

REPORT DOCUMENTATION PAGE

Form Approved OMB No. 0704-0188

Public reporting burden for this collection of information is estimated to average 1 hour per response, including the time for reviewing instructions, searching existing data sources, gathering and maintaining the data needed, and completing and reviewing the collection of information. Send comments regarding this burden estimate or any other aspect of this collection of information, including suggestions for reducing this burden to Washington Headquarters Services, Directorate for Information Operations and Reports, 1215 Jefferson Davis Highway, Suite 1204, Arlington, VA 22202-4302, and to the Office of Management and Budget, Paperwork Reduction Project (0704-0188), Washington, DC 20503.

1. AGENCY USE ONLY (Leave blank)		2. REPORT DATE 1994		3. REPORT TYPE AND DATES COVERED Final Report	
4. TITLE AND SUBTITLE XVI International Symposium on Discharges and Electrical Insulation in Vacuum				5. FUNDING NUMBERS F6170894W0503	
6. AUTHOR(S) Gennady A. Mesyats					
7. PERFORMING ORGANIZATION NAME(S) AND ADDRESS(ES) University of South Carolina 901 Sumner Street Columbia, South Carolina				8. PERFORMING ORGANIZATION REPORT NUMBER N/A	
9. SPONSORING/MONITORING AGENCY NAME(S) AND ADDRESS(ES) EOARD PSC 802 BOX 14 FPO 09499-0200				10. SPONSORING/MONITORING AGENCY REPORT NUMBER CSP-94-1015	
11. SUPPLEMENTARY NOTES					
12a. DISTRIBUTION/AVAILABILITY STATEMENT Copying of material in this book for internal use or personal use or for the internal or personal use of specific clients, beyond the fair use provisions granted by U.S. Copyright Law is authorized by SPIE subject to payment of copying fees. Other copying or any form of reproduction is prohibited except with permission in writing from the publisher.				12b. DISTRIBUTION CODE	
13. ABSTRACT (Maximum 200 words) The International Society for Optical Engineering (SPIE) Conference Proceedings for the XVI International Symposium on Discharges and Electrical Insulation in Vacuum held 23-30 May 1994 , Moscow - St Petersburg, Russia.					
14. SUBJECT TERMS				15. NUMBER OF PAGES 638	
				16. PRICE CODE	
17. SECURITY CLASSIFICATION OF REPORT UNCLASSIFIED	18. SECURITY CLASSIFICATION OF THIS PAGE UNCLASSIFIED	19. SECURITY CLASSIFICATION OF ABSTRACT UNCLASSIFIED	20. LIMITATION OF ABSTRACT UL		

NSN 7540-01-280-5500

Standard Form 298 (Rev. 2-89)
Prescribed by ANSI Std. Z39-18
298-102

PROCEEDINGS



SPIE—The International Society for Optical Engineering

XVI International Symposium on

Discharges and Electrical Insulation in Vacuum

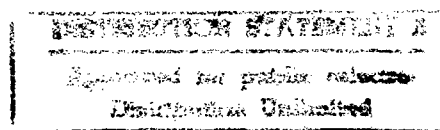
Gennady A. Mesyats
Chair/Editor

23–30 May 1994
Moscow–St. Petersburg, Russia



ISDEIV

Sponsored by
SPIE—The International Society for Optical Engineering

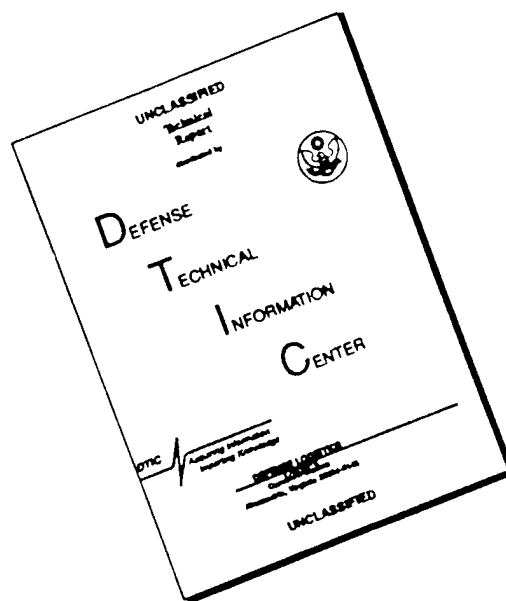


19970113 017



Volume 2259

DISCLAIMER NOTICE



THIS DOCUMENT IS BEST QUALITY AVAILABLE. THE COPY FURNISHED TO DTIC CONTAINED A SIGNIFICANT NUMBER OF PAGES WHICH DO NOT REPRODUCE LEGIBLY.



SPIE—The International Society for Optical Engineering

PROCEEDINGS

XVI International Symposium on

Discharges and Electrical Insulation in Vacuum

Gennady A. Mesyats

Chair/Editor

23–30 May 1994

Moscow–St. Petersburg, Russia

Sponsored by

SPIE—The International Society for Optical Engineering

In Cooperation with

IEEE Dielectric and Electrical Insulation Society—DEIS

Supported by

Russian Science Foundation

Russian Ministry of Science

Russian Academy of Science

Ural Branch, Russian Academy of Science

Institute of Electrophysics, Ural Branch, Russian Academy of Science

European Office of Aerospace Research and Development—EOARD

Pulsed Power Sciences, Sandia National Laboratories (USA)

The William and Mary Greve Foundation, Inc. (USA)

University of New Mexico, Albuquerque (USA)



Volume 2259

SPIE (The Society of Photo-Optical Instrumentation Engineers) is a nonprofit society dedicated to the advancement of optical and optoelectronic applied science and technology.



The papers appearing herein comprise the proceedings of the meeting mentioned on the cover and title page. SPIE has published this proceedings on behalf of the conference organizers and sponsors. The contents of this volume have been determined by the organizers and editors and reflect the authors' opinions, published as submitted and without change. Their inclusion in this publication does not necessarily constitute endorsement by the publisher (SPIE).

Please use the following format to cite material from this book:

Author(s), "Title of paper," in *XVI International Symposium on Discharges and Electrical Insulation in Vacuum*, Gennady A. Mesyats, Editor, Proc. SPIE 2259, page numbers (1994).

Library of Congress Catalog Card No. 94-66132
ISBN 0-8194-1581-2

Published by
SPIE—The International Society for Optical Engineering
P.O. Box 10, Bellingham, Washington 98227-1101 USA
Telephone 206/676-3290 (Pacific Time) • Fax 206/647-1445

Copyright ©1994, The Society of Photo-Optical Instrumentation Engineers.

Copying of material in this book for internal or personal use, or for the internal or personal use of specific clients, beyond the fair use provisions granted by the U.S. Copyright Law is authorized by SPIE subject to payment of copying fees. The Transactional Reporting Service base fee for this volume is \$6.00 per article (or portion thereof), which should be paid directly to the Copyright Clearance Center (CCC), 222 Rosewood Drive, Danvers, MA 01923. Other copying for republication, resale, advertising or promotion, or any form of systematic or multiple reproduction of any material in this book is prohibited except with permission in writing from the publisher. The CCC fee code is 0-8194-1581-2/94/\$6.00.

Printed in the United States of America.

Contents

xv	Conference Committee
xvii	Preface
xix	Dyke Award
xx	Chatterton Young Investigator Award

SESSION 1 VACUUM BREAKDOWN AND PREBREAKDOWN PHENOMENA

2	Electrohydrodynamic phenomena on an explosive-emission liquid-metal cathode [2259-03] L. M. Baskin, Institute of Telecommunications (Russia); A. V. Batrakov, S. A. Popov, D. I. Proskurovsky, Institute of High-Current Electronics (Russia)
6	Measurements of current intensities from 10^{-18} A to 10^{-6} A emitted from niobium samples under high dc electric fields [2259-04] M. Boussoukaya, A. Curtoni, A. Zeitoun-Fakiris, Ctr. d'Etudes de Saclay/CEA (France)
10	High-speed imaging of explosive exoemission from an alumina ceramic in vacuum [2259-05] B. M. Coaker, N. S. Xu, Aston Univ. (UK); F. J. Jones, EEV Ltd. (UK); R. V. Latham, Aston Univ. (UK)
14	Discharge in commercial vacuum at high voltage [2259-06] G. M. Kassirov, F. G. Sekisov, V. N. Chekrygin, Tomsk Polytechnical Univ. (Russia)
17	Vacuum-breakdown properties of oxygen-free copper electrodes machined by diamond turning for mirror finish [2259-08] S. Kobayashi, Y. Hashimoto, Saitama Univ. (Japan); Y. Saito, National Lab. for High Energy Physics (Japan); Y. Nagai, Y. Yamamoto, Hitachi Cable, Ltd. (Japan); K. Takeuchi, T. Sugano, Mechanical Engineering Lab. (Japan)
21	Carbon coatings to increase electric strength of vacuum gap [2259-09] L. V. Loginov, A. S. Pokrovskaya-Soboleva, All-Russian Electrotechnical Institute (Russia)
25	Properties of ectons in a vacuum discharge [2259-10] G. A. Mesyats, Institute of Electrophysics (Russia)
30	Non-self-maintained discharge in vacuum [2259-11] M. M. Nikitin, Institute of Electrophysics (Russia)
35	Influence of electrode area on conditioning in vacuum-gap breakdown [2259-12] T. Shioiri, T. Kamikawaji, E. Kaneko, M. Homma, I. Ohshima, Toshiba Corp. (Japan)
39	Pulsed electric discharge in vacuum diodes with electrodes made of low- and high-temperature superconductors [2259-13] S. I. Shkuratov, Institute of Electrophysics (Russia)
45	Another cause of vacuum insulation electrical strength decrease following the bakeout of metal-insulation electrode system [2259-14] N. V. Tatarinova, Moscow Physical Engineering Institute (Russia)

- 49 **Total voltage effect and electrode porosity** [2259-15]
N. V. Tatarinova, Moscow Physical Engineering Institute (Russia); Yu. V. Grigoriev, All-Russian Electrotechnical Institute (Russia)
- 53 **Emission processes arising during a pulse discharge in solid dielectrics** [2259-16]
Y. N. Vershinin, A. A. Podrezov, S. V. Barahvostov, Institute of Electrophysics (Russia)
- 58 **Discharge initiation system in electrothermal launcher** [2259-17]
A. V. Chebotarev, I. L. Kolensky, Ju. A. Kulikov, A. V. Melnik, E. Ja. Shcolnikov, Moscow Engineering Physics Institute (Russia)
- 60 **Real-time optical study of dc and pulsed-field breakdown events in high-voltage vacuum-insulated gaps** [2259-18]
N. S. Xu, R. V. Latham, Aston Univ. (UK)
- 64 **Influence of prebreakdown currents on the electric strength of vacuum gaps at large electrode areas** [2259-180]
N. N. Koval, Yu. D. Korolev, P. M. Shchanin, Institute of High Current Electronics (Russia)

SESSION 2 VACUUM ARCS

- 70 **Dependence of nonstationary behavior of arc cathode spots on discharge duration (Invited Paper)** [2259-19]
B. Jüttner, W. Löffler, C. Weber, G. Ziegenhagen, Max-Planck-Institut für Plasmaphysik (FRG)
- 76 **Influence of current instabilities on the parameters of the vacuum arc plasma jet** [2259-21]
B. Alterkop, I. Beilis, R. L. Boxman, S. Goldsmith, Tel Aviv Univ. (Israel)
- 82 **Physical model of low-current density vacuum arc** [2259-22]
A. V. Bolotov, A. V. Kozyrev, Yu. D. Korolev, High Current Electronics Institute (Russia)
- 86 **Arcing and breakdown in near-electrode plasma** [2259-24]
D. P. Borisov, N. N. Koval, P. M. Shchanin, Institute of High Current Electronics (Russia)
- 90 **Filtered vacuum arc deposition of semiconductor thin films** [2259-25]
R. L. Boxman, S. Goldsmith, A. Ben-Shalom, L. Kaplan, D. Arbilly, E. Gidalevich, V. Zhitomirsky, A. Ishaya, M. Keidar, I. Beilis, Tel Aviv Univ. (Israel)
- 96 **Criterion for type-2 spot originating under pulse-discharge conditions** [2259-26]
A. I. Bushik, I. A. Bakuto, P. S. Zachepilo, V. A. Shilov, Physical-Technical Institute (Belarus)
- 100 **Emission and arc studies of contacts with metal-oxide inclusions** [2259-27]
A. M. Chalyi, V. A. Nevrovsky, ANTECH Ltd. (Russia)
- 105 **Electrode geometry and material effects on cathode-spot dynamics in a high-current vacuum arc** [2259-29]
A. M. Chaly, Tavrida Electric LTD (Russia); A. A. Logatchev, S. M. Shkol'nik, A.F. Ioffe Physical-Technical Institute (Russia)
- 109 **Sheath model of negatively biased substrate in vacuum arcs with cathode spots** [2259-30]
Z. Cheng, J. Zou, Huazhong Univ. of Science and Technology (China)

- 114 **Two-dimensional MHD model of the plasma jet originating from a vacuum-arc cathode spot** [2259-32]
V. N. Gavrilov, E. A. Litvinov, G. A. Mesyats, D. L. Shmelev, Institute of Electrophysics (Russia)
- 118 **Investigation of striking characteristics of a pulsed low-pressure discharge in magnetic field** [2259-33]
N. V. Gavrilov, S. P. Nikulin, Institute of Electrophysics (Russia)
- 122 **Vacuum-arc plasma-beam motion in curved magnetic fields** [2259-34]
E. Gidalevich, S. Goldsmith, R. L. Boxman, Tel Aviv Univ. (Israel)
- 128 **Approaches to two-dimensional models of expanding vacuum-arc plasmas** [2259-35]
E. Hantzsche, Max-Planck-Institut für Plasmaphysik (FRG)
- 132 **Appearance of vacuum-arc cathode spots imaged by emitted light** [2259-36]
E. Hantzsche, B. Jüttner, Max-Planck-Institut fuer Plasmaphysik (FRG)
- 136 **Experimental research on a high-voltage low-current vacuum arc** [2259-37]
R. Yu. Ivanov, S. V. Puzanov, Yu. M. Yashnov, Titan Scientific-Research Institute (Russia)
- 140 **Nonstationary macroparticle charging in arc plasma jet** [2259-39]
M. Keidar, I. Beilis, R. L. Boxman, S. Goldsmith, Tel Aviv Univ. (Israel)
- 146 **Modeling non-steady-state processes at the electrode and in the electrode regions of pseudospark devices** [2259-40]
I. V. Kozlov, E. A. Litvinov, E. Yu. Sadovskaya, Institute of Electrophysics (Russia)
- 149 **High-current vacuum-arc discharge with gas-filled electrodes** [2259-41]
A. A. Logatchev, S. M. Shkol'nik, A.F. Ioffe Physical-Technical Institute (Russia)
- 153 **Numerical simulation of the high-current vacuum arc** [2259-42]
M. T. Glinkowski, A. Greenwood, P. Stoving, Rensselaer Polytechnic Institute (USA)
- 160 **Boundary conditions and solution stability in dynamics of cathode spots in vacuum arcs** [2259-44]
A. Z. Nemirovskii, A. A. Emelianov, Institute of Electrophysics (Russia)
- 164 **Experimental and theoretical study of the temperature of a hot-anode vacuum arc** [2259-46]
H. Rosenthal, I. Beilis, S. Goldsmith, R. L. Boxman, Tel Aviv Univ. (Israel)
- 170 **Ion potential distribution of high-current arcs in vacuum** [2259-47]
C. Rusteberg, M. Lindmayer, Institut für Elektrische Energieanlagen (FRG); B. Jüttner, H. Pursch, Max-Planck-Institut für Plasmaphysik (FRG)
- 179 **Behavior of vacuum arcs between spiral contacts with reduced spacing** [2259-48]
M. B. Schulman, Cutler-Hammer (USA)
- 183 **Interrupting abilities of vacuum interrupters with horseshoe electrode** [2259-49]
W. Shang, H. Schellekens, HOLEC Syst. & Comp. B.V. (Netherlands)
- 187 **Moving characteristics of electrodes for vacuum circuit breaker** [2259-50]
S. Yuan, Northeastern Electric Power Test and Research Institute (China); J. Wang, Xi'an Jiaotong Univ. (China)

- 191 **Microscopical high-speed investigations of vacuum-arc cathode spots** [2259-51]
P. Siemroth, T. Schülke, T. Witke, Fraunhofer Institute for Materials Physics and Surface Engineering (FRG)
- 195 **Vacuum-arc plasma deposition: macroparticle filtering, scaling, and other problems** [2259-52]
A. Anders, S. Anders, I. G. Brown, R. A. MacGill, M. R. Dickinson, Lawrence Berkeley Lab. (USA)
- 199 **Calculation of plasma MHD flow in vacuum spark discharge** [2259-53]
V. A. Skvortsov, A. Yu. Krukovsky, A. A. Otochin, High Energy Density Research Ctr. (Russia)
- 203 **HF-reignition phenomena related to post-arc current in vacuum interrupters** [2259-54]
R. P. P. Smeets, Eindhoven Univ. of Technology (Netherlands); H. Li, Xi'an Jiaotong Univ. (China); N. J. G. Lamerichs, Eindhoven Univ. of Technology (Netherlands); E. Kaneko, Toshiba Corp. (Japan)
- 207 **Measurement of cathode-spot parameters with pulsed-laser diagnostics** [2259-55]
N. Vogel, J. Heinzinger, F. Cichos, Univ. of Technology Chemnitz-Zwickau (FRG)
- 211 **Calculation of film-thickness distribution provided by vacuum-arc deposition** [2259-56]
H. Wang, J. Zou, L. Yang, L. Cheng, Huazhong Univ. of Science and Technology (China); H. Yang, Hunan Univ. (China)
- 215 **Characterization of the cathode spot in vacuum-arc deposition** [2259-57]
H. Wang, J. Zou, M. Li, L. Cheng, Huazhong Univ. of Science and Technology (China); H. Yang, Hunan Univ. (China)
- 219 **Currents collected at the metal shield in high-current vacuum arcs** [2259-59]
Z. Załucki, J. Kutzner, Z. Boruta, Technical Univ. of Poznań (Poland)
- 224 **Number of half-cycles of HF vacuum arc** [2259-176]
H. Q. Li, Xi'an Jiaotong Univ. (China); R. P. P. Smeets, Eindhoven Univ. of Technology (Netherlands)

SESSION 3 SWITCHING IN VACUUM

- 232 **Electron tubes for industrial applications (Invited Paper)** [2259-61]
B. Gellert, Thomson Elektronenröhren AG (Switzerland)
- 239 **Phases of vacuum and plasma discharges and control of their parameters** [2259-62]
E. N. Abdullin, High Current Electronics Institute (Russia); G. P. Bazhenov, Institute of Electrophysics (Russia); S. M. Chesnokov, G. P. Erokhin, V. V. Kiselev, O. B. Ladyzhensky, High Current Electronics Institute (Russia)
- 243 **Triggered vacuum interrupter with a switching accuracy up to microsecond units** [2259-63]
D. F. Alferov, V. A. Sidorov, V. A. Vozdvijenskii, All-Russian Electrotechnical Institute (Russia)
- 247 **Switching characteristics of the submicrosecond triggered vacuum switch** [2259-64]
D. F. Alferov, V. A. Sidorov, V. A. Vozdvijenskii, All-Russian Electrotechnical Institute (Russia)
- 251 **Repetitive generators based on the plasma opening switch** [2259-65]
N. U. Barinov, G. S. Belenki, G. I. Dolgachev, Yu. I. Kovalev, L. P. Zakatov, A. G. Ushakov, Kurchatov Institute (Russia)

- 254 **Mega-ampere nanosecond current switching from external unstable light liner to inner load in vacuum on Angara-5-1** [2259-66]
A. N. Batunin, A. V. Branitsky, I. N. Frolov, E. V. Grabovsky, D. V. Kuznetsov, A. G. Lisitsyn, S. F. Medovschikov, V. O. Mishensky, S. L. Nedoseev, G. M. Olejnik, Troitsk Institute of Innovation and Thermonuclear Investigations (Russia); P. V. Sasorov, Institute of Theoretical and Experimental Physics (Russia); V. P. Smirnov, A. N. Starostin, S. V. Trofimov, G. S. Volkov, E. G. Utjugov, S. V. Zakharov, M. V. Zurin, Troitsk Institute of Innovation and Thermonuclear Investigations (Russia)
- 258 **High-current electron switch with deep compensation of volume charge** [2259-67]
A. B. Bogoslovskaya, K. N. Ulyanov, All-Russian Electrotechnical Institute (Russia)
- 262 **Simulation of the MAG II generator** [2259-68]
V. Bulan, V. V. Zajivikhin, Troitsk Institute of Innovation and Thermonuclear Investigations (Russia); B. Etlicher, Ecole Polytechnique Palaiseau (France)
- 266 **Vacuum-state estimation of vacuum circuit breakers** [2259-69]
G. C. Damstra, N.V. KEMA and Eindhoven Univ. of Technology (Netherlands); R. P. P. Smeets, H. B. F. Poulussen, Eindhoven Univ. of Technology (Netherlands)
- 270 **Series resonance inverter with triggered vacuum gaps** [2259-70]
G. C. Damstra, N.V. KEMA and Eindhoven Univ. of Technology (Netherlands); X. Zhang, Qinghua Univ. (China)
- 273 **Electrical characteristics of pseudospark discharge** [2259-71]
G. Bauville, A. Delmas, Paris VI and Paris XI Univ. (France)
- 277 **Mass erosion and surface-voltage holdoff recovery of insulators used in a high-current high vacuum surface discharge switch** [2259-72]
T. G. Engel, S. L. Wester, M. Kristiansen, L. L. Hatfield, Texas Tech Univ. (USA)
- 283 **Energy concentration in Z-pinch experiments** [2259-73]
E. M. Gordeev, V. D. Korolev, V. I. Liksonov, V. V. Zazhivikhin, I.V. Kurchatov Institute (Russia)
- 287 **100-kA vacuum current breaker of a modular design** [2259-74]
V. P. Ivanov, V. A. Vozdvijenskii, All-Russian Electrotechnical Institute (Russia); V. A. Jagnov, S. G. Solodovnikov, A. V. Mazulin, Troitsk Institute of Innovation and Thermonuclear Research (Russia); V. M. Ryjkov, Moscow Engineering-Physical Institute (Russia)
- 291 **Strengthened magnetic-field contacts for vacuum interrupters** [2259-75]
A. A. Pertsev, L. A. Rylskaya, All-Russian Electrotechnical Institute (Russia); S. P. Chistyakov, NPP ELVEST (Russia)
- 295 **Dynamic test and analysis of shield potential in vacuum interrupters** [2259-78]
C. Wang, Xi'an High Voltage Apparatus Research Institute (China); J. Wang, Z. Ma, Xi'an Jiaotong Univ. (China)
- 301 **Post-arcing recovery characteristics of vacuum interrupters under a high-rising rate of recovery voltage** [2259-79]
C. Wang, Xi'an High Voltage Apparatus Research Institute (China); J. Wang, Xi'an Jiaotong Univ. (China)
- 304 **Nonstability of post-arcing recovery process in vacuum interrupters** [2259-80]
C. Wang, Xi'an High Voltage Apparatus Research Institute (China); Z. Ma, J. Wang, Xi'an Jiaotong Univ. (China)

- 308 **Experimental investigation on the ion-diffusion performance in vacuum interrupter by multichannel array probe** [2259-82]
J. Wu, Xi'an Jiaotong Univ. (China); S. Yuan, Northern Electric Power Test and Research Institute (China); Y. Wang, Dalian Univ. of Technology (China); J. Wang, Xi'an Jiaotong Univ. (China)
- 312 **Dynamic insulation in vacuum interrupters** [2259-83]
J. Zou, J. He, L. Cheng, Huazhong Univ. of Science and Technology (China)
- 317 **Effect of a prebreakdown current on the hold-off voltage and discharge initiation in the pseudospark switches** [2259-179]
V. D. Bochkov, A. V. Kolesnikov, Yu. D. Korolev, V. G. Rabotkin, O. B. Frantz, I. A. Shemyakin, High Current Electronics Institute (Russia)
- 321 **Anode melting and evaporation in vacuum interrupters** [2259-181]
V. A. Nevrovsky, ANTECH Ltd. (Russia); A. A. Pertsev, L. A. Rylskaya, All-Russian Electrotechnical Institute (Russia)

SESSION 4 SURFACE FLASHOVER

- 328 **Inhomogeneous charging characteristics of polycrystalline alumina surfaces** [2259-85]
T. Asokan, T. S. Sudarshan, Univ. of South Carolina (USA)
- 332 **Surface charging and flashover of insulators in vacuum** [2259-86]
I. D. Chalmers, J. H. Lei, B. Yang, Univ. of Strathclyde (UK)
- 336 **Surface flashover sensitivity of silicon in vacuum** [2259-87]
G. Gradinaru, G. Korony, T. S. Sudarshan, Univ. of South Carolina (USA)
- 340 **Microwave surface flashover of dielectrics in vacuum** [2259-88]
A. A. Ravaev, E. A. Galstjan, Moscow Radiotechnical Institute (Russia)
- 344 **Influence of dielectric surface properties on the generation of surface microplasmas** [2259-89]
T. S. Sudarshan, C. R. Li, Univ. of South Carolina (USA)
- 348 **New method for characterization of the space charge in insulators** [2259-91]
B. Vallayer, S. Fayeulle, Ecole Centrale de Lyon (France); C. Le Gressus, CEA-DAM (France); G. Blaise, Univ. Paris-Sud (France); D. Treheux, Ecole Centrale de Lyon (France)
- 354 **Temporal behavior of electric field at triple junction and its relation to flashover of bridged vacuum gaps** [2259-92]
O. Yamamoto, T. Hara, H. Matsuura, M. Hayashi, Kyoto Univ. (Japan); K. Yukimura, Doshisha Univ. (Japan)

SESSION 5 VACUUM INSULATION (MAGNETIC INSULATION, ACCELERATORS, ETC.)

- 360 **Effect of pulsed electron-beam treatment of electrodes on the electric strength of the vacuum insulation** [2259-94]
A. V. Batrakov, A. B. Markov, G. E. Ozur, D. I. Proskurovsky, V. P. Rotshtein, Institute of High-Current Electronics (Russia)

- 364 **Influence of in-situ ion-beam sputter cleaning on the conditioning effect of vacuum gaps**
[2259-98]
S. Kobayashi, H. Kojima, Saitama Univ. (Japan); Y. Saito, National Lab. for High Energy Physics (Japan)
- 368 **Estimation of vacuum-insulation degradation after long-lasting nonvoltage state of the system**
[2259-99]
K. Siodła, Technical Univ. of Poznań (Poland)
- 372 **Image-processing analysis of discharge phenomena under nonuniform electric field in vacuum**
[2259-100]
H. Okubo, M. Fujimori, S. Yuasa, N. Hayakawa, M. Hikita, Nagoya Univ. (Japan)
- 378 **Influence of cobalt-molybdenum-alloy coating on the surface of copper electrodes upon electric strength of unconditioned vacuum-insulation systems** [2259-101]
W. Opydo, J. Miła, R. Batura, J. Opydo, Technical Univ. of Poznań (Poland)
- 382 **High-voltage design of vacuum components** [2259-102]
J. M. Wetzter, P. A. Wouters, Eindhoven Univ. of Technology (Netherlands)
- 386 **Electrical insulation problem in quasi-stationary high-current relativistic e-beam injectors**
[2259-103]
M. A. Zavjalov, V. I. Perevodchikov, All-Russian Electrotechnical Institute (Russia)

SESSION 6 HIGH-CURRENT DIODES AND INTENSE PARTICLE BEAMS

- 392 **Generation and transformation of 0.4-MJ ribbon beam with the U-2 device** [2259-104]
A. V. Arzhannikov, V. B. Bobylev, V. S. Nikolaev, S. L. Sinitsky, A. V. Tarasov, Budker Institute of Nuclear Physics (Russia)
- 396 **Relativistic electron-beam generation in plasma-filled diode and foilless injection into dense plasma** [2259-107]
V. S. Burmasov, I. V. Kandaurov, E. P. Kruglyakov, O. I. Meshkov, Budker Institute of Nuclear Physics (Russia)
- 399 **High-current annular electron- and ion-beam sources based on magnetron discharge in the $E \times H$ fields** [2259-108]
A. A. Chagin, E. M. Oks, P. M. Schanin, Institute of High Current Electronics (Russia)
- 403 **Electron-beam focusing and unfocusing experiments** [2259-109]
A. L. Filatov, Y. A. Kotov, V. A. Motovilov, V. A. Scotnikov, Institute of Electrophysics (Russia)
- 409 **Investigation of an ion-optical system of technological ion-gas source** [2259-110]
N. V. Gavrilov, Institute of Electrophysics (Russia); O. M. Ivanov, A. F. Stekolnikov, Byelorussian State Univ. of Information and Radioelectronics (Belarus)
- 412 **Intensive ion beams in the transverse magnetic field of an electromagnetic separator**
[2259-111]
A. Goncharov, N. Datsko, I. Soloshenko, Institute of Physics (Ukraine)
- 416 **Formation of an electron beam in its squeezed state** [2259-113]
A. M. Ignatov, V. P. Tarakanov, General Physics Institute (Russia)

- 419 **Physics of electron emission from ferroelectric cathodes** [2259-118]
G. A. Mesyats, Institute of Electrophysics (Russia)
- 423 **E-beam behavior accelerated by short-time high-voltage pulses** [2259-119]
V. V. Osipov, V. M. Orlovsky, V. I. Solomonov, Institute of Electrophysics (Russia)
- 427 **Compact high-current ribbon e-beam diode** [2259-121]
V. G. Shpak, M. I. Yalandin, S. A. Shunailov, Institute of Electrophysics (Russia)
- 431 **Current addition by MITL in vacuum** [2259-122]
E. V. Grabovsky, S. L. Nedoseev, V. E. Pichugin, V. P. Smirnov, V. V. Zajivikhin, G. M. Olejnik, Troitsk Institute of Innovation and Thermonuclear Investigations (Russia)
- 435 **Experiments on microsecond electron-beam generation in a plasma-filled diode** [2259-123]
S. V. Lebedev, M. A. Shcheglov, S. G. Voropaev, Institute of Nuclear Physics (Russia)
- 439 **Powerful wideband amplifier based on hybrid plasma-cavity slow-wave structure** [2259-124]
M. A. Zavjalov, L. A. Mitin, V. I. Perevodchikov, V. N. Tskhai, A. L. Shapiro, All-Russian Electrotechnical Institute (Russia)

SESSION 7 DISCHARGE IN THE SPACE ENVIRONMENT

- 444 **Vacuum-chamber simulation of high-voltage breakdown in space** [2259-126]
A. C. Logue, L. B. Gordon, Univ. of Texas/Arlington (USA)
- 448 **Mechanics and physics of swift dust-particle impact** [2259-127]
N. A. Inogamov, S. I. Anisimov, Landau Institute for Theoretical Physics (Russia)
- 452 **Phenomena of fault-arc propagation on cables and wires for space applications in vacuum and oxygen-enriched atmosphere and air** [2259-129]
F. R. Frontzek, D. König, Technical Univ. of Darmstadt (FRG); M. D. Judd, ESA/ESTEC (Netherlands); H. J. Reher, DASA-ERNO (FRG)
- 459 **Vacuum insulation on the moon** [2259-131]
L. B. Gordon, Univ. of Texas/Arlington (USA); K. L. Gaustad, Battelle Memorial Institute/Pacific Northwest Lab. (USA)

SESSION 8 EMISSION PROCESSES

- 464 **Thin superconducting films at field emission** [2259-133]
S. A. Barenholts, E. A. Litvinov, I. V. Uimanov, Institute of Electrophysics (Russia)
- 469 **Field emission from nanometer protuberances at high current densities** [2259-134]
G. N. Fursey, D. V. Glazanov, S. A. Polezhaev, St. Petersburg Bonch-Bruевич Telecommunications Univ. (Russia)
- 473 **Dynamic processes on a surface of iridium field emitters produced by the actions of high temperature and electric field** [2259-135]
O. L. Golubev, V. N. Shrednik, A.F. Ioffe Physical-Technical Institute (Russia)
- 477 **Design of field electron emission spectrometer, field ion microscope, and field electron emission microscope combination** [2259-136]
S. N. Ivanov, S. N. Shilimanov, S. I. Shkuratov, Institute of Electrophysics (Russia)

- 479 **Effect of emitter surface structure on field-ionization and electron-emission processes** [2259-137]
V. A. Ivchenko, N. N. Syutkin, Institute of Electrophysics (Russia)
- 483 **Liquid-metal surface under the artificial stimulation of microcapillary waves** [2259-138]
A. L. Kovalev, L. M. Baskin, G. N. Fursey, L. A. Shirochin, St. Petersburg Bonch-Bruевич Telecommunications Univ. (Russia)
- 486 **Experimental determination of work function of silver alloys** [2259-139]
A. Lefort, M. Akbi, M. Parizet, Univ. Blaise Pascal (France)
- 491 **Emission of a liquid metal interface in vacuum** [2259-140]
G. Neron de Surgy, J. P. Chabrierie, Lab. de Genie Electrique de Paris (France); J. E. Wesfreid, Lab. d'Hydrodynamique et Mecanique Physique (France)
- 497 **Field evaporation of HTS materials as a nonequilibrium process** [2259-141]
V. N. Shrednik, A.F. Ioffe Physical-Technical Institute (Russia)
- 501 **Thermionic emission investigation of materials for directly heated cathodes of electron tubes** [2259-177]
B. Gellert, W. Rohrbach, Thomson Elektronenrohren AG (Switzerland)

SESSION 9 HIGH-POWER MICROWAVES

- 506 **High-power microwave Cherenkov oscillators with high-current relativistic electron beams (Invited Paper)** [2259-142]
S. D. Korovin, S. D. Polevin, I. V. Pegel, V. V. Rostov, A. M. Roytman, Institute of High Current Electronics (Russia); V. L. Bratman, G. G. Denisov, A. V. Smorgonsky, Institute of Applied Physics (Russia)
- 512 **Surface breakdown phenomena in alumina rf windows (Invited Paper)** [2259-143]
Y. Saito, National Lab. for High Energy Physics (Japan)
- 518 **Prebunched-beam free electron maser** [2259-145]
M. Arbel, D. Ben-Chaim, M. Cohen, M. Draznin, A. Eichenbaum, A. Gover, H. Kleinman, A. Kugel, Y. Pinhasi, S. Witman, Y. Yakover, Tel Aviv Univ. (Israel)
- 522 **Experiments with an S-band vircator** [2259-146]
D. E. T. F. Ashby, J. Allen, K. C. Hawkins, AEA Technology (UK)
- 526 **Comparison between experiment and computer modeling for simple MILO configurations** [2259-147]
D. E. T. F. Ashby, J. Allen, J. W. Eastwood, K. C. Hawkins, L. M. Lea, AEA Technology (UK)
- 530 **Excitation of UHF oscillations in a magnetically insulated slow-wave line** [2259-148]
V. A. Balakirev, D. Yu. Sidorenko, G. V. Sotnikov, Yu. V. Tkach, Kharkov Institute of Physics and Technology (Ukraine)
- 534 **Near-surface secondary emission vacuum HF discharge in magnetic insulation conditions** [2259-149]
L. G. Blyachman, V. E. Nechaev, Institute of Applied Physics (Russia)

- 538 **Relativistic pulse-periodic mm-wavelength cyclotron masers with hot cathodes** [2259-150]
V. L. Bratman, I. E. Botvinnik, Yu. V. Grom, Yu. K. Kalynov, M. M. Ofitserov, Institute of Applied Physics (Russia)
- 542 **Interaction of REB with electromagnetic field in overmoded slow-wave structures near the high-frequency boundary of the transmission band** [2259-151]
I. A. Chernyavsky, M. P. Deichuly, V. I. Koshelev, High Current Electronics Institute (Russia); V. M. Pikunov, Moscow State Univ. (Russia)
- 546 **Superradiance of ensembles of classical electron oscillators as a method for generation of ultrashort electromagnetic pulses** [2259-153]
N. S. Ginzburg, Yu. V. Novozhilova, A. S. Sergeev, Institute of Applied Physics (Russia)
- 550 **Use of two-dimensional distributed feedback for synchronization of radiation of powerful sheet and tubular relativistic electron beams** [2259-154]
N. S. Ginzburg, N. Yu. Peskov, A. S. Sergeev, Institute of Applied Physics (Russia)
- 554 **Nonlinear processes in relativistic Cerenkov microwave resonance sources** [2259-155]
V. I. Kanavets, A. S. Nifanov, A. I. Slepikov, I. G. Bakharev, Moscow State Univ. (Russia)
- 557 **Powerful microwave oscillator of microsecond pulse duration driven by relativistic electron beam** [2259-157]
O. T. Loza, P. S. Strelkov, General Physics Institute (Russia)
- 561 **Investigation of TW output circuit for relativistic klystrons** [2259-158]
D. V. Fedyaev, V. M. Pikunov, A. N. Sandalov, Moscow State Univ. (Russia)
- 565 **Measurement of spectrum and power of microwave radiation from relativistic plasma microwave oscillator** [2259-159]
A. G. Shkvarunets, D. K. Ulyanov, General Physics Institute (Russia)
- 569 **Multiwave interaction in high-current microwave devices** [2259-160]
A. N. Vlasov, Moscow State Univ. (Russia); V. A. Cherepenin, Institute of Radioengineering and Electronics (Russia)
- 573 **400-kV 400-A microsecond electron accelerator with a hot cathode** [2259-161]
N. I. Zaitsev, E. V. Ilyakov, G. S. Korablyov, I. S. Kulagin, Institute of Applied Physics (Russia)
- 577 **Radio-frequency interference generated by a high-voltage system with vacuum insulation** [2259-162]
W. Ziomek, H. Mościcka-Grzesiak, Technical Univ. of Poznań (Poland)

SESSION 10 COMMERCIAL APPLICATION AND OPPORTUNITIES

- 582 **Microwave amplifier based on a compact high-voltage modulator** [2259-165]
E. B. Abubakirov, M. I. Fuchs, N. F. Kovalev, N. I. Zaytsev, Institute of Applied Physics (Russia); J. P. Brasil, G. Jean-Francois, M. Simon, Thomson-Shorts-Systemes (France)
- 586 **Pseudospark switches for high-power applications** [2259-166]
A. Görtler, J. Christiansen, S. Döllinger, K. H. Frank, U. Herleb, S. Insam, T. Mehr, M. Schlaug, A. Schwandner, R. Tkotz, Univ. of Erlangen-Nuremberg (FRG)

- 590 **Unsteady shock-wave propagation from an electrical foil explosion** [2259-167]
N. G. Karlykhanov, S. V. Dem'yanovskiy, I. V. Glazyrin, A. A. Kondrat'ev, Y. A. Kucherenko, A. T. Litvin, A. V. Pavlenko, M. S. Timakova, A. D. Zoubov, All-Russian Scientific Research Institute of Technical Physics (Russia)
- 594 **Alternating current investigations of the insulation of HV equipment in theory and practice with a new PD-measuring method** [2259-168]
E. Keil, Bundesforschungs- und Prüfzentrum Arsenal (Austria)
- 598 **Compact PC-controlled tester of electric strength** [2259-169]
V. D. Okunev, Moscow Institute of Radio-Electronics & Automatics (Russia); V. I. Pozdnyakov, S. V. Puzanov, Y. M. Yashnov, Titan Scientific-Research Institute (Russia)
- 601 **Designing field-emission devices to avoid impedance collapse** [2259-170]
R. Olson, California State Univ./Northridge (USA)
- 605 **Self-propagating phase transformations in metastable media induced by ion bombardment** [2259-171]
V. V. Ovchinnikov, Institute of Electrophysics (Russia)
- 609 **Plasma flare of pulsed-microwave surface discharge in vacuum for thin film deposition and materials processing** [2259-172]
A. A. Ravaev, A. V. Medvedovsky, P. S. Chernyshev, Moscow Radiotechnical Institute (Russia)
- 613 **Ion-beam surface treatment: a new capability for rapid melt and resolidification of surfaces** [2259-173]
R. W. Stinnett, D. C. McIntyre, R. G. Buchheit, Sandia National Labs. (USA); J. B. Greenly, M. O. Thompson, Cornell Univ. (USA)
- 619 **Atomic structure and phase state of quenched FePd₂Au alloy after bombardment by Ar⁺ ions** [2259-174]
E. F. Talantsev, N. N. Syutkin, V. V. Ovchinnikov, V. I. Chernoborodov, Institute of Electrophysics (Russia)
- 623 **Composite plastic coatings and face rolled materials technology, energy- and environment-saving, based on irradiation of liquid monomers by broad and high-current electron beams in vacuum** [2259-178]
D. Vaisburd, Tomsk Polytech Univ. and High Current Electronics Institute (Russia)

SESSION 11 ADDITIONAL PAPERS

- 628 **In-situ surface charge distribution measurement of alumina insulator surfaces after impulse voltage application in vacuum** [2259-182]
Tumiran, S. Kobayashi, H. Imada, M. Maeyama, T. Ishii, Saitama Univ. (Japan); Y. Saito, National Lab. for High Energy Physics (Japan); N. Sato, Saitama Univ. (Japan); N. Kawada, Mitsubishi Heavy Industries, Ltd. (Japan)
- 632 **Enhanced field emission from extremely small metallic microtips** [2259-183]
R. Z. Bakhtizin, V. G. Valeyev, Bashkir State Univ. (Russia)
- 635 *Author Index*

Conference Committee

Conference Chair

Gennady A. Mesyats, Institute of Electrophysics (Russia)

Local Organizing Committee

G. A. Mesyats, Chairman
V. A. Ivchenko, Secretary
S. P. Bugaev
V. E. Fortov
G. N. Fursey
V. A. Glukhikh
E. P. Kruglyakov
M. I. Petelin
V. I. Rakhovsky
A. A. Rukhadze
V. N. Shrednik
V. P. Smirnov

Permanent International Scientific Committee

J. E. Thompson, Chairman, USA
R. L. Boxman, Secretary, Israel
H. C. Miller, Treasurer, USA
S. P. Bugaev, Russia
I. Chalmers, United Kingdom
G. H. Ecker, Germany
A. Guenther, USA
R. Hackham, Canada
E. Hantzsche, Germany
L. Hatfield, USA
W. Jimei, China
J. Kutzner, Poland
D. Konig, Germany
R. V. Latham, United Kingdom
C. Le Gressus, France
V. I. Rakhovsky, Russia
W. Rieder, Austria
E. Schade, Switzerland
R. Stinnett, USA
S. Yanabu, Japan

Preface

The XVIth International Symposium on Discharges and Electrical Insulation in Vacuum is held in unusual surroundings—on board a ship traveling from Moscow to St. Petersburg, Russia. During extended breaks between technical sessions the attendees and their guests will have an opportunity to see the beautiful sights and nature of central Russia.

The sites of previous symposia in this series were:

- Cambridge (USA) 1964 and 1966
- Paris (France) 1968
- Waterloo (Canada) 1970
- Poznań (Poland) 1972
- Swansea (United Kingdom) 1974
- Novosibirsk (USSR) 1976
- Albuquerque (USA) 1978
- Eindhoven (The Netherlands) 1980
- Columbia (USA) 1982
- Berlin (GDR) 1984
- Shoresh (Israel) 1986
- Paris (France) 1988
- Santa Fe (USA) 1990
- Darmstadt (Germany) 1992

There are over 185 scientists from 16 countries participating in this meeting, including nearly 100 attendees from Russia and the CIS countries. There are 178 invited and contributed papers, including 106 from Russia and the CIS countries. The Table of Contents of this proceedings gives a good overview of recent work which is presented on the properties of vacuum discharges and the increasing importance of vacuum discharges in industrial applications.

The Local Organizing Committee gratefully acknowledges the scientific and financial support of the Symposium sponsors listed. We also thank the members of the Permanent International Scientific Committee, especially its Chairman, Professor James E. Thompson, for the assistance and guidance given in organizing this symposium. Finally, we would also like to thank SPIE staff for their assistance in putting together this proceedings.

Papers published in this proceedings will be reviewed by the Permanent International Scientific Committee and selections will be made for papers to be considered for publication in forthcoming Special Issues of the *IEEE Transactions on Plasma Science* and the *IEEE Transactions on Electrical Insulation*. We believe that the XVIth ISDEIV will be interesting and useful to you. We anticipate stimulating exchanges of scientific information between scientists from different countries, and that the environment of the symposium will promote personal contacts for collaborative ventures.

In conclusion, I wish to express my deep appreciation to all the attendees for their contribution to the works presented at the Symposium. I wish you a fruitful symposium and a nice rest.

G. A. Mesyats

Dyke Award for Distinguished Work on Discharges and Electrical Insulation in Vacuum

Endowed by the Toshiba Corporation

The Dyke award has been established by the International Symposium on Discharges and Electrical Insulation in Vacuum (ISDEIV) to recognize outstanding contributions to the field. The Award is given by the Symposium to a worthy person identified by the Awards Committee of the Permanent International Scientific Committee. The Award is presented at the Banquet of the Biennial Symposium.

The Dyke Award for the XVIth ISDEIV Honors Professor Burkhard Jüttner for his Pioneering and Continuing Technical Contributions on the Subject of Electrical Discharges in Vacuum

Prof. Jüttner has explored prebreakdown and breakdown phenomena in vacuum for many years. His pioneering work on nanosecond discharges with clean electrodes in ultrahigh vacuum provided significant information concerning processes in vacuum breakdown and cathode spots. More recently notable have been his experimental investigations into substructures of cathode spots. Other valuable contributions have been his reviews of vacuum breakdown and cathode phenomena. Prof. Jüttner's 25 years of work has contributed greatly to the fields covered by this symposium.

Prof. Burkhard Jüttner was born in Prague, Czechoslovakia in 1938. He received the diploma in physics from Humboldt University, Berlin in 1962, and the degrees of Dr.rer.nt., Dr.sc., and Professor of Physics from the Academy of Sciences, Berlin in 1971, 1983, and 1985, respectively. He worked in basic research on vacuum breakdown, vacuum arcs (especially cathode phenomena), and electrode processes of gaseous arcs, as well as in the technical applications of these phenomena. Special note should be paid to his pioneering work on nanosecond discharges with clean electrodes in ultrahigh vacuum, which provided significant information concerning processes in vacuum breakdown and cathode spots. Of particular recent interest have been the experimental investigations of Prof. Jüttner and colleagues into substructure of cathode spots. Other valuable contributions have been his reviews of vacuum breakdown and cathode phenomena.

Prof. Jüttner has been working with electrical discharges in vacuum for over 25 years, formerly with the Central Institute of Electron Physics, and now with the Max Plank Institute for Plasma Physics. He has published over 100 technical papers.

The ISDEIV Permanent International Scientific Committee would like to gratefully acknowledge the Endowment of the Dyke Award by the Toshiba Corporation.

**Chatterton Young Investigator Award for Outstanding Achievement
of Young Investigators in the Field of Discharges and Electrical
Insulation in Vacuum**

**Supported by CALOR EMAG Elektrizitäts, AG
Member of the ABB Group**

The Chatterton Young Investigator Award was established by the ISDEIV in honor of the late Paul A. Chatterton. The purpose of this award is to recognize outstanding achievement of young investigators in the field of discharges and electrical insulation in vacuum, and aims at encouraging young scientists and engineers to enter this field of research.

The Chatterton Award recipients for the Darmstadt Symposium and the Moscow—St. Petersburg Symposium will be announced at the banquet of this symposium. The ISEIV Permanent International Scientific Committee would like to gratefully acknowledge CALOR EMAG Elektrizitäts AG, Member of the ABB Group, for supporting this Award.

SESSION 1

Vacuum Breakdown and Prebreakdown Phenomena

Electrohydrodynamic phenomena on the explosive-emission liquid-metal cathode

Lev M. Baskin[†], Alexander V. Batrakov, Sergey A. Popov, and Dmitry I. Proskurovsky

Institute of High-Current Electronics, Russian Academy of Sciences, Tomsk 634055

[†]Institute of Telecommunications, St.Petersburg 191065, Russia

ABSTRACT

The paper describes the results of a direct experimental observation of the development of an electrohydrodynamic instability at an explosive-emission liquid-metal cathode along with a theoretical analysis of the growth and destruction of the protrusion formed on the cathode surface.

1. INTRODUCTION

The study of electrohydrodynamic phenomena at liquid-metal cathodes operating in the explosive-emission mode is of interest for a better insight into the mechanism of the development of vacuum discharges and the peculiarities of the operation of this type of cathode. The surface of a liquid metal is known¹ to be unstable in a strong electric field. In recent years, the behavior of a liquid metal in a strong electric field has been extensively studied theoretically^{2,3}. However, direct observations of the time variation of the shape of a liquid metal have not been carried out till now. Only a few attempts have been taken^{4,5} to observe some phases of the development of an electrohydrodynamic instability at the surface of a liquid metal. Nevertheless, conditions for experimentation with a liquid metal cathode may be chosen, which would allow one to readily observe the growth and destruction of a protrusion on the surface of a liquid-metal. The present paper describes experimental observations of these processes with analyzing them theoretically. In addition, the data obtained are used to explain the sluggish nature of liquid-metal needle emitters.

2. EXPERIMENT

A liquid-metal cathode of diameter 4 or 2 mm (see Fig. 1,a) and a plane anode formed a vacuum gap of length 4 mm. The surface of the cathode base was wetted with a working liquid ($\text{In}_{0.25}\text{Ga}_{0.75}$ alloy). A vacuum of no worse than 10^{-5} Pa was produced by oilless pumping tools.

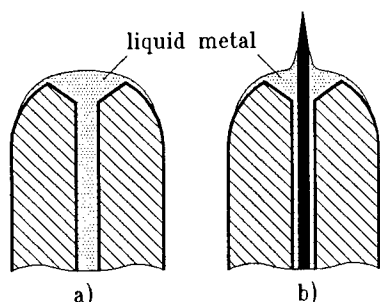


Fig.1

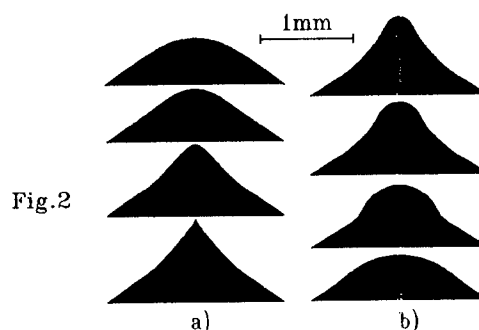


Fig.2

High voltage pulses which resulted, at electric fields $E_0 \sim 10^5$ V/cm and more, in the development of an electrohydrodynamic instability at the surface of a liquid metal, the formation of a protrusion, and the initiation of explosive electron emission were applied to the vacuum gap at a frequency of 20 to 50 Hz. The explosive electron emission caused a 50 to 250 pF capacitor connected to the gap to discharge into vacuum during 10^{-7} s. The peak current was 20 to 40 A. During the discharge, the gap voltage dropped and the protrusion started destructing. The reproducibility of the delay time to discharge and the cathode processes attained upon this repetitively pulsed action made it possible to use stroboscopic shadow photography for the operating cathode surface. For this purpose, the gap was illuminated by a flash lamp producing light flashes of duration 5 μ s. By controlling the delay of starting the flash lamp with respect to the beginning of the voltage pulse, we were able to indicate various phases in the oscillation of the liquid

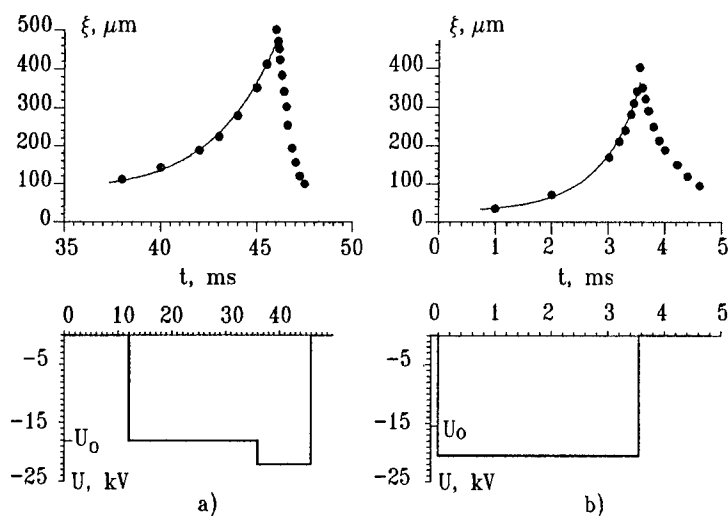


Fig.3

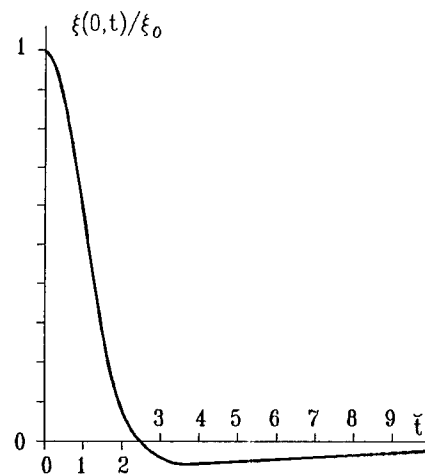


Fig.4

metal surface. Typical photographs of the protrusion profiles taken at different times are presented in Fig. 2. The technique used allowed a spatial resolution of $\sim 10\mu\text{m}$.

Figure 3,a illustrates the case where a stepped voltage pulse was applied to a cathode of diameter 4 mm, oriented in opposition to the force of gravity. The amplitude of the voltage pulse first step was somewhat lower than the threshold voltage U_0 for the development of an instability leading to the initiation of explosive electron emission. In this phase, no perturbation at the liquid metal surface was noticed. At the second voltage step, an instability developed, which led to the formation of a conical protrusion of the "cusp" type (see Fig. 2,a). The cone angle near the protrusion apex was close to the Taylor angle. Once explosive electron emission had been initiated, the conical protrusion stopped growing and destroying, with a wave being generated on the liquid metal surface (see Fig. 2,b). In Fig. 3, the variation of the protrusion height within the cycle $\xi(t)$ is shown with dots. Figure 3,b presents the results of measuring $\xi(t)$ for a cathode of diameter 2 mm, placed horizontally, to which rectangular pulses of peak voltage $U > U_0$ were applied. In this case, the growing and destroying protrusions were similar in shape to those shown in Fig. 2. Note that the upper points on the curves $\xi(t)$ correspond to the locations of the cathode flares.

3. THE DYNAMICS OF PROTRUSION GROWTH AND DESTRUCTION

Let us consider the dynamics of "deep" nonviscous liquid in a strong electric field. The dispersion equation for gravitational capillary waves on the surface of a liquid metal in the presence of an electric field has the form⁶:

$$\omega_k^2 = k \left(g + \frac{\alpha}{\rho} k^2 - \frac{E_0^2}{4\pi\rho} k \right), \quad (1)$$

where g is the free fall acceleration, ρ is the density of the liquid, and α is the surface tension coefficient. For an axially symmetrical system (r, z) , the liquid boundary $z = \xi(r, t)$ can be approximated linearly as

$$\xi(r, t) = \int_0^\infty \xi_k(t) J_0(kr) k dk. \quad (2)$$

For the given form of the initial perturbation at the boundary $\xi(r, 0)$ and the initial velocity of the boundary $\frac{\partial \xi(r, t)}{\partial t} \big|_{t=0}$, the initial conditions $\xi_k(0)$ and $\dot{\xi}_k(0)$ are determined and then, with Eqs. (1) and (2) taken into account, the boundary shape at a time t is found³. In the below discussion, we will assume for simplicity that $\dot{\xi}(r, 0) = 0$.

For a strong electric field, within some range of $k_1 < k < k_2$, we have $\omega^2(k) < 0$. The shape of the protrusion pooled will then be adequately described by the relation

$$\xi(r, t) \approx \int_{k_1}^{k_2} \xi_k(0) \text{ch} \left(k \frac{E_0}{2\sqrt{\pi\rho}} t \right) J_0(kr) k dk. \quad (3)$$

If we assume that the initial boundary shape is described by the Gaussian

$$\xi(r, 0) = \xi_0 \exp\left(-\frac{r^2}{\lambda^2}\right), \quad (4)$$

and if the field at the boundary is such that $k_2\lambda \gg 1$ and $k_1\lambda \ll 1$, what holds with a margin for the conditions of our experiment, then the motion of the liquid metal boundary can be described, to a high accuracy, by the expression

$$\xi(r, t) = 2\xi_0 \int_0^\infty e^{-y^2} \operatorname{ch}(y\tilde{t}) J_0(y\tilde{r}) y dy, \quad (5)$$

where $\tilde{t} = E_0 t / \lambda \sqrt{\pi\rho}$ and $\tilde{r} = 2r/\lambda$. The position of the protrusion apex is given by

$$\xi(0, t) = \xi_0 \left(1 + \frac{\sqrt{\pi}}{2} \tilde{t} \exp\left(\frac{\tilde{t}^2}{4}\right) \Phi_0\left(\frac{\tilde{t}}{2}\right)\right), \quad (6)$$

where Φ_0 is the error integral.

The cross size of the surface in the experiment was limited, therefore the spectrum of initial perturbations appeared to be continuous rather than discrete. This, however, only slightly affected the results obtained for the field $E_0 > 10^5$ V/cm and surface cross sizes over 1mm.

The experimental dependencies $\xi(t)$ are best approximated by Eq. (6) (solid lines in Fig. 3) for the λ values close to the cathode diameter, what corresponds to the development of the principal mode of liquid oscillations on the liquid cathode surface. The amplitude of the initial perturbation ξ_0 was $\sim 80\mu\text{m}$ for the case presented in Fig. 3,a and $\sim 20\mu\text{m}$ for the case presented in Fig. 3,b. These values of ξ_0 may be accounted for by the fact that the liquid surface was originally curved.

Let us consider the destruction of a protrusion after disappearance of the electric field as a result of explosive electron emission. If we, as earlier, describe the initial shape of the protrusion by Gaussian (4) and put the initial velocity of protrusion growth equal to zero, then we will have

$$\xi(r, t) = 2\xi_0 \int_0^\infty e^{-y^2} \cos(y^{\frac{3}{2}}\tilde{t}) J_0(y\tilde{r}) y dy, \quad (7)$$

where $\tilde{t} = t\sqrt{8\alpha/\rho\lambda^3}$. The position of the protrusion apex as a function of time, calculated from Eq. (7), is shown in Fig. 4. It can be seen that the destruction of the protrusion stops at a time of 2.5, i.e. the total destruction time is $t_p \simeq 2.5\sqrt{\rho\lambda^3/8\alpha}$. Putting, for example, $\lambda \simeq 500\mu\text{m}$, we find $t_p \simeq 800\mu\text{s}$.

Note that with this analysis of the protrusion destruction, it is difficult to attain good quantitative agreement of the predictions with experimental data. This is not only due to the fact that the final emitter shape in the growth phase is far from a Gaussian, but, first of all, for the reason that the liquid metal has some initial velocity gathered in the process of development of an instability in the field. The numerical simulation has shown that, with allowance for this velocity, the destruction time in our case increases four times. However, estimates show that the expedition of the protrusion destruction by the pressure of the explosive emission plasma is not essential, since the discharge current is low and short-term.

4. THE VOLUME OF THE LIQUID-METAL PROTRUSION

An interesting result has been obtained on measuring the final volume of the protrusion formed at various peak voltages U . Figure 5 gives the volume ratio V/V_0 for protrusions formed at voltages U and U_0 as a function of the overvoltage U/U_0 . Based on the result obtained, we have supposed that taking into account the dependence of the final volume of the protrusion formed on a liquid metal surface on the overvoltage might provide a better description for the dependence of the delay time to the emission of charged particles τ on the overvoltage for a needle liquid-metal emitter. According to Ref. 2,

$$\tau \simeq \frac{3\eta V}{h^2 \sin \alpha} \left(\frac{U^2}{U_0^2} - 1\right)^{-1}, \quad (8)$$

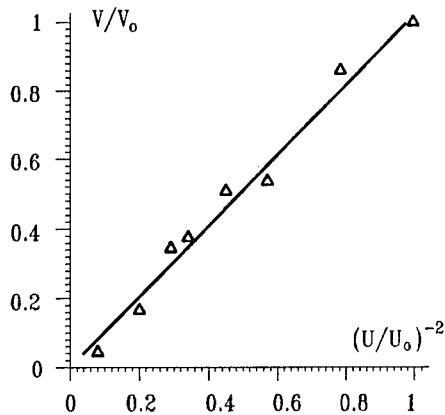


Fig.5

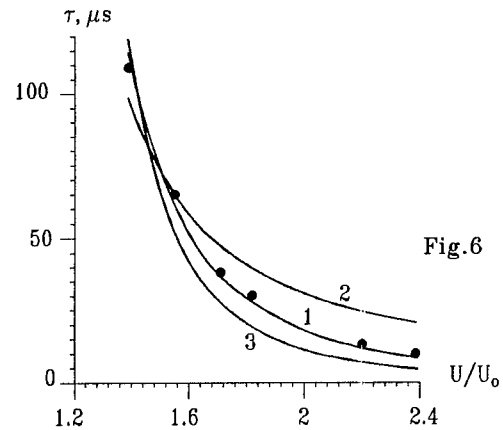


Fig.6

where η is the coefficient of viscosity, V is the final volume of the conical protrusion, h is the initial thickness of the film on the needle apex surface, and α is the half the angle of the needle conical part. Assuming that the dependence $V = V_0(U^2/U_0^2)^{-1}$ presented in Fig. 5 also holds for a needle cathode at whose surface a viscous liquid flow mode is realized, we obtain

$$\tau \simeq \frac{3\eta V_0}{h^2 \sin \alpha} \left(\frac{U^2}{U_0^2} \right)^{-1} \left(\frac{U^2}{U_0^2} - 1 \right)^{-1}, \quad (9)$$

Shown with dots in Fig. 6 is a typical dependence of the delay time to the start of electron emission from a needle cathode (see Fig. 1,b) on the overvoltage. Curve 1 has been obtained from experimental data using approximating expression (9). Herein, the results of approximation of our experimental data using Eq. (8) (curve 2) and the expression given in Ref. 7 (curve 3), where $\tau \sim \left(\frac{U^2}{U_0^2} - 1 \right)^{-2}$, are shown. It can be seen that the best description of the dependence of the emission sluggishness on the overvoltage is provided by Eq. (9). The film thickness h estimated from Eq. (9) is $\sim 0.5 \mu\text{m}$, which is in accordance with the data given in Ref. 2.

Thus, the allowance for the dependence of the final volume of the protrusion formed on a liquid metal surface on the overvoltage provides a more accurate description for the dependence of the delay time to the electron emission from a liquid metal emitter on the voltage.

5. REFERENCES

1. L. Tonks, "A theory of Liquid Surface Rupture by a Uniform Electric Field", *Phys. Rev.*, Vol. 48, p. 562, 1935.
2. S.P. Thompson, P.D. Prewett, "The Dynamics of Liquid Metal Ion Sources", *J. Phys. D: Appl. Phys.*, Vol. 17, pp. 2305-2321, 1984.
3. L.M. Baskin, "Development of Aperiodic Instability on Liquid Metal Surface Perturbed by Thermal Fluctuations", *IEEE Trans. Electr. Insul.*, Vol. 24, pp. 929-931, 1989.
4. Bartashus I.U., Pranevichus L.I., Fursey G.N., "Investigation of Explosive Electron Emission from a Liquid Gallium Cathode", *Zh. Tekn. Fiz.*, Vol. 53, pp. 1943-1948, 1971.
5. L.M. Swanson, G.A. Schwind, "Electron Emission from a Liquid Metal", *J. Appl. Phys.*, Vol. 49, pp. 5655-5662, 1978.
6. L.D. Landau, E.M. Lifshits, "Theoretical Physics. Electrodynamics of Continuous Media", *Gostekhizdat*, 1957.
7. V.G. Dudnikov, A.L. Shabalin, "Peculiarities of Transient processes of Electrohydrodynamic Ion Emission", *Zh. Tekn. Fiz.*, Vol. 57 pp. 185-187, 1987.

MEASUREMENTS OF CURRENT INTENSITIES FROM 10^{-18} A TO 10^{-6} A EMITTED FROM NIOBIUM SAMPLES UNDER HIGH DC ELECTRIC FIELDS

Mustapha Boussoukaya, Aline Curtoni, Anne Zeitoun-Fakiris
DAPNIA-SEA, CEA SACLAY
F 91191 Gif-sur-Yvette Cedex FRANCE

ABSTRACT

An experimental set-up allowing measurements of DC field emission currents in the range of 10^{-18} A to 10^{-6} A in ultra high vacuum ($P < 10^{-10}$ Torr) at room temperature has been developed. The detection of currents in the range of 10^{-18} A to 10^{-12} A was carried out with an electron multiplier located behind a grid anode. Higher currents were measured using a massive anode and a picoammeter. The whole system was designed to study niobium samples from sheets used to build electron superconducting accelerator cavities. Comparisons of the electron field emission from samples prepared by different surface treatments as chemical etching, electropolishing, oxide coating by anodization, were done. Some of the obtained results are presented below

1. INTRODUCTION

Development of linear colliders in the TEV range using normal or superconducting structures is tied to the realisation of high accelerating electric fields. The electric field limitations for both structures are essentially due to their surface electron field emission. Consequences of the field emitted currents are not the same on superconducting accelerator cavities and on the normal ones. For both, field emission currents of a few microamps may induce high degradation of the microwave parameters. The quality factor of the structures decreases leading to a decrease of the accelerating field magnitude. For the superconducting ones, the local surface temperature may also increase and transition from the superconducting to the normal state can occur. The aim of these studies is the understanding of the electron emission mechanism under high electric field condition. A great number of papers have been published on the subject^{1,2}, but the level of the measured current was always higher than 10^{-13} A. In this paper, we present our investigations on electron field emission using a device that allows measurements of current as low as 10^{-18} A to values as high as 10^{-6} A. Planar niobium samples of macroscopic sizes ($\approx 1 \text{ cm}^2$) having different surface treatments were studied. We compare, at the end, the results obtained for the very low EFE regime ($I < 10^{-12}$ A) with the "usual" one ($I \geq 10^{-13}$ A). Some results characteristic of the very low current regime are presented.

2. EXPERIMENTAL CONDITIONS AND PROCEDURE

In order to detect DC field electron currents in a large current range (10^{-18} A to 10^{-6} A), an experimental set-up has been developed, in which ultra high vacuum is permanently realised in the test chamber by a 600 l/s ion pump and a titanium sublimator (Fig.1). To avoid baking out after each sample loading, the samples are introduced through two intermediate chambers in which vacuum is respectively of the order of 10^{-2} and 10^{-7} Torr. Currents in the range of 10^{-18} A to 10^{-12} A are measured with an electron multiplier (EM) which collects the electrons and preamplifies the signal. Then the signal passes through fast amplifiers and a discriminator to a 100 MHz scaler counting the pulses whose amplitude exceeds the electronic noise. The gap between the sample (S) and the anode can be adjusted from 1/10 mm to more than 2 mm before measurements. The gap geometry is then a planar cathode (C) opposite a grid (G). The electron multiplier is located just behind this grid. For higher current measurements ($I \geq 10^{-12}$ A) a planar anode (A) is used and the current is measured by a Keithley ammeter. In both cases, experiments are automatically driven. A maximum voltage of 25 kV can be applied to the surface in study. The experiments were performed at room temperature.

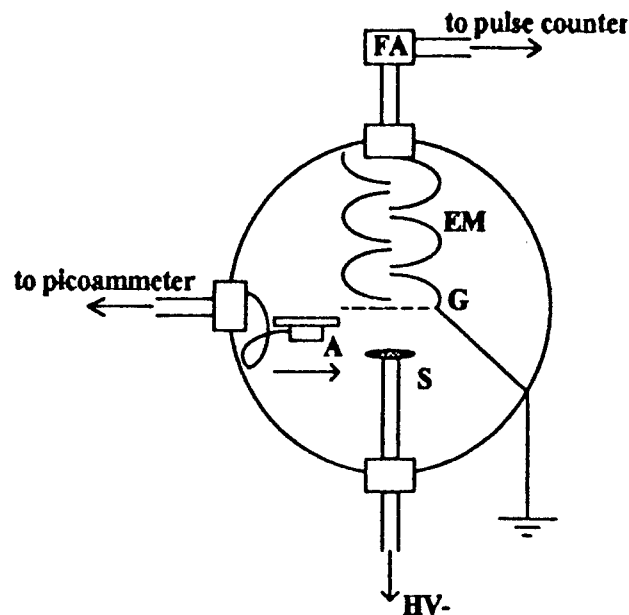


Figure 1. A view of the experimental chambers where S is the sample in study, G the grid, A the planar anode. The working pressure is $P < 10^{-10}$ Torr.

For a given gap and detector, the measurements of the electronic current I versus voltage V for a tested sample were first performed with increasing V -values and after, eventually, with decreasing ones. Results are plotted in the following coordinates : -a) $\ln(I/E^2) = f(1/E)$ or Fowler-Nordheim (FN)¹ : -b) $\ln(I/E) = f(\sqrt{E})$, or Poole-Frenkel (PF)³ where $E = V/d$ is the applied electric field.

3. RESULTS AND DISCUSSION

For each sample more than three curves were consecutively recorded. The decreasing voltage plot was always

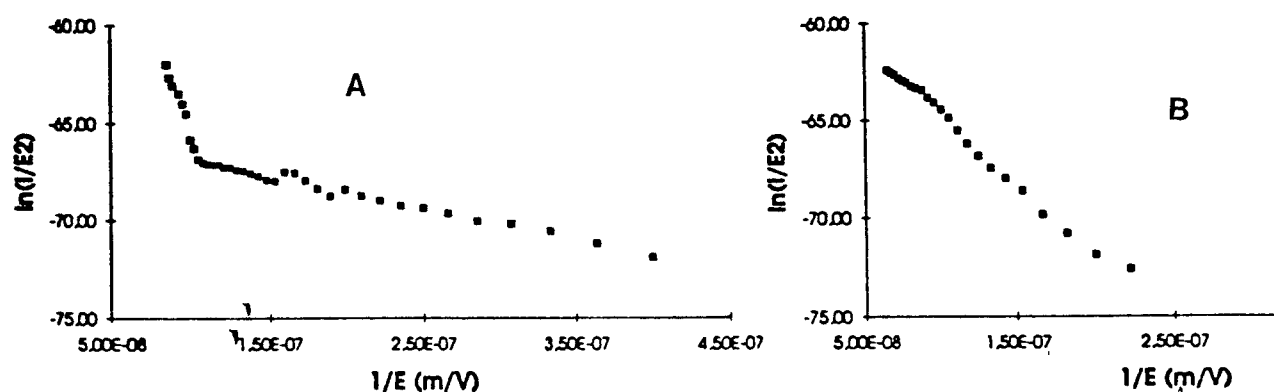


Figure 2. A First test of a chemically polished niobium sample ; B fifth test for the same sample.

smoother than the increasing voltage one (Fig.3). A possible explanation for that is a change in the surface conditions (degassing, emission of loosely attached particles, smoothing of the adsorbed gas coverage...) during

the increase of the voltage. Some of these changes seem to be permanent, as the first plot for a virgin sample was different from the next ones. This can be seen when comparing the FN plots A and B on Fig.2 and on Fig.3. For instance, the first plot for chemically etched electrodes presents a low current tail which disappears on the next curves. This may be an emission of exoelectrons trapped by the rough surface of the sample. So, for next records the same current-values appear at higher electric fields. This phenomenon is less important for electropolished or anodized electrodes.

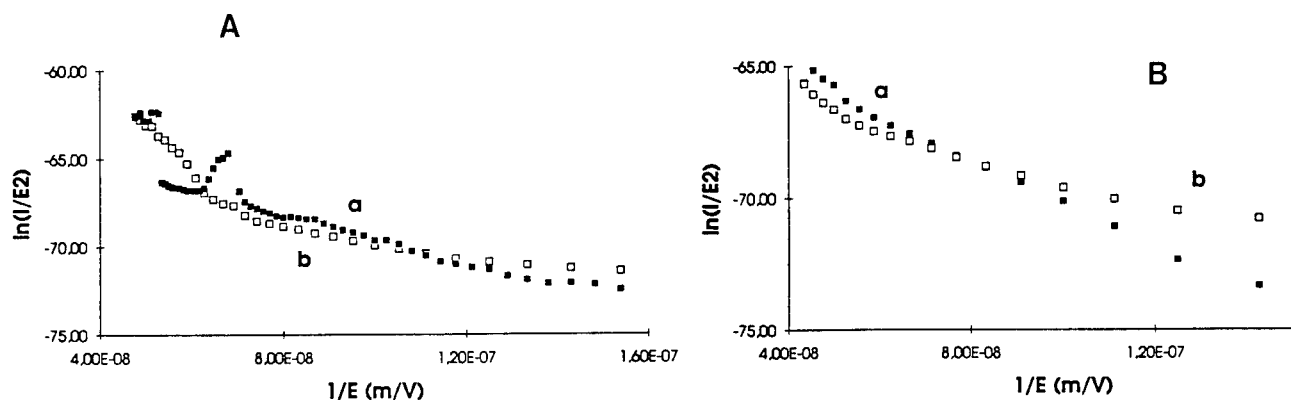


Figure 3. A First test of an electropolished niobium sample ; B sixth test for the same sample. -a) increasing , -b) decreasing voltages plot.

In the low current range, the experimental plots have a "nearly hyperbolic" form when plotted in the FN coordinates (Fig.2). This situation is similar to the one observed for semiconducting emitters⁴. This may be due to

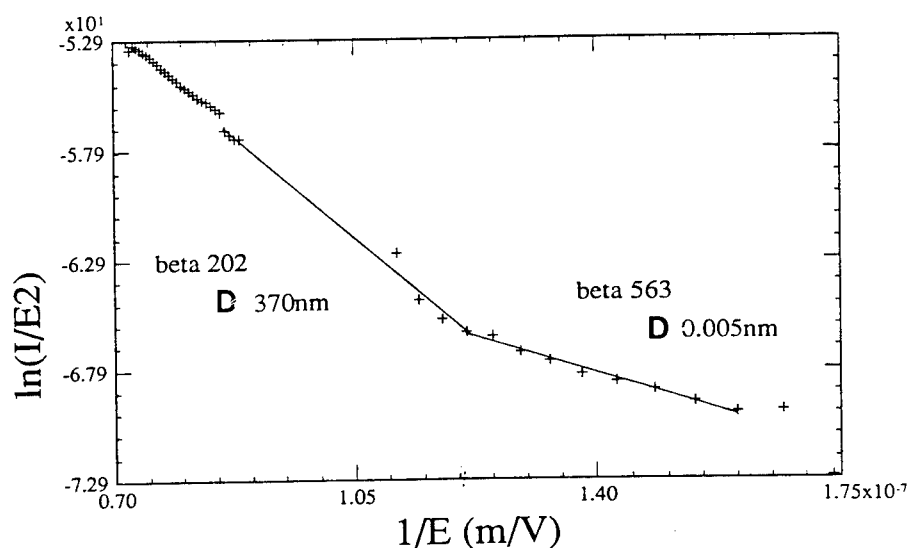


Figure 4. Plot of a chemically polished niobium sample in both the low current regime (right part of the curve) and the high current regime (left part).

the superposition of two (or more) different quasi-linear curves coming from different emitting conditions in competition. Also, the calculation of FN plot parameters β and s give quite different results for lower field current values than for higher ones : for very low currents the β -values are larger as can be seen on Fig.4.

Searching for an alternative explanation of that, the experimental measurements have, also, been plotted in the PF coordinates. An example is given on Fig.5 concerning the curves presented on Fig.3. The plots show reproducible quasi-linear parts. The values of their slopes seem compatible with the possibility of an emission of electrons from the metal to the vacuum through the semiconducting surface oxide layer (essentially Nb_2O_5). This hypothesis needs further experimental and theoretical studies that are, actually, going on.

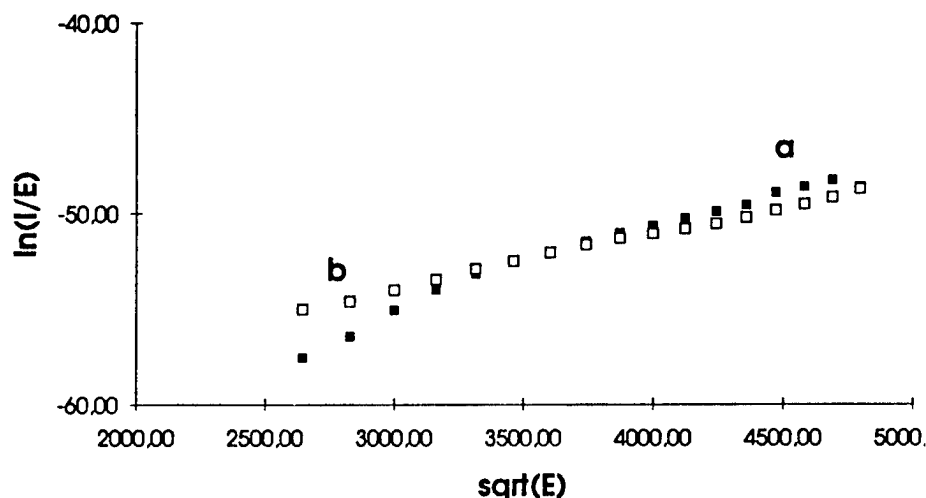


Figure 5. PF characteristic of : A the chemically etched, B the electropolished niobium samples of respectively Fig.2. and Fig.3.

4. CONCLUSION

The experimental set-up used in our experiences permitted measurements of field emitted currents as low as 10^{-18} A. We observed differences in the emission tied to the nature of the treatments of the surface of niobium samples essentially for low level currents. We also observed changes in the plots between the first test and the later ones for the same sample. Plotting low-current results in the PF coordinates exhibits linear dependence which could be interpreted as an emission through the oxide upper layer.

5. REFERENCES

- ¹ R.H.GOOD jr and E.W.MÜLLER *Field Emission Handbuch der Physik* vol.XXI (1956) 176-231
- ² R.W.LATHAM *High Voltage Vacuum Insulation* Academic Press London New York (1981)
- ³ G.JOUVE *Phil.Mag.* vol 64 (1991) 207-18
- ⁴ P.G.BORZIAK, A.F.YATSENKO, L.S.MIROSHERCHENKO *F.E. from high resistance Si and Ge* *Phys.Stat.Sol.* vol 14 (1966) 403-23

High-speed imaging of explosive exoemission from an alumina ceramic in vacuum

B M Coaker[†], N S Xu[†], F J Jones[‡] and R V Latham[†]

[†] Surface Science Group, Department of Electronic Engineering and Applied Physics,
Aston University, Birmingham, UK B4 7ET

[‡] Cold Cathode Engineering, EEV Limited, Carholme Road, Lincoln, UK LN1 1SF

ABSTRACT

A fast-video imaging technique was used to observe the pulsed breakdown behaviour of an alumina tube, having two concentric planar electrodes on its end-face. Voltage-pulses, typically of 5kV amplitude ($5\text{kV } \mu\text{s}^{-1}$ time rate-of-rise), were applied to the radial M-I-M insulator-electrode regime under ultra-high vacuum (pressure $< 10^{-8}$ Torr), with video recordings made at 1000 frames per second. Images of the observed breakdown phenomena are presented, viewing along the centre-axis and also in the plane of the M-I-M structure. These images are discussed in relation to plasma-jets associated with vacuum arcs, and the nature of the ion species within such jets.

1. INTRODUCTION

The surface-breakdown of a solid-insulator, under the influence of a fast-rising voltage pulse, has widely been used as a trigger mechanism in triggered vacuum gap (TVG) switches;¹ TVGs offer a low trigger-voltage, high hold-off voltage, high-current switching capability, over a wide range of operating voltages.¹ Despite this extensive characterisation of TVG operation, there remains much discussion of the physical nature of the surface-flashover process across the trigger insulator, which leads to the 'firing' of the TVG tube.² Long-standing physical models of surface-flashover describe electrons emitted from the cathode triple-junction 'hopping' along the insulator surface; as the electrons strike the insulator, gas is desorbed from the surface and ionised by the hopping electrons.³ Recently, 'solid-state' models of insulator surface-flashover have emerged; namely the avalanching of charge-carriers injected into the insulator surface-layers,⁴ and the explosive de-stabilisation of trapped-charge within the dielectric.⁵

In recent work,⁶ we described DC prebreakdown phenomena viewed on the end-face of a metallized alumina tube. In order to deepen the understanding of the surface-flashover process across an insulator in vacuum, a development from this early work has been the observation of *pulsed breakdown* events, again on an alumina insulator. An intensified high-speed digital video technique allowed the acquisition of real-time optical images associated with pulsed-breakdown events. Images of pulsed surface-flashovers are presented, viewed along the centre-axis of the alumina tube, and also viewed orthogonal to the tube axis. Visible features of the pulsed-breakdown images are described, with additional comment made upon the nature of the observed phenomena.

2. EXPERIMENTAL

2.1 Experimental System

The specimen regime has the standard form described elsewhere,⁶ consisting of an alumina tube (Al_2O_3 , 94% purity), with two concentric rings of Mo/Mn metallized onto one end-face of the alumina sample: a nominal 300 μm spacing separated the two metallized rings. Figure 1 shows the mounting of the metallized alumina specimen in a stainless-steel vacuum chamber, that forms part of a dedicated experimental system that was described in detail in an earlier paper.⁶ The vacuum system was operated at a pressure of 5×10^{-9} Torr, and the alumina specimen initially baked *in vacuo* for 2 hours at 400°C.

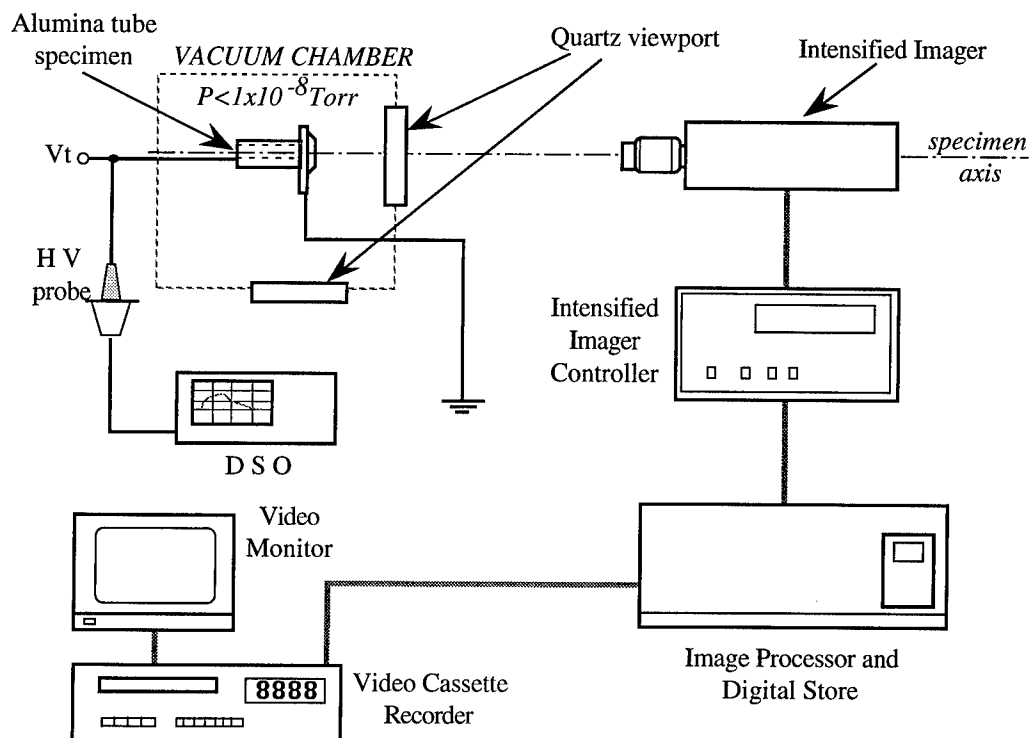


Fig. 1. Schematic arrangement of the experimental system.

Electrical connection was made between the inner metallized-ring of the alumina sample and a high-voltage pulsed power supply, with the outer metallized-ring brazed to an earthed copper tag. A monochrome CCD camera (768 pixels x 576 lines resolution) imaged the alumina specimen through quartz viewports in the vacuum chamber wall.

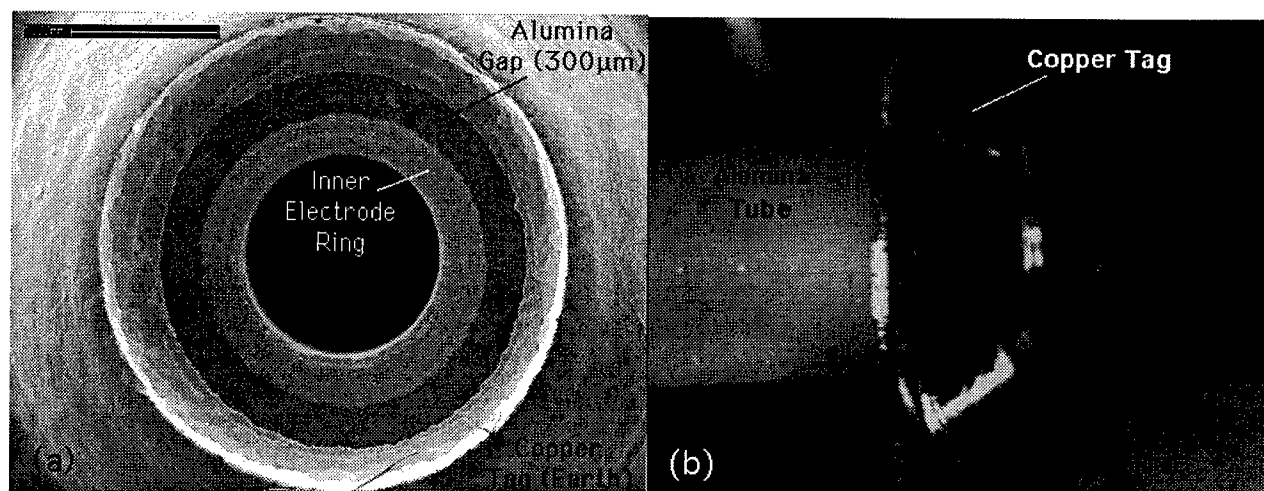


Fig. 2. (a) Front-view electron-micrograph and (b) side-elevation view of metallized alumina specimen

Figure 2(a) illustrates an electron-micrograph of the end-face of the alumina specimen; a second viewport allowed observation of the specimen orthogonal to its centre axis, and an illuminated side-view of the specimen is shown in Fig 2(b). All background illumination was then removed for the duration of the experiment. An intensified high-speed video camera (256 x 256 pixels resolution) complemented the high-resolution CCD camera, and imaged the fast optical processes associated with pulsed flashover

events at the end-face of the alumina specimen. The operation of this camera, and the acquisition of digitised frames showing fast optical events from the ceramic specimen, are described in Section 2.2.2.

2.2 Procedures and Measurements

2.2.1 Voltage-bias and Electrical Waveform-capture A positive voltage pulse, V_t , was applied to the inner electrode-ring of the specimen: this pulse was derived from the first half-cycle of a damped-sinusoidal voltage, having a maximum amplitude of +5kV (see Fig 3(a)). Voltage-waveform acquisition was performed using a 50MHz-bandwidth digital storage oscilloscope (DSO). The metal-insulator-metal (M-I-M) structure of the metallized end-face of the alumina tube was found to break-down at V_t values around +3kV: a typical pulsed-breakdown voltage waveform is shown in Fig 3(b).

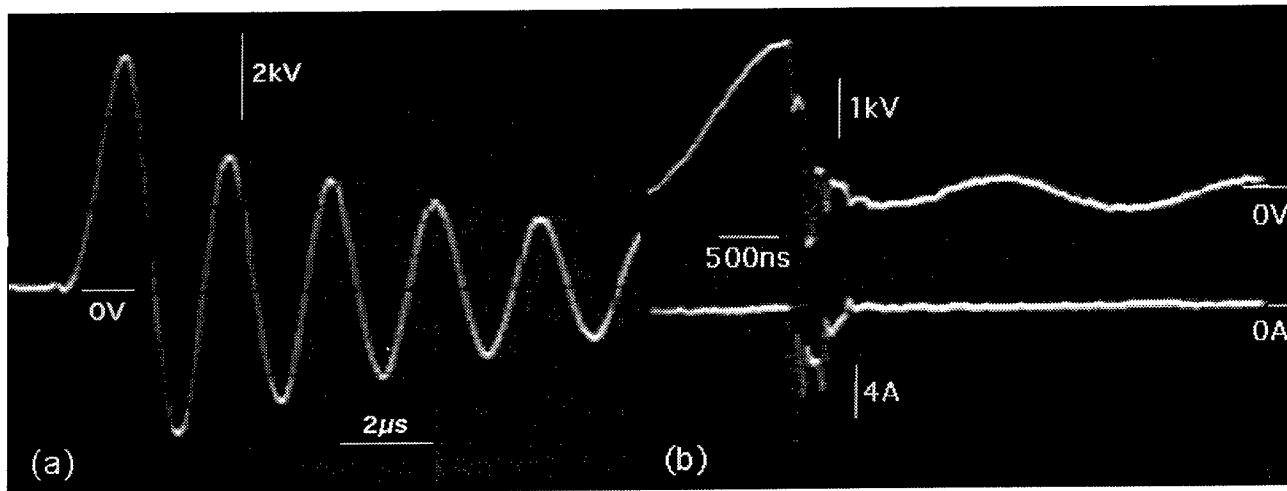


Fig.3. (a) Oscillogram of applied voltage waveform (open-circuit load), and (b) voltage-breakdown waveform (amplitude $V_t \approx +3\text{kV}$), together with the current-pulse waveform recorded through a transparent anode

2.2.2 Optical Image Capture: The high-speed video apparatus was operated in a 'rolling' recording mode, whereby 1ms frames were continuously read into a 1200-frame digital memory.

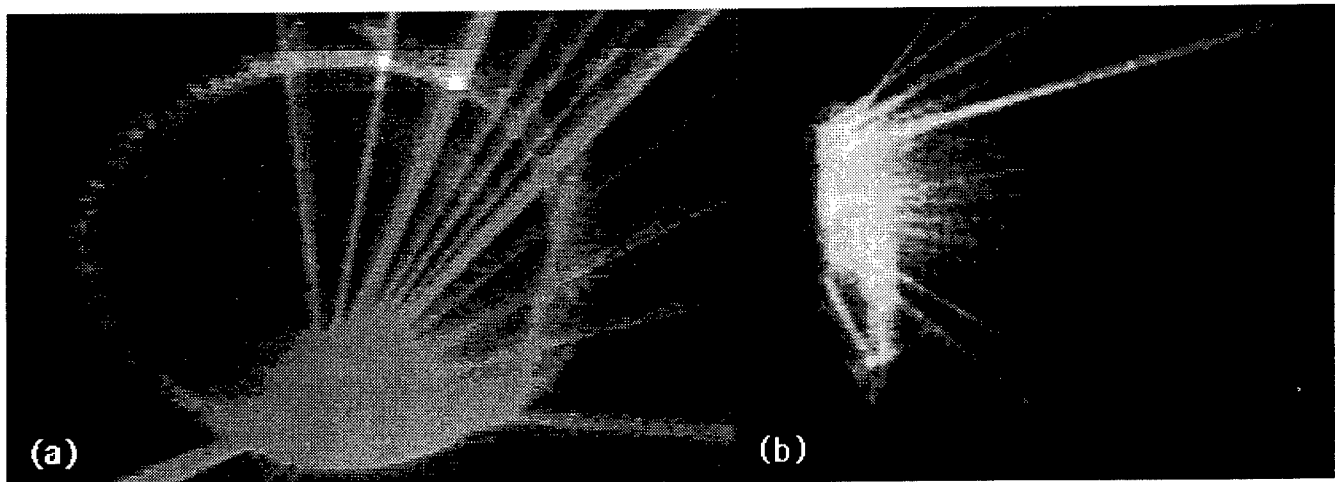


Fig.4. 1ms frames of exoemission events, viewing (a) the front and (b) the side elevation of an alumina specimen

Viewing the end-face of the alumina tube along the specimen axis (as shown in Fig 2(a)), and applying a voltage pulse (V_t) to the inner electrode-ring, the image depicted in Fig 4(a) was observed. Figure 4(b) displays an emission image observed perpendicular to the centre-axis of the alumina specimen, i.e.

across the front-face of the specimen as shown in Fig. 2(b).

2.2.3 Emission Current Waveform Capture A transparent anode⁶ was introduced into the experimental regime, and located at a spacing of 2mm parallel to the end-face of the alumina tube; the anode was terminated to 0V via a 10Ω current-viewing resistor (CVR). Figure 3(b) shows an oscillogram of a negative current-pulse collected through the anode, of approximately 10A amplitude, indicating an emission of negative current from the alumina specimen, coincident in time with the collapse of the applied-voltage (V_t) across the alumina insulator, and exceeding an estimated 1A of capacitive displacement current.

3. DISCUSSION AND CONCLUSIONS

This study has presented real-time images of photon-emission processes resulting from electrically-induced pulsed-breakdown flashover across an alumina insulator in vacuum. Referring to Figs. 4(a) and 4(b), two types of optical phenomena have been identified from the pulsed-breakdown flashover of the alumina specimen, namely

- an explosive 'luminous centre', within the 300 μ m alumina gap between the ring-electrodes, and
- bright 'jets', emitted out of the alumina specimen, propagating with straight-line trajectories, and which appear to emanate from a luminous centre within the alumina gap.

Graphical projection of the jet-trajectories does not show a single point of convergence: instead, the trajectories appear to stem from several points, suggesting a finite *distribution* of jet sources within the alumina gap; some jets appear to showing modulation of the recorded intensity along their length (Fig. 4(b)).

Studies of the vacuum plasma-efflux from an alumina-insulated spark plug, by Buraczyk *et al*⁷, detected ionised species of aluminium (Al) and oxygen (O) from the alumina insulator. This observation may be consistent with an apparent explosive emission of material from within the 300 μ m alumina gap of the metallized samples used in this work, as indicated by the pulsed-breakdown images of Fig. 4; a predominant emission of negative ion species (such as O^{n-}) and electrons in the jets observed in this work may contribute to the observed negative current collected from these jet phenomena (Fig. 3(b)).

ACKNOWLEDGEMENTS

The authors wish to thank the Engineering Board of the SERC for their provision of the high-speed video imaging equipment. Some of the authors (BMC, NSX and RVL) also wish to thank EEV Limited for their continued support in this programme. This work was carried-out under the Science and Engineering Research Council (SERC) Total Technology studentship scheme, award number 91302542.

REFERENCES

1. G A Farrall, "Low Voltage Firing Characteristics of a Triggered Vacuum Gap", *IEEE Trans. Elec. Dev.*, vol. 13, pp. 432-438, 1966
2. R L Boxman, "Triggering Mechanisms in Triggered Vacuum Gaps", *IEEE Trans. Elec. Dev.*, vol. 24, pp. 122-128, 1977
3. R A Anderson & J P Brainard, "Mechanism of pulsed surface flashover involving electron-stimulated desorption", *J. Appl. Phys.*, vol. 51, no. 3, pp. 1414-1421, 1980
4. N C Jaitly & T S Sudarshan, "DC surface flashover mechanism along solids in vacuum based on a collision-ionisation model", *J. Appl. Phys.*, vol. 64, no. 7, pp. 3411-3418, 1988
5. G Blaise & C Le Gressus, "Charging and flashover induced by surface polarisation relaxation process", *J. Appl. Phys.*, vol. 69, no. 9, pp. 6334-6339, 1991
6. B M Coaker, N S Xu, F J Jones & R V Latham, "Electrical and Optical DC Vacuum Emission Phenomena from a Ceramic-Insulated Planar electrode Configuration", *IEEE Trans. Plasma Sci.*, vol. 21, no. 5, pp. 400-406, 1993
7. D E Buraczyk, G G Edelman & K W Zieher, "Time-of-Flight Analysis of a Plasma Jet from a Spark Plug in Vacuum", *J. Appl. Phys.*, vol. 73, no.7, pp. 3169-3171, 1993

Discharge in commercial vacuum at high voltage

G.M. Kassirov, F.G. Sekisov, and V.N. Chekrygin

High Voltage Institute, Tomsk Polytechnical University
2a Lenin Str., Tomsk 634050, Russia

ABSTRACT

The results of the investigation of amplitude and spatial-time characteristics of the initial conduction current at pulse voltage of a microsecond duration in the centimeter gaps in commercial vacuum are presented and discussed.

1. INTRODUCTION

Numerous investigations of electric insulation in commercial vacuum, the operating conditions of a majority of electrophysical devices showed that the discharge evolution has remarkable peculiarities therein. The peculiarities can hardly be explained in terms of the field emission breakdown model only. They involve, first of all, a decrease, by one or two orders of magnitudes in the average breakdown electric field in the discharge gap; well pronounced effect of the total voltage; evolution of light phenomena in the stage of initial conduction; dependence of the main discharge characteristics on the vacuum parameters. The difference between the breakdown development in commercial vacuum and under highly-pure conditions get stronger with increasing the discharge gap length.

Our investigations of the electrical discharge in centimeter vacuum gaps at quasirectangular voltage pulses of a microsecond duration have provided an additional information on the current dynamics in the vacuum discharge gaps in a wide range of peak currents and the current dependence on the experimental conditions. When conducting the experiments we used five oscilloscopes adjusted synchronously to different amplitude-time regions of the oscillograms from initial conduction current. A pumped-out Faraday cylinder used for measuring the electron component of the initial conduction current was placed behind thin plane anode. The cathode was a sphere 12 cm in diameter. To indicate and analyze weak light emission we used the photomultipliers, the monochromators, and the spectrographs operating used in the visible wavelength range.

2. EXPERIMENTAL RESULTS

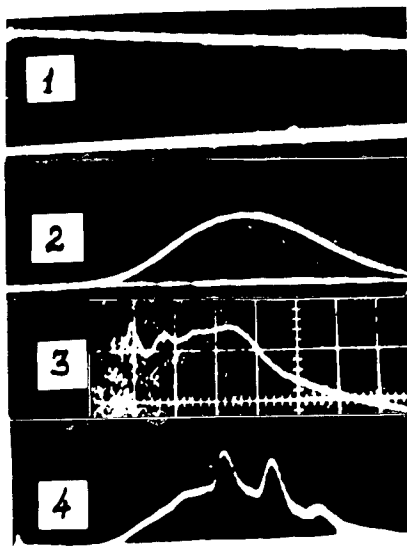


Fig. 1. The voltage (1), the microdischarge current (2), the pressure burst (3), and the prebreakdown current (4) oscillograms

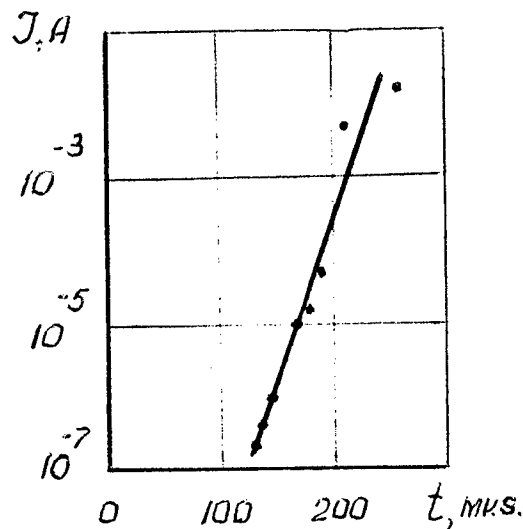


Fig. 2. Current rise on the microdischarge front

At the voltages far below the breakdown voltage, the vacuum gap current has a character of a single self-damping pulse (Figs. 1, curve 2) of several tens of microseconds in duration. During the pulse risetime, the current increases exponentially in the range of several orders of magnitude (Fig. 2). The microdischarge peak current depends on many factors. With increasing the pressure of residual gases from 2.6×10^{-5} to 3.6×10^{-3} Pa the microdischarge current decreases by four orders of magnitude. It is strongly influenced by electrode

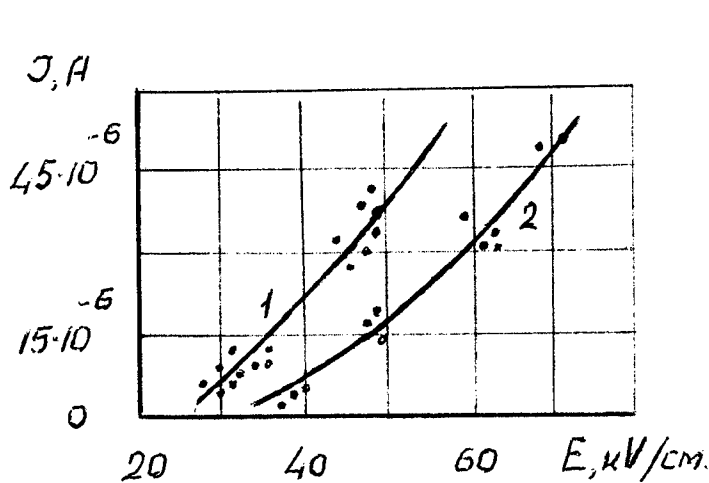


Fig. 3. Microdischarge peak current for gap spacings 8 (1) and 6 cm (2)

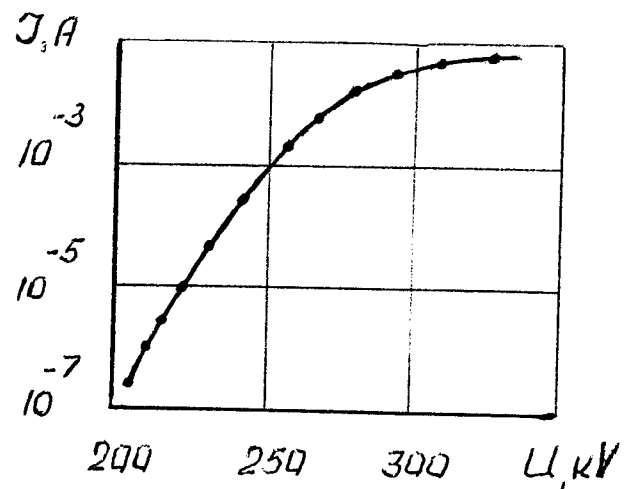


Fig. 4. Microdischarge current-voltage characteristic

conditioning. Increasing the number of pre-burning pulses from 50 to 250 leads to a decrease in the microdischarge peak current by two orders of magnitude. The cathode heating up to 300 °C leads to a decrease in current by five orders of magnitude. Under other equal conditions, the microdischarge peak current is higher in the longer gaps (Fig. 3). The current-voltage characteristic is saturated in the range of high voltages (Fig. 4). By means of electron-ionization transducer, pressure bursts were been indicated which appeared in step with the microdischarge current and enhanced the residual gas pressure in the experimental chamber near by an order of magnitude (Fig. 1, curve 3). The pressure burst amplitude increases linearly with increasing in microdischarge current. A weak glow appeared in the gap in step with the microdischarge current. Photometrical analysis of its spatial structure has shown that the glow was spatial in character. The intensity is high near the cathode, on the gap axis but reduces monotonically in radius.

When the gap voltage approaches the breakdown one, strong deformations in the oscillogram of the microdischarge current take place. The falling waveform branch exhibits fast current bursts (see Fig. 1, curve 4) of periodic character and high enough amplitude. The time between the current bursts depends on the electrode separation. When it gets shorter the current oscillation period proportionally decreases. With one of these bursts, the discharge was observed to go into a high-current stage and the gap eventually breaks down.

In this case, essential changes in the spatial discharge structure took place. In the stage of initial high-voltage conductance, the space discharge was localized at small areas of the cathode surface. First at the cathode, and then at the anode, the brightly luminous flares were formed. As they approach each other, the discharge becomes irreversible and the gap is eventually broken down.

3. DISCUSSION

Microdischarge as a form of high-voltage conduction of the discharge gaps in commercial vacuum and its more intensive forms, high voltage vacuum discharge, were investigated thoroughly^{1,2}. It should be noted that in a lot of studies microdischarge was considered as an independent discharge process which was related to a subsequent breakdown. The use of a pulsed voltage and high resolution in current in our experiments allowed us to reveal new elements in the time behavior of the microdischarge current and to indicate an essential connection between the microdischarge and the subsequent breakdown. Our earlier work³ has shown that for a nonovervolted breakdown, the stage of comparatively slow current rise and the stage of fast current rise terminating with breakdown may be inferred from the same oscillogram.

Even at low overvoltages, the stage of abrupt current rise was seen to come across the falling branch on the oscillogram of the microdischarge current to reach its peak values. For overvoltages exceeding 10%, both current stages were merged and indiscernable on one oscillogram.

These experimental results and the above mentioned evidences on the development of the microdischarge current instabilities may draw to the conclusion that microdischarge encourages the conditions for breakdown in commercial vacuum. As for the physical mechanism, one may suggest that positive ions retained in the gap after the microdischarge enhance the cathode field to the value high enough to cause field emission from the cathode surface irregularities. At a threshold current density, the field emission destroys the irregularities and produces metallic plasma which is necessary for breakdown to occur. In this case, the breakdown criterion may be the achievement of some critical current density of the positive ions. As for the physical mechanism of microdischarges in commercial vacuum, our studies confirm the concepts available in the literature.

The above experimental results as well as the evidence for the microdischarge ability develop under dropping voltage at the gap electrodes, and to extinguish at a steady voltage; non-metallic nature of the discharge plasma; low threshold voltage for the microdischarge initiation; strong influence of the electrode conditioning on their characteristics make it possible to speak about them as being a discharge process in the environment of the gases desorbed from electrodes and the electrode contaminant. At pulsed voltages of microsecond duration, the dynamic higher pressure regions of desorbed gases are able to form and electron avalanches to develop in the centimeter vacuum gaps. Quantitative estimation, comparison of the calculated and experimental data on the peak microdischarge current and its dynamics at the front and the time evolution argue in favor of their justifiability.

4. REFERENCES

1. H.P.S. Powell and P.A. Chatterton, "Prebreakdown conduction between vacuum insulated electrodes", *Vacuum*, Vol. 20, N 10, pp. 419-429, 1971.
2. Yu.E. Kreidel, N.N. Koval, and P.M. Schanin, "Pulse space discharge in vacuum", *Proc. VIII Intern. Symp. on Discharges and Electrical Insulation in Vacuum*, Albuquerque, USA, pp. F2-1—F2-7, September 1978.
3. I.I. Kalyatsky, G.M. Kassirov, and F.G. Sekisov, "On the impulse electrical breakdown of centimeter vacuum gaps", *IEEE Trans. Electr. Insul.*, Vol. EI-20, pp. 701-703, 1985.
4. G.M. Kassirov, "Desorption model of initial conductivity in commercial vacuum", *Proc. 8 All-Union Symp. on High-Current Electronics*, Vol. 3, Sverdlovsk, 1990.

Vacuum breakdown properties of oxygen-free copper electrodes machined by diamond turning for mirror finish

Shinichi Kobayashi*, Yasuyuki Hashimoto*, Yoshio Saito**, Yasuchika Nagai***, Yoshiki Yamamoto***, Kiyomatsu Takeuchi**** and Takeshi Sugano****

*Saitama University, 255 Shimo-ookubo, Urawa, Saitama, 338, Japan (FAX 81 48 855 0940)

**National Laboratory for High Energy Physics, 1-1 Oho, Tsukuba, Ibaraki, 305, Japan

***Hitachi Cable, Ltd., 3550 Kidamari, Tsuchiura, Ibaraki, 300, Japan

****Mechanical Engineering Laboratory, 1-2 Namiki, Tsukuba, Ibaraki, 305, Japan

Abstract

The electrodes used in this investigation to experimentally evaluate the effect of diamond turning on electrical breakdown characteristics in vacuum were first roughly machined by turning, and then machined to a mirror finish by diamond turning. Residual stresses of the electrode surfaces were measured by an X-ray diffraction method before and after the diamond turning. Several electrodes were annealed in vacuum for one hour at 400°C or 700°C before the diamond turning. Vacuum breakdown experiments using impulse voltages with the wave form of 64/700 μ s revealed that the diamond turning improves breakdown strength, that the conditioning of vacuum gaps is achieved by only few tens of breakdowns, and that annealed electrodes have a better hold-off voltage capability.

1. Introduction

Particle accelerators, vacuum interrupters, and other such devices, must have good insulating properties, and for better performance, the vacuum gaps must have higher hold-off voltages. In these devices oxygen-free copper (OFC) is often used in the high-voltage electrodes in vacuum, and vacuum breakdown phenomena are greatly affected by the surface condition of these electrodes. Because one cause of the electrical breakdown of vacuum gaps is the field electron emission from small protrusions on the cathode, electrode surfaces are usually polished or machined to be smooth. Polishing or machining, however, sometimes increases residual surface stresses that will affect breakdown strength. Diamond turning can be used not only to produce a mirror finish, but also to reduce the residual surface stresses caused by machining or polishing.

We therefore experimentally evaluated the residual surface stresses of OFC electrodes before and after diamond turning, and we measured the breakdown strength of diamond-turned OFC electrodes after they had been annealed under several conditions.

2. Preparation of sample OFC electrodes

Figure 1 shows the shape of OFC electrode used in this investigation. The purity of the electrodes satisfied the standards for ASTM-F-68 Class 1. Typical chemical compositions were as follows: copper was more than 99.996%, hydrogen gas content was less than 0.5 ppm and oxygen gas content was less than 2 ppm. We had previously found that Class 1 OFC electrodes have high breakdown strength and a significant conditioning effect.¹ These electrodes were first roughly machined by turning them to the mushroom shape shown in Fig. 1. Several electrodes were then

annealed in vacuum for one hour at 400°C or 700°C. These electrodes were then machined by diamond turning to a mirror finish. The cutting condition of the diamond turning of the OFC electrodes have been given in Ref.2. Residual stresses of electrode surfaces were measured by X-ray diffraction method before and after the diamond turning.

Figure 2 is a phase-contrast photomicrograph of the electrode surface after the diamond turning. It shows that the pitch is 15 μm , and the surface roughness was 0.06 μm . Diamond turning reduces residual stresses, for example, from 158.8 MPa to 42.5 MPa (Table 1).

Three pairs of OFC electrodes making three vacuum gaps were prepared in this investigation:

Gap A: Only the diamond turning

Gap B: Annealed at 400°C in vacuum and the diamond turning

Gap C: Annealed at 700°C in vacuum and the diamond turning

The experimental procedure was as follows. All of the electrodes were first ultrasonically cleaned in an acetone bath for 10 minutes and then placed into a vacuum chamber, where their surfaces were cleaned by He ion bombardment. Afterwards, a series of 500 vacuum breakdowns was carried out for each test gap. The voltages applied were positive impulses (64 μs rise and 700 μs decay) reaching a maximum of 100 kV. The pressure in the vacuum chamber before breakdown test was reduced by sputter ion pumps and Ti-getter pumps to $1\text{--}3 \times 10^{-8}$ Pa.

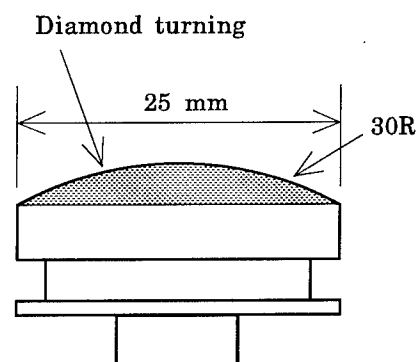


Figure 1.

Shape of the OFC electrodes.

Table 1.

Residual stresses of OFC electrodes before and after the diamond turning.

Samples	Residual stresses [MPa]			
	Before		After	
	Anode	Cathode	Anode	Cathode
Gap A	- 21.8	- 62.4	+ 66.9	+ 47.7
Gap B	+112.8	+ 76.1	+ 34.8	+ 46.8
Gap C	+158.8	+205.7	+ 42.5	+ 42.4

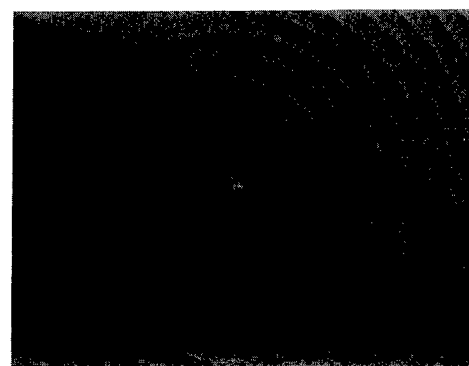


Figure 2.

Micrograph of electrode surface after diamond turning.

3. Experimental results and discussion

3.1 Breakdown field

The dependence of breakdown fields (breakdown voltage/gap-length) on the number of breakdowns is shown in Figure 3. Breakdown fields at the first voltage application are 71.4 MV/m for Gap A, 49.4 MV/m for Gap B, and 14.9 MV/m for Gap C. As a result of the conditioning effect,

these values gradually rise as the number of breakdowns increases, and then they then settle down to final breakdown fields averages of settled down values: 160 MV/m for Gap A, 230 MV/m for Gap B, and 250 MV/m for Gap C. On the other hand, in breakdown test without He ion bombardments³ the first breakdown fields were 12.5 MV/m for Gap A, 12.4 MV/m for Gap B, and 11.8 MV/m for Gap C and the final breakdown fields were 140 MV/m for Gap A, 150 MV/m for Gap B, 200 MV/m for Gap C. In the present experiments, using the He ion bombardment technique to clean the electrode surface increased the breakdown strength.

Both the first and the final breakdown fields are very important values for representing the breakdown strength, since the difference between these two values shows a degree of the effect of conditioning. The values obtained from the data shown in Fig. 3 are summarized in Table 2.

Comparing the values in Table 2 with the values obtained in another experiment carried out with electrodes machined by ordinary turning⁴, confirmed that the diamond turning results in higher breakdown fields, that is, greater breakdown strength. This is because the diamond turning of OFC electrodes releases surface residual stresses due to machining or polishing.

Furthermore, the diamond turning results in a different conditioning effect. The conditioning effect shown in Fig.3 is no longer apparent after about 100 breakdowns, whereas with only the ordinary turning of electrodes the conditioning effect continued through 500 breakdowns. Similar trends are seen in the results of the OFC⁴ and stainless steel⁵ electrodes polished with electro chemical buffing (ECB). Either diamond turning or ECB makes the electrode surfaces mirror-like, greatly reducing the size and number of small protrusions and the amount of gas adsorbed on the electrode surfaces. It is therefore expected that the conditioning of vacuum gaps can be achieved with few breakdowns.

The values listed in Table 2, we show that the final breakdown fields of Gap B and Gap C (annealed) are higher than those of Gap A (unannealed). This is because the annealing reduces gas content, and changes the quality of the electrode surface (recrystallization). Breakdown strength can thus increased by annealing of electrodes in vacuum before the diamond turning.

3.2 Electrode surface conditions

Scanning electron microscope (SEM) photographs of electrode surfaces after 500 breakdowns of Gap A are shown in Figs. 4(a) and 4(b), which show the center of the electrode surfaces magnified 50,000 times. Figure 4(a) shows the anode surface, and Figure 4(b) shows the cathode surface. These figures show many small particles, and the density of the particles is lower on the cathode surface than on the anode surface. Furthermore, grain boundaries are seen in Figure 4(b). These

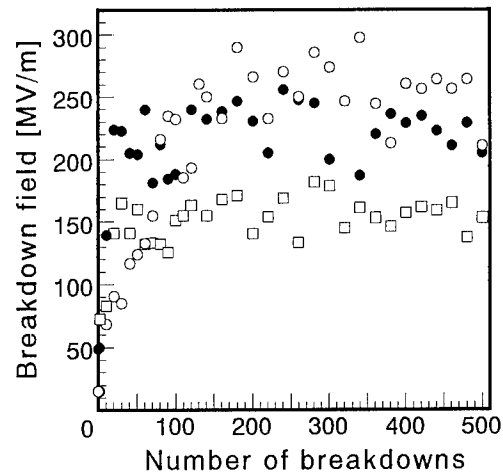


Figure 3.

Dependence of breakdown field on the number of breakdowns.

- Gap A: Diamond turned
- Gap B: Annealed at 400°C and diamond turned
- Gap C: Annealed at 700°C and diamond turned

Table 2.

First and average breakdown fields. Number in () denote the range of breakdown fields averaged.

Samples	Breakdown fields [MV/m]	
	First	Average
Gap A	71.4	160 (50-500)
Gap B	49.4	230 (50-500)
Gap C	14.9	250(150-500)

features, many small particles and grain boundaries, are not seen on the surface of OFC electrodes prepared by ordinary turning, and they indicate that the Bailby layers due to 500 breakdowns were removed.

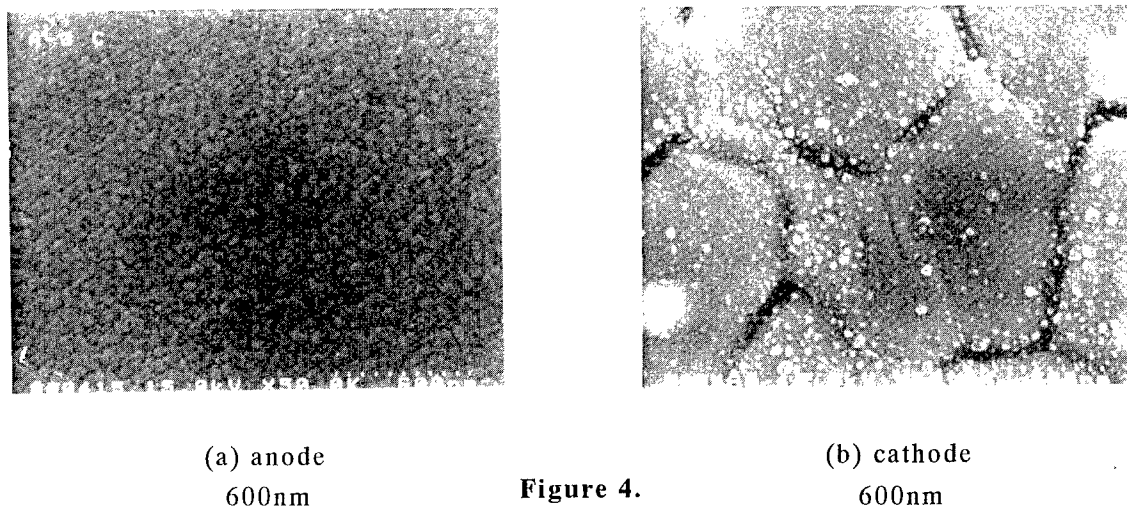


Figure 4.
Micrograph of electrode surface
after 500 breakdowns. (Gap A)

4. Conclusions

1. The diamond turning of OFC electrodes improves breakdown strength and the conditioning effect.
2. Annealing electrodes in vacuum greatly affects breakdown strength, and annealing electrodes in vacuum before the diamond turning improves breakdown strength even more.
3. SEM pictures of electrodes after 500 breakdowns show grain boundaries due to vacuum breakdown.

5. References

- 1 S. Kobayashi, Y. Saito, Y. Nagai, and Y. Yamamoto, "Vacuum Breakdown Strength Of Vacuum Degassed Oxygen Free Copper Electrodes," *Proc. 15th International Symposium on Discharges and Electrical Insulation in Vacuum*, pp. 80-84, Darmstadt, 1992.
- 2 K. Takeuchi, T. Sugano, and Y. Yoshida, "Diamond Turning of Oxygen-Free Copper for Mirrors," *Transactions of the Japan Society of Mechanical Engineers*, Vol. 57, No. 542-C, pp. 151- 156, 1991 (in Japanese).
- 3 S. Kobayashi, Y. Hashimoto, Y. Saito, Y. Yamamoto, Y. Nagai, K. Takeuchi, and T. Sugano, "Electrical Breakdown Strength of Vacuum Gaps between Vacuum Degassed Oxygen-Free Copper Electrodes Machined by Diamond Turning for Mirror Finish," To be presented in *Journal of the Vacuum Society of Japan*, 1994 (in Japanese).
- 4 S. Kobayashi, Y. Saito, Y. Hashimoto, and Y. Yamamoto, "Vacuum Breakdown Properties and Surface Conditions of Vacuum Degassed Oxygen Free Copper Electrodes," *Proc. 8th International Symposium on High Voltage Engineering*, Vol. 1, pp. 311-314, Yokohama, 1993.
- 5 T. Shioiri, T. Kamikawaji, E. Kaneko, M. Ohkawa, and I. Ohshima, "Conditioning Effect of Stainless Steel Electrodes in Vacuum," *Proc. 8th International Symposium on High Voltage Engineering*, Vol. 1, pp. 473-480, Yokohama, 1993.

Using of carbide coatings
to increase electric strength of vacuum gap

I. V. Loginov, A. S. Pokrovskaya-Soboleva

All-Russian Electrotechnical Institute, Moscow, 111250
Russia

1. INTRODUCTION

Stability of output parameters of power high-voltage vacuum devices is connected with the problem of interelectrode vacuum gap electric strength and electrode thermal loads increase as well as development of stable form electrodes. One of the way to solve this problem is using graphite being a well as known in electronics material or some other materials on the base of carbon with their unique mechanical and thermophysical properties as soon as their essential defect, the low electric strength is eliminated.

The coal-graphite materials are successfully used in those cases, when the electrode forced cooling is difficult if their form have to be saved.¹ The advantages of the carbon materials are evident: high melting temperature, high radiation and thermal conductivity coefficients, low coefficient of second emission and absence of thermal deformation.

Despite the all advantages, use of graphite and the coal graphite materials in power electron devices is limited because of disadvantages being the cause of the high-voltage vacuum gaps low electric strength. They are the following: porosity determining the high sorption ability and content of big gas volume in the electrode depth and this leads to discharge progress in the pores², relatively low mechanical strength, which in strong electric fields is the cause of slightly connected particles.³ Partly these disadvantages could be eliminated by use in the electrodes graphite condensed by pyrolytic carbon and by use a composite carbon-carbon material.

2. EXPERIMENTAL RESULTS

The experiments within the work showed that the best results of vacuum gap electric strength can be achieved after high-melting metal carbide coatings are deposited on coal graphite electrodes. The high-melting metal carbides are chemically passive to graphite and composites on the base of carbon, they surpass high-melting metals by some physical characteristics, such as melting temperature, modulus of elasticity, hardness and have less evaporation velocity as well as low coefficient of thermal expansion. From checked high melting metal carbides tantalum carbide (TaC) was used to be deposited on the graphite electrodes. The thickness, quality and structure of the coating are determined by the coating forming method. Of the four checked coating forming methods: powder sintering, vacuum deposition, plasma deposition and thermal gas-diffusion forming the latter was chosen. During the thermodiffusion tantalum atoms depositing onto the graphite surface are being formed while thermal dissociation of tantalum chloride molecules (TaCl)⁴. The realized coating has high mechani-

cal strength, uniformity, homogeneity and can be coated on electrodes of any form. The deposited coating purity grade depends on preliminary treatment of the electrodes. On polished pyrographite a mirror coating, on which any defects (omissions, cracks, chips etc) are completely absent, is created. Such coatings bear thermocycles at temperatures up to 1500 C. The thermodiffusion method makes it possible to vary the coating thickness from 50 till 200 m.

Electric strength of a vacuum gap with graphite electrodes coated by TaC are determined by the breakdown probability curves presented in Fig.1⁵. The curves were measured at the interelectrode distance of $d = 1.5$ mm in the same vacuum conditions with the oilless pumping out. The curve 1 corresponds to the pure graphite electrodes, the curve 2 corresponds to the electrodes of graphite condensed by pyrolytic carbon, the curve 3-the pyrographite electrodes coated by TaC. To be compared the electric strength curve for stainless steel electrodes gap of $d = 1.5$ mm is presented. It is evident that curves 3 and 4 are practically coincident and it means that a carbide - tantalum coating on graphite allows increasing breakdown voltage of a vacuum gap three times and make it closer to breakdown voltage of stainless steel.

The essential increasing breakdown voltage of a vacuum gap after the carbide - tantalum coating is deposited can be caused by several reasons. One of them is absence of slightly connected particles and consequently, - decreasing probability of the graphite electrode surface ledges forming with raised intensity of local electric field.⁶ The second likely explanation ahypothesis of Tatarinova N. V.² gives. The matter of it is that breakdown can appear at the field intensity which is essentially less than it is needed for autoelectron emission. Porosity decrease when depositing and consequently gas - saturation reduce leads to lessening ionization probability in the graphite electrode micropores which usually sharply decrease the electric strength.

In the work some physical constants of the graphite TaC coating are received: gas penetrability at the 100 μ coating thickness and room temperature- 10^{-13} mm Hg l/cm²s; second electron emission coefficient at the voltage up to 5 kV- less than 1; effective work function of electron at the 1470 - 1970 K temperatures- 3.55 - 3.7 eV; integral radiation coefficient- 0.25 - 0.35.

The high electric strength and positive data on some physical properties of the coating made it possible to use successfully graphite electrodes with the TaC coating when creating high-current, high-voltage accelerators.

In Fig. 2 a photograph of an accelerator diode with the mosaic cathode of lanthanum hexaboride is presented. The cathodic electrode, accelerating greed and cathode housing are made of graphite with the TaC coating. The cathode - greed interval is equal to 10 mm. In cold state the accelerator diode has been training by high voltage for several hours up to 300 V. Under the heated cathode conditions operation voltage was equal to 100 kV at the 400 A beam current and 100 μ s pulse width. After the vacuum being lost the second training time much shortened and the operation voltage value was achieved within 10- 15 minutes.

3. CONCLUSIONS

As a result of the carried out work it is established, that the electric strength of the vacuum gaps with graphite

electrodes can be increased more than three times when using high-melting metal carbide coatings and achieve the values corresponding to the stainless steel electrodes.

4. References.

1. A. S. Pokrovskaya-Soboleva, A. L. Shapiro and others. "Studies of Pyrocarbon Properties as a Construction Material for Gas-discharge Devices". Electron technics, Ser. 4, Iss. 6, p. 79, 1975
2. N. V. Tatarinova. "Mechanism of Electric Insulation Disturbance when gas Discharge Igniting in the Electrode Surface Micropores". Moscow, MIFI, 1983
3. N. B. Rosanova. Vacuum breakdown initiated by macroparticles, IV of the USSR Academy of Sciences, Ser. Phys.V. 26, # 11, p. 1438, 1962
4. N. N. Repnikov, N. S. Gorbunov. "Physical - chemical Conditions of Niobium Carbide Deposition onto Graphite", Volume "Temperature-stable Coatings, Nauka, p. 124-130, 1963
5. A.S. Pokrovskaya-Soboleva et al. "Dependence of vacuum breakdown probability upon surface condition of electrodes", 10th International Conference on Phenomena in Ionized Gases, Oxford, p.92, 1971.
6. A. S. Pokrovskaya-Soboleva, V. V. Kraft and others. "Effect of a Cathode Surface Microrelief on Vacuum Breakdown", JTF, V. X[[, p. 1318, 1972

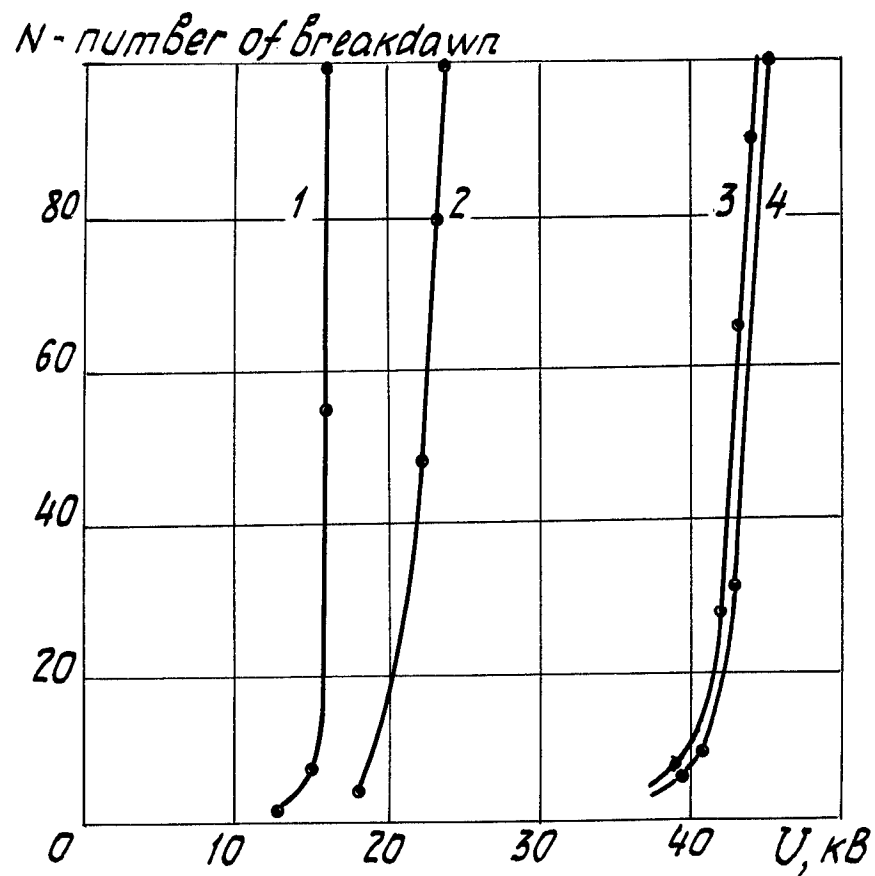


Fig.1-Electrical strength of the vacuum gap, $d=1.5\text{mm}$.
 1-graphitic electrodes, 2-pyrolytic graphitic electrode,
 3-carbide tantalum coated graphitic electrodes, 4-stain-
 less steel electrodes.

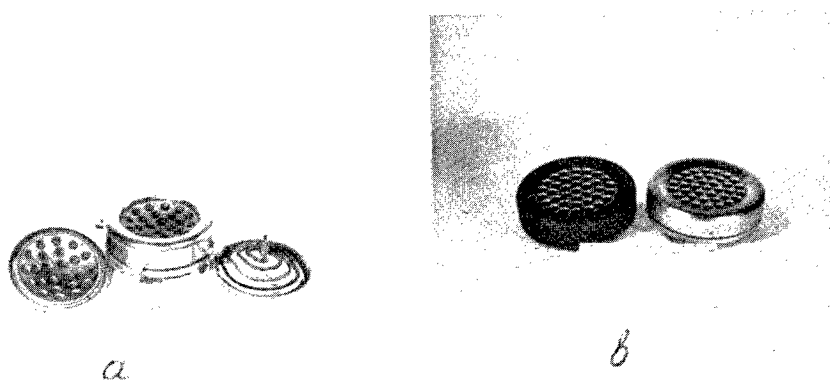


Fig.2a,b-Photos of accelerator diode electrodes made of
 graphit covered with TaC.

Properties of ectons in a vacuum discharge

G. A. Mesyats

Institute of Electrophysics
Ural Division, Russian Academy of Sciences
Ekaterinburg 620219, Russia

ABSTRACT

The paper deals with ectons, emission centers produced on the surface of a cathode as a result of heating and explosion of its material due to large specific energy accumulated in cathode microvolumes. The criteria for the initiation and self-sustaining of ectons are given and their parameters and types are discussed.

1. INTRODUCTION

It has been shown¹⁻³ that the microexplosions occurring on a cathode cause intense electron emission accompanied by ejection of electrons, plasma, metal vapor and microdrops. This phenomenon was named Explosive Electron Emission (EEE)^{3,4}. It was believed that there exists only one mechanism for microexplosions: heating of the cathode microexplosions due to field emission (FE)⁵. EEE plays a fundamental part in a vacuum discharge². The goal of this paper is to show that there exist a number of microexplosion mechanisms and FE is only one of a few possible initiating phenomena.

For instance, consider how the FE-initiated EEE appears and proceeds. When the current density j is greater than 10^8 A/cm², a microexplosion on the cathode surface takes an energy of the order of 10^4 J/g and explodes in time t_d , which can be found for many metals from the relation

$$\bar{h} = \int_0^{t_d} j^2 dt, \quad (1)$$

where \bar{h} is named a specific action. Its value for metals, such as Cu, Al, Au, Ag, Ni, and Fe is, respectively, 1.91, 0.92, 0.83, 1.04, 0.73, $0.54 \cdot 10^9$ A² · cm⁻⁴ · s.

Once an explosion occurs, an EEE current starts flowing and a microcrater appears on the cathode. When the EEE current exceeds some threshold value i_{thr} (a few amps), the current produced by the first microexplosion ceases (in a time of the order of $10^{-9} - 10^{-8}$ s), the process becomes self-sustaining, and each new microexplosion behaves in fact like the secondary electrons in a gas discharge, that appear at the cathode under the action of ions, photons, metastables, and the like. I have named this phenomenon an ecton, since the zone of EEE operation is often referred to as an explosion center. The term 'ECTon' has been constructed using the first letters of these English words. An ecton is a short electron burst emitted from a localized region on a cathode.

Thus, for a primary electron to appear, it is necessary that the specific energy in a cathode microvolume be high enough ($> 10^4$ J/g), and for the primary ecton to be able to initiate one or several secondary ectons, its current should be greater than some threshold current. These are in fact two principal criteria for the appearance and self-sustaining of ectons. It can readily be shown, however, that these conditions may be provided not only by field emission, but also by other similar processes.

2. INITIATION AND SELF-SUSTAINING OF ECTONS

The energy density needed to be accumulated in a cathode microvolume for a microexplosion to occur can be provided by an intense flow of laser radiation, plasma, or ions, a fast microparticle impact, a discharge over the surface of a dielectric in the place of its contact with a point (triple point), by producing metallic cathode-anode bridges, etc. These processes, however, not necessarily should result in microexplosions. There exist some accompanying effects, which appear at comparatively weak energy fluxes, that further promote the accumulation of energy in cathode microvolumes. The most important of them is the interaction of the cathode surface with

plasma. Plasma may be generated, in particular, as a result of evaporation of cathode material from a microarea or gas desorption under the action of high temperatures and subsequent ionization of the gas and metallic vapor by an electric field. The short time scale of the electron emission in an ecton is conditioned by the facts that the emitted current is low and exists for a short time and that eventually the self-cutoff of current occurs due to cooling of the emission zone. The criterion for an ecton to be initiated is that the needed energy be accumulated in microvolume W_0 of the cathode at its surface in a time shorter than the characteristic time of energy scattering τ :

$$\frac{dW}{dt} > \frac{W_0}{\tau}, \quad (2)$$

where W_0 is of the order of the sublimation energy and $\tau = b/v_s$ (b is the linear dimension of the explosion region and v_s is the velocity sound). If energy scattering occurs through heat conductance, it is necessary to have $b \ll \sqrt{a\tau}$, where a is the thermal diffusivity.

Let us now discuss the criteria for an ecton to be self-sustained. The self-sustaining is due to the plasma - metal surface interaction. Scattered ectons appear, as a rule, as a result of charging dielectric films and inclusions present on the cathode by plasma ions. If we assume that an ecton is produced when the electric field inside the dielectric reaches $E > 10^6$ V/cm, then, in order that this film be charged in $t < 10^{-9}$ s, it is necessary to have

$$n_i v_i > 10^{23} \text{ cm}^{-2} \cdot \text{s}^{-1}, \quad (3)$$

where v_i is the velocity of ions and n_i the ion density. If $v_i \approx 10^6$ cm/s, then, for an ion density $n_i \approx 10^{17}$ cm $^{-3}$, we may expect that ectons will appear under the action of the plasma coming at the cathode.

Grouped ectons appear, to our opinion, due to an increase in the current density through the neck formed during the detachment of a drop from the cathode surface or through cathode microprotrusions. If we assume that the main current component is ionic, then, in order that the current density through the neck be 10^9 A/cm 2 , it is necessary that the inequality

$$n_i v_i > \frac{10^{28}}{\beta_j}, \quad (4)$$

where β_j is the current density enhancement factor, be satisfied. If we even assume that $\beta_j \approx 10^2$ to 10^3 , then, for grouped ectons to appear, it is necessary that the plasma density be 2 to 3 orders of magnitude greater for the same ion velocity 6 .

Let us consider how the value of β_j can be estimated for variously shaped microprotrusions. Let the surface area of a microprotrusion be equal to S and the place of its contact with the cathode has the shape of a circle of radius r . Then the ion current $j_i S$ incident on the microprotrusion surface will have the density in the place of contact $j_i S / \pi r^2$. The current density enhancement factor will then be

$$\beta_j = \frac{S}{\pi r^2}. \quad (5)$$

For instance, for a cylinder on a plane, β_j will be $2h/r$, where h is the cylinder height; for a cone l/r , where l is the length of the cone generating line, and for a sphere $4R^2/r^2$, where R is the sphere radius. The h/r value for cylindrical microprotrusions is well known from measurements, because it is also a characteristic of the electric field enhancement, and typically it is 10^2 or more 7 . For a spherical microprotrusion, β_j may be 10^3 or greater. This effect increases the plasma ion flow density onto the cathode, what may lead to appearance of secondary ectons.

Using the EEE phenomenon as an example, let us show why an ecton exists for a short time ($\sim 10^{-9}$ to 10^{-8} s) and then disappears, giving rise to new ectons. This is due to the fact that the crater formed as a result of the Joule heating of the cathode by the EEE current is increased in radius, evaporates atoms, and ejects hot liquid metal. This causes the crater to cool and the emission to cease. It was already mentioned that there exist two

types of ecton. The first-type ectons are realized, when the craters formed on the cathode surface do not touch each other in the geometrical sense, while the second type of ecton corresponds to the case, where secondary craters appear in the place of the primary ones or away from them. Ectons of the first type appear due to the expansion of plasma over the cathode surface or the charging and subsequent breakdown of dielectric films and inclusions, what was said above. The second-type ectons are formed as a result of energy accumulation at the cathode during the liquid metal - plasma interaction. We mentioned that an efficient mechanism for the production of secondary ions may be the explosion of the liquid metal neck formed during the detachment of a drop from the cathode. In this case, the ion current density onto a spherical drop may reach more than 10^6 A/cm². Taking into account that in this case $\beta_j = 4R^2/r^2 \geq 10^3$, we have that, according to Eq. (1), the explosion of the neck will occur in a time $t_d < 10^{-9}$ s. In vacuum arcs⁸ and at EEE³ the number of microdrops γ varies between 10^7 and $5 \cdot 10^7$ C⁻¹ for various metals. Then, supposing that the threshold current i_{thr} needed for self-sustaining of ectons is equal to the current at which though one drop will appear within the cycle time τ_e , we shall obtain the criterion for the self-sustaining of ectons in the form

$$\gamma \tau_e i_{thr} \geq 1. \quad (6)$$

For the above value of γ and $\tau_e \approx 10^{-8}$ s, the current i_{thr} should be equal to a few amps, which agrees with experimental data for EEE³ and vacuum arcs⁹.

3. ESTIMATION OF THE ECTON PARAMETERS

For ectons scattered over a plane metal surface, which are formed in a time of the order of 10^{-9} s, the radius of the crater produced by an ecton and the mass removed from the crater can be estimated from relations derived with the use of a simple Joule model:

$$r_{cr} = \left(\int_0^{\tau_e} i^2 dt / 4\pi^2 \bar{h} \right)^{\frac{1}{4}}, \quad (7)$$

$$M_1 = \frac{\rho}{3\sqrt{2\pi}} \left(\int_0^{\tau_e} i^2 dt / \bar{h} \right)^{\frac{3}{4}}. \quad (8)$$

Note that the current in these formulas is lower than the threshold current. For example, for Cu ($\tau_e = 10^{-9}$ s) and $i = 1$ A we have $r_{cr} \sim 10^{-5}$ cm and $M_1 \approx 0.5 \cdot 10^{-13}$ g.

The situation is more complicated when $i \geq i_{thr}$. Then the effect of ecton self-sustaining takes place. If we assume that the self-cutoff of current occurs at the instant when heat removal starts playing a part and that $r_{cr} = \sqrt{at}$, then the time needed for an ecton to operate is determined from the relation

$$\tau_e = \frac{i^2}{4\pi^2 a^2 \bar{h}}, \quad (9)$$

and the crater radius is found from

$$r_{cr} = \frac{i}{2\pi(a\bar{h})^{\frac{1}{2}}}. \quad (10)$$

Recall the values of the thermal diffusivity a for various metals. For Ag, Al, Au, Cu, Mo, Fe, W, and Ni it is, respectively, 2.6, 1.1, 1.03, 1.41, 0.59, 0.25, 0.75 and 0.26 cm²/s.

In deriving formulas (9) and (10) it was assumed that the current i does not vary in time. This is also valid for an arc. For $i \sim 10$ A we have for copper from Eqs. (9) and (10) $\tau_e \sim 10^{-9}$ s and $r_{cr} = 3 \cdot 10^{-5}$ cm. The time τ_e for lower currents will be shorter than the measured time of an ecton cycle, because the supposition that the emission ceases only due to the onset of influence of heat conductance seems to be not fully correct. There exist more sluggish processes. For instance, from the drop model of ecton self-sustaining it follows that a new ecton will

appear only when though a single drop escapes from the crater. Therefore, the minimum cycle time should not be shorter than the time needed for metal ejection from the crater to occur:

$$\tau_e > \frac{r_{cr}}{v}. \quad (11)$$

Here, v is the velocity of motion of the liquid metal. For copper and $i = 1$ to 100 A, we have $v \sim 10^4$ cm/s, then, with Eq. (7) taken into account, we obtain that the minimum cycle time should be no shorter than one nanosecond.

In explosive electron emission, as a contrast to an arc, the current increases with time. Let $i = kt$ be valid, then we have

$$\tau_e = \frac{12\pi^2 a^2 \bar{h}}{k^2}, \quad (12)$$

$$r_{cr} = \frac{2\pi\sqrt{3} a^{\frac{3}{2}}}{k} \sqrt{\bar{h}}. \quad (13)$$

It is difficult to determine experimentally the threshold current for EEE, since an ecton develops at a high rate of current rise, $\frac{di}{dt}$. Therefore, to estimate the threshold current for metals, it would be better to use the data by Kesaev⁹ obtained in vacuum arc experiments. For instance, for Cu, Ag, Au, Al, Mo, W, Fe, and Ti, the threshold current for an arc is, respectively, 1.6, 1.2, 1.4, 1.0, 1.5, 1.6, 1.5, and 2.0 A.

Let us now consider on a qualitative level the reason for the current cutoff in an ecton. This problem is directly related to the mechanism for electron emission from a metal. There is no doubt now that this is thermal electron emission enhanced by the Schottky effect due to the electric field present at the plasma - metal boundary. In terms of the classical thermal model, we supposed that in a time of $\sim 10^{-9}$ s the cathode temperature becomes much higher than the boiling temperature. If we assume that the Richardson - Schottky formula is valid for this case, we may write:

$$j = AT^2 \exp\left(\frac{-(e\varphi - \alpha E^{\frac{1}{2}})}{k_B T}\right), \quad (14)$$

where $A = 120.4$, $\alpha = 3.79 \cdot 10^{-4}$, φ is the work function ($\varphi = 4.4$ eV for copper), E is the electric field at the emission surface, V/cm, T is the cathode temperature, K, and j is the electron current density, A/cm².

Modeling the processes occurring in an ecton has shown that the field E is no greater than 10^5 V/cm. This suggests that the correction for the Schottky effect, $\alpha E^{\frac{1}{2}}$, in the exponent term is not of principal importance in determining the current density j . According to the estimates, for copper with the input energy equivalent to 10^4 and $7 \cdot 10^3$ K, the current density will be $\sim 10^8$ and only $5 \cdot 10^6$ A/cm², respectively. That is, when the ecton zone is cooled by 30 orders of magnitude.

Thus, the process of current cutoff in an ecton can be imagined as follows. Once an ecton has been initiated, the current density is about 10^9 A/cm². Then there occurs fast heating in a microvolume of cathode metal and its explosion, giving rise to efficient field-assisted thermal electron emission. As the explosion develops, the emission zone expands, heat removal intensifies, and more and more heat is removed due to the evaporation and ejection of hot liquid metal. This decreases the temperature in the ecton operation region and the current density of field-assisted thermal electron emission. The decrease in emission current density in turn results in that the cooling of the emission zone becomes more rapid due to less intense Joule heating.

On the basis of the available results on EEE, we may estimate the parameters of ectons and the aftereffects they cause. Let us do this for a plane copper surface with a current close to the threshold current.

First, we find how many electrons per cycle are emitted by an ecton. It is obvious that

$$N_e = \frac{i_{thr} \tau_e}{e}, \quad (15)$$

where e is the electron charge. That is for $i_{thr} \sim 1$ A and $\tau_e \sim 10^{-8}$ s we have $N_e \approx 10^{11}$. If we assume that the current linearly increases with time, we may use Eq. (12). For the current rise rate 10^{10} A/s and $\tau_e = 10^{-8}$ s, we obtain $N_e \approx 10^{12}$. The energy needed to initiate an ecton, W_e , can be estimated by the specific energy W_0 needed to remove from a crater a portion of metal of mass M_1 . Since $W_0 \approx 10^4$ J/g and $M_1 \sim 10^{-12}$ g, then we have

$$W_e = M_1 W_0, \quad (16)$$

i.e. $W_e \approx 10^{-8}$ J.

Recall that the reduced mass removed from the ecton operation region is $\sim 10^{-5}$ g/C. In the process of ecton operation, the current density decreases from 10^9 to about 10^8 A/cm². When an ecton operates, metal drops, vapor, and plasma are ejected. The velocity of plasma expansion is $\sim 10^6$ cm/s, the velocity of drops is $> 10^4$ cm/s, and the number of drops is $> 10^7$ C⁻¹. In the region of ecton operation, the plasma density is of the order of 10^4 atm and the plasma temperature is 4 to 5 eV.

4. ECTON TYPES

As we mentioned above, ectons may be scattered or grouped, depending on the cathode surface condition. For a surface covered with dielectric films and inclusions, much lower plasma density and temperature are required for secondary ectons to appear. So it seems that the critical vacuum arc current is lower for a contaminated surface than for a clear one.

Besides the classification associated with the surface properties, there exists a classification of ectons based on the value of the emitted current. If the current is higher than the threshold current, the ecton is referred to as a self-sustaining ecton, otherwise it is referred to as a non-self-sustaining ecton. All above discussed ectons were in fact self-sustaining ectons and we named them ectons for simplicity.

Finally, ectons may be classified by the type of the electrode where they appear. All above discussion was about cathode ectons, i.e. cathode microexplosions which eject an electron burst. However, there is no doubt that, when a microexplosion occurs at an anode, the plasma produced will emit positive ions, i.e. an anode ecton will be initiated. It seems that such an anode ecton should be non-self-sustaining, since an ion current is always much lower than the corresponding electron current, all other conditions being the same. In a vacuum discharge, for instance, the anode ecton is of minor importance. It promotes the initiation of a cathode ecton. The properties of anode ectons are still not well studied. This is the matter of future.

5. REFERENCES

1. G. A. Mesyats, *Studies on the Generation of Intense Nanosecond Pulses*, Doctoral Thesis, Tomsk, Polytechnical Inst., 1966.
2. G. A. Mesyats and D. I. Proskurovsky, *Pulsed Electrical Discharge in Vacuum*, Springer, Berlin - Heidelberg, 1989.
3. G. A. Mesyats and D. I. Proskurovsky, 'Explosive electron emission from metallic points', *Pisma Zh. Eksp. Teor. Fiz.*, Vol. 13, pp. 7-11, 1971.
4. G. A. Mesyats, 'The role of fast processes in vacuum breakdown', *Proc. Xth Intern. Conf. on Phenomena in Ionized Gases*, Vol. 2, Inv. Pap., pp. 333-363, Oxford, 1971.
5. G. N. Fursei and Vorontsov-Veljaminov, 'A qualitative model of the initiation of a vacuum arc', *Zh. Tekh. Fiz.*, Vol. 37, pp. 1870-1888, 1967.
6. G. A. Mesyats, 'Ectons in electrical discharges', *Pisma Zh. Eksp. Teor. Fiz.*, Vol. 57, pp. 88-99, 1993.
7. I. N. Slivkov, *Processes at High Voltages in Vacuum*, Energoatomizdat, Moscow, 1986.
8. T. Utsumi and J. H. English, 'Study of electrode products emitted by vacuum arcs in form of molten metal particles', *J. Appl. Phys.*, Vol. 46, pp. 126-131, 1975.
9. I. G. Kesaev, *Cathode Processes of an Electric Arc*, Nauka, Moscow, 1968.

THE NON-SELF-MAINTAINED DISCHARGE IN VACUUM.

M.M. NIKITIN

Institute of Electrophysics Russia Academy of
Sciences (laboratory of electron-ion technology, Moscow)

ABSTRACT

For production of ionized atom fluxes a method of evaporating materials in vacuum by means of non-self-maintained discharge was developed. The conditions of the initiation discharge were examined. The necessary conditions are attainment of fixed vapor or gas pressure between the electrodes and presence of pre-breakdown current. The characteristics of the discharge in the voltage range from 30 to 700 V with currents of 1 to 50 A were investigated. The discharge plasma was studied with the assistance of electrostatic probes.

The considered discharge region occupies the transition region from glow to arc. The cathode temperature is one of the fundamental parameters which defines the type of discharge and its burning. The regulation of temperature and discharge power influences on the processes which proceed on the cathode and in the space between the electrodes. The operation in different regimes results in the ability to control of ionization degree from 2 to 100%.

1. INTRODUCTION

In 1967 the method, in which the evaporation of metals was created by means of non-self-maintained discharge was proposed for vacuum deposition of thin films and coatings /1/. Use of discharge resulted in the ionization of evaporated atoms. The ionization of deposited atoms and control over the energy allowed to deposit of the coatings with controllable microstructure and physical properties /2-3/. The method is used in a wide variety of applications. In this paper the results of investigations of the main characteristics of discharge in metal vapor are given.

2. EXPERIMENTAL CONDITIONS.

The principle of vacuum deposition by means of non-self-maintained discharge is shown schematically in Fig.1. The evaporator consists of a heated tungsten ring cathode, an anode (material to be evaporated) and a system of magnetic and electrostatic focusing. The cathode was grounded. This evaporator is similar to the construction of conventional electron beam gun with a ring cathode. It differs, however, in one important aspect that a cathode-anode assembly, a power source and a system of

focusing produce the initiation of the discharge in deposit vapor.

The accelerated electron flux bombards an anode. The deposit material is heated and evaporated. As a result of collisions with the electrons the evaporated atoms are activated and ionized. The probe ion current is appeared /Fig.2./. With increase of the heating power a vapor pressure between electrodes and a current are increased. At some values of the evaporation rate and pre-breakdown current, which depend on the thermophysical properties of deposit material and on the design parameters, between two electrodes the discharge in the vapor of the deposited material is initiated. The discharge initiation is characterized by the appearance of the luminous plasma. The light of the ionized vapor spreads deeply into the chamber. The stabilization of the discharge with the lowering characteristics is reached by the use of a power source with a suitable performance and a additional resistance. Copper, chromium, silver, titanium and nickel were evaporated. The extractive plasma discharge was studied with the assistance of electrostatic probes.

Initiation of the discharge in vacuum is produced by operating the evaporator as an electron-beam gun for the attainment of fixed vapor pressure, or leakage in gas between the electrodes. The first scheme of initiation the greatest application has found. The dependance of the conditions of initiation discharge and its burning were considered due to the vacuum, the evaporated metals, the cathode/anode distance and the cathode temperature.

3.RESULTS AND DISCUSSION.

The vacuum conditions in evaporator may influence profoundly on stability of the discharge in metal vapor. In a chamber under the pressure more than 0.1 Pa is initiated the glow discharge in residual gases simultaneously with evaporation of metals. The shunting degree of main discharge by glow depends on the pumping speed, the rate of desorption of the evaporator components and degassing of the evaporant. With the decrease of pressure less 0.01 Pa the glow discharge disappears, a burning of discharge in metal vapor is stabilized. A starting pressure of residual gases in a chamber must not be more than 0.005 Pa.

According to the obtained results, the necessary conditions for initiation of the discharge are attainment of fixed vapor pressure between the electrodes and ionization of evaporated atoms. The necessary power for initiation is decreased with decreasing heat of metal vaporization and the distance cathode/anode.

The characteristics of the discharge were considered in the voltage range from 30 to 700 V with currents of 1 to 50 A. Change of the regime is achieved by control of the discharge power and the use of the power source with suitable performance. The fundamental dependences were obtained under examination of the high voltage region discharge (voltage from 100 to 700 V with currents up to 10 A).

The study of an electrical discharge through gas at low pressures shows that its character is determined mainly by processes at the cathode /4/. At the non-self-maintained discharge these processes depend on the cathode temperature. The two regions of the cathode work were considered, in field of negative space charge (the cathode temperature more 2100 C) and limitation of the thermoelectronic emission (the cathode temperature 1800-1900 C).

In first instance the discharge current is provided by thermoelectron emission completely. The power does not change at the discharge burning practically. At ground potential the probe current is negative as a result of very high electron mobility. The fluctuation appearance is possible. The fluctuations disappear, the luminescence intensity strengthens, the probe current is made positive at increasing of discharge power.

In the second the discharge current is considerably greater than the thermoelectronic emission current. The additional electron emission is attained due to secondary electron emission. The power increases at the transition in the discharge. The discharge plasma characterizes by the intensive luminescence. The probe current is positive. The less the cathode temperature the higher the discharge voltage.

4. CONCLUSION.

Change of the cathode temperature provides the different electron emission mechanisms and influences on the parameters of the discharge. By regulation of the cathode heating and the discharge power may to influence on the processes, which take place at the cathode and in the space between electrodes, and, therefore, to change the ionization of evaporated atoms.

The glow discharge transitions to arc with increasing of the discharge current at work in region of low voltage, less than 100 V (Fig.3.). The thermal ionization occurs simultaneously with ionization by collisions the energetic electrons with the vapor atoms. The ionization degree of evaporated atoms increases and may to approach 100%. As a result of this investigation, the recommendations of discharge use in the processes of vacuum deposition and surface modification were developed.

REFERENCES

1. M.M. Nikitin, G.N. Klebanov, M.X. Shorshorov, N.N. Rycalin. USSR Patent No. 213533 (1967)
2. M.M. Nikitin, Technology and equipment of vacuum deposition, Metallurgia, Moscow, 1992
3. J.E. Greene, Sol. St. Technol., 30 (1987) 115
4. A. von Engel, Ionized gases, Clarendon Press, Oxford, 1955

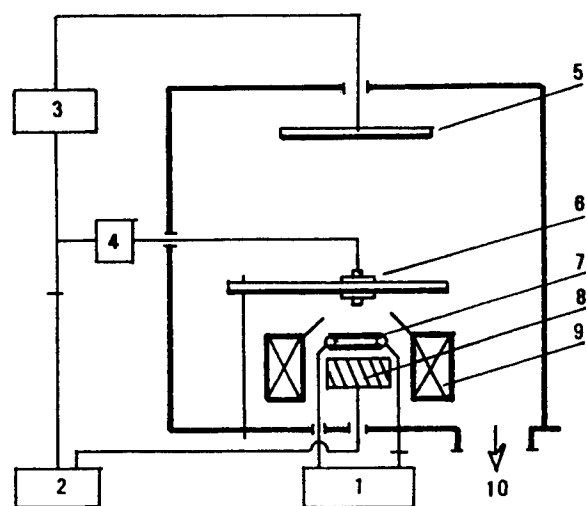


Figure 1. Schematic diagram of vacuum deposition by means of non-self-maintained discharge. Power sources of cathode heating(1),discharge(2),bias voltage(3) and plasma diagnostic(4);substrate(5);shutter with current sensor(6);heated cathode(7);evaporated material(8);system of electromagnetic focusing(9);diffusion pump connection(10).

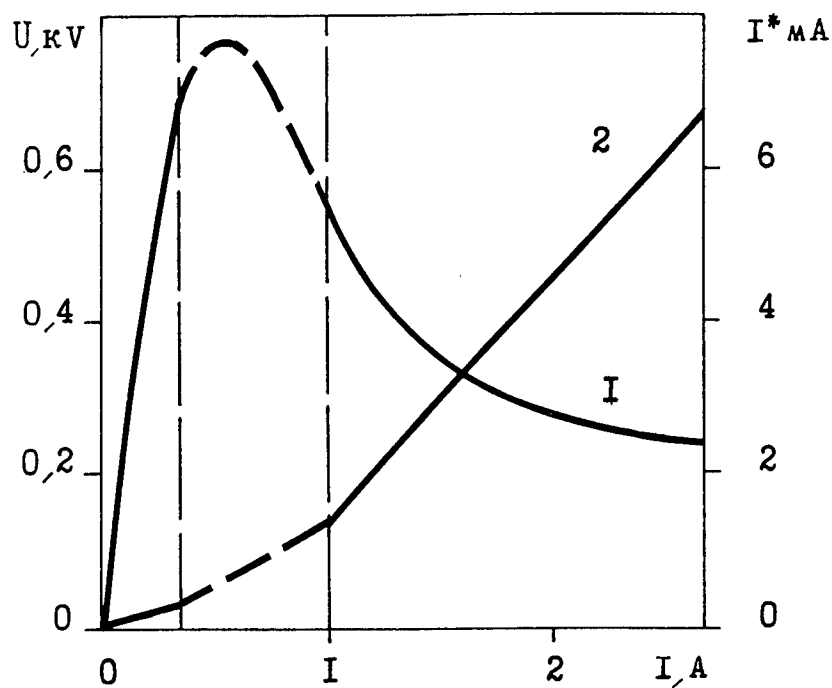


Figure 2. Current-voltage characteristic of initiation of the non-self-maintained discharge in vapor metal(1) and variation of the probe current(2).

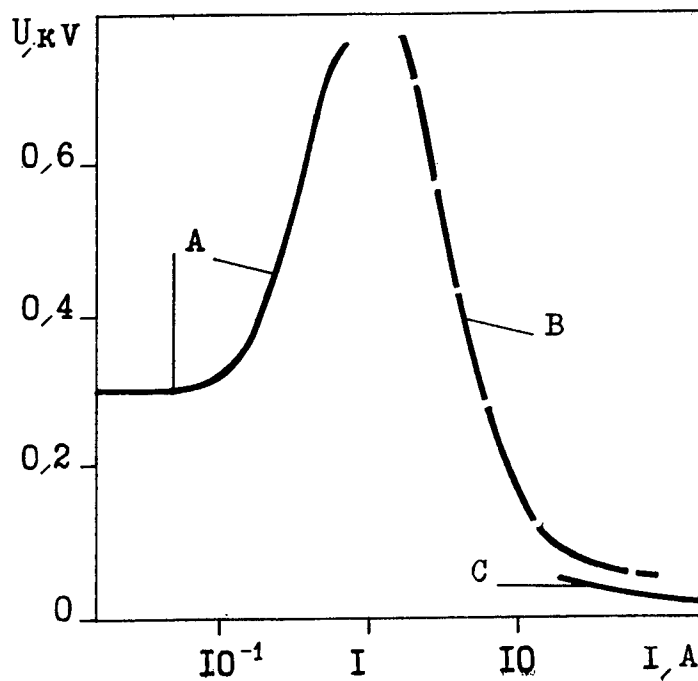


Figure 3. Current-voltage characteristics of an electrical discharges at low pressures. A- the glow discharge, B- the cathode arc, C- the non-self-maintained discharge.

Influence of Electrode Area on Conditioning in Vacuum Gap Breakdown

T. Shioiri, T. Kamikawaji, E. Kaneko, M. Homma, I. Ohshima

Toshiba Corporation
Tokyo, Japan

ABSTRACT

Using three kinds of copper electrodes with different surface areas, experiments were performed to investigate the influence of electrode area on conditioning effect, which is a characteristic of dielectric breakdowns in vacuum gaps. The conditioning process varied with electrode area: the smaller the electrode area, the sooner conditioning ended. Breakdown voltages after completion of conditioning also depended on electrode area: the smaller the electrode area, the higher the breakdown voltage.

1. INTRODUCTION

In research and development on vacuum interrupters for vacuum circuit breakers with a high vacuum as an insulating and arc extinguishing medium, studies on the materials and the surface conditions of electrodes are important, because dielectric breakdown characteristics in a vacuum depend greatly on electrode surface conditions such as roughness, depositions and oxides.¹⁻³ A phenomenon known of the effects of such factors is the "conditioning effect," which means that repeated dielectric breakdowns cause breakdown voltages to be improved. Treatments with the conditioning are generally employed in vacuum apparatus to which high voltages are applied. From past investigations, it is considered that a conditioning effect is achieved by removing adsorbed gas and deposits, forming a melted layer and smoothing microprotrusions due to the surface melting in dielectric breakdowns.⁴ It is also known that the dielectric breakdown characteristics of vacuum gaps vary with electrode surface area.² A new investigation was carried out of variations in conditioning processes with electrode surface area.

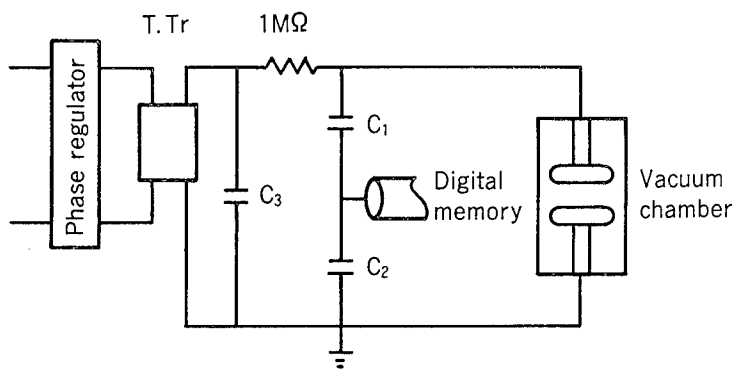
2. TEST METHOD

Conditioning processes in which breakdown voltages were gradually raised by repeated dielectric breakdowns were compared for three electrode shapes: a) hemisphere - hemisphere (20mm in diameter), b) plane - plane (34mm in diameter) and c) plane - plane (79mm in diameter). The electrode material was oxygen-free copper (Cu: 99.99% or up, O₂: 10 ppm or less). The gap length was 1.5mm. For thermal treatment, the chamber and electrodes were baked beforehand at around 150°C. To measure breakdown voltage V_b and pre-breakdown current I_e , the measuring circuit shown in Fig. 1 was used. One of the measured waveforms of the pre-breakdown current is shown in Fig. 2. The applied voltage waveform was of a 50Hz AC voltage with the polarity of the first wave phase-adjusted, and the application time was 50ms. The breakdown voltage measured was that at the first wave of the applied voltage. The relation between breakdown voltage/pre-breakdown current and the number of voltage applications was obtained.

3. CONDITIONING EFFECT

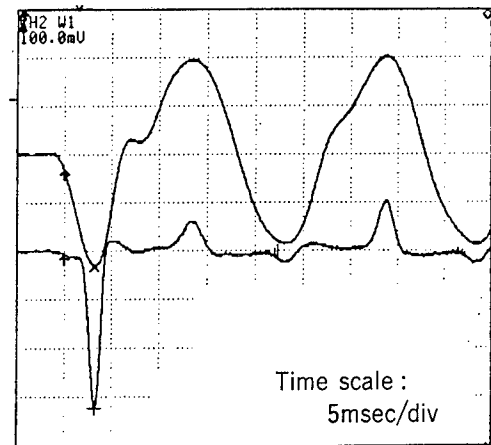
The conditioning effect is the phenomenon of the breakdown voltage being raised by repeated dielectric breakdowns, which can be attributed to the following three factors: First, as the electrode surface is melted by dielectric breakdowns, adsorbed gas and deposits evaporate, cleaning the electrode surface. Second, as the electrode surface is melted by dielectric breakdowns, microprotrusions on it are flattened, causing the electric field emission from the cathode surface to be reduced. Third, as the electrode surface is melted, it is cooled rapidly, causing a fine structure layer to be formed.

The conditioning process, as an index of the rate of breakdown voltage rises, is usually represented by the relation between breakdown voltage V_b and number of voltage applications N . It is empirically known that this relation is as shown in Fig. 3. V_b rises exponentially with N from the initial value V_1 to the limit value V_L . We then tried to formulate this V_b - N relation in the conditioning process as



T. Tr : test transformer
 C_1, C_2 : capacitance dividers
 C_3 : capacitor capacitance

Fig.1 Test circuit



Upper trace : Applied voltage 35.9kV/div
 Lower trace : Prebreakdown current 585μA/div

Fig.2 Waveforms of applied voltage and prebreakdown current

$$V_{bn} = V_1 + V_a [1 - \exp \{-(N-1)/\alpha\}] \quad (1)$$

$$V_a = V_L - V_1 \quad (2)$$

where V_{bn} represents the breakdown voltage at Nth voltage application in conditioning and α is a conditioning coefficient as an index of the rate of breakdown voltage rises for number of voltage applications. The smaller the value of α , the sooner the conditioning process ends.

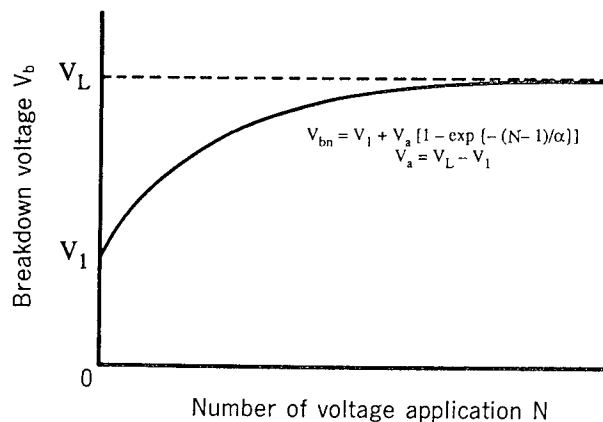


Fig.3 Relation between breakdown voltage V_b and number of voltage application N

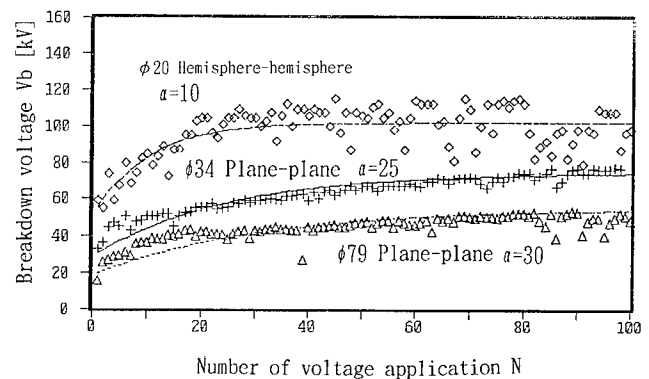


Fig.4 Relation between breakdown voltage V_b and number of voltage application N

4. EXPERIMENTAL RESULTS

4.1 Variations in conditioning process

Fig. 4 shows the V_b - N relations for the three kinds of electrodes with different shapes. The larger the electrode, the smaller the value of conditioning coefficient α , involving faster conditioning. Fig. 5 shows micro-graphs of electrode surfaces. In terms of electric field strength, the locations of dielectric breakdowns concentrated on the zone with electric field strength 90% or higher of the maximum. The area of this zone was defined as the effective area S_{eff} (the area of the

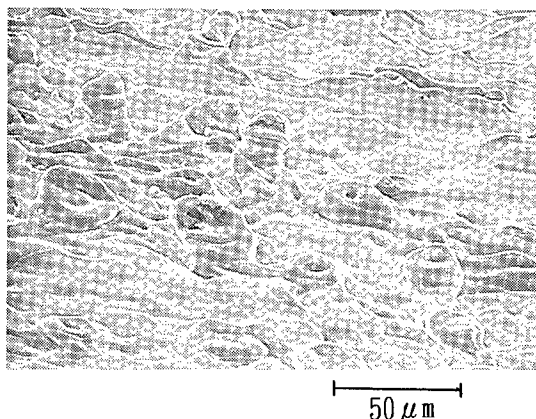


Fig.5 SEM photograph of electrode surface after conditioning

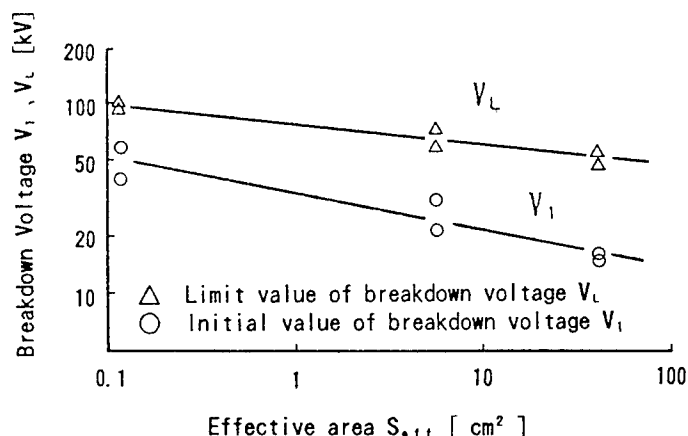


Fig.6 Relation between breakdown voltage V_1 , V_L and effective area S_{eff}

zone related to the generation of dielectric breakdowns). The smaller the effective area, the smaller the value of α , requiring a smaller value of N for the breakdown voltage to reach its limit: Fig. 6 shows the relation between initial value V_1 and limit value V_L of breakdown voltage and effective area S_{eff} . As S_{eff} increases, both V_1 and V_L decreases. Thus, the conditioning process varies greatly with the effective area S_{eff} of the electrode.

4.2 Variations of pre-breakdown current

The currents measured in the conditioning process include micro-discharge currents due to desorption and ionization of adsorbed gas and field emission currents (Fig. 2), which meet the Fowler-Nordheim equation.^{5,6} The measured field emission currents were adjusted using the Fowler-Nordheim equation to obtain field intensification factor β , which can be derived from the equation. Fig. 7 shows the relation between field intensification factor β and voltage V_{1mA} with which the field emission current reaches 1mA in the conditioning process. Field intensification factor β decreases with number of voltage applications N , saturating at limit value β_L . In contrast, V_{1mA} increases with N , reaching saturation. This shows that microprotrusions on the electrode surface are flattened by conditioning with the repetition of dielectric breakdowns, causing field emission currents to be obstructed. Fig. 8 shows the relation between limit value β_L of field intensification factor and effective area S_{eff} . As reported previously, field intensification factor β_L after conditioning increases and decreases with S_{eff} .²

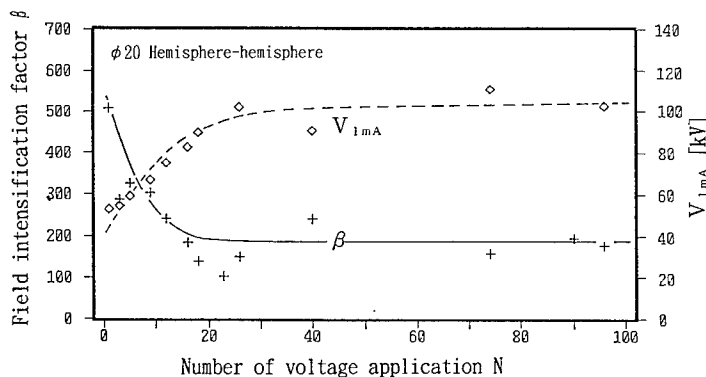


Fig.7 Relation between V_{1mA} (voltage causing field emission current of 1mA), β and number of voltage application N

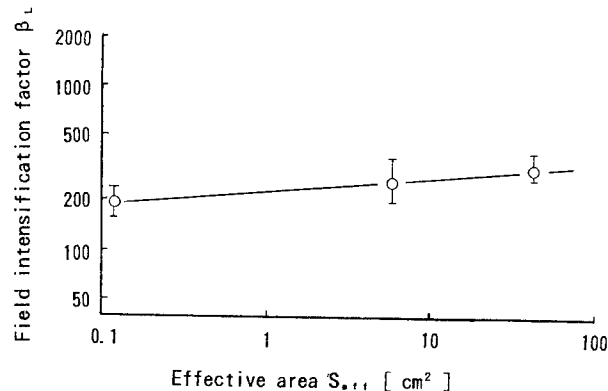


Fig.8 Relation between field intensification factor β_L and effective area S_{eff}

5. DISCUSSION

As described above, the conditioning process depends greatly on the electrode area: the smaller the electrode surface area,

the faster the conditioning process is completed. As the breakdown voltage rises, the field intensification factor decreases in the conditioning process. This shows that microprotrusions on the electrode surface responsible for dielectric breakdowns are gradually smoothed by conditioning. Breakdown voltage rises in the conditioning process, however, can be ascribed not only to the field emissions from microprotrusions but also to the removal of adsorbed gas and deposits.⁴ Dielectric breakdowns are generated in weaker zones with microprotrusions, adsorbed gas and deposits. Probably, as dielectric breakdowns are repeated, their locations shift to weaker and weaker zones, causing the breakdown voltage to rise. This suggests that when the locations of dielectric breakdowns have spread over the effective area, conditioning is completed and the breakdown voltage reaches saturation.

The breakdown voltage after conditioning depends on the electrode surface area. As shown in Fig. 5, the electrode surfaces after conditioning are covered with damage due to dielectric breakdowns. Critical field strength E_c for microprotrusions in the zone damaged by the generation of dielectric breakdowns is given by $E_c = \beta_L \cdot V_b/d$. Fig. 9 shows the relation between critical field strength E_c and effective area S_{eff} . E_c is constant irrespective of S_{eff} . This shows that dielectric breakdowns after conditioning are determined by field emissions from the damaged zones. The value of critical field strength E_c agrees with the one in our previous report and the one in the report produced by Tsuruta et al.^{2,7} This proves that the dependence of dielectric breakdowns after conditioning on the electrode surface area is due to the dependence on the electrode surface area of field intensification factor β_L as an index of field emissions from damaged zones.

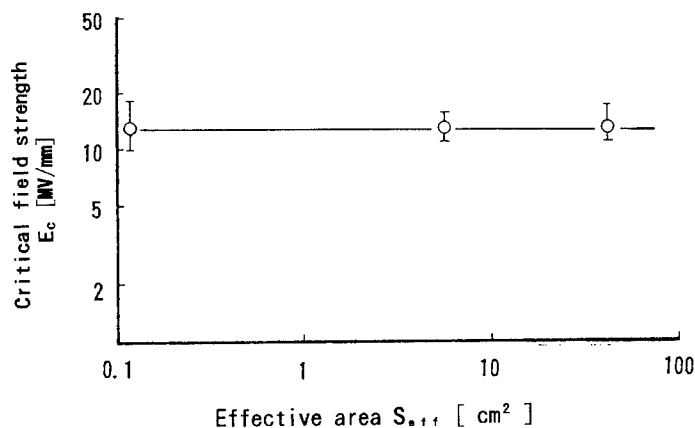


Fig. 9 Relation between critical field strength E_c and effective area S_{eff}

6. CONCLUSION

Experiments were carried out to investigate the effect of electrode surface area on the conditioning process of a vacuum gap. It was found that the conditioning process varied with electrode surface area; the smaller the electrode surface area: the faster the conditioning process ended. The locations of repetitive dielectric breakdowns probably shifted successively to weaker zones with adsorbed gas, deposits and microprotrusions, causing the breakdown voltage to rise. The breakdown voltages after conditioning also depended on electrode surface area; the smaller the electrode surface area, the higher the breakdown voltage.

7. REFERENCES

1. T. Shioiri, I. Ohshima, M. Honda, H. Okumura, H. Takahashi, H. Yoshida: "Impulse Voltage Field Emission Characteristics and Breakdown Dependency upon Field Strength in Vacuum Gaps," IEEE Trans. on Power Apparatus System, PAS-101, pp.4178-4184, 1982
2. M. Okawa, T. Shioiri, H. Okubo, S. Yanabu: "Area Effect on Dielectric Breakdown of Copper and Stainless Steel Electrode in Vacuum," IEEE Trans. on Electrical Insulation, 23, pp.77-81, 1988
3. T. Shioiri, R. Murase, M. Okawa, S. Yanabu: "Effect of Oxidation on Vacuum Gap Breakdown Characteristics and Surface Cleaning Effect of Vacuum Heating Treatment," IEEE of Japan, B-111, pp.777-783, 1991
4. T. Shioiri, T. Kamikawaji, E. Kaneko and M. Homma, "Conditioning Effect of Stainless Steel Electrodes in Vacuum," 8th ISH 38. 05, pp.473-476, Aug. 1993
5. J.M. Meek and J.D. Craggs, "Electrical Breakdown of Cases," Willy & Sons, pp.151, 1978
6. R.H. Fowler and L. Nordheim, "Electron Emission in Intense Electric Field," Proc Roy. Soc., Vol. 119, pp.173, 1928
7. K. Tsuruta, "Impulse Electrical Breakdown Fields of Short Vacuum Caps," IEEE Trans. on Electrical Insulation, Vol. EI-22, pp.77-78, 1987

Pulsed electric discharge in vacuum diodes with electrodes made of low and high temperature superconductors

Sergei I. Shkuratov

Institute of Electrophysics, Urals Division of the Russian Academy of Sciences
34, Komsomolskaya Str., GSP-387, Ekaterinburg, 620219, Russia

ABSTRACT

Results are presented of studies of pulsed electric strength and threshold current densities for niobium cathodes in the superconducting and normal states. The process of heating and failure of cathode microemitters under the action of high density field emission current is analyzed. Data of the work function, limiting current densities and tensile strength of $\text{YBa}_2\text{Cu}_3\text{O}_{7-x}$ cathode tips, effect of emission current on the superconducting properties of $\text{YBa}_2\text{Cu}_3\text{O}_{7-x}$ thin films and peculiarities of prebreakdown phenomena in vacuum gap with $\text{YBa}_2\text{Cu}_3\text{O}_{7-x}$ electrodes are given.

1. INTRODUCTION

Fundamental studies have shown that microexplosions on the cathode surface are one of the main reason in the initiation of a vacuum discharge.^{1,2} One of the causes of such microexplosions is heating of cathode microtips by field emission current due to Joule and Nottingham effects. The absence of resistive heating of the superconducting emitter and the finiteness of the time required for the superconducting-normal (S-N) state phase transition give one hope to expect that an increase in the delay time to explosion of microemitters and, respectively, increase of pulsed electric strength of the vacuum gap.

Progress achieved in quench and melt-growth processing technologies for the fabrication of bulk high-temperature superconductors (HTSC) opens opportunities for their application in a wide range of dc, ac and pulsed devices. With this view, there appears a necessity for information on the behaviour of HTSC surface in strong electric fields: work function and limiting current densities of HTSC microemitters, prebreakdown phenomena in vacuum gap with HTSC electrodes. All this has stimulated our research of electric discharge in vacuum diodes with electrodes made of low and high temperature superconductors.

2. EXPERIMENTAL

The studies were conducted with the use of three specially designed setups:

a) A **Field Electron Spectrometer/Field Ion Microscope/Field Emission Microscope Combination** (FIM/FEM/FES setup) made it possible to investigate the emission characteristics and the electronic properties of microemitters in direct correlation with their real atomic structure visualized in FIM.³

b) A **Metal-Glass UHV Cryostat** with precisely displaceable anode probe allowed us to study emission properties, prebreakdown characteristics of local areas of electrodes and the effect of field emission on the superconducting properties of the cathode.⁴

c) An **UHV Cryostat Impedance-Matched with Pulsed Transmission Line** was used to investigate of electric discharge with a nanosecond resolution.⁵

Also used were: transmission electron microscope (TEM), scanning electron microscope (SEM) and scanning tunneling microscope (STM).

3. DISCHARGE IN VACUUM GAP WITH LOW TEMPERATURE SUPERCONDUCTING ELECTRODES

3.1. Effect of superconducting state of a cathode on the breakdown delay time

Extended electrodes were made of Nb (S-N transition temperature $T_c=9.2$ K), Ta ($T_c=4.4$ K) and Pb ($T_c=7.2$ K). Investigations have shown that the maximum pulsed electric strength is possessed by electrodes: i) made of spectroscopically-clean metals, ii) the surface of which were subjected to special treatment (electrochemical polishing, washing and conditioning by pulsed discharges in UHV).

Figure 1 shows dependences: vacuum breakdown delay time t_d vs macroscopic field for various Nb cathode temperatures. The cooling of the cathode from 300 to 4.2 K leads to the increase in t_d and pulsed electric strength of

vacuum gap. The transition of Nb cathode to the superconducting state has no effect in the t_d . Similar results were obtained for Ta and Pb cathodes.

3.2. Threshold current densities of Nb microemitters at cryogenic temperatures

Measurements of breakdown delay time give an integral picture of vacuum discharge. With this in view, we carried out a study of the threshold current densities in the superconducting and normal states of cathode microprotrusions (CMs) formed after vacuum discharge on Nb cathode of limited area (10^{-3}cm^2) and of Nb cathode tips (CTs) prepared by electrochemical polishing and smoothed by high temperature annealing (their radius at the apex r , cone angle θ and surface state were monitored by TEM and FEM).

The experiments were conducted in the steady-state and pulsed modes. Figure 2 shows typical direct and pulsed current-voltage characteristics (CVCs) of CM and CT. In the pulsed sector there is distinctly visible the effect of space charge of emitted electrons both in the case of CT and CM. FIM and FES investigations have shown the identity of field ion images and electronic spectra of Nb CMs and CTs. It allows one to draw the conclusion that CMs and CTs have identical atomic structure and electronic properties.

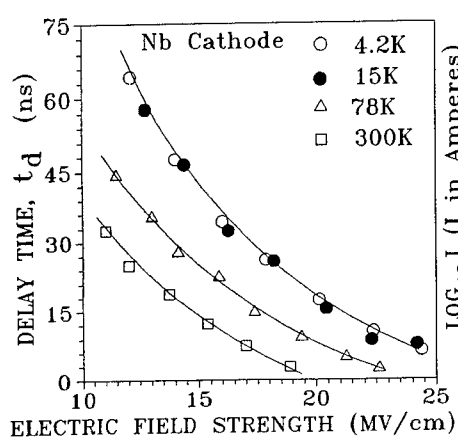


Figure 1.

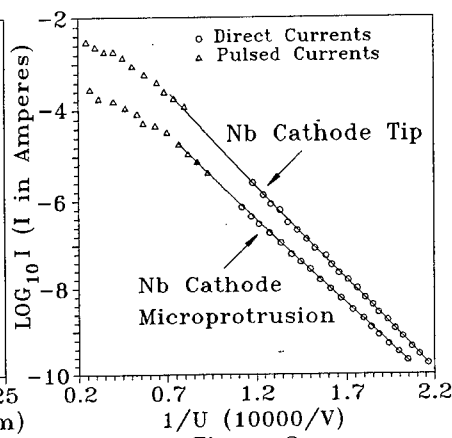


Figure 2.

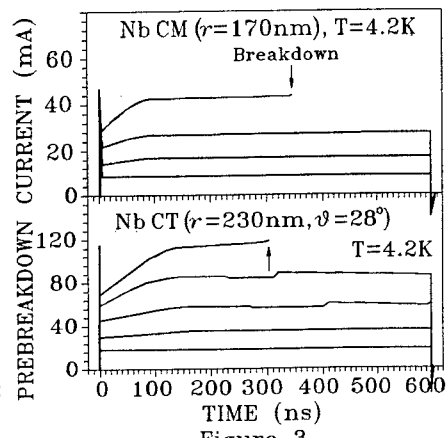


Figure 3.

Figures 3 and 4 show series of oscillograms of the prebreakdown currents of CMs and CTs for various initial temperatures. We discovered in the waveforms of the prebreakdown current close to the threshold current I_t a rising section. Its length and rate of current rise significantly depended on the initial cathode temperature. The CVCs, TEM and FEM images of emitters taken before and after pulsed current extraction indicate that there are no changes in the shape and state of emitting surface. The dominant effect of initial cathode temperature and absence of any residual effect suggest that observed rising section is due to the heating of the emitter apex by the self emission current.

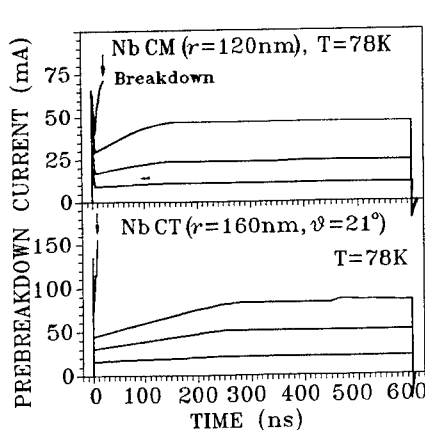


Figure 4.

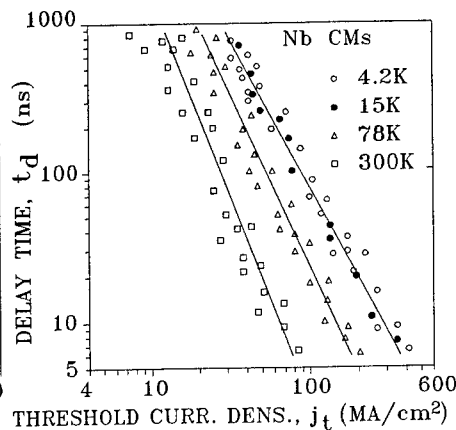


Figure 5.

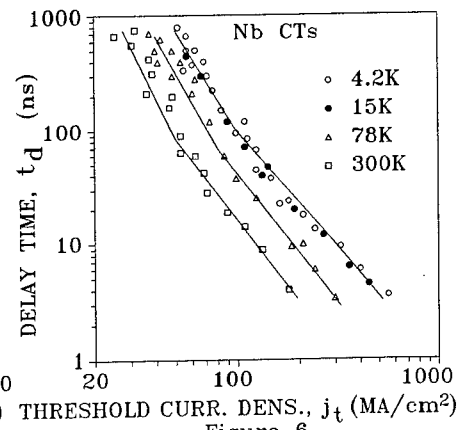


Figure 6.

In Figures 5 and 6 are presented dependences: delay time to explosion of CMs and CTs t_d vs threshold current

density $j_t = I_t / \pi \cdot r^2$ for various initial temperatures. The analysis of experimental results allows one to draw the following conclusions: (1) The cooling of the cathode from 300 to 4.2 K results in a monotonic increase in j_t . (2) The transition of Nb cathode to the superconducting state has no effect in j_t in the range of $t_d = 10^{-9}$ - 10^{-6} s. (3) Thermal processes are identical in CMs and CTs.

The current from a superconducting emitter is limited by three factors: the existence of a critical magnetic field which destroys superconducting properties of the emitter, the existence of the energy of decomposition of Cooper pairs and Nottingham effect. Since the magnitude of j_t of Nb cathode in the range of $t_d = 10^{-9}$ - 10^{-7} s exceeds the critical current densities of superconductor determined by a critical magnetic field ($2 \cdot 10^8$ A/cm²) and by the energy of decomposition of Cooper pairs (10^8 A/cm²), one can draw the conclusion that the S-N transition of the Nb cathode is a result of action of all three limiting factors. In the range of $t_d = 10^{-7}$ - 10^{-6} s the S-N transition of a cathode is a result of Nottingham heating.

A monotonic increase of j_t with colling of Nb cathode from 300 to 4.2 K cannot be explained in terms of the model suggested by Prof. Fursey's group⁶ (expanding of the region where Nottingham effect takes place with cooling of a cathode), because their model predicts that the most important temperature range is 4.2 to 20 K.

3.3. Dynamics of heating and failure of Nb microemitters

For the understanding of dynamics of heating of emitter from cryogenic temperatures and for the evaluation of the roles Joule's and Nottingham's effects in various temperature ranges we numerically solved the problem of heating of emitter with account taken of the nonuniformity of electric field distribution over the apex, the effect of space charge of emitted electrons and the temperature dependences of thermophysical parameters.^{7,8} The Nottingham effect was involved as a surface energy source.

Figure 7 shows calculated dependences: delay time to explosion of Nb CMs t_d vs threshold current densities j_t for various initial cathode temperatures. These dependences are in good agreement with experiment (Fig.5). Calculations have shown: (1) The main contribution to the tip heating from 4.2 to 300 K is due to the Nottingham effect; with $T > 300$ K it is the Joule's effect that predominates. (2) The cooling of the cathode to cryogenic temperatures strengthens the heat removal and this is just the the reason for the observed monotonic increase in the breakdown delay time and threshold current density (Figs.1, 5 and 6). (3) The magnitude of j_t of CM shows strong dependence on its height at cryogenic temperatures, therefore, one can expect a considerable increase of electric strength of vacuum gap after cooling of perfectly smoothed cathode.

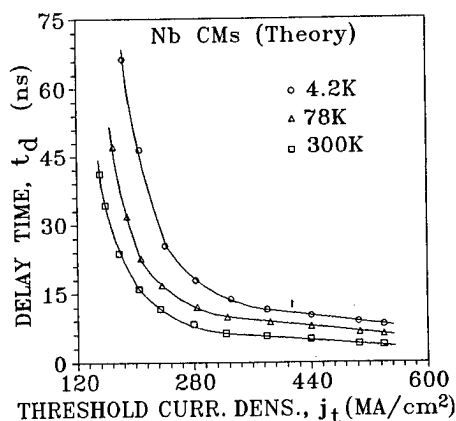
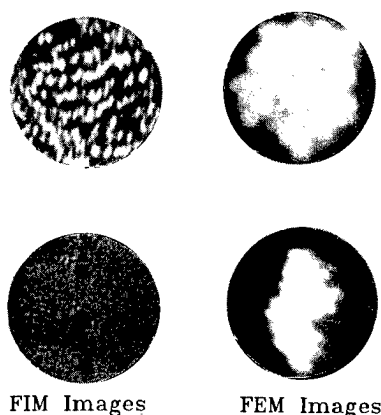


Figure 7.



YBaCuO Cathode Tips
Figure 8.

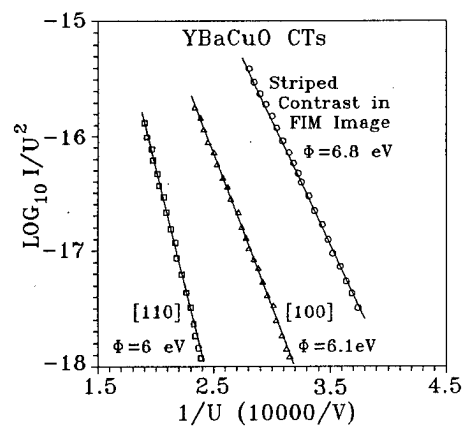


Figure 9.

The spontaneous rise of prebreakdown currents (Figs.3 and 4) is due to the propagation of the heat wave to the periphery of the tip apex and thermal field emission from an area where there is no space charge influence. The cooling of the cathode leads to the increase of thermal conductivity and, correspondingly, to the faster setting of a steady-state temperature in the peripheral area of the tip apex. The shorter length of rising section in the case of CM is due to the effect of the massive cathode. Calculated lengths of rising section are in good agreement with experimental results for various cathode temperatures.

Calculations have shown that a steady-state temperature in the emitter sets in during a time interval not exceeding 100 ns, i.e. with $t > 100$ ns there is no avalanche type interdependent growth of apex temperature and emission

current. This conclusion is confirmed by the cardinal difference in the dynamics of prebreakdown current in various t_d ranges (Figs.3 and 4). Thus, delay times $t_d > 100$ ns cannot be explained within the framework of the traditional thermal model. Analysis of TEM images of CTs, dynamics of prebreakdown current, dependences t_d vs j_t together with calculations of thermal processes in the emitter and data on the tensile strength for Nb at various temperatures has revealed the important role of mechanical loading in the failure of the microemitter in the $t_d > 100$ ns.⁵

4. DISCHARGE IN VACUUM GAP WITH HIGH TEMPERATURE SUPERCONDUCTING ELECTRODES

4.1. Properties of HTSC surfaces in strong electric fields

For gaining the information on the behaviour of HTSC surfaces in strong electric fields in UHV we conducted a series of FIM/FEM/FES investigations of $\text{YBa}_2\text{Cu}_3\text{O}_{7-x}$ single crystal ($T_c=92$ K) CTs prepared by electrochemical polishing.

Figure 8 shows $\text{YBa}_2\text{Cu}_3\text{O}_{7-x}$ FIM images and corresponding FEM images. In Figure 9 are presented CVCs of various oriented $\text{YBa}_2\text{Cu}_3\text{O}_{7-x}$ CT surfaces cleaned by field evaporation in UHV and values of work function ϕ .

FES of atom-clean surfaces of $\text{YBa}_2\text{Cu}_3\text{O}_{7-x}$ CTs has demonstrated a metallic-like behaviour of electronic spectra at different temperatures.^{3,9,10} At the same time, the transformation of $\text{YBa}_2\text{Cu}_3\text{O}_{7-x}$ from a superconductor into a semiconductor and dielectric with a decrease oxygen content leads to the emergence of a number of special features in the behaviour of $\text{YBa}_2\text{Cu}_3\text{O}_{7-x}$ in UHV. Figure 10(2) shows the electronic spectrum of an atom-smooth $\text{YBa}_2\text{Cu}_3\text{O}_{7-x}$ CT surface after holding of CT in UHV ($T=300$ K) for 15 hours. The absence of a signal in the vicinity of the Fermi level is due to the escape of oxygen from the CT subsurface layer. The field evaporation of 10 atom layers of the material leads to the restoration of initial $\text{YBa}_2\text{Cu}_3\text{O}_{7-x}$ properties (Fig.10(1)). At 75 and 115 K we did not observe any transformation of $\text{YBa}_2\text{Cu}_3\text{O}_{7-x}$ similar to that shown in Fig.10.

4.2. Limiting current densities of $\text{YBa}_2\text{Cu}_3\text{O}_{7-x}$ microemitters

Investigations of limiting current densities of $\text{YBa}_2\text{Cu}_3\text{O}_{7-x}$ CTs at 115 and 75 K in the steady-state mode have shown that the extraction of high-density field emission current ($j=(3-10)10^4$ A/cm², $t=3$ s) does not change FIM and FEM images of CTs, but leads to changes in the electronic spectra (Fig.11). The analysis of results shows that this effect is due to Nottingham heating of the tip apex, escape of oxygen under UHV condition and, correspondingly, the transformation tip apex properties into semiconductor ones.^{11,12}

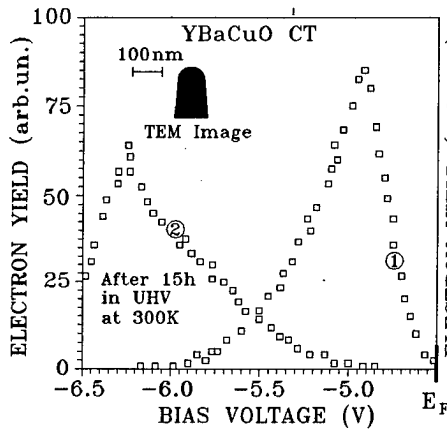


Figure 10.

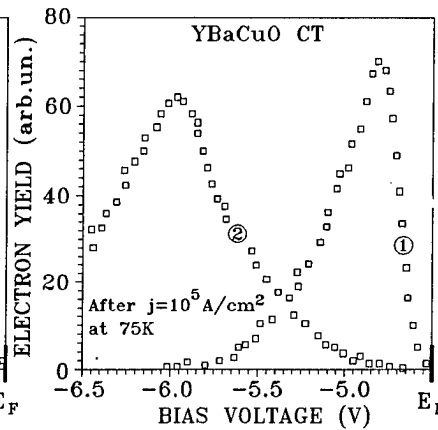


Figure 11.

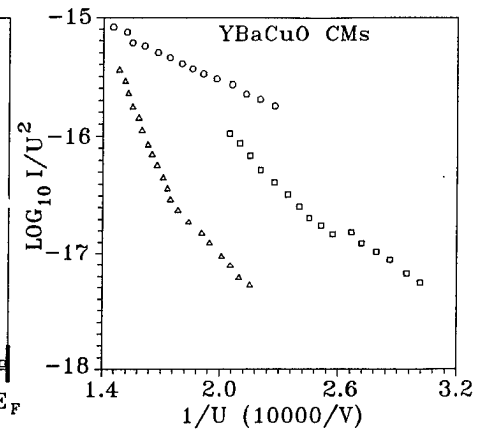


Figure 12.

Investigations of threshold current densities of $\text{YBa}_2\text{Cu}_3\text{O}_{7-x}$ CTs have shown that over a $t_d=(1-2)10^{-6}$ s range the superconducting state of CT does not affect the magnitude of $j_t=(0.7-2.2)10^6$ A/cm². The analysis of thermal processes shows that low (more than 10 times less) $\text{YBa}_2\text{Cu}_3\text{O}_{7-x}$ j_t , as compare with Nb (Figs.5 and 6), is due to essentially different thermophysical properties of HTSC (high resistivity, low thermal conductivity and thermal capacity).^{8,13}

Measurements of tensile strength σ of $\text{YBa}_2\text{Cu}_3\text{O}_{7-x}$ microemitters by loading CTs with electric field ponderomotive forces in the FIM¹⁴ have yielded the following results: $\sigma=3.5$ GPa (almost 3 times less than for Nb).

4.3. Electric discharge in vacuum diodes with electrodes made of HTSC

Investigations of $\text{YBa}_2\text{Cu}_3\text{O}_{7-x}$ single crystals removed from the melting crucible into an UHV cryostat without any processing have revealed that the macroscopic breakdown field is $(1.5-2) \cdot 10^5$ V/cm at 300 K, this value not changes with the cooling of the cathode and its transition to the superconducting state.

Figure 12 shows CVCs of local areas of $\text{YBa}_2\text{Cu}_3\text{O}_{7-x}$ cathode. The analysis of CVCs on the assumption work function 6 eV yields enhancement factor for cathode microtips $\beta=150-200$. SEM images of cathode surface did not show microtips which could ensure such values of β . FES of cathode microtips shown typical semiconductor electronic spectra (Fig.13). This make it possible to draw the conclusion that nonmetallic inclusions on the surface of $\text{YBa}_2\text{Cu}_3\text{O}_{7-x}$ cathodes are centers initiating vacuum breakdown as in the case of extended metallic cathodes before special treatment of their surfaces.²

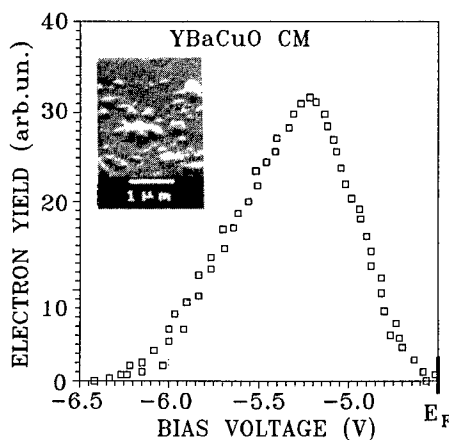
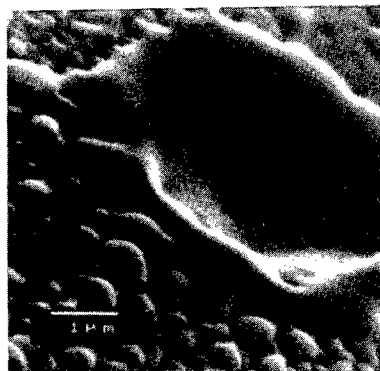


Figure 13.



YBaCuO Cathode
Figure 14.

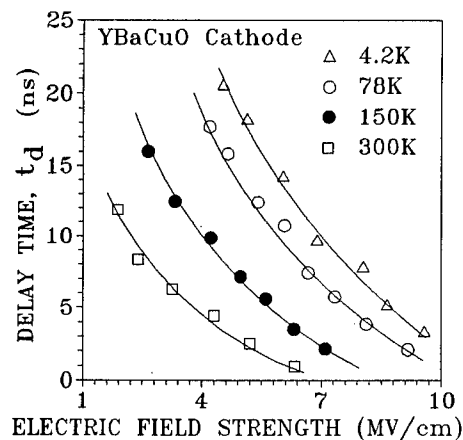


Figure 15.

X-ray microanalysis (JEOL JCSA-733 Superprobe) has shown that remelting of microscopic areas on the $\text{YBa}_2\text{Cu}_3\text{O}_{7-x}$ cathode resulting from the vacuum discharge (Fig.14) leads to the escape of oxygen and, therefore, transforms the initial material into a semiconductor or dielectric.

In Figure 15 are shown dependences breakdown delay time vs macroscopic field for $\text{YBa}_2\text{Cu}_3\text{O}_{7-x}$ cathode, the surface of which was conditioned by pulsed vacuum discharges. The growth of electrical strength with the cooling of cathode is, evidently, due to changes in the properties of the dielectric layer, coating the cathode.

The velocity of the cathode plasma expansion in the vacuum gap with $\text{YBa}_2\text{Cu}_3\text{O}_{7-x}$ electrodes was $v=(1.6-2) \cdot 10^6$ cm/s, i.e., did not differ from the v values typical for most of the metals studied till now.¹

The mass loss of $\text{YBa}_2\text{Cu}_3\text{O}_{7-x}$ cathode material by explosive electron emission process was $m = (1.4-3.2) \cdot 10^{-4}$ g/(A²s)^{-3/4}. The high value of m (almost two orders of magnitude greater than for Nb) is due to the high electrical resistance, low thermal conductivity and mechanical strength of $\text{YBa}_2\text{Cu}_3\text{O}_{7-x}$.^{8,13}

4.4. S-N switching of $\text{YBa}_2\text{Cu}_3\text{O}_{7-x}$ thin film under the action of field emission current

The investigations of the superconducting properties of $\text{YBa}_2\text{Cu}_3\text{O}_{7-x}$ thin films in strong electric fields have shown that the extraction of field emission current 3-4 orders of magnitude lower than the critical transport current leads to S-N switching of the films.^{4,12} The analysis of experimental results allows us to draw the conclusion that there exist a thermal mechanism of S-N transition caused by field emission: with high emission current densities the microemitter on the $\text{YBa}_2\text{Cu}_3\text{O}_{7-x}$ film surface becomes a point thermal source leading to the formation of a normal phase in the HTSC film.⁴

5. SUMMARY

Thus, studies have shown that Nottingham effect plays a fundamental part in the failure of electric insulation in vacuum diodes with superconducting electrodes and for breakdown delay time more than 100 ns this is just the reason for S-N transition of cathode microtips. The colling of Nb cathode from 300 to 4.2 K strengthens the heat removal and leads to a monotonic increase in threshold current densities and pulsed electric strength of vacuum gap. The relatively low threshold current densities of $\text{YBa}_2\text{Cu}_3\text{O}_{7-x}$ cathodes are due to the high resistivity and low thermal conductivity

of these materials. The complex chemical composition of oxide superconductors and their relatively weak atomic bond result in essential difficulties in the preparation of HTSC clean surfaces in UHV by traditional methods.

6. ACKNOWLEDGEMENTS

The author are very grateful to G.A. Mesyats, V.F. Puchkarev, D.I. Proskurovsky, A.V. Batrakov, V.G. Mesyats, N.N. Syutkin, S.N. Shilimanov, S.N. Ivanov, and E.F. Talantsev for their help during this work.

7. REFERENCES

1. G.A. Mesyats, D.I. Proskurovsky, *Pulsed Electric Discharge in Vacuum*, Springer-Verlag, Heidelberg, 1985.
2. R.V. Latham, *High Voltage Vacuum Insulation: The Physical Basis*, Academic Press, London, 1981.
3. S.I. Shkuratov, S.N. Ivanov and S.N. Shilimanov, "Field electron microscopy and spectroscopy HTSC perfect monocrystals", *Surf. Sci.*, Vol.266, pp.224-231, 1992.
4. S.I. Shkuratov, S.N. Shilimanov and V.N. Skokov, "Effect of switching over $\text{YBa}_2\text{Cu}_3\text{O}_{7-x}$ thin films from the superconducting to the normal state under the action of field-emission currents", *Phys. Rev. B*, Vol.48, No.9, pp.6456-6459, 1993.
5. S.I. Shkuratov, "Pulsed electric discharge in vacuum at cryogenic temperatures", *Cand. Sci. Thesis*, Inst. of Electrophysics, USSR Academy of Sciences, Sverdlovsk, 1987.
6. G.N. Fursey, V.M. Zhukov, L.M. Baskin, "Limiting densities of FEE and pre-explosive effects", in: *Emission Electronics*, Novosibirsk, 1984.
7. S.A. Barengolts, S.I. Shkuratov, E.A. Litvinov, V.G. Mesyats and V.F. Puchkarev, "Pulsed electric current and the value of critical current at cryogenic temperatures", *IEEE Trans. on Elect. Insul.*, Vol.25, No.2, pp.341-350, 1990.
8. S.A. Barengolts, "Theoretical study of emission properties of metals and HTSC", *Cand. Sci. Thesis*, Inst. of Electrophysics, USSR Academy of Sciences, 1989.
9. S.I. Shkuratov, "High-temperature superconductors in strong electric fields", *Surf. Sci.*, Vol.266, pp.88-99, 1992.
10. S.I. Shkuratov, S.N. Ivanov and S.N. Shilimanov, "Field electron emission microscopy and spectroscopy $\text{YBa}_2\text{Cu}_3\text{O}_{7-x}$ single crystals at different temperatures", *Physica C*, Vol.213, pp.321-326, 1993.
11. S.I. Shkuratov, S.N. Ivanov and S.N. Shilimanov, "Limiting current densities of $\text{YBa}_2\text{Cu}_3\text{O}_{7-x}$ single crystal submicron specimens", *Physica C*, Vol.211, pp.158-164, 1993.
12. S.I. Shkuratov, "High-temperature superconducting thin films in strong electric fields", *J. Vac. Sci. Technol. B*, Vol.11(2), pp.353-361, Apr/Mar. 1993.
13. V.G. Mesyats and S.I. Shkuratov, "Explosive electron emission from high-Tc superconductor $\text{YBa}_2\text{Cu}_3\text{O}_{7-x}$ ", *Sverchprovodimost: fizika, khimiya, tekhnika*, Vol.3, pp.2046-2049, 1990.
14. E.F. Talantsev, "Field ion microscopy of HTSC", *Cand. Sci. Thesis*, Inst. of Electrophysics, USSR Academy of Sciences, Sverdlovsk, 1990.

ANOTHER CAUSE OF VACUUM INSULATION ELECTRICAL STRENGTH DECREASE FOLLOWING THE BAKEOUT OF METAL - INSULATION ELECTRODE SYSTEM

Nina V. Tatarinova

Moscow Physical Engineering Institute
Kashirskoe shosse - 31, 115409, Russia

ABSTRACT

The cause of pre-breakdown currents appearing between metal electrodes copper soldered with ceramics after bakeout in vacuum up to 200...440°C was established. Quest for it was conducted from the viewpoint of a hypothesis suggested by author earlier on vacuum insulation violation. "Tripple point" - metal-insulator contact in vacuum - is referred to as a pore in the gas medium of which ionisation process resulting in various kinds of vacuum insolation violation develop. Experimental results confirm the hypothesis suggested.

1. INTRODUCTION

The process giving rise to prebreakdown currents, microdischarges and arc (vacuum breakdown) were shown [1-4] to take place in high voltage electrode pores electrical field strength exceeding 0.1 MV/m being insufficient for FEE to appear. External field sagging into pore volume gas results from resonance desorption as well as charged particles. Voltage increasing ionisation process lead to swift current build-up and appearance of plasma formations. Previously influence of electrode gas saturation and pore size on insulation characteristics of vacuum was demonstrated [1-4]. Poresize and configuration define not only electrical field sagging but pore volume gas pressure as well. These relations resemble Paschen curve for gas. But the mechanism sustaining discharge in the pores of high voltage electrodes in vacuum differs from that from classical gas discharge, the limitation on paper dimension preventing from a comparison of both in detail here.

Anode playing a special role, the electrons from the cathode getting into its pores of the optimum size may result in appearance of plasma formations at the anode. Earlier this was noted in paper [5] when electron beam hit cracks or scratches on the anode. Ion flow from anode plasma formations enters a cathode pore thus promoting ionization processes. Dielectric in vacuum gap given, "triple point" can be regarded as pores along seal perimeter where the processes mentioned are promoted anode pores being locked exactly to the "triple point" of the cathode. This latter, on a level with possible charging of dielectric, is one of the causes of electrical strength decrease for vacuum in presense of dielectric.

Dielectric given, characteristics of vacuum insulation can be explained from the viewpoint of the hypothesis discussed . The include breakdown voltage dependence on the negative slope of cylindrical insulator having minimum for negative angles of 5...20° [7] and a similar in appearance dependence of pulsed breakdown voltage on the width of the slot (gap) between insulator and the second electrode (cathode or anode). Both the "anode" and "cathode" curve minimums are registered for 100 μ slot [8].

From the viewpoint of both existing hypotheses and the one under discussion gas desorption decreases, mostly off the insulator, must result in electrical strength improvement. In this case preliminary bake-out of high voltage electrodes with dielectric insulation should be desirable. However, we found out bake-out up to 225°C in high vacuum to have notably increased pre-breakdown currents while further temperature elevation was accompanied by plasma formations appearing at dielectric surface. Based on hypothesis suggested, studies of metal-dielectric contact spots were carried out.

2. EXPERIMENT

The experimental block was an electrode system of metallic rings 35 mm in diameter sandwiched with 22XC insulator 2.3 mm thick rectangularly copper soldered. Metal rings were of the same size, the internal diameter of dielectric being 2 mm greater (Fig. 1). Six electrode blocks sealed into separate glass envelopes were studied each envelope being connected to a common vacuum pipeline. Thus measurement process for each block was independent of the rest. Insulators of three blocks were chamfered at an angle of 45° on all the four edges (both anode-cathode and internal-external).

Currents were measured under pressures less than 0.0001 Pa; this condition was supported when baking out the blocks.

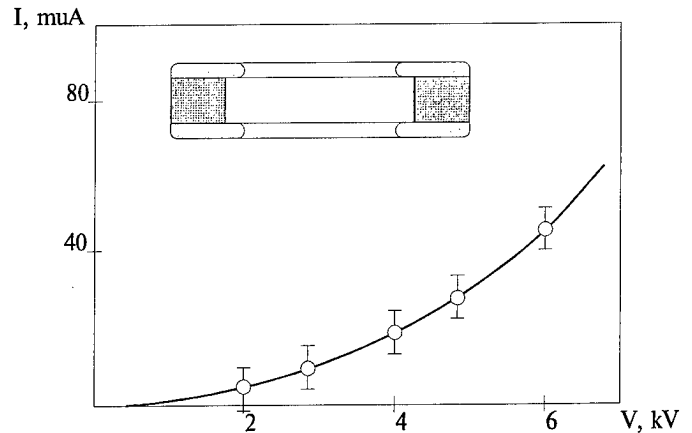


Fig. 1

3. EXPERIMENTAL RESULTS

Voltage-current characteristics of devices with electrode system under study were measured. Before bakeout their values were less than 1 nA at voltage of 7 kV (field strength $E=3$ MV/m). Notable current increase for facetless insulators appeared already following bakeout up to 225°C , while the maximum value after 385°C (Fig. 1). Current rise was five orders of the initial value approaching 0.1 mA. In some places of facetless samples fine glowing columns of reddish colour were observed, those short circuiting electrodes across the surface of insulator and rapidly heating ceramics.

EM pictures of those places with plasma formations were cameredated, showing microstructure before and after bakeout for both cathode (Fig. 2) and anode (Fig. 3) joint. (Before bakeout to the left, after to the right). Seal thickness is shown with arrows. Before bakeout the seal is smooth for both electrodes, though it doesn't fit ceramics tightly in all places (Fig. 3). After bakeout it became porous. Typical patterns were observed along the whole perimeter. Some crashes were not less than 100 μ m. The patches of seal untightly fitting the ceramics are also seen. At such pore size equipotential line equal to hydrogen ionisation potential sags into at the field strength being about 1 MV/cm thus resulting in rapid current buildup.

The influence of low-temperature bakeout was confirmed for other samples. Those differed of material, size and construction of the "triple point". Porcelain insulations had the form of a continuous cylinder 20 mm in diameter and length. External field strength being 0.3 MV/m non-stationary currents with peak values of some milliamperes followed vacuum bakeout up to 225°C . One had to find out the causes of seal microstructure variation. Those could be mechanical tensions resulting from the difference thermal-expansion coefficients as well as explosive character of gassing from the nearby surface layers. The cause was created out in the experimental with the second design of samples. Durable degassing of sample seals in vacuum at room temperature preceded bakeout procedure. After the latter no currents higher than 1 nA were observed even for field strength 3 MV/m. Hence seal was destroyed when baking out by gassing.

4. SUMMARY AND CONCLUSION

Appearance of porosity in "triple point" both for cathode and anode following vacuum bakeout

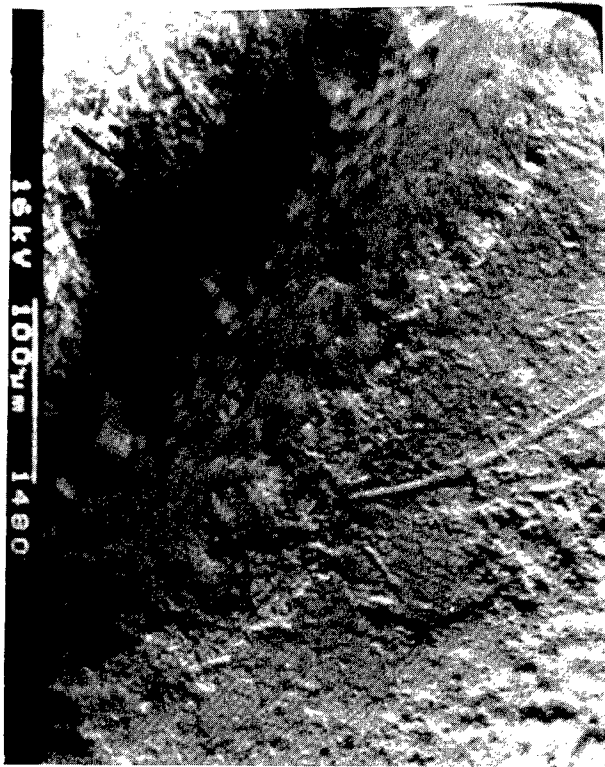
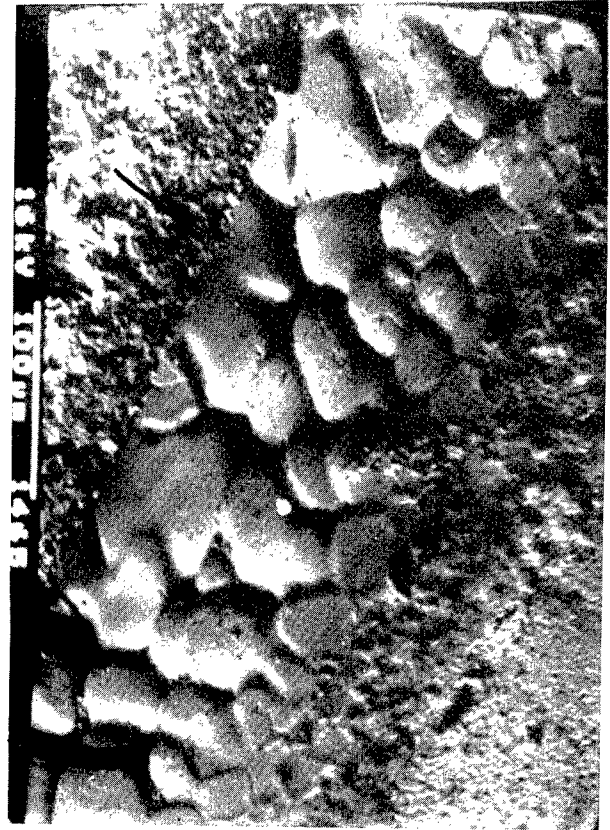
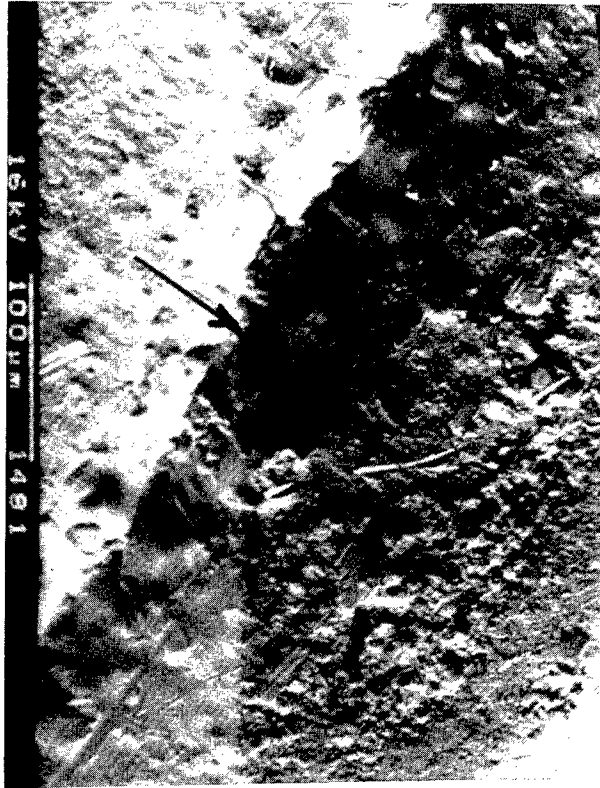


Fig. 2

Fig. 3

results in high prebreakdown currents. The latter induce irreversible insulator conductivity[9].

Preliminary seal bakeout at room temperature omits this limitation on vacuum bakeout, this procedure being so necessary for high voltage devices and facilities.

The results obtained confirm the suggested hypothesis of vacuum insulation violation once again more.

4. REFERENCES

1. N.V. Tatarinova. Mechanism of Vacuum Insulation Damage.-Proc. of XIII Int. Symp. on DEIV, Paris, pp. 78-81, 1988.
2. N.V. Tatarinova. A new Kind of Vacuum Insulation Damage, Pore-Electron Emission from Metal-Dielectric Contact.- Proc. of XIV Int. Symp. on DEIV, Santa-Fe, USA, pp. 381-387, 1990.
3. N.V. Tatarinova. Processes in Surface Layer Micropores of High Voltage Electrodes and Vacuum Electroinsulation. - Proc. of XV Int. Symp. on DEIV, Darmstadt, pp. 761-765, 1992.
4. B.S. Kulvarskaya, N.V. Tatarinova. About Nature of Electron Emission of Porous Cold Cathode. - Radiotekhnika i elektronika, v.37, No.2, pp.362-365, 1992.
5. V.P. Gamarsky, G.G. Gontarev. New Property of Surface Bombarded Electrons Metals.- Elektronnaya Tekhnika, v. 1 (61), pp.22-27, 1978.
6. N.V. Tatarinova, Yu.V. Grigoriev. Total Voltage Effect and Electrode Porosity. - Proc. of this Symp.
7. H.G. Miller. Flashover of Insulators in Vacuum Techniques to Improve the Holdoff Voltage.- Proc. of XV Int. Symp. on DEIV, Darmstadt, pp.165-174, 1992.
8. A.A. Avdeenko, A.P. Lisenko. Flashover of Insulators in Vacuum for Nanosecond Impulses.- Preprint JNP SO AN USSR, Novosibirsk, 1970.
9. G.S. Grishutin, V.M. Zhurtov, A.S. Pokrovskaya-Soboleva, A.L. Shapiro, A.A. Shevchukov. Influence of Hydrocarbon Compounds on the Electrode on the Electrical Strength of Insulator.- Proc. of XI Int. Symp. on DEIV, Berlin, pp. 347-349, 1984.

TOTAL VOLTAGE EFFECT AND ELECTRODE POROSITY

N. V. Tatarinova

Moscow Engineering Physical Institute
Kashirskoe Shosse 31 Moscow 115409 Russia

Yu. V. Grigoriev

All-Russian Electrotechnical Institute
12, Krasnokasarmennaya str. Moscow Russia

ABSTRACT

"The total voltage effect" being a main characteristic of vacuum insulation is explained from an earlier offered mechanism of vacuum insulation deterioration point of view [1 - 3]. When an external electric field sagging in the negative electrode cracks and pores in their volume ionization processes occur. Gas medium in the pores appears as a result of the resonance gas desorption from the pores surface. "The total current effect" is explained by the same processes.

1. INTRODUCTION

It is known, that the so called "total voltage effect" is revealed as a decrease of the field intensity with the gap increase under vacuum breakdown conditions. Abrupt decrease of this value (sometimes by an order) can be observed both in very short (0.01 mm) and in long (up to 1 mm) gaps. However, in some works this dependence is absent, and in some other works it changes during its measurements. The cause is probably determined by the fact that surface state changes because of vacuum breakdowns. As well the situation relates to the gap size dependence of an external electric field intensity at a constant current passing through the gap. The phenomenon is called "the total current effect". In experiments with fully metal electrodes preliminarily cleaned of oxide and mechanically destroyed layer [4 - 5] "the total current effect" depended on the electrode state. It is shown in Fig. 1 that after the electrodes had been cleaned, in the vacuum gap measuring interval the effect is absent, but it appears again after one microbreakdown took place and it is clearly defined after a number of microbreakdowns occurred. One can propose that these properties are determined by the surface microstructure (appear of craters, peaks, cracks etc.) as the surface monitoring before and after breakdown showed that nonmetal inclusions were absent. [4]. These inclusions registration was realized by means of the after-discharge electron emission.

Interesting results were received when studying an electrode system consisting of a fully metal electrode and a porous foil (Fig. 2). On the base of the measured voltage - current characteristics with the porous electrode different polarity the following vacuum gap length dependences of an external electric field intensity were plotted: curve 1 (transition to the exponential region of the voltage - current characteristics), curve 2 (a constant current passes), curve 3 (vacuum microbreakdown occurs). As it can be seen from Fig. 3, all curves for the both cathodes are practically parallel. Curves 1 and 2 illustrate "the total current and voltage effect". However, the difference between field intensity on curves 1 and 3 for the porous cathode is essentially less.

We'll consider these relationships from the viewpoint of the processes inside pores creating the vacuum insulation deterioration conditions. The foil cathode has artificial pores of approximately 30 μ m size. In other cases defects in the form of pores weren't checked. After vacuum breakdowns pores are located in the oxide film at grain boundary in the form of cracks, craters and scratches. When an external electric field sagging at the boundary of a solid body and vacuum, equilibrium due to different conductivity between the thin surface layer with deteriorated crystal lattice directed toward vacuum, from one hand, and layers located near the surface, from the other hand, is disturbed. Electron flow toward vacuum appears. These electrons interact with adsorbed layers of water and oxygen and the resonance gas desorption from pores surface arises. The most

probability of this process corresponds to the electron energy of several eV, i. e. near to Fermi energy. As a result of interaction with the pore surface electrons both neutral and negative particles are desorbed into its volume. A gas medium is created in the pore volume and charged particles create current in the vacuum gap. Doing so they increase gas desorption from the pore surface. The greater an external field, the greater it sags into pores, i. e. gas desorption surface increases. That's why the first region of the voltage - current characteristics looks like a linear one. This relationship is clearly defined for fully metal coatings with big porosity [1 - 3]. Without preliminary heating, in presence of an oxide film, at a big pore gas pressure, this region current, as a rule, is less than μA . However, as for a porous surface with through pores, degassing goes essentially faster and we can observe initial regions being close to linear dependence (Fig. 2). The fact that current value of the initial region is dependent on the cathode gas saturation was convincingly showed in the previous works [1, 2].

When voltage following raising equipotentials being equal to the gas ionization potentials sag into pores. Charged particles appearing as a result of the gas resonance desorption take part in pore ionization process. The second region closed to exponent develops. Transition to it can be both smooth and abrupt. The latter takes place at a big pore pressure, for example, after pumping out from atmospheric pressure. In spite of temporal decreasing the initial region current is stable. At the exponential region current fluctuations and jumps occur. During the following current increase plasma is forming, glowing of which can be seen in many cases. It means that a self-keeping discharge is fixed transiting into an arc at a determined current density. This arc can be short time or stationary.

The moment, when the initial region transits to the exponential one, is determined by the pore geometry (width, depth, symmetry etc.) as well as by relation of these values with the gap length. The second cause is the gas pressure and its composition but here they are not considered here. To explain "the total current and voltage effect" it must be proposed that the equipotential being equal to some ionization potential at short vacuum gaps sags in a pore volume by a less distance in comparison with the long ones. Such a task was set and the sagging of an external field depending on the vacuum gap length with different pore configurations was considered. The proposal was confirmed and the first results were published in the work [3]. In this article the vacuum gap length dependence of the field sagging grade in the pore volume at different pore sizes are presented.

2. EXPERIMENTS

As is clear from earlier experiments with specially prepared porous surfaces [3], the most currents through a vacuum gap were observed for the sizes near 100 μm , and current density of tens $\mu A/cm$ were measured under steady state conditions at the $4 MV/m$ field intensity. The calculation program was developed for these conditions. A cathode pore is schematically presented in Fig. 4. Sagging of the 10 and 20 V equipotentials at the $4 MV/m$ constant intensity of the macrofield was considered. With regard to initial energy of negative particles emitted into the pore volume these values correspond to ionization spectrum of the desorbed from pore surface gas. In Fig. 5 vacuum gap length dependences of the two being considered equipotentials are presented in the interval, where "the total current and voltage effect" is best defined. These curves once again confirm the fact that for big pores with sizes being closed to studied ones, the field sag is less in case of short gaps, i. e. "the total current and voltage effect" takes place.

It is best defined for the pores with big sizes, depth of which is comparable with the width of the pore or more. It is shown in Fig. 6. So, the reveal grade of the considered effects is determined by the pore size relative to the gap length. As the field sag measuring results showed, for the radius being by an order less than considered ones these effects are absent. In this case, as a rule, vacuum insulation disruption field intensity increases. This picture is observed on microchannel plates with essentially less pore size, i.e. the studied effects are practically absent [6].

Porous cathode peaks, on which an external field influence was 100 times strengthened is determined.

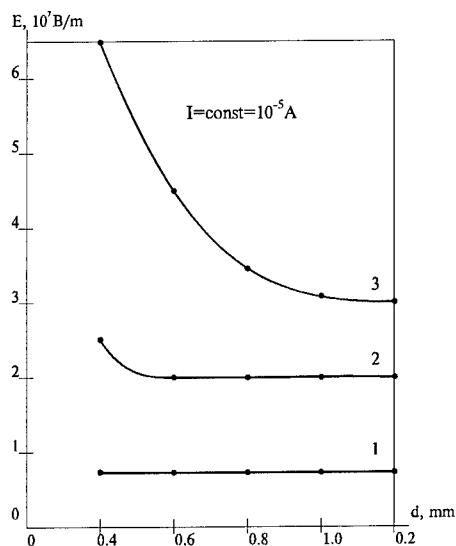


Fig. 1. Total current effect after glowing discharge treatment (1), after one vacuum micro-breakdown (2), after a number of breakdowns (3).

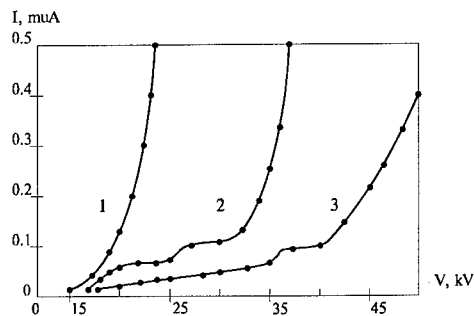


Fig. 2. Voltage - current characteristics for a cathode of porous foil with through pores.

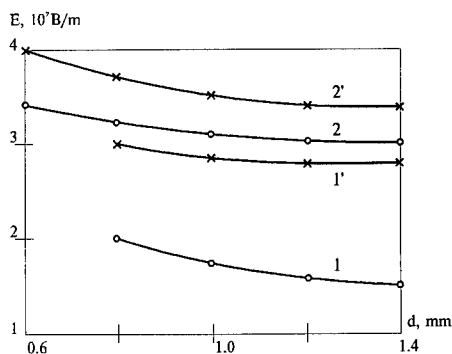


Fig. 3. Field macrostrength versus vacuum gap length for cases: 1, 1' - transition to exponential part of current-voltage characteristics (according to fig. 2); 2, 2' - vacuum breakdown. X-porous cathode, O - full metal cathode.

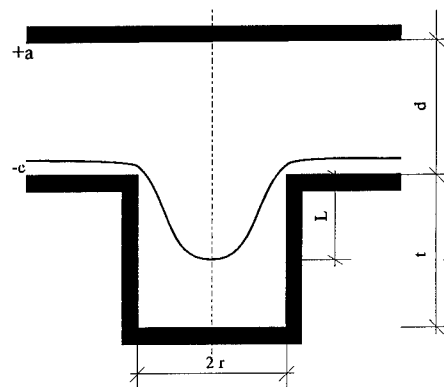


Fig. 4. A schematic picture of a cathode pore; d : vacuum gap length(cathode-to anode interval), r : pore radius, t : pore depth, l : sag grade of the being studied equipotential into the pore.

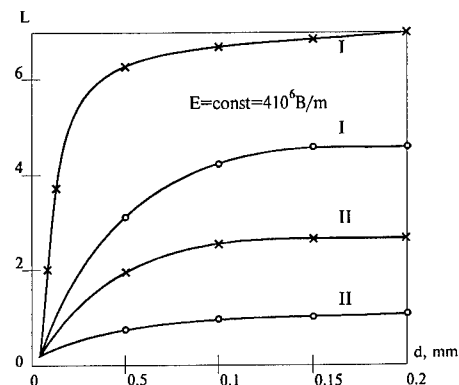


Fig. 5. Sag in the 10 (X) and 20 (O) V equipotentials in relative units depending on the vacuum gap length, the pore depth is 100 μ ; I - pore radius is equal to 50 μ , II - pore radius is equal to 25 μ .

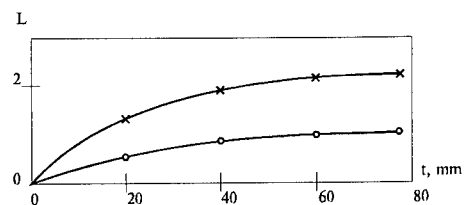


Fig. 6. Sag of the 10 (X) and 20 (O) V equipotentials in relative units depending on the pore depth t , pore radius $r = 25$, vacuum gap length $d = 0.1$ mm.

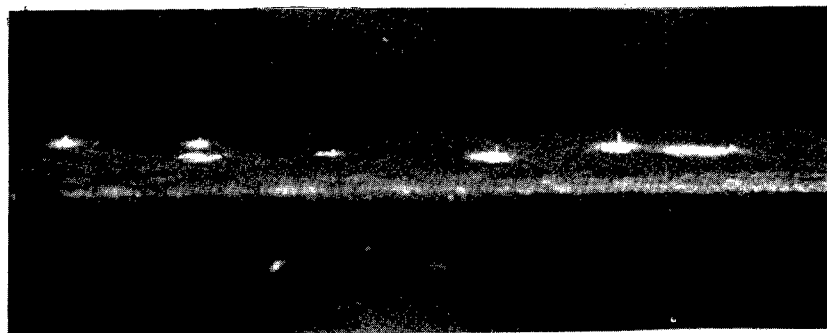


Fig. 7. A photo of a porous cathode after peaks appeared (the gap voltage-current characteristics didn't change)

When studying a porous cathode with the pore radius $r = 50 \mu\text{m}$ and with foil anode, micropeaks on the anode appeared after a number of discharges melting the anode through. These peaks were visible by the unaided eye and were shot by a photocamera (Fig. 7). After the peaks appeared the porous cathode voltage - current characteristics practically didn't change. The electric field sag calculation with a cathode having such peaks for the above mentioned pore size showed that the sag value was somewhat less. These experiments attest that under the considered field intensities an influence of autoemission is absent. The fact is also confirmed by the calculation results (an external field gain at the pore edge decreases with the vacuum gap increasing and its value for short gaps is no more than 10).

3. SUMMARY AND CONCLUSIONS

The received results confirm the possibility to explain "the total current and voltage effect" using processes occurring primarily in a cathode pores. Influence of an anode pores is considered in [7]. The experiment and calculation results confirm the proposed hypothesis validity for all kinds of vacuum insulation damage indicators.

4. REFERENCES

1. N.V. Tatarinova. Mechanism of Vacuum Insulation Damage.-Proc. of XIII Int. Symp. on DEIV, Paris, pp. 78-81, 1988.
2. N.V. Tatarinova. A new Kind of Vacuum Insulation Damage, Pore-Electron Emission from Metal-Dielectric Contact.- Proc. of XIV Int. Symp. on DEIV, Santa-Fe, USA, pp. 381-387, 1990.
3. N.V. Tatarinova. Processes in Surface Layer Micropores of High Voltage Electrodes and Vacuum Electroinsulation. - Proc. of XV Int. Symp. on DEIV, Darmstadt, pp. 761-765, 1992.
4. P.N. Chistyakov, A.L. Radionovsky, N.V. Tatarinova, D.S. Treshnikova. Vacuum Electrical Insulation Characteristics under Controlled Conditions of the Electrode Surface. Proc. of V Int. Symp. on DEIV, Poland, pp. 361-365, 1972.
5. N.V. Tatarinova. Mechanism of Vacuum Insulation Damage in Consequence of Discharge in Surface Layer Micropores. - Preprint of Moscow Physical Engineering Institute, pp. 76-88, 1988.
6. N.V. Tatarinova. Total Voltage effect and Enhanced Electric Macrofield Strength in Vacuum Breakdown Experiments.- Proc. of VII Int. Symp. on DEIV, Novosibirsk, Russia, pp. 113-116, 1976.
7. N.V. Tatarinova. Another Cause of Vacuum Insulation Electrical strength Decrease Following the Bakeout of Metal-Insulator Electrode System. - Proc. of this Symp. (to be published).

Y.N. Vershinin, A.A. Podrezov, S.V. Barahvostov

Institute of Electrophysics Urals Division of the Russian Academy of Sciences
34, Komsomolskaya Str., Ekaterinburg, 620219, Russia

ABSTRACT

The effect of injection processes on the pulse discharges propagation mechanism in solid dielectrics has been shown. It has been established, that during a cathode discharge these processes are analogous to laser action on solids, while in the case of an anode discharge they are similar to detonations of explosives.

1.INTRODUCTION

According to traditional conceptions established in the physics of solid dielectric breakdown, the basic mechanism, determining regularities of this process, is the shock ionization of valence electrons by conduction electrons. With cathode discharge conduction electrons get into the discharge gap as a result of injection from the cathode or from the head of the discharge channel. With anode discharge this happens as a result of inward injection of valence electrons through the forbidden zone. The difference between the dynamic characteristics of these discharges is explained, usually, by the difference in resulting electric fields in the region of volume homo- and heterocharges. The values of critical fields E_m , for which there occurs a disruption in the condition electron velocity distribution function have been termed criteria of shock ionization or criteria of breakdown. This point of view, which is correct for narrow-gap semiconductors, cannot be extended to wide-gap dielectrics for many reasons.¹

Earlier it has been established,² that

$$E_k < E_m < E_l, \quad (1)$$

Here E_k, E_l - are critical field intensities, limiting the range of fields in which overheat instability of S - type conduction electrons appears, which leads to cord of the current. This occurs with electron energies $\epsilon_n \leq 1.5eV$, which are allowed by energy zones of electrons.

Coincidence of criteria (1) is physically justified. Indeed, for the development of S - type instability it is necessary, that in the range of fields $E_k < E < E_l$ in the fluctuation region either the electron concentration n_e , or electron mobility μ_e gets increased. Criterion E_m , fulfilled with $\epsilon_n \cong 0.1eV$ testifies to the latter. Of fundamental significance for the formation of a qualitatively new approach to the description of injection processes with the emergence and spreading of pulse discharges was the experimentally determined dependence.³

$$V_{cd} < C_0 < V_{ad}, \quad (2)$$

where V_{cd}, V_{ad}, C_0 - are respectively rates of discharges from the cathode, and, anode, and velocity of sound in solid dielectrics.

There were developed electro - and magneto - hydrodynamic (EHD and MHD) theories of these processes.^{4,5} Quantitative analysis of calculation correlations, ensuing from these theories, has led to the following results.

2.DISCHARGE FROM THE CATHODE.

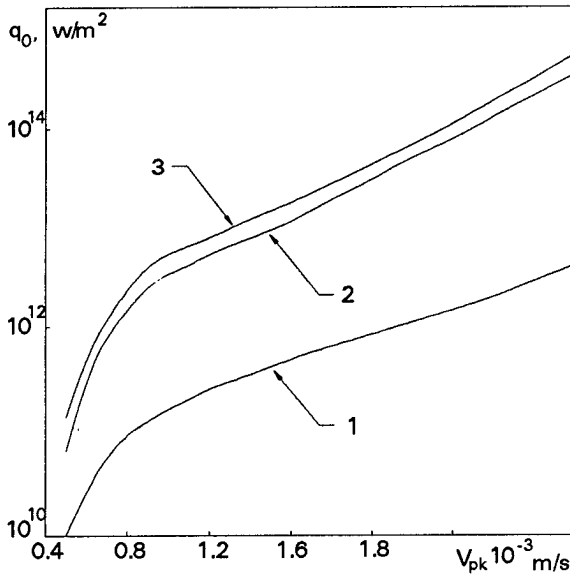


Fig. 1 The density of the power at the cathode discharge. 1, 2 - on phase surfaces F_1 and F_2 , 3 - Σq_0 .

$W_0 = 0, B = 3.33 \cdot 10^2$. It has been determined, that criterion (3) is not fulfilled on the assumption of existence in the discharge channel of one PS (F_0), on which the "solid - gas (plasma)" transition occurs. In this case, if $P_1, T_1 < P_c, T_c$, then $V_{cd} = D < V_{cd, \min} \cong 800$ m/s. If $8 \cdot 10^2 \leq V_{cd} \leq 3 \cdot 10^3$ m/s, then $P_1, T_1 > P_c, T_c$. At the same time, criterion (3) is satisfied by the consecutive transformation of solid dielectric first into a melt (F_1), and then - into a gas (plasma) (F_2). Power density on the surface.

$$q_2 = \Delta h V_{cd} = \frac{l}{\sigma} \left\{ \frac{\epsilon \epsilon_0}{r_0^2} \left[2 \frac{dU}{dt} \left(r_i + \frac{l}{\ln(l/r_0)} \right) + \left(\frac{r_i}{h} \right)^2 V_{cd} U_0 \right] \right\}^2 \quad (5)$$

where r_0, r_i - are radii of the injecting part of the discharge channel and of the volume charge, l - is the length of the melt zone, σ - is its electrical conductivity, Δh - is the change in enthalpy per unit mass, h - is the magnitude of the discharge gap, $U_0, dU/dt$ - are instantaneous values of parameters of the pulse voltage when the discharge channel appears. (Fig.1) Comparison of values $q(V_{cd})$ with data⁷ on the dependence $D(q)$ with laser action on Al is shown in Fig.2. This is evidence of the closeness of the physics nature of these, at the first glance, quite different processes.

It is known,⁶ that in case of propagation of the phase transition front (PTF) at velocities $D < C_0$, the substance state parameters behind the PTF are less than critical, i.e.

$$P_1, T_1 < P_c, T_c, \quad (3)$$

Calculation of pressure P_0 on the phase surface (PS) with $D = V_{cd} < C_0$ were carried out using formula⁶

$$P_0 = B \frac{R_0 T_n}{\mu_a} \exp\left(\frac{W_0}{k T_n}\right), \quad (4)$$

where $P_0 = P_n, T_n$ - are the pressure and temperature at PS, R_0 - is the gas constant, μ_a - is the gram-atomic weight, W_0 - is the phase transition potential barrier, $B/\rho_0 = 10^2 + 10^3$, ρ_0 - is the density of

saturated vapours. For NaCl with $T_n = T_c = 3400$ K, $P_0 = P_c = 35$ MPa, $\rho_0 = \rho_c = 220$ kg/m³,

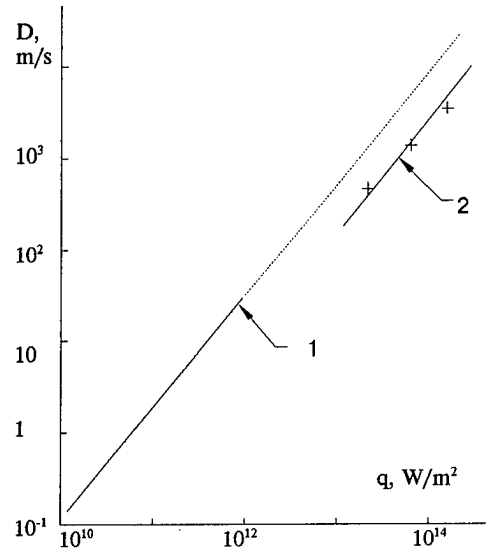


Fig. 2 Velocities of the spreading of phase passages at the laser influence on Al(1) and at the cathode dis-

3.ANODE DISCHARGE.

With pulse voltage, especially in the nanosecond range, when $dU/dt > 10^{14}$ V/s, the density of the injection current j_i at head of the channel in section S_0 , closing on the displacement current $j_c = S_0^{-1} dQ/dt$, exceeds

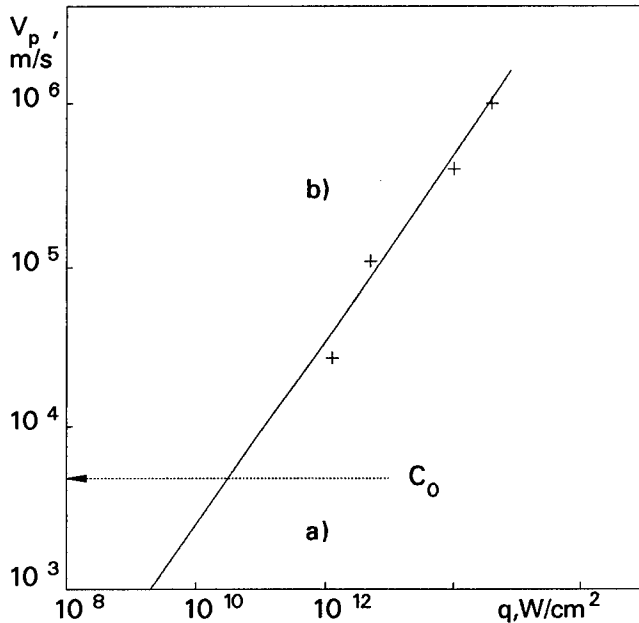


Fig. 3 Densities of the power at pulse discharge in KCl. C_0 - sound speed; a, b - areas of cathode and anode discharges.

$j_j = j_c > 10^6$ A/cm². These values of j_j approach those, which with the injection of electrons from the cathode induce a number of phenomena, called explosive electron emission.⁸

At the same time, the use of known quantum - mechanics formulas for determining j_j shows that when the width of the forbidden zone in dielectrics $\epsilon_g > 5$ eV, such current densities can be attained only in fields, $E \geq 10^8$ V/cm, which hardly can be fulfilled in experimental conditions. The elimination of this contradiction is connected with the exceptionally supersonic mechanism of propagation of the anode discharge and, as a consequence, with the generation of the shock wave (SW) phase transition front. It is known,^{9,10} that the action of a SW on dielectrics leads to a reduction of ϵ_g and to an increase of the temperature of the substance behind the front SW. Thus, for NaCl ($P_0=1$ bar)/ ϵ_g ($P_0=220$ kbar) = 3.5 and $T_n \approx 1300$ K. Under these conditions the requirement that $j_j = j_c$ is easily fulfilled at the expense of thermoautoelectron emission with $E \leq 10^7$ V/cm. An additional source of energy, released behind

the SW front, is the conversion of energy, stocked in the dielectric ($\sim \epsilon \epsilon_0 E_0^2/2$) into heat before the SW front.

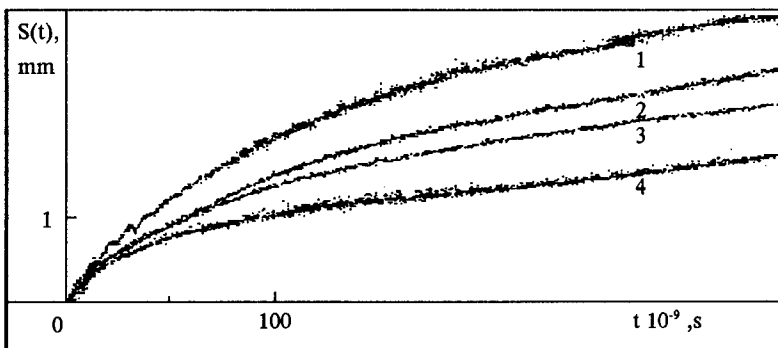


Fig. 4 Cronogrammes of the outflow of the highspeed component of the plasma from the channel of the anode discharge in KCl. 1 - 3 - $U_0 = 320, 270, 170$ kV; $C = 10^{-9}$ F. 4 - $U_0 = 250$ kV; $C = 4 \cdot 10^{-11}$ F.

The shock nature of these processes leads to that the anode discharge gains features, which are typical of the detonation of explosives. The common features for these processes are : exceptionally supersonic and constant speed of propagation of PTF the with generation by this front of SW; presence behind the SWF of an extensive "reaction zone" in which there take place phase transformations in the substance; the same laws of motion for the substance in this zone; dependence of substance state parameters (P ,

T , Δh) on the Mach number. With anode discharge the magnitude of M must be redetermined with account taken of field E ⁵. It is no coincidence, that in the range of velocities V_{ad} , coinciding with detonation velocities D ,

the equations describing the detonation of solid explosives,¹¹ prove to be correct in the calculation of anode discharge parameters.

If one imagines the "reaction zone" as a semiellipsoid of rotation with semiaxes l_p and r_0 , then the power density at the end of the reaction zone will be equal to:

$$q_a = \Delta h V_{ad} = 1.84 \cdot 10^{-2} \epsilon \epsilon_0 \left[\frac{U_0^2 V_{ad}}{r_{0,min}^2} + 2.88 \frac{\epsilon \epsilon_0}{r_0^4} \left(\frac{dU}{dt} \right)^2 \frac{l_p^3}{\sigma} \right], \quad (6)$$

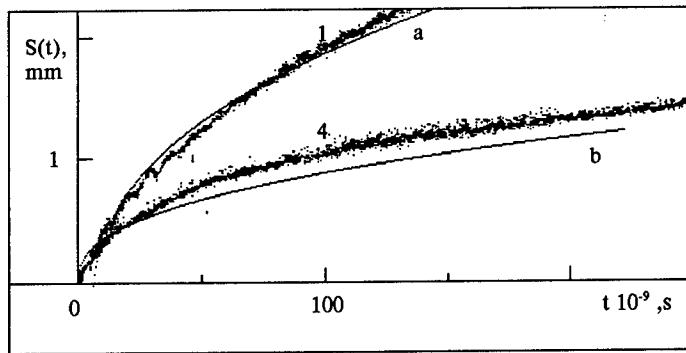


Fig. 5 The comparison of experimental and calculated magnitudes $S(t)$. 1,4 - Fig.4; a,b - calculate (7), $E_0(a) = 1$ J, $E_0(b) = 10^{-2}$ J.

theory of point explosion¹³ for the description of this process. It has been established, that the initial stage of the outflow of the high-speed plasma component is described by the automodel equation.¹³

$$S(t) = \left(\frac{\epsilon_0}{\alpha \rho_1} \right)^{1/5} t^{2/5}, \quad (7)$$

where $S(t)$ - is a shock wave coordinate depending on time t , ϵ_0 - is the energy of a point explosion, ρ_1 - is density of air, α - is a coefficient, with $1.1 \leq \gamma \leq 3$ and spherical symmetry $\alpha = 0.5$. At later stages of propagation of SW ($t > 50$ ns) experimental values of $S(t)$ exceed those calculated according to (7). This means (Fig.5), that behind the SW front supplementary energy¹³ is released.

Values of energy ϵ_0 , for which $S(t)$, calculated according to formula (7), coincided with experimental ones, were compared with the energy $W = CU^2/2$, stocked in the pulse voltage source. It has been found that the part of the energy, expended on the formation of the high-speed plasma component, is $(10^{-2} - 5 \cdot 10^{-2}) W$.

4. CONCLUSION

Thus, the difference in spatial-time regularities of discharges from cathode and anode is linked with essentially different injection mechanisms and their energy consequences. With discharge from the cathode they lead to processes, analogous to those, which take place with laser action on solids. With discharge from the anode we have processes, that are typical of explosive detonation.

As is known¹¹, the detonation process can be imagined as a joint action of shock wave and chemical reaction. The shock pulse initiates the reaction, and the energy of the reaction maintains the amplitude of the wave.

In our case, the shock pulse leads to a reduction of the width of the forbidden zone ϵ_g and to an increase of temperature behind the SW front. In its turn this creates conditions for an internal shock thermoautoelectronic emission of electrons and to the release behind the SWF of considerable specific energy, which maintains the SW amplitude. Hence, the anode discharge propagation mechanism has been termed electron-detonative.

5. REFERENCES

1. M.A. Lampert, P. Mark, "Current injection in solids", N.-Y.-L., 1970.
2. Y.N. Verzhinin, Y. Zotov, "Overheated instability in crystal isolators," *Sov. Phys. Sol. St.*, t. 17, Vol. 3, p. 826, 1975.

Here $r_{0,min} \cong 10^{-5}$ cm - is the minimum radius of the reaction zone; l_p, σ - are its length and electrical conductivity.

The enthalpy change Δh was determined according to a calculation and experimental method¹² with simultaneous electronic - optical registration of discharge speeds V_{ad} . Power densities power $q = V_{cd} \Delta h$, that developed at the PTF with pulse discharges in KCl crystals are shown in Fig. 3.

Analysis of chronograms of plasma outflow from the discharge channel (Fig.4) has confirmed the possibility of using the

3. Y.N. Vershinin, "Correlation of velocities of electric discharge and solid dielectric," *Jorn. of Techn. Phys.*, t. 59, Vol. 2, p. 158, 1984.
4. Y.N. Vershinin, A. Pleshanov, "To common equations of breakdown of condensed media," *News of USSR Acad. of Scien., Energy and Transp.*, N 6, p. 75, 1987.
5. Y.N. Vershinin, "Descarrega per impulsos en els dielectrics solids," *Butll. Soc. Cat. Cien.*, Vol. XII, N 2, p. 533, 1991.
6. "Physics of high energy density," *Pros. of the Intern. Sch. of Phys., "Eurico Fermi"*, N.-Y.-L., 1971.
7. S. Anisimov, Ja. Imas, G. Romanov, "Effect of the radiation of much power on materials", *Science*, Moscow, 1970.
8. G.A. Mesyats, "Electron explosive emission and electrical discharge in vacuum", *Proc. VI Int. Symp. on Discharges and Electrical Insulation in Vacuum*, pp. 21-47, 1974.
9. "Solid under pressure," ed. by W. Paul and D.M. Warschauer, N.-Y.-S., Fr.-T.-L., 1963.
10. L. Altschuler, "Application of shock waves in physics of high pressures," *U.F.N.*, t. 85, Vol. 2, pp. 197-258, 1965.
11. "Kurzzeitphysik," herausgegeben von K. Vollrath und J. Thomer, W.-N.-Y., 1967.
12. Y. Vershinin, A. Podrezov, S. Barahvostov, A. Pleshanov, I. Rogdestvensky, "Diagnostics of the parameters of state in the channel of nanosecond discharge in the solid dielectric," *Proc. IEEE International Conference on Properties and Application of Dielectric Materials*, pp. 1189-1191, 1991.
13. B. Korobeinikov, "Problems of the theory of the point explosion", *Science*, Moscow, 1970.

Discharge initiation system in electrothermal launcher

Chebotarev A.V., Kolensky I.L., Kulikov Ju.A., Melnik A.V., Shcolnikov E.Ja.

Moscow Engineering Physics Institute,
115409, Moscow, Kashirskoye shosse, 31

ABSTRACT

A discharge initiation system is developed which is intended for discharge gap breakdown in an electrothermal launcher. It consists of a high voltage transformer, a pulse sharpening discharge element and a nonlinear inductance or magnetic switch. The high voltage transformer with air as dielectric produces output voltage up to 130 kV. It permits to realize with certainty the breakdown of gaps with length up to 3 cm. The breakdown occurs along the surface of dielectric dividing the gap electrodes, polyethylene, fluoric plastic and ceramics being used as a material between electrodes.

The repetitive operational regime of an electrothermal launcher which is used as an equipment for producing coatings out of powder materials¹ requires a foilless discharge initiation system. Commonly, as in case of rocket plasma launchers an additional high voltage electrode is used which triggers the gap initial break-down. The specific discharge camera construction as well as characteristic discharge parameters of the electrothermal launchers motivated us to develop an initiation discharge system in which the triggering high voltage pulse is applied directly to the gap's electrodes. The schematic clarifying the system principle of operation is presented in Fig. 1.

A high voltage capacitor C_0 is charged from a high voltage source. At a certain voltage level the pulse sharpening gap S_1 is triggered and the capacitor C_0 gets connected to the main gap S_0 of the discharge circuit which consists of a nonlinear inductance (magnetic switch) L_s and preliminary charged capacitive store C_0 . After breakdown of the gap S_0 the magnetic switch L_s is moved into saturation regime due to the discharge current and its inductance drops to a small value.

The ferrite rings ($\mu=80$; $B_{\max}=0.4$ T) with inner and outer diameters correspondingly 60 and 100 mm were used as magnetic flux path in the switch. Several windings are wound around the rings and connected in parallel with the purpose of diminishing the magnetic switch inductance in saturation regime and avoiding the effects of ampere forces and wire heating. The number of windings and number of turns in each winding depend on the discharge circuit operational regime and discharge gap geometry. The latter has the shape of a cylindrical cavity surrounded by dielectric walls and having two electrodes: a pin-electrode at the input butt end and a ring-electrode at the output.

As an energy source the high voltage pulse transformer is used the primary winding of which is connected to a capacitor by means of a tiristor switch. The capacitor was charged up to the voltage not exceeding 600 V.

The transformer secondary winding contains 1000 turns which are wound by sections on a framework made of the organic glass. The framework is placed inside the insulating drum outside of which the primary winding is wound. The latter consists of 4 turns made of three copper bus-bars connected in parallel. For magnetic field concentration and coupling coefficient enhancement ferrite rings separated by insulating disks are placed into the space inside the secondary winding. The high voltage is being withdrawn along the drum axis by means of the cable central strand. The transformer dimensions are as follows: the length is 236 mm, the diameter is 116 mm. The primary and secondary windings inductances μH were 0.9 and 28.2 μH correspondingly, the coupling coefficient being equal to 0.7.

The loadless maximum voltage value at the secondary winding output without electrical breakdown was 60-70 kV. For the purpose of this value increasing some transformer oil was poured inside the insulating tube that resulted in obtaining output voltage values up to 120-130 kV. It appeared to be enough to realize with certainty the break-down of air discharge gaps with length up to 2.5-3 cm, the pressure in the gap being atmospheric. The break-down occurred along the inner surface of cylindrical dielectric. Polyethylene, fluoric plastic and ceramics were used as dielectrics.

REFERENCES

1. United States Patent; 4,142,089; Feb. 27. Pulsed coaxial thermal plasma sprayer.

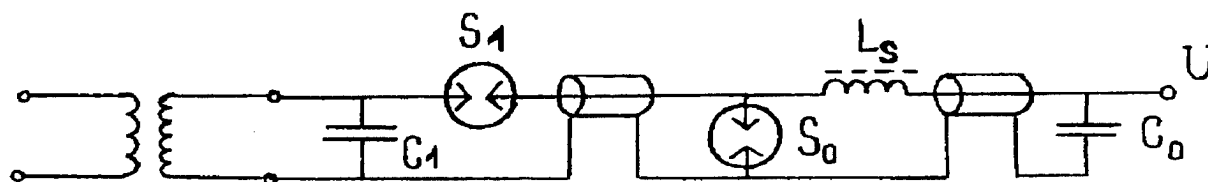


Fig. 1. Discharge initiation circuit.

A REAL-TIME OPTICAL STUDY OF DC AND PULSED-FIELD BREAKDOWN EVENTS IN HIGH-VOLTAGE VACUUM-INSULATED GAPS

N S Xu and R V Latham

Department of Electronic Engineering and Applied Physics, Aston University, Birmingham B4 7ET, UK.

ABSTRACT

A 'transparent anode' imaging technique has been used to display the spatial distribution of prebreakdown emission sites and the location of subsequent breakdown events. Using a real time video recording technique, it has been possible to address the following issues: (i) whether or not a spatial correlation exists between a DC prebreakdown emission site and the location of a subsequent DC or pulsed-field (PF) breakdown event, and (ii) the evolutionary character of both DC and PF breakdown processes.

1. INTRODUCTION

It has been long assumed that the field-induced prebreakdown electron emission processes associated with particulate-like surface microstructures are responsible for initiating the breakdown of a HV vacuum gap formed by broad-area electrodes [1]. However, there is no direct evidence confirming that breakdown events (both DC and PF) can be initiated from a DC prebreakdown emission site (PES). Also, there is a need to obtain a clearer physical picture of the breakdown mechanism itself. This paper describes how the Transparent Anode imaging technique [2] has been adapted for an experimental study aimed at addressing the above needs.

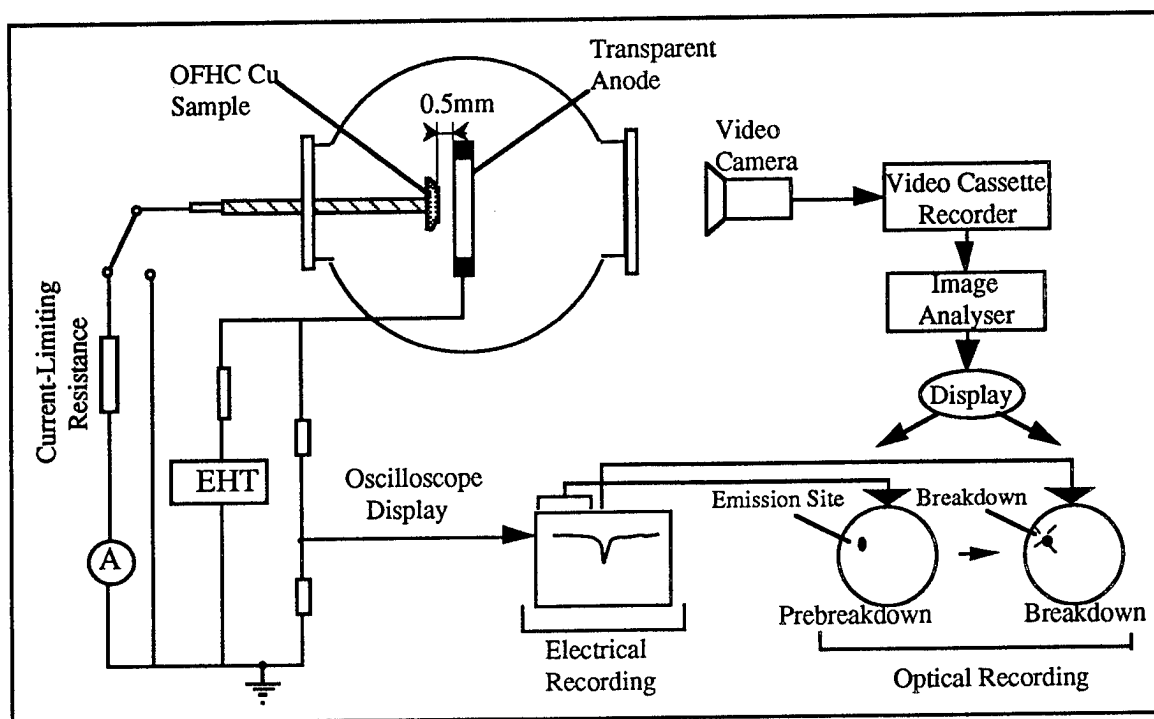


Fig 1 The experimental set-up for the present study.

2. EXPERIMENTAL

2.1 SYSTEM

As illustrated in Fig 1, the study is based upon a UHV vacuum chamber ($<10^{-9}$ mbar) containing a test gap formed between a transparent anode and a 15mm diameter Cu cathode. The transparent anode is made from a glass substrate coated with conducting tin-oxide, and is used to record the spatial distributions of both prebreakdown emission sites and the locations of breakdown arcs. Thus, the visible light (transition radiation) generated on the anode by the impact of electrons can be directly correlated to the position of emission sites [2]. A video camera with a frame speed of 40ms is used to record optical images in real-time sequences. To complement these recordings, an oscilloscope (Techtronix 7904) is used to monitor the time-profile of the collapsing gap voltage. Finally, an in-house built HV pulse generator provides output pulses of magnitude up to 15 kV with a rise time of $\sim 1\mu\text{s}$.

2.2 PROCEDURES

A common preparation procedure was employed for both types of experiment illustrated in Fig 2. Thus, the test surface of an as-machined Cu cathode is firstly mechanically polished and cleaned in an ultrasonic spirit bath. It is then mounted in the chamber and carefully adjusted to form a 0.5mm plane-parallel gap with the transparent anode. The chamber is then pumped down to its operating pressure of $\leq 10^{-9}$ mbar.

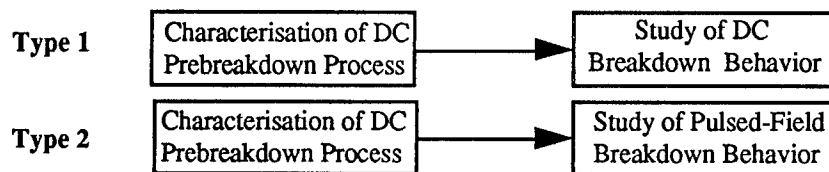


Fig 2 Illustrating the two types of evolutionary experiment reported in this paper.

In each of the following electrical measurements, a video camera system is set to make a continuous and concurrent record of all optical activity that occurs in the gap, thus making it possible to correlate the optical and electrical characteristics of the test cathode.

DC Prebreakdown Characterization This involves very slowly increasing the field applied to the virgin specimen until its "first generation" of emission sites are switched-on to establish a reversible prebreakdown current of $\sim 1\text{-}10\mu\text{A}$. The map of these sites is recorded on video film and can be used as a reference for a later spatial correlation analysis. In addition, the I-V data are collected in order to derive an effective β -value for the given population of sites.

DC Breakdown Study To initiate a breakdown of the test gap, the applied field is slowly increased until there is a sudden jump in the gap current, accompanied by a collapse of the gap voltage.

PF Breakdown Study For this type of study, the amplitude of the pulsed-field is increased incrementally in 500V steps, starting from a value that is $\sim 75\%$ of the maximum DC field used to record the prebreakdown I-V characteristic of the gap. At each pulsed field level, up to 15 pulses are fired to determine whether or not breakdown events occur. The reason for doing this will be explained later. If breakdown events do occur, then pulses are continuously fired until no more such events are observed at this field level. The magnitude of the pulse is then again incrementally increased and the process repeated.

2.3 FINDINGS

Type 1 Measurement Fig 3a illustrates the typical optical images obtained from two sequential video frames. Frame 1 displays the spatial distribution of DC prebreakdown sites just before breakdown, whilst Frame 2 shows the locations of the subsequent breakdown arcs. It is important to note that the position of one of these arcs coincides with the prebreakdown site. In fact this study has shown that 80% of DC breakdown events are initiated at DC prebreakdown emission sites. In addition, Frame 2 shows that a DC breakdown event can consist of a number of localised arcs.

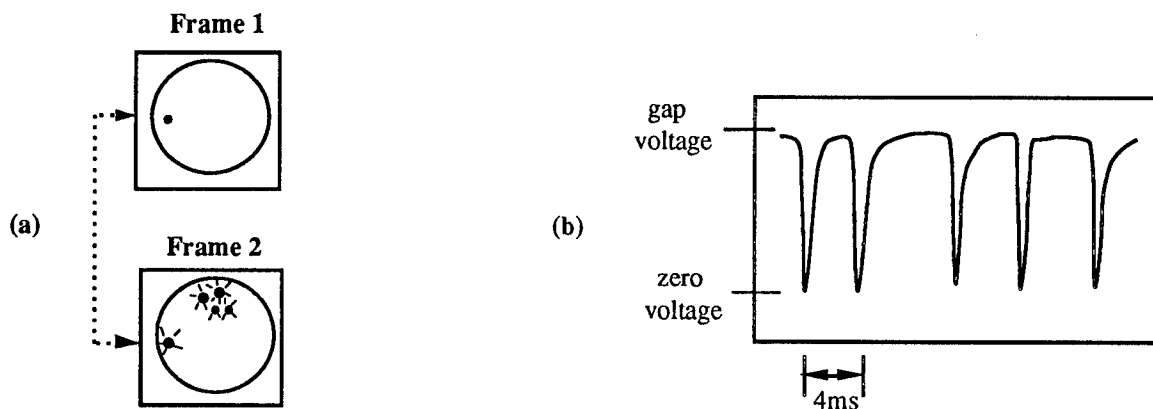


Fig 3 Illustrating (a) how two optical images from consecutive video frames confirm that a spatial correlation exists between a PES and the primary arc of a breakdown event, (b) the associated record of the collapsing gap voltage.

To complement this optical data, Fig 3b illustrates a typical oscilloscope trace of the time profile of the collapsing gap voltage during a period of ~20ms of a DC breakdown process, where each collapse is seen as a downwards pointing peak. As can be seen, 5 peaks are recorded, where the time interval between two successive peaks can be as short as ~4ms.

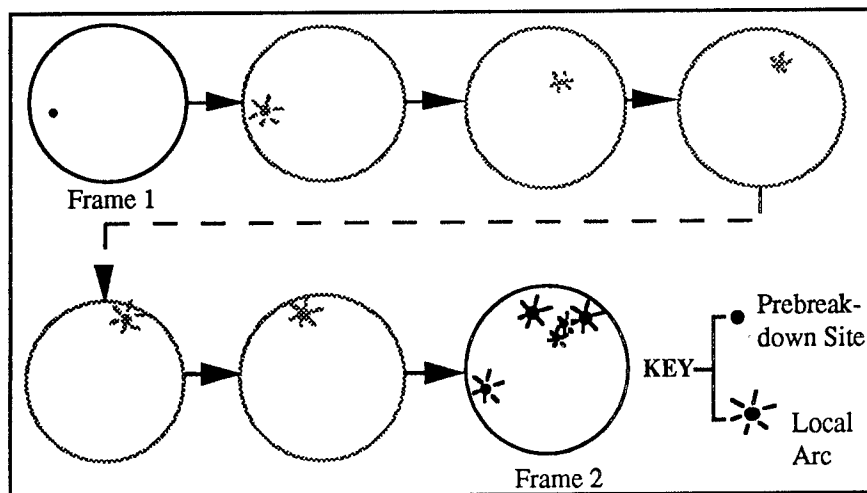


Fig 4 A schematic illustration of the time-resolved evolutionary process assumed to be responsible for the integrated image of a DC breakdown event shown in Fig 3a.

From a comparison of the gap voltage profile of Fig 3b and the optical breakdown image of Fig 3a, it will be seen that there is an apparent numerical correspondence between the number of breakdown arcs and collapses of the gap voltage. It is therefore reasonable to assume that a DC breakdown event involves a sequence of spatially random localised-arcs as illustrated in Fig 4. To experimentally verify this, it would be necessary to employ a higher frame speed recording technique.

Type 2 Measurement Fig 5 illustrates the typical findings obtained from optical imaging and electrical measurements recorded with the PF technique described in Section 2.1 above. Thus, Fig 5a illustrates how a PF breakdown arc is typically initiated at a PES. If this same cathode is now subjected to a further sequence of constant-value pulses, it is found to exhibit three distinct evolutionary phases in its response. Thus, referring to Fig 5b, it is found that, during Phase I, corresponding to ~6 pulses, no breakdown events are initiated. In contrast, Phase II is typically associated with ~25 breakdown events, where each pulse produces one breakdown event. In the following Phase III, up to a further 20 or more pulses can be applied to the gap without initiating a further breakdown event; ie it has become stable at this field. However, if the magnitude of the pulsed field is now increased, the typical three-phase process described above again repeats itself.

The typical spatial locations of the complementary optical processes is illustrated schematically in Fig 5b. This shows that the PF breakdown arcs associated with any given sequence tend to be clustered within a localised region of the cathode surface.

3. DISCUSSION

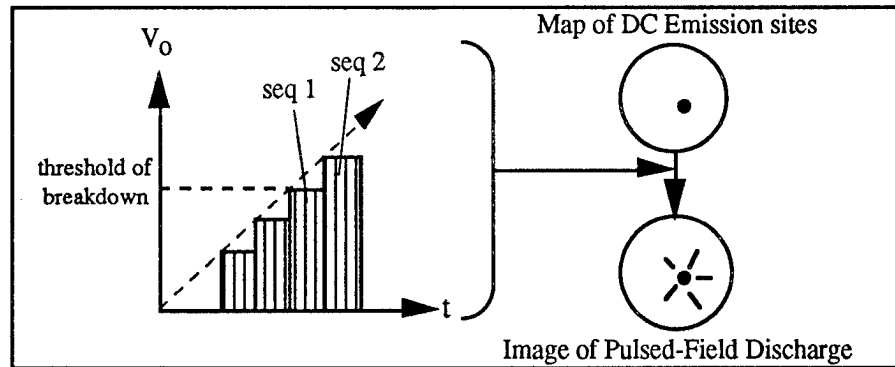
The first important finding to emerge from this study is the confirmation that a spatial correlation exists between a DC-PES and the location of a subsequent primary DC or PF breakdown arc. This therefore represents direct experimental evidence in support of the belief that a breakdown event is likely to be initiated at particulate-like surface microstructures that have a semiconducting or insulating nature; ie identical to those that are now accepted to be responsible for DC prebreakdown emission processes [1].

The second important finding is that a DC breakdown event is characterised by a primary arc followed immediately by a sequence of spatially random secondary localised discharges. The causes for the secondary discharges are not clear at the present. However, it is probable that they are breakdown events associated with new electron emission sites formed on the cathode surface, as the result of particulate materials being deposited on cathode surface during a previous discharge.

The third important finding is that a sequence of constant-value high-field pulses can de-stabilise potential emission sites; ie modify their electronic properties to the point where they are likely to initiate a breakdown event. In practical terms, a pulsed-field breakdown appears to be typically "delayed" by a sequence of ~6 pulses. This indicates that the pulsed-field breakdown processes that have been observed in the present experiments are very likely to be associated with non-metallic

emitters [1]: not least, because one would not anticipate a time delay in the occurrence of a breakdown event with metallic emitters.

(a) Spatial Correlation



(b) Evolutionary Characteristics

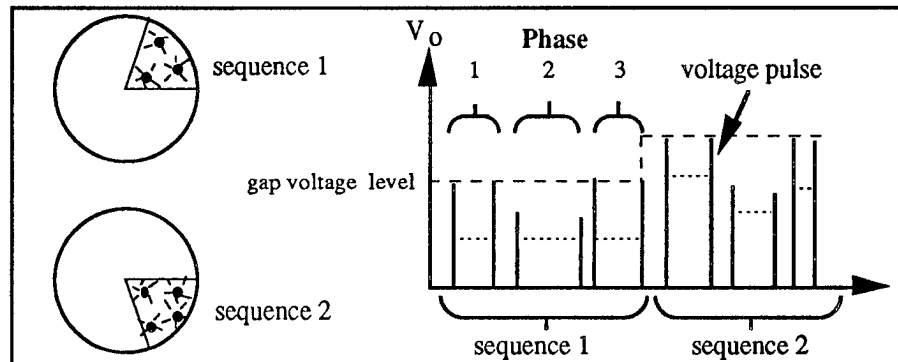


Fig 5 (a) Illustrating how successively applied pulse-sequences of incrementally increasing magnitude eventually lead to a PF breakdown event that is initiated at a DC-PES. (b) Illustrating how the breakdown arcs associated with a particular sequence of pulses are clustered within localised region of the cathode surface. NB: Each sequence consists of 15 to 25 constant-magnitude pulses, where the individual pulses are shown as single vertical lines: pulses that do not achieve the full gap voltage level correspond to the occurrence of PF breakdown events.

4. CONCLUSIONS

The following conclusions can be drawn from the present study.

- A spatial correlation exists between a DC prebreakdown emission site and the location of a subsequent DC or PF breakdown initiating arc.
- A DC breakdown event consists of a sequence of spatially random localised arcs.
- Potential emission sites can be "promoted" to initiate a breakdown by the application of a sequence of constant magnitude pulses.

5. ACKNOWLEDGEMENT

This work was supported by the Strategic Defense Initiative Organization's Office of Innovative Science and Technology (SDIO/TIN) through contract number N60921-91-C-0078 with the Naval Surface Warfare Center.

6. REFERENCES

- 1 R V Latham and N S Xu, "Electron Pin-Holes: The Limiting Defect for Insulating High Voltages by Vacuum, a Basis for New Cold Cathode Electron Sources", *Vacuum*, 42, pp1173-1181,1991.
- 2 R V Latham, K H Bayliss and B M Cox, "Spatially Correlated Breakdown Events initiated by Field Electron Emission in Vacuum and High Pressure SF₆", *J Phys D: Appl Phys*, 19, pp 214-231, 1986.

Influence of prebreakdown currents on the electric strength of vacuum gaps at large electrode areas

N.N. Koval, Yu.D. Korolev, and P.M. Shchanin

Institute of High Current Electronics, Siberian Division of the Russian Academy of Sciences, Tomsk 634055, Russia

1. INTRODUCTION

Electrode systems with electrode areas exceeding a few square meters and interelectrode gap spacings reaching several tens of centimeters are used in physical experiments for the production of large-cross-section charged-particle beams as well as for the separation and deflection of the particles. Under commercial vacuum condition, the breakdown voltage is strongly affected by the electrode size and surface condition and the electrode separation. Thus, for a 1-mm gap, increasing the electrode area a hundred times reduces the breakdown voltage by about one half, all other conditions being the same. Large and intricately shaped electrodes make the system degassing and conditioning more complicated. Prebreakdown currents produce an extra load on the power supply circuits and, in pulsed accelerators, they distort the beam currents waveform and often disturb the normal operation of the accelerator. This has stimulated the study aimed at refining the factors affecting the breakdown voltage, elucidating the mechanism for the prebreakdown conductance in the electrode gap, and developing the methods for suppressing prebreakdown currents.

2. EXPERIMENTAL SETUP

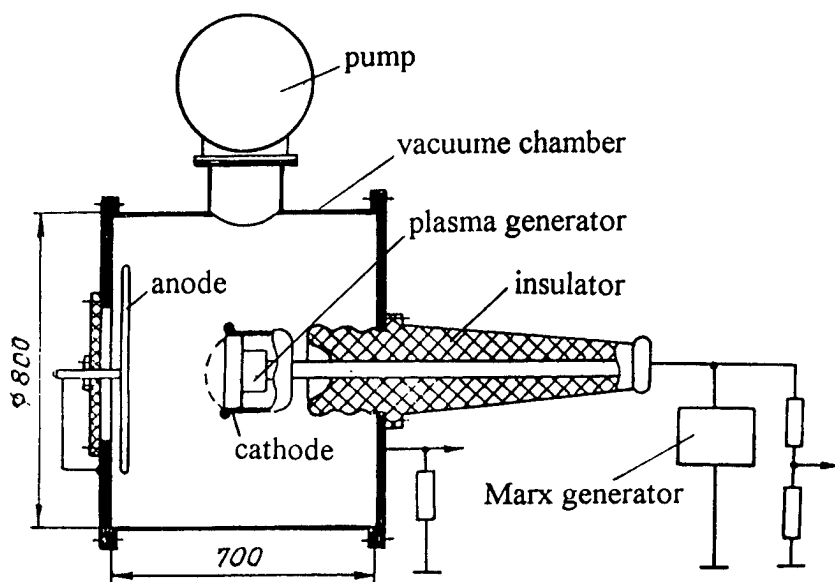


Fig. 1. Schematic of the experimental setup

Experiments were carried out on a diode-type electron accelerator, which is shown schematically in Fig. 1. In the vacuum chamber, a plasma cathode¹ of diameter 200 mm and length 250 mm with an emission plasma generator placed inside it was mounted on a bushing insulator. Experimentation was performed with the plasma cathode switched-on or switched-off. In the former case, an electron beam of pulse duration 50 μ s and current of a few amps was injected into the gap through a grid emitter electrode, while in the latter case, the emitter electrode was replaced for a solid disc. A pulsed voltage of FWHM duration 1 ms and peak voltage controlled in a range of 100 to 300 kV was applied to the cathode from a Marx generator. Served as an anode were the vacuum chamber and a movable disc of diameter 500 mm. By moving the disc, the gap spacing could be varied from 2 to 20 cm. In some tests, the disc was replaced for a foil window, through which the electron beam was extracted into the air. The currents flowing in the circuits of the vacuum chamber and disc anode were measured by resistive voltage dividers and Rogowski coils and recorded by a memory oscilloscope. The vacuum chamber was pumped out to a pressure of 10^{-4} Pa with the use of a nitrogen-trap diffusion pump. The pressure in the chamber was varied from 10^{-4} to 10^{-1} Pa by bleeding-in a gas (air, xenon). The pressure change caused by the predischage current flow in the gap was measured by a magnetodischage manometer placed behind the anode disc, opposite to a hole of diameter 10 mm, which was covered with a grid or foil to eliminate the influence of the discharge plasma on the readings of the manometer. Prior to measuring the pulsed pressure change, the manometer was calibrated by slowly varying the pressure in the vacuum chamber.

ing the disc, the gap spacing could be varied from 2 to 20 cm. In some tests, the disc was replaced for a foil window, through which the electron beam was extracted into the air. The currents flowing in the circuits of the vacuum chamber and disc anode were measured by resistive voltage dividers and Rogowski coils and recorded by a memory oscilloscope. The vacuum chamber was pumped out to a pressure of 10^{-4} Pa with the use of a nitrogen-trap diffusion pump. The pressure in the chamber was varied from 10^{-4} to 10^{-1} Pa by bleeding-in a gas (air, xenon). The pressure change caused by the predischage current flow in the gap was measured by a magnetodischage manometer placed behind the anode disc, opposite to a hole of diameter 10 mm, which was covered with a grid or foil to eliminate the influence of the discharge plasma on the readings of the manometer. Prior to measuring the pulsed pressure change, the manometer was calibrated by slowly varying the pressure in the vacuum chamber.

3. EXPERIMENTAL RESULTS

In a high vacuum with unconditioned electrodes, application of a pulsed voltage of more than 100 kV to the electrode gap initiates a high-voltage vacuum discharge (HVD), which is characterized by prebreakdown currents reaching 20 A, large (20 to 300 μ s) delay to the onset of the discharge with respect to the instant of voltage application, and spontaneous extinction of the discharge at high voltages²⁻⁴. In the majority of cases, the HVD results in a breakdown of the electrode gap, during which the voltage falls to zero in less than 1 μ s and the current rises to several kiloamps (Fig. 2).

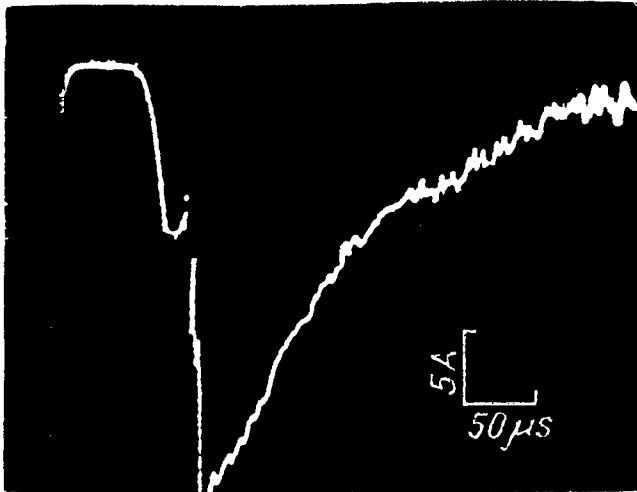


Fig. 2. Gap breakdown pulse waveform

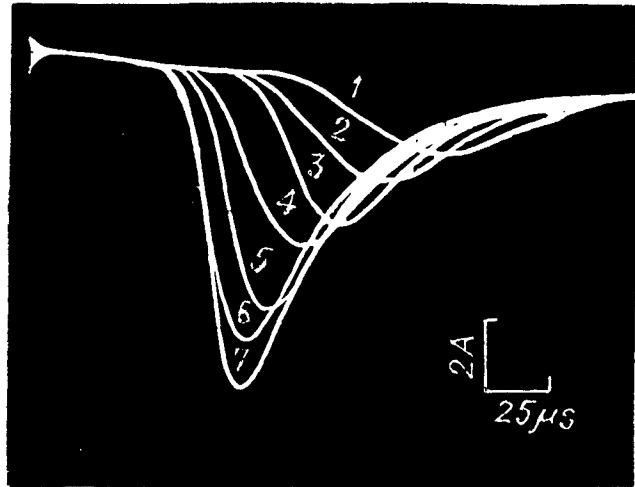


Fig. 3. Waveforms of HVD current for a voltage of 180 (1), 190 (2), 200 (3), 210 (4), 220 (5), 230 (6), and 240 kV (7). Pressure = 5×10^{-4} Pa; anode-cathode distance = 10 cm.

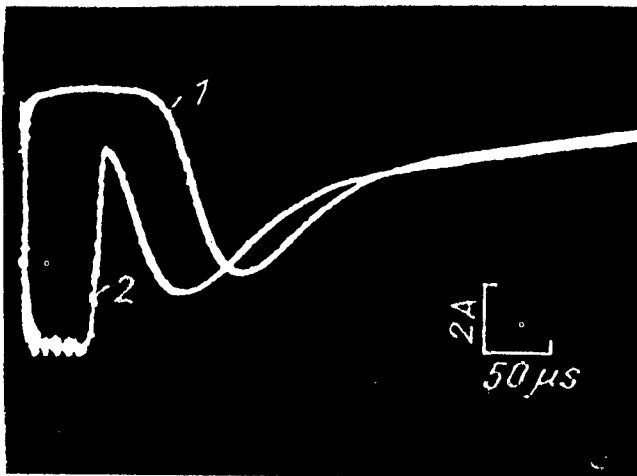


Fig. 4. E-beam and HVD current waveforms. 1 — HVD current, 2 — e-beam and HVD current. Voltage = 200 kV; anode-cathode distance = 10 cm.

ponds to the voltage applied across the gap. To elucidate the role played by electrons in the initiation and operation of a HVD, an electron beam was injected into the gap from the plasma cathode. Typical beam and discharge current waveforms are presented in Fig. 4. The injected beam current changes the discharge current only slightly, but decreases the delay time to discharge with respect to the instant of voltage application. As noted in Ref. 4, most obscure are the reasons for the self-extinction of a HVD and the factors affecting this event, since no electrode con-

Increasing the voltage applied to the gap increases the HVD current and decreases the delay time to HVD (Fig. 3). In prolonged operation, the conditioning effect is observed, which results in a decrease in discharge voltage. Thus, the current decreased two-fold after 80 pulses and four-fold after 130 pulses. However, at a voltage of 240 kV and pressure of 10^{-4} Pa, the discharge could not be completely suppressed. The HVD is strongly affected by a change in the pressure in the electrode gap. The discharge ceased, as the pressure was increased to 1.5×10^{-2} Pa. Meanwhile, the discharge could be suppressed at a smaller in pressure, when a heavier gas (xenon) was used.

As in the microdischarges occurring at a dc voltage^{5,6}, the main HVD current is carried in the gap by electrons, and, as shown in experiments with electron extraction through a foil, the electron energy approximately corres-

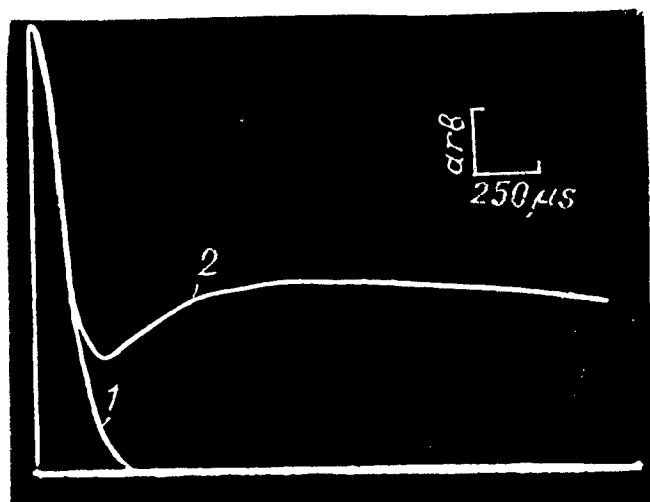


Fig. 5. HVD current (1) and gap pressure (2) waveforms

ditioning occurs in a single pulse and the next pulse is similar to the preceding one. The strong effect of a change in pressure on the HVD suggests that the discharge extinguishing during a pulse is also related to the increase in pressure in the discharge development. Shown in Fig. 5 (curve 2) is a pressure waveform measured by a magnetodischarge manometer. The burst at the early stage appears to be caused by the high-energy electrons that have found their way into the manometer, since it coincides with the pulse recorded in a test where the manometer inlet was covered with a foil (curve 1). The pressure increases by an order of magnitude and equals to or exceeds the pressure at which an HVD is suppressed at a constant or slowly varied pressure. Figure 6 shows the parameters of an HVD onto the disc electrode and vacuum chamber as functions of the distance between the cathode and the movable disc electrode. These data complement the experimental results that provide for an explanation to the effect of pressure on the operation of an HVD.

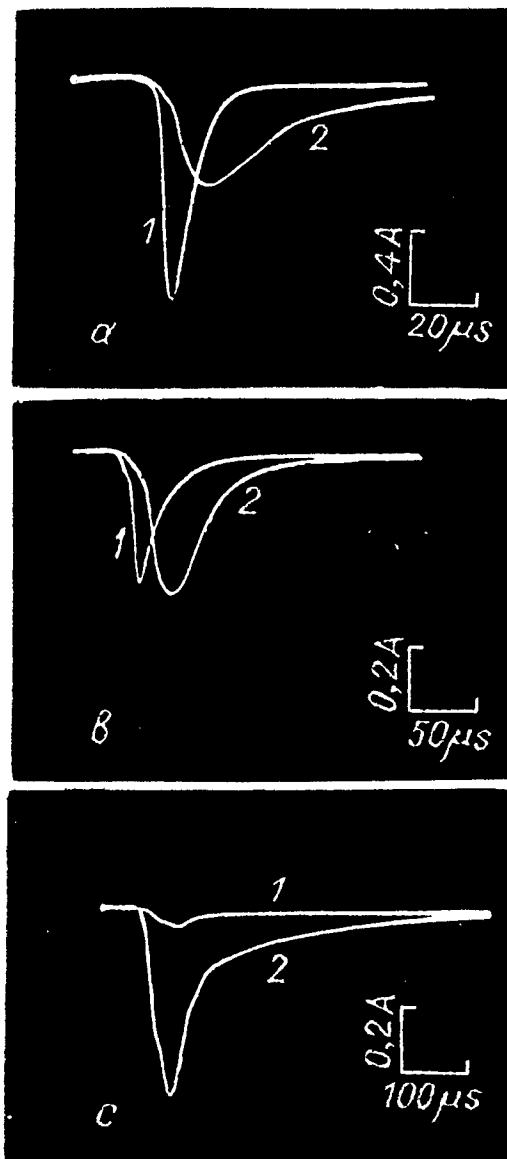


Fig. 6. Disc anode (1) and vacuum chamber (2) circuit current waveforms for a disc anode — cathode distance of 2.5 (a), 5 (b), and 7.5 cm (c). Voltage = 200 kV, pressure = 5×10^{-4} Pa.

4. DISCUSSION

The experimental results obtained suggest that the ion-exchange processes^{2,6} are the mechanism for the initiation of both microdischarges and a high-voltage vacuum discharge, despite the large difference in current. On application of a pulsed high voltage across a gap, the HVD current is the sum of the current of microdischarges occurring in the main at dielectric inclusions and contaminated regions of the electrodes. The current increases exponentially and, as shown in Ref. 2, can be described by the expression

$$I_t = \frac{(1 + A + C)e}{T} \exp[(t/T - 1/2) \ln(AB)]$$

where A is the number of negative ions knocked from the cathode by a positive ion, B is the number of positive ions knocked from the anode by a negative ion, C is the number of electrons knocked from the cathode by a positive ion, e is the electron charge, T is the time required for an ion to doubly cross the gap, t is the current time. Calculations have also shown that the discharge fails to develop, if the coefficient AB is less than unity.

The discharge self-extinction can also be associated with the disruption of the ion-ion exchange between the electrodes as a result of the scattering of ions on the gas molecules in the gap. Our calculations show that at the pressures over 10^{-2} Pa, at which the discharge is suppressed, the ion range becomes shorter than the gap spacing, therefore the ion scattering is a rather probable process. The increase in pressure in the passage of the discharge current is the result of gas desorption occurring in the interaction of electrons with the anode. The desorption coefficient (the number of molecules knocked from the anode by one electron) may be, under certain conditions⁷, greater than 10.

Based on the mechanism discussed, the more rapid extinction of the discharge in the cathode – disc electrode gap can also be explained (Fig. 6). As the HVD operates, electrons bombard mainly the disc anode, and the pressure increases first in this gap. This is just the reason why the discharge ceases more rapidly in this gap than between the cathode and the vacuum chamber wall.

5. ACKNOWLEDGMENT

This paper is supported by the Russian Foundation for Fundamental Research (Project code 93-02-17418).

6. REFERENCES

1. N.N. Koval, E.M. Oks, P.M. Schanin, Yu.E. Kreindel, and N.V. Gavrilov, "Broad beam electron sources with plasma cathodes", *Nucl. Instrum. Meth. Phys. Res.*, Vol. A321, pp. 417-428, 1992.
2. W.A. Smith, M.J. Inness, K.A. Fielding, and R. Pradhan, "Impulse breakdown of large gaps in vacuum", *Proc. IV Intern. Symp. on Discharges and Electrical Insulation in Vacuum*, Waterloo, Canada, pp. 96-101, 1970.
3. G.M. Kassirov, N.N. Koval, and V.N. Chekrygin, "Prebreakdown phenomena in the vacuum insulator of a 1.3-MV pulsed power system", *Prib. Tekh. Eksper.*, No 3, pp. 99-101, 1989.
4. Yu.E. Kreidel, N.N. Koval, and P.M. Schanin, "Pulse space discharge in vacuum", *Proc. VIII Intern. Symp. on Discharges and Electrical Insulation in Vacuum*, Albuquerque, USA, pp. F2-1—F2-7, September 1978.
5. L.I. Pivovarov and V.I. Gordienko, "Microdischarges and predischage currents between metallic electrodes in high vacuum", *Zh. Tekh. Fiz.*, Vol. 28, pp. 2289-2294, 1958.
6. V.I. Gerasimenko, "On the theory of microdischarges in interelectrode gaps", *Zh. Tekh. Fiz.*, Vol. 38, pp. 155-162, 1968.
7. E.N. Abdullin, G.P. Bazhenov, S.P. Bougaev, G.P. Erokhin, O.B. Ladyzhensky, and S.M. Chesnokov, "Generation of quasi-stationary electron beams on the basis of a vacuum discharge", *IEEE Trans. Plasma Sci.*, Vol. PS-13, N 5, pp. 338-339, 1985.

SESSION 2

Vacuum Arcs

Dependence of the non-stationary behavior of arc cathode spots on the discharge duration

B. Jüttner, W. Löffler, C. Weber, and G. Ziegenhagen

Max-Planck-Institut für Plasmaphysik, Research Group Electrode Processes
Hausvogteiplatz 5/7, D-10117 Berlin, Germany

ABSTRACT

In nanosecond vacuum arc discharges, the size of cathode plasmas has been found to have the order of 10 μm . This outcome has decisive consequences for particle density, current density, time constants, and radiation properties. The present paper explores the question whether there occur principal changes in longer discharges. Experimental methods were: imaging the spots of μs -discharges by absorption and emission techniques, and monitoring the shape of spectral lines in the range of nanoseconds through milliseconds. It has been found that in the light of atomic or ionic lines the diameter of emission pictures have the order of 100 μm , irrespective of the discharge duration in the range 10 ns through 100 μs . Pictures obtained by differential laser absorption¹ in the time range 100 ns through 50 μs yielded a size ≤ 30 μm . Time-integrated analysis of emitted spectral lines yielded broadened profiles for discharges of 800 ns duration with a FWHM (full width at half maximum) up to 0.5 nm. This indicates the effect of high densities and magnetic fields, possible only with small spots. The same has been found for discharge durations up to 100 ms. Thus, it is suggested that the spot size remains small up to discharge durations of milliseconds. This outcome is associated with a principal non-stationary spot nature.

1. INTRODUCTION

Parameters of cathode spot plasmas are controversial since decades, mainly because it is difficult to measure their exact size. There exist two different conceptions: (i) interpreting the spot as a quasi-stationary phenomenon² with a diameter ≥ 100 μm , time constants > 1 μs , plasma densities $< 10^{24}$ m^{-3} , and current densities $< 10^{10}$ A/m^2 , and (ii) interpreting the spot as a quasi-explosive phenomenon³ with a diameter $\ll 100$ μm , time constants < 100 ns, plasma densities $\gg 10^{24}$ m^{-3} , and current densities $\gg 10^{10}$ A/m^2 . A decision between these conceptions can be made when determining the size of the spot plasma.

In recent experiments¹ spot imaging by laser absorption resulted in plasma diameters ≈ 10 μm , particle densities $\geq 5 \times 10^{26}$ m^{-3} , and time constants < 10 ns, thus favouring conception (ii). These measurements were performed for times < 1 μs , so the question arises whether there is a transition to case (i) for longer discharges. This might be possible when the cathode becomes hot, but when the cathode as a whole remains cold, the rapid spot movement could preserve the basic parameters found in the ns-region. The present paper examines this question by several experimental methods. The most simple of them is photographing the spots. However, as shown in refs.⁴⁻⁶, even with very high time resolution this method yields too large dimensions when using the light from excited atoms and ions (instead of the continuum), because before radiation the excited particles fly 20-100 μm due to the limited transition probability and the high expansion velocity of the plasma. The second method is the absorption technique developed in ref.¹. Because it is possible only when the spots appear at the contour of the cathode, the spot motion renders it increasingly difficult for longer discharges. The third method is based on the idea that the quoted spot parameters for case (ii) should markedly influence the profile of emitted spectral lines. While in general the conditions are too complicated for quantitative evaluation, a transition

of the spot regime from case (ii) to case (i) should cause changes of the line profiles that are sufficient for qualitative conclusions.

2. EXPERIMENTAL SETUPS

Vapor-free vacuum systems were used with a base pressure $<10^{-6}$ Pa. The electrodes consisted of copper or titanium. They formed a point-to-plane gap, the anode being a cylinder of 10 mm diameter. The cathode diameter was 0.3 mm for discharges ≤ 100 μ s, and 1 mm for longer discharges. Due to numerous arcs, the cathode surface was thoroughly cleaned. Figure 1 shows the experimental systems: The current pulse was produced by discharging a charged coaxial cable CCC, which for discharges >1 μ s was backed by a capacitor bank C and connected to the discharge gap via a limiting resistor R2. When using the capacitor bank C the pulse length was limited by a short-circuiting switch SCS. The whole system was matched to an impedance of 50 Ω . For discharges ≤ 100 μ s the cable mantle was charged instead of the inner conductor. The advantage is that the input of the inner conductor could be grounded via the resistor R1=50 Ω so that pulses partially reflected at the electrodes could not be reflected again at the input. This is especially important when the whole discharge was registered in an open shutter mode. When the spark gap SG was fired, a pulse appeared at the inner conductor with the opposite polarity of the charging voltage U and a rising edge of ≤ 5 ns. The current was measured by a low inductivity shunt SH. It was varied in the range 30 - 150 A for discharges ≤ 100 μ s, and 5-350 A for the longer discharges. The arc was ignited at the closest distance to the anode by a breakdown (for short discharges) or by an additional trigger electrode (for long discharges, not shown in Figure 1). Due to the magnetic field of the current flow in the cathode, for times >1 μ s the spots were driven out of the gap and moved away from the anode along the circumferential surface of the cathode cylinder.

Three optical systems were used:

1. Imaging by laser absorption (Figure 1, system 1). At a preselected time during the discharge the gap was homogeneously illuminated by a laser beam LB. In the light of this beam (tuned to a desired wavelength with an accuracy of 10 pm) the spot plasma produced absorption structures that were registered via a magnifying optic MO by a CCD-camera and digitally processed. The duration of the laser pulse was 0.4 ns (=time resolution of the exposure), the spatial resolution was about 3 μ m. For the light emitted by the spot itself, the CCD-camera operated in an open shutter mode. This light was reduced by metal interference filters MIF with a FWHM of 6-9 nm, matched to the selected wavelength of the laser pulse. To reduce optical disturbances, a reference picture was taken without discharge, and the discharge picture was subtracted from this reference. The resulting pictures show absorption structures as bright areas, and emission structures as dark areas. More details can be found in ref.¹. In spite of the open shutter mode for the emission structures, the spot movement allowed a certain time resolution of about 1 μ s. The spectral resolution of the emission pictures was given by the metal interference filter.
2. Time resolved emission pictures by using a Hamamatsu-streak camera (Figure 1, system 2). The time resolution amounted to 2 ns, the spectral resolution was 6-9 nm (as in case 1), and the spatial resolution was about 10 μ m. The main results obtained with this method are reported in refs.^{5,6}. Here it was used to test whether the time resolution by the spot motion (case 1) was sufficient.
3. Time and spatially integrated measurement of line profiles (Figure 1, system 3). The emitted light was focused by the optic FO onto the entrance slit of a spectrograph SP having a spectral resolution of about 0.1 nm. For short discharges many exposures have been superimposed. For some exposures a polarization filter PF has been used.

3. EXPERIMENTAL RESULTS

Figure 2 shows a combined picture of absorption structures (at the contour, bright) and emission structures (in the middle, dark) caused by an arc of 80 A at a titanium cathode of 0.3 mm diameter. The discharge duration was 100 μ s, the laser for production of the absorption image was fired at $t=52 \mu$ s. The laser was tuned to the Ti-resonance line at 501.418 nm, the used filter was centered at 497 nm. The latter means that the emission image was mainly produced by five Ti I - lines at 498.173, 499.107, 499.951, 500.721, and 501.418 nm, having transition probabilities (ref.⁶) of about 7.6×10^7 , 6.9×10^7 , 7.1×10^7 , and $8 \times 10^7 \text{ s}^{-1}$, respectively. The emission images were always broad as in Figure 2, having diameters around 100 μ m and extending 50-100 μ m beyond the cathode contour. In contrast to this outcome, the diameter of the absorption structures was $<30 \mu$ m in spite of the used resonance line. A more exact study of the size of emission images was performed with the optical system 2 according to Figure 1. The results, presented in detail in ref.⁶, showed no systematic change of the size when varying the time from 10 ns to 100 μ s. Thus, their large size is not due to the spot movement. As Figure 2 indicates, no pronounced change was found also for the size of absorption images in the studied time range of 100 ns to 50 μ s.

As expected, the profiles of some spectral lines (system 3 in Figure 1) were broadened. For titanium with pulses of 800 ns at 100 A and superimposition of several thousand shots, FWHM-values up to 0.5 nm have been obtained. This is shown in Figure 3. The use of polarization filters reduced the width of the profiles (Figure 3b). For example, the FWHM of the Ti I line at 499.107 nm amounted to 0.46 nm, while a polarization filter reduced this value to 0.27 nm. A similar result was obtained with copper in discharges of 1-100 ms duration. Polarization effects have been found as well, and also some influence of the current, as shown in Table 1. Since the spectrum contained also lines with a width of about 0.1 nm, we can exclude trivial errors (as e.g. instabilities of the optical system). Interference by neighbouring lines might contribute in some cases, but it cannot explain the effect as a whole (in particular the influence of polarization filters).

Table 1: Observed FWHM $\Delta\lambda$ for Cu I Lines (in nm) in Dependence on the Total Current for Millisecond Arcing Times

CURRENT (A)	TIME (ms)	WAVE LENGTH λ (nm)					
		515.323		521.820		529.252	
		no PF	with PF	no PF	with PF	no PF	with PF
5	0.1	0.3	0.24	0.3	0.28	0.36	0.3
10	1	0.35		0.32		0.49	
40	10	0.38	0.34	0.42	0.30	0.80	0.52
180	25	0.54	0.36	0.84	0.36		0.75
350	40	0.60	0.30	0.84	0.30		0.40

PF - polarization filter oriented such as to obtain maximum reduction of FWHM.

4. DISCUSSION

According to section 3, absorption pictures at 50 μs indicate small diameters of the spot plasma like in the case of times $<1 \mu\text{s}$, reported in ref.¹. Emission pictures do not show principal changes in the time span 10 ns - 100 μs , although they are larger than the former because of the unavoidable time of flight effect of excited particles. If one accepts the conclusions from ref.¹ on high densities in nanosecond discharges, broad emission pictures obtained in microsecond discharges do not constitute an objection, because they are broad already at a few nanoseconds. So we do not find a transition of the spot operation when going from nanoseconds to microseconds.

Data on a millisecond time scale are difficult to obtain by the imaging techniques because of the complication by the spot motion. For these times, however, qualitative information is possible from the gross behavior of line radiation. According to table 1 we found for some lines broadening of $\Delta\lambda/\lambda \approx 10^{-3}$. Even if most line radiation stems from outside the spot core at distances $r=20\text{-}50 \mu\text{m}$ (ref.⁶), it should be influenced by the densities of particles and current. According to ref.⁷ at $r=50 \mu\text{m}$, $I=50 \text{ A}$ (arc current), for copper the particle density amounts to about $2 \times 10^{23} \text{ m}^{-3}$. This should lead to considerable pressure broadening (Stark effect) near the observed values of $\Delta\lambda/\lambda$. However, also splitting of the lines due to the self-magnetic fields of the spots should contribute (Zeeman effect) as demonstrated in ref.⁸. This is evident from the influence of polarization filters on $\Delta\lambda/\lambda$ (Table 1). Because of the limited resolution of our spectrograph, Zeeman splitting will appear as line broadening. It will slower decrease with increasing distance r from the spot center than the Stark effect, because the magnetic field varies as r^{-1} whereas the pressure decreases with r^{-2} . To obtain $\Delta\lambda/\lambda > 10^{-4}$ we need magnetic fields $>1 \text{ T}$, thus current densities $>10^{11} \text{ A/m}^2$. According to Table 1, $\Delta\lambda/\lambda$ reacts on the arc current only when registered without polarization filter. In this case, the increase with current can be due to superimposition of the spot field with the fields of neighbouring spots the number of which grows with the current. The enhanced magnetic field will then influence the magnetized components of the lines. The absolute value of the observed broadening can be explained only by a combination of Stark effect and Zeeman effect. Other mechanisms as e.g. Doppler broadening by the plasma expansion can be neglected ($\Delta\lambda/\lambda < 10^{-4}$).

Since line broadening was found with discharges of 800 ns duration as well as with millisecond duration, a change of spot mechanisms seems to be absent in this time range. Spot imaging allows the same conclusion for the range 10 ns - 100 μs . Thus, the quasi-explosive spot mechanism is important not only for nanosecond discharges.

5. ACKNOWLEDGMENTS

The present work was supported by the contract DFG Ju 227/3-2 of the Deutsche Forschungsgemeinschaft. The authors are indebted to Prof. W. Böttcher and his colleagues, University Hannover, for very helpful discussions and their aid with hardware and software.

6. REFERENCES

1. A. Anders, S. Anders, B. Jüttner, W. Böttcher, H. Lück, and G. Schröder, "Pulsed Dye Laser Diagnostics of Vacuum Arc Cathode Spots", *IEEE Trans. Plasma Sci.*, Vol. **20**, pp. 466-472, 1992.
2. V. I. Rakhovsky, "Experimental Study of the Dynamics of Cathode Spots Development", *IEEE Trans. Plasma Sci.*, Vol. **PS-4**, pp. 81-102, 1976.

3. G. A. Mesyats and D. I. Proskurovsky, *Pulsed Electrical Discharge in Vacuum*, Springer, Berlin, 1989.
4. A. Anders, S. Anders, E. Hantzsch, B. Jüttner, and G. Ziegenhagen, "Optical Investigation Of Arc Cathode Spots in Vacuum", *Proc. XXIth Int. Conf. Phen. Ionized Gases*, Vol. I, pp. 3-4, Bochum, 1993.
5. E. Hantzsch and B. Jüttner, "On the Appearance of Vacuum Arc Cathode Spots Imaged by the Emitted Light", this Symposium.
6. E. Hantzsch, B. Jüttner, and G. Ziegenhagen, "Why Arc Cathode Spots Appear Larger Than They Are", prepared for publication.
7. B. Jüttner, "On the Plasma Density of Metal Vapour Arcs", *J. Phys. D: Appl. Phys.*, Vol. **18**, pp. 2221-2231, 1985.
8. N. Vogel and B. Jüttner, "Measurements of the Current Density in Arc Cathode Spots from the Zeeman Splitting of Emission Lines", *J. Phys. D: Appl. Phys.*, Vol. **24**, pp. 922-927, 1991.

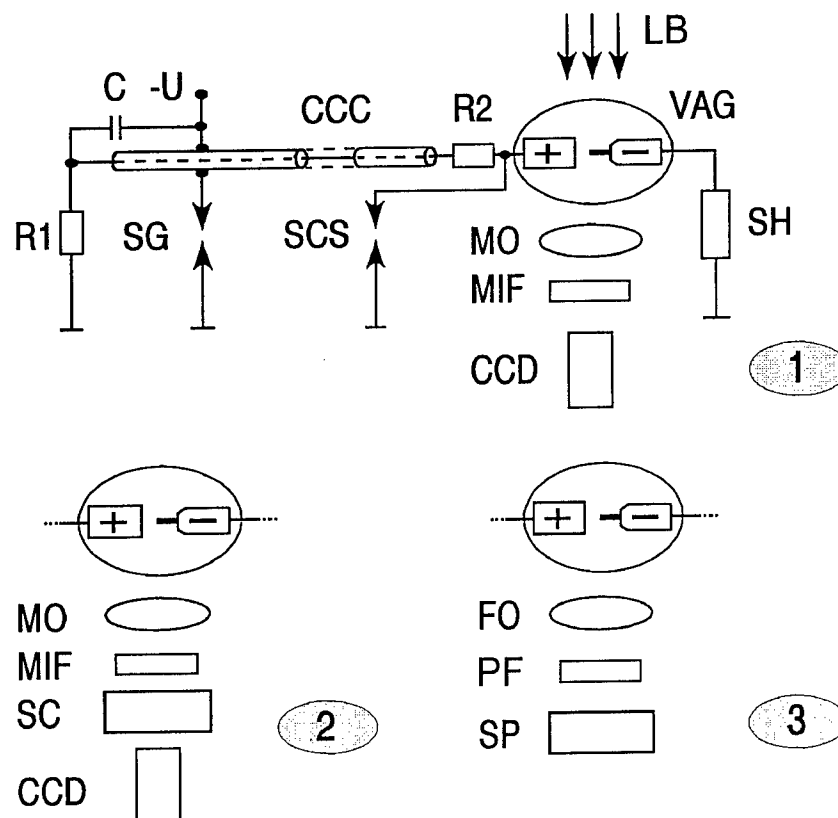


Fig. 1: Experimental setups. 1) Absorption and Emission Pictures, 2) Time-resolved Emission Pictures, 3) Time and Spatially Integrated Profiles of Spectral Lines.

R1, R2 - resistors, C - capacitor bank, CCC - charged coaxial cable, U - charging voltage, SG - pressurized spark gap, SCS - short-circuiting switch, VAG - vacuum arc gap, SH - shunt, LB - laser beam, MO - magnifying optic, FO - focusing optic, MIF - metal interference filter, PF - polarization filter, CCD - camera, SC - streak camera, SP - spectrograph.

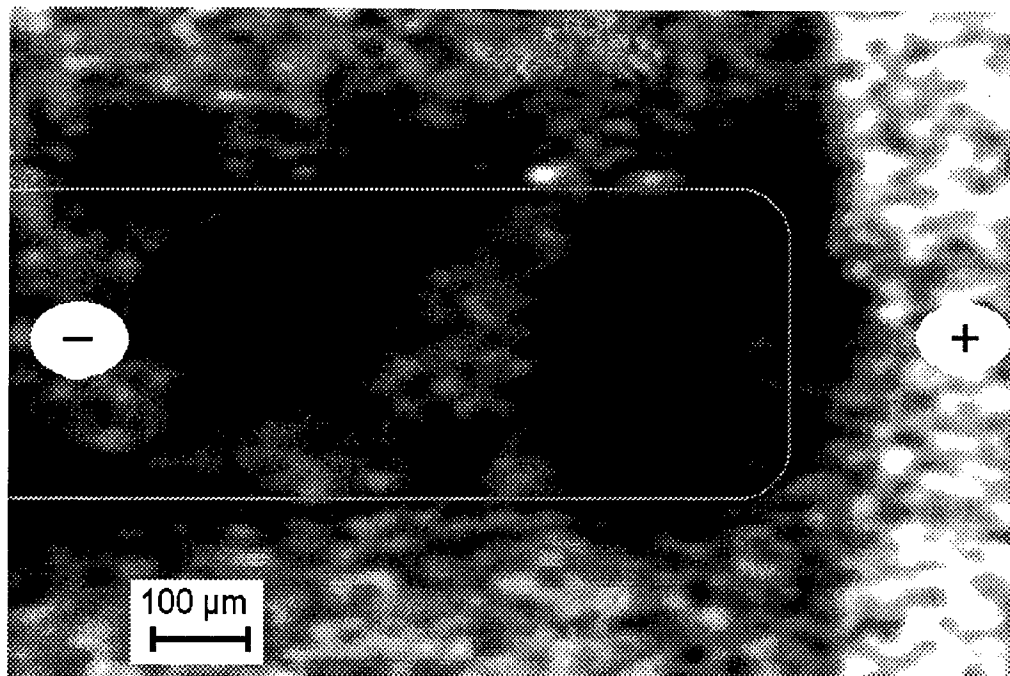


Fig. 2: Absorption and emission images of a Ti- arc of 80 A with 100 μ s duration (setup 1 according to Figure 1). Two absorption structures at the upper contour of the cathode cylinder can be seen (bright), and broad emission structures extending beyond the contour of the cathode (black, due to inverted presentation). The imaging laser was tuned to the resonance line Ti I at 501.418 nm and fired at $t=52 \mu$ s. The metal interference filter MIF was centered at 497 nm. While the absorption structures were taken with 0.4 ns exposure time, the emission structures were taken in an open shutter mode.

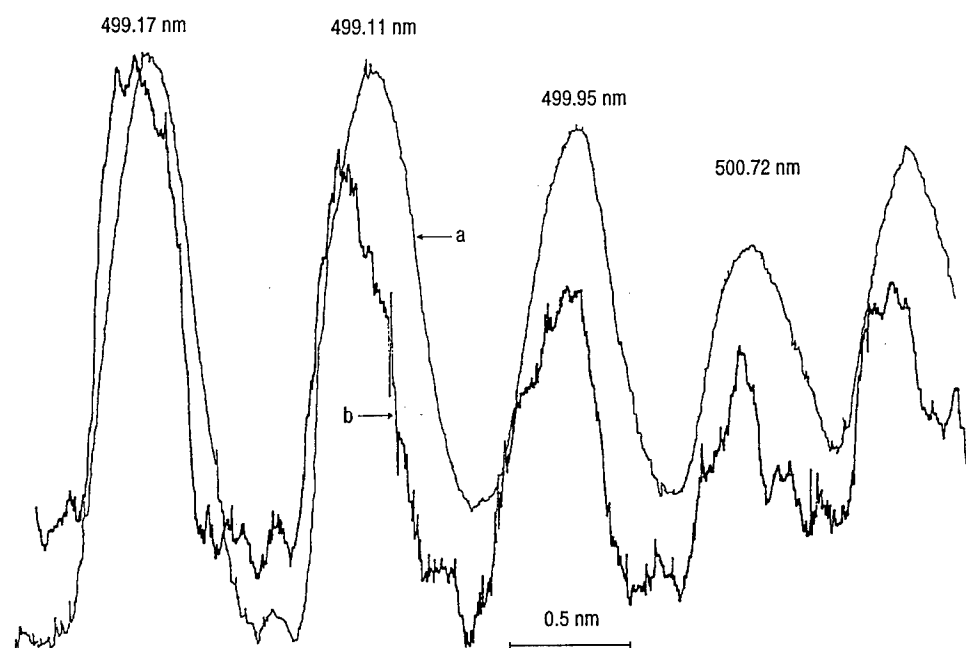


Fig. 3: Broadened Ti I lines obtained by superimposing of several 1000 shots with 800 ns duration and 100 A current. a - without polarization filter, b - with polarization filter.

INFLUENCE OF CURRENT INSTABILITIES ON THE PARAMETERS OF THE VACUUM ARC PLASMA JET

B. ALTERKOP, I. BEILIS, R. BOXMAN, S. GOLDSMITH
Electrical Discharge and Plasma Laboratory. Tel Aviv University
P.O.B. 39040, Tel Aviv 69978, ISRAEL

ABSTRACT

The influence of the Buneman instability on the parameters of a current carrying plasma is investigated. By using the quasi-linear approximation the analytical expressions which connect the plasma parameter changes and the turbulent electrical conductivity with the energy of the unstable electrostatic field fluctuations were obtained. The latter is expressed by the plasma supercriticality. The experimental data of the arc discharge in an extended gap are analyzed. It is shown that the changes of the electron temperature and potential drop can be explained by this instability.

1. INTRODUCTION

The efficient use of the arc discharge in technological applications depends on arc plasma jet parameters such as temperature and density. The latter can be changed if unstable fluctuations develop in the plasma. In particular, in discharges with a long interelectrode gap, the expanding plasma jet has a region where collisions between the particles are rare and the electrons have a sufficiently large drift velocity for existing unstable plasma perturbations. Aksenov *et al.*¹ used the Buneman instability² to explain the large kinetic energy and wide energy spectrum of the ions which were measured in the vacuum arc discharge. During this instability, which is realized when the current exceeded a critical value, the electrostatic field perturbations increase exponentially. In this paper a consistent theoretical analysis of the excitation conditions for the Buneman instability and its influence on the plasma jet parameters will be presented. The theoretical results will then be compared with experimental data¹.

2. LINEAR THEORY OF THE BUNEMAN INSTABILITY OF A CURRENT-CARRYING PLASMA

Let us consider the region of a vacuum arc plasma jet, where the plasma has expanded so much that the electron mean free path is greater than the region size and collisions between particles can be neglected. The potential drop in this region is small because the resistivity is so small, and we shall neglect it for simplicity. The electron drift velocity relative to the ions will be considered a constant. In this region the plasma is the homogeneous, isotropic and fully ionized and the distribution functions of the electrons and ions are Maxwellian:

$$f_{\alpha} = \frac{n_{\alpha}}{(\sqrt{2\pi} v_{\alpha})^3} \exp\left[-\frac{(\mathbf{v} - \mathbf{u}_{\alpha})^2}{2 v_{\alpha}^2}\right] \quad (1)$$

where n_{α} , u_{α} , $v_{\alpha} = \sqrt{T_{\alpha}/m_{\alpha}}$, T_{α} , and m_{α} are the density, drift velocity, thermal velocity, temperature, and mass, respectively, of the α -component plasma particles, with $\alpha = e, i$ representing electrons and ions respectively. Usually, there are ions with different charge states in the plasma jet. For simplicity we shall consider them as a single component having averaged parameters.

We want investigate the stability of this current-carrying plasma state with respect to perturbations in which both the electrons and ions take part. Because their velocity is much less than the light velocity, we can consider the electric field of these perturbations as electrostatic and neglect their magnetic field.

To describe the dynamics of the perturbations we use the Boltzman-Vlasov kinetic equations:

$$\frac{\partial f_{\alpha}}{\partial t} + \mathbf{v} \cdot \nabla f_{\alpha} + \frac{e_{\alpha}}{m_{\alpha}} \mathbf{E} \cdot \frac{\partial f_{\alpha}}{\partial \mathbf{v}} = 0 \quad (2)$$

and Poisson's equation:

$$\text{div } \mathbf{E} = \sum e_{\alpha} n_{\alpha} / \epsilon_0 = \sum e_{\alpha} / \epsilon_0 \int f_{\alpha} d\mathbf{v} \quad (3)$$

where e_{α} is the particle charge and \mathbf{E} is the electric field. For infinitesimal perturbations Eq. (2) can be considered in the

linear approximation. Distinguishing the equilibrium stationary values (subscript "o") and perturbations (subscript "1") and expanding the perturbations in a Fourier series over the plane waves:

$$f_{o\alpha}(\mathbf{r}, \mathbf{v}, t) = \frac{1}{2} \sum_{\mathbf{k}} f_{\alpha k}(\mathbf{v}) e^{-i\omega t + i\mathbf{k}\mathbf{r}} + c.c., \quad E_1(\mathbf{r}, t) = \frac{1}{2} \sum_{\mathbf{k}} E_k e^{-i\omega t + i\mathbf{k}\mathbf{r}} + c.c. \quad (4)$$

where ω and \mathbf{k} are the wave frequency and wave vector, taking into account the condition of the quasi-neutrality $\sum_{\alpha} e_{\alpha} n_{o\alpha} = 0$, from Eqs. (1)-(4) we obtain that $E_{1\mathbf{k}} \neq 0$ only if the following condition is satisfied³:

$$1 + \sum_{\alpha} \varepsilon_{\alpha}(\omega, \mathbf{k}) = 0, \quad \varepsilon_{\alpha}(\omega, \mathbf{k}) = i \frac{\sigma_{\alpha k}}{\varepsilon_o \omega} = \frac{(1 - J(\xi_{\alpha}))}{k^2 D_{\alpha}^2} \quad (5)$$

Here by definition $\varepsilon_{\alpha}(\omega, \mathbf{k})$ and $\sigma_{\alpha}(\omega, \mathbf{k})$ are the contributions of the α -species to the permittivity and conductivity, respectively, $D_{\alpha} = (\varepsilon_o k T_{\alpha} / e_{\alpha}^2 n_{\alpha})^{1/2}$ is the Debye length, and:

$$J(\xi_{\alpha}) = -\xi_{\alpha} e^{-\xi_{\alpha}^2/2} \left(i \sqrt{\frac{\pi}{2}} - \int_0^{\xi_{\alpha}} \exp(\tau^2/2) d\tau \right) = -i \sqrt{\frac{\pi}{2}} \xi_{\alpha} W(\xi_{\alpha} / \sqrt{2}), \quad \xi_{\alpha} = \frac{\omega - k u_{\alpha}}{k v_{\alpha}} \quad (6)$$

where the function $W(\xi)$ is the tabulated probability integral on a complex argument.

The function $J(\xi)$ may be approximated by the asymptotic series:

$$J(\xi) = 1 + \frac{1}{\xi^2} + \frac{3}{\xi^4} + \dots - i \sqrt{\frac{\pi}{2}} \xi e^{-\xi^2/2}, \quad |\xi| > 1 \quad (7)$$

$$J(\xi) = \xi^2 - \frac{\xi^4}{3} + \dots - i \sqrt{\frac{\pi}{2}} \xi, \quad |\xi| < 1$$

Equation (5) is the plasma dispersion relation. It determines the spectrum $\omega = \omega(\mathbf{k})$ of the plasma waves as a function of the wave number \mathbf{k} and the plasma equilibrium parameters. In the general case the frequencies determined from Eq. (5) are complex $\omega = \omega_k + i\gamma_k$. The sign of γ_k determines the wave stability because $E \sim E_k e^{\gamma_k t}$.

Let us consider on the basis of Eq. (5) the Buneman instability in a current-carrying plasma. This instability is an example of a wave instability with "negative" energy⁴. It is so named because the plasma energy with this wave is less than without it. This is possible only in a non-equilibrium plasma. The said wave amplitude increases when its energy decreases, due to dissipation or interaction with a positive energy wave. In the problem examined here, the plasma is non-equilibrium owing to the electrical current, and the negative energy waves are the space charge slow waves in the electron flow. For these waves $|\xi_e| \gg 1$ in Eq. (5). However two cases can be distinguished depending on the value of ξ_i , and will be analyzed in the following paragraphs.

Kinetic Case

We define the kinetic case by $|\xi_i| \leq 1$, and then Eq. (5) has the form:

$$1 - \frac{\omega_e^2}{(\Omega - k u)^2} \left(1 + 3 \frac{k^2 v_e^2}{(\Omega - k u)^2} \right) + \frac{1}{k^2 D_i^2} \left(1 - \frac{\Omega^2}{k^2 v_i^2} \right) = \frac{1}{k^2 D_i^2} \left[\frac{Z T_i}{T_e} \frac{k u - \Omega}{k v_e} \exp\left(-\frac{(\Omega - k u)^2}{2 k^2 v_e^2}\right) - \frac{\Omega}{k v_i} \exp\left(-\frac{\Omega^2}{2 k^2 v_i^2}\right) \right] i \sqrt{\frac{\pi}{2}} \quad (8)$$

$$\text{where: } \Omega = \omega - k u_i, \quad u = u_e - u_i, \quad \omega_{\alpha} = \left(\frac{e_{\alpha}^2 n_{\alpha}}{\varepsilon_o m_{\alpha}} \right)^{1/2}$$

In this equation the left side describes a space charge wave in the electron flow and quasi-static ion perturbations, while the right side describes a resonance interaction between waves and particles. For slow electron waves $\Omega \ll k u$ and

$$\Omega \approx k u - \omega_e \left(1 + \frac{3}{2} \frac{v_e^2}{u^2} \right)$$

To solve Eq.(8) we put: $\Omega = \Omega_k + i\gamma_k$, $\gamma_k \ll \Omega_k \ll ku$, $u > v_e$ and then obtain that the growth rate is:

$$\frac{\gamma_k}{kv_i} = \sqrt{\frac{\pi}{8}} \left[\frac{\Omega_k}{kv_i} e^{-\frac{\Omega_k^2}{2k^2 v_i^2}} - \frac{T_i}{ZT_e} \frac{u}{v_e} e^{-\frac{u^2}{2v_e^2}} \right], \quad (9)$$

where Ω_k satisfies the equation:

$$1 - \frac{\omega_e^2}{(ku)^2} \left(1 + 3 \frac{v_e^2}{u^2}\right) + \frac{1}{k^2 D_i^2} \left(1 - \frac{\Omega_k^2}{k^2 v_i^2}\right) = 0 \quad (10)$$

From Eq. (9) one can see that in this case the cause of the instability is the resonance interaction between the waves and ions (Landau damping). The minimal value of relative electron drift velocity $u=u_0$ which corresponds to the plasma stability threshold ($\gamma=0$) is determined from the conditions¹

$$\Omega_{k_0} = k_0 v_i, \quad \eta \exp \frac{1-\eta^2}{2} = \frac{ZT_e}{T_i}, \quad \eta = \frac{u_0}{v_e} \quad (11)$$

From Eq. (10), we obtain for the critical value of the wave number $k=k_0$, corresponding to maximal value of the growth rate γ_k :

$$\left(\frac{k_0 u}{\omega_e}\right)^2 = 1 + 3 \frac{v_e^2}{u^2} \quad (12)$$

Thus, near the stability threshold the instability growth rate is:

$$\gamma_k = \gamma_{\max} \left(1 - \frac{u_0}{u}\right), \quad \gamma_{\max} \cong \omega_i \left(\eta - \frac{1}{\eta}\right) \sqrt{\frac{T_i}{ZT_e}} \quad (13)$$

Here the factor $q_0=1-u_0/u$ defines the plasma supercriticality. The plasma is unstable if $q_0>0$.

Hydrodynamic Case

Far away from the stability threshold (or if $ZT_e > T_i$) Landau damping is unessential and the instability develops in a hydrodynamic regime for which $|\xi_e| \gg 1$ and $|\xi_i| \gg 1$ and the dispersion relation takes the form:

$$1 - \frac{\omega_e^2}{(\Omega - \mathbf{k}\mathbf{u})^2} \left(1 + 3 \frac{k^2 v_e^2}{(\Omega - \mathbf{k}\mathbf{u})^2}\right) - \frac{\omega_i^2}{\Omega^2} \left(1 + 3 \frac{k^2 v_i^2}{\Omega^2}\right) = 0 \quad (14)$$

In this equation the last term describes the ion plasma oscillations $\Omega \approx \omega_i$, which have a positive energy. In this case the instability growth rate has a maximum under the same condition (12) and Eq. (14) takes the form:

$$\left(\frac{\Omega_{k_0}}{\omega_e}\right)^3 \left(1 + 6 \frac{v_e^2}{u^2}\right) = -\frac{Zm_e}{2m_i} \left(1 + 3 \frac{v_e^2}{u^2} + 3 \frac{k_0^2 v_i^2}{\Omega_{k_0}^2}\right)$$

The unstable solution of this equation is:

$$\begin{aligned} \text{Re } \Omega_{k_0} &= \frac{\omega_e}{2} \left(\frac{Zm_e}{2m_i}\right)^{1/3} \left[1 - \frac{v_e^2}{u^2} + \left(\frac{2m_i}{Zm_e}\right)^{2/3} \frac{v_i^2}{u^2}\right], & \gamma_{k_0} &= \text{Im } \Omega_{k_0} = \omega_e \frac{\sqrt{3}}{2} \left(\frac{Zm_e}{2m_i}\right)^{1/3} \left[1 - \frac{u_0^2}{u^2}\right], \\ u_0^2 &= v_e^2 + \left(\frac{2m_i}{Zm_e}\right)^{2/3} v_i^2 \end{aligned} \quad (15)$$

The instability develops when $u > u_0$. However the condition $|\xi_i| \gg 1$ or $\Omega_{k_0} \gg k_0 v_i$ is satisfied only if $u \gg u_0$, i.e. far away from the stability threshold, when the supercriticality $q=1-u_0^2/u^2 \approx 1$. Thus, the excitation conditions and the stability threshold of the Buneman instability are determined by the kinetic regime. Far away from the stability threshold the

instability development is determined by the hydrodynamic regime, where the thermal motion of the particles is not essential for the development of the instability.

3. INFLUENCE OF THE UNSTABLE OSCILLATIONS ON THE PLASMA PARAMETERS.

To investigate the plasma parameter changes caused by these unstable oscillations let us average the kinetic equation (2) over a length much greater than a wave length. We obtain:

$$\frac{\partial \bar{f}_\alpha}{\partial t} = - \frac{e_\alpha}{m_\alpha} \bar{\mathbf{E}}_1 \frac{\partial \bar{f}_{1\alpha}}{\partial v} \quad (16)$$

where the overbar represents the average value. Multiplying Eq. (16) consecutively on 1, v , and v^2 and integrating over the velocity we obtain the equations expressing conservation of particles, momentum, and energy:

$$\frac{d \bar{n}_\alpha}{dt} = 0, \quad \frac{d \bar{u}_\alpha}{dt} = \frac{e_\alpha}{m_\alpha n_\alpha} \bar{n}_{1\alpha} \bar{\mathbf{E}}_1, \quad \frac{n_\alpha m_\alpha}{2} \frac{d \bar{u}_\alpha^2}{dt} = \bar{\mathbf{j}}_{1\alpha} \bar{\mathbf{E}}_1 \quad (17)$$

From the first equation one can see that the mean density of the plasma components are constant. By using for perturbations the Fourier series such as (4) and relations, which follows from linear approximation:

$$n_{\alpha k} = \mathbf{k} \mathbf{j}_{1\alpha k} / \omega, \quad \mathbf{j}_{\alpha k} = \sigma_\alpha(\mathbf{k}, \omega) \mathbf{E}_k$$

we transform Eq. (23) to the form:

$$m_\alpha n_\alpha \frac{\partial \bar{u}_\alpha}{\partial t} = \text{Re} \sum_k \frac{\mathbf{k}}{2\omega} \sigma_{\alpha k} |E_k|^2, \quad n_\alpha \frac{\partial T_\alpha}{\partial t} = \text{Re} \sum_k \frac{1}{3} \left(1 - \frac{\mathbf{k} \bar{u}_\alpha}{\omega}\right) \sigma_{\alpha k} |E_k|^2, \quad (18)$$

where the temperature is defined as $T_\alpha = m_\alpha (\bar{U}_\alpha^2 - \bar{U}_\alpha^2)$ and $\sigma_{\alpha k}$ is the electrical conductivity of the α -component of the plasma. We see that the plasma parameter changes are determined by the electrical field energy of the perturbations, for which from the current continuity equation $\partial \mathbf{E}_1 / \partial t + \sum \mathbf{j}_{1\alpha} / \epsilon_0 = 0$ we obtain:

$$\frac{\partial |E_k|^2}{\partial t} = - \frac{2}{\epsilon_0} \sum_\alpha \text{Re} \sigma_{\alpha k} |E_k|^2 = 2 \gamma_k |E_k|^2 \quad (19)$$

where to obtain the last equality we used the relations following from the dispersion equation (5):

$$\text{Re} \sum_\alpha \sigma_{\alpha k} / (\epsilon_0 \omega) = 0, \quad \text{Re} \sum_\alpha \sigma_{\alpha k} / \epsilon_0 = -\gamma_k \quad (20)$$

By using Eqs. (20) and from Eqs. (18)-(19) we obtain the conservation laws for the momentum and energy of the particles and waves:

$$\sum n_\alpha m_\alpha \bar{u}_\alpha = \text{const}, \quad \sum (3n_\alpha T_\alpha / 2 + n_\alpha m_\alpha \bar{u}_\alpha^2 / 2) + \epsilon_0 \sum |E_k|^2 / 4 = \text{const} \quad (21)$$

From the first Eq. (21) we see that the ion drift velocity changes caused by perturbations are much less than the value of the electron drift velocity:

$$u_i(t) - u_i(0) \equiv \Delta u_i = -m_e \Delta u_e / m_i \ll \Delta u_e \quad (22)$$

Taking into account Eqs. (20) and (22) we can represent the first Eq. (18) in a form $du/dt = -v_{\text{eff}} u$, where the effective electron collision frequency is given by:

$$v_{\text{eff}} = - \sum_k \frac{\mathbf{k} \bar{u}}{2} \text{Re} \frac{\sigma_{ek}}{\omega} \frac{|E_k|^2}{m_e n_e u^2} \quad (23)$$

Because from (19) it follows that $|E_k|^2 \sim e^{2\gamma_k t}$, then at $t > 1/\gamma_{\text{max}}$ the main terms on the right sides of Eqs. (18) and (23) have $k=k_0$ corresponding to $\gamma(k_0, u) = \gamma_{\text{max}}$. Therefore in the pre-exponential expressions we can set $k=k_0$. Then these expressions can be represented in the form:

$$\operatorname{Re} \sigma_{\alpha k o} / \epsilon_o \omega = -\gamma_{k o} A_{\alpha} / \mathbf{k} \mathbf{u}, \quad \operatorname{Re}(1 - \mathbf{k} \mathbf{u}_{\alpha} / \omega) \sigma_{\alpha k o} / \epsilon_o = \gamma_{k o} B_{\alpha} \quad (24)$$

It follows from Eq. (24) that:

$$A_i = -A_e, \quad B_i + B_e = A_e^{-1} \quad (25)$$

By using (19) and (24) we can integrate Eq. (18). Considering that the initial oscillation energy is infinitesimally small, we obtain:

$$\Delta u_{\alpha} = u_{\alpha}(t) - u_{\alpha}(0) = -A_{\alpha} \sum_{\mathbf{k}} \frac{|E_{\mathbf{k}}|^2 \epsilon_o}{4 n_{\alpha} m_{\alpha} u} \quad (26)$$

$$\Delta T_{\alpha} = T_{\alpha}(t) - T_{\alpha}(0) = -\frac{1}{3} B_{\alpha} \sum_{\mathbf{k}} \frac{|E_{\mathbf{k}}|^2 \epsilon_o}{2 n_{\alpha}} \quad (27)$$

And for the effective collision frequency we have:

$$\nu_{eff} = \gamma_{max} A_e \sum_{\mathbf{k}} \frac{|E_{\mathbf{k}}|^2 \epsilon_o}{2 m_e n u^2} \quad (28)$$

From (5) and (7) we obtain for the Buneman instability:

$$A_e = 2, \quad B_e = 1 - \Omega_{k o} / (\mathbf{k} \mathbf{u}), \quad A_i = -2, \quad B_i = \Omega_{k o} / (\mathbf{k} \mathbf{u}) \quad (29)$$

From Eqs. (26) and (27) it follows $\Delta T_i / \Delta T_e \approx \Omega_{k o} / \mathbf{k} \mathbf{u} \approx v_i / u \ll 1$, i.e. the electron heating is much greater than the ion heating. Because $A_e > 0$, from Eqs. (21) and (29) it follows that electrons are decelerated and ions are accelerated by the unstable electric field fluctuations, and $\Delta u_e \gg \Delta u_i$. Further, from (27)-(29), we have that:

$$\sum 3 n_{\alpha} T_{\alpha} / 2 = \epsilon_o \sum |E_{\mathbf{k}}|^2 / 4$$

Thus, during the Buneman instability only a small part of the electron flow energy is expended on heating and acceleration of the ions. Half of the principal part of the energy loss by the electron flow goes into the perturbations of the electrostatic field and half goes to electron heating.

To determine the electrostatic energy of the oscillations in the nonlinear stationary state of the plasma, we assume that the electron drift velocity will be decreased until it reaches the plasma stability threshold, which changes because of electron heating. At this state the plasma supercriticality q_s will be equal zero, the growth rate $\gamma_{ks} = \gamma_{max} q_s = 0$, and from Eq. (26), $|E_{\mathbf{k}}|^2 = |E_{ks}|^2 = \text{const}$. So, if the initial value $q = 1 - u_o / u = q_o > 0$ and in the stationary state $q_s = 0$, i.e. $u_s = u_{os}$, then putting $u_s = u + \Delta u$, and $u_{os} = u_o + \Delta u_o$, we obtain:

$$q_o = \frac{\Delta u_o}{u} - \frac{\Delta u}{u} = -\frac{\Delta u}{u} + \sum_{\alpha} \frac{1}{u} \frac{\partial u_o}{\partial T_{\alpha}} \Delta T_{\alpha} \quad (30)$$

where we take into account that $u_o = u_o(T_{\alpha})$.

From Eq. (30) one sees that if $\Delta u, \Delta u_o \ll u$ then it is necessary that $q_o \ll 1$. From Eqs. (26), (27), (30) it follows that the oscillation electrostatic energy may be determined from:

$$q_o = (A_e + \sum_{\alpha} B_{\alpha} \frac{u}{u_o} \frac{\partial m_e u_o^2}{\partial T_{\alpha}}) \sum_{\mathbf{k}} \frac{|E_{\mathbf{k}}|^2 \epsilon_o}{4 n m_e u^2} \quad (31)$$

Substituting (29) into Eq. (31) we obtain:

$$\sum_{\mathbf{k}} \frac{|E_{ks}|^2 \epsilon_o}{2 n m_e u^2} = \frac{2 q_o}{2 + \eta^2 \frac{u}{u_o} (1 - \frac{\Omega_{k o}}{k_o u})} \quad (32)$$

and from Eq. (28) for the effective collision frequency:

$$v_{eff} = \gamma_{ko} A_e \sum_k \frac{|E_{ks}|^2 \epsilon_0}{m_e n u^2} \cong \frac{\gamma_k}{2 + \eta^2 \frac{u}{u_0}} \quad (33)$$

We notice that near the stability threshold the Buneman instability cannot provide the essential acceleration and heating of the ions. In so far as the hydrodynamics regime is concerned, there are some results in the literature⁵, which point out that it is possible.

4. COMPARISON WITH EXPERIMENTAL RESULTS

Let us compare the theoretical results with the experimental data¹. In this work the vacuum arc plasma jet parameters are measured in a discharge with a Ti cathode and an interelectrode length of 50 cm. The discharge current was $I=100$ A and the anode surface area was $S \leq 5 \times 10^2 \text{ cm}^2$. From the experimental results the plasma density at the anode was $n_a = 7 \times 10^9 \text{ cm}^{-3}$ and slowly increased in the direction of the cathode. The temperature of the titanium ions ($Z=2$) was $T_i=20$ eV, while the electron temperature was $T_e=1.25$ eV and the scatter in the data increased with increasing distance from the cathode, reaching a value of 20 % of the mean for distances of 35-40 cm, defining a region of length $L=15$ cm. The amplitude of the electric field also decreases in this region.

We assume that this effects is caused by the Buneman instability. Under the experimental conditions $T_i=8ZT_e$ and from Eq. (11) we obtain $\eta=2.67$ and $u_0=1.25 \times 10^6$ m/s. Near the anode $u=I/(en_a S_a) \geq 1.8 \times 10^6$ m/s and hence $u > u_0$ and there are suitable conditions for the Buneman instability to develop. Thus $q_0=0.3 < 1$ and we can use our theory. From Eqs. (26), (27), and (32) we obtain the plasma parameter changes.

$$\frac{\Delta u}{u} = \sum_k \frac{\epsilon_0 |E_k|^2}{2nm u^2} = 5 \times 10^{-2}, \quad \frac{\Delta T_e}{T_e} = 0.2, \quad \frac{\Delta T_i}{T_i} = 3 \times 10^{-5}$$

The electron temperature change corresponds to the maximum value of the experimental spread ΔT_e in the examined region. From Eq. (33) we determined the effective collision frequency $v_{eff} \approx 210^7 \text{ s}^{-1}$ and plasma turbulent electrical conductivity: $\sigma_{eff} = \epsilon_0 \omega_e^2 / v_{eff} \approx 210^2 \text{ ohm}^{-1} \text{ m}^{-1}$. We can compare the classical and turbulent electron free path. for the experimental conditions and obtain $l_{eff} = v_e / v_{eff} \approx 2.5$ cm and $l_{cl} \approx 2 \times 10^{11} / n$, cm. In the examined region $n \leq 2 \times 10^{10} \text{ cm}^{-3}$ and we see that $l_{eff} \ll L \leq l_{cl}$.

Now we can calculate the electric field which is necessary to transport the stationary current $j_s = en u_{0s}$ over the turbulent region as $E_s = j_s / \sigma_{eff} = 8$ V/m. Assuming that this value is present in all of the turbulent region, we obtain across the length $L=10-15$ cm a potential drop $\Delta V = 0.8-1.2$ V, which corresponds well to the experimental data.

Thus the experimental plasma parameter variations can be explained by the Buneman instability if the electron drift velocity u is considered as independent of position within the examined region. There are no experimental data on the current density variations¹. But there are the data on the plasma density which increases by a factor of about 1.5-2 across the examined region. Our explanation is correct if the current density changes proportionally to the plasma density change, i.e. by a factor of 1.5-2 which is possible in this experiment.

REFERENCES

1. I. I. Aksenov, I. I. Kononov, V. G. Padalka, V. L. Sezonenko, V. M. Khoroshikh, "Instabilities in a plasma of a vacuum arc with gas in the discharge gap," Sov. J. Plasma Phys., Vol. 11, pp. 187-191, 1985.
2. O. Buneman, "Dissipation of current in ionized media", Phys. Rev. Vol. 115, pp. 503-517, 1959.
3. V. L. Ginsburg, A.A. Rukhadze, *Waves in Magnetoactive Plasmas*, Nauka, Moscow, 1970.
4. B. B. Kadomtzev, *Collective Phenomena in Plasma*, Nauka, Moscow, 1976.
5. S. V. Bulanov, P. V. Sasorov. "On the acceleration of ions in the non-linear stage of the Buneman instability," Fiz. plasma, Vol. 12, pp.54-58, 1986.

Physical model of low current density vacuum arc

Alexander V. Bolotov, Andrey V. Kozyrev, and Yuri D. Korolev

High Current Electronics Institute
Russian Academy of Sciences, Siberian Division
634055, Tomsk, Russia

In this paper the processes in the low arc current (less then 1 kA) on a cathode with moderate melting temperature are discussed. In this arc an anode typically plays a passive part, acting only as a collector of the microparticles, metal vapor, ion and electron flux, which are ejected into a gap from the cathode spot region.

Two types of cathode spots are distinguished: type 1 are the quick moving spots with a low erosion rate and a small crater dimension ($< 1\mu\text{m}$)¹ and type 2 that are characterized by slow motion, a large crater dimension and a high erosion rate^{1,2}. We will discuss the physical model for cathode spots of type 2 on clean smooth surfaces.

Most investigators dealing with the cathode spot research use some assumptions which have taken a power of axioms, although none of these assumptions are immediately evident from experimental results. These postulates are the following. 1) A value of cathode voltage drop, U_c , must be lower then an arc operating voltage, U_a , i.e. the electrical potential raises monotonically from a cathode to an anode. 2) The generation of ions inside the cathode voltage drop region, l_c , does not take place. The ion current to a cathode flows only from plasma region and has got the value of Bohm's equation. 3) The value of electron emission current must be close to a value of the total current.

We believe these assumptions are contrary to the experimental data, therefore this paper deals with the model of vacuum arc using nonmonotonical potential distribution across the gap. Plyutto et al were the first who proposed this idea³, but their point of view has not received the further development.

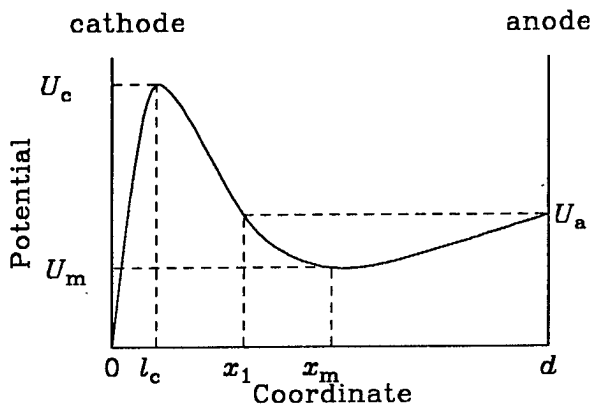


Fig. 1.

However, our papers⁴⁻⁶ and the paper⁷ give an substantial justification for the above approach. Thus, a new results of application of the potential hump model are presented here. The potential distribution along the discharge axis is schematically shown in Fig. 1. Near the cathode a plasma region with the high particle density exists, which is named a cathode flare. Its boundary approximately corresponds to coordinate x_m . The rest of the gap, from x_m to d , forms a vacuum diode with ion neutralization. The cathode voltage drop, U_c , being in excess of the discharge operating voltage, U_a , is concentrated along l_c .

During the process of arc operation a neutral flux $j_a(T_c)$ is evaporated from the cathode, whose value depends on the cathode surface temperature, T_c . Some part of these evaporating atoms are ionized before their arrival in the point of the potential maximum ($x = l_c$). These atoms return on the cathode as ions constituting an ion current, j_{ic} . The rest of the atoms are ionized in the cathode

flare region, $l_c x_1$. These ions are accelerated by an electric field and may arrive to the anode constituting the anode ion current, j_{ia} . It is obvious that $j_{ic} + j_{ia} \leq j_a(T_c)$. The value of ion current at the cathode is determined by the ionization constant, $k_i(T_c)$, and the velocity of the atoms, v_a

$$j_{ic} = j_a(T_c) \left\{ 1 - \exp \left[- \frac{k_i(T_c)}{v_a} \int_0^{l_c} n_e(x) dx \right] \right\}. \quad (1)$$

Our model assumes that the electrons in cathode flare plasma obey the Boltzmann energy distribution. A certain share of the plasma electrons can overcome the potential barrier eU_c and they form the electron back flow to the cathode, j_{eb} .

Thus, the total current at the cathode consists of three components

$$j = j_{ic} + j_{em}(T_c, E_c) - j_{eb}, \quad (2)$$

where j_{em} is the current of thermionic emission, calculated with the Schottky effect taken into account, and $E_c(j_{ic}, U_c)$ is the electric field at the cathode surface given by McCown's equation. The energy balance equation for the cathode has the form

$$j_{ic}(eU_c + \varepsilon + I_i - \phi) + j_{eb}(\phi + 2T_e) - j_a \varepsilon - j_{em}(\phi + 2T_e) = Q_r - Q_{ext}, \quad (3)$$

where ε is an evaporation energy per atom, ϕ is an electron work function, I_i is an atom ionization energy. Terms in the right side of the equation show other reasons of heat removal, Q_r , or heating, Q_{ext} , on the cathode, which do not indicate in the left side. For instance, Q_{ext} implies a possible heating by means of independent external source.

We have shown⁶, that the set of Eqs. (1)–(3) makes it possible to calculate the values U_c , T_c , T_e , j_{ic} , j_{em} , j_{eb} , E_c at a given j . In order to find U_m we can write the current balance at U_m . Without the loss of generality it is believed that $U_m \approx U_a$. Then the total current is the sum of the following components: thermionic current of the electrons, which have not lost their energy in collisions within the cathode flare region, δj_{em} ($\delta < 1$); the current of thermal electrons from plasma, $j_{ep} = j_{eb} \exp(eU_m/T_e)$; and the ion current, $j_{ia} \approx j_a(T_c) - j_{ic}$:

$$j = \delta j_{em}(T_c, E_c) + j_{ep} - j_{ia}. \quad (4)$$

Another necessary equation is the integrated energy balance for the discharge system

$$ejU_m + Q_{ext} = Q_r + j_{ia}[e(U_c - U_m) + \varepsilon + I_i - \phi] + \delta j_{em}(eU_m + \phi) + j_{ep}(\phi + 2T_e). \quad (5)$$

In our simulations we have supposed that the anode is cold and made of the same material as the cathode. Eqs. (4) and (5) define two unknown parameters: δ and U_m . Thus, the set of Eqs. (1)–(5) can be solved to find the principal characteristics of the vacuum arc.

Unfortunately, the cathode spot processes are far from our ideal model. In spite of respectively invariable total current in external circuit, a cathode spot is not a steady-state object. As a rule, the cathode spot moves over the cathode surface and it can consist of a few cells, moreover some cells disappear, while other ones come into being. In the process of cathode spot operation the current density varies with time and position. However, a new form of vacuum arc with diffused cathode spot has been found recently^{8,9}, in which an actual processes are close to our steady-state model of the cathode spot. A typical value of this cathode spot area is a few cm^2 , that is why there are solid experimental data on the basic parameters of arc: current density, j , cathode temperature, T_c , electron temperature, T_e , operating voltage, U_a , and erosion rate^{8,9}.

Let us consider an example of steady-state vacuum arc with a current density up to 100 A/cm^2 on gadolinium (Gd) cathode⁹. For Gd-cathode the equilibrium flux of thermionic emission, j_{em} , is about 20 times excess of the evaporating atoms flux, j_a . In this case a problem arises how to explain the mechanism of keeping of the high cathode temperature ($> 2000 \text{ K}$). To compensate the emission cooling it is required for each ion to bring at the cathode surface the energy of $> 200 \text{ eV}$, while the arc operating voltage, that was measured, to be no more then 100 V . The above discussed model clarifies this contradiction. Experiments⁹ have been carried out under the condition of radiative cooling cathode, when Q_r is proportional to T_c^4 . Fig. 2 shows calculated relationships between U_c , U_m and j for the

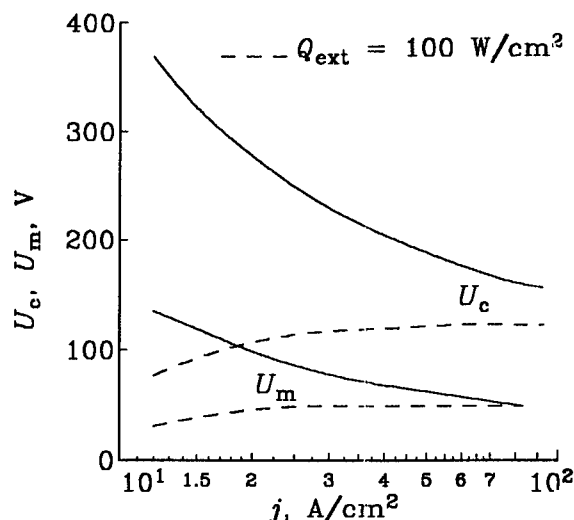


Fig. 2.

self-sustaining mode of arc operation, $Q_{\text{ext}} = 0$ (solid curves) and $Q_{\text{ext}} = 100 \text{ W/cm}^2$ for the externally heated cathode (dash curves). In both cases U_c is much in excess of $U_m \approx U_a$. In the mode with $Q_{\text{ext}} = 0$ about 90 % of evaporated atoms return to the cathode as ions being appeared within the cathode voltage drop region. In order to provide this high ionization rate, it is required that T_e in the plasma ranges from 8 to 15 eV, depending on j . If we bear in mind that the cathode material vapour density in the gas discharge gap is $\leq 10^{15} \text{ cm}^{-3}$, these values of temperature seem to be quite reasonable. An additional heating of the cathode from an external source reduces T_e , U_c , and U_a by several times. This is in a good agreement with experiment⁹.

Our model, as applied to the diffused cathode spot on the chromium (Cr) cathode⁸, also adequately explains the experiments. For Cr-cathode the thermionic emission flux is negligible as compared with the flux of evaporated atoms, i.e. this property of Cr is opposite to one of Gd. Our calculations have demonstrated that the total current on the cathode surface almost entirely consists of the ion current. That is why there is no need for a conception of "abnormal emission", as authors of paper⁸ have done.

In spite of the preceding doubt concerning the usefulness of the model to describe the constricted cathode spot it is of interest to know the results of formal calculations. For steady-state vacuum arc with a bulk cold cathode at given value of the total current I_0 we must substitute $Q_r = 2\lambda T_c(\pi I_0/j)^{1/2}$ in Eqs. (3) and (5). Here λ is thermal conductivity of the cathode material, and the flux of heat within the thickness of cathode is assumed having a spherical symmetry. Some calculated cathode spot parameters are shown in the Table 1.

Table 1. Calculated parameters of steady-state cathode spot on a bulk cold cathode. Value of the current $I_0 = 5 \text{ A}$.

Metal	$j, \text{ A/cm}^2$	$T_e, \text{ eV}$	$U_c, \text{ V}$	$U_m, \text{ V}$	$j_{ic}/j, \%$	$G, \text{ g/C}$	$n_{e0}, \text{ cm}^{-3}$
Mg	$8 \cdot 10^5$	0.8	9	2	81	$4 \cdot 10^{-3}$	$2 \cdot 10^{20}$
Cu	$2 \cdot 10^5$	4.5	32	9	66	$7 \cdot 10^{-5}$	$5 \cdot 10^{18}$
Ni	$1 \cdot 10^5$	1.8	16	4	60	$4 \cdot 10^{-4}$	$2 \cdot 10^{19}$
Ti	$6 \cdot 10^3$	2.5	20	9	26	$6 \cdot 10^{-5}$	$7 \cdot 10^{17}$

Here G is an erosion rate, n_{e0} is the plasma density at the cathode voltage drop boundary, l_c . The value of j should be read as denoting the average current density in the cathode spot. As might be expected from the versatility of the set of Eqs. (1)–(5), the calculated parameters are not in conflict with the experimental data.

Thus, the presented model of the vacuum arc can be effectively applied to an analysis of both diffused and constricted cathode spot. The value of maximum plasma density, n_{e0} , allows an estimation for free path of a heavy particle. In all cases with the exception of Mg the free path is comparable to the size of the cathode spot. The almost collisionless character of ion motion is the reason why a potential hump region builds up in the gap. Without resort to the idea of the potential hump region one cannot adequately explain the current transfer in a gap. The existence of the potential hump region is responsible for ion acceleration towards both the anode^{3,5} and the cathode. This model gives an interpretation a number of other problems. Among them there are the phenomena of current cutoffs and voltage spikes; a problem of the current density value in the spot; the reverse motion of the spot in the magnetic field.

It is common knowledge that in operation of the vacuum arc with a large ballast resistor there are spikes in the operating voltage oscillogram. The duration of this spikes is in the order of a few nanoseconds, and its amplitude can be up to a few hundreds volts. In the frames of the potential hump conception this phenomenon can be explained as follows. When the atom flux into the gap decreases, i.e. n_{e0} decreases in the hump region, the value of U_m increases (ref. Eq. (4)) in order to hold the value of total current, which is being stabilized by a large ballast resistor. Just when U_m will be closed to U_c , the hump is fully destroyed. As a result the mechanism of atom ionization by means of the electrons oscillation ceases to operate, the gap resistance and the gap voltage drop dramatically increase. After that a new explosion centre is generated as a results of raising of the electric field strength near the cathode surface. The rate of atom evaporation increases, the potential hump is restored to its original form and the operating voltage decreases again.

The different procedures for determination of the spot dimension give the difference in a few orders of the current density values. At the beginning of the cathode surface explosion j may be as great as 10^8 A/cm², but once the crater dimension increases, the current density decreases. If it is believed that the cathode voltage drop is not high ($U_c \approx U_a$), then one cannot explain the high value of current density, $\approx 10^8$ A/cm², and the occurrence of small-size craters within the area of a single cathode spot. In our model there is no this problem.

The rather high ionization rate of the cathode material vapour by oscillating electrons inside the cathode voltage drop region is one of the necessary conditions for continuous operation of the cathode spot. It is known that the imposition of a magnetic field on a plasma as a rule leads to raising of the ionization processes, because of a magnetic field confines an electron plasma component. At position where a magnetic field strength is elevated the value of plasma density is larger than another position. That situation takes place when an external magnetic field strength is added to the current magnetic field strength in one side of the cathode spot and it is subtracted in opposite side. That is why the cathode spot has to move in the direction of increasing magnetic field strength. This phenomena is known as the reverse motion of the cathode spot in the magnetic field.

Thus, the potential hump conception explains a variety of the experimental facts and the theoretical estimations of some parameters of the vacuum arc correlate well with measurements.

ACKNOWLEDGMENT

This work is supported by the Russian Fund of Fundamental Research (project 93-02-17418).

REFERENCES

1. G.A. Mesyats and D.I. Proskurovskii, *Pulsed Electrical Discharge in Vacuum*, Springer, Heidelberg, 1989.
2. C.W. Kimblin, "Erosion and ionization in the cathode spot regions of vacuum arcs", *J. Appl. Phys.*, Vol. 44, N 7, pp. 3074-3081, 1973.
3. A.A. Plyutto, V.N. Ryzhkov, and A.T. Kapin, "High speed plasma beams in vacuum arcs", *Sov. Phys. JETP*, Vol. 20, pp. 328-337, 1965.
4. A.V. Bolotov, A.V. Kozyrev, and Yu.D. Korolev, "Vacuum arc cathode processes influenced by the local maximum potential", *Proc. of XIX Inter. Conf. on Phenomenon in Ionized Gases*, Part I, pp. 114-115, Belgrade, 1989.
5. A.V. Bolotov, A.V. Kozyrev, Yu.D. Korolev et al., "Current cutoff in vacuum plasma-filled diode", *Proc. of XV Inter. Symp. on Discharges and Electrical Insulation in Vacuum*, pp. 683-685, Darmstadt, 1992.
6. A.V. Bolotov, A.V. Kozyrev, and Yu.D. Korolev, "Model for the cathode layer of vacuum arc at nonmonotonical distribution of a potential in a near-cathode plasma", *Fizika Plasmy*, Vol. 19, N 5, pp. 709-719, 1993. (in Russian)
7. V.F. Puchkarev and S.M. Chesnokov, "Erosion rate and voltage distribution in contracted (with cathode spot) and diffuse (spotless) low current vacuum arcs", *J. Phys. D: Appl. Phys.*, Vol. 25, pp. 1760-1766, 1992.
8. A.I. Vasin, A.M. Dorodnov, and V.A. Petrosov, "Vacuum arc with a distributed discharge on an expendable cathode", *Sov. Tech. Phys. Lett.*, Vol. 5, N 12, pp. 634-636, 1979.
9. S.N. Pararin, V.P. Polistchook, P.E. Sytchev et al. "Experimental study of the thermal regime of heated evaporated cathode in stationary vacuum arc with diffuse spot", *Teplofizika Vysokikh Temperatur*, Vol. 24, N 3, pp. 422-429, 1986. (in Russian)

Arcing and breakdown in the near-electrode plasma

D.P. Borisov, N.N. Koval, and P.M. Shchanin

Institute of High Current Electronics
Siberian Division of the Russian Academy of Sciences
Tomsk 634055, Russia

1. INTRODUCTION

Vacuum and low-pressure arcs are widely used to produce intense electron and ion beams^{1,2}, in switches³, as well as in devices producing plasma-ion treatment of materials and articles in application of coatings. To attain an appropriate rate of treatment for articles in plasma ion spraying, it is necessary to produce in the operating space a plasma, which would provide for supplying the required energy to the surface under treatment. This energy is determined by both the bias voltage applied to the article and the ion energy in the plasma. The bias voltage is restricted by the breakdown of the near-electrode sheath formed around the electrode placed in the plasma. The probability of breakdown depends on the electrode surface condition, the duration of voltage application, and the plasma density. In this paper we shall discuss the peculiarities of the arc discharge in large interelectrode gaps and the breakdown of the near-electrode plasma sheath depending on the surface condition.

2. EXPERIMENTAL SETUP

A schematic diagram of the experimental setup is given in Fig. 1. The arc initiated by a discharge over the surface of an insulator placed between cathode 1 of diameter

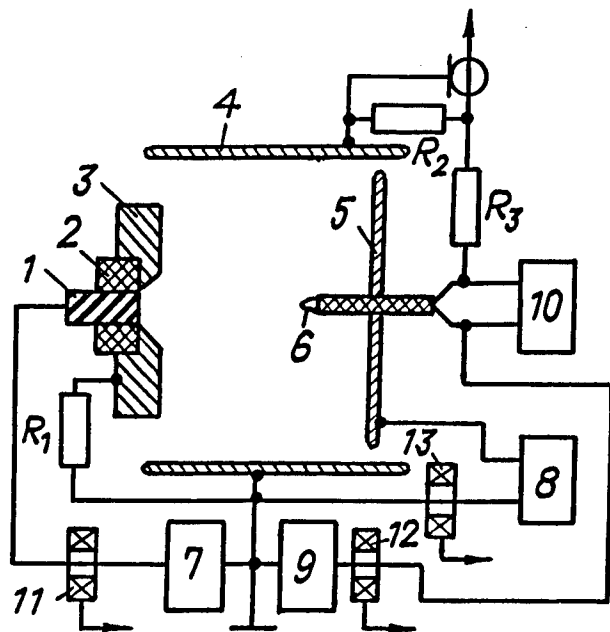


Fig. 1. Schematic of the experimental setup

The ion velocity distribution was investigated by an optical method based on measuring the Doppler shift of the radiation spectrum lines. The discharge system was arranged in such a way that the arc could operate alternately in two opposite directions (see Fig. 3). The light from two discharge regions passed through quartz windows and was projected by a lens with a focus distance of 112 mm onto a spectrograph with a reverse linear dispersion equal to 0.38 nm/mm. The electron energy spectrum was measured by a multigrid electrostatic analyzer. The operating pressure controlled by additional bleed-in of a gas (Ar, N₂) was 10⁻³ to 10⁻² Pa.

2–4 mm and trigger electrode 2 operated in the gap between the cathode and hollow cylindrical anode 4 of diameter 270 mm and length 400 mm, whose functions were fulfilled by a vacuum chamber. The arc was powered from power supply 7 produced rectangular pulses of duration 0.1 to 1 ms with the current controlled within a range from 0.1 to 1 kA. Inside the chamber, a movable plane electrode 5 was placed and a negative bias dc voltage, varied between zero and -200 V was applied to it, or this electrode was connected to the anode. Hot probe 6 made of tungsten wire of diameter 0.2 mm was inserted into the discharge gap through a hole in electrode 5. The length of the probe part protruded outward from the ceramic insulator was 10 mm. A rectangular pulse of duration 150 μ s with a voltage controlled between 0.1 and 4 kV was applied to the probe from power supply 9 with a delay of 500 μ s with respect to the instant of arc ignition. To degas and clean the probe, it could be heated to 1200 °C. Currents were measured by Rogowski coils 11, 12, and 13; voltage divider R_2R_3 was used for measuring the pulsed voltage.

The ion velocity distribution was investigated by an optical

3. EXPERIMENTAL RESULTS AND DISCUSSION

In a pulsed arc operating in a large electrode gap, two characteristic regions with highly different integrated light intensities are observed. Near the cathode, a bright flare 5 to 7 mm in diameter can be seen, which is separated by a sharp boundary from another, weakly luminating, part of the discharge. A photograph of a glow in the near-cathode region taken for a discharge current of 100 A and pulse duration of 100 μ s is given in Fig. 2. Herein, the distributions of the plasma glow intensity (in relative units) in the axial and radial directions obtained by photometry are shown. The plasma potential with respect to the cathode at the flare boundary was +90 V, then it gradually increased at a rate of 2 V/cm and reached its maximum (depending on the gap spacing) near the anode. The negative anode potential drop, depending on the discharge current and gap spacing, was 20 to 50 V.

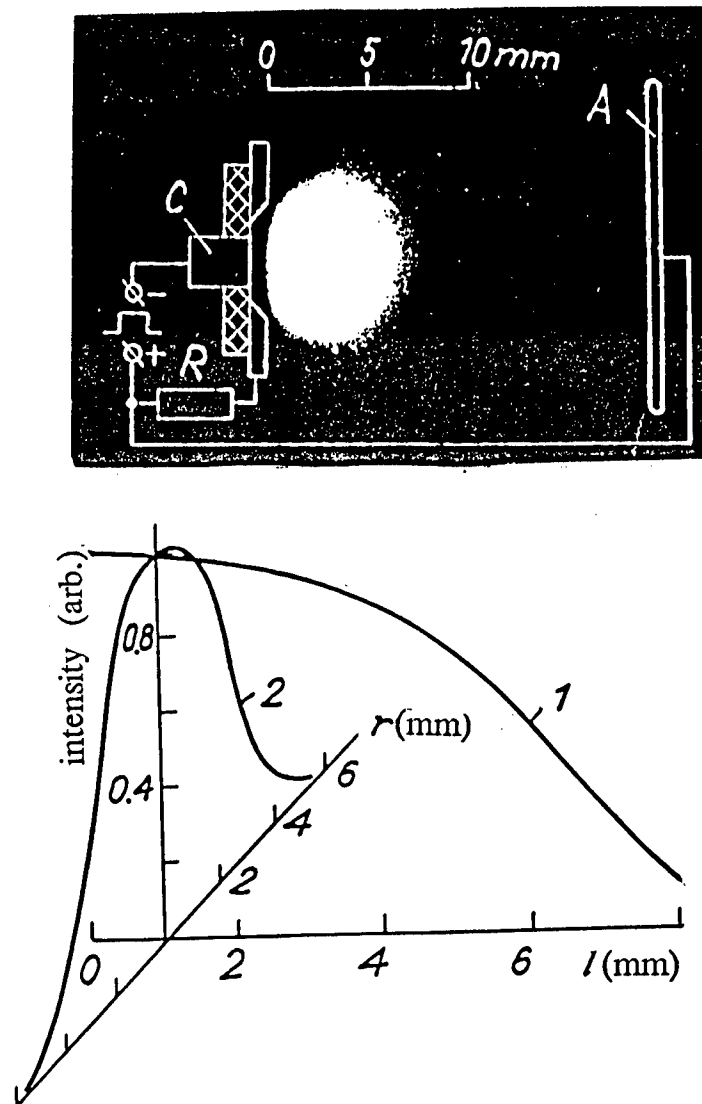


Fig. 2. Discharge plasma light intensity distribution in the near-cathode region along (1) and transverse to (2) the system axis

Spectroscopic investigation of the velocity distribution for the cathode material excited ions (Mg II, 2790.8 Å) has shown that the flare contains magnesium ions which move toward both the cathode and the anode (Fig. 3, curve 1), while outside the flare only fast ions moving toward the anode are observed (Fig. 3, curve 2). In measuring the

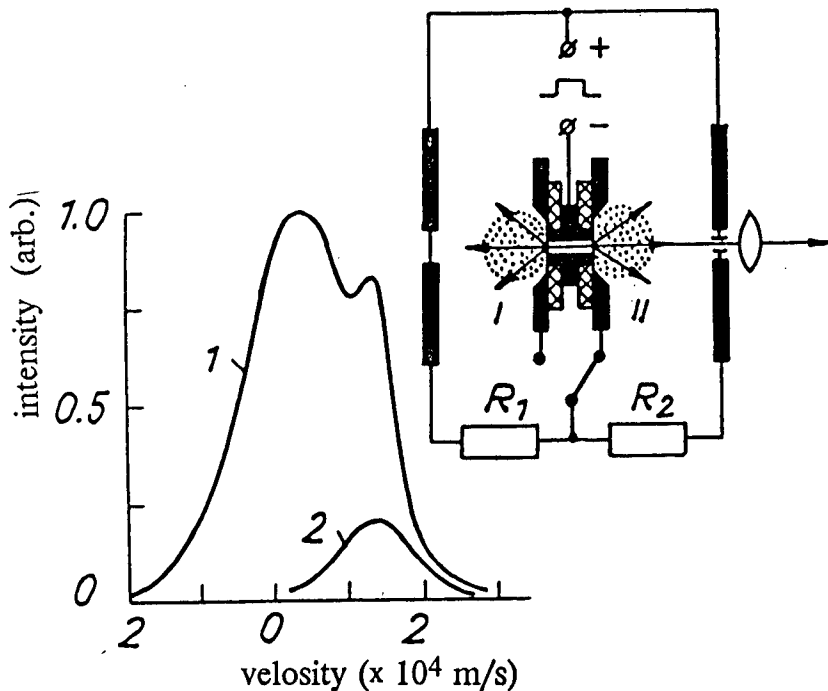


Fig. 3. Schematic of spectroscopic measurements and the velocity distribution of excited magnesium ions along the system axis (1) and at 6 mm from the axis (2)

Doppler shifts and spectral line profiles for magnesium atoms (Mg I, 3829.4 Å and Mg I, 3932.3 Å), an abrupt decrease in spectral line intensity was observed in the weakly luminating plasma region, and, for a discharge propagating in the viewer direction, the line shift toward the short-wavelength spectral region was detected. For the Doppler effect, this corresponds to an accelerated motion of particles away from the cathode.

In the anode part of the discharge, two groups of electrons — slow electrons with an energy of 5 to 10 eV and fast electrons with an energy of 60–80 eV — were detected. It seems that electrons acquire high energies at the flare boundary, where an abrupt increase in plasma potential is observed. In this region, ions moving toward the anode appear. The accelerated motion of ions can be accounted for by the fact that they are entrained by the fast electron flow due to the action of electron-ion friction forces, if these forces are turbulent in nature⁵.

The slow plasma ions and the fast ions, when getting on the surface of an electrode placed into the plasma, discharge dielectric inclusions present on the surface and, if the surface charge density is high, they may cause a breakdown of the dielectric film by initiating the formation of cathode spots and a breakdown of the space charge near-electrode sheath.

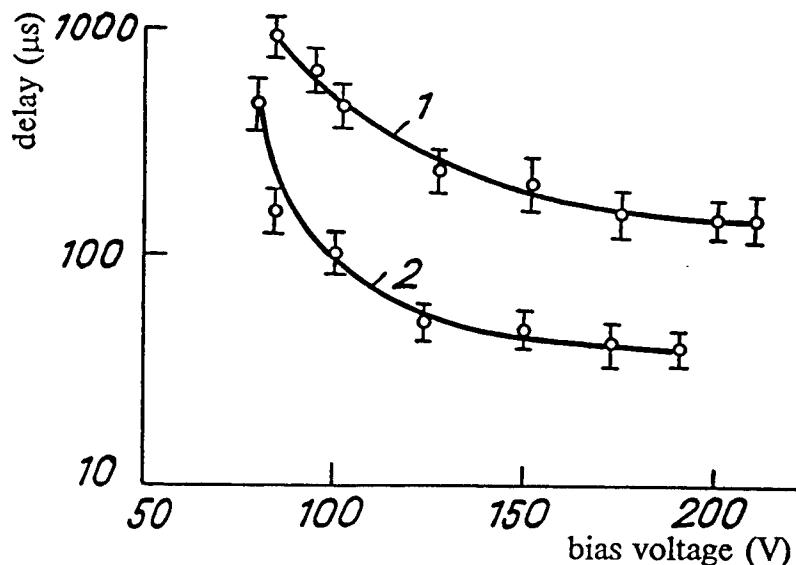


Fig. 4. Breakdown delay time versus bias voltage for a plane electrode at a discharge current of 150 A (1) and 600 A (2)

In our experiment, the time to sheath breakdown, t_d , was measured from the instant of arc ignition to the abrupt current rise in the circuit of electrode 5 and the corresponding voltage drop. Figure 4 presents the breakdown delay time t_d as a function of the negative bias voltage V_b applied to the electrodes for two values of discharge current corresponding to the saturation ion current density 6 mA/cm² (curve 1) and 24 mA/cm² (curve 2). In the experiment with a probe, heating the latter allowed two breakdown modes, one being realized with dielectric inclusions present on the surface and the other corresponding to a clean surface. When a pulsed bias voltage was applied to a cold probe, the sheath was broken down at voltages over 1.2 kV with a wide spread in delay time throughout the pulse duration range under investigation. At voltages over 3 kV,

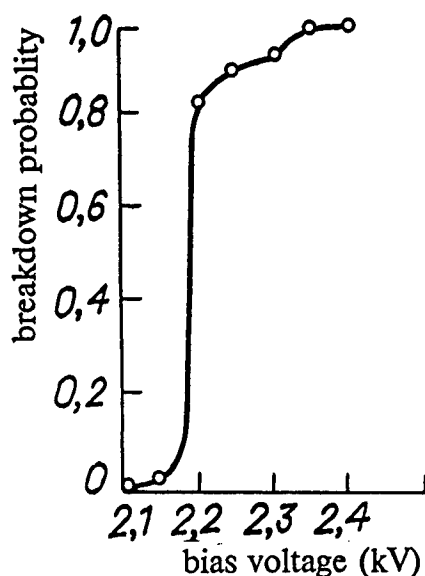


Fig. 5. Breakdown probability versus hot probe voltage

the breakdown probability was 100%. The breakdown probability is given in Fig. 5 as a function of bias voltage for a clean probe heated to 1200 °C. For the ion current density onto the probe 45 mA/cm², breakdowns did not occur at a bias voltage below 2.1 kV and occurred without any delay in each pulse at a voltage over 2.4 kV.

The experiments performed suggest that there exist two mechanisms of breakdown for the near-electrode sheath near a negative electrode placed into a plasma. In the first case, the sheath breakdown is initiated by the breakdown of dielectric inclusions present on the electrode surface, which are charged by ions coming from the plasma. Theoretical estimates show that when the negative voltage at the electrode is lower than the arc operation voltage, the ion charge is neutralized by electrons. Thus, in the experiment discussed, for an arc operation voltage equal to 60 to 80 V, an electron current was indicated in the negative electrode circuit at a bias voltage below -80 V. The delay time to breakdown for the sheath decreases with increasing the bias voltage at a cold probe and the plasma density. Moreover, no breakdown of the sheath occurs, if the pulse duration is shorter than the time needed for the charge density at the dielectric inclusion surface to reach some critical value.

In the absence of dielectric inclusions for a high-density plasma or high bias voltage, the breakdown of the sheath occurs, once the electric field at the electrode surface reaches a critical value; therefore the breakdown has a threshold nature.

4. REFERENCES

1. A.T. Forrester, *Large Ion Beam: Fundamentals of Generation and Propagation*, John Wiley & Sons, New York, 1988.
2. *Charged Particle Sources with a Plasma Emitter*, Ed. by P.M. Shchanin, Nauka, Ekaterinburg, 1993.
3. *Vacuum Arcs*, Ed. by J.M. Lafferty, John Wiley & Sons, New York, 1980.
4. B.S. Danilin and V.D. Kireev, *Application of Low-Temperature Plasma for Etching and Cleaning of Materials*, Energoatomizdat, Moscow, 1987.
5. V.P. Borzenko, O.L. Volkov, V.I. Krasov, I.A. Krinberg, V.L. Paperny, and V.G. Simonov, "Resistive acceleration of ions in current-carrying plasma jets", *Fizika Plazmy*, Vol. 17, pp. 360-368, 1991.

Filtered vacuum arc deposition of semi-conductor thin films

Raymond L. Boxman, Samuel Goldsmith, Amir Ben-Shalom, Larissa Kaplan, David Arbilly,
Evgeny Gidalevich, Vladimir Zhitomirsky, Amiel Ishaya, Michael Keidar, and Isak Beilis

Electrical Discharge and Plasma Laboratory, Tel Aviv University, POB 39040, Tel Aviv 69978, ISRAEL

ABSTRACT

The cathode spot vacuum produces a jet of highly ionized plasma plus a spray of liquid droplets, both consisting of cathode material. The droplets are filtered from the plasma by passing the plasma through a curved, magnetized duct. A radial magnetic field may be applied to the face of the cathode to rotate and distribute the cathode spots in order to obtain even erosion and avoid local overheating. The choice of axial magnetic field strength in the vicinity of the cathode is a compromise between a relatively high field desired to collimate a large fraction of the plasma flux, and the need to collect a substantial fraction of the plasma at the anode in order to reduce arc voltage and insure arc stability. The transmission of the filter duct increases with magnetic field strength until a saturation value. Entrainment of the droplets in the plasma jet can decrease the effectiveness of the filter at high plasma flux. Semiconducting thin films of amorphous silicon were prepared using cathodes of heavily B-doped Si. Arcs of 35 A current produced a deposition rate of 10 Å/s. The electrical conductivity of the films was similar to conventional a-Si:H films deposited by conventional Silane based CVD at high temperatures, but had a higher room temperature conductivity, despite the absence of hydrogen to terminate dangling bonds. Transparent conducting films on Sn-O were deposited at rates of up to 100 Å/s using 160 A arcs on a Sn cathode while injecting O₂ gas in the vicinity of the substrate. Adjustment of the O content is critical for optimizing conductivity, and complicated by pumping effects of the arc. Optimal conductivity was achieved at an oxygen pressure of 6 mTorr. Conductivities equal to the best reported to date were achieved by subjecting the room temperature deposited films to a 30 s rapid thermal annealing at 350 C. Both the as deposited and annealed films are amorphous. The deposition rates achieved by the filtered vacuum arc technique for these semiconductor films are an order of magnitude greater than achieved with conventional methods, while the conductivities are equivalent or better. The results contravene accepted assumptions that hydrogenation is necessary for high conductivity a-Si, and that high conductivity Sn-O requires a crystalline microstructure. It is suggested that the unusual results achieved are a result of higher density coatings caused by the high energy of the depositing ions.

1. INTRODUCTION

The cathodic vacuum arc produces a jet of highly ionized, energetic, vapor of the cathode material, which will form a coating on any substrate upon which the jet impacts. Vacuum arc deposition has been studied in the previous century by Wright¹ and Edison², and in the present time cathodic vacuum arcs deposition is in wide scale industrial use for producing wear protective coatings of TiN and related materials on cutting and forming tools, as well as decorative coatings on plumbing fixtures and jewelry³. A by product of the cathode spot vacuum arc is a spray of molten or solid particles of the cathode material which may become imbedded in the coating⁴. These macroparticles (MP's) are thought to be deleterious, but not critical, in wear protective coatings.

Semi-conducting thin films are highly desired for microelectronics and electro-optics, but must be free of macroparticle contamination. Silicon thin films have been deposited by Naoe *et. al.*⁵ and later by Muchizuki⁶. Generally the films were multi-crystalline, and a substantial fraction of the films appears to be from the deposition of macroparticles. Muchizuki, however, did obtain smooth, amorphous coatings of Si at a very low deposition rate (0.1 Å/s) by arcing on a heated Si cathode in a gas background, and facing his substrate away from the cathode. Presumably atoms or ions of Si were scattered by the gas atoms onto the substrate.

High quality amorphous carbon films were obtained by Aksenov *et. al.* at deposition rates of up to 50 Å/s using a graphite cathode, and passing the plasma through a magnetized quarter torus macroparticle filter⁷. Electron energy loss spectroscopy (EELS) as well as diffraction studies show that these films are quasi-amorphous but have a diamond nano-structure with predominantly sp³ bonding.^{8,9} While most of the attention has been focused on the mechanical properties of these films, McKenzie *et. al.* have fabricated heterostructure semiconductor rectifying diodes by filtered vacuum arc deposition (FVAD) of a diamond like carbon thin film onto a crystalline Si wafer substrate.¹⁰ The FVAD technique has also been used for deposition of optical thin films of metal oxides including TiO₂ and Al₂O₃, by introducing an oxygen gas flow in the vicinity of the substrate.^{11,12} Generally these films could be deposited by FVAD at higher deposition rates than by conventional technologies, while having indices of refraction and loss coefficients as good as achieved by any technique.

In the present work the FVAD technique has been adapted for deposition of semi-conducting thin films of amorphous silicon, and transparent tin oxide. The deposition process will be presented, including aspects of controlling the location and motion of the cathode spots, and transport of the plasma through the macroparticle filter. Characterization of the microstructure of the films will be presented, as well as measurements of the film conductivities. Finally, potential applications for these films will be surveyed.

2. CATHODE DESIGN AND CATHODE SPOT CONTROL

Neither Sn nor Si are good structural materials -- Si is brittle, and cannot be machined, while Sn is soft, and melts at a low temperature. Thus the cathodes were designed as compound structures, with a supporting structure of Cu for thermal control, electrical current connection, and structural strength, holding an active surface of the desired deposition material.

The Cu support structure for the Sn cathode was in the form of a hollow cup, into which Sn could be melted or cast. A hollow region behind the cup facilitated water cooling. A 100 turn coil which produced a generally radial field in the vicinity of the cathode surface was also located in this hollow region. In a 160 A arc, generally about 5 cathode spots were visible simultaneously when operating in vacuum, but the number greatly increased as did the random spot velocity when operated in an oxygen atmosphere. Unlike arcs on Hg cathodes, no tendency was noted for the arc to anchor itself at the Sn-Cu interface. As the level of the Sn decreased due to erosion, the increasingly exposed Cu cup side wall was also coated with Sn, and did not suffer any significant arc erosion. The application of a radial magnetic field tended to rotate the cathode spots in the retrograde direction, and thus spread the heat load and cathode erosion over the cathode surface.

Design of a Si cathode is complicated by the low room temperature electrical conductivity of intrinsic Si. Several different designs have been tested. (1) A hollowed Cu cylinder upon which a 5 mm thick 100 mm diam heavily doped Si disc attached using silver epoxy. Water cooling in the hollow cavity prevents overheating of the epoxy. (2) A Cu clamp holding a 55 mm thick, 100 mm diam heavily doped Si cylinder. And (3), a Cu clamping arrangement supporting an array of halogen lamps on one end, and a 55 mm thick, 100 mm diam intrinsic Si cylinder. Heavy doping supplies the requisite electrical conductivity to support the arc in designs (1) and (2), while heating to approximately 600 C substantially increases the conductivity of the intrinsic Si in design (3).

Designs (1) and (2) have been successfully tested. It was found that at currents of 150 A in design (1), the cathode spot tended to be stationary despite the presence of a magnetic field, and severe erosion, and cracking through the depth of the Si wafer readily occurred. Operation at 20-30 A was possible without severe damage, however. Imposition of a relatively strong magnetic field could produce cathode spot rotation at relatively low velocities, and in a distinct narrow radial groove. The groove radius could be varied by using a superposition of magnetic fields produced by a coil with the hollow cooling cavity, and an external field coil, with the currents in the opposite directions. Varying the ratio of the currents would alter the location at which the field was purely radial, and the groove diameter. Design (2) was successfully tested at 20-30 A also. The thickness of the Si cylinder made it more difficult to impose an effective radial field, but the stationary arc produced little damage under these circumstances. As of this writing design (3) is currently in preliminary testing.

3. PLASMA TRANSPORT THROUGH A MACROPARTICLE FILTER

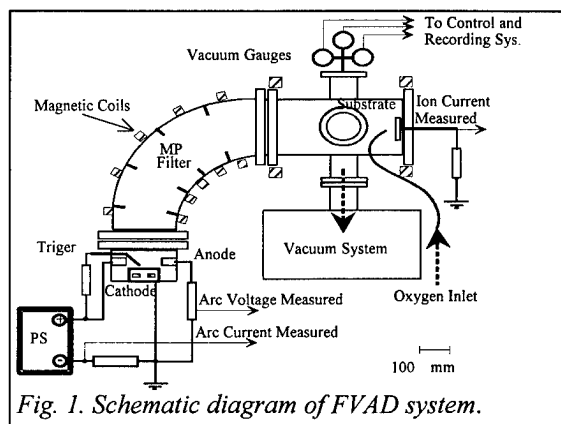


Fig. 1. Schematic diagram of FVAD system.

The plasma produced by the cathode spots is extracted through an annular aperture of 122 mm diameter in the anode and passed through a quarter-torus duct with a minor radius of 80 mm, and a major radius of 300 mm, into a deposition chamber (Fig. 1). The plasma beam is collimated with a magnetic field coil in the vicinity of the electrodes, a set of five coils around the quarter-torus, and a pair of Helmholtz coils around the deposition chamber. The objective of this arrangement is to filter out macroparticles from the plasma beam, and thus the plasma transport system can be characterized by its throughput of plasma, and its rejection of MP's.

Design of the electrodes and duct, and choice of the operating parameters involves a compromise between the competing desires to maximize plasma throughput, MP rejection, and arc stability. For example, increasing the magnetic field strength and the anode aperture tend to give higher plasma fluxes through the anode aperture, but at the same time, by separating the plasma from the anode higher arcing voltages are required, and there is an

increasing tendency for the arc to extinguish (Fig. 2). Indeed, this very same configuration was used by Gilmour and Lockwood¹³ as a d.c. opening switch.

Fig. 2. Arc voltage and lifetime as a function of the magnetic field in the vicinity of the cathode.

Arc Voltage and Lifetime

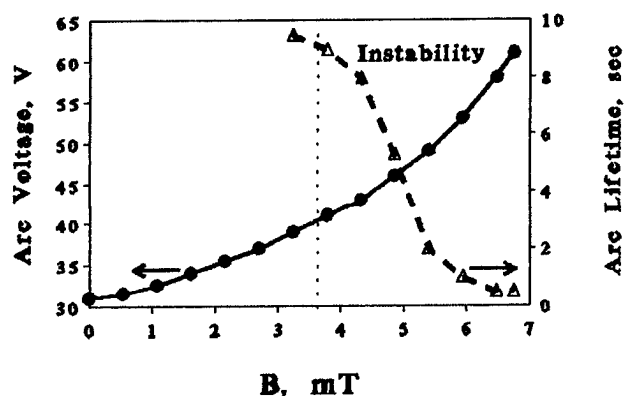
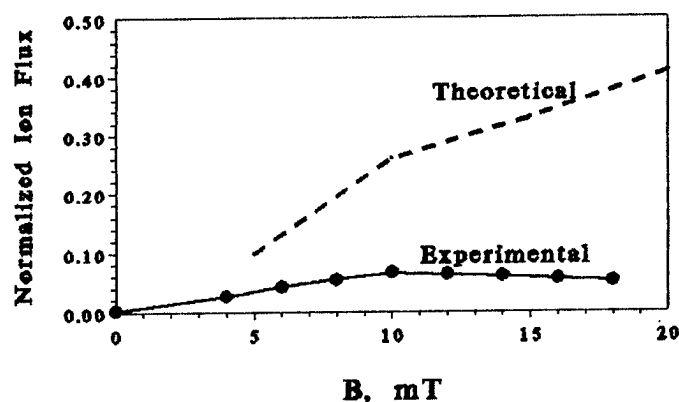


Fig. 3. Ion transmission fraction in MP filter as a function of magnetic field, measured for Ti, calculated for Cu.

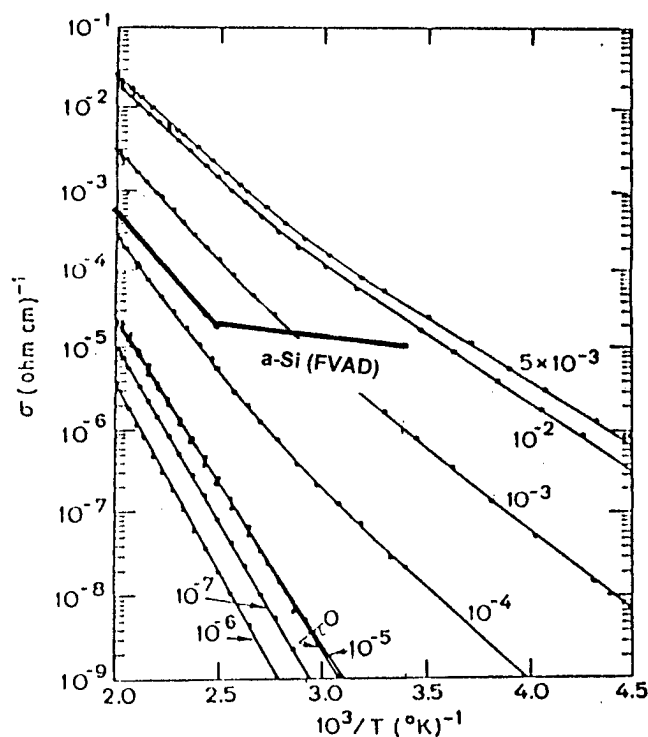
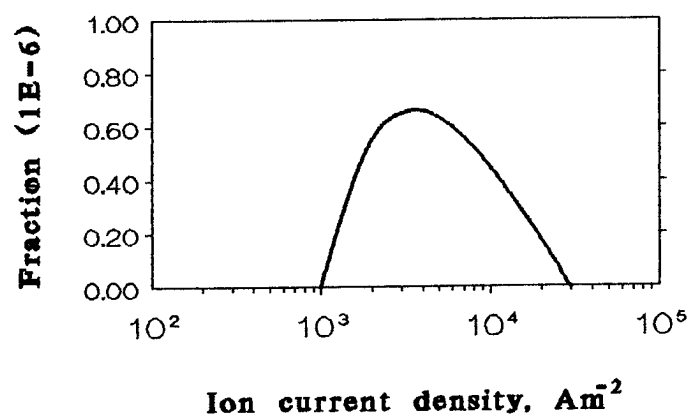
Normalized Ion Flux VS Field



Generally, the magnetic field strength used in the quarter-torus duct is such that the Larmour radius of the electrons is quite small with respect to the torus minor radius, but the Larmour radius of the fast ions is comparable or larger. The plasma as a whole is collimated by virtue of the collimation of the electrons, and the electrostatic field set up by the negative space charge resulting from the loss of ions. In the large radius quarter-torus duct used in the present experiments, the conditions are approximately hydrodynamic, and a two-fluid model of the plasma transport¹⁴ shows qualitatively an increase in plasma flux as a function of magnetic field, as shown in Fig. 3 for a Cu plasma. Also shown is the measured output flux for a Ti plasma. The decrease in output flux is attributed to arc instabilities at the cathode, as illustrated in Fig. 2.

Fig. 5. Conductivity of FVAD α -Si films with 4.4×10^{-4} B fraction, as a function of $1/T$. Shown for comparison are curves for glow discharge CVD α -Si:H films, where the parameter is the molecular fraction of B in the feed gas. \rightarrow

Fig. 4. Calculated macroparticle transmission fraction (ppm) due to entrainment in a Cu plasma beam. \downarrow



While ideally any MP striking the walls of the duct will adhere to it, and thus be removed from the plasma beam, in practice some of the impacting MP's are reflected, or splattered, from the walls. This effect can be minimized by corrugating the duct¹⁵, or in our case, by inserting baffle plates within the duct. In addition, a theoretical analysis indicates that some of

the smaller of the MP's can become entrained in the plasma beam, and reach the torus exit. This effect has a maximal value of about 1 ppm at an optimal ion current density within the filter, as shown in Fig.4.

4. AMORPHOUS SILICON DEPOSITION AND THIN FILM PROPERTIES

Silicon thin films were prepared using a heavily B-doped Si cathode (B content 440 ppm), and arc currents of 20-30 A. Typically the background pressure was around 5×10^{-5} Torr. Deposition rates of about 8-10 Å/s were obtained. Secondary Ion Mass Spectroscopy (SIMS) measurements indicated that the B content of the films was the same as in the cathode material. Transmission Electron Microscopy, Scanning Electron Microscopy, Electron Diffraction, and X-ray Diffraction all indicate that the films are amorphous.

The electrical conductivity of the amorphous silicon (a-Si) films as a function of temperature is shown in Fig. 5. Shown for comparison are the electrical conductivities of a-Si films prepared by the conventional Silane glow discharge process¹⁶. The parameter in the figure is the fraction of B molecules in the feed gas, which is approximately equal to the B fraction in the coatings¹⁷. It may be seen that the electrical conductivity is comparable to the conventional films at high temperatures, while it is considerably better at low temperatures. It should be noted that the conventional films are hydrogenated. It is generally held that a-Si has numerous 'dangling bonds', which serve as traps to conduction electrons, and in order to achieve a reasonable conductivity, the dangling bonds must be tied with hydrogen atoms. Conventional a-Si films typically contain up to 20% hydrogen for this purpose.¹⁸ Thus it is noteworthy that the conductivity of the FVAD a-Si films is equal to or better than the conventional films, despite the lack of hydrogenation in the FVAD films. In addition, the deposition rate achieved (8-10 Å/s) is considerably faster than typical in the conventional Silane glow discharge process (3 Å/s).

5. CONDUCTING TRANSPARENT TIN OXIDE DEPOSITION AND FILM PROPERTIES

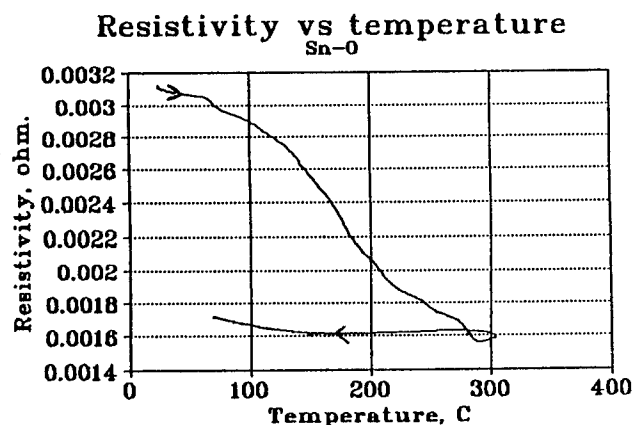
While stoichiometric SnO_2 is an insulator, SnO_{2-x} is an n-type semiconductor due to the excess of Sn donor atoms with respect to the O_2 .¹⁹ This material is characterized by a large band gap, and is thus transparent in the visible range.

Tin oxide thin films were prepared with the apparatus shown in Fig. 1, with a flow of O_2 gas in the vicinity of the substrate. The preparation procedure included pumping the chamber to a pressure of 5×10^{-5} Torr, adjusting the needle valve which controls the gas flow for a pressure of 500-800 mTorr while pumping only with a mechanical roughing pump, and igniting the arc. Initially, the plasma beam is confined to the vicinity of the electrodes. However, during the course of the first 5-15 s of arcing, the plasma beam pumps the gas in the chamber in a manner similar to a Ti sublimation pump, during which time the plasma beam gradually advances until it propagates along the entire length of the system, and the pressure in the deposition chamber decreases to the 1-10 mTorr range. When the steady state pressure was reached, depositions at rates up to 100 Å/s were obtained.²⁰

The characteristics of the coatings obtained depend very much on the deposition and post deposition parameters, and most particularly, on the oxygen pressure and on post deposition annealing. All of the films obtained at deposition substrate temperatures less than 350 C were amorphous. As a function of increasing O_2 pressure, both the optical transmission and the conductivity of the films improved, while the deposition rate decreased. Generally optimal sheet conductivities were obtained at a pressure of about 6 mTorr.

Post arc annealing to temperatures in excess of 350 C caused the films to begin to crystallize, and for the conductivity to decrease. Films heated to temperatures of over 550 C were totally crystallized. X-ray diffraction of the crystallized films revealed reflections characteristic of SnO_2 when the films were prepared with pressures in excess of 6 mTorr, but contained reflections characteristic of SnO if the films were prepared at lower pressures. In contrast, if the films were annealed to temperatures of less than 300 C, a non-reversible increase in conductivity was observed, as shown in Fig. 6. The best films had optical transmissions in excess of 85-90%, and a conductivity of $7 \times 10^{-4} \Omega\text{-cm}$, which is equivalent to the best value reported in the literature for undoped tin oxide thin film.²¹ The deposition rate obtained using FVAD was an order of magnitude faster than with the previous method, however.

Fig. 6. Non-reversible decrease in resistivity by post deposition annealing.



6. APPLICATIONS

Transparent conductor and a-Si thin films have numerous applications, present and future, as indicated in Table I. Several applications are particularly noteworthy, as they would exploit the combined abilities of FVAD to produce high quality films at high deposition rates.

Photovoltaic solar cells have the potential to provide energy in convenient electrical form from a 'free' source. The difficulty is the current high cost of producing the solar cells per power production capacity, 5-8\$/W, limit the economical use of solar cells to isolated installations such as satellites, and cellular telephone repeater stations. Amorphous silicon solar cells, based on p-i-n diode structure, with a transparent conductor window-electrode, have been proposed as a means of lowering the cost, due to the potential for low cost mass production. While cells are this nature are now routinely produced in large scale, so far their price has not gone below that of 'expensive' single crystal wafer solar cells, due to the cost of Si in the form of Silane gas (SiH_4) and its attendant safety and health hazards, as well as the low deposition rates in the conventional production technologies. In addition, a-Si solar cells suffer from a radiation degradation effect, believed to be associated with rearrangement of the H atoms. In contrast, FVAD produced heavily doped a-Si films with good conductivity without hydrogenation, using solid Si as the feedstock, and at a deposition rate larger than the conventional Silane glow-discharge method. Furthermore, increases in the deposition rate are expected with the introduction of multi-finger independently driven cathodes. Thus, while much work remains to be done, FVAD has the potential for producing solar cells with better performance and lower cost.

Active Matrix Liquid Crystal Displays (AMLCD's) have become increasingly popular in high-end 'laptop' and 'notebook' personal computers. Each picture element Each picture element (pixel) is a multilayer device including transparent conducting electrodes, the liquid crystal, and in a corner of the pixel a thin film a-Si field effect transistor. The cost of these devices could probably be lowered if a higher deposition rate coating technology could be employed to improve the throughput, without adversely affecting defect-free yield. FVAD, with its higher deposition rate for both the transparent conductor and the a-Si layers, may have this potential.

In addition, there are many applications for transparent conductors alone; automobile windshield defrosters will be discussed as an example. The basic concept is simple: the transparent conductor is applied onto a vehicle windshield, and used as a heating element. This concept has been applied to aircraft cockpits for some time, and more recently to luxury automobiles. Using conventional sputtering technology, the available coatings are expensive, and their high resistivity requires a supplemental power supply. Further development of the FVAD process to achieve resistivities of $10^{-4} \Omega\text{-cm}$ and modest improvements in the macroparticle filter throughput to levels already achieved in other laboratories would permit the deposition of a 1 μm thick, 1 Ω/\square coating which could be powered from the native automotive alternator and melt a layer of ice in about 5 minutes. The cost of the deposition in a mass production environment is projected to be approximately \$10, which would facilitate its deployment even in popularly priced vehicles.

7. DISCUSSION AND CONCLUSIONS

FVAD thin-films have unique and surprising properties, when viewed in the context of results achieved with other techniques. In the tin oxide films, best conductivity was achieved so far with amorphous, rather than crystalline, films. With the a-Si films, good conductivity doped films were achieved without hydrogenation to tie dangling bonds. The explanation for these results may prove to be prosaic. The poor conductivity of the crystalline tin oxide films may be due to grain boundaries and stresses induced during post deposition crystallization, and perhaps better results will be achieved if high substrate temperatures are used to deposit crystalline films directly. The high room-temperature conductivity of the FVAD a-Si films may be the result of undesirable hopping conduction.

On the other hand, it is also possible that the explanation is more profound, namely that FVAD amorphous films are different than amorphous films produced by other techniques. From the analogous work in carbon films, it has been shown that FVAD films have predominantly sp^3 bonding, while hydrogenated films deposited by other techniques have predominantly sp^2 bonding. Furthermore, there are reports that FVAD diamond like carbon films are denser and harder than natural diamond. Molecular dynamic simulation of Ti deposition have shown that when low energy atoms form a film, the low surface mobility results in a low density structure with micro-voids, while a high density structure is obtained if a mix of low energy and high energy particles form the film. One may speculatively extrapolate that if all the depositing particles were high energy, as would be typical in FVAD, that even higher density would be achieved. Applied to the covalent sp^3 structure of both C and Si, it may be that low energy deposition leads to voids, and hence dangling bonds, while the high energy of the depositing particles in FVAD leads to a denser structure with fewer dangling bonds, and hence to good conductivity without hydrogenation in the FVAD a-Si films.

In conclusion, FVAD has been shown to produce films of doped a-Si and undoped amorphous tin oxide having conductivities equivalent or better than those produced by other techniques at deposition rates 3-10 times larger. With further development, the FVAD technique may find application in the production of solar cells, AMLCD's, windshield defrosters, and other electronic and optical applications. Further work on the correlation of film properties to deposition conditions are indicated, including, in particular, the effect of substrate biasing.

8. ACKNOWLEDGMENTS

The authors gratefully acknowledge financial support from the Israel Ministry of Energy and Infrastructure, the Israel Ministry of Science and Technology, the RAMOT Fund, and the Friends of Tel Aviv University in France. The technical assistance of Hanan Yaloz is greatly appreciated.

REFERENCES

- ¹ A.W. Wright, "On the production of transparent metallic films by the electrical discharge in exhausted tubes", *Am. J. Sci. Art*, 3rd Ser., Vol. 13, No. 73, pp. 49-55, 1877
- ² T.A. Edison, "Process of duplicating phonograms", U.S. Patent 484,582, Oct. 18, 1892
- ³ R.L. Boxman and S. Goldsmith, "Principles and applications of vacuum arc coatings", *IEEE Trans. Plasma Sci.*, Vol. PS-177, pp. 705-712, 1989.
- ⁴ R.L. Boxman and S. Goldsmith, "Macroparticle contamination in cathodic arc coatings: generation, transport, and control", *Surface and Coating Technology*, Vol. 52, pp. 39-50, 1992
- ⁵ M. Naoe and S. Yamanaka, "Evaporation of silicon by vacuum-arc discharge", *Japan. J. Appl. Phys.*, Vol. 8, pp. 287-8, 1969.
- ⁶ M. Muchizuki, "Thin-film deposition by the vacuum-arc evaporation method", thesis, Kanazawa University, Japan, 1992.
- ⁷ I.I. Aksenov, S.I. Vakula, V.G. Padalka, V.E. Strel'nitskii, and V.M. Khoroshikh, "High-efficiency source of pure carbon plasma", *Sov. Phys. Tech. Phys.*, Vol. 25, pp. 1164-6, 1980.
- ⁸ V.E. Strel'nitskii, V.G. Padalka, and S.I. Vakula, "Properties of the diamond-like carbon film produced by the condensation of a plasma stream with an rf potential", *Sov. Phys. Tech. Phys.*, Vol. 23, pp. 222-4, 1978.
- ⁹ D.R. McKenzie, D. Muller, B.A. Pailthorpe, Z.H. Wang, E. Kravtchinskaia, D. Segal, P.B. Lukins, P.D. Swift, P.J. Martin, G. Amaratunga, P.H. Gaskell, and A. Saeed, "Properties of tetrahedral amorphous carbon prepared by vacuum arc deposition", *Diamond and Related Materials*, Vol. 1, pp. 51-9, 1991.
- ¹⁰ G.A.J. Amaratunga, D.E. Segal, and D.R. McKenzie, "Amorphous diamond-Si semiconductor heterojunctions", *Appl. Phys. Lett.*, Vol. 59, pp. 69-71, 1991.
- ¹¹ T.D. Schemmel, R.L. Cunningham, and H. Randhawa, "Process for high rate deposition of Al_2O_3 ", *Thin Solid Films*, Vol. 181, pp. 597-601, 1989.
- ¹² P.J. Martin, R.P. Netterfield, T.J. Kinder, L. Descotes, "Deposition of TiN, TiC, and TiO_2 films by filtered arc evaporation", *Surf. Coat. Technol.*, Vol. 49, pp. 239-243, 1991.
- ¹³ A.S. Gilmour and D.L. Lockwood, "Pulsed metallic-plasma generators", *Proc. IEEE*, Vol. 60, pp. 977-990, 1972.
- ¹⁴ E. Gidalevich, S. Goldsmith, and R.L. Boxman "Vacuum arc plasma beam transport in curved magnetic fields" (in these Proceedings).
- ¹⁵ J. Storer, J.E. Galvin, and I.G. Brown, "Transport of vacuum arc plasma through straight and curved magnetic ducts", *J. Appl. Phys.*, Vol. 66, pp. 5245-50, 1989.
- ¹⁶ Z.S. Jan, R.H. Bube, and J. Knights, "Field effect and thermoelectrical power on boron doped amorphous silicon", *J. Appl. Phys.*, Vol. 51, pp. 3278-81, 1980.
- ¹⁷ C.C. Tsai, "Characterization of amorphous semiconducting silicon-boron alloys prepared by plasma decomposition", *Phys. Rev. B*, Vol. 19, pp. 2041-55, 1979.
- ¹⁸ K. Takahashi and M. Konagai, *Amorphous Silicon Solar Cells*, North Oxford Academic, 1986, pp. 113-4, 127-131.
- ¹⁹ K.L. Chopra, S. Major and D.K. Panday, "Transparent conductors - a status review", *Thin Solid Films*, Vol. 102, pp. 1-46, 1983
- ²⁰ A. Ben-Shalom, L. Kaplan, R.L. Boxman, S. Goldsmith, and M. Natan, "SnO₂ transparent conductor films produced by filtered vacuum arc deposition", *Thin Solid Films*, 236, pp. 20-26, 1993.
- ²¹ R. Banerjee and D. Das, "Properties of tin oxide films prepared by reactive electron beam evaporation", *Thin Solid Films*, Vol. 149, pp. 291-31, 1987.

Suggestion of criterion of type 2 spot originating under pulse discharge conditions

A. I. Bushik, I. A. Bakuto, P. S. Zachepilo and V. A. Shilov

Physical-Technical Institute, Belarus Academy of Sciences
Minsk 220730, Belarus

ABSTRACT

The paper discusses experimental data which indicate that type 2 cathode spots originate only on oxide-cleaned metal surfaces. The suggestion is made that an instant at which an ion resonance recharging starts to play an active role in a near-cathode region can be taken as a criterion of type 2 spot origination.

1. INTRODUCTION

At present a spot type is usually characterized by a set of parameters such as spot velocity, luminosity, life time, current and a character of a metal erosion¹. Type 1 spots are faint and rapidly moving, have short life time and a small spot current. They produce branchy eroded areas on a cathode surface. Type 2 spots are characterized by a low mobility, high luminosity, prolonged life time, a great spot current and a deep metal erosion in the form of fused craters^{3,4}. The aforesaid also pertains to spots freely functioning in a discharge zone. A significant alteration of one or several spot parameters can be obtained by changing a surface microstructure with the rest remaining unchanged. The same effect can be also achieved by some other external factors, e. g. a magnetic field. This results in some uncertainty when identifying spots. Thus, slowed-up type 1 spots remain faint with a small erosion effect and accelerated type 2 spots retain a high luminosity but decrease the degree of a surface erosion². The above facts motivate a need for an extensive study of cathode spots under various conditions and thus a search for a criterion of type 2 spot originating.

2. EXPERIMENTAL CONDITIONS

The dynamics of cathode spots in vacuum was studied using multiple high-current pulse discharges repeated at one and the same site with electrodes placed coaxial for the purpose of decreasing a magnetic field effect of current-carrying elements. A face of 30-mm dia. cylinder served as a cathode working surface. The cathode was placed inside an anode which was made in the form of a hollow copper cylinder with an internal diameter of 50 mm. The base of the anode was capped with a copper mesh (1 x 1 mm cell) which had a 15-mm dia. window in the center for observation of a charge development. A triggering tungsten wire electrode 0.5 mm in diameter was placed near the cathode working surface. The interelectrode length i. e. the distance between a cathode face surface and an anode mesh was 5 mm. The discharges were burnt in a vacuum of $5 \cdot 10^{-5}$ Pa at an initial capacitor voltage of 2 kV.

A unipolar current pulse had a shape close to that of a bell with $2.5 \cdot 10^{-4}$ -s duration and a maximum current of $2 \cdot 10^3$ A at $6 \cdot 10^{-5}$ s.

The dynamics of these processes was studied with the aid of high-speed photorecorder in a framewise regime with the exposure of $4 \cdot 10^{-6}$ s. The high-speed photorecording was carried out normal to a cathode working surface. Commercial pure metals such as copper, iron, zirconium, aluminium, magnesium, zinc and tin with corresponding oxides were used as cathode materials.

3. EXPERIMENTAL RESULTS

As it follows from high-speed photograms the first discharge occurring on oxidized cathodes made of all metals under study is characterized by a radially expanding zone with a more bright boundary formed by rather uniformly and closely distributed spots (Fig. 1 a).

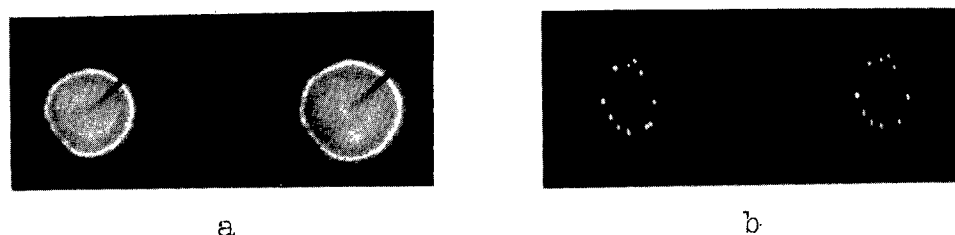


Fig. 1. Fragments of high-speed photograms of discharges (2 kA) in vacuum ($5 \cdot 10^{-5}$ Pa) on Cu cathode: b) without and a) with oxide film.

The velocity of a spot (70 to 100 m/s), a character of its luminescence and surface erosion are indicative of type 1 spot formation. However, a higher luminosity and a lower velocity (30 m/s) of spot expansion in the form of a ring are observed only with a discharge occurring on zinc or magnesium cathodes. The velocity of expanding a ring formed by type 1 spots increases with enhancing the number of discharges repeated at one and the same site. For example, the velocity amounts to 200 m/s for a 30th discharge on a copper. In this case a discontinuous ring-like area is observed and bright type 2 spots originate in a central discharge part.

The originating of type 1 spots is observed during subsequent discharges only in the form of independent bounded clusters which expand at a great velocity from a site of a discharge initiation to a periphery. Except several isolated type 2 spots formed near a triggering site most of these spots originate in a central cathode part in the form of a ring expanding at a much slower velocity.

After passing several discharges there occurs a complete surface cleaning from oxides and contaminations and an evolution pattern of each subsequent discharge is actually repeated. In this case type 2 cathode spots are immediately formed in the site of a discharge initiation in the shape of a ring expanding at the velocity of 30 to 60 m/s (Fig. 1 b).

The electron temperature was evaluated relative Al ion line intensities such as 448, 451.2 and 452.9 for spots of both types on an aluminium cathode². T_e is equal to $(16-19) \cdot 10^3$ K and $(11-15) \cdot 10^3$ K for type 2 and type 1 spots, respectively. From this evaluation of electron temperature values it follows that processes occurring in type 2 spots have a higher energy level than those in type 1 spots.

4. DISCUSSION

The experiments conducted indicate that a behaviour of type 1 spots is associated with their originating and functioning on a cathode surface layer. The latter is characterized by the presence of oxides and elements loosely bound to a basis. The layer has sharp microirregularities which is inevitable result of grinding and polishing. It would appear reasonable to suggest that the layer can easily interact with an expanding plasma and "be burnt out" by it at a relatively low process energy level. This can account for a branchy shape of type 1 spot traces, a high spot velocity which is comparable with that of a plasma scattering, a short life time and a weak erosion effect. Therefore, an artificial contraction of spots which results in their higher density does not lead to a significant increase of a surface erosion and luminosity. Thus, there occurs a situation at which type 1 spots are functioning though their velocity is not high. It can be inferred that a plasma component of type 1 spots is contaminated or multicomponent with an uncertain relationship between the components. So cleaning the surface provides the basis for originating and functioning of new-type spots with a greater plasma density over them and a higher energy level of internal processes. This is the cause of their stability, sufficient independence, prolonged life time, a low mobility and consequently a great erosion effect. These spots require an additional energy source the role of which can be fulfilled by an ion resonance recharging. The latter can ensure an effective heating of a neutral component in a plasma over a spot up to a level of a significant thermal ionization. The density and purity of a spot vapour are necessary and sufficient conditions for this process to occur. This, probably, completely ensures the conditions for originating type 2 spots only on a cleaned surface of both fusible and refractory metals. Therefore, starting an active ion resonance recharging can be reasonably considered the instant of originating type 2 spots and accepted as a criterion of this phenomenon. So the identification of type 1 spots can be effected by taking into account the absence or a very low intensity of an ion resonance recharging due to a contamination of a medium. The acceptance of this criterion simplifies and allows a more exact identification of spots. It should be noted that Rakhovsky and Beilis³ and Nagaibekov⁴ consider the process of ion resonance recharging as that having a big value of section. In the paper³ the authors state that the above process results in establishment of Maxwell ion distribution in a near-cathode layer and in the paper⁴ the author thinks that it leads to the formation of a near-cathode ion layer which increases an electric field strength.

The conditions for originating type 2 spots are established by a surface cleaning and heating a base metal. As it follows from

the experiments these conditions are primarily achieved in the areas of a higher type 1 spot density and especially pronounced when the temperature of decomposition and melting of oxides is higher than that of metals. This is responsible for a faster originating of type 2 spots on tin, zinc and magnesium than on more stable metals. A surface cleaning results in a surface roughness increase and as a consequence establishment of conditions required for increasing an effectiveness of an explosive electron emission mechanism⁵. This ensures a sufficient density of a near-cathode plasma with the parameters adequate for proceeding the process of ion resonance recharging and stable functioning of type 2 spots.

5. CONCLUSION

Thus, the experimental data indicate that type 2 cathode spots originate only on cleaned surface of the metals investigated. Probably, the general cause of this factor is an ion resonance recharging in a near-cathode plasma layer. The classification of spots helps to distinguish with a substantial degree of certainty between type 1 and type 2 spots on assumption of a dominant role played by an ion resonance recharging in type 2 spots and its absence in type 1 spots.

6. REFERENCES

1. G. A. Lyubimov and V. I. Rakhovsky, "Cathode spot of vacuum arc", UFN, Vol. 125, N 4, pp. 665-706, 1978.
2. M. K. Mitskevitch, A. I. Bushik et al., "Electroerosion processing of metals", pp. 56-75, Nauka i Technika, Minsk, 1988.
3. I. I. Beilis and V. I. Rakhovsky, "About theory of cathode mechanism of arc discharges", TVT, Vol. 7, pp. 620-625, 1968.
4. R. V. Nagaibekov, "About influence of recharging on cathode spot processes", Izvestia Akad. Nauk Uz. SSR, Ser. Phys.-Mat. Nauk, N 1, pp. 95-97, 1972.
5. G. A. Mesyats and D. I. Proskurovsky, "Pulse electric discharge in vacuum", Nauka, Novosibirsk, pp. 206-238, 1984.

Emission and arc studies of contacts with metal oxide inclusions

A.M. Chalyi, V.A. Nevrovsky

"ANTECH Ltd", Kazarmenny per., 6, bld. 1, 109028 Moscow, Russia

ABSTRACT

This paper reports studies of contact admixtures effects on recovery voltages of contact pairs when admixtures have a form of multiple inclusions of some metal oxides introduced into standard contact material CuCr 50/50.

The breakdown and recovery voltage studies of these materials were carried out at a simulating circuit with load current up to 300 A and frequencies 50 kHz - 120 kHz. Grains of alumina, and hafnium, lithium and lanthan oxides were used as inclusions. CuCr 50/50 with small tungsten chips was used as reference material. Statistical characteristics of recovery voltages were obtained for these materials and some promising compositions were selected for future studies.

2. INTRODUCTION

One of the ways to improve high-frequency performance of vacuum circuit breakers (and first of all to decrease recovery voltage U_r after arc extinction) is suggested to use additives of easily evaporative substances to standard copper-chromium contacts. The authors [1] demonstrated that e.g. lithium oxide inclusions reduced significantly recovery voltage in a special device simulating a vacuum switch. This effect was attributed to low ionization potential of lithium and, probably, to low work function of metallic lithium.

This paper reports results of similar tests for inclusions of following oxides: Li_2O , Al_2O_3 , HfO , La_2O_3 embedded into CuCr matrix. Application of these oxide inclusions has an additional advantage that they increase voltage of cold breakdown comparing to standard CuCr contacts [2] in contrast to the Latham's concept of emission sites as dielectric or semiconductive inclusions [3].

3. EXPERIMENTAL

Experiments were carried out in a high-vacuum chamber oil-free pumped with residual pressure as low as 10^{-9} Tor. Contacts being tested were separated with interelectrode gap 0,1-0,25 mm. An electrical circuit simulating the real electrical circuit in which vacuum breakers are used is shown at the Fig. 1. Changable inductance coils L and a group of capacities C_2 allowed to have frequencies of arc current oscillations in the range 50-120 kHz.

Samples for tests were manufactured by sintering of 51 vol. % of chromium, 44 vol. % of copper and 5 vol. % of an oxide of specific metal. The reference samples consisted of 51,2 vol. % of chromium and 48,8 vol. % of copper and were formed by melting. They had tungsten chips embedded into a matrix. These latter samples were practically pore-free.

Samples with alumina inclusions were of two types - with macro-size inclusions ($\sim 20+50$ mK μ m dia) and with sub-micron inclusions of alumina.

Samples were formed as cylinders with diameter 14 mm. Their butts were polished, degreased in alcohol and then washed in an ultrasonic cleaner in mixture of acetone and alcohol.

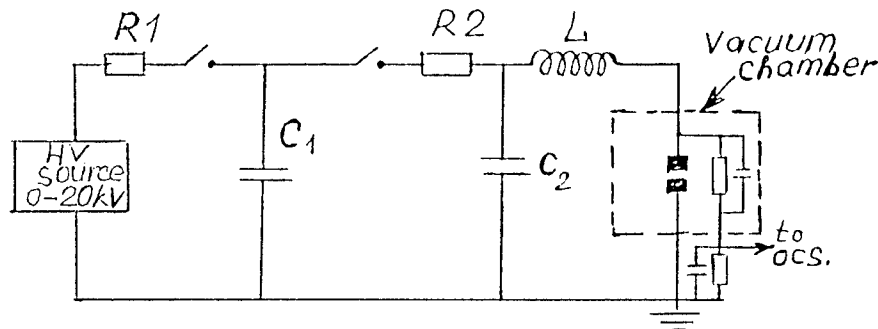


Fig. 1. Test circuit for recovery voltage studies.

An oscilloscope Tektronix 7623 A was used for recording voltage measured by an RC-divider at the electrode pair. Arc current was monitored by a current shunt. The experiments reported here were carried out at arc current amplitude I_{arc} up to 300 A.

4. RESULTS

Typical experimental oscillograms of recovery voltage for material with Li_2O inclusions are shown at the Fig. 2. Fig. 2a) shows details of an arc stage of current interruption whereas Fig. 2b) demonstrates a sequence of multiple voltage transients and reignitions of arc in the simulating circuit. We demonstrate this latter oscilloscope trace only to show that repetitive breakdown of the gap takes place at reduced voltage comparing to the first

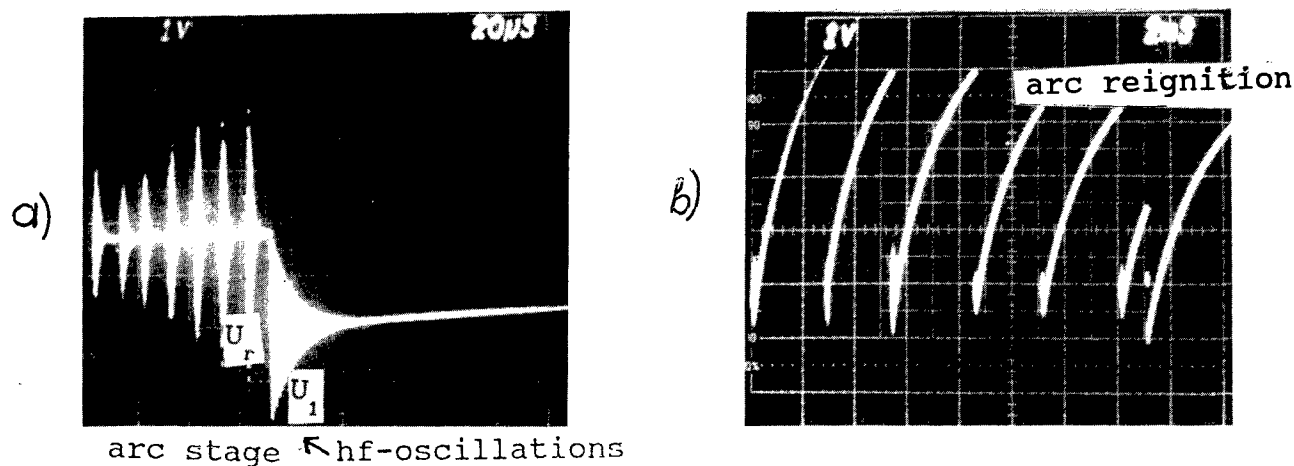


Fig. 2. Typical oscillograms of transient recovery voltage (gap 0,1 mm between electrodes with Li_2O).

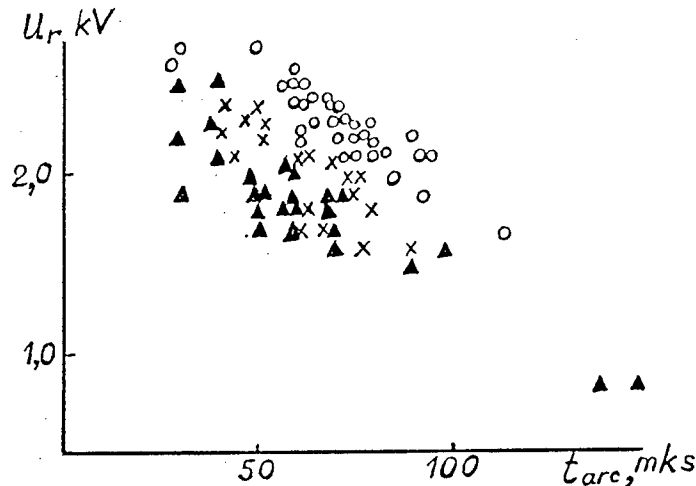


Fig. 3. Correlation between arc burning time and recovery voltage (gap 0,1 mm, electrodes with micro-sized alumina: Δ - first run, x - second run, o - third run, $L = 120$ mK).

breakdown of tested electrode gap (4,9 kV in this example). This result is known as "hot breakdown" voltage [4] and some speculations on its nature are proposed using correlation between the voltage and the time elapsed after arc extinction. However, we observed poor correlation between this time and "hot breakdown" voltage. So we shall not speculate on the result. Definite correlation was obtained for arc stage duration and the recovery voltage for all materials tested and typical groups of data are shown at Fig. 3.

We observed also unusual fast arc reignitions (in about ten mKs after arc extinction) in $\sim 5\%$ of tests for samples with HfO or Li_2O inclusions (see Fig. 4). Data on arc burning time and recovery voltage were statistically treated for all samples of materials. We got cumulative probability, distribution function and Weibull plots for recovery voltage data (see Table). All samples with inclusions are seen to have reduced mean values of recovery voltage comparing to the reference material CuCr/W chips. Weibull plot index m shows the spread of data and this parameter depends on the circuit inductance and on the material.

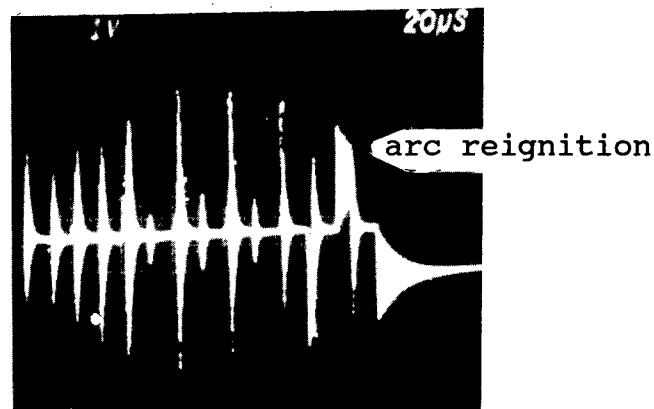


Fig. 4. An example of fast arc reignition for electrodes with Li_2O inclusions.

Table

	L = 120 mKHz				L = 60 mKHz			
	U_r kV	t_{ar} aver. mks.	m	i A/s	U_r kV	t_{ar} aver. mks.	m	i A/s
CuCr/W _{chips}	5,1 6,14*	79,5 81	3,86	$4,3 \cdot 10^7$ $5,1 \cdot 10^7$	3,26	74	3,36	$5,4 \cdot 10^7$
CuCr/Al ₂ O ₃	2,29	72	9,1	$1,9 \cdot 10^7$	2,2	52	6,3	$3,7 \cdot 10^7$
CuCr/Al ₂ O ₃ microsized	2,29 2,0**	69	8,15	$1,4 \cdot 10^7$	2,3	52,5	5,7	$3,8 \cdot 10^7$
CuCr/Li _{oxide}	1,67	63	5,45	$1,8 \cdot 10^7$	1,39	55	3,6 ^a	$2,3 \cdot 10^7$
CuCr/Hf _{oxide}	2,18	82	5,15 ^a	$1,7 \cdot 10^7$	2,02	74	—	$3,3 \cdot 10^7$
CuCr/La _{oxide}	2,06 2,4*	71 73	6,25 7,9	$2 \cdot 10^7$	1,89	62	4,35	$3,15 \cdot 10^7$

L = 20 mKHz				
CuCr/W _{chips}	2,2	28	1,21	$1,1 \cdot 10^8$
CuCr/Al ₂ O ₃	0,63	30	4,5	$3,15 \cdot 10^7$
CuCr/Al ₂ O ₃ microsized	1,3	10	2,7	$6,5 \cdot 10^7$
CuCr/Li _{oxide}	0,29	35	—	$1,45 \cdot 10^7$
CuCr/Hf _{oxide}	0,45	33	—	$2,3 \cdot 10^7$
CuCr/La _{oxide}	0,64	33	2,74 ^a	$3,2 \cdot 10^7$

*) - after long-term (~ 600 arcings) conditioning,

**) - after opening of the vacuum chamber and rearrangement of the samples,

^a) - Weibull plot is slightly curvy

Another parameter determining high-frequency oscillations of voltage is $k = U_1/U_r$ (where U_1 is marked at the Fig. 2a), and depends on L and stray capacity of electrodes in the vacuum chamber: L = 20 mKHz, $k = 1,45$; L = 60 mKHz, $k = 1,79$; L = 120 mKHz, $k = 1,9$.

The table shows di/dt corresponding to recovery voltage: $di/dt = U_r/L$. This parameter is proposed sometimes to be a criterium of recovery voltage in switches. If it is so it would be a constant specific for certain material for wide range of circuit parameters (e.g. inductance L). The table shows that it is not the case.

5. ACKNOWLEDGMENTS

The authors would like to acknowledge the assistance of V.M. Rossomagin and A.P. Alexeyev in experimentation.

6. REFERENCES

1. M. Lindmayer, E.-D. Wilkening, "Breakdown of short gaps current zero of high frequency arcs", *Proc. XIV Intern. Symp. on Disch. and El. Insul. in Vacuum*, pp.234-241, Santa Fe, 1990.
2. A.P. Alexeyev, A.M. Chalyi, V.A. Nevrovskiy, V.I. Rakhovskiy, "Study of breakdown characteristics of copper-chromium with multiple inclusions", *Proc. of the Intern. Symp. on El. Contacts. Theory and Applications*, pp. 110-113, Almaty, 1993.
3. R.V. Latham, "Prebreakdown electron emission", *IEEE Trans. Electr. Insul.* Vol. 12, pp. 194-203, 1983.
4. Y.H. Fu, R.P.P. Smeets, "An experimental investigation on high frequency vacuum arc interruption at small gap lengths", *Proc. XIV ISDEIV*, pp. 475-479, Santa Fe, 1990.

Electrode geometry and material effects on the cathode spot dynamics in a high-current vacuum arc

A.M.Chaly*, A.A.Logatchev**, S.M.Shkol'nik**

*Tavrida Electric LTD

Dorozhnyi proezd, 9/10, Moscow, Russia

** A.F.Ioffe Physical-Technical Institute RAS,
Polytechnicheskaya 26, St.Petersburg, 194021 Russia

ABSTRACT

Comparative characteristics of the cathode processes in the discharge with electrodes of pure metal and of CuCr composition are presented. The effect of the gap, electrode shape and other geometric factors on the cathode spots dynamics is investigated. The accomplished investigations allowed to elaborate methods to influence the cathode spot dynamics by geometric factors.

1. INTRODUCTION

In the diffuse mode of a high-current vacuum arc the cathode is the main source of plasma producing substance. The plasma parameters in the gap and consequently the arc integral characteristics are determined by the dynamics of the emission centers - cathode spots (CS). It has been shown that at the discharge initiation in the center of substantial butt preliminary trained electrodes (a clean surface) of a pure metal at symmetric current supply the cathode spots form an expanding ring¹. The influence of the current waveform and cathode material on the ring expanding rate V has been studied. The summary of the results is given in². Ascertained is that the CS motion is due to the self-magnetic field: $V=K \cdot B$ (K - constant, the characteristic of the cathode material). The CS dynamics on bimetallic electrodes is investigated in³.

In the vacuum circuit breakers (VCB) the place of ignition and the electrode center generally do not coincide; at the first milliseconds after ignition the gap is shorter than that studied in¹. Therefore is necessary to investigate the CS dynamics at a non-central ignition, as well as at small gaps. As electrode materials for VCB the main attention is attracted by compositions Cu/Cr.⁴ Possible peculiarities of CS dynamics on the like compositions are of interest. The arc transition out a diffuse mode into a contracted one with current arise restricts the VCB interrupting capacity. Usually are considered two possibilities to solve this problem using special contacts shapes: by a generation of a radial or of a longitudinal self-magnetic field⁵. Of interest is an investigation of contact configurations changing azimuth component of the self-magnetic field. This permits to affect the CS dynamics, to keep the spots near the discharge axis, or retain their motion to the periphery, and therefore reduce side ion losses. Additionally this should reduce the plasma column constriction. Investigated were also other ways of influencing these processes with the help of geometric factors.

2. EXPERIMENTAL SET-UP AND METHODS

The experiments were carried out in a vacuum chamber at continuous pumping ($p \sim 10^{-5}$ Torr). The electrodes were made of composition CuCr50W3 and OFHC Cu. Three types of pair electrodes were used (Fig.1). Also were used substantial butt electrodes with ring shaped groove on the butt. Internal groove diameter and its depth were fixed at 16 and 2mm respectively. Two electrodes of this type were tested: D1 - with 1mm groove

width and D2 - with 2mm width. The contact gap $h=1\div 8$ mm. The discharge was ignited in the cathode center (except special experiments) and fed by a special rectangular voltage pulse generator ($U=115$ V, duration 0-5 ms), enduring of $I\leq 6$ kA. The current

(<100 μ s front) was adjusted by a resistor in series. Registered were the current and discharge voltage; there were led spectroscopic measurements, the cathode surface was observed at a small angle by a high speed photography (HSP) camera (more details in⁶).

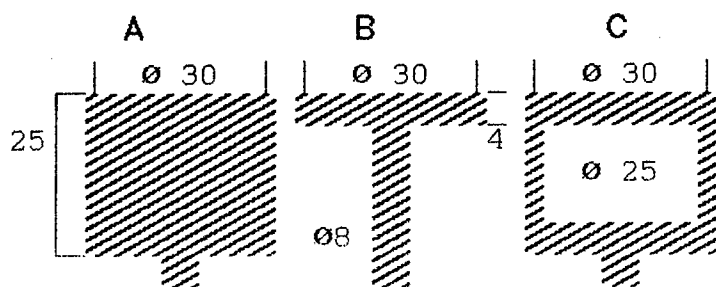


Fig. 1.

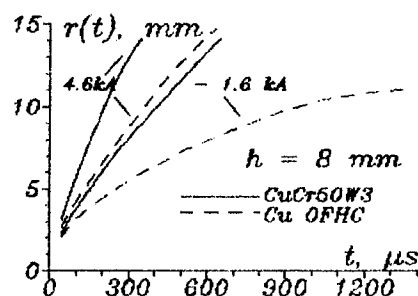


Fig. 2.

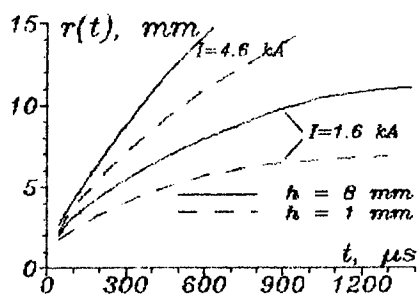


Fig. 3. CS-dynamics on Cu OFHC

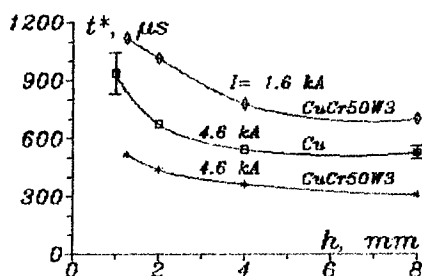


Fig. 4.

3. EXPERIMENTAL RESULTS AND DISCUSSION

3.1. The cathode spot dynamics on copper chromium composition (A-type electrodes). Unlike the pure metal ele-

ctrodes with clean trained surfaces where CS form an expanding ring with only occasional spots inside, high CS activity has been observed inside the ring for copper chromium electrodes. The ring radius $r=r(t)$ is increasing under other equal conditions faster than, for instance, on the OFHC Cu (fig.2). Reaching the electrode edge, the spots run on the side surface. There begin intensive oscillations of the current and of the voltage. Our experience obtained with gas filled electrodes prompts to explain described peculiarities by the substantial amount of dissolved gases in a composite material. Intensive lines of different gas admixtures (hydrogen, nitrogen, oxygen) have actually been observed in the discharge radiation spectrum. We have also noted that CS activity inside the ring slightly diminishes with the number of discharge though remains high enough after lot of arcing.

3.2. The effect of the contact gap on the CS dynamics (A- type electrodes). Fig.3 presents the dependencies of the CS ring radius on time. Fig.4. presents the dependencies of the value t^* ($r(t^*)=0.9R$) on the gap. As it is obvious from fig.3,4 the rate of ring expansion tends to decrease with gap decrease. The explanation of CS ring expansion in¹ does not take into consideration such dependence. According to¹ the rate of CS ring expansion should not depend on the contact gap. Thus, according to the presented results (see fig.4) this explanation may be directly applied only for relatively long gaps (>4 mm). The reason of the observed phenomena may be as follows. In short gaps the pressure of erosion products increases. It is known that this may lead to the decreasing of CS velocity⁷. Another reason may be determined by the growth of the probability of CS occurrence in the region of increased pressure, i.e. near the center of the electrode. We must to mention that the authors of¹ investigating CS dynamics for gaps 3-5 mm did not observe such effects. This might happen because of the use of the grid anode (necessary for the cathode observation) that did not allow to increase the pressure.

3.3. The effect of the discharge ignition location. (A- type electrodes) The experiments were carried out at the discharge ignition at a distance of 7 or 12 mm from the center of the electrode out of CuCr composition. The gap $h=4\text{mm}$. HSP showed that the CS form a ring structure, which, expanding with the rate like that at the central discharge initiation, reaches the nearest edge of the electrode. Some spots runs on the side surface; the discharge however remains relatively low noisy. The main part of CS continue to propagate over the butt. An essential peculiarity of the process is the growing CS front deformation, finishing with tearing off and running ahead of a CS group. In some cases this results in a formation of small CS ring near the main ring. The tearing off occurs on the electrode part diametrically opposed to that where the spots have already reached the cathode edge. After the CS has embraced the whole cathode butt the ring joins. The number of CS running on the side surface increases. The discharge becomes noisy. Thus at a non-central ignition there is observed a tendency to embrace by the CS ring the whole cathode, to the discharge symmetrization.

3.4. The effect of the self magnetic field azimuth component variation on the CS dynamics. Using the B and C type electrodes we expected to vary the value of the self magnetic field azimuth component near the cathode surface and to effect in accordance with the rate of the CS ring expansion. One may expect that for B type electrodes this rate will be decreased and for C type - increased compared with that for A type. However further experiments have shown that for copper electrodes for different currents ($\leq 6\text{ kA}$) and contact gaps ($1\div 8\text{ mm}$) the dependencies $r(t)$ have no differences for A, B and C type electrodes. In contrast for CuCr electrodes we observed the variation for different electrode types. These variations were most essential for high current (fig.5.) The behavior of $r(t)$ curve for B type electrodes corresponded to our expectation, in contrast for C type electrodes. Experimental results at different gaps are presented in fig.6a. It is clearly visible that variations of the CS dynamics become negligible with the decrease of contact gap. Fig.6b. presents obtained results for relatively low current. The accuracy of t^* determination in low currents experiments is lower because the expansion rate is small especially at $h=1\text{ mm}$. The discrepancy of obtained experimental results for composite electrodes with the expected ones in the C- type case may be explained based on the notions, discussed in 3.2. Really if the rate of CS expansion for short gaps drops because of the increase of the erosion products pressure, the increase of the azimuth component of self magnetic field will cause the growth of the $\vec{j}\times\vec{B}$ force preventing plasma radial expansion. And vice versa - the decrease of the azimuth component will cause the decrease of the $\vec{j}\times\vec{B}$ force as well. Thus there are at least two factors affecting the CS dynamics; note that for C- type electrode they affect in a contrary way. Although the absence of noticeable effects for the Cu electrodes makes the presented explanation doubtful, but it does not give sufficient reasons to reject it.

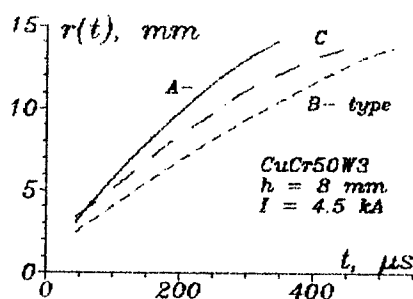


Fig.5.

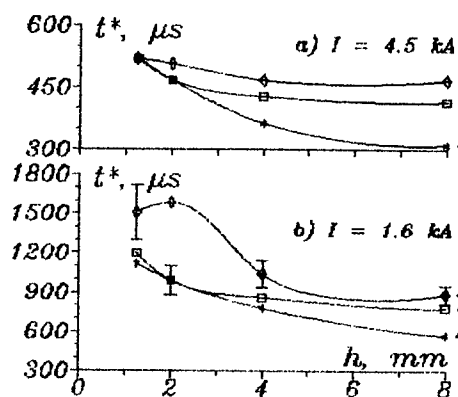


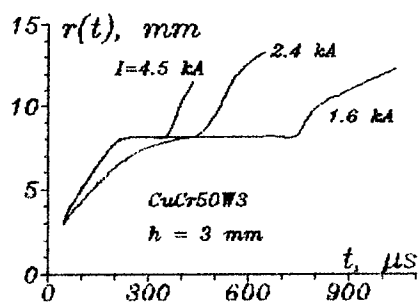
Fig.6.

The results, received at testing the composite electrodes of the B- type allow to expect an increase of the interrupting capacity of the like contact systems. The effect may be strengthened by taking away the central part of the electrode butt. Actually interrupting capacity tests carried out on special set-up for the ring shape electrodes proved nearly 50% higher interrupting capacity then that for the substantial butt electrodes of the same diameter. The CS dynamics

investigations on the ring electrodes, enable to suggest, that this is a result of a more optimal CS distribution on the electrode – a significant part of the CS is retained near the inner ring edge and only a small part of the CS runs from the exterior edge on the side surface.

3.5. The efficacy of the cathode surface grooving. Since on the clean surface a new spot is formed at the distance $x \sim \rho$ (ρ – a spot radius) from the existing one, it may be

expected to delay or even to restrict the CS expansion by the cathode grooving. The experiments indicated, that the grooving effect is the stronger the greater is the groove width and the less are the current and the contact gap. For instance, on the electrodes D1 at $h=8\text{mm}$, $I=5\text{kA}$ the groove practically did not effect on the CS dynamics. But at $I=1.5\text{kA}$ the spots were retained on the inner groove side for $\Delta t \approx 100 \mu\text{s}$. The groove widening (electrodes D2) leads to an appearance at the same gap and $I=5\text{kA}$ of a small delay, and at $I=1.5\text{kA}$ – to an increase of the delay up to $\Delta t \approx 180$



μs . The reducing of the gap had an essential effect: $I=1.5\text{kA}$ at $h=3 \text{ mm}$ – $\Delta t \approx 550 \mu\text{s}$; $h=2 \text{ mm}$ – during the whole recording period (1500 μs) the CS did not overcome the groove. The dependence on the current is illustrated in the fig.7. It is essential, that for a short gap even at $I=5 \text{ kA}$

Fig.7.

many CS did not overcome the groove. HSP of the cathode surface during the last 1.5 ms of the 4.5 ms discharge duration indicated that a majority of CS is retained on an interior groove side. By changing the parameters, as well as the number of the grooves the spot dynamic on the cathode surface may be effectively managed if measures are taken to centralize the ignition.

4. ACKNOWLEDGMENTS

The work has been carried out under the financial support of the Tavrida Electric LTD and of the Russian Fundamental Investigation Fund (project 93-02-17416).

5. REFERENCES.

1. J.C. Sherman, R. Webster, R. Holmes, " Cathode spot motion in high- current vacuum arc on copper," J.Phys.D:Appl.Phys, Vol.8, pp.696-702, May 1975.
2. Н. Е. Перский, В. И. Сысун, Ю. Д. Хромой, "Динамика катодных пятен вакуумного разряда", ТВТ, Т. 27, С. 1060-1067, ноябрь-декабрь 1989.
3. А. И. Бушик, Б. Ютнер, Х. Пурш, "Динамика катодных процессов на биметаллических электродах в сверхвысоком вакууме", ТВТ, Т. 18, С. 713-720, июль-август 1980.
4. F.Heitzinger, H.Kippenberg, K.E.Saeger, K.-H. Schroder, "Contact materials for vacuum switching devices", Proc. XV ISDEIV, Darmstadt, Germany, p.273-278, 1992.
5. K. Frohlich et al, "Fundamental research on vacuum interrupters at technical universities", ibid, p.261-271.
6. A.A.Logatchev, S.M.Shkol'nik, "Arc discharge in vacuum with gas- filled electrodes", Proc. XVI ISDEIV, Russia, 1994.
7. C.J.Gallagher, "The retrograde motion of the arc cathode spot," J.Appl.Phys., Vol.21, p.768, July 1950.

Sheath model of negatively biased substrate in vacuum arcs with cathode spots

Cheng Zhongyuan, Zou Jiyan

Huazhong University of Science and Technology
Department of Electric Engineering, Wuhan, Hubei, P.R.China

ABSTRACT

Plasma sheath near the substrate acts an important role in Vacuum Arc Deposition Technology(VADT). To analyze the sheath characteristics of the substrate in VADT, the unique ejection pattern of the cathode region must be taken into account. This paper describes a steady-state, two-dimension sheath model in which ions distribute specially according to a cosinoidal law. The model equations can be numerical solved under specified conditions, to describe the sheath behavior of the substrate in the process of titanium film deposition using VADT. The model can be used for calculation of ion flux and heat flux flowing to the substrate in VADT, or in some other cases in which biased conductors were in vacuum arcs with cathode spots.

1. INTRODUCTION

Vacuum arcs have been extensively studied for tens of years because of their importance as circuit-breaking components in vacuum switchgears^[1]. Recently vacuum arcs have been used for surface modification, i.e. for the deposition of various films on workpieces that need some special surface performances, such as microhardness, wear- and corrosion-resistance, colour etc. Pure metals, alloys and compound films can be produced by Vacuum Arc Coating Technology(VADT). Some reviews^{[2] [3] [4] [5]} and various coating processes and devices have been introduced in the literatures.

While it has been widely utilized in commercial purpose, VADT has been studied in laboratory by a lot of researchers. However, theoretical knowledge still remains not enough to uncover the essential principles of VADT at present. Some researchers suggested a theoretical outline in which a step-by-step model works, i.e. the process of VADT can be divided into three continuous steps according to movement of the deposition species^{[4] [6]}. The deposition particles are generated in the electrode regions (here and below we refer them to cathode regions), then transport in the arc column from their source to the substrate which is usually negatively biased. At last they reach the sheath around the substrate and deposited to or reflected from the substrate. Fig.1. shows schematically the different region according to the above theoretical outline.

It is the sheath region that connects the plasma in the arc column to the deposition surface. Before impacting and deposited to the substrate, the ions are attracted and accelerated by the sheath region. Ion energy is critical to the structure of the film, the temperature of the substrate and deposition rate. The effects of ion bombardment on the film formation are introduced by some authors^{[7] [8]}. The ions gain great part of their kinetic energy in the sheath region around the substrate. Obviously, the behaviour of the sheath region must be of great importance to the quality of the deposited film.

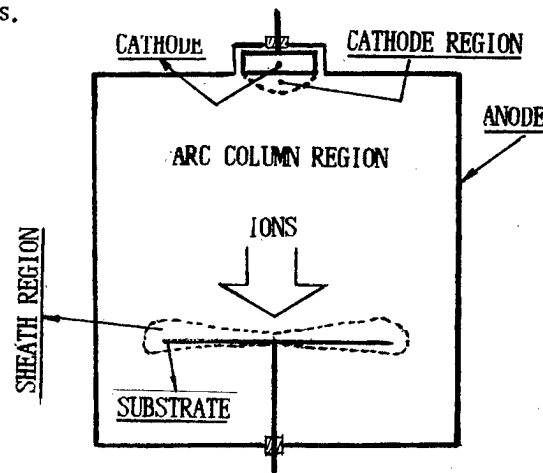


Fig.1 Three Regions in VADT Process

2. MODEL OF THE SHEATH

2.1 Statement of the problem

Vacuum arcs in VADT are reasonably similar to those in vacuum interrupters under the same vacuum, current, magnetic field and electrode arrangements. Especially, the arcs have similar processes in the cathode spot region. The cathode material is locally evaporated in the spots sized several microns, and the evaporants are intensively ionized in a hemisphere of several tens of microns diameter just before the cathode region. According to the popular non-stationary model of the cathode spots, the current density in the spots gets to 10^{12}A/m^2 , the plasma density $10^{25} - 10^{26} \text{m}^{-3}$ [9] [10]. However these values decrease sharply in the arc column. The plasma stream ejects so rapidly from the cathode region that any correct modeling of the sheath in the vacuum arc with cathode spots must take the ejection pattern of the spots into account.

The sheath problem has been extensively studied by many authors since Langmuir's work. Most of the authors formulated the problem using Poisson's equation together with assumptions of Boltzmann's distribution for electrons and some other distribution patterns for ions, or together with hydrodynamic equations for electrons and ions [11] [12] [13] [14]. As has been pointed out above, the spots of vacuum arcs provide plasma streams with a very rapid directed velocity backward the spots. Thus the plasma is not that kind of hot electrons and 'cold' ions as supposed in most models. In the arc column electron temperature T_e is not higher than 1-3eV, while the ions fly with a velocity v of $1-2 \times 10^4$ [10] [15], i.e. with a kinetic energy of about 100eV for the ions of titanium cathodes, due to the expansion and acceleration from the spots. Simple estimation reveals that the ion acoustic speed V_A is much smaller than v . Furthermore, when the substrate is biased to above several tens of volts, the non-equation $kT_e \ll e u_b (k: \text{Boltzmann constant, } e: \text{electron temperature, } u_b: \text{the bias voltage of the substrate})$ stands. This implies that Bohm's criterion plays a less important role here.

2.2. Model of the problem

The basic assumptions are as follows,

- neglecting collisions in the sheath region, thus neglecting any charge exchanging processes;
- neglecting magnetic field in the sheath; only electric force affecting the ions in the sheath;
- for electrons: thermo-equilibrium, thus a Boltzmann distribution;
- for ions: a cosinoidal distribution in the plasma jet from the spots; random energy $kT_i \ll 0.5 M_i v^2$ (directed kinetic energy); $0.5 M_i v^2 \gg kT_e$;
- steady-state; cylindrical symmetry

It must be pointed out that collisions must be taken into account when the background gas pressure is higher enough, for example in the process of TiN film coating using VADT the pressure is usually higher than 0.1Pa due to the infilling of nitrogen, or when the arc current is sufficiently large, just like the case in vacuum circuit breakers. In fact in most VADT devices except those with plasma collimation or filtering using magnetics, the magnetic field in the sheath can be neglected. Electrons' thermo-equilibrium is a result of their relatively small inertia, with such an assumption, the problem can be modelled jumping over the electron time scale. According to the study of Tuma, Juntter et al. [15] [16], metal ions ejected from the cathode region obey a cosinoidal distribution pattern. Ion current density can be written

$$J_i = \gamma f I \cos \theta / (2 \pi r^2), \quad (1)$$

where ' γ ' is a constant ($\gamma \approx 4$, according to [15]), ' f ' the fraction of ion current, ' I ' total arc current, ' r ' the distance from the cathode spots, ' θ ' the angle with the normal of the cathode surface.

In VADT the cathode spots are driven by a local magnetic field. They move symmetrically on the cathode surface just like a circular spring. Thus in a steady-state model the center of the cathode can be taken as the 'average position' of the cathode spots. Thus this position can be used as the reference point of θ and r .

Traditionally, the following normalized variables are introduced: $U = -eu/kT_E$, $V = v/V_A$, $N_I = Zn_I/n_{E0}$, $N_E = n_E/n_{E0}$. Here 'u' is the potential in the sheath, 'v' the velocity of the ions, 'Z' the average charge state of the ions, 'n_E', 'n_I' are respectively the density of the electrons and ions in the sheath (here and below, subscript E, I, S and 0 represent for values of the electrons, ions, in the arc column and on the boundary between the sheath and the plasma, respectively), 'n_{E0}' the plasma density in arc column. V_A is ion sound speed, $V_A = (2ZkT_E/M_I)^{0.5}$, where 'M_I' is the ion mass. L_d is Deby length, $L_d = (\epsilon_0 * kT_E / (e^2 n_E))^{0.5}$.

The sheath equations are as follows (see Fig. 2),

$$\nabla^2 U = L_d^{-2} (N_I - N_E) \quad (2)$$

$$N_I = (1 + U [V_S \cos(\theta_S)]^{-2})^{-0.5} \quad (3)$$

$$N_E = \exp(-U) \quad (4)$$

Eq. 3 is obtained by coupling the equations of mass and energy conservation in the z direction. They are written below,

$$0.5 M_I (v_S \cos(\theta_S))^2 = 0.5 M_I v_z^2 + Zeu \quad (\text{energy conservation})$$

$$n_I v_z = n_{I0} v_S \cos(\theta_S) \quad (\text{mass flux conservation})$$

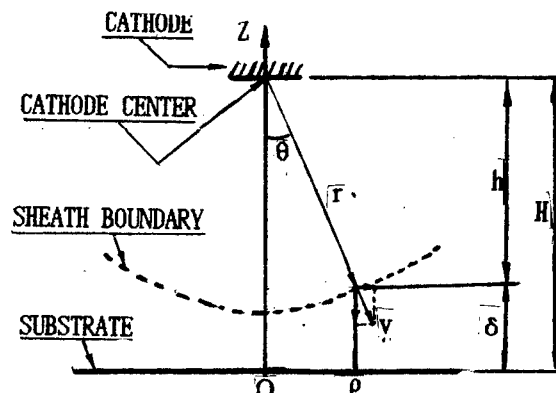


Fig. 2 Coordinates for Modelling

in Eq. 3 the normalized velocity $V_S \cos(\theta_S)$ can be obtained by Eq. 1 and mass flux conservation equation on the sheath boundary, i.e.,

$$J_I = v_S n_{I0} e Z = \gamma f I \cos(\theta_S) / (2\pi r g). \quad (5)$$

Thus,

$$V_S \cos(\theta_S) = \{ [\gamma f I / (2\pi H^2)] / (e Z n_{I0} v_S) \} * [hH / (h^2 + \rho^2)]^2, \quad (6)$$

where H, h and ρ are illustrated in Fig. 2.

Let $J_1 = \gamma f I / (2\pi H^2)$, $J_2 = e Z n_{I0} v_S$, Eq. 6 becomes

$$V_S \cos(\theta_S) = (J_1 / J_2) * \{hH / (h^2 + \rho^2)\}^2 \quad (7)$$

The sheath model consists of Eq. 2, Eq. 4 and Eq. 7. The boundary conditions are

$$\begin{aligned} U=0, \quad dU/dz=0, \quad \text{when } z=\delta \quad (\delta \text{ is the sheath thickness at a specified radius } \rho) \\ U=U_b, \quad \text{when } z=0 \quad (\text{where } U_b \text{ is the normalized bias voltage, } U_b > 0). \end{aligned}$$

2.3. Calculation method of the model

The radial component of electric field in actual VADT devices can often be neglected due to the high bias voltage. In a symmetrical cylindrical system Eq. 2 can be simplified as

$$d^2 U / dz^2 = L_d^{-2} (N_I - N_E) \quad (8)$$

Eq. 8 looks one dimensional but it contains co-ordinate ρ in its right side. In the Eq. 4, Eq. 7 and Eq. 8, the potential U and the sheath thickness δ are all unknown variables. However it is possible to integrate Eq. 8 once, using the boundary conditions given above. So the differential equation can be lowered to the first order. It can be written as follows when N_I, N_E was substituted in,

$$dU/dz = -\{4 \cdot k(\rho, \delta) * [(1 + k(\rho, \delta) U)^{1/2} - 1] + 2(\exp(-U) - 1)\}^{1/2}, \quad (9)$$

where $k(\rho, \delta) = (J_1/J_2)^2 [(h^2 + \rho^2)/(hH)]^4$. The negative sign has been selected before Eq.9 because dU/dz decreases with increased z . The boundary conditions for Eq.9 is as follows,

$$U=U_b, \text{ when } z=0; U=0, \text{ when } z=\delta. \quad (10)$$

Eq.9 and Eq.10 can be numeritically solved. The pricipal procedure is described here; for a given radius ρ , calculate $k(\rho, \delta)$, where δ may be given an initial value; integrate Eq.9 until the absolute value of U gets nearly zero(Runge-Kutta method provides good performance here), thus a value of δ can be obtained; next, use this value for the next iteration, integrate Eq.8 again, until the second condition of Eqs.10 is satisfied. Therefore we can get the spacial distributions of electric potential and ion densities, together with sheath thickness distribution around the substrate.

3. REMARKS AND FUTURE WORK

3.1. About the model

The above model are established under some critical assumptions. These assumptions limit its valid range to high vacuum, low current, no magnetic fields around the substrate and high bias voltage. The calculation of the model needs such easily getatable parameters such as the deposition chamber size, arc current and bias voltage. But it also needs the electron density, the electron temperature, the mean charge of the ions in the arc column and the mean velocities of the ions leaving from the cathode spots. These later group of parameters can be obtained only by plasma diagnostics. In our calculations, the electron density and temperature in the arc column were obtained by plasma diagnostics using a Langmuir probe. The experimetental setup was introduced in detail in [17]. The mean charge number and speed of the ions are results in literatures[1], [15] and [16], etc. Some relations can be made to connect the deposition rate and the temperature rise of the workpieces with the process parameters such as arc current, bias voltage and workpiece positions. The results of the calculation will be given some elsewhere in the near future.

The model is somewhat complicated when the radial component of electric field is considered. When one needs only sheath thickness Child-Langmuir relation is a good method for estimation^[17].

3.2. Future Work

(1) Using the model frame to deal with more complicated deposition atmosphere i.e. taking the interactions between the plasma with the back ground gas into account during the deposition of composite material TiN. Collision paramers will be introduced in.

(2) Plasma diagnostics will be carried out duing the actural process of TiN deposition with electric probe and Farady cup.

4. REFERENCES

1. J. M. Lafferty, Ed. *Vacuum Arc: Theory and Application*, Wiley-Interscience, New York, 1980.
2. B. Rother, 'Cathode arc evaporation as a coating technique', *Surf. Engin.*, Vol.4, No.4, 1988.
3. D. Sanders, 'Review of ion-based coating processes derived from the cathodic arc', *J. Vac. Sci. Technol.*, A7(3), 1989.
4. R. L. Boxman, et.al., 'Principles and applications of vacuum arc coating', *IEEE Trans. on Plasma Sci.*, Vol.17, No.5, 1989.
5. J. Vyskocil, et.al., 'Cathode arc evaporation in thin film technology', *J. Vac. Sci. Technol.*, A10(4), 1992.
6. R. F. Bunshah, 'Critical issues in plasma-assisted vapor deposition process', *IEEE Trans. on Plasma Sci.*, Vol.18, No.6, 1990.

7. L. Hutman, et.al., 'Low energy ($\sim 100\text{eV}$) ion irradiation during growth of TiN deposited by reactive magnetron sputtering: effects of ion flux on film microstructure', *J. Vac. Sci. Technol.*, A9(3), 1991.
8. P. Martin, ionization-assisted evaporation processes; techniques and film properties', *IEEE Trans. Plasma Sci.*, Vol.18, No.6, 1990.
9. S. Anders, et.al., 'On modes of arc cathode operation', *IEEE Trans. on Plasma Sci.*, Vol.19, No.1, 1991.
10. V. I. Rokhovskiy, 'Critical parameters of the cathode region of a vacuum arc', *IEEE Trans. on Plasma Sci.*, Vol.18, No.3, 1990.
11. F. F. Chen, 'Electric probe', in *Plasma Diagnostic Techniques*, ed. by R. H. Huddleston, et.al., Academic Press, New York, 1965.
12. V. A. Godjak, et. al., 'Smooth plasma-sheath transition in a hydrodynamic model', *IEEE Trans. on Plasma Sci.*, Vol.18, No.6, 1991.
13. Kyu-Sun Chung, 'A Kinetic theory of ion collection by a probe in flowing unmagnetized plasma', *J. Appl. Phys.*, Vol.69, No.6, 1991.
14. G. A. Emmert, et.al., 'Numerical simulation of plasma sheath expansion, with applications to plasma-source ion implantation', *J. Appl. Phys.*, Vol.71, No.1, 1992.
15. B. Juttner, 'Characterization of cathode spot', *IEEE Trans. on Plasma Sci.*, Vol.PS-15, No.5, 1987.
16. D. T. Tuma, et.al., 'erosion products from the cathode region of a copper vacuum arc', *J. Appl. Phys.*, Vol.49, 1978.
17. Z. Cheng, 'Characteristics of the sheath around the substrate in the process of vacuum arc deposition of Ti film', *Proc. of IC-ECAAA*, Xi'an, 1993.

2-D MHD model of the plasma jet originating from a vacuum-arc cathode spot

V.N. Gavrilov, E.A. Litvinov, G.A. Mesyats and D.L. Shmelev

Institute of Electrophysics, Russian Academy of Sciences, Ural Division
34, Komsomolskaya st., Ekaterinburg 620219, Russia

ABSTRACT

The paper presents a two-dimensional hydrodynamic model of the plasma jet running out of the cathode spot of a vacuum arc, which is an outgrowth of the one-dimensional problem that we have solved earlier. Also given are refined equations of state for a matter in a transitory phase, which conceivably might allow a through numerical simulation of a cathode spot from cold metal to hot plasma.

1. MODEL OF A PLASMA JET

The 2-D MHD model of the vacuum-arc plasma jet presented here is in outgrowth of the 1-D hydrodynamic model discussed by us in Ref [1,2,3,6]. The computations carried out in 1-D approximation have provided the principal characteristics of a cathode jet being in satisfactory agreement with experimental data. Nevertheless, these results cannot be considered completely adequate, since actually the plasma parameters of a cathode jet are distributed highly nonuniformly over its cross section. Furthermore, a 1-D model fails to take into account the effects related to the influence of the self-magnetic field of the cathode jet.

The 2-D model of a plasma jet is based on the two temperature non steady-state MHD equations.

$$\begin{aligned} \frac{\partial n_i}{\partial t} + \operatorname{div}(n_i \mathbf{v}) &= n_e (\alpha_{i-1,i} n_{i-1} - \beta_{i,i-1} n_i n_e - \alpha_{i,i+1} n_i + \beta_{i+1,i} n_{i+1} n_e) \\ n &= \sum_i n_i \quad n_e = z n \quad \mathbf{v}_e = \frac{\mathbf{j}}{e z n} + \mathbf{v} \\ m_i n \left(\frac{\partial \mathbf{v}}{\partial t} + (\mathbf{v} \nabla) \mathbf{v} \right)_j &= - \frac{\partial n T}{\partial r_j} - \frac{\partial n_e T_e}{\partial r_j} + \frac{1}{c} [\mathbf{j} \times \mathbf{H}]_j \\ \left(\frac{\partial T}{\partial t} + \mathbf{v} \frac{\partial T}{\partial \mathbf{r}} \right) + \frac{2}{3} T \operatorname{div} \mathbf{v} &= \frac{2 m_e}{m_i} \frac{1}{\tau_{ei}} (T_e - T) \\ \left(\frac{\partial T_e}{\partial t} + \mathbf{v}_e \frac{\partial T_e}{\partial \mathbf{r}} \right) + \frac{2}{3} T_e \operatorname{div} \mathbf{v}_e + \frac{2}{3 n_e} \operatorname{div} \mathbf{q}_e &= - \frac{2 m_e}{m_i} \frac{1}{\tau_{ei}} (T_e - T) + \frac{2 m_e}{3 \tau_{ei}} \left(\mathbf{v}_e - \mathbf{v} - \frac{3 \mathbf{q}_e}{5 n_e T_e}, \mathbf{v} - \mathbf{v}_e \right) + Q_e \\ \frac{\partial \mathbf{H}}{\partial t} &= \operatorname{rot} [\mathbf{v} \times \mathbf{H}] - \frac{c^2}{4 \pi} \operatorname{rot} \frac{1}{\sigma} \operatorname{rot} \mathbf{H} - \frac{c}{e} \operatorname{rot} \frac{1}{n_e} \operatorname{grad} n_e T_e \end{aligned}$$

where Q_e are terms associated with energy absorption or liberation in the processes of ionization and recombination; α and β are, respectively, the ionization and recombination coefficients in Born's approximation; ions with a charge from 1 to 6 are taken into consideration. The problem geometry is shown in Fig. 1. The Z -axis is the axis of cylindrical symmetry for the plasma jet and the R -axis coincides with the cathode surface. It is supposed that the emission and erosion regions match and are confined within the crater radius R_0 . Specified for the lower boundary are the mass flux, the ion density, and the total current, for the Z -axis the condition of symmetry, and for the rest boundaries the conditions that the normal derivatives of the main variables are zero.

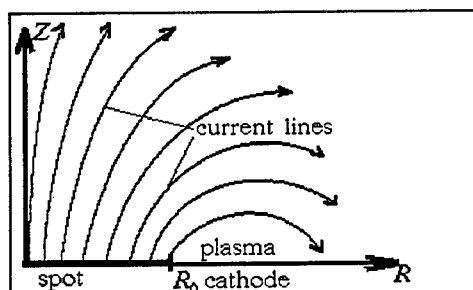


Fig. 1. The problem geometry.

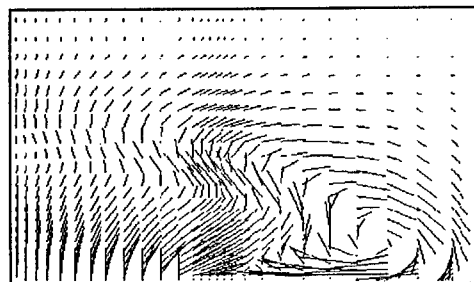


Fig. 2. The electron current distribution.

Computations carried out in terms of the 2-d model have shown that the account of the self-magnetic field for the conditions of the given problem, on the one hand, has little effect on the scattering of ions and, on the other hand, results in a highly nonuniform electron current distribution in the jet (Fig. 2). It can be seen that there exists a considerable reverse current, which can be inferred directly from the solution of the equation for h , and no additional mechanism should be involved in the model to describe this current like in the 1-d model.

According to the computations, the radial distribution of the reverse electron current has a pronounced maximum, which shifts in the course of time forward the peripheral regions of the cathode spot. The reverse electron current is comparable to the total cathode spot current and it decreases with time. It also depends on the total current through the spot and decreases with increasing the latter. This may be responsible for the nonlinear current dependence of the cathode spot radius observed in experiment.

The electron current is distributed nonuniformly over the jet cross section. At the early stage of spot operation, the current density is the maximum in the peripheral regions; in the course of time the current constricts forward the center of the jet and the current density in the jet reaches its maximum at distances from cathode, comparable with the size of cathode spot. The maximum current density is higher than the current density at the cathode. In some computations the temperature in these regions reached 20 eV and the average ion charge was 6. Our solutions show interesting that there exist interesting objects, ring-shaped (more exactly, toroidal-shaped) current vortices, responsible for which is the third form on the right side of the equation for H . However, sharply defined nonuniformities are shown to exist for about 0.25 ns. Steady-state solutions give cross-sectional current profiles being in qualitative agreement with our 1-D steady-state solutions.^{3,6}

We believe that the model discussed offers new view of the processes occurring during the formation of a vacuum arc.

2. CHOOSING A WIDE-RANGE EQUATION OF STATE

Our subsequent efforts will be focused on a numerical simulation of the whole process of development of a cathode spot. Our interest will be not only with the plasma flare but also with the transitory metal-plasma region as well as with the processes of melting and evaporation in the cathode spot crater. To do this requires a knowledge of a wide-range equation of state for the cathode material, since the temperature varies from room temperature to several electronvolts and the material density decreases from the solid (10^{23} cm^{-3}) to plasma (10^{15} cm^{-3}) density. We will consider a copper cathode.

Some of several model wide-range equations of state for copper proposed to date are given in Refs. [4-6]. We should choose that one which would offer the most adequate description of the material properties within a given range of temperatures and densities and, at the same time, approach asymptotically the known solid-state equations (for the limiting case of high densities and low temperatures) and plasma equations (for the limiting case of high temperatures and low densities). Let us explain the last statement. The total pressure in a material is the sum of the electron pressure, P_e , the ion and neutral pressure, P_0 , and the elastic pressure, P_{el} , and the energy per unit volume is the sum of the electron energy, E_e , the ion and neutral energy, E_0 , the elastic energy, E_{el} and the ionization energy, E_i :

$$P(\rho, T) = P_e + P_0 + P_{el} ;$$

$$E(\rho, T) = E_e + E_0 + E_{el} + E_i ;$$

The expressions for $P(\rho, T)$ and $E(\rho, T)$ are such that the following limits should hold:

Plasma:	$E_e = 1.5kT_e n_e,$	$E_0 = 1.5kT_0 n_s,$	$E_{el} = 0,$	$E_i = \sum_{j=1}^L \left(\sum_{k=j}^L n_k \right) I_j$
$(n \rightarrow 0, T \rightarrow \infty)$	$P_e = n_e k T_e,$	$P_0 = n_s k T_0,$	$P_{el} = 0,$	$Z \rightarrow Z_s.$
Solid State:	$E_e = (0.6\epsilon_m + \pi^2 k^2 T_e^2 / (4\epsilon_m)) n_e,$	$E_0 = 3kT_0 n_s,$	$E_{el} = -E_{subl},$	$E_i = 0,$
$(n \rightarrow 10^{23}, T \rightarrow 0)$	$P_e = 0.667 E_e,$	$P_0 = \gamma E_0,$	$P_{el} = 0,$	$Z \rightarrow 1.$

ϵ_m is the maximum energy of the degenerated electron gas in a crystal [7], $n_s = \sum_0^L n_i$, L is the nuclear charge, I_j is the j ionization potential, Z_s is Saha's ionization degree, γ is the Gruneisen factor. The ion charge j must be a multiple of the unit charge. From this table it can be inferred that when calculating the ionization equilibrium it is necessary to take into account the decrease in ionization potential with an increase in material density, since for a crystal we have $E_i = 0$, but $Z = 1$, so $I_1 = 0$ [8]. It should be noted that the ionization degree Z will be changed rather substantially at near critical densities (2.4 g/cm³), because copper may be considered to be a metal in the region $\rho > \rho_c$, while at $\rho < \rho_c$ it is a dielectric. In choosing interpolation relationships, we will assume that $Z(\rho_c, T_c) = 0.5$.

As shown above, very important processes occurring in the cathode spot of a vacuum arc are Joule heating, heat exchange between the electron and ion subsystems, and electron heat conductance. Therefore, it is of great importance to find interpolation relationships for the electron-ion time, τ , through which the electrical conductivity and the heat conductivity are expressed:

$$\sigma = n_e e^2 \tau_{\sigma ei} / m_e \quad \chi = n_e k^2 T_e \tau_{\chi ei} / m_e$$

Let us now consider the asymptotic limits for the electron-ion relaxation time in the plasma and solid-state cases.

Plasma limit ($n \rightarrow 0, T \rightarrow \infty$)

$$\tau_{\sigma ei} = 0.75 \sqrt{m_e} (kT_e)^{1.5} / (\sqrt{2\pi} (e^2 e_i^2 n_i \Lambda))$$

$$\frac{\tau_{\chi ei}}{\tau_{\sigma ei}} = \frac{2.5}{1.3 + 0.565 e^2 n_e / (n_i e_i^2)} \quad [9],$$

Solid State limit ($n \rightarrow 10^{23}, T \rightarrow 0$)

$$\frac{\chi}{\sigma T_e} = \frac{k^2 \pi^2}{3e^2} \quad \text{the Wiedemann - Franz law}$$

$$\frac{\tau_{\chi ei}}{\tau_{\sigma ei}} = \frac{\pi^2}{3}$$

The conductivity of copper under normal conditions (room temperature) is known. So we may check whether the interpolation relations for $\tau_{\sigma ei}$ provide in this case a realistic result. Using the equations given in Refs. 4 - 6, 8 and entering in them, if necessary, our own correction factors, we have obtained interpolation expressions for pressure, internal energy, ionization degree, and electron-ion relaxation time, which meet all above requirements. These expressions are as follows:

$$\begin{aligned}
P_e &= 0.667 n_e E_e, & P_0 &= \frac{\gamma + a/3}{1 + a/2} E_0 n_e, & P_a &= 0.00195 n_e^3 - 0.0376 n_e^{7/3} \\
E_e &= 0.457 \varepsilon_m Z \ln \left\{ 3.728 ch \left(\frac{3.27 T_e}{\varepsilon_m Z} \right) \right\}, & E_0 &= \frac{2+a}{1+a} 1.5 T_0, & E_a &= 2.12 \{ 2(n_e/85)^2 - 3(n_e/85)^{4/3} \} \\
E_i &= \sum_{j=1}^L \left\{ \sum_{k=j}^L n_k \right\} I_j / n_e, & I_j &= I_{0j} \left[1 - \ln \{ 1 + \exp(4.55 - 6.37 I_{0j}^{1/2} / n_e^{1/3}) \} \right] \\
Z &= \sum_{j=1}^L j n_j / n_e, \quad \varepsilon_m = 0.364 n_e^{2/3}, & a &= 673.46 \frac{T_0}{n_e^{1.479}}, & \gamma &= 1.917 \quad (\text{for Cu}), \\
n_j &= 6 T_e^{1.5} (n_{j-1} / n_e) A_j' \exp(-I_{0j} / T_e), & A_j' &= 1 + (10 n_e / T_e^{1.5}) \exp(I_j / T_e \{ 1 - (I_j / I_{0j})^4 \} - T_e)
\end{aligned}$$

Here I_{0j} is the ionization potential for the j multiple ions in a rarefied plasma, the energy E is given on a per-particle basis, n is expressed in 10^{21} cm^{-3} , P in 1.602 kbars, T and E in eV. The electron-ion relaxation time that determines the electrical conductivity and thermal conductivity are written (in the CGSE units) as follows:

$$\tau_{ei} = A^{\sigma, \chi} \frac{\sqrt{m_e} k^{1.5} (1.5 T_e + \varepsilon_m)}{Z^2 n_e e^4 \Lambda S(0)} \left\{ 1 - \frac{B^{\sigma, \chi} T_e}{T_e + \varepsilon_m} \right\}^{-1}$$

Here Λ is Coulomb's logarithm, k is Boltzmann's constant, the structure factor $S(0) = (1 + T_m / (0.027 T_0))^{-1}$, T_m is the melting temperature for copper; the numerical factors are as follows:
 $A^\sigma = 0.65$, $B^\sigma = -3.0$, $A^\chi = 1.74$, $B^\chi = -9.64$.

3. ACKNOWLEDGMENTS

This work is partially supported by the Russian Fundamental Research Foundation, Project 93-02-17349.

4. REFERENCES

1. E.A. Litvinov, G.A. Mesyats, A.G. Parfyonov, N.B. Volkov, "An explosive emission model of the vacuum arc cathode spot", in *Proc. XIII ISDEIV*, pp. 158-160, Paris, 1988.
2. E.A. Litvinov, A.G. Parfyonov, D.L. Shmelev, "Potential distribution across the plasma of a vacuum arc", in *Proc. XIV ISDEIV*, pp. 266-268, Santa-Fe, 1990.
3. E.A. Litvinov, A.G. Parfyonov, D.L. Shmelev, "Nonstationary model of the cathode and near-cathode processes in a vacuum arc", in *Proc. XIII ISDEIV*, pp. 356-360, Darmstadt-1992.
4. S.N. Kolgatin, A.V. Chatchatur'ants, "Interpolation metal equations of state," *Tepl. Vys. Temp. (Russia)*, Vol. 20, 3, pp. 447-451, 1982.
5. I.M. Bespalov, A.J. Polishuk, "Thermophysical properties of a plasma in a wide range of densities and temperatures," *Pis'ma v JTF (in Russia)*, Vol. 15, 2, pp. 4-8, 1989.
6. A.G. Parfyonov, "Nonstationary model of the cathode and near-cathode processes in a vacuum arc," Doctor's thesis, Russia, Ekaterinburg, 1992.
7. V.G. Levitch, *Course of Theoretical Physics*, Vol. 1, Nauka, Moscow, 1969.
8. A.G. Polishuk, "Thermo- and transport- properties of electrons in dense matter," Doctor's thesis, Russia, Moscow, 1991.
9. V.P. Silin, *Introduction to Kinetic Theory of Gases*, Nauka, Moscow, 1971.

INVESTIGATION OF STRIKING CHARACTERISTICS OF A PULSED LOW-PRESSURE DISCHARGE IN MAGNETIC FIELD

N.V.Gavrilov, S.P.Nikulin

Institute of Electrophysics,
34, Komsomolskaya st., 620219, Ekaterinburg, Russia.

INTRODUCTION

Hollow-cathode glow discharge, which operates at gas pressures as low as those corresponding to a vacuum regime with $\lambda \geq d$, where λ is the free path length of electron, d is the size of a cavity, is used in electron and ion beam sources with plasma emitter.¹ However, a significant difference in value between igniting and operating discharge voltages motivates the use of special systems for discharge ignition. Such systems, operating under increased pressures as compared to the pressure in the hollow cathode or using a high voltage ignition pulses, complicate source design and its electric power supplies.

To decrease gas pressure and keep out a need for gas bleeding into a discharge gap a hollow-cathode system in magnetic field has been developed which don't require an ignition system to be used.² Moreover, such a systems, based on a glow discharge in magnetic field, may be used as initiating ones to ignite an arc with a cathode spot.³ However, the mechanism of pulsed breakdown in long (1-10 cm) interelectrode gaps in weak electric (0.1-1 kV/cm) and magnetic ($B = 1-10$ mT) fields at low pressures is still not clearly understood and this plagues the optimization of discharge system design and power supply. A necessity to ensure a reproducible ignition conditions, stable beam generation and increase in the limiting rate of pulse repetition determines the importance of investigating the discharge ignition characteristics in specific electrode systems of charged-particle-beams gas-discharge-plasma sources, operating in a pulse-repetitive mode.

Here we report a series of experiments aimed at studying the dependencies of delay time τ and threshold voltage U_t of hollow-cathode glow discharge ignition in magnetic field on magnetic induction B , gas pressure p and pulse repetition rate f .

EXPERIMENTAL SETUP AND RESULTS

A schematic drawing of the plasma electron source² electrode system used in experiments is shown in Fig.1. 3-mm dia, 50-mm length tungsten rod anode 1 was set co-axially with a cylindric hollow cathode 2 with covered ends. The diameter and the length of the cathode made of stainless steel were 56 mm. Magnetic field was created by solenoid 3. Argon was used as a working gas. Gas pressure was controlled by varying of gas flow into a vacuum

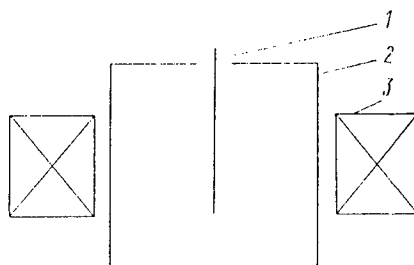


Figure 1: Electrode scheme. 1 - anode, 2 - cathode, 3 - solenoid

chamber. The discharge electrode system was connected with vacuum chamber via a hole 12-mm in dia, placed in the

centre of a cathode end. The gas pressure was measured in the vacuum chamber. It was assumed that the pressure in the cavity was close to that in the chamber, at least, during the pauses between the discharge current pulses.

The discharge was ignited by a pulse power supply with a peak voltage U_a up to 1400 V, pulse duration of up to 300 μ s and a pulse repetition rate controlled in the range from 10 to 250 Hz. The resistor limited the peak current in a range of up 0.1 to 2 A. Risettime of voltage pulse was about 1 μ s.

The breakdown delay time, measured at experiments, includes the first stage, during which the primary electron emerges in the gap, and the second one, corresponding to a discharge formation.⁴ Under experimental conditions of low pressures and weak magnetic field the value of τ was mainly determined by space charge formation phase. Statistical spread in values of τ was negligible.

The plots of $\tau(B)$ for various gas pressures and peak pulse voltages are shown in the Fig.2. The value of τ increases when p and U_a are decreased. The minimal value of magnetic induction B_0 , allowing a discharge initiation,

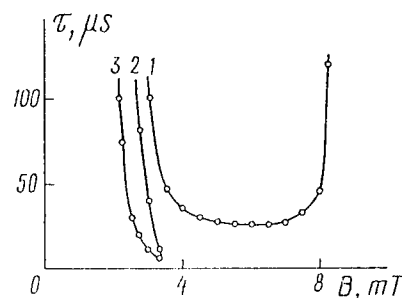


Figure 2: Delay time vs. magnetic induction. p (Pa) : 1 - 0.12; 2,3 - 0.28. U (kV) : 1,3 - 1.4; 2 - 1.1.

is also increases when p and U_a are decreased. The delay time has maximum value near B_0 and abruptly decreases with increasing B . However, further behavior of τ with increasing B depends on a gas pressure. The delay time decreases practically to zero and transition to high-current glow discharge takes place at a leading edge of voltage pulse at higher pressure, but at low one τ decreases to about 25 μ s, then the delay increases, and finally, when $B \gg 8$ mT, discharge ignition didn't occur.

The plots of threshold voltage, below which discharge ignition is impossible, as a function of B for various pressures are shown in Fig.3. The qualitative changes in curve behavior take place with p variation. At high pressures

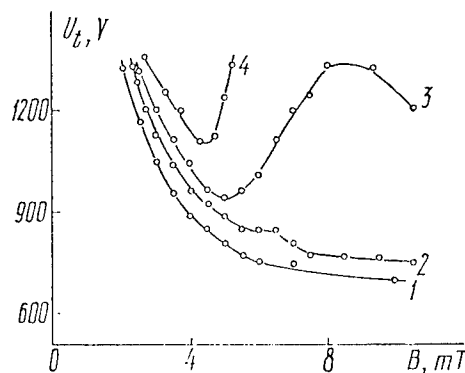


Figure 3: Threshold voltage vs. magnetic induction. p (Pa) : 1 - 0.25; 2 - 0.2; 3 - 0.15; 4 - 0.1.

U_t continuously decreases while B is increased. At lower pressure the function $U_t(B)$ becomes nonmonotonic and, at lowest pressures, the magnetic field range, in which discharge ignition is possible, has not only lower but also upper bound. However, despite on nonmonotonic character of function $U_t(B)$, the decreasing of pressure uniquely causes increase in U_t at given B .

At lower values of B the difference between igniting and operating discharge voltages and also their ratio increase. The values of operating discharge voltage U_d , shown at the Fig.4., were measured at a discharge current

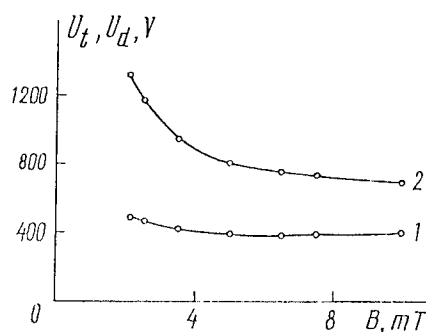


Figure 4: Operation (1) and ignition (2) voltages vs. magnetic induction at $p = 0.25$ Pa.

$I_d = 1$ A, but, it should be note, that variations of I_d have no significant effect on U_d , because discharge volt-ampere characteristic is close to horizontal one.

Under pulsed exciting of discharge in such systems, which are characterized by combination of low pressure, large surface of electrodes and high ion current density, gas sorbed on electrodes may essentially influence the processes of discharge initiation and sustaining. In measurements of dependencies $\tau(B)$ it was observed the change of curves behavior with value of current passing through the discharge gap after initiation. If at low I_d increase in f causes decrease in τ , then at high I_d dependency $\tau(f)$ becomes rising (Fig.5). Growing of τ with increase

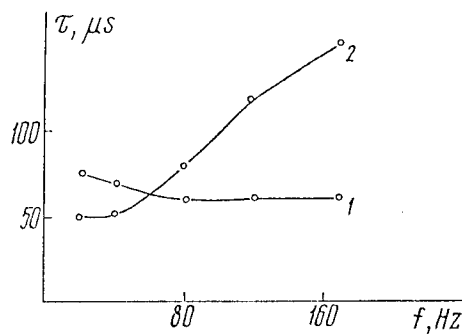


Figure 5: Delay time vs. pulse repetition rate at $B = 2.75$ mT, $p = 0.2$ Pa, I (A) : 1 - 0.15; 2 - 1.8.

in f is determined by decrease in number of gas molecules, adsorbed on cathode surface during pauses between pulses as a result of both pause shortening and surface heating. Correspondingly, intensity of desorption processes, occurring during breakdown and causing increase of pressure and acceleration of discharge development, decreases.

Essential affecting of f on the threshold voltage U_t was not observed. It may be explained by weak influence of desorption on initial stage of breakdown. At first, electron multiplication is governed by ionization of gas molecules, which are in the discharge gap, and only with essential increasing the number of ions, bombarding cathode surface,

the growth of desorption give rise to gas pressure. It should be noted, that in further experiments, in which discharge current and pulse duration were increased by the order of magnitude, an increase of U_i and U_d was observed with magnification of f . This is connected with gas heating in the cathode cavity and decreasing of neutrals concentration in it though the pressure in the vacuum chamber was kept constant.

CONCLUSIONS

1. At low gas pressures the stage of space charge accumulation in discharge gap makes the main contribution in delay time τ of hollow-cathode glow discharge ignition in weak magnetic field. Statistical spread in values of τ is negligible.

2. Delay time decreases with increasing pressure and applied voltage. Behavior of delay time and ignition voltage dependencies on magnetic induction changes with the pressure qualitatively. At low pressure these dependencies are nonmonotonic.

3. The change of delay time with pulse frequency is an evident of essential influence of sorption processes at cathode surface on discharge development.

4. The difference between voltages of discharge ignition and operation increases with magnetic induction B decreasing. At low B for reliable ignition it is necessary to apply voltage which is 2-3 times higher, then operating voltage.

REFERENCES

1. V. G. Grechanii, F. S. Metel, "Hollow cathode glow discharge in vacuum conditions of the cathode cavity", *T. V. T.*, vol. 22, N 3, pp. 444 - 448, 1984.
2. N. V. Gavrilov, M. A. Zavjalov, S. P. Nikulin, F. V. Ponomarev, "Isobaric gas regime of powerful electron source, based on discharge in magnetic field", *Pis'ma Zh. T. F.*, N 21, pp. 57 - 60, 1993.
3. "Charged-particle Beam Sources with a Plasma Emitter", edited by P. M. Tshanin, p. 44, Nauka, Ekaterinburg, 1993.
4. Yu. D. Korolev, G. A. Mesyats, "Physics of Pulse Breakdown in Gases", p. 9, Nauka, Moscow, 1991.

Vacuum arc plasma beam motion in curved magnetic fields

E. Gidalevich, S. Goldsmith, R. Boxman,

Electrical Discharge and Plasma Laboratory, Tel Aviv University, P.O.B. 39040, Tel Aviv 69978, ISRAEL

ABSTRACT

A theoretical model is presented for transport of vacuum arc generated metal vapor plasma through a magnetized quarter-torus duct used for filtering out macroparticles in order to deposit high quality thin films. The model utilizes a two fluid approximation which takes into account collisions among the plasma particles. It is found that centrifugal forces must lead to a charge separation generated field, that determines plasma drift in the centrifugal force direction to the duct wall and give rise to ion loss.

Another cause for plasma loss is the plasma pressure gradient. The plasma output flux is an increasing function of the magnetic field strength. The plasma flux in the output plane is asymmetrically skewed to favor the outside half. A further asymmetry in the flux distribution in the direction of the toroidal axis of symmetry is introduced if ions of different charge states are present in the plasma.

1. INTRODUCTION

High quality thin film production from a vacuum arc vapor source requires the removal of molten droplets, or macroparticles, produced as a by-product by the cathode spots. This is typically accomplished by passing the plasma extracted from the vacuum arc through a curved duct, often in the form of a quarter torus, which has a curved magnetic field parallel to the duct walls [1]. Plasma transport in curved magnetic field has been studied using the one-particle approximation [2,3] and a Monte-Carlo method [4]. There are some works where charged particles behavior was investigated on the basis of the plasma-optic approximation [5].

The basic assumption of the plasma-optic model is that the ion time of flight is much less than the ion Larmor precession period, and hence that the magnetic field has negligible direct effect on the ion motion. In this model the electrons are collimated magnetically, and the ions are trapped by the negative space charge remaining in the plasma column after a few of the ions escape, which sets up a retarding electrostatic field.

In some devices of interest, the system parameters include an electron density of 10^{18} - 10^{22} m⁻³, ion temperatures of a few eV, lengths on the order of 1 m, and magnetic field strengths of 0.02 T [6,7]. Under these conditions the ion time of flight approaches the ion Larmor radius, the magnetic field has a direct influence on the ion motion, and collisions may play an important role as an ion loss mechanism.

The objective of the present paper is to analyse the plasma transport in a magnetized torus under the above conditions. Towards this goal a two-fluid model consisting of interacting electrons and ions will be presented and analyzed.

2. EQUATIONS OF MOTION

Consider the electron and ion motion equations (neutrals are neglected):

$$\begin{aligned} (v_e \nabla) v_e + \frac{kT}{m_e} \nabla \ln n_e + \frac{e}{m_e} E + \omega_e [v_e h] + \sum_k v_{ek} (v_e - v_k) &= 0 \\ (v_k \nabla) v_k + \frac{kT}{m_i} \nabla \ln n_k - \frac{Z_k e}{m_i} E - Z_k \omega_i [v_k h] + \frac{m_e}{m_i} v_{ke} (v_k - v_e) &= 0, \end{aligned} \quad (1)$$

where v_e and v_k are the electron and k -times ionized ion velocities respectively, Z_k represents a charge number ($Z_k=1,2,3$), ω_e and ω_i are the gyrofrequencies of the electrons and singly charged ions respectively, h is a unit vector coinciding with the magnetic field direction, n_e and n_k are the electron and k -ion concentrations respectively, $v_{ke} = 2(\frac{kT}{m_e})^{0.5} \sigma_{eI} Z_k^2 n_e$ is the frequency of k -ion-electron collisions and $v_{ek} = 2(\frac{kT}{m_e})^{0.5} \sigma_{eI} Z_k^2 n_k$ is the frequency of electron - k -ion collisions, σ_{eI} is an effective cross-section of electron - singly ionized ion collisions.

The first term is nonlinear with respect to velocity and describes the centrifugal acceleration, which does not depend on the mass and charge of the plasma particles. Therefore if longitudinal velocities of electrons and ions are equal to each other and have significantly larger value than other velocity components, then $(v_k \nabla) v_k$ is equal to $(v_e \nabla) v_e$. Multiplying first equation by n_e and second by n_k , and summing over the index " k ", an expression for the electrical current density is obtained:

$$j = \frac{e}{\omega_e} \left[\frac{m_i}{m_e} \sum n_k h \times (v \nabla) v + \frac{kT}{m_e} h \times \nabla (\sum n_k + n_e) \right] \quad (2)$$

Hence, there are two forces driving the electric current: the centrifugal force and the pressure gradient. Kirchoff's law demands that $\nabla \cdot j = 0$. Making use of vector identities, the following equation is obtained:

$$\frac{\omega_e}{e} \nabla j = - \frac{m_i}{m_e} \sum n_k h \nabla \times (v \nabla) v + \frac{m_i}{m_e} (v \nabla) v \nabla \sum n_k - \frac{kT}{m_e} h \nabla \times \nabla (\sum n_k + n_e) \quad (3)$$

Since $\nabla \times (\nabla \Phi) = 0$, where Φ is any scalar, it appears that the first term in expression (2) does not satisfy Kirchoff law and therefore is depressed by a polarization field produced by charge accumulation at the edges of the plasma. Thus one can calculate the polarization field and then use the electric current resulting from the gradient of pressure. Making use of the electron motion equation in order to obtain an electric field, the following equations are eluded:

$$\lambda_0 E^* = j_I + \frac{\omega_e}{\sum v_{ek}} [jh] - \left[\frac{kT}{m_e} \nabla \ln n_e + (v \nabla) v \right] \frac{en_e}{\sum v_{ek}}, \quad (3)$$

where λ_0 is plasma conductivity in the absence of magnetic field, and

$$j_I = \frac{e}{\omega_e} \frac{m_i}{m_e} \sum n_k h \times (v \nabla) v, \quad (4)$$

The expression for electrical field of polarization and the current

$$j = \frac{e}{\omega_e} \frac{kT}{m_e} h \times \nabla (\sum n_k + n_e) \quad (5)$$

are substitute into the second equation of (1) and taking into account that $n_e = \sum n_k Z_k$ and $v_{ke} \ll \omega_e$ in any real case, an expression for the k -ion velocity is obtained:

$$v_k = \left(\frac{1}{Z_k} - \frac{\sum n_k}{n_e} \right) \frac{m_i}{m_e} \frac{1}{\omega_e} h \times (v \nabla) v + \frac{m_i}{m_e} \frac{\sum n_k}{n_e} \frac{1}{\omega_e} \frac{\sum v_{ek}}{\omega_e} (v \nabla) v - \frac{v_{ke}}{\omega_e n_e} \frac{kT}{m_e} \nabla (\sum n_k + n_e) \frac{1}{\omega_e} \frac{1}{Z_k} + \frac{1}{Z_k} \frac{kT}{m_e} \frac{1}{\omega_e} h \times \nabla \ln n_k \quad (6)$$

It convenient to use a toroidal coordinate system [9] since one of the coordinate surfaces can be set to coincide with the walls of the torus. In this case, where longitudinal component of velocity has a value much larger then the other components, it is possible to deduce the following approximation:

$$\begin{aligned} [(v \nabla) v]_\sigma &= - \frac{\sin \sigma}{a} v_\phi^2 \\ [(v \nabla) v]_\tau &= \frac{1 - \cosh \tau \cos \sigma}{a \sinh \tau} v_\phi^2 \end{aligned} \quad (7)$$

where σ, τ, ϕ are the space coordinates in the toroidal coordinate system (for detailed description see [9]), a is a system parameter which is slightly less than the major radius of the torus, v_ϕ is the longitudinal component of the plasma velocity, which is assumed to be identical for all plasma components and constant within the inner part of the torus. Hence, the k -ion velocity components are:

$$\begin{aligned} v_k^\sigma &= \frac{1 - \cosh \tau \cos \sigma}{\sinh \tau} \alpha g_2 \left(\frac{1}{Z_k} - \frac{\sum n_k}{n_e} \right) - \alpha g_1 \frac{\sum n_k \sum n_k Z_k^2}{n_e n_0} \sin \sigma - \\ &- Z_k \frac{g_1}{n_0} (\cosh \tau - \cos \sigma) \frac{\partial}{\partial \sigma} (\sum n_k + n_e) - \frac{1}{Z_k} g_2 (\cosh \tau - \cos \sigma) \frac{\partial \ln n_k}{\partial \tau}. \\ v_k^\tau &= \sin \sigma \alpha g_2 \left(\frac{1}{Z_k} - \frac{\sum n_k}{n_e} \right) + \alpha g_1 \frac{\sum n_k \sum n_k Z_k^2}{n_e n_0} \frac{1 - \cosh \tau \cos \sigma}{\sinh \tau} - \\ &- Z_k \frac{g_1}{n_0} (\cosh \tau - \cos \sigma) \frac{\partial}{\partial \tau} (\sum n_k + n_e) + \frac{1}{Z_k} g_2 (\cosh \tau - \cos \sigma) \frac{\partial \ln n_k}{\partial \sigma}. \end{aligned} \quad (8)$$

where $g_1 = \frac{2 \left(\frac{kT}{m_e} \right)^{1.5} \sigma_e I n_0}{a \omega_e^2}$ and $g_2 = \frac{kT}{a \omega_e}$. Here g_1 and g_2 are diffusion tensor components when $\omega_e^2 \gg v_{ek}^2$, n_0 is the initial total ion concentration, and $\alpha = \frac{m_i v_\phi^2}{kT}$.

Using the continuity equation for the k -ions

$$\begin{aligned} \frac{\partial \ln n_k}{\partial \phi} &= - \frac{\sinh \tau}{v_\phi} \left[v_\sigma \frac{\partial \ln n_k}{\partial \sigma} + v_\tau \frac{\partial \ln n_k}{\partial \tau} + \frac{\partial v_\sigma}{\partial \sigma} + \frac{\partial v_\tau}{\partial \tau} - \right. \\ &\quad \left. - 2v_\sigma \frac{\sin \sigma}{\cosh \tau - \cos \sigma} + v_\tau \frac{1 - \cosh \tau \cos \sigma - \sinh^2 \tau}{\sinh \tau (\cosh \tau - \cos \sigma)} \right] \end{aligned} \quad (9)$$

and the formulae for velocity components (8), an equation is obtained describing the spatial distribution of the ions at any cross-section within the torus.

3. CALCULATED RESULTS

Analysis of the last factor in the first term of equations (8) shows that the ion charge distribution has a significant effect on the ion spatial distribution. If all the ions have the same charge, a case which we will call homogeneously charged plasma, the first term in equations (8) disappears. On the other hand, this term is non-zero in the non-homogeneous case. The first term is the only term which produces a motion in the direction normal to both the centrifugal acceleration and to the longitudinal velocity component. Thus in the homogeneous case, the plasma motion is symmetrical with respect to a plane bisecting the torus and containing a unit vector in the ϕ -direction (which we shall term the horizontal plane), while in the non-homogeneous case the plasma will be displaced above or below this plane.

The above equations were solved numerically for conditions approximating the toroidal filter used in Tel-Aviv University. The minor and major radii are 8 cm and 20 cm respectively. The following properties of plasma were assumed for simplicity: $T_i = T_e = 10^4$ K, $v_\phi = 10^4$ m/s, initial density n being 10^{12} cm $^{-3}$. It is assumed that

each ion striking the toroidal wall is removed from the plasma. Results for the homogeneously charged plasma are presented in the Figures 1-3. Anywhere density normalization relatively initial plasma density is used. Plasma flow in the magnetic and electrical (polarization) fields, directed perpendicular to each other, appeared to be symmetrical in respect to horizontal plane of the torus and considerably asymmetrical in respect to its vertical plane in the exit cross-section of torus. The dependence of the flux on the magnetic field is shown in the Fig. 2. A non-homogeneous ion charge distribution characteristic of a Cu-vapor plasma consists of approximately 16% of Cu^+ , 64% of Cu^{2+} , and 20% of Cu^{3+} [10] is considered in Figs. 4-6. Ions. Asymmetry with respect to the vertical plane of the torus was calculated to occur mainly for Cu^+ (Fig. 4) and to a much smaller extent for Cu^{2+} ions (Fig. 5). As may be seen in Fig. 6, the partial and integral flux increases with magnetic field strength.

4. CONCLUSIONS

The above analysis shows that the plasma flux exiting a toroidal filter increases with magnetic field strength, while this dependence cannot be obtained from the one-particle approximation. The exiting plasma spatial distribution is asymmetric in the vertical direction, as obtained in previous analysis. Furthermore, the present analysis shows that the distribution may be asymmetric in the horizontal direction if ions of several degrees of ionization are present simultaneously. The above calculations may be utilized for designing and optimizing the performance of toroidal macroparticle filters for vacuum arc deposition, as well as an aid in the proper positioning of deposition substrates.

REFERENCES

1. I. I. Aksenov, V. G. Padalka, V. T. Tolok and V. M. Khoroshikh, *Sov. J. Plasma Phys.* **4**, 425, 1978.
2. I. I. Aksenov, V. G. Padalka, N. S. Repalov and V. M. Khoroshikh, *Sov. Plasma Phys.* **6**, 173, 1980.
3. I. I. Aksenov, V. A. Belous, V. G. Padalka and V. M. Khoroshikh, *Sov. Plasma Phys.* **6**, 504, 1980.
4. D. M. Sanders, D. B. Boercker and S. Falabella, *IEEE Trans. Plasma Science* **18**, 883, 1990.
5. D. S. Harned, *Phys. Fluids*, **26**, 1320, 1983.
6. R. L. Boxman and S. Goldsmith, *IEEE Trans. Plasma Sci.*, PS-17, 705, 1989.
7. R. L. Boxman and S. Goldsmith, *Surface and Coating Technology*, **33**, 153, 1987.
8. L. Spitzer, Jr., *Physics of Fully Ionized Gases*, New-York - London, 1962
9. G. Korn, T. Korn, *Mathematical Handbook for Scientists and Engineers*, Mc Graw-Hill, New-York, 1961.
10. I. G. Brown, X. Godechot, *IEEE Trans. Plasma Science*, **19**, 713, 1991.

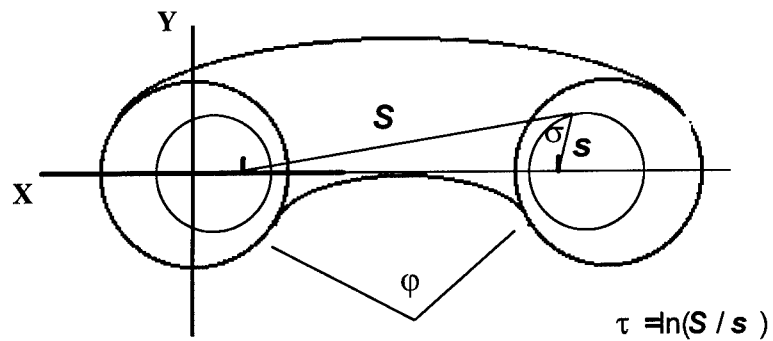


Fig1. Torroidal macroparticle filter, illustrating coordinates (x,y) at output plane, and torroidal coordinates used in model..

ϕ - azimuthal angle ,

σ - angle between straight lines, S and s connecting point with two poles of system.

τ - logarithm of the ratio of the lengths S and s (see formula in draught).

Take into account that torroidal coordinate surfaces are not concentric, but co-poleness.

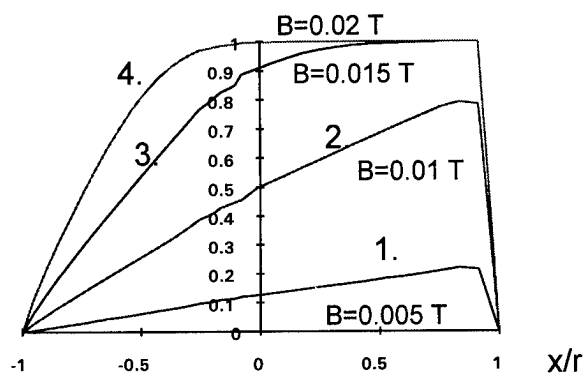


Fig. 2. Normalized uniform charged ion density distribution at the exit plane of the torus. 1 - 0.005 T, 2 - 0.01 T, 3 - 0.015 T, 4 - 0.02 T.

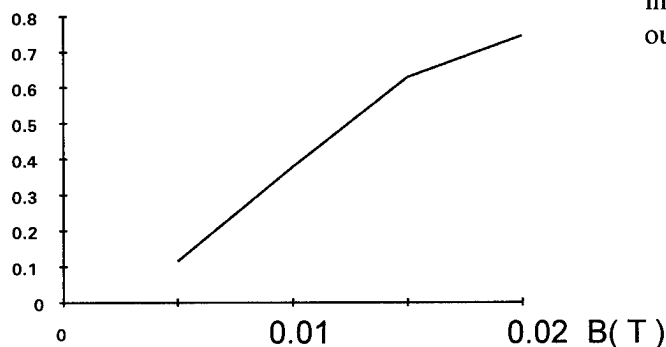


Fig. 3. Normalized ion flux dependence from the magnetic field strength for the homogeneously charged plasma.

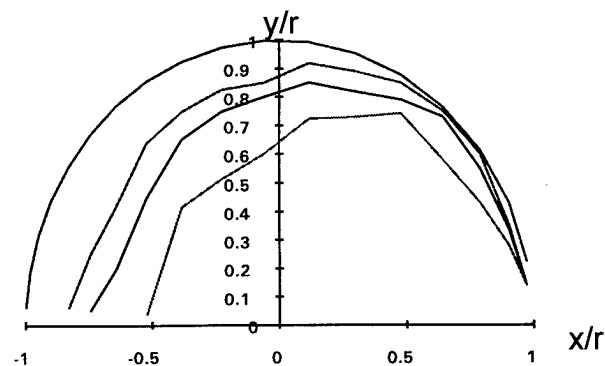


Fig. 4. Normalized isodensities (0.8, 0.6, 0.4) at the toroidal exit. $B=0.02$ T. (Outward line - toroidal wall).

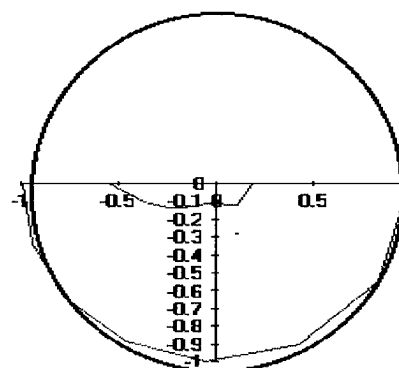


Fig. 5. Normalized 0.5 isodensity line for Cu^+ in a simulated Cu vacuum arc plasma at torus output plane. $B=0.01$ T.

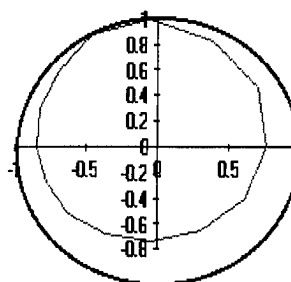


Fig. 6. Normalized 0.5 isodensity line for Cu^{3+} ions in a simulated Cu vacuum arc plasma at torus output plane. $B=0.015$ T.

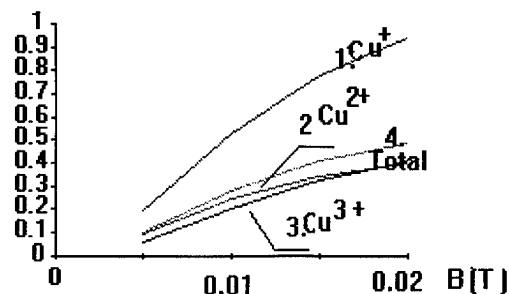


Fig. 7. Normalized ion flux at torus output plane, 1 - Cu^+ , 2 - Cu^{2+} , 3 - Cu^{3+} , 4 - total flux.

Approaches to two-dimensional models of expanding vacuum arc plasmas

Erhard Hantzsche

Max-Planck-Institut für Plasmaphysik, Bereich Berlin

ABSTRACT

Multifluid equations describing the plasma of vacuum arcs expanding anisotropically from a cathode spot are given and discussed. Some first and preliminary results from an approximate analytical integration of such a system of equations are presented. Though the dependence of the plasma parameters on the direction is weak, the inclusion of angular terms and angular equations changes some results significantly, compared with the experiences from usual one-dimensional models.

1. INTRODUCTION

By intensive evaporation and ionization, partly also by explosive processes, each cathode spot of a vacuum arc generates a small plasma ball of very high density which rapidly expands towards the anode and the walls. The properties of such plasmas are investigated intensively for many years, e.g.^{1,2}. In long-duration arcs with constant current - sufficient are lifetimes $\tau > \max(t_r, t_i)$, (with the averaged residence time constant of an arc spot t_r = crater excavation time, and the free flight time of ions t_i to the most distant walls) - this expanding plasma is in a quasi-stationary state, though superimposed by rapid fluctuations. As can be shown by the solution of a system of multifluid equations describing the components of this plasma (e.g.³⁻⁴) the acceleration of the plasma is caused by three forces: the electric field, the pressure gradient, and the electron-ion friction. The expansion is neither adiabatic nor isothermal. Approximately, the motion of ions and electrons can be formulated analytically.

This theoretical plasma model was strictly one-dimensional, presupposing a purely radial and isotropic expansion (though the confinement to a jet with a solid angle $\omega < 2\pi$ can easily be supplemented). Indeed, the expansion of a geometrically undisturbed spot plasma without magnetic fields seems to be almost isotropic - at least beyond a minimum distance $r = r_{\min}$ » a (spot radius), where the form and structure of the spot surface loses its influence on the expanding plasma. However, a certain angular (ϑ)-dependence (fig. 1) could be observed even at $r > r_{\min}$ (e.g.^{5,6}) which can be described to be somewhere between an isotropic and a cosine distribution. Such a weak anisotropy is plausible for at least three reasons: 1) The preferential current flow towards the anode, 2) the Lorentz force caused by the self-magnetic field of the arc current, 3) the contact of the plasma with the cathode surface outside of the spot, which acts as a plasma sink.

2. EQUATIONS

For these reasons, a two-dimensional (or even three-dimensional) extension of the arc plasma model is desirable in order to consider this angular dependence in a suitable form. Such a model has been developed and shall be outlined.

We use the following variables and designations: Index $k = e, i, (n)$ relating to electrons or ions (or neutrals), respectively, n density, $\rho = nm$ mass density, p pressure, T temperature, Ze charge, $\rho_{el}^* = Ze\rho/m$ space charge density, j current density = $e(Zn_i v_i - n_e v_e)$, R friction force ($\sim (v_e - v_i)$), R_T thermal force ($\sim \nabla T$), Q friction energy flow, Q_T temperature equalization term ($\sim (T_e - T_i)$), $\underline{\sigma}$ stress tensor, q heat flux density (heat conduction $\sim \nabla T$, and convection $\sim (v_e - v_i)$), $n\epsilon_{th}$ thermal energy density ($\epsilon_{th} = 3/2 kT$), E^* electric field strength, B^* magnetic field strength (induction), $\mu = m_e/m_i$.

We apply a spherical coordinate system r, ϑ, φ (fig. 1, but see below) and assume symmetry around the discharge axis, i.e. independence of the azimuthal angle φ . Moreover, we consider only time-independent (or time-averaged) conditions and only one kind of ions, with an averaged charge Z , and the B^* -field is assumed to be generated by the arc current only. As before, inelastic collisions are completely neglected.

With these preconditions we get the following system of plasma fluid equations:

1) equations of continuity

$$\nabla (\rho_k v_k) = 0 \quad (1)$$

2) momentum equations

$$\rho_k (v_k \cdot \nabla) v_k = \rho_{eL,k}^* E^* - \nabla p_k \pm R_{ei} \pm R_{ei,T} + \nabla \cdot \underline{\sigma}_k' + (j_k \times B^*) \quad (2)$$

3) equations of the energy flux

$$\nabla [\rho_k v_k \left(\frac{v_k^2}{2} + \frac{\epsilon_{th,k}}{m_k} + \frac{p_k}{\rho_k} \right) - (v_k \cdot \underline{\sigma}_k') + q_k] = (j_k E_*) \pm Q_{ei} \pm Q_{T,ei} \quad (3)$$

Compared with the equations of former model variants³⁻⁴, in addition to the dependence on the second coordinate, the Lorentz force and the stress tensor have been included. If several kinds of ions or neutrals are considered, further collision terms have to be added. Written explicitly, the system (1) - (3) becomes very voluminous and cannot be given here. The \pm terms change their sign between $k = e$ or i , respectively.

3. SOLUTION

Since a general solution of (1) - (3) seems to be hopeless, probably further simplifications may be unavoidable. In spite of the high complexity of the equations, in principle approximate solutions in an analytical form must be derivable, using asymptotic semi-convergent series, similar to the one-dimensional case, but much more extended and not so easy to handle. Moreover, there arise some new problems (see below) which are not sufficiently settled up till now. In this way a general solution can be derived only step by step. The evaluation is still in a very early state.

We start again with an expansion approach of the kind

$$X = \sum_{n=0}^{n_{\max}} \alpha_n^{(X)} r^{-\beta_n} f_n^{(X)}(\cos \vartheta) \quad (4)$$

where X is symbolizing all plasma parameters ($X := \{n_e, n_i(z), T_e, T_i(z), v_{e,r}, v_i(z), r, v_{e,\vartheta}, v_i(z), \vartheta, E_r^*, E_\vartheta^*\}$ a.s.o.), while the coefficients $\alpha_n = \text{const}$. The functions f_n have to be chosen in a suited way to represent the angular dependences.

An extremely simple (and therefore possibly questionable) first step towards a solution is achievable with the help of the following presuppositions and assumptions:

- 1) We consider one kind of ions only (index i , averaged charge Ze), and no neutrals.
- 2) The functions $f(\vartheta)$ in (4) are used in this form: $\{X, X_r\} = \{X_0(r), X_{r0}(r)\} [\beta^{(X)} + (1 - \beta^{(X)}) \cos \vartheta]$, and $X_\vartheta = X_{\vartheta0}(r) \sin \vartheta$, where $X := \{n_e, n_i, T_e, T_i\}$, and the vector components $X_r := \{v_{e,r}, v_{i,r}, E_r^*\}$, $X_\vartheta := \{v_{e,\vartheta}, v_{i,\vartheta}, E_\vartheta^*\}$, with $\beta^{(X)} = \text{const}$.
- 3) We assume the applicability of the relation $X_{\vartheta0} = (r_0^{(X)}/r)^{\xi(X)} X_{r0}$, with $r_0^{(X)} = \text{const}$, $\xi(X) = \text{const}$.
- 4) We assume that β , r_0 , and ξ are independent of the corresponding variable X .
- 5) The series (4) are used only up to terms of the first order.
- 6) We consider the equations only near to the axis, i.e. where $\vartheta \ll \pi/2$.
- 7) The contributions of heat conduction, heat convection and the stress tensor are neglected.
- 8) "Renormalization" of the largest terms in the series expansion (from internal friction and Lorentz force) by their mutual compensation.
- 9) Quasineutrality of the plasma (i.e. $n_i = n_e/Z$).
- 10) All terms $\sim \mu$ or $\sim \mu^{1/2}$ are neglected ($\mu = \text{mass ratio } m_e/m_i$).

- 11) The T_i -dependence of $R_{ei,T}$ and the collisional heat transport caused by this term are omitted.
- 12) The Coulomb logarithm in the plasma conductivity is taken constant.

If we apply the boundary conditions of Cu arc spots, with $Z=1.8$, $\delta = v_{i,r}/v_{e,r} = 0.08$, and with spot currents of about $I_s \approx 50$ A (or about 25 ... 100 A), the following results can be derived:

$$kT_{e,0} \approx \frac{T_{e0}^*}{r^{2/5}} \left(1 + O\left(\frac{1}{r^{2/5}}\right) \right) \quad (5a)$$

$$(T_{e0}^*)^{5/2} = \frac{5eI_s(1-\delta)}{(7+2c_0)c_2\sigma_0} \approx 6.79 I_s^{2/5} \quad (5b)$$

(where r is used in the unit μm , $c_0 \approx 0.71$, c_2 = effective solid angle $< 2\pi$, and the electrical conductivity $\sigma = \sigma_0/T_e^{3/2}$, with $\sigma_0 = \text{const}$). Moreover,

$$v_{e,r0} \approx v_{e0}^* \left(1 - 0.0892 \frac{T_{e0}^*}{r^{2/5}} + O\left(\frac{1}{r^{4/5}}\right) \right) \quad (5c)$$

where $v_{e0}^* = \text{const}$ is given by the asymptotic mean kinetic ion energy $E_{i\infty} = m_i (\delta v_{e0}^*)^2/2$, and, therefore, by the arc energy balance. Finally, we get $T_{i0}^* \approx 0.578 T_{e0}^*$, and $r_0^{2/5} \approx -0.00186 T_{e0}^*$, while the plasma density is given by

$$n_{e,0} \approx \frac{N_{e0}^*}{r^2} \left(1 + 0.0985 \frac{T_{e0}^*}{r^{2/5}} + O\left(\frac{1}{r^{4/5}}\right) \right) \quad (5d)$$

with $N_{e0}^* = I_s/c_2 e(1-\delta)v_{e0}^*$. The electric field strength is $E_{r0}^* \approx e\eta_1/r^{7/5}$, and $e\eta_1 \approx 0.8536 T_{e0}^*$. Some of the results (kinetic energy of ions, electron temperature) are shown in fig. 2, where the angular dependence is indicated too.

4. DISCUSSION

Thus, as before in the one-dimensional models, integrals of the multifluid plasma equations can be found in an analytical form with asymptotic semi-convergent series, which, however, are much more complex than in one-dimensional approaches. They cannot be given here explicitly. Up till now the derived solution is a very much simplified one, and the evaluation of this solution is in a preliminary and incomplete state only. Some further consequences are:

1. Both T_e and T_i are higher than in the one-dimensional model, and the asymptotic ratio $T_i/T_e \approx 0.58$ is considerably increased compared with the one-dimensional results.
2. Consistent results call for a reduction of the asymptotic ion energy (e.g. $E_{i\infty} \approx 80$ eV) and of the effective solid angle of the expansion ($c_2 \approx 0.6$) in comparison with the one-dimensional case.
3. Plausible values of the new constants are $\xi = 2/5$, $\beta = 5/3$ (from renormalization).
4. The asymptotic contributions of the single forces to $E_{i\infty}$ are: + 26.9 % by the electric field, +24.3 % by the pressure gradient (composed of 20.2 % density gradient, and 4.1 % temperature gradient), +57.7 % by the electron-ion friction, - 8.9 % by the thermal force (friction terms together 48.8 %).

All numerical results presuppose that r is taken in the unit μm . The limitations in the range of r where the solution may be used remain essentially unchanged compared with one-dimensional models. Since we have restricted the solution to small ϑ , the effects of plasma-surface interaction near $\vartheta \approx \pi/2$ are excluded (an extrapolation to such angles is possible, but not realistic).

Altogether, the main results can be summarized by these statements:

1. If compared with the outcomes of one-dimensional models^{3,4} the principal r -dependence of all plasma parameters (which is given by functions of $(l_0/r)^{2/5}$) remains unchanged.
2. Generally, the ϑ -components of all vectors are much smaller than the r -components (e.g. $|v_\vartheta| \ll |v_r|$, $|E_\vartheta^*| \ll |E_r^*|$), and the ϑ -dependence of plasma scalars and r -components is weak ($\sim \vartheta^2$).
3. In spite of that, there are (partly) significant quantitative changes in the results (due to changes of the series coefficients) caused by ϑ -dependent terms and, especially, by the momentum equations in ϑ -direction which have to be fulfilled simultaneously. In this way further conditions and restrictions are imposed on the solution, e.g. by an interconnection between otherwise independent boundary conditions.
4. All these results must be considered as very preliminary ones, a) because of too many simplifying presuppositions, b) because of too few free parameters used in this approach, which is not enough flexible up till now for a good adaptability to the ϑ -dependent equations, and there remains some ambiguity in the solutions. However, the discussed solution represents a first step towards a consistent theoretical description of the non-isotropic plasma flow in the whole acceleration zone. Further improvements by dropping the most important simplifications (and partly shortcomings) are necessary and planned.

Another possibility to consider the two-dimensional problem is the introduction of an ellipsoidal coordinate system which is better suited than the spherical system. Especially, the transition zone from the dense plasma layer in front of the spot surface to the almost freely expanding plasma at greater distances can be treated as a one-dimensional problem in a much better approximation with the help of such ellipsoidal coordinates than with spherical ones. Some first results from this model are already derived.

REFERENCES

1. W.D.Davis, H.C.Miller, "Analysis of the products emitted by dc arcs in a vacuum ambient"; J. Appl. Phys. Vol. 40, pp. 2212-2221, 1969
2. V.M.Lunev, V.G.Padalka, V.M.Khoroshikh, "Plasma properties of a metal vacuum arc", Sov. Phys. Tech. Phys. Vol. 22, pp. 858-861, 1977 (Zh. Tekh. Fiz. Vol. 47, pp. 1491-1495)
3. E.Hantzsch, "Theory of the expanding plasma of vacuum arcs", J. Phys. D, Vol. 24, pp. 1339-1353, 1991
4. E.Hantzsch, "A hydrodynamic model of vacuum arc plasmas", IEEE Trans. Plasma Sci., Vol. 20, pp. 34-41, 1992
5. J.E.Daalder, P.G.E.Wielders, "Angular distribution of charged and neutral species in vacuum arcs", Proc. 12th ICPIG Eindhoven, p. 232, 1975
6. J.Kutzner, "Angular distribution of ion current in dc copper vacuum arc", Proc. 8th ISDEIV Albuquerque, pp. A1,1-15, 1978

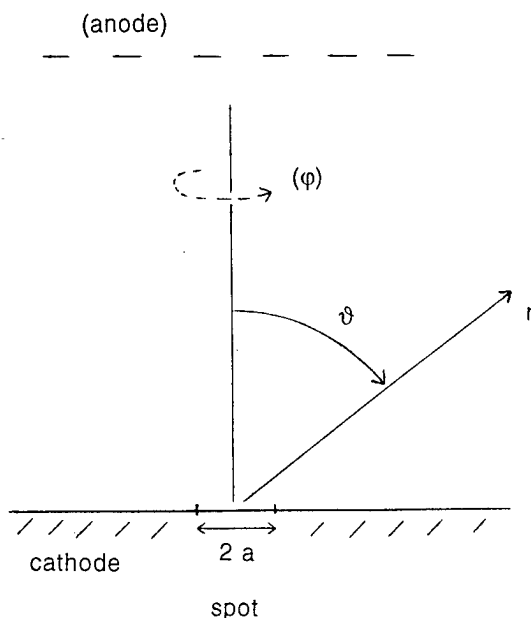


Fig. 1: Schematic view of the used spherical coordinate system

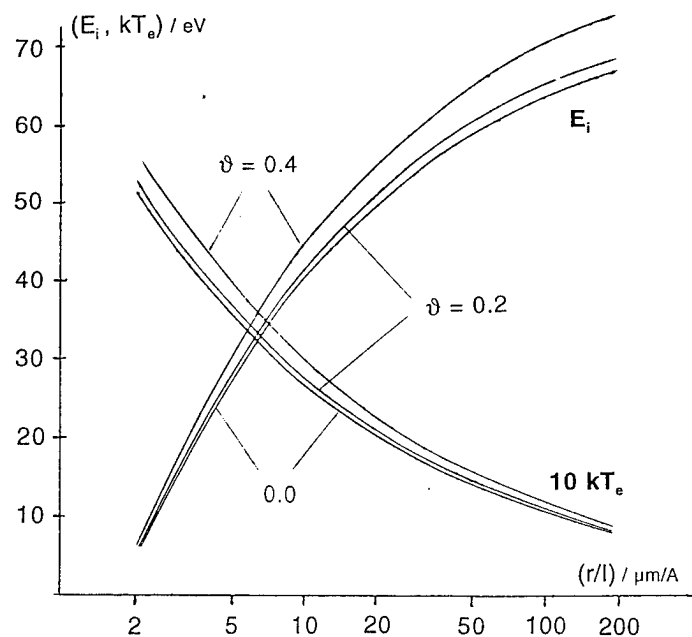


Fig. 2: Averaged kinetic ion energy E_i and electron temperature T_e in Cu arc plasmas as a function of distance r from the spot center (with $l=l_0$), and dependence on angle ϑ near the axis ($\vartheta=0$)

On the appearance of vacuum arc cathode spots imaged by the emitted light

E. Hantzsche and B. Jüttner

Max-Planck-Institute for Plasma Physics, Research Group "Electrode Processes"
Hausvogteiplatz 5/7, D-10117 Berlin, Germany

ABSTRACT

The present paper discusses the appearance of arc cathode spots observed in emission. Photographs yield a size of about 100 μm when using line radiation, whereas imaging by absorption techniques¹ or emission pictures with continuum radiation² result in values of about 10 μm , comparable to the crater traces left at the surface. Besides the size, the slope of the spot profiles is considered. Experimentally, it is found that the light intensity decreases with the distance r from the spot center proportional to r^{-2} . This slope is much less than the expected dependence proportional to $r^{-\beta}$, $\beta > 4$, i.e. the observed spot edge is much less sharp than expected. The behavior of the radiation is theoretically studied by modelling the radial dependence of particle densities and temperature. It is shown that the line radiation stems from a region which is greatly influenced by the plasma expansion in competition with the finite transition probability of excited levels. It is concluded that emission pictures of cathode spots yield considerably higher spot diameters than corresponding to the spot core.

1. INTRODUCTION

The current conduction at the arc cathode is associated with hot mobile surface spots where cathodic material is evaporated and ionised, thus forming a dense ball of vapor plasma. The size of the active spot is important for evaluating decisive parameters. In spite of this, the results in the literature are contradictory since many years. Emission pictures of vacuum arc plasmas are known to yield diameters of 100-200 μm . However, absorption pictures of short duration vacuum arc spots yielded a radius $\leq 10 \mu\text{m}$ ¹. Also, craters left at the surface after the arc have small radii $< 10 \mu\text{m}$, for dc-arcs as well as for nanosecond arcs. On the other hand, it seems natural to take the visible appearance of a spot as its real size. Thus, there is an obvious contradiction that must be explained.

As schematically shown in Figure 1, we distinguish 3 light emitting spot zones: The inner **Zone 1** at $r < 10 \mu\text{m}$ represents the dense core. With a density $> 10^{26} \text{ m}^{-3}$, ref.¹, it will be highly collisional. From the ion charge distribution measured outside the spot, an electron temperature $\geq 5 \text{ eV}$ is deduced³. In this region, the plasma starts to expand with subsonic velocity. The emitted light is determined by continuum radiation due to free-free transitions. The outer **Zone 3** at $r > 20 \mu\text{m}$ consists of a collisionless plasma that expands with a supersonic velocity of $v = 10\text{-}20 \text{ km/s}$. At distances $r \geq 1 \text{ mm}$ the electron density behaves as coming from a point source with constant velocity. The electron temperature amounts to 1-2 eV. The radiation preferentially consists of lines from excited atoms and ions. In the transition **Zone 2**, the plasma is accelerated to supersonic velocity, thus the density should decrease more rapidly than with r^{-2} (because for expansion from a point source $nvr^2 = \text{const.}$). The temperature is decreasing from 5 to 1 eV. There occur all kinds of radiation (continuum & lines). The present paper discusses the consequences of the radiation from these zones for the visible spot structure.

3. EXPERIMENTAL BACKGROUND

Figure 2 shows a streak picture of 3 arc cathode spots on a Ti-cathode taken with a vacuum arc of 80 A, using mainly line radiation from Ti I at 456.263 nm and Ti II at 458.995 nm due to a metal interference filter centered at 458 nm and having a FWHM of 9 nm. The transition probabilities of these lines are $3.4 \times 10^5 \text{ s}^{-1}$ and $2.4 \times 10^6 \text{ s}^{-1}$, respectively (more details in ref.²). One finds broad structures with diameters around 100 μm and blurred edges. The decrease of brightness at these edges can be approximated⁴ by a power law $r^{-\beta}$ with $\beta \approx 2$, r being the distance to the spot center. No systematic temporal change could be found in the range 10 ns - 100 μs . However, when imaging the spots with the emitted continuum, small structures with sharp edges ($\beta \approx 4$) have been found². Figure 3 gives an example for a Ti-arc, 80 A, using an interference filter centered at 512 nm. Obviously, judging the spot size by its optical appearance is less trivial as commonly assumed.

4. THEORETICAL ANALYSIS

1) The excitation rates R_{ex} of both continuous and line radiation are $\propto n_e n$ (where $n(r)$ is the density of atoms or ions, n_e the density of electrons), resulting in $\beta \geq 4$ in the Zones 2 and 3 ($dv/dt \geq 0$). Moreover, if we apply a very simple model of the excitation cross section σ ($= 0$ for electron energies $E < E_{\text{ex}}$ (excitation threshold), or $= \sigma_{\text{ex}} = \text{const}$ for $E > E_{\text{ex}}$, respectively) and assume a Maxwellian distribution of the electron energies, we get

$$R_{\text{ex}} \approx \sqrt{\frac{8}{\pi m_e k T_e}} n_e n \sigma_{\text{ex}} (E_{\text{ex}} + k T_e) \exp \left[- \left(\frac{E_{\text{ex}}}{k T_e} \right) \right] \quad (1)$$

resulting in a further increase of β (> 4), see Figure 4, since the electron temperature T_e is slowly decreasing with r , ref⁵.

2) The spontaneous emission of line radiation is delayed with a time constant $\tau = 1/A$ (transition probability). We consider two limiting cases: a) $\tau \ll t_{\text{ex}}$ (expansion time constant $t_{\text{ex}} = n/(v|dn/dr|) \approx r/2v \approx 2 \dots 3 \text{ ns}$), i.e. immediate (local) emission resulting in $\beta \approx 4$, and b) $\tau \gg t_{\text{ex}}$ with almost constant emission probability, the excited atoms radiate according to their density n^* , i.e. $\beta \approx 2$. From the measured spectral intensities² and the known transition probabilities of Ti we derive an averaged time constant τ^* increasing from about 5 ns at $r \approx 20 \mu\text{m}$ to 10 ns at $50 \mu\text{m}$. Therefore, $\tau^*/t_{\text{ex}} \gg 1$.

3) The calculation of the combined action of collisional excitation and spontaneous radiation in Zone 2 + 3 is simplified by assuming an averaged $\tau^* = \text{const}$, $v = \text{const}$, and an effective net excitation rate coefficient $R^* = R_{\text{ex}}/n_e n = \text{const}$. In this case the number of excited atoms $N^*(r)dr$ in the hemispherical shell $2\pi r^2 dr$ (neglecting any angular dependence) is determined by

$$\frac{dN^*}{dr} = \frac{\epsilon}{r^2} - \alpha N^* \quad (2)$$

where $\epsilon = R^* N_{e1} N_1 / 2\pi v$, $N_{e1} = N_e(r_1)$, $N_1 = N(r_1)$, $\alpha = 1/\tau v$, while $r = r_1$ is the boundary of Zone 1 where the condition of a detailed balance between excitation and de-excitation is assumed to hold. If we

neglect radiation, we have an increase of excited atoms: $N^* = N_1^* + \varepsilon(1/r_1 - 1/r)$ and $\beta < 2$. If we neglect excitation, the number of excited atoms is decreasing according to $N^* = N_1^* \exp[-\alpha(r - r_1)]$, with $\beta > 2$. An approximate solution of equ. (2) applied to the conditions of our Ti-discharge results in $\beta \approx 2.0 \dots 2.5$ in the range $r \approx 20 \mu\text{m} \dots 60 \mu\text{m}$ (Figure 4).

6. DISCUSSION

The analysis shows that line radiation is inevitably influenced by time of flight-effects that enlarge the spot appearance. These effects cause a blurred spot edge with a decrease near r^{-2} , in agreement with the experiment. Imaging by absorption techniques¹ or using the emitted continuum² avoids the time of flight-effects, thus yielding the characteristic spot size with a sharp edge ($\beta \geq 4$). Emission pictures using line radiation reflect the process of plasma expansion rather than the active spot zone where electrons are emitted and atoms are evaporated. These pictures do not contradict the smaller absorption pictures and the surface craters that indicate current densities $>10^{11} \text{ A/m}^2$ and particle densities $>10^{26} \text{ m}^{-3}$.

8. ACKNOWLEDGMENTS

The present work was supported by the contract DFG Ju 227/3-2. We are indebted to Prof. W. Böttcher, Hannover, for very helpful discussions.

9. REFERENCES

1. A. Anders, S. Anders, B. Jüttner, W. Böttcher, H. Lück, and G. Schröder, "Pulsed Dye Laser Diagnostics of Vacuum Arc Cathode Spots", *IEEE Trans. Plasma Sci.*, Vol. **20**, pp. 466-472, 1992.
2. E. Hantzsche, B. Jüttner, and G. Ziegenhagen, "Why Arc Cathode Spots Appear Larger Than They Are", prepared for publication.
3. E. Hantzsche, "Consequences of Balance Equations Applied to the Diffuse Plasma of Vacuum Arcs", *IEEE Trans. Plasma Sci.*, Vol. **17**, pp. 657-660, 1989.
4. A. Anders, S. Anders, E. Hantzsche, B. Jüttner, and G. Ziegenhagen, "Optical Investigation of Arc Cathode Spots in Vacuum", *Proc. XXIth Int. Conf. Phen. Ionized Gases*, Vol. **I**, pp. 3-4, Bochum, 1993.
5. E. Hantzsche, "A Hydrodynamic Model of Vacuum Arc Plasmas", *IEEE Trans. Plasma Sci.*, Vol. **20**, pp. 34-41, 1992.

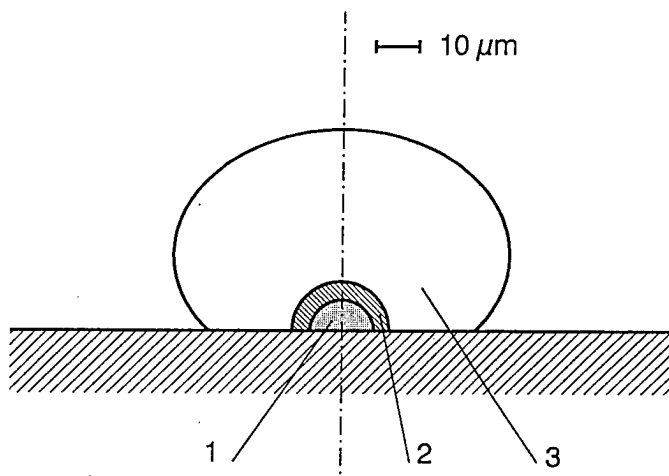


Fig. 1: Light emitting zones of cathode spots (schematically):
1 - dense core, 2 - zone of plasma acceleration,
3 - zone of plasma expansion.

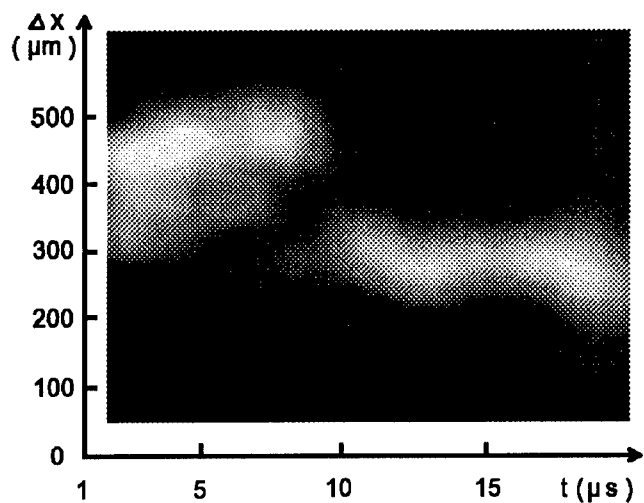


Fig. 2: Streaked emission picture for a Ti-arc viewed through an interference filter centered at $\lambda=458$ nm, $I=80$ A. Discharge duration $40 \mu\text{s}$.

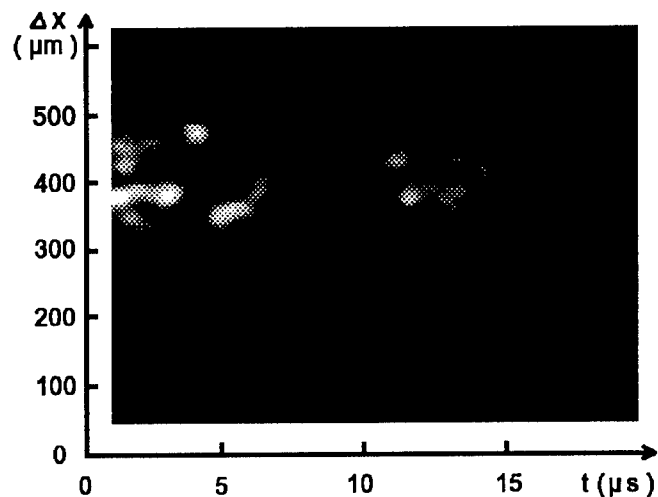


Fig. 3: Streaked emission picture from the continuum at $\lambda=512$ nm. Ti, $I=100$ A, $40 \mu\text{s}$.

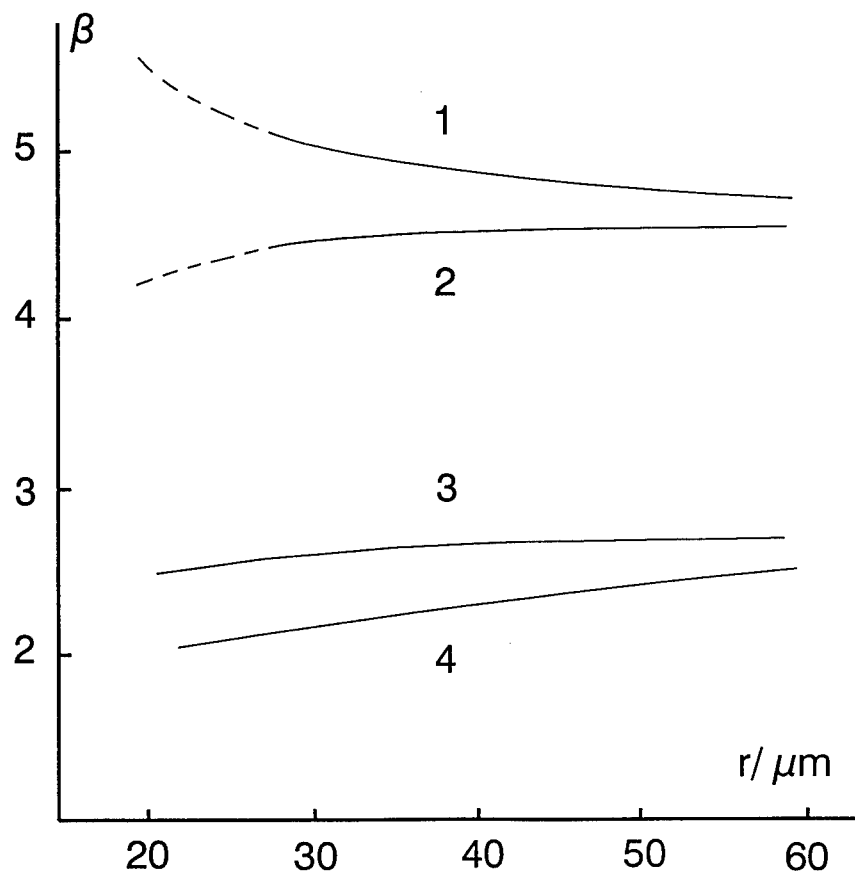


Fig. 4: Power $\beta(r)$ of the spot radiation $I_\lambda \propto r^{-\beta}$ when assuming instantaneous emission at the locus of excitation and spherical expansion (curve 1), and with a geometric correction due to flattening (curve 2); delayed emission in the expansion zone without new excitation, from the superposition of Ti lines (curve 3), and delayed radiation with additional excitation in the expansion zone (curve 4). r -distance from the spot centre. Current $I=50-100$ A.

Experimental research of high-voltage low-current vacuum arc

Ivanov R.Yu., Puzanov S.V., Yashnov Yu.M.

Scientific-Research Institute "Titan", Moscow

ABSTRACT

Voltage-current and other characteristics of the poorly explored type of discharge has been investigated and was found out to be quite different from the characteristics of other wide-known types of vacuum and gas discharges.

A high voltage ($U \sim 100-1000$ V) low current ($I \sim 10-100$ mA) vacuum arc was observed for the first time at the end of the sixties in the tests of vacuum gaps with metal electrodes in a pulsed operation with a pulse duration of an order of 100 mcsec, there being a protrusion on the cathode comparable in dimensions with the vacuum gap.¹ After 1970 until recently there were no publications on this discharge differing to a considerable extent from other well known types of gas and vacuum discharges.

The purpose of this work was a study of conditions of high voltage low current vacuum arc initiation, reading of its voltage-current characteristics (VCC) when stepping-up and down voltage, determination of dependence of arc current and voltage on the electrodes spacing and also frequency characteristics of the arc.

The tests were conducted in a chamber with oil-free vacuum on the level of 10^{-7} Torr, which was provided by an electrodisharge pump. Electrodes were out-gassed by heating to 600°C in vacuum directly in the chamber before the tests. A high voltage of selectable polarity was applied from a three-phase high voltage rectifier with a control of the output over the primary circuit of a step-up transformer. A ballast resistor from 100 to 900 kOhm was inserted for limitation an arc current between the rectifier output and vacuum gap.

In multiple tests of vacuum gaps with plane-parallel electrodes of copper, molybdenum, tungsten, stainless and electrical steel the arc was not observed ever neither in the pulsed operation nor in the continuous mode.

The arc occurred only in the tests of gaps with an impregnated tungsten thermoemission cathode (both heated and cold) as one of the electrodes. Emitting material-impregnated cathode tablet was activated directly in the test chamber.

The arc occurred after one or several gap breakdowns (point "A" in the Fig.1) appearing as a very bright point glow in the vacuum gap with a sharp step-up of the current in the gap (from dozens-hundreds mA to dozens-hundreds mA) and step-down of the voltage in the gap because of the voltage drop on the

ballast resistor (section "arc" in the Fig 1.).

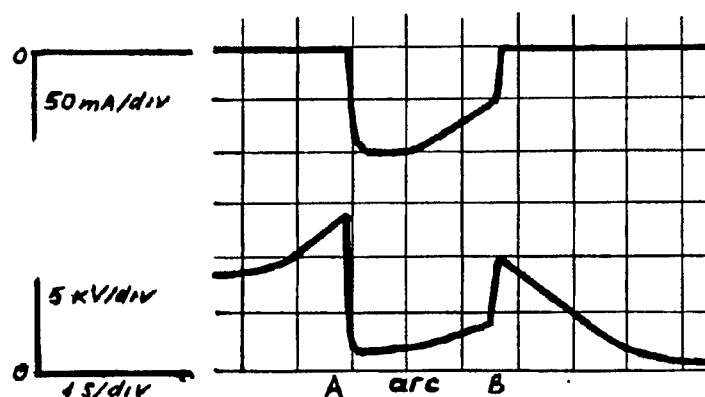


Fig.1. The initiation of the arc after breakdown (point "A") and it's going out (point "B").The arc voltage - lower curve, current - upper curve.

Typical arc current and voltage oscillograms' images with step-up and step-down of the rectifier output voltage are given in Fig.2. It is characteristic that with a step-up of the rectifier output voltage (section 1) the arc current increases, with a step-down of the output voltage (section 2) it decreases, while the arc voltage goes on the contrary.

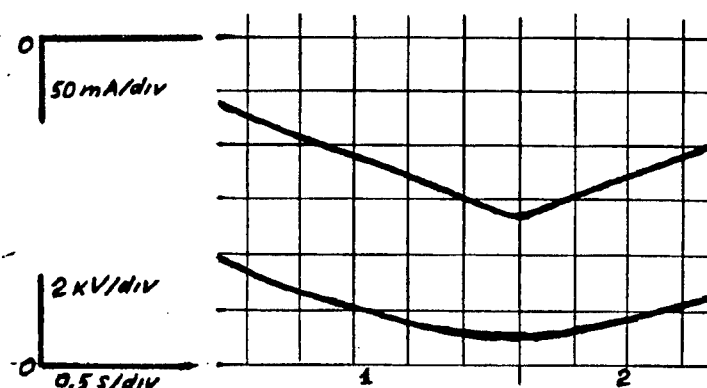


Fig.2. Conduct of the arc voltage (lower curve) and current (upper curve) with the output voltage step-up (section 1) and step-down (section 2).

The VCC of the arc had the form of hiperbola. With an error maximum 10% a discharge power along the VCC curve could be considered to be constant in the range from 90 to 140 W in the dependance on the ballast resistor, the material

of the electrode opposite to the thermocathode, an electrode spacing (from 0.2 to 0.5 mm) and high voltage polarity. The arc went out if the output voltage of the rectifier could not provide the supply of the present level of power to the gap through the ballast resistor (point "B" in the Fig 1.).

The movement apart of the electrodes with a change of electrodes spacing 2-4 times (from 0.2 to 0.8 mm) and recording of current and voltage oscillograms (images in Fig.3) was carried out to study of the spacing influence upon the arc characteristics in the gap after the arc initiation. In the oscillograms the arc current and voltage remain invariable with the spacing variation.

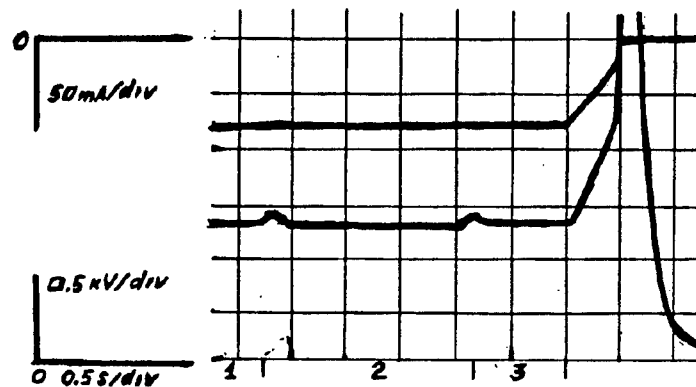


Fig.3. Conduct of the arc voltage (lower curve) and current (upper curve) with the electrodes spacing increase: 1-d=0.4mm; 2-d=0.6 mm; 3-d=0.8 mm.

The most of the energy consumed by the arcing goes for the anode heating by the electron bombardment. The latter is testified by rapid (some seconds) anode heating to the temperature of high red glow with the cathode remaining dark and cold. Therefore carriers of the arc current are basically electrons.

Besides the gap increase during the arcing electrodes were mutually moved in parallel with their plane surfaces. The arc was found out to be "tied" to the negative-potential electrode, the latter being either thermocathode tablete or metall one. The arc conjunction was observed directly in the chamber and by a melted trace of a width from the tenths fractions to 1 mm on the positive electrode surface. When the thermocathode tablet had positive potential a tapered off-projection with a crater of the thermocathode evoparization products due to the electron bombardment was observed on the opposite electrode after arcing and its extinction.

The arc might be connected to the non-uniformity on the negative potential electrode. So far as the arc ion current is much less than the electron one and there was no noticable cathode heating the electron emission from the cathode occurs most likely due to the field-emission mechanism and is

determined by the field in Langmuir layer of the near-cathode plasma (hence invariability of the arc current and voltage when moving the electrodes apart). Photoemission of electrons activated by the arc radiation is also possible.

Arc frequency characteristics were also studied by means of oscillography of the arc current and voltage by storing oscillograms with subsequent increase of sweep speed from 0.5 sec/sm to 1 mcsec/sm. No noticable (in comparison with current and voltage level) pulsation of the arc current and voltage in the frequency band up to 10 MHz were not discovered.

The tests with heated up to 800°C electrodes have not showed any differences in the arc characteristics in comparison with the tests with cold electrodes.

REFERENCES

1. B.N.Klyarfeld and A.S.Pokrovskaya-Soboleva, "Dugovoy razryad v vacuume s vysokim napryagением gorenija", Journal of Technical Physics, Vol.XL, N 1, pp.206-210, 1970.

NON-STATIONARY MACROPARTICLE CHARGING IN ARC PLASMA JET

M. KEIDAR, I. BEILIS, R.L. BOXMAN, S. GOLDSMITH
Electrical Discharge and Plasma Laboratory, Tel Aviv University
P.O.B. 39040, Tel Aviv 69978, ISRAEL

ABSTRACT.

In this work the kinetics of macroparticle charging in the rarified part of the arc plasma jet are studied. The sheath in the vicinity of the macroparticle is collisionless and the problem with different Debye length to macroparticle radius ratio is analysed. Maxwellian velocity distribution functions with different temperatures for the electrons and ions in an arbitrary ratio are allowed in the model. The influence of the plasma drift velocity on the macroparticle charging is discussed.

1. INTRODUCTION.

The erosion products of vacuum arc cathodes consist of ions, neutral vapour, and macroparticles (MP). The MP's are molten droplets or solid particles which are generated in the cathode spot region by action of the plasma pressure¹. MP's are small in size (0.1-100 μm) and have decreasing size distribution function^{2,3}. Suspended particles have been observed also in radio frequency plasmas⁴. The macroparticles become electrically charged through their interaction with the interelectrode plasma. The charged macroparticles move in the plasma and affect the flow field of the plasma. Practical applications of the vacuum arc, and modeling of the plasma flow require the understanding of the macroparticle charging processes. In the steady state the macroparticles develop a floating potential, so that the electron current is balanced by the ion current⁵. In the general case the charging time is defined by the plasma parameters and in each particular case the relation between charging time and the characteristic process time is changed. Thus in some cases the macroparticles don't have time to reach the floating potential.

The kinetics of the MP charging is determined by the ion and electron flux to the macroparticle surface, which is influenced by a potential distribution in the sheath surrounding the MP. The first detailed analysis of the probe in an electrical discharge was provided by I. Langmuir and H.M. Mott-Smith⁶. Expressions for the ion and electron flux to the probe were obtained in order to analyze the current-voltage characteristic without solving the Poisson equation in the probe vicinity. A method for solving the probe problem by analyzing all possible trajectories of the charged particles in the sheath around spherical probes immersed in low-density plasmas was developed by I. B. Bernstein and I. N. Rabinowitz⁷. The appropriate Boltzmann equation was solved, yielding the particle density and flux as functions of the electrostatic potential. J. Laframboise solved this problem in the case of Maxwellian velocity distributions and finite current collection for both ions and electrons⁸. An iterative numerical scheme was used in which an initial trial function was assumed for the charge density near the probe. A method was developed to obtain theoretical predictions of the current collected from a plasma by an electrically conducting probe having cylindrical or spherical symmetry, but results were presented only for the cylindrical case. Poisson's equation was integrated to provide the electric potential field. E.C. Whipple found the potential distribution in the sheath around a body which is emitting electrons. In the case of attracted particles (ions) the assumption was made that there were no extrema of the effective potential curves⁹. Also a second approach of a monoenergetic ion distribution was used. In all probe problems the probe potential is set, which is the boundary condition for the sheath surrounding the probe.

In the case of an isolated MP, the situation is different in that the both MP potential and plasma response time evolution is determined by the self-consistent solution of the set of equations. This problem was formulated in the planar case by J.W. Ciolla and M.B. Silevich¹⁰. The one-dimensional model for the time-dependent behaviour caused by placing an uncharged conducting surface in contact with a uniform equilibrium plasma was studied. Both the probe potential and plasma response are unknown *a priori* but are specified through a set of self-consistent model equations and boundary conditions.

In the present work the kinetics of MP charging in the interelectrode gap of the vacuum arc are studied. In order to define the mathematical model the following assumptions are made:

- (1) The plasma consists of two species of charged particles. In many experimental cases thermal equilibrium between two species is not achieved and therefore an arbitrary temperature ratio is assumed.
- (2) The plasma is so rarified that Debye length (L_D) is much smaller than the mean free path for electron-ion collisions (L_c) and thus the sheath around MP can be considered as collisionless.
- (3) The spherical case is discussed for $R_p \ll L_D$ and $R_p \approx L_D$, where R_p is the MP radius.
- (4) The plasma jet flow is not substantially obstructed by the MP's, and thus spherical symmetry of the plasma density relative to the macroparticle is assumed.
- (5) There is no magnetic field present.

2. PROBLEM FORMULATION.

The kinetics of the MP charging is controlled by the ion and electron flux to the MP which depend on the potential distribution in the sheath. The Poisson equation is solved to obtain this distribution

$$\nabla^2 U(r) = e/\epsilon_0 [N_e(r) - N_i(r)] \quad (1)$$

where $N_e(r)$ and $N_i(r)$ are the electron and ion densities, respectively, e is the electron charge; and ϵ_0 is the permittivity of vacuum. This equation is solved in the region $[R_p; R_\infty]$, where R_p is the MP radius, R_∞ is the external boundary of the sheath where the following conditions are fulfilled:

$$(R_\infty) = 0; \quad \partial U(R_\infty)/\partial r = 0; \quad (2)$$

The magnitude of the electric field $E(r)$ changes with time according to the relation:

$$\epsilon_0 \partial E(r)/\partial t = -[J_i(r) - J_e(r)] \quad (3)$$

where $J_e(r)$ is the electron current density; and $J_i(r)$ is the ion current density; The time derivative of the electric field is a function of the radius r . The simple estimation seems that the characteristic time of the electric field changes is smaller with radius and the maximum time we have at the macroparticle. Then equation (3) was solved only at the radius R_p . In order to solve the system of equations (1) and (3), the electron and ion density and flux must be obtained.

3. ELECTRON and ION DENSITY and FLUX.

In our assumption framework both species are described by a Maxwell-Boltzman distribution function of the constants of motion, namely the total energy (E) and the angular momentum (L)¹¹. The radial flux of a carrier is governed by the effective potential energy $U_{eff}(r) = L^2/2mr^2 + qU(r)$, where q, m are the particle charge and mass, respectively, $L = mv_\theta r$ is the angular momentum relative to the center of force, v_θ is the tangential projection of particle velocity vector, r is the distance from center of force, and $U(r)$ is the local potential. A charged particle with total energy E and angular momentum L has a nonzero radial velocity projection at the radius r if next condition is fulfilled:

$$E \geq U_{eff} \quad (4)$$

The density and flux are moments of the distribution function in the range of L and E which is fulfilled by condition (4). At the initial time the more mobile electrons charge the macroparticle negatively. Therefore let us discuss electrons as are retarded and ions are attracted particles. In case of electrons $qU(r) > 0$ and the electrons are repelled by the effective potential. Integration of the distribution function yields an expression for electron density as function of local potential¹²

$$N_e(z) = N_0/2 \{ \exp(-\varphi) [1 + \operatorname{erf}[(\varphi_p -)^{1/2}] + (1-z^2)^{1/2} \exp\{z^2(\varphi_p - \varphi)/(1-z^2)\} (1 - \operatorname{erf}\{(\varphi_p - \varphi)/(1-z^2)\}^{1/2})] \}; \quad (5)$$

where $\varphi = q_e U(r)/kT_e$, $z = R_p/r$; and erf is the error function; N_0 is the electron density in the bulk of plasma; T_e is the electron temperature; k is the Boltzman constant; and we use the subscript p to indicate all parameters at the MP surface. The electron flux current density flowing to the spherical body, obtained from the analysis of $U_{eff}(r)$ is given by¹²:

$$J_e = J_{e0} \exp(-\varphi_p) \quad (6)$$

where J_{e0} is the electron flux in the absence of a field;

In the case of attracting particles (ions) the potential energy $qU(r) < 0$ and therefore U_{eff} consists of two terms with different signs. The resulting sign of U_{eff} depends on the magnitude of L . In general we have a family of $U_{eff}(r)$ curves which correspond to different values of L (fig. 1). Let L_a be the value of L at which $U_{eff} < 0$ for all r and L_{cr} is the value of L at which U_{eff} has no extremum and for all r $U_{eff} > 0$. For an arbitrary L in the interval $L_a < L < L_{cr}$ U_{eff} has extremums. Let us discuss situation for the ion with an angular momentum L in this range. At the radius r the total energy of ion must satisfy the condition:

$$E \geq U_{eff}(r_{max}) \quad (7)$$

where r_{max} is the radius at which function U_{eff} has maximum. Let us discuss the general case of the potential distribution and in place of condition (7) we use at some radius $r < r_{max}$ the condition:

$$E \geq U_{eff}(r) \quad (8)$$

This means that the probability of an ion passing by the MP without colliding with it does not depend on the potential distribution, but rather only on the local potential. The model potential in this case has some plateau a-a' is presented in fig. 1.

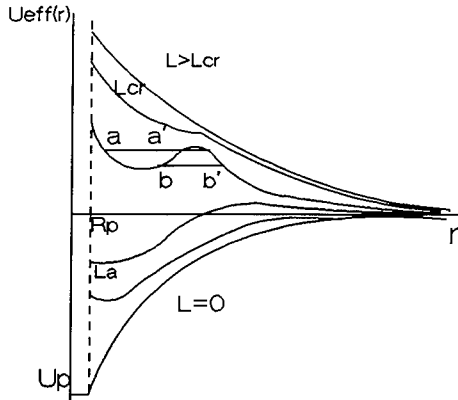


Fig.1. Effective potential curves for ion.

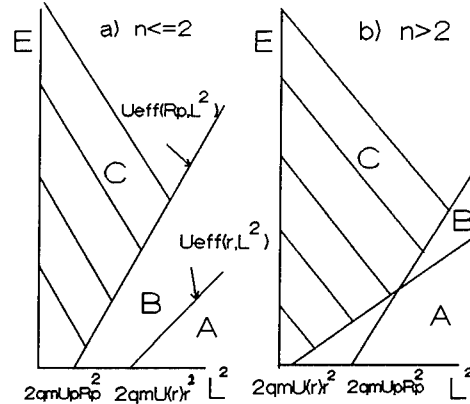


Fig.2. Relation between ion energy and angular momentum

Then in the $E-L^2$ plane we have only two types of ion trajectories which correspond to the two potential distributions $U(r) \approx 1/r^n$ with $n \geq 2$ and $n < 2$ (fig. 2), where region C correspond to the ions captured by the MP and region B to the ions penetrate to a radius r but are unable to reach the MP. The same two types of trajectories was discussed by Whipple⁹. In this model framework we can obtain analytical expressions for the ion density versus local potential:

$$N_i(z) = N_0 \left\{ (-\phi/\pi\beta)^{0.5} + 0.5 \exp(-\phi/\beta) (1 - \text{erf}(-\phi/\beta)^{1/2}) + ((z^2\phi_p - \phi)/\beta\pi)^{1/2} + 0.5(1-z^2)^{1/2} \exp[(\phi - z^2\phi_p)/\beta(z^2-1)] (1 - \text{erf}((\phi - z^2\phi_p)/\beta(z^2-1))^{1/2}) \right\} \quad (n < 2)$$

$$N_i(z) = N_0 \left\{ (-\phi/\pi\beta)^{0.5} + 0.5 \exp(-\phi/\beta) (1 - \text{erf}(-\phi/\beta)^{1/2}) + 0.5(1-z^2)^{1/2} \exp[(\phi - z^2\phi_p)/\beta(z^2-1)] \right\} \quad (n \geq 2) \quad (9)$$

In order to determine the ion flux let us discuss the two different situations presented in figure 2. In case (a) the corresponding integral of the distribution function has form:

$$J_i = J_{i0} (1 - \phi_p/\beta) \quad (10)$$

where J_{i0} is the ion flux in the absence of a field, $\beta = T_i/T_e$; This expression was first obtained by Langmuir⁶. In case (b) the situation is more difficult. If the electric potential in the vicinity of the MP decreases more rapidly then $1/r^2$, then we have the case illustrated in the fig.3. The region D in the $E-L^2$ plane appears. This region is defined by lines $U_{\text{eff}}(r)$, where r is changed from R_p up to R_∞ . If we know this region than we can define ion flux in his case. Let us determine the equation of the curve which limit this region.

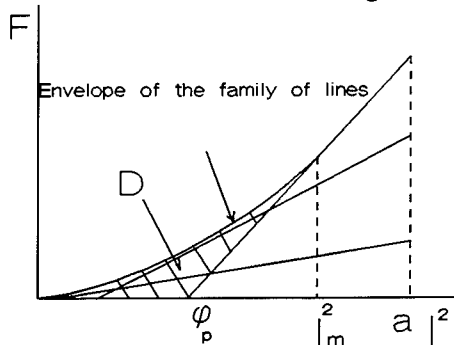


Fig.3. Definition ion flux to the MP in the case $n > 2$

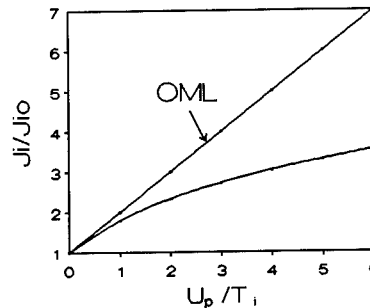


Fig.4. Ion current density vs MP potential

The problem is to find the envelope of a family of a lines. In the case of a line with constant length a which moves with its ends on two perpendicular lines, this curve is a hypocycloid of four cusps¹³. The equation of this curve in the XY plane is:

$$X^{2/3} + Y^{2/3} = a^{2/3} \quad (11)$$

In the $F - l^2$ plane we have that in our case the functional relation between F and l^2 has form

$$F^{2/3} + (l^2 - a)^{2/3} = a^{2/3} \quad (12)$$

Here we use dimensionless variables $F = E/kT_e$; $l^2 = L^2/[M_i R_p^2 k T_e]$ and $x = r/R_p$ and the constant a is the length of lines $a = (2 + 2^{0.5})\phi_p$. By substitution $F = \phi_{eff} = \phi_p + l^2$ the upper limit l^2_{max} of the region D is obtained from equation (12). The solution of this equation $l^2_{max} \approx 2.207 \phi_p$

By integration of the distribution function in the $F - l^2$ plane an analytic expression for the ion current density is obtained:

$$J_i = J_{i0} \left\{ \exp[(\phi_p - l^2_{max})/\beta] + \int_0^{l^2_{max}} \exp[-(a^{2/3} - (a-x)^{2/3})^{3/2}] dx \right\} \quad (13)$$

Fig. 4 shows the influence of the potential distribution on the ion current density. The upper curve corresponds to the Orbital Motion Limit (OML) ion density with $n \leq 2$ (Eq. 10) and the lower curve if defined by equation (13).

4. RESULTS.

4.1. Small Macroparticles ($R_0 = R_p/L_D \ll 1$)

The potential distribution in the vicinity of small MP's ($R_0 = R_p/L_D \ll 1$) in the moments of non-dimensional time $\tau = 1, 10, 20$ ($\tau = t/(L_D/V_{th})$), where V_{th} is the ion thermal velocity, is shown in figure 5. In the particular case $R_0 = 0.01$; $\beta = 0.5$; $M_i = 47.9$ (Titanium) the stationary distribution is settled during $\tau = 10$. Initially the charging process is controlled by electrons ($J_e \gg J_i$) but the charging time is limited by the ion time scale. For comparison a distribution with slope $1/r^2$ is shown in the figure 5. The index $n=2$ divides between two types of ion trajectories (fig. 2a, 2b).

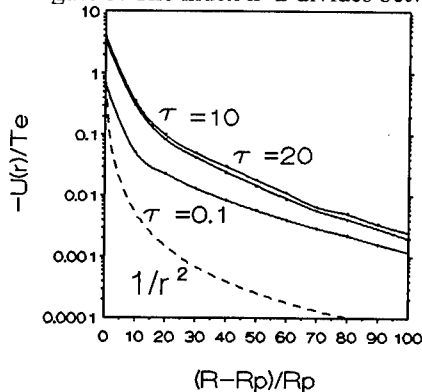


Fig.5. The potential distribution as a function of position $R_p/L_D = 0.01$; $T_i/T_e = 0.5$; $M_i = 47.9$

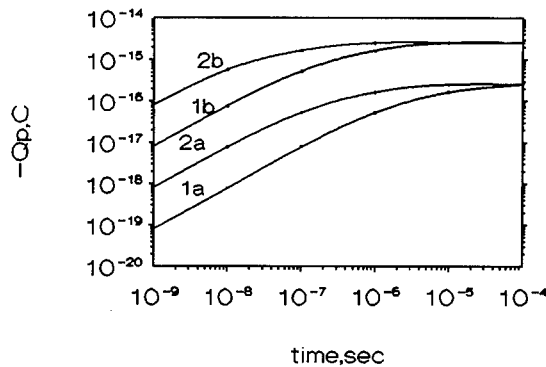


Fig.6. The evolution of the MP charge $1 - N_e = 10^{16} \text{ m}^{-3}$; $2 - N_e = 10^{17} \text{ m}^{-3}$; $a - R_p = 0.1 \mu\text{m}$; $b - R_p = 1 \mu\text{m}$

Fig.6 shows the time evolution of the MP charge in the case of a titanium plasma with $T_e = 6 \text{ eV}$; $\beta = 0.5$ and for electron densities $N_e = 10^{16} - 10^{17} \text{ m}^{-3}$ and for MP radii $0.1 - 1 \mu\text{m}$. The maximum charging time is 10^{-5} sec , and occurs if $N_e = 10^{16} \text{ m}^{-3}$ and $R_p = 0.1 \mu\text{m}$. The charge which accumulated on the macroparticle depends on the electron temperature. In the case of $T_e = 6 \text{ eV}$; $\beta = 0.5$; $R_p = 0.1 \mu\text{m}$ the charge is $2 \times 10^{-16} \text{ C}$ or is about 1250 electron charges. The dependence of the MP charge from parameter β with $T_e = \text{const}$ is shown in figure 7. This function has an extremum in our framework at $\beta = 3$. This happens because with large T_i the ion flux isn't influenced by the MP potential and is controlled only by J_{i0} and therefore the steady state charge is smaller. In the case of $R_0 \ll 1$ the potential distribution decrease with increase of r slower than $1/r^2$. This means that the electron and ion fluxes aren't influenced by potential distribution and controlled only by the MP potential.

4.2. Large Macroparticles ($R_0 \approx 1$)

In the large macroparticle case ($R_0 = 1$) we also assume that all types of ion trajectories are possible. But in this case the potential distribution differs from that in the previous case (Fig. 8). In the case $R_0 = 1$ the potential decreases with increasing r more rapidly than $1/r^2$. The ion flux is smaller than OML and is defined by equation 13.

The stationary potential distribution is formed during a time $\tau=0.5$. In this case the steady state MP potential is larger than previously, because the ion flux is smaller. In this case the steady state electrical field at the macroparticle surface is larger than in case a and the MP charge is larger than in the previous case.

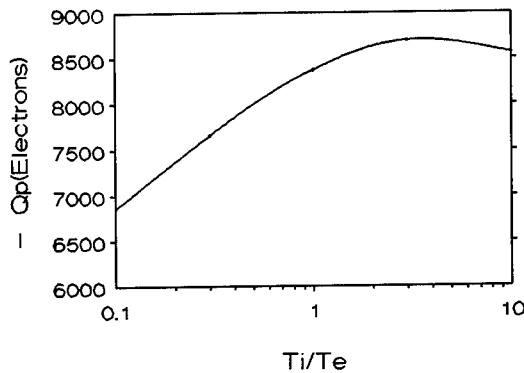


Fig. 7. MP charge vs T_i/T_e ($R_0 \ll 1$ model); $T_e=3$ eV; $R_p=1$ μm

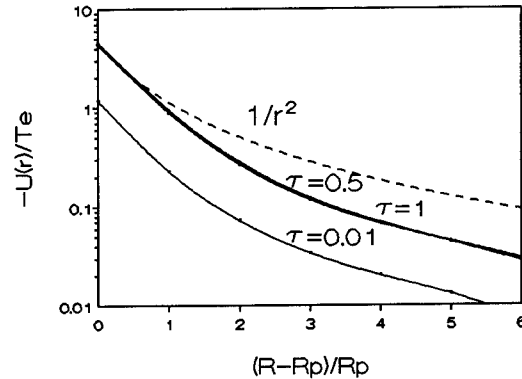


Fig. 8. The potential distribution as a function of position
 $R_0=1$; $\beta=0.5$; $M_i=47.9$

5. THE INFLUENCE OF THE PLASMA DRIFT ON THE MP CHARGING.

The vacuum arc plasma jet has a high directed energy. The relation between thermal ion energy and directed energy was analyzed by Lunev V. et. al.¹⁶. They shown that the ratio W_{i0}/T_i where W_{i0} is the directed energy, depends on the arc current, and for the Mo vacuum arc it is between 1.5-5. The ion flux to the macroparticle is determined by the directed and thermal energy. If the drift velocity is U_0 , the distribution function is Maxwellian when referred to a frame moving with the velocity U_0 . In order to determine the flux, let use assume that: (a) the MP is small ($R_0 \ll 1$); and (b), that the sheath is symmetric around the MP and isn't distorted by the drift. This means that in this system the total energy and angular momentum are conserved. As $1/R_0$ becomes infinity it is found that the ion flux approaches a limiting form, which can be obtained by the application of the d'Hopital rule. This method was used by H. M. Mott-Smith and J. Langmuir⁶.

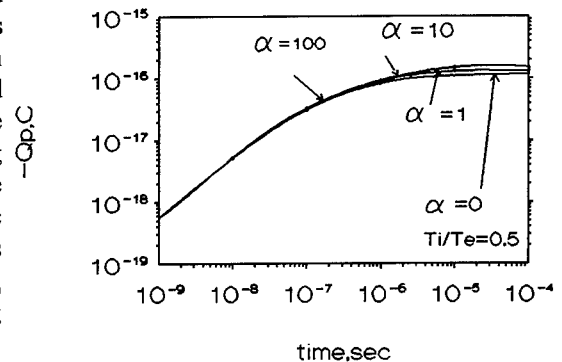


Fig. 9. The evolution of the MP charge.
 $T_e=3$ eV; $V_i=1.27 \cdot 10^4$ m/s; $N_e=10^{17} \text{ m}^{-3}$; $R_p=0.1$ μm .

The resulting expression for the ion flux has the form:

$$J_i(\alpha) = J_{i0} \{ \pi^{0.5} / (2\alpha) \operatorname{erf}(\alpha) [0.5 + \alpha^2 - \phi_p/\beta] + 0.5 \exp(-\alpha^2) \} \quad (14)$$

where $\alpha = U_0 / (2K_B T_i / M_i)^{1/2}$. The results of the calculation of the evolution of MP potential with time for different α are presented in the fig. 9. In the particular case of titanium with a mean plasma directed velocity¹⁷ $U_0 = 1.27 \cdot 10^4$ m/s, $T_e = 3$ eV, $R_p = 0.1$ μm , $N_e = 10^{17} \text{ m}^{-3}$, this influence is small in the wide range of α (0-100).

6. DISCUSSION.

In this work the MP charging in the interelectrode plasma of the vacuum arc is discussed. This process is characterized by a charging time and by the magnitude of the charge which accumulates on the MP. The charging time is determined by parameters of the plasma and macroparticles. In a particular case where $N_e = 10^{16} \text{ m}^{-3}$, $R_p = 0.1$ μm ; $T_e = 6$ eV the charging time is about 10^{-5} sec. This means that that MP's in shorter duration arcs and fast MP travelling through small plasma jets will not be fully charged. The dependence of the non-dimensional charging time on parameter R_0 is shown in the figure 10. Physically this means that the charging time is smaller in dense plasmas. In¹⁴ significant reduction was observed in the number of macroparticles reaching substrates placed in the arc plasma jet, as a result of negative biasing of the substrate relative to the anode. These results can be explained by the electrostatic repulsion of the negatively charged macroparticles, i.e. by fulfilling the conditions: $Q_p U_{\text{bias}} > \frac{1}{2} M_p v_p^2$ where U_{bias} is the bias voltage; v_p , M_p are the MP velocity and mass; Q_p is the MP charge.

The fraction of MP's repelled from a negatively biased substrate was calculated using the distribution of R_p from ¹⁵ with experimental conditions which are close to the conditions in ¹⁴. By calculation of the maximum MP radius R_{pmax} which fulfilled condition mentioned above for U_{bias} and using the distribution of R_p - $F(R_p)$ the fraction of repelled MP's by bias U_{bias} is calculated:

$$f = \int_0^{R_{pmax}} F(R_p) dR_p$$

The results are shown in figure 11, where v_p is the parameter, and the results of ¹⁴ are also shown for comparison. A good agreement is obtained for v_p close to 30 m/s using the $R_0 \ll 1$ model, and for v_p close to 50 m/s for $R_0 \approx 1$ model.

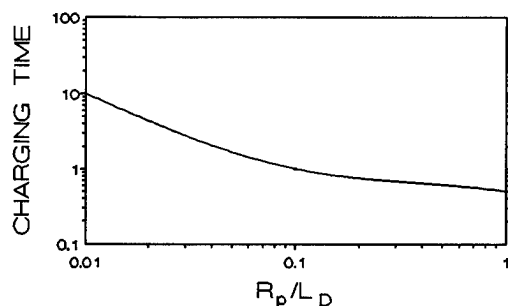


Fig.10. Charging time vs R_p/L_D ratio. $T_e=3$ eV;

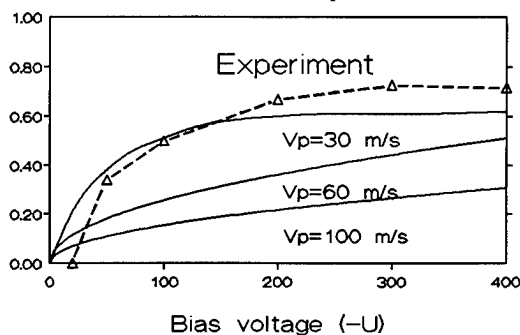


Fig.11. The fraction of MP's repelled by bias. $R_0 \ll 1$ model

7. REFERENCES.

1. G. W. McClure. Plasma expansion as a caused of metal displacement in vacuum arc cathode spot. J. Appl. Phys. vol.45, pp.2078-2084, 1974.
2. J. E. Daalder. Vacuum arc and cathode spot. Physica C, vol.104, pp.91-106, 1981.
3. T. Utsumi, J. H. English. Study of electrode products by vacuum arc in form of molten metal particles. J. Appl. Phys. vol.49, pp. 3821-3831, 1978.
4. G. S. Selwyn, E. F. Patterson. Particle trapping phenomena in radio frequency plasmas. J. Vac. Sci. Technol. A. vol. 10(4), pp. 1053-1059, 1992.
5. R. L. Boxman, S. Goldsmith. The interaction between plasma and macroparticles in a multi-cathode-spot vacuum arc. J. Appl. Phys. vol.52(1), pp.151-162, 1981.
6. H. M. Mott-Smith, J. Langmuir. Collectors in the gaseous discharges. Phys. Rev. vol.28, pp. 727-763, 1926.
7. I. B. Bernstein, I. N. Rabinowitz. Theory of electrostatic probes in a low density plasma. Phys. Fluids. vol 2, pp. 112-120, 1959.
8. J. Laframboise. Rarefied Gas Dynamics, Theory of cylindrical and spherical langmuir probes in a collisionless plasma at rest. vol.II, Academic Press, N-Y, pp. 22-44, 1966.
9. E. C. Whipple. Theory of the spherically symmetric photoelectron sheath: A thick sheath approximation and comparison with the ATS 6 observation of a potential barrier. J. Geoph. Res. vol.81, pp. 601-607, 1976.
10. J. W. Cipolla, M. B. Silevitch. On the temporal development of a plasma sheath. J. Plasma Phys. vol.25, pp. 373-388, 1981.
11. A. V. Gurevich. The distribution of the particles in a centrally symmetric field. Geomag. and aeron. vol.3, pp.151-164, 1963.
12. J. D. Swift, M. J. R. Schwar, Electrical probes for plasma diagnostics, Iliffe books, London, 1970.
13. D. J. Struik. Lectures on classical differential geometry. Addison Wesley Publishing Company, 1965.
14. C. N. Tai, E. S. Koh and K. Akari. Macroparticles on TiN films prepared by the arc ion plating process. Surf. Coat. Technol. vol.43-44, pp.324-335, 1990.
15. A. W. Baouchi, A. J. Perry. A study of the macroparticle distribution in cathodic-arc-evaporated TiN films. Surf. Coat. Technol. vol.49, pp.253-257, 1991.
16. V. M. Lunev, V. D. Ovcharenko, V. M. Khoroshich. Plasma properties of a metal vacuum arc I. Sov. Phys. Tech. Phys. vol.22(7), pp.855-858, 1977.
17. J. Kutzner, H. C. Miller. Integrated ion flux emitted from the cathode spot region of a diffuse vacuum arc. J. Phys. D: Appl. Phys. vol.25, pp.686-693, 1992.

I.V. Kozlov, E.A. Litvinov, and E.Yu. Sadovskaya

Institute of Electrophysics
Ural Division, Russian Academy of Sciences
Ekaterinburg 620219, Russia

ABSTRACT

The paper deals with modeling processes at the electrode regions of pseudospark devices. We have analyzed the physical processes that could result in the initiation and development of explosive electron emission.

It has been proposed [1] that in pseudospark devices, explosive electron emission occurs at the cathode. We have analyzed the physical processes that could result in the initiation and development of explosive electron emission.

Let us consider the processes that occur inside a hollow cathode beginning with the formation of a cathode plasma. The external electric field penetrates through the cathode hole into the hollow cathode. If we assume that the electric field in the gap, (E_0), is uniform and the cathode hole dimensions (the cathode hole radius $\alpha \ll x_m$) are much less than the cathode transverse dimensions, then, according to Smythe [2], the potential of the electric field behind the cathode is given by

$$U = \alpha E_0 k_1 [k_2 - 1/\pi(k_2 \arccot k_2 - 1)],$$

where $k_1 = \frac{x}{\alpha k_2}; \quad k_2 = \frac{r}{\alpha}.$

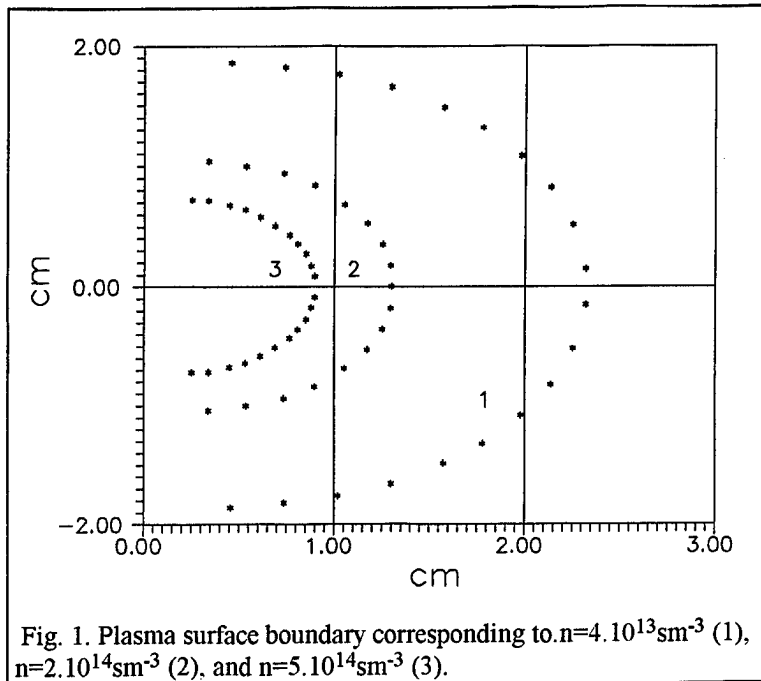


Fig. 1. Plasma surface boundary corresponding to $n=4 \cdot 10^{13} \text{sm}^{-3}$ (1), $n=2 \cdot 10^{14} \text{sm}^{-3}$ (2), and $n=5 \cdot 10^{14} \text{sm}^{-3}$ (3).

The origin of the coordinates is placed into the hole center. In the generation of plasma inside the hollow cathode, a region free from plasma forms near the hole, since the plasma is forced out by the electric field penetrating through the hole. The boundary of the plasma surface is determined by the equality of pressures between the plasma and the electric field inside the hollow cathode. From Fig. 1 showing the plasma surface boundary for different plasma densities, it can be seen that the plasma surface is shaped as a paraboloid of revolution, whose dimensions decrease with increasing the plasma density. Assuming that the electron emission from the plasma surface is uniform and the initial electron velocities are zero, we may follow the trajectories of the emitted electrons for different discharge stages with their associated plasma densities.

From Fig. 2 it can be inferred that at the lowest plasma density the electrons emitted from the plasma surface, while moving under the action of the electric field, scatter by the inner wall of the cathode.

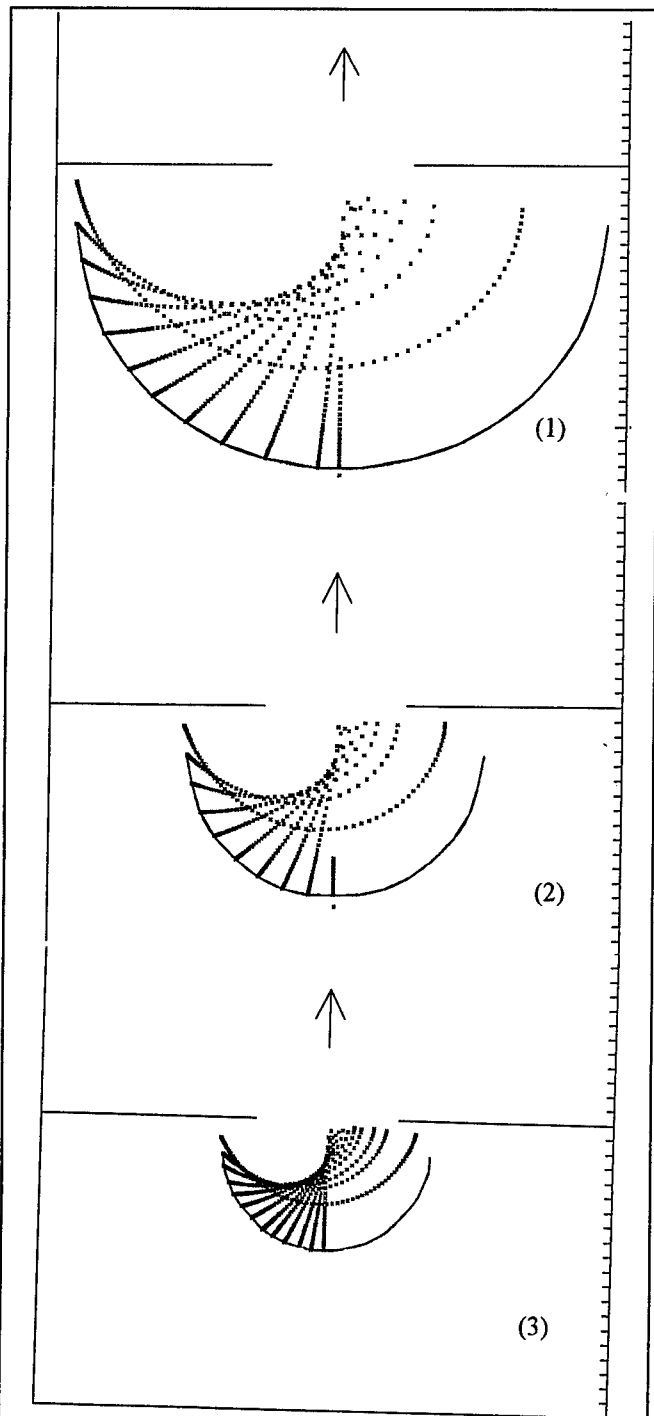
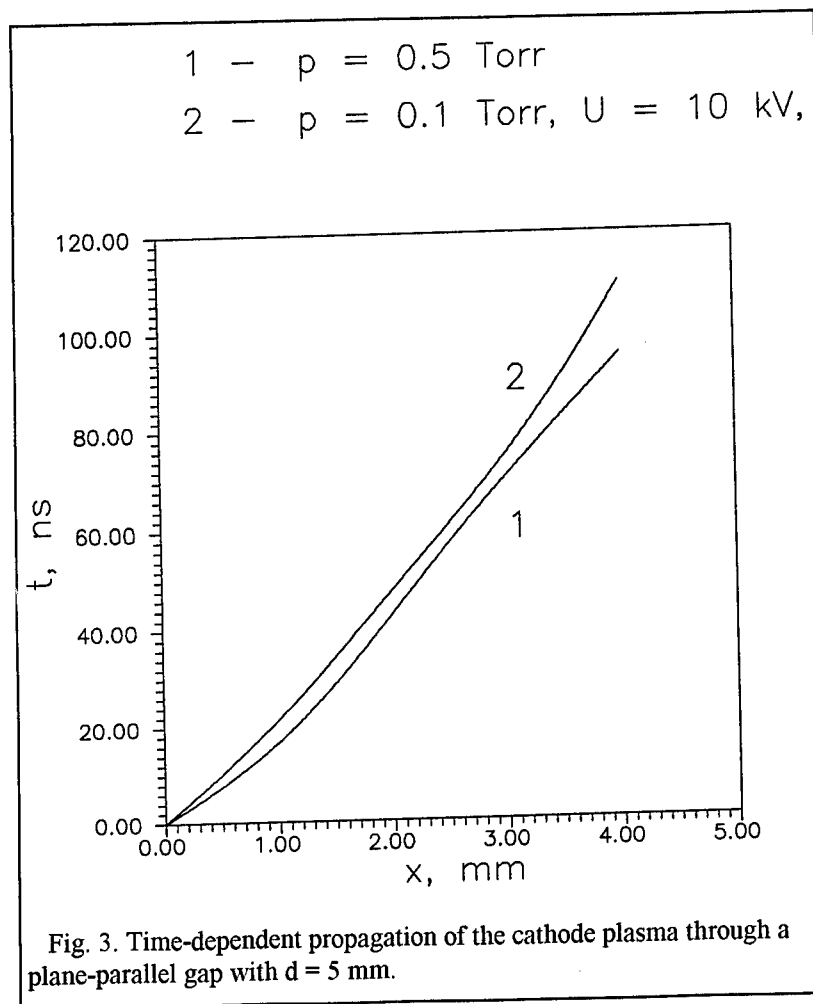


Fig. 2. Trajectories of electrons emitted from the plasma surface for $n=4.10^{13}\text{sm}^{-3}$ (1), $n=2.10^{14}\text{sm}^{-3}$ (2), and $n=5.10^{14}\text{sm}^{-3}$ (3).

Moreover, the electrons emitted from the plasma surface near the cathode wall, those whose trajectories are the longest, execute oscillatory motions under the action of the electric field inside the plasma-free region, ionize the residual gas, thereby increasing the total number of electrons in the beam. As the plasma density increases and the plasma-free region contracts, more and more electrons pass through the hole. The enhancement of the external electric field at the edges of the cathode hole and the bombardment of the cathode by the cathode plasma electrons initiate the processes of desorption and ionization in the region of the cathode hole. This may eventually result in explosive electron emission at the cathode edge. The plasma produced as a result of the cathode processes expands and bridges the cathode - anode gap. However, the velocity of plasma expansion observed experimentally at explosive emission

$(v \approx 10^6 \text{ cm/s})^3$ gave no way of providing an explanation

for the conductance time 100 ns measured by [4,5] with co-workers and the fact that the conductance time depends on the gas pressure in the gap. Therefore, we considered the ionization of the residual gas by an electron beam and the motion of the ions in a self-consistent non-steady-state electric field in a cathode-anode gap. We used our previously developed model of a low-pressure gas discharge with a plasma boundary propagating from cathode to anode.^{6,7,8,9} The numerical simulation was carried out as a one-dimensional approximation (plane-parallel geometry) for a gap of spacing $d = 0.5 \text{ cm}$ and gas (nitrogen) pressure of 0.5 and 1 Torr at $U = 10^4 \text{ V}$. The shorter conductance time (see Fig. 3) in comparison to the time needed for expanding cathode plasma to bridge the gap, predicted by modeling the discharge process, is due to the nonmonotonic potential distribution in the gap. The nonmonotonicity (potential well) is caused by the accumulation of positive ions produced as a result of the ionization by the electrons beam. Since the voltage applied to the gap is 10^4 V and the electron impact ionization is a maximum at 100 V^{10} , the potential well is located near the cathode or at the expanding cathode plasma. The region of local reduction in potential, first, slows down the positive ions generated in this region and, second, accelerates the cathode plasma ions deep into the discharge gap. As the cathode plasma absorbs the ions produced in the gap, the depth of the potential well decreases, the cathode plasma stops accelerating, and the next potential well forms at the distance from the cathode plasma boundary, corresponding to the potential 100 V. An increase in residual gas pressure favors more rapid accumulation of ions and decreases the time intervals between the stepwise propagation of the plasma deep into the gap.



REFERENCES

1. G. A. Mesyats, V. F. Puchkarev, "On mechanism of emission in pseudosparks" in *Proc. XIII ISDEIV*, pp.356-360, Darmstadt-1992.
2. W. R. Smythe, *Static and Dynamic Electricity*, Moscow, 1954.
3. G. A. Mesyats and D. I. Proskurovsky, *Pulsed Electrical Discharge in Vacuum*, Springer, Berlin - Heidelberg, 1989.
4. K.A. Klimenko, A.V. Kolesnikov, Yu.D. Korolev, V.G. Rabotkin, and I.A. Shemyakin, "Investigation into the mechanism for discharge initiation in low-pressure pseudospark gaps", *Fizika Plazmy*, Vol. 17, pp. 1256-1262.
6. N.N. Koval, Yu.E. Kreindel, and E.A. Litvinov, "Development of a Knudsen arc with a cathode spot", *Dokl. AN SSSR*, Vol 300, pp. 1108 - 1111.
7. Yu.E. Kreindel, E.A. Litvinov, and E.Yu. Sadovskaya, "Development of a Knudsen discharge with a space-charge-limited current", *Zh. Tekh. Fiz.*, Vol. 59, pp.47 -53.
8. M.Yu. Kreindel and E.A. Litvinov, "Formation of a Knudsen discharge by a nonmonotonic potential distribution in a gap", *Zh. Tekh. Fiz.*, Vol. 62, N 5, pp.159 - 164.
9. G.P. Bazhenov, O.B. Ladyzhensky, E.A. , S.M. Chesnokov, "On the formation of the cathode-flare-plasma emission boundary at explosive electron emission", *Zh. Tekh. Fiz.*, Vol.47, N 10, pp.2086 - 2091.
10. B. M. Smirnov *Physics of the Weakly Ionized Gas*, Moscow, Nauka, 1979.

High-current vacuum arc discharge with gas-filled electrodes.

A.A.Logatchev, S.M.Shkol'nik

A.F.Ioffe Physical-Technical Institute RAS,
Polytechnicheskaya 26, St.Petersburg, 194021 Russia

ABSTRACT

The results of investigation of high-current vacuum arc with Ti cathode filled by deuterium till $x \approx 1$ (at.D/at.Ti) are presented. Electric and erosion characteristics were measured. The investigations proved this discharge to be very differing from the arc with degassed electrodes. The results obtained indicate the gas-filled electrodes have good prospects for some technical applications.

1. INTRODUCTION

The characteristics of a vacuum arc with a metal cathode, filled with the hydrogen till $x \approx 1$ (x - a ratio of hydrogen atom number to the metal atom number in the sample) essentially differ from those of an arc with degassed electrodes. Gas-filled metals formerly were used in vacuum commutation devices only for triggering¹, but not as main discharge electrodes. The discharge with gas-filled electrodes (GFE) remained unstudied. The preliminary results of our investigations were published recently².

2. EXPERIMENTAL SET-UP AND METHODS

Investigated was a discharge fed by a special generator of rectangular voltage pulses with an amplitude $U=115V$ and regulated duration $t \leq 5$ ms enduring loads of $I \leq 6$ kA. The current was regulated by a ballast resistor. The discharge was ignited in a vacuum chamber ($p \sim 10^{-5}$ Pa) during a continuing pumping. The electrodes were butt ones with a diameter $2 \cdot R=20$ mm, the gap $h=(1-16)$ mm. The cathodes and the anodes were made of oxygenless Cu. On the cathode butt was a Ti-layer 10 or 45 μm thick filled with deuterium till $x \approx 1$. In control experiments were used Cu cathodes without any coating and the cathodes of titanium VT-1 specially degassed. The degassing was carried out at $T \approx 1100K$ during 2-6 hours in a vacuum $\sim 10^{-4}$ Pa. The discharge was ignited in the center by a current break in the auxiliary circuit.³ The current and the discharge voltage were recorded by digital stored oscillographs. The processes on the cathode were observed at a small angle by high-speed photography (HSP). For spectroscopic measurements there were used two monochromators with photomultipliers. The radiation was led out on the splits of monochromators with the help of two fibers whose other ends could be replaced on the plane of twice reduced discharge image. The space resolution $\approx 1mm$. The metal erosion was determined by a weight method, and the gas expense - by the pressure change after arcing in a chamber with cut-off pumping.

3. RESULTS AND DISCUSSION

3.1. It is known that in a discharge with degassed electrodes the life-time of the discharge with a rather low noise level τ is determined by the current, the size and the material of the electrodes, the gap length⁴. For instance: at $I=5$ kA, $2 \cdot R=20$ mm, $h=8$ mm for a cathode out of degassed Ti $\tau \sim 180-200$ μs ; of oxygenless Cu $\tau \sim 300-320$ μs . In the GFE discharge a low noise level is maintained during the whole pulse even in the case its duration reaches the value of $1-5000 \mu s$, maximally accessible in our experiments (fig.1). In initial discharge development stages the current

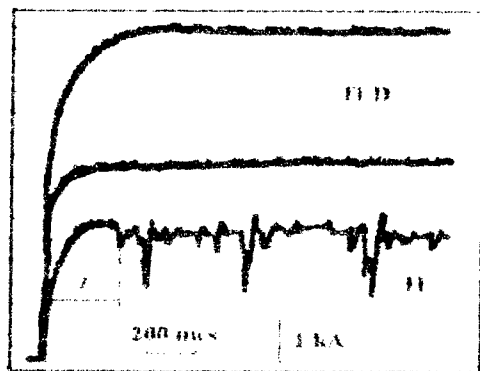


Fig. 1. Current oscillogram.

mately on 1.5 V lower, than that of the degassed electrode. The VAC-sloping is also essentially different. Note the presence of two plots with different VAC-slopes of the GFE discharge especially clear at long h .

One of the most significant high-current vacuum arc characteristics is the current I_c critical for the anode spot formation. In the discharge with a degassed Ti at $h=3\text{ mm}$ $I_c \approx 4\text{ kA}$, and at $h=8\text{ mm}$ $I_c \approx 3\text{ kA}$. In the GFE discharge an anode spot formation for $h \leq 12$ has not been observed until the maximal current, provided by a feeding source: $I \leq 6\text{ kA}$.

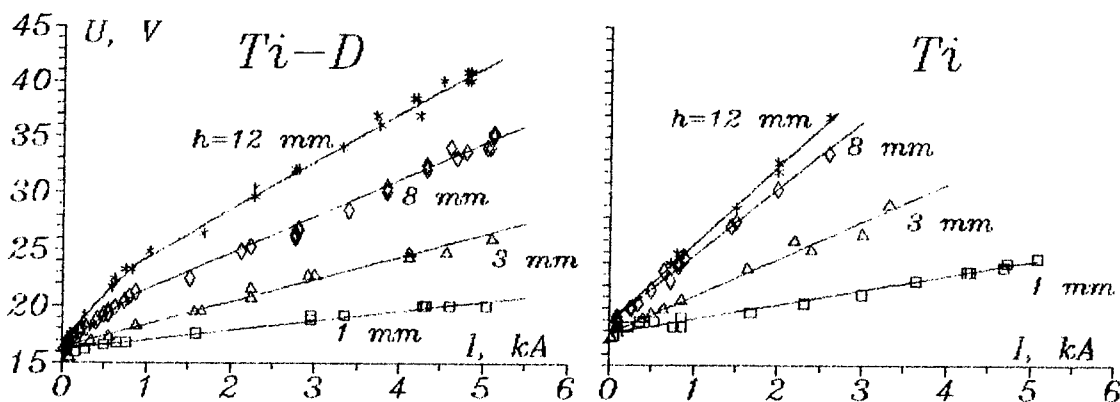


Fig. 2.

3.2. The described electric characteristic peculiarities of the GFE discharge partially are elucidated during the comparison with the cathode process investigation results. It is known that after the discharge excitement on the degassed preliminary trained electrodes the cathode spots form an expanding ring. The analysis of HSP data showed that on the GFE not a ring, but a circle of spots is formed practically uniformly filled by cathode spots. The circle radius r is growing in time under other equal conditions much more quickly than the ring radius on the degassed electrodes (fig.3). Note that on badly degassed electrodes the surface processes were partially like those observed on GFE: inside the cathode spot ring some activity was noticed, which was more expressed – the worse degassed the electrode was. The analysis of the VAC-slope dependence on the gap length h , made in accordance with [6] at sufficiently long h ($h \gg 1\text{ mm}$), when the model [6] may be applied, also showed that in the GFE discharge the current density distribution is more uniform. In fact, in the discharges with electrodes of degassed Ti this dependence has a logarithmic character, meanwhile in GFE discharge for the both characteristic VAC-plots its character is a linear one (fig.4).

The high rate of the spot circle expanding provides a high rate of a current inc-

rease and correspondingly - a quick attainment by the current of a quasi stationary level in the GFE discharge. On the degassed material the spot ring diameter $2 \cdot r(t)$ after the time τ becomes equal to that of the cathode $2 \cdot r(\tau) = 2 \cdot R$ (e.g. on Ti at $I = 5 \text{ kA}$ $\tau = 200 \mu\text{s}$ (fig.3)), and at $t > \tau$ the major part of spots passes over on the side surface of the cathode cylinder. The cathode jets flow outside of the gap, the discharge burning becomes unstable, the noise level increases. On the GFE the spots after a quick propagation over the cathode even at the maximal current remain on the butt (on the gas-filled coating) during the whole pulse (till $500 \mu\text{s}$); therefore the noise level remains low (fig.1). HSP of the cathode surface for $I \sim 100 \text{ A}$ enabled the estimation of the current passing through one spot on the GFE: $I = (15-20) \text{ A}$. It is essentially less than that for the spot on degassed Ti: $I \sim 70 \text{ A}$.

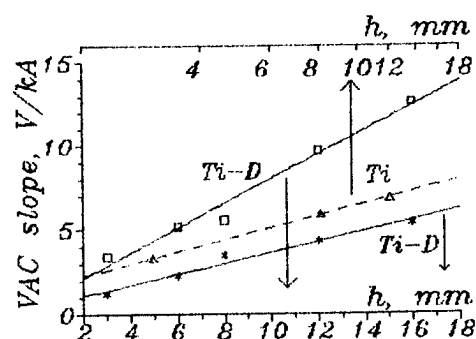


Fig.4.

relatively low currents $I < 1 \text{ kA}$ there was noticed a an expense increase. At the current $I > 1 \text{ kA}$ a characteristic significance of deuterium expense: (3 ± 6) gas atoms per one Ti-atom. (Apparently these values are underestimated as the Ti sputtered by the discharge covered the surfaces of the chamber inside and absorbed the deuterium released out of the cathode.) This indicates that the gas is released not only because of breaking the crystal lattice during the spot burning (remember that in the layer $\sim 1 \text{ D}$ atom is per Ti atom), but possibly, the gas is released out the cathode surface surrounding the spot under ion bombardment. Also it may be a result of heating by the discharge. The resource of GFE is not a small one. For the $45 \mu\text{m}$ thickness of gas-filled layer on the electrode of 20 mm in diameter it makes $\sim 10^3 \text{ C}$.

3.4. In the radiation spectrum of the GFE discharge intensive D_α and D_β lines were observed. The radiation intensity is increasing approximately in proportion to the current. The duration of the pulse front of the photomultiplier signal coincides with that of the discharge current front. The differences in the signal appearance in the center and at the electrode edge is not more than several μs . This sharply distinguishes the deuterium line oscillograms from that of both Ti-atoms and ions for which is noticed a significant delay of the signal appearance at the electrode edge relatively to the moment of the signal appearance in the center (fig.5). The observed delays clearly correlate with the propagation time τ of the cathode spots along the cathode surface from the center to the periphery, discussed in the previous section. The results received show that unlike the Ti ions the motion of the deuterium atoms released by

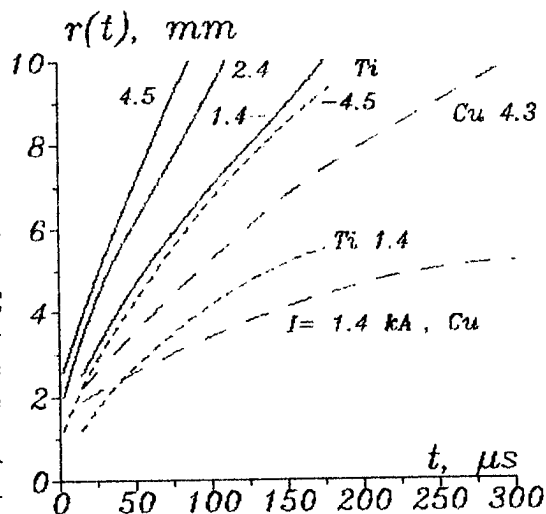


Fig.3. Solid - TiD (layer $10 \mu\text{m}$), dashed - degassed Ti and Cu.

3.3. The character of the erosion damage, visible through a microscope, is also strongly different. On the degassed Ti even at a small magnification there can be seen spot craters. On the GFE up to the magnification of $\times 100$ the surface looks out only slightly rough. We have no exact quantitative data on the erosion in the droplet phase, however it can be stated that in the discharge with GFE it is not stronger than that with a degassed Ti. The erosion rate measurements for Ti in a GFE discharge give $\sim 3 \cdot 10^{-5} \text{ g/C}$ against $\sim 5 \cdot 10^{-5} \text{ g/C}$ for Ti in the discharge with degassed electrode. The gas expense (deuterium atoms/Ti atoms) has somewhat changed from sample to sample. At $I > 1 \text{ kA}$ the expense does not depend on the current. At

the discharge out of the electrode volume is in a significant degree randomized.

In the degassed Ti discharge radiation spectrum there were noticed hydrogen lines, however very weak. An essential peculiarity is the delay of the appearance of hydrogen line luminosity on the discharge periphery, which is analogous to that observed for Ti. Apparently small hydrogen admixtures released during the destroying of the crystal lattice are rather effectively entrained by the spot plasma jet.

3.5. The results received and the assumptions seeming reasonable, that the major part of the gas released from the gas filled Ti layer has no high directed velocities, the gas motion being in a significant degree chaotic, permit to think that Fig.5.

the use of GFE facilitates the compensation of the charge of electrons, emitted by the cathode. This is as well promoted by an obvious ion side losses decrease provided by a rather uniform distribution of the spots along the cathode butt and by their tendency not to abandon the gas filled coated butt. The result is an essential increase of I_c in the GFE discharge.

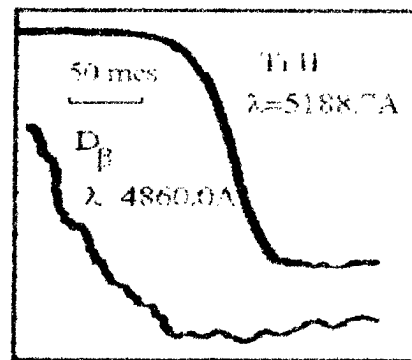
3.6. The described peculiarities enable to hope for a successful utilization of GFE in the commutating devices. The study of the GFE discharge is of interest also because of the fact, that in plasma devices using hydrogen as a plasma-producing substance the metal surfaces are necessarily saturated with the hydrogen. For instance - this has to be taken into consideration during the study of conditions and causes of unipolar arc formation on the first wall of thermonuclear fusion devices.

4. ACKNOWLEDGMENTS

The work has been carried out under the financial support of the Russian Fundamental Investigation Fund (project 93-02-17416).

5. REFERENCES

1. J.M. Laferty, "Triggered vacuum gaps," Proc.IEEE, Vol.54, pp.23-32, January 1966.
2. A.A. Logatchev, S.M. Shkol'nik, "Arc discharge in vacuum with gasfilled electrodes", Pis'ma.Zh.Tekh.Fiz, Vol.20, pp.53-57, February 1994. (in russian).
3. S.M. Shkol'nik, "The plasma parameters of the interelectrode gap of the vacuum arc," IEEE Trans.Plas.Sci, Vol.PS-13, pp.336-338, October 1985.
4. A.M. Chaly, A.A. Logatchev, S.M. Shkol'nik, "Electrode geometry and material effects on the cathode spot dynamics in a high-current vacuum arc," Proc. XVI ISDEIV, Russia, 1994.
5. J.C. Sherman, R. Webster, R. Holmes, "Cathode spot motion in high-current vacuum arc on copper," J.Phys.D: Appl.Phys. Vol.8. pp.696-702, May 1975.
6. J.C. Sherman, R. Webster, J.E. Jenkins, R. Holmes, "The voltage, self generated magnetic field and current distribution in a high-current vacuum arc," J.Phys.D: Appl.Phys, Vol.11, pp.379-388, February 1978.
7. C.M. Kimblin, "Erosion and ionization in the cathode spot region of vacuum arcs," J.Appl.Phys. Vol.44, pp.3074-3081, July 1973.



Numerical simulation of the high current vacuum arc

Mietek T. Glinkowski, Allan Greenwood and Paul Stoving

Rensselaer Polytechnic Institute, Electric Power Engineering Department
Troy, New York 12180-3590

1. INTRODUCTION

The paper presents the numerical implementation of the state-variable model of the high current arc interruption. The differential equations governing the sheath development in vacuum plasma after the main frequency current zero (CZ) are coupled with the electrical circuit equations representing the power system and solved simultaneously using Advanced Continuous Simulation Language software (ACSL). The mathematical formulation of the arc interruption is in the form of a black-box, i.e. the two "external" variables are voltage, $u(t)$ and current, $i(t)$. Other black-box variables are "internal", i.e. they are only needed to specify the physical conditions of the arc plasma. These internal variables are: plasma density, N_{i0} , its space distribution between contacts at CZ and its time decay due to diffusion, ion velocity, v_i , time delay between the beginning of the TRV and CZ, t_0 , and the equivalent arc diameter at current zero, D .

2. BLACK-BOX MODEL OF THE INTERRUPTION PROCESS IN VACUUM

2.1 MODEL DESCRIPTION

The main difficulty to develop a two-terminal black-box model of a vacuum circuit breaker is that the inherent plasma parameters of the arc at current zero are space and time dependent, i.e. there is no simple function to describe them; rather a distribution of parameters should be used.

An extensive treatment of vacuum arc and the interruption processes at current zero can be found in Glinkowski¹. A complex, finite-difference (FD) software was developed that had taken into account the space distributions of plasma parameters such as ion velocity, ion/electron density, electric field, and electric potential⁴. However, this program is not practical to use as a simple and portable design tool that could be easily combined with other softwares. Therefore, a simplified model of vacuum arc in the post arc current region was developed. The model is a combination of the "ion matrix"² and Child-Langmuir space-charge-limited models³ for low density plasmas subjected to electric fields resulting from the application of transient recovery voltages (TRV).

Mathematical modeling equations of the transition model are as follows

$$t^2 = \frac{4\epsilon_0 U_0}{9eZN_i} \left[\left(1 + \frac{u(t)}{U_0} \right)^{3/2} + \frac{3u(t)}{U_0} - 1 \right] \quad (1)$$

$$U_0 = \frac{M_i}{2e} \left(v_i + \frac{d\ell}{dt} \right)^2 \quad (2)$$

$$\frac{d\ell}{dt} = \frac{4i(t)}{\pi D^2 Z N_i e} - v_i \quad (3)$$

where N_i , ion density at the sheath edge, $\approx 10^{18} - 10^{23} \text{ [m}^{-3}\text{]}$ for diffuse arcs, dynamically changing.
 Z , average charge multiplicity number ($\approx \text{const.}$),
 $\approx 1.3 \div 1.5$ for copper based materials and diffuse arcs.
 v_i , ion velocity at the sheath edge ($\approx \text{const.}$),
 $\approx 10^4 - 2 \cdot 10^4 \text{ [m/s]}$ for copper based materials and diffuse arcs, see¹ for other materials,
 D , equivalent diameter of the discharge in the vicinity of the current zero, for short gaps and high dI/dt 's (100A/ μs) a value of 1 mm is representative (Lindmayer, Wilkening⁹).

$$\pi = 3.14159, \epsilon_0 = 8.854 \cdot 10^{-12} \text{ [F/m]}, e = 1.6 \cdot 10^{-19} \text{ [C]}.$$

ℓ is a sheath length. This is a thickness of the ion space charge developed in front of the ex-anode (new cathode after a current zero) and it is a result of the voltage (TRV) applied to the electrodes after current zero. $u(t)$ is the transient recovery voltage applied across the contacts by the external circuit. In the black-box representation it is one of the two output variables. U_0 is almost constant if the sheath velocity does not reach an extreme value. Typical values of U_0 for copper type materials are of the order of 20 V to 35 V. $i(t)$ is a post arc current and it is the other of the two output variables of the black-box. This current includes two components. A displacement current, proportional to the sheath velocity ($d\ell/dt$) is due to the changing voltage across the contacts, $u(t)$. The second component is a conduction current,

$$i(t) = i_{\text{displacement}}(t) + i_{\text{conduction}}(t) \quad (4)$$

M_i is an ion mass, (for Cu $M_i = 1.06 \cdot 10^{-25} \text{ kg}$ (atomic weight = 63.57)).

In summary, the transition model consists of three equations (1-3) and four unknowns, ℓ , $u(t)$, $i(t)$, U_0 . Therefore, it can be viewed as "black-box", i.e. by adding one more equation, for instance an equation describing an external electrical circuit, the system of four equations will be solvable. Two out of the four unknowns are output variables $u(t)$ and $i(t)$. The remaining two, ℓ and U_0 , are needed only for internal calculations within the model. The block representation of the model is shown in Fig. 1.

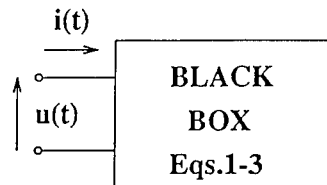


Figure 1. Black-box model of the vacuum interrupter

2.2 Application of black-box model

The vacuum model as described by (1-3) represents the state of the post arc plasma after the application of the power frequency current. It is known⁵⁻⁷ that the beginning of the recovery voltage in vacuum arcs is delayed and does not coincide with the current zero by several nanoseconds. Times of up to 40-60 ns are reported in⁷ for copper electrodes and high di/dt 's. This delay is caused by a flux of positively charged ions moving from the ex-cathode to the ex-anode, i.e. against the arc voltage and the main flux of electrons. Therefore the simulation process using a black-box model starts t_0 [ns] after current zero (CZ). The situation is depicted in Fig. 2.

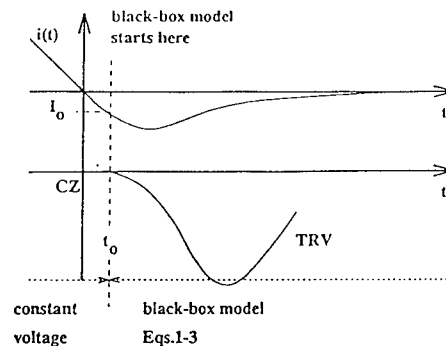


Figure 2. Delay TRV after CZ in vacuum switch.

2.3 Model limitations

The ion velocity, v_i , is a constant value in this model. The work described in^{1,4} and many others, indicates that the velocity is a parameter that varies in time and in space. The velocity has its own distribution, therefore, to assume a fixed constant

value could lead to errors.

The ion density N_i is also a complex function of time and space. The change in the ion density results from at least two phenomena. First, the diffusion of plasma due to the pressure gradient causes ions and electrons to escape from the interelectrode volume and tends to equalize the density in the gap. Second, since the density in the equations (1-3) is taken at the edge of the ion sheath, the location of the sheath will have an effect on the density if it is different at the ex-cathode and the ex-anode. In an attempt to include the two described processes an analytical expression for N_i has been created,

$$N_i = N_{i0} \cdot \exp\left(-\frac{t-t_0}{\tau}\right) \cdot \left(\text{Amp} \cdot \frac{\ell^2}{\text{gap}^2} + 1.0\right) \quad (5)$$

\uparrow
 initial density
 at the ex-anode
 $t \leq t_0$

\uparrow
 decay in time due
 to diffusion residual
 ionization, etc.

\uparrow
 change in space due
 to the location
 of the sheath

The initial density, N_{i0} , is determined from the initial post arc current $I_0 = i(t_0)$ (Fig. 2).

$$N_{i0} = \frac{4 \cdot I_0}{v_i \cdot \pi \cdot D^2 \cdot Z \cdot e} \quad (6)$$

and derived from the fact that at t_0 the total post arc current consists only of the conduction component

$$I_0 = \underbrace{N_{i0} v_i}_{\substack{\uparrow \\ \text{ion flux}}} \cdot \underbrace{Z \cdot e}_{\substack{\uparrow \\ \text{ion current} \\ \text{density}}} \cdot \underbrace{\frac{\pi D^2}{4}}_{\substack{\uparrow \\ \text{equivalent} \\ \text{cross-section of the discharge at } t_0}} \quad (7)$$

The time constant, τ , of the diffusion can be adjusted to match the experimental results. In most simulations τ was chosen between 0.5 μs to 10 μs . It is expected that this parameter will be a function of the gap length ("gap") and the diffuse or constricted mode of the arc. Some influence of the di/dt at CZ is also possible. The Amp factor controls how different the density at the ex-cathode is compared to the density at the ex-anode. At the ex-anode $\ell = 0$ and $\left(\text{Amp} \cdot \frac{\ell^2}{\text{gap}^2} + 1.0\right) = 1.0$ whereas at the ex-cathode $\ell = \text{gap}$ and $\left(\text{Amp} \cdot \frac{\ell^2}{\text{gap}^2} + 1.0\right) = 1.0 + \text{Amp}$. This accounts for a nonuniform distribution of ions across the gap. The shape of the distribution was chosen as quadratic due to a spherical nature of expansion of plasma from the cathode spot of the ex-cathode. The Amp factor can be adjusted to match the experimental results as long as it has some physical justification. In most simulations Amp was chosen between 0 and 10. An example of the density function $N_i(t, \ell)$ is shown in Fig. 3 for gap = 10 mm, $N_{i0} = .8 \cdot 10^{21} [\text{m}^{-3}]$ Amp = 5, $\tau = 10 \mu\text{s}$.

Another limitation of the model is the exclusion of residual production of plasma after CZ. It is highly possible^{1,6,7} that the ionization of neutrals in the metal vapor continues well after current zero. It is primarily due to the high electric field that exists when the TRV is applied. This residual ionization exhibits itself in the "long tail" of the post arc current signal even after the sheath traveled through the gap and reached the opposite electrode (ex-cathode). Quasi representation of the residual ionization is possible using a parameter τ in eq. (5). τ of 10 μs in Fig. 3 represents such a situation.

A series limitation of the vacuum model is its numerical stability. The coupled equations (1-3) are strongly nonlinear in nature. In many instances during testing of the vacuum black-box the solution became unstable and several adjustments of the parameters were required. These numerical instabilities depend on the values of N_i , v_i as well as the frequency and the magnitude of TRV.

To better understand that let's analyze the equations (1-3). The sheath length, ℓ depends on the voltage across the contacts,

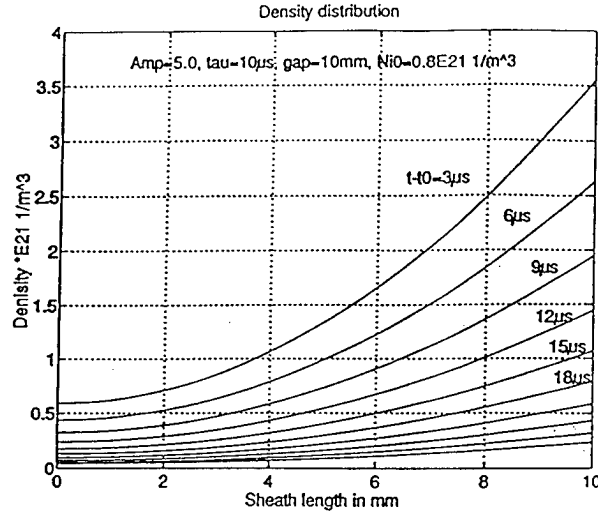


Figure 3. Example of N_i as a function of time and sheath position.

$u(t)$ (eq. 1). The higher the voltage the longer the sheath. The movement of the sheath results in $d\ell/dt$ which in turn results in the displacement current which increases the total current $i(t)$. This increased total current results in the increased $d\ell/dt$ (eq. 3) which in turn accelerates the sheath even more (eq. 1) and so on. In addition, in later stages of post arc simulations the density N_i tends to decrease which increases the sheath length even more. As a result the sheath velocity tends to be low at first and then increases very rapidly later in the process. For this reason, dynamic smoothing subroutines (filters)⁸ were built in the vacuum black-box model to control the rate of change of some parameters.

2.4 Breakdown/Failure Criteria

The black-box model has the ability to predict the post arc current in vacuum after power frequency CZ when the initial parameters are specified. The model equations (1-3) do not contain any failure criteria, i.e. they will never indicate if the interruption was successful or not. In⁷ for instance the authors point out that there are few different mechanisms of failure in vacuum. To accommodate these criteria it was proposed that the black-box model be augmented by

- a field breakdown regime - When the electric field at the ex-anode exceeds a specified value, E_{\max} , the program will indicate a breakdown. The electric field at the ex-anode is calculated as

$$E = 2 \sqrt{\frac{ZeN_i}{\epsilon_0} \left(\sqrt{u(t) \cdot U_o + U_o^2} - U_o \right)} \quad (8)$$

- a thermal breakdown regime - A thermal breakdown can be associated with the power density delivered to the ex-anode. If the power density exceeds a specified value, P_{\max} , the interruption failure will be reported. The power density is calculated as

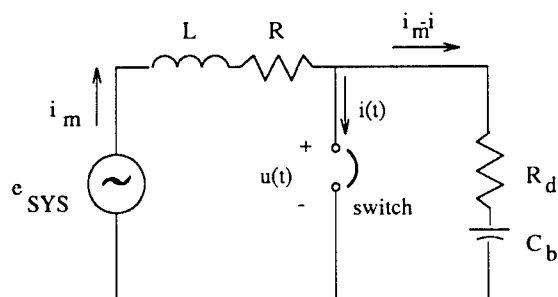
$$P = N_i M_i v_i \left(\frac{v_i^2}{2} + \frac{Ze u(t)}{M_i} \right) \quad (9)$$

where N_i and v_i are the ion density and velocity at the sheath edge, as before.

- a sheath reversal regime - When the voltage across the contacts reaches a maximum (peak of the TRV) and its value is not high enough to move the sheath across the full gap to the ex-cathode the sheath edge will try to reverse its direction and move back towards the ex-anode. This is physically impossible. Therefore, when the program detects the negative sheath velocity it will terminate and report the interruption failure.

3. VERIFICATION OF THE MODEL PARAMETERS USING EXPERIMENTAL DATA

The application for the vacuum arc model is shown in Fig. 4. The equations (1-3) were coupled with the state-variable equations for v_c and i_m ,



$$\begin{cases} \frac{di_m}{dt} = \frac{1}{L} (e_{SYS} - Ri_m - u) \\ \frac{dv_c}{dt} = \frac{1}{C_b} (i_m - i_a) \end{cases} \quad (10-11)$$

Figure 4.

The strong nonlinear coupling between the equations and nonlinear derivative terms like $\left(\dots + \frac{d\ell}{dt}\right)^2$ cause potential numerical instability.

An explanation is also required for the parameters D and v_i . Some experimental evidence of Lindmayer and Wilkening⁹ suggests that for high di/dt vacuum arcs D is approximately equal to 1 mm. This value was also adopted here. The ion velocities were chosen as less than 2.25 km/s.

In order to verify the vacuum model and its parameters the experimental results of Dullni¹⁰ were used and compared against the simulations. The sample Dullni test is reproduced in Fig. 5. The circuit parameters, such as L , e_{SYS} , and C_b were calculated from the peak 50 Hz current (56 kA), inherent RRRV of 2 kV/ μ s and 66 kV_p TRV. The values were found as $L = 1.88$ mH, $e_{SYS} = 33$ kV_p @ 50 Hz, $C_b = 85$ nF. R_d was set to a value of 200 Ω . Figure 6 illustrates the same test simulated

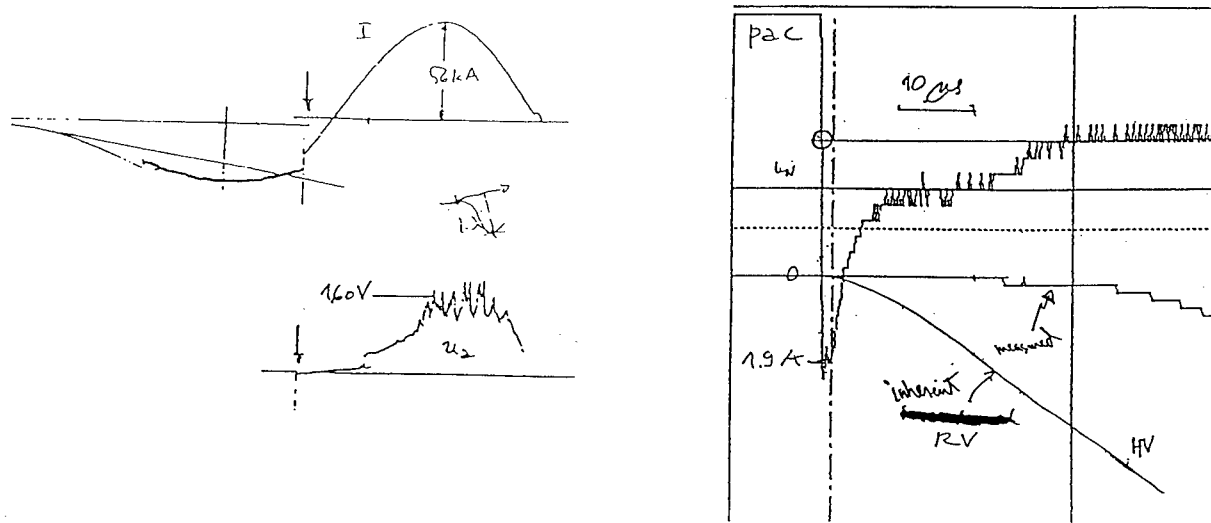


Figure 5.

by the software program. A very good match of the post-arc current was obtained by setting $D = 1.25$ mm, $v_i = 2.25$ km/s, gap = 10 mm, $\tau = 10$ μ s, Amp = 5, $I_0 = 1.9$ A. However, this does not mean that the values are unique for this particular

device. It does not even imply that the arc was in the diffuse mode at the time of interruption. The matching simply illustrates that the program is capable of reproducing the experimental data. Therefore, it was decided to rerun the simulation with lower values of I_0 that would make the sheath travel faster across the gap (lower density N_i). Indeed, it was again possible to reproduce the experimental waveforms. This simulated run is illustrated in Fig. 7 and is believed to better resemble the physical phenomena in the arc plasma.

4. CONCLUSIONS

It was shown that a simple but strongly nonlinear model of the vacuum arc interruption processes can be assembled as a two-terminal black-box. The model contains two external variables, $u(t)$, $i(t)$, that are easy to verify, and several internal

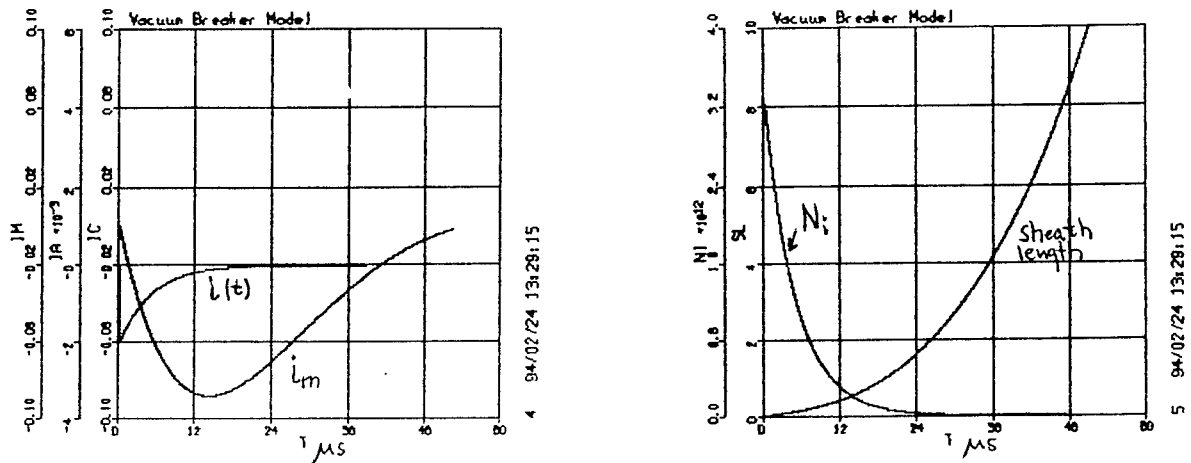


Figure 6. Simulated test from Fig. 5 with $I_0 = 1.9$ A corresponding to $N_{i0} = 3.5 \cdot 10^{12}$ 1/mm³.

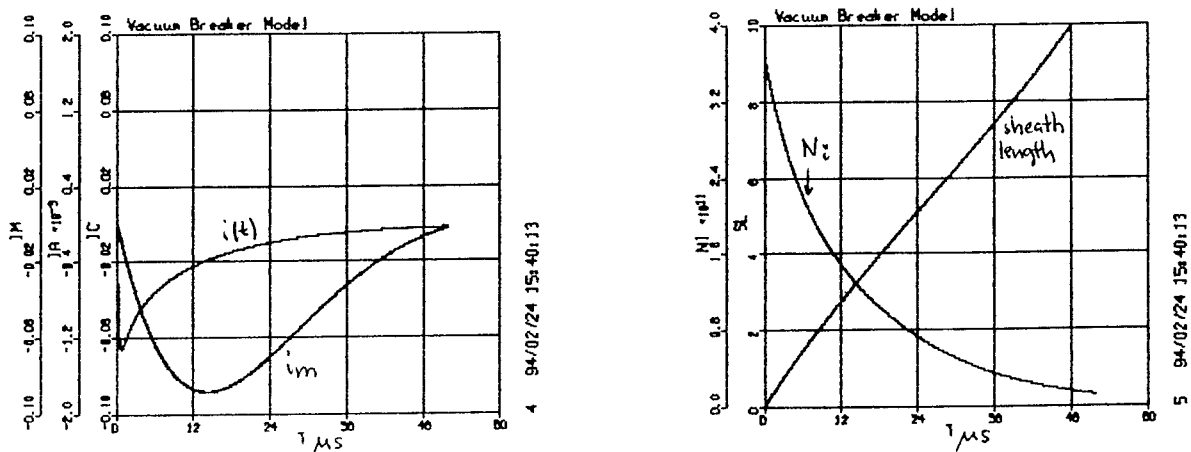


Figure 7. Simulated test from Fig. 5 with $I_0 = 0.1$ A corresponding to $N_{i0} = 3.5 \cdot 10^{11}$ 1/mm³.

variables that have to be adjusted based on the knowledge of the physical phenomena. The model simulations could produce results that match given measurements of external variables for different values of internal variables and parameters. Therefore, caution and close inspection of results are required when applying the model. By rerunning the simulation several times the set of parameters was found that satisfied the measurements of voltage and current and internal processes inside the arc. The attractiveness of the described simulation software stems from the fact that a sensitivity analysis of all internal plasma parameters can be performed without the need for an extensive experimental program. The model could also be used as a design tool for a new vacuum switches in a wide range of voltage and current levels.

5. ACKNOWLEDGMENT

The experimental results of the post arc current measurement were provided by E. Dullni whose willingness to share the data is greatly appreciated.

6. REFERENCES

1. M. Glinkowski, "Behavior of Vacuum Switching Devices for Short Gaps," Ph.D. Thesis, Rensselaer Polytechnic Institute, Troy, NY, December 1989.
2. R.H. Varey, K.F. Sander, "Dynamic Sheath Growth in a Mercury Plasma, "British Journal of Applied Physics, Vol. 2, p. 541, 1969.
3. J.G. Andrews R.H. Varey, "Sheath Growth in a Low-Pressure Plasma," Phys. Fluids, Vol. 14, pp. 339-343, 1971.
4. M.T. Glinkowski, E-D. Wilkening, "Spatial and Time Characteristics of Short Gap, High di/dt Discharges," Proceedings of XVth Intern. Symposium on DEIV, Darmstadt, Germany, pp. 449-453, Sept. 6-10, 1992.
5. S. Childs, A. Greenwood, "A Model for DC Interruption in Diffuse Vacuum Arcs," IEEE Trans. on Plasma Science, Vol. PS-8, No. 4, pp. 289-294, December 1980.
6. M. Glinkowski, A. Greenwood, "Computer Simulation of Post-Arc Plasma Behavior at Short Contact Separation in Vacuum," IEEE Trans. on Plasma Science, Vol. 17, No. 1, pp. 45-50, February 1989.
7. M. Glinkowski, A. Greenwood, "Some Interruption Criteria For Short High-Frequency Vacuum Arcs, "IEEE Trans. on Plasma Science, Vol. 17, No. 5, p. 741, October 1989.
8. Advanced Continuous Simulation Language, Reference Manual, Edition 10.1, Mitchell and Gauthier Associates, Concord, MA, 1993.
9. M. Lindmayer, E.-D. Wilkening, "Breakdown of Short Vacuum Gaps After Current Zero of High Frequency Arcs," XIVth Intern. Symposium on DEIV, Santa Fe, NM, 1990.
10. E. Dullni, Private communication, 1993.

Boundary conditions and solutions stability in dynamics of cathode spots in vacuum arcs.

Nemirovskii A.Z. Emelianov A.A.

Institute of Electrophysics of Russian Academy of Sciences,
34 Komsomolskaya Street, Yekaterinburg 620219, Russia.

ABSTRACT

While one is trying to create the model of high speed charged particles flows from the cathode spot in vacuum arcs, the attention to be paid to the non-contradictory choice of boundary conditions system⁴. For example, in² the necessary amount of boundary conditions (BC) is set on the semisphere r_0 (cathode) independently of the problem solution in the electrode body. The values of parameters were chosen in correlation with that, from the experiments, or from some evaluations. But the local parameters in the vicinity of the cathode in the papers are obtained in the different experiments. Application of this data often leads to the solutions not corresponding to the cathode jet. From the viewpoint of¹ in the paper² the assumption that gas flow velocity on the cathode surface is equivalent to the sound velocity seems to be unjustified. Really, with the simultaneous solution of the problem in the cathode body and on the surface³, the equality of gas flow velocity v_2 on the right side of the gap to the sound velocity v_s leads to the solution nonequilibrium (Fig.1,2). The dynamic and energetic parameters show the nonequilibrium behaviour. Such mode in the deflagration area is well-known, but the attention paid to (for example⁴) impossibility of this mode in the experiments. It is quite clear, that this unstability connected with the nonequilibrium of the specific energy growth to the heat loss (due to fast mass erosion, transmitting the accumulated heat) ratio. It's interesting to note that the solution of the equations system in this model with the BC $v_2 = v_s$ (current value $J=1A$, current density on the cathode surface $j=4 \cdot 10^8 A/cm^2$) gives the nonequilibrium boundary solution. The reasonable values: initially $v_2 = v_s$ and then $v_2 < v_s$ corresponds to the really existing experimental results.

DISCUSSION

Using the results of calculations one can analyse possible BC, which define the medium state from the right side of the gap. In the most common case the conditions system on the hydrodynamic and electrodynamic gap may be described as⁵.

$$\begin{aligned}
\{\rho u\} &= 0 & m\{u\} + \{P\} - (1/8\pi)\{E^2\} &= 0 \\
m\left\{\frac{\gamma}{\gamma-1}\frac{P}{\rho} + \frac{u^2}{2}\right\} &= 0 & \{E\} &= 4\pi\sigma_P \\
\{p\} &= 0 & \{q(u+bE)\} &= 0 & m &= \rho u
\end{aligned} \tag{1}$$

Where ρ - the environment density, q - spatial charge, u - velocity component normal to the gap front, P - pressure, E - electric field strength component normal to the gap front, φ - potential, σ_P - surface charge, b - agility factor, γ - specific heat capacities ratio. Equations (1) are valid in the coordinate system, where the tangential velocity component is equal to zero, the figure brackets means the parameters values difference before and after the gap. In the text below the values before and after the gap would have the indexes 1 and 2, respectively. Define the dimensionless parameters:

$$\begin{aligned}
P &= \frac{P_2}{P_1}; \quad V = \frac{V_2}{V_1}; \quad L = \frac{E_2^2 - E_1^2}{8\pi P_1}; \quad M_k = \frac{u_k}{a_k}, \quad k = 1, 2 \\
\Pi &= 1 + \frac{1}{\gamma M_1^2} - \frac{L}{\gamma M_1^2}; \quad \beta = \frac{\gamma-1}{\gamma+1} + \frac{2}{(\gamma+1)M_1^2}; \quad a_k^2 = \frac{\gamma P}{\rho k}
\end{aligned} \tag{2}$$

The value L is connected with the surface charge σ_P by the equation $L = -\sigma_P^{-1} (2\pi\sigma_P + E_1)$, and besides $L \leq E_1^2 / (8\pi P_1)$ independently of σ_P . Write down the second and the third expressions as:

$$P = -\gamma M_1^2 V + (1 - L + \gamma M_1^2) \tag{3}$$

$$\frac{\gamma}{\gamma-1} (PV - 1) + \gamma \frac{M_1^2}{2} (V^2 - 1) = 0 \tag{4}$$

excluding subsequently from equations (3,4) P and M_1^2 one can obtain

$$V_{\pm} = \frac{\gamma\Pi}{\gamma+1} \left\{ 1 \pm \left[1 - \frac{(\gamma+1)^2 P_1^2}{(\gamma\Pi)^2} \right]^{1/2} \right\} \tag{5}$$

$$P = \frac{\gamma-1}{\gamma+1} (L-1) + \frac{2\gamma}{(\gamma+1)^2} [(\gamma+1)L + 2] \left(V - \frac{\gamma-1}{\gamma+1} \right)^{-1} \tag{6}$$

The nonnegativity of expression under the root in the right side of the formula (5) restricts the parameters before the gap front (from the left side of the gap) (M_1, P_1, E_1), defining the existence of stationar flows with the above type gap. With $\Pi > 0$ from (5) we have

$$L \leq 1 + \beta^* M_1^2, \quad \beta^* = \gamma - (\gamma+1)\beta^{1/2} \tag{7}$$

With $\Pi < 0$ the values V_{\pm} in equation (5) are negative, that's why this case has no physical reason. The equal sign in (7) corresponds to the following conditions:

$$V_+ = V_- = \frac{\gamma\Pi}{\gamma+1}, \quad P_+ = P_- = \frac{\gamma\Pi M_1^2}{\gamma+1}$$

This case the flow velocity behind the gap front is equal to the sound speed (Juge wave), because Mach is $M_2^2 = M_1^2 V P^{-1} = 1$

If $L < 0$ then the equations (5), (6) always have two different real solutions. With $L = 0$ ($\sigma_P = 0$) the electric field is persistent on the gap and the expressions (5), (6) can be reduced to the common gasodynamic equations Gugonio for the impact wave. Expression (6) gives the system of impact adiabates, depending on parameter L for electrohydrodynamic gaps with the given value of σ_P . On Fig. 3, 4 the probable cases of the impact adiabat location in the PV plane are shown. The adiabat is the hyperbole with asymptots I and II which can be described with the equations:

$$P = \frac{\gamma-1}{\gamma+1} (L-1), \quad V = \frac{\gamma-1}{\gamma+1}$$

Fig.3,4 correspond to the $L>1, 0<L<1$ intervals. The points of cross between the hyperbole and the straight, which is given by the equation (3) of the impulse preservation law, and passing through the point $A(1;1-L)$. Coefficient $(-; M_1^2)<0$, that's why one can reach only the parts DC and D'C' situated on the same or different parts of hyperbole (6). The exception is the existence of the reachless part D'C' of lower branch of hyperbole in case of $L>1$ (Fig.3), as a result of condition $M_1^2>L-1$ with $\Pi>0$ (on this branch in the area $V>0$ always $P<0$). For gases the physical essence is only in the adiabat parts, situated in the area $V>0, P>0$ of PV plane. It should be noted, that the parts DF, where $P>1, V>1$ simultaneously ($L>0$), (Fig.3,4) and D'F where $V<1, P<1$ ($0<L/(1-\gamma)$) can't be reached with any parameter values. The straight $P=M_1^2 V$, corresponding to the $M_1=1$, divides the area $P>0, V>0$ into two parts. The first, where $M_1<1$ (above the straight), and the second, where $M_1>1$ (under the straight). Define $(P^*; V^*)$ as the point of cross between the straight $P=M_1^2 V$ and the straight (3). $(P^*; V_a^*)$ is the cross coordinates between the straight $P=P^*$ and the upper branch of hyperbole (6). $V_a^*\leq V^*$ is always right, when inequality (7) is fulfilled.

In the case of $L>0$ check up the adiabat (6) part DC located in the $P>1, V>1$ area. Fig.3,4 show that the slope angle α of the secant from A point to the any point of adiabat on the DC part related to the absciss axe can't be less than the α_0 angle of tangent AB. As $\tan(\alpha)$ is equal to the γM_1^2 coefficient, the mass flow through the gap surface $m=M_1(\gamma P/q_1)^{1/2}$ can't be less than some limit. The same situation appears in gasodynamics. In the contact point B, Mach behind the impact wave is $M_2=1$, and the secant location corresponds Mach before the gap front (left) $M_1^2=P/V>1$, because in the point B: $P>1, V>1$. From this fact and considering that for the rest points of CD part $\alpha>\alpha_0$, one can obtain that $M_1>1$ in adiabat points on the CD part. In the B point the inequality is fulfilled $dM_1/dP<0$, where the derivation is made with fixed q_1 . With $M_1>M_1^*$, where $M_1^*=\gamma^{-1/2} \arctg(\alpha_0)$ the $(V;P)$ point corresponds to the concentrating shifts like $M_1>1, M_2<1$, the $(V;P)$ point - to the shifts like $M_1>1, M_2>1$.

Fig.4 shows that with $0<L<1$ one can find reachless part of adiabat D'C', the fragment of which D'G (including the B' contact point) located in $P>0, V>0$ area. This fragment corresponds to the disconcentrating shifts, as if here $V>1, P<1$. Similar to the above, $M_1=1, M_2<1$ is in the B' point, in the D'B' points: $M_1<1, M_2<1$. On the B'G part: $M_1<1, M_2>1$. The mass flow through the gaps of this kind is limited as in the previous case. With $\alpha<\alpha_0$ point $(V;P)$ gives the disconcentration shift, where $M_1<1$ and $M_2<1$; point $(V;P)$ - the shift, where $M_1<1, M_2>1$ as it is in the calculations on Fig.1,2. In the case of $L>0$ the normal component shift of the impulse flow $\Delta\Pi<0$. The Gugenio adiabat is situated under the adiabat (6), and the material compression in the electrodynamic concentrating shifts of $M_1<1, M_2<1$ kind with the same Mach M_1 is smaller than that in gasodynamic. The calculations also approve this fact.

CONCLUSION

Based on the previous analysis one can confirm, that the value of emitted mass (on the right side of hydrodynamic and electrodynamic gap, the last includes the nonequilibrium) is restricted up and below. That restriction depends sharply on the BC system choice. As a result the right choice of BC system is impossible without the simultaneous solution in the cathode body, on its surface and in plasma jet in the vicinity of the cathode.

REFERENCES

1. Beilis I.I., Zexcer M.P., Lubimov G.A. J.Tech.Physics vol.58, no.10, 1988, p.1861 - 1870.
2. Moijes B.J., Nemchinsky V.A. J.Tech.Physics vol.50, no.1, 1980, p.78-86.
3. Nemiróvskii A.Z., Puchkarev V.F., Tarbeev O.I. 15th International Symposium on Disch. and Elec. Insulation in Vacuum.(Darmstadt) 1992 p.339-344.
4. Cherny G.G. "Gas dynamics", Moscow, 'Science' 1988, 421 pgs.
5. Gogosov V.V., Polyansky V.A. PMM vol.35, no.5, 1971, p.761-772.

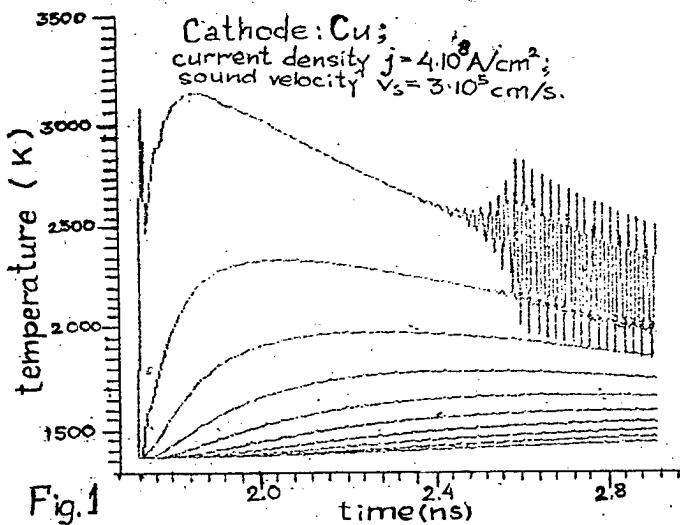


Fig.1

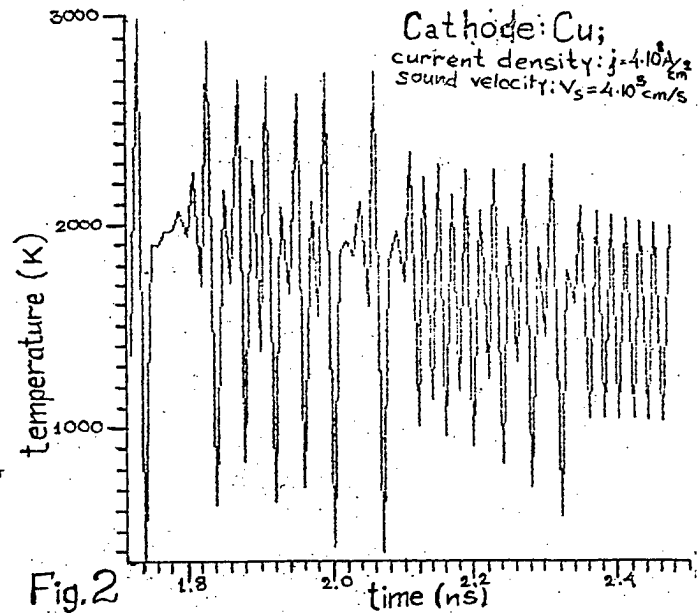


Fig.2

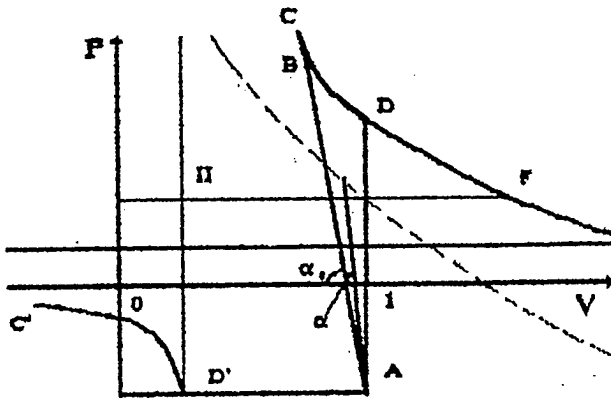


Fig.3 Impact adiabat in $L > 1$ case

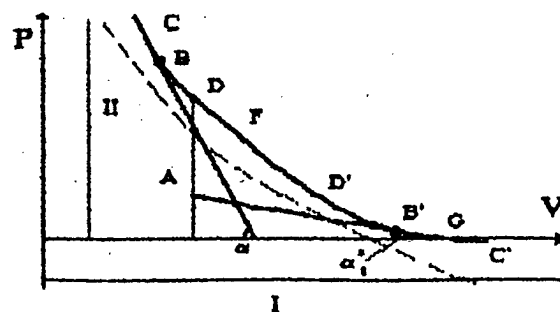


Fig.4 Impact adiabat in $0 < L < 1$ case

Experimental and Theoretical study of the Temperature of a Hot Anode Vacuum Arc

H. ROSENTHAL, I. BEILIS, S. GOLDSMITH and R.L. BOXMAN

Electrical Discharge and Plasma Laboratory
Tel-Aviv University, P.O.B. 39040, Ramat-Aviv 69978, ISRAEL

ABSTRACT

Heat transfer to a thermally isolated graphite anode in a long duration vacuum arc was investigated. Anode bulk temperatures were measured as a function of time using two high temperature thermocouples. The anode surface temperature was optically determined. Surface temperatures of 2300 K were obtained in a 340 A arc. A one dimensional non-linear heat flow model for the anode was developed. A solution was obtained using a dynamic numerical method and the effective anode potential was determined to be approximately 6 V.

1. INTRODUCTION

The hot anode vacuum arc (HAVA) is a long duration electrical discharge between electrodes in vacuum ambient, in which the anode is thermally isolated. Vapor evaporated from the hot anode may play a significant role in the discharge process. In some cases, the anodic plasma plume can prevent the cathodic plasma jets from reaching the anode (1), and there are some reports that the cathode spots may even disappear (2). The HAVA is of interest both fundamentally and practically, because it serves as a physical model of the more complex transient anode spot vacuum arc mode which causes rapid electrode destruction and limits the interruption ability of vacuum arcs, and because of its applications in depositing metal vapor coatings (3) and in synthesizing macroscopic diamond crystals (4). While it is obvious that the anode surface temperature plays a decisive role in determining the characteristics of the discharge, through its control of the anodic evaporation rate, only little quantitative information is available in the few published works on the HAVA discharge. The objectives of this work are to measure the anode temperature as a function of time, to establish a model for the heat transfer in the anode, and to formulate a theoretical model for the energy flow into the anode.

2. EXPERIMENTAL SETUP AND PROCEDURE

2.1. Vacuum Chamber and Electrode Assembly

The arc was run in a cylindrical stainless steel chamber 500 mm long and 160 mm in diameter, inside which the two electrodes are mounted. The chamber is pumped down to a pressure of 10^{-5} torr, by an oil diffusion pump and a conventional mechanical pump, before arc initiation. The arc was run at currents of 175 and 340 A, sustained by a 100 kw dc power supply, for periods up to 200 s. Arc voltage and current were measured using a resistive voltage divider and shunt. Their signals were presented and stored using a personal computer, equipped with a data acquisition card. Several runs were conducted for each experiment in order to check the reproducibility of results, and observe its statistical scatter. The cathode-anode assembly is shown schematically in fig.1. The cathode is attached to a water cooled, 30 mm diameter, copper cylinder.

The cathode had a disc shaped protrusion of 10 mm diameter and 5 mm height, to enable the operation of the mechanical trigger. It also ensured that the discharge was initiated near the axis of the electrodes.

The anode assembly is shown in fig. 2. The anode (1) is a graphite cylinder (DFP-1 POCO Graphite Inc.) of 32 mm diameter and 30 mm height. The anode surface (4) facing the cathode is beveled by less than 5 deg to allow spectroscopic observation of its surface. Two Mo radiation shields (5) surround the anode to reduce radiative heat losses. As we shall show below the radiation flux through the outer shield is negligible. A tungsten stem (6) closes the electrical circuit. The anode bulk temperature is measured with two high temperature thermocouples (2 and 3). The thermocouple wires were made of W-5%Re and W-26%Re alloys and are welded at their tips. The thermocouples are placed 5 mm and 25 mm below the anode surface, as shown in fig. 2. The thermocouple wires, insulated from the arc by ceramic tubes,

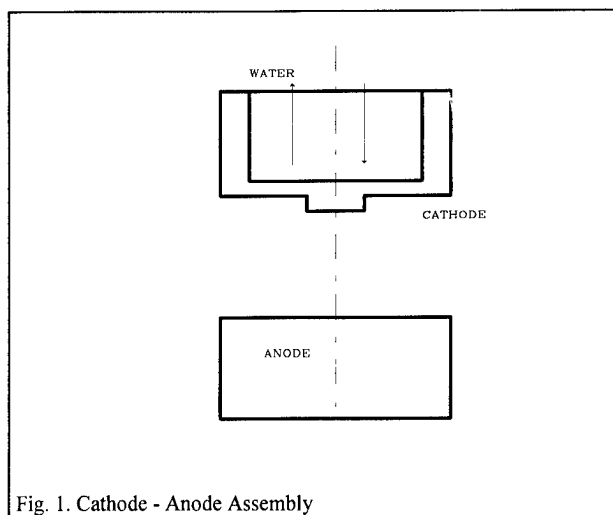


Fig. 1. Cathode - Anode Assembly

extend outside the vacuum chamber and were connected to copper leads. These leads and the "cold" junction are at uniform room temperature and do not contribute to the generated EMF (5). The response time of the thermocouple was determined to be less than 0.1 s. The thermocouple that is located close to the upper anode surface is connected to an isolated transmitter (TCT-4 CONLAB, Israel) which is a 4 wire system that converts the thermocouple voltage into a standardized load-independent linear signal, with a CMRR (common mode rejection ratio) of 132 db and a time response of 320 ms (0-98%). The transmitter has electronic cold junction compensation. The linearity, calibration and transmitter gain have been also determined by recording the input and output signals while the thermocouple sensor tip was placed inside pure Sn at its melting point, and in boiling water. The gain of the transmitter was $G=135\pm2\%$.

The transmitter amplified signal was sampled by the data acquisition card at a rate of 1-2 Hz, and presented and stored by the PC mentioned above. No higher rate is required in this experiment. The overall experimental temperature accuracy was better than 3%.

The second thermocouple was connected directly to a DVM (digital multi-voltmeter). The DVM reading was corrected to match cold junction room temperature. In some experiments both thermocouples were located 5 mm below the anode surface diametrically opposed positions. Differences in their readings could arise from nonuniformity over the anode surface of the incoming flux. The difference between the two signals was less than 5% at lower temperatures, i.e. for the first few seconds after arc initiation, and less than 1% for higher temperatures. The factor limiting temperature measurement accuracy was its fluctuation.

2.2. Anode surface temperature

The anode surface temperature was determined by measuring the specific intensity, using a monochromator in the near IR. The radiometric method applied allowed us to obtain both temporal, and spatial distribution of the anode surface temperature, T_a , across a chord along the anode surface. The optical detection system (see fig. 3) was calibrated to measure the absolute specific intensity using a calibrated tungsten ribbon lamp. The 5° bevel in the anode surface allowed the imaging of a selected region on the anode surface onto the entrance slit of the monochromator. The band pass of the monochromator in this case was 0.8 Å, while the monochromator resolution was 0.3 Å.

A CCD (charge coupled device) black and white TV camera (HCS model MX-5) was placed at the exit focal plane of the spectrograph, and recorded the radiation intensity across the anode surface. The radiation intensity from the anode surface was determined at preselected wavelengths where no spectral lines are radiated by the arc plasma, and where continuum radiation from the arc is negligible. The camera video signal output was recorded by commercial VCR (Sony SLV-X55ME). The images were converted to a digital signal and analyzed with a PC using a commercial frame grabber digitizer, DT2851. The intensity scale of the digitized images is given by 256 gray levels. With a fixed camera gain (20db), the pixel values are directly proportional to the radiation intensity, within the CCD's dynamic range. The dynamic range of the system was determined by use of a set of gray filters, whose density changed in steps of

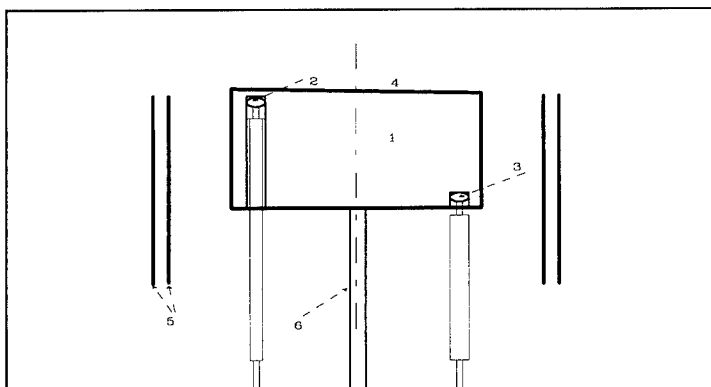
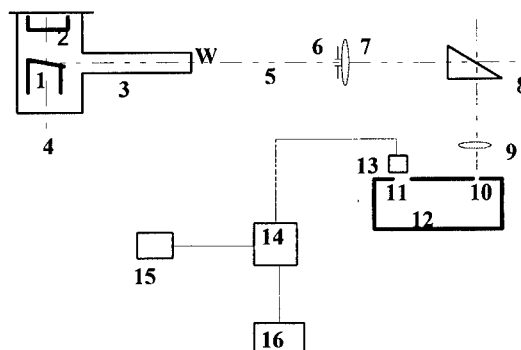


Fig. 2. Anode Assembly: (1) Anode. (2) TC-u, (3) TC-l, (4) surface. (5) Radiation Shields. (6) W-stem.

Fig. 3 Optical System. 1-anode. 2-cathode. 3-vacuum chamber. 4-arc axis. 5-optical axis. 6- pupil. 7-lens. 8-prism. 9-lens. 10-spectrometer entrance slit. 11-spectrometer exit focal plane. 12-spectrometer. 13- ccd tv camera 14-image processor/pc. 15-vcr. 16- monitor.



0.1D. The time resolution of the intensity measurement was 40 ms, while the spatial resolution was 0.15 mm along the imaged chord and 3.7 mm across it. The lower limit for detection was 1400 K.

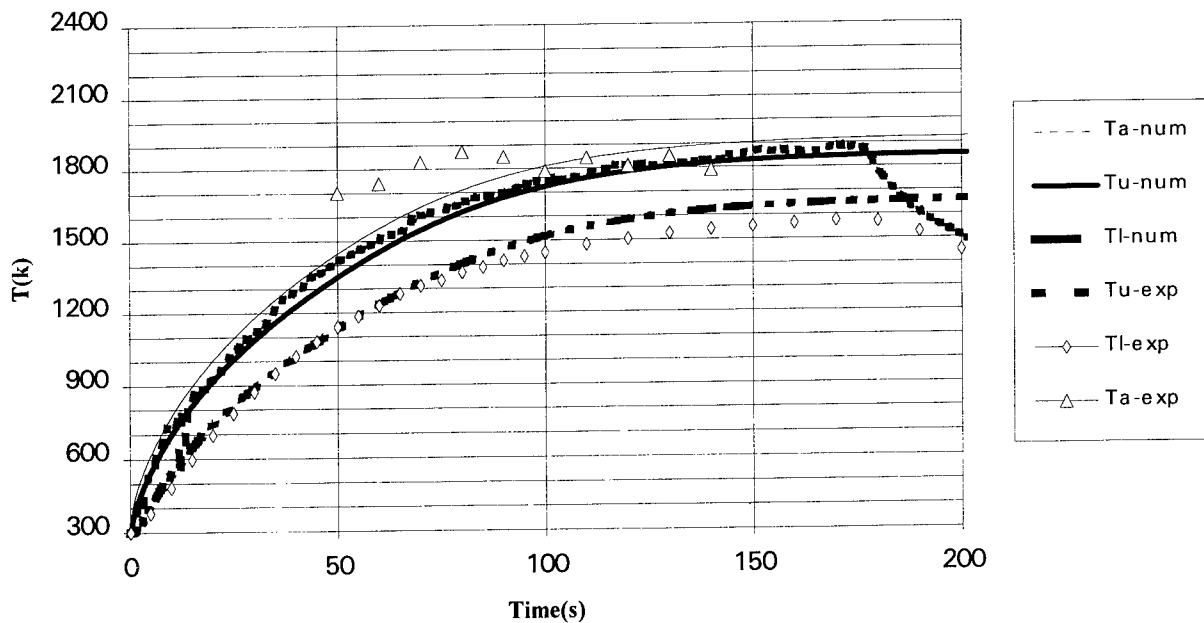
The anode surface temperature was determined by assuming that the graphite radiation intensity closely approximates that of black body, but with (known) spectral emissivity $\epsilon_{\lambda G}$. In the final analysis T_a is expressed as a function of the pixel value of the recorded signal. Designating by P_{VT} and P_{VG} the pixel values corresponding to the tungsten lamp signal and the graphite signal, respectively, at 7500 Å, we obtain an expression for T_a . The value of $\epsilon_{\lambda G}$ is given by the graphite manufacturer.

3. RESULTS

3.1. Temperature measurements

The time dependence of T_a , anode surface temperature, T_u , the temperature measured by the upper thermocouple, and T_l , the temperature measured by the lower thermocouple are presented in figs. 4-5. Model calculated temperatures (see sec. 4) are shown as well. The data of fig. 4 corresponds to arc current of 175 A, while the data of fig. 5 were obtained with a 340 A arc. In both figures the upper curve gives the surface temperature measured radiometrically. The middle curve corresponds to T_u , while the lower curve gives T_l .

Fig.4. Experimental and Calculated Temperatures. 175 A



The model calculated temperatures are shown in the same order. In both cases the measured temperatures reach a steady state. In both figures the cooling process of the anode after the interruption of the arc is also shown. The temperature measurements were highly reproducible. When the two thermocouples were located at the upper position (not shown), both thermocouples readings increased with time at the same rate, reaching approximately the same steady state temperature at approximately the same time.

4. THEORY OF THE HEAT FLOW IN THE ANODE

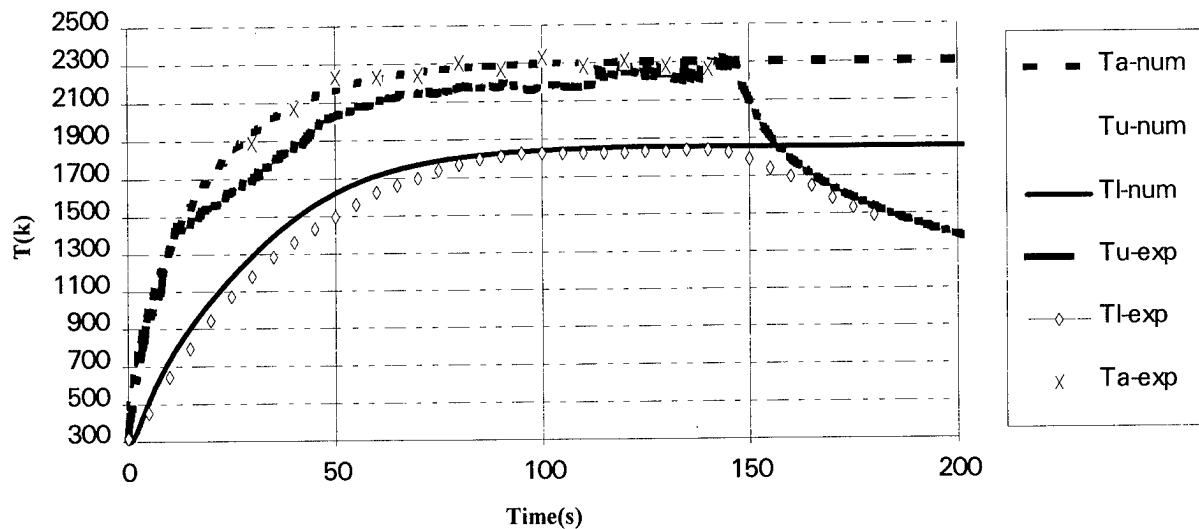
In this section we develop a heat flow model for the anode of the HAVA, using the basic heat conductivity equation. The model results will be compared with the experimental results.

4.1. Thermal model and main assumptions

A solid cylindrical anode with diameter d and length L , and surrounded by two radiation shields, as described above, is assumed. Anode radiation losses are mainly from the upper and lower surfaces of the anode. The radiation shields reduce

markedly the radiative losses from the side surface of the anode. However, we have included in the model losses from the side surface by radiation through the gaps between the upper surface of the anode and the upper end of the inner shield, as well as through the shields. In some of the calculations conduction losses through the tungsten stem are also considered.

Fig.5 - Experimental and Calculated temperatures. 340 A



The upper surface of the anode is subjected to an incoming heat flux from the arc, and specifically from the incidence of cathode plasma jets. Since there may be several cathode spots moving randomly over the cathode surface, each producing a plasma jet, a nonuniform and fluctuating heat flux at the anode surface may result. However, because of the relatively short period of the fluctuations we assume in the model that q_i (the incoming flux) is uniformly distributed over the anode surface, i.e. the model incoming heat flux q_i is the effective average of the incoming flux, and it may vary slowly due to the change in the average arc voltage and other arc conditions. The anode is also heated by the arc current flowing through it and loses heat by atomic evaporation. Conduction losses through the tungsten stem will be neglected in the model.

4.2 Two dimensional steady-state model

The steady-state temperature distribution assuming cylindrical symmetry was calculated as a function of q_i using the shareware finite element computer program ELCUT. It was found that the radial temperature gradients were much smaller than the axial gradients, which justifies the use of a 1-dimensional model to be presented below.

4.2. One-dimensional transient model - mathematical formulation

As a consequence of the above 2-dimensional analysis we assume that the temperature T within the anode varies only with time and distance x from the upper surface. During the course of the arc, the temperature of the anode rises from room temperature to rather high values. In as much as the thermo-physical constants of the anode material vary with temperature, and heat losses are likewise dependent on temperature, the heat flow in the anode is governed by the following non-linear heat conduction equation and the appropriate boundary and initial conditions:

$$\rho(T)c(T) \frac{\partial T}{\partial t} = \lambda(T) \frac{\partial^2 T}{\partial x^2} + \rho_e(T)J^2 - \frac{4}{d} \epsilon \beta(x) \sigma_{SB} T^4 \quad (1)$$

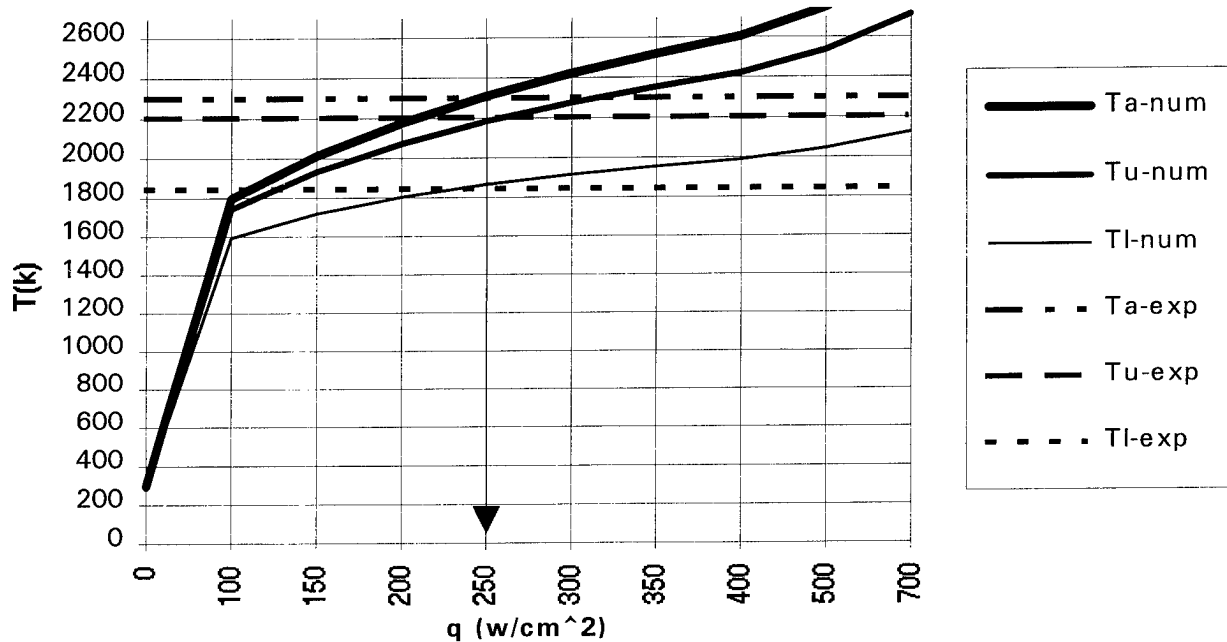
$$-\lambda(T) \frac{\partial T}{\partial x} = q_i(T) - q_{r0}(T) - q_{ev}(T) \quad \text{at } x = 0. \quad (2)$$

$$-\lambda(T) \frac{\partial T}{\partial x} = q_{rL}(T) \quad \text{at } x = L. \quad (3)$$

$$T(\mathbf{x}, t) = T_0 \quad \text{at } t = 0. \quad (4)$$

where ρ , c , λ , ρ_e and ε are anode material density, heat capacity, thermal conductivity, electrical resistivity and total emissivity, respectively, and where q_i , q_{r0} and q_{rL} are the temperature depended incoming heat flux, that flux radiated by the upper surface, and the flux radiated by the lower surface, respectively. The evaporated heat flux q_{ev} will be neglected. In this formulation conduction through the stem is neglected, but radiation from the side surfaces is taken into account in the last term in Eq. (1). The parameter β is a correctin factor which takes into account the fraction of the radiation flux which escapes from the sides of the anode via the gap between the anode and the radiation shield, as well as radiation through the

Fig. 6 - Temperatures Input-flux dependence . 340 A



shields, and J is the current density in the anode. In general, $\varepsilon\beta$ can be defined as: $\varepsilon\beta = \varepsilon F + \varepsilon_{eff}(1-F)$. In our case : $F = a \cdot \exp(-bx)$, where $a = 0.5$, $b = 0.8 \text{ cm}^{-1}$, $\varepsilon = 0.84$ and $\varepsilon_{eff} = 0.06$. In the above equation the flux radiated by the distant surrounding walls and absorbed by the anode has been neglected.

5. ANALYSIS

In this section the thermal model will be applied to analyze the experimental measurement of temperature in the anode. First, we shall study the steady state temperatures to derive the energy flux reaching the anode from the cathode. Second, we shall study the dependence of the measured temperature on time.

5.1. Steady State Analysis

In steady state the left side of equation (1) is equal to zero. The differential equation obtained in this way was solved numerically for different values of q_i , the incoming energy flux. It should be recalled that all parameters in that equation depend on T , making the problem non-linear. The dependence of the thermo-physical parameters on T was provided by the manufacturer for the whole temperature region, and to simplify the solution were very closely approximated by polynomial functions of T .

Fig. 6 presents graphically the dependence of the surface temperature T_a , as well as the temperatures at the thermocouple locations, T_u and T_l , on the input flux. The three horizontal lines represent the steady state temperature

measured when arc current was 340 A. The intersection of the horizontal lines with the appropriate temperature curves determines the energy flux to the anode, q_i . The obtained values of q_i show a very small scatter (1%). The total energy input is 2000 W, and $q_i=249 \text{ W/cm}^2$. The total energy flux to the anode for arcs running at 175 A was determined to be 1050 W, or $q_i=131 \text{ W/cm}^2$. The corresponding effective anode potential ($V_{\text{eff}}^a=q_i/I$) is calculated to be approximately 6 V for both cases. The calculated total energy flow to the anode is found to be in both cases to be approximately 27% of the arc power H , where $H=IV$, and where V is the arc voltage. The derived values of q_i is used to calculate the transient time dependence of T_a , T_u and T_l .

5.2. Time dependent analysis

In figs. 3-4 we present the temperature time dependence evaluated using a numerical solution, at the same three locations where anode temperature were measured in the experiments (T_s , T_u and T_l). These figures may be compared with the experimental measurements. It can be seen that the numerical and experimental results agree with each other, both during the transient phase and during steady state.

6. DISCUSSION

The effective anode potential determined here of 6 V is surprisingly low. Measurements in a cathode spot arc with a cold anode (5), as well as models for the multi-cathode-spot (MCS) arc (6), gave the effective anode potential as approximately 13 V minimum. The model for the MCS arc indicates that the anodic heat flux has two components, from depositing electrons and depositing neutral atoms, and it is assumed that every particle arriving at the anode deposits all of its energy therein (i.e. the coefficient of accommodation is unity). In the present experiment, however, the hot anode behaves quite differently than the cold anode in that it does not collect a coating. Clearly a new model of the interelectrode plasma, and in particular of the plasma-anode interface, which takes into account re-evaporation of any deposited cathode material, interaction of the re-evaporated cathode material, and/or reflection of incident ions from the hot surface, is required in order to understand the low effective anode potential determined here.

7. CONCLUSIONS

The isolated graphite anode reaches a steady-state temperature distribution in about 110 s for a 175 A arc, and in 80 s for a 340 A arc. In steady-state, the energy flux input is balanced mainly by radiation from the front surface of the anode, but radiation from the side surfaces through the space between the anode and the shields, as well as from the bottom of the anode, is not negligible. The effective anode heating potential is approximately 6 V. A model for the interelectrode plasma and the plasma-anode interface is needed to explain this result.

REFERENCES

1. R.L. Boxman and S. Goldsmith, "Momentum interchange between cathode-Spot plasma jets and background gases and vapor and its implication on vacuum arc anode spot development", *IEEE.Trans.Plasma.Sci.* **18**, 231-6, 1990.
2. A.M. Dorodnov et al., "New anode vapor vacuum arc with a permanent hollow cathode", *Sov. Tech. Phys. Lett.* **5**, p. 418-9, 1979.
3. H. Ehrich *et al.*, "The anodic vacuum arc.II. Experimental study of arc plasma", *J. Vac. Sci. Tech.* **A6**, p. 2499-503, 1988.
4. S. Goldsmith, H. Rosenthal, P. Avivi and R.L. Boxman, "Diamond growth in Hot Anode Vacuum Arcs", **4th** European conference on diamond, diamond-like and related materials, Portugal, 1993.
5. M.P. Reece, "The vacuum switch. Part 1: Properties of the vacuum arc", *Proc. IEE.* **110**,793-802, 1963.
6. R.L.Boxman and S. Goldsmith, "Model of the anode region in a uniform multicathode-spot vacuum arc", *J.Appl.Phys.***54**,592-602,1983.

On the Ion Potential Distribution of High Current Arcs in Vacuum

C. Rusteberg*, M. Lindmayer*, B. Jüttner**, H. Pursch**

* Institut für Elektrische Energieanlagen, TU Braunschweig,
Pockelsstrasse 4, D-38 106 Braunschweig, Germany

** Max-Planck-Institut für Plasmaphysik
Hausvogteiplatz 5-7, D-10 117 Berlin, Germany

With the experiments presented in this paper applications of a retarding field analyser (RFA) for the measurement of ion potentials U_i in a vacuum arc plasma are discussed. The ion potential is defined by the formula $U_i = E_i / (Z \cdot e)$ (E_i - ion energy, Z - ion charge number and e - electron charge).

The examined plasma was produced by a sinusoidal half-wave vacuum arc current. The experiments were concentrated on evaluating the plasma parameters at the last three milliseconds before current zero.

In a current range from 300 A_{rms} to 10 kA_{rms} the ion potential distributions and their peak values were evaluated. With the increase of the arc current a decrease of the ion potential was found. By additional investigations of the angular distribution of the ion energies, a transition from a collision dominated interelectrode plasma to a freely expanding plasma was observed, depending on the arc current.

1. INTRODUCTION

For currents below a few kA the vacuum arc is in a state of a diffuse arc mode with single cathode spots [1]. These spots are the source of metal vapor and electrons. Within the ionization zone in front of the cathode the metal vapor is ionized by the accelerated electrons. Due to the acceleration by the high pressure gradient, the friction between ions and electrons and the electric field the plasma ions expand with high kinetic energy from the cathode region to the anode [2]. Typically the ion current which flows opposite to the voltage polarity, lies in a range of 7% -10% of the total arc current [3].

One of the first measurements of the ion energy distribution was presented by Plyotto et al. [4]. They determined ion energies of low current stationary vacuum arcs for copper up to 70 eV by using a retarding potential analyser.

Davis and Miller [5] measured the ion energy distribution in a dc current range between 30 A and 250 A for various metals and also found potentials for the majority of the ions higher than the arc voltage. They used a combined mass and electrostatic energy analyser and found that the fraction of single charged ions increases with an increasing arc current. The peak values of the ion energy distributions shift towards lower energies as the current rises.

Other authors have also examined the angular distribution of the plasma ions. Kutzner [6] found an anisotropic ion flux for vacuum arcs caused by dc currents lower than 200 A which is directed to the anode. The angular distribution was described by an exponential function. Some authors [7,8] determined an angular distribution for current with an amplitude below 1 kA which follows nearly a cosine curve.

2. EXPERIMENTAL CIRCUIT AND RETARDING FIELD ANALYSER

All experiments were carried out in a synthetic laboratory circuit. The sinusoidal half-wave currents between 300 A_{rms} and 10 kA_{rms} were generated with an LC circuit. The frequency was about 50 Hz. These currents were switched off by the CuCr-75/25-contacts operating in a dismountable vacuum chamber with a pressure less than $5 \cdot 10^{-5}$ Pa. The contacts were opened mechanically shortly after current closing at a speed of 1.7 m/s. The diameter of the spiral contacts was 60 mm and the final contact distance was 12 mm. The arcing time was around 9 ms. The cathode was grounded and the stainless steel vessel of the vacuum chamber (fig. 1A) was floating during all the measurements. The measured potentials refer to the cathode potential. All mentioned arc currents are rms values unless otherwise specified.

The plasma parameters were measured by using a retarding field analyser RFA [17] as shown in figure 1B with a collector of 6 mm diameter, two removable grids and one aperture plate. The analyser housing was floating during all experiments.

For the determination of the ion potential with a retarding field analyser it is necessary to separate the plasma ions from the electrons. Therefore we used the metal grids G1 and G2 in figure 1B. The nickel wires of the grids had a diameter of $2r=0.02$ mm and the spacing between the wire axes was $d=0.1$ mm. The transparency calculated with the formula [9]

$$\delta_T = (d - 2r)^2 / d^2 \quad (1)$$

was 0.64.

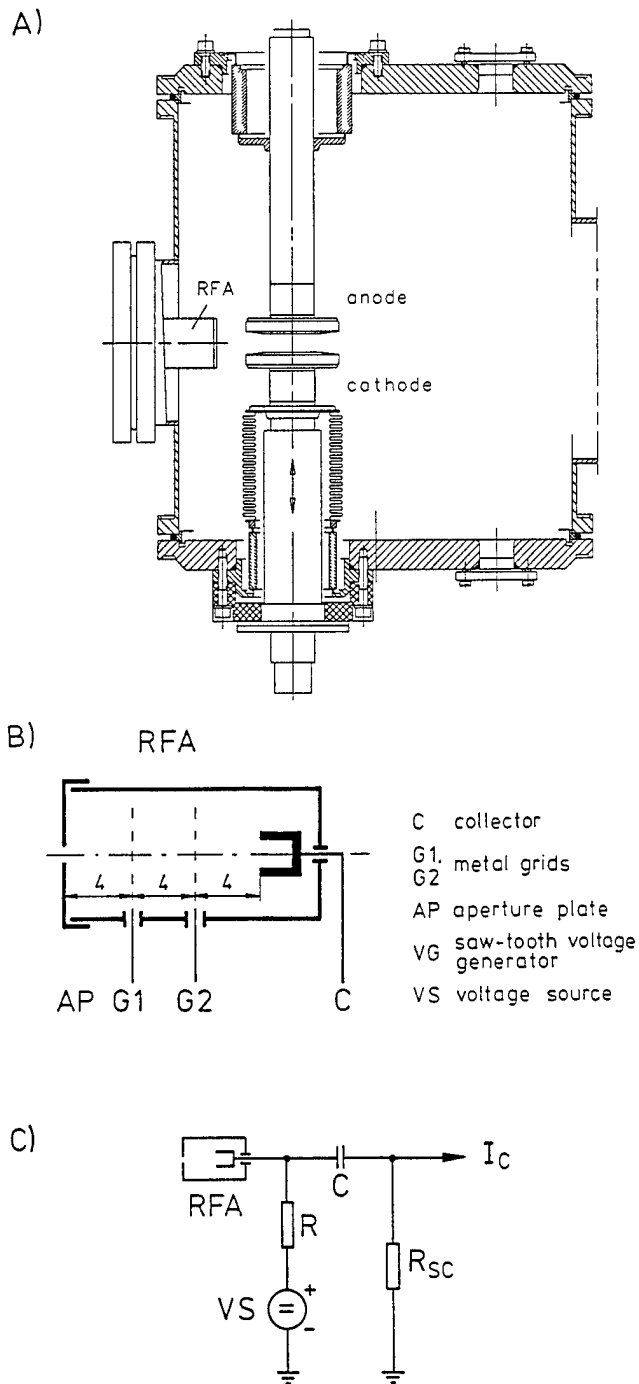


Fig.1. Cross section of the vacuum chamber (1A) and of the retarding field analyser RFA (1B), circuit diagram of the RFA (1C).

A voltage between 20 V and 50 V lower than the plasma potential U_p was applied at these grids, thus repelling the electrons by the electric field [10]. The spacing d between the grid wires is a very important value for an efficient separation [10]. It must not be larger than half the Debye Length :

$$d \leq \lambda_D/2 \quad (1)$$

with

$$\lambda_D = \sqrt{\frac{\epsilon_o k T_e}{2e^2 n_e}} \quad (2)$$

(ϵ_o - permittivity of vacuum, k - Boltzmann constant, T_e - electron temperature, e - electron charge and n_e - electron density). The electron density n_e increases with increasing arc current [12]. This means that for a grid with a given spacing d the plasma density resulting from equations (2), (3) must meet the condition

$$n_e \leq \frac{\epsilon_o k T_e}{8e^2 d^2} \quad (3)$$

In order to adapt the different plasma densities to this requirement for an optimal separation of ions from electrons, an aperture plate is used to reduce the plasma density. Its orifice diameter is varied, depending on the arc current. This diameter is much larger than the Debye Length, so that ion current density passing through the aperture remains unaffected and the charge carrier concentration within the RFA is proportional to the aperture area.

After the ions are separated from the electrons, they fly against the retarding field of the collector. The collector voltage U_c was changed in a range between -20 V and 100 V with respect to the cathode. The diagram for the collector circuit is shown in figure 1C.

The ion potential distribution was determined by measuring the ion current I_c and the collector voltage U_c which causes the retarding field for ions. A typical $U_c I_c$ -characteristic of the retarding field analyser is shown in figure 2. The curve is subdivided into three ranges :

- **Saturation area A:** The collector voltage U_c is much lower than the plasma potential U_p . Therefore all ions which reach the analyser housing are accelerated to the collector. The ion saturation current depends on the ion density n_i , the diameter of the orifice and the transparency of the electron retarding grids.
- **Transition area B:** The collector current I_c decreases strongly because the collector voltage approaches the plasma potential (ca. 20-30 V) and the ions are no longer accelerated towards collector. The plasma potential U_p was determined by Langmuir probe measurements.

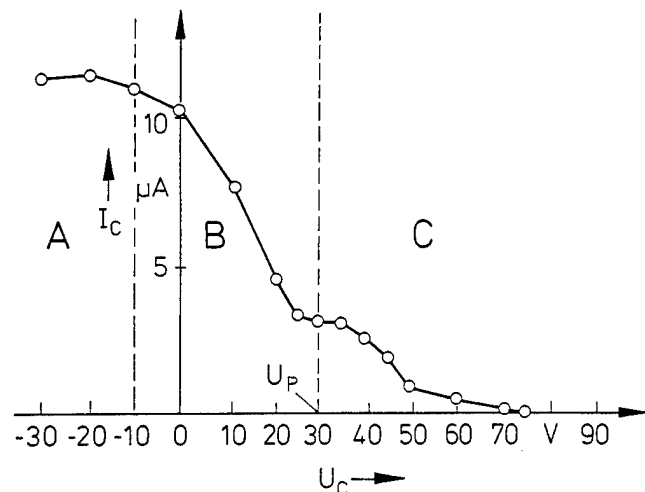


Fig.2. Typical $U_c I_c$ -characteristic of the retarding field analyser ($I = 1.75 \text{ kA}$, $U_{G1} = -10 \text{ V}$, $U_{G2} = -15 \text{ V}$)

- **Retarding area C:** The ions that fly to the collector with their drift velocity are repelled by the retarding field between separation grid 2 and the collector. In this case the collector voltage U_c is higher than the plasma potential.

Since the ions are not monochromatic, a retarding curve is obtained in region C. From the equations (ion potential $U_i =$ collector voltage U_c) [12]

$$I_c = c_1 \cdot \int_{E=e(U_c-U_p)}^{\infty} f(E_i) dE_i \quad (4)$$

$$E_i = U_c \cdot Z \cdot e \quad (5)$$

the distribution function $f(E_i)$ of the ion potential can be calculated by numerical differentiation

$$f(E_i) = \frac{1}{c_2} \cdot \frac{dI_c}{dU_c} \quad (6)$$

In the case of figure 2 the retarding field analyser was situated perpendicularly to the contact axis at a distance of 50 mm (19 mm from the contact rim) looking at the center of the interelectrode gap.

3. MEASURED RESULTS

3.1. The ion potential as a function of arc current

Typical curves of the collector current signal I_c at the last three milliseconds before current zero of a 1 kA arc are shown in figure 3. As expected, the ion current decreases with the decreasing sinusoidal arc current. The ion current is plotted for different collector voltages. Every point shown in the curve is the average of ten or more measuring points from separate identical experiments. The collector voltage U_c was changed in 5 V steps. For the last three milliseconds before current zero the measured points were evaluated in steps of 0.25 milliseconds. For the results in fig. 3 approximately 200 experiments had to be made.

The U_c/I_c -characteristic of the RFA for an arc current of 1 kA is shown in figure 4 for selected times during arcing. Obviously there are ions with higher potentials than the plasma potential of approximately 20 V. In the retarding part C of the characteristic an ion current signal was measured at the collector up to retarding voltages U_c of 60 V.

These U_c/I_c -characteristics were measured for different arc currents in a range between 300 A and 10 kA. Due to the changing orifice diameter of the aperture plate and the increasing plasma density, the amplitude of the ion current is varying. For a better comparison of the results the measured ion current is normalized to the ion saturation current I_0 at a collector voltage of 0 V for each curve.

By numerical differentiation of the standardized U_c/I_c -characteristics the ion potential distribution for the retarding part C was determined. In the saturation and transition part of the curves ions with potentials lower than the plasma potential are superimposed by accelerated ions. This acceleration occurs

between the electron separation grids and the collector for collector voltages below the plasma potential because of the negative grid voltages.

Figure 5 shows ion potential distribution functions for different currents at two milliseconds before current zero. It is obvious to see, that the ion potentials decrease for higher arc currents. For instantaneous current values higher than 8 kA the maxima of the potential distributions have nearly the value of the plasma potential. This means that the plasma ions of higher arc currents do not have the same high drift velocities like at lower currents. At the end of the arcing time the instantaneous values of the arc currents decrease and the maxima of the potential distributions grow up to higher values. This effect can be seen in figure 6. The curves show the maxima of the ion potential distribution versus the time during arcing for different currents. For example at an arc current of 2.5 kA the most frequent ion potential grows from 39 V up to 47 V during the last two milliseconds of the arcing time. As a reference the floating potential U_f of the plasma is also plotted in the figure 6. This potential is related to the plasma potential by [13]

$$\delta U = U_p - U_f = \frac{kT_e}{2e} \cdot \ln \frac{T_e m_i}{T_i m_e} \quad (7)$$

It is easier to measure the floating potential with a simple electric plasma probe instead of measuring the plasma potential, which must be evaluated by determining a complete Langmuir characteristic. In our case we found, that the floating potential is normally 5 V lower than the plasma potential.

The maxima of the ion potential distribution function for equal instantaneous currents of arcs with different 50 Hz rms currents show no significant differences (figure 7). Only a small decrease of the ion potential from 42 V to 39 V could be observed in an arc current range between 2.5 kA and 7.5 kA. This means that the ion energy follows the 50 Hz current nearly instantaneously compared to the time frame of milliseconds.

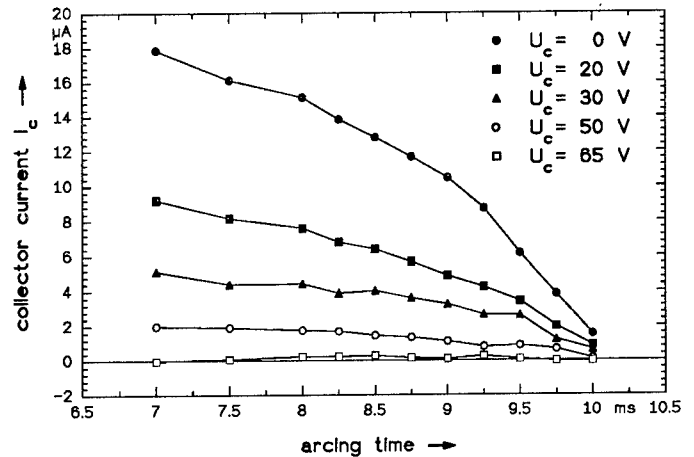


Fig.3. Collector current signal I_c at the last three milliseconds before current zero ($I=1$ kA)

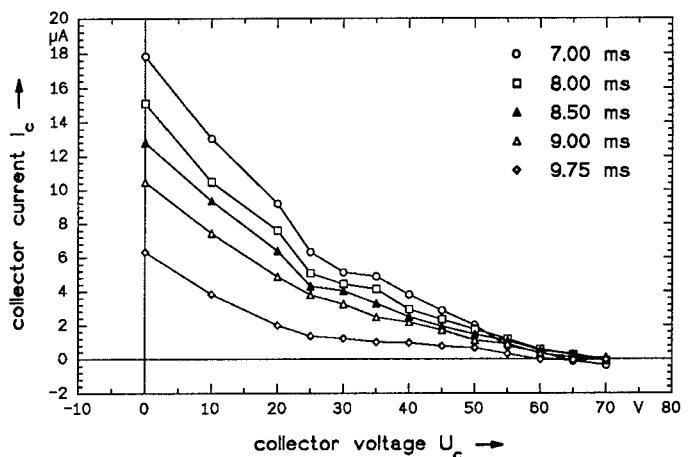


Fig.4. Collector current I_c versus retarding voltage U_c ($I=1$ kA)

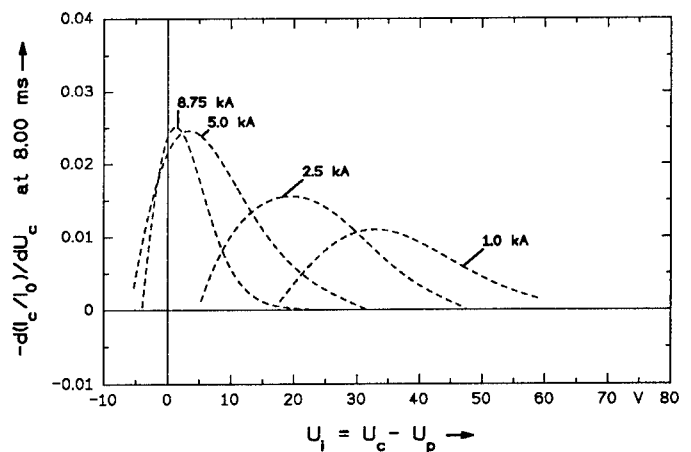


Fig.5. Ion potential distribution functions $f(U_i)$ for different arc currents at two milliseconds before current zero

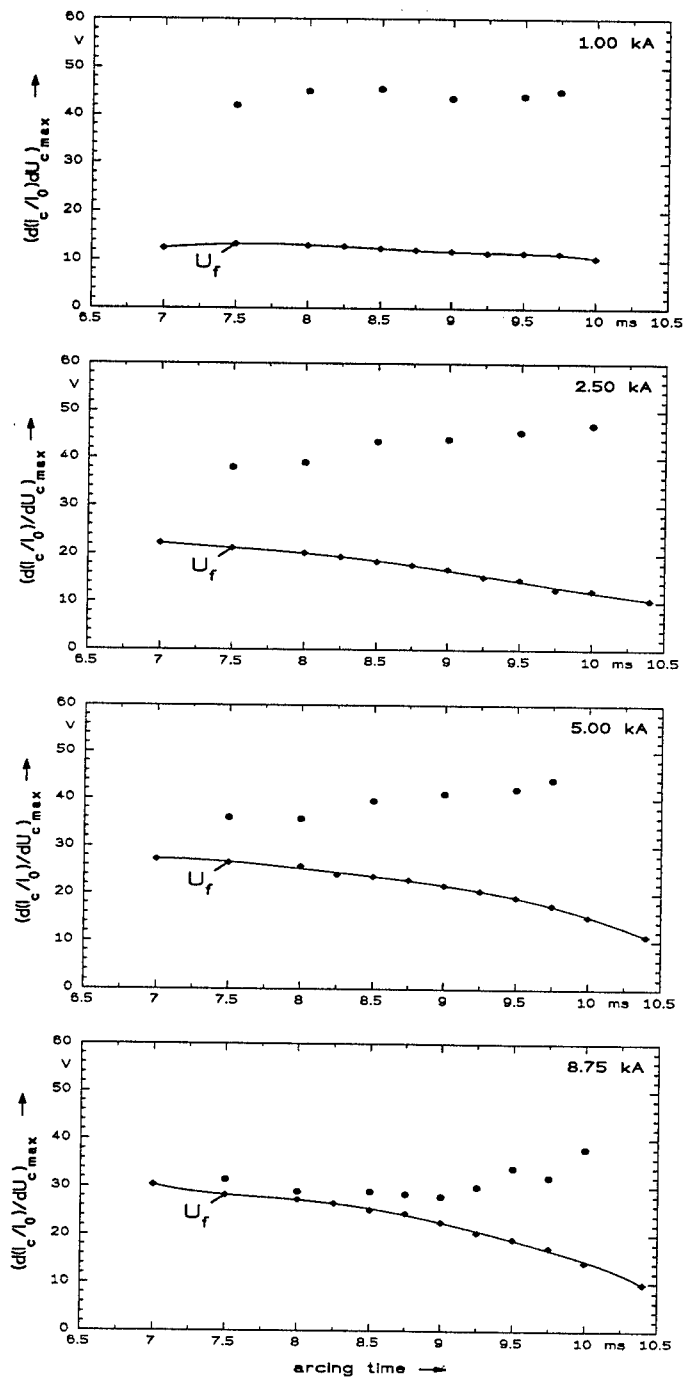


Fig.6. Maxima of the ion potential distribution function $f(U_i)$ versus time during arcing for different currents (floating potential U_f as reference)

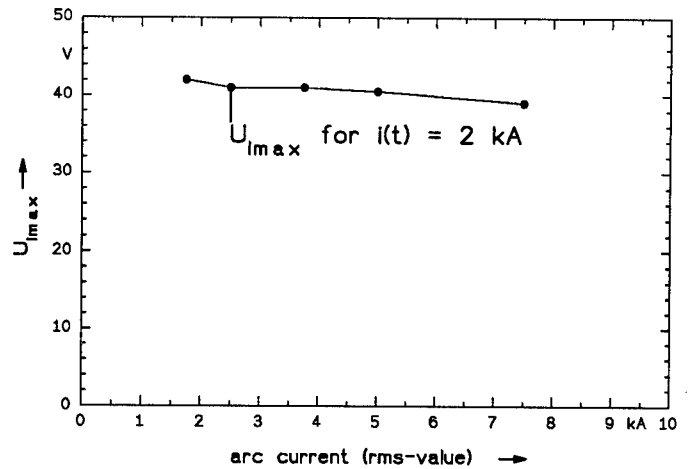


Fig.7. Maxima of the ion potential distribution function for instantaneous currents with different rms-values

3.2. Angular distribution

For the determination of the angular distribution the retarding field analyser was fixed at a constant distance of 50 mm from the axis in different angular positions in steps of 5° (figure 8). A positive angle means that the analyser looks onto the cathode. For all settings the ion saturation currents (figure 2, area A) were measured. All points are averages of 20 measurements.

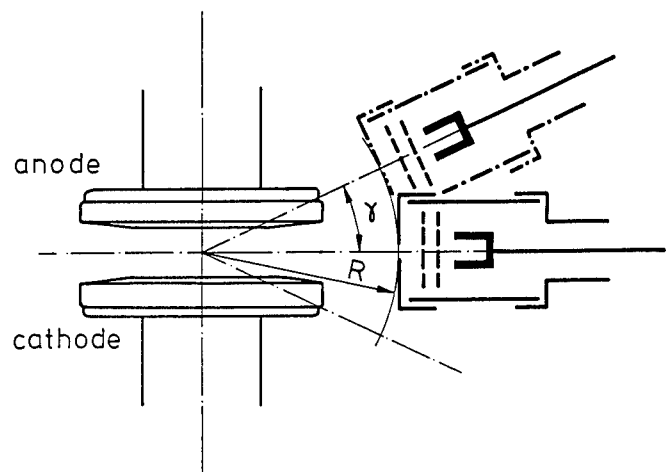


Fig.8. Measurement of the angular distribution; the analyser was fixed in a constant distance of $R=50$ mm in different angular positions γ in steps of 5°

For lower arc currents (time $t < 9$ ms, momentary current $i \leq 1.5$ kA) the maximum of the ion saturation current lies at $\gamma = 25^\circ$, from where the analyser looks towards the cathode surface. This is an indication that the ions that mainly emanate from the cathode spots are expanding towards the anode and radially outwards rather collisionlessly. For a momentary current of 3 kA ($t=7$ ms, fig.9) the maximum lies at $\gamma = 5^\circ$ which is nearly perpendicular to the contact axis. This effect is only possible if the plasma density has so considerably increased that collisions between the particles occur in the interelectrode gap. For 5 kA (fig.10) the alteration in the angular distribution happens later than for 2.5 kA, but the instantaneous arc current values are similar ($i \simeq 1.8$ kA).

4. DISCUSSION

The high ion potentials measured at lower ac arc currents ($i \leq 1$ kA) are in good agreement with measurements of dc vacuum arcs known from the literature [4,5]. But for higher ac current vacuum arcs a strong reduction of these high values was found. Considering the results of the angular distribution it seems that collisions between the plasma particles caused by the increasing plasma density are the reason for the decreasing ion potentials. For high arc currents the maximum of the angular distribution is perpendicular to the contact axis. This is only possible if the interelectrode plasma is collision dominated.

Boxman et al. [14] also characterized the plasma bulk as collision dominated in their multicathode-spot model (MCS), because they found that the electron mean-free path is shorter than the typical electrode scale length.

At lower instantaneous values of the arc current the plasma density and the probability of collisions in the interelectrode space decreases. Related to the same moment before current zero, the angular distribution indicates that the ion motion is much more directed to the anode and the ion potentials tends to higher values (fig. 6,9). Near current zero we found much higher ion potentials than at earlier times where the current was higher.

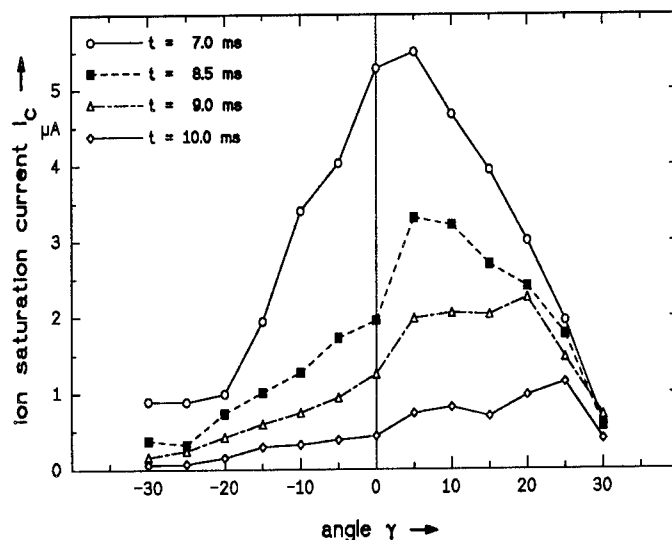


Fig.9. Angular distribution of the ion saturation current ($I=2.5$ kA)

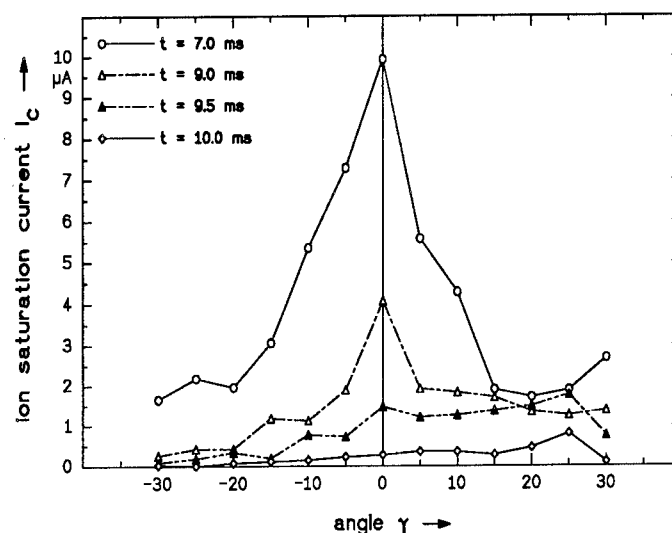


Fig.10. Angular distribution of the ion saturation current ($I=5$ kA)

As figure 7 shows, there is only a small reduction in the ion potential for the same instantaneous current at different rms currents. If the ion potential and the angular distribution is influenced by collisions in the interelectrode gap, this effect depends only on the plasma density. Investigation of the vapor density with laser-induced fluorescence showed that a delay time up to 0.8 ms exists between the arc current and the density maximum [15]. So the slightly falling curve in figure 7 can be attributed to such inertia. The RFA supplies no information about the masses of the plasma ions and the ion charge number. Investigations of Anders et al. [16] showed that the ion charge number is changing during short pulse vacuum arcs. For copper ions they found a decrease of the mean ion charge number Z from 2.6 down to 1.85 for the first 500 μs of a 100 A current impulse. With the definition of the ion potential (eq. 6)

$$E_i = U_i \cdot Z \cdot e$$

and under the assumption that these processes occur in a reversible way at current zero, the increase of the charge number Z would lead to higher ion energies. So this possible effect does not change the general tendency, found in our investigations with a retarding field analyser.

5. CONCLUSIONS

- For low sinusoidal arc currents ($i \leq 1$ kA) high ion potentials up to 60 V were found.
- A strong reduction of the ion potentials down to values near the plasma potential was determined for higher arc currents.
- Near current zero the ion potentials increase with the decrease of the arc current.
- The ion potentials tend to higher values in the same range of the arcing time, in which the direction of the ions changes from nearly perpendicular to the contact axis towards the anode.
- At arc currents below a momentary current $i \leq 1.8$ kA the maximum of the RFA ion saturation current lies at an angel which is directed towards the anode. This indicates that the plasma ions which mainly emanate from the cathode spots are expanding towards the anode and radially outwards rather collisionless.
- For higher momentary currents $i \geq 1.8$ kA the maximum of the RFA ion saturation current lies at an angel which is nearly perpendicular to the contact axis. This effect is only possible if the plasma density has so considerably increased that collisions between the particles occur in the interelectrode gap. In the literature, the current value for the transition collisionless-collisional is controversial. The present paper offers a simple experimental means for determining this value (about 1.8 kA for our conditions).

Acknowledgements

The authors gratefully acknowledge the support by the Deutsche Forschungsgemeinschaft DFG.

REFERENCES

- [1] Lafferty J.M. (Editor), Vacuum arcs - theory and application, John Wiley & Sons, New York 1980.
- [2] Hantzsche E., A simple model of diffuse vacuum arc plasma, **Contrib. Plasma Phys.** **30**, (1990) 5, pp.575-585.
- [3] Kimblin C.W., Erosion and ionisation in the cathode spot regions of vacuum arcs, **J. Appl. Phys.**, Vol. 44, No. 7, July 1973, pp.3074-3081.
- [4] Plyutto A., Ryzhkov V.N., Kapin A.T., High speed plasma streams in vacuum arcs, **Soviet Physics JETP**, Vol.20, No. 2, Feb. 1965, pp.328-337.
- [5] Davis W.D., Miller H.C.: Analysis of the electrode products emitted by dc arcs in a vacuum ambient, 1969, **J. Appl. Phys.**, Vol. 40, No. 5, pp.2212-2221.
- [6] Kutzner J., Miller H.C.: Ion flux from the cathode region of a vacuum arc, 1989, **IEEE Trans. Plasma Sci.**, Vol. 17, No. 5, pp. 688-694.
- [7] Lunev V.M., Ovcharenko V.D., Khoroshikh V.M., Plasma properties of a metal vacuum arc I, **Sov. Phys. Tech. Phys.**, Vol. 22, No. 7., pp.855-861.
- [8] Cohen Y., Boxman R.L., Goldsmith S., Angular distribution of ion current emerging from an aperture anode in a vacuum arc, **Proc. 13th Int. Symp. Disch. Electr. Insul. Vac.**, Paris 1988, pp.300-302.
- [9] Pitts R.A.: Ion Energy, Sheath Potential and Secondary Electron Emission in the Tokamak Edge, 1990, Thesis, Univ. of London.
- [10] Lindmayer M., Rusteberg C., Klajn A., Measurement of the plasma parameters of high current arcs in vacuum, **Proc. 7th Int. Conf. Switching Arc Phenomena**, Lodz (Poland), 1993, pp.326-332.
- [12] Ivanov V.A., Konyshov M., Anders S., Jüttner B., Pursch H., Sünder D.: On the Energy of Electrons and Ions of a Pulsed Metal Vapour Arc in Vacuum, 1990, Preprint 90-4, Akad. d. Wiss. der DDR, Zentralinstitut für Elektronenphysik.
- [13] Dosse J., Mierdel G., Der elektrische Strom im Hochvakuum und in Gasen, Verlag S. Hirzel, Leipzig 1945.
- [14] Boxman R.L., Goldsmith S., Izraeli I., Shalev S.: A model of the multicathode-spot vacuum arc, 1983, **IEEE Trans. Plasma Sci.**, Vol. PS-11, No. 3, pp.138-145.
- [15] Hayeß E., Jüttner B., Lieder G., Neumann W., Pursch H. Measurements on the behaviour of neutral atom density in a diffuse vacuum arc by laser-induced fluorescence (LIF), **IEEE Trans. Plasma Sci.** PS-17 (1989), p. 666-671.
- [16] Anders A., Anders S., Jüttner, B., Brown I.G., Time dependence of vacuum arc parameters, **IEEE Trans. Plasma Sci.**, Vol. 21, No. 3, June 1993, pp.305-311.
- [17] Prokopenko S.M.L., Laframboise J.G., Goodings J.M., Evaluation of an orifice probe for plasma diagnostics, **J. Phys. D: Appl. Phys.**, Vol. 5, 1972, pp.2152-2160.

The behavior of vacuum arcs between spiral contacts with reduced spacing

M. Bruce Schulman

Cutler-Hammer
200 Westinghouse Circle, Horseheads, New York, 14845

ABSTRACT

The use of reduced gaps in applications of high-current vacuum arc devices presents a number of interesting challenges. Specifically, standard contact designs have been developed over several decades to achieve controlled motion of high-current ac arcs in vacuum interrupters. For medium-voltage applications, the optimal maximum contact gap can typically range from about 6 mm to about 2 cm. However, the influence of the contact design may be gap dependent, so additional research may be appropriate if the contacts are to be used at smaller gaps. For example, the current through spiral contacts produces a magnetic field perpendicular to the arc column, but this will force the arc to move outward and run along the periphery of the petals only if a threshold separation is achieved. In this investigation, a framing camera was used to record the appearance and motion of drawn vacuum arcs between spiral-petal contacts with final gaps of 2 to 3 mm. After the rupture of the molten bridge, a high-pressure arc column formed and expanded across the width of the spiral arm. At the reduced gap, an intense anode spot formed if the peak current exceeded ~ 15 kA. Compared to results previously obtained at larger gaps, the arc motion was greatly reduced, and severe contact damage was observed at lower currents.

1. INTRODUCTION

The vacuum interrupter is widely established as the technology of choice for the many applications of medium-voltage switching from 5 kV to 38 kV. An overview of the theory of operation and the internal components of the vacuum interrupter is provided in Ref. 1, along with a description of the two main types of contacts used commercially for high currents. Both of these contact types use a self-generated magnetic field to control the drawn vacuum arc and promote its transition from the columnar mode to the diffuse mode. In the first type of contact, a magnetic field is impressed perpendicular to the arc column to force it to move rapidly around the contact surface. In the second type, an axial magnetic field is generated which forces the high-current arc to go diffuse within a few milliseconds after separation of the contacts.^{1,2}

Research on vacuum arcs continues to be important for the optimization of vacuum interrupters and the development of wider applications of the technology.³ In particular, the spiral contact design is widely used in commercial interrupters to promote motion of the high-current columnar arc. This work extends an earlier investigation of spiral contacts which resulted in plots of the characteristic arc appearance as a function of instantaneous ac current up to 70 kA peak and contact gap up to 8 mm.⁴ These *appearance diagrams* showed how current-gap space was divided into regions of diffuse or columnar arcing modes, and these were compared with previous results for drawn arcs on simple butt-type contacts⁵ and slotted cup contacts.⁶ Reports of the arc appearance in other experimental studies with spiral contacts have been more descriptive in nature.⁷⁻⁹

High-current columnar vacuum arcs were previously observed to run on spiral vacuum interrupter contacts for gaps greater than ~ 4 mm, and the spiral slots effectively promoted the transition to a diffuse arc by breaking up the moving column.⁴ This work presents detailed results from high-speed photographic and electrical analyses of high-current arcs at gaps of 2 to 3 mm. For gaps up to 3 mm the arc motion is limited, with the column moving less than half way around the contacts. The conditions which produced the limited arc motion are identified. These results can be compared to analogous studies of the hesitation time and minimum gap required for initial motion of high-current arcs in air on runner-type electrodes (see Ref. 10, for example).

2. EXPERIMENT

A diagram of the apparatus is shown in Fig. 1. The Cu-Cr contacts were mounted in a vacuum chamber which was operated at a base pressure of $\sim 10^{-4}$ Pa. The contacts were electrically isolated from the chamber, which was isolated from the circuit and ground. The upper contact was fixed, and the lower contact was attached to a stainless steel bellows. Motion of the lower contact was activated by a pulsed double-coil repulsion and latching actuator which provided an approximately linear opening speed. The stainless steel arc shield was 21 cm in diameter, and it was electrically connected to the chamber. It had a screen-

TABLE I
Experimental Parameters

Peak current I_p (kA)	7.70 - 36.3
Separation current I_s (kA)	7.70 - 29.0
Separation delay (ms)	1.0 - 2.2
Contact speed (m/s)	1.0
Maximum gap d (mm)	2, 3

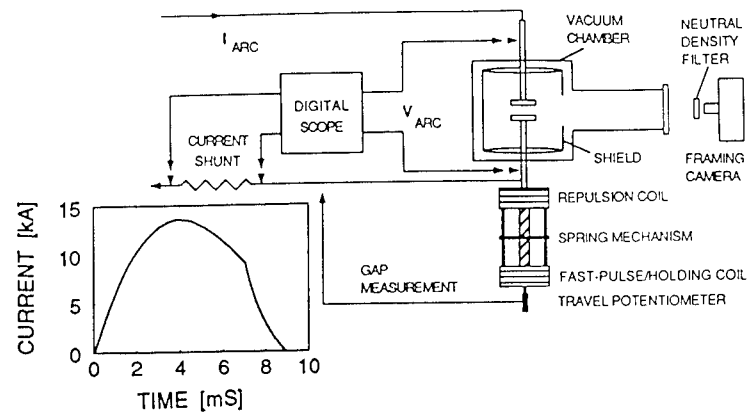


Fig. 1. Diagram of experimental apparatus and current waveform.

covered window for photographing the arcs with a framing camera at ~7000 frames per second. Table I gives the ranges of experimental conditions. A 420-V electrolytic capacitor bank supplied the arc current. A plotted current pulse is included in Fig. 1; it follows a 60 Hz waveform up to the crowbar at 7 ms. The 62-mm diameter contacts had four spiral arms and 4-mm wide slots⁴ (see Fig. 2), and were mounted with the arms of one overlapping the slots of the other. They were conditioned with a flowing, 100 W RF argon discharge, followed by repeated diffuse vacuum arcs at ~3 kA and several higher current arcs.⁴

3. RESULTS

The columnar vacuum arcs which formed over the range of currents investigated were not observed to move more than about one-half of the way around the gap's circumference. One or two *bridge column arcs*⁵ formed upon contact separation and then became anchored at nearby spiral slots. If only one column formed initially, a second column would sometimes appear and stick at another slot before the gap reached about 1 mm. In other instances, part of the arc would expand across the slot, split off and move away from the original column to the next slot. No arcing to the shield was observed for the tests with final gaps of 2 to 3 mm. Previously, at gaps of 4 mm or greater, more vigorous arc motion around the periphery of the contacts was observed, and arcing to the shield could be triggered as the running column passed over a slot and became unstable.⁴ Examples of movie frames from tests with a maximum gap of 2 mm are shown in Fig. 2. Intense anode activity and contact damage at the anchored arc roots are shown for cases with one or two columns.

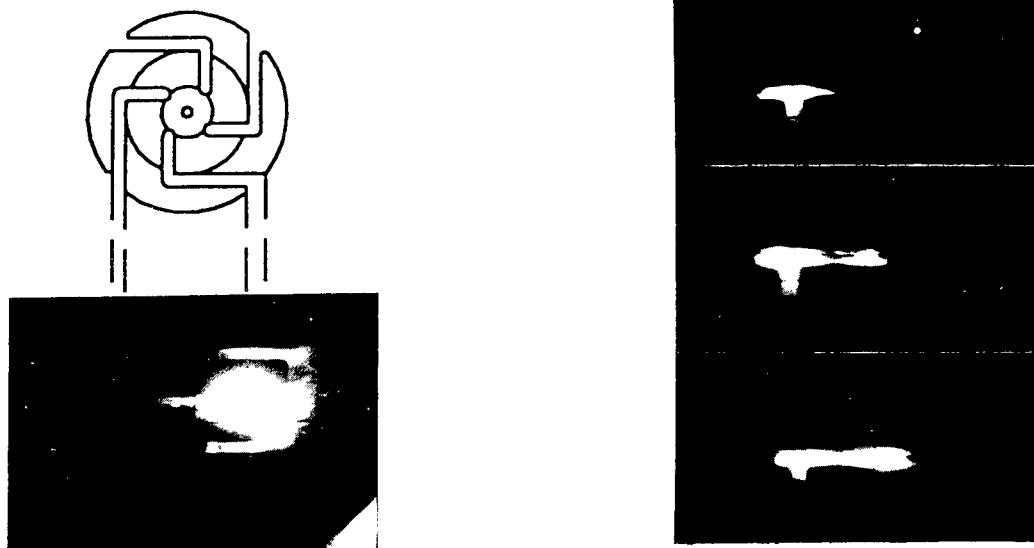


Fig. 2. Left: frame from a test with $I_p = 21$ kA, a full gap of 2 mm, and a single anchored bridge column. Molten contact material is visible as bright droplets ejecting to the right. The orientated view of the cathode contact is shown to the same scale. Right: three frames from a test with $I_p = 36$ kA, a full gap of 2 mm, and two parallel arc columns. The second column formed by splitting of the original bridge column at a cathode slot, as seen in the second frame.

On the left in Fig. 2 is a frame of a single column with $I_p = 21$ kA. There was no motion of the arc after the bridge column formed adjacent to a slot on the lower contact (cathode). Molten material is visible as bright droplets ejecting from the intense anode spot. The orientated top view of the cathode is shown to the same scale. The sequence at right was obtained from a test with $I_p = 36$ kA. The top frame shows an arc column anchored at a cathode slot 1.32 ms after the contacts separated with $I_p = 18$ kA. The second frame shows the column splitting at the slot 1.18 ms later. The second column became anchored at the next slot and developed an intense anode spot. The lower frame shows the arc after another 3.68 ms, during the interval of decreasing current. Dark molten material is seen falling from the anode through the center of the gap at the right-hand edge.

Figs. 3 and 4 show the ranges of peak current for which various arcing modes were observed. Fig. 3 was constructed for experiments with a single arc column from the time of contact separation until the current dropped and the arc went diffuse (at ~ 10 kA for $I_p \geq 29$ kA).⁴ With I_p less than about 13 kA, the bridge column arc transitioned directly to a *diffuse columnar mode*.^{5,11} During the time of a stable diffuse columnar mode, the anode discharge probably entered the footpoint spot mode.¹² For I_p higher than about 13 kA, the arc developed into a *constricted column*;⁵ i.e., the column boundaries became visibly well defined, and it was more constricted near the anode. Intense anode activity was identified by a glowing spot which continued after a column began to go diffuse. Of particular interest is the observation that intense anode activity was seen for currents above $I_p \approx 15$ kA, which is about 2 kA above the peak current for which the arc column began to constrict. No running arc motion was observed until I_p exceeded ~ 32 kA, at which point the column would begin to move away from the position where the initial bridge column arc formed to the tip of the spiral arm on which it was located. At that point, it would become anchored at the petal tip. For $I_p \geq 21$ kA, intense activity occurred which caused severe contact damage, with molten electrode material being visibly liberated from the anode spot. This degree of anode damage previously was not observed when the gap was increased to 4 mm or more, even for currents as high as 35 kA peak.⁴ This is attributed to the ability of the arc column to overcome the anchoring forces and run along the contact periphery and briefly attach to the shield.

For the experiments corresponding to Fig. 4, two parallel arc columns had formed before the gap reached ~ 1 mm. The parallel columns generally had about the same brightness when the current was near its peak. Constriction of the parallel columns was observed for $I_p \geq 29$ kA, consistent with the trend of the observations at larger gaps.⁴ As judged by the relative brightness of the columns, the current transferred increasingly into one column as the current decreased to zero. This can explain why intense anode activity was observed near the end of the cycle for $17 \text{ kA} \leq I_p < 29 \text{ kA}$, even though the parallel arcs retained a diffuse columnar appearance. Although the instantaneous current in the longer-lived parallel column was not large enough to cause it to constrict, a high rate of heat input was maintained as the other column became unstable and extinguished first. This suggests that the onset of intense anode activity depends on integrated heating. On the other hand, the threshold peak current for ejection of molten material from the anode was significantly increased above the corresponding level for one arc column.

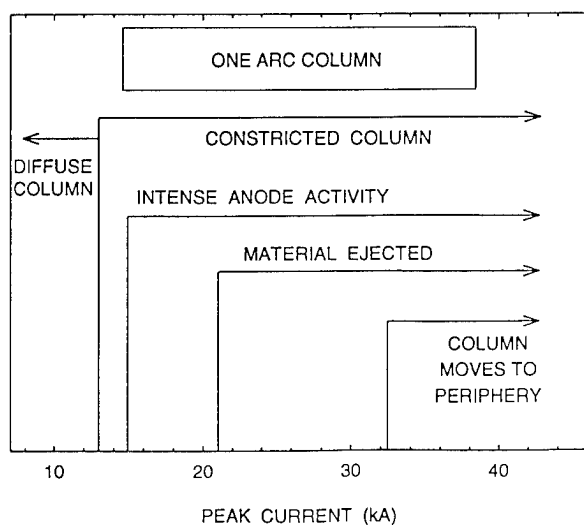


Fig. 3. Ranges of peak arc current for the observed appearance of various arcing modes with a full gap of 2 mm and a single arc column.

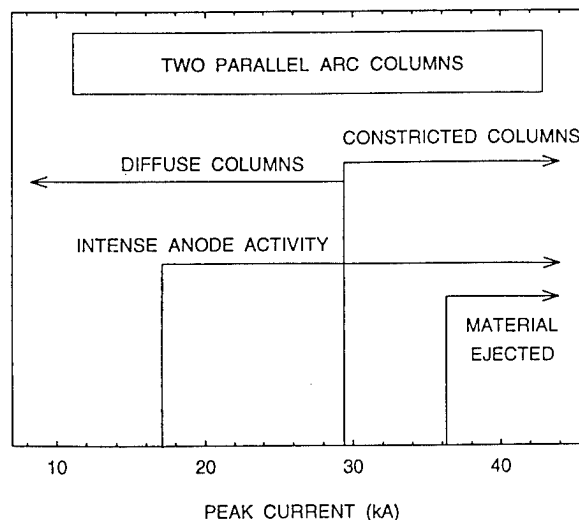


Fig. 4. Ranges of peak arc current for the observed appearance of various arcing modes with a full gap of 2 mm and two parallel arc columns.

4. DISCUSSION

Arc appearance diagrams for high-current drawn arcs on butt-type (Heberlein and Gorman⁵) and spiral-petal (Schulman⁴) contacts have been reported previously. Heberlein and Gorman used 100-mm butt-type contacts with final gaps of 12 to 25 mm and separation speeds of 2.4 to 5 m/s. Within the first ~3.5 mm of travel, they observed a boundary between the diffuse columnar and constricted columnar arc modes at an instantaneous current of 15 to 16 kA, with anode spot modes forming as the gap continued to increase. The corresponding results in Fig. 3 show that when the gap is limited to 2 mm, the constricted column boundary is shifted to slightly lower current. While the anode spot boundary did not shift below 15 kA, the very short constricted arcs did not assume the hourglass or separated jet appearances observed at longer gaps.^{4,5} Using identical spiral contacts at gaps of 4 to 8 mm and opening speeds of ~2 m/s, Schulman⁴ found that arcs initiated on the steeply rising current would always pass through an intermediate stage of two parallel columns before transforming into a single column at 3 to 6 mm. This condition of current sharing between parallel fixed columns is desirable, as it shifts the threshold for anode damage to higher currents. However, it was only observed for roughly half of the trials with maximum gaps of 2 to 3 mm. Schulman⁴ also found that for larger gaps, if an arc column became anchored at a slot, it could not resume or begin running unless it developed a *wedge instability*.⁵ This allowed it to expand out from the gap and attach to the shield. It then began to move and quickly returned to the contact gap. Heberlein and Gorman observed that the wedge instability only occurred for gaps above ~3 mm. This establishes that for these small gaps, the spiral contacts behave as essentially butt-type contacts, and do not provide a mechanism for inducing the instability required for the column to begin or maintain motion over the slots.

5. CONCLUSIONS

This work establishes that final gaps of 2-3 mm are smaller than the minimum gap necessary to allow high-current arcs to pass over the slots in these standard spiral contacts. The immobility of the arc columns lowered the threshold peak current for severe contact heating at the anode arc root. Heavy anode damage was observed in progress for $I_p \geq 21$ kA when there was a single arc column. For single arc columns, the arc was constricted for I_p above ~13 kA; intense anode activity appeared for $I_p > 15$ kA. No arcing to the large-diameter cylindrical shield was observed for maximum gaps in the present range. This eliminated an important mechanism by which anchored columnar arcs can resume their motion.⁴ The observed arc modes are similar to those reported for previous experiments on drawn arcs during the first few millimeters of opening to larger final gaps.^{4,5}

6. ACKNOWLEDGMENTS

John Bindas provided skilled assistance, and expert guidance and advice was provided by Dr. Paul Slade.

7. REFERENCES

1. P. G. Slade, "The vacuum interrupter contact," *IEEE Trans. Comp. Hybrids Packag.* vol. CHMT-7, pp. 25-32, March 1984.
2. M. B. Schulman, P. G. Slade and J. V. R. Heberlein, "Effect of an axial magnetic field upon the development of the vacuum arc between opening electric contacts," *IEEE Trans. Comp., Hybrids, and Manuf. Tech.*, vol. 16, pp. 180-189, March 1993.
3. A. Luxa, R. Renz and W. Branston, "Vacuum interrupters engineering requirements," *Proc. 15th Int. Symp. Discharges and Electrical Insulation in Vacuum*, Darmstadt, Germany, Sept. 1992.
4. M. B. Schulman, "Separation of spiral contacts and the motion of vacuum arcs at high ac currents," *IEEE Trans. Plasma Sci.* vol. 21, pp. 484-488, Oct. 1993.
5. J. V. R. Heberlein and J. G. Gorman, "The high current metal vapor arc column between separating electrodes," *IEEE Trans. Plasma Sci.* vol. PS-8, pp. 283-288, Dec. 1980.
6. I. Paulus, "The short vacuum arc—Part I: Experimental investigations," *IEEE Trans. Plasma Sci.* vol. 16, pp. 342-347, 1988.
7. T. Yokoyama and Y. Kashitani, "An observation of arcing under vacuum," *Meiden Rev.* vol. 56, pp. 60-64, 1979.
8. L. P. Harris, "Small-scale anode activity in vacuum arcs," *IEEE Trans. Plasma Sci.* vol. PS-10, pp. 173-180, Sept. 1982.
9. E. Dullini, "Motion of high-current vacuum arcs on spiral-type contacts," *IEEE Trans. Plasma Sci.* vol. 17, pp. 875-879, 1989.
10. A. Lee, Y.-K. Chien, P. P. Koren and P. G. Slade, "High-current arc movement in a narrow insulating channel," *IEEE Trans. Comp., Hybrids, and Manuf. Tech.*, vol. CHMT-5, pp. 51-55, March 1982.
11. M. B. Schulman and P. G. Slade, "Sequential modes of drawn vacuum arcs between butt contacts for currents in the range 1 kA to 16 kA," *Proc. 17th Int. Conf. on Electrical Contacts*, Nagoya, Japan, July 1994.
12. H. C. Miller, "A review of anode phenomena in vacuum arcs," *Contrib. Plasma Phys.*, vol. 29, pp. 223-249, 1989.

The Interrupting Abilities of Vacuum Interrupters with Horseshoe Electrode

W. Shang

H. Schellekens

HOLEC Syst. & Comp. B.V., Postbus 23, 7555 AA, Hengelo, The Netherlands

ABSTRACT

In this paper, the high current vacuum arc behaviour with horse shoe electrode has been described. These are dynamic vacuum arc distribution, the maximum current density related to the interrupting limit and factors which influences the interrupting limits. Then based on the above analyses, several vacuum interrupters within $\phi 70$ mm outside diameter have been tested. From the results, it shows that the small size vacuum interrupters can be made with the oblique, ellipse shaped horseshoe electrode. The interrupting ability of such type vacuum interrupters is further increased.

1. INTRODUCTION

The interrupting abilities of vacuum interrupters depends on many factors. These factors are normally influenced by each other and show collective effects on the interrupting abilities. There are many literatures about the high current vacuum arcs [1]-[7]. In this paper the following items are tested and analyzed for horseshoe electrode. The diffusing process of vacuum arcs; the maximum current distribution at maximum interrupting abilities; the influence of direct diffusing space on the interrupting abilities. Based on these tests and analyses, several different types of vacuum interrupters are tested and compared. As a results within the same outside diameter of vacuum interrupters, not only large contact area is important but also large diffusing volume plays very important role also to increase further the interrupting abilities. The vacuum interrupter electrode with oblique, ellipse shaped horse shoe electrode shows very promising results.

2. DYNAMIC DIFFUSING PROCESS OF VACUUM ARC WITH HORSESHOE ELECTRODE

For horseshoe electrode the vacuum arcs can be kept diffusely under strong axial magnetic field. These have been described in [1], [2]. The diffusing process of vacuum arc with horseshoe electrode are tested with divided electrode as shown in Fig. 1(a).

The electrode is divided in 14 segments and behind every segment there is one Rogowski coil to measure the differential of the current which flows through the segment. By using the integration of the measured signal, the current which flows in the segments can be determined.

By using this principle, the calibration is very important. The measured signal is composed with 14 different imposed signals:

$$U_i = U_{ic} + \sum_{\substack{j=1 \\ i \neq j}}^{14} U_{ij} \quad (i=1, \dots, 14) \quad (1)$$

In which U_{ic} is the signal from the current flowing through the i -th segment and U_{ij} is the signal of the influence from the j -th segment. From this, the current flowing in each segment can be derived as:

$$U_i = K_{ic} * I_i + \sum_{\substack{j=1 \\ i \neq j}}^{14} K_{ij} * I_j \quad (i=1, \dots, 14) \quad (2)$$

In which I_i , I_j are the current flowing in different segment. K_{ic} , K_{ij} are the coefficients to be determined by the calibration. By using individual current flowing in each segment, the coefficient K_{ic} , K_{ij} are experimentally determined. By using this

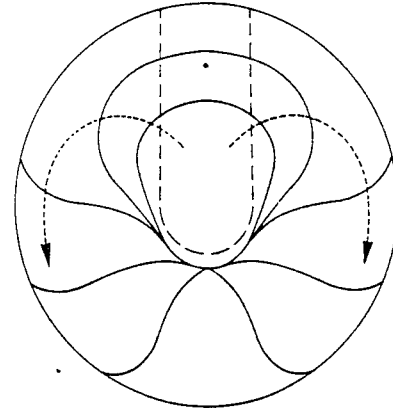
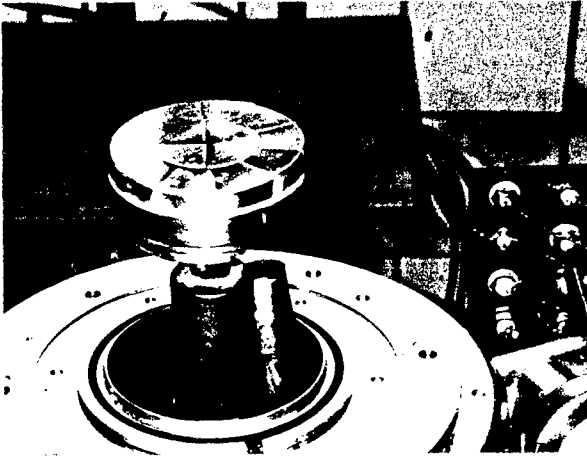


Fig. 1 The vacuum arc distribution with divided electrode.

1(a) The measurement arrangement; 1(b) The dynamic vacuum arc development;

method, the vacuum arc distribution is measured for horseshoe electrode. The dynamic development of the vacuum arcs can be given as in Fig.1(b). The vacuum arc started in the middle of the electrode, and then the vacuum arc moves along the middle line of the horseshoe to the edges of electrode, and finally the vacuum arc moves to the strong axial magnetic field area. After this diffusing process, the vacuum arcs kept in diffusing mode during high current phase.

3. THE CURRENT DISTRIBUTION OF VACUUM ARCS WITH HORSESHOE ELECTRODE

With the above mentioned experiment setup the current distribution with 10,3kA(t-op) are analyzed and simulated. Based on measurement the current density on the anode can be simulated with the following relations:

$$J(r, \theta) = J_{zm} (r/R_0) \text{EXP}(-r^2/A(\theta)) \text{EXP}[-(\theta/\theta_0)^3] \quad (3)$$

in which $A(\theta)$ is functions of θ , θ , r are the coordination on the electrode. θ_0 is angel of the arcing limit on the electrode (from experiments θ_0 is from 80-110 degree). R_0 is the electrode radius. From the experiment mentioned above, the functions $A(\theta)$ can be given as follows:

$$A(\theta) = K_1 R_0^2 * [1 + (2\theta/\pi)^2] \quad (4)$$

in which K_1 is one constant from 0.6 - 0.8. Based on these results assume that the current distribution with horse shoe does not change with current increase. Then the maximum current density on the maximum interrupting current can be derived. Due to the maximum interrupting current with horseshoe can be given as [1]:

$$I = 240.89 * R_0^{1.555} \quad (5)$$

in which R_0 is the electrode radius in mm, I is the interrupting current in A (top) and the contact material is based on Cu/Cr and the electrode distance is 10mm. By integrating the equation (3), the following equation can be derived.

$$J_{zm} = 374.227 * R_0^{-0.445} \quad \text{A/mm}^2 \quad (6)$$

From these expressions, we can get the information that at the maximum interrupting ability the maximum current density is reached to the order of 10^7 A/M^2 . Which is in the order of anode spot formation [4]. So that means that the maximum interrupting abilities of vacuum interrupters are really limited by the thermal stress to the electrode, although with the help of axial magnetic field. The maximum current density at the interrupting limit is also electrode diameter dependent.

4. THE INFLUENCE OF DIRECT DIFFUSING VOLUME FOR VACUUM ARCS (OR NEUTRALS, IONS AND ELECTRONS).

The volume of vacuum interrupters plays very important role on the interrupting abilities of vacuum interrupters. The volume here is defined as the direct diffusing volume between the inter-electrode space and the shielding. This volume has critical influence on the neutral density after current zero. The neutral density is very important factor to determine the maximum interrupting abilities. The neutral density directly after the current zero determines the voltage recovery ability of the gap. The neutral density should be kept lower than the vacuum breakdown region. Otherwise the main gap can have breakdown direct after current zero.

By assuming that the cathode is one perfect evaporation source of the neutral, because the multiple cathode spots give metal neutral to the gap and at the same time the cathode is one imperfect condensation surface, so there is one neutral generation effect on the cathode. The anode is also one neutral source. The shielding is one perfect condenser for the metal neutrals. At the same time, assuming that the generated neutrals from the electrode are immediately distributed in the space. This is based on the fact that the neutral velocity is high and the electrode temperature is also high. The condensation rate is much more lower than the generating rate. Then the following equations can be derived.

$$\frac{\partial N_n}{\partial t} = \frac{S_c N_{gc} I_m \sin(\omega t)}{\Delta V} + \frac{S_a N_{ga} I_m \sin(\omega t)}{\Delta V} - S_s N_{as} \quad (7)$$

in which S_c , S_s are the electrode surface and shielding surface area. N_{gc} , N_{ga} are the rate of the generated neutrals by per ampere, per unite area and per second by cathode and anode. N_{as} is the absorb rate of per unite area per seconde. ΔV is the effective pressure increasing space. For simplicity, N_{gc} , N_{ga} are considered to be constant, ΔV is the cylinder space of diameter of the shielding and the length is the contact distance. Then neutral density at current zero can be derived.

$$N_n = \frac{2 * S_c I_m (N_{gc} + N_{ga})}{\Delta V} - S_s N_{as} \Delta t_{arc} \quad (8)$$

From this equation we could assume that there is one critical neutral density N_{nc} at which the vacuum gap could have breakdown direct after current zero. From these we could also get the maximum current I_{mp} at which breakdown happens directly after current zero.

$$I_{mp} = (N_n + S_s N_{as} \Delta t_{arc}) \Delta V / (2 * (S_c I_m (N_{gc} + N_{ga}))) \quad (9)$$

The maximum interrupting current has the relation with this current I_{mp} shown above:

$$I_{mi} \propto I_{mp}^k \quad (10)$$

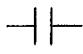
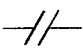
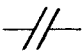
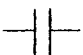
in which k is one constant. From above equations, the volume of the effective diffusing space for the neutral vapour density has direct relation with the maximum current at which breakdown could happens and the maximum interrupting current of the vacuum interrupters.

5. THE INTERRUPTING ABILITIES OF VACUUM INTERRUPTERS WITHIN $\phi 70$ mm DIAMETER

Based on the above analyses the current density and the direct diffusing volume of vacuum interrupters are two very important factors. Four different type of vacuum interrupters, with $\phi 70$ mm outside diameter, are designed and tested. The results are given in the table I.

Table I

The interrupting abilities of different designs
(Based on IEC ratings)

Electrode design	Interrupting ability (kA)	Electrode area (%)	Direct diffusing space (%)	Contact Shape
Conventional design	20	100%	100%	
Oblique construction with the same contacts as above	23,5	100%	105%	
Oblique with ellipse shaped electrode	25,0	110%	105%	
Conventional electrode with larger diameter and diffusing space	27,5	153%	122,6%	

From these results, it shows that two factors has vital influences on the interrupting abilities of vacuum interrupters. Not only the electrode area is an important factor but direct diffusing space is also an important factor.

6. CONCLUSIONS

From the experiments, the following conclusions can be drawn:

The maximum current density at the limit of interrupting abilities can reach to the current density of anode spot formation that is in the order of $1.0E7 \text{ A/m}^2$.

The maximum current interrupting ability of vacuum interrupters is influenced by the direct diffusing space.

The ellipse shaped and oblique construction vacuum interrupters with horseshoe electrode provide promising direction to increase the interrupting abilities of vacuum interrupters with small size.

7. REFERENCES

- [1] W. Shang et al, 'Experimental Investigations into the Arc Properties of Vacuum Interrupters with Horseshoe Electrode, Four Pole Electrode, and their Applications', IEEE Trans. Plasma Sci., vol.PS-21, No. 5, pp.474-477, October, 1993.
- [2] H. Schellekens et al, 'Vacuum Interrupter Design Based on Arc Magnetic Field Interaction for Horseshoe Electrode', IEEE Trans. Plasma Sci., Vol. PS-21, No. 5, October, 1993.
- [3] R. L. Boxman et al, 'A model of the anode region in a uniform multi-cathode-spot vacuum arc', J. Appl. Phys., vol. 54, pp. 592-602, 1983.
- [4] H. Schellekens, 'Modelling of the diffuse arc in a vacuum circuit-breaker (Eindhoven University of technology, Eindhoven), Thesis, 1983.
- [5] G. R. Mitchell, 'High-Current Vacuum Arcs' Part I and Part II, Proc. Inst. Electr. Eng. Vol. 177, pp. 2315-2332, 1970.
- [6] E. Dullni et al, 'Electrical and pyrometric measurements of the decay of the anode temperature after interrupting of high current vacuum arcs and comparison with computations', IEEE Trans. Plasma Sci., vol.PS-17, no. 5, pp.644-648.
- [7] M. S. Agarwal et al, 'Current flow pattern in high current metal vapour arcs' Proc. 7th Int. Conf. on Gas Disc. and Appl., pp.62, London, 1982.

MOVING CHARACTERISTICS OF ELECTRODES FOR VACUUM CIRCUIT BREAKER

Yuan Shun

Northeastern Electric Power Test & Research Institute, Shenyang (110006), P. R. China

Ji-meí Wang

Dept. of Electrical Engineering, Xi'an Jiaotong University P. R. China

ABSTRACT

This Paper analyzes the effect of the gap of electrodes on the state of vacuum arc by experiment and theory. And the model of vacuum arc is set up. The optimal gap can be deduced from controlling the vacuum arc to be diffusion state, in order to get the optimal moving characteristics of electrodes.

1. INTRODUCTION

The phase angle of interrupting current is random at the moment which electrodes separate for vacuum circuit breaker (VCB). The vacuum arc modes are dependent on electrode gap and interrupting current during arcing. The limit interrupting current is relative with the material, the size and gap of electrodes¹. Usually, the investigation on cathode phenomena deals with low current only. When the current is high enough to make the anode become active, the gross erosion on the cathode surface takes place², too. The arc current can be extinguished successively at current zero under diffusion arc and footpoint arc. It is possible for arc current to not be interrupted when anode spot appears or the anode erosion is very serious. The constriction of arc often be found before anode spot appears³. The anode spot will take place when arc contraction at anode is kept in diffusion mode. For a certain material and size of electrodes, the arc mode can be controlled by electrode gap and magnetic field under arc current.

2. ANALYSIS BY EXPERIMENT

Test circuit is shown in fig. 1. The fig. 2 is about the relationship between the electrode gap and interrupting current. There is a optimal gap zone to break a interrupting current effectively. For example, the interrupting current is 25kA, optimal gap zone is 3—8mm.

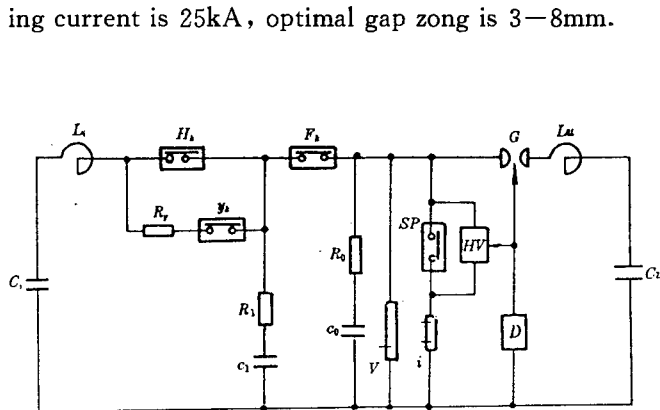


Fig. 1 Test circuit

Ci, Li; current source; G; trigger

Cu, Lu; voltage source; R; resistance

C; capacitor; V, i; dividers

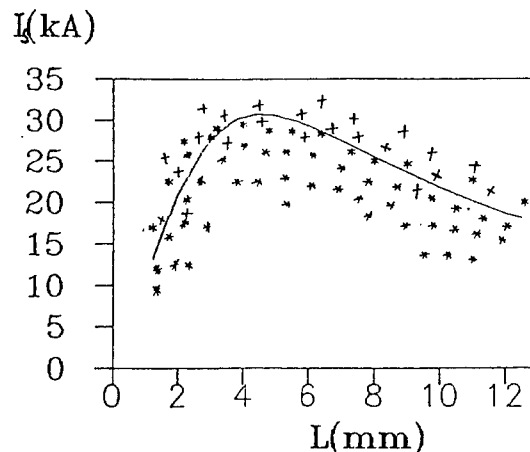


Fig. 2 The relationship between the electrode gap and current

* — successful interruption;

+ — not successful.

3. MODELLING OF VACUUM ARC

3. 1. The Basic Hypotheses

The vacuum arc can be usually divided into three regions, cathode, plasma—column and anode. Before the anode spots formation, the electrons, ions and metal vapour are supplied by cathode under low current. The

particles are produced by the cathode spots of which the number is proportional to the arc current. A large number of the particles jet from the rapidly moving spots. Because of the rapid movement of the spots, the distribution of the particles nearby the cathode surface is basically uniform. Therefore the arc radius in neighbourhood of cathode is approximately equal to the electrode radius. For the plasma, the mean free path of all particles is far small compared to the characteristics dimension collision is dominant. Thus, it is quite approximate that macroscopical one—fluid plasma theory is used to describe the physical process of vacuum arc. The anode may act as an additional source of the particles due to anode column. Therefore, the physical process are more complicate. In this paper, only the vacuum arc without anode spots or prior to the anode spot forming is discussed. The fig. 3 is a picture for vacuum arc to be the diffusion state by high speed camera.

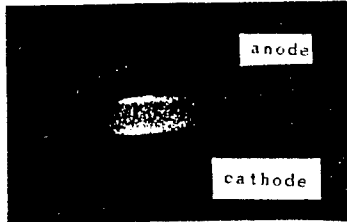


Fig. 3 Vacuum arc

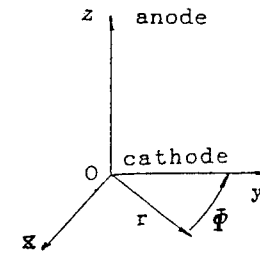


Fig. 4 Coordinate system

3. 2. The stationary Vacuum Arc Equation

Hypotheses conditions

1) The system is local quasineutrality. Because the plasma as a whole is neutral, there must be some scale on which quasineutrality is valid. This scale the Debye length:

$$\lambda = \left(\frac{\epsilon_0 K T}{2 n e^2} \right) = 69.0 \sqrt{\frac{T}{n}} \quad \text{For the valid parameters: } T = 2 \times 10^4 \text{K; } n = 2 \times 10^{21} \text{m}^{-3}, \lambda = 2.2 \times 10^{-7}$$

It is much smaller than the characteristic dimension of the system studied. Then it can be assumed that the ion density is equal to the electron density.

- 2) The electron mass is neglected to compare with the ion mass.
- 3) The pressure is isotropic due to many collisions during a characteristic time.
- 4) To neglect the displacement current.
- 5) The viscosity effects is out of regard.
- 6) The vacuum arc is axisymmetrical approximately. So J_z can be expressed as

$$J_z = I / \pi R^2 = J_0 \left(R_0 / R \right) \quad (1)$$

where, $J_0 = I / \pi R^2$ is the current density near by the cathode. Momentum transport

$$\rho_m \left(\frac{\partial V_t}{\partial t} + V_r \frac{\partial V_r}{\partial t} + V_z \frac{\partial V_r}{\partial r} \right) = - \frac{\partial P}{\partial r} - J_z \cdot B_\phi + J_\phi \cdot B_z \quad (2)$$

$$J_z \cdot B_r = J_r \cdot B_z \quad (3)$$

Maxwell's equations

$$\frac{\partial (r \cdot B_r)}{r \partial r} + \frac{\partial B_z}{\partial z} = 0 \quad (4)$$

$$\frac{\partial B_r}{\partial z} - \frac{\partial B_z}{\partial r} = -\mu_0 \cdot J_\phi \quad (5)$$

$$\frac{\partial(r \cdot B_r)}{r \partial r} = -\mu_0 \cdot J_z \quad (6)$$

Continuity equations of electric current

$$\frac{\partial(r \cdot J_r)}{r \partial r} + \frac{\partial J_z}{\partial z} = 0 \quad (7)$$

B; Magnetic field; n; Density; B_r; Radial magnetic field; n_e; Electron density; p; Pressure B; Azimuthal magnetic field; n_i; Ion density; e; Electron charge; R; Arc radius; I; Current R₀; Electrode radius; J; Current density; T; Temperature; J_r; Radial current density; V; Velocity; J_z; Axial current density; V_r; Radial velocity; k; Boltzmann constant; V₀; Initial velocity; K; Electrode parameter; λ; Debye length; L; Gap length; μ₀; Permeability; m_e; Electron mass; ρ_m; Mass density; m_i, m_n; Ion, neutral mass.

The stationary mode is valid in 90 % interval during arcing time for the current with power frequency [6]. Thus the derivative with regard to time is negligible.

The arc radius equation deduced from above expressions is

$$\left[1 - \frac{B_z^2}{\mu_0} - \rho_m V_0^2 \left(\frac{R_0}{R}\right)^4\right] \frac{d^2 R}{dz^2} - \rho_m \left(\frac{R_0}{R}\right)^4 \frac{1}{R} \left(\frac{dR}{dz}\right)^2 + \left[3\rho_m V_0^2 \left(\frac{R_0}{R}\right)^4 \frac{1}{R} + \frac{B_z^2}{\mu_0 R}\right] \frac{dR}{dz} + \frac{\mu_0 R}{2} J_0^2 \left(\frac{R_0}{R}\right)^4 - \frac{2B_z^2}{\mu_0 R} + \frac{2P_0}{R} = 0 \quad (8)$$

The arc current should be less than 3 kA/cm² to prevent serious melting of the surface of anode in an arcing time. Supposing that the arc radius of the surface of anode is k R₀ under the limit state which arc current density is 3 kA/cm².

Supposing the shape of vacuum arc is shown in fig. 5. Then

$$R = R_1(1 - z/L) + k \cdot R_0 \quad (9)$$

$$dR/dt = -R_1/L \quad (10)$$

Where R₁ = R₀ - k R₀;

R = k R₀ (k < 1) when z = L.

Thus equation (8) is

$$L^2 - bL - c = 0$$

where $b = [R_1(3\rho_m V_0^2/K^4 + B_z^2/\mu_0)] / [\mu_0 R_0^2 J_0^2/2K^2 - 2B_z^2/\mu_0 + 2P_0]$

$$c = [\rho_m R_1^2/K^4] / [\mu_0 R_1^2 J_0^2/2K^2 - 2B_z^2/\mu_0 + 2P_0]$$

then the root of the above equation is

$$L_1 = [b + \sqrt{b^2 + 4c}] / 2$$

For stationary arc, L₁ is the longest gap length to keep the arc state mentioned above. The anode spots can't be found when L < L₁. But L can't be less than a certain value because the density of arc current is very high in small gap. At this time, The serious erosion takes place not only on the surface of anode, but also on the surface of cathode. The state in small gap can't be expressed in above equations. L_{min} is supposed to be the limit value. The arc state is high density in the case L < L_{min}. The arc constriction leads to the melting of the surface of anode on the case L > L₁. L₁ is relative with the axial magnetic intensity. The next relationship can be gotten if k = 1

$$B_z^2 = \mu_0^2 R_0^2 J_0^2 / 4 + 2 P_0 \quad (11)$$

3.3. The Equation of Moving Electrode Velocity

Hypotheses is that the current is certain. Thus, the relationship between the velocity and the gap length is expressed as

$$\rho_m V_0 R_1 R_0^2 \frac{dL}{dt} = - \left[\frac{\mu_0 R_0^2}{2K^2} J_0^2 - \frac{2B_z^2}{\mu_0} + 2P_0 \right] L + R_1 \left[\frac{3\rho_m V_0^2}{K^4} + \frac{B_z^2}{\mu_0} + \frac{3\rho_m R_0}{K} \right] L + \rho_m R_1^2 / K^4 = 0 \quad (12)$$

The displacement curve of moving electrode is not one solution because the moment which electrodes sepa-

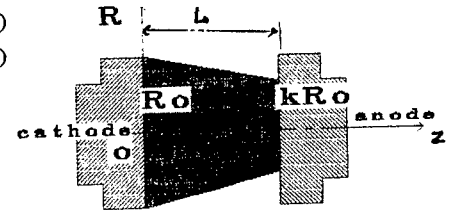


Fig. 5 The state of arc

rate is random. So there is a significance to analyze the velocity of moving electrode. Under the arc current is peak value and the velocity is zero, then $J_0 = I_{\max} / \pi R_0^2$; supposing

$$\rho_m V_0 R_0^2 R_1 (dL/dt) = -A \cdot L^2 + B \cdot L + C = 0$$

Then the root of the above equation is

$$L_m = [B + \sqrt{B^2 + 4 \cdot A \cdot C}] / (2A)$$

L_m is the longest gap of electrode to interrupt a current effectively from above time—dependent equations. The velocity of the electrode is positive when $L < L_m$. The moving electrode moves continually. The velocity is zero when $L = L_m$, then the moving electrode stops.

4. THE OPTIMAL MOVING CHARACTERISTICS OF ELECTRODES

L_m is larger than L_1 . The optimal moving characteristics of electrodes is shown in fig. 6. Δt is very short. It means that the electrode should move to L_{\min} as possible as quickly.

The electrode should move at low speed from L_{\min} to L_1 . The electrode stops when the gap is L_m . The velocity characteristics is shown in fig. 7.

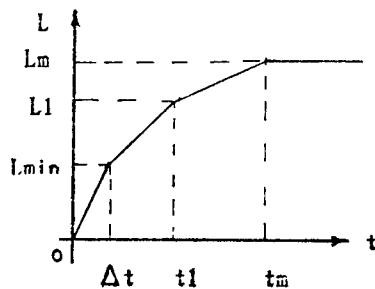


Fig. 6 The optimal moving curve of electrodes

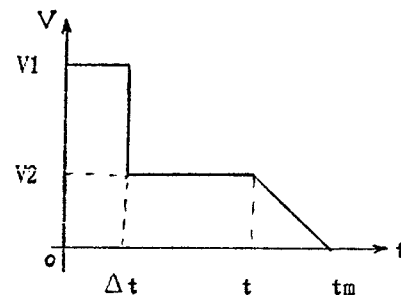


Fig. 7 The optimal velocity of electrodes

5. ACKNOWLEDGEMENT

This research work has been supported by the Doctor Subject Foundation Commission of State College Committee in china. To whom the authors would like to express their grateful thanks.

6. REFERENCES

1. Ji—mei Wang, et al, "Vacuum arc theory and its application", Published by Xi'an Jiaotong University, Chapter 1, PP2—6, 1986
2. Yi Wang, "The measurement of vacuum arc by light intensity and modelling analysis", Thesis, Xi'an Jiaotong University, 1989
3. H. C. Miller, "A review of anode phenomena in vacuum arcs", XIth Int. Symp. Disch. Insul. Vac., pp115—122, 1984
4. L. P. Harris, et al "Small—scale anode activity in vacuum arcs", IEEE Trans. Plasma Sci., Vol. PS—10, pp 173—180, 1982
5. R. L. Boxman, et al, "Measurement of anode surface temperature during a high—current vacuum arc", J. Appl. Phys., Vol. 46, pp4701—4704, 1975
6. J. H. Wang, "Anode spot phenomena in vacuum arcs and effect of axial magnetic field", Thesis, Xi'an Jiaotong University, 1985

Microscopical high speed investigations of vacuum arc cathode spots

P. Siemroth, T. Schülke, T. Witke

Fraunhofer-Institute for Materials Physics and Surface Engineering (IWS), Helmholtzstraße 20, D-01069 Dresden, Germany

ABSTRACT

The main parameters and dimensions of cathode spots were under discussion since years. To solve these current questions, a new system was especially designed. The image converting High Speed Framing Camera **HSFC**, which combines a microscopical resolution of 5 μm with a nanosecond time resolution and a very high optical sensitivity. This camera was used to study the microscopical behaviour of vacuum arc cathode spots in a pulsed high current arc discharge on copper. The direct observation of these spots with high resolution revealed the conclusions that one single cathode spot, as normally observed by optical means consists of a number of simultaneously existing microscopical sub-spots, each of them with a diameter of about 15 μm and a mean distance of 30...50 μm between them. The mean existence time of these sub-spots on copper was found to be about 3.2 μs , where the position of a sub-spot remains unchanged (with an upper limit of about 2...3 μm) during its existence time. An upper limit of the crater surface temperature was estimated by a comparison between the brightnesses of a cathode spot and of a black body radiation lamp to about 3000 K.

1. INTRODUCTION

The main parameters and dimensions of single cathode spots, especially of the current carrying plasma cloud, the existence time and the character of its displacement were under discussion since many years. There was an uncertain difference between the crater dimensions of about 10 μm , measured post mortem with scanning electron microscopes (e.g. /1/, /2/, /3/) and the photographically measured dimensions of the bright plasma cloud of about 100 μm (/4/, /5/, /6/). Consequently, it was impossible to determine the current density within the cathode spot - a key value for each theoretical explanation - from the experimental data. Values between 10^9 and 10^{12} A/m² have been offered by different authors /7/. Therefore the question of spot dimensions and current density is the task of a long lasting discussion (e.g. /3/, /9/), carried out on the base of experimental data but also on obsessions and prejudices. Really, it is difficult to understand by what means the current would pass through an area, outside the molten craters and on the other hand, the (Spitzer-)conductivity is much lower than it must be, to transport the arc current through the small craters forced by only the cathode drop voltage. Consequently, new experimental methods and arrangements are inevitable to get more insides of the arc spot.

Another motivation of more detailed studies of the arc spot process is the development of new vacuum arc applications. In the last few years, the arc based thin film deposition (e.g. hard films, like TiN, anticorrosive films and decorative coatings) has become a new important technology. This new application where the arc is used as an effective source of highly ionised plasma has stimulated new investigations. For the coating technology it is important, to find out, by what means the degree of ionisation can be regulated and how to minimize the droplet fraction.

In the present paper, a new high speed camera with microscopical resolution will be described and the first results are reported of the current program of high speed investigations of the cathode spot behaviour.

2. EXPERIMENTAL SET-UP

Due to the insufficient local and temporal resolution of the available high speed cameras, a new system was especially designed for our tasks. This new technology high speed framing camera **HSFC**, developed by the PCO Computer Optics GmbH Kelheim combines a microscopical resolution of better than 5 μm with a nanosecond time resolution and a very high optical sensitivity. Therefore a high-resolution long-distance microscope QUESTAR is combined with a four channel intensifying CCD camera. Each channel can be triggered separately (delay 0...1 ms in 1 ns steps), moreover the optical amplification factor (gain; variation range about 6 orders of magnitude) as well as the exposure time (width; 5 ns...1 ms in 1 ns steps) can be adjusted independently. Hence the camera allows a variety of observation modes. It can be used to take a sequence of four frames with or without interval, with the same parameters or with especially chosen parame-

ters for each single picture. Moreover the four frames can be taken at one time with different gains, to enlarge the dynamic range or with different filters for selected wavelength, to detect the radiation of special ions and so on. The four pictures are transferred by a video-multiplexer into the computer, where the information will be stored and analysed. The resolution of the QUESTAR mirror objective is limited only by diffraction to about $3\text{ }\mu\text{m}$. With the highest magnification, one CCD-pixel corresponds to an area of $(1 \times 1)\text{ }\mu\text{m}^2$ on the observation field. The inhomogeneous structures of the image intensifying multi-channel-plate (MCP) and of the fiber optical taper which connects the MCP and the CCD give additional distortions. Therefore the usable resolution is limited to about $5\text{ }\mu\text{m}$.

The arc spot studies have been carried out at the HCA (High Current Arc) device, a new type of pulsed arc evaporator /9/. As cathodes flat cylinders (diameter 30 mm) made of various metals or carbon were been used which are mounted in a special cathode holder. In the centre of the cathode a trigger electrode is situated. The discharges are ignited by high-voltage pulses over the trigger electrode. During the arc observation experiments the pressure in the vacuum chamber has a value of $10^{-4} \dots 10^{-3}\text{ Pa}$. The voltage between anode and cathode delivered by a condenser unit amounts to 600 V before the arc is ignited. Sinusoidal current pulses (peak current: $3 \dots 5\text{ kA}$, duration: $0.5 \dots 1\text{ ms}$, repetition rate: single pulses $\dots 300\text{ s}^{-1}$) are formed by a resonant pulse forming circuit ($L=35\text{ }\mu\text{H}$, $C=3\text{ mF}$). Due to the repelling forces, the cathode spots run radially from the ignition point to the rim of the cathode. In the first experiments described here were the HSFC was used to observe cathode spots on a copper cathode. The observation area of $900 \times 700\text{ }\mu\text{m}^2$ was situated at a distance of about 6 mm apart from the centre.

Similar observations on other metals (titanium, aluminium) and also on carbon have been carried out and will be reported soon.

3. RESULTS AND DISCUSSION

Conventional short time observations have shown cathode spots as large bright areas of homogeneous luminosity and diameters of about $100\text{ }\mu\text{m}$ (e. g. /4/, /5/. To compare conventional photographic observations with the HSFC pictures, a series of arc spot images with three different resolutions is shown in fig. 1:

- An open shutter photograph - lateral resolution about $80\text{ }\mu\text{m}$ - shows a number of arc spot traces running from the ignition point in the centre to the rim of the cathode.
- Using a gated, intensified CCD-camera with a standard objective - exposure time 200 ns, resolution $\sim 40\text{ }\mu\text{m}$, a ring of simultaneously existing spots can be seen.
- With higher magnification it turns out, that each spot has dimensions of about $100\text{ }\mu\text{m}$, remarkably larger than the lateral resolution of the used optical system.
- The HSFC picture shows the inner structure of the large spot - a number of small spots (diameter about some μm) existing at the same time and separated one from each other for about $20 \dots 50\text{ }\mu\text{m}$.

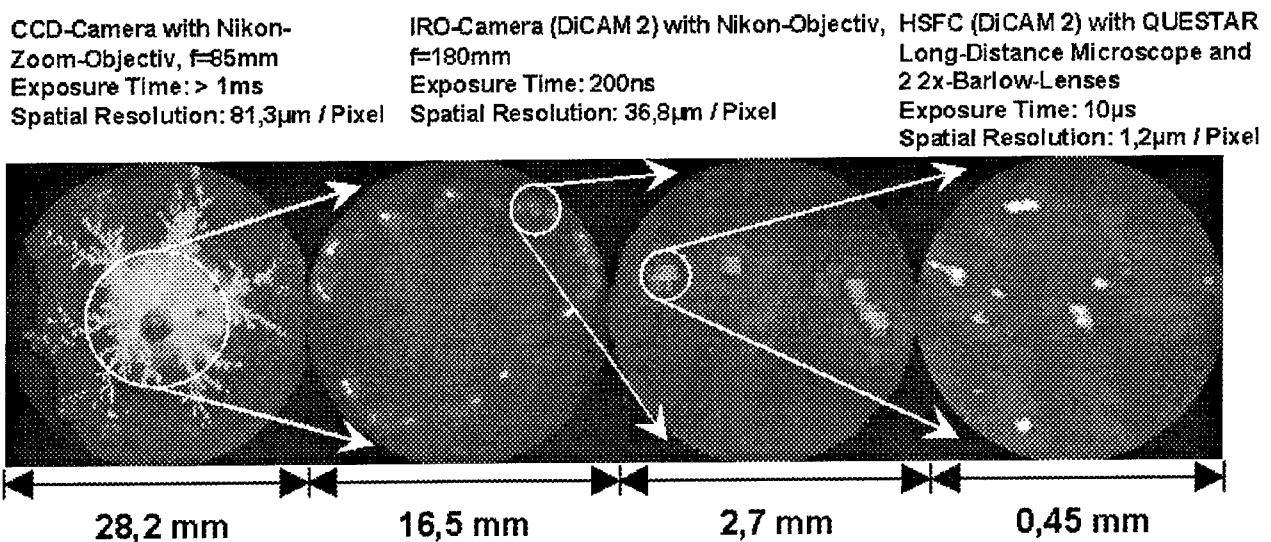


Fig. 1 Series of spot images with three different resolutions

The dimensions of the small sub-spots are in the order of $10\text{--}20\text{ }\mu\text{m}$, that means they are similar to those of the microscopically observable post-mortem craters (comp. /3/, /4/) but also to the dimensions found in the only microscopical photography (resolution about $0.4\text{ }\mu\text{m}$) of arc spots showing micrometer structures, which were been carried by Eckhardt /10/ on anchored spots on mercury. The dimensions and the observation of numerous parallelly existing spots found in our experiments is also consistent with the absorption pictures taken by Anders and Anders /11/ by a side-on passage of a sub-nanosecond dye laser pulse through the plasma cloud in front of the cathodes.

To determine the life span of a single spot, as a first test, a number of sequences of four frames with exposure=delay time of 50 ns were taken. In sharp contrast to the commonly accepted arc spot models, which predict spot life times of some tens of nanoseconds /4/, /6/. In our pictures mostly no changes at all can be seen during the 200 ns .

To determine the mean spot existence time, the number of spots were been counted on frames with different exposure times (20 ns , 100 ns , $1\text{ }\mu\text{s}$, $10\text{ }\mu\text{s}$) each of them interlocked in the middle of the next longer. By a statistical estimation, the mean life time of the small spots was deduced from the numbers of spots counted in the different frames to about $3.2\text{ }\mu\text{s}$. As an example the four frames of one typical shot are shown in fig. 2.

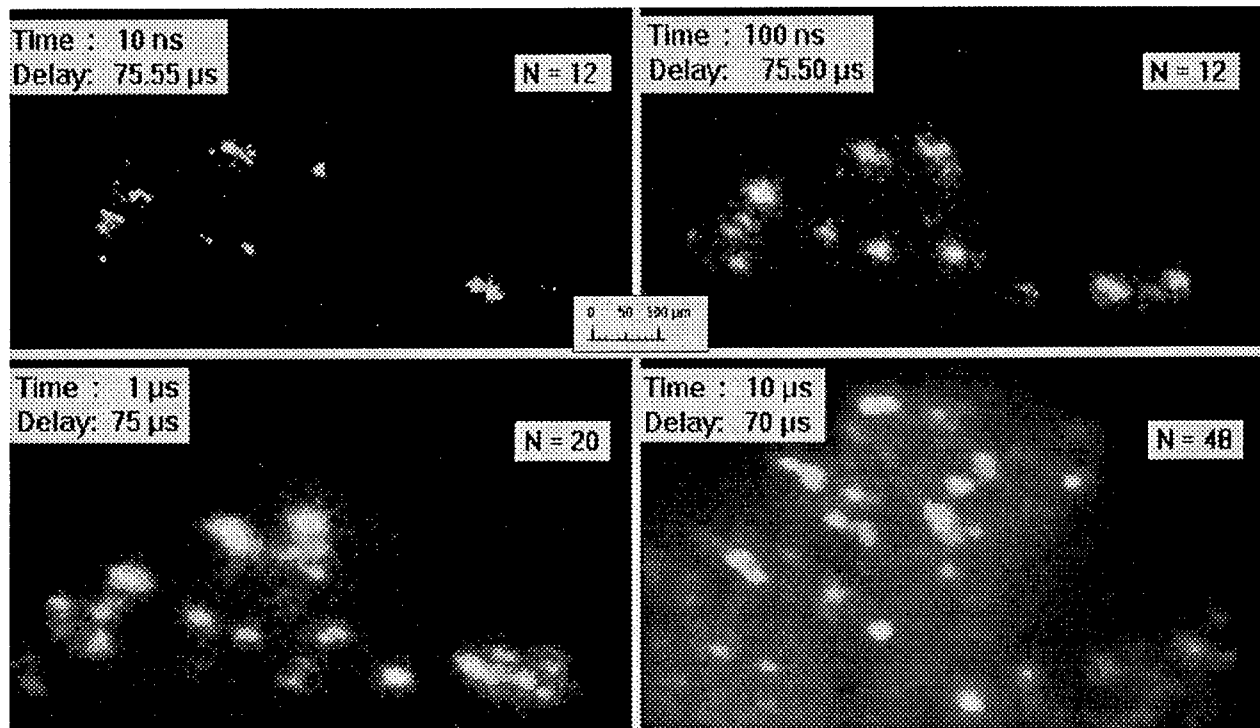


Fig. 2 Number of spots, counted in frames with different exposure times taken with the same middle time

By only counting the number of spots, it cannot be proved, whether the spot exists really at one place all the time or it moves randomly with a step width below the resolution limit. Therefore the brightness distribution of these spots was measured in dependence on the exposure time. It was established, that the width of this distribution is about $(15\pm 3)\text{ }\mu\text{m}$, independently on the exposure time (in the range $20\text{ ns}\text{--}1\text{ }\mu\text{s}$). By a numerical simulation /12/, it was shown that the width of the brightness distribution should be proportional to the square root of the exposure time, if a small spot is moving randomly: Therefore it can be concluded, that the spot positions remain stable over its existence time of about $3\text{ }\mu\text{s}$ with an uncertainty of less than $2\text{--}3\text{ }\mu\text{m}$.

The maximum brightness inside the small spots was compared with the brightness of a standard light source (black body radiation with $T=2700\text{ K}$). The mean brightness of spot was found to be 3.7 times higher than that of the standard lamp. Taking into account, that the thermal emission is only a (small) part of the light emitted by the spot, only an upper limit of the crater temperature can be estimated by this way. In the case of copper, this upper limit was found to be about 3200 K , a temperature much lower than in most theoretical estimations but consistent with the temperature established by Utsumi /13/ from the Maxwellian velocity of metal vapor atoms, emitted from the cathode spot.

4. CONCLUSIONS

The direct observation of these spots with high resolution revealed the following main features:

- ☐ One single cathode spot, as normally observed by optical means and having dimensions of about 100 μm consists of a limited number of simultaneously existing microscopical sub-spots.
- ☐ The brightness distribution of a single (sub-)spot has a radial symmetrical bell-like shape with a FWHM of about 20 μm .
- ☐ The distance between such neighbouring sub-spots is in the range of 30 ...50 μm .
- ☐ The existence time of these small cathode spots (sub-spots) on the studied materials was in the range from some 100 ns to several microseconds, e. g. for copper the mean life time was found to be about 3.2 μs .
- ☐ During the existence time, the position of a sub-spot remains unchanged (with an upper limit of about 2...3 μm).
- ☐ The optical emission of the spot consists of two parts: a line spectrum of plasma emission and a continuum from the thermal emission of the crater surface. Taking into account, that the thermal emission is only a (small) part, an upper limit of the crater temperature can be estimated. In the case of copper, this upper limit is about 3000 K.

5. ACKNOWLEDGEMENTS

Thanks are due to B. Schultrich H.-J. Scheibe and Mr R. Wilberg and for their permanent support and useful discussions. The development of the high current arc plasma source was supported by the Bundesminister für Forschung und Technologie, grant No. 13 N 5950A and by the firm "Vakuumentchnik Dresden" (VTD). The development of the HSFC system was supported by the *Sächsisches Staatsministerium für Wissenschaft und Kunst*, grant No. 4-7541.81-IWS/1.

6. REFERENCES

- /1/ Puchkarev, V.F., Murzakayev, A.M.; *Autographs of the cathode spot and the current density on the nanosecond time scale of arc operation*; Proc. XIIIth ISDEIV; 1988.
- /2/ Daalder, J.E.; *Diameter and current density of single and multiple cathode discharges in vacuum*; IEEE Trans. Pow. App. Syst. **PAS-93** (1974) 1747-1758.
- /3/ Hantzsch, E., Jüttner, B.; *Current Density in Arc Spots*; IEEE Transact. Plasma Sci. **PS-13**(1985)230- 234.
- /4/ Beilis, I.I., Zektser, M.P., Rakhovskii, V.I.; *Current density in the cathode spot of a vacuum arc: Gradients of the temp. and concentrations of charge particles*; Doklady Akademii Nauk SSSR; **282**(1985)854-857; Soviet Physics Doklady (USA), **30** (1985)476-478.
- /5/ Djakov, B.E., Holmes, R.; *Cathode Spot Structure and Dynamics in Low-Current Vacuum Arcs*, J. Phys. D: Appl. Phys., **7**(1974)569-580
- /6/ Rakhovsky, V.I.; *Critical parameters of the cathode region of a vacuum arc*; IEEE-Transaction on Plasma Science; **PS-18**(1990) 677-681.
- /7/ Anders, S., Jüttner, B., Pursch, H., Siemroth, P., *Investigations of the Current Density in the Cathode Spot of a Vacuum Arc*; Contr. Plasma Phys.; **25**(1985) 467-473.
- /8/ Rakhovsky, V.I.; *State of the art of physical models of vacuum arc cathode spots*; IEEE Transaction on Plasma Science (USA) ;**PS-15** (1987) 481- 487.
- /9/ B. Schultrich, P. Siemroth, Th. Schülke; *High-Current Arc - A new Source for High Rate Deposition*; Proc. TATF 1994.
- /10/ Eckhardt, G.; *Properties of Anchored Cathode Spots of a DC Mercury Vacuum Arc*; IEEE Trans. Plasma Sci. **PS-8** (1980) 295-301.
- /11/ Anders, A., Anders, S., Jüttner, B., Böttcher, W., Lück, H. and Schröder, G.; *Pulsed Dye Laser Diagnostics of Vacuum Arc Cathode Spots*, IEEE Trans. Plasma Sci. **PS-20**, (1992) 466-472.
- /12/ Anders, S., Anders, A.; *Simulation of the brightness pattern of a moving cathode spot*; Proc. XVth Int. Symp. Disch. El. Ins. Vac., p. 294-298; Darmstadt, 1992.
- /13/ Utsumi, T., *Measurements of Cathode Spot Temperature in Vacuum Arcs*, Appl. Phys. Lett., **18**(1971)218-220.

Vacuum arc plasma deposition: macroparticle filtering, scaling, and other problems

**André Anders, Simone Anders, Ian G. Brown,
Robert A. MacGill, and Michael R. Dickinson**

Lawrence Berkeley Laboratory,
University of California, Berkeley, CA 94720

ABSTRACT

Micron-size macroparticles can be removed from vacuum arc plasmas using magnetic filters, permitting the deposition of high-quality thin films of the cathode material. The principle of magnetic filtering is explained, and ways of improving filter efficiency using additional electric and magnetic fields are explored. Under optimum conditions, about 25% of all ions entering the filter can be used for deposition. Other problems such as down or upscaling of deposition facilities are briefly discussed.

1. INTRODUCTION

Vacuum arc plasma deposition is an emerging film deposition technique having a potentially wide range of industrial applications such as the production of metallurgical coatings. It does not require any hazardous solutions such as those used in conventional wet-chemical plating. The material to-be-deposited is used as the cathode material in a vacuum arc discharge and transformed into a plasma at the cathode spots. Along with the plasma, macroparticles up to a few microns in size are produced at the cathode spots. Contamination of the films by macroparticles is a major obstacle to broad application of vacuum arc plasma deposition. Attempts have been made to solve this problem by steering the cathode spots by a magnetic field, and by removing the macroparticles by magnetic filters (see, e.g., review [1]). More applications would be possible if the macroparticle contamination problem was solved; for example, smooth amorphous diamond films could be used as protective layers for computer hard disks, multilayer structures for magnetic recording or X-ray mirrors, transparent conductive layers in solar cells, etc.

In this paper we report about problems associated with macroparticle filtering, scaling of vacuum arc plasma deposition facilities, and summarize our results obtained so far.

2. MACROPARTICLE REMOVAL BY MAGNETIC FILTERING

The idea of filtering is to guide the vacuum arc plasma by a magnetic field through a straight or curved duct to the substrate. Macroparticles move along nearly straight trajectories due to their inertia and are lost at the duct walls; the contamination of the plasma at the substrate location is therefore drastically reduced (straight duct) or even completely removed (curved duct). Additional measures have to be taken to handle bouncing of macroparticles from the duct walls.

Pioneering experiments were carried out by Aksenov and his group in the late 1970's [2]. They used a curved (90°) duct with a guiding magnetic field strength of up to 80 mT, with the option of biasing the duct wall. Such a configuration has been used by many researchers. We have modified this approach by using pulsed vacuum arc plasma sources and filter systems in which the arc current is used to generate a pulsed guiding magnetic field [3]. Our "small" vacuum arc plasma source [3] is comprised of a central rod as the cathode (diameter 6 mm), surrounded by a ceramic insulator, and annular anode. By applying a high-voltage pulse to a trigger electrode, a surface discharge creates a small plasma which triggers the main arc. Cathode spots move randomly over the cathode surface (front face of the rod) and produce a plasma of the cathode material; the anode is passive and acts as an

electron collector. Typically, arc current is in the range 50 - 300 A and arc duration is between 100 μ s and 10 ms. The plasma contains electrons, ions with charge states between 1+ to 5+, a low fraction of neutral atoms, and macroparticles. The plasma streams away from the source with a velocity of $1\text{--}2 \times 10^4$ m/s, and the macroparticle velocities are much smaller. A 90° duct was attached to this plasma source, and high-quality thin films of the cathode material have been deposited [3]. As a duct material we have used welded bellows to minimize bouncing of macroparticles.

3. OPTIMIZING MACROPARTICLE FILTERING

The plasma flux at the substrate is reduced by the macroparticle filter since a fraction of the plasma recombines at the duct walls. To improve plasma transport from source to substrate, understanding of the basic transport mechanism is important. An analysis of characteristic lengths and frequencies shows that electrons are magnetized, i.e., the electron Larmor radius is much smaller than the minor radius of the duct and the collision frequency is smaller than the gyration frequency (assuming a typical magnetic field strength of a few mT or tens of mT). Therefore, electrons gyrate around the magnetic field lines and cannot reach the wall without collisions (field lines are parallel to the duct wall). Although ions are not magnetized, their motion is bound to the electrons by plasma internal electric fields. Thus, the whole plasma motion is determined by the magnetic field but ion transport can be influenced by electrostatic fields since electric sheaths penetrate into the plasma due to the presence of the magnetic field ("plasma-optics" or "flux tube" model). Consequently both magnetic and electric fields improve the plasma filter throughput.

The findings of Aksenov and his group [2] that a positive wall bias improves plasma transport have been confirmed in our experiments, see Fig.1.

The data of Fig.1 have been obtained using a 90° copper duct (minor radius 34 mm, major radius 76 mm, 100 turns solenoid). The anode of the plasma source was at ground potential, and the duct wall could be biased. More details of the experiment can be found in [4]. The output of an optimally biased duct is increased by almost a factor of 10 over that of a grounded duct, which represents a substantial improvement.

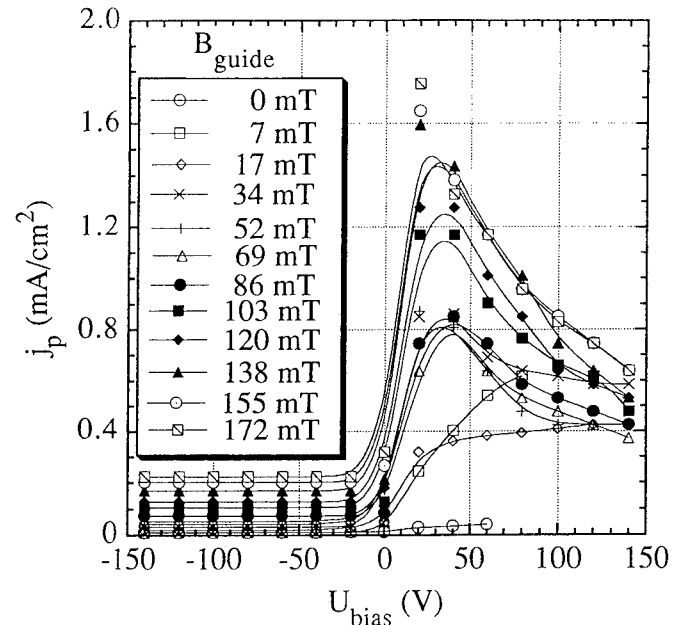


Fig. 1: Ion saturation current density to a Langmuir probe as a measure of the filter output as a function of the duct potential, with the guiding magnetic field strength as a parameter. Titanium cathode, 100 A, 600 μ s discharges.

Another way of increasing the efficiency is to apply an axial magnetic field to the plasma source which focuses the plasma into the filter [5]; we refer to this axial field as the focusing field. The plasma source was equipped with a solenoid (10 turns over a length of 20 mm) which was electrically in series with the arc current. A magnetic field strength of about $B_{focus}(\text{in mT}) \approx 0.6 I_{arc}(\text{in A})$ was established at the position of the cathode surface, where I_{arc} is the arc current. Using the plasma source without filter but with focusing field, the total ion saturation current reached about 10% of the arc current. Combining the efficient plasma source (i.e., with focusing field) with a magnetic filter gives a maximum ion current of 2.5% of the arc current (Fig.2), i.e., about 25% of the ions entering the filter are usable for film deposition.

To investigate the influence of the guiding and focusing magnetic field strengths, the arc current and the currents for the magnetic field coils were driven independently (Fig. 3). At small or moderate focusing field, the output increases with increasing guiding field. Maximum output is reached at a focusing field of about 30 mT. A higher focusing field is not advantageous, and plasma instabilities have been observed at much higher magnetic field strength [6].

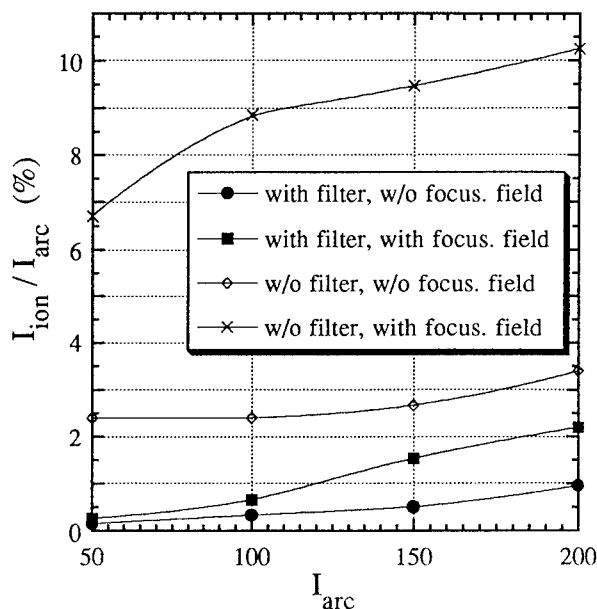


Fig. 2 Ratio of ion current to arc current (in %) for various source and filter arrangements. Arc current, focusing and guiding field coils are electrically in series. Titanium cathode, 5 ms discharges.

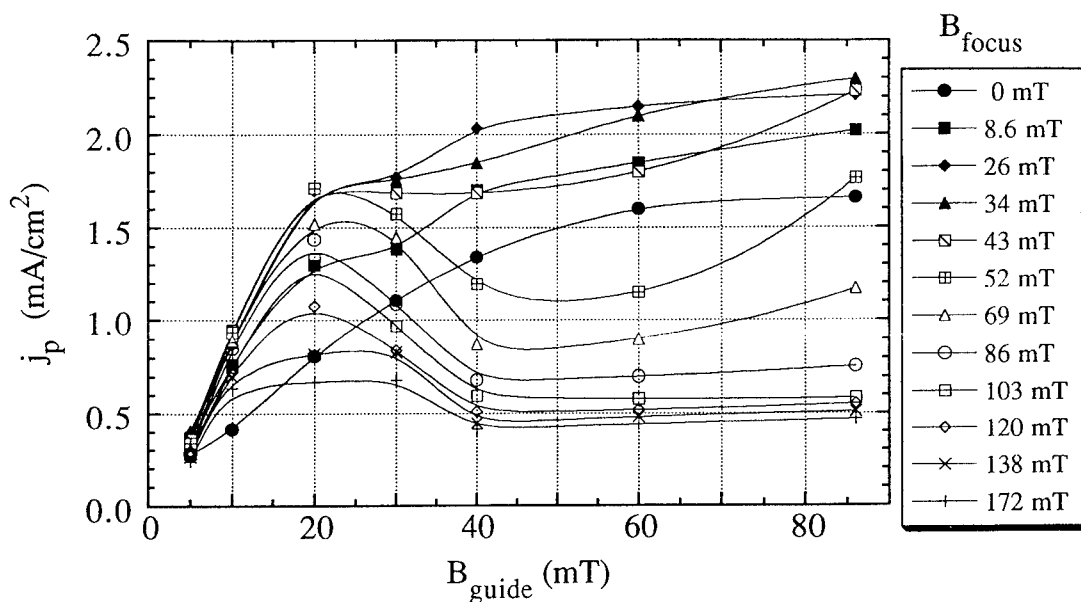


Fig. 3: Ion saturation current density as a function of the guiding magnetic field strength, with the focusing field strength as a parameter. Titanium cathode, 100 A, 5 ms discharges.

5. UPSCALING OF PLASMA SOURCE AND FILTER

Large fluxes of plasma are required for the deposition of thick films (e.g., ≥ 500 nm). Increasing plasma production by increasing the arc current is limited due to the appearance of anode

4. DOWNSCALING OF PLASMA SOURCE AND FILTER

Smaller devices must be capable of handling the average power which can be estimated by $\bar{P} \leq \delta U I_{arc}$ where δ is the arc duty cycle and U is the burning voltage. Vacuum arcs require a minimum arc current ("chopping current", typically a few amperes), and a finite arc lifetime has been observed even for currents greater than the chopping current. This effect is associated with the nonstationary nature of cathode spots. Since U is of order 20 V, the duty cycle must be lower than 10^{-2} to keep the heat load low.

Another consideration of downscaling is to keep the necessary electrical insulation between anode, cathode, and trigger. Cathode erosion, heat load and insulation limit the scaling; one feasible device that we have developed is shown in Fig. 4. It has been used for deposition of *thin* films (≤ 10 nm).

spots which may destroy the plasma source anode, its cooling system, or other parts. The arc current is therefore typically smaller than 1 kA. Large plasma fluxes can be obtained by using a high arc duty cycle, up to DC operation.

Heat removal from the plasma source-filter system and from the substrate becomes essential. A

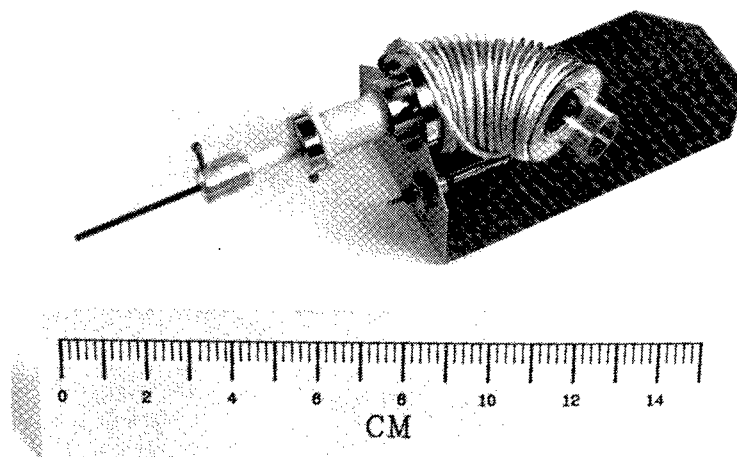


Fig. 4 Miniature vacuum arc plasma source with magnetic macroparticle filter.

large system has been developed (cathode diameter 5 cm) in which cathode, anode, duct, and substrate are water-cooled. In a quasi-DC mode of operation (pulse length up to 1 sec) various metal films have been deposited with thickness of up to 100 μm . Different trigger schemes have been tested, including a surface discharge trigger and electromechanical trigger mechanisms. In the first case, deposition of cathode material on the insulating surface is a problem which can be overcome by a suitable insulator shape. In the case of a movable trigger pin, coating of the pin and eventual welding of trigger pin and cathode remained a problem if thousands of discharges were required.

6. "DUST" PRODUCED IN DEPOSITION FACILITY

If the films deposited are strained, they may eventually crack and delaminate. This is true not only for films deposited on substrates but also for films which are deposited on the plasma source anode and duct wall. In particular, if carbon is used as the cathode to deposit amorphous diamond films, microscopic flakes of cracked films are "blown" with the plasma stream towards the substrate although macroparticle filtering has been shown to work properly. More work is needed to solve this problem.

ACKNOWLEDGMENT

This work was supported by the Electric Power Research Institute under RP 8042-03 and by the U.S. Department of Energy, Office of Basic Energy Sciences, under Contract No. DE-AC03-76SF00098.

REFERENCES

- [1] R.L. Boxman and S. Goldsmith, "Macroparticle contamination in cathodic arc coatings: generation, transport and control," *Surface and Coatings Technology* vol. 52, pp. 39-50, 1992.
- [2] I.I. Aksenov, V.A. Belous, V.G. Padalka and V.M. Khoroshikh, "Transport of plasma streams in curvilinear plasma-optics systems," *Sov. J. Plasma Phys.* vol. 4, pp. 425-428, 1978.
- [3] S. Anders, A. Anders and I. Brown, "Macroparticle-free thin films produced by an efficient vacuum arc deposition technique," *J. Appl. Phys.* vol. 74, pp. 4239-4241, 1993.
- [4] A. Anders, S. Anders and I.G. Brown, "Effect of duct bias on transport of vacuum arc plasmas through curved magnetic filters," to be published in *J. Appl. Phys.* (May 1994).
- [5] S. Anders, A. Anders and I. Brown, "Focused injection of vacuum arc plasmas into curved magnetic filters," to be published in *J. Appl. Phys.* (May 1994).
- [6] A. Anders, S. Anders and I.G. Brown, "Transport of vacuum arc plasmas through magnetic macroparticle filters," submitted to *Plasma Sources Sci. & Technol.*

CALCULATION OF PLASMA MHD-FLOW IN VACUUM SPARK DISCHARGE

V.A.Skvortsov, A.Yu.Krukovsky, A.A.Otochin
High Energy Density Research Center,
Russian Academy of Sciences,
127412, Moscow, Izhorskaya 13/19

ABSTRACT

The present paper deals with the creation of a new mathematical model for 2D-computer simulation of the axisymmetrical radiative plasma magnetohydrodynamics (MHD) flows under vacuum spark discharge. In difference with the earlier works (see, for example,¹ and its references) we use not only one-but also two temperature approximation and take into consideration not only electrical but also magnetic fields in equation's system of the mathematical model. Created MHD-model is based on implicit full conservative difference scheme in combined Eulerian and Lagrangian (CEL) approach. The system of difference equations is solved by using of Newton-like iteration procedure. Groups of equations are selected in accordance with the similar character of physical processes and the energy balance calculation is carried out for the convergence control.

1. INTRODUCTION

The goal of this work is the development of computer code to simulation of MHD processes in emissive center on the cathode surface under high voltage discharges. The solution of such a problem has a key significance for the creation of quantitative theory of explosive electronic emission (EEE)². One of the main problem is the correct description of electro-magnetic fields and electric currents in the emission region along with self-consistent solution of hydrodynamical equations.

Thermophysical, electrophysical and optical properties of real substances in wide range of parameters are taken into account in our work. The using of nonequidistance difference grids and two temperature approximation makes it possible to investigate the processes in the near-cathode region not only for small (as it was made earlier with the aid of the model¹) but also for big gaps between the electrodes.

This circumstance considerably increases the validity of the created model because makes it possible to provide practically important scientific and engineering calculations of perspective devices in micro- and high power electronics, micrometallurgy².

2. MODEL FORMULATION

The mathematical model of the explosive and the destructive processes of the cathode microinhomogeneities under vacuum discharge are based on the system of the 2-D nonstationary axisymmetrical magnetohydrodynamic equations³:

$$\begin{aligned}
\partial \rho / \partial t + \operatorname{div}(\vec{V} \rho) &= 0, \\
\rho d\vec{V} / dt &= -\nabla(P + \hat{D}) + [\vec{j}, \vec{B}] / c, \\
\rho d\varepsilon / dt &= -(P + \hat{D}) \nabla \vec{V} - \nabla \vec{W} + G_j, \\
\vec{W} &= -\hat{\alpha} \operatorname{grad} T, \\
\operatorname{rot} \vec{B} &= \frac{4\pi}{c} \vec{j}, \\
\operatorname{rot} \vec{E} &= -\frac{1}{c} \frac{\partial \vec{B}}{\partial t}, \\
\operatorname{div} \vec{B} &= 0, \\
\vec{j} &= \hat{\sigma} \cdot (\vec{E} + [\vec{V}, \vec{B}] / c).
\end{aligned} \tag{1}$$

Here ρ - density of matter, \vec{V} - hydrodynamics velocity vector of matter (two components), P - pressure, ε - specific internal energy, $\vec{B} = (0, B_\phi, 0)$ - vector of magnetic field, $\vec{E} = (E_r, 0, E_z)$ - vector of electric field density, T - temperature, c - velocity of light, $\hat{\alpha} = \hat{\alpha}(\rho, T, \vec{B})$ - total coefficient of thermal and radiative heat transfer, $\hat{\sigma} = \hat{\sigma}(\rho, T, \vec{B})$ - electric conductivity coefficient, $j(r, z, t)$ - density of current, $G_j = (j)^2 / \hat{\sigma}$ - Joule dissipation, \hat{D} - displacement part of tension.

Thermal and electrical conductivity were calculated using the method, which includes effects of non-ideal plasma and electron degeneration^{4,5}. The system of hydrodynamical equations was completed by wide-range equation of state⁶ (EOS).

Boundary conditions include Nottingham's effect⁷ (for solid state cathode surface or ordinary electron emissive cooling for the plasma surface) and surface thermal black body emission:

$$\frac{\partial T}{\partial n} = \frac{j_{\text{em}}}{e} W_n + \sigma_{SB} \cdot T^4. \tag{2}$$

Here W_n is the mean energy carried out by single electron, j_{em} - density of emissive current.

The peculiarity of our approach is the calculations of nonstationary electric and magnetic fields and currents. To make these calculations we've divided our region into two parts - matter and vacuum. Then we should take into account evolution of:

- spatial distribution of strong electric fields in vacuum;
- spatial distribution of electro-magnetic fields and current inside the tip and plasma corona.

As the first step of calculations at each moment of time (i.e. at each step of hydrodynamical calculations to take into account rapid changes of geometry and electrical conductivity) we solve Laplace equation in the vacuum:

$$\Delta \phi = 0, \tag{3}$$

where ϕ is the electric potential. Then we calculate the density of emissive current j_{em} at the interface between solid state matter and

vacuum using relationships⁸ and between plasma and vacuum using recommendations⁹. (We disregarded metal-plasma emission as in¹⁰). For this, we construct additional grid between electrodes every time-step and solve the equation (3). Then we may calculate the density of emissive current and magnetic field on the boundary:

$$B_{\text{boundary}} = \frac{2}{cr} \int_{\Omega} \vec{j}_{\text{em}} \cdot d\vec{S} \quad (4)$$

for Maxwell's equations (see (1)), using which we can find the distributions of current densities inside the tip and energy, deposited into the tip (or another kind of emissive center geometry). Here Ω - emissive surface, which is limited by circumference with radius r .

The discrete model is implemented on the base of implicit full conservative finite-difference scheme corresponding the difference system of MHD equations (1) and used the technique of adaptive grid¹¹.

The algorithm for solution the system of finite-difference equations derive a few groups of equations depending on physical processes. There are motion, energy, field groups. Every group of equations is solved by means of Newton-like iteration procedure³.

The energy balance calculation is carried out for the convergence control during the solving of the discrete MHD equations. The full conservative method ensure us to obtain most correct physical effects in discussion problems.

Numerical generation of grids has recently found extensive application to problems in physics and engineering. This is because many problems of practical interest, such as flows bounded by curved surfaces, can be calculated in curvilinear coordinates more accurately and conveniently than in Cartesian coordinates. In flow problems, the boundary conditions have to be represented accurately in the numerical formulation since the region in the immediate of solid surfaces is generally dominant in determining the character of the flow, especially at high Reynolds numbers.

We used an adaptive-node method having next ingredients:

- an orderly method of numbering (or mapping) nodes distributed over the physical region of interest;
- a means of "communicating" between nodes so that the distribution of nodes remains fairly regular as they are shifted;
- a measure of the error in the discrete values that bears some relation to the truncation error;
- a means of redistributing the nodes as indicated by the measure, so as to reduce solution error.

At first, the nodes are held stationary in physical space one or several time-steps, after which the measure is computed. Then, the nodes are shifted in response to the measure to their new positions. During the calculation the measure, we used the the information about coordinates of the node, form of domain, and node velocities.

3. SUMMARY

The computer simulations were performed for investigation of the electro-explosion of the different micro-inhomogeneities (cylindrical and conic microtips, hot spots) on the aluminum cathode surface, during nanosecond vacuum discharges.

A new results of such computer simulations will be discussed in

this symposium (the limited volume of this paper does not permit us to demonstrate all interesting results). Note only, that in some cases the induction of magnetic field may reaches up to 100 T during nanosecond discharges, that is very important to account in describing the dynamics of emissive centers. But when the magnetic fields are not such high the results of computer simulations are in a good agreement in major details with that received earlier (in electrohydrodynamic approach as in¹).

Thus the constructed model made available to produce computer simulation of the high speed processes of initiation of electron explosive emission at the spark stage of vacuum discharges in any axisymmetrical geometry and with taking into account the effects of magnetic fields.

4.ACKNOWLEDGEMENTS

The authors wish to acknowledge G.A.Mesyats and V.E. Fortov for stimulating discussions and attention to this work. The authors also grateful to R. Borisov and I. Lomonosov for submitted tables of data of transport coefficients and EOS.

5.REFERENCES

- 1.G.A.Mesyats, V.A.Skvortsov, V.E.Fortov, V.A.Moroz, "Electrohydrodynamics of cathode microtorch". Proc.XXI Int.Conf. on Phenomena in Ionized Gases, Vol.1, pp.15-16, Buchum, 1993.
- 2.G.A.Mesyats, D.I.Proskurovsky, "Pulsed electrical discharge in vacuum", Springle-Verlag, Berlin, 1989.
- 3.V.A.Gasilov, A.Yu. Krukovsky, A.A.Otochin, "Program complex for calculation of 2-D axisymmetrical radiative MHD-flow", Preprint. Inst. Appl. Mathem., the USSR Academy of Sciences, No 160, 1990.
- 4.W.Ebeling, V.E.Fortov, V.K.Gryaznov, A.Forster, A.Ya.Polishchuk, "Thermophysical properties of hot dense matter", Teubner-Texte zur Physik, Leipzig, 1990.
- 5.G.R.Gathers, "Thermophysical Properties of Liquid Copper and Aluminum", International Journal of Thermophysics, Vol. 4, No. 3, pp.209-226, 1983.
- 6.A.V.Bushman, I.V.Lomonosov, V.E.Fortov, "Models of wide-range equations of state for matter under conditions of energy density", Sov. Tech. Rev. (B), Therm. Phys., Vol.5 (1), pp.1-44, 1993.
- 7.W.R. Nottingham, "Remarks on Energy Losses Attending Thermo-Ionic Emission of Electrons from Metals", Phys.Rev., Vol. 59, pp.906-907, 1941.
- 8.E.L.Murphy, R.H.Good, "Thermionic Emission, Field emission, and the Transition Region", Phys. Rev., Vol. 102, No.6, pp.1464-1473, 1956.
- 9.F.R. Schwirzke, "Vacuum Breakdown on Metal Surfaces", IEEE Trans. Plasma Sci., Vol. 19, pp.690-698, 1991.
- 10.E.A.Litvinov, G.A.Mesyatz, A.G. Parfenov, "Peculiarities of transition of metal- plasma at initial stage of explosive emission cycle at the cathode", Dokl. Acad. Sci. USSR, Vol. 320, No. 2, pp.319-321, 1991.
- 11.V.A.Gasilov, A.Yu. Krukovsky, Al.A.Otochin, An.A.Otochin, "Full conservative difference scheme in CEL variables for calculations of axisymmetrical MHD-flows", Preprint. Inst. Appl. Mathem. the USSR Acad. of Sciences, No. 5, 1991.

HF-Reignition phenomena related to post-arc current in vacuum interrupters

René P. P. Smeets¹, Honqun Li², Nico J.G. Lamerichs¹, Eiji Kaneko³

¹ Eindhoven University of Technology, Eindhoven, the Netherlands

² Xi'an Jiaotong University, Xi'an, P.R. of China

³ Toshiba Corporation, Fuchu Works, Tokyo, Japan

ABSTRACT

After interruption of a high-frequency (hf) current by a vacuum arc, two distinct types of reignition can be observed. The first type follows immediately after interruption, the second type tends to allow a currentless pause of a few tenths of a microsecond. The post-arc current that flows after hf-current interruption has been measured and has a peak of several A and a decay time of a several hundreds of ns. A dynamic sheath model for the decaying plasma after hf current interruption has been used successfully to model the measured post-arc current waveshapes. The first type of reignition may be attributed to thermal stress during the period in which no ion sheath has been formed yet, the second type to high electric fields, either due to the ion sheath, or due to the TRV, the weight of each depending on gaplength and di/dt .

1. INTRODUCTION

In circuit breakers, the post-arc current (the manifestation of the decaying residual plasma that is present a short time after current interruption) has a negative influence on the current interruption ability. This is documented for the interruption of power frequency currents of very high magnitudes¹. Currents that flow after reignition of interrupters are much smaller (few hundred of A) than the just mentioned short circuit currents, but their frequency is orders of magnitude higher than 50 Hz, dictated by the parasitic circuit in the vicinity of the interrupter. This causes the steepness (di/dt) of reignition current to be in the same order or higher than in the case of a short circuit current. Thanks to the excellent interrupting ability of vacuum interrupters, currents with di/dt of hundreds of A/ μ s may still be interrupted. The question whether or not a reignition current can be interrupted is important in estimating the probability of over-voltage generation in power distribution networks by processes such as voltage escalation and virtual current chopping². In this contribution, the relation between hf current interruption ability and post-arc current will be discussed.

2. POST-ARC CURRENT MEASUREMENT

HF currents were obtained by letting an opening vacuum interrupter breakdown soon after contact separation at a gaplength smaller than 500 μ m. The discharge of a parallel LC circuit generates currents of several 100 kHz, such as occur in power distribution systems. By this method, typical waveshapes as shown in fig. 1 are obtained.

Immediately after interruption of the hf current, the (small) gap is stressed by the transient recovery voltage (TRV) that has an extreme steepness, in our case approx. 100 kV/ μ s. This TRV originates from the parasitic capacitance of the interrupter (from 50 pF to 15 pF depending on the momentary gaplength) and the total inductance of the hf current loop (in the order of few tens of μ H). In order to obtain the plasma component of the post-arc current, the capacitive current due to the TRV was subtracted from the measured current using the appropriate interrupter capacitance.

From fig. 1 it is clear that two types of reignition are present³:

- immediate reignition (the first three zero passages in fig. 1) without a noticeable rise of voltage;
- delayed reignition (the 4th zero passage), in which a currentless pause of several tens of ns allows the TRV to rise to a level of several kV, whereupon the gap reignites.

At the fifth zero passage, definite current interruption takes place.

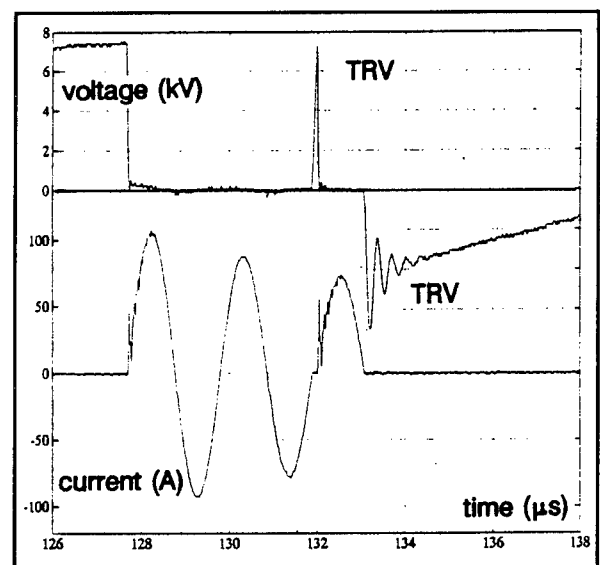


Fig. 1: Voltage and current during reignition

The problem in measuring post-arc current is its small value following pre-zero amplitudes of many hundreds of A. Especially in hf current interruption, the time between appearance of current maximum and post-arc current is only in the order of a μs . A very fast clipping device is constructed that limits the output of a broadband current transformer. This device is realised with a coaxial array of fast diodes. Extensive checks guaranteed that the clipping of the current transformer output signal did not influence the near zero current period.

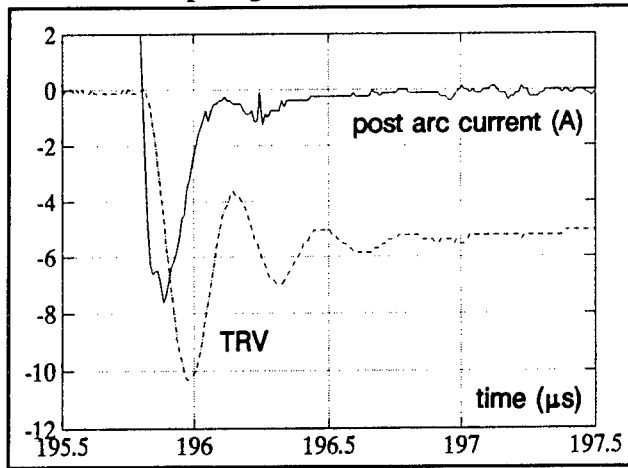


Fig. 2: Measured post-arc current and TRV

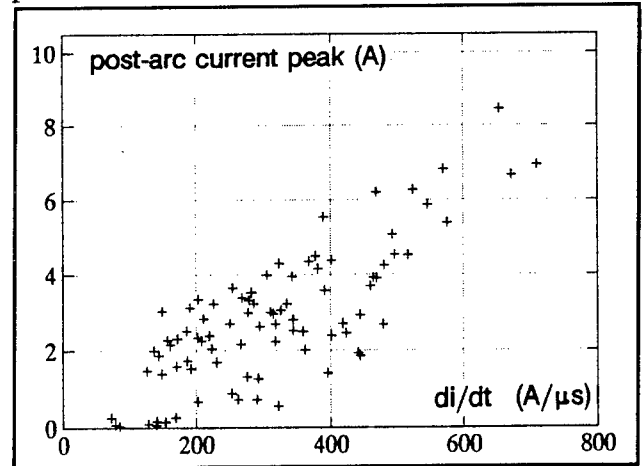


Fig. 3: Peak of post-arc current vs. current zero di/dt

A typical oscillogram of a post arc current can be seen in fig. 2. Its peak is typically a few A, decaying to zero in less than a μs . This peak value is in the same order as after 50 Hz short circuit current interruption¹ (with axial field-type contacts). The duration, however, is much shorter in our case, due to the small gaplength.

By varying the frequency of the current and the breakdown voltage, the peak value of post-arc current (\hat{I}_{pa}) was investigated as a function of current steepness at current zero (S_i). This results in fig. 3. As can be seen, the post-arc current increases approximately proportional to current steepness. The vertical spread is due to the difference in gaplength. When the post-arc current peak value is plotted against gaplength at constant di/dt (of 300 A/ μs) then it becomes clear that post-arc current rises steeply with gaplength until a saturation value is reached. This is shown in fig. 4, together with \hat{I}_{pa} calculated from eq. (2).

The same tendency is observed for the 6 different contact materials under investigation. It was striking to notice that the post-arc current peak is roughly independent of the contact material when gaplength and di/dt are kept the same, although the reignition behaviour of the materials differs considerably.

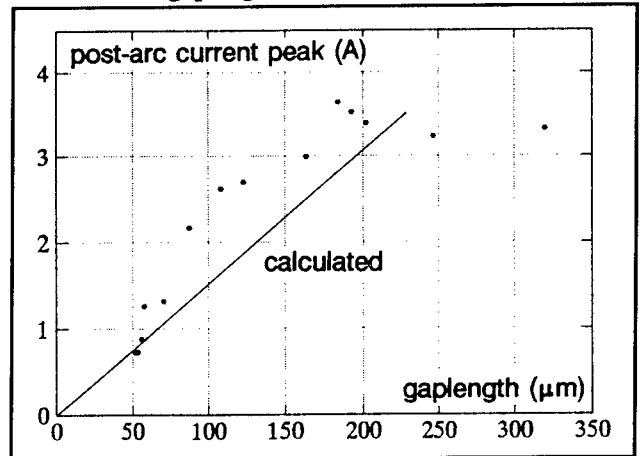


Fig. 4: Post-arc current vs. gaplength for fixed di/dt

3. MODELLING OF POST-ARC PHENOMENA

At current zero, the ion velocity is roughly equal to the electron velocity. Thereafter, the electron velocity decreases until the electrons reverse direction at a time t_1 . From current zero to t_1 , the former arc plasma remains an excellent conductor and no TRV can develop. Starting from t_1 , electrons leave the plasma at the ex-cathode side, leaving behind an ion space charge at the ex-anode side over which the TRV can develop.

As an initial condition, the ion density at current zero (n_{i0}) has to be estimated. Assuming a constant ion velocity v_i near current zero, all the ions that are present in the gap (with length d) at current zero are created in a time interval $\tau = d/v_i$ before current zero. Therefore, n_{i0} can be estimated from the arc current waveshape a time τ ago as follows:

$$n_{i0} = \frac{1}{zeV} \int_{-\tau}^0 0.1 i(t) dt = \frac{S_i d}{5ze\pi D^2 v_i^2} \quad (1)$$

with V the cylindrical volume of the discharge with diameter D , ze the ion charge and the factor 0.1 accounting for the

well known fact that 10% of the arc current is carried by ions.

It is this initial ion density that roughly determines the value of the post-arc current (i_{pa}) at t_1 because at that instant the post-arc current is solely carried by ions, giving for this current and for the "TRV delay time" t_1 the following estimation:

$$i_{pa}(t_1) = \frac{\pi D^2 z e v_i n_{i0}}{4} = \frac{d S_i}{20 v_i} \quad \text{this yields for } t_1: \quad t_1 = \frac{i_{pa}(t_1)}{S_i} = \frac{d}{20 v_i} \quad (2)$$

in which the sinusoidal arc current is linearised between the time τ before current zero and t_1 after current zero.

For the analysis of the complete post-arc current waveshape, the Andrews-Varey transition model⁴ has been used in order to describe the expansion of the space charge sheath starting at t_1 . A series of 5 differential equations can be set up in order to couple the dynamics of this sheath with the parasitic circuit in the vicinity of the arc⁵. With the assumption $v_i = 10^3$ m/s and $d = 1$ mm these equations can be solved relatively easy. A typical result is presented in fig. 5, where a 170 A 165 kHz current was interrupted in a 260 μm gap. The initial ion density is in the order of 10^{22} m^{-3} .

Comparing the measured waveshape with the calculated one, it may be concluded that the model reasonably explains the post-arc phenomena. From fig. 5, it can be seen that the peak value of i_{pa} is only slightly higher than $i_{pa}(t_1)$, estimated above. Therefore, the proportionality of post-arc current peak with di/dt and with gaplength as suggested by figs. 3 and 4 may be understood within the model outlined above. The flattening at longer gaps is because linearisation of hf current is no longer allowed for larger τ .

4. REIGNITION AND POST-ARC CURRENT

The importance of the post-arc current for reignition of the gap lies in the fact that the presence of the ion sheath creates an electrical field (E_{pa}) at the ex-anode. The absolute magnitude of this electrical field can be estimated as follows⁶:

$$E_{pa} = 2 \sqrt{\frac{z e n_i}{\epsilon_0} \sqrt{u U_0 + U_0^2} - U_0}, \quad U_0 = \frac{m}{2e} \left(v_i + \frac{dl}{dt} \right)^2 \quad (3)$$

with n_i the decaying ion density, u the voltage over the sheath (TRV), l the increasing sheath thickness, m the ion mass.

This field only exists during the period that a post-arc current is drawn. After this - when the sheath has reached the ex-cathode, the remaining electric field originates from the TRV, yielding $E_{trv} = u/d$. Using the Andrews-Varey model with the appropriate initial estimations the total field can be calculated.

This is visualised in fig. 6 showing the electrical field (vertical axis) at the ex-anode as a function of time (0 - 1 μs) after t_1 and gaplength (30 - 465 μm) after interruption of 335 A/ μs current. For small gaps, E_{trv} dominates over E_{pa} , whereas the opposite is true for larger gaps. Also, the time of maximum of E_{pa} drifts further away from t_1 at longer gaps; the maximum value of E_{trv} always occurs at half the inverse TRV frequency, in our case 230 ns after the start of TRV at t_1 .

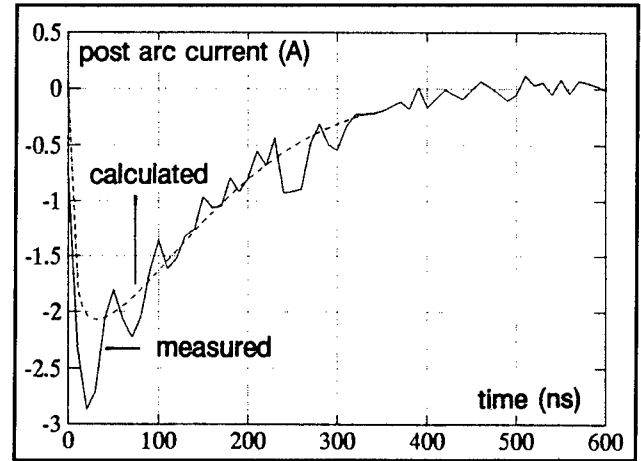


Fig. 5: Measured and calculated post-arc current

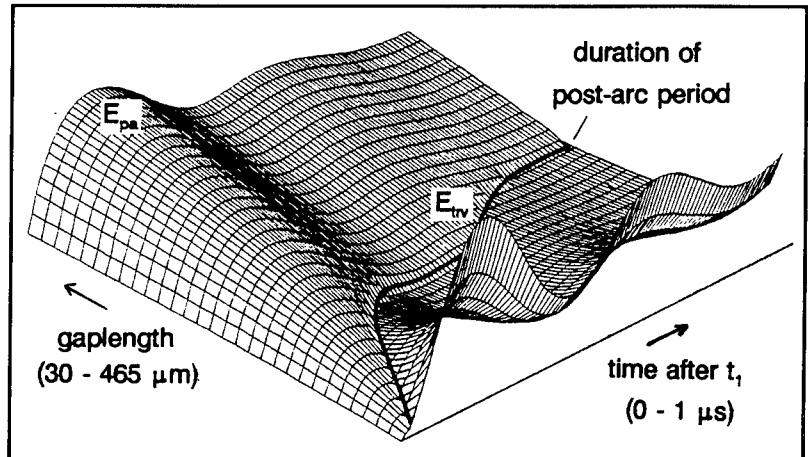


Fig. 6: Calculated electric field vs. time and gaplength

The two types of reignition, mentioned in sect. 2 and shown in fig. 1, may now be explained as follows:

- immediate reignition always occurs between current zero and t_1 under the influence of a linear rising post-arc current $i_{pa} = S_i t$ and negligible voltage (much less than arc voltage) that decelerates the electrons. Ion bombardment of the ex-anode will probably thermally lead to new cathode spot formation.
- delayed reignition is due to a sufficiently high field at the ex-anode, either caused by the TRV directly (E_{trv}) at small gaps and relatively low S_i (too small \hat{I}_{pa}) or by the field due to post-arc current (E_{pa}) at larger gaps.

The propositions above are verified indirectly by investigating the frequency of occurrence of each type of reignition at varying gap-length. This is done in a fixed vacuum gap that suffers breakdown by a 65 kV pulse, followed by a hf current that is independent of the breakdown voltage⁷. The result is given in fig. 7, where the fraction of immediate reignitions of the total number of reignitions is plotted (CuCr contactmaterial). At smaller gaps, in the absence of a significant post-arc current, the large value of E_{trv} causes delayed reignition, while at larger gaps (with decreasing E_{trv}) the increasing value of both post-arc peak current \hat{I}_{pa} and t_1 causes a more severe thermal stress on the ex-anode, more easily leading to immediate reignition. Also, the shift from immediate to delayed reignition within one series of reignitions as in fig. 1 can be explained by realising that the decreasing di/dt reduces the post-arc current thus relieving the thermal stress and giving way for the E-field to reignite the gap.

5. SUMMARY AND CONCLUSIONS

After interruption of current with steep rate of fall, post-arc current can be observed. The post-arc period is divided in two time-intervals:

- $0 < t \leq t_1$: The post-arc plasma is a perfect conductor. TRV can not rise yet. Reignition in this period is due to thermal stress on the ex-anode. The post-arc current peak and the initial ion-density increases proportional to the gaplength (up to a saturation level) to di/dt prior to current zero [eq. (2)]. At t_1 an ion space charge sheath starts to develop at the ex-anode.
- $t > t_1$: The ion sheath is sweeping the gap, starting from the ex-anode, whereby the post-arc current first increases slightly before falling to zero in less than a μs . In this period, a high electric field may be built up by the sheath formation, and thereafter by the usual TRV. At small gaps, the latter dominates due to the small initial ion-density whereas at larger gaps the former can more easily cause reignition. Reignition in this period is accompanied by a steep (up to 100 kV/ μs) reignition peak of several kV.

No significant difference in post-arc current has been observed for six different contact materials. Their different sensitivity for reignition (e.g. breakdown field strength) accounts for the different capability of interrupting high di/dt current.

6. REFERENCES

1. S. Yanabu, Y. Satoh, M. Honma, T. Tamagawa, E. Kaneko, "Post arc current in vacuum interrupters", *IEEE Trans. on Power Delivery*, Vol. 1, No. 4, pp. 209-214, Oct. 1986
2. R.P.P. Smeets, R.C.M. Kardos, J.P. van Oostveen, R.G.C. Dirven, H.Q. Li, E. Kaneko, "Essential parameters of vacuum interrupter and circuit related to the occurrence of virtual current chopping in motor circuits", *IVth IEE Japan Power & Energy Soc. Meeting, Sapporo, July 1993*
3. R.P.P. Smeets, T. Funabashi, E. Kaneko, I. Ohshima, "Types of Reignition Following HF Current Zero in Vacuum Interrupters with Two Types of Contact Material", *IEEE Trans. on Plasma Sci.*, Vol. 21, pp. 478-483, 1993
4. J.G. Andrews and R.H. Valey, "Sheath growth in a low-pressure plasma", *Phys. Fluids*, Vol. 14, pp. 339, 1971
5. M. Lindmayer and E.-D. Wilkening, "Breakdown of Short Vacuum Gaps after Current Zero of High Frequency Arcs", *XIVth Int. Symp. on Disch. and Elec. Ins. in Vacuum*, Santa Fe, USA, pp. 234-241, Sept. 1990
6. S. Childs and A.N. Greenwood, "A Model for DC Interruption in Diffuse Vacuum Arcs", *IEEE Trans. on Plasma Sci.*, Vol. PS-8, No. 4, pp. 289-294, Dec. 1980
7. H.Q. Li and R.P.P. Smeets, "Gap-length Dependent Phenomena of High-frequency Vacuum Arcs", *Eindhoven University of Technology Report 93-E-280, Eindhoven, the Netherlands, Nov. 1993*

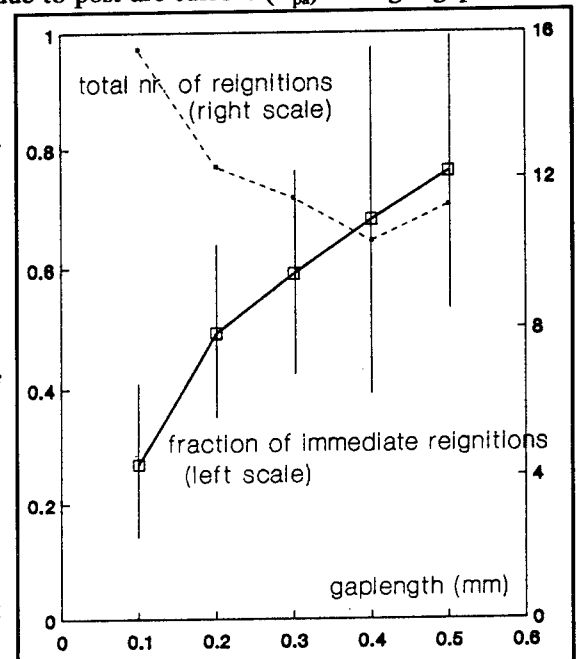


Fig. 7: Fraction of immediate reign. vs. gaplength

Measurement of cathode spot parameters with pulsed laser diagnostics

Nadja Vogel, Jan Heinzinger, Frank Cichos

University of Technology Chemnitz-Zwickau,
Department of Physics, Sub dept. of Optical Spectroscopy and Molecule Physics, POB 964,
09009 Chemnitz, Germany

ABSTRACT

The cathode spot formation within first 22 ns was investigated by laser absorption photography and ps-pulse interferometry. The discharge was initiated between W -, Ag -, AuNi -, Pd - electrodes with cathode-anode distance below 100 μm , the arc duration was some milliseconds and arc current 5A. A ps-pulse holographic interferometer and momentary absorption photography enabled us to determinate spatial-temporal density distributions in the ignition phase of the cathode spot. An absolute electron density value of order of $3 \cdot 10^{26} \text{ m}^{-3}$ has been determined indicating high conductivity values of the metal vapour plasma. Present measurements show that cathode spot plasma is essentially non-ideal and verify theoretical calculations resulting in an ionisation potential decrease in dense cathode plasmas.

1. INTRODUCTION

Many parameters of cathode spot plasmas are still controversial, especially the plasma size. Whereas Rakhovskii¹ reports about 100 μm as typical plasma radius, Anders et al.² found values around 10 μm by using spot imaging by laser absorption. Still smaller values ($<5\mu\text{m}$) have been deduced in ref.³ by evaluating Zeeman-splitting of Cu-resonance lines in vacuum. This indicates a possible substructure not resolved in ref.². Probably with clean surface in ultra high vacuum the spot fragments remain too close to each other ($\Delta x < 10 \mu\text{m}$) to be optically resolved. When using oxidised surfaces remaining crater distribution indicates a separation of fragments. Thus, the study of such surfaces promises easier detection of fragments. However the oxide layers will quickly be removed by the arcs. In air the layers can be restored. Thus, for arcs in air should facilitate the demonstration of small spot fragments.

There is evidence that the surrounding air has little influence on the nature of the spot core: Zeeman splitting is found with break arcs³ in air as well streak measurements⁴ revealed high frequency fluctuations of the spot core ($6 \cdot 10^{17} \text{ Hz}$) as in the case of vacuum arc spots, while the surrounding air region changed in a slower time scale (e.g. rotation with time constants of about 30 μs). Possible differences between spot plasmas in vacuum and air refer to distances $> 100 \mu\text{m}$ from the spot centre because of the high vapour pressure that separates the spot core from the surroundings. Thus, investigation of spot fragmentation in air for distances $< 10 \mu\text{m}$ should be applicable also for vacuum arc spots.

The present paper reports an experimental study of spot fragmentation in air by laser absorption and interferometry.

2. EXPERIMENTAL

The investigated electrodes formed a point-to-point gap of 50-200 μm . Materials were Pd, W, Ag, AuNi. The applied voltage was 30-90 V. Arcs with currents of 5 A were ignited by focusing a IR-laser beam, duration 100 ps, onto the circumferential surface of the anode. At a preselected time, 0,1-22 ns after ignition, the gap was illuminated by a second laser beam for achievity absorption images and holographic interferograms. Figure 1 shows the optical set-up. The laser system consisted of an actively mode-locked oscillator, a single pulse selection unit, two amplifiers, a generator for producing the second and third harmonics, a set elation's for extending the pulse durations. The laser operated with a repetition frequency of 10 Hz or with single shots. The ignition beam operated at the fundamental frequency ($\lambda = 1064 \text{ nm}$). With a focus area of diameter $< 40 \mu\text{m}$ the maximum surface power density was $4 \cdot 10^{18} \text{ W/m}^2$.

The electrode system was placed in one arm of Michelson interferometer. When using only one mirror, this arrangement was used for producing absorption pictures on a CCD camera. The probing laser beam passing the interferometer was optically delayed with respect to the ignition beam (3 prisms in fig. 1). Spot imaging was achieved with a magnification optics ($\times 14$) and a 10 nm interference filter centred at $\lambda = 532 \text{ nm}$ to reduce the light emitted by the spots. The CCD

images were digitised with 8 bit depth with a 512×512 pixel frame. The distributions of interference phases was determined by a linear FFT algorithm (analogously to the 2D-algorithm developed by Kreis⁵).

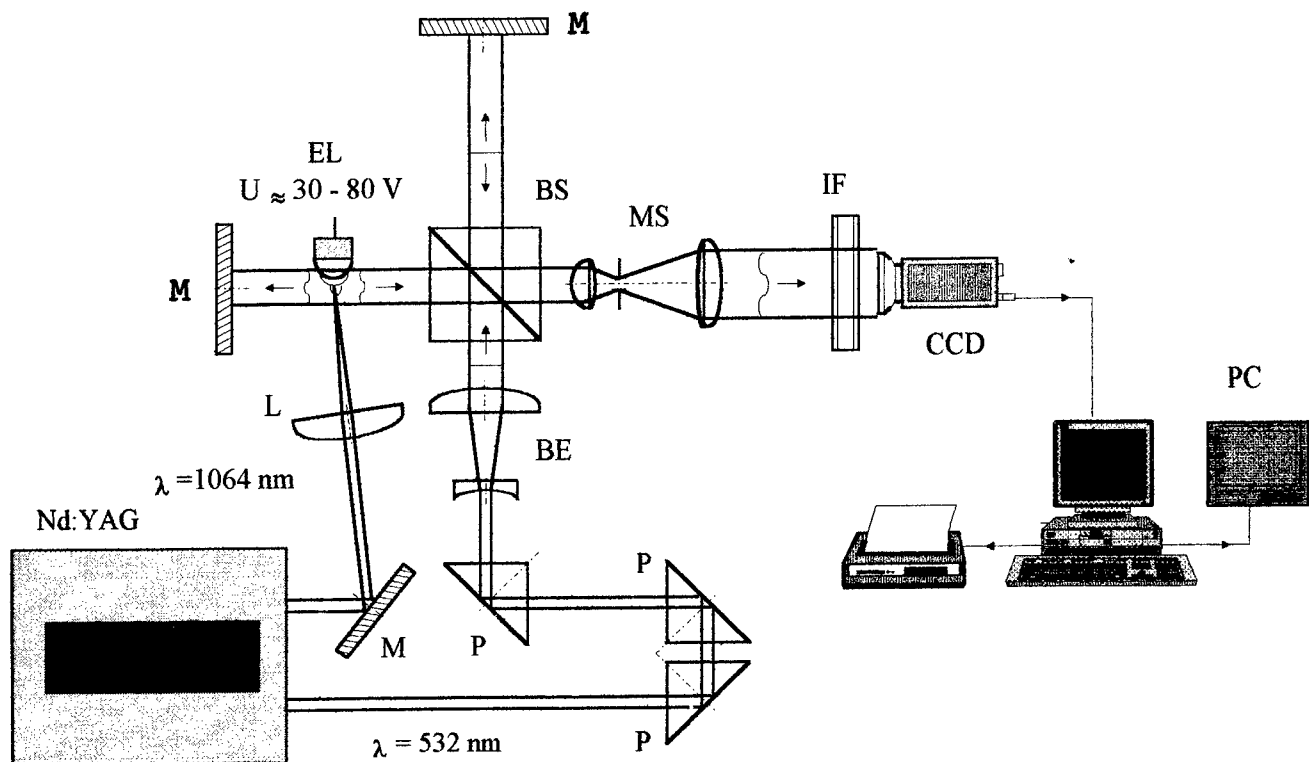
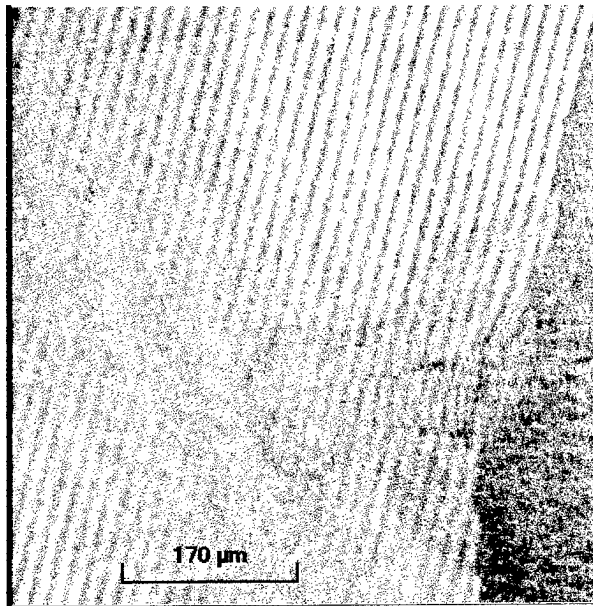


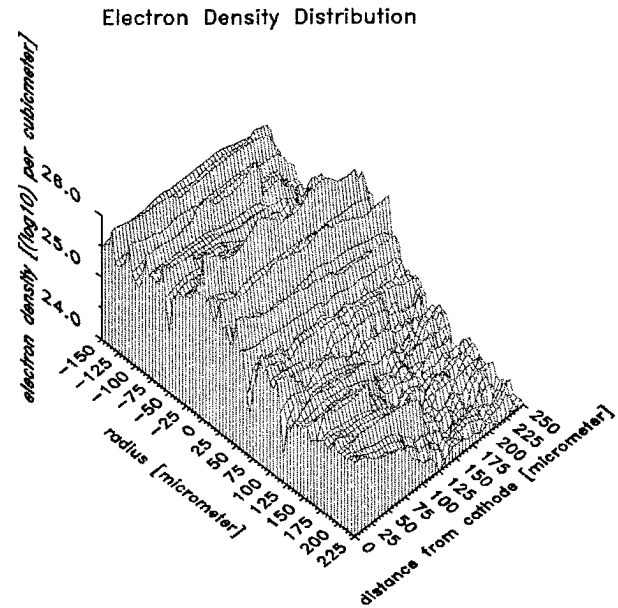
Fig. 1. Optical set-up: EL - electrodes configuration; Nd:YAG - laser system; L - lenses; M - mirrors; BE - beam expander system; BS - beam splitter cube; P - prisms; MS - magnification system; IF - interference filter; CCD - camera; PC - automatic image processing.

3. RESULTS

Fig. 2 shows a combined interference and absorption image of the anodic trigger plasma. It exhibits large absorption structure with a size $\approx 200 \mu\text{m}$, showing discernible shifts of interference fringes in the centre. The peculiarities and properties of such laser induced plasmas should be discussed in a forthcoming paper⁶. By means of this plasma it was easy to ignite anode spots, whereas the probability for production of cathode spots was < 1 . In the case of occurrence of cathode spots an internal structure could be observed. Fig. 3 gives an example for a Pd - cathode. The conditions of this picture were: current 5 A, exposure time 100 ps, time elapsed after ignition 9,1 ns. The overall spot size amounts to about $20 \mu\text{m}$. It exhibits internal fragments with a diameter $< 5 \mu\text{m}$. This can clearly be seen in the line scan though the spot shown in fig. 4. In fig. 3 some fringes around the spot indicate the shock wave produced in the surrounding air by the spot plasma.



a).



b).

Fig. 2. a). Holographic interferogram of the laser induced plasma 2.2 ns after the ignition laser pulse, b). Electron density distribution corresponding to this interferogram

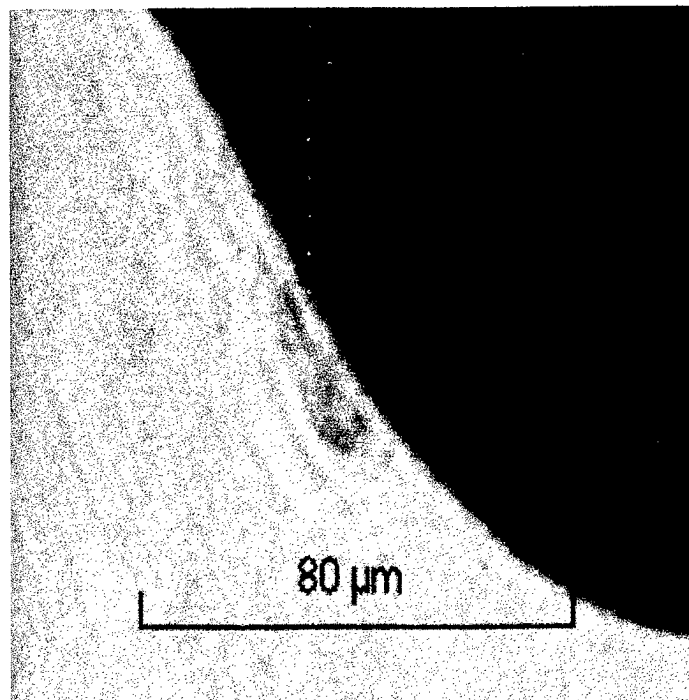


Fig. 3. Absorption photograph of the cathode spot plasma 9.1 ns after IR - laser pulse ignition .

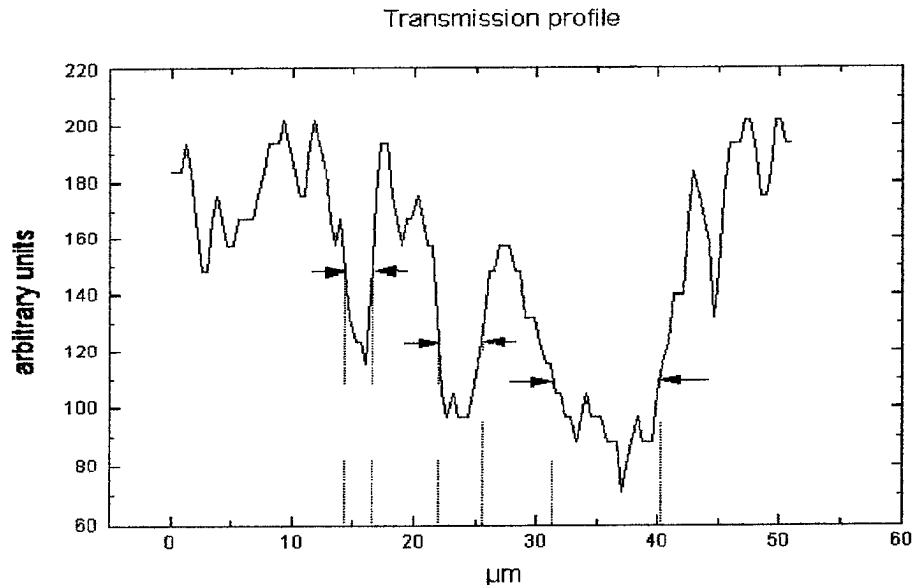


Fig. 4. Transmission scanning profile through the absorption picture, the pointers show the dimensions of the fragments in cathode spots

4. DISCUSSION

Fig. 3 and 4 yield direct evidence for the fact that the small plasma structures of a metal vapour spot ($< 20 \mu\text{m}$) can consist of an agglomerate of still small fragments ($< 5 \mu\text{m}$). From the absorption coefficient of the whole plasma a mean electron density $> 3 \cdot 10^{26} \text{ m}^{-3}$ and a current density $> 10^{11} \text{ A/m}^2$ can be estimated (compare ref.²). Within the fragments, the density must be $\geq 10^{27} \text{ m}^{-3}$ and the current density $\geq 10^{12} \text{ A/m}^2$. The latter explains the Zeeman splitting observed in ref.³. Probably, the occurrence of shock wave strings (fig. 3) was possible only by our short exposure time. During this time the plasma expanding with a velocity of 10 - 20 km/s covers a distance of 1 - 2 μm , sufficiently small to preserve the fringe structure. These will disappear with larger exposures. It might also be that exposure times $> 1.1 \text{ ns}$ (as in ref.²) are not sufficient to resolve internal fragments because of the plasma expansion.

5. ACKNOWLEDGEMENTS

The present work was supported by the contract DFG Vo 527/1-1 of the Deutsche Forschungsgemeinschaft.

6. REFERENCES

1. V. I. Rakhovskii, "Experimental study of the dynamics of cathode spots development", IEEE Trans. Plasma Sci., Vol. PS-4, pp. 1-102, 1976
2. A. Anders, S. Anders, B. Jüttner, W. Böttcher, H. Lück and G. Schröder, "Pulsed dye laser diagnostics of vacuum arc cathode spots", IEEE Trans. Plasma Sci., Vol. 20, pp. 466-472, August 1992
3. N. Vogel and B. Jüttner, "Measurements of current density in arc cathode spots from the Zeeman splitting of emission lines", J. Phys. D: Appl. Phys. Vol. 24, pp. 922-927, 1991
4. N. Vogel, "The cathode spot plasma in low-current air and vacuum break arcs", J. Phys. D: Appl. Phys., Vol. 26, pp. 1655-1661, 1993
5. T. Kreis and W. P. O. Jüttner, "Fourier-transform evaluation of interference patterns: demodulation and sign ambiguity", SPIE Vol. 1553, Laser Interferometry IV: Computer-Aided Interferometry, pp. 263-273, 1991
6. N. Vogel, to be published

Calculation of film thickness distribution provided by vacuum arc deposition

Hao Wang, Ji-yan Zou, Lei Yang, Li-chun cheng
Huazhong University of Science and Technology, Department of Electrical Engineering
Wuhan, Hubei, 430074, P.R.China

Hong-lin Yang
Hunan University, Department of Electrical Engineering
Changshan, Hunan, 410012, P.R.China

ABSTRACT

Computer calculation of pure metal film thickness distribution, using vacuum arc deposition technique, is presented in this paper. For random arc with a lower arc current, a model of single cathode spot with ion beam flux taking into account the cosine function spatial distribution is deduced. For arc steered by an external magnetic field, which is parallel to the cathode surface, a multiple cathode spots model is developed. And, in the case of random arc, calculation comparison between static substrate and rotating substrate is made. Results show that, film thickness distribution is non-uniform when the arc is not controlled and tends to be uniform when the arc is steered by external parallel magnetic field with cathode geometry and substrate location being well choosed. Also, film thickness distribution is more uniform on a rotating substrate than on a static substrate.

1. INTRODUCTION

Recently, vacuum arc deposition technique has been widely used as an efficient method of metal surface modification both in laboratory and in industrial use. It has many advantages over other deposition methods, such as high ionization, high energy and fast deposition rate.¹⁻⁴

Film thickness is one of the key points to film properties, which effects directly on the modification efficiency. Few papers about theoretical analysis on film thickness distribution in this field were found than that in the field of vacuum evaporation. The difficulty is the complication of determining the ion current spatial distribution in the plasma beam, particularly in the case of steered arc. Boxman et al.,⁵ developed an approximate model to calculate the film deposition rate, taking into account the ion current with the cosine function spatial distribution. For steered arc, magnetic field influence on cathode spot distribution, motion, propagation and collimation of the plasma, makes it difficult to determine the ion current distribution accurately.

In the present work, a simple model is employed to calculate the film thickness distribution on the substrate, both for random and steered arc. The calculation is based on the deposition configuration as shown in Fig. 1. It consists of a circular, planar source cathode, and an aperture anode being coplanar with the cathode surface. The substrate is located outside the interelectrode region and the deposited material is conveyed to it by an ion beam extracted from the arc. Before the calculation, some presumption are made:

- a. No collision between metal ions and remaining gas molecules exists.
- b. No second emission on substrate surface.
- c. Only pure metal film of cathode material are deposited.

2. CALCULATION MODEL

2.1. Random arc deposition

Random arc is characterized by cathode spots move randomly on the cathode surface.⁶ In the case that arc current is less than 100A, only one cathode spot exists.⁷ Close to the cathode spot, we are faced with a strong vapor and plasma jet and with extremely high current density.⁸ As shown in Fig. 1, there is a current-carrying plasma channel of current density line between the cathode spot and somewhere on the anode surface. In plasma jet, ion current component I_1 may be given by⁹

$$I_i = fI \quad (1)$$

Where I is the arc current, f is a constant ranging from 0.07 to 0.12, depending on the cathode material. The ion current density from cathode spot jet, has a cosine function angular distribution

$$J_i(\theta) = \frac{fI \cos \theta}{2\pi l^2} \quad (2)$$

Where θ is the solid angle from cathode spot to point B, on the substrate surface, l is the distance between cathode spot and point B. $J_i(\theta)$ means the ions going into the solid angle. In unit time, the film thickness on point B is given by

$$D = u_D = \frac{J_i(\theta) M_i \cos \alpha}{eZ\rho} \quad (3)$$

Where Z is the average degree of ionization of the ions, ρ is the film density, M_i is the mass of the cathode material ion. And the relation between the geometry parameters are

$$\cos \theta = \cos \alpha = \frac{h}{l} \quad (4)$$

$$l^2 = h^2 + x^2 \quad (5)$$

Where x is the distance between point B and the source point of substrate (o')

Combining equation (2), (3), (4), and (5) film thickness D_x is given by

$$D_x = \frac{fI \cos \theta \cdot M_i \cdot \cos \alpha}{eZ\rho \cdot 2\pi l^2} = \frac{M_i fI}{2\pi eZ\rho} \cdot \frac{h^2}{(h^2 + x^2)^2} \quad (6)$$

When $x=0$, film thickness on point O is

$$D = D_0 = \frac{M_i fI}{2\pi eZ\rho} \cdot \frac{1}{h^2} \quad (7)$$

Then, film thickness distribution on the substrate is given by

$$\frac{D_x}{D_0} = \frac{h^4}{(h^2 + x^2)^2} \quad (8)$$

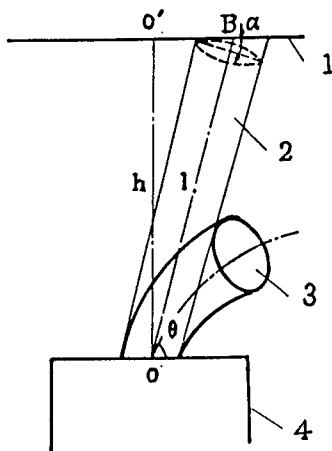


Fig.1 Configuration for random arc deposition
1.Substrate 2.Ion beam channel
3.Discharge channel 4.Cathode

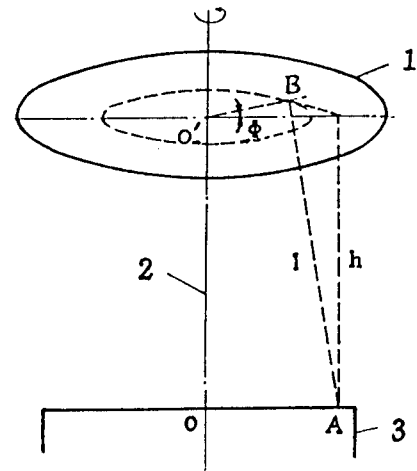


Fig.2 Calculation of rotating substrate
1.Substrate 2.Circulating axle 3.Cathode

2.2. Rotating substrate deposition

If the substrate can circle around the central-axis, as shown in Fig.2, the film thickness distribution based on random arc deposition can be given by

$$\frac{D_x}{D_0} = \frac{\int_0^{2\pi} (h^2 + x^2 + y^2 - 2xy \cos \Phi)^{-2} d\Phi}{\int_0^{2\pi} (h^2 + y^2)^{-2} d\Phi} \quad (9)$$

Where y is the distance between cathode spot and the source point of cathode plate. (o)

2.3. Steered arc deposition

"Steered arc" was first introduced in an international patent.⁹ It means that, on the influence of external magnetic field being parallel to the cathode surface, cathode spot was controlled to move according to the direction of $-J \times B$ (i.e. retrograde). For the reason of high velocity and short lifetime of the cathode spot, we can consider that cathode spots exist continually along a certain circumference and form a cathode spots ring on the cathode surface. At the mean time, cathode spots ring shrink and expanse. So, it seems that cathode spots distribute on all of the cathode surface.

As shown in Fig.3, A is a point on cathode surface, B is a point on substrate surface. Projecting point B on X-Y plane, projective point is B'. x is the distance between B' and Y-axis. h is the distance between B and B'. Then, the distance between A and B is l .

$$l^2 = h^2 + r^2 + x^2 - 2xrcos\Phi \quad (10)$$

Where r is the radius of the ring, where point A is on. Φ is the angular coordinate of point A.

Summing all the fluxes from each cathode spot jets, the ion current flux in solid angle θ is

$$J_i(\theta) = \frac{1}{2\pi R} \int_0^R \int_0^{2\pi} \frac{fI \cos \theta}{2\pi l^2} d\Phi dr \quad (11)$$

The film thickness distribution is

$$D_x / D_0 = \int_0^R \int_0^{2\pi} (h^2 + r^2 + x^2 - 2xrcos\Phi)^{-2} d\Phi dr / \int_0^R \int_0^{2\pi} (h^2 + r^2)^{-2} d\Phi dr \quad (12)$$

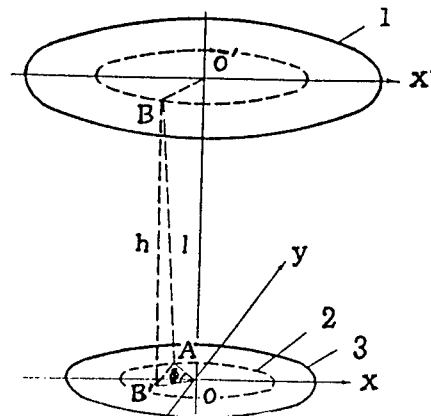


Fig.3 Calculation of steered arc deposition 1.Substrate 2.Cathode spots ring 3.Cathode

3. RESULTS AND DISCUSSION

Calculation results are shown in Fig.4, by using the former model. In Fig.4a, a comparison of thickness distribution between static and rotating substrate is made in random arc deposition. From the comparison, we can see there is a more uniform film thickness distribution on a rotating substrate than that on a static substrate. For the reason of the randomness, cathode spot is not in the source point of cathode plane. The film thickness distribution is less uniform than the calculation curve 1 in Fig.4a. In Fig.4b, film thickness distribution of steered arc deposition with different cathode geometry and

substrate location are made. When the ratio of substrate location (h) and cathode radius (R) is well chosen, a more uniform film thickness distribution can be got. According to the calculation, the best ratio is $h/R=2$. In Fig. 4c, comparison between random and steered arc deposition with different substrate location is made. There are a little difference between the two conditions. When the distance between substrate and cathode surface is more than a certain value, the difference does not exist. However, for the randomness of the cathode spot in random arc deposition, film thickness distribution of steered arc deposition is a little more uniform than that of random arc deposition.

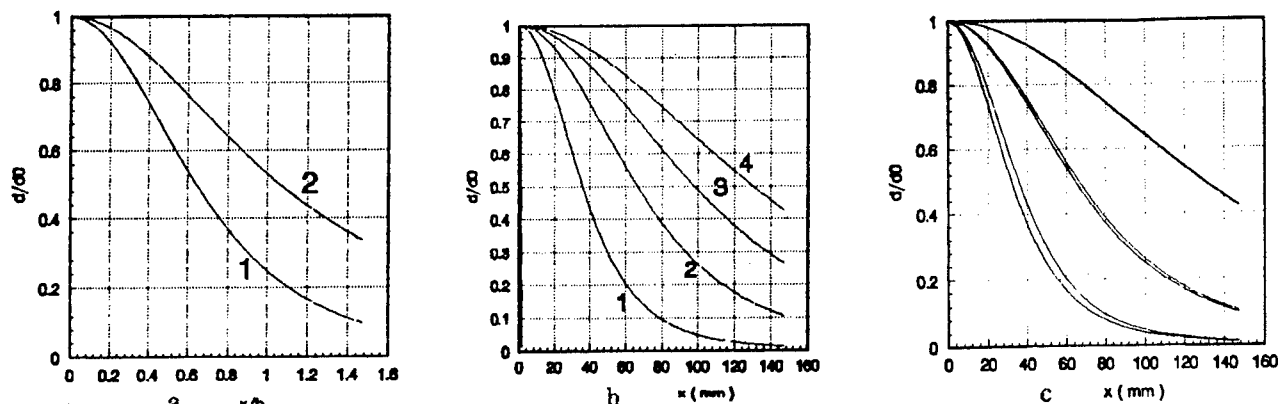


Fig.4 Calculation results

- a. Comparison between static and rotating substrate 1.Static substrate 2.Rotating substrate
b. Film thickness distribution of steered arc deposition 1. $h/R=5$ 2. $h/R=4$ 3. $h/R=3$ 4. $h/R=2$
c. Comparison between random and steered arc deposition

4. CONCLUSION

- In random arc deposition, film thickness distribution with a rotating substrate is much more uniform than that with a static substrate.
- In steered arc deposition, the ratio between substrate location and cathode radius is important to the film thickness distribution. When the ratio is well chosen, a more uniform film thickness distribution can be got.
- In general, the film thickness distribution provided by steered arc is a little more uniform than that by random arc.

5. REFERENCES

- R.L.Boxman and S.Goldsmith, "Principles and applications of vacuum arc coatings", IEEE Trans. on Plasma Science, Vol.17, No.5, pp.705-712, Oct. 1989.
- D.M.Sander et. al., "Coating technology based on the vacuum arc-a review", IEEE Trans. on Plasma Science, Vol.18, No.6, pp.883-894, Dec.1990.
- P.J.Martin, "Ionization-assisted evaporative process: techniques and film properties", IEEE, Trans. on Plasma Science, Vol.18, No.6, pp.855-868, Dec.1990.
- B.Rother, Thin solid films, Vol.188, pp.293, 1990.
- R.L.Boxman and S.Goldsmith, "Cathode spot arc coatings: physics, deposition and heating rates, and some examples", Surface and Coatings Technology, Vol.33, pp.153-167, 1987.
- J.M.Lafferty, "Vacuum arcs-theory and application", John Wiley, New York, 1980.
- J.Vyskocil and J.Musil, "Arc evaporation of hard coatings: process and film properties", Surface and Coatings Technology, Vol.43/44, pp.229-311, 1990.
- H.O.Schrade, "Arc cathode spots: their mechanism and motion", IEEE Trans. on Plasma Science, Vol. 17, No.5, pp.635-637, Oct.1989.
- S.Ramalingam, Inter. patent 85/03954, 1985.

Characterization of the cathode spot in vacuum arc deposition

Hao Wang, Ji-yan Zou, Mao-lin li, Li-chun cheng
Huazhong University of Science and Technology, Department of Electrical Engineering
Wuhan, Hubei, 430074, P.R.China
Hong-lin Yang
Hunan University, Department of Electrical Engineering
Changshan, Hunan, 410012, P.R.China

ABSTRACT

Characterization of the cathode spot, which connects to a vacuum dc arc on a consumable cathode as a source of material for deposition, is studied using high speed photograph technique. For a titanium cathode, external magnetic field effect on the behavior of the cathode spot is given with respect to number, size, and motion. Lastly, some discussion to the experimental results are presented.

1. INTRODUCTION

In the present work, we study on a kind of vacuum arc ion source used for hard film deposition, which employs a high current and low-voltage dc arc on a consumable cathode in a vacuum as an ion source of material for deposition. The extracted ions from the source have the energy of up to several hundred eV and the charge states about 2+, respectively.¹⁻⁴ For the reason of its manifest virtues, including high density, high adhesion and fast deposition rate, in the last decade, this source has been commercially employed for producing coatings on the surface of machine cutting tools with metal nitrides to extend their lifetime. The typical coatings are the wear resistant coatings of TiN and TiC.

Vacuum arc plasma has been researched deeply in the field of high power switching.⁵ In which, vacuum arc discharge is typically characterized by cathode spots, which are usually highly unstable and jump statistically over the cathode surface. In a magnetic field being parallel to the cathode surface, the cathode spots move in the retrograde direction, i.e., opposite to the Ampere rule.⁶⁻⁸ The spots eject electrons and metal vapor of cathode material extensively. The current density in the spot is in the range from 10^8 A/m² to 10^{12} A/m² or even more, depending on different theoretical models and experimental results.^{7,9,10} The velocity of cathode spot motion is about 1~10 m/s in random arc⁹ and several hundred m/s in external magnetic field steered arc.⁸ The mean lifetime of the cathode spot is in the range of 10^{-8} ~ 10^{-9} s.^{9,10}

In this paper, we concentrate our attention on the design of the vacuum arc ion source used for film deposition, the characterization of the cathode spot observed by high speed photograph camera.

2. EXPERIMENTAL ARRANGEMENT

An outline of the source is shown in Fig.1. It is composed of a water cooled, circular, planar source cathode, an aperture anode, in one limiting case, being coplanar with the cathode, an external permanent magnet behind the cathode and a shield around the outside circumference of the cathode.

When a high current, low voltage electrical discharge is ignited by a mechanical trigger in a vacuum, a substantial portion of the conducting medium consists of ionized cathode material generated at minute highly luminous regions of high current density on cathode surface known as cathode spots. Each cathode spot produces a high velocity jet of hot concentrated plasma expanding away from the minute ionization zone adjacent to the cathode spot into the surrounding vacuum. The aperture anode is used as an ion beam extractor here. The energy of the extracted ions are in the range 20~180 eV, for a variety of cathode materials. Multiple ionization are common, except for graphite and high vapor pressure cathode materials. For example, in a titanium arc in this work, ion energy is 76 eV, 67% of the ion flux is doubly ionized, 6% is triply ionized, and average charge state is 1.78.¹¹ The external magnetic field presented by the permanent magnet includes transverse and axial component near cathode surface. The transverse component will lead the high velocity retrograde motion of the cathode spot, and a uniform erosion of the cathode

surface can be achieved. The axial component can collimate the plasma jets along the axial direction. The position of the magnet can be regulated by the regulation pole, thus, the distribution of the magnetic field can be regulated. The surrounding shield is used to avoid the cathode spot generating on the outside circumference of the cathode.

The schematic of the experimental arrangement is shown in Fig. 2. The source is attached to and injecting into a 50-cm-high, 45-cm-diam vacuum chamber which is pumped to a pressure in the 10^{-1} Pa range. A high speed film scanning camera with a rotary drum and a rotary exposure plate is arranged behind the observation window, which is faced to the cathode surface of the source. The rotary speed of the drum is 2820r/min, and of the exposure plate is 500r/min.

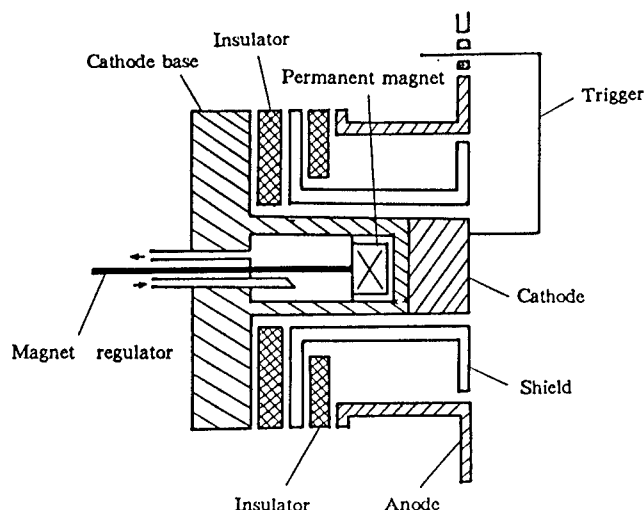


Fig.1 Outline of the vacuum arc ion source

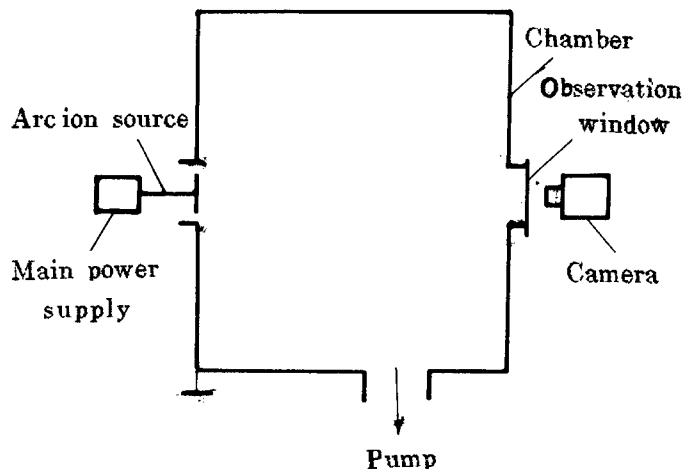


Fig.2 Schematic of experimental arrangement

3. EXPERIMENTAL RESULTS

Some experimental results are presented in this section, first, the characterization of the cathode spot, in the process of TiN film deposition, with arc current 75A, at the pressure of $1.33 \times 10^{-1} \sim 5.32$ Pa.

A series of regular camera photographs of different exposure time is shown in Fig.3. In most cases, arc current is concentrated in one cathode spot, which covers a tract of luminous region. However, multiple cathode spots existing at the same time are also observed under the same arc condition. In this case, the luminous region is divided into two or more smaller luminous region. When only one cathode spot exists, the spot is a few millimeters in size, and the appraised current density is about 4×10^6 A/m².

When the spot divides into two or more spots, the size of each spot tends to be smaller. If the arc current takes into account the average distribution in each spot, the appraised current density in each spot is about $3 \times 10^6 \sim 10^7$ A/m².

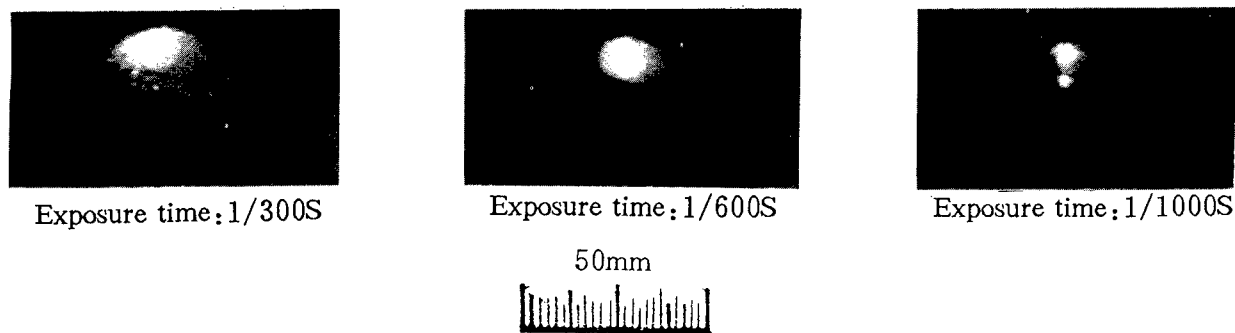


Fig.3 Regular camera photographs of cathode spot

A series of high speed camera photographs under different external magnetic field is shown in Fig. 4. The exposure time is 6 μ s, the time between each frame is 60 μ s.

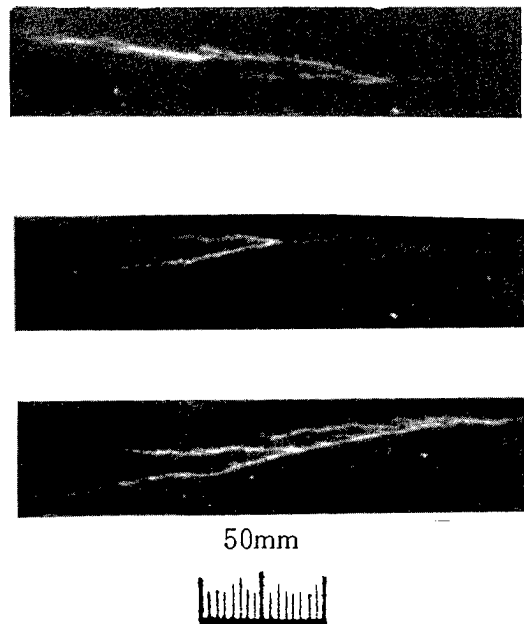


Fig.4 High speed camera photographs of cathode spot(exposure time 6 μ s, 60 μ s per frame)

Each frame shows the development of cathode spot during the spot lifetime period. At the beginning of the period, cathode spot is concentrated in one most luminous region, which is about 5mm in size. With time going on, the region disperses into two or more less luminous regions, which are 0.5~1mm in size. Then, two or more luminous spots developing channel create, and each channel has a number of burrs on both side, i.e., the dispersed spots continue to disperse. Last, the luminous channel tends to be dark gradually, and spots tend to disappear. However, a few micro-seconds later, a new cathode spot will generate at another place on the cathode surface. The average lifetime of each cathode spot is about 2 μ s, derived from the photographs. The current density in each spot and the velocity of the spot motion change with the magnetic field. The relation between each other are shown in Fig.5.

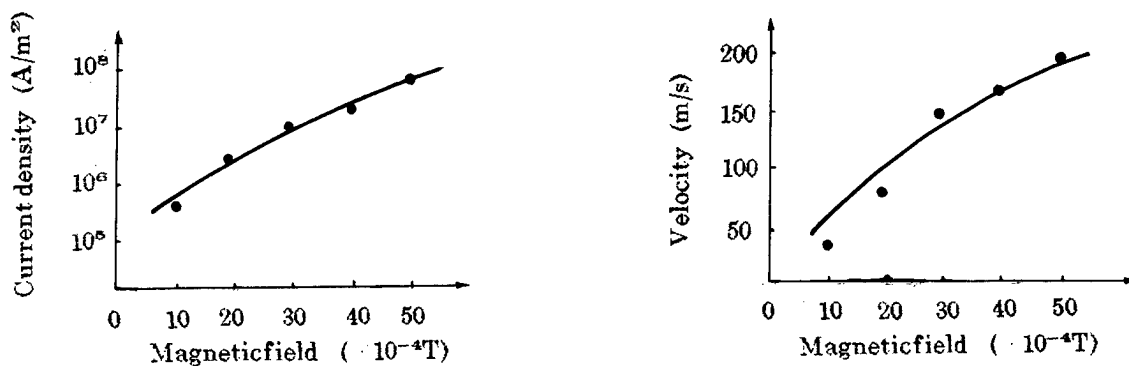


Fig.5 Relation between magnetic field and current density, velocity of cathode spot

4. DISCUSSION

The current density of cathode spot has been determined by two kind of means. One way is by determining the size of the crater on cathode surface after arcing. Another way is by determining the size of cathode spot during arcing, which is used in the present work. For the crater may be caused not only by cathode spot, but also by metal droplet ejection, the current density determined by the former way is less than the real value.

However, the problem of being difficult to determine the boundary between luminous region and dark region, is also raised in the later way. For example, the current density derived from Fig. 3 is quite different from that from Fig. 4. In Fig. 3, there is a luminous center in cathode spot luminous region. The size of the center is difficult to be determined, so the whole luminous region is taken as the size of cathode spot. In Fig. 4, the boundary is more clear and the size of spot is easy to be determined.

5. CONCLUSION

According to the experimental results, we can draw conclusion as follow. With the enhancement of transverse magnetic field, the number of cathode spots increase, the size of cathode spots tend to be smaller, the current density in each cathode spot increase, and the velocity of cathode spots motion increase.

6. REFERENCE

1. R.L.Boxman and S.Goldsmith, "Principles and applications of vacuum arc coatings", IEEE Trans. on Plasma Science, Vol.17, No.5, pp.705-712, Oct. 1989.
2. D.M.Sander et. al., "Coating technology based on the vacuum arc-a review", IEEE Trans. on Plasma Science, Vol.18, No.6, pp.883-894, Dec.1990.
3. P.J.Martin, "Ionization-assisted evaporative process: techniques and film properties", IEEE, Trans. on Plasma Science, Vol.18, No.6, pp.855-868, Dec.1990.
4. B.Rother, Thin solid films, Vol.188, pp.293, 1990.
5. J.M.Lafferty, "Vacuum arcs-theory and application", John Wiley, New York, 1980.
6. H.O.Schrade, "Arc cathode spots: their mechanism and motion", IEEE Trans. on Plasma Science, Vol. 17, No.5, pp.635-637, Oct.1989.
7. H.O.Schrade et.al., "Analysis of the cathode spot of metal vapor arcs", IEEE Trans. on Plasma Science, Vol.PS-11, No.3, pp.103-110, Sept.1983.
8. J.Vyskocil and J.Musil, "Arc evaporation of hard coatings: process and film properties", Surface and Coatings Technology, Vol.43/44, pp.229-311, 1990.
9. V.I.Rakhovsky, "Critical parameters of the cathode region of a vacuum arc", IEEE Trans. on Plasma Science, Vol.18, No.3, pp.677-681, June 1990.
10. B.Jutter, "Characterization of the cathode spot", IEEE Trans. on Plasma Science, Vol.PS-15, No.5, pp. 474-480, Oct. 1987.
11. J.Kutzner and H.C.Miller, "Ion flux from the cathode region of a vacuum arc", IEEE Trans. on Plasma Science, Vol.17, No.5, pp.688-694, Oct. 1989.

CURRENTS COLLECTED AT THE METAL SHIELD IN HIGH-CURRENT VACUUM ARCS

Z. Załucki, J. Kutzner, and Z. Boruta

Technical University of Poznań
Institute of Electric Power Engineering
60-965 POZNAŃ, POLAND

ABSTRACT

The shield current distribution in a vacuum arcs between CuCr40 contacts was studied by means of three cylindrical shields arrangement. It was found that the total shield current is affected by the arc mode. For a high-voltage oscillation sequence a significant effect on shield current distribution has an anode plasma jet. Then a great increase of the shield current is observed and the ratio of shield current to arc current was even more than 20%.

1. INTRODUCTION

The most investigations of shield ion currents were so far carried out for dc diffuse vacuum arc, usually at long arcing time [1-3]. Relatively little part of measurements of the ion current has been made at higher alternating currents [4]. Kimblin [5] found that for moderate dc arc current the anode ion flux is a linear function of arc current, and the anode ion flux starts from zero at the critical current for anode spot formation. There is a plausible necessity to study the behaviour of shield current in high-current arcs, especially in the range where a transition from diffuse to constricted arc mode occurs.

In this paper we present the values, dynamic and behaviour of these currents measured at the metal shields surrounding the arc electrodes.

The behaviour of the arcs with the active anode is investigated by measuring: the total shield ion current (i_j), the component currents flowing to three segments (upper - i_{iu} , central - i_{ic} and bottom - i_{ib}) of the metal shield connected to the cathode potential, the arc voltage (u_a) and the floating shield potential (u_c).

2. EXPERIMENTAL APPARATUS AND METHOD

The measurements of currents collected at the metal shield in the ac vacuum arcs have been carried out for a sinusoidal arc current with peak value (I_{am}) of 2,5-4-6kA and with a half-cycle of 900Hz and 150Hz (semiwave duration of 0,55ms and 3,33ms respectively). The electrodes were made from Cu60Cr40 and spaced 10mm apart in a plane of butt contact geometry (anode was 30mm in diameter, cathode of 50mm with 150mm radius of curvature). Three-elements cylindrical vapour shield with an inner diameter of 100mm were made from stainless steel. The base of central shield of 43mm height was situated in the cathode plane. The upper and bottom shields, each of 90mm height were insulated from the central shield and each other by 1mm distance.

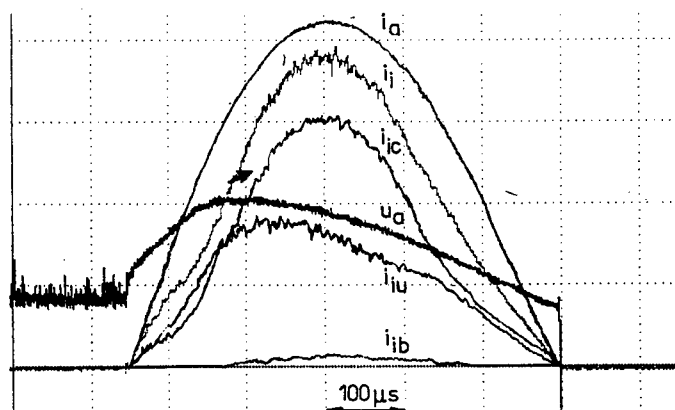


Fig.2. Waveforms of arc current (i_a), total shield current (i_j), arc voltage (u_a) and current of central (i_{ic}), upper (i_{iu}) and bottom (i_{ib}) shield, for arc current crest 2.5kA and $f=900\text{Hz}$. Scale: i_a -600A/div; i_j -50A/div; i_{ic} , i_{iu} and i_{ib} -40A/div; u_a -20V/div

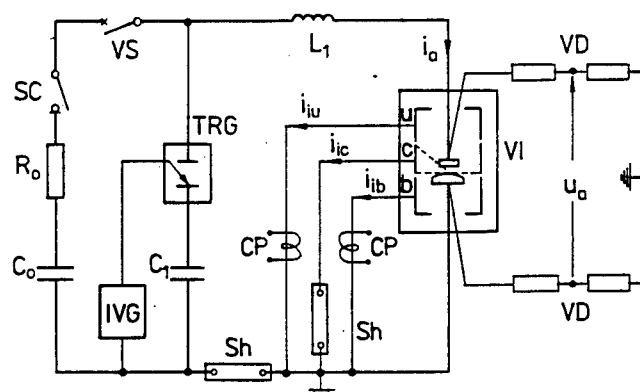


Fig.1. Circuit schematic for shield current measurements. VI-demontable vacuum chamber; TRG-trigatron; IVG-generator of ignition voltages; VS-vacuum interrupter; SC-contactor; CP-current probe; Sh-coaxial current shunt; VD-voltage divider; u,c,b-shields

The test circuit is shown in Fig.1. The source of current was the oscillating circuit C_1, L_1 . An additional branch C_0, R_0, SC and VS was applied in order to produce preliminary discharge of direct current in the testing vacuum chamber VI. The flow of dc current started at the moment of closing the contactor SC. The separation of contacts in the interrupters VS and VI caused the ignition of an arc in them. When the contact gap of VI reached the required length, the trigatron TRG was ignited and then a sinusoidal current was superposed on the current flowing from the circuit of C_1, L_1 . The preliminary current at the time of TRG ignition was 10A, therefore it created an arc with single cathode spot.

3. RESULTS OF INVESTIGATIONS AND ANALYSIS

Fig.2 shows typical example of waveforms of ion currents $i_i, i_{iu}, i_{ic}, i_{ib}$, and arc voltage u_a for arc current crest $I_{am}=2.5kA$ at the current frequency $f=900Hz$. The ratio i_i/i_a and u_a as a function of time is shown in Fig.3. We can conclude from the carried out measurements the following features or properties:

- Currents i_i and i_{ic} are almost symmetrical with a small oscillation level. The ratio i_i/i_a for $i_a=2.5kA$ is included in the range from 6.8% to 9.1%. The average value of i_i/i_a rises with the increase of i_a from 4.6% at 0.5kA to 7.7% at 2.5kA.
- At the initial period, the current i_{iu} has the values close to i_{ic} . The ratio i_{iu}/i_{ic} for $i_a=2.5kA$ is included in the range from 0.4 to 0.6. The clear asymmetry of i_{iu} is a result of spot random distribution on the cathode surface.
- The ratio i_{ib}/i_i is small and is equal to a few percent for $i_a=2.5kA$. Current i_{ib} appears with a delay of about 100 μs .
- Arc voltage is asymmetrical taking higher values during the current increase.
- Floating shield potential differs slightly from arc voltage.
- Currents flowing to the shield during arc burning are ion currents.

Similar measurements were made for $I_{am}=4.0kA$ and $f=900Hz$. Figures 4-7 show currents at the shields, voltages and the results of calculation. From the obtained results we can conclude that:

- After initiating a large voltage arc oscillations, the high-amplitude oscillations appear in currents collected by the shield. These oscillations start at $i_a=3.2kA - 3.6kA$ and thereafter, they collapse at $i_a \approx 3kA$ after the current crest.
- The ratio of i_i/i_a increases with current i_a .
- Current i_{ic} is in the shape similar to the total ion current i_i (Fig.4 and 5).
- Current i_{ib} appears with a delay of about 100 μs and rises quietly until the large oscillations in arc voltage are developed. At that moment a large oscillations in i_{ib} begin. For $i_a=4.0kA$ the ratio i_{ib}/i_{ic} is included in the range from 0.5 to 0.7.
- In the initial period, the current i_{iu} is close to value of i_{ic} and then reaches its crest value after 110 $\mu s - 140\mu s$ (before the beginning of high oscillations in u_a).
- During these oscillations, the current i_{iu} is of small values ($i_{iu}/i_{ic} < 0.1$). (A similar interrelation between i_{iu} and i_{ic} was found also at 150Hz - see Fig.6).

From comparison of results obtained for current frequencies of 900Hz and 150Hz at the arc-current crest value of 4kA, we can also ascertain that during the current increase, the higher value of i_i/i_a and u_a will occur for frequency of 900Hz (see Fig.7).

Shapes and values of the measured shield currents are considerably varied in successive trials of the same parameters. For example, for $f=900Hz$ and $I_{am}=4.0kA$, the ratio i_i/i_a near the current crest value is included in the range of 9.2-15.4 percent. This variety is caused by many factors including: the cathode spots position in the preliminary discharge at

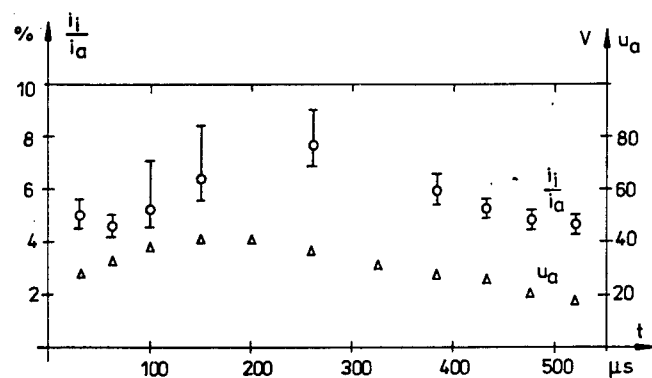


Fig.3. The ratio of i_i/i_a (o) and arc voltage u_a (Δ) versus time for $I_{am}=2.5kA$ and $f=900Hz$

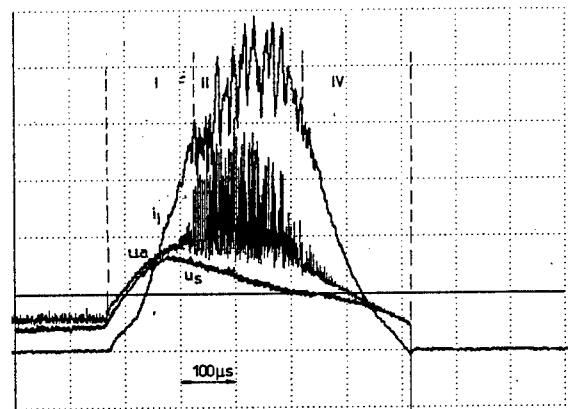


Fig.4. Waveforms of shield current (i_i), arc voltage (u_a) and floating shield potential (u_s) for $I_{am}=4.0kA$ and $f=900Hz$. Scale: i_i -125A/div; u_a and u_s -30V/div

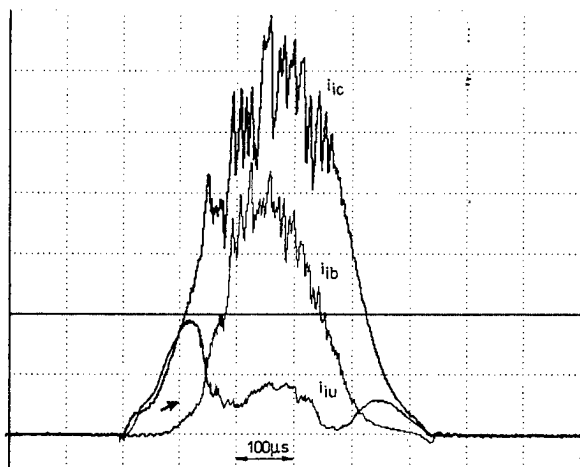


Fig.5. Waveforms of shield currents i_{ic} , i_{ib} and i_{iu} for $I_{am}=4.0kA$ and $f=900Hz$. Current scale: 75A/div

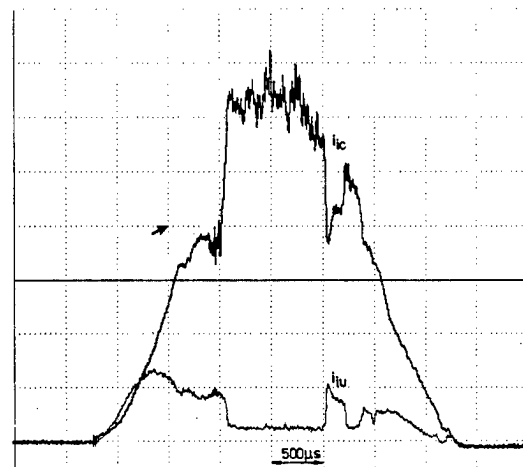


Fig.6. Waveforms of shield currents i_{ic} and i_{iu} for $I_{am}=4.0kA$ and $f=150Hz$. Current scale: 50A/div

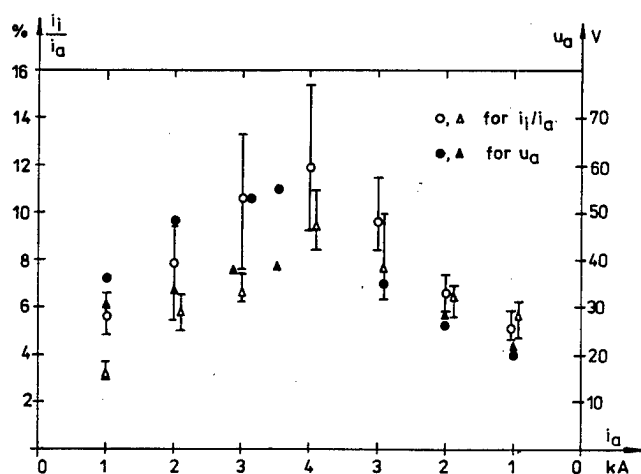


Fig.7. The ratio of i_i/i_a (○, △) and mean arc voltage (●, ▲) for instantaneous values of arc current during the current increase and decrease. Current frequency of 900Hz (○, ●) and 150Hz (△, ▲). Arc current crest 4.0kA

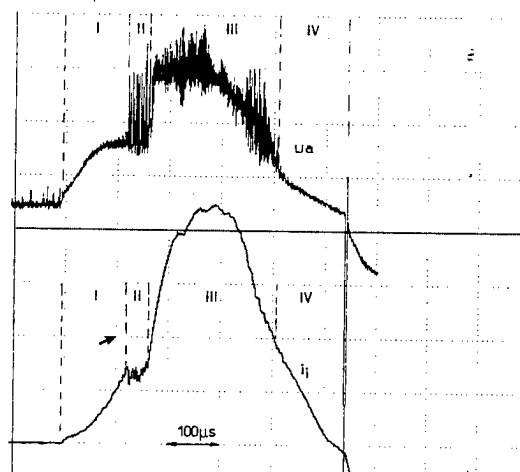


Fig.8. Typical arc voltage (u_a) and current shield (i_i) waveforms for $I_{am}=6.0kA$ and $f=900Hz$. I, II, III and IV - regions. Scale: i_i -400A/div, u_a -40V/div

the moment when the high-current semiwave starts, the dynamics of generation and expansion of new cathode spots, the distribution of active points on the anode from which evaporation takes place, and spatial distribution of anode ion fluxes.

The increase of shield currents during high oscillations of arc voltage is caused mainly by anode ion formation after the anode thermal activation. The possibility of occurrence of this effect increases with the anode voltage drop, which can be deduced from comparison the waveform of arc voltage with floating shield potential - see Fig.4.

We supposed that for 4kA arcs, the analyzed currents collected by the shields are generated mainly as a result of positive ion flux flow.

For greater arc currents, the characteristics of shield currents and arc voltage will be performed on the basis of measurements carried out for $I_{am}=6kA$ and $f=900Hz$. The obtained results and oscillograms are shown in Fig.8÷10. In the waveforms of shield current and arc voltage, we can distinguish four characteristic regions, which are essential from the point of view of the specific properties and essence of the shield currents. These Regions are shown in Fig.8, and they also occur for currents greater than 6kA.

Region I

In this Region, there is an oscillationless shield current rises with the arc current i_a , until about 4kA arc current will be reached. The average values of i_i/i_a increase from 6.6% at $i_a=1kA$ to 14.9% at $i_a=4kA$. The average arc voltage changes from about 17V at the moment of arc flow initiation, to 68V at $i_a=4kA$ (Fig.9). At the initial period, there is a rapid arc voltage increase with small oscillation amplitudes. In a later period, this increase is slower with a moderate increase of high-

frequency oscillations. In the whole Region I, there is a small difference between arc voltage and floating shield potential u_s (Fig.9). In the final phase of this Region, the upper shield current and its floating potential begin to decrease. This effect is caused by a retarding action on the cathode ions of already quite high anode potential. The change of cathode ion trajectories and the initiation of anode ion generation is one of the reasons of a higher increase of currents i_{jc} and i_{jb} in the final phase of Region I. There are experimental evidences to state that the measured shield currents are the ion currents.

Region II

The shield current typically contain a sequence of oscillations, similar to those which appear near the arc-current crest of $I_{am}=4.0kA$. Their existing time is in the range of tenths microseconds. In arc voltage, there also appear oscillations of high amplitude and frequency, at a small increase of its base value. Such a behaviour of arc voltage results from positive ion starvation in the anode Region. The voltage increase must cover a large energy losses in the plasma, and force the flow of charged carriers between the electrodes with an increasing circuit current. The needs to generate an increased amount of charged carriers result from large dispersion of positive ions to the space surrounding the contact gap. It can be assumed that also in this Region, the currents collected by the shields are generated by positive ion flow.

Region III

In this Region, a large and fast changes of shield current are observed (Fig.8). It is characterized quantitatively by the ratio of i_i/i_a shown in Fig.10. It results from the obtained data, that in Region III, the ratio i_i/i_a usually exceeds value of 0.2. At $i_a=6.0kA$ the values of i_i/i_a are included in the range from 22% to 37%. Current i_i flows mainly to the central and bottom shields. Upper shield current is small (for $i_a=6.0kA$ and $i_u/i_i < 0.05$).

In arc voltage, it is observed a rapid or even abrupt increase of the mean arc voltage value of about 40V, and high-frequency oscillations are still relatively large. After exceeding the arc-current crest, the mean value of arc voltage systematically decreases and its high-amplitude oscillations disappear at current of 4kA.

Large increases in arc voltage in Region III should be located mainly across the anode voltage drop region. This results from the comparison of mean values of arc voltage with floating shield potential, shown in Fig.9. The difference of these voltages near the arc current crest reaches 90V. In these conditions, there is an intensive anode heating as a result of large power density flow to the anode.

Large currents to the shields in Region III are a result of abundant positive ion generation in the anode region after reaching the thermal activity by the anode and creating an intensive plasma fluxes directed from the anode toward the central and bottom shields. However, the possibility of simultaneous appearance of parallel arcs burning between the shield and the anode, cannot be eliminated..

Region IV

There is a decrease of shield ion current down to zero, practically without oscillations and a decrease of arc voltage with small oscillations to the level below 20V near arc current zero. The ratio of i_i/i_a is included in the range from 5 to about 16%, and higher values of i_i/i_a occur for greater instantaneous values of arc current. Shield currents are created by positive ions collection from the plasma.

It should be stressed that Region I, II and IV occur also in the waveforms of shield voltage and currents for smaller arc currents (Fig.4).

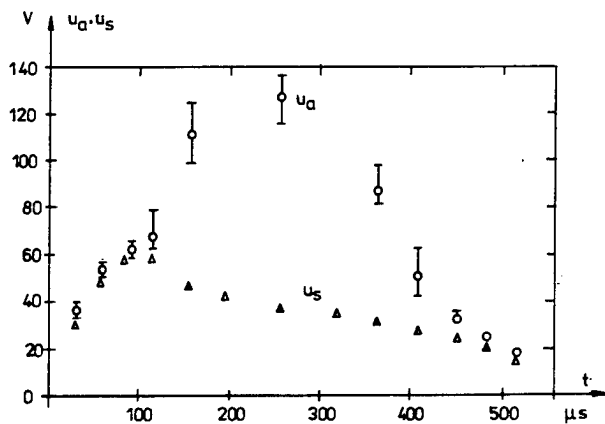


Fig.9. Mean arc voltage (u_a) and floating shield potential (u_s) for $I_{am}=6.0kA$ and $f=900Hz$

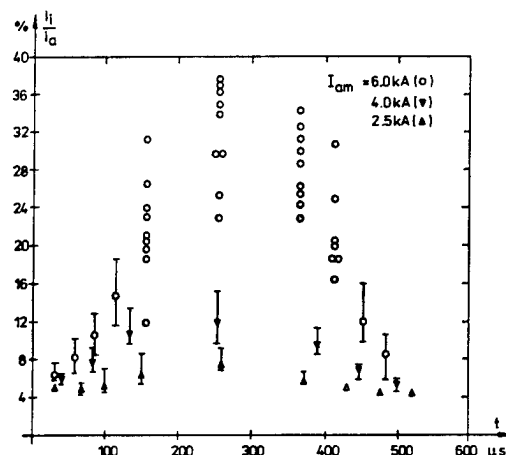


Fig.10. The ratio of i_i/i_a versus time for crest arc current 2.5kA (Δ), 4.0kA (∇) and 6.0kA (\circ), $f=900Hz$

Fig.10 contains the mean values and dispersions of i_i/i_a as a function of time for currents of the amplitude 2.5kA, 4.0kA and 6.0kA for frequency of 900Hz. Because of large dispersions of shield currents in Region III, the figure shows their values obtained in successive measurements. The compiled results characterize values and dynamics of changes of the shield current as a function of time and arc current amplitude.

4. CONCLUSIONS

During the current increase before initiation of high-amplitude oscillation in the arc voltage, the shield current - to - arc current ratio i_i/i_a is not a constant value, but it rises with the instantaneous value of arc current and also with its frequency. For $i_a \leq 4\text{kA}$ the ratio i_i/i_a is in the range from 4.5 to about 18 percent. In the most experiments it was found, that at the same instantaneous value of current on the semiwave, the shield current was greater during the current decrease than for the current increase period. Furthermore, this effect takes place when the arc voltage is clearly lower while the current decreases. During the high voltage oscillations sequence, when at the same time the base component of arc voltage is greater, a significant increase of the shield current is observed ($i_i/i_a > 20$ percent). The shield current distribution depends on the arc mode. For diffuse arc mode, this distribution is mainly affected by the cathode ion flux and also by anode potential. For high voltage oscillation sequence a significant effect has the anode plasma jet which can be confirmed by change in a current distribution between particular shields.

5. ACKNOWLEDGMENTS

This work was supported by State Committee for Scientific Research within the research project No 3.0621.9101.

The authors would like to express their deep gratitude to DEGUSSA AG. Company for supplying contact materials for the study.

6. REFERENCES

1. C.W.Kimblin, "Vacuum arc ion currents and electrode phenomena", *Proc.IEEE*, vol.59, pp.546-553, April 1971
2. J.V.R.Heberlein and D.R.Porto, "The interaction of vacuum arc ion currents with axial magnetic field, *IEEE Trans.Plasma Science* , vol.PS-8, pp.283-288, No 4, 1980
3. J.Kutzner and Z.Zalucki, "Ion currents emitted from the cathode region of a dc copper vacuum arc", *Proc.III Int.Symp.Switching Arc Phenomena*, pp.210-216, Łódź 1977
4. H.Toya, T.Hayashi, and H.Sasao, "Voltage / current characteristics at the metal shield surrounding high-current vacuum arcs", *J.Appl.Phys.*, vol.65, pp.64-69, January 1989
5. C.W.Kimblin, "Ion currents associated with the anode spots of vacuum arcs", *Proc.XII Int.Conf.Phenomena in Ionised Gases*, p.243, Eindhoven, 1975

Number of half-cycles of HF vacuum arc

H.Q. Li* R.P.P Smeets**

* Dept. of Electrical Engineering, Xi'an Jiaotong University, Xi'an, P.R. of China

** Dept. of Electrical Engineering, Eindhoven University of Technology, P.O.Box 513, 5600 MB Eindhoven, the Netherlands

ABSTRACT

An experimental circuit which can be used to measure the phenomena of HF (high frequency) vacuum arc is built. Numerous measurements are carried out and the number of half-cycles of the HF vacuum arc, which is considered important to the over voltage caused by multiple reignition of vacuum switch, is input into computer. A calculating method is developed to calculate the mean value of the number of half-cycles of vacuum arc at various fixed gap-lengths and circuit parameters. The calculated results fit the experimental ones very well. It is concluded that the number of half-cycles of HF vacuum arc depends strongly to the frequency dependent decaying constant of the high HF circuit and the parasitic or lumped capacitor parallel to the vacuum interrupter.

1. INTRODUCTION

When a vacuum switch is used to switch an inductive circuit a transient phenomenon called multiple reignition may occur. This multiple reignition can cause voltage escalation and, especially in the three-phase circuit case, another phenomenon called virtual current chopping. Attention had already been paid to these phenomena in early 1970's^{1,2} because the overvoltage caused by the phenomena is hazardous. It is found that the surges caused by such phenomena may endanger the turn-to-turn insulation of the load such as motors and transformers, even if the crest value of the surges is not so high. So the two factors being responsible for the mentioned surges, circuit parameters and the behaviour of HF vacuum arc, are constantly the subject of those who are interested in the phenomena.

Analytical and simulation methods are used to consider the effect of the parameters of the different circuits on the overvoltage resulting from the HF arcing^{1,2,3}. Meanwhile experimental and theoretical methods are used to understand the phenomena and behaviour of HF vacuum arc. M. Lindmayer and E.-D. Wilkening measured the effects of circuit parameters on the reignition voltage distribution of short vacuum gaps (mostly gap length being 64 μm) of different contact materials⁴ and deduced that at high currents, where low reignition voltages dominate, the reignitions occur

in the old arc channel, favoured by the strong field of the space charge sheath in front of the new cathode⁵. Z. Zalucki^{6,7} measured the phenomena of HF vacuum arc at a gap length of 0.3 mm and also estimated that if high frequency arcs developed from one point there are high concentrations of cathode spots and high power densities on the anode.

From the overvoltage producing view point the important parameter of HF vacuum arc (contains a series of reignitions) is the total arcing time or the number of half-cycles of the HF vacuum arc. In the fact, during the HF arcing period the load inductance is charged by the power source to a certain value of current which in turn produces a overvoltage over the vacuum interrupter if the HF vacuum arc extinguishes. If there is another reignition and therefore another HF vacuum arc, the higher overvoltage would increase the probability of virtual current chopping. This is because the high current in the HF arcing phase will cause high induced current in the other phases through the coupling between the different phases.

The aim of this research is to study the relation between the circuit parameters, gap-length and the number of HF vacuum arcs.

2. EXPERIMENTAL SET-UP

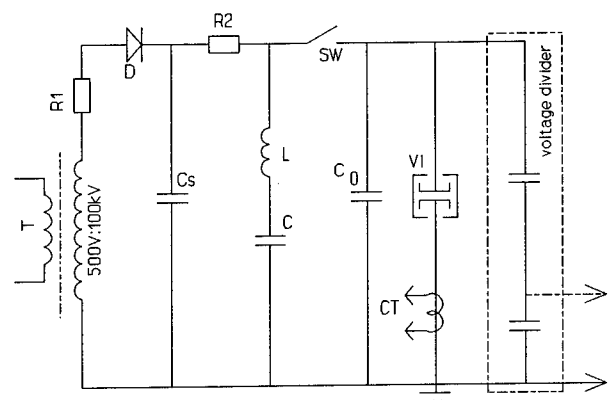


Fig.1 Experimental circuit for HF arcing phenomena measurement with fixed gap length

The experimental circuit for HF arcing phenomena

measurement is shown in Fig.1. Capacitor C, inductor L (147 μ H) and the vacuum interrupter VI constitute the HF circuit which supplies the HF current to HF arcing. C₀ is a changeable capacitor, which, together with the inductor L, forms the ultra high frequency (UHF) circuit producing UHF recovery voltage over VI after each half-cycle of current of HF arcing.

The gap length of the vacuum interrupter is fixed during one shot (measurement) and is measured by a digital vernier calliper.

The fixed gap HF arcing phenomena measuring process is as follows. First, fix the vacuum gap to a predetermined length and charge the capacitor C to a required voltage. Then, SW is switched on and at the same time a UHF transient voltage is applied to the gap of the vacuum interrupter VI. This transient voltage breaks down the vacuum gap of VI and initiates the HF vacuum arcing. At last the waveform of current and voltage are recorded by a LECROY 9400 digital oscilloscope (sampling time 10ns) through a Pearson current transformer (20 A/V) and a self-made capacitive voltage divider (6.05 kV/V). In this paper a reignition means one half-cycle of HF arcing and a reignition voltage the voltage which starts (by breakdown of the gap) the reignition.

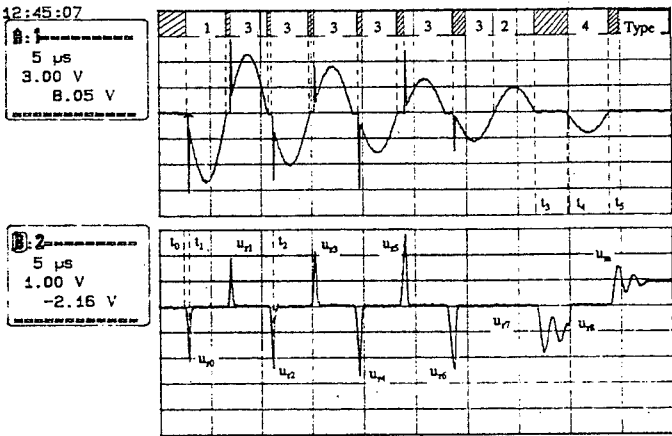


Fig.2 A typical voltage and current waveform of measurement. Current (upper trace): 60A/div, voltage (lower trace): 6.05kV/div and time: 5 μ s/div

A typical waveform of current and voltage of one shot is shown in Fig.2. In the figure, t₀ stands for the instant at which the switch SW is closed electrically (there is a pre-breakdown of the air gap), t₁ the breakdown of the fixed gap of VI, t₂ the second reignition, t₃ the temporary interruption, t₄ the reignition of the gap and t₅ the final interruption of the HF arcing current (Fig.2 is measured from a vacuum interrupter with AgWC contact material and a gap length of 0.4mm).

The quantity of data for the different contact materials used is given in Tab.1.

Tab.1 Data volume of the measurement

contact material	Cu	CuCr
nr. of data files	24	22
nr. of shots	527	555
nr. of data points	5260	4885

3. DATA PROCESSING AND ANALYSIS

When the current of a vacuum arc passes zero and is interrupted the diffusion of the residual plasma causes the recovery of the vacuum gap from the conducting state to the insulating state. There is a race between the speed of dielectric recovery and the rate of rise of transient recovery voltage (RRTRV) which is supplied by the circuit. At the moment the recovery voltage is higher than the momentary voltage withstanding ability of the vacuum gap, the gap will breakdown and the current starts to flow in the vacuum through the residual plasma again. For HF vacuum arc the situation is the same. The extent of the recovery of the vacuum gap after each current zero is reflected by the following reignition voltage (u_r).

Fig.3 and Fig.4 show the results of the measurement of CuCr vacuum interrupter with capacitor C being 10nF and gap length being 0.1mm and 0.5mm respectively. In those

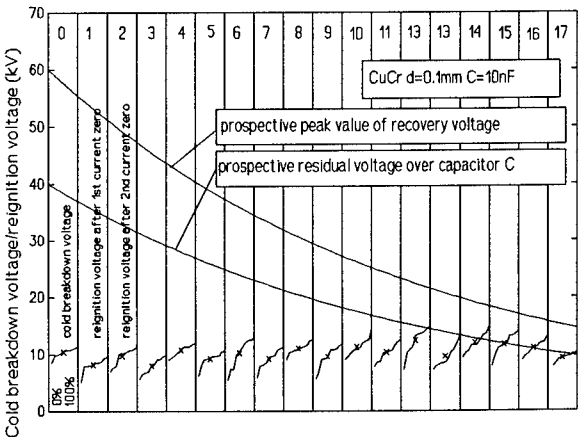


Fig.3 The measured mean values (x) and distributions (erratic short line) of reignition voltages after each current zero for CuCr contact material with d=0.1mm

figures each vertical stripe which expresses the distribution and mean value of reignition voltages (indicted by x) after a certain numbered current zero is denoted by a number at the top of the stripe, which stands for the sequential number of the corresponding current zero.

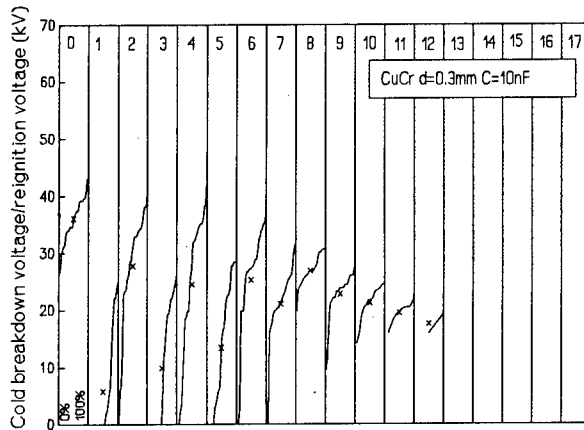


Fig.4 The measured mean values and distributions of reignition voltages after each current zero for CuCr contact material with $d=0.3\text{mm}$

3.1 COLD BREAKDOWN VOLTAGE

For each shot of the measurement the initial breakdown voltage is taken as the cold breakdown voltage. The mean value of the cold breakdown voltage vs gap length for Cu and CuCr are shown in Fig.5 and Fig.6 respectively. The relation between U_b and gap length d is fitted by $U_b = a_E \cdot d + a_U$, where U_b is the cold breakdown voltage (in kV) and d the gap length (in mm). The coefficient a_E and a_U for Cu and CuCr are listed in Tab.2.

Tab.2 Coefficient of cold breakdown characteristics

contact material and C	a_E (kV/mm)	a_U (kV/mm)
Cu C=10nF	53.4	0.6
Cu C=3.4nF	70.8	-1.2
CuCr C=10nF	106.3	0.3
CuCr C=6.6nF	106.7	1
CuCr C=3.3nF	110.9	0.4

For CuCr the cold breakdown characteristic is not so sensitive to the capacitor C. This is why CuCr is widely used in vacuum interrupters to obtain higher voltage withstanding ability after arcing.

3.2 INTERRUPTING ABILITY OF HF VACUUM ARC

The interrupting ability of HF arcing is expressed in the final maximum recovery voltage U_m against the gap length. Fig.7 and Fig.8 give the results. In those two figures each point represent a pair of U_m and d , and the mean values are calculated for the data belong to each gap length.

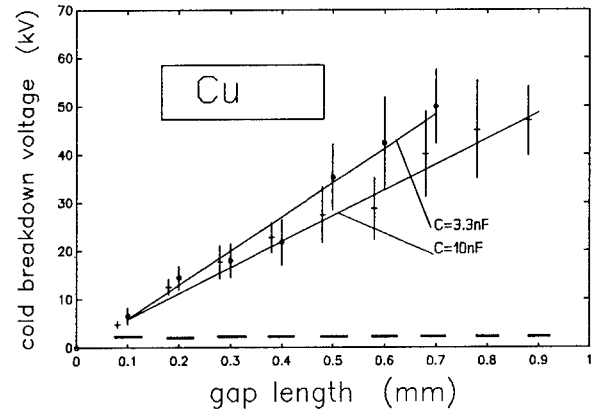


Fig.5 The cold breakdown voltage vs gap length for Cu with $C=3.3\text{nF}$ and 10nF

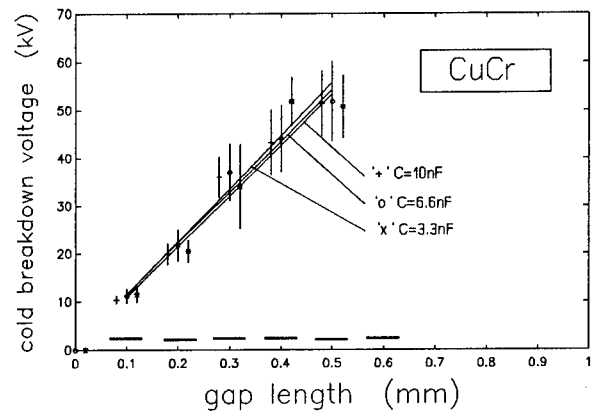


Fig.6 The cold breakdown voltage vs gap length for CuCr with $C=3.3\text{nF}$, 6.6nF and 10nF

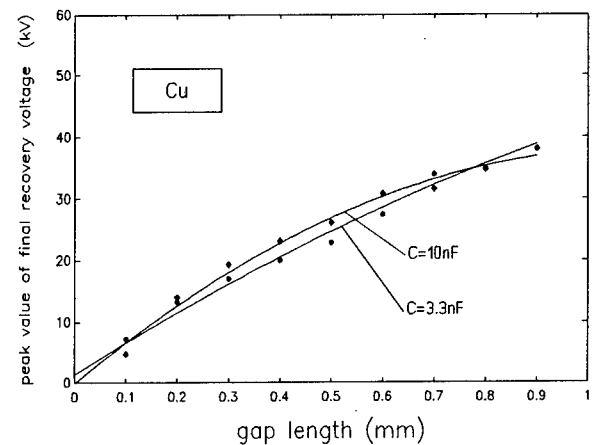


Fig.7 The peak value of final recovery voltage U_m against gap length d for Cu contact material

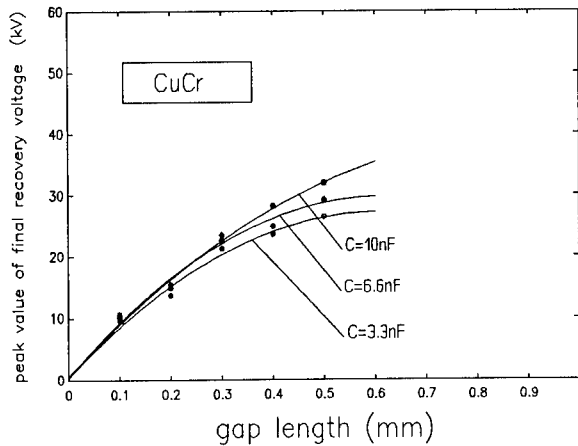


Fig. 8 The peak values of final recovery voltage against gap length d for CuCr

The relation between U_m and d is expressed as

$$U_m = 0.4 + 91d - 67.3d^2 \quad (\text{for CuCr}) \quad (1)$$

and

$$U_m = 0.8 + 59.8d - 20.1d^2 \quad (\text{for Cu}), \quad (2)$$

where U_m in kV and d in mm.

3.3 NUMBER OF HALF-CYCLES OF HF vacuum arc

The measured number of half-cycles of HF vacuum arc is shown in Fig. 9 and Fig. 10. In these two figures the gap

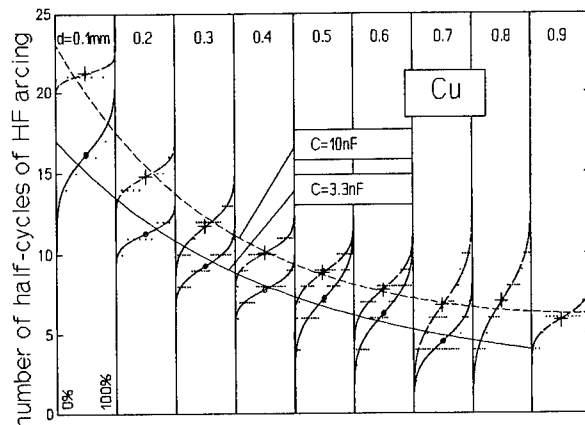


Fig. 9 The measured mean values and distributions of number of half-cycles of HF vacuum arcing for Cu with different gap length

length d is shown at the top of the figure. The figures also show the cumulative distribution of number of half-cycles.

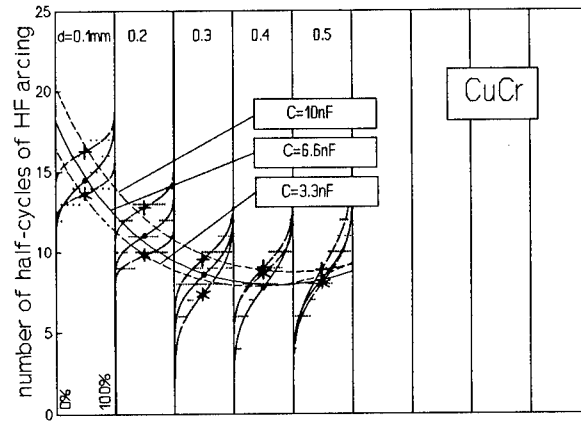


Fig. 10 The measured mean values and distributions of number of half-cycles of HF vacuum arcing for CuCr with different gap length

Take Fig. 9 for example, in the range of $d=0.1\text{mm}$, the left boundary stands for 0% and the right boundary for 100%. The dots are the measured data and they are fitted with a normal distribution function. From the figures, it is obviously seen that the number of half-cycles of HF arcing increases with C and decreases as gap length increases. Because the period of HF arcing increases as C increases, the arcing time would increase much more with C . This must be kept in mind when estimation of reignition or virtual current chopping overvoltage is under consideration.

3.4 CALCULATION OF THE NUMBER OF HF ARCING

In a RLC circuit the voltage across the capacitor can be written as,

$$U_C(t) = U_C(0) \exp(-a_1 \cdot t) \cos(\omega \cdot t) \quad (3)$$

where $a_1 = R/2L$ is the decaying constant and $\omega = 1/\sqrt{LC}$ is the angular frequency of the oscillation. If only the values of voltage of capacitor at each current zero are under consideration, the voltage U_C can also be expressed as,

$$U_C(n) = U_C(0) \exp(-a_n \cdot n) \quad (4)$$

where n is the sequential nr. of current zero at which the voltage is measured. The relation between a_1 and a_n is,

$$a_n = 0.5 \cdot \pi \cdot a_1 / \omega \quad (5)$$

For the circuit shown in Fig. 1, if there is an arc between the contacts in VI the effect of C_0 to the HF circuit will scarcely exist because the arc voltage is very low compared with the residual voltage of capacitor C . So the circuit will work according to the principle described above.

From the view point of energy conservation, the number of half-cycles of HF vacuum arc can be determined as follows. The energy stored in capacitor C before HF arcing is $\frac{1}{2}C \cdot U_C(0)^2$. If there is not a vacuum gap in HF circuit, that is to say the circuit only consists of R, L and C, the energy stored in capacitor C at each HF current zero can be expressed as

$$\begin{aligned} E_C(n) &= \frac{1}{2}C(U_C(n))^2 \\ &= \frac{1}{2}C[U_C(0) \cdot \exp(-a_n \cdot n)]^2 \\ &= E_C(n-1) \cdot \exp(-2a_n) \end{aligned} \quad (6)$$

Considering the vacuum gap in the circuit, the energy dissipation caused by reignition voltage $U_r(n)$ and the capacitor paralleled to vacuum interrupter C_0 , $E_r(n)$ must be taken into account. It is known from the measurement that the energy dissipation by U_r is very fast (in the time of less than one tenth of the period of HF circuit). So it is reasonable to consider $E_r(n)$ a integral energy loss at the beginning of each half cycle of current (reignition). So,

$$E_C(n) = (E_C(n-1) - E_r(n)) \cdot \exp(-2a_n) \quad (7)$$

and the voltage of the capacitor C at each current zero will be

$$U_C(n) = \sqrt{U_C^2(n-1) - \frac{C_0}{C} U_r^2(n-1) \cdot \exp(-2a_n)} \quad (8)$$

If the overshoot factor of the circuit is f_p , the maximum recovery voltage which the circuit can provide at n-th current zero is $U_C(n) \cdot f_p$. So

$$U_C(n) \cdot f_p > U_{ri} \quad (9)$$

is the criterion of the occurrence of n-th reignition. The number of half-cycles of HF vacuum arc will increase one by one until the condition of the equation 9 is not satisfied any more.

It must be emphasized that it was found in the measurement that the decaying constant a_i is a function of the frequency of HF circuit. This is because the energy radiated in the form of an electromagnetic wave and the skin effect increase with the frequency. The inherent decaying constant of the circuit is defined as the decaying constant when the reignition voltage is zero. The inherent decaying constant is measured in the experimental circuit. It should be mentioned here that the decaying constant a_i and a_n mentioned above are inherent decaying constants. The measured a_i as a function

of frequency f is obtained as follows

$$a_i(f) = b + a \cdot f \quad (10)$$

with $a = 0.35$ and $b = -2.4e3$ (valid for $f > 0.5\text{MHz}$).

The calculated number of half-cycles of HF arcing are shown in Fig.11 (for Cu) and Fig.12 (for CuCr). In the

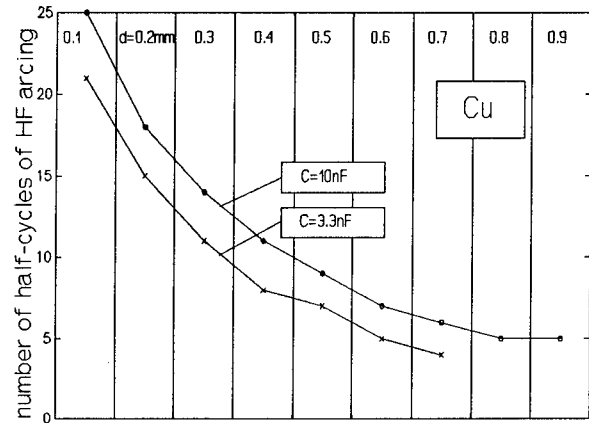


Fig.11 The calculated number of half-cycles of HF vacuum arcing for Cu with different gap length

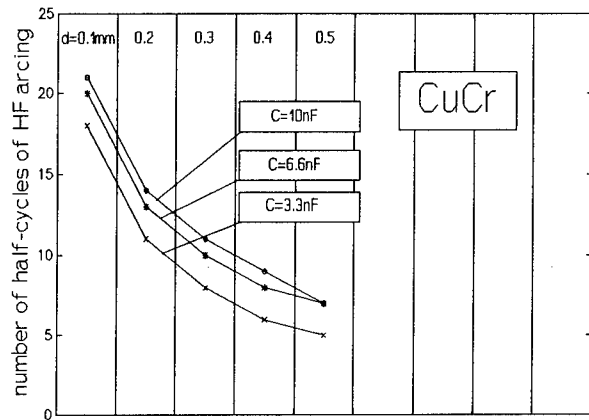


Fig.12 The calculated number of half-cycles of HF vacuum arcing for CuCr with different gap length

calculation $U_r(n)$ takes one value which is equal to the mean value of final peak value of recovery voltage U_m given by equation 1 (for Cu) and equation 2 (for CuCr). The inherent decaying constant comes from equation 10.

4. CONCLUSIONS

1. The cold breakdown voltage of vacuum interrupters having a fixed gap length ($< 0.9\text{mm}$) was measured with a 650 kHz (frequency of UHF circuit) 60 kV impulse voltage.

For a gap length less than 1 mm the following breakdown field strengths were found for the two contact materials under study:

Cu: $534\text{kV/cm} < E_b < 708\text{kV/cm}$
 CuCr: $1063\text{kV/cm} < E_b < 1109\text{kV/cm}$

2. The measured interrupting ability of HF vacuum arc (with small gap length) is expressed as U_m vs d :

$$U_m = 0.4 + 91d - 67.3d^2 \quad (\text{for CuCr})$$

and

$$U_m = 0.8 + 59.8d - 20.1d^2 \quad (\text{for Cu})$$

where U_m in kV and d in mm.

3. The decaying constant is a function of the frequency of the circuit. In this research the experimental equation is

$$a_i(f) = 0.35 - 2.4 \times 10^{-5}f$$

where a_i and f are both in 1/s

4. Number of half-cycles of HF arcing is affected by the contact material and gap length (through $U_r(n)$ in the model), HF circuit parameters (through a_i in the model), parasitic capacitor C_0 and the initial voltage of capacitor C (or energy stored in capacitor) C . In the range of frequency used in the measurement, the number of half-cycles of the HF vacuum arc increases with C , and $U_c(0)$, and decreases as gap length and C_0 increase. Both the result of measurement and theoretical analysis meet each other very well.

ACKNOWLEDGEMENTS

The authors gratefully acknowledge prof. G.C. Damstra for his advice. The authors also wish to thank mr. J.W.G.L. Vossen, mr. L.A.H. Wilmes and mr. A. van Staalduinen for their technical support.

REFERENCES

1. M. Murano, T. Fujii, H. Nishikawa, S. Nishiwaki, M. Okawa, "Voltage Escalation in Interrupting Inductive Current by Vacuum Switches", IEEE Trans. Power Apparatus and Systems, vol. 91, pp. 1897-1903, no.5 Sep./Oct. 1972.
2. J. Panek, K.G. Fehrle, "Overvoltage Phenomena Associated with Virtual Current Chopping in Three Phase Circuits" IEEE Trans. on Power Apparatus and Systems, vol. PAS-94, no. 4, July/August 1975.
3. R.P.P. Smeets, R.C.M. Kardos, J.P. van Oostveen, R.G.C. Dirven, H.Q. Li, E. Kaneko, "Essential Parameters of Vacuum Interrupter and Circuit Related to the Occurrence of Virtual Current Chopping in Motor Circuits", Proceedings of the Fourth Annual Conference of Power & Energy Society IEE Japan (International Session), (1993)
4. M. Lindmayer, E.-D. Wilkening, "The Influence of Circuit Parameters and Contact Materials on the Reignition of High Frequency Vacuum Arcs" Proceedings of 35th IEEE- Holm Conference on Electrical Contacts, USA, September 1989.
5. M. Lindmayer, "Breakdown of Short Vacuum Gaps after Current Zero of High Frequency Arcs" Proceedings of XIVth Int. Symp. on Disch. and Elec. Ins. in Vacuum, pp. 234-241, Santa Fe, New Mexico USA, September 1990.
6. Z. Zalucki, "The Ability of High Frequency Current Interruption In Vacuum at Small Gap Length" Proc. of XIVth ISDEIV, pp. 536-541, USA 1990.
7. Z. Zalucki, "Interrupting Capacity of Vacuum Interrupter Dependence on Frequency of current" Proc. of XVth ISDEIV, pp. 540-545, Germany 1992.

SESSION 3

Switching in Vacuum

Electron Tubes for Industrial Applications

B.Gellert

THOMSON ELEKTRONENRÖHREN AG
CH-5600 Lenzburg

ABSTRACT

This report reviews research and development efforts within the last years for vacuum electron tubes, in particular power grid tubes for industrial applications. Physical and chemical effects are discussed that determine the performance of today's devices. Due to the progress made in the fundamental understanding of materials and newly developed processes the reliability and reproducibility of power grid tubes could be improved considerably. Modern computer controlled manufacturing methods ensure a high reproducibility of production and continuous quality certification according to ISO 9001 guarantees future high quality standards. Some typical applications of these tubes are given as an example.

1. INTRODUCTION

Vacuum electron tubes show a large variety of applications. Depending on the type and frequency range it is possible to classify into power grid tubes, microwave tubes, display tubes, image intensifiers and many more. For all of these tubes there are industrial applications.

In order to be more detailed this review is restricted to power grid tubes. Power grid tubes operate in the kW to MW range of output power. They compete with semi-conductors in many fields and have been predicted to die out many times in the past. Nevertheless there are well-established applications that require the special properties that can be offered just by electron tubes. These are among others their reliability, simplicity and their performance in surroundings with strong electrical noise. Electron tubes have thus gained a market share for certain applications that can not be taken by other electronic devices. Possibly it is now even the time, when a return from existing semi-conductor solutions to electron tubes may become attractive again. Industrial applications utilise mainly triodes and tetrodes that are offered in water or air-cooled versions. Typical examples are given in fig.2. and fig.3. Fig.2 shows a tube of ITK30 type, which e.g. can be used in generators for induction or dielectric heating at frequencies up to 27 MHz. Fig. 3 shows as an example of a tetrode the type IQK25-1 that is used in modern laser generators.

2. FUNDAMENTAL PHYSICAL EFFECTS IN VACUUM ELECTRON TUBES

Main components of a power grid tube are cathode, grid(s), anode and ceramics. Although there are also glass tubes on the market, greater progress has been made with ceramic tubes. Therefore the main physical effects are described for tubes with these components only.

Fig. 1

*Variation of potential energy near a metal surface:*¹

$V_0(x)$: image potential

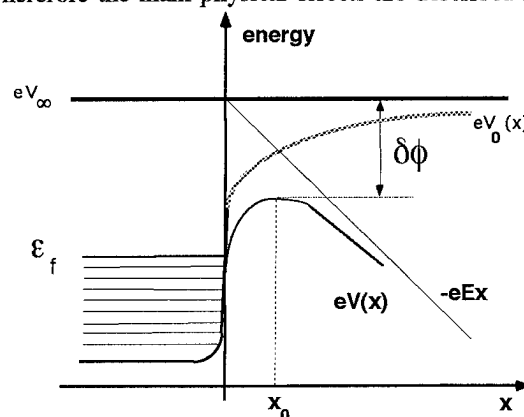
$V(x)$: potential in the case of an applied field E

x_0 : position of the maximum in the potential

eV_∞ : energy of vacuum level for $x = \infty$

ϵ_f : Fermi energy

$\delta\phi$: lowering of work function due to the applied field

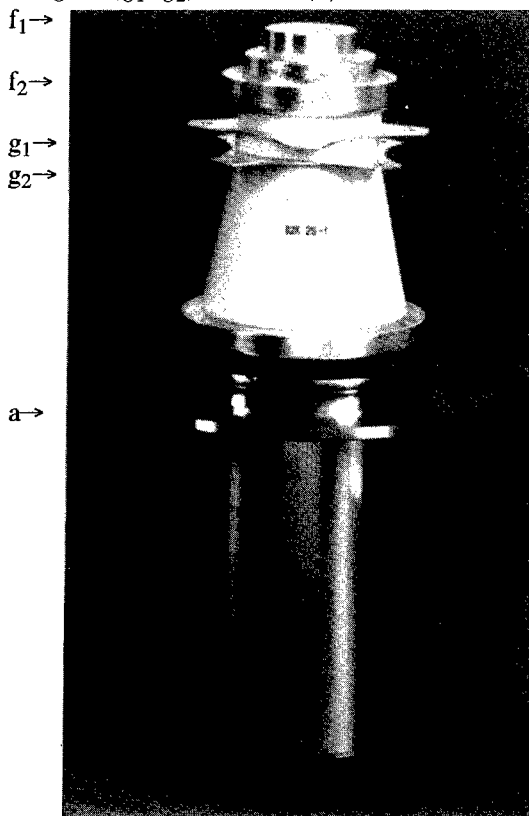


2.1. Cathodes

The cathode of a vacuum electron tube should deliver as high a current density as possible at lowest heating temperature. It functions mainly as a thermionic emitter. Theoretical models of thermionic emission are well-known and can be found e.g. in ¹. Electrons that leave the bulk of a clean metal into vacuum require an energy that is given by the work function ϕ of the material. The work function ϕ is then given as the potential difference between the Fermi level of energy ϵ_f and the energy of the vacuum level eV_∞ . If an electrical field is present, the potential barrier of the solid is reduced by $\delta\phi$ due to the Schottky effect (fig.1).

Fig. 3

Water cooled industrial tetrode IQK 25-1 which is used e.g. in laser generators with electrical connections for cathode filament (f_1, f_2), two grids (g_1, g_2) and anode (a)



$f_1 \rightarrow$

$f_2 \rightarrow$

$g \rightarrow$

$a \rightarrow$

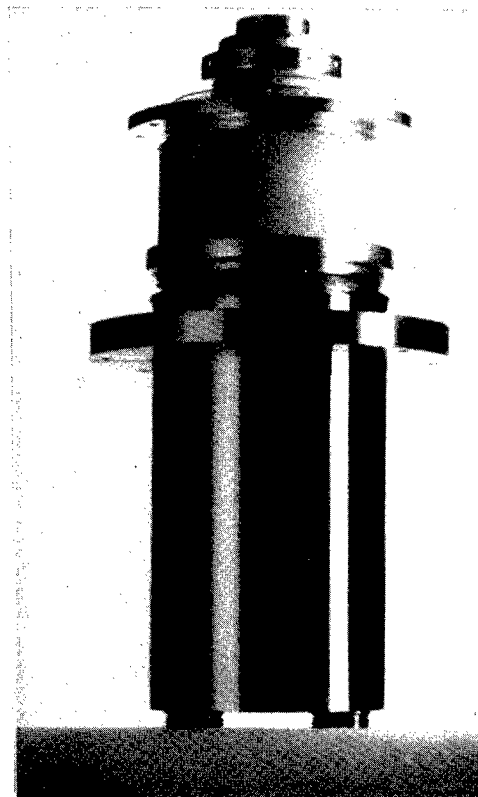


Fig. 2

Water cooled industrial triode ITK 30 which is used for induction and dielectric heating with electrical connections for cathode filament (f_1, f_2), grid g and anode a

The thermionically emitted current is rather well described by the Richardson-Dushman equation (1). The saturation current density J of electrons emerging from clean homogeneous metal surface at temperature T is

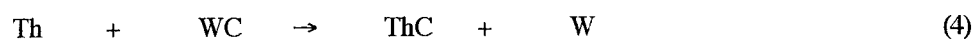
$$J = A^* (1 - r_e) T^2 \exp(-\phi / k_b T), \quad (1)$$

$$A^* = \frac{4 \pi m k_b e}{h^3} = 120 \text{ A cm}^{-2} \text{ degree}^{-2},$$

m, e = electron mass, charge
 h = Planck's constant,
 k_b = Boltzmann's constant
 r_e = mean value of the zero-field reflection coefficient for the incident electrons²

Main parameters to obtain high emission are the temperature T , the work function ϕ and the Richardson-Dushman constant A preceding the exponential. Materials are utilised of low work functions ϕ and high constant A that work at the lowest temperature possible. A possibility to reduce the work function was found in the past, when material compositions were investigated instead of pure metals. For such a multi-component system the complicated theoretical description may be approached by the static substrate model of Gurney³. The model is explained e.g. in⁴. The reduction of work function by mono-layers or attached atoms is well known in literature. Typical values can be found e.g. in⁵.

Thoriated tungsten that is mainly used as cathode material in commercial applications can be manufactured by powder metallurgical processes, sintering, pressing and drawing. It contains several per cent of ThO_2 . In order to make use of the reduced emission potential of atomic thorium on tungsten, a mono-layer of thorium atoms has to exist at the surface continuously. To achieve this state, a special chemistry takes place to continuously reduce the oxide. The basic mechanism of this method is the reduction of the oxide in a coating of W_2C around the tungsten wire. The process to coat tungsten wires in the appropriate way is known as "carburisation" and described e.g. in⁶. Key reactions at the surface and in the layers are the following



Reaction (2) describes the generation of thorium atoms at the surface of a tungsten filament even without W_2C coating. This reaction is important at high temperature. The W_2C coating allows a thorium production at lower temperature and therefore lower thorium evaporation by reaction (3). The unwanted side-reactions (4) and (5) contribute only little in the temperature range considered. Reaction (6) is the carburisation process itself, whereas reaction (7) is a loss process producing WC which again prohibits thorium formation at the surface e.g. by reaction (4).

In the last years new materials with similar properties as thoriated tungsten are investigated worldwide⁷⁻⁹.

The emission process is understood for the existing commercially available material for some time. The knowledge about the processes with new materials however is not yet complete.

For existing industrial applications there are also other requirements that need to be fulfilled. Special technical requirements for industrial tubes are

- ° large emission reserves
- ° short-time overload capability
- ° strong construction with high mechanical stability
- ° long life-time

In order to fulfil these requirements specific constructions are chosen. In industrial tubes mainly mesh cathode structures are used. By a special design high permeance and good stability can be achieved to withstand possible system voltage fluctuations or overloads and to become insensitive to different switching pulse shapes. Special physico-chemical processes are developed for the carburisation of cathode filaments, by which the mechanical stability of a specific design is essentially improved. To optimise such methods metallurgical research and development is an important help. Simultaneously with the improvement of the stability the life-time of the cathodes can be increased. The main limiting mechanism is the decarburisation, i.e. the back-reaction of reaction (6) forming tungsten and carbon from W_2C . There are now tubes in the field which work under extreme conditions for more than 10'000 hours.

2.2. Grids

It is the task of the grids to control and modulate the power of a tube with as little losses as possible. Physically, grids must behave strictly neutral, i.e. they should not generate further electrons. Apart from that the characteristic curve of the tube must not be changed under different operation conditions. E.g. any grid distortions at high temperature must be avoided or compensated, since the gap spacings inside the tube may change with varying temperature. Technically these requirements are realised by the choice of an appropriate material and corresponding chemical treatment. For industrial tubes the operational

reliability depends strongly on the reserve dissipation capability of the grids. Since the cathodes run at temperatures in excess of 2000 K the grids are heated excessively by the radiation from the cathode. Furthermore, the grid current and RF charging currents heat the grids considerably. The two main properties of the materials involved are therefore their radiation characteristic and their secondary emission behaviour. Fig. 4 shows the secondary emission factor α as a function of the accelerating voltage U_a for some typical materials. α is

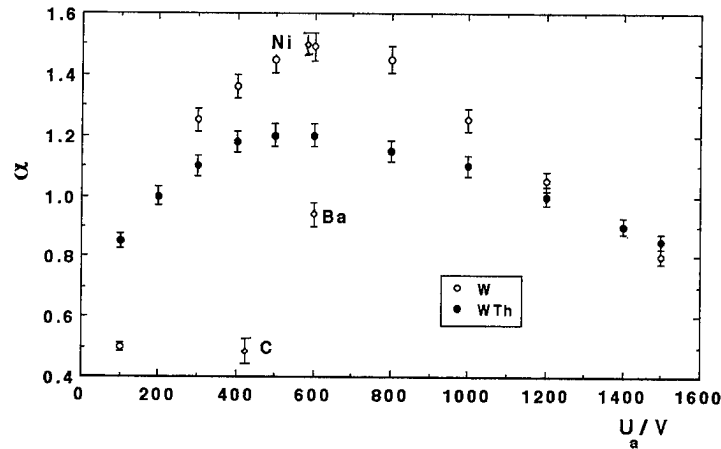


Fig. 4
Secondary emission factor α as a function of the accelerating voltage U_a for tungsten (W) and thoriated tungsten (WTh). Also given are values for barium (Ba), nickel (Ni) and carbon soot (C).

defined as
$$\alpha = I_2 / I_1, \quad (8)$$

I_1 = incident current density = primary electron current,

I_2 = resulting secondary electron current.

The measurements are obtained by sputtering experiments in vacuum. The figure demonstrates that pure tungsten shows a relatively poor behaviour, whereas e.g. carbon has better properties.

At the high temperatures involved it is tried to optimise the back-radiation from the grid as a means of cooling. Fig. 5 shows the radiation measured from typical grid material in the visible spectrum at around a wavelength $\lambda = 668$ nm compared to blackbody radiation. For blackbody emission Planck's law holds:

$$I_{pl} = \frac{2 h c^2}{\pi \lambda^5} \left(\exp \left(\frac{h c}{k_b \lambda T} \right) - 1 \right), \quad (9)$$

c = velocity of light,

λ = wavelength.

Radiation from heated substrates differs from blackbody radiation by a factor ϵ (spectral radiant emissivity) depending upon wavelength λ , emission angle Φ , and temperature T . ϵ is a characteristic quantity for every material. Thus the emitted radiative power is reduced and given by

$$I(\lambda, \Phi, T) = \epsilon(\lambda, \Phi, T) I_{pl}(\lambda, T), \quad (10)$$

Φ = angle of emission.

$\epsilon(\lambda, \Phi, T)$ is material dependent. As can be seen from fig. 5 radiation is reduced considerably, if the surface is treated mechanically or chemically, because the angular and material dependence has a strong influence on the total radiation.

As a consequence two main approaches are followed for industrial tubes:

- chemically treated pure metal grids - mainly on a tungsten or molybdenum basis, or
- pyrographitic grids (pyrobloc®), which make use of the advantages of pure carbon.

Main efforts in research and development of the last years for new grid types was in these fields. For the pure metal grids special coatings and ways to apply these have been developed. Apart from different carbide coatings also new systems have

evolved. $ZrPt_3$ is an example of a coating that suppresses any grid emission strongly. The advantages of the pyrobloc® technology are the low vapour pressure, good heat conductivity, low sputtering rate and optimum ion capture. With these grids very short gap lengths can be realised which results in very steep tube characteristics.

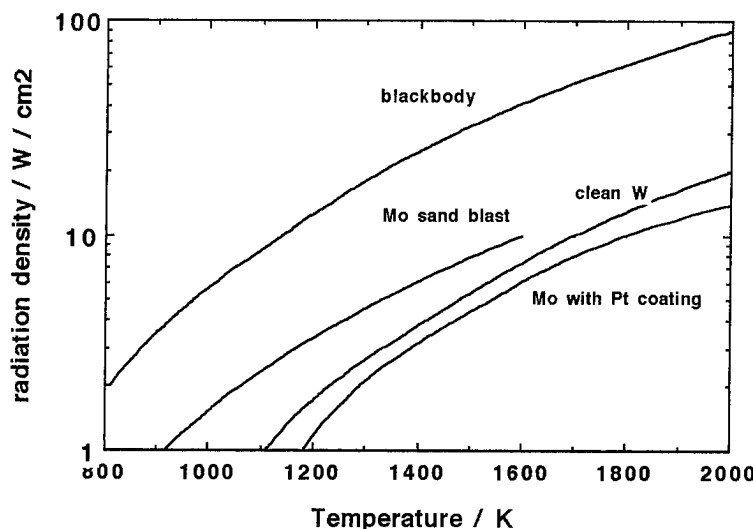


Fig.5

Emission properties of sand blast Mo, clean tungsten, molybdenum with platinum coating compared to blackbody radiation

2.3 Anodes

Anodes are heated by the current to the anode and the thermal irradiation. They are made of OFHC copper and have an overload capability to allow for mismatching. They are designed with adequate thermal capacity and good thermal and electrical conductivity. In order to reduce reflection from the inner walls and thus not to contribute to further grid heating the anodes are often chemically treated at the inside. Development in the field of anodes is mainly concerned with optimising the design and applying high quality materials.

2.4. Ceramics

High grade aluminium oxide ceramics are used for the housing which provides the required mechanical and dielectric strength and has high thermal withstand capability. Great progress has been made in the last years in metal ceramics joining technologies. It is now possible to reproducibly and precisely bond the ceramic to the metal by computer controlled manufacturing methods. It is thereby also possible to perform very precise welding and brazing operations under buffer gas as well as in vacuum. The resulting excellent dielectric strength is partly due to the special design of the metal fittings and ceramic part and partly to the optimised manufacturing possibilities.

3. PRODUCTION TECHNOLOGY

Although there is still a lot of skillful work to be done by hand, the greatest quality improvements and cost reduction by rationalisation was achieved by introducing modern production technologies to the manufacturing of electron tubes. The large number of spots welds of the cathodes and the grids e.g. can easily be monitored and recorded for every single weld by computers. Similar controls can be established for all different brazing or pumping steps in the process of the production of an electron tube. The increased control and documentation of all process steps has achieved a very high standard of reproducibility and quality.

Quality control does not only concern the production methods themselves, but also all other activities including testing, research and development, process support, logistics etc. that are necessary to perform as a high quality supplier on the market. That is why quality tests by independent international organisations are more and more used to guarantee the standard for the future. In that way certification according to the ISO 9001 norm has lead to a continuous striving for optimised processes. Introducing ISO 9001 to companies that produce electron tubes has again achieved a jump forward in technological quality.

4. APPLICATIONS

Most of the triodes are used in generators up to 27 MHz. They are used to heat a substrate either inductively or dielectrically. There are applications for many purposes e.g. plastic or pipes welding, wood bonding, wood laminating, all kinds of drying (textile, paper etc.), sterilisation, food processing (cooking, defrosting), tin remelting etc. Special "high μ " (high

amplification) triodes find applications in RF oscillators or amplifiers for plasma or laser applications. To be adopted to any kind of mounting industrial tubes do not need special sockets as e.g. broadcast tubes, but can be equipped with flexible leads. A typical generator scheme is sketched in fig.6. The main part consists of the oscillator part with the triode and a matching network to the load which serves also as feed-back suppression.

Contrary to some triode applications new applications of amplifiers arise with laser and plasma technologies. They require pulsing and special RF pulse shaping. Nearly any RF pulse shape up to 100 kHz at any repetition rate can be achieved without repercussions of the supply, if a high quality tetrode is used in the self-oscillating mode¹⁰. Switching within μs is possible with an increase in power by a factor of 4.

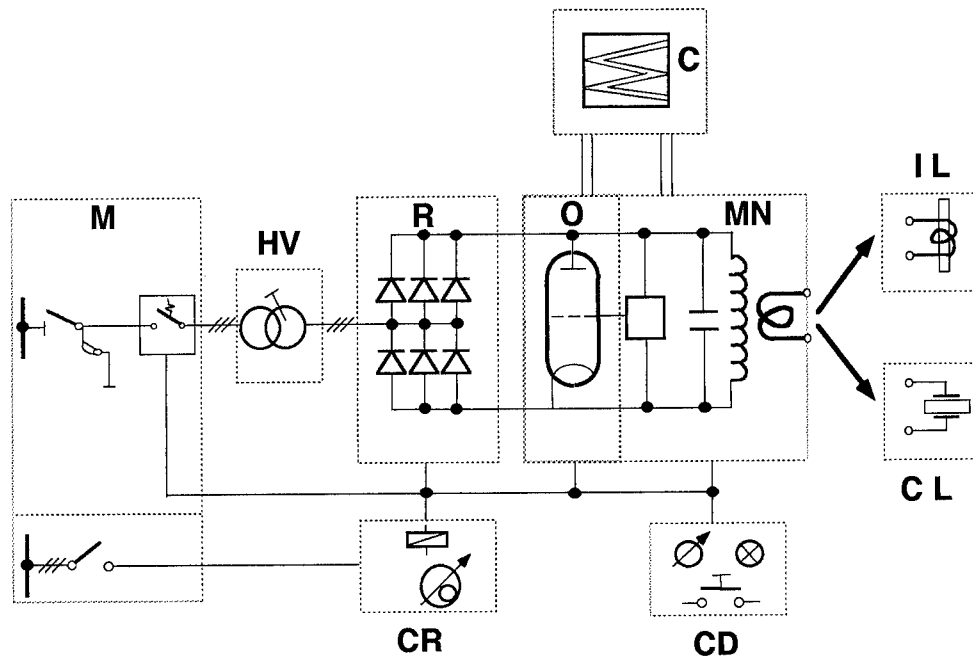


Fig. 6

Principal set-up of a radio frequency generator with mains input M, high voltage transformer HV, high voltage rectifiers R, oscillator part O, matching network and feedback suppression MN, cooling system C, control rack CR and control desk CD. The load is either an inductive load IL or a capacitive, i.e. dielectric load CL.

Fig. 7 shows the basic control circuit of a self-oscillating RF generator with a tetrode.

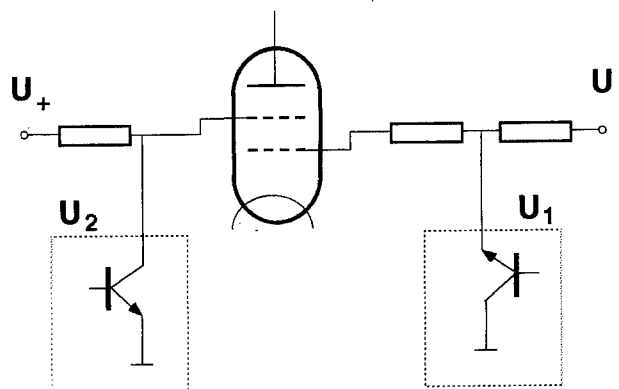


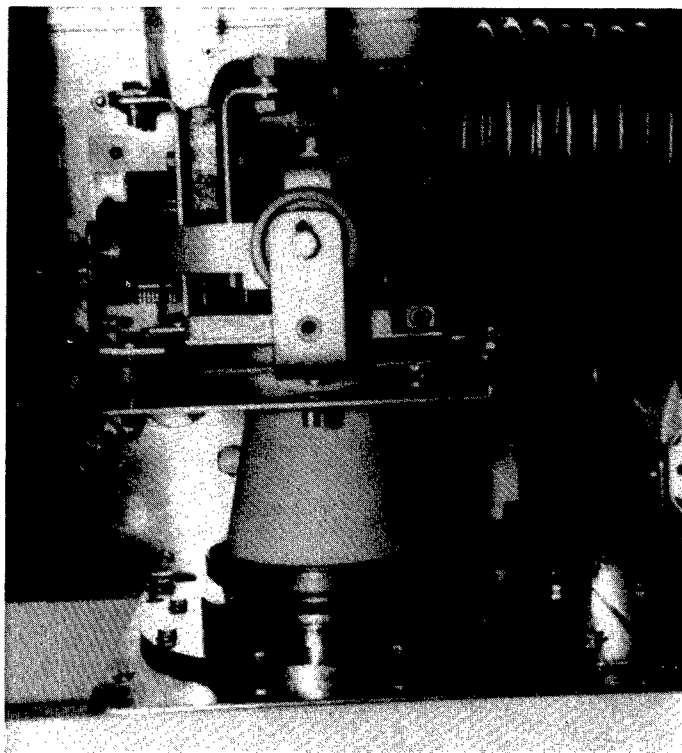
Fig. 7

Basic control circuit of a self-oscillating RF generator with a tetrode. (Negative grid voltage U_- , screen grid voltage U_+ , pulse generator control voltages U_1 , U_2)¹⁰

The advantages of a freely pulsating generator with tetrodes are manifold compared to externally controlled transmitters. Only small space is needed. Components like smoothing filters or e.g. for high voltage transformation can be left out, which can

mean a considerable cost reduction. Stepless power changes from 0 to 100% can be achieved via screen grid control. The efficiency is enhanced from typically 50% to above 70%. Finally fast super-pulse modes can be realised reliably. Fig. 8 shows the industrial tetrode IQK 25 in a 27 MHz oscillator.

Fig. 8
Industrial tetrode IQK25
in a 27 MHz laser oscillator
(taken from ¹⁰)



5. SUMMARY

Research and development efforts within the last years for vacuum electron tubes, in particular power grid tubes for industrial applications have been reported. Physical and chemical effects at the cathode and the grids determine the performance of today's devices. Due to the progress made in the fundamental understanding of materials and newly developed processes the reliability and reproducibility of power grid tubes could be improved considerably. Modern computer controlled manufacturing methods ensure a high reproducibility of production and continuous quality certification according to ISO 9001 guarantees future high quality standards. Typical applications of these tubes are inductive as well as dielectric heating in many ways. New applications arise in RF oscillators or generators for laser and plasma applications.

6. ACKNOWLEDGEMENTS

The author acknowledges the stimulating discussions about applications with R. Chaudet responsible for clients' support (Thomson Tubes Electroniques, 13 avenue Morane Saulnier, Bâtiment Chavez, Velizy Espace, BP121, F 78141 Velizy-Villacoublay Cedex, France) and W. Rohrbach's assistance with the manuscript.

5. REFERENCES

1. J. Hölzl, F. K. Schulte "Work function of Metals", Springer Tracts in modern Physics, vol. 85, Berlin, 1979
2. J. W. Gadzuk "The structure and chemistry of Solid Surfaces" ed G. A. Somorjai, Wiley, N.Y. 1969, p.43-1
3. R. W. Gurney, "Theory of electrical double layers in adsorbed films", Phys. Rev. 47, 479 pp., 1935
4. B. Gellert, W. Rohrbach, "Investigation of materials for directly heated cathodes of electron tubes", Proc. XVI Int. Symp. on Disch. and Electr. Insul. in Vac., Moscow, 1994
5. V. S. Fomenko, "Handbook of thermionic properties", ed G. V. Samsonov, Plenum Press, N.Y. 1966
6. Walther H. Kohl, Materials and Techniques for Electron Tubes, Reinhold Publ., N.Y. 1960
7. D. M. Goebel et al., "Large area LaMo electron emitters", Rev. Sci. Instr. 56 (19), pp 1888, 1985
8. Zhou Meiling et al., "A study of the properties of Mo - La₂O₃ thermionic emission material" Proc. 13th Int. Plansee Seminar, vol. 1, Eds. H. Bildstein, R. Eck, Reutte (Austria) 1993
9. C. Buxbaum, G. Gessinger, CH-Patent 579 824, 1976
9. K. R. Spangenberg, "Vacuum Tubes", Mc Graw Hill, N.Y., 1948
10. K. Roth, L. Eggerszegi, "New tetrodes for industry", ABB Review, vol. 10, 1992, pp. 3

Phases of vacuum and plasma discharges and control of their parameters

E.N. Abdullin, G.P. Bazhenov*, S.M. Chesnokov, G.P. Erokhin, V.V. Kiselev, O.B. Ladyzhensky

High Current Electronics Institute, Russian Academy of Sciences, Siberian Division

634055, Tomsk, Russia

* Institute of Electrophysics, Russian Academy of Sciences, Ural Division,

620219, Ekaterinburg, Russia

Linear electric circuit with constant parameters becomes a nonlinear one with parameters variable in time after vacuum discharge gap is connected to it. Change of discharge parameters occurs by cycle. Full vacuum discharge cycle includes predischage, spark, arc phases and current break phase (Fig. 1). Discharge development by incomplete cycle as well as development of one and the same discharge by several parallel channels with different cycles are possible.

Every moment discharge current I is limited by one of the factors and namely - cathode emission ability I_c , plasma emission ability I_p , vacuum gap conductivity P , outer circuit resistance R - but it can not be limited by simultaneous influence of several these factors. Fragment of the scheme (Fig. 2) reflecting succession of turning on of current limiting factors may present how the process of every discharge goes on.

Connections between current limiting factors are realized by the physical processes in electrodischarge system. Discharge gap is one of subsystems in this system. Main processes going on simultaneously result in secondary processes which are interactions of the main processes. Multiplicity of processes accompanying and providing discharge consists of multiplicity of essential processes in discharge (D) and multiplicity of the ones outside the discharge (S). Fig. 3 presents a diagram of multiplicity of D - processes sorted out, according to the accepted division of processes in the discharge, to the cathode (C), anode (A) ones, processes in the gap (G), information about contribution of C, A, G processes and their interaction in realizing of discharge gap commutation. Contribution of each process was estimated by Fisher criterion of importance on the basis of results of the full factor experiment ²³. Influence of changes inserted was judged from commutation time t_c changes. We can see, that A*C interaction has more significant effect on t_c than factor A, and A*G interaction is superior in significance to factor G. We have enough evidences of significance of S - processes and interactions of C, A, G - processes with S - processes.

Processes and their interactions in electrodischarge system set the form of volt - ampere characteristic (VAC) of a discharge. Proper section of VAC corresponds to each phase of discharge. Location region of VAC sections corresponding to spark and arc phases, as well as current break phase is limited by the threshold current I_0 at which self - maintained discharge is possible as well as by cathode drop of potential U_c and loading characteristic of power supply (DS - interaction). VAC section corresponding to predischage phase is limited by the axes of coordinates, I_0 line, and line of the lowest voltage of discharge excitation. Fig. 4 presents schematically (without keeping to scale) VAC of the vacuum discharge gap inserted into a circuit from a source of constant voltage U_0 with constant inner resistance R . Equilibrium states in this circuit are located in the points of crossover of VAC discharge gap with loading straight line of power supply.

Circuit stability is breaking before the discharge beginning, when differential resistance of the gap r decreases to zero (point 1 of VAC) and then becomes a negative one and increases on absolute value due to high intensity of C - processes. Until $|r| < R$, current in the discharge gap I increases spontaneously. At the moment $|r| = R$ (point 2 of VAC) current rise stops. Duration of circuit staying in equilibrium state is limited by plasma appearance on the cathode. Now, circuit current is determined by P , and circuit state is determined not only by C processes but also by G - ones. Cathode plasma expansion breaks circuit equilibrium, $|r|$ becomes higher than R , spontaneous current rise renews. When "emission reserve" is sufficient and $U_0/R > I_0$, current reaches the value I_0 , self-maintained discharge (spark phase) begins. Intensity of G - processes begins to decrease in point 3 of VAC but current I is determined by P as before. Again $|r| < R$, velocity of I rise decreases and electrodischarge system rushes to a new equilibrium state. Physical reason of discharge transition into a stable state is saturation of cathode plasma emission ability. In point 3 of VAC sections of cathode plasma surface appear for which I_p becomes current limiter. In point 4 current from all the cathode plasma surface is limited by I_p . Conditions at which plasma quantity lost due to deionization on the cavity walls is equal to plasma quantity supplied by the cathode can

be realized by plunging of emitter into a cavity. Position of cathode plasma emission boundary becomes stable. Emission surface form and gap conductivity are regulated by the cavity dimensions and the depth of emitter plunging. Next breakdown of discharge stability results from sharp intensification of A, AC, AG - processes with anode plasma appearance. $|r|$ increases, gap geometry changes, I value is determined by P. In the point 5, exhaustion of source of plasma-forming medium on the anode, voltage decrease on the discharge gap promote $|r|$ lowering, decrease of current rise velocity and discharge transition into a new equilibrium state (point 6). Discharge spark phase comes to an end, R determines discharge current, arc phase begins. But in this state, discharge resides during limited time also. Growth of emission center quantity on the cathode surface, increase of cathode surface area collecting ion flow from cathode plasma are accompanied by decrease of emission ability of I_p plasma generated by cathode as well as by decrease of C-process intensity. I_c becomes a current limiter. A tear is formed between cathode and plasma. This results in further I_p lowering until $|r|$ exceeds R. As a result, discharge loses its stability. Loss of stability displays itself by current I drop. I drop to I_0 (point 7) completes current break phase and establishment of postdischarge emission current (point 8) completes discharge cycle. I break is possible at the discharge stability breaking at point 4 if C - processes intensity begins to decrease before anode plasma appearance and at point 2 if plasma generated on the cathode or outer circuit is not able to provide current I_0 .

Multiplicity of apparently and not apparently working back - couplings is formed owing to interaction in the electrodischarge system. Discovering and application of these relations allow to control discharge and namely: to reduce or protract discharge phases, to stabilize or modulate discharge current, to affect the form and position of charged particle beams generated by the discharge, to regulate composition of ion beams.

In a gap with cathode having two points made of the same materials, discharge current I_2 depends on the distance between the tops of the points l (Fig.5). I_2 can exceed twice the discharge current in the gap with one - point cathode I_1 at the fifth second already. I_2/I_1 changes with l change are due to electron beam interaction in the gap. By sight, this interaction can be easily observed by the tracks of anode erosion. Fig.5 also presents erosion pictures after discharge being broken in (8 - 10) ns from the moment of spark phase beginning: a - $l/d < 0,5$; b - $0,5 < l/d < 1,8$; c - $l/d > 1,8$. I_2/I_1 dependence on l/d and erosion tracks have been obtained at the interelectrode gap $d = 0,35$ mm.

Fig.6 presents current oscillograms of separate points of two - point cathode in the gap with the length $d = 1$ mm. The points are made of Cu and C, their I_0 values differ by more than an order of magnitude. In cases a and b, $l/d = 10$ and interaction of electron beams with each other as well as the ones of the plasma of one point with the surface of another point are absent. Interaction is realized through the outer circuit. A couple of oscillograms a is typical of the voltage pulse $U_0 = 25$ kV and b is typical of $U_0 = 15$ kV. At higher U_0 , discharge inevitably passes a cycle along the channel with C point omitting the arc phase and it passes the whole cycle along the channel with Cu point. At lower U_0 , discharge passes the whole cycle along the channel with C point and it does not exceed the boundaries of predischage phase along the channel with Cu point. In case $l/d = 0,1$ (oscillograms c) plasma of the functioning point stimulates emission center formation on the surface of nonfunctioning point. At the discharge beginning, point C is always a functioning one. Plasma of this point initiates discharge from Cu point. Discharge from Cu point transits to the phase of current breaking which lasts about 10 ns. Cu point current rise occurs owing to C point current drop since total discharge current can not be increased with switching on of the second emitter at the given l/d (Fig.5). Delay of discharge initiation from Cu point decreases with U_0 growth. Investigation of jointly functioning couples of emitters made of C, Pb, In, Cd, Cu, Mo, Al in different combinations allow to conclude that on the materials with higher I_0 , intensity of C - processes is higher and on the materials with lower I_0 , gap transition into the discharge spark phase occurs at lower intensity of C - processes. In other words, with the rise of cathode material I_0 , time of discharge delay grows and time of vacuum gap commutation decreases.

Dependence of one - and two - discharge ions containing in plasma on I_0 value of the cathode material evidences for increase of C - processes intensity with I_0 growth (Fig.7). Compositional cathode plasma contains mainly ions of material with high I_0 even at insignificant content of material with I_0 essentially exceeding I_0 of the rest of materials forming the cathode. E.g., ion beam extracted from plasma of the cathode containing 90% of Pb and 10% of Ti consists by almost 70% of Ti ions. Surface erosion of cathode made of simple substances with essentially different I_0 looks equally homogeneous on macrolevel after exploitation in equal conditions for equal time. Surface erosion of compositional cathodes made of the same materials put to the same tests is nonuniform and more intensive.

Cathode plasma interaction with cathode surface becomes more intensive with increase of the velocity of current I rise. This effect reveals in shortening of emission excitation delay time from the surface of non - functioning emitters, velocity increase of cathode generated plasma flow, increase of multicharged ions containing in plasma. Fig.8 presents mass -

spectrograms of ion beams extracted from plasma of quasistationary and forced discharges. Decrease of current rise velocity lowers interaction intensity and can be used to control the discharge.

Regulation of emitter current rise velocity was used to increase spark phase duration. Emission and current I_1 from one of the points E_1 of a two - point cathode were initiated by auxiliary discharge. Appearance of current I_2 from the second point E_2 was stimulated by plasma E_1 and occurred during discharge transition along the channel between E_1 and anode into the final stage of a spark phase (Fig.9). We can see from oscillograms given that E_2 switching on interrupts arc discharge generation and restores the discharge into a spark stage owing to current redistribution. Discharge between E_1 and anode breaks and discharge cycle renews but between E_2 and anode. Now, E_1 turning on prevents from arc discharge ignition along the channel between E_2 and anode. When resistance is inserted into the every emitter circuit, the process is realized automatically. False operations are blocked by a condensator preventing from potential difference appearance between emitters at short - time current throws.

Duration of t_{ST} discharge stable state at point 4 of VAC decreases with the rise of current density of electron beam j_e bombarding anode. For a plane discharge gap $t_{ST} \sim j_e^{-1}$. In the gaps with spherical and cylindrical geometry, t_{ST} is lower or higher than in the plane gap depending on whether inner electrode is cathode or anode. Electron bombardment of anode surface stimulates gas desorption. Desorption efficiency $\gamma \sim (1-10)$ molecule/electron, velocity of the desorbed gas flow $v \sim (3,5-5)10^4$ cm/s, molecule concentration in the stream $n \sim j_e \gamma / e v$. In a plane discharge gap, potential difference between the gas stream front and anode U_g is proportional to the depth of the desorbed gas layer $d_g = vt$. Discharge ignition in the desorbed gas layer in accordance with the Pashen's law is supposed to be the reason of t_{ST} limitation. Dependence of t_{ST} on j_e and discharge gap geometry qualitatively agrees with this interpretation of anode plasma origin.

At the electron beam power density on the anode lower than 10^5 W/cm² only desorbed gas is the medium from which anode plasma is generated. Reserve of gas adsorbed by anode surface is limited. During discharge adsorbed gas layer exhausts. Time is necessary to restore the layer. Desorption processes may be applied to control current break process and to realize plasma interrupters. Fig.10 presents electron - optical pictures of glowing with 2 - μ s exposure duration and discharge current oscillogram of 4000 - μ F capacity condensator through 2000 μ H - inductance to a 4 - cm - long vacuum gap (cathode is above). Initial voltage on the condensator is 180 V. Discharge initiation was realized by the firing pulse on the cathode. After appearance of cathode plasma, the anode one is observed to be generated. Anode plasma volume and brightness of glowing grow in due course, reach the maximum and then decrease resulting in the discharge current break. Current break phase is presented in Fig.11 in details. Presence of high inductance in the circuit provides ~ 100 - fold voltage increase at the discharge gap in the current break phase as compared with the initial one. Fig.12 presents integral pictures of the discharge glowing at the first switching after a long break (a), at the switching in 4 (b), 2 (c) and 1 minutes (d) after the previous switching of discharge. Volume and brightness of glowing decrease with the decrease of interval between switchings.

Autonomous plasma source on the discharge gap anode or cathode allows to realize special discharge form and namely, plasma discharge. Peculiarity of this discharge form consists in the fact that before voltage is applied, interelectrode space volume set beforehand is filled by plasma with such composition and concentration distribution at which predischage and spark phases in the discharge cycle are absent after voltage is applied. From the moment of discharge gap connection up to the power supply, I is limited by R . Cathode drop layer and the value U_c at reaching $I \sim I_0$ are sufficient for exciting of emission centers on the cathode and subsequent functioning of C - processes since they proceed in the arc phase of the discharge. Transition from current limitation by factor R to limitation by factor I_p , formation of tear in plasma, expansion of tear and partial or full I drop may be organized at any moment by regulation of the gap filling by plasma. Fig.13 presents I and U_D oscillograms illustrating distinctions of vacuum discharge from plasma one. Oscillograms 1 correspond to vacuum discharge, plasma was not injected into the gap. Oscillograms 2 correspond to plasma discharge with I breaking. Owing to SR - interactions, voltage on the gap U_D increases up to 2,0 - 2,2 MV that is 1,5 - 1,8 times higher than the initial voltage U_0 of Marx generator. Oscillogram 3 corresponds to the case when I is determined by R due to insufficient generator power and energy reserve during all the time of discharge proceeding. Here U_D is lower than resolution system.

At a partial filling of discharge gap by plasma from the anode side before applying voltage, discharge begins from spark phase. This is a vacuum discharge with plasma anode. Plasma anode application allows to decrease intensity of AC - interaction conditioned by uncontrolled generation of anode plasma, to increase the time t_{ST} and beam current density j_e . Electron beams with $j_e \sim 1$ kA/cm², $t_{ST} \sim 100$ μ s and $t_{ST} \sim 3,5$ μ s at the electron energy of 5 - 10 keV and ~ 100 keV, respectively, have been obtained in the discharge with plasma anode. In the last case, spark phase duration was limited by generator discharge.

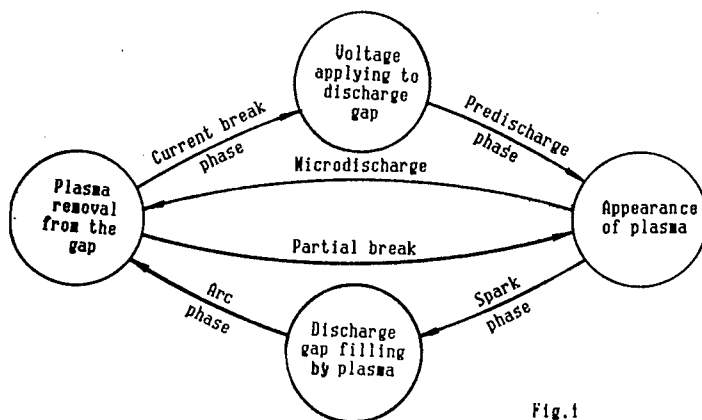


Fig. 1

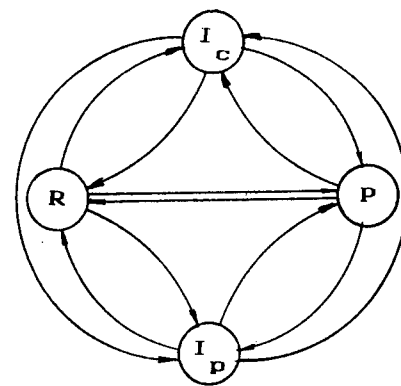


Fig. 2

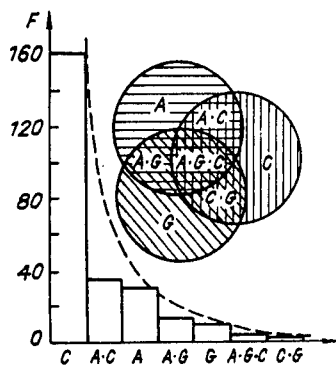


Fig. 3

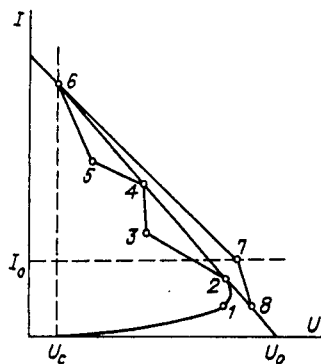


Fig. 4

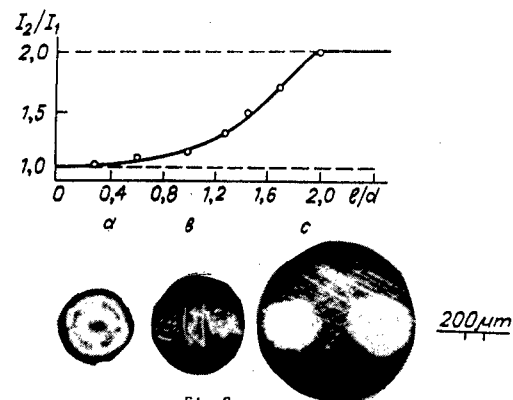


Fig. 5

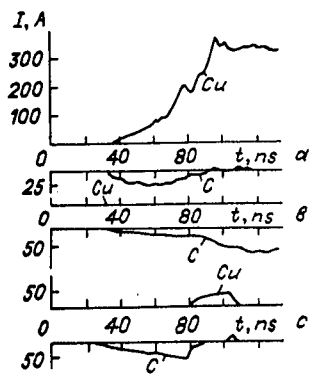


Fig. 6

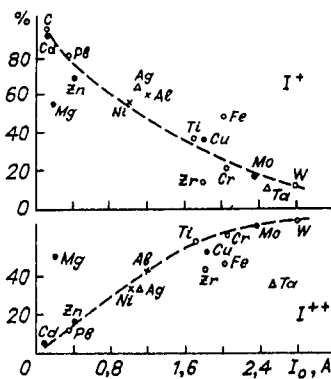


Fig. 7

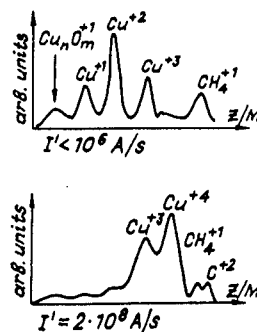


Fig. 8

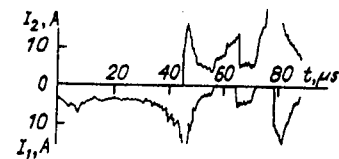


Fig. 9

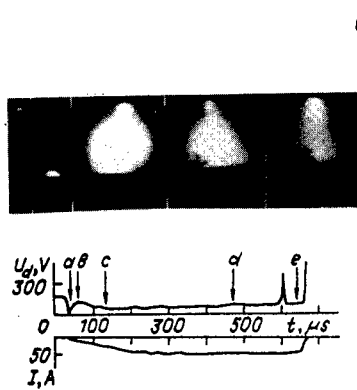


Fig. 10

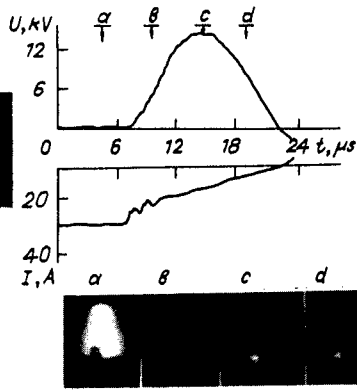


Fig. 11

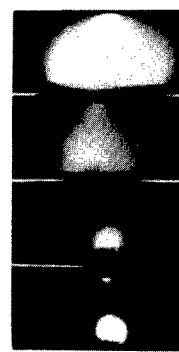


Fig. 12

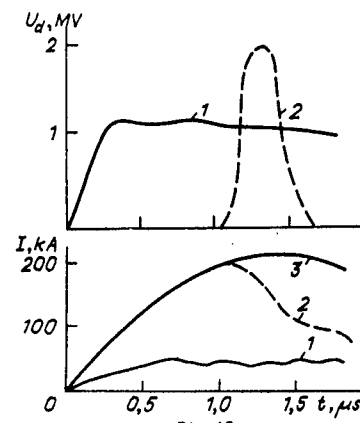


Fig. 13

TRIGGERED VACUUM INTERRUPTER WITH A SWITCHING ACCURACY UP TO MICROSECOND UNITS

D.F. Alferov, V.A. Sidorov, V.A. Vozdvijenskii

All-Russian Electrotechnical Institute
12 Krasnokazarmennaja st., Moscow 111250, Russia

ABSTRACT

Switching characteristics of the triggered vacuum interrupter (TVI) combining the properties of vacuum interrupter and triggered vacuum switch are studied. In order to reduce the chopping current electrode insertions made of a highly arcing-proof composite material are used. Along with the expected low chopping current less than 1 A the TVI has good switching capabilities both at anode and cathode modes of operation with a trigger current $I_t > 100$ A and trigger voltage $U_t > 500$ V.

The effect of the load on the switching capability of the interrupter at the anode mode of operation is investigated. The obtained results make it possible to specify the requirements for trigger source output parameters with the aim to provide a reliable switching for different polarities of the main electrodes. Model tests of TVI in power frequency networks showed the possibility of its utilization under controlled switching with an accuracy to microsecond units and keeping all the properties of the vacuum interrupters.

1. INTRODUCTION

For many applications in power networks it is of great promising to make a vacuum interrupter combined with a triggered vacuum switch (TVS). Such offer has been already done in literature¹. However it hasn't yet been realized to date.

The expected conditions of utilization of such unit, which will be referred to hereinafter as the triggered vacuum interrupter (TVI), differ essentially from those of the TVS in pulse equipments: switching currents of (0.1-1) kA at 50 Hz; trigger cycle duration of the order of (0.1-10) s; a charge per cycle is to 1000 K; instantaneous operating voltage range from 0.5 to 10 kV; triggering is done to an accuracy to tens of microseconds at any polarity of the network voltage. The main feature of the above pointed operating conditions are a small value of the current at a large pulse duration and starting cycle. Here, high chopping currents are not allowable.

With regard for the above given requirements a model TVI has been designed on the basis of a commercial vacuum interrupter. The model made it possible to carry out investigations of its starting characteristics and to determine optimum conditions of the trigger unit start. The obtained results showed that it is characteristic of a high switching capability in either mode of operation (cathode or anode) at a trigger voltage $U_t > 500$ V. The interrupter trigger unit ensures a persistent flowing of a trigger current $I_t \geq 20$ A at 100 Hz and mean voltage drop at the trigger gap from 25 V to 30 V. A switch-on delay time of TVI when it is started with the cathode doesn't exceed 1 μ s. A mean value of the chopping current is on the order of (0.5-1) A.

The paper gives the TVI scheme and discusses peculiarities of its triggering at the anode mode of operation taking into account the effect of parameters of loads of the main discharge circuit. The switching capabilities of TVI has been proved by means of its testings in a 50 Hz network at 220 V.

2. INTERRUPTER SCHEME

The TVI is a vacuum interrupter tube controlled in general by travel of a movable electrode 1. A trigger unit containing the dielectric cylindrical insertion between trigger 2 and main electrodes is placed in the center of the fixed electrode 3. The electrode system scheme is presented in Fig. 1. In order to reduce a chopping current at the main electrode surface a highly arcing-proof composite material insertions are soldered in. Measurements were done at the electrode contact surfaces spaced to 5 mm. In this case a minimum distance between the trigger unit and opposite electrode surface was about 9 mm. At application of a control pulse to the trigger electrode the TVI connects quickly the network with the load at a specified voltage phase. When the trigger cycle is terminated a command to close the movable electrode is given and the interrupter is switched on completely.

3. SWITCHING ON CONDITIONS OF THE TVI IN ANODE MODE OF OPERATION

After the control pulse is applied a triggering plasma is formed close to the anode surface. At the moment of approaching the triggering plasma to the cathode a space charge layer (a near-cathode layer) is produced in the vicinity of its surface. The generated layer is subjected to practically the whole voltage value occurred at the interelectrode gap. In a prebreakdown phase until cathode spots are appeared a discharge is of a self-dependent nature. In this phase the current in the near-cathode layer consists of electron I_e and ion I_i components.

$$I = I_i + I_e = f \cdot I_t - S \cdot e \cdot n_e \cdot v_e \cdot e^{-\frac{eU}{kT_e}} \quad (1)$$

where S - the area under the space charge layer, e , n_e , v_e and T_e - the charge, density, thermal velocity and temperature of electrons, respectively. A change in the ion current versus the time imitates practically dynamics of the trigger current. Its amplitude is proportional to the trigger current amplitude. The proportionality factor f depends on the trigger unit electrode material and in our case it is $5 \cdot 10^{-2}$. An electron component is defined by a Boltzman distribution under deceleration regime and decreases exponentially with increasing the voltage U at the layer. A prebreakdown current in the layer specifies the field strength E_k at the cathode. If E_k exceeds a certain field strength value E_{kbr} a breakdown of the near-cathode layer takes place and the TVI is switched on². If the prebreakdown current is determined mainly by the ion component the conditions of the layer breakdown can be represented as follows:³

$$I_t(t) \sqrt{U(t)} > G, \quad G \sim \frac{d^2}{f \sqrt{M}} \cdot E_{kbr}^2 \quad (2)$$

Here, d - the minimum distance from the trigger unit to the cathode, M - molecular ion weight. The value of E_{kbr} depends on the cathode material and its surface condition.

Let us consider the dynamics of the current in the near-cathode layer for the case of switching on TVI in a low-frequency LC circuit at a starting voltage U_0 (Fig.1). Let us assume that the triggering plasma is quasi-neutral and propagates isotropically from the trigger unit: $n_e = z n_i = f \cdot I_t / 2\pi \cdot d^2 \cdot z \cdot e \cdot v_i$, where z - the mean ion charge, v_i - the averaged drift ion velocity. Taking into account a comparatively low prebreakdown phase duration $t_t \ll T = 2\pi \sqrt{LC}$ one may obtain the following set of equations, describing the dynamics of the discharge current ($S \approx 2\pi \cdot d^2$)

$$U = U_0 - L \frac{dI}{dt} \quad I = f \cdot I_t \left(1 - \frac{v_e}{v_i} \cdot e^{-\frac{eU}{kT_e}} \right) \quad (3)$$

According to (3) two main conditions of the current dynamics may be singled out as a function of I_t and U_0 (when estimating boundary conditions assume $v_e/v_i \approx 10^2$, $T_e \approx 5$ eV).

Provided $f \cdot \frac{dI_t}{dt} \ll \frac{U_0}{L}$, ($|U| > 35$ V) the current in the discharging gap is only defined by a trigger current $I(t) \approx f \cdot I_t(t)$. In this case the highest probability of realization of the breakdown conditions takes place close to a maximum I_t when $dI_t/dt = 0$ ($U = U_0$) and ion density in the layer is maximum.

If $f \cdot \frac{dI_t}{dt} \gg \frac{U_0}{L}$, ($|U| < 35$ V) the discharge current is representative of significant electron components and dynamics of the current is specified by parameters of the external circuit. Here, breakdown condition (2) can't be satisfied till $I_i > \frac{U_0}{L} \cdot t$. At $I_t < \frac{U_0}{L} \cdot t$ a chop of the discharge current occurs as a result of reduction in the particle density in the layer. At this moment ($dI/dt < 0$) the voltage U increases abruptly and fulfillment of condition (2) becomes probable.

The duration t_T of the unipolar half-wave trigger current pulse with amplitude I_{tm} may be estimated provided a breakdown takes place at the trigger current value close to its maximum

$$t_T \geq 2 \cdot f \cdot I_{tm} \cdot L / U_0 \quad (4)$$

It is to be pointed out solution of (3) makes it possible to estimate triggering plasma parameters (v_e/v_i and T_e) under field testing conditions

4. EXPERIMENTAL RESULTS

At the first stage of investigations conditions of the discharging gap breakdown were determined as a function of a trigger current amplitude I_{tm} at $t_T = 300 \mu s$. The measurements were carried out by using the technique described in³ at $U = \text{const}$. The obtained results are depicted by a relation of $I_{tm} \cdot U^{0.6} \geq 4 \cdot 10^3 [A \cdot B^{0.6}]$, which agrees well with (2). Subsequently, to ensure a reliable TVI switch on in the whole range of operating voltages $U_0 = (0.2-2) \text{ kV}$ the trigger current amplitude was $I_{tm} \approx 160 \text{ A}$.

Studies of TVI switching capability at the anode mode of operation were performed by means of a single start in a low-frequency LC circuit (Fig. 1; $C \approx 600 \mu F$; $L \approx 600 \mu H$). At $|U_0| < 200 \text{ V}$ ($f \cdot dI_T/dt > U_0/L$) the voltage across the TVI drops sharply practically to zero immediately after a trigger pulse has been applied. A value of the prebreakdown current is defined in this case by parameters of the external circuit. Here, a drop of the voltage and increase of the current are of a monotonous character. If $|U_0| \leq 150 \text{ V}$ then, at the trigger current decrease (at $t \approx 270 \mu s$), events of the discharge current chopping are observed and upon significant oscillations the voltage is restored to the starting U_0 .

At $|U_0| > 300 \text{ V}$ ($f \cdot dI_T/dt \leq U_0/L$) the beginning portion of the current increase is determined by the ion component of the current. Typical current and voltage oscillograms for such case is shown in Fig. 2. This condition is characteristic of noticeable voltage oscillations in the prebreakdown phase of the discharge. Their appearance may be explained by an inherent nonmonotonicity of the ion current. A change in the ion current derivative versus the time leads to bumps in the voltage $\Delta U \sim L \cdot dI_T/dt$. With increasing $|U_0|$ an averaged drop in the voltage across the gap $|U| = |U_0 - L \cdot f \cdot dI_T/dt|$ also increases. After a breakdown has occurred the voltage $|U|$ decreases quickly down to zero. At this moment a bend is taken place in the current curve as its rate of rise increases drastically to $dI/dt \approx U_0/L$.

Voltage oscillations in the breakdown phase may be practically fully excluded by means of shunting the TVI with a RC circuit. Parameters of the circuit ($R < U_0/3f \cdot I_T$ and $C > t_T/2R$) were chosen so that a prebreakdown current is defined by the ion current flowing through RC circuit and $U \approx U_0$.

To verify switching characteristics of the TVI at a frequency operation it was tested in a commercial frequency circuit at a network voltage of 220 V. The testing oscillograms are given in Fig. 3. If the TVI is triggered close to the maximum voltage $U_m = 220 \cdot \sqrt{2} \approx 310 \text{ V}$ it is switched on both at a negative and positive voltage polarity. In the case of shifting the trigger phase there are events of a failure in switching on the anode.

5. CONCLUSION

The cycle of investigations carried out on a model TVI showed the possibility of using it for a fast controlled switching on with maintaining all characteristics of the vacuum interrupter.

The investigation of the TVI switching capability under anode mode of operation made it possible to found out the effect of load parameters on development of the prebreakdown discharge phase. As a result of this breakdown conditions at the discharging gap were defined as a function of parameters of the control current pulse and external circuit. Optimum parameters of the control unit ensured a reliable triggering TVI in anode and cathode modes of operation at frequency conditions are estimated.

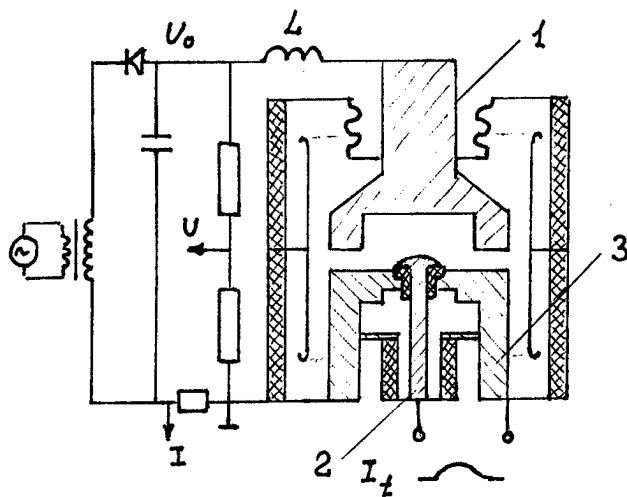


Fig. 1

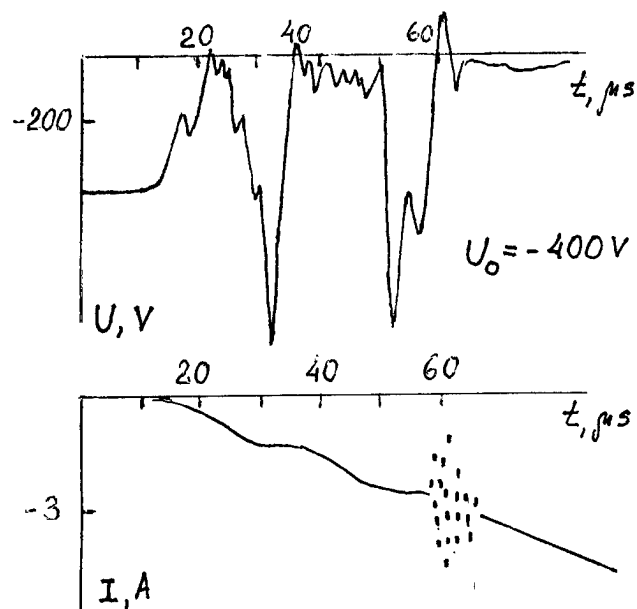


Fig. 2

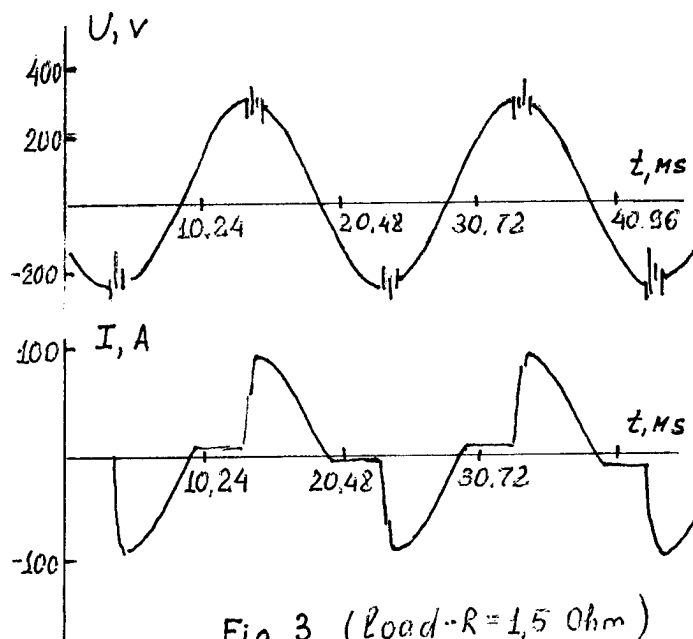


Fig. 3 (load $R = 1.5 \text{ Ohm}$)

6. ACKNOWLEDGMENTS

We gratefully acknowledge the support of this work by the Russian Fundamental Research Fund (grant No. 93-02-17425)

7. REFERENCES

1. Vacuum Arcs. Theory and Application, J.M. Lafferty ed., John Wiley & Sons, New York, 1980
2. R.L. Boxman, "Triggering mechanism in triggered vacuum gaps", *IEEE Trans. Electr. Devices*, Vol. ED-24, pp. 122-128, February 1977
3. D.F. Alferov, V.A. Vozdvijenskii, I.O. Sibiriak, "Formation of the cathode spots under the vacuum discharge plasma", *Proc. XIV ISDEIV*, Santa Fe, pp. 546-549, Sept. 1990

SWITCHING CHARACTERISTICS OF THE SUBMICROSECOND TRIGGERED VACUUM SWITCH

D.F. Alferov, V.A. Sidorov, V.A. Vozdvijenskii

All-Russian Electrotechnical Institute
12 Krasnokazarmennaja St., Moscow 111250, Russia

ABSTRACT

The small-size sealed-off triggered vacuum switch TVS-7 designed to switch current pulses to 10 kA at high repetition rate to 1 kHz and maximum voltage to 25 kV is described. TVS switching characteristics are studied systematically versus the trigger current parameters for different polarities of the main electrodes. It is shown the TVS ensures a monotonous current rise of submicrosecond duration with a rate of current rise up to 10^{11} A/s and a minimum switch-on delay time of 50 ns at a trigger current amplitude of $I_t \geq 100$ A. In the cathode mode of operation the TVS is reliably triggered with reducing of trigger current up to $I_t \geq 1$ A. But in this case current and voltage oscillations occur at an initial discharge development stage. This unstable stage of discharge burning is subjected to investigation. A minimum trigger energy, of about 10 mJ is required to ensure stable conditions of discharge burning with any polarity at the main electrodes. Under the condition power losses at switch-on stage of the TVS are substantially reduced in comparison with those of traditional vacuum switches. This became possible because of the use a two-stage trigger system of the erosion type and a small main vacuum gap.

1. INTRODUCTION

Progress in the pulse technique makes more and more increasing demands to switching devices intended to provide fast and reliable connection of the energy accumulators both under monopulse mode of operation at currents to hundred kiloamperes with a pulse duration to several millisecond and high-repetition-rate mode at currents from units to tens of kiloamperes with a pulse duration from hundreds of nanoseconds to tens of microseconds. The application of triggered vacuum switches (TVS) to meet these requirements is highly promising¹. These devices are filamentless three-electrode sealed-off units, the residual gas pressure in which doesn't exceed 10^{-4} Pa. They are capable to switch on quickly (for less than 1 μ s) and to operate over a wide range of voltages and currents: $U=(1-100)$ kV; $I=(0.1-200)$ kA. The TVS is characteristic of rapid recovery, compactness, noiseless, fire-proof, ecological purity in production and operation, reliable service in a vast variety of environmental conditions.

At present the TVS is used mainly in high current applications having comparably high pulse duration from tens of microsecond to units of milliseconds²⁻⁷. In the case of shorter submicrosecond pulses with a rate of rise of the current over 10^{11} A/s energy losses at the initial stage of discharge development are essentially increased. This is due to the occurrence of unstable condition of burning discharge accompanied by current and voltage oscillations⁸.

The present work considers switching parameters of a small-size sealed-off high-repetition-rate triggered vacuum switch (type TVS-7). By choosing an adequate trigger gap geometry and respective trigger conditions the starting losses were considerably reduced.

2. TVS-7 FEATURES AND TEST CONDITIONS

The TVS-7 design was specified by requirements to ensure a high rate of current rise above 10^{11} A/s at a submicrosecond pulse duration, to withstand a maximum voltage (to 25 kV) across the gap and to reduce start energy losses to level under 10% of the full switching pulse energy. The TVS-7 tube comprises two ceramic cylinders of 36 mm in outside diameter and 100 mm in height, connected through a flat copper sealing which is at the same time a cathode holder (Fig.1). The main electrodes are mounted inside ceramic cylinder 1. Cylinder 2 serves as an insulation for a triggering electrode. To reduce the tube size the TVS-7 is made without a separate screen system unlike the other types of the sealed-off TVS^{4,6}. For a specified rate of current-rise to be ensured a double-stage trigger system is used that proved well itself in TVS-3⁶. The minimum interelectrode main gap was about 3 mm.

A testing circuit of the TVS-7 is presented in Fig.1. The trigger circuit is charged to U_t and discharged to the TVS trigger system through a control switch S1. When S1 is started trigger electrode 3 is applied with voltage U_t resulting in a

breakdown at the surface of the trigger unit dielectric insertion. Occurrence of the breakdown leads to formation of a trapezoidal current pulse whose amplitude is controlled by change of voltage $U_t=(1-8)$ kV and resistance $R_t=(10-1000)$ Ohm. To decrease the circuit inductance L to 300 nH the main test oscillatory circuit LC is coaxial. At storage capacitance $C=32$ nF the wave circuit resistance was about 3 Ohm. Several microseconds prior to application of a trigger pulse the capacitance C was charged to voltage $U_0=(0.5-20)$ kV by switch S_2 . The S_2 trigger circuit is similar to this of S_1 shown in Fig. 1. Type triggered vacuum switches served as switches S_1 and S_2 .

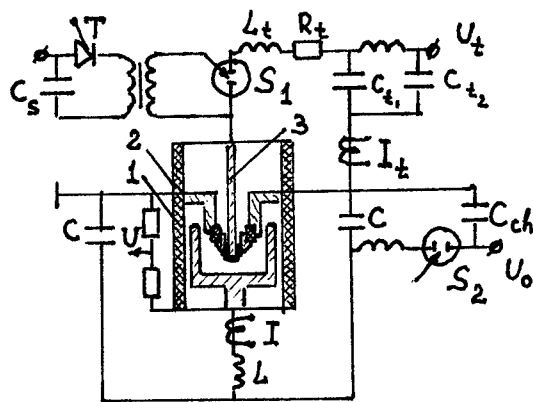


Fig. 1 Schematic of TVS-tube and test circuit.

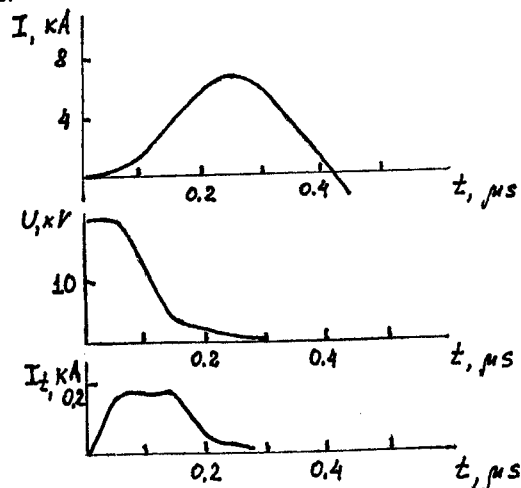


Fig. 2 Typical current and voltage pulses at cathode mode of operation.

3. TEST RESULTS

3.1. Cathode mode of operation

A minimum value of the breakdown voltage at the trigger unit is dependent of the relationship between main discharge current and trigger current parameters that is characteristic of the erosion firing mechanism. So, at a trigger current above several per cent of the main current a minimum trigger unit breakdown voltage was (2-3) kV. With decreasing the trigger current the breakdown voltage drops, being below 1 kV at I_t on the order of several Amperes.

The main discharge development depends on the trigger current form and value⁸. There are two main modes of its behaviour: an unstable burning at the initial main current development phase followed with current and voltage oscillations, and steady-state current flow at a monotonous rise of the current and decrease of the voltage. Realization of either of the modes is defined by the relationship between main discharge current and trigger current parameters. A steady state progress of the discharge development in the whole range of operating voltages at the TVS-7 takes place at $I_t > 100$ A with a trigger current front duration of 50 ns. Typical current and voltage oscillograms at these conditions are presented in Fig. 2. The trigger current duration corresponds to about a quarter of the main current period. Changes in current and voltage with time is as a rule steady. A voltage drop duration during discharge current rise doesn't exceed 100 ns. With decreasing U_0 qualitative form of time-dependent current and voltage are maintained up to the discharge current amplitude $I_m=(300-500)$ A. In subsequent decreasing I_m the current is turned off when it crosses zero and the TVS passes only the first half-wave of the discharge current. A switch-on delay time t_d decreases with increasing in the trigger current. A minimum delay time $t_d=(40-50)$ ns was obtained at $I_t=300$ A.

It should be pointed out TVS start energy losses at these conditions are low and practically negligible at the level of measurement errors. The active resistance of the discharging circuit estimated through the damping of discharge current sinusoidal oscillations amount to ~ 0.25 Ohm. The minimum energy consumed in the trigger unit circuit to ensure steady state conditions isn't higher than 10 mJ.

At comparatively small trigger current (below a threshold one for a given charge voltage) current and voltage oscillations take place at the front of the discharge current and at the drop in the voltage. At $U_0=20$ kV such unstable phase is generally marked by a small current peak ($<20\%$ of the amplitude) at the beginning of the voltage decrease. The duration of the

unstable phase and number of oscillations increase with reducing U_0 at a fixed trigger current. The switch-on delay time at the given conditions is $t_d \approx (200-400)$ ns if defined upon finishing the unstable discharge burning phase. The presence of the unstable phase leads to appreciable energy losses during the turn on event. These losses estimated through a decrease in the first discharge current half-wave amplitude relative to a calculated one at $U_0 = 20$ kV are about 5%.

3.2. Anode mode of operation

The anode mode of operation is carried out by application of a negative polarity voltage $U_0 < 0$ to bottom electrode 5 (Fig. 1). In this case the upper electrode 4 remains to be grounded. At the conditions after a number of the first switching on the trigger voltage U_t required to break trigger gaps increases abruptly. An absolute magnitude of the minimum voltage when a trigger unit is broken reliably can be a little reduced to $|U_t| \sim 8$ kV by reversing the trigger electrode polarity $U_t < 0$.

Upon a breakdown at the trigger gap the plasma formed at the anode propagates into the main vacuum gap and an ion current starts passing in the main discharge circuit. Its value is limited by conductance of the space charge layer between the anode plasma emission surface and cathode surface. And if the voltage at the vacuum gap remains constant the form of the ion current repeats qualitatively the trigger current form with a front and drop prolonged in time. A delay in the ion current appearance against the beginning of I_t is attributed to the time of the trigger plasma propagation to the cathode. The ion current amplitude at comparatively low anode voltage $U_0 < 5$ kV is about of 8% of the trigger current amplitude.

Breakdown conditions in the main gap depends essentially on the relationship between a trigger current and voltage across the main gap⁹. At a fixed I_t a probability of a breakdown drops with decreasing U_0 from unity to practically zero. By using the technique minimum trigger current I_{tmin} and voltage U_{0min} necessary to switch on TVS reliably were defined. The obtained relationships are approximated by a function of $I_{tmin} \sim (U_0)_{min}^{-1.2}$ (Fig.3) which differs essentially from a similar relationship for a TVS with an external plasma source⁹. The cause of this phenomenon isn't yet clear for us. To explain it additional model experiments have to be carried out. But it is worth noting in the case of the conditioned trigger unit when its internal resistance becomes infinite (above 10^9 Ohm) high frequency oscillations with a period of 10-30 ns and a double amplitude of 10 A occur in trigger and ion currents. In our opinion appearance of such oscillations make the breakdown process essentially nonstationary (type time become comparable with a flight time of near-cathode layer ions) leading to a higher probability of a breakdown¹⁰. In this case the breakdown takes place, as a rule, at the front of the ion current. The obtained data on measurements of the switch-on delay time justify this. The delay time remains practically constant $t_d \approx 100$ ns in a wide range of trigger currents $I_t = (2-100)$ A and voltages $U_0 = (5-20)$ kV. Typical current and voltage oscillograms taken at significant exceeding the threshold breakdown conditions are shown in Fig.4.

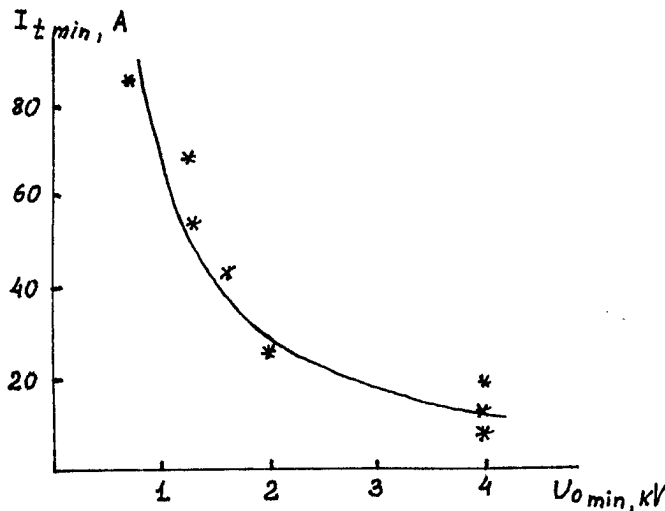


Fig.3 TVS switch-on condition at anode mode of operation.

The curve is defined by eq. $I_{tmin} = 3 \cdot 10^5 U_{0min}^{-1.2}$.

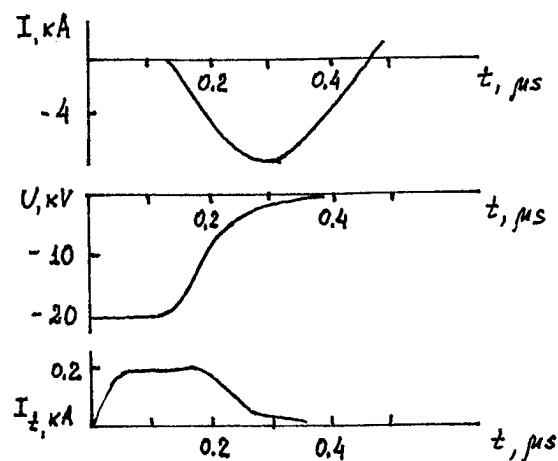


Fig.4 Typical current and voltage pulses at anode mode of operation.

3.3. High-repetition-rate test

TVS was tested on a high repetition rate of 1 kHz at $U_0=+4$ kV, $I_{\max}=500$ A with a pulse duration of 1 μ s under forced air cooling. It was subjected to 10^6 switches on and no markable changes in its electrical characteristics were found out.

4. CONCLUSION

The new high-repetition-rate triggered vacuum switch TVS-7 developed in VEI showed the capability to switch submicrosecond pulses at a rate of rise of the current higher than 10^{11} A/s at any polarity of the main electrodes. The minimum trigger energy at a steady state switch condition is 10 mJ in the whole range of operating voltages of $\pm(1-20)$ kV. The use of a double-stage erosion triggering system and a small main gap enables to considerably reduce energy losses during the turn-on event over those of conventional vacuum switches.

5. ACKNOWLEDGMENTS

We gratefully acknowledge the support of this work by the Russian Fundamental Research Fund (grant No. 93-02-17425)

6. REFERENCES

1. Vacuum Arcs, Theory and Application, J.M.Lafferty ed., John Wiley & Sons, New York, 1980.
2. L.M.J. Vries, G.C.Damstra, "Triggered vacuum gaps in a high power three-phase synthetic test circuit", *IEEE Trans. Plasma Sci.*, Vol. PS-17, pp. 755-758, October 1989.
3. G. Bauville, A. Delmas, N. Haddad, C. Rioux "Study of recovery phenomena in a high-current pulse-triggered vacuum switch", *IEEE Trans. Plasma Sci.*, Vol. PS-17, pp. 781-784, October 1989.
4. D.F.Alferov, V.A.Vozdvijenskii, I.O.Sibiriak, V.A.Sidorov, "Controlled vacuum discharger with staggered electrodes", *Instrum. Exp. Tech.*, Vol.33, No.5, Part 2, Sept.-Octob. 1990 / April 1991.
5. R. Dethlefsen, V.A. Sidorov, V.A.Vozdvijenskii, "Triggered vacuum switch testing for millisec. pulses", *Proc. 8th Int. Pulsed Power Conf.*, San Diego, pp 511-514, June 1991.
6. V.A.Vozdvijenskii, V.A.Sidorov, "Triggered vacuum switch RVU-3", *Prib. Tekh. Eksp.*, pp. 104-111, April 1992 (in Russian).
7. H. Arita, K. Suzuki, Y. Kurosawa, "Switching characteristics of the triggered vacuum gap for a high-repetition-rate pulse-power source", *IEEE Trans. Plasma Sci.*, Vol. 20, pp. 76-79, April 1992.
8. D.F.Alferov, N.I.Korobova, I.O.Sibiriak, "Evolution of pulsed high current electrical discharge in vacuum", *Fiz. Plasmy*, Vol.19, pp.339-410, March 1993 (in Russian).
9. D.F.Alferov, V.A.Vozdvijenskii, I.O.Sibiriak "Formation of cathode spots under the vacuum discharge plasma", *Proc. XIV ISDEIV*, Santa Fe, pp.546-549, Sept. 1990.
10. M.Yu. Kreindel, E.A. Litvinov, G.E. Ozur, D.I. Proskurovsky, "High-voltage pulsed breakdown of the nonstationary near-cathode layer in a plasma-filled diode", *Proc. XV ISDEIV*, Darmstadt, pp. 707-710, Sept. 1992.

Repetitive generators based on the plasma opening switch

N. U. Barinov, G. S. Belenki, G. I. Dolgachev, Yu. I. Kovalev,
L. P. Zakatov, A. G. Ushakov

Russian Research Center "Kurchatov Institute" , Moscow, Russia, 123182

ABSTRACT

The paper considers pulsed power repetitive systems using plasma opening switches (POS). The solutions of a row of technical problems connected with both repetitive operation of accelerator having high peak power and x-ray radiation converter are proposed. These machines are to be prospective for advanced radiation technologies.

Within the frames of military conversion a certain class of pulsed electron accelerators previously used for military purposes comes to radiation industrial technologies. In these technologies for example in potable water decontamination or wasted water disinfecting in big cities the average power of 10 MWt and the electron beam energy of 5-10 MeV are required. According to Dr. G.Yonas¹ the prospective ways to realize mentioned parameters lay in the concepts possessing high peak power.

One of the ways recently being developed for pulsed power accelerators is an inductive storage system with a plasma opening switch (POS). The experimental level allows to establish the principal appropriates of POS operation and to create POS-based machines in a wide range of parameters.²

In 1991 the first repetitive-ray generator RS-20 which uses POS was constructed. The parameters are as follows: electron beam current 20 kA, electron energy - 2-3 MeV, average power 20 kWt, repetition frequency 2-4 Hz.³

POS Voltage increase up to 5-10 MeV requires drive current increase up to values substantially higher than 100 kA to provide a magnetic insulation. With these parameters of peak power reaching average power of MegaWatt is possible with repetition frequencies up to 10 Hz. POS operation analysis shows that there are no physical limitations regarding these parameters disinfecting

Two year period of RS-20 exploitation allowed to clear up and to resolve a row of problems stipulated by repetitive regime of accelerator operation.

The machine uses 4 20-stage Marx pulse voltage generators with 1 MV output voltage as primary source. Marx generators are placed around the insulator close to its surface. The potential of gradient rings is determined by the stage voltages. Marx generator inductiveness is minimized due to the fact that each stage constitutes a circuit containing a capacitor and a switch and a magnetic fields of adjacent circuits go opposite directions.⁴ This connection allows to reduce the inductiveness of the one stage of Marx generator 20% as low as that of the single circuit including capacitor and triggering switch.

A POS anode illustrated in Fig.1 looking like a "squirrel's cage" is made from brass with a diameter changing in a longitudinal direction. The rods inserted into the ring are placed at the high-voltage drive. This design⁵ allows to reduce electron component of the current to the anode hence increasing its transparency with plasma volume shifting.

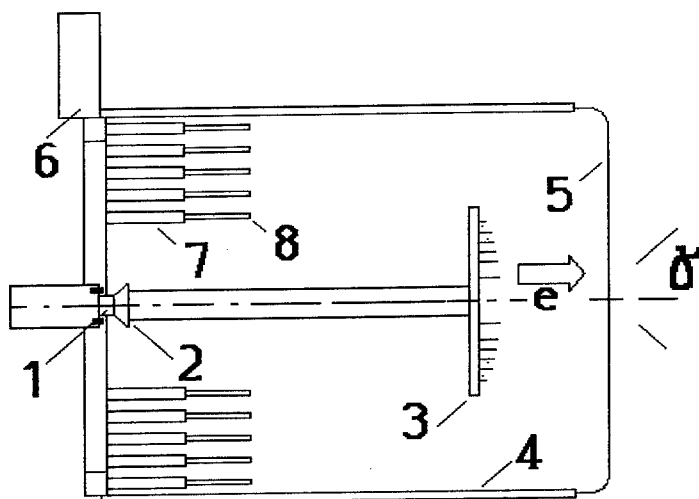


Fig.1. RS-20 generator POS scheme: 1 - 12 plasma guns, 2 - deflector, 3 - diode cathode, 4 - anode holder, 5 - x-ray converter, 6 - POS anode (a ring from a stainless steel), 7- 32 anode rods, 8 - tungsten rods

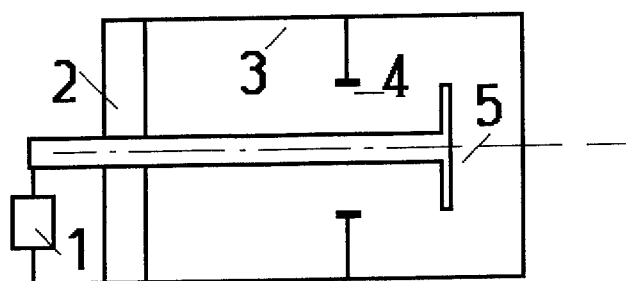


Fig.2. A new concept of POS for repetitive generator. 1 - Marx generator, 2 - high voltage insulator, 3 - vacuum chamber, 4 - plasma guns (placed at the cathode), 5 - x-ray target (POS anode).

allows to increase the average power density up to 50 Wt/cm² and durability up to 10⁷ pulses without a drop in a dose rate of x-ray radiation.

A new scheme of POS is proposed in which the plasma volume is placed into the break of outer electrode of a vacuum coaxial line as it given in Fig.2. In the scheme a magnetic field pressure of the drive current going at coaxial line pushes plasma in a radial direction resulting in a decrease of both plasma density and current being interrupted. This scheme has prospects from a

Plasma guns are placed at the butt-end of POS cathode⁶ having ground potential. With a flashover of plasma gun dielectric surface plasma goes longitudinal direction toward deflector and fills POS radial gap. This design allows to protect plasma gun dielectric surface from an ion bombardment and so to prevent gas emission from its surface and to increase the resource. Diode is switched in parallel to POS where its anode is used as x-ray radiation converter. The exploitation show an advisability of charging resistor substitution with a specially constructed inductiveness that resulted in energy losses decrease in elements used for charging from 7% down to 1% and enhanced the reliability of the Marx. Under testing with active load the density of power transformed by the Marx generator was 50 kWt/cm³.

The specially designed multi-layer target is used to reach the goal of x-ray converter high durability. High pulsed power of the beam results in fast 10³-10⁴ pulses destruction of tungsten (or tantalum) target (having optimum sickness for a dose power) with an average power density 20 Wt/cm². Using combined target made from several layers of materials (see Fig.3)

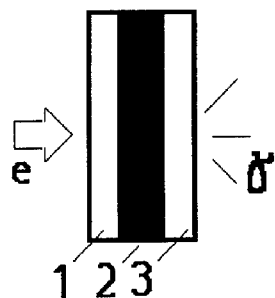


Fig.3. A scheme of multi-layer target. 1 - protective layer (carbon $p=0.06 \text{ g/cm}^2$), 2 - highly dispersed tungsten or tantalum ($p=1 \text{ g/cm}^2$), supporting layer (carbon $p=0.2 \text{ g/cm}^2$).

viewpoint of x-ray emission increasing because all electron part of the drive current comes to the x-ray converter.

Experiments on a sterilizing at the RS-20 generator show that the sterilizing which uses x-ray pulse radiation with the high peak dose rate is preferable and requires lower doses than a continuous irradiation does.

REFERENCES

1. G. Yonas A report at the Opening of 9th Int. Conf. on High Power Particle Beams BEAMS'92 Washington DC May 25-29, 1992 (Private communication).
2. G. I. Dolgachev, L. P. Zakatov, A. G. Ushakov, Sov. Journ.of Plasma Phys. "Fizika Plazmy", "Microsecond plasma curcuit breakers", vol.17(10), pp.1171-1183, Oct.1991.
3. V. M. Babykin, R. V. Chikin, Yu. P. Golovanov, Yu. I. Kovalev, G. I. Dolgachev, A. G. Ushakov, L.P.Zakatov Proc. of 9th Int. Conf. on High Power Particle Beams BEAMS'92 Washington DC May 25-29 1992, "Development of microsecond generators with plasma current interrupting switches in Kurchatov Institute of Atomic Energy. Frequency operation of generators", vol.1, p.517-523.
4. V. M. Babykin, L. P. Zakatov, G. I. Dolgachev, Yu. I. Kovalev, A. G. Ushakov, "Pulse voltage generator", Patent of the Russian Federation N 5040386.
5. V. M. Babykin, G. I. Dolgachev, L. P. Zakatov, A. G. Ushakov, "Electron accelerator", Patent of the Russian Federation N 5040387.
6. V. M. Babykin, G. I. Dolgachev, L. P. Zakatov, A. G. Ushakov, "Plasma opening switch", Patent of the Russian Federation N 5040385.

MEGAAMPER NANOSECOND CURRENT SWITCHING FROM EXTERNAL UNSTABLE LIGHT LINER TO INNER LOAD IN VACUUM ON "ANGARA-5-1"

A.N.Batunin, A.V.Branitsky, I.N.Frolov, E.V.Grabovsky,
D.V.Kuznetsov, A.G.Lisitsyn, S.F.Medovschikov, V.O.Mishensky,
S.L.Nedoseev, G.M.Olejnuk, P.V.Sasorov, V.P.Smirnov,
A.N.Starostin, S.V.Trofimov, G.S.Volkov, E.G.Utjugov,
S.V.Zakharov, M.V.Zurin.

Troitsk Institute of Innovation and Thermonuclear Investigations,
Troitsk, Moscow reg. Russia. *-Institute of Theoretical and
Experimental Physics, Moscow, Russia.

Introduction

We made some experiments on "Angara-5-1" (2-3 MA, 100 ns) [1], using low linear mass liner (10-40 mkg/cm) as a part of double Z-pinch. The low mass liner surrounded coaxially a cylindrical load of higher mass (100-200 mkg/cm). Current instability and poor compression of the low mass liner were specific features of that inhomogeneous Z-pinch. We registered ~0.5 TW pulse of soft X-ray radiation from inner load in the instability moment. We treat the effect as a Plasma Opening Switch (POS) process in external current shell of double pinch.

Schematic of an experimental devise

Schematic of target unit of the parallel double pinch is shown at Fig.1. It was proposed and investigated as a double liner scheme for inertial confinement fusion in [2]. In our experiments cathode nozzle could produce a low mass annular flux of Xe with linear mass $M_{lin} \approx 10-40$ mkg/cm, 2-3 cm diameter as an external shell. Microcellular foam inner loads (agar-agar, doped 20% KCl and 20% Mo) 200-300 mkg/cm of 1-3 mm diameter were situated at the axis of the nozzle between solid cathode and anode net, cathode-anode gap being of 1 cm. A current $I=2-3$ MA, after 100 ns passed through the double pinch in the experiment.

Visible light streak-camera was used with two slits- radial at the middle of the gap and axial, directed along pinch axis. X-ray streak - camera with radial slit and collimated X-ray filtered diodes (XRD) were used for soft X-ray time-resolved measurements. Time integrated X-ray spectrometer, X-ray pinhole cameras were used as well.

Experimental results

In our experiments low mass current shells became unstable at rather small compression ratios. Visible light streak pictures show radial and azimuthal splitting of lighting layers of current shell (Fig.2). The instability occurs in the beginning of current shell compression. Shell stops its radial movement and the inner foam load bursts into shining in 2-3 ns at this moment, axial slit indicates simultaneous lighting of whole length of the pinch. Some nanosecond later another wave of radiation passes in axial (from cathode to anode) direction through the pinch with

the velocity of $\sim 10^8$ cm/s. After that an axial inhomogeneity of its lighting occurs. XRD signals have two oscillating maximums: the former coincides with the beginning of foam load flash, the latter related to the total compression of Z-pinch (Fig.3). Time integrated pinhole camera shows nicely shaped, nonexpanded foam load and intensive X-ray radiation from the axis of the foam. This radiation has an axial inhomogeneity, and a fine tubular structure in some cases (Fig.4). Time- and space-integrated X-ray spectrum shows He- and H-like K and Cl lines as for 20%KCl doping, so for 20%KCl+20%Mo doping of the foam load. Ne-like Mo spectral lines are rather intensive as well. It allows to conclude that significant part of foam plasma has an electron temperature of ~ 1 keV.

Discussion

Two alternative explanations of the sharp X-ray pulse from inner load are possible:

1. The current instability generates an anomalous resistivity in external current shell and the POS process in the double pinch. In that case, the current of 1-2 MA could switch itself from external shell to inner foam load during some

nanosecond, giving more than 10^{14} A/s of dI/dt value, and producing the X-ray pulse as a result of current compression and heating of the inner load. A theory of anomalous resistivity of low density high current plasma, based on the Electron MHD [3,4], can explain POS effect in our case. The theory proposes a criterion of its validity as $v_e > v_A$, it is equivalent to

$$(\omega_{pi} \cdot a/c) \leq 1, \quad (1)$$

where v_e - electron current velocity, v_A - Alfven velocity, a - specific size of plasma, (for example, liner plasma length or thickness), c - light velocity, ω_{pi} - plasma ion frequency. This criterion is fulfilled for parameters of Z-pinches plasma in our experiments. So, as follows from [3], the anomalous conductivity σ_{eff} can be used to explain the POS process in our case:

$$\sigma_{eff} \sim \sigma_{spitzer} / (1 + \omega_{He} \tau_{ei})$$

The Hall parameter is $\omega_{He} \tau_{ei} \gg 1$ in our case. Current plasma erosion decreases plasma density as [3]:

$$n_e(t) = n_{eo}(t-t_A)^2/t_A^2, \quad t_A = a / v_A, \quad v_A = v_A(I, r, n_i, M_i)$$

Consequently, $n_e(t) \rightarrow 0$ and $\sigma_{eff} \rightarrow 0$ at $t \rightarrow t_A$ and POS process happens at $t = t_A$. For fixed current $I = 1-3$ MA and liner parameters given, $t_A \sim 60-20$ ns.

A criterion of other instability, the ion sound instability,

$v_e > C_s$, can be fulfilled for rather wide band of parameters of the external current shell as for this experiment, so for the experiment [2], using greater linear mass. Here C_s is an ion sound velocity. The condition $v_e > C_s$ can be re-written as

$$I_{[MA]} > I_{cr} \sim 1.4 \cdot 10^5 (Z_i/M_i)^{3/2} T_e^{1/2} M_{lin}[g/cm^2]$$

For $I = 2$ MA, $M_{lin} = 180$ mkg/cm², $T_e = 50$ eV it is valid, if $Z_i < 5$.

2. An alternative proposal, based on radiative MHD simulations [5], explains the experimental data as a result of fast shock wave generation in Xe shell. Really, in a current shell plasma with multicharged ions, a thermal pressure is small comparing with magnetic pressure due to radiative losses. An intensive shock wave, generated by the current shell in a fading inner profile of annular external gas, accelerates ions to the velocity, greater then implosion velocity of current shell. The ions can have rather high energy in comparison with plasma temperature. For example, Xe ion with velocity $v_i = 5 \cdot 10^7$ cm/s has kinetic energy 150 keV, the thermal ion energy being only 30-50 eV. This ion flux can deliver its energy to inner load earlier the moment of current shell compression, being responsible at least for the former maximum of X-ray radiation.

We are reluctant to insist strongly on the POS process, because we have not direct measurements of a current in the inner load now. But some indirect witness of current effects in the foam load, as an inhomogeneous radiation of foam plasma at the axis, "hot spots", which are usual for high current dense Z-pinches, allows as to prefer POS process to explain experimental results.

References

1. E.V.Grabovsky, S.L.Nedoseev, et.al. "Angara-5-1" pulsed power system for ICF-experiments //Proc.of the 7-th International Conf. on High-Power Particle Beams/ Jul.1988, Karlsruhe,FRG/ EC-5/p.331.
2. V.P.Smirnov, E.V.Grabovsky, V.I.Zaitsev, S.V.Zakharov, S.L.Nedoseev, V.Ia.Tsarfin, I.R.Yampolsky Progress in investigation on a dense plasma compression on "Angara-5-1" /Proc.of the Eight International Conf. on High-Power Particle Beams/ July 2-5 1990, Novosibirsk,USSR/ p.p.61-78..
3. П.В.Сасоров, "К теории плазменных размыкателей", ПЖЭТФ, 1992, 56, 614-617.
4. L.I.Rudakov, "Stability of plasma shell, accelerated by magnetic field". Proc. of 2-nd Intern Conf.on Dense Z-Pinches, Laguna- Beach, USA, 1989,p.p.290-299.
5. В.А.Гасилов, С.Ф.Григорьев, С.В.Захаров. "Динамика магнитного сжатия газовых струй". Препринт ИАЭ, 4767/6, 1989.

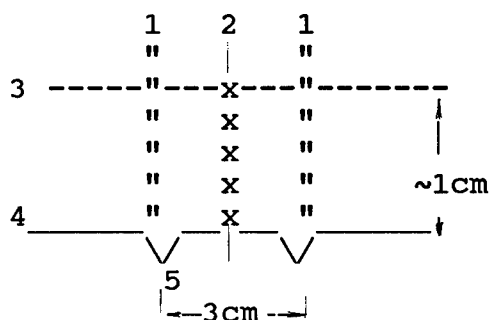


Fig.1
Schematic of target unit of
double Z-pinch
1-external gas shell, 2-inner
foam load, 3-anode grid, 4-ca-
thode, 5-gas nozzle

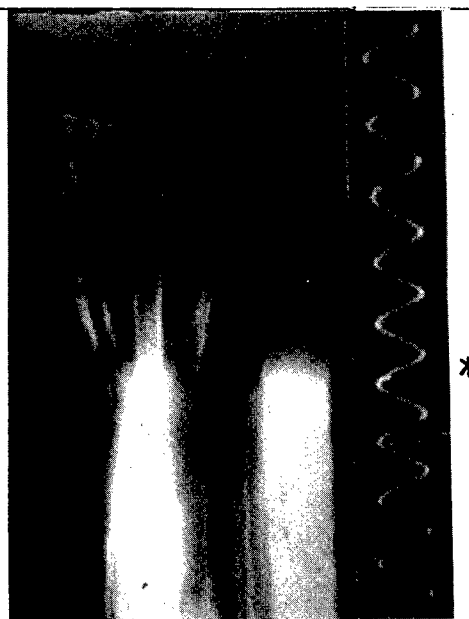


Fig.2 Visible light streak pic-
tures; a-horizontal slit, b-ver-
tical slit, $f=100\text{MHz}$, *-POS moment

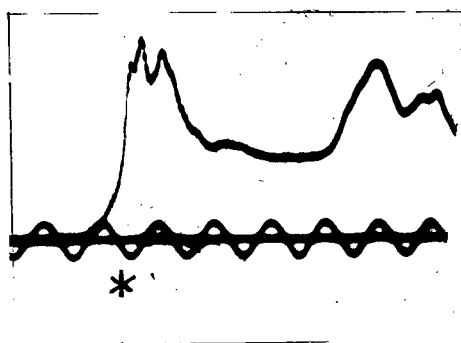


Fig.3
Soft X-ray detector
signal
 $f=100\text{ MHz}$, *-POS moment

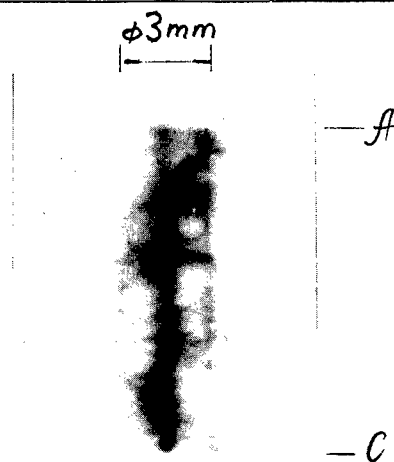


Fig.4
Inner foam load soft X-ray
image (time integrated)

High current electron switch with deep compensation of volume charge

A.B.Bogoslovskaya, K.N.Ulyanov

All-Russian Electrotechnical Institute, Moscow, Russia

ABSTRACT

The current switching by means of a gas-filled electron switch has been studied experimentally and theoretically. Under deep volume charge compensation conditions the switch showed complete controllability. The switched current density was more than current density of a similar vacuum switch by an order.

1.INTRODUCTION

One of the main problems in the field of the high-current electron switch development is the problem of current density increasing. A method of current density increase by the partial ion compensation of electron volume charge is known, for example, by ion beam from the plasma anode. In this case current density increases, however, its value order doesn't change. Earlier¹ the method by an electron beam of deep charge compensation with the help of ions generated a special bled gas of low density was proposed. In this case electron and ion volume charge distribution are similar, an extremely deep compensation, the increasing current density in diode by one-two order in plasma-less mode takes place.

2.EXPERIMENTAL AND CALCULATION RESULTS

This work is dedicated to studying of current switching with the help of an electron gas-filled triode. The experiments were carried out with using of the model with plane geometry of the electrodes, the current density of Ba-Ni cathode being limited by 3 A/cm². The accelerating electrode was a grid with high transparency placed at a distance of 1.4 cm from the cathode, the distance between the grid and the anode was equal to 1.1 cm. A constant voltage was applied to the anode and was regulated from 0 to 10 kV. The triode turned off when a negative voltage relative to cathode had been applied to the grid. When a positive rectangular voltage pulse (front time less than 10⁻⁷ s) had been applied to the grid the triode was turned on. The amplitude of the voltage pulse was smoothly regulated from 0 to 10 kV, the voltage pulse time was changed from 1 to 20 mks. During the experiments air was pumped out from the switch down to 10⁻⁶ Torr. Then the switch was filled with argon up to a necessary pressure. The cathode, grid and anode pulse currents were measured. The experiments showed the switching possibility and its complete controllability in plasma-less conditions. In this

case the current pulse had a rectangular form, front and fall times were equal to the voltage pulse (less than 10^{-7} s). The experiments were carried out under different pressures and different grid and anode potentials. In case when plasma had been generated unstable conditions appeared and the current increase sharply. For the experiment results could be explained we calculated the potential, electric field strength, volume charge and current density distribution under different pressures and grid and anode potentials using the method². The triode potential distribution is described by the equation:

$$\left(\frac{dy}{dt}\right)^2 = A + B - 1 + \sqrt{y} + \gamma_1 \int_{\max(y, y_1)}^1 \frac{\sigma(y')\sqrt{y'-y}}{dy'/dt} dy' \quad (1)$$

$$y = \frac{U}{U_2}, \quad y_1 = \frac{U_1}{eU_2}, \quad Z = \frac{x}{x_2}, \quad t = \frac{4}{3} K^{1/2} Z, \quad \gamma_1 = \frac{3}{4} K^{-1/2} \left(\frac{m_i}{m_e}\right)^{1/2} n_0 \sigma_m x_2,$$

$$K = \frac{9\pi j_e x_2^2 m_e^{1/2}}{(2e)^{1/2} U_2^{3/2}}, \quad A = (y'_{t_2})^2, \quad B = (y'_{-0})^2 - (y'_{+0})^2.$$

The boundary conditions are used for the equation as follows: the cathode potential is equal to 0 in x_1 point, the grid potential is equal to U_1 in 0 point, the anode potential is equal to U_2 in x_2 point. Due to the high transparency of the grid almost all ions being generated in the grid-anode space found themselves in the cathode-grid space. The equation (1) was solved as follows. The value of the electron current density and K corresponding to it were set with set up values of the electrode coordinates, potentials and gas density. Then beginning from the anode the equation (1) was solved for the different values of the anode electric field (the parameter A). Then the value of the parameter K' corresponding to the set value of A was calculated². The solution of the equation $K'(A)=K$ defines the A value corresponding to the gas density set value. The equation (1) was solved for this A value and the potential, electric field and volume charge distribution in the grid-anode space was calculated. The calculations for the different values of j_e allowed defining the maximum value of j_e . The grid electric field is equal to 0, the value of j_e is maximum. The plasma was generated near the grid after the current density had reached the high values. The anode boundary of the plasma was unstable, and a stationary state was impossible. The equation (1) was solved in the cathode-grid space after the parameters in the grid-anode space calculated (dependence $A(K)$ definition). The boundary condition $U(x_1)=0$ was realized by selection of the B parameter. In that way the dependence $B(K)$ for the first gap was defined. A maximum possible value of the current density was defined by calculation for each n_0 value (the electric field is equal to 0). At high current densities the stable current through the first gap is impossible because in this case plasma

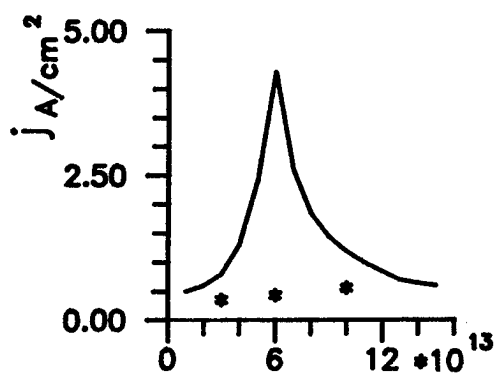


Fig.1 Dependence $j_{lim}(n_0)$ for $U_1=5\text{kV}, U_2=7\text{kV}$

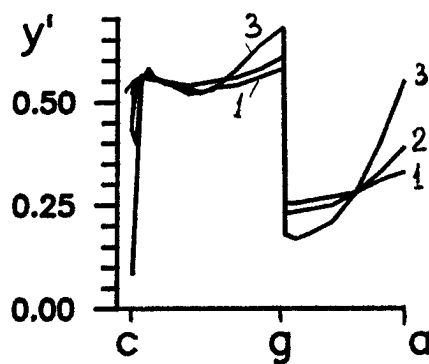


Fig.2 Dependence $y'(z)$: $n_0=5 \times 10^{13} \text{ cm}^{-3}$, $j: 0.5 \text{ A/cm}^2$ (1), 1 A/cm^2 (2), 2.4 A/cm^2 (3).

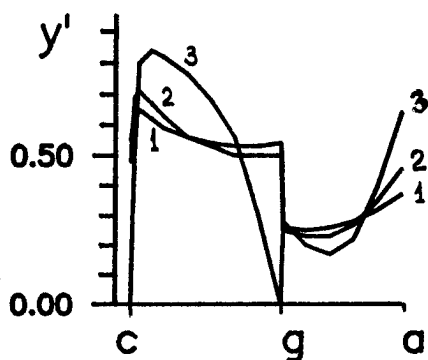


Fig.3 Dependence $y'(z)$: $n_0=6 \times 10^{13} \text{ cm}^{-3}$, $j: 1 \text{ A/cm}^2$ (1), 2 A/cm^2 (2), 4.3 A/cm^2 (3).

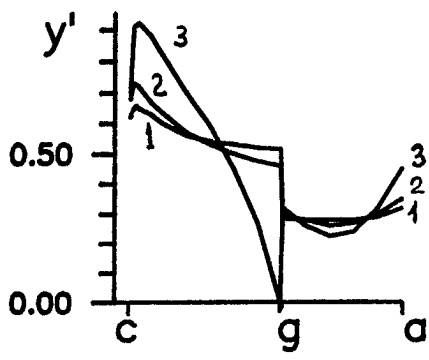


Fig.4 Dependence $y'(z)$: $n_0=7 \times 10^{13} \text{ cm}^{-3}$, $j: 0.5 \text{ A/cm}^2$ (1), 1 A/cm^2 (2), 2.6 A/cm^2 (3).

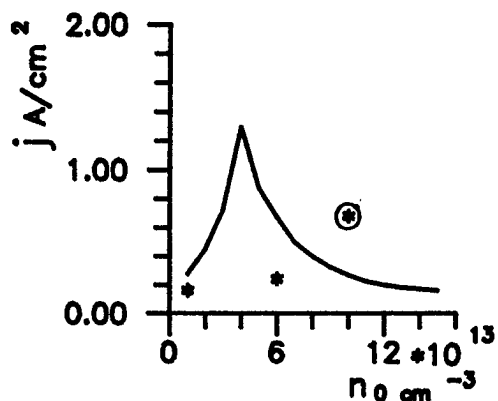


Fig.5 Dependence $j_{lim}(n_0)$ for $U_1=3\text{kV}, U_2=5\text{kV}$.

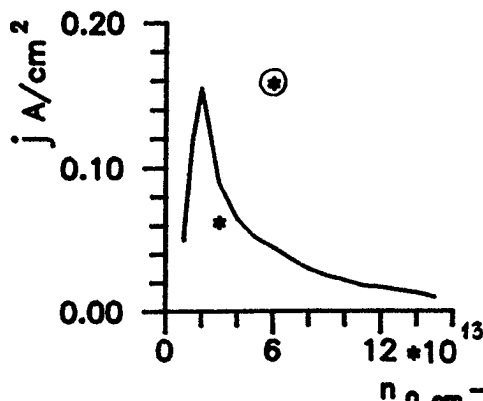


Fig.6 Dependence $j_{lim}(n_0)$ for $U_1=1\text{kV}, U_2=3\text{kV}$.

through the grid penetrates into the second gap. Fig.1-6 show the calculation results of three pairs of different values of the grid and anode potentials. The size of the first gap defines stable conditions of the experiments. In Fig.1 the limit current calculation results at the $U_1=5$ kV and $U_2=7$ kV effected by n_0 are presented. The maximum value of the limit current density takes place when n_0 is equal to $6 \cdot 10^{13} \text{ cm}^{-3}$. The dependence of the limit current density upon n_0 is increased when $n_0 < n_0^*$. This dependence is decreased when $n_0 > n_0^*$. The space charge at the cathode limit the current. This limitation defines the limit current density for $n_0 < n_0^*$. The limitation for $n_0 > n_0^*$ is defined by the zero electric field at the grid. In the curve maximum the electric field is equal to 0 both at the cathode and the grid in the first gap. Fig.2-4 represent the distributions of the electric fields in the first and the second gaps for the different value of the current density and the values of n_0 corresponded to the left branch ($5 \cdot 10^{13} \text{ cm}^{-3}$), to the maximum ($6 \cdot 10^{13} \text{ cm}^{-3}$) and to the right branch ($7 \cdot 10^{13} \text{ cm}^{-3}$). The increase of the j_e accompanied by the decrease of the electric field at the cathode is shown on the left branch (Fig.2), the electric field is equal to 0 for the limit current density (Fig.1). Fig.3 ($n_0=n_0^*$) shows the increase of j_e accompanied by the decrease of the electric fields at the cathode and the grid. The electric fields are equal to 0 for the limit value of j_e . This limit value of j_e is more than the same one for the analogous vacuum gap by an order. The distributions of the electric field for $n_0 > n_0^*$ are represented in Fig.4. The electric field becomes equal to at the grid when the current density has increased. the increase of n_0 is accompanied by the decrease of the limit current density. It's bound with that fact that the greater value of n_0 is corresponded to the dreater value of the volume charge, and the electric field becomes equal to 0 for the less value of j_e . The calculation results of the limit states for $U_1=3$ kV and $U_2=5$ kV are represented in Fig.5. Fig.6 shows the same results for $U_1=1$ kV and $U_2=3$ kV. Fig.1,5,6 represent also the experimental points for the stable * and the unstable ⊙ currets. This points were obtained for the different values of n_0 . The theoretical and experimental facts coincide: the stable poits get to the stable space, the unstable ones get to the unstable space. This cycle of theoretical and experimental works allows to optimize the electron-optic system and the work states of the gas-filled electron switches. One can forecast the limit parameters of such switches: the current - 10-30 kA, the accelerating voltage - 10-20 kV, the switched voltage - hundreds of kV, the current edges - $(2-8) \cdot 10^{-8} \text{ s}$.

3. REFERENCES

1. N.I.Korobova, L.P.Menahin, I.O.Sibiryak, K.N.Ulyanov, "Compensation space charge in gas-filled diode," Radioengineering and Electronics, v.28, pp.599-605, 1983.
2. A.B.Bogoslovskaya, K.N. Ulyanov, "Calculation of the parameters of the electron-optical systems of gas-filled triod taking into account gas ionization in the gap," Radioengineering and Electronics, v,34, N.4, pp.859-864, 1989.

Simulation of the MAG II generator.

Vladimir Bulan, Vladimir Zajivikhin, Bernar Etlicher*

TRINITI, Troitsk, Moscow region, 142092, Russia;

*Ecole Polytechnique, Laboratoire de Physique de Mileux, Palaiseau, F-91128, France

Abstract

In this report the results of the optimization of the multi-module mcs-scale PEOS-based generator parameter's are presented. The PEOS parameters influence on the energy transfer efficiency was studied, the PEOS being considered as the part of the magnetically self-insulated line.

1. Introduction.

The generator consists of the Marx bank, magnetically insulated lines (MITL) with plasma erosion opening switch (PEOS) and fast liner load. To obtain the requirements on general parameter's of the system the simple lumped element's circuit model was used. It was shown that to optimize output parameter's of generator it is important to define relation of inductance's of system before and after the PEOS. To define these values in a real system and to obtain the current density distribution in transition lines the 2D Laplace task was solved.. Those data was used to check the magnetic insulation conditions in the PEOS area and downstream of it. The simulation model for PEOS and MITL are presented. As the source of parameters the specification of the MAG II facility were used, which is under construction in Ecole Polytechnique.

2. Lumped element's model with magnetic flux conservation.

The model do not take into account wave processes in transmission lines, electron and ion leakage currents. The currents and voltage are linked by means of Kirhgoff equation and liner motion is described in terms of the 0D approximation. The PEOS is considered as lumped time-varying resistance. It is supposed that PEOS resistance is zero up to the moment of opening stage, then linearly grows to some value, and, then, remains constant. The system considered consists of K(8) parallel modules connected to one common load (liner). The values for inductance's, capacitance's and currents are presented per one module..

However, even in such simple model the system characteristics depend on a too large set of parameters. Subsequent

system simplification can be achieved under the following assumptions. The inductance is initially filled with current I_0 . The PEOS is represented by very large resistance. Then magnetic flux conservation takes place and liner motion equation has the integral of energy (see eq. (1)). This model can be close to real case while liner impedance is smaller than PEOS resistance.

$$L_1 \cdot I_0 = (L_1 + L_2 + 2K (\mu_0 H / 4\pi) \cdot \ln(r_0/r)) \cdot I$$

$$(Mu^2/2 + E_0 \alpha_1 / (1 + \alpha_2 \xi)) = \text{Const} \quad (1);$$

Here: I - current flowing through liner, r , r_0 , M , H - liner radius, initial radius, mass and height, μ_0 - $4\pi \cdot 10^{-7}$ H/m, u - liner velocity, E_0 - energy saved in generator and

$$\alpha_1 = L_1 / (L_1 + L_2);$$

$$\alpha_2 = 2 (\mu_0 H / 4\pi) / (L_1 + L_2);$$

$$\xi = \ln(r_0/r)$$

The efficiency ϵ can be derived from (1) as

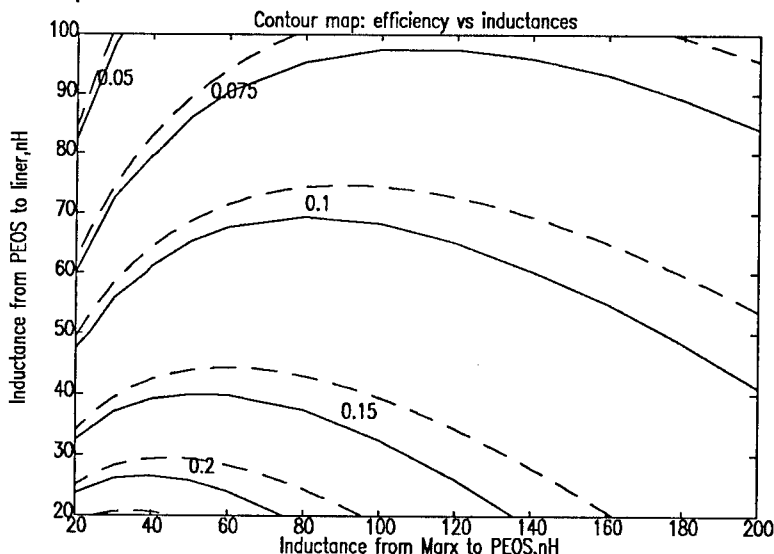


Fig.1. The contour map: efficiency versus inductance's "before" and "after" PEOS. Solid lines are for "real" system (capacitance + PEOS + ...). Dashed lines are for the system with magnetic flux conservation

$$\varepsilon = \alpha 1 \cdot \frac{\alpha 2 \cdot \xi \cdot K}{1 + \alpha 2 \cdot \xi \cdot K} \quad (2)$$

The results of the calculations on full lumped-circuit model ($C_{\text{Marx}}=2830 \text{ nF}$) are presented in fig.1 as a contour diagram (solid lines). The levels shown are the levels of constant efficiency. At the same figure the results of analytical calculations on (2) are presented as dashed lines levels.

The results demonstrate the existence of optimum value for inductance L_1 , provided the value L_2 is defined. This maximum can be found from (2): $\varepsilon_{\text{opt}} = \eta / (1 + \sqrt{1 + \eta})^2$; $(L_2/L_1)_{\text{opt}} = 1/\sqrt{1 + \eta}$

$\eta = 2 \frac{\mu_0 H}{4\pi L_2} \xi K$ In the working range the change in L_1 may give some rise in efficiency: about 1% of overall energy. If we do not change the system configuration (number of modules and so on), the maximal efficiency increase can be achieved by reducing of L_2 value - the value of inductance from PEOS to liner. However, it will not be sufficient: with constant L_1 , this increase will be partially counterbalanced by drift from optimum value of L_2/L_1

3. THE INDUCTANCE'S EVALUATION.

The inductance's of the system are the sum of three almost independent parts: Marx and oil-vacuum interface inductance, MITL inductance, central unit inductance. The Marx and oil-vacuum interface inductance can not be changed. The central unit inductance is defined by the liner geometrical parameters and, perhaps, the requirements of liner visualization. To increase the efficiency, it is necessary to diminish the value of "after PEOS" inductance. The reducing of overall MITL inductance may be of use too.

To calculate the inductance's of line we have used a simple model, that give possibility to use the decision of 2D plain Laplace task. The equations do not contain sources and 1-st order members. Such a model supposes that the gap is small in comparison with the other dimensions of line and that the gap is constant along the line. However, the decision can be expanded to the lines with varying gap. The decision will be accurate if the level of constant gap follows the levels of constant magnetic flux. To solve the Laplace task two methods were used: "complex boundary elements" method¹ and "finite element method".

The complex boundary elements method was used to find the values of the inductances and to roughly estimate the

fields in the lines. The finite element method was used to obtain the detailed picture of current and flux distribution. In the case of varying gap, the inductance is recalculated. The area enclosed between two levels of magnetic flux was prescribed to some average constant gap.

The local magnetic field needed for the magnetic self-insulation (SMI) calculations is defined by the local current density.

The typical results and boundary conditions definition are presented in fig. 2.

The 2D field distribution was used to calculate inductances and to obtain the parameters for evaluation of the SMI conditions at the PEOS area and downstream of that area. The voltage at the upstream region is small, so the SMI conditions are not violated. The form of MITL should satisfy insulation requirements, minimize "after PEOS" inductance and matches the size of PEOS area. The optimized geometry

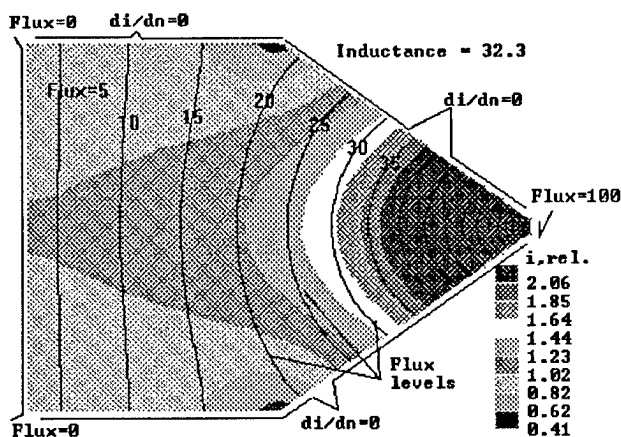


Fig. 2. Example of flux and current density distribution. The width of line is 80 cm, the length of line is 80 cm. The levels of current density are shown as gray areas of different intensity. The relative values of current density: the value divided by I/h , where I - current in line, h - line width.

differs from the shown at the Fig.2. One of the reasons to reject it, is the difficulties for observation of processes in the central unit.

For the "acceptable" case, the minimal central unit inductance (from entry size of 3 cm) was estimated as 15-25 nH per one line. The overall minimal "after PEOS" inductance is more than 50 nH for 1 cm gap and close to 30 nH for 0.5 cm gap.

If the "after" PEOS inductance will be made 30 nH, it can be of use to reduce inductance between Marx and PEOS. According to results of Section 1 the transfer energy efficiency will be 15-17% in that case.

4. NUMERICAL MODEL OF THE LINE WITH MAGNETIC INSULATION AND PEOS

The voltage pulse is delivered to the load in pulsed power systems by MITL. Efficiency of transport is defined by both MITL geometry and the load. If the load impedance R is greater than $U/I_{cr}(U)$ (U -line voltage, $I_{cr}(U)$ -current, ensuring SMI² then electron flow across MITL gap is absent and energy losses are due to impedance mismatch. In opposite case, the electron losses occur in MITL. They are localized near the load and near the non-uniformity line region and can substantially decrease the energy transmission efficiency. Usually minimum current $I_m(U)$ (calculated for Brillouin flows) is adopted as a critical current I_{cr} . This current is close to that of ensuring the line energy minimum. Liner is the time-varying load. The voltage at the MITL entry is a function of time too. As a result, the analytical description of process in MITL is impossible. To calculate the output parameters of the system the one dimensional model was used^{3,4}. In this model the wave processes in MITL were described by telegraph equations with nonlinear electron leakage current $J(U, I)$. The voltage pulse $U(t)$ is applied from the Marx generator with capacitance C_m and inductance L_m to each MITL through the interface with inductance L_p , the capacitance being charged to. The entry MITL circuit is described by Kirghoff equations (see Sec.1). The outputs of each MITL is connected to the central unit of inductance L_c with liner. To describe liner motion OD-model was used.

The MITL model permits incorporation of the PEOS to numerical code. The PEOS is considered as some nonlinear element with varying in time impedance (wave and active) and is represented as part of the MITL with its own wave impedance and leakage current J_s , differed from those of regular MITL. To determine J_s and R_s the erosion model⁵ and the expressions for minimum SMI current and ion current density obtained in the framework of Brillouin model in⁶ was used. There is no any adequate physical model describing conduction phase consistently but as was revealed by Zakatov⁷ on the base of experimental data (obtained on different facilities) analysis, the charge value flowing through the PEOS unit length during conduction phase ranges between 0.1 and 0.5 C/m. It is the charge per unit PEOS length, we chose as a parameter of the transition to the opening stage.

5. NUMERICAL SYSTEM SIMULATION FOR EXPERIMENTAL CONDITIONS.

In all calculations it has been assumed that generator consisted of 8 separate modules connected in parallel to liner load. Each module contained Marx (capacitance 2823 nF (C_m), charge voltage 120 kV(U_m), inductance 40 nH(L_m)), and vacuum strip line. The inductance of transition from Marx to MITL was 15 nH(L_p). The MITL geometry choice is based on the results obtained in Sec.3 and was chosen to avoid the MITL domains with reduced magnetic field. It has been approximated in calculations as follows. The MITL width W_g has been linearly decreased from 80 to 40 cm at the entry section from insulator surface to PEOS location, and gap D has been remained constant and equalled to 3 cm. The region with length 9 cm (l_p) occupied by PEOS has been followed. Then the transition of 3 cm length to gap of 2 cm has been located. Further MITL width and gap linearly have been decreased down to 3 cm(W_l) and 0.5 cm (D_{acl}). Each module MITL has been connected with liner by means of convolution section. The convolution and initial liner inductance have added up to 4 nH or 32 nH per one module. So, the one module inductance before PEOS, L_1 , has been 84 nH(L_1), and after PEOS inductance (including central unit) 51.8 nH(L_2). The beginning of the opening has been defined by charge value Q_{cr} (0.4 C/m), which was carried through PEOS length unit. In the following runs, the liner parameters have been put equal to $H = 1$ cm, $r_0 = 1$ cm, $m = 0.26$ mg. Plasma density n_p , width of the PEOS, the value of the gaps D_{acg} and D_{acl} , values of the critical charge Q_{cr} , generator and PEOS jitter have been varied during simulation.

Before discussing the result, note, that as was shown by calculations, the losses connected with electron leakage in MITL are small outside the PEOS because the MITL current significantly exceeds minimum MITL current I_m . Such result confirms the validity of utilization of the model in Sec.2. However it is necessary to take into account phenomena of SMI when the PEOS operation and its interaction with other system parts are considered. The density of plasma injected into interelectrode gap is one of the main parameters, determining PEOS behavior. The energy transmitted to the liner is decreased with PEOS plasma density current is greater than the minimal current of SMI I_m , then electrons in PEOS would

be magnetized; leakage current through PEOS would be small and PEOS - opened. In opposite case PEOS current will be equaled the minimal one, and only $U(I_m)/R_l$ will be delivered to the load. These two regimes were called load and switch limited one in⁸. Thus minimal current of SMI in PEOS is important parameter determining system behavior. It is inversely proportional D_s thickness of the vacuum gap in PEOS and growth. This is caused by the influence of the load on PEOS operation^{8,9}. As was noted at the beginning of Sec.4, if the load directly proportional W_s , plasma will occupy region width. The more D_s , the smaller minimal current, and as the result, the better condition for switching. Calculations made confirm the qualitative picture drawing above. The plasma density was the parameter which defines D_s value. Kinetic liner energy E_k and final value of the PEOS resistance R_s and thickness D_s dependence on plasma density are represented in Fig 3a,b. For smaller densities, E_k and R_s at $W_s=40\text{cm}$ have no considerable change (solid curve in Fig 3 a). For $n_p > 2 \cdot 10^{15} \text{ cm}^{-3}$ abrupt drop is observed. The explanation of such a behavior is that PEOS is magnetized at this n_p and output characteristic are defined by load rather than PEOS. When transition from magnetized to uninsulated state takes place (point of inflection at R_s , E_k dependencies on n_p). PEOS is partially closed and the portion of current delivered to the load depends on D_s and, hence, on plasma density.

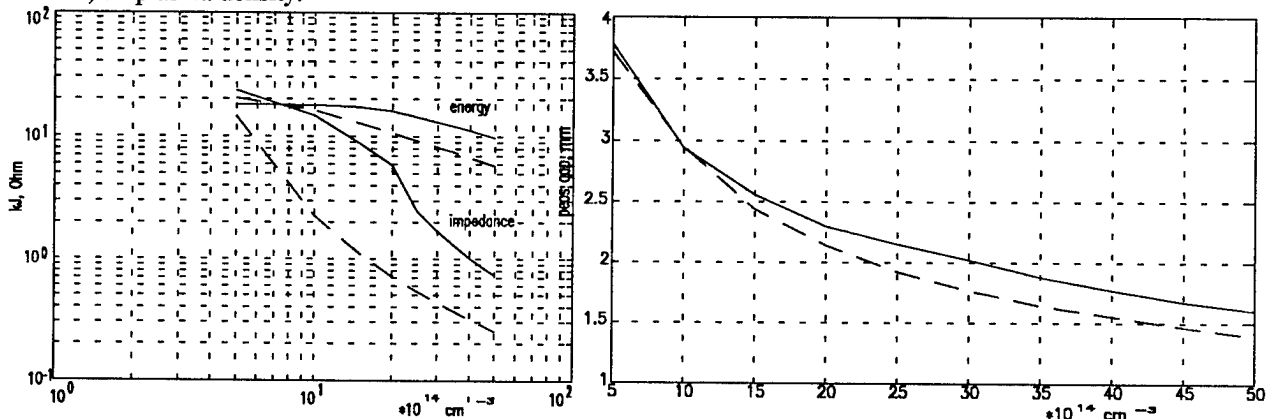


Fig. 3. Liner kinetic energy, PEOS impedance (a), PEOS gap thickness (b) as a function of plasma density, for two value of PEOS width W_s , dashed line- $W_s=60 \text{ cm}$, solid line - $W_s=40 \text{ cm}$.

So, the gap $D_s \sim 2.5 \text{ mm}$ is a critical one for appearance of SMI. Note, that parameters of the PEOS under investigation are close to those for HAWK accelerator⁸. Both simulation and experiment give approximately the same value for the thickness $D_s \sim 2-2.5 \text{ mm}$. As can see from fig.3 increase in $W_s=60 \text{ cm}$ decreases liner kinetic energy as large as twice. To analyze the dependence of output parameters on short circuit current of PEOS the value of the critical charge Q_{cr} have been ranged in value from 0.1 to 0.6 C/m. The corresponding value of the switching current lay between 326 and 663 kA. For reasonable range of value Q_{cr} , the difference in liner kinetic energy does not exceed 10%.

As has been shown by the calculations jitter of generator switching on leads to reducing liner kinetic energy on 25% for jitter $\Delta T=25 \text{ ns}$ and 50% for $\Delta T=50 \text{ ns}$. Such abrupt decrease is connected with PEOS behavior in delayed modules. PEOS in system under consideration is the space where zero magnetic field point is occurred⁹, because wave impedance is minimal here and PEOS have been remained in closed state owing to absence of electron flow insulation. The value of the PEOS resistance has not exceeded 0.5 Ohm, while for zero jitter it has been equaled to 5 Ohm with the same PEOS plasma density. In other set of calculation PEOS jitter has been analyzed. The modules have been divided to two groups. They have been differed by the value of the critical charge. We have put $Q_{cr} = 0.3(0.2) \text{ C/m}$ in one group and $Q_{cr} = 0.4 \text{ C/m}$ in another one with jitter equal to 0.1(0.05) C/m the corresponding liner kinetic energy decrease has not been exceeded 30%(50%).

REFERENCES.

1. T.Hromadka II, C.Lai. The complex variable boundary element method in engineering analysis. Springer-Verlag, NY., 1987.
2. L.I.Rudakov, et. al. Generation and focusing of the high current REB's. M., Energoatomizdat., 1990. (Rus)
3. V.V. Bulan, et. al. Thesis of the 6th All-union symposium on high current electronics, v.2, p.183, Tomsk, 1986 (Rus.)
4. V.V. Bulan, V.V. Zajivikhin. Proc. 8 Int. Con. on High Power Particle Beams. v.2, p.990-995. 1990, Novosibirsk, USSR
5. P.F. Ottinger, S.A. Goldstain, R.A. Meger, J. Appl. Phys. vol. 53, pp. 774-784, 1984.
6. L.E. Aranchuck, et. al. Journal of the Technical Physics, 1989, v. 59, n. 2, pp. 142-151. (Rus.)
7. G.I. Dolgachev, L.I. Zakatov, A.G. Ushakov, Physika Plasm, v. 17, n 7., pp. 1171-1182. (Rus..)
8. R.J. Comisso et. al., Phys. Fluids B vol. 4, pp. 2368-2376.
9. V.V. Zajivikhin. Proc. 9 Intl. Conf. on High Power Particle Beams. vol. 1, pp. 592-597, 1992, Washington, US

Vacuum state estimation of vacuum circuit breakers

G.C. Damstra^{1,2}, R.P.P. Smeets², H.B.F. Poulussen²

¹ N.V. KEMA, Arnhem, the Netherlands

² Eindhoven University of Technology, Fac. of Elec. Eng., Eindhoven, the Netherlands

ABSTRACT

The vacuum state of vacuum switching elements after production is checked normally by Penning- or Magnetron methods (combined electrical and magnetic field). Vacuum in the range of 10^{-1} - 10^{-4} Pa can be measured in this way. After assembly into circuit breakers however, these methods are not applicable. HF interruption performance during making operation has been proposed earlier as a possible alternative. Further investigations show that differences in the number of HF prestrike current loops can be found in the pressure range of 10^{-1} - 10^{-5} Pa. Current chopping of DC arcs between 5 and 30 A during opening operation, may be another option for determination of the pressure range by measuring the lifetime of the arc, but the resolution in the vacuum range below 10^{-1} Pa is too poor.

1. INTRODUCTION

Vacuum circuit breakers, load switches and contactors have been introduced in MV distribution and industrial applications during more than a quarter of a century. The experiences are very good and the absence of means to verify the status of the vacuum has never got great priority. The manufacturers have improved the vacuum soldering techniques and the choice of material to such a level of quality that long lifetimes are guaranteed. Production tests after assembly are made in the factory by Penning or Magnetron methods. Voltages up to 5 kV and magnetic fields up to 0.1 T are applied simultaneously. The ion current between contacts or between contacts and screen is a measure for the vacuum but the value is design-dependent. After a period of storage by the manufacturer the tests are repeated and vacuum tubes with increased ion currents are rejected. These methods are not useful for utilities because the vacuum tubes have to be disassembled from the switchgear with all the risks of improper remounting. Although the lifetime of modern vacuum tubes is estimated as more than twenty years, failures of early interrupters can not be excluded completely. For industrial application after a large number of operations, inleak may occur by fatigue of the metal bellows. But also in distribution application with negligible number of operations the vacuum quality may be reduced by long term diffusion, intercrystalline corrosion or deactivation of the getter material. Hence it would be very practical to have on site tests methods for vacuum interrupters of earlier year of production.

2. DIELECTRIC TESTS

Most utilities have AC and DC testing equipment for test voltages up to 30-50 kV. Hence it is quite evident that these methods have been also used for tests on vacuum switchgear. Unfortunately the voltage withstand in vacuum is already at maximum from 1 Pa and below. Tubes with a vacuum from 1 - 10^{-5} Pa (atmospheric pressure) can be selected by applying a test voltage. In case the tubes are mounted in SF₆ (GIS) they will be filled with SF₆ and the voltage withstand is high and not sufficient differences between good and bad tubes will be found.

There also exists commercial testing equipment for good-bad selection of vacuum tubes using AC or DC supply, with the same limitations. We have tried to improve the sensitivity of the AC method by measuring the DC component of the emission current from the low voltage contact. This work was a continuation of earlier work on Fowler-Nordheim measurements [1]. In an experimental tube on a pumped system we found at a pressure 10^{-1} Pa an emission current of 30 nA decreasing to less than 5 nA at 10^{-2} Pa under an AC voltage of 25 kV_{RMS}. At the same time also the DC potential of the shield electrode of the vacuum tubes has been measured by a 10.000 MΩ Brandenburg HVDC meter (20 kV range). A remarkable effect occurred, just between 0.1 - 1 Pa shield potentials up to 1 kV have been found. The physical explanation of those effects needs further research. Tests on vacuum tubes of

different manufacturers have to be made also.

It is important that the structure of the switchgear is discharge-free up to the maximum test voltage, otherwise the results will be influenced by external discharges.

3. HIGH-FREQUENCY INTERRUPTION PERFORMANCE

The status of the vacuum in the tube can be determined in principle by interruption tests at suitable current levels. At network frequency and voltage this approach is less practical by the high KVA demand of the supply circuit.

Proposals have been made to use the HF interrupting performance as an indicator for the pressure [2]. The advantages of this testing method is that relatively high di/dt and du/dt can be obtained by relatively compact capacitive storage. The frequency of the discharge current is given by the capacitance and inductance of the circuit, the steepness of the recovery voltage by an RC network. Tests have been performed at high frequencies (250 kHz, 15 kV, 200 A) and medium frequencies (16 kHz, 25 kV, 800 A) during making operation of the contact system. A typical oscillogram of such an operation is shown in fig. 1. The number of pre-ignition current loops (of the first reignition wavetrain) as well as the time between first reignition and contact touch (pre-ignition time) has been measured (see fig. 2) at varying pressure. This time varies between 0.2 - 2 ms.

The sensitivity of the hf-current interruption performance for changes in pressure was measured in two ways:

1. By evacuating a demountable laboratory interrupter in an oil-free vacuum system until 10^{-5} Pa (after baking out and arc conditioning) and allowing a controlled leak of air through a precision valve increasing the pressure 10 times every measuring sequence until 1 Pa;
2. By evacuation of a commercial interrupter with a diffusion and turbo-molecular pump, and arc conditioning at the lowest possible pressure.

Both methods did not show a significant difference in interrupting performance with respect to high frequency current in the pressure range 10^{-5} - 10^{-1} Pa.

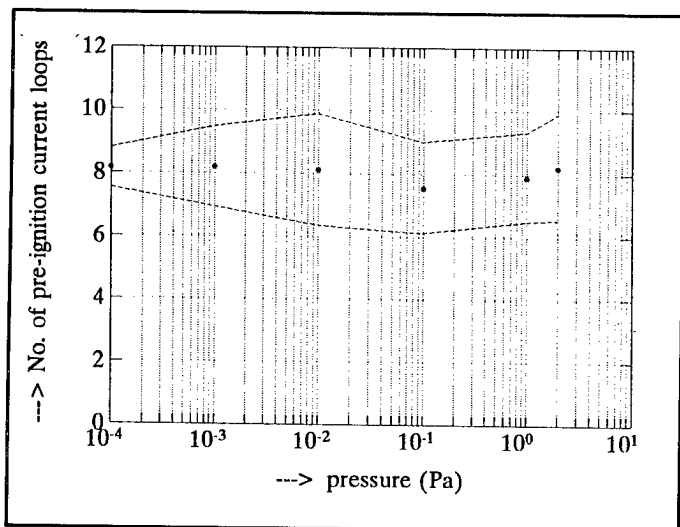


Fig. 2: Number of pre-ignition current loops vs. pressure

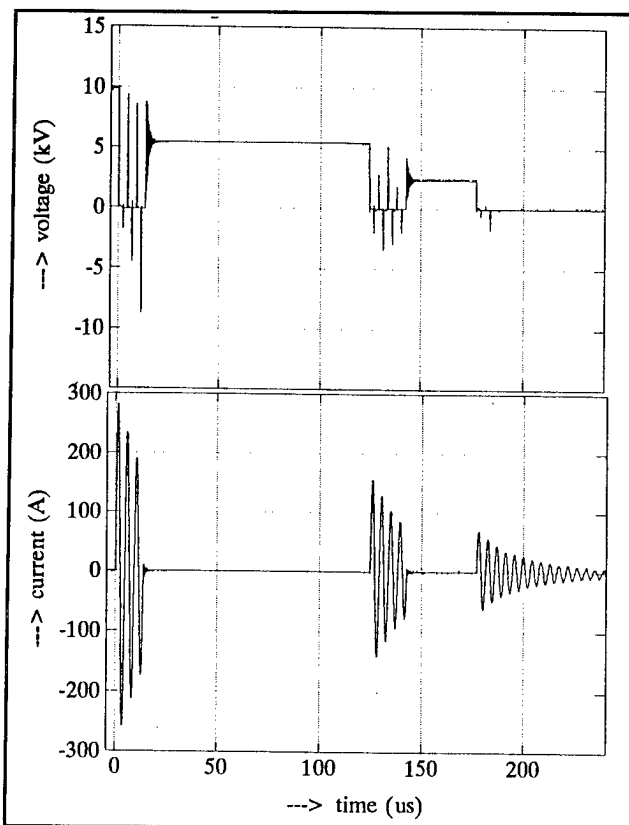


Fig. 1: Voltage (upper) and current (lower) at pre-ignition in high frequency LC circuit in laboratory interrupter. The number of current loops is 6. Contact touch is at 185 μ s.

4. CABLE DISCHARGE TESTS

thereafter the cable is discharged by a closing operation of the VCB. The discharge current of a cable is more or less rectangular caused by the distributed parameters, with a peak current of U/Z . For 15 kV and $Z = 25 \Omega$ a peak current

This method could be used in the field, where often cables are connected to the circuit breakers. One of the cable cores is charged by a DC source of 15 - 30 kV,

of 600 A is made with a high di/dt . The frequency of the discharge is determined by the length of the cable. We have made tests with cable lengths of 300 m in the laboratory and 2 km in the field (frequency 100 and 16 kHz). The pre-ignition time and the DC arc lifetime (see sect. 5) have been measured in three circuit breakers with nine vacuum tubes (2 km cable). The results are shown in fig. 3. From the results it may be concluded that the vacuum quality of the T-pole of the third circuit breaker may be suspected of loss of vacuum quality. The number of pre-ignition current loops was varying between 1 and 3, showing no evident correlation with the other measured quantities.

5. DC ARCING TESTS

The interrupting performance of low current DC arcs could have a relation to the pressure in the vacuum tube. This effect has been investigated with a DC supply ± 300 V with a three phase rectifier from the 380 V low voltage network. The current is stabilized by series capacitors of 50, 100, 200 or 300 μ F, giving currents of 5 - 10 - 20 or 30 A. An inductance of 30 mH is inserted in the DC path. The capacitance in parallel to the VCB is important for the value of the life time and the overvoltage generated after the current chopping. At high pressure (> 1 Pa) the arc will burn more or less permanently (> 30 sec), when opening the contacts. At low pressure the lifetime of the arc varies between 0.1 - 10 sec, depending on the current, capacitances parallel to the arc and the surface conditions of the contacts. For arc life time measurements, the degree of surface contamination has probably more influence than the background pressure in the bottle. For this reason, it is advisable to keep the arc lifetime sufficiently small, in order to avoid conditioning of the contacts by the measurement itself. An impression of the average DC arc lifetime, obtained in the two experimental set-ups described in sect. 3 with its standard deviation can be obtained from fig. 4. As can be seen, no evidence of pressure dependency in the interesting range below 10^{-2} Pa can be gained from this measurements. This is in accordance with earlier findings [4].

6. CONCLUSIONS

Vacuum state estimation by AC or DC test voltages is only effective for pressures higher than 2 Pa. For pressures lower than 1 Pa the test voltage can be withstood and sensitive emission current measurements (1-100 nA) give some indication if not superimposed by external discharges.

In the pressure range 10^{-2} - 1 Pa shield potential rises up to 1.5 kV have been observed during AC tests with 25 kV.

The high frequency interruption ability of preignition arcs during a making operation give a decreasing number of current loops for lower pressure down to approx. 0.1 Pa. Below 0.1 Pa the number of loops has no significant relation with the pressure.

Interruption of cable discharge currents with longer cables (1 - 3 km) gives a smaller number of loops than short cables (100 - 300 m), probably due to the lower di/dt . DC arc lifetime measurements with currents of 20 - 30 A have a tendency to give a shorter lifetime for lower vacuum

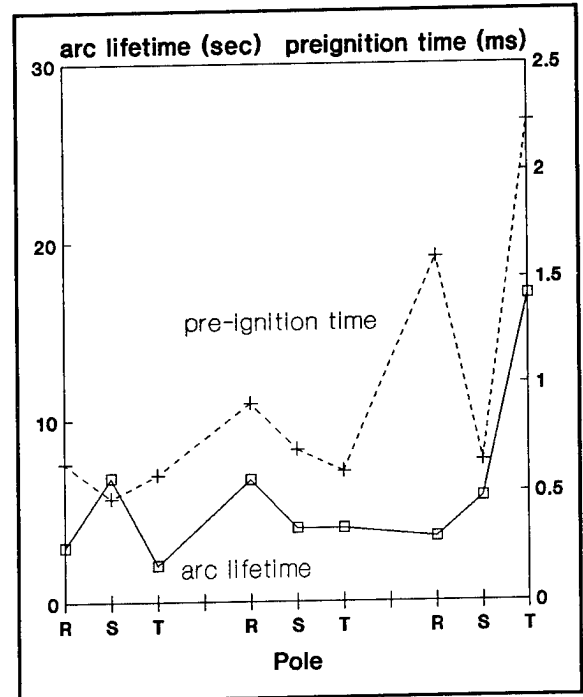


Fig. 3: DC arc lifetime (at 30 A) and pre-ignition time for 9 vacuum tubes in 2 km cable discharge

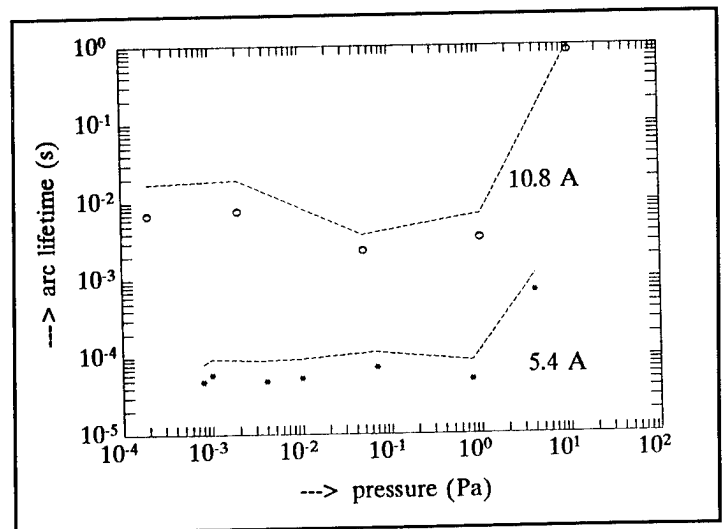


Fig. 4: Points: Average DC arc lifetime (commercial bottle 10.8 A, laboratory bottle 5.4 A). Line : upper standard deviation

downto approx. 1 Pa. For pressures below 1 Pa, arc lifetime does not seem a suitable indicator. For pressures above 1 Pa the arc is not interrupted due to a rapid increase in lifetime.

During field tests of cable discharges a correlation between pre-ignition time and DC arc time have been found. Further research for the vacuum pressure dependence of these effects is necessary.

7. REFERENCES

- [1] L.M.J. Vries, G.C. Damstra, "Pre-breakdown emission current measurements in a 24 kV vacuum circuit breaker with butt contacts", Proc. XIIth ISDEIV Shresh, pp. 27-30, September 1986
- [2] F.R. Frontzek, D. König, R. Heinemeijer, "Electrical methods for verifying internal pressure of vacuum interrupters after long time service", IEEE Trans. on Elec. Ins., vol. 28, pp. 635 - 641, August 1993
- [3] F.R. Frontzek, D. König, "Measurements of emission currents immediately after arc polishing of contacts", IEEE Trans. on Elec. Ins., vol. 28, no. 4, August 1993, pp. 700 - 705
- [4] S. Anders and B. Jüttner, "Influence of residual gases on cathode spot behavior", IEEE Trans. on Plasma Sci., Vol.19, No.5, pp. 705-712, Oct. 1991

Series resonance inverter with triggered vacuum gaps

G.C. Damstra^{1,2}, X. Zhang³

¹ N.V. KEMA, Arnhem, the Netherlands

² Eindhoven University of Technology, Eindhoven, the Netherlands

³ Qinghua University, Beijing, China

ABSTRACT

Series resonance inverters based on semi-conductor switching elements are well-known and have a wide range of application, mainly for lower voltages. For high voltage application many switching elements have to be put in series to obtain sufficient blocking voltage. Voltage grading and multiple gate control elements are needed.

There is much experience with the triggered vacuum gaps as high voltage/high current single shot elements, for example in reignition circuits for synthetic circuit breaker tests. These elements have a blocking voltage of 50 - 100 kV and are triggerable by a light fibre control device.

A prototype inverter has been developed that generates 0.1 Hz, 30 kV AC voltages with a flat top for tests on cables and capacitors of many micro farads fed from a low voltage supply of about 600 V.

Only two TVG elements are needed to switch the resonant circuit alternatively on the positive or negative supply. The resonant circuit itself consists of the capacitance of the testobject and a high quality inductor that determines the frequency and the peak current of the voltage reversing process.

1. INTRODUCTION

For on site tests of long run of high voltage cables DC tests at 3 - 4 U_0 have been used since years but proved to be less adequate for polyethen HV cables [1]. On the other hand for AC tests at 2 - 3 U_0 appreciable capacitive currents have to be compensated by reactors in parallel or series resonant circuits. The supply network has to deliver the ohmic losses of the test circuit, the greatest part of these losses is caused by the compensating reactors, the smallest part by the dielectric losses of the cable under test. These losses may be in the order of 100 kV. Using a lower test frequency, for example 0.1 Hz, the capacitive current will be proportionally lower. In 1986 a prototype 0.1 Hz test generator was developed at KEMA High Power Laboratory for 30 kV and 5 km cable length [2]. Two regulated rectifiers for positive and negative polarity are coupled by metaloxide elements to the cable under tests. This principle is quite advantageous for medium voltage and commercial apparatus are available now. But up-scaling to high voltage application causes a serious dissipation problem with the metaloxide elements. Hence another line of development was chosen. The voltage at the cable capacitance will be held constantly positive or negative for about 5 sec, with a quick reversal through a resonant inductor. As switching elements semiconductors can be used but due to the relatively low blocking voltage many elements have to be put in series. Also voltage grading and multiple gate control elements will be necessary.

Another line of development at KEMA has been the application of triggered vacuum gaps (TGV) for multiple reignition circuits for HV synthetic circuit breaker test schemes [3, 4, 5] and the Tesla transformer. TVGs are typical single shot devices, with a high current capability (5 kA). The triggered circuit can be operated free from ground by a light fibre control device.

2. TRIGGERED VACUUM GAP INVERTER

For the first time we use the TVG in a periodic mode with one triggering per ten seconds (0.1 Hz). Two TVGs are needed to connect the resonant circuit consisting of the grounded capacitors of the cable under test through a reactor of appropriate inductance, alternatively to a positive and a negative DC supply source (Fig. 1). This source consists of a voltage doubler (600 V) fed by the local LV network (230/400 V). The smoothing of the DC voltages is made by a number of series connected electrolytic capacitor of 350 V, 2000 μ F each.

The voltage amplification is determined to a large extend by the quality factor of the reactor. A compromise has to be made between a low frequency voltage reversal with a low peak current and a high frequency reversal with a high peak

current. To avoid current chopping of the TVG the current must not be too small. The quality of the reactor can be improved using winding techniques with parallel wires of relatively small cross sections to reduce the eddy currents.

3. TRIGGER CIRCUIT

The TVGs are normally triggered by a pre-charged capacitor (20 nF, 10 kV) and an auxiliary air sparkgap ignited by a pulse transformer. This is activated by a thyristor fired by an optical transmitted pulse. The circuit gives a high discharge frequency of about 1 MHz in the triggergap loading for about 5 μ sec. The current rise in the main gap must be rather high to avoid disruption of the main current after the trigger circuit is damped out. This could result in overvoltages by current chopping. The trigger circuit is shown in fig. 2.

We also carried out experiments with two stage triggering. A low voltage circuit (1 μ F, 1 kV) is added to sustain the trigger current over a larger period.

Some of the TVG we used were made in China and showed to have a low resistance trigger electrode. These tubes can also be triggered by a low voltage circuit only. This facilitates the design and the power consumption of the trigger circuit considerably.

The pulses for the trigger circuits are made by an electronic timer with a cycle time of 10 seconds. The pulse sequence can be varied but normally a 50/50 ratio is chosen.

4. EXPERIMENTS

In an experimental set-up a capacitor of 4.2 μ F resonates at 1500 Hz using a 2.7 mH reactor. With \pm 300 V supply voltage peak voltages of \pm 20 kV can be obtained. The peak current during the voltage reversal is 800 A. The final voltage is reached after about 60 voltage reversals.

5. CONCLUSIONS

The proposed circuit offers the possibility to make flat top low-frequency test voltages on capacitive loads and cables. The application of trigger vacuum gaps makes test voltages of 20 - 60 kV possible with a small number of components. A high quality coil design allows a high amplification factor, so a supply from LV sources is simple and reliable. For higher test voltages, series connection of TVG is an option that deserves further investigation.

6. REFERENCES

- 1 C. Aucourt, W. Boone et al., "Recommendations for a new after laying test method for HV extruded cable systems", CIGRE, Report 21-105, pp. 1-11, 1990
- 2 W. Boone, C.G. Damstra et al., "A very low frequency HV generator for testing cables after laying", 5th Int. Symp. on HV Eng., Braunschweig, Rep. 62-04, pp. 1-3, 1987
- 3 L.M.J. Vries, G.C. Damstra, "A reignition installation with triggered vacuum gaps for synthetic fault interruption testing", IEEE Trans. on Power Del. Vol. PWRD-1, no. 2, pp. 75-80, April 1986
- 4 L.M.J. Vries, "The three phase reignition installation", KEMA Newsletter, no. 3, pp 2-3, April 1988

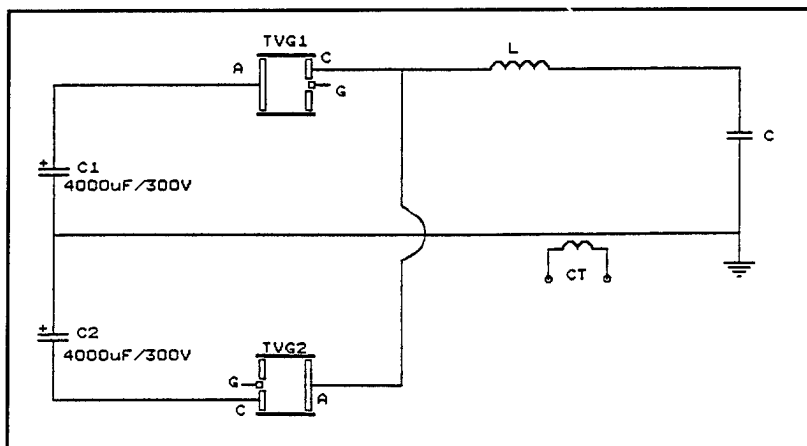


Fig. 1: The test circuit

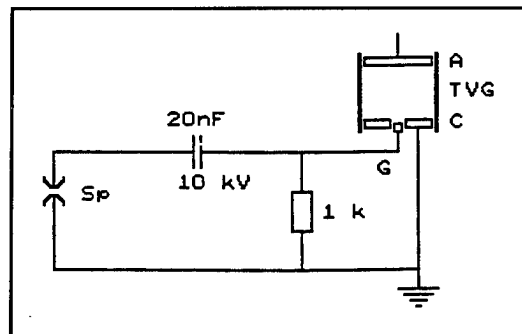


Fig. 2: The trigger circuit

- 5 G.C. Damstra, "A new 6 pulse reignition installation for three phase synthetic tests", KEMA Newsletter, no. 8, pp. 3. June 1991
- 6 G.C. Damstra and J.A.J. Pettinga, "A six pulse 400 kV Tesla transformer", 5th Int. Symp. on HV. Eng., Braunschweig, Report 62-13, pp. 1-3, 1987

Electrical characteristics of Pseudospark discharge.

Gérard Bauville, Alain Delmas
Paris VI and Paris XI Universities
Electrotechnical Laboratory
Bt 214, 91405 Orsay, France

ABSTRACT

The studies, carried out on high inductive energy transfer, has lead the Electrotechnical Laboratory to test switch device. Our works on trigger vacuum switches has shown switch off capacities, [4]. In preliminary studies, we have shown possibilities to pseudospark discharge for zero current switching off, [5]. Our purpose here is to define electrical characterisation of this kind of discharge. An axial magnetic field, pressure of gas (air), differents shapes of geometrical electrode was the network constant of the pseudospark discharge. The surface observation of the cathode and the anode show us that a pseudospark discharge diffuse all over the electrode surface.

1. INTRODUCTION

The "Pseudo-spark discharge" behaviour is characterised by two phases [1],[2].

1) a "z-pinch" discharge

2) a glow discharge at low pressure define by a height current density electron beam at the anode.

This high electronic density (10^6 A/cm^2), [2], is produced without arcing like vacuum electrical discharge. This arcing produces erosion of the electrode surface. Thus, the Pseudo-spark discharge presents a great interest in closing switching. The ignition phase and hollow cathode discharge with the formation of "virtual anode" in the hollow cathode are subjects of many researches and publications. However, the high current main phase and their capacity to zero current opening switching was not very developed for time discharge more than $10 \mu\text{s}$ at $200 \mu\text{s}$.

2. EXPERIMENTAL DEVICE

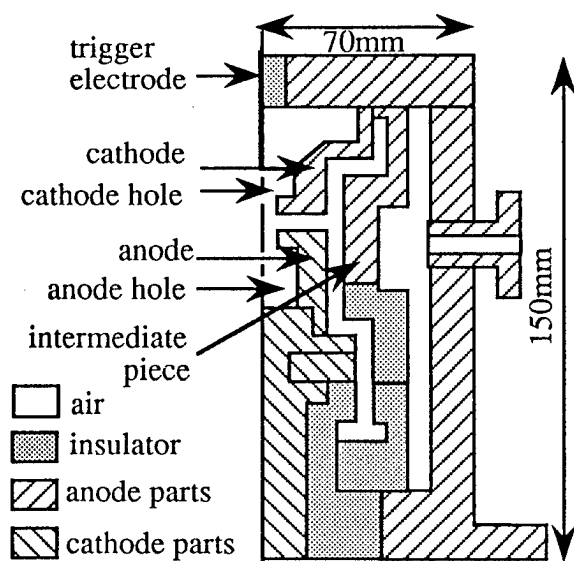


Figure 1: Prototype device

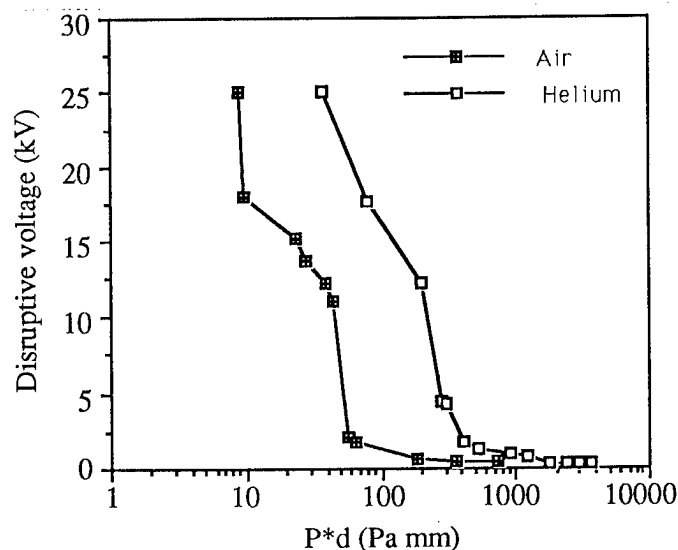


Figure 2: Experimental Paschen curves

The "Pseudospark" switch, figure 1, is a cylindrical revolution type, comprising two fixed hollow electrodes with a usual spacing of 5mm. The predischage (ignition of Pseudo-spark switch) starts to the system axis. A Teflon part maintains an insulation between the height voltage element (anode) and the cathode elements. Aluminium (Au4G) chamber stands as return circuit. An oil diffusion pump ensures an

adjustable pressure up to 10^{-4} Pa. The usual gas is air, but some experimentation was made with helium. According to behaviour of the "Pseudo-spark", we use hollow electrodes (hole diameter $\varnothing=6$ mm, cavities: $\varnothing=20$ mm, height=15mm), and the experimental pressure is located at the left side of experimental Paschen curves, figure 2.

The determination of the electrical characteristics needs the knowledge of voltage and current discharge []. The current is measured with an inductive probe derivative to a classical Rogovsky probe. The measure of voltage discharge (few ten volts) needs a special electrical test, [3]. The voltage and the current of discharge allows us to obtain mean voltage, the product of voltage by the current give us the power and the integration of power, the dissipative energy during the discharge. To a basic outline (Air, $P=1$ Pa, time discharge= $27\mu\text{s}$), we have experimented a largest time= $265\mu\text{s}$, and we study the effect of an axial magnetic field, the increase pressure and the effect of geometrical parameter like the anode shape.

3.VOLTAGE DISCHARGE

3.1 Effect of time discharge

The overvoltage appears, for two different time discharge, for a peak current upper than 6,5kA. A Fast Fourier Transformer of voltage signals get us a characteristic frequency of 2MHz. (in helium, for short pulse, this frequency is 18MHz). Noted that this overvoltage appears before I_{peak} , ($dI/dt > 0$). The ratio between Q and I_{peak} is 0,0154 Cb/kA for short pulse ($T/2=27\mu\text{s}$) and 0,13Cb/kA for long pulse ($T/2=265\mu\text{s}$).

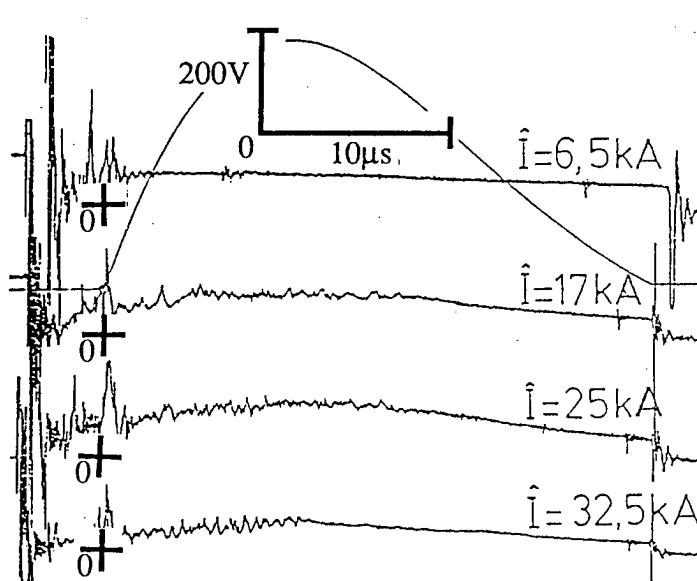


Figure 3: Voltage, $T/2=27\mu\text{s}$, Air, $P=1$ Pa

It seems that the emission and conduction process are similary for the two times discharges, two different domain of transfered charge, and two dI/dt different.

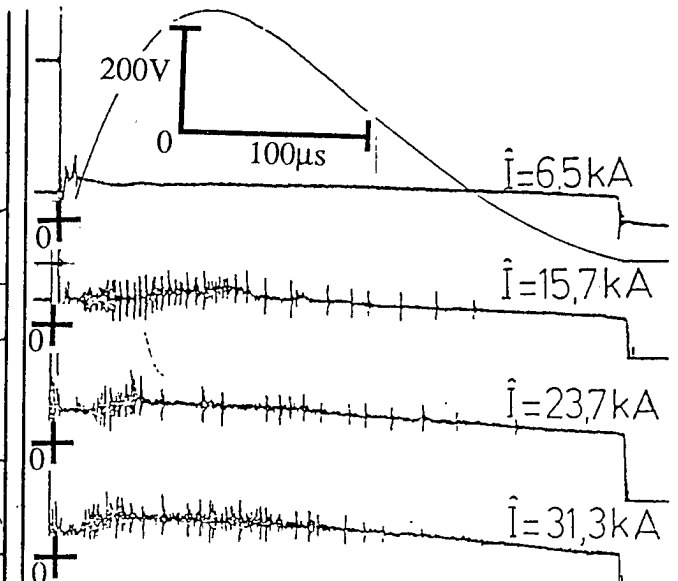


Figure 4: Voltage, $T/2=265\mu\text{s}$, Air, $P=1$ Pa

3.2 Effect of gaz pressure

For the short pulses, a closing up to Paschen minimum induce a quiet voltage and a decrease of the over voltage intensity. We think that an increase of pressure gas give it an important part to the ionization process. To the long pulse ($265\mu\text{s}$), the over voltage endures near the Paschen minimum(air; $U_d \approx 500$ V; Pressure*gap= 100 Pamm). We think that the phenomena area electrode emission is most important to creation charge than the effect of the gas. An observation of electrode surface show a diameter fusion of 16mm or short pulse and 40mm for long pulse. An another mean to induce a over voltage reduction is to apply a steady magnetic field, $0 < B < 40$ mT. This axial magnetic field prevent a radial expansion of the discharge in space gap between the electrodes.

4. MEAN VOLTAGE, ENERGY

4.1 $\langle U \rangle, E$ versus pressure and time discharge

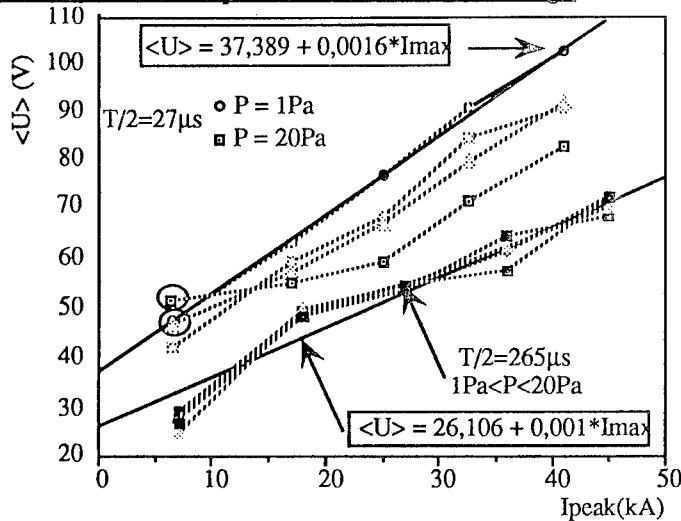


Figure 5: Mean voltage versus peak current, air

Short pulses: For $P=1\text{Pa}$: An increase of 400% of I_{max} imply one increase of 90% for the mean voltage, for $P=20\text{Pa}$, the increase is only 70%.

Long pulses: mean voltage by unit time. The same evolution was observed than short pulse with upper values. The mean voltage and dissipative energy are independent to pressure, we think that the charge transferred is so important that the effect of electrode surface supply the discharge and the gas, for the long pulse, have lower influence in the process of conduction phase.

The influence of axial magnetic field is significative from a value of 40mT, the decrease of mean voltage and energy reach 25% for $I_{\text{peak}}=6,5\text{kA}$. the influence of the magnetic field on energy is light.

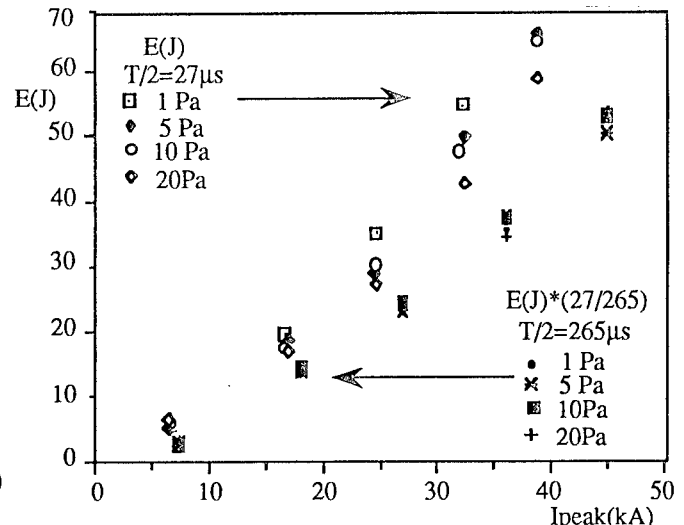


Figure 6: Energy versus peak current, air

4.2 Effect of geometry anode.

The figure 7 and 8 shows the values of energy and mean voltage for three different couple of electrodes: the first: anode and cathode hollows, the second cathode allow and flat anode and the third anode ant cathode flats. For the third case, the discharge is not a pseudo spark discharge but an arc.

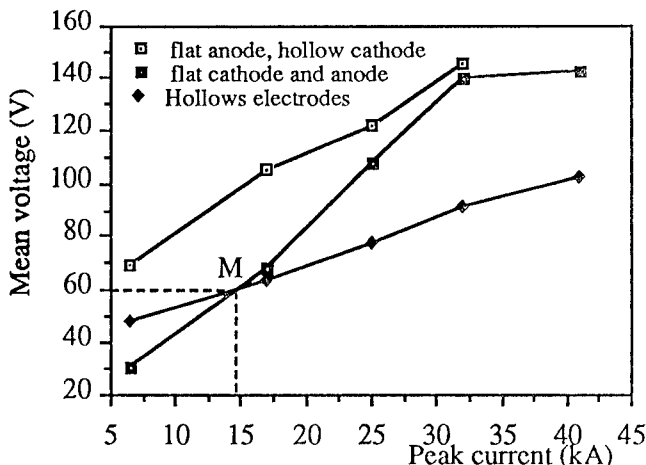


Figure 7: Mean voltage versus peak current

A flat anode facing hollow cathode induce an increase of the mean voltage and dissipative energy, for a peak current of 30kA, the rise is 75% for $\langle U \rangle$ and 90% for the energy. We show the preponderant part of the hollow anode in the behaviour of Pseudo-spark discharge. We think that the hollow anode is a trap for electron or negative charge which reach anode surface collector and thus increase radial diffusion strength in

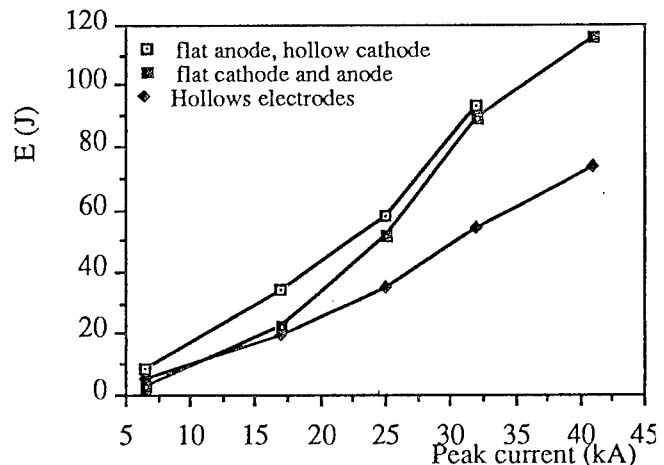


Figure 8: Dissipative energy versus peak current

the space gap. Another point noted on figure 7 is a crossing between the two mean voltage curves (flat and hollow electrodes), this is a limit of a constricted vacuum arc and a diffuse vacuum arc.

5. VOLTAGE VERSUS CURRENT.

The curves of the voltage versus current discharge allows us to define a threshold voltage U_0 , and a dynamical resistance, R_0 . These two quantities define the decrease current phase (dI/dt). The spreading of the discharge in the space gap ($dI/dt > 0$) is at the origin of the over voltage.

R_0 is the slope of voltage versus current during the current decrease. U_0 is defined by the voltage at zero current, end of conduction phase.

-short pulses ($T/2=27\mu s$): $U_0=25V$ (experiments with helium and short pulses: $U_0=22V$)

-long pulses ($T/2=265ms$): $U_0=10V$

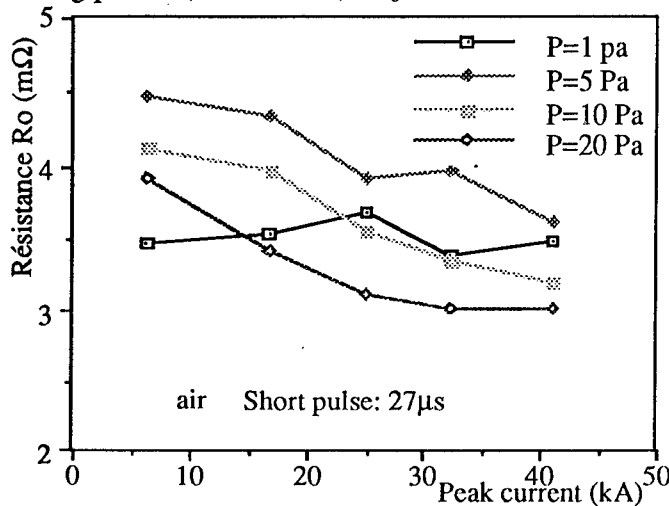


Figure 9: Dynamical resistance versus peak current

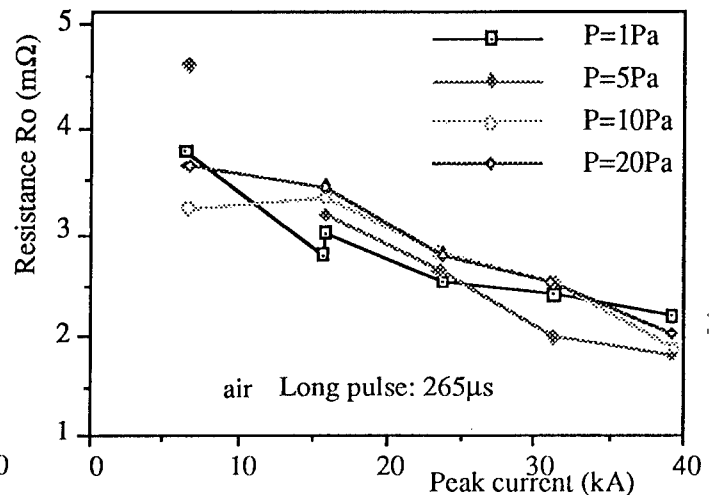


Figure 10: Dynamical resistance versus peak current

6. CONCLUSION

Short time conduction ($27\mu s$): High dI/dt prevents a good spread discharge, and gives upper mean voltage. Higher residual gas pressure, or axial magnetic field continuous field, reduce this one.

Long time conduction ($265\mu s$): The diffusion of discharge is effective all over the electrodes surfaces. Mean voltages and dissipative energies are independent to pressure and are lower than one's for short pulse.

For all cases, the voltage discharge can be represented by a relation type: $U=U_0+R_0I$. The hollow geometry allows to obtain a diffuse discharge in conditions which it's difficult to obtain with an arc. All this information's could be used to define the best configuration experimental (gas, pressure, electrode geometry) to use this pseudo spark device like a zero current opening switch.

7. REFERENCES

1. K. Frank, E. Boggash and J. Christiansen, "High power pseudospark and BLT switches", IEEE Trans on Plasma Science, 1988, vol 16, p 317-323.
2. W. Hartmann, G.F. Kirkman and M.A. Gundersen, "Evidence for large area super emission into a high current glow discharge", Appl. Phys. Letter, 1988, vol 53, p1699.
3. P. Lequitte and A. Delmas, "Arc voltage of a fast triggered vacuum gap", IEEE Trans on Plasma Science, october 1993, vol 21, n°5.
4. G. Bauville, A. Delmas and C. Rioux, "Study of recovery phenomena in a high-current pulse triggered vacuum switch.", IEEE Trans on Plasma Science, vol 17, n°5, october 1989, pp 781-785.
5. G. Bauville, A. Delmas, "Study of hollow cathode discharge", 9th International Pulsed Power Conference, Albuquerque, New Mexico, June 1993.

Mass Erosion and Surface Voltage Holdoff Recovery of Insulators Used in a High Current, High Vacuum Surface Discharge Switch *

T.G. Engel, S.L. Wester, and M. Kristiansen

Texas Tech University, Department of Electrical Engineering, Pulsed Power Laboratory
P.O. Box 43102, Lubbock, Texas 79409-3102

L.L. Hatfield

Texas Tech University, Department of Physics and Engineering Physics
P.O. Box 41051, Lubbock, Texas 79409-1051

ABSTRACT

A high current surface discharge across the surface of an insulator in high vacuum is investigated. The mass erosion of the insulator and its surface voltage holdoff recovery are the two most important parameters of this investigation. Typically, the discharge current reaches ~ 350 kA peak with a pulse length of ~ 60 μ s (~ 5 periods of a damped sinusoidal pulse). The vacuum level is maintained at $\sim 10^{-6}$ Torr. The insulator materials tested include a variety of polymeric (i.e., polyethylene, nylon, epoxy-fiberglass composites, and polyurethane) and ceramic (alumina, silicon nitride, and zirconia) insulators. Insulator mass erosion and surface voltage holdoff recovery versus electrode material has also been investigated. The electrode materials used include stainless steel, molybdenum, copper, copper-tungsten, brass, aluminum, and lead. Insulator materials that have low mass erosion and good surface voltage holdoff recovery have potential applications in high power vacuum switches. Breakdown voltage histories and mass erosion data were obtained for the plastics, but only breakdown voltages were obtained for the ceramics.

2. INTRODUCTION

The purpose of this research is to find insulator materials that can withstand high current (~ 350 kA) discharges while in high vacuum (10^{-6} Torr). The materials tested in this experiment include polyethylene, Lexan¹, Lucite², polyurethane, blue nylon, G-10, alumina, silicon nitride, and TTZ (transformation toughened zirconia)³. In this document, a description of the experimental setup will be given, along with experimental results.

There are two primary mechanisms affecting the holdoff voltage characteristics of insulators; decomposition of the insulator surface and electrode material deposited on the insulator surface from the previous breakdown. It was previously found⁴ that ceramics tend to metallize while polymers and elastomers tend to pyrolyze (i.e., carbonize). The electrode material deposited on the insulator surface was not studied extensively in that previous work or in this investigation. It is to be noted that in the above referenced study, the tests were limited to gas discharges at atmospheric pressure. To the authors' knowledge, high current, high vacuum surface discharge tests investigating the nature of the insulator mass erosion and surface voltage holdoff recovery have not been reported before.

* This work was supported by SDIO/TNI through DNA/RAEV under contract #DNA001-90-C-0110.

3. EXPERIMENTAL SETUP

The basic requirements for the experimental setup were to simulate a ~ 350 kA fault condition across different insulator materials in a high vacuum, 10^{-6} Torr. The discharge across the insulator sample was self commutating. A capacitor bank was charged using a high-voltage dc power supply until an arc formed across the insulator sample. After a discharge, the original vacuum level was reestablished by waiting 5 minutes before another discharge was attempted. As seen in Figure 1, there are fifteen 60 kV, $1.85 \mu\text{F}$ Scyllac capacitors connected in parallel via a parallel plate transmission line. Also shown in this drawing is the vacuum chamber where the discharge occurs. The capacitor bank was charged negatively with the bottom plate of the transmission line at experiment ground.

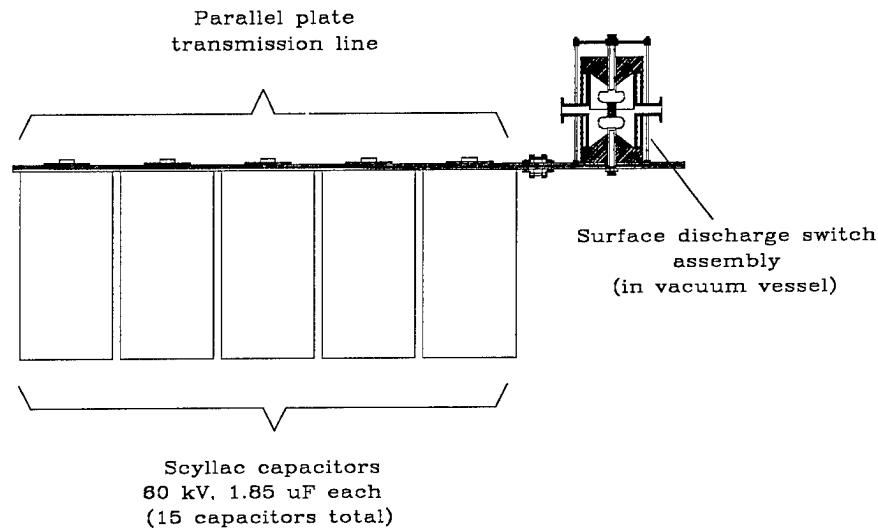


Figure 1. Experimental setup.

Table 1 shows the operating characteristics of the system. The voltage breakdown level was measured with a 10,000:1, 1 MHz high-voltage probe connected to a 300 kilosample/second A-D converter. A computer program was written to monitor the voltage from the probe, detect the voltage peaks occurring at discharge, and record the voltage signal to an ASCII file. A typical discharge waveform is shown in Figure 2.

TABLE 1. OPERATING CHARACTERISTICS.

PARAMETER	VALUE
Voltage (typical)	40 kV
Current (typical)	350 kA
Discharge current oscillation frequency	250 kHz
Energy (typical per shot)	22.2 kJ
Effective charge transfer (typical per shot)	10 C
Vacuum level	10^{-6} Torr

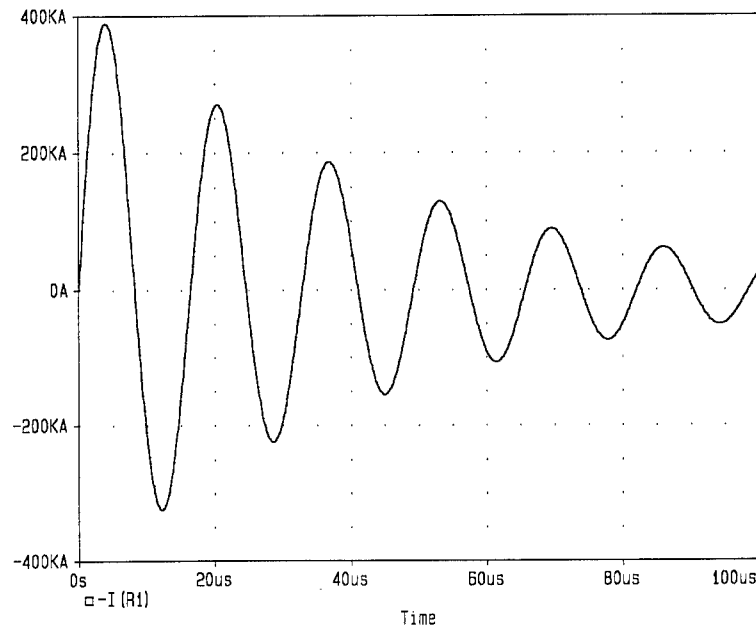


Figure 2. Typical discharge current waveform.

The electrodes were machined to have field enhancement points along the insulator surface (to ensure breakdown across the insulator sample) with the samples actually sitting in 0.32 cm deep recesses in the electrodes. The insulators were 2.54 cm in diameter and 2.54 cm in length, leaving a 1.91 cm gap between the electrodes. The complete vacuum chamber and electrode assembly can be seen in Figure 3.

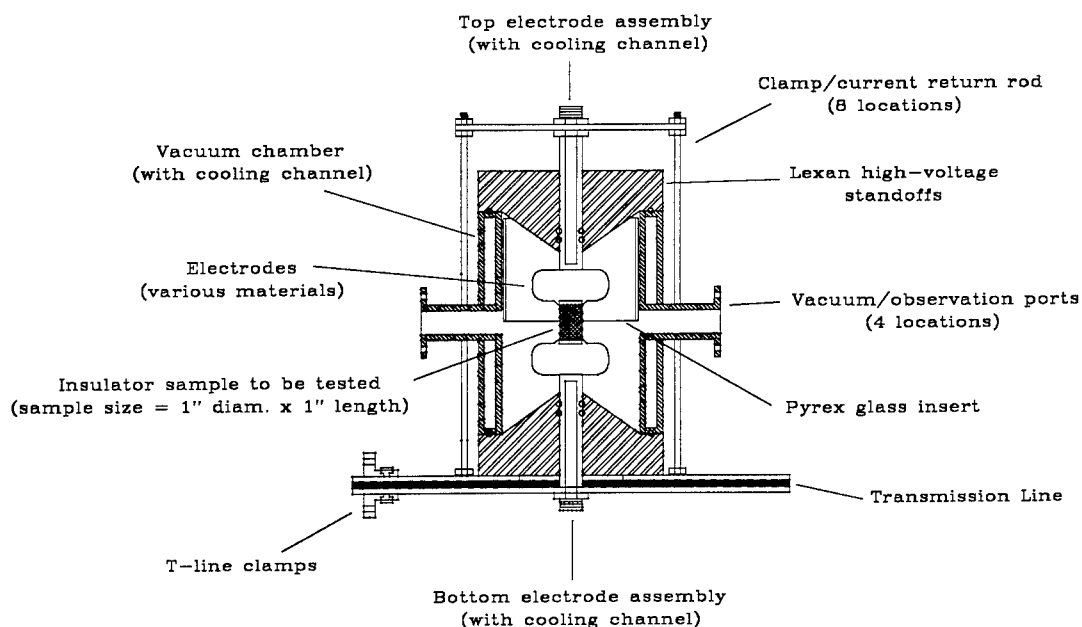


Figure 3. Illustrating vacuum chamber and electrode assembly (side view).

4. EXPERIMENTAL RESULTS

In the following experimental results, the breakdown voltage history was determined by averaging the results of 3 different samples subjected to a 12 discharge test sequence. Polyethylene was the insulator material most extensively used in this experiment and was tested with copper, lead, stainless steel, aluminum, and graphite electrodes. The polyethylene voltage breakdown history using the stainless steel electrode material can be seen in Figure 4. There was little difference in the voltage breakdown history plot when the other electrode materials were used.

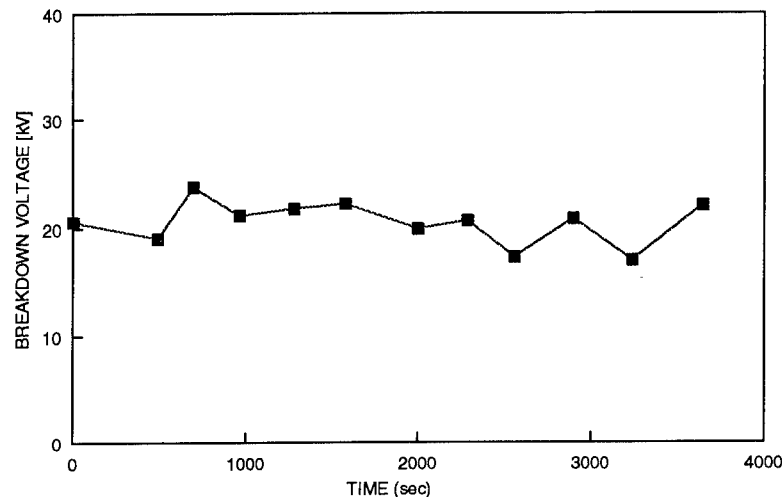


Figure 4. Polyethylene average breakdown voltage using stainless steel electrodes.

Additionally, the total energy of the run could be calculated from the breakdown voltages recorded. The mass erosion rate was calculated as mass erosion of the insulator per amount of total energy in the run or in units of $\mu\text{g/J}$. The mass erosion rates for polyethylene (averaged over three test sequences) versus electrode atomic weight can be seen in Figure 5. As seen in this figure, the mass erosion rate increased linearly as the atomic weight of the electrodes was increased. The exception to this was the lead electrode test, where it was assumed that deposited electrode material skewed the mass erosion data. It was calculated that ~ 2000 monolayers of lead would have to be deposited on the surface to bring the mass erosion rate for lead to the linear portion of the graph.

It was shown in reference [4] that increased electrode atomic weight increased the amount of UV radiation given off during a surface discharge in air. The higher the UV flux, the more molecular bonds are broken and more conductive/semi-conductive materials are formed leading to poor surface voltage holdoff recovery. In this experiment, because the discharge occurs in vacuum, no stable gases like carbon dioxide or carbon monoxide are formed from decomposed material. It is believed that the lack of a gaseous ambient during the discharge leads to an explosive emission of both insulator and electrode materials leaving deposits on the inside of the chamber.

In surface flashover studies in air, a conditioning phase for the insulator was found. The conditioning phase is a number of shots that occur at breakdown voltages each higher than the one before⁴. Since there is a reported correlation between the "conditionability" of the insulator and its water

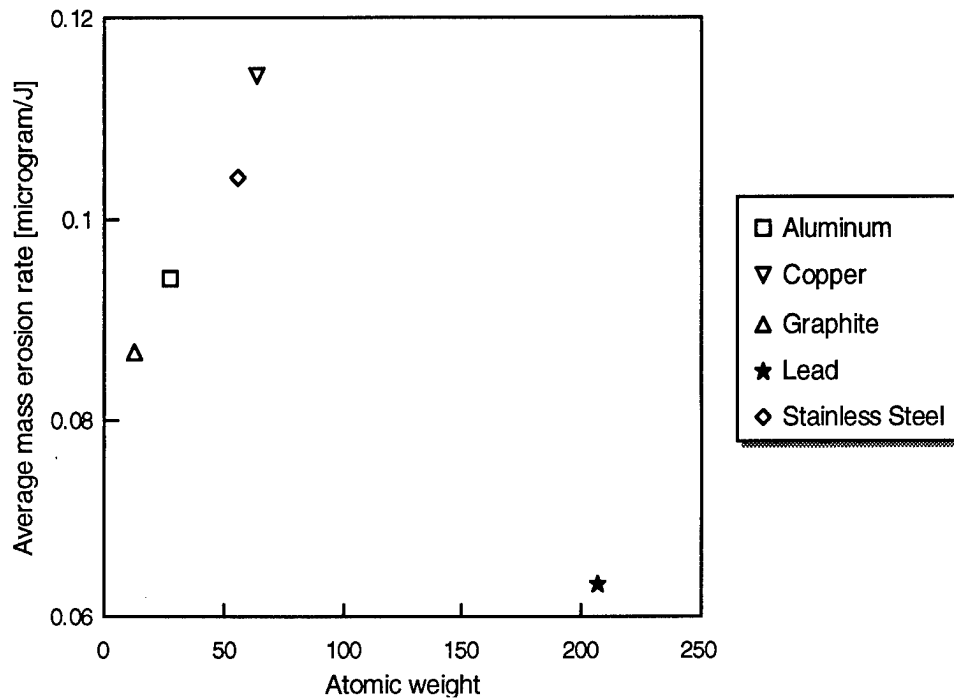


Figure 5. Polyethylene average mass erosion rates versus the electrode atomic weight.

vapor absorption coefficient⁴, a water vapor or gas layer presumably exists on a dielectric surface in air and acts as “a source of virtual charge that lowers the (dry) surface breakdown strength and serves as a ‘sacrificial’ surface coating, absorbing and efficiently removing some of the incident arc energy that would otherwise cause insulator decomposition.” Since this experiment tested insulators in vacuum, the surface water or gas layer would be removed, and would explain the absence of a conditioning phase.

Three different ceramics were tested in this experiment (with stainless steel electrodes); alumina (Al_2O_3), TTZ (transformation toughened zirconia), and silicon nitride (Si_3N_4). To be consistent with earlier work, the lifetime of the insulator material is referred to as the number of discharges required to reduce the breakdown voltage to the half power level (i.e., $V_{\text{initial}}/\sqrt{2}$) of the initial breakdown voltage⁴. The lifetime of the alumina was two discharges which is unexpected because when tested in air, alumina is a multi-discharge material (>140 shots)⁴. The TTZ and silicon nitride had slightly longer lifetimes lasting ~ 5 discharges. The current levels at breakdown for all three ceramic insulators are lower than similar tests on polymers which is attributed to the higher ceramic dielectric constants. To obtain higher currents on the order of 350 kA, the lengths of the samples will need to be increased. TTZ and silicon nitride are single shot materials when tested in air⁴. Therefore, the lifetime of the material was substantially increased in vacuum. It is predicted, however, that for higher current levels, the lifetime will be reduced to either one or two shots.

Several other materials were tested with the stainless steel electrodes. These insulator materials included; Lucite, blue nylon, Lexan, polyurethane, and G-10 (glass fabric reinforced epoxy). Their lifetimes were > 12 discharges (i.e., the extent of the tests) with the exception of G-10 which had a 3 discharge lifetime. Their erosion rates are listed in Table 2.

TABLE 2. MASS EROSION RATES FOR OTHER MATERIALS

MATERIAL	EROSION RATE [$\mu\text{G/J}$]
Blue Nylon	0.085
G-10	0.132
Lexan	0.17
Lucite	0.193
Polyurethane	0.175

5. CONCLUSIONS AND FUTURE WORK

From the results of this experiment, it appears that all thermoplastics (i.e. polyethylene, Lexan, Lucite, blue nylon, and polyurethane) are good, high current vacuum insulators. G-10, a thermoset, pyrolyzed after several shots. The holdoff voltage decreases as the amount of carbonization on the insulator surface increases. Ceramics performed poorly and would not be good candidates for vacuum insulators exposed to high currents. The ceramics tend to metallize quite easily, reducing their holdoff voltage. Additionally, their higher dielectric constants yield higher electric fields and lower breakdown voltages.

It has also been noted⁴, that the type of electrode material will affect the mass erosion rate for insulator samples. This was shown to be true in these tests for polyethylene samples tested with aluminum, graphite, copper and stainless steel electrodes. It appears that there is a correlation between the atomic weight of the electrode material and the mass erosion rate. Additionally, since the vacuum arc formed on the insulator surface is more diffuse than a gas discharge, lower mass erosion rates were found for the plastics tested in this experiment than in similar tests in air discharges⁴.

Monitoring the peripheral location of the discharge site, as it varies from discharge to discharge, would be an interesting study for future investigations perhaps yielding additional information about the level of insulator damage. This could be accomplished using four fiber optic cables placed at the four quadrants around the insulator sample. During a discharge, the light intensities from the four fibers would be compared using photomultiplier tubes (PMT's). This location could be compared to the location of the next discharge. At the present time, the fiber optic cable has been prepared along with a vacuum feedthrough. The PMT's are also available, but need calibration for relative measurements. One of the remaining problems is determining how to mount the fiber optic assembly inside the chamber at the required location.

6. REFERENCES

1. General Electric tradename.
2. DuPont tradename.
3. Coors Ceramics tradename.
4. T. G. Engel, Insulator degradation by high current discharges" PhD. Dissertation, Texas Tech University, December 1990.

Energy concentration in Z-pinch experiments.

Gordeev E.M., Korolev V.D., Liksonov V.I., Zazhivikhin V.V.

Russian Research Center "I.V. Kurchatov Institute"
Moscow 123182, Russia.

ABSTRACT

The vacuum energy concentrator has been designed on the 0.15 Ohm, 10 TW pulse power 8 module generator S-300. A vacuum 3-D EC was constructed on the base of MITLs, connected parallelly at the central unit. For the total output inductance of 7.7 nH the concentrator provides currents of 5 - 7 MA. The calculations show that the transportation of efficiency electrical energy to the liner kinetic energy is about 30%.

INTRODUCTION

For a development of experimental investigation in the field of ICF in RRC "Kurchatov Institute" the 8-module pulse power (10 TW) generator S-300 was worked out¹. This installation will provide a generation of 300kJ electrical pulse at a voltage level of 1.3 MV with FWHM of 33 ns. A high - voltage pulse developed at the output of the water pulse - forming line enters into the vacuum energy concentrator (ES) through the ring type high - voltage insulator of 1 m diameter. The S-300 installation with output impedance of 0.15 Ohm provides a total current of 5 - 7 MA with a rise time of 60 ns on liner load.

NUMERICAL CALCULATION.

For obtaining the required current in experiments on investigation of liner implosion it is necessary to minimize the output inductance of the installation. For the choosed ring type insulator geometry with a total inductance of 2 nH, the minimum inductance can be provided by the EC constructed on the base of MITLs which are parallelly connected.² A simulation of the energy transportation in the EC was carried out on the base of a model described in the nonstationary processes in MITLs. The EC consists of 16 triplate transmission lines, which are parallelly connected to 8 triplate nonhomogeneous lines of the central unit. Each MITL of the central unit is connected to 2 triplate MITLs of the concentrator, which are situated in a single vertical plane (see Fig.1). In this model wave processes in a MITL were described by telegraph equation with a nonlinear current of an electron leakage.³

$$\frac{1}{c} \frac{\partial A_z}{\partial t} + \frac{\partial V}{\partial z} = 0, \quad \frac{\partial Q}{\partial t} + \frac{\partial I}{\partial z} = -j_1(V, I),$$

where A_z - is the component of the vector potential, V - the electrical potential, Q and I - the charge per unit length and the line current respectively, j_e - the electron leakage current per unit length. A MITL was divided to segments. Inside each segment a condition of magnetic self - insulation was analysed and the leakage current was calculated on the base of a superposition of incident and reflected waves. The generator load was taken into account as a boundary condition. In calculations the installation was represented as 16 effective parallelly connected to liner load generators with each impedance equal to 2.4 Ohm. Each generator has the following parameters: the insulator inductance of a MITL is 56 nH - 114 nH, the depending on the cathode - anode gap, the liner unit inductance 32 nH - 56 nH. This leads to the value of the output "cold" inductance of 7.7 nH at 1 cm gap. The voltage pulse form of a generator was obtained from experiments in which the operation of one of 8 modules of the S - 300 installation was investigated. Boundary condition at the load was defined from a solution of the liner motion equation per 0 - dimensional approximation. The charge Q and magnetic flux A_z are connected with the current and voltage by means of the equations

$$Q = C_0 V, \quad A_z = \frac{1}{c} L_0 I.$$

where L_0 and C_0 - are the inductance and the capacitance of the MITL per unit length, which are equal to their vacuum values. For the calculation of the electron leakage density $j(V, I)$ was used the Child - Langmuire formula, generalised on relativistic voltages. In case when the line current I exceeded minimum current of insulation I_{min} , the leakages were settled to zero. As a result of simulations the following parameters of the energy concentrator was obtained:

concentrator MITL quantity.....	16
concentrator MITL length.....	40 cm
concentrator MITL width.....	8 cm
central unit MITL quantity.....	8
central unit MITL length.....	14 cm
central unit MITL width.....	4-7 cm
MITL's gap.....	1 cm

From the results of the calculations it follows that at $V = 1.3$ MV for liner with 2 cm in diameter, 2 cm in height and 420 mg of weight transportation efficiency of the generator electrical energy to the kinetic energy of the liner achieves 30%. For this case liner kinetic energy is equal to 100 kJ and the liner current - 5.7 MA. The leakage current in EC is less than 0.8 MA during the first 10 ns, the leakage current density - 3kA/cm² and the total energy of electron losses - 7.5 kJ.

The dependences of liner radius $R(t)/R_0$ (R_0 - the initial liner radius), its velocity $V(t)$, and current on time for voltage which corresponds to a half of the installation power are shown in Fig.2. In this case the kinetic energy is equal 46 kJ, that corresponds to the efficiency of 30%.

In the calculations it was set that the losses are cut off when $I > I_{min}$. Generally speaking a critical current I_{cr} of magnetic

insulation can exceed I_{min} because of the change of an electron shell structure. In case when $I_{cr}=1.5 I_{min}$ calculations have shown (see Fig.3) that although the current of electron losses increase twicely the total energetic losses rise in less than 5%. The values of the current and the kinetic energy practically don't differ from the case when $I_{cr}=1.5 I_{min}$.

Energy transportation efficiency essentially depends on the gap value of MITLs. At increasing the gap value from 1 cm up to 2 cm the total "cold" inductance increases from 7.7 nH up to 11 nH and transportation efficiency decreases up to 20%.

The gap value is limited by the movement of a plasma created on the electrodes of a MITL by the explosion emission electrons and radiation coming from the imploding liner. The experiments on the investigation of the transportation efficiency in a concentrator carried out on Module A5-1 ($\rho=0.04$ Ohm, $I=4.6$ MA, $T=100$ ns) showed that there exists a critical line gap of 5-6mm below which the losses increase 5-10 times. These losses are connected with local plasma flows, which expand across millimeter gaps with velocities of $(1-5) \cdot 10^7$ cm/sec. The appearance of the plasma in a gap which was registered by overall photography of EC by framing cameras leads to a closing of the interelectrode gap and to the characteristic time-laging trailing edge of the current pulse (see Fig.4,5).

ACKNOWLEDGMENTS

The others wish to express their gratitude to Prof.L.I.Rudakov for his support to this work.

REFERENCES

1. L.I.Rudakov. "Kurchatov Institute Program of Soft X-ray Flash Generation for ICF Study on the Base of Pulse Power Application. "Seminare C.E.A./DAM - INSTITUTE KURCHATOV. Z-pinches et tres hautes pulssanges pulsees Laboratoire de Physique des Milieux Iionises. ECOLE POLYTECHNIQUE, p.9, 1993.
2. A.V.Gordeev, V.D.Korolev, V.P.Smirnov. Annals of the New York Academy of Sciences, Vol. 251, p.668. 1975.
3. V.V.Bulan, V.V.Zajivikhin. Proc. of 8th Conf. on High Particle Beams, Novosibirck, USSR, Vol.2, p.990. 1991.
4. G.A.Mesyatz, D.I.Proskurovskii, Pis'ma Zh Exsp.Teor.Fiz., Vol.15, p.7.1971.
5. E.M.Gordeev, V.V.Zajivikhin, V.D.Korolev et al, J Plasma Phys., Vol.19, p.1101.1993.

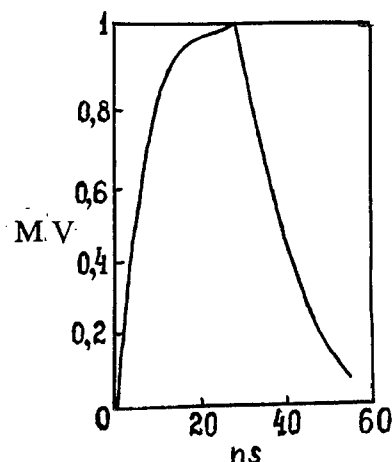
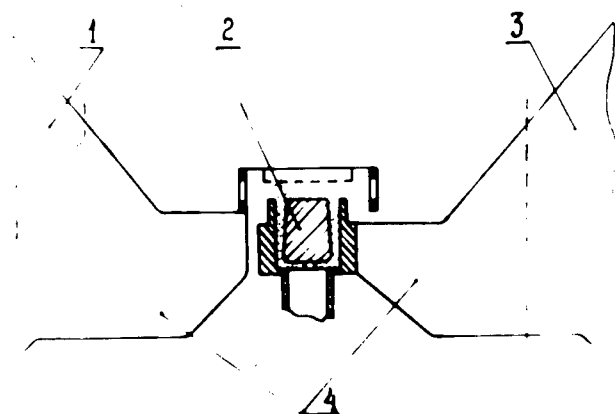


Fig.1. Energy concentrator. a: 1,3 - electrodes of concentrator, 2 - valve, 4 - electrodes of central unit, b: voltage waveform.

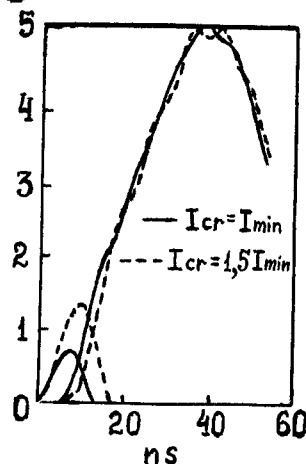
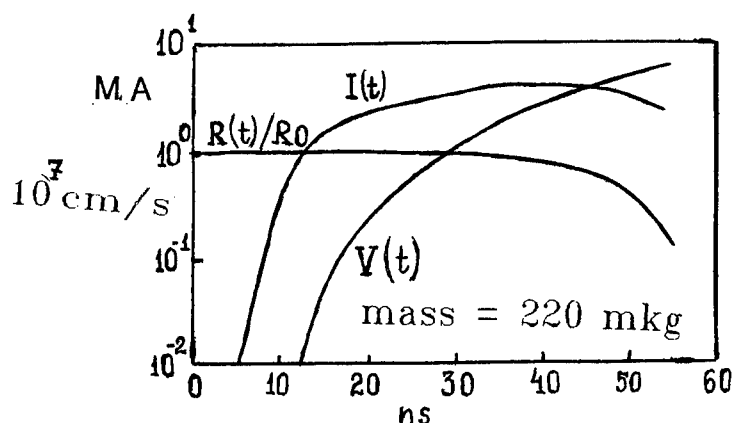


Fig.2. Dependence of the liner radius $R(t)/R_0$, the velocity and the current vs the time.

Fig.3. Dependence of the liner current I and the total leakage current vs time for two values of the critical current of the magnetic insulation.

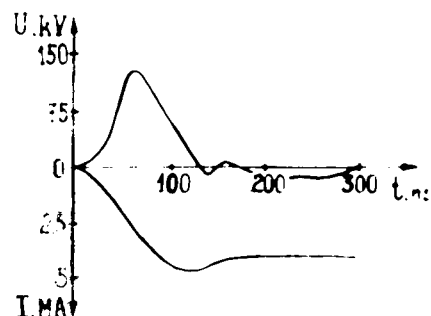
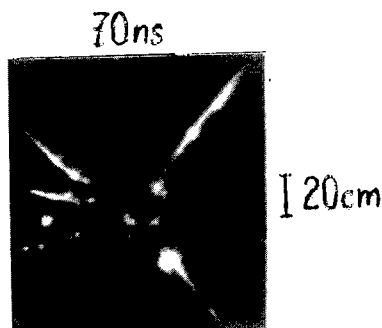


Fig.4. Visible light overall photograph of the energy concentrator. Exposure time 15 ns.

fig.5. Experimental traces of the voltage V and current at the concentrator unit.

100 kA VACUUM CURRENT BREAKER OF A MODULAR DESIGN.

Ivanov V.P., Vozdvijenskii V.A.
All - Russian Electrotechnical Institute, Moscow.

Jagnov V.A., Solodovnikov S.G., Mazulin A.V.
Institute of Innovation and Thermonuclear Researches, Troitsk, Moscow region.

Ryjkov V.M.
Moscow Engineering-Physical Institute, Moscow.

ABSTRACT.

Direct current breaker of a modular design is developed for the strong field tokamak (SFT) power supply system. The power supply system comprises four 800 MW alternative current generators with 4 GJ flywheels, thyristor rectifiers providing inductive stores pumping by a current up to 100 kA for 1 - 4 sec. To form current pulses of various shapes in the tokamak windings current breakers are used with either pneumatic or explosive drive, at a current switching synchronosity of not worse than 100 mks. Current breakers of these types require that the current conducting elements be replaced after each shot. For recent years vacuum arc quenching chambers with an axial magnetic field are successfully employed as repetitive performance current breakers, basically for currents up to 40 kA. In the report some results of researches of a vacuum switch modular are presented which we used as a prototype switch for currents of the order of 100 kA.

1. INTRODUCTION.

SFT power supply system is rather complex. It uses multi-coiled inductive stores of toroidal and cylindrical shapes of both transformer and conventional types. A simplified circuit of the transformer type toroidal inductive store (TTIS) is presented in Fig.1. It has two multi-coiled windings, L1 - primary winding and L2 - secondary one. TTIS has the following parameters:

- primary winding inductance, mH	- 70
- secondary winding inductance, mH	- 0.5
- number of coils of primary and secondary windings	- 32
- maximum current via a coil, kA	$I_1 = 150$ $I_2 = 830$
- windings coupling coefficient	- 0.92

Primary winding coils are connected in series-in-turn with resistors shunted by opening switches, secondary winding coils can be connected in parallel to a common load, or in series-in-turn with the toroidal field winding coils. The TR must provide current input and output according to a program and current sustaining in the load during the pulse.

Energy delivery to TTIS starts when switches S1 - S8 shunting the resistors in the primary winding in the course of energy storage are opened. When energy output must be stopped the resistors are shunted again by closing switches. To reduce the overvoltage level opening switches are actuated under a strict sequence, the next one operates only after the previous one. The total switch operation time should not be longer than that of energy delivery to the load.

In this circuit reduction of maximum power per a switch is achieved by using non-linear thermal resistors.

At primary winding currents of the order of 100 kA it is possible to achieve a 800 kA current pulse with a current rise time of 20 ms and total pulse duration of 200 ms in the secondary one. Switching voltage across a single switch must be 40 kV.

All the above-mentioned requirements can be met if a vacuum arc quenching chamber KQB - 20-100/1600 developed and designed in the Institute is used as a switching element. A required service life can be achieved by using several chambers connected in parallel¹. Vacuum arc - quenching chambers employment provides repetitive operation in both opening and closing mode.

2. VACUUM CHAMBER DESIGN

Most perspective are vacuum chambers with axial magnetic field, which reduces arc voltage and sustains its burning. The arc is of a diffuse type with many cathode spots, uniformly distributed along the contact surface. Opening switches with such chambers are exploited in some experimental facilities.

The vacuum chamber developed in the All-Russian Electrotechnical Institute with contacts producing an axial magnetic field has the following parameters (all the values for 50 Hz frequency):

$I_{\text{open}}/I_{\text{therm}}/I_{\text{ee,dynamic}}, \text{ kA} = 100/100/260$

$U_{\text{nom}} = 15.75 \text{ kV}$, weight = 50 kg

over all dimensions - 720 x 280 mm.

The arc quenching chamber has contacts made of chromium - copper compound (Cu - Cr 50/50). Magnetic field value H_m at minimum voltage across the arc and at arc current of 5 kA is 30 mT, the ratio $H_m/I_{\text{arc}} = 6 \text{ mT/kA}$ being constant in the wide range of currents. The main advantage of a new contact system developed in the Institute is the possibility to have any values of the ratio H_m/I_{arc} and to attain a precise value of U_{min} .

The contacts of this chamber are not float and in the close position they touch each other only by central parts with effective radius $R = 30 \text{ mm}$ (diameter of the contact is 190 mm). When the contacts start to separate arc always occurs only in the center. Contact erosion is weak along the whole surface excepting the central part where a constricted arc always occurs. Specific contact erosion is $w = 4.8 \cdot 10^{-4} \text{ g/K}$.

The chamber has the following peculiarities in the design:

- silfon are provided on the sides of both movable and unmovable contacts, which greatly reduces the stresses in the ceramic frame.
- On the back side of the field producing coil there are provided rigid elements, they prevent its strain due to electrodynamics stresses.

3. VACUUM SWITCH MODULAR DESIGN

Vacuum switch module consists of two equal vacuum chambers arranged vertically in a rigid metal frame with the following dimensions: 0.5 x 1.0 x 1.8 m. Both parallel and series connections are possible via equalizing resistors and additional inductances with one - turn saturable reactors. The contact resistance of the switch in the close - position is of the order of 35 mΩ, the necessary pressing is provided by two springs for each chamber, the total force - 150 kg. The contacts are driven pneumatically by a pressure $2 \cdot 10^7 - 4 \cdot 10^7 \text{ Pa}$. The rod of the operating plunger is connected to the electrodes by a link and is isolated from the contact system to a voltage of 30 kV. The contacts moved apart to a distance of 17 mm for time no longer than 25 mks. There is a position indicator which produces a control pulse triggering a counter-current capacitance at the moment when the interelectrode distance is of a required value / from 5 to 15 mm /.

The counter-current system exploits a 4-member LC forming line with pulse capacitor banks IKM - 50/9 (50 kV, 9 mF). Vacuum valve **PBY** - 40 also developed in the Institute is used as a closing switch².

4. ANALYSIS OF THE BASIC SWITCHING RESTRICTIONS

Counter-current system must provide such current decreasing rate in zero vicinity that there could not occur a repetitive break-down in the gap. One of the causes for repetitive break-downs is a higher value of electric field in the negative electrode vicinity E_0 than the critical one - E_0 mainly determined by electrode material and its surface condition.

We have presented a physical model in which the mean life time - τ of ions in the inter electrode gap is the key parameter. The analysis shows that maximum electric strength at the negative electrode during the so-called after-arc period occurs within time of the order of τ . The ratio of τ and T times for which discharge current decreases from its maximum value I_0 to zero determines restrictions upon counter-current system parameters:

$$(dI/dt)^2 (dU/dt) < 2 (\epsilon_0 E_0^2 / 2)^2 (S^2 m) / g^2 w^2 q \tau^3 \quad (1)$$

$$I_0^2 (dU/dt) < 2 (\epsilon_0 E_0^2 / 2)^2 (S^2 m) / g^2 w^2 q \tau \quad (2)$$

where $\epsilon_0 = 8.85 \cdot 10^{-12}$ F/m; S - negative electrode area; m and q - effective mass and charge of ions respectively, w - factor connecting material mass vapoured from the cathode and electric charge through the arc; g - ion share in the vapoured cathode material, non-dimensional factor $0 < g < 1$; $\tau = L/2V$ L - interelectrode distance, V - characteristic ion velocity in quasineutral plasma.

The first restriction is valid at slow current output, when $\tau < T$, and the second one - for a rapid current output when $\tau > T$.

5. EXPERIMENTAL RESULTS

Switching capability of vacuum current breaker was tested in a conventional circuit with a standard IS. As a primary energy source for IS charging capacitor banks were used at nominal voltage - 2.5 kV. IS inductance 300 - 100 mH, maximum testing current - 30 kA. A low inductance 1 Ohm resistor was connected in parallel to VS.

A characteristic switching oscillogram is presented in Fig.2, where I_s - current through the breaker; I_{cc} - counter-current system current; 1 - oscillograms in the close position; 2 - the contacts moved apart to a distance of 10 mm. At 15 kA current and 10 msec arc burning the vacuum breaker reliably operated with zero-current duration of 30 mks and current output rate $dI/dt = 109$ A/sec. Counter-current capacitance was $C = 72$ mF, $U = 5$ kV, iron cross section of the reactor - 400 cm².

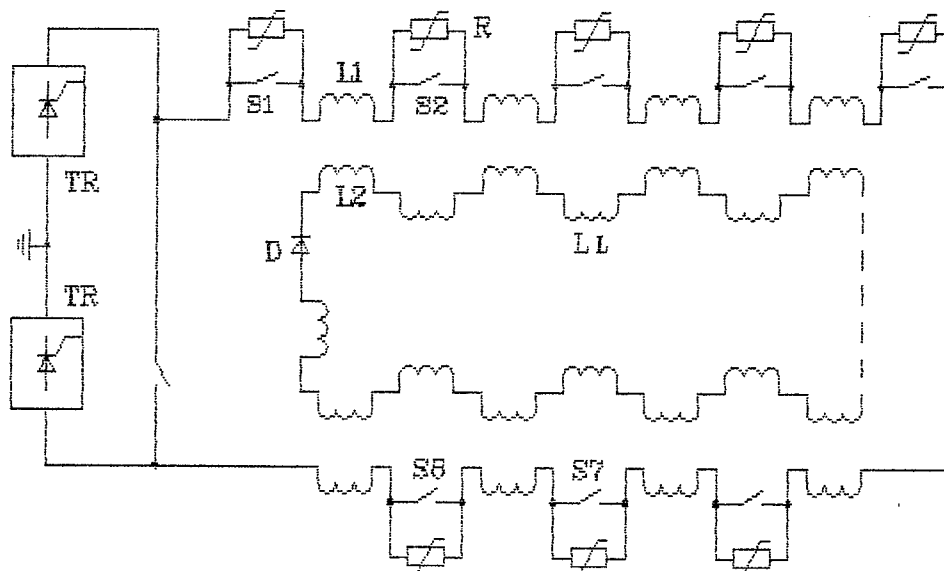


Fig.1.

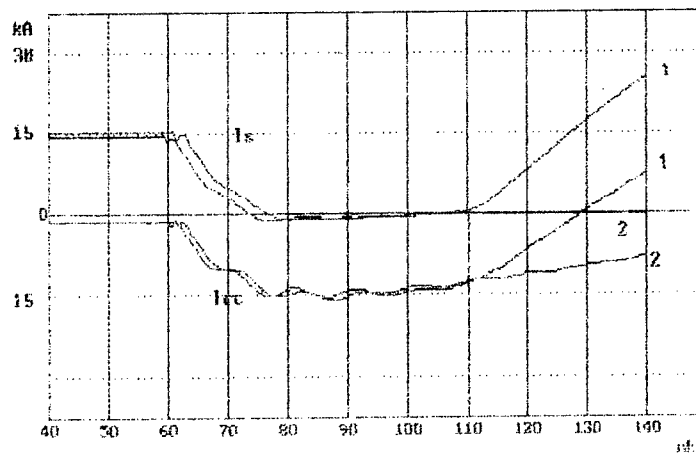


Fig. 2

6. CONCLUSIONS

The vacuum chambers with an axial field developed in the Institute for alternative current switches can be successfully used in switches of quasidirect current. At currents through a chamber of the order of 30 kA zero-current duration does not exceed 50 mks with recovery voltage rate $dU/dt = 200$ V/mks.

7. REFERENCES

1. V.P.Ivanov, V.A.Vozdvijenskii, V.V.Fedorov, "Vacuum interrupters use in the current switches for inductive energy storages", *Proc. International Workshop on Physics and Technique of High Power Opening Switches*, Novosibirsk, p.57, 1-2, July 1989
2. D.F.Alferov, V.A.Vozdvijenskii, I.O.Sibiriak, V.A.Sidorov, "Controlled vacuum discharger with staggered electrodes", *Instrum. Exp. Tech.*, Vol. 33, No. 5, Part 2, Sept.-Octob. 1990/April 1991

Strengthened magnetic field contacts for vacuum interrupters

A.A. Pertsev*, L.A. Rylskaya*, S.P. Chistyakov **

* All-Russian Electrotechnical Institute (VEI), Krasnokazarmennaya str. 12, 111250, Moscow, Russia

** NPP "ELVEST", Shefskaya str. 1, 620040, Ekaterinburg, D-40, Russia

ABSTRACT

Contacts design with amplified axial magnetic field for vacuum interrupters is described. Axial field specific induction reaches 10 mT/kA, that is the cause of time reduction for high current (>10 kA) arc transition from contracted to quasidiffuse modification. The arc movement on contacts surfaces is controlled by radial magnetic field up to arc transition from contracted to quasidiffuse modification. Both high current arc modifications control permits to decrease contacts separation velocity. During one pole tests 25-27 kA current was interrupted by contacts with diameter near 70 mm at 35 kV recovery voltage, 50 Hz, both at 1,1 m/s and 0,8 m/s separation velocity.

1. INTRODUCTION

In some specific fields of application, such as a commutation of steel melting furnaces transformers, there is a requirement for vacuum circuit-breakers, having a resource up to 100 thousand cycles. It is easier to make this circuit-breaker and it will be cheaper, if circuit-breaker elements are less given to mechanical actions and it may be achieved by reducing vacuum interrupter contacts velocity, particularly during current interruption. However, there is arc time increasing in this case because of a smaller contact velocity and accordingly lesser contact gap at the first current zero moment, contact gap is broken under recovery voltage and the arc recommences. As a result of the contact velocity reduction the share of interruptions increases not at the first current zero passing but at the second one, contacts heating is increased and the vacuum interrupter current interruption ability is decreased. Besides it, when using vacuum interrupters with axial magnetic field in circuit-breakers, it is need to restrict existence time of moving contracted arc (this arc certainly appears when the second half-wave of current begins [1]) by two-four milliseconds, there will be the arc transition to quasidiffuse modification during this time. Essential exceeding of this time can lead to advantages loss of axial magnetic field contacts. In particular, there is heat load increasing on a steam screen, surrounding contacts, during the contracted arc existence, that is caused by more than tenfold increasing of ion current, flowing towards the screen. As a result it can be overheating and in the case of insufficient arc movement velocity it can be even overwelding of the screen. The contracted arc can prove to be the cause of an extreme disturbance of recovery voltage distribution between the contacts and the steam screen [2]. If after quasidiffuse arc modification the screen potential is caused by interelectrode capacities of an interrupter in 10-30 μ s after current interruption and its value is almost near to the mean-square value of both contacts potential, than after contracted arc modification the recovery voltage distribution in accordance with interelectrode capacities begins in 75-140 μ s. Up to this time expiration the screen potential is practically equal to the positive contact potential, and all recovery voltage, including transient recovery voltage amplitude, is held just by one half of the interrupter insulating tank length and one half of the interelectrode gaps. This recovery voltage distribution disturbance keeps during a lot of half wave periods of rated frequency, increasing the probability of an interrupter internal insulations breakdowns. There is a description of contacts in [3], these contacts excite an axial magnetic field and admit the work at the reduced velocity. This property is achieved by increasing of an axial and radial magnetic field components of induction and by induction distribution optimization at the contact surface. The description of main design features of contacts and test results of vacuum interrupter with such contacts at short circuit clearing at normal (1,1 m/s) and reduced (0,8 m/s) separation velocity, are given below. Vacuum interrupters applications examples at this or another contact movement velocity in circuit-breakers for different use are presented.

2. CONTACT DESIGN

Fig.1. shows a schematic view of the contacts [1]. Each contact contains an inductor, which has an annular form, consisted of two stepped arc-similar elements. The starting parts of elements are joined with a current-conducting stem, the ending ones are free. The starting and ending parts of the adjacent elements of the inductor are mutually overlapped at a

length $P=(0,5-3)H$, where H is inductor height. The inductor covers disk-like electrode, which has a diameter somewhat lesser than the inner diameter of the inductor. The electrode has an electrical connection with both arc-similar elements due to electrode lugs. The electrode is deepened by 2-3 mm relative to the inductor surface, and as a result when the contacts are closed, they touch by the inductors. The electrode and the inductor contact surface have arc-resistant covering made, for example, from copper-chrom composition. The current I_0 , flowing through the stems and distributing the inductor arc-similar elements as indicated by the arrows, forms two one-direccted circular currents, exciting magnetic field with an axial-dominated component of induction in the contact gap. It is expected that control for the high current arc (amplitude more than 10 kA) in all its modifications will be achieved by contacts with such configuration. The control can be provided for all arc modifications: stationary contracted arc, appearing just after contacts opening, when the distance between them does not exceed 2- 3 mm [4]; a quasidiffuse (multichannel) arc, generated in a contact gap with a length more than 2-3 mm on condition that there is an excited axial magnetic field with sufficient induction in the contact gap; a moving contracted arc, generated in the contact gap with a length more than 2-3 mm due to restrike or reignition, and existing in it up to transition to the quasidiffuse modification [1].

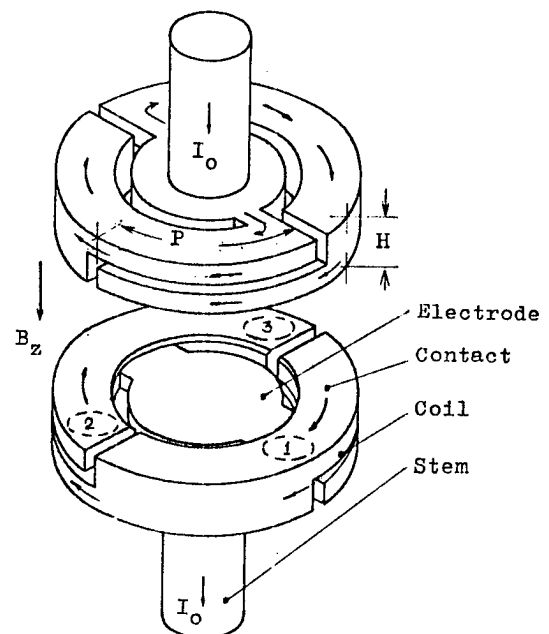


Fig.1. Contacts design with strengthened magnetic field induction. (The dotted line shows the places 1-3 of metallic stems, imitated the vacuum arc)

3. TEST RESULTS

The value of a specific axial magnetic field component B_z at different distances d between contacts surfaces was measured. The contracted arc was imitated by one metallic stem, which was placed turn by turn on parts 1-3, fig.1, providing electrical connection between two contacts. The quasidiffuse arc was imitated by three stems placed on the indicated parts simultaneously. B_z is characterized by data of table 1 (the outer diameter of inductor is 70 mm).

TABLE 1

$d, \text{ mm}$	2	18	40
$B_z, \text{ mT/kA}$	9,8 - 10	6,8 - 7,2	4,4 - 4,7 (6,5)

* B_z was chosen as an average on a circular area with diameter 20 mm. The area was placed in the middle of two contacts and had the same axis with them. The measurements were carried out at 50 Hz alternating current. The limits of changing B_z at variation of member and location of stems, imitating the arc, were pointed out. The result in the round brackets - the value of B_z on the disk electrode surface.

tion up to 2 the number of arc-similar elements, and then by their angular length increasing. The first admitted to raise the inductor circular current up to 0,5 I_0 , and the second - to make the circular current path in inductor a little bit more than one turn. The induction raise above the "optimal" value is dictated by the aim to short the time of the arc transi-

As follows from the table 1, the change of one stem location or the number of stems on the contact surface, has no influence on B_z component in practice. The value of B_z component reaches 10 reduces up to 4,4-4,7 mT/kA at $d = 40$ mm. As the field is not uniform B_z values increases directly near contacts surface. As one can see B_z value at contact surface is 1,4 times as much as in the middle of the gap at $d = 40$ mm. Of course, other field components, including B_r , increase together with B_z .

These B_z values are essentially more than usually realized "optimal" values, reaching 3-5 mT/kA for contacts with similar dimensions. It is known there is minimum arc voltage at the "optimal" induction [1]. Higher magnetic field induction, excited between contacts, fig.1, is caused by more magnetomotive force, developed by inductors. In turn, that is defined, first of all, by reduction

tion from contracted to the quasidiffuse modification. It is actually at the reduced separating contact velocity, when the cases of restrikes and reignitions become more frequent. These cases can lead, as it was noted, to the moving contracted arc appearance, with more intensified acting on contacts and steam screen in comparison with quasidiffusive arc. The reduction of the local influence of the contracted arc on the contacts and the screen is provided not only by the arc existence time shorting, but also by increasing the arc movement velocity on contacts and preventing its fixation on the edges of the radial slots which are on the contact surfaces. The prevention of the arc fixation is achieved due to mutual overlapping of the stepped arc-similar elements on the length P , that leads to increasing the field component B_r in the vicinity of the radial slots.

Magnetic field pressure on the contracted arc also becomes stronger because its base spots move directly on the inductor surfaces, near which B_r component has the most value. This circumstance is favourable not only for the positive influence on movement velocity of the moving contracted arc. Because of the forced value of B_r component at the contact surface, the existence time of stationary arc at the first stage of the contact movement is shortened ($d < 2$ mm and the output of the melted drops is decreased).

The contact interrupting capability at the average separation velocity 1,1 and 0,8 m/s is defined by interrupting 50 Hz current with value up to 27 kA in a single phase circuit at the recovery voltage 34-35 kV and the transient recovery voltage amplitude 69-81 kV. These electrical effects are typical for the circuit-breakers, destined for the work at 35 kV rated voltage. The contacts stroke was equal to 16 mm. The results are presented in table 2.

TABLE 2

Contact velocity m/s *	Interrupting current, kA	The number of interruptions successfull	unsuccessfull	The limits of the arc time values, ms
1,1	24 - 27	12	1	4 - 14
0,8	24 - 26	8	2	13 - 23

*) The average value of velocity at the first 10 mm of contact stroke is shown.

**) When the interruption was unsuccessfull the current was interrupted by the additive protective circuit-breaker in 60-90 ms from the moment of the tested interrupter contact separation.

One can see from the table 2 that the arc time did not exceed 14 ms at the velocity 1,1 m/s and the interrupting current 24-27 kA.

One of 13 interruption operations was unsuccessfull, the current was not interrupted by the interrupter, the arc time was 60 ms and was caused by current interruption with the help of the additional preventive circuit-breaker. The execution of the following current interruption operations did not reveal any aggravation in the interrupter work.

At 0,8 m/s velocity the arc time increased and was in 13-23 ms interval, that is caused by flowing the second half-wave

of the current. The corresponding arc voltage and interrupting current oscillograms are presented in fig.2. The first one of them gives the possibility to determine existence time of different arc modifications. From the moment T_1 when the contacts are opened till the first current zero passing, the arc undergoes the next modifications. There is the stationary arc up to the moment T_2 , until $d < 2$ mm. In T_2 - T_3 interval the quasidiffusive arc development takes place. This arc fills both contact surfaces and disk electrode surfaces. From the moment T_3 quasidiffusive arc exists, which shortly before current zero modifies into diffusive arc, extinguishing at the current zero passing. The arc voltage is characterized by the absence of the high frequency peaks in T_3 - T_4 interval, maximum arc voltage value at current magnitude does not exceed 60 V, that is exactly inherent in quasidiffusive arc. The arc voltage at the beginning of the second current half wave and T_4 - T_5 interval are characterized by the presence of high frequency peaks with amplitude 100 V and more. It shows that there is the moving contracted arc between the contacts, which are separated 9-11 mm distance from each other to this time. The axial magnetic field component in the gap of such length, taking into account table 1 data, is 8-9 mT/kA, and as can be seen from oscillogram, the contracted arc in these conditions turns into the quasidiffusive one for time not more than 2,5 ms. From the moment T_5 the voltage curve indicates on the quasidiffusive arc existence in the gap. The local acting of the diffusive arc on the contact surface is considerably less in comparison with the contracted arc influence. As a result there is cooling of the local contacts parts and the screen, heated by the contracted arc, in T_5 - T_6 interval. The steam density in the contact gap decreases and at the moment T_6 during the next current zero passing the current is interrupted.

The measurement results at 0,8 m/s velocity are presented in table 2. These results show, that the tendency of increasing the number of unsuccessful interruption operations is outlined under keeping the value of the interrupted current at 24-26 kA level. If at 1,1 m/s velocity there was one unsuccessful interruption from thirteen, then at 0,8 m/s velocity there were two unsuccessful interruptions from ten. We must note, that though the arc time in each of these two unsuccessful operations reached 90 ms, the following successful operations did not reveal the decrease of the current interruption capability of the interrupter. It proves, that examined contacts design is stable to the thermal overloads, appearing at the arc existence during several current half waves. Contacts and interrupter screen examination after such thermal overloads did not show any essential faults.

The contacts under consideration were applied in commercial type interrupters KДВ-35-25/1600 YXN2. These interrupters are used in type БВЦ-35 circuit-breaker at 35 kV rated voltage and type БВЗ-110 circuit-breaker at 110 kV rated voltage, produced by NPP "ELVEST" (Ekaterinburg city)[5]. The contact velocity is 0,7-0,8 m/s, the contact stroke 13-14 mm. The pole of БВЗ-110 circuit-breaker contain four interrupters, connected sequentially. Mechanical life of 35 kV circuit-breaker is 100 thousand "close-open" cycles at one time change of an interrupter. Mechanical life of 110 kV circuit-breaker is 40 thousand cycles without an interrupter change. Rated interrupting current is 20 kA. The pointed types circuit-breakers are used for the transformer commutation of electrothermal installations, where they are successfully exploited. In 35 kV type БВН-35 network circuit-breaker an interrupter contact velocity is raised up to 1,1-1,2 m/s, the stroke is increased up to 16-17 mm, owing to that rated interrupting current reaches 25 kA. Electrical and mechanical life of circuit-breaker is 20 thousand cycles at 1600 A current.

4. ACKNOWLEDGMENTS

Financial support of the reported research by the Russian Fundamental Research Fund (grant No. 93-02-17425) is gratefully acknowledged.

5. REFERENCES

1. S. Yanaby et al., "Vacuum arc under an axial magnetic field and its interrupting ability," IEE Proc. Vol.126, No.4, april 1979.
2. R. Gebel "Shield potential in vacuum interrupters after clearing of short circuits," IEEE Trans. on Plasma Science, Vol. 17, No. 5, p. 834, 1989.
3. A.C. 1725681 (СССР). "Контактная система для вакуумной дугогасительной камеры," А.А. Перцев, С.П. Чистяков. Публ. в Б.И., N 23, 1993.
4. С.М. Селикатова, И.А. Лукацкая, "Некоторые особенности движения вакуумной дуги отключения в магнитном поле," Журнал технической физики, т. XLII, в. 7, 1972.
5. Проспект НПП Элвест, "Вакуумные выключатели," г. Екатеринбург, 1993 г.

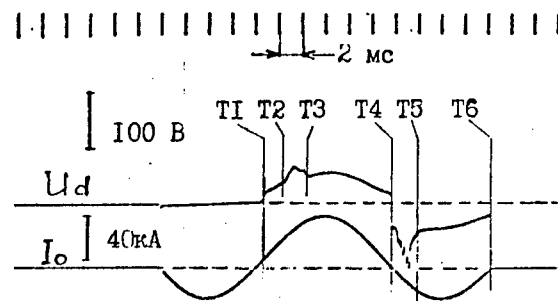


Fig.2. The arc voltage U_d between the contacts fig.1, at the arc existence during two current I_o half waves.

(T1 - contacts separation moment and stationary contracted arc appearance; T2 - T3 - the interval of the quasidiffusive arc modification formation; T3-T4 - the interval of the quasidiffusive and diffusive arc modifications existence; T4 - the second current half wave recommence moment; T4 - T5 - the interval of the moving contracted arc modification existence; T5 - T6 - the interval of the quasidiffusive and diffusive arc modifications existence; T6 - current interruption moment. The contact gap 16 mm is achieved to the moment T6).

Dynamic test and analysis of shield potential in vacuum interrupters

Wang Chengyu

Wang Jimei Ma Zhiying

No.4 Dept., Xi'an High Voltage Apparatus Research Institute,
Xi'an, 710077, P.R.China

Electrical Apparatus Div., Xi'an
Jiaotong University,
Xi'an, 710049, P.R.China

ABSTRACT

This paper studies the arcing and post-arcing medium-intensity recovery of vacuum arcs during short-circuit breaking of a vacuum interrupter by measuring the dynamic change waveforms of the relationship between shield potential, arc voltage and recovery voltage. On the basis of the experimental results, it makes mathematical derivation for the relationship between the vacuum interrupter shield potential and the voltage in contact gap. It also makes a theoretical analysis of changing regularity of the shield potential. It is proven that this method is feasible for deeper study of vacuum interrupter performance.

1. INTRODUCTION

When a vacuum interrupter is in static state, the shield potential is determined by its stable distribution capacitors against the anode and the cathode. While in course of short-circuit breaking, the dispersion of arc plasma toward the outside of contact gap and the bombardment of charge carriers cause the shield potential to change. The change features a transient nature. Therefore, we can study the dynamic change process inside the vacuum interrupter by measuring the dynamic waveforms of the shield potential.

2. METHOD TO MEASURE THE SHIELD POTENTIAL

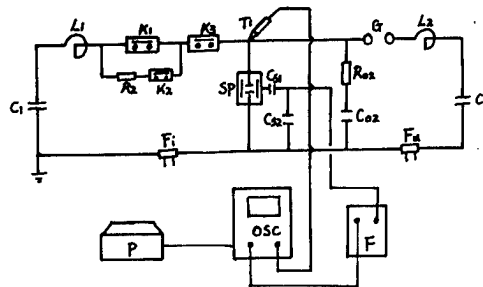


Fig.1 Test circuit for experiment

The power supply for the experiment is a synthetic circuit. A coaxial shunt is used to measure the arc current. A Tek-P6015 high-voltage probe is used to measure the arc voltage or recovery voltage. A capacitance divider is used to measure the shield potential. All the measured waveforms are memorized and printed by a memory oscilloscope. In order to get a true and complete picture of the dynamic change of vacuum interrupter during arc breaking, the response time of the measurement system is limited within 100ns; especially, the C_{s1} is less than $3pF$.

The experiment samples are commercially available vacuum interrupters of cup-shaped axial magnetic field (AMF) contacts and cup-shaped cross magnetic field (CMF) contacts.

In the following discussion, without special specification, the arc voltage division ratio is 1:1000V; the shield potential division ratio is 1:100V.

3. EXPERIMENTAL RESULTS

3.1 Analysis of arcing process

3.1.1 Influence of arc current and contact gap on arcing

There is a difference between the waveform of the arc voltage and that of the shield potential. When the arc current and the contact gap increase, the difference increases gradually. So does the high-frequency division superimposed on the waveforms, as shown in fig.2. This indicates that the arcing stability decreases. The dispersion of arc plasma toward the outside of contact gap increases. Under this circumstance, it is impossible and also incorrect to analyze arcing states by means of arc voltage values. We have to analyze arcing states according to waveforms.

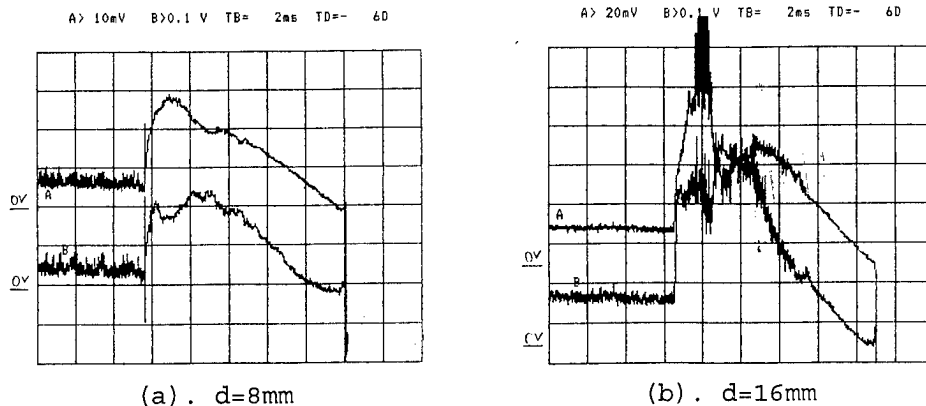


Fig.2 AMF contact contact diameter: 40mm. $I=15kA$.

3.1.2 Comparison of experimental results of AMF and CMF contacts

Under the same contact gap and the same arc current, we made an experiment by means of AMF and CMF contacts with the same contact diameter and the same shield diameter. The waveform shown in fig.3 was obtained.

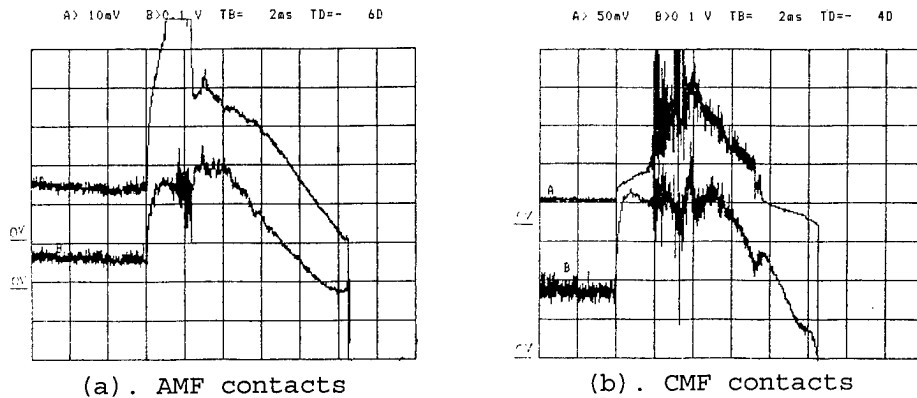


Fig.3 $d=8mm$, $I=15kA$

From fig.3, we can see that for vacuum arcs under the action of AMF contacts and those under the action of the CMF contacts, their non-stable states happen at different moments. For the AMF contacts, the superimposition of high-frequency division on the arc voltage and the shield potential waveforms happens mostly in the first $1/4$ period. This shows that for the AMF contacts, the arcing stability within the first $1/4$ period is poor. While for the CMF contacts, the superimposition of high-frequency division on the arc voltage and the shield potential waveforms happens mostly near the peak value of the arc current. This shows that for the CMF contacts, the arcing stability near the arc current peak value is poor.

3.2 Analysis of the post-arcing recovery process

In vacuum interrupters, many post-arcing breakdowns are often caused by the breakdowns in the space between the contacts and the shield. Therefore, in the following part, we will analyze the post-arcing recovery process by means of the recovery voltage and the shield potential waveforms.

The ratio of the contact diameter to the shield diameter is big, as shown in

fig.4. When the breaking current is small, the waveform of the recovery voltage conforms with that of the shield potential, as shown in fig.4(a). When the breaking current is large, distortion happens to the shield potential waveform, as shown in fig.4(b). This phenomenon has been well explained by Rudolf¹.

The ratio of the contact diameter to the shield diameter is small, as shown in fig.5. When the breaking current increases, the shield potential waveform is different from the recovery voltage waveform in not only phase but also amplitude. The difference increases when the breaking current increases.

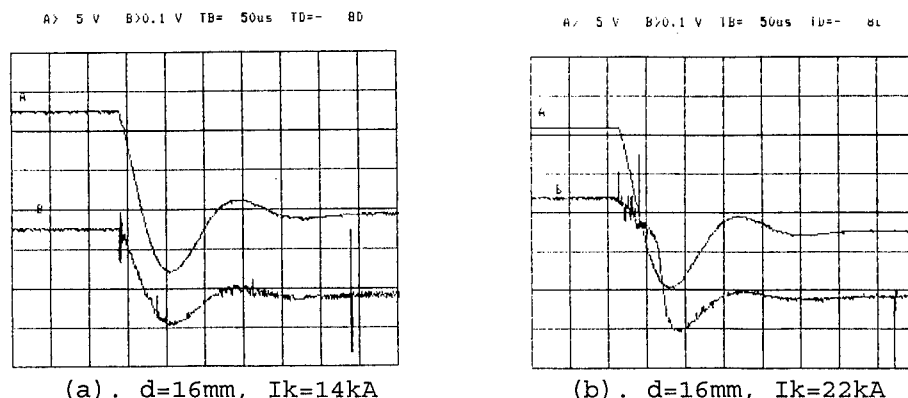


Fig.4. Waveforms of recovery voltage and shield potential
AMF contact diameter: 60mm; shield diameter: 85mm

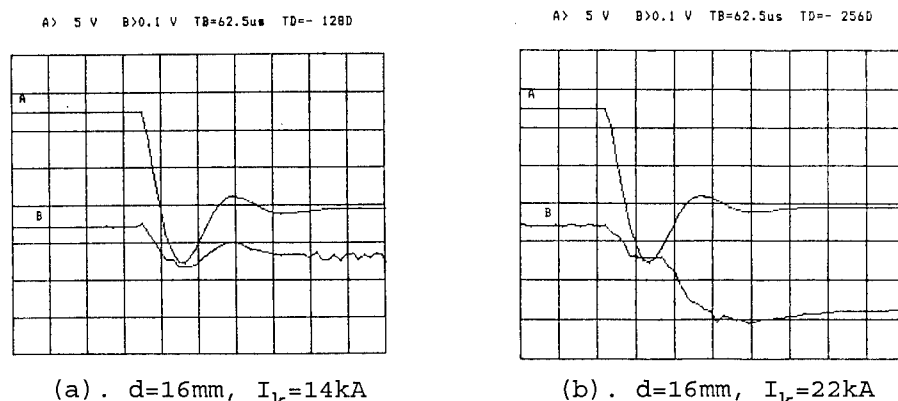


Fig.5. Waveforms of recovery voltage and shield potential
AMF contact diameter: 40mm; shield diameter: 120mm

From the above analysis we can see that to reduce the shield diameter properly is beneficial for the post-arcing recovery process of vacuum interrupters.

4. MATHEMATICAL ANALYSIS OF THE RELATIONSHIP BETWEEN SHIELD POTENTIAL AND VOLTAGE IN CONTACT GAP

From the above experimental results, we can see in the post-arcing recovery process, the shield potential is different from the voltage in the contact gap. From this difference, we can analyze the dynamic change of the arc plasma in the vacuum interrupter. This is very important for the deeper study of the running state of the vacuum interrupter.

4.1 Mathematical derivation of the relationship between the shield potential and the arc voltage in the contact gap

A mathematical model shown in fig.6 was set up.

In the model shown in fig.6, we can see that in the arcing process of vacuum interrupters, capacitance values of C_A and C_K are constant. The equivalent resistors R_A and R_K are leakage resistors caused by some of the charge carriers when they disperse toward the outside of the contact gap. The influence of the

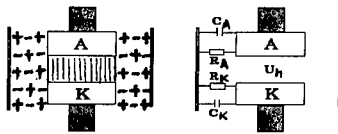


Fig.6 Illustration of arcing model

change of the arcing column is reflected on the values of the equivalent resistors R_A and R_K and hence on the shield potential waveform.

From this, we can obtain the following differential equation group on the relationship between the shield potential U_Z and the arc voltage U_h :

$$C_A \frac{dU_A}{dt} + \frac{U_A}{R_A} = C_K \frac{dU_K}{dt} + \frac{U_K}{R_K} \quad (1)$$

$$U_A + U_K = U_h \quad (2)$$

$$U_Z = U_K \quad (3)$$

The initial condition: $U_Z|_{t=0} = 0$.

In order to find the relationship between the shield potential and the arc voltage in the arcing process, we can make the following assumptions:

(a). The relationship between the arc voltage U_h and time is expressed as: $U_h = U_{hm} \sin \omega t$.

(b). The values of the equivalent resistance R_A and R_K are not related to time. From the assumptions, we can get:

$$U_Z = U_h \frac{R_K(1+j\omega R_A C_A)}{(R_A+R_K)+j\omega R_A R_K(C_A+C_K)} \quad (4)$$

In the design of vacuum interrupters, the geometrical positions of the two contacts against the shield should be as symmetrical as possible. So we have: $C_A \approx C_K$. This has been proven by experiments.

Hence equation (4) can be written as: $U_Z = \rho U_{hm} \sin(\omega t + \phi)$ (5)

where,

$$\rho = \left\{ \frac{[R_K(R_A+R_K)+2(\omega R_A R_K C_A)^2]^2 + [\omega R_A R_K C_A(R_A+R_K)-2\omega R_A R_K^2 C_A]^2}{[(R_A+R_K)+(2\omega R_A R_K C_A)^2]^2} \right\}^{1/2}$$

$$\phi = \text{tg}^{-1} \left[\frac{\omega R_A C_A (R_A - R_K)}{R_K(R_A+R_K) - 2R_K(\omega R_A C_A)^2} \right]$$

We can see the shield potential expressed in equation (5) differs from the arc voltage both in phase and amplitude. The amplitude of U_Z is ρ times of that of U_h ; while the phase difference between U_Z and U_h is ϕ . From the formula, we can see that this value can be positive or negative. U_Z may advance or lag in phase with U_h . When $R_A > R_K$, $\phi > 0$, U_Z advances in phase with U_h . Otherwise, it lags in phase behind U_h .

4.2. Mathematical derivation of relationship between the shield potential and the recovery voltage

The model shown in fig.6 can be used as a reference for this part of discussion. But the A and K poles should be reversed.

The resistors R_A and R_K are closely related to the dispersion process of the residual particles between the post-arcing contact and the shield. The dispersion state is reflected on their resistance values and hence on the shield potential waveform. So we can get the differential equation group of the shield potential U_Z and the recovery voltage U_H :

$$C_K \frac{d(U_H - U_Z)}{dt} + \frac{U_H - U_Z}{R_K} = C_A \frac{dU_Z}{dt} + \frac{U_Z}{R_A} \quad (6)$$

The initial condition: $U_Z|_{t=0} = 0$.

In the post-arcing recovery process, a shell is formed on the surface of the

cathod pole². This shell will extend gradually to the anode pole until the recovery process ends. Most of the transient recovery voltages fall on the shell. Therefore we will consider the resistance value of the shell to be very great in our following discussion.

One of the typical cases of the functional relationship between the post-arcing recovery voltage and time can be expressed as:

$$U_H(t) = U_{Hm} [1 - e^{-\alpha t} \cos \beta t].$$

where, the parameters U_{Hm} , α , and β are determined according to different waveforms.

Next, we will discuss the development of the post-arcing process by dividing it into five stages. In the discussion of each of the stages, we will regard R_A and R_K as constant values, as shown in fig.7.

a). The stage immediately after the arc current zero, as shown in fig.7(a). At this stage, the whole space of the shield is filled with post-arcing residual charge carriers. So we have: $R_A \ll \frac{1}{\beta C_A}$, $R_K \ll \frac{1}{\beta C_K}$.

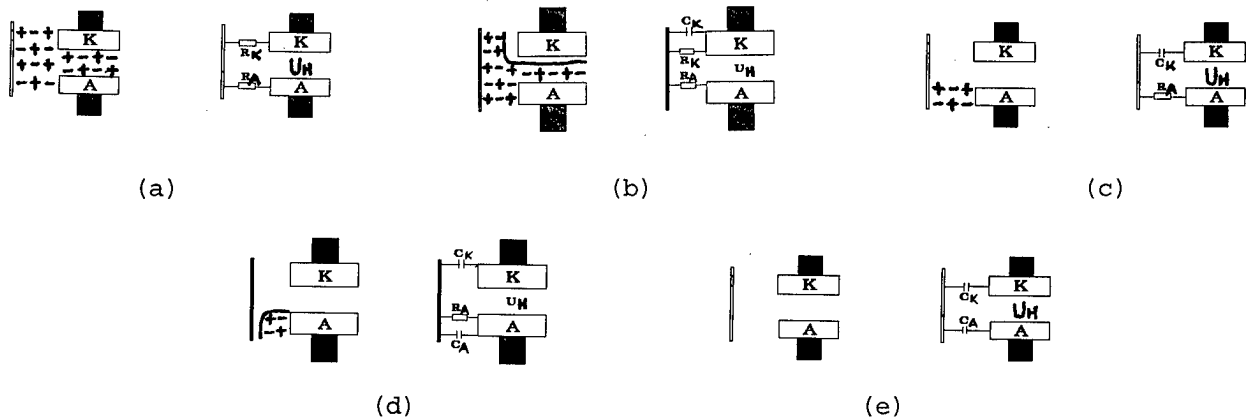


Fig.7. Post-arcing recovery process of vacuum interrupters

From equation (6), we will get:

$$U_Z = \frac{R_A}{R_A + R_K} U_H$$

For $U_H=0$, the shield potential $U_Z=0$. At this time, both the shield potential and the recovery voltage start from zero.

b). According to the post-arcing recovery model of medium intensity set up by Andrews and Varey², the recovery will start first from the cathode, as shown in fig.7(b).

At this stage, since the equivalent resistor R_K reaches a certain value $R_K \gg R_A$, because of the formation of the cathode shell and $R_A \ll \frac{1}{\beta C_A}$, to solve equation (6), we have:

$$U_Z = U_{Hm} [1 - e^{-\alpha t} \cos \beta t] - \frac{U_{Hm}}{\tau} e^{-t/\tau} \{ \tau (e^{t/\tau} - 1) - \frac{1}{(1/\tau - a)^2 + \beta^2} [e^{(1/\tau - a)t} (\langle 1/\tau - a \rangle \cos \beta t + \beta \sin \beta t) - (1/\tau - a)] \}$$

where, $\tau = R_A C_K$, which is a constant.

c). When the dispersion of the post-arcing residual charge carriers enters the state shown in fig. 7(c), $R_K \rightarrow \infty$. To solve equation (6), we will have:

$$U_Z = U_{Hm} e^{-\alpha t} (A \cos \beta t + B \sin \beta t)$$

where,

$$A = \frac{a/\tau - a^2 - \beta^2}{\beta^2 + (a - 1/\tau)^2} \quad B = \frac{\beta/\tau}{\beta^2 + (a - 1/\tau)^2}$$

If at a certain moment t_0 of this stage, $U_H \rightarrow U_{Hm}$ is a constant value, equation (6) will become:

$$C_K \frac{dU_Z}{dt} + \frac{U_Z}{R_A} = 0 \quad (7)$$

The initial conditions:

$$U_Z|_{t=0} = 0, \quad U_Z|_{t \rightarrow \infty} = \frac{C_K}{C_A + C_K} U_{Hm}$$

To solve equation (7), we have

$$U_Z = -\frac{C_K}{C_A + C_K} U_{Hm} (1 - e^{-(t-t_0)/\tau})$$

At this time, the shield potential is determined by the post-arcing recovery parameters of vacuum interrupters. It will decrease by exponential law until it finally approach to a constant value.

d). When the dispersion of the post-arcing residual charge carriers reaches the stage shown in fig. 7(d), $R_K \rightarrow \infty$, R_A is at a constant value.

For we have $C_A \approx C_K$, to solve equation (6),

$$U_Z = U_{Hm} e^{-\alpha t} (A \cos \beta t + B \sin \beta t)$$

where

$$A = \frac{a/\tau - 2a^2 - 2\beta^2}{4\beta^2 + (2a - 1/\tau)^2}, \quad B = \frac{\beta/\tau}{4\beta^2 + (2a - 1/\tau)^2}$$

The case described at the end of stage c may also happen here. The result will be the same as that described in stage c.

e). When the dispersion of the post-arcing charge carriers ends, the condition inside the shield is shown in fig. 7(e). At this stage, $R_A = R_K \rightarrow \infty$, C_A and C_K are all constants. To solve equation (6), we have

$$U_Z = \frac{C_K}{C_A + C_K} U_{Hm}$$

Therefore, after this stage the shield potential waveform will conform with the recovery waveform. But their amplitudes are different.

5. CONCLUSIONS

1. In the arcing process of vacuum interrupters, the phases of the waveforms for the shield potential and the arc voltage are different. The difference changes when the arcing state changes. Hence we can analyze the change of arcing states by means of the phase difference between the two waveforms.

2. In the post-arcing recovery process of medium intensity, the relationship between the shield potential and the recovery voltage changes throughout the whole recovery process. This includes amplitude difference and amplitude attenuation relationships. In the different stages of the post-arcing recovery, the relationships change.

3. By comparing the arcing waveforms of vacuum interrupters of AMF and CMF contacts, we find that the arcing non-stability of the AMF contacts happens at the rising stage of the arc current. While the arcing non-stability of the CMF contacts happens near the peak value of the arc current.

6. REFERENCES

1. Rudolf Gebel, "Vapor shield potential in vacuum interrupters after clearing of short circuits", IEEE Trans. on Plasma Science, Vol.17, No.5, Oct. 1989.
2. J.G. Andrews and R.H. Valey, "Sheath growth in a low pressure plasma", Phy. Fluids, vol.14, 1971.
3. Qu Xiuying, Thesis, Xi'an Jiaotong University, 1982.

Post-arcing recovery characteristics of vacuum interrupters under a high rising rate of recovery voltage

Wang Chengyu

Wang Jimei

No.4 Department, Xi'an High-voltage Apparatus Research Institute, Xi'an, 710077 PR, China

Department of Electrical Engineering, Xi'an Jiaotong Univ. 710049, PR, China

ABSTRACT

This paper studies post-arcing recovery characteristics of vacuum interrupters under the action of a high rising rate of recovery voltage (rrrv) by analyzing waveforms of recovery voltage and shield potential. It discovers that in the post-arcing recovery, there are two processes: electric recovery process and plasma recovery process. The two processes relate closely with the performance of a vacuum interrupter. The success of the breaking of a vacuum interrupter will rely on the plasma recovery process.

1. INTRODUCTION

The recovery speed of the post-arcing medium intensity of a vacuum interrupter is very high. Generally, arcing is put off after the first arc current zero. For this reason, vacuum interrupters are used more and more to break special circuits with high rrrv. Therefore, we think it necessary to make a deep study of the post-arcing recovery characteristics of medium intensity under the action of a high rrrv.

2. EXPERIMENT METHOD

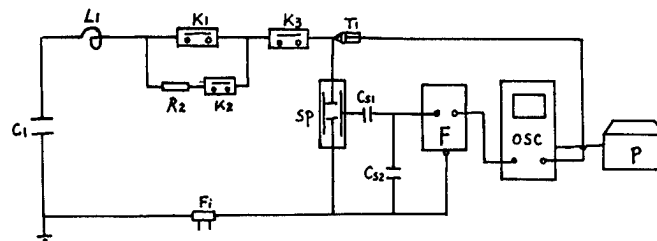


Fig.1 Test circuit for the experiment

The power supply for the experiment is an LC oscillation circuit. A Tek P6015 high-voltage probe T1 is used to measure the recovery voltage. A capacitance divider is used to measure the shield potential. All the experimental waveforms are printed by a Fluke & Philips PM3335, 60MHz memory oscilloscope. The rrrv is approximately 1.2kV/us. The response time of the measurement system is restricted within 100ns.

The experimental samples are commercially available vacuum interrupters constructed with cup-shaped axial magnetic field (AMF) contacts and cup-shaped cross magnetic field (CMF) contacts.

In the following discussion, without special description, waveform (a) will be the recovery waveform. Its voltage division ratio is 1:1000V. Waveform (b) will be the shield potential waveform. Its voltage division ratio is 1:100V.

3. EXPERIMENTAL RESULTS AND ANALYSIS

3.1 Analysis of the experimental results of AMF contacts

The post-arcing recovery voltage waveform is determined by the circuit parameters. It has nothing to do with the performance and the construction of the vacuum interrupter. While the shield potential waveform relates closely with the state of the post-arcing medium intensity recovery, as shown in fig.2. From fig.2(b), we can see that in the shield potential waveform, three parameters, i.e. electric recovery time (the time from the zero point to the peak value), plasma

recovery time (the time from the zero point to the end of the horizontal line) and the biggest amplitude value of the waveform oscillation, change with the breaking state of the vacuum interrupter. Among the three parameters, the plasma recovery time is most critical. It relates closely with the post-arcing dispersion state of electrically conducted residual particles. It embodies the post-arcing recovery of medium intensity.

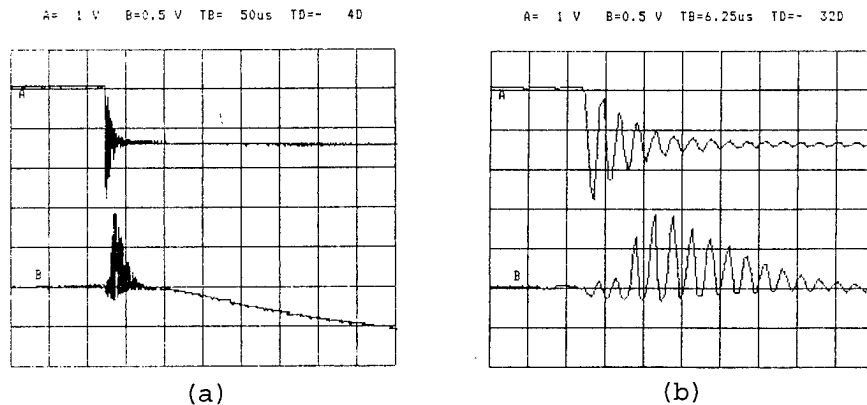


Fig.2 Recovery waveform of vacuum interrupter with AMF contacts

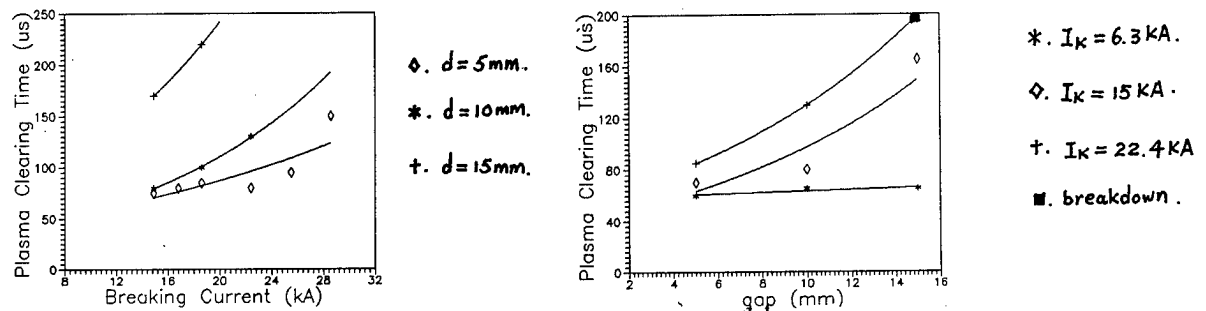


Fig.3 Relationship between the plasma recovery time and the breaking state

From the experimental results, we can see when the breaking current and the contact gap increase, the electric recovery time becomes longer. So does the plasma recovery time. But the oscillation amplitude of the shield potential decreases, as shown in fig.3.

3.2 Analysis of the experimental results of the CMF contacts

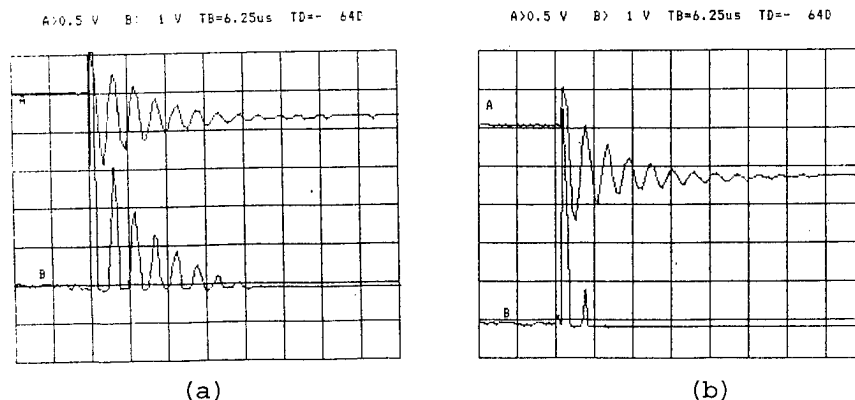


Fig.4 Post-arcing recovery waveform of the CMF contacts

By comparing the post-arcing recovery process for the AMF and CMF contact vacuum interrupters, we find that the waveform oscillation of the post-arcing shield potential of AMF contacts first increases and then attenuates to zero; while the waveform oscillation of the post-arcing shield potential of CMF contacts

always attenuates. The waveform for the AMF contacts is off-zero-line positive and negative oscillation; while the waveform for the CMF contacts is single-pole oscillation. From the experiment, we can see that the time for post-arcing plasma recovery of the CMF contacts is much longer than that of the AMF contacts.

Personally, we think these differences may be caused by the delay effect of the AMF contact post-arcing vortex on the attenuation of the axial magnetic field. The delay effect limits the dispersion of charge carriers and buffers the oscillation of the shield potential waveform. However, such delay effect and buffering do not exist in the vacuum interrupter with the CMF contacts.

3.3 Analysis of the waveform for breaking failure

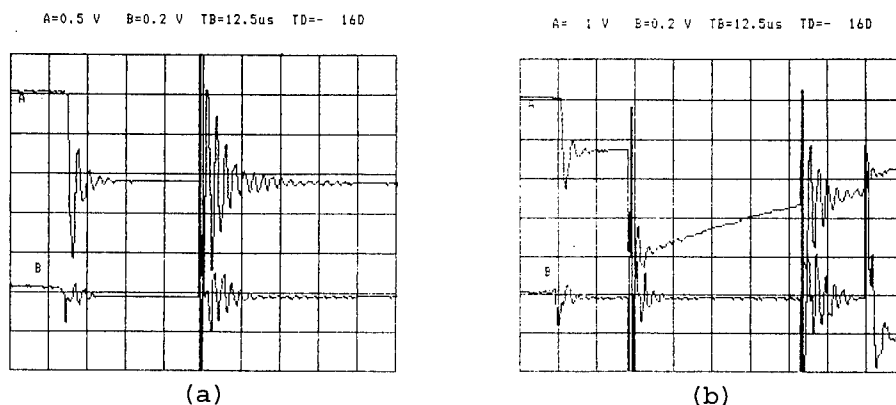


Fig.5 Waveform for breaking failure of vacuum interrupter with AMF contacts

In fig.5(a), breakdown happens to the recovery voltage waveform after 40us of current zero. The same thing happens on the shield potential waveform at this moment. Then the breakdown to the two waveforms recover by itself. From the breaking current waveform, we can see the breaking succeeds. While in fig.5(b), breakdown happens to the recovery voltage waveform after 24us of current zero. The same thing happens on the shield potential waveform. Then, the breakdown-recovery-breakdown process repeats for several times. From the breaking current waveform, we can see the breaking fails. Therefore, we think that each breakdown happens in the plasma recovery process.

4. CONCLUSION

From the analysis for the experimental results, we think there is a great deal of residual plasma in the contact gap and the shield space immediately after the current zero. With the elapse of time, the cathod shell begins to extend gradually. The recovery voltage is mainly applied to this shell.

In the post-arcing recovery process, there is electrically conducted residual plasma (not neutral metal vapor) left in the shield space. It short circuits the shield and the anode. The recovery voltage mainly drops on the shell that grows on the cathod surface and extends continuously. Therefore, the electric field intensity inside the shell is usually very great. In addition, the recovery process is unstable. These factors cause the shell to breakdown and hence make the breaking fail.

Non-stability of post-arcing recovery process in vacuum interrupters

Wang Chengyu

Ma Zhiying Wang Jimei

No.4 Department,Xi'an High-voltage
Apparatus Research Institute
Xi'an, 710077, PR,China

Electrical Apparatus Div.
Xi'an Jiaotong Univ.
Xi'an, 710049, PR, China

ABSTRACT

This paper measures and analyzes the waveforms of recovery voltage and shield potential. It discovers that in the shield potential waveform, when the breaking current is close to its limit, an irregular distortion happens to it. It is proved that not only the speed of post-arcing recovery process varies, but also non-stability exists in the process. This non-stability increases as the breaking current reaches its limit. The non-stability may cause post-arcing breakdown and breaking failure.

1. INTRODUCTION

In short-circuit current breaking process in a vacuum interrupter, at the moment of arc current zero, there are a large number of residual arc ions, electrons, neutral particles and metal vapour particles in the spaces of the contact gap and between the contacts and the shield. With the dispersion of these residual particles, the post-arcing voltage standing capability of the vacuum interrupter increases gradually until it becomes a steady value which is determined by the contact surface conditions. In the dispersion process of the residual particles, if at an arbitrary moment, the transient recovery voltage value is greater than the medium recovery intensity, post-arcing breakdown will happen, which will cause breaking failure. Therefore, the success of breaking of the vacuum interrupter will mostly rely on the post-arcing recovery state of medium intensity.

2. METHOD TO MEASURE THE SHIELD POTENTIAL

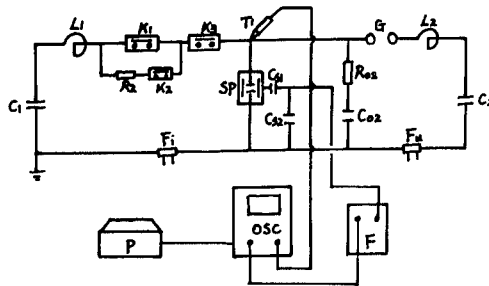
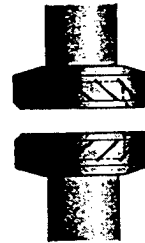
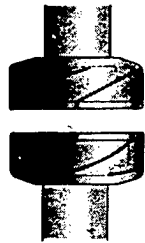


Fig.1 Test circuit of the experiment

The power supply of the experiment is a synthetic circuit or an LC oscillation circuit. A Tek-P6015 high-voltage probe is used to measure the recovery voltage. A capacitance divider is used to measure the shield potential. All the measured waveforms are printed with a PM3335, 60MHz memory oscilloscope. To perform the experiment with a synthetic circuit, the amplitude of the recovery voltage is 15.5kV; the rising rate is about 0.34kV/us. To perform the experiment with an LC oscillation circuit, the rising rate of recovery voltage (rrrv) is about 1.2kV/us. In the experiment, we pay more attention to the phase or time difference between waveforms than to the amplitudes of waveforms. Since the time for the post-arcing recovery is very short (generally at the class of micro second), we have limited the response time for the measurement system within 100ns in order to get a real and complete picture of the post-arcing recovery process.

The samples for the experiment are commercially available cup-shaped axial magnetic field (AMF) contacts and cup-shaped cross magnetic field (CMF) contacts, as shown in fig.2.

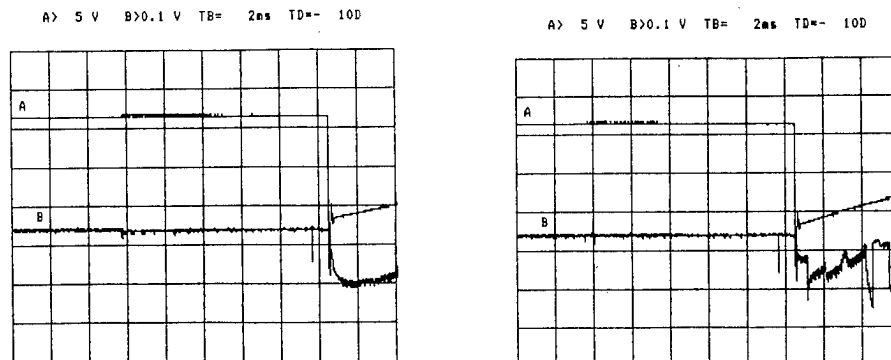
In the following discussion, without further specification, waveform (a) will be the recovery voltage waveform. Its voltage division ratio is 1:1000V. Waveform (b) will be the shield potential waveform. Its voltage division ratio is 1:500V.



(a) AMF contacts (b) CMF contacts
Fig. 2 Sample contacts for experiment

3. EXPERIMENTAL RESULTS AND ANALYSIS

3.1. Standard 10kV class recovery voltage being applied



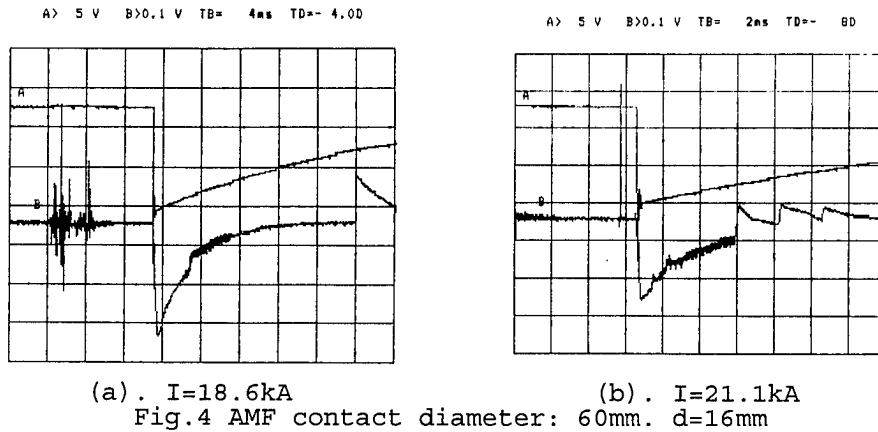
(a) $I=25.5\text{kA}$ (b) $I=28.6\text{kA}$
Fig.3. Diameter of the AMF contacts: 60mm.
Diameter of the shield: 120mm. $d=6\text{mm}$.

Under the action of 10kV class recovery voltage, when the contact gap is small ($d=6\text{mm}$) and the breaking current reaches its limit, as shown in fig.3(a), the waveforms of the recovery voltage and the shield potential keep smooth. This indicates that the post-arcing recovery process of medium intensity is stable. When the breaking current reaches its limit (The breaking for this current for the second time fails.), as shown in fig.3(b), a very serious fluctuation will happen to the shield potential waveform. This shows the non-stability of the post-arcing recovery process under this state. Namely, the dispersion process of the residual particles fluctuates unregularly.

When the contact gap is big ($d=16\text{mm}$), we find the poles for the shield potential reverse, as shown in fig.4. If the breaking current is small, the time for the pole reversion is longer, as shown in fig.4(a). With the increase of the breaking current, the pole reversion time becomes shorter, as shown in fig.4(b).

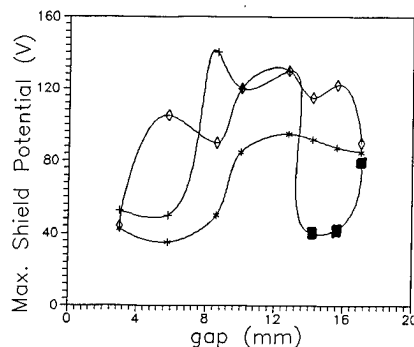
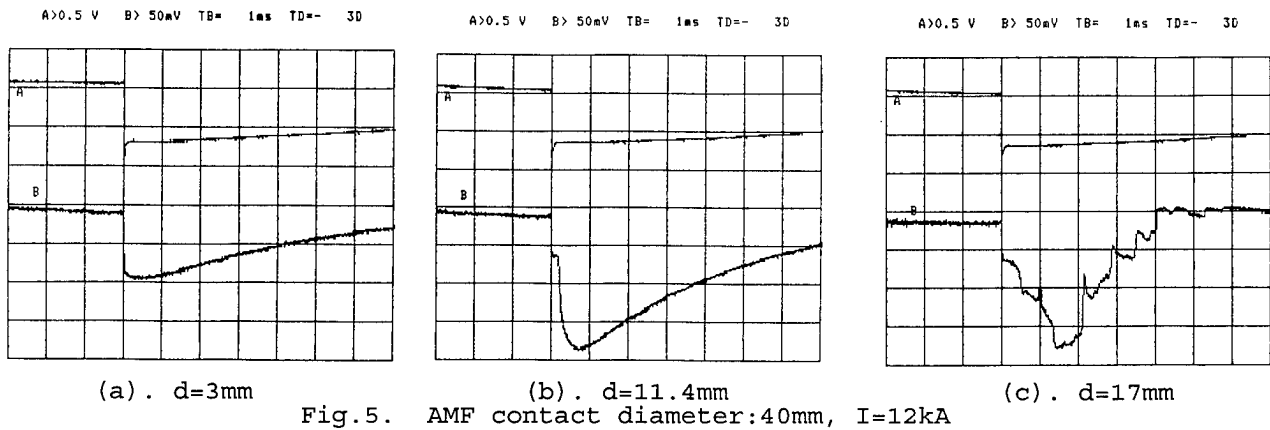
The reversion of the poles of the shield potential is caused by the surplus positive ions accumulated on the shield because of the bombardment of the post-arcing residual particles. Or it is because a large number of secondary electrons are emitted and make the shield potential higher. This will cause the electric field intensity between the shield and the contacts to increase. Under this circumstance, breakdown is likely to happen. From this result, we can see the pole reversion of the shield potential indicates only the breaking current is very close to its limit. It has not reached its limit.

From the above, we can see that the dispersion of the residual post-arcing particles is a ununiform oscillation process. Hence, we think the recovery of post-arcing medium intensity is a unstable process.



3.2. High rising rate of recovery voltage

Next, we will study the stability of post-arcing medium intensity by increasing the rrrv from 0.34kV/us to about 1.2kV/us .



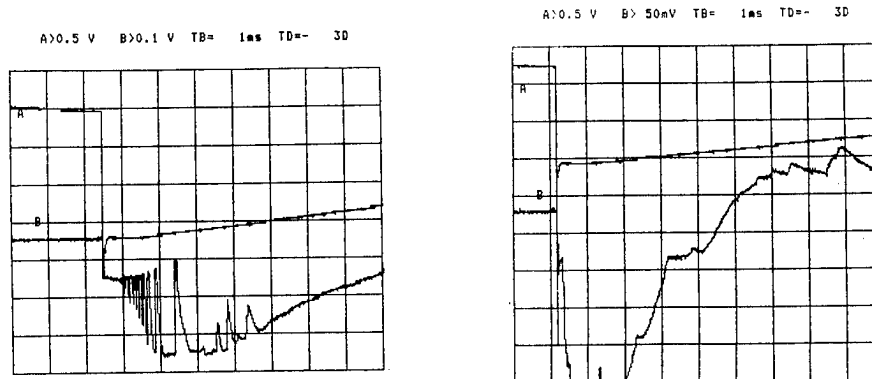
- *. Curve 1.
- + . Curve 2.
- ◇. Curve 3.
- . Pole reversion.

Fig.6 Relationship between the contact gap and the shield potential

1. AMF contact diameter:40mm; shield diameter:120mm; $I_K=12\text{kA}$
2. AMF contact diameter:60mm; shield diameter:120mm; $I_K=20\text{kA}$
3. AMF contact diameter:60mm; shield diameter: 85mm; $I_K=22\text{kA}$

In fig.6, we used the same AMF contacts with diameter of 60mm. The shield diameters are 120mm and 85mm respectively. We can see that for the shield with diameter of 85mm, until the contact gap becomes 17mm, pole reversion does not happen. This shows that its post-arcing recovery is good.

When the breaking current and the recovery voltage become constant, as the contact gap increases, the amplitude of the shield potential increases gradually until unstable oscillation and pole reversion happen, as shown in fig.5. One phenomenon deserves our attention: as the contact gap or the breaking current increases, there is a step in the shield potential waveform. The step tends to last longer. The step often becomes shorter and even disappears when the breaking current is close to its limit. Instead of the step, non-stability or pole reversion happens to the shield potential waveform, as shown in fig.7.



(a). $d=21.7\text{kA}$

(b). $d=22.4\text{kA}$

Fig.7. AMF contact diameter:80mm. $d=10\text{mm}$

4. CONCLUSION

When the breaking current of in the vacuum interrupter is close to or reaches its limit, a serious non-stability will happen to the post-arcing recovery process. Therefore, we can judge the limit value of the breaking current by observing whether there is an unstable oscillation or pole reversion on the shield potential waveform.

5. REFERENCES

1. Rudolf Gebel, "Vapor shield potential in vacuum interrupters after clearing of short circuits", IEEE Trans. on Plasma Science, Vol.17, No.5, Oct. 1989.

EXPERIMENTAL INVESTIGATION ON THE ION DEFFUSION PERFORMANCE IN VACUUM INTERRUPTER BY MULTI-CHANNEL ARRAY PROBE

Wu Jian—wen

Xi'an Jiaotong

Uni. Xi'an(710049),

Shaanxi, P. R. C

Yuan Shun .

Northern Ele. Power

Test & Research

Insti. Shenyang, P. R. C

Wang Yi

Dalian Uni.

of Technology P. R. C

Wang Ji—mei

Xi'an Jiaotong

Uni. P. R. C

ABSTRACT

In this paper, the multi-channel array probes have been applied. And the computer measuring system has been adopted to deal with the measuring results to get the electron density and electron temperature at the point of the probe in vacuum chamber. And the electrode with self-axial magnetic field can be analysed comparing with electrode with self-radial magnetic field by the distribution of electrode density in the chamber to study the effect of magnetic field on the diffusion ion.

1. INTRODUCTION

Vacuum arc is metal vapour arc. Metal vapour, electrons and ions come mainly from cathode under low current. But the electron, ion and metal vapour come from the spot or several spots on the surface of the cathode. The cathode spots move at very high speed on the surface of cathode. The current density forming the cathode spots is very high. Electron emission is due to heat-field emission. The position where spots appear is relative with the roughness of cathode surface. Many scientists focus their working on the contact surface, the material of electrodes and forming process of anode spot¹. Some scientists studied the diffusing procedure of ions and electrode. For example, prof. R. L. Boxman researched the electron and vapour densities in a high current vacuum arc by interferometric measurements. The distribution of electrode density is obtained on the electrode density(see fig. 1)². H. Toya measured the electron temperature by the spectroscopic measurement. The measuring results is shown in fig. 2.³

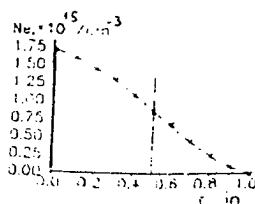


Fig.1 I-3kA. D-lin

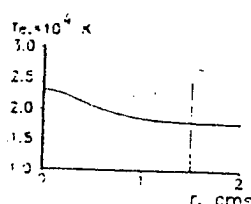


Fig.2 I-10kA D-3cm

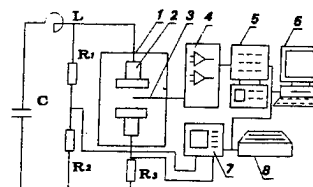


Fig.3 Testing and measuring circuit
1-chamber 2-electrode 3-probes 4-measuring circuit
5-transient recorder 6-computer 7-recorder 8-printer

In this paper, the axial and radial distribution of electron has been gauged whether inside the arc column of outside the arc column by the axial and radial array probe. The diffusion performance of electron and the formation of anode spot can be observed when interrupting a high current.

2. TEST SETUP AND MEASURING RESULTS

Testing circuit is shown in fig. 3. The vacuum degree is 8×10^{-5} Pa in a detachable chamber. Cup structure contact with axial magnetic and spiral structure with radial magnetic has been used in this experiment(see fig. 4, 5). High voltage pulse trigger has been fixed on the down electrode to form the vacuum arc between electrodes.

The distance between electrodes is adjustable. Axisymmetric array probes have been applied to solve the effect of space potential of ions by single probe. Meanwhile, the probe characteristics curve of double array probe is better than single probe as to magnetic field. Three group of double array probes (a), (b) and (c) is horizontal section. The position of probe can be adjustable. The probes are made of Mo wire(diameter 0.6mm and length 3mm). Each group of probes is applied by sew voltage, the peak value is minimum for the group which is the nearest one to center. But the output current is maximum.

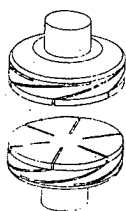


Fig.4 The electrode with cup axial-magnetic field structure

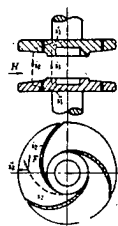


Fig.5 The electrode with spiral radial-magnetic field structure

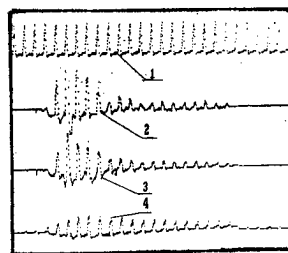


Fig.6 The probe voltage and current
1-probe voltage 2-(a)probe current
3-(b)probe current 4-(c)probe current

Probe current turns to voltage by high frequency current transformer and resistance. The signal has been collected and restored by multichannel transient recorder. Then, the data is handled to draw the curve of voltage and current of probe(fig. 6) At last, the electron temperature and electron density deduced from voltage and current curve above.

In this experiment, the arc current is 2kA—12kA. And charged voltage is 400~1000V for hypothetic circuit.

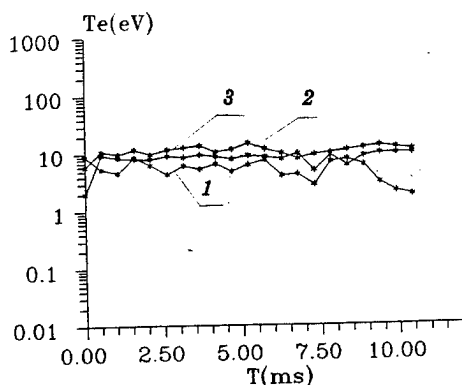


Fig.7 The relationship between electron temperature and arcing time for axial-magnetic field electrodes

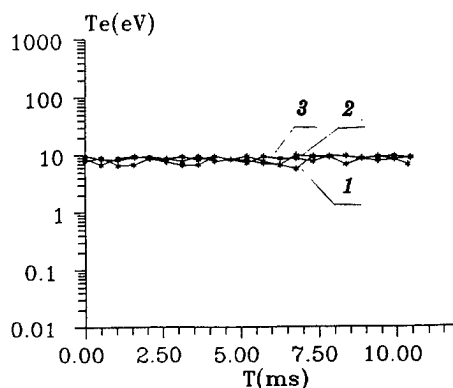


Fig.8 The relationship between electron temperature and arcing time for spiral radial-magnetic field electrodes

3. DISCUSSION

The relationship between electron temperature and density for axisymmetric double probes is following^{4,5}

$$kT_e = \frac{eI_{i0}}{2 \left. \frac{dI_d}{dV_D} \right|_{I_D=0}} \quad (1)$$

$$Ne = \frac{I_{i0}}{\alpha \cdot Z \cdot e \cdot Si} \sqrt{\frac{mi}{2kT_e}} \quad (2)$$

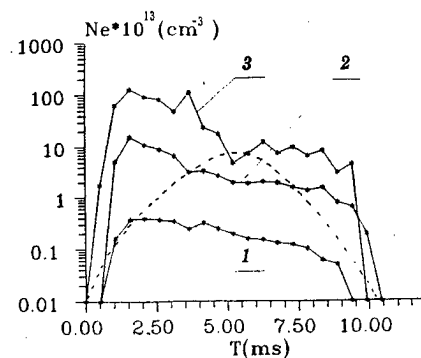


Fig. 9 The relationship between electron density and arcing time for axial-magnetic field electrodes

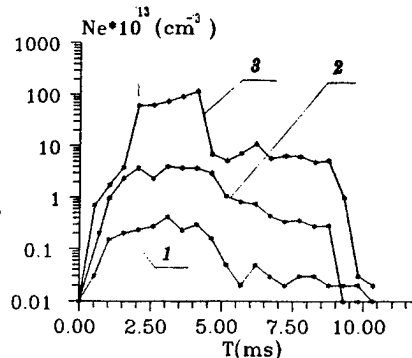


Fig. 10 The relationship between electron density and arcing time for spiralradial-magnetic field electrodes

Where; I_{io} : ion saturation current. I_d : probe current. V_d : probe voltage. α : constant ($=0.4 \sim 1.0$). Z : ionizing parameters ($=1$). S_i : surface area of probe. m_i : atom mass of copper. k : constant.

Electron density and temperature can be calculated with formula (1), (2) by computer to get the fig. 7, fig. 8, fig. 9 and fig. 10. [1—(a) probe; 2—(b) probe; 3—(c) probe]

Fig. 7 and fig. 9 are about diameter 60mm CuCr electrode with axial magnetic field. The distance between electrodes is 16mm. The array probe is the center position between electrodes.

Fig. 8 and Fig. 10 are about diameter 60mm spiral structure with radial magnetic field. The distance between the electrodes is 16mm. The array probes are the center between electrodes. The electron temperature near the center of the vacuum arc is lower for axial magnetic field. And the electron temperature is higher far from the center of arc. It is different with other kinds of arcs. By many experiments, the total temperature is lower because of low power electron constrained in arc column and high power electron escapes from vacuum arc column. so the electron temperature is higher far from vacuum arc column. But there is not this phenomena far electrodes with radial magnetic field structure (see fig. 9).

The electron density is proportional to arcing times or arc current (see fig. 8, 9) from so much experimental data. A great part of data shows the movement at electron density peak is earlier than the moment at current peak. It is because the metal vapour density is low in 1~2ms when arcing begins. Metal atom is seldom ionized and main conductor in the vacuum arc are electrons.

Fig. 11 is the distribution of electron density. The electrode density dropped down more quickly at radial direction outside of vacuum arc for axial magnetic structure than radial magnetic structure. The total electron density spread freely in vacuum is more quickly than column gas and ball shape gas. This tells us the electron move at a certain direction and influenced by electric field and magnetic field.

The distribution of the electron density at axial direction for spiral structure under same current is shown in fig. 12. From fig. 12, the nearer to center of arc column, the higher electron density is. This is because of serious constriction of arc.

The relationship between electron density and the gap between electrodes is shown in fig. 13. There is a maximum value of electron density at a certain position.

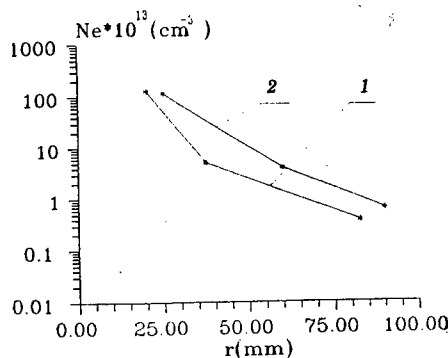


Fig.11 The distribution at radial radition
1-for axial-magnetic field electrodes
2-for spiral radialmagnetic field electrodes

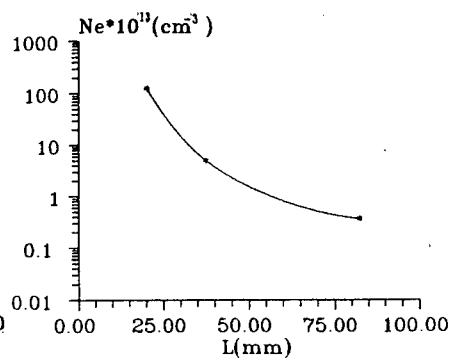


Fig.12 The distribution of electron density at
axial radition for radial-magnetic field electrodes

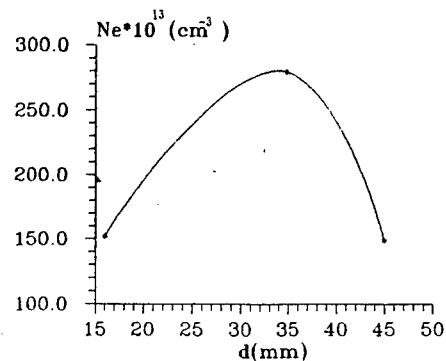


Fig.13 The relationship between of electron density
and gap length for axial-magnetic field electrodes

The axial magnetic field is weaker than other positions when the gap between electrodes is becoming large. And the diffusion of the center of arc is serious. So the electron density (the gap between electrodes is 45mm) is lower than the electron density of the center of vacuum arc (the gap between electrodes is 35mm).

4. CONCLUSION

- The electron temperature is not lower from the center to outside of arc at radial direction. The electron temperature outside of arc is higher than in the arc.
- The electron density for radial magnetic field structure is: lower than the one for axial magnetic field under same current.
- The electron density for radial magnetic field is drop down more *slowly* than the one for axial magnetic field.
- The distribution of electron density and temperature at radial direction is relative with the gap between electrdes. And the distribution property is dependent on the diffusion and the constriction of vacuum arc under a different gap between electrodes.

5. REFERENCES

1. C. R. Mitchell, "High—Current Nacvmm Aarcs", P. IEE. , 1970
2. R. L. Boxman "Interfermltic measurments ofelection and Vapor densitis in high—current Vacuum arc" J. Appl phys 45, 1974
3. H. Toya, el all "Spectroscopic measurements and analysis of high—current vacuum arc near copper cathode" IEEE Trans. plas. Sci. , 14, august, 1986
4. Phys Fluids, 8, 73(1965)
5. Ann physic, 15, 69(1965)

Dynamic insulation in vacuum interrupters

Zou Jiyan; He Junjia; Cheng Lichun

Department of Electric Engineering
Huazhong University of Science and Technology
Wuhan, Hubei, 430074, P.R.China

ABSTRACT

Breaking capacity of vacuum circuit breakers (VCB's) is limited by dynamic voltage withstanding of their vacuum interrupters in a sense. Dynamic insulation in a vacuum interrupter can be represented externally by their dielectric recovery behaviour and the stability of voltage withstanding. The internal feature of dynamic insulation includes two sides: one is the weak points under high electric stress, the other is macro-particles produced in the process of breaking high current. Some experiments were made to investigate these features. After analysis of the results, we give some measures to improve dynamic insulation of vacuum interrupters.

1. INTRODUCTION

Vacuum circuit breakers (VCB's), as a new generation of switches, have found wide applications in power system. As the development of VCB's, they were asked having higher breaking capacity and higher reliability. One of the key questions is the dynamic insulation of their vacuum interrupters during the process of breaking high current. As distinct from static insulation, that is represented by static voltage withstanding of new vacuum interrupters, dynamic insulation means a voltage withstanding on the process of dielectric recovery and in some sense, the stability of insulation after high current breaking. Generally, the static voltage withstanding of a new vacuum interrupter is very high, but, when it is used to break high current it may fail to withstand recovery voltage, that is much lower in peak than the static breakdown voltage. Besides, the static voltage withstanding after high current breaking or just after some stand idle times will be deteriorated, we looked it as also a question of dynamic insulation.

Dielectric recovery is an external feature of dynamic voltage withstanding of vacuum interrupters. A former work gave some investigations on it and showed that the sheath field enhancement is the main cause of dielectric breakdown^[1]. Dielectric recovery behaviour was also affected by micro-surface reinforcement and thermo-reinforcement, which also indicates the internal causes of dielectric breakdown.

Latham R.V. analysed the breakdown in vacuum gaps and defined two field enhancement factors, β_0 and β_w , as the macro-enhancement and the micro-enhancement respectively^[2]. The points with high β factor and easy to cause a breakdown under high electric field stress were called "weak points". Generally they are micro-protrusions, impurities, and absorbed gas layers on the surface of the electrodes and the shields. He also showed that macro-particles, both conductive or insulative, made a large contribution on breakdown. Arc discharge can eliminate most of the weak points, but after the arcing they will be reproduced again by whiskey, edge of spot sites, impurities, and explosive gases from electrode materials. Besides, Gellert B., et al gave out a measurement of particles and vapor density after high current vacuum arcs by laser techniques^[3] and got verification of macro-particles existed in the gap when the arc extinguished. So the question of dynamic voltage withstanding should include two internal causes: the weak points and the macro-particles. And all our efforts were made just in these two fields. By means of experiments, we can find their action mechanism and the way to improve dynamic insulation.

2. EXPERIMENT SET-UP

A group of commercial vacuum interrupters were taken as the samples, they have the same ratings of 10kV/20kA-630A and same contact material, but different magnetic field constructions. Experiments

began from the process of conditioning after the vacuum chambers were sealed up. The source for conditioning was an AC transformer with the rating of 150kV-100kVA. A generally spark conditioning procedure was made in the air, and an ultra-high voltage conditioning was made with the samples immersing in transformer oil. The current breaking tests were made by a LC oscillated loop as showed in Fig.1, that can give out a rated load current of 10kV-630A, or a short circuit current of 10kV-20kA in power frequency. We measured the voltage withstanding of the samples before and after current breaking by impulses of $1.2 \times 50 \mu s$, and taken the highest impulse level that the sample can withstand 15 times continually as the breakdown voltage.

At the last, we dissected the samples and investigated the surface state of contacts by SEM, and related it with their dynamic voltage withstanding. The samples were acted by a single phase actuator S_p , and the signals were measured by F and D separately.

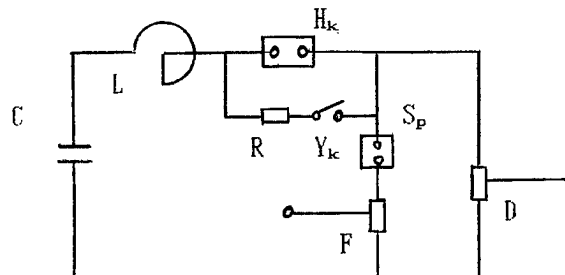


Fig.1 Test circuit for current breaking

3. RESULTS AND DISCUSSIONS

Before we find a solution on dynamic voltage withstanding, analysis of mechanism on breakdown of a new vacuum interrupter is necessary. As discussed above, we have to investigate it from the internal causes of breakdown, and look for a practical way to improve the dynamic insulation of VCB's.

3.1. Weak points-distribution and elimination

For a vacuum interrupter just sealed, the distribution of weak points is mainly within two regions: on the surfaces of the contacts (the main gap), and the other surfaces of the shields and electrode system (the additional gaps). One of the useful ways to eliminate or blunt weak points is voltage (spark) conditioning. Two groups of samples with same electrode construction and same contact material of CuCr, were conditioned by a generally conditioning procedure and an ultra-high voltage conditioning procedure, respectively. Fig.2 shows the relation between the gap length L and breakdown voltage U_b . In general case, the conditioning in the air was finished as the curve begins to saturation, although it was limited by flash over as the case of curve(a). This kind of conditioning procedure can only eliminate and blunt weak points on the main gap. It can not destroy the weak points on the additional gaps, that will ignite a breakdown in the process of dielectric recovery or and decrease the voltage withstanding after high current breaking. Curve(b) is the case that an ultra-high voltage was made with the samples immersing in transformer oil. When the discharge got enough, conditioning can be made to both main gap and additional gaps thoroughly, that can improve dynamic voltage withstanding to a large extent and increase the stability of their insulation.

A former worke showed that^[4], if we use an impule source for conditioning, the curves in Fig.2 can be got also, but the breakdown voltage is not stale. When the contacts were acted by arc or by impact, even by standing some idle time, breakdown voltage will decrease again. This unstability was not found when using an AC voltage source. This result shows again that discharge energy is most important in the process of conditioning.

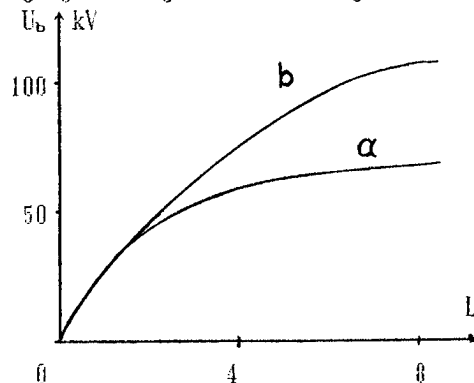


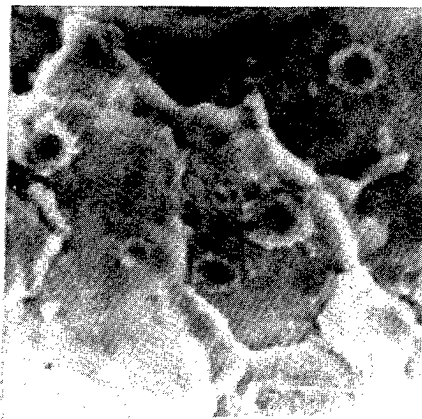
Fig.2 Conditioning voltage to gap length

3.2. Destruction and reproduction of weak points

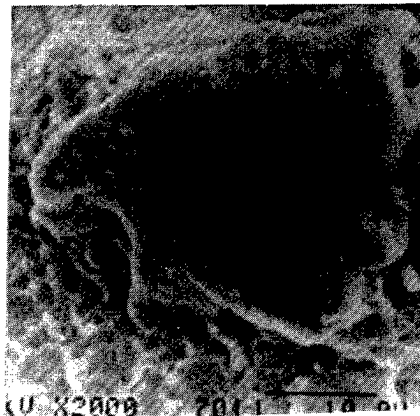
Destruction and reproduction of weak points after current breaking dominate the dynamic voltage withstanding of vacuum interrupters in general case. It is well known that, a current conditioning can destroy weak points effectively, but a high current breaking will reproduce weak points, that is to say, destruction and reproduction of weak points is a process of dynamic equilibrium. The question is from which current level the β factor begins to increase. Fig.3 shows some SEM photographs of contact surfaces after breaking 630A rated load current 10,000 times(a) and 24.5kA short circuit current 30 times(b). Electrodes of the samples were with axial magnetic field and CuCr material. Apparently, the micro-constructure was destroyed seriously in the case of breaking high current, and the voltage withstanding measurement showed that, its breakdown voltage was decreased also. Table 1 lists some test results after breaking different current; the samples were same as above, but got different magnetic field states, axial magnetic field (AMF), or transverse magnetic field (TMF).

Table 1 Voltage withstanding after current breaking

Sample No.	Breaking current (kA, rms)	Breakdown voltage (kV, 1.2 · 50 μ s)	Magnetic field state
101	0.63 (10 ⁴ times)	84	AMF(12mT kA)
102	12.5 (100times)	84	AMF(12mT kA)
103	20.0 (30 times)	84	AMF(12mT kA)
104	24.5 (30 times)	75	AMF(12mT kA)
105	29.5 (5 failure)	60	AMF(12mT kA)
111	20.0 (30 times)	60	TMF
121	24.5 (30 times)	84	AMF(18mT kA)



(a) Sample 101=



(b) Sample 104=



(c) Sample 105=

Fig.3 SEM photographs of contact surfaces after breaking currents

For the convenience of analysis, we set a model of the arc spot site as showed in Fig.4, which can cover most of the micro-constructure in the contact surfaces like that in Fig.3. Curvature radii r_1 and r_2 formed in the process of condensation of melting material, dominate the micro-enhancement factor β_m . If we can enlarge r_1 or and r_2 , the breakdown voltage will increase. When the tension of a metal in liquid state is high, curvature radius r_1 formed in the process of condensation will large. CuCr is just this kind of metal. We found a smooth surface after high current breaking, and the SEM photographs was also provable for this feature. F.Yanhong's work used a similar model as Fig.4, and showed that [8].

r_2 was dominated by energy input and the motion velocity of cathode spots. Based on the discussions above, we can define a parameter of w , as the energy density input on the surface of contact, which can be related directly to the β_u factor, then the dynamic voltage withstanding. So, we have:

$$w = f(I, C) \quad (1)$$

where I is the arc current including the conditioning current and breaking current; C is the construction factor, including the effects of magnetic field and contact material, diameter etc. A qualitative relation between w and β_u is showed in Fig.5. Two special points w_1 and w_2 should be corresponding to conditioning current I_1 and rated short circuit breaking current I_2 , respectively. Vacuum interrupters are expected to work in the region between w_1 and w_2 . In order to get a low energy density input, a diffused arc model is prerequisite, that can be ensured by enough axial magnetic field. This concept is specially important in the design of higher voltage vacuum interrupters.



Fig.4 A model of arc spot site

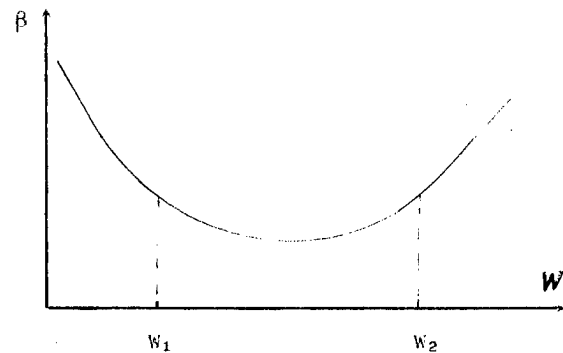


Fig.5 Input energy density to β factor

3.3. Effect of macro-particles

One of the mechanisms on breakdown of vacuum gaps is particle ignited. For a vacuum interrupter well treated by vacuum processing, the particles commonly from arcing. Macro-particles produced by vacuum arc are unavoidable. They will exist in the gap even after the arc died out. Gellert's work^[53] gave an extreme condition, the pulsed current made a great di/dt . However, when the arccurrent in power frequency is very high, or the contact surface is eroded seriously, a great number of macro-particles will appear on the surface of contacts or in the gap, that makes a lower dynamic voltage withstanding, and the current breaking will be failure, like the case in Fig.3 (c).

We can suppose that, macro-particles with dimension smaller than $10\mu\text{m}$ have less effect on breakdown. This is because, tiny particles with smaller mass and very high speed ($>200\text{m/s}$) will fly out off the gap in a small angle with the contact plane before transient voltage is set up. But for macro-particles with larger dimension, flying or attached on the surface of contact, they are active easy to contribute to the process of breakdown. So, all the work we can do for macro-particles is controlling their dimension.

Contact material is the most important on the macro-particles control. It is well known that, CuCr has advantage over other materials like CuBi in voltage withstanding. P. Frey, et al investigated the breakdown behavior of CuCr electrodes^[67], and found that, surface of contacts after arcing with smaller current, would form a layer with thickness about $50\mu\text{m}$, which contains Cr in fine dispersion and leads to forming a more even fracture surface, the breakdown voltage increased. That is to say, a current conditioning is helpful to reduce macro-particles when the breaking current is not too high.

In order to restrain macro-particles with large dimension after high current breaking, we have to do more work on CuCr material or try to find better materials. A former work showed that, a contact material with higher density and higher hardness will get higher voltage withstanding and lower electric erosion^[71]. A new technique called **hot-isopressing** treatment can densify CuCr material and be expected to restrain large macro-particles. The other efforts in this field were trying new additive

elements or new materials. Ta and Nb were reported to improve breakdown voltage level to a great extent. Again the arc energy density takes an important role in production of macro-particles. Keeping the arc diffused whenever is a prerequisite.

4. CONCLUSIONS

1. The question of dynamic insulation of a vacuum interrupter includes two internal causes: the weak points and the macro-particles. The first effort we can do to improve it is conditioning. When the discharge got enough, conditioning can be made to both main gap and additional gaps thoroughly, that can eliminate and blunt the weak points, increase not only the breakdown voltage but also the stability of insulation. Discharge energy is most important in the process of conditioning, that can be ensured by an AC voltage source instead of a impulse source.
2. Destruction and reproduction of weak points is a process of dynamic equilibrium in the process of breaking current. The energy density input on the surface of contact, that can be related directly to the βu factor then the dynamic voltage withstanding, is a dominant parameter. There is an optimum region of energy density input where βu has the minimum value and the rated short circuit breaking should be within this region, that can be ensured by diffused arc model and enough axial magnetic field.
3. Macro-particles appeared on the surface of contact or in the gap will deteriorate dynamic voltage withstanding, and made current breaking failure. In order to restrain macro-particles after high current breaking, we have to do more work on CuCr material such as hot-isopressing treatment. The other efforts in this field were trying new additive elements, like Ta and Nb.

5. REFERENCES

1. Zou Jiyan, et al "Interaction of Dielectric Strength Recoery of VCB", *Proc. 14th ISDEIV*, pp 343-346, 1990.
2. R.V. Latham, *High Voltage Vacuum Insulation*, London, Academic Press, 1981
3. B. Gellert, et al "Measurement of particles and vapor density after high current vacuum arcs by laser techniques", *IEEE Tr. on Plasma Science*, Vol.15, pp. 545-551, 1987
4. Zou Jiyan, et al "Improvement on Voltage Withstanding level of VI's", *Proc. IEE ICAPSCOM*, Hong Kong, 1993
5. Fu Yanhong, "Cathode Surface Effects and HF Behaviour of Vacuum Arcs", *Doctoral Dissertation*, Eindhoven University, 1990
6. P. Frey et al, "Metallurgical Aspects of Contact Materials for Vacuum Switching Devices", *IEEE Tr. on Plasma Science*, Vol. 17, No.5, pp.734-740, 1989
7. Zou Jiyan, "High Current Vacuum Arcs and Its Contact Materials", *Doctoral Dissertation*, Xi'an Jiaotong University, 1987

Effect of a prebreakdown current on the hold-off voltage and discharge initiation in the pseudospark switches

V.D. Bochkov, A.V. Kolesnikov, Yu.D. Korolev, V.G. Rabotkin, O.B. Frantz, I.A. Shemyakin

High Current Electronics Institute
Russian Academy of Sciences, Siberian Division
634055, Tomsk, Russia

INTRODUCTION

Considerable interest has recently been generated in a new type of high-voltage switches that depend on a low pressure gas discharge with a cold cathode, often named the pseudospark switches¹⁻³. They are considered as an alternative to the hydrogen thyratrons in facility where the high level of currents and di/dt are required. One of the problems for such switches is to increase the static breakdown voltage since this parameter is very important in itself and, besides, determines the ability for a switch to operate in high frequency mode. In order to solve the above mentioned problem Christiansen et al^{1,2} use the special design in which a positive potential is applied to additional blocking electrode from auxiliary power unit.

The goal of the present paper is to investigate the effect of the prebreakdown currents on the static breakdown voltage and to research the mechanism that is responsible for an action of the blocking potential on this voltage.

2. EXPERIMENTAL SETUP

The schematic of the electrode system and circuit design are shown in Fig. 1. The electrodes are placed into a ceramic cylindrical chamber of internal diameter 86 mm with the flanges. This construction enables us to replace the inner parts of the switch in the course of experiment. The main electrodes *C* and *D* form two cavities that communicate through axial holes. The interelectrode separation in the main gap being of 4 mm and the axial holes of the electrodes *B*, *C* and *D* are also 4 mm in diameter. The switch is filled in air at pressure range from 10^{-2} to $6 \cdot 10^{-2}$ Torr.

To initiate the high current discharge in the main gap, a triggering unit based on an auxiliary steady-state glow discharge is used. It consists of two hollow electrodes, *A* and *B*, and glow discharge current is provided by power supply $+V_1$. In initial position the electrode *B* as it is shown in Fig. 1 is positive with respect to the grounded cathode of the main gap, *C*. Once triggering pulse, $-V_T$, is applied to resistor R_T the electrode *B* becomes negative, the axial electron flux from auxiliary glow discharge is injected into the main gap, and it results in triggering of the switch. The operation of such a switch type is described in more detail in papers⁴⁻⁶.

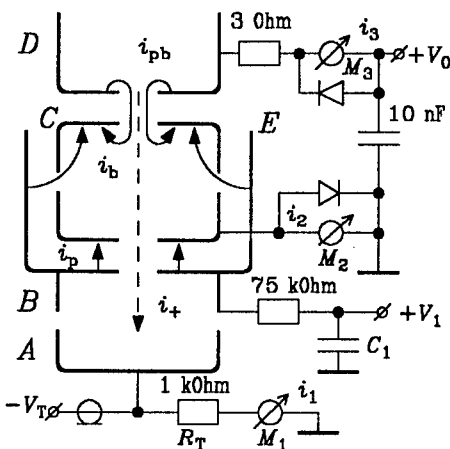


Fig. 1

The blocking electrode, *E*, exerts an effect on breakdown voltage due to the 12 holes 3 mm in diameter that are located on the side wall of the main cathode cavity (Fig. 1). Traditionally, this electrode is positive with respect to the main cathode and a positive potential is supplied from independent power unit^{1,2}. Our electrode system and method of triggering give us ability to use potential V_B for blocking electrode, i.e. the glow-discharge-drop voltage.

The current in the prebreakdown stage is measured by means of devices M_1 , M_2 , and M_3 . Since in the case of occasional breakdown a high value of current will flow through devices M_2 and M_3 , they are protected by high frequency diodes. When a weak prebreakdown current takes place the voltage drop on the devices is very small and the diodes have a large resistance in compare with M_2 and M_3 resistance also they are put in forward direction. In the case of breakdown the main share of total current flows through the diodes.

A distinctive feature of the pseudospark switch is that at low pressure the free electron path for ionization is in substantial excess of an interelectrode separation. Thus, for both the static breakdown and the external trigger mode a considerable values of prebreakdown currents are required to initiate the main discharge^{7,8}. The results of measurements for various types of such currents are presented below.

3. RESULTS AND DISCUSSION

Now let analyze the currents that can flow in the switch in the prebreakdown stage and the reasons for their occurrence. These currents are shown in Fig. 1. The prebreakdown current in the main gap, i_{pb} , can be caused by a field emission and by photoemission which is initiated due to irradiation of the cathode from glow discharge in triggering unit and from parasitic prebreakdown current over a surface of ceramic switch chamber. This weak emission current is enhanced, since the hollow cathode effect comes into force. As a result, the prebreakdown current reaches the value which is large enough to trigger a high current discharge in the main gap^{7,8}. The device M_3 serves for measurement of the current i_{pb} . Notice, that in the case of forced discharge initiation the electron flux from triggering unit into the main gap should be sufficiently large to ignite the main discharge in the voltage range lower than static breakdown voltage.

It is known that in prebreakdown phase the fast ions which are accelerated in the main gap CD propagate along the switch axis in the form of a narrow beam¹⁻³. The current i_+ is a component of i_{pb} current, however, we can measure i_+ separately by means of device M_1 . This device is also intended for registration of the glow discharge current in triggering unit.

In order to understand the action of blocking electrode the experiments were carried out both without side holes on electrode C and with side holes. In the former case at condition $V_0 = 0$ the device M_2 enables to measure the current i_p . We name this component as parasitic current. It flows in the gap BC due to irradiation of the cathode from glow discharge. Besides, the hollow electrode B operates as an anode with respect to electrode C . Hence, an ion flux can be extracted from the cavity B . This ion current is also a certain component of the current i_p .

In the second case, i.e. when the side holes are present, there appears a blocking current, i_b . Formally, this current, along with current i_p , flows between electrodes B and C , however we distinguish i_b in our consideration. The point is that the design of electrode C foresees the ability for potential $+V_B$ to penetrate into the main cathode cavity through the side holes. Thus, the current i_b flows to inner walls of the cavity, or in another words, this current is provided by charge carriers that originate within the cavity. That is the reason why the blocking potential exerts the action on the breakdown voltage.

It is interesting to note that the potential V_B may also penetrate into main cathode cavity through the axial hole resulting in blocking effect. This is especially true when the ion beam is available at the switch axis since the beam manifests itself as an "original conductive bridge" between cathode cavity and electrode B . However in the set of experiment under discussion the part of the axial hole appears to be negligible.

Taking the above mentioned into account we can write the equation for the current i_2

$$i_2 = i_{pb} - i_+ + i_b + i_p.$$

Fig. 2 shows the dependence of static breakdown voltage on gas pressure for different electrodes designs with the availability of a glow discharge in triggering unit and without it. Curve 1 corresponds to the conditions in which the glow discharge is absent, the side holes in electrode C is closed and points A and B are grounded. The same case, but under the presence of the glow

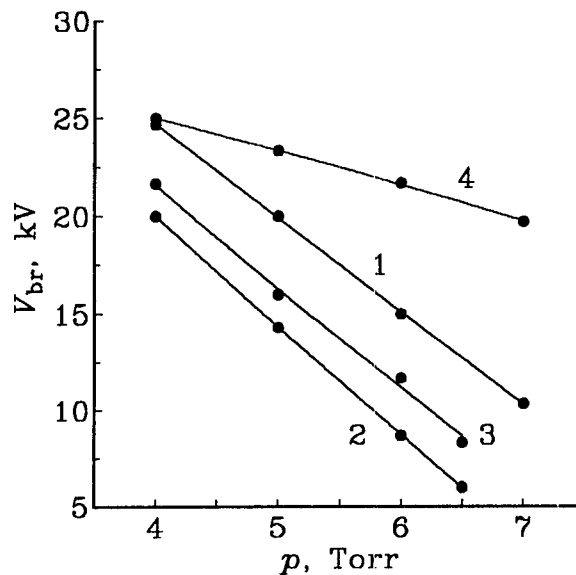


Fig. 2.

discharge is demonstrated by the curve 2. One can see that the breakdown voltage decreases. Once the side holes are opened and glow discharge is available than the breakdown voltage increases again (curve 3). Thus, in this case we can see the effect of blocking potential.

Let us consider now the results of current measurements in prebreakdown phase for the conditions corresponding to Fig. 2. The first two lines in Table 1 demonstrate a current-voltage characteristic of the triggering discharge and the third line shows the parasitic current i_p . Notice, that the discharge in triggering unit can operate in low-current mode and in abnormal glow discharge mode as it is shown in Table 1. The above modes are described in more details in papers^{5,6}. The parasitic current depends strongly on voltage V_B and only slightly on the glow discharge mode and glow discharge current. In our opinion, the current i_p by its nature is a non-self-sustained one with any weak ionization amplification.

Table 1. $p = 4 \cdot 10^{-2}$ Torr, $i_2 = i_p$

	low-current discharge							↓	abnormal discharge	
V_B , V	450	460	500	560	590	670	725		330	350
i_1 , mA	0.1	0.2	0.4	0.8	1.0	2.0	3.0		9.6	14
$i_p = i_2$, μ A	4	6	8	13	15	23	30		5	6

$p = 6 \cdot 10^{-2}$ Torr, $i_2 = i_p$

	low-current discharge						↓	abnormal discharge		
V_B , V	355	365	390	420	430	440		295	320	330
i_1 , mA	0.1	0.2	0.4	0.8	1.4	1.8		3.7	8.4	14
$i_p = i_2$, μ A	3	4	5	6	7.5	8		2	3	5

Table 2 shows the results of measurements for prebreakdown current i_3 and for i_2 . Since the side holes of electrode C are closed the device M_2 registrates the value $i_2 = i_{pb} - i_+ + i_p$. It is seen that in absence of glow discharge ($V_B = 0$, $i_p = 0$) the prebreakdown current begins to be registrated at a high anode voltage, $V_0 = 18$ kV. The glow discharge operation results in an irradiation of the main gap and the current i_{pb} appears at lower level of V_0 voltages. Also the source of radiation (triggering unit) is far from the main gap, CD , however, the prebreakdown current at anode voltage of about 15 kV is in excess of parasitic current. We consider that current in the main gap flows in non-self-sustained mode with a substantial ionization amplification. This amplification appears to be due to hollow cathode effect in vicinity of the axial hole of electrode C .

Table 2. $p = 4 \cdot 10^{-2}$ Torr

V_0 , kV		0	5	10	15	18	20	24
$V_B = 0$	i_2 , μ A	0	0	0	0	1	2	3
$i_p = 0$	i_3 , μ A	0	0	0	0	1	2	3
$V_B = 340$ V	i_2 , μ A	5	5.5	6	8	12	15	breakdown
$i_p = 5$ μ A	i_3 , μ A	0	1	2	4	7	10	
$V_B = 520$ V	i_2 , μ A	9	10	12.5	17	22	26	
$i_p = 9$ μ A	i_3 , μ A	0	1.5	4	8	13	17	
$V_B = 600$ V	i_2 , μ A	15	17	22	28	35	41	
$i_p = 15$ μ A	i_3 , μ A	0	3	7	14	20	26	

Now let analyze the action of blocking potential basing on the results that are given in Table 3. We can not measure the blocking current i_b , but can calculate it as $i_b = i_2 - i_3 - i_p$. The presence of blocking electrode leads to reducing of the prebreakdown current i_{pb} . For instance, when $V_B = 400$ V and the side holes are closed the variation of the anode voltage from 8 kV to 14 kV results in ranging of current i_3 from 4 A to 33 A. If the side holes are available, it can be seen from Table 3 that current i_3 ranges only from 0.3 μ A to 1.5 μ A.

Table 3. $p = 5 \cdot 10^{-2}$ Torr, $V_{br} > 16$ kV

$V_B = 320$ V	V_0 , kV	0	8	10	12	14	16
$i_1 = 6$ mA	i_2 , μ A	4	4.5	4.5	5	8	15
(abnormal discharge)	i_3 , μ A	0	0.2	0.2	0.8	2.5	8
$i_p = 4$ μ A	$i_b = i_2 - i_3 - i_p$	0	0.3	0.3	0.2	1.5	3
$V_B = 400$ V	V_0 , kV	0	8	10	12	14	16
$i_1 = 0.2$ mA	i_2 , μ A	4	4.5	5	5.5	7	11
(low-current discharge)	i_3 , μ A	0	0.3	0.5	0.8	1.5	4
$i_p = 4$ μ A	$i_b = i_2 - i_3 - i_p$	0	0.2	0.5	0.7	1.5	3
$V_B = 490$ V	V_0 , kV	0	8	10	12	14	16
$i_1 = 1$ mA	i_2 , μ A	7	8	9	10	11	16
(low-current discharge)	i_3 , μ A	0	1	1.2	1.5	2	5
$i_p = 7$ μ A	$i_b = i_2 - i_3 - i_p$	0	0	0.8	1.5	2	4

The action of blocking potential manifests itself in the fact that a some share of electrons originated within the cathode cavity C are collected on the electrode E . As a result, this share of electrons does not take part in ionization and the prebreakdown current reduces. It should be stressed that the reducing in current i_{pb} is not a simple redistribution of electron flux between electrodes D and E , but this is the suppression of the hollow cathode effect and corresponding suppression of prebreakdown current.

Curve 4 in Fig. 1 shows the static breakdown voltage for other design where three blocking electrodes 2.5 mm in diameter are directly inserted into the main cathode cavity through the side holes. Also for conditions of curve 4 the glow discharge and irradiation of the main gap are present, however, the breakdown voltage appears to be higher then for the curve 1.

REFERENCES

1. K. Frank, E. Boggasch, J. Christiansen et al, "High-power pseudospark and BLT switches", *IEEE Trans. on Plasma Science*, Vol. 16, No 2, pp. 317-323, 1988.
2. G. Mechttersheimer, R. Kohler, T. Lasser, and R. Meyer, "High repetition rate, fast current rise, pseudo-spark switch", *J. Phys. E.: Sci. Instrum.*, Vol. 19, pp. 466-470, 1986.
3. M.A. Gundersen, "Plasma-based device concepts based on the pseudospark and BLT", *Physics and Applications of Pseudosparks*, Plenum Press, New York, 1990, pp. 331-341.
4. K.A. Klimenko, A.V. Kolesnikov, Yu.D. Korolev et al, "Low pressure discharge in pseudosparks", *XX Intern. Conf. on Phenomena in Ionized Gases*, Contributed papers 2, Pisa, Italy, 1991, pp. 492-493.
5. K.A. Klimenko, A.V. Kozyrev, Yu.D. Korolev et al, "Electrical breakdown mechanism in pseudospark switches", *XV-th Intern. Symp. on Discharge and Electr. Insulation in Vacuum*, Darmstadt, Germany, 1992, pp. 467-469.
6. K.A. Klimenko, Yu.D. Korolev, V.G. Rabotkin et al. "Triggering mode for pseudospark switch with triggering unit based on auxiliary glow discharge". *Zhurnal tekhnicheskoi fiziki*, Vol. 62, No 10, pp. 74-80, 1992 (in Russian).
7. K.A. Klimenko, A.V. Kolesnikov, Yu.D. Korolev et al. "Investigation of discharge initiation mechanism in low-pressure pseudospark switches", *Fizika plasmy*, Vol. 17, No 10, pp. 1256-1262, 1991.
8. A.V. Kozyrev, Yu.D. Korolev, V.G. Rabotkin, and I.A. Shemyakin "Processes in the prebreakdown stage of a low-pressure discharge and the mechanism of discharge initiation in pseudospark switches", *J. Appl. Phys.*, Vol. 74, No 9, pp. 5366-5371, 1993.

ACKNOWLEDGMENT

This paper is supported by Russian Foundation on Fundamental Research (code of the project 93-02-17418).

Anode melting and evaporation in vacuum interrupters

V.A. Nevrovsky*, A.A. Pertsev**, L.A. Rylskaya**

* "ANTECH Ltd", Kazarmennyi per. 6, bld.1, 109028 Moscow, Russia

** All-Russian Electrotechnical Institute (VEI), Krasnokazarmennaya str. 12, 111250 Moscow Russia

ABSTRACT

A one-dimensional nonstationary model of material melting and evaporation in anode spots of vacuum arc is developed. Calculations of melting and evaporation rates of copper and copper-chromium contacts were carried out and concentration of copper atoms was evaluated when the arc was burning and after its extinguish.

The model of anode melting that accompanies its evaporation permits to assess the time of liquid metal film existence at the anode in the ablation approximation of the model.

Experiments with vacuum interrupters having CuCr contacts showed that current was successfully interrupted when contacts began to separate 2-2,5 ms before zero current provided energy Q released in the arc was less than 700 J. If Q is higher the current is not interrupted in the first zero and an arc of opposite polarity is initiated at voltage of some tens volts. Separation of contacts 5 ms before zero current resulted in successful interruption even if arc energy released was as high as 3400 J.

2. INTRODUCTION

Dynamics of evaporation into a vacuum gap between contacts when a hot spot exists at the anode controls the process of interruption of high currents of industrial frequency by a vacuum interrupter. Residual vapor concentration at the moment of arc extinction if this moment coincides virtually with current zero seems to influence on reignition of arc and hence on failure of an arc switch. And this concentration depends on the temperature of heavy loaded spots on electrodes.

Experimental observations of heavy currents interruptions in vacuum switches suggests that heat inputs into an anode would be in the range of hundreds and thousands of Joules with typical time of input in milliseconds range.

This paper discusses heating and evaporation of anodes under action of heat flux from arc plasma taking into account Stephan nature of the problem and compares results with experimental observations in vacuum interrupters with CuCr contacts.

3.A MODEL OF HEATING AND PHASE TRANSITION

In this paper we apply the one-dimensional model of semi-infinite solid heating by heat flux $q(t)$. One-dimensionality is granted by fulfillment of inequality: $\kappa t < R^2$, where $R \geq 3$ mm - radius of the

heating circle and $\kappa \approx 0,3 \text{ cm}^2/\text{s}$, $t \approx 2 \div 3 \text{ ms}$.

For calculation of front surface temperature an ablation model of the paper [1] is used:

$$\frac{d}{d\eta} \left[\frac{\vartheta}{1 - \frac{AL}{q_0 \sqrt{T}} \exp(-\frac{H}{T})} \right] = q/q_0 - \frac{LA}{q_0 \sqrt{T}} (1 + \varepsilon \vartheta) \exp(-\frac{H}{T}) \quad (1)$$

$$\eta = t/t_0, \text{ scale time } t_0 \approx 0,793 \cdot \frac{\lambda (T_k - T_0)^2}{\kappa \cdot q_0^2}$$

q_0 - scaling heat flux, κ - thermal diffusivity, λ - thermal

conductivity, $\vartheta = \frac{T - T_0}{T_k - T_0}$.

T_k - asymptotic temperature is obtained from the condition of stationary evaporation:

$$LA (1 + \varepsilon \vartheta) \exp(-\frac{H}{T_k}) = \sqrt{T_k} \cdot q_0$$

parameter $\varepsilon = \frac{C}{L} (T_k - T_0)$ shows the effect of heat accumulation by thermal capacity, L - heat of evaporation. Evaporation is believed to obey the law [2]:

$$\omega = \frac{A}{\sqrt{T}} \cdot \exp(-\frac{H}{T})$$

Specific solution of (1) depends on the form of heat flux $q(t)$. It is often accepted for simplicity to be constant. Fig. 1 shows temperature ϑ evaluation in this case. It is seen that the dimensionless results are virtually the same for the heat flux range considered.

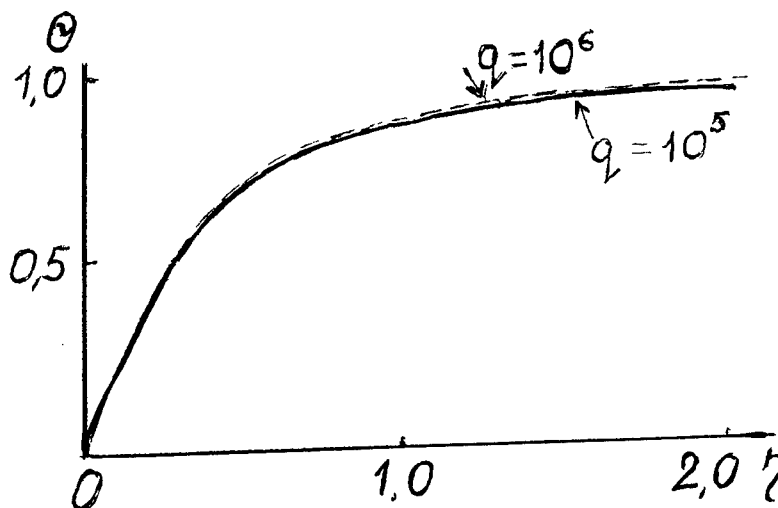


Fig. 1. Surface Temperature growth of evaporated CuCr-composite (case $q = \text{const}$, $0,7 \cdot 10^5 \leq q \leq 1,5 \cdot 10^6 \text{ W/cm}^2$).

For the problem of current interruption this result means that the highest temperature of the electrode hot spot occurs by the end of arc burning. In practice of current interruption q decreases often linearly to zero in time (see the insert at Fig. 2). If vaporization can be neglected, peak temperature occurs exactly at $t = t_1/2$.

Vaporization flattens the temperature curves around their apexes, as Fig. 2 shows. To calculate these curves the initial equation (1) should be modified since it is valid only for non-decreasing heat flux ($dq/dt \geq 0$). The modification is based on subtraction of linearly growing heat flux $q = q_0 \cdot t/t_1$ from constant one: $q = q_0(1 - t/t_1)$. Resulted equations of the ablation model are:

$$\frac{d}{d\eta} \left[\frac{\vartheta_1^2}{1 - r} \right] = 1 - (1 + \varepsilon \vartheta) r \quad (2)$$

$$\frac{d}{d\eta} \left[\frac{\vartheta_2^2 t_1}{\eta \cdot t_0} \right] = 1 - \varepsilon \cdot r \cdot \vartheta \quad (3)$$

where $r = \frac{AL}{q_0 \sqrt{T_1 - T_2}} \cdot \exp(-\frac{H}{T_1 - T_2})$, $\vartheta_1 = \frac{T_1 - T_0}{T_k - T_0}$, $\vartheta_2 = \frac{T_2 - T_0}{T_k - T_0}$

The front surface temperature in question is

$$T_f = T_1 - T_2 = T_0 + (T_k - T_0)(\vartheta_1 - \vartheta_2)$$

Initial conditions are $\vartheta_1 = 0$, $\vartheta_2 = 0$ at $\eta = 0$. There were made numerical integrations of the eq.(2) and (3) with $\kappa = 0,3 \text{ cm}^3/\text{s}$, $\lambda = 1,2 \text{ W/cm} \cdot \text{deg}$,

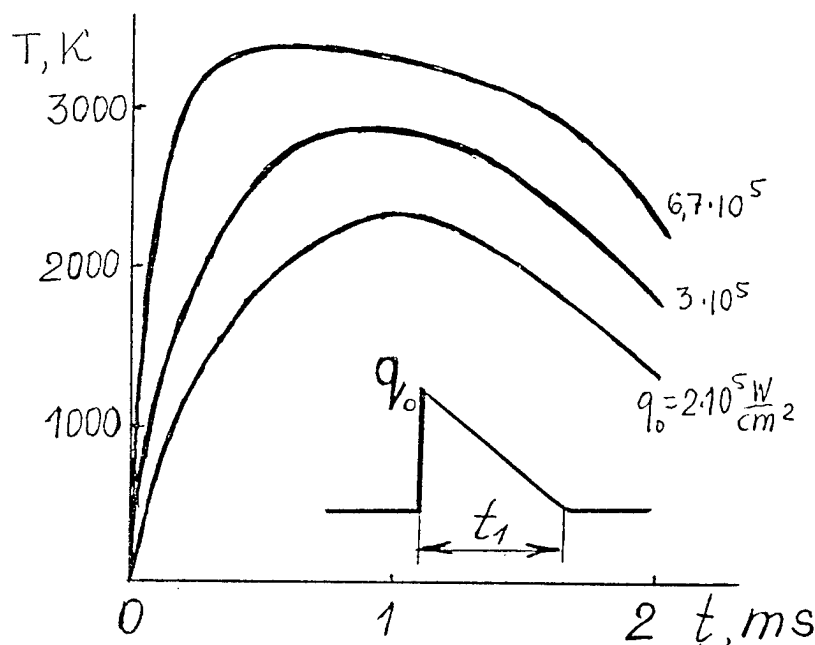


Fig. 2. Temperature curves for "triangle" heat flux: 1 - $q = 6,7 \cdot 10^5 \text{ W/cm}^2$, 2 - $q = 3 \cdot 10^5 \text{ W/m}^2$, 3 - $q = 2 \cdot 10^5 \text{ W/cm}^2$.

typical for CuCr composite. H and L were taken from [2] and standard tables for Cu as a more easily evaporative constituent. Fig. 2 shows results of calculations for three values of q_0 . It is interesting to compare two concentrations of vapor in equilibrium with hot solid at the end of arc burning. One value is got for $q = \text{const}$, and another one - for linearly decreasing heat flux. Total amount of heat $Q = \int q dt$ is the same. Fig. 3 shows that approximation of $q = \text{const}$ results in too high concentration (curve 1) comparing to the "triangle" heat flux.

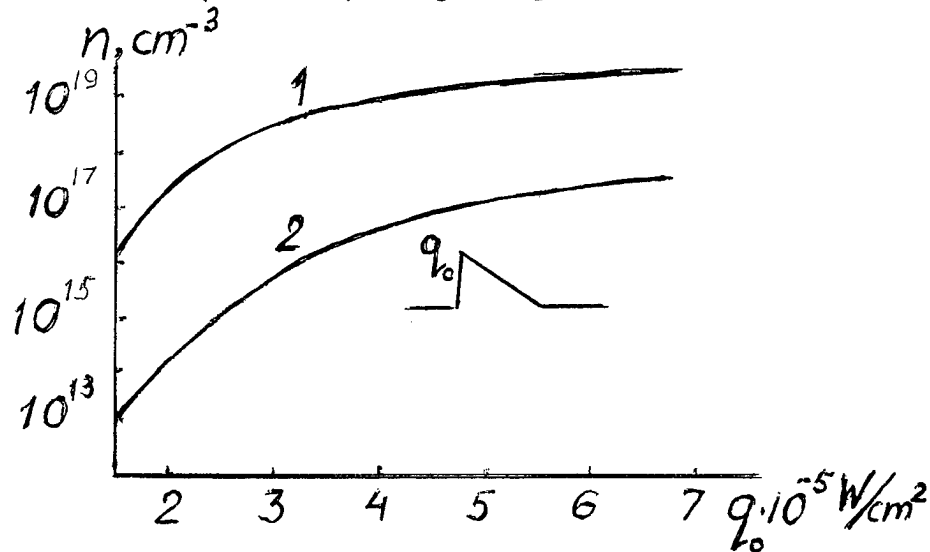


Fig. 3. Concentration of copper atoms by the end of 2 ms heat pulse. 1 - $q = \text{const}$, 2 - "triangle" heat pulse.

4. EXPERIMENTAL OBSERVATIONS AND DISCUSSION

Some heavy current vacuum interrupters were tested at a high power facility. Typical modes of current interruption are shown at the Fig. 4 (denoted 1 and 2). Contact separation speed is 1 m/s. So arc length is about 2 mm (in 2 ms after separation start) by the moment of arc removal by magnetic field (mode 1) or by the moment of current zero (mode 2).

It was found that industrial currents with crest value of 50 kA were successfully interrupted in mode 2. Higher currents of 60 kA were not reliably switched off and of 70 kA failed to be interrupted.

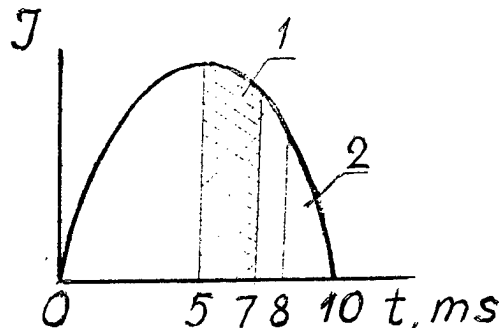


Fig. 4. Modes of current interruption

Voltage between contacts did not exceed 100 V at the moment of successful interruption. Interruptions were successful for currents up to 95 kA when operating in mode 1.

Taking arc voltage to be ~ 20 V and sharing released arc energy equally between electrodes we have $Q = 330$ J accepted by an electrode at successful interruption, and 400 J or more for failure (mode 2). The successful interruptions in mode 1 means $Q \approx 3400$ J of arc energy and 1700 J accepted by an electrode.

The crucial but unknown value is the spot area. Dullni and Schade [3] measured $S \approx 0,5 \text{ cm}^2$ for 20 kA arc on CuCr. For higher currents of our tests $S \approx 0,5 \div 1 \text{ cm}^2$, seems to be acceptable. In this case $q_{av} = 1,65 \cdot 10^5 \text{ W/cm}^2$ for $q = \text{const}$ approximation, and $q_0 = 2q_{av} = 3,3 \cdot 10^5 \text{ W/cm}^2$ for more realistic "triangle" approximation of $q(t)$, provided $Q=330$ J. So $n=1,6 \cdot 10^{16} \text{ cm}^{-3}$ when an interrupter operates successfully in mode 2 and $n=4 \cdot 10^{16} \text{ cm}^{-3}$ when it fails. This result follows from Fig. 3 curve 2. Having in mind interelectrode distance d at the moment of current zero $d=0,2 \text{ cm}$ we have $nd=3,2 \cdot 10^{15} \text{ cm}^{-2}$ (interruption) and $nd=8 \cdot 10^{15} \text{ cm}^{-2}$ (failure).

Interruptions in mode 1 were always successful at the highest current attainable, whereas heat flux into an electrode was as high as $q=1,2 \cdot 10^6 \text{ W/cm}^2 \approx \text{const}$. This result suggests comparatively fast decrease of electrode temperature after arc removal. The model of non-stationary evaporation used in the paper allows to calculate temperature decrease followed after instant vanishing of heat flux.

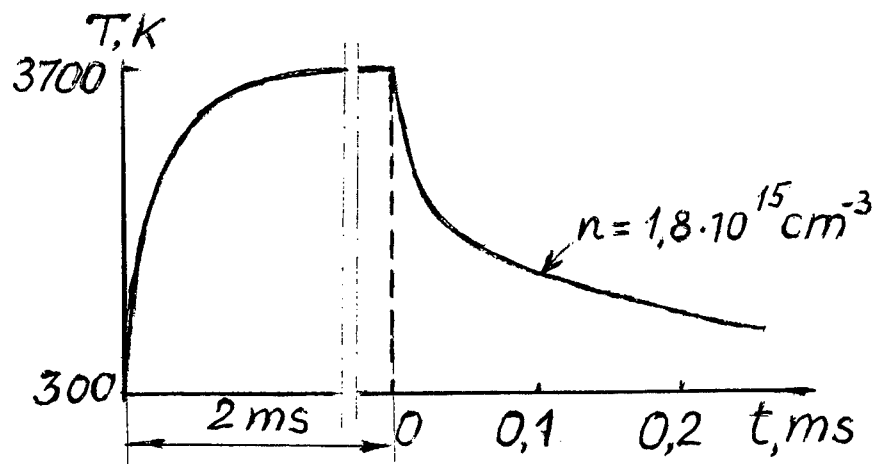


Fig. 5. Temperature decay of evaporating surface after heat pulse vanishing.

Fig. 5 shows the temperature plot for this case. Temperature decay does not virtually depend on the heat pulse duration (only for intensive evaporation) and in this example it takes only 120 mks for reduction of vapor concentration below $2 \cdot 10^{15} \text{ cm}^{-3}$. In addition to evaporation the solid is melted. The influence of melting on evaporation is negligibly small. It is seen from the fact that asymptotic rate of evaporation is $U_0 = \frac{q}{\rho L(1+\epsilon)}$ for $q=\text{const}$, and

melting leads to the corrected relation:

$$U_1 = \frac{(1 + \varepsilon) \bar{U}_0}{1 + \varepsilon + L_m/L},$$

where L_m - melting heat. For copper correction is about 4 %.

In this case both fronts of phase transition move with the same velocity U and thickness of melt h can be deduced roughly from the complete model of the problem [1]. Since the model includes the law of temperature decrease into a solid.

For the last example ($q = 1,2 \cdot 10^6$ W/cm²) thickness $h = 0,15$ mm. According to the complete model of ablation the time of resolidification of the melt after heat pulse vanishing is about 0,8 ms. So an electrode would be solid by the moment of current zero when the mode 1 of interruption is in operation.

References

1. V.A.Nevrovsky, "On the transit stage of non-stationary ablation", Sibirsky physico-tekhnich. zhurnal. 1991, N1, pp.38-44.
2. Y.Groshkovski, "Tekhnika vysokogo vakuumu", Moscow, 1975.
3. E.Dullni, E.Schade, "Recovery behavior of vacuum circuit-breakers at the current interruption limit". Proc.XIV ISDEIV, Santa Fe, 1990 pp. 517-521.

SESSION 4

Surface Flashover

Inhomogeneous charging characteristics of polycrystalline alumina surfaces

T. Asokan and T. S. Sudarshan

Department of Electrical and Computer Engineering
University of South Carolina, Columbia, SC 29208, USA

ABSTRACT

Electron-induced surface charging characteristics of sintered alumina were studied in relation to the polycrystalline features, such as (a) grain boundaries (b) non-uniform distribution of grain size and (c) orientation of grains, by adopting the scanning electron microscope (SEM) "electrostatic mirror technique." Significant variation in the charging characteristics of grains and grain boundary regions were not observed for bombardment with low energy (< 8 keV) electrons corresponding to secondary electron yield (δ) > 1 . Interestingly, for higher energies (> 8 keV) corresponding to $\delta < 1$, the grain boundary regions were found to charge more negatively than the grains. The electrostatic mirror studies reveal that (i) the mirror image formation is not possible at high density defect zones, (ii) the size of the mirror images, formed at one location varies significantly from that formed at another location, due primarily to the variation in the defect prone grain boundary volumes and, (iii) the size of the image, formed on one grain, varies from that formed on another, due to variation in the crystallographic orientation of the grains. The results suggest that alumina undergoes inhomogeneous charging under electron bombardment.

1. INTRODUCTION

It is well established that the insulator-surface flashover is governed by a surface charging process, resulting from the interaction of the insulator surface with the electrons emitted from the insulator-cathode-vacuum triple junction by field emission process¹. Electron-induced surface charging of insulators is also commonly observed in an SEM; hence, the study of charging of insulators in an SEM is believed to be an experimental simulation of surface flashover phenomena². The secondary electron emission yield is a quantitative measure of surface charging of insulators. The surface charging capability of a polycrystalline solid varies significantly from one region to the other, due primarily to the lattice inhomogeneity, caused by the presence of grain boundaries and pores (voids). The influence of inhomogeneous charging of polycrystalline dielectrics on the surface flashover process is not yet understood. The present work is carried out to determine a correlation between the polycrystalline features (e.g., grain, grain boundary and grain orientation) and the electron charging of ceramic dielectrics.

2. ELECTROSTATIC SEM MIRROR IMAGE FORMATION

An insulator surface is known to be charged, under electron bombardment, either positively or negatively depending on the energy of the incident primary electrons. The polarity of the surface charge is controlled primarily by the total electron yield σ , which varies as a function of the primary electron energy. The insulator would be charged positively when the electron yield $\sigma > 1$; it would be charged negatively when $\sigma < 1$. Depending on σ , a mirror image is formed in an SEM as discussed below. The insulator surface is bombarded with a high energy (~ 25 keV; $\sigma < 1$) electron beam which would result in the formation of negative charges on the surface. After a specific duration (~ 1 to 3 minutes) the electron beam is turned off and the surface probed with a low energy electron beam (< 5 keV). The low energy electrons are deflected near the negatively charged surface region, and consequently probe the SEM components (e.g., pole piece), instead of the insulator surface². The secondary electrons produced by the bombardment of the deflected primary electrons on the SEM components would result in the formation of an image of the SEM internal components.

3. RESULTS AND DISCUSSION

3.1. Effect of Surface Damage on the Mirror Image Formation

In general, the formation of an electrostatic mirror image is more difficult on polycrystalline materials (e.g., alumina) than on single crystals, due to the inhomogeneous nature of the polycrystalline surface, caused by the presence of grains, grain boundaries, pores and structural damages (e.g., scratch marks). The dielectric properties of localized regions, consisting of grains and grain boundaries, are significantly different, since (a) the lattice structure and (b) the chemistry (e.g., non-stoichiometry and the oxidation state of the cation) of these regions vary significantly. Besides, the surface of a polycrystalline material is often found to exhibit structural damages (e.g., scratches, voids and cracks) that are usually caused by the mechani-

cal processing (machining, polishing etc.). We made attempts to form an electrostatic mirror image on such an alumina surface. We did not succeed despite the fact that the test was conducted at more than 20 different locations, indicating that the implanted charges leak away due to the predominance of shallow defect level sites on the surface. To support our view, the as-machined samples were subjected to mechanical polishing to eliminate or minimize the surface damages caused by the machining process. After polishing with a 3 μm diamond abrasive, the surface irregularities and machining-induced damages are removed (Fig. 1). The 3 μm diamond polished samples were ultrasonically cleaned in de-ionized water for a few hours and dried in an oven at $\sim 150^\circ\text{C}$ for 30 minutes. An electrostatic mirror image of the pole piece was easily observed on the polished samples, suggesting that structural homogeneity (i.e., fine surface finish with low damage) of the surface is a prerequisite for the formation of a mirror image. The size of the pole piece image, formed at different locations of the polished specimen, however, was found to vary significantly. The above results suggest that the dielectric properties of alumina vary significantly from one location to the another.

3.2. Effect of grain boundaries on the SEM mirror image

The principal feature of polycrystallinity is the presence of defect prone grain boundary regions which are known to possess a high degree of lattice disorder and non-stoichiometry compared to the grains. In addition, impurity atoms are usually segregated at the grain boundary regions. Hence, the secondary emission characteristics of the grain and grain boundaries are believed to differ significantly. To support the above view, high purity polycrystalline α -alumina samples are studied under electron irradiation in an SEM. Prior to the SEM studies, the surface of the specimens were polished to a fine finish using 6 μm abrasive diamond paste and subjected to heat treatment at 1600°C for a few hours. The heat treatment of the samples was performed to etch the grain boundary regions, partially, by volatilization process (i.e., thermal etching) to attain a well defined surface.

The electron yield (σ) of alumina is reported to be higher than 1 (i.e., positive charging) when the primary electron energy is $> \sim 20 \text{ eV}^3$. Also, σ of alumina is reported to be below 1 when the primary electron energy is $> 8 \text{ keV}^4$. Hence our thermally etched alumina specimen (without metal coating) was probed with a low energy beam (2 keV) to attain a condition that $\sigma > 1$. A typical micrograph of the alumina surface, obtained at 2 keV, is shown in Fig. 2 (i). Significant variation in the charging contrast between the grain and grain boundary regions is not observed. The energy of the electron beam was increased in steps of 1 keV. The grain and grain boundary regions did not exhibit significant charging contrast up to about 8 keV. Appreciable charging contrast was observed at energies above 8 keV. A typical micrograph of the specimen, obtained at 10 keV and shown in Fig. 2 (ii), indicates that the grain boundary regions are bright compared to the grains. Besides, some of the grains also appear bright (e.g., grain B). It may be recalled that alumina charges negatively (when the energy of the primary electron beam is $> 8 \text{ keV}^4$). Hence, the observed variation in the contrast can be attributed to the higher charging of the grain boundary regions (negatively) compared to the grains. The inhomogeneous charging is believed to be due to the variation in the concentration of lattice or crystallographic defects.

3.3. Effect of grain size distribution on the SEM mirror image

During the electrostatic mirror image test, the selection of the location on a polycrystalline surface for charge implantation is usually made randomly in the pore-free regions, because the microstructure of an as-polished surface does not reveal the grain boundaries (Fig. 1). The randomly-selected pore-free location for the mirror test may include either the grain or grain boundary regions. Also, the grain size of the material is not uniform, as seen in Fig. 3. If the initial high energy electron bombardment (in the spot mode) is performed at the center of a large crystal (i.e., A in Fig. 3), the charged volume will be within the grain. Hence, the respective pole piece image would be a characteristic of crystal A. Contrarily, if the electron implantation is carried out in region B (Fig. 3), the mirror image may be characteristic of the fine crystals and the grain boundary regions. The amount of charge trapped in the above two locations is likely to differ, and the size of the pole piece image is expected to change. In order to confirm this view, regions similar to that of A and B are subjected to mirror tests. The size of the mirror images, corresponding to those regions, was found to be significantly different. The variation of the grain boundary regions, constituting the charged volume in the above two cases, is therefore believed to be the primary cause for the observed variation in the size of the mirror images.

3.4. Effect of grain orientation on the SEM mirror image

The observed variation in the degree of charging among the grains of alumina seems to be a new and interesting phenomenon. The major variable in a polycrystalline matrix is the crystallographic orientation of the different grains. To

understand the influence of the orientation of the grains on the degree of charging, mirror images are studied as described below. Initially, a grain possessing weak charging ability (i.e., grain A in Fig. 2 (ii)) was bombarded with a 20 keV electron beam for 3 minutes in the spot mode. As the electron beam diameter used was < 100 nm (in the spot mode) the electron-insulator interaction volume was small ($< \text{a few } \mu\text{m}^3$), and so the charging occurred only within the grain. The charged region was then probed with a low energy beam (1 keV) in the normal scanning mode. The low energy probing electrons were deflected from the corresponding equipotential surface, without reaching the insulator-surface, and probed the SEM chamber, resulting in the formation of the SEM component image. The mirror obtained on grain A of Fig. 2 (ii) is shown in Fig. 4 (i). Similarly, a grain possessing strong charging ability [grain B in Fig. 2 (ii)] was subjected to mirror image formation [Fig. 4 (ii)]. The experimental conditions in both the cases were the same. The size of the image formed on grain B is much larger (i.e., strong charging ability) than the size of the image obtained on grain A (i.e., weak charging ability). The observed correlation between the charging ability and the mirror image size appears to be in good agreement with the results of Gong, et al.⁵ Briefly, the charging ability of $\alpha\text{-SiO}_2$ single crystals is found to decrease as the orientation angle (with respect to the basal plane) of the crystal increases from 0° (i.e., z-cut) to 60° . Hence, it may therefore be stated that the variation in the crystallographic orientation of the grains is responsible for the observed changes in the degree of charging of grains in alumina [Fig. 2 (ii)].

3.5. Large area charging effect

The mirror images represent the characteristics of the individual grains or localized regions. For a polycrystalline solid, the degree of charging varies significantly from one location to another due to the grain boundaries and grain orientation, as discussed before. To characterize a polycrystalline surface, it is essential to form a mirror that represents both the grain and grain boundary regions. An attempt has therefore been made to form a mirror image of a large surface area of the polycrystalline alumina. The alumina surface, at a low magnification, was bombarded with a 20 keV electron beam in the normal scanning mode (Note: not in the spot mode) for about 3 minutes. The charged region (area $\sim \text{mm}^2$) was then probed with a 1 keV beam in the normal mode again, resulting in a mirror image. The size of the above mirror, obtained via large area charging, is much larger than that of the image obtained in the localized charging (spot) mode. Besides, the size of the images formed by the large area charging on other regions is found to be nearly the same. It is important to note that the images, formed by large area charging, represents the aggregate (i.e., grain and grain boundary) behavior of the alumina surface. If the mirror method is used to evaluate a material property (e.g., permittivity) or to make comparison of the surface properties of two materials, the conditions of the experiment must be carefully monitored before valid conclusions can be drawn.

4. CONCLUSIONS

Polycrystalline alumina, under electron bombardment, undergoes inhomogeneous charging, due to the presence of grain boundary regions and a random orientation of grains. We have shown qualitatively that the size of the mirror images varies due to grain boundary regions (constituting the charged volume) and the orientation of grains. Mirror image formation using large area charging is proposed to be a suitable method for the evaluation of polycrystalline surfaces.

5. ACKNOWLEDGMENTS

We gratefully acknowledge the support of this work by NSF (grant no. DMR-9113500).

6. REFERENCES

1. N. C. Jaitly and T. S. Sudarshan, *IEEE Trans. Elect. Insul.*, 23, 261- (1988).
2. C. Le Gressus, et al., *J. Appl. Phys.*, 69, 6325-6333 (1991).
3. P. H. Dawson, *J. Appl. Phys.*, 37, 3644-45 (1964).
4. T. S. Sudarshan, J. D. Cross and K. D. Srivastava, *IEEE Trans. Elect. Insul.*, 12, 200-208 (1977)
5. H. Gong, C. Le Gressus, et al., *J. Appl. Phys.*, 74, 1944-1948 (1993).

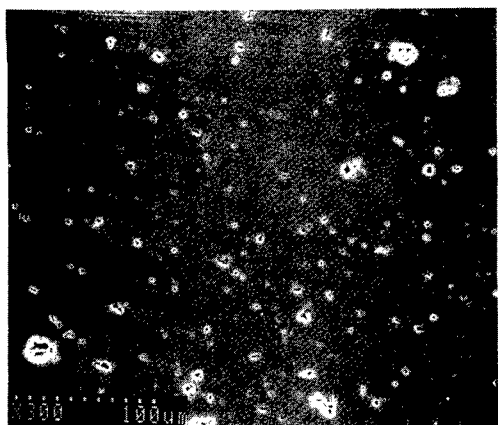


Fig. 1 Micrograph of a polished (3 μm diamond finish) alumina surface



Fig. 3 A typical micrograph of a thermally etched alumina surface, showing non-uniform grain size distribution.

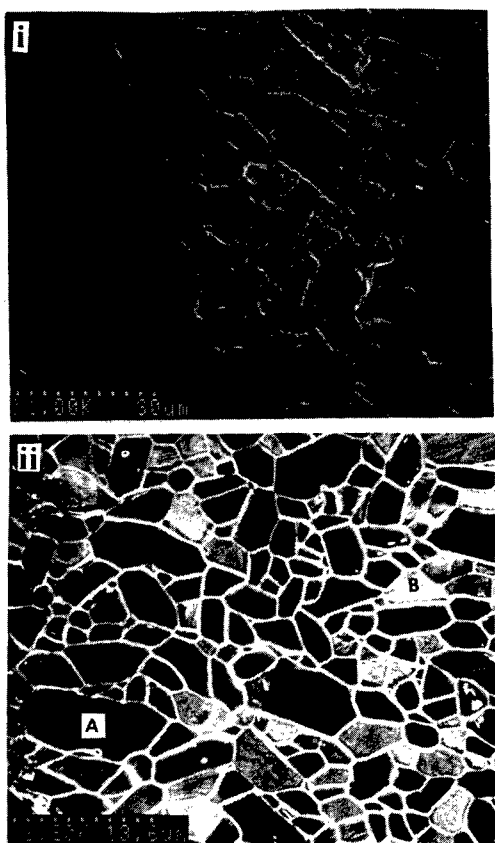


Fig. 2 Micrographs of the thermally etched alumina surface (without any metal coating) obtained at acceleration voltages of (i) 2 keV and (ii) 10 keV.

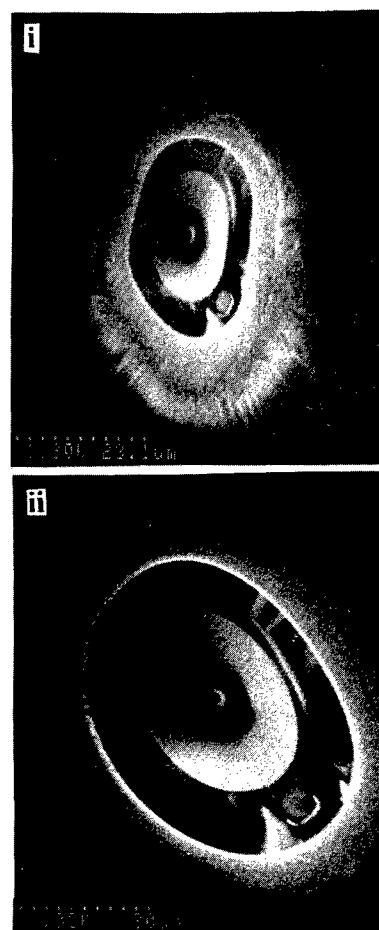


Fig. 4 SEM mirror images obtained on (i) a crystal of weak charging ability (gain A), and (ii) a crystal of strong charging ability (gain B) of Fig. 2 (ii).

Surface charging and flashover of insulators in vacuum

I D Chalmers, J H Lei and B Yang

Dept of Electronic and Electrical Engineering
University of Strathclyde
Glasgow, UK

ABSTRACT

Investigations have been carried out on right cylindrical teflon spacers in vacuum under DC stress to study the effect of cathode geometry on surface charging and flashover. Three cathode support arrangements were used. Type I involved a recess in the cathode into which the spacer was located. Type II was a simple flat plate cathode while type III had a raised insert on the cathode surface over which the spacer was located. In all cases the surface charge density and distribution is primarily dependent upon the magnitude of the electric stress. Using the type I arrangement inception for charge deposition was always about 10kV even when the spacer had been subjected to repeated flashovers and at applied voltages greater than this the density of the charge, which was fairly uniformly-distributed around the surface, was more or less proportional to the applied voltage. For the type II and III arrangements, a distinct, uniformly-distributed negative charge of up to $20\mu\text{C}/\text{m}^2$ was always detected at low values of applied stress and at a fairly well defined transition voltage this gave way to a distribution which was substantially uniform in the case of type II but quite filamentary in type III and both involved the deposition of positive charge.

1. INTRODUCTION

It is well known that the voltage hold-off capability of a vacuum gap is considerably reduced by the introduction of an insulator between the electrodes and therefore surface flashover has been a subject of considerable interest over the years¹. No undisputed model for surface breakdown has emerged from these studies² although all proposed mechanisms involve the final breakdown phase developing in a localised high pressure gas environment desorbed from the dielectric surface. There are basically two proposals. One³ involves electron emission from the cathode and the development of secondary emission electron avalanches (SEEA) at the insulator/vacuum interface. In an alternative scheme^{4,5} the physical processes taking place just below the dielectric surface are considered and a mechanism is proposed which involves propagation of electrons in the conduction band of the insulator. The source of electrons is assumed to be surface traps in the material and such electrons produce essentially an avalanche within the solid material but close to the surface. Some of the electrons produced in this avalanche are ejected into the vacuum and are accelerated towards the anode giving the appearance of a secondary emission electron avalanche. At the same time gas is desorbed from within the material by electron collision, and ionisation in the gas phase at the dielectric surface leads to breakdown in the usual way.

Regardless of the breakdown mechanism considered, it is clear that surface charging of insulators with the associated modification of the electric field in proximity to the insulator is an important prebreakdown phenomenon and indeed the nature of the surface charging prior to breakdown may ultimately help in differentiating between the two proposed schemes. It has been shown^{6,7}, for example, that the polarity and magnitude of the surface charge is a function of the shape of the insulator, in particular of the vertex angle when conical insulators are used. Additionally the nature of the cathode/insulator contact has been found to affect the surface charge accumulation and it has been reported⁸ that the dc and impulse flashover voltage of a cylindrical insulator can be increased by about 25% by incorporating a metal insert into the insulator at the cathode end which relieves the field at the cathode triple junction. Similar effects^{8,9} have been observed when the insulator is recessed into the electrode. It is clear that reducing the field at the triple junction in this way will reduce the emission of electrons but it is also probably of importance that the modification of the electric field will also mean that the surface charging process is affected. The present work was aimed at examining the process of surface charging of right cylindrical spacers under dc conditions and determining the effect on surface charging and flashover of different electrode/insulator geometries.

2. EXPERIMENTAL SET UP AND PROCEDURE

The experimental vessel has been described previously¹⁰. Briefly, it consists of a number of stainless-steel vacuum sections with a 150kV high-voltage input bushing, a pirani, penning and ionisation gauge, viewports and an oil diffusion pump and rotary pump capable of maintaining a vacuum of around 10^{-8} mbar. The test gap is formed from a pair of uniform-field brass electrodes,

50mm in flat diameter, the lower of which can be moved both rotationally and axially. In order to study the behaviour of dielectric surface charge, the uniform field electrodes are bridged by a right cylindrical spacer, 25mm diameter and effectively 10mm long. Stressing of the sample is then achieved by applying dc voltage between the electrodes.

The surface charge at any position on the sample was measured by an electrostatic shielded probe coupled to a high-impedance charge amplifier. A special support arrangement involving spring-bound retention of the spacer allowed the entire spacer surface to be scanned when the electrodes were moved apart. After the desired stressing period, the applied voltage was removed and the bottom electrode carrying the spacer was lowered until the electrode surface was below the centre line of the probe. The probe could then be moved in until its tip came within the desired distance from the spacer surface. By rotating the spacer using a low speed (0.5 rps) motor, a measure of the charge density around the circumference at that particular axial position was obtained. By lowering the spacer in steps, the circumferential charge distribution at various axial positions between the cathode end and the anode end could be obtained. The charge distribution was displayed on a storage CRO, the digitised output from which is fed to a computer and the complete set of data for that test was stored on disk.

The present observations and measurements were confined to teflon samples and three cathode/insulator geometries were used as shown in figure 1. Before any experiment, the electrodes were polished with grade 1-W-47 diamond paste and the electrodes

and insulating sample were cleaned in alcohol in an ultrasonic bath and degassed for at least 16 hours. The procedure adopted was as follows. The dc applied voltage was increased in steps of 5kV at an average rate of 20kV/min. At each step the insulator was stressed for 10 minutes and then the surface charge was measured. The voltages V_i , V_f and V_h are defined respectively as the voltage at which positive charge is first measured, the voltage at which the first surface

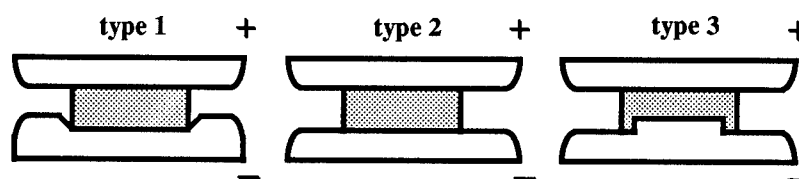


Figure 1. Three cathode geometries used in the investigation.

flashover takes place and the maximum voltage which can be applied for 10 minutes without flashover occurring. It should be noted here that in many cases V_h was greater than V_f . This is because the early breakdowns clearly result in some dynamic conditioning effect which enables considerably higher voltages to be subsequently withstood for the 10 minute period. When 20 flashovers occurred in any test period, the test was concluded. At this stage the surface charge was removed by increasing the system pressure to around 1mbar and the sample was then degassed before commencing a second similar test sequence. In general 3 such tests were performed on successive days on any sample in order to observe any longer term conditioning which might take place

3. RESULTS

3.1 Surface charge measurement

Surface charge is never absolutely uniformly distributed on the spacer surface and therefore it is difficult to ascribe to any particular distribution a unique value. However, since it has been found that in all cases the overall distribution is similar from one test to the next for any given set of conditions, in the interests of comparison, we have ascribed to each set of conditions a value corresponding to the maximum value recorded during the surface scan. Figures 2, 3 and 4 show these maximum values as a function of applied voltage for the three tests performed on successive days. For the recessed cathode (type 1, figure 2), the charge density which is always positive, is clearly a unique function of applied voltage and no conditioning effect, either short term or long term is observed. The charge appears as more or less uniformly distributed around the spacer circumference (ie no tendency towards filamentary channels) with a maximum density of about $30\mu\text{C}/\text{m}^2$ at an applied voltage of around 50kV. At voltages in excess of this there appears to be a reduction in charge density as the breakdown voltage of 60kV is approached.

Types 2 and 3 (figures 3 and 4 respectively) are similar to one another in the fact that at low values of applied field a fairly uniform distribution of negative charge is always observed. As the applied voltage is increased this negative charge increases until it gives way to positive charge accumulation at a fairly repeatable and well-defined transition voltage which, for both types of arrangement, depends strongly upon the history of the spacer. In general, the transition voltage increases as the tests proceed (with repeated sparking and/or exposure to stress) and this is much more evident for the type 3 arrangement where, in the first test, the transition to positive charge was just over 45kV whereas, for the third test, the transition did not occur until something over

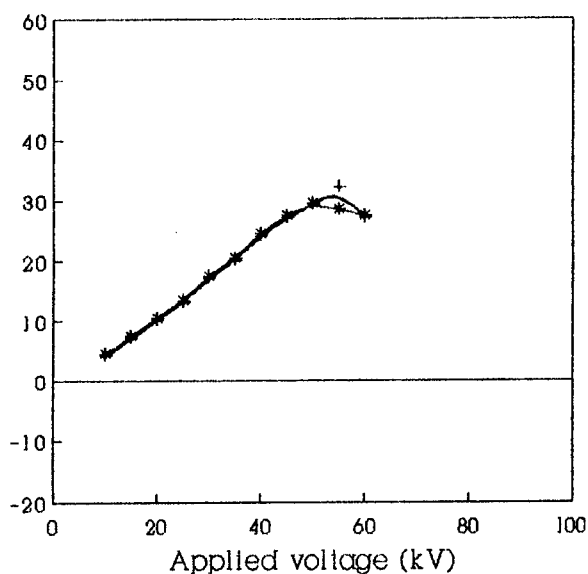


Figure 2

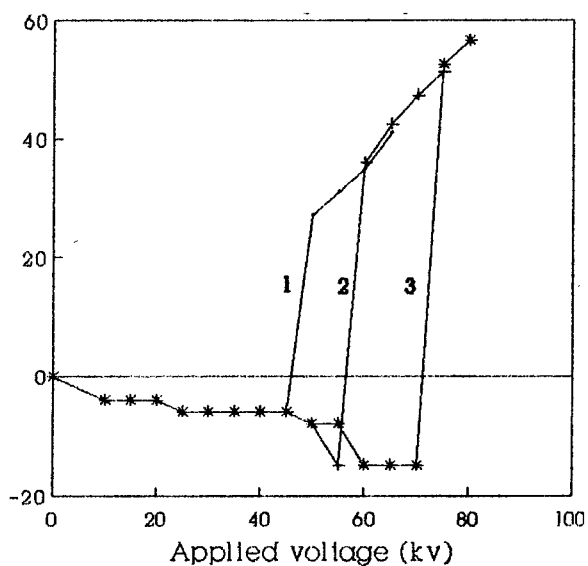


Figure 4

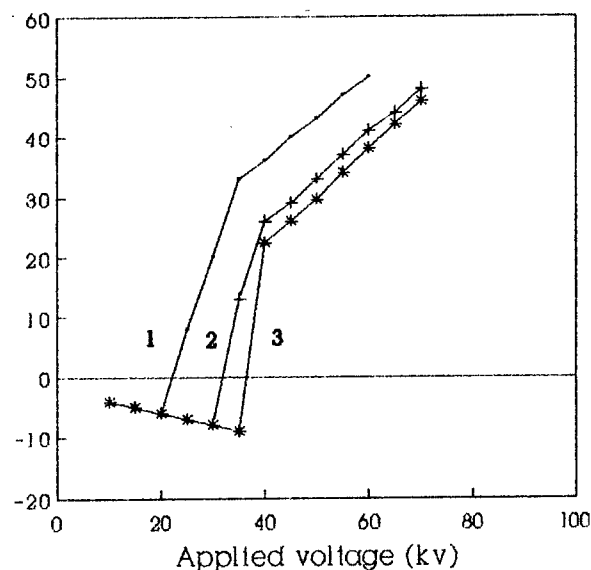


Figure 3

Figures 2, 3 and 4.

**Maximum surface charge density ($\mu\text{C}/\text{m}^2$)
as a function of applied voltage for the types
1, 2 and 3 cathode geometry respectively.**

• test 1 + test 2 * test 3

70kV had been reached. Since it is not easy to imagine that repeated sparking or prolonged exposure to applied stress could significantly affect the electric field distribution, this strongly suggests that by some process the insulator surface is being modified such that there is a greater tendency towards negative charge accumulation.

In all cases there is a well-defined axial distribution of charge in which the maximum value appears around 2 to 4mm away from the cathode and the density decreases fairly linearly towards both electrodes. Around the circumference at any axial position the distribution appears to be a function of the cathode arrangement. As indicated above, for the type 1 arrangement the circumferential distribution, whilst not absolutely uniform, is certainly not filamentary. The same distribution is found for the type 2 arrangement although the positive charge tends to accumulate more on one side of the spacer than the other. With the type 3 arrangement there is a definite tendency for filamentation. At the present time we have no explanation for this behaviour although it is believed that the pattern of charge accumulation is probably of significance.

3.2 Flashover and conditioning

Table 1 shows typical values of V_i , V_f and V_h for three tests conducted on successive days for the three types of cathode geometry. It is clear that the worst geometry in terms of withstand capability is initially type 1 although after two test periods, the performance of the type 1 geometry has improved and is superior to that of type 2 although the inception voltage for positive charge accumulation remains unchanged at 10kV. Type 3 always exhibits the highest withstand and inception voltages.

In terms of conditioning, types 1 and 3 condition fairly dramatically with repeated sparking and testing while type 2 does condition but less so than the other two.

Cathode geometry	Type 1	Type 2	Type 3
	$V_i/V_f/V_h$	$V_i/V_f/V_h$	$V_i/V_f/V_h$
Test 1	10/20/15	25/20/30	50/35/45
Test 2	10/25/45	35/35/40	60/60/55
Test 3	10/60/55	40/40/45	75/75/70

Table 1. Typical values of V_i , V_f and V_h (in kV) for the three arrangements

4.DISCUSSION

The present work has shown that both the flashover and the charge accumulation characteristics of spacers are related to the cathode support geometry. Clearly the most efficient form of support is that involving a cathode insert which relieves the electric field at the triple junction. However it can readily be demonstrated by field computation that the arrangement of type 1 where the spacer is recessed into the cathode results in a similar reduction in macroscopic field at the triple junction and thus it seems unlikely that the electrons in this case originate at the triple junction. It is possible that electrons are emitted from the raised shoulder on the electrode. However an important difference between the geometries of the type 1 and type 3 supports must be taken into account. That is that the electric field at the insulator surface in proximity to the cathode tends to accelerate electrons towards the insulator surface in the case of type 1 and away from the surface in type 3. This is probably the fundamental reason for the absence of negative charging in the type 1 arrangement. The fact that prolonged exposure to stress and repeated flashovers for the types 2 and 3 geometries increases the tendency to negative charge accumulation strongly suggests some change in the insulator surface. At the present time this is not understood and perhaps an explanation for this aspect of the behaviour will be found only after detailed microscopic or other examination of such surfaces.

5.ACKNOWLEDGEMENTS

The work reported was part of a project supported by the US SDI organisation through Auburn University. Receipt of funding under contract N60921-91-C-0078 is gratefully acknowledged.

6.REFERENCES

1. H. Craig Miller, "Surface flashover of insulators", IEEE Transactions on Electrical Insulation, **24**, pp 765-786, 1989.
2. R.A.Anderson, "Surface flashover-three decades of controversy", 14th ISDEIV, pp 311-317, 1990.
3. R.A.Anderson and J.P.Brainard, "Mechanism of pulsed surface flashover involving electron-stimulated desorption", J.Appl.Phys., **51**, pp 1414-1421, 1980.
4. J.P.Vigouroux, O.Lee-Deakon, C.LeGressus, C.Juret and C.Boiziau, Surface processes occurring during breakdown of high-voltage devices. IEEE Transactions on Electrical Insulation, **18**, pp 287-291, 1983.
5. C..LeGressus, P.H.Maire and J.P.Duraud, "The influence of surface phenomena on the insulation of discharge gaps in vacuum", IEEE Transactions on Electrical Insulation, **24**, pp 969-977, 1989.
6. H. Boersch, H. Hamisch and W. Erlich, "Surface discharge over insulators in vacuum", Z. Angew. Physik, **15**, pp 518-525, 1963.
7. O.Yamamoto, T.Hara, I.Nakanishi and M.Hayashi, "Monte Carlo simulation of surface charge on angled insulators in vacuum", Proc 14th ISDEIV, pp 400-404, 1990.
8. A.SS.Pillai and R.Hackam, "Influence of metal insulator junction on surface flashover in vacuum" J.Appl.Phys., **61**, pp 4992-4999, 1987
9. M.J.Kofoid, "Effect of metal-dielctric junction phenomena on insulator flashover in vacuum" AIEE, pp 999-1004, 1960.
10. I.D.Chalmers, J. H.Lei and J.W Bethel, "Dielectric surface charge in vacuum", Proc 14th ISDEIV, pp 324-327

SURFACE FLASHOVER SENSITIVITY OF SILICON IN VACUUM

G. Gradinaru, G. Korony, and T. S. Sudarshan
Department of Electrical and Computer Engineering
University of South Carolina, Columbia, SC 29208, USA

ABSTRACT: The high flashover sensitivity of high resistivity silicon in vacuum is discussed. Surface flashover fields of 5 - 30 kV/cm are common in silicon-vacuum systems, even though the intrinsic critical fields of silicon and vacuum are >300 kV/cm. The influences of the material (bulk quality and surface processing), contact technology, contact geometry and electrode configuration on the preflashover and surface flashover characteristics of wafer samples in vacuum are analyzed.

I. INTRODUCTION

The severe limitation of a photoconductive power switch (PCPS), due to the breakdown of the semiconductor-dielectric system, generally by surface flashover (SF), led to many experiments in the last decade on high field (HF) semiconductor systems, including Si-vacuum systems. In all papers on this topic [1-6] very low SF fields are reported for Si-vacuum systems. In all the cited papers, attention is focused on the SF response itself and on the possible mechanisms responsible for the SF process. The conclusion from [2-5] is that SF is a breakdown process located in the semiconductor, most probably in a region near the surface of the device. Our results of HF tests in Si-vacuum systems [6] (using cylindrical samples between parallel plane electrodes) are discussed using a new physical model of the prebreakdown and breakdown phenomena in semiconductor-dielectric systems [7]. In our model SF is an interface phenomenon strongly related with semiconductor processes (ohmic conduction, contact injection, collision-ionization generation, thermal effects, surface phenomena), ambient dielectric properties (density, electronegativity, dielectric strength), interface processes (gas desorption, electron bombardment), and the system configuration.

Here, new results on Si-vacuum systems at HF are reported using wafer shaped Si devices with different electrode configurations. For the first time the major influence of the contact technology and electrode configuration on the SF field, and also on the preflashover response in vacuum, is emphasized.. A discussion of results based on our SF model [7] is presented.

II. EXPERIMENTAL

The experimental set-up described in earlier works [7,8] was modified to incorporate advanced optical diagnostics, computer data acquisition interfaces, and a microprocessor based control system [9]. The applied voltage was a 0.39/3.0 μ s double-exponential pulse, allowing a time resolved analysis of the prebreakdown and breakdown response of the system. A medium vacuum (10^{-5} - 10^{-6} Torr) was used and the following electrode configurations: (1) Parallel plane electrode (PPE) configurations (Fig. 1) with variants: (a) sharp edged slot electrode, one-side contact; (b) chamfered electrode, one-side contact; (c) two-side contact. (2) Pillar hemispherical electrode (PHE) configurations with perpendicular or oblique pillar electrodes having hemispherical ends [Fig. 2(a,b)].

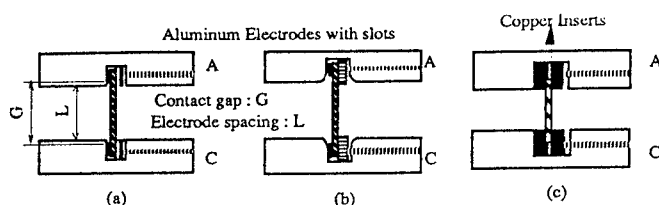


Fig. 1. Parallel plane electrode (PPE) configurations: (a) sharp edge, one-side contact; (b) chamfered, one-side contact; (c) two-side contact.

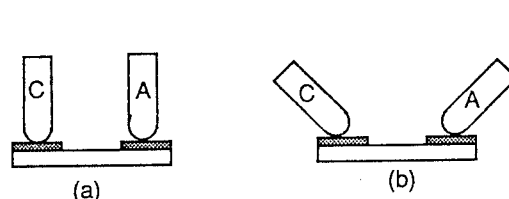


Fig.2. Pillar hemispherical electrode (PHE) configurations: (a) perpendicular; (b) oblique.

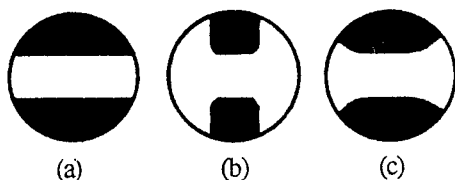


Fig. 3. Contact geometries

Wafer devices with contact geometries (deposited generally on one face), presented in Fig. 3(a,b,c), with gap lengths of 5-12 mm, were fabricated using ~ 35 k Ω cm Si(p) one inch diameter wafers, mirror-polished on both faces by the manufacturer. Essentially, three types of contacts were used (with variants in the annealing temperature, deposition temperature, cleaning procedure, and thickness of the metallic layer):

(1) Au contacts: after cleaning (ultrasonic - DI water), a first 600 \AA Au layer is sputter - deposited at room temperature, followed by a 200 $^{\circ}$ C/ 30 min.

annealing in air; then a second layer (1200-2000 Å) of Au is deposited.

(2) Cr/Au contacts: after cleaning (ultrasonic-DI water), 100 Å Cr was sputter-deposited at room temperature, then baked in air at 450°C/ 30(60) min.; then a second layer of 2000 Å Au was deposited.

(3) NiCr/Au contacts: after cleaning (RCA method or ultrasonic-DI water), a first layer of 600 Å NiCr mixture is sputter-deposited at 25-350°C (mostly at ~100°C); then a ~1000 Å Au layer is deposited by thermal evaporation at the same temperature of the wafer, without exposure to air.

III. RESULTS

For 35 kΩcm Si(p) cylindrical samples in the classical PPE configuration, in vacuum, we have reported [6] low SF fields in 10-16 kV/cm range, with a relatively low influence of the lateral surface processing. The main SF properties reported in [6] for cylindrical samples have also been observed in the case of wafers: (1) high SF sensitivity, (2) time delay of the SF event from the voltage peak, (3) SF conditioning (recovery) effect, and (4) light emissions during breakdown.

A distribution of the SF field values obtained in vacuum for different conditions is presented in Fig. 4 (each data point represents a certain SF field value obtained on a certain number of specimens). For Au, sharp edge contacts [Fig. 3(a)], in sharp or chamfered one-side contact PPE, most SF fields lie in 5-10 kV/cm range (Δ). Using NiCr/Au contacts with the same geometry in chamfered one-side contact PPE, larger values of 10-16 kV/cm (◻) are obtained. For NiCr/Au rounded contacts [Fig. 3(b,c)], using PHE systems, most SF fields are larger than 20 kV/cm (○); in many cases the test was stopped before SF (⬆). However for a device with NiCr/Au sharp edged contacts, using PHE system, the SF in vacuum was obtained at ~16 kV/cm. Note that no SF track or surface filament [7,9] was observed after SF in all conditions. However, for SF fields >20 kV/cm, especially for repeated SF events, the metal contact is often eroded in PHE; in PPE configurations, for SF fields generally <20 kV/cm, no contact erosion was observed.

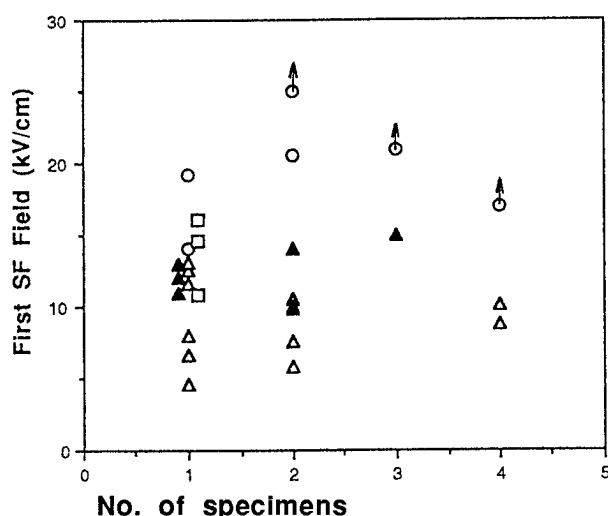


Fig.4. Statistical distribution of first SF field of Si in vacuum for different contact conditions and electrode configurations: (▲) cylindrical samples; (Δ) wafer, sharp geometry Au, one-side sharp or chamfered PPE; (◻) wafer, sharp geometry NiCr/Au, one-side chamfered PPE; (○) wafer, rounded geometries NiCr/Au, PHE; (⬆) test stopped before SF (Each data point represents the total number of samples with first SF at a given field)

A correct understanding of the breakdown phenomena in semiconductor-dielectric systems is not possible without the analysis of the *prebreakdown response* of the system. Until now, the preflashover characteristics of semiconductor-dielectric systems were totally neglected due, probably, to the high SF sensitivity in vacuum. However, under the experimental conditions presented above, there are some important observations to be made indicating the strong influence of the contact technology and shape, electrode configuration, and HF stress on the *preflashover* characteristics in vacuum:

(1) For one-face contact devices tested in PPE configurations, the conduction current up to SF (5-10 kV/cm) is very low (2-10 mA), much smaller than the displacement current.

(2) A significant preflashover nonohmic current component (0.1-3 A), with a clear delay (>500 ns) from the voltage peak, either without or with very low light emission, appears in the PPE systems in the following cases:

(a) at >300°C annealing or deposition temperature (e.g. 450°C/60 min annealing for Cr/Au contact, 350°C/30 min annealing for Au contact, and 350°C deposition temperature for NiCr/Au contact).

(b) after HF test in air or SF₆ at >25 kV/cm involving significant nonohmic currents.

(c) for two-face Au contact devices in the PPE system; the nonohmic component already present was significantly increased by including silver paste between the device contacts and electrodes.

An example of a large nonohmic current response in vacuum (750 mA/6 kV/cm) is presented in Fig. 5. A typical SF characteristic with a large preflashover current is presented in Fig. 6(a). At the SF event the sharp increase of the current

is accompanied by the total collapse of the applied voltage; at the same time a significant light (visible and IR) is emitted persisting a long time after the breakdown. The location of the visible light emission is obtained using an ICCD camera: for a 10^3 photonic gain and 10 μ s window time, the SF plasma light emission is filling the gap [Fig. 6(b)], while for 10^2 photonic gain and 1.5 μ s window time, the initiation of the SF light emission at the cathode can be observed [Fig. 6(c)].

(3) Using PHE configurations, in addition to much larger SF fields than in PPE configurations, different preflashover characteristics are obtained:

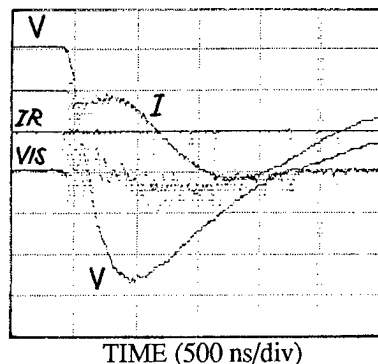
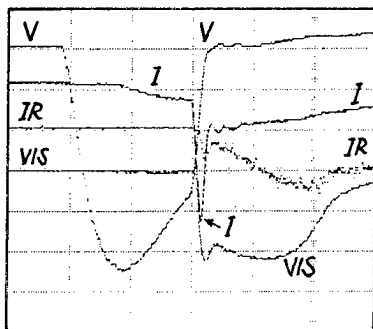


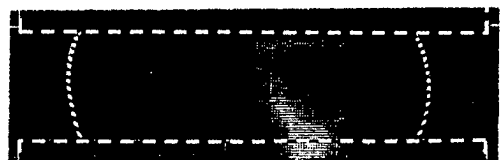
Fig.5. Significant nonohmic current response (V: 0.85 kV/cm; I: 0.35 A/div; IR: 5 mV/div; VIS: 5 mV/div)



(a) TIME (500 ns/div)



(b)



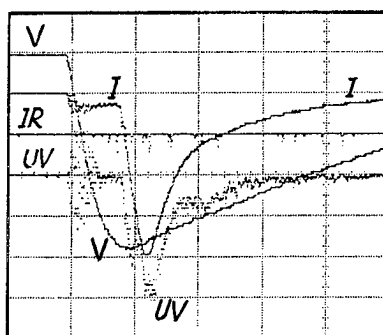
(c)

Fig. 6: (a) SF with large preflashover current (V: 1.7 kV/div; I: 15 A/div; IR: 300 mV/div; VIS: 250 mV/div); (b) SF-CCD image ($G_p = 10^3$; $t = 10 \mu$ s); (c) SF-CCD image ($G_p = 10^2$; $t = 1.5 \mu$ s)

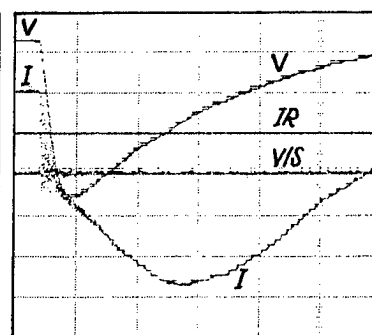
(a) The ohmic preflashover current is strongly dependent on the contact and surface processing. Good devices, with a very low current (< 1.5 A) up to 60 kV/cm in SF₆ (1-1.5 atm.), also presented relatively low ohmic currents in vacuum, lower than 15 mA up to 15-20 kV/cm. This is the case of NiCr/Au contacts deposited at $\sim 100^\circ\text{C}$ after a RCA cleaning.

(b) For NiCr/Au contacts deposited at 25-250 $^\circ\text{C}$ (mostly rounded and some sharp edged contacts), starting at 15-22 kV/cm, a sharp increase of the UV emission was observed, accompanied, generally, by a significant increase of the current (50-1000 mA) near V_{max} (Fig. 7). No IR emissions were detected and no CCD images were captured. In these cases the SF process is believed to be related to the UV-current generation phenomenon. This behavior was not observed with PPE systems for all types of contacts. Also, the UV-current burst-phenomena were not observed in devices with deposition temperature $> 300^\circ\text{C}$ for NiCr/Au or Au. More important, the noted effect disappears totally in SF₆. Devices with high UV-current emissions in vacuum above 16 kV/cm, but having a relatively low ohmic current, exhibited very low currents in SF₆ and a quasi-ohmic response up to 60 kV/cm, as noted above.

(c) For contact deposition temperatures $> 300^\circ\text{C}$, the above effect in vacuum was not observed even for > 22 kV/cm; instead, a large nonohmic current well delayed from the voltage peak was obtained (Fig. 8), without light emissions, starting at relatively low fields (6 kV/cm for Au, where only the first layer of 300 \AA was deposited at $\sim 380^\circ\text{C}$, and 9.5 kV/cm for NiCr/Au-350 $^\circ\text{C}$). As noted, the SF in vacuum in these cases was not obtained up to ~ 24 kV/cm, even though the total current was very large (~ 5 A). The nonohmic current was much larger for wafers with Au than for those with NiCr/Au in the 6-20 kV/cm range, but the currents were similar for higher fields. More important, in all cases, when this behavior was present in vacuum, the same very large currents were obtained in subsequent HF tests in SF₆, indicating bulk degradation.



TIME (500 ns/div)



TIME (1 μ s/div)

Fig. 7. Pulsed UV and current in PHE configurations (V: 3.4 kV/div; I: 0.35 A/div; IR: 20 mV/div; UV: 20 mV/div)

Fig. 8. Large preflashover current for high deposition temperature of NiCr/Au (350 $^\circ\text{C}$) (V: 1.7 kV/div; I: 0.035 A/div; IR: 10 mV/div; VIS: 100 mV/div)

IV. DISCUSSION

The very limited space allows us only a "telegraphic" discussion of the experimental results. Without having to develop detailed explanations for each case, we note that all experimental results could be satisfactorily explained using the following ideas:

(1) In all cases, the device subjected to HF must be considered an unitary system; the device response is, in fact, the system response, with significant contributions from all the constituting parts: semiconductor (bulk, surface), ambient dielectric, and electrodes.

(2) We consider four main factors in the SF "game" (as well as in the preflashover response) in Si-vacuum and, in general, in HF semiconductor-dielectric systems: (a) the defect distribution in the semiconductor which controls the current distribution in the device and, therefore, the electrical activity at the semiconductor-vacuum interface; (b) the field distribution in the device due to significant field enhancement effects in the device bulk and surface, mainly determined by the contact technology, contact geometry, and electrode configuration; (c) the intensity and effectivity of triple-junction-emitted electrons depending on the electrode configuration and contact geometry; (d) gas desorption from the material.

(3) When the defect density in the bulk is significantly increased (by high temperature treatments or high fields inducing large nonohmic currents), the surface current component is reduced, decreasing significantly the SF sensitivity and the interface activity in the preflashover stage.

(4) A much smaller effectivity is supposed for the triple-junction-emitted electrons in PHE configurations than in PPE ones; the field values (15-20 kV/cm) that cause SF in all PPE cases, only cause an interface effect producing pulsed UV light emission and current in PHE systems.

(5) Good bulk quality, high resistivity Si subjected to HF in vacuum, is dominated by interface processes, as is true with solid dielectrics.

(6) The very high SF sensitivity of Si in vacuum compared with other ambient dielectrics (SF₆, air, N₂, etc) is due to a significantly higher efficiency of the triple-junction emitted electrons at the interface.

(7) The very high SF sensitivity of Si in vacuum, compared with solid dielectrics, is caused by much larger currents in the semiconductor surface, with a high surface activity when the device is subjected to HF and electron bombardment from the cathode. The thermal effects of the semiconductor currents in the surface region and the electron bombardment produce significant gas desorption [4]. Interface collision-ionization processes cause UV emissions and current increase, leading, finally, to SF.

V. CONCLUSIONS

The HF Si-vacuum system has some unique characteristics governed by major influences of the bulk and the surface of the semiconductor material, contact contour and process technology, and electrode configuration on the preflashover and SF response. The high SF sensitivity of Si in vacuum can be explained in terms of the physical model proposed in [7].

ACKNOWLEDGEMENT

The support from BMDO/ONR for this work is gratefully acknowledged.

REFERENCES

1. B. L. Thomas, *et al*, in *Proc. of 6th IEEE Pulsed Power Conf.* (Arlington, VA, 1987), p. 149.
2. R. Feuerstein and B. Senitzky, in *Proc. of 7th IEEE Pulsed Power Conf.* (Monterey, CA, 1989), p. 358.
3. R. Feuerstein and B. Senitzky, *J. Appl. Phys.* **70**, 288 (1991).
4. F. E. Peterkin, *et al*, *IEEE Trans. Electron Devices* **37**, 2459 (1990).
5. P. F. Williams, *et al*, in *Proc. of 7th IEEE Pulsed Power Conf.* (Monterey, CA, 1989), p. 890.
6. G. Gradinaru, *et al*, in *Proc. of 15th ISDEIV* (Darmstadt, Germany, 1992), p. 208.
7. G. Gradinaru and T. S. Sudarshan, *J. Appl. Phys.* **73**(11), 7643 (1993).
8. S. H. Nam and T. S. Sudarshan, *IEEE Trans. Electron Devices* **37**, 2466 (1990).
9. T. S. Sudarshan, *et al*, in *Proc. of 6th SDIO/ONR Pulse Power Meeting* (Chicago, IL, 1993).

Microwave surface flashover of dielectrics in vacuum

Alexander A. Ravaev, Eugene A. Galstjan

Moscow Radiotechnical Institute, Russian Academy of Sciences
Warshawkoe Shosse, 132, Moscow 113519, Russia

ABSTRACT

There is no need to explain an importance of a titled phenomenon study. Microwave surface flashover (MWSF) of dielectric articles - such as insulators, focusing lenses, waveguide windows, etc. - in vacuum is the primary factor limiting the applicable microwave intensities in physical and industrial installations. Besides this "negative" sense, MWSF also takes an applied significance. The present work is devoted to description of MWSF phenomenon itself and consists of two following parts.

Threshold characteristics of pulsed dielectric surface breakdown in vacuum, obtained at various experimental conditions, are considered in detail. As would be expected, the breakdown time delay τ_d - supposing that τ_d is less than MW pulse duration τ_p - depends on many initial parameters, such as MW intensity J , nature of irradiated material and its surface quality, vacuum characteristics, etc. At the same time experimental results, arrived at MW intensities above "continuous wave" threshold up to 10^7 W/cm², showed that the value $W = J \cdot \tau_d \approx \text{const}$; i.e. W looks like some energetic invariant for a given material and its exploitation conditions. An increase of pulsed MWSF thresholds after surface training by preliminary discharge series or under supplying constant electrical potential to the article from external source was observed and measured too. Obtained results are of great interest from the purely practical view point.

Experimental data allowed us to make the physical model of MWSF phenomenon more clear. It is based on the dominating role of the saturated secondary electron emission avalanche, electron stimulated gas desorption, and following MW breakdown of near surface gas cloud. Experimental results and theoretical estimations are in a satisfactory agreement.

1. INTRODUCTION TO THE PROBLEM

By now, the realistic physical picture of pulsed MWSF is far from being fully understood. It should be borne in mind that the physical mechanisms leading to *microwave* surface breakdown are in many respects similar to the processes of *high voltage* pulsed flashover (HVF) of insulators in vacuum.¹ Several models have been proposed to describe high voltage flashover.

Bugaev, Iskoldskii and Mesyats were among the first to carry out the correct experimental investigations and to consider the HVF mechanism.² An extended HVF model, so called "gaseous model", was suggested and theoretically estimated by Avdienko.³ More recent works - theoretical analysis⁴ and the use of novel high-speed diagnostics in experimental investigations⁵ - essentially amplified HVF theory. In particular, the existence of dielectric surface charging and a saturation of the current amplification mechanism in early phase of flashover, the major role of desorbed gases from the insulator surface and following gaseous discharge near the surface were pointed out there.

On the other hand, *microwave* surface flashover has a number of specific distinctions: the absence of any conductors and electrodes, of a fixed direction of the discharge front moving, etc. The same is applied to particularities of secondary electron emission discharge (SEED) in high-frequency electric fields.

The first step on the way of determining MWSF threshold was made by Kossiy and co-authors⁶. They have developed microwave SEED theory in case of its most general polyphase form. It allowed to estimate the "first" threshold of MWSF, corresponding to $\tau_d \rightarrow \infty$, in a variety of operating conditions.

At the same time the next step was not done. Well understanding the importance of gas desorption mechanism (Kossiy, Ref. 1, chapter 8), the authors⁶ have not combined mentioned phenomena. A time delay τ_d and, consequently, a "second" threshold of the *pulsed* MW surface breakdown were not considered and determined. Furthermore, many of investigators know and use in practice aforementioned invariant W , but nobody has explained this fact in detail.

Below an attempt is made to fill in this gap. Let us begin with description of some experimental results obtained in Moscow Radiotechnical Institute with participation of colleagues from General Physics Institute.

2. EXPERIMENT

The studies of MWSF characteristics were conducted with a usual experimental set-up consisting of high-power microwave generator, focusing system, anechoic vacuum chamber, and diagnostic apparatus. Two types of pulse MW generators and auxiliary equipment were used: magnetron (incident MW intensity in focal zone reached 10^6 W/cm², wavelength - 16 cm, pulse duration $1 \div 50$ μ s); multichannel generator based on clystron amplifiers ($J_{\max} \approx 3 \cdot 10^4$ W/cm², $\lambda = 4.3$ cm, $\tau_p = 1 \div 1000$ μ s). To increase an effective MW intensity on a sample surface, a standing-wave regime was realized as needed. We also used a super-power MW generator, relativistic carsinotron, for a qualitative examination of pulsed MWSF thresholds at intensities up to 10^7 W/cm².

Time characteristics of flashover were measured with optical and X-ray diagnostics (using photo-electron amplifiers) with resolution of 50 ns, and semiconductor detectors of reflected and transmitted MW radiation (based on hot-electron effect) with time resolution ~ 1 ns. Foil filters with cut-off energy of ~ 3 keV were placed before X-ray plastic scintillator, therefore we registered fairly hard part of X-ray discharge emission.

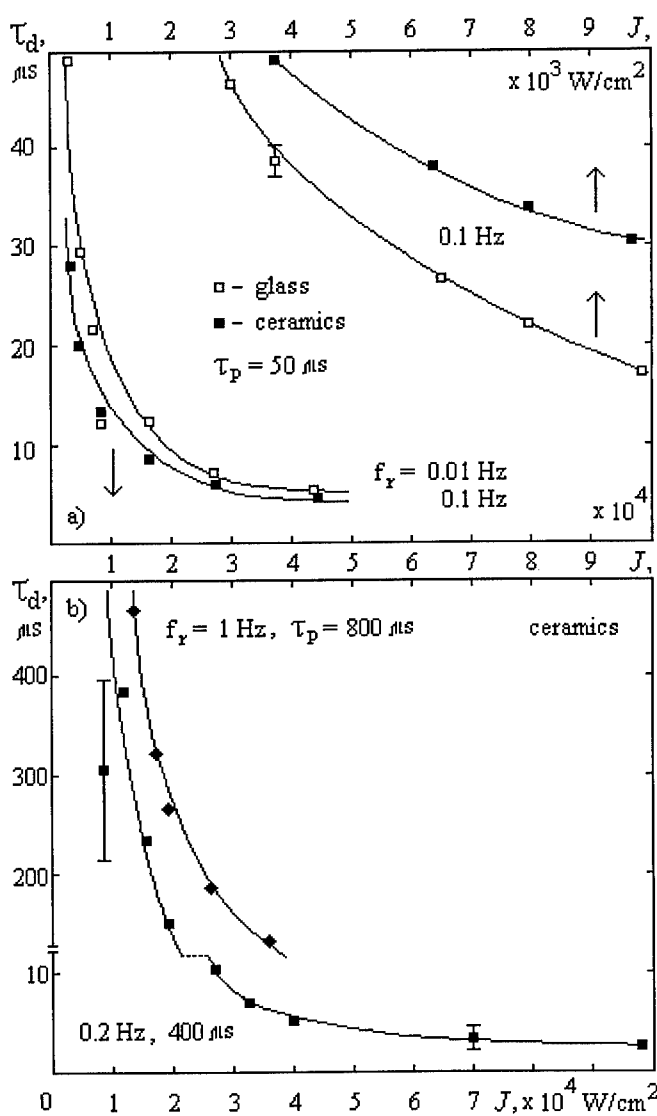


Fig 1. Time delay τ_d of MWSF vs. radiation intensity J at various pulse repetition rates f_r and pulse duration τ_p . a) $\lambda = 16$ cm; b) 4.3 cm.

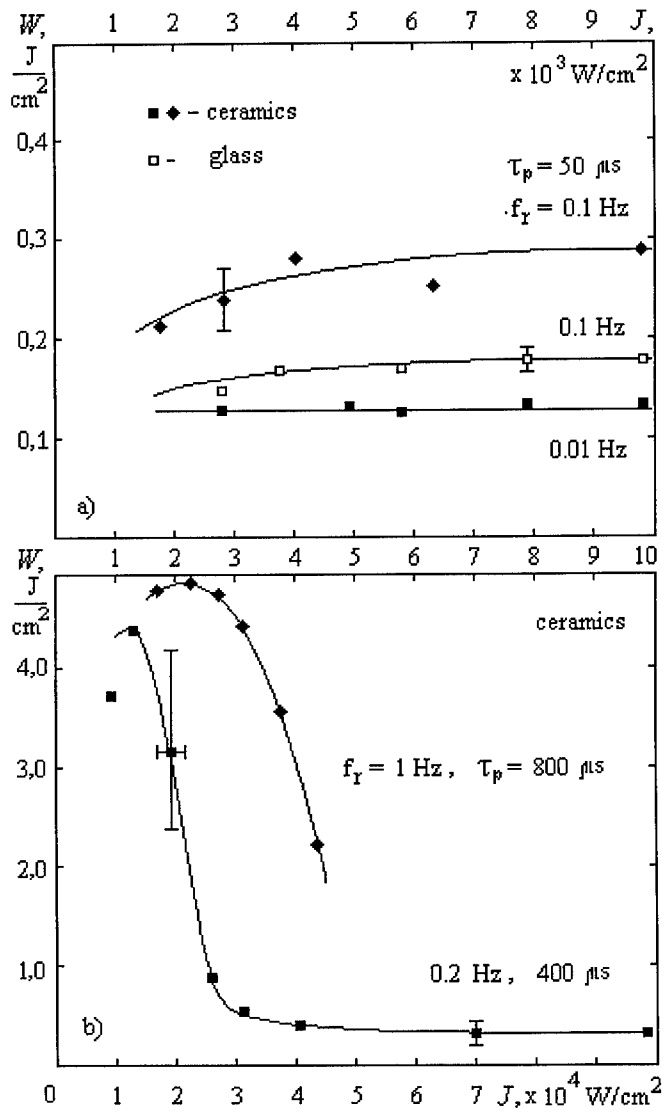


Fig. 2. Value $W = J \cdot \tau_d$ vs. radiation intensity J at various experimental conditions. a) $\lambda = 16$ cm; b) 4.3 cm.

We have studied two sorts of materials. The first sample represented a glass cylinder with quite smooth surface. Another was made of composite ceramics, carborundum being a good microwave absorber. Its surface roughness was about 100 μm - an average dimension of SiC powder granules.

As would be expected, starting from some values $J \approx J_1$ and on, we have observed microwave breakdown at the samples' surface, accompanied by intense light and X-ray emission, sharp radiation reflectivity growth and passage rate decreasing. The last testifies that discharge plasma concentration exceeds its critical value, that may be used as MWSF criteria. In contrast to results of Hegeler et al.,⁵ a sharp growth of X-ray emission takes place at the final phase of flashover, and may be explained by nonlinear generation of strong Langmuir waves and fast electrons production in a plasma resonance region of the plasma flare.⁷ At low MW intensities a "weak" optical luminosity was observed too.

Experimental dependencies $\tau_d(J)$, obtained at various repetition rates f_r and pulse duration τ_p , are presented in Fig.1.; associated curves W , as functions of intensity J , are depicted in Fig.2. From these figures notice that "continuous wave" limit is approximately equal to J_1 , corresponding to the first critical potential of a sample material. Value J_1 depends on wave frequency as $\sim 1/\omega^2$, but is weakly dependent on the nature and surface quality of the material itself. Above J_1 , parameter $W \cong \text{const.}$ and looks like "energetic invariant" independent on radiation frequency and net material properties. This fact and an increase of τ_d with increasing MW pulse repetition rate (that is equivalent to surface training) confirm gas-desorption model of MWSF. It is in agreement with independence of invariant W on material characteristics in "dirty" vacuum.

Strong influence of an external potential U , supplied to the ceramic sample, on pulsed MWSF threshold was observed in our experiments. The dependencies $\tau_d(U)$ and $W(U)$ rise sharper in the case of negative potential. This circumstance and values of the first threshold J_1 tell us about electron nature of initial stage of the MWSF phenomenon considered.

3. THEORETICAL ESTIMATIONS

Let us consider an infinite dielectric plane eliminating by MW so, that the MW electric field is directed along the surface of the plane (in the X direction and the Z is perpendicular to the plane). At the beginning there are only background electrons in vacuum space above the dielectric plane. In the initial stage of MWSF these electrons bombard the surface providing a way for SEED to be born. The energy of a background electron therewith have to be more than A_1 - the lower of the two energies, at which the SEED rate $\sigma = 1$. In addition, there is a need to have a force returning the secondary emission electrons to the surface. Before the surface has been essentially charged, the only returning force is Miller's one.⁷ Maximum value of Miller's quasi potential corresponds to the point $z_m = \lambda/4$ and is equal to

$$A_m = (\epsilon - 1)e^2 E_0^2 / (\sqrt{\epsilon} + 1)^2 m \omega^2 = 1.8 \cdot 10^3 (\epsilon - 1) E_0^2 / (\sqrt{\epsilon} + 1)^2 \omega^2 \text{ (eV)},$$

where ϵ is a permittivity of the dielectric, e , m are the charge and the mass of electron, E_0 (in kV/cm) is an amplitude of the MW electric field, ω (in GHz) is MW frequency. The dependence of Miller's potential in moving from z_m to the plane is approximately giving by function $(4z/\lambda)^2$, where λ is MW wavelength. Furthermore, we assume that the secondary emission electrons are moving in a uniformly charged layer with upper bound $z_0 < z_m$ and a total charge of electrons in the layer is equal to a positive charge of the plane. Electrostatic potential in this situation may be written in the form

$$A_c = 4\pi e^2 n \cdot (z - z^2 / 2z_0) = 1.8 \cdot 10^{-6} n (z - z^2 / 2z_0) \text{ (eV)},$$

where n (in $1/\text{cm}^2$) is the number of electrons in the layer per unit area. We assume also that the secondary emission electrons are uniformly distributed over angle and have the mean energy $A_0 = 4 \text{ eV} < A_m$. All of the preceding allow us to write down an equation, describing dependence of n upon time:

$$dn / dt = (\sigma - 1) n V_0 / z_0,$$

where V_0 (in cm/s) is the velocity of the secondary emission electrons, $\sigma(A) = A/A_1$ is secondary emission rate averaged over angle (A is mean energy of electron) and z_0 (in cm) is

$$z_0 = \sqrt{A_0 / 2 A_m} (\sqrt{1 + A_c^2 / 2 A_0 A_m} - A_c / \sqrt{2 A_0 A_m}) \cdot \lambda / 4.$$

At the beginning a charge of the plane is very small and behavior of electrons is defined by Miller's force. In this case the equation may be simplified and gives as the solution exponential rise of the number of the secondary emission

electrons $n = n_0 \exp(t/\tau_m)$, where $\tau_m = \lambda(A_0/A_m)^{1/2}/4V_0(\sigma-1)$ is characteristic time of SEED development. This solution holds up to $n_1 \approx 10^6$ 1/cm². As the charge density on the plane increases, the boundary of the layer moves to the plane, so that the electrostatic potential A_c starts to determine the behavior of electrons. The electrons are pressed by electrostatic field to the plane so, that the mean energy decreases to the value whereby $\sigma = 1$. In that event the equation also may be simplified and its analytical solution is

$$n = n_{\text{lim}} [1 + C_1 \exp(-2\alpha t)] / [1 - C_1 \exp(-2\alpha t)],$$

where $n_{\text{lim}} = 8.2 \cdot 10^{-2} \omega E_0 / A_1^{1/2}$ is maximum value of the number of electrons per unit area, $C_1 = \ln[(n_1 - n_{\text{lim}})/(n_1 + n_{\text{lim}})]$ is constant, $\alpha = n_{\text{lim}} V_0 10^{-6} / A_0$ (in 1/sec).

By this means SEED has stabilized at time interval of the order of 50 - 300 nsec. The thickness of the electron layer, after this time moment, is $\approx \lambda A_0 / 10^{-5} n_{\text{lim}} = 10^{-4} - 10^{-3}$ cm and the amplitude of the surface current is about 30 - 300 mA/cm. From the outset the electron bombardment of the surface is accompanied by gas molecule desorption and this process defines the second stage - gas discharge. Production of a gas cloud and its ionization go hand in hand to lead to a critical plasma density creation. We assume that each electron knocks about 10^2 molecules out the surface. Consequently, a number of molecules rises lineary as function of time $N = 10^{-4} \omega^2 E_0^2 \cdot t$. Equation of gas ionisation can be obtained as

$$dn_e / dt = \nu(t) \cdot n_e,$$

where n_e is the plasma electron density, ν is collision frequency. The solution of this equation $n_e = n_{e0} \exp(\beta t^2/2)$ let us estimate the total discharge time $\tau_d \approx (2 \ln n_{cr} / \beta)$. For $\lambda = 4$ cm and hydrogen molecules it becomes

$$\tau_d = 3 \cdot 10^{-3} / E_0^2 \sqrt{E_0 - 37.5 / E_0}, \quad \text{if } 8 < E_0 < 12 \text{ kV/cm}$$

$$\tau_d = 2 \cdot 10^{-4} / E_0^2, \quad \text{if } E_0 > 12 \text{ kV/cm}.$$

From where the value of the above-mentioned energetic invariant is $W = J \cdot \tau_d \approx 0.26$ J/cm² and is in the good agreement with experimental one (Fig. 2). Its independence from MW intensity and frequency is attributable to peculiar features of gas ionization cross-section in the electron energetic range from 20 eV to 70 eV.

So, SEED is but an initiator of MW surface flashover, the most of τ_d is time of gas molecules desorption and ionization. Even simple theoretical estimation in the framework of the gaseous model gives us the good agreement with experiment.

4. REFERENCES

1. I. N. Slivkov, *Processes at High Voltage in Vacuum*, Energoatomizdat, Moscow, 1986.
2. S. P. Bugaev, A. M. Iskoldskii, and G. A. Mesyats, "Investigation of the pulsed breakdown mechanism at the surface of a dielectric in vacuum. I. Uniform field," *Sov. Phys.- Techn. Phys.*, vol. 12, no. 10, pp. 1358-1362, April 1968.
3. A. A. Avdienko and M. D. Malev, "Surface breakdown of solid dielectrics in vacuum," *Zhurnal Technicheskoi Fiziki*, vol. 47, no. 8, pp. 1697-1711, Aug. 1977; vol. 49, no. 5, pp. 987-997, May 1979 (in Russian).
4. A. S. Pillai and R. Hackam, "Surface flashover of solid dielectric in vacuum," *J. Appl. Phys.*, vol. 53, no. 4, pp. 2983-2987, April 1992.
5. F. Hegeler, G. Masten, H. Krompholz, and L. L. Hatfield, "Current, luminosity, and X-ray emission in the early phase of dielectric surface flashover in vacuum," *IEEE Trans. on PS*, vol. 21, no. 2, pp. 223-227, April 1993.
6. L. V. Grishin, A. A. Dorofejuk, I. A. Kossiy, G. S. Lukianchikov, and M. M. Savchenko, "A study of polypfase secondary electron emission discharge," *Proc. of Lebedev Phys. Inst. (FIAN) - Dissipation of Electromagnetic Waves in Plasmas*, vol. 92, pp. 82-131, Nauka, Moscow, 1977.
7. G. A. Askar'jan, G. M. Batanov, and I. A. Kossiy, "Energy conversion of intense radiation in plasma flare," *Proc. of General Physics Inst. - Generation of Nonlinear Waves and Quasi-Stationary Currents in Plasmas*, vol. 16, pp. 3-10, Nauka, Moscow, 1988.

Influence of dielectric surface properties on the generation of surface microplasmas

T.S.Sudarshan and C.R.Li
Department of Electrical and Computer Engineering
University of South Carolina
Columbia, SC 29208, USA

Abstract

Alumina samples with different surface polishing (unpolished, 9 μm diamond-finished, and 9 μm SiC-finished samples) were used in our studies in vacuum, under pulse excitation, to understand the influence of surface preparation on the surface predischage associated with microplasmas. The unpolished sample exhibited very active predischage events, consisting of active localized plasmas on the surface, with associated large predischage current and high intensity of luminosity, and low electrical breakdown strength. Compared to the SiC-finished sample, the diamond-finished sample showed more active predischage events and lower conditioned and hold-off voltages. There seems to be a correlation between the predischage activity and the surface preparation. Our experimental studies indicate that the phenomena of predischage localized plasmas are related to the physical state of the dielectric surface.

I. Introduction

In recent years, physical models proposed to explain the dielectric surface flashover phenomenon suggest that the electrical breakdown strength of an insulator is related to the type of surface treatment.¹ Some results have shown that mechanical polishing of the surface can minimize the surface irregularities or defects caused by the machining process, thereby resulting in higher breakdown strength for a polished insulator compared to that of an unpolished sample.² However, the mechanisms responsible for the improvement in flashover strength caused by surface polishing are not yet understood. In the present work, investigations have been aimed towards understanding the effects of different polishing media (like SiC abrasives and diamond paste) on the predischage phenomena and the flashover strength of polycrystalline alumina samples.

II. Experiment setup and procedure

A nonuniform field test system was employed, consisting of aluminum finger-type electrodes placed on the flat surface of a test specimen. The distance between the two electrodes was 10 mm, while the radius of curvature of the electrodes at the tip was 9 mm. The electrodes were polished initially by 9.5 micron alumina abrasive followed by 0.05 micron alumina abrasive to attain a mirror finish. The insulators studied were 99.9% pure polycrystalline alumina in the form of right circular cylinders, 10 mm thick and 25.4 mm in diameter. Four alumina samples were chosen. One sample was tested as machined, without subjecting it to any kind of surface polishing. The others were polished by SiC abrasive discs and diamond paste. The sequence of polishing adopted for the experiments had two distinct phases. Initially, all the samples were polished using SiC abrasive discs ranging from 60 grit (268 μm) to 600 grit (16 μm). The SiC polishing was used to eliminate heavy or macro surface damages and to attain a flat surface. In the final phase, one sample was subjected to 9 μm diamond final finish. The other was subjected to 800 grit (9 μm) SiC final finish. After polishing, the sample, as well as the electrodes, was cleaned ultrasonically in deionized water for one hour.

The experimental arrangement used has been discussed in detail elsewhere.³ Briefly, a 0.39/3 μs electrical pulse generated by a Marx generator was applied to the test specimen in the vacuum chamber at 2×10^{-6} torr. The current and voltage waveforms were measured using a 50 Ω current viewing resistor and an E dot probe respectively, both having a response time of 1 ns. A gatable high speed (50 ns) 2D intensified CCD camera (spectral response from 320ns to 820ns) was focused on the surface of the tested sample in order to obtain spatially-resolved images. The gain of the ICCD camera was set to be high ($\sim 10^4$ photonic gain) to capture weak light emissions from the surfaces. In addition, a photomultiplier tube (R632 spectral response between 300 nm to 1200 nm) with a rise time of 2 ns was used to provide time-resolved information of the optical activities.

The sample was subjected to voltage pulses beginning at about 15 kV. The voltage was then progressively increased in steps of 1.0 kV. At each voltage level the sample was subjected to ten shots. If the sample did not experience a breakdown,

the voltage was increased by 1.0 kV. This procedure was continued until the sample experienced a flashover. This voltage level was called the first breakdown level, V_{bd} . If the sample underwent breakdown in the two subsequent applications at V_{bd} , the same voltage level was also termed the conditioned voltage, V_{co} . Otherwise, the voltage was increased again in steps of 1.0 kV until the specimen underwent breakdown. The voltage at which three out of three successive voltage applications resulted in breakdown was called, as noted above, the conditioned voltage. The voltage level below the conditioned value, at which the sample did not breakdown, was termed the "hold-off voltage", V_{ho} .

III. Results

1. Predischarge activity associated with microplasma

The predischarge activity detected in our system is usually associated with a several milliamper pulse current and luminosity of 10^{-3} lm. Fig.1(a) shows typical voltage, current and light emission signals as a function of time during preflashover. The first peak in the current response is the displacement current. The current pulse near the voltage peak, accompanied by a light signal from the PMT, is the preflashover activity. Once the light and current signals occur simultaneously, some small light sources distributed on the surface of the sample can be captured by our weak light imaging system. Fig.1(b) shows an image of the light sources, captured on the ICCD camera, corresponding to the light emission from the PMT in Fig.1(a). It is interesting to note that the number and the intensity of the light sources increase with current, indicating that these light point sources are related to the surface current conduction. According to their light and electrical conduction characteristics, the light point sources are identified as localized plasmas on the surface. In the nonuniform field electrode arrangement, the preflashover activity is relatively high.

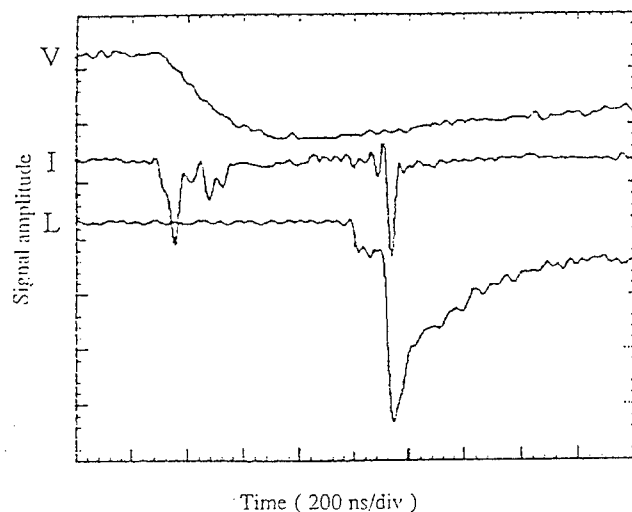


Fig.1(a) Typical voltage, current and light signals as a function of time showing preflashover activity.
V:8.5 kV/div, I:88 mA/div, L: 10^{-3} lm/div.

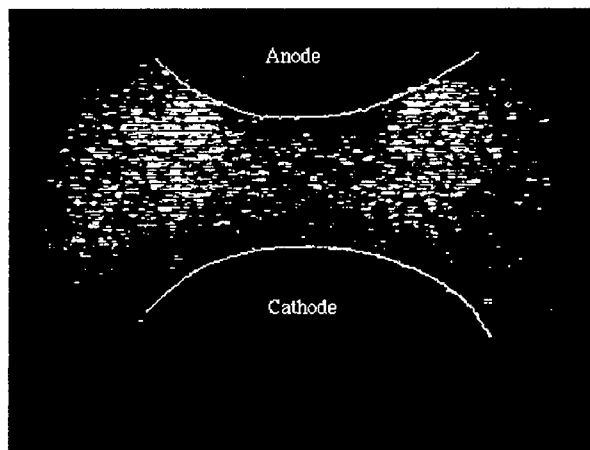


Fig.1(b) The ICCD camera image corresponding to the waveform shown in Fig.1(a).

2. Effect of Surface Finish on the Electrical Characteristics

Table 1 summarizes the values of V_{bd} , V_{co} and V_{ho} for the tested samples prepared with different surface finishes. On all four days, the unpolished sample shows very poor breakdown voltage levels and does not exhibit any significant conditioning. The surface flashover behavior of this unpolished sample may be related to scratches and deformations caused by the machining operations since the surface damages or deep scratches are believed to introduce significant defect complexes on the surface.² Compared to the 9 μ m diamond-finished sample, the 9 μ m SiC-finished sample shows marginally better performance on the first day. On the second and third day, the 9 μ m SiC-finished sample shows superior conditioning and, in general, exhibits higher conditioned and hold-off voltage levels. On the fourth day, the electrical performances of the 9 μ m SiC-finished sample are much better than those of the 9 μ m diamond-finished sample, showing an enhancement of about 7

kV in the value of V_{CO} . Usually, when samples are tested over a period of four days, they exhibit very poor performances on the fourth day, due to the formation of permanent microcracks and channels conducive to electronic conduction on the surface of the insulator, caused by several flashovers on the previous days. The fact that V_{HO} (the hold-off strengths) of the SiC-finished sample are relatively much closer to V_{CO} (the conditioned level) suggests that the SiC-finished samples are probably not permanently affected by the repeated application of voltage pulses and hence have higher hold-off levels on the fourth day. In comparison, the diamond-finished sample shows lower levels of breakdown strength, lesser conditioning, and very low hold-off levels (15 kV) on the fourth day, indicating that they might have undergone permanent damage. To confirm this trend, tests for 9 μm SiC and diamond-finish samples were extended to the fifth day. The 9 μm diamond-finished sample shows still very low V_{HO} of 15.8 kV on the fifth day, while the 9 μm SiC-finished sample still exhibits a high hold-off flashover strength of 24 kV on the fifth day. Comparison of electrical strengths of samples polished with almost the same particle size but with different polishing mediums shows that the breakdown voltage levels may be influenced by surface preparation. Transmission electron microscopy (TEM) studies reported by Hockey have shown that a diamond-abraded alumina surface exhibits higher density of dislocations on the surface, as well as within the near surface regions.⁴ These defects, induced by diamond polishing, may be responsible for the poor electrical performance of a 9 μm diamond-finished sample.

Table 1 The Electrical Performance of the Different Samples

Surface finish		Unpolish	9 μm Diamond	9 μm SiC
1st Day	Vbd	14 kV	16.7 kV	19.9 kV
	Vco	14 kV	18.6 kV	22.8 kV
	Vho	13.2 kV	17 kV	20.2 kV
2nd Day	Vbd	16.9 kV	19.9 kV	26.7 kV
	Vco	16.9 kV	23.3 kV	26.7 kV
	Vho	15.7 kV	19 kV	20.9 kV
3rd Day	Vbd	16.9 kV	23.5 kV	27.3 kV
	Vco	16.9 kV	23.5 kV	27.3 kV
	Vho	15 kV	20.4 kV	25.3 kV
4th Day	Vbd	15 kV	20 kV	27 kV
	Vco	16 kV	20 kV	27 kV
	Vho	14 kV	15 kV	25 kV
5th Day	Vbd		17.3 kV	26 kV
	Vco		18.3 kV	26 kV
	Vho		15.8 kV	24 kV

Table 2 The Predischage Performance of the Different Samples

Surface finish		Unpolish	9 μm Diamond	9 μm SiC
1st Day	P	35.8%	31%	17.6%
	E	1.1 mJ	0.55 mJ	0.32 mJ
2nd Day	P	30.1%	28%	22.6%
	E	9.5 mJ	0.6 mJ	0.4 mJ
3rd Day	P	36%	27%	18%
	E	0.9 mJ	0.81 mJ	0.56 mJ
4th Day	P	38%	36%	24%
	E	2.3 mJ	0.85 mJ	0.61 mJ
	Pv	35%	30%	21%

P: Probability of predischage occurrence
E: Marximum predischage energy
Pv: Average probability of predischage occurrence

2. Effect of surface finish on the predischage activity

Table 2 shows the predischage performances of the tested samples with different surface finishes. It is clear from Table 2 that predischage activity is influenced by the surface preparation of a sample. The unpolished sample exhibited very active preflashover through all the tested days. Compared to the other samples, the unpolished sample exhibited much higher average probability of preflashover occurrence (~ 35% of all shots applied) and much larger maximum preflashover energy (~ 9.6 mJ), which was calculated using time-coordinated current and voltage waveforms. The 9 μm diamond-finished sample exhibited larger maximum predischage energy (~ 0.85 mJ) and higher average probability of the predischage occurrence (~ 30%) than the 9 μm SiC-finished sample (E~0.6 mJ, P~21%). Comparing the electrical breakdown performances of the tested samples shown in Table 1, there seems to be a correlation between the predischage activity and the breakdown characteristics of a sample. The results show that the more active the predischage activity is on a sample, the poorer the breakdown characteristics will be. It is interesting to note from Table 2 that the maximum predischage energy of the *polished samples* increases with tested days (i.e., number of flashover shots). The increase in the maximum predischage energy of the polished samples may be due to the probable formation of new defects on the surface and the various defect complexes that grow with repeated voltage applications. Another interesting observation to be noted here is that the electrical performance of a sample starts to deteriorate with the increase in the maximum predischage energy and the probability of the predischage occurrence for the polished samples. In fact the samples show definite signs of permanent damage and exhibit low voltage withstand capability when the predischage energy and the probability of the predischage occurrence reach certain high levels. For example, the hold-off voltage of 9 μm diamond-finished sample deteriorates to 15 kV when the maximum predischage energy reaches a value of 0.85 mJ and the probability of predischage occurrence reaches ~36% on the fourth day.

IV. Conclusions

Results reported here provide some evidence that the surface preparation of a dielectric plays an important role in the predischage activity and the electrical performance of the insulator. There are indications of a correlation between the electrical performance of the insulator, the high field predischage activity of the insulator, and the surface preparation of the insulator. The larger the defect density is on the surface of the insulator, the more active the predischage localized plasma is, and the poorer the flashover performance of the insulator will be.

V. Acknowledgments

The authors wish to thank NSF for the support of this research under grant no.DMR-9113500.

VI. References

1. H.C. Miller, "Surface Flashover of Insulators", IEEE Trans. Electr. Insul., 24, 765-86 (1989).
2. T. Asokan and T.S. Sudarshan "Importance of Surface Treatment on the Surface Flashover Properties of Alumina Ceramics", XVth ISDEIV, Darmstadt, Germany, 1991.
3. C.R.Li, R.Sundaraman and T.S.Sudarshan, "Spectroscopic Investigations of Surface Flashover Across an Insulator in Vacuum Under Pulsed Excitations", IEEE. Trans. Plasma Science, 21, No.5, pp.598-604 (1993).
4. B.J. Hockey, "Observations on Mechanically Abraded Aluminum Oxide Crystals by Transmission Electron Microscopy", pp.333-339 in the science of ceramic machining and surface finishing, Edited by S.J. Schneider, Jr. and R.R. Rice, NBS special publication, Washington, D.C. (1972).

A new method for characterization of the Space Charge in insulators.

* B. VALLAYER; * S. FAYEULLE; ** C. LE GRESSUS; *** G. BLAISE; * D. TREHEUX;

* Ecole Centrale de Lyon, URA CNRS 447, 69131 ECULLY Cedex, F.

** CEA-DAM, BP 12, 91680 Bruyères-le-Chatel, F.

*** Lab. de Physique du Solide, Université PARIS-Sud, 91405 ORSAY Cedex, F.

ABSTRACT.

A new method called the "Miroir Method" for characterization of charging properties of insulators is presented. This method consists in the characterization of electrical potential formed after irradiation of a sample with 30 kV electrons in a scanning electron microscope. Analytical and numerical calculations allows to relate the electrical potential with intrinsic properties of materials such as the dielectric constant. Experimental results on various materials are well fitted by the models. The role of contamination layers is underlined. Relation between charging and mechanical properties are described owing to friction experiments.

1. INTRODUCTION.

It has been recently established that the flashover occurrence is related to space charge relaxation. The Space Charge Physics, based on the "Polaron" concept (1-2), has been recently developped by Blaise (3-4). It shows that if electrical charges can be trapped in the bulk of an insulator on special location where the local polarizability decreases, polarization energy is stored in the whole material. Under various stresses (mechanical, electrical...), this energy can be released and produce fracture or breakdown. Breakdown has been observed without any electrical field, but with a strong space charge in the bulk of the insulator (5). Since space charge is the cause, and not the consequence of the behaviour of dielectrics, it is usefull to develop a new method which allows to charaterize :

- Charge traps in the material.
- The space charge formation in an insulator.
- Stability of the charge distribution.

The aim of this paper is to present a method fullfilling those three issues. It is called : "the Mirror Method" (6).

2. PRINCIPLE OF THE MIRROR METHOD.

Two steps have to be completed in order to achieve a mirror experiment:

- Injection of electrical charges in the sample through irradiation in a Scanning Electron Microscope (SEM).
- Characterization of the electrostatical state of the sample after irradiation.

2.1) Injection of the electrical charges.

The primary electron beam of the SEM is described with several parameters:

- Injection voltage : V_i , gives the initial kinetic energy of the primary electrons which enter the chamber of the SEM (30 kV for our experiments).
- Intensity I_i of the beam, and time t_i of application of the electron beam on the sample give the total quantity of charge : Q_i , sent in the sample.
- Focalization gives the size of the electron beam spot on the surface of the insulator.

The whole electron emission yield (backscattered and secondary electrons) is well known as a function of the primary electron energy (7). If this energy is high (30 kV), a double layer is formed in the sample, made of positive charges trapped near the surface, and more negative charges below the surface (figure 1). In the following of this paper, we consider that there is only a negative charge Q , trapped in the sample, but the influence of this double layer will be discussed later.

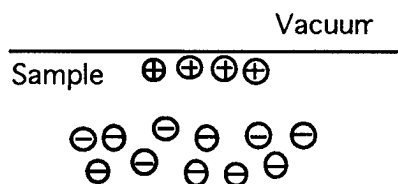


figure 1: Double layer in the sample after the injection of charge. the final distribution is considered as a negative trapped charge in the sample : Q .

2.2) Characterization of the space charge.

During the injection, charges can be trapped in the insulator. If so, an electrical field appears in the chamber of the SEM. When the sample is observed with a low potential : V_s , this electrical field can be strong enough to deflect or reflect the low energy electron beam (figure 2-a). Therefore, an image of the chamber is formed on the screen of the SEM (figure 2-b). A black spot (diameter d) is seen in the center of the screen. This black spot is the image of the last output diaphragm (diameter d') of the electron gun (electrons e_1 on figure 2-a).

The reverse of this diameter d is plotted as a function of the scanning potential : V_s . The aim of the next part of this work is to understand the meaning of these curves.

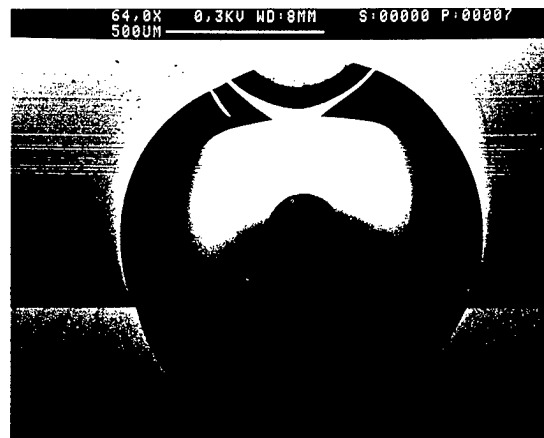
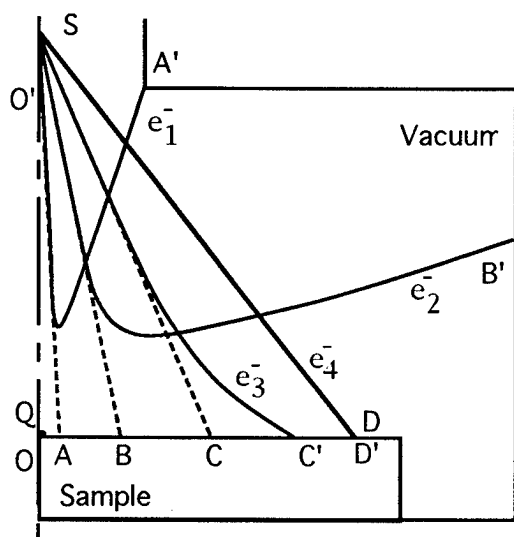


Figure 2-a : schematic view of the electron trajectory deflections. The trajectory e_4 is not deflected, while the three trajectories e_3 , e_2 and e_1 are deflected. The microscope put the image of A', B', C' in A, B, C : the mirror effect appears. A is the image of the last output diaphragm of the electron gun: $2OA=d$ and $2O'A'=d'$.

Figure 2-b : View of the chamber of the SEM through a mirror effect on the sample. The black spot of diameter d (trajectory e_1 , figure 2-a) is in the center of the image.

3) CURVES $1/d = f(V_s)$.

A finite element code solving the Poisson law has been used to calculate the electrical potential in the chamber of the SEM as a function of several parameters:

- Macroscopic parameters: which define environment and size of the sample. A major parameter is the thickness of the sample : h . The walls of the chamber of the SEM are at the ground potential.

- Microscopic parameters: which define the shape of the trapped charge zone. In a first approach, the geometry of this zone is modelled as a cylinder of diameter d_c and thickness p_c

When the potential follows an hyperbolic law {1}, analytical calculation based on the Gaussian optical theory is used to link the scanning potential value V_s with the diameter d of the black spot (figure 3) :

{1} $V = A \cdot \frac{Q}{R}$ The trapped charge Q is in O , center of the equipotential. The radius of the equipotential is R . A is a constant which depends on macroscopic parameters.

The Gaussian hypothesis are verified : the incident angle ($OO'A$) is small, and R very small compared to L . Then, we calculate $OA=d/2$ as a function of $O'A'=d'/2$, constant of the microscope:

$$\{2\} \quad OA = \frac{R}{4L} O'A'$$

{1} and {2} give an expression of $1/d$ as a function of V_s :

$$\{3\} \quad \frac{1}{d} = \frac{4L}{d'} \frac{1}{AQ} V_s$$

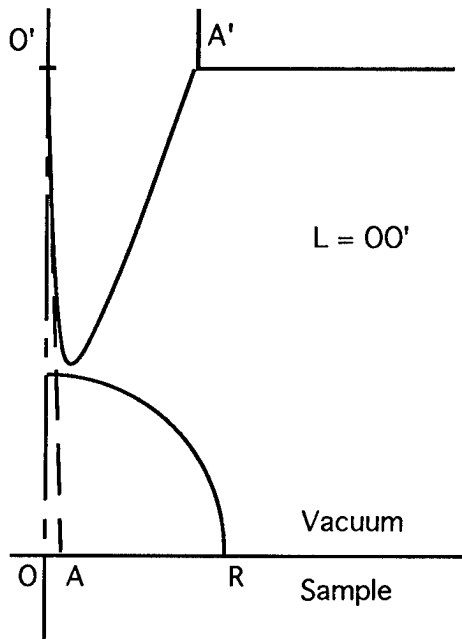


Figure 3 : The equipotential V_s is spherical, and its radius is R . The trajectory that gives the diameter of the black spot is shown on this figure.

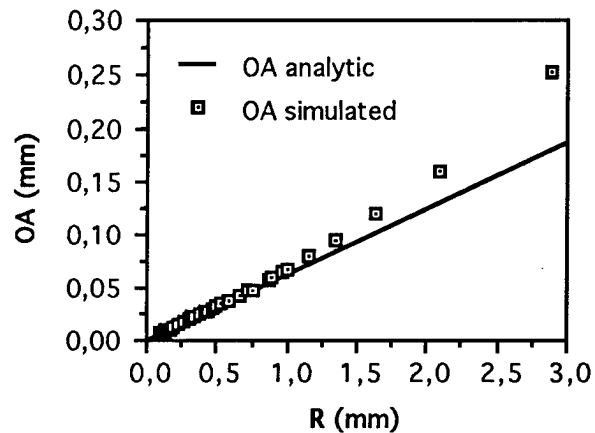


Figure 4 : Correlation between analytical and numerical theory. The analytic curve is given by the expression {2}. The simulated curve fits the analytical theory until $R=1\text{mm}$ ($L=10\text{mm}$) as the Gaussian hypothesis of R very small compared to L is true.

This calculation compared with the results of numerical simulation of $OA=d/2$ as a function of R (figure 4) shows that:

- A good correlation of the two theory is observed if the radius of the equipotential is small compared to L .
- For large radius, the theory is no more accurate.

If we apply this theory for the curve $1/d=f(V_s)$ we expect three different parts : 0), I), II).

-Part 0): This part corresponds to the largest equipotentials. The influence of the wall of the chamber of the SEM changes the shape of the equipotentials. The potential does not follow the hyperbolic law {1} : the analytic theory is not applicable.

-Part I): The influence of the wall of the chamber disappeared and the size of the trapped charge zone is small compared to the radius of the equipotential : the potential follows an hyperbolic law {1}, with:

$$\{4\} \quad A = K(h) \cdot A_{\infty} \quad \text{where:} \quad A_{\infty} = \frac{1}{2\pi\epsilon_0(\epsilon_r+1)} \quad \text{and } K(h) \text{ is a parameter which depends on } h \text{ (fig. 5)}$$

$$\{4\} \quad A = K(h) \cdot A_{\infty} \quad \text{where:} \quad A_{\infty} = \frac{1}{2\pi\epsilon_0(\epsilon_r+1)} \quad \text{and } K(h) \text{ is a parameter which depends on } h.$$

The curve $1/d=f(V_s)$ is a straight line which passes through the origin. The slope of this straight line is related to the dielectric constant of the material, the quantity Q of trapped charges, and some geometric constants {5}.

$$\{5\} \quad \frac{1}{d} = \frac{4L}{d'} \frac{1}{K(h)A_{\infty}Q} V_s$$

If the dielectric constant of the tested material is known, it is now possible to calculate the real quantity of trapped charges during the injection by the 30kV electron beam, as a function of the slope of the straight line. If this quantity of trapped charges is related to the quantity Q_i (total quantity of charges sent by the primary electron beam), it is possible to calculate the full (backscattered and secondary electrons) electron emission yield.

-Part II): This part shows the deformation of the equipotentials near the trapped charge zone : the curve becomes parallel to the horizontal axis.

Finally, the figure 5 shows an experimental curve $1/d=f(V_s)$ which shows the three parts 0, I, II.

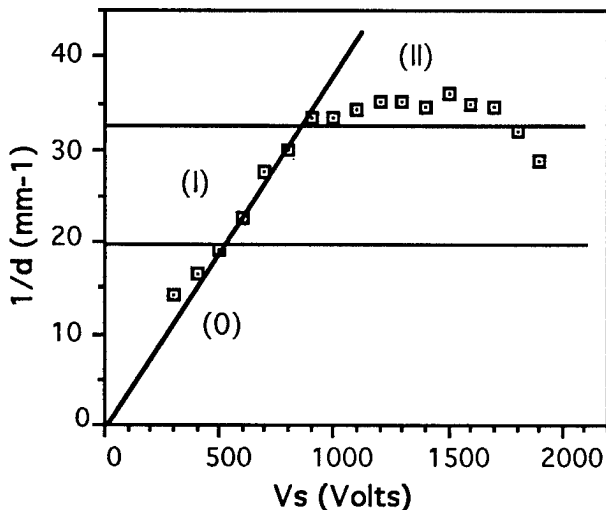


Figure 6 : Experimental curve on Yttrium Oxide (Y2O3), polycrystal. The three parts of the curve are clearly defined.

4) EXPERIMENTAL RESULTS.

4.1) Effect of contamination layer on charging capacity.

Mirror experiments have been performed on as cleaved single-crystal samples of magnesium oxyde (MgO, $\epsilon_r=9,8$) ($X=10\text{mm}$, $Y=10\text{mm}$, $Z=5\text{mm}$). Charging and mirror effect have been detected, and the figure 7 shows the variation of Q : real quantity of trapped charges in the material, as a function of Q_i : the quantity of charges injected by the 30kV electron beam. In this case Q was equal to Q_i : the electron emission yield was 0.

In order to remove contamination layers due to the cleaving process, the samples of MgO have been heated (500°C , 1h30, in air). After this treatment, charging effect was no more observed : Q was equal to zero while Q_i changed from 10^{-11}C to 5.10^{-10}C .

This results demonstrates the influence of contamination layers on the mirror method. We assume that the contamination layers act as a potential barrier for the electrons. The primary electrons of 30kV have a high energy and pass through this barrier, entering the bulk of the material. Then, the secondary electron are emitted below this barrier and cannot go outside of the sample.

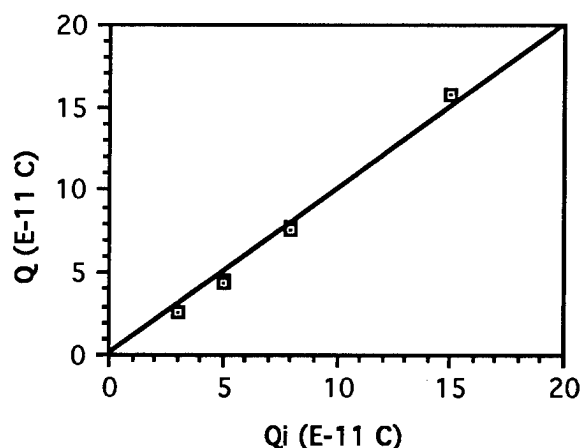


Figure 7 : experimental curve : Q , quantity of trapped charges in MgO as a function of Q_i , quantity of charge injected by the 30kV electron beam.

4-2) Effet of friction on charging capacity.

High purity, single-crystal sapphire and polycrystalline alumina (99,5% purity) were used. Surfaces ((001) plane) of the single crystal were polished to an average R_a value lower than $0,01\mu\text{m}$. Before the friction tests, the samples were annealed for 4 h at 1500°C in air, to remove defects resulting from machining and polishing. Some samples were irradiated with a polychromatic X-ray beam (molybdenum anticathode, 40 keV, 20 mA, 2 h) over their whole surface or only on the part of the surface which is outside of the wear track during the friction test.

The friction test were performed on a reciprocating flat-on-flat tribotester where a flat sapphire sample slid on a sapphire plane. The normal load was 21 N and the average speed was $3,33 \cdot 10^{-3} \text{ ms}^{-1}$. The conditions, corresponding to a very low contact pressure ($21 \cdot 10^{-2} \text{ MPa}$) allow friction to be achieved without the formation of macroscopic wear debris. Friction measurements were performed at room temperature in dried argon under unlubricated conditions. The relative humidity was controlled during the test and was kept to less than 1%. During each test, the friction coefficient μ was recorded.

The Mirror Method has been used before and after the friction test in order to characterize charge traps in the sample. Before a mirror experiment, the samples are heated (200°C , 1h) in the chamber of the SEM, in order to remove contamination layers.

Before friction test, and at room temperature, the sapphire did not produce any charging effect. Then, some test were carry out at -100°C . The figure 8 shows the evolution of the diameter of a given equipotential (300V) during heating of the samples after initial charging at -100°C . Results are given for pure and irradiated sapphire, and for α -quartz for comparison. For the sapphire samples, the diameter remained nearly constant and dropped suddenly to zero at 30°C for pure sapphire and at 80°C for irradiated samples. The initial plateau shows that the energy of all the trapped charges was nearly the same for a given sample.

In contrast, for α -quartz, the slowly decreasing curve revealed an energy distribution of the traps. The differents nature of the traps detected after irradiation is indicated be the higher temperature of detrapping.

Measurements of the friction coefficient for a 1000-cycles test are summarized in fig. 9. For pure sapphire, the coefficient increased slowly to reach 0,35 at 1000 cycles, while for fully irradiated samples, friction coefficient was greatly increased to reach 1 at the end of the test. Finally, for partially irradiated sapphire, the friction coefficient became higher than for pure sapphire after 300 cycles and reached more than 0,5 at the end. Those measurements show that the charging properties of ceramics can give informations on their mechanical behavior.

The figure 10 gives the results of a mirror experiment after a five-cycle friction test, performed at room temperature inside and outside the wear track. Both areas revealed similar charging capacities, as indicated by the two curves having the same slope, while the same sample before friction does not produce any charging effect. Then, we assume that friction induces modification of intrinsic charging properties of ceramics.

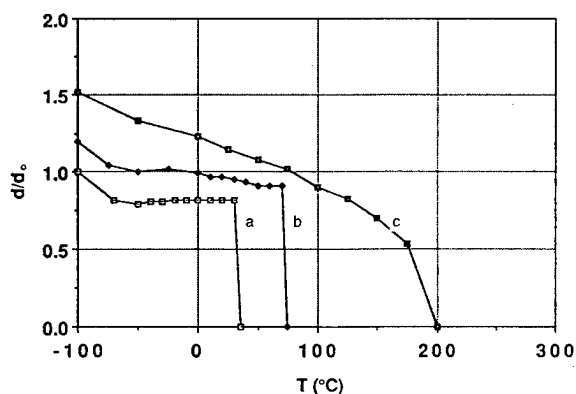


figure 8 : Diameter of the 300V equipotential as a function of temperature : (a) pure sapphire, (b) irradiated sapphire, (c) a-quartz.

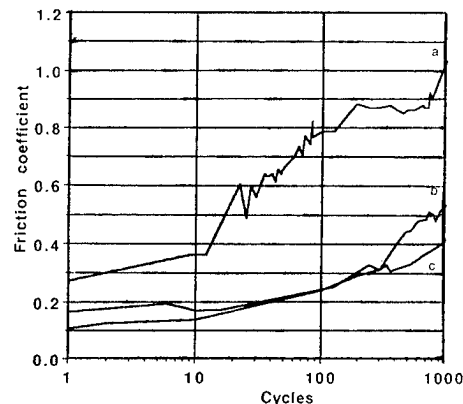


figure 9 : Friction coefficient evolution during 1000-cycle friction test : (a) totally irradiated sapphire, (b) partially irradiated sapphire, (c) pure sapphire.

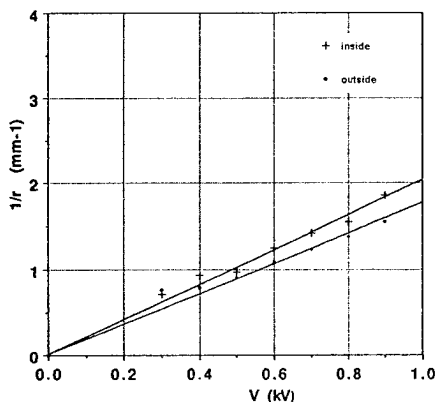


figure10 : Mirror experiment on pure sapphire at room temperature after 5-cycle friction test

5) CONCLUSION.

A new method has been developed for the characterization of the charging capacity of dielectrical materials. This method is supported by analytic calculation and numeric simulation and gives important information on intrinsic parameters of insulators.

Experimental results shows that the charging capacity plays a major part in the behaviour of insulator under mechanical stresses (friction). Moreover, ceramic machining, modelled by a friction test, triggered modification of the intrinsic properties of the material.

As a result, the Mirror Method, associated with Space Charge physics and some other methods of space charge characterization, appears to be an interesting experiment in order to develop selection criterions for insulators.

6) REFERENCES.

- 1) L. Landau et E. Lifchitz: Electrodynamique des milieux continus. Edition MIR, 1969.
- 2) I.G. Austin and N.F. Mott : Polarons in crystalline and non-crystalline materials. Advances in Physics, Vol 18, n° 71, 1969.
- 3) G. Blaise, Proceedings, Congress of dielectrics, Antibes, March 1992.
- 4) G. Blaise, Journée d'études sur les diélectriques, Conférence, CEA-DAM, Bruyères-le-Châtel, Sept. 1993.
- 5) C. Le Gressus, M. Gautier, J.-P. Duraud, Propriétés de surface et propriétés techniques des céramiques. Fracture mécanique et claquage diélectrique. Revue Scientifique de la Défense, 2^{ème} trimestre 1990.
- 6) C. Le Gressus, F. Valin, H. Henriot, M. Gautier, J.-P. Duraud, T.S. Sudarshan, R.G. Bommakanti, G. Blaise, J. Appl. Phys., May 1991, 6325.
- 7) F. Maurice, L. Meny, R. Tixier, Microanalyse et Microscopie Electronique à Balayage, Les Editions de Physique, 1978.

Temporal Behavior of Electric Field at Triple Junction and its Relation to Flashover of Bridged Vacuum Gaps

O. Yamamoto, T. Hara, H. Matsuura, M. Hayashi and K. Yukimura*

Department of Electrical Engineering, Kyoto University, Kyoto, 606 Japan

*Department of Electrical Engineering, Doshisha University, Kyoto, 602 Japan

ABSTRACT

Temporal change in electric field strength at the insulator-cathode-vacuum interface accompanied by charging of the insulator have been studied by using a two-dimensional Monte Carlo simulation. The study employed cylindrical insulators and conical insulators. Each of the insulators was made of PMMA, polyimide or Al_2O_3 . The field strength with cylindrical insulators show an abrupt increase, and with conical insulators considerable rapid reduction. Dependencies of the field change on the applied voltage height and material are well demonstrated. Flashovers occur after the simulated field change.

1. INTRODUCTION

The surface charging of an insulator caused by the secondary electron emission avalanche (SEEA) and associated electron stimulated gas generation are possible mechanisms which lead the bridged vacuum gap to electrical breakdown¹. Anderson and Brainard² has demonstrated a rapid charging of their insulator by observing V-t characteristic. Our purpose is to understand how the charging progresses with different shapes and materials.

In this paper, the SEEA charge accumulation is analyzed by employing a two-dimensional Monte Carlo simulation method. Then the temporal behavior of the electric field at cathode triple junction is observed taking the simulated charge into account. The simulation is performed both for cylindrical and conical insulators. As we have proved that positively angled conical insulators scarcely acquire the SEEA charge³, we employ a negatively angled insulator. Each of the insulators is made of PMMA, polyimide or Al_2O_3 . The field at the triple junction depends strongly both on the insulator shape and the material, and also on voltage height being applied. The cylindrical insulators show an abrupt increase of the field strength. Negatively angled insulators show a considerable decrease of the electric field. Experimental observation has shown that the flashover occur at a time which is later than those respective field changes.

2. INSULATORS EXAMINED

The secondary electron emission rate δ is a function of the kinetic energy of electron (A_i) impinging upon the insulator surface. General shape of the relation can be expressed as shown in Fig.1, where δ is unity at $A_i=A_1$ with comparatively low energy, and also at $A_i=A_2$ with a higher energy. For energies between $A_1 < A_i < A_2$, δ is greater than unity and has the maximum (δ_m) at a energy $A_i=A_m$. Table 1 provides A_1 , A_2 , δ_m and the relative permittivity ϵ_r for each of the insulators^{4, 5, 6}.

The cylindrical insulators have 10mm in radius and 10mm in height. The conical insulators have a cone angle $\alpha=-45^\circ$. The upper radius of the frustums is $r_u=10\text{mm}$ and the height is 10mm. Each of the insulators is placed between two plane parallel electrodes made of aluminum.

Table 1 Characteristic values of insulators

	A_1	A_2	δ_m	ϵ_r
PMMA	56	1062	2.3	3.0
Al_2O_3	52	11800	6.4	9.2
polyimide	43	517	1.9	3.2

$A_1, A_2: (\text{eV})$

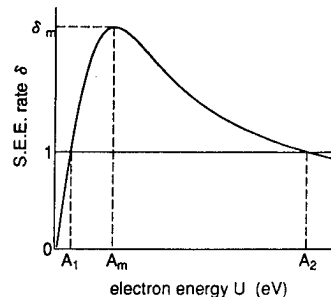
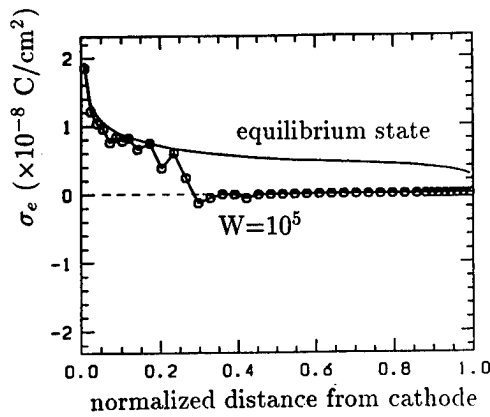
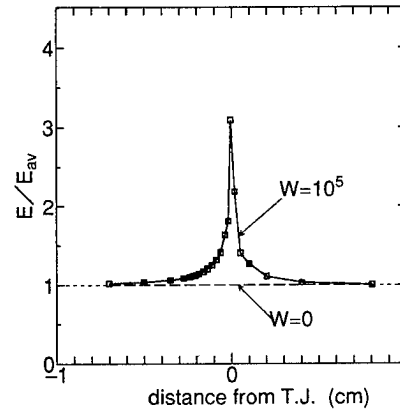


Fig.1 Secondary electron emission rate



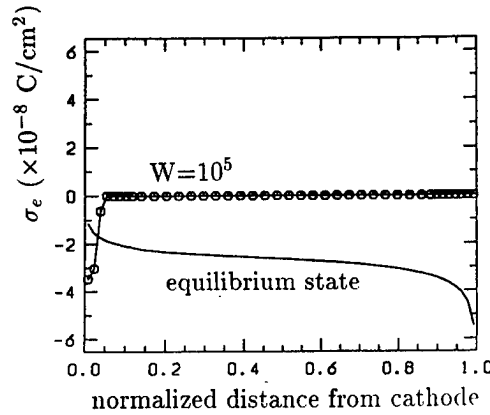
(a) charge distribution



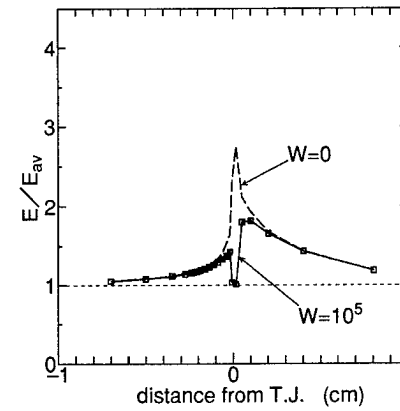
(b) field distribution on cathode

Fig.2 Results on cylindrical insulator

(PMMA, $V=50\text{kV}$, $E_{av}=50\text{kV/cm}$, $N=10^5/\text{cm}$, $W=10^5$, $M=6.28 \times 10^{10}$, $t=5.6 \times 10^2 \mu\text{s}$)



(a) charge distribution



(b) field distribution on cathode

Fig.3 Results on conical insulator

(PMMA, $\alpha=-45^\circ$, $V=100\text{kV}$, $E_{av}=100\text{kV/cm}$, $N=10^5/\text{cm}$, $W=10^5$, $M=6.28 \times 10^{10}$, $t=78\text{ns}$)

3. METHOD OF ELECTRIC FIELD CHANGE ANALYSIS

The analysis starts with the simulation of surface charge distribution, which varies as the number of electrons M released from the triple junction increases. The simulation consists of a two-dimensional field calculation and an electron trajectory analysis by employing Monte Carlo simulation. Details of this simulation has been described elsewhere³. As the simulation is two-dimensional and it is necessary to save the computing time, a bundle of electrons with density $N(\text{/cm})$ is released for W times from the triple junction, so that the number of electron in this study is given as $M=2\pi r_u N W$, where r_u is the radius of the initial electron bundle.

Examples of the charge distribution are shown in Fig.2(a) for the cylindrical and Fig.3(a) for the conical insulators, where solid lines show the charge in equilibrium³. Figs.2(b) and 3(b) are normalized electric field distributions on the cathode, where values at distance $l=0$ give the field strength at the triple junction.

The field strength at the triple junction can be denoted as $E_j(M)$ as it varies with M . In order to understand the temporal behavior of the field $E_j(t)$, we transform the electron number M into time t . When the number of electrons increases from M to $M+\Delta M$, the time Δt necessary for providing ΔM electrons can be estimated by using a field emission current. Assuming that field strength is constant during Δt , and that actual field strength at the junction is multiplied by ϵ_r , taking a small vacuum gap at the interface into account, the field emission current I can be obtained by substituting $\epsilon_r E_j(M)$ into Fowler-Nordheim equation. Thus, for a given $M=\sum \Delta M$, t is given as $t=\sum \Delta t=\sum e(\Delta M)/I$.

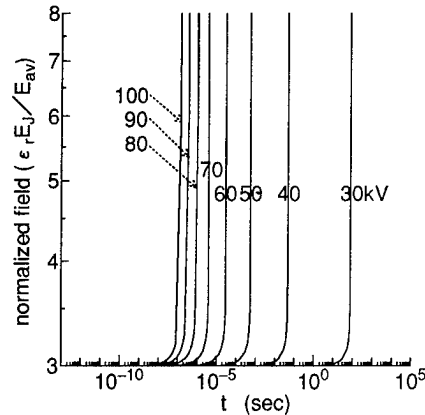


Fig.4 Voltage dependence of cylindrical insulator(PMMA)

Table 2 Flashover voltages

	flashover voltage (kV)		
	$\alpha=0^\circ$	$\alpha=-45^\circ$	$\alpha=+45^\circ$
PMMA	53	163	217
Al ₂ O ₃	40	25	97
polyimide	95	213	242

4. RESULTS AND DISCUSSIONS

4.1. Voltage dependence

Fig.4 shows the field changes of the cylindrical PMMA insulator, where the insulator is exposed to stepwise constant voltages with different height (V). It is seen that each of the fields increases suddenly from its geometrical value to a higher one. This is because the positive charge accumulation as shown in Fig.2 causes a positive feed back effect on the field emission current. The increase occurs at about $t=60\text{ns}$ when $V=100\text{kV}$ and at about $t=50\text{s}$ when $V=30\text{kV}$. This result demonstrates that the reduction in voltage height by 30% brings into a charging speed multiplication of 10^{-9} .

4.2. Field change at flashover voltage

4.2.1. Flashover voltage and time lag

Flashover voltages of insulators exposed to $\pm 2/50(\mu\text{s})$ impulse voltages are measured and shown in Table 2, where results with a positive angle are also shown for a reference. Spark conditioning was conducted before each of the measurements. It is interesting to note that the polyimide insulator is superior than the other insulators. It is also interesting to note that Al₂O₃ insulator has the lowest flashover voltage at the negative cone angle.

Statistical distributions of the flashover time lag t_l were observed for each of the insulators and it was found that the flashovers took place during $2 \leq t_l(\mu\text{s}) \leq 30$. Among those distributions, the flashover delays with Al₂O₃ were shorter than that of the other two materials and distributed mostly in $t_l \leq 3(\mu\text{s})$.

4.2.2. Field change at flashover voltage

Fig.5 shows the field changes at around respective flashover voltages of the cylindrical insulators. The field with Al₂O₃ insulator increases at $t=3\text{ns}$. This is shorter than that of the other insulators although the applied voltage is lowest. The field with polyimide increases at around $t=400\text{ns}$. From these results we can deduce that the field enhancement with above two insulators occurs immediately after the crest of the impulse voltage is reached, even if a charging during the voltage rise is neglected. Thus the simulated results are consistent with the observed time lag. A wide distribution of the time lag with polyimide could be attributed to a statistical time lag of the discharge initiation in a gas generated during the charging.

The field enhancement with the cylindrical PMMA insulator occurs at $t=560\mu\text{s}$, which is too late to explain the experimental flashover delay. Since a intense degradation at the cathode side edge of this insulator was observed after the test, it is considered that the degradation lowered the flashover voltage.

Fig.6 shows the field changes with the conical insulators. These fields demonstrate a similar decreasing curve. The field at $t=1\mu\text{s}$ is approximately 17% (polyimide), 21% (PMMA) and 6% (Al₂O₃) of those respective geometrical values.

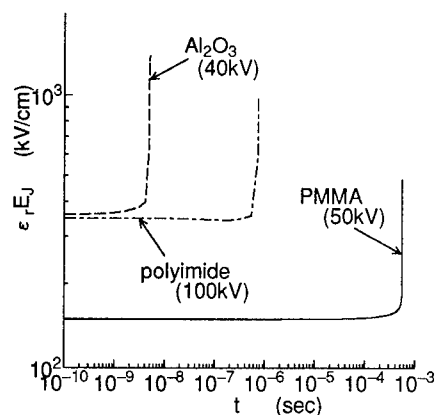


Fig.5 Field changes of cylindrical insulators at flashover voltage

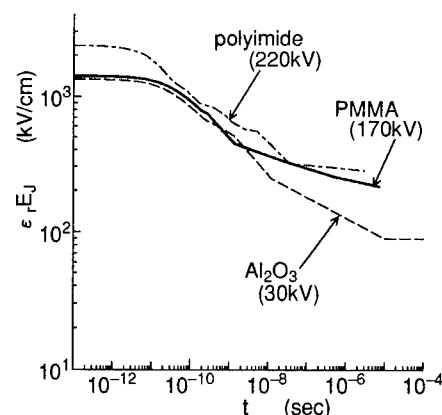


Fig.6 Field changes of conical insulators at flashover voltage ($\alpha = -45^\circ$)

After this instant, each of the fields goes down much slower than before because of the decrease in the field emission current. It is difficult to explain the relationship between the field reduction and the flashover occurrence in these cases, however, we consider that a electron stimulated gas desorption occurring with the negative charging up to $t=1\mu s$ is responsible for the flashover.

5. CONCLUDING REMARKS

Temporal changes in the electric field strength at cathode triple junction due to the accumulation of charge on insulators have been analyzed. It has been demonstrated that the temporal behavior of the field depends strongly on both insulator shape and material, and also on the voltage height being applied. Cylindrical insulators show a abrupt increase in the field strength. Negatively angled insulators show a considerable reduction in the electric field. Experimental observation has shown that the flashover occurs at a time which is later than the considerable field change, excepting a special case in which a degradation of insulator takes place.

ACKNOWLEDGEMENT

The authors thank Mr. Y.Suzuki, Nissin Electric Co., and Mr. M.Kinouchi, UBE, who provide us the insulators for this investigation.

REFERENCES

1. H.C.Miller, "Flashover of Insulators in Vacuum. Review of the Phenomena and Techniques to Improve Holdoff Voltage", IEEE Trans. on EI, vol.28, No.4, pp.512-527 (1993)
2. R.A.Anderson and J.P.Brainard, "Mechanism of Pulsed Surface Flashover Involving Electron Stimulated Desorption", J.Appl. Phys., Vol.51, pp.1412-1421 (1980)
3. O.Yamamoto, T.Hara and I.Nakanishi et al., "Monte Carlo Simulation of Surface Charge on Angled Insulators in Vacuum", IEEE Trans. on EI, Vol.28, No.4, pp.706-712 (1993)
4. E.A.Burke, "Secondary Emission from Polymers", IEEE Trans. on NS, Vol.27(60), pp.1760-1764 (1980)
5. R.F.Willis and D.K.Skinner, "Secondary Electron Emission Yield Behaviour of Polymers", Solid State Communications, Vol.13, pp.685-688 (1973)
6. P.H.Dawson, "Secondary electron emission yield of some ceramics", J.Appl. Phys. Vol.37, p.3644 (1964)
7. C.H. de Turreil and K.D. Srivastava, "Mechanism of Surface Charging of High-Voltage Insulators in Vacuum", IEEE Trans. on EI, Vol.8, no. 1, 1973, pp.17-21.

SESSION 5

Vacuum Insulation (Magnetic Insulation, Accelerators, etc.)

The Effect of Pulsed Electron-Beam Treatment of Electrodes on the Electric Strength of the Vacuum Insulation

Alexander V. Batrakov, Alexey B. Markov, Gregory E. Ozur, Dmitry I. Proskurovsky, and Vladimir P. Rotshtein

Institute of High-Current Electronics, Russian Academy of Sciences, Tomsk 634055

ABSTRACT

A method for preliminary treatment of electrodes by a microsecond low-energy intense electron beam is proposed. It has been demonstrated that such a beam melts off the electrode surface and cleans the surface layers from impurities and dissolved gases. In combination with subsequent conditioning of the vacuum gap by low-current pulsed discharges, high breakdown electric fields can be attained.

1. INTRODUCTION

The electric strength of a vacuum insulation depends in large measure on the surface condition of the electrodes after preliminary treatment. Typical treatment of the electrodes involves mechanical and/or electrochemical polishing followed by washing with distilled water. The electric strength of a vacuum gap may further be increased by conditioning the electrodes in vacuum without breakdowns or with breakdowns at a limited discharge current¹⁻³. We propose a method for preliminary treatment of electrode surfaces by low-energy high-current electron beams (LEHCEBs) of microsecond duration⁴. This method has been made feasible owing to the creation of broad-LEHCEB sources⁵. In the process of LEHCEB treatment of electrodes, the surface layers are quickly heated to high temperatures, melted, and cleaned from impurities and dissolved gases. Superfast cooling of the surface layers results in forming a highly homogeneous structure in this layers. This treatment has the effect of improving the insulating properties of the vacuum gap. The paper presents some data on the peculiarities of the pulsed e-beam treatment of electrodes and the effect of such treatment on the insulating properties of vacuum gaps.

2. ELECTRODE SURFACE MODIFICATION UPON LEHCEB TREATMENT

2.1. Electrode treatment conditions

Electrode pairs made of stainless steel (SS), copper, titanium, and nickel. The electrodes were shaped as 4-mm diameter rods with rounded edges. Upon being manufactured, all electrodes (Ti excluded) were electrochemically polished in standard modes described in the literature, and washed in distilled water. The washed and dried electrodes were stored in plastic boxes until being used. Subsequently, some electrodes were treated by LEHCEBs and placed again in plastic boxes. Unirradiated electrode pairs were used for comparison measurements.

Electrode irradiation was performed on a setup described in Ref. 5. The beam pulse duration τ_p was 0.7 to 1.5 μ s, the average electron energy in a pulse was 7 to 15 keV, and the beam energy density Q was 2 to 6 J/cm². These beam parameters provided a smooth transition from the mode of initial surface melting to the mode of initial evaporation of the surface layer. The number of shots N_s was varied from 1 to 200.

2.2. Thermal processes at electrodes on LEHCEB irradiation

The thermal processes occurring at electrodes were analyzed by solving a time-dependent one-dimensional heat equation⁶. Figure 1 shows the position of the melt-solid interface as a function of time t/τ_p for various materials at $\tau_p = 0.8 \mu$ s and $Q = 5.6$ J/cm². The velocity of propagation of the crystallization front increases, as the surface is approached, and reaches, depending on the material, 3 to 30 m/s. The rate of cooling of the electrode material at the crystallization front also increases, as the surface is approached, and reaches 10⁹ to 10¹⁰ K/s. This superfast cooling results in for stainless steel, as for carbon steels⁶, the formation of a nanocrystalline structure in the surface layer. On the action of an electron beam on polycrystalline iron, as a result of recrystallization, a subgrain structure (with a grain size of 2 to 5 μ m) with a reduced density of dislocations and point defects is formed⁷.

Increasing the beam energy density increases the thickness of the molten layer which starts intensely evaporating. Figure 2 gives the thickness h of a layer evaporated per shot as a function of beam energy density, obtained by the weighing method.

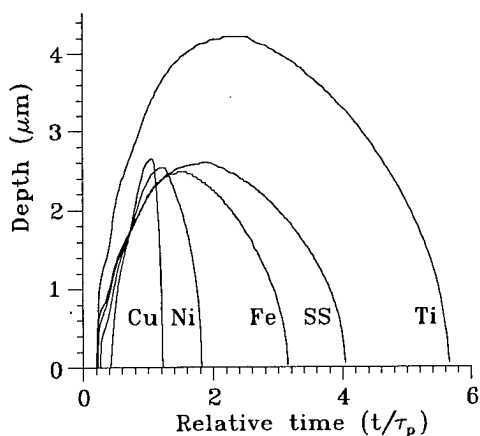


Fig. 1

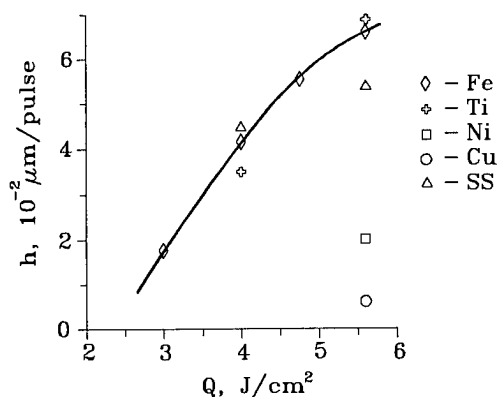


Fig. 2

2.3. Formation of the electrode surface microrelief

It has been established that the initial melting of the electrode surface is preceded by the formation of craters of diameter from a few micrometers to some tens of micrometers and depth of some micrometers. The highest density of microcraters is characteristic of the stainless-steel and copper electrodes. Figure 3,a,b presents typical photographs showing the morphology of the surface stainless-steel electrodes. With increasing the beam power density, the density of craters increases slightly, but their diameter increases substantially. Note that we observed similar microcraters in studying the dynamics of erosion processes on the anode during the spark stage of a pulsed breakdown in vacuum³. It was found that the microcraters were solidified liquid phase centers having appeared on an unmolten anode surface under the action of the electron beam. This selective character of the initial melting indicates that microcraters appear in the places where inclusions of other phase (sulphides, phosphides, carbides), capable of forming low-melting-point eutectics with the matrix, are present. The regions with nonmetallic inclusions are known² to show elevated emissivity and be responsible for the initiation of breakdown.

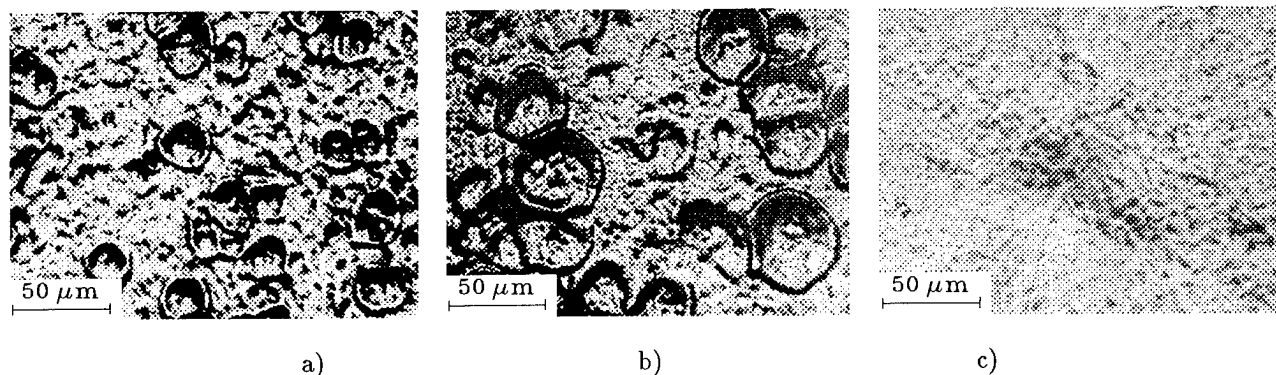


Fig. 3. Photographs of the surface of stainless-steel electrodes after LEHCEB treatment: a) $Q \simeq 2 \text{ J/cm}^2$, $N_s=1$; b) $Q \simeq 5 \text{ J/cm}^2$, $N_s=1$; c) $Q \simeq 5 \text{ J/cm}^2$, $N_s=50$.

To clean the surface layers of an electrode from impurities, it is purposeful to treat it in a cyclical manner by an LEHCEB in the initial evaporation mode. During this treatment, various impurities and dissolved gases will be efficiently trapped by the crystallization front, crop out at the surface, and be removed from it. A direct indication for the efficiency of the surface layer of stainless steel from detrimental impurities is its strongly enhanced resistance to corrosion⁸. Besides, Auger spectroscopy of the surface layers of titanium alloys⁹ has shown that LEHCEB treatment cleans these layers from oxygen and carbon. The number of shots necessary for cleaning should apparently correspond to the thickness of the removed layer comparable with the microcrater depth. As can be inferred from Fig. 2, the desired effect, e.g. for stainless-steel electrodes, can be attained by cyclical treatment with $Q \simeq 5 \text{ J/cm}^2$ and $N_s=50$.

The result of this treatment is illustrated in Fig 3,c. In addition, LEHCEB treatment of electrodes makes the surface microrelief smoothed off. The best smoothed surfaces are obtained for titanium electrodes, they gain mirror lustre. Smoothing should also add to the electric strength of the vacuum gap.

3. THE EFFECT OF PULSED E-BEAM TREATMENT OF ELECTRODES ON THE ELECTRIC STRENGTH OF VACUUM INSULATION

3.1. Experimental technique

The experiment was carried out in an oilless vacuum of $\sim 10^{-6}$ Pa. The electrode gap d was varied from 70 to 200 μm . The prebreakdown current-voltage characteristics were measured with the use of a highly sensitive dc amplifier and a highly stable constant-voltage power-supply source until a first breakdown and after conditioning of the electrodes at a pulsed voltage (voltage pulse duration $\sim 3 \mu\text{s}$, discharge current up to 0.5 A). The dc breakdown voltages U_1 were measured by a kilovoltmeter with slowly ($\sim 10 \text{ kV/min}$) increasing gap voltage, the limiting resistance in the discharge circuit was 50 M Ω . To measure the pulsed breakdown voltage U_2 , a half-sinusoidal voltage of peak value up to 45 kV and duration 1.5 ms was applied to the electrode gap. Taken as the U_2 value was the minimum peak voltage at which breakdown took place. The voltage U_2 was recorded using an oscilloscope. The discharge current was limited by a 75 k Ω resistor.

3.2. Prebreakdown currents

An analysis of the effect of discharge conditioning and electron beam treatment of electrodes on the prebreakdown current (see Fig. 4) has shown following:

1. Discharge conditioning of unirradiated stainless-steel and nickel electrodes increases the prebreakdown current. The low prebreakdown currents for initial electrodes are due to the presence on the surface of a hard passive film formed upon electrochemical polishing. Discharges destroy this film and microprotrusions appear on the cathode as a result of both explosive electron emission and material transfer from anode to cathode, what is just the reason for the increase in prebreakdown current. Discharge conditioning of unirradiated titanium and copper electrodes reduces the prebreakdown current by two orders of magnitude. These results are in good agreement with well-known observations¹⁻³.

2. LEHCEB treatment of stainless-steel and nickel electrodes increases the prebreakdown current by about an order of magnitude, what seems to be related to the destruction of the passive film. However, as compared to the case where the film was destroyed only by discharges, the increase in current is not so great. This is related to the fact that the destruction of the film is accompanied by cleaning and smoothing off of the electrode surface. The result of LEHCEB treatment of Ti and Cu electrodes is a decrease in prebreakdown current by about three orders of magnitude, what is related to the fact that the electrodes are cleaned from impurities.

3. Discharge conditioning of electrode pairs reduced prebreakdown current. This effect is most pronounced for Cu electrodes. This is possibly related to the fact that copper electrodes are not cleaned well enough upon LEHCEB treatment. Actually, as follows from calculations and experiments (see Fig. 2), for $Q=5.6 \text{ J/cm}^2$, the thickness of the

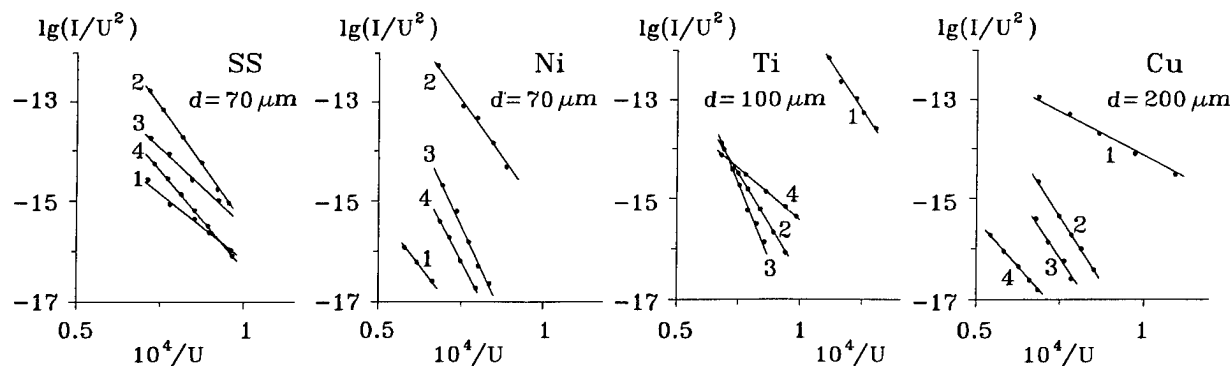


Fig. 4. Prebreakdown current-voltage characteristics measured for various electrode pairs: 1 – unirradiated, before conditioning; 2 – unirradiated, after conditioning; 3 – irradiated, before conditioning; 4 – irradiated, after conditioning.

layer removed from a copper electrode in one shot is about an order of magnitude smaller than that for electrodes made of other metals. Therefore, for more efficient cleaning of copper electrodes, it is necessary to increase the beam energy density.

3.3. Breakdown electric fields

Curves 1 and 2 in Fig. 5 illustrate a typical process of conditioning for vacuum gaps with unirradiated electrodes. LEHCEB irradiation of electrodes increases both the dc (curves 3) and the pulsed (curves 4) electric strength. The highest breakdown electric fields, E_{br} , have been achieved for stainless-steel and Ni electrodes. When it is considered that for the materials investigated the critical electric field at cathode micropoints, at which breakdown is initiated, is $E_{cr} = \beta E_{br} = (5 \text{ to } 7) \cdot 10^7 \text{ V/cm}$ (see Ref. 3), the effective factor of field enhancement at these micropoints β turns out to be 10 to 30. These values of β are indicative of good condition of the surface treated by an electron beam and conditioned by discharges.

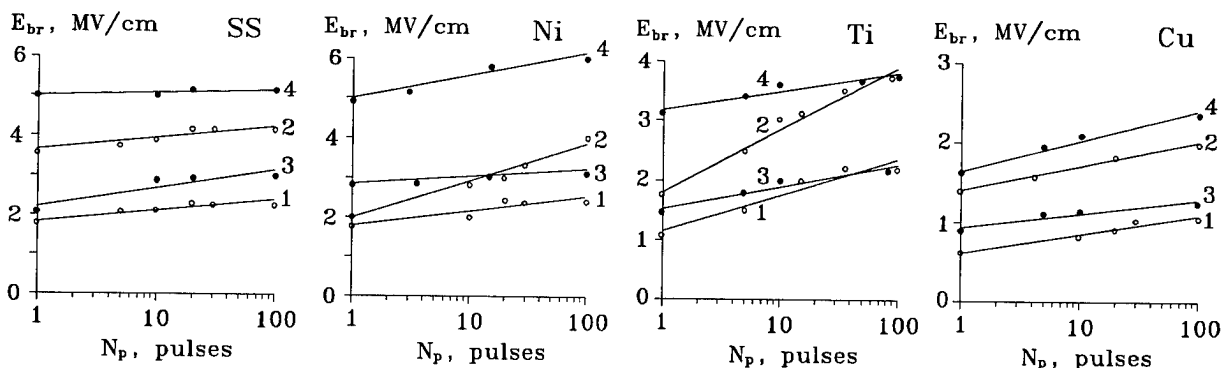


Fig. 5. Breakdown electric field E_{br} vs the number of conditioning pulses N_p : 1 – unirradiated electrodes (\circ), dc voltage; 2 – unirradiated electrodes (\circ), pulsed voltage; 3 – irradiated electrodes (\bullet), dc voltage; 4 – irradiated electrodes (\bullet), pulsed voltage.

4. REFERENCES

1. N.I. Slivkov, "Electrical Insulation and Discharge in Vacuum", *Atomizdat, Moscow*, 1972.
2. R.V. Latham, "High Voltage Vacuum Insulation: the Physical Basis", *Academic Press, London*, 1981.
3. G.A. Mesyats, and D.I. Proskurovsky, "Pulsed Electrical Discharge in Vacuum", *Springer-Verlag, Berlin*, 1989.
4. A.V. Batrakov, G.E. Ozur, D.I. Proskurovsky, and V.P. Rotshtein, "The Effect of Pulsed Electron-Beam Irradiation on the Emissive Properties of Electrodes in Strong Electric Fields", *Digest of the XXI All-Union Conf. on Emission Electronics, Leningrad, USSR*, Vol. 1, p. 302, 1990.
5. G.E. Ozur and D.I. Proskurovsky, "Generation of Low-Energy Electron Beam in the Diode with Plasma Anode", *Proc. XIV Intern. Symp. on Discharges and Electr. Insulation in Vacuum, Santa Fe, USA*, pp. 665-670, 1990.
6. Yu.F. Ivanov, V.I. Itin, S.V. Lykov, et al., "Phase and Structure Changes in Steel 45 under the Action of a Low-Energy, High-Current Electron Beam", *Izv. RAN, Metall*, No. 3, pp. 130-140, 1993.
7. E.F. Dudarev, L.A. Kornienko, S.V. Lykov, et al., "The Dislocation Substructure Formed in Iron as a Result of its Irradiation by a Low-Energy, High-Current Electron Beam", *Izv. Vyssh. Uchebn. Zaved., Fizika*, No. 5, pp. 42-47, 1993.
8. I.M. Goncharenko, V.I. Itin, S.V. Isichenko, et al., "Enhancement of the Corrosion Resistance of the 12X18H10T Steel upon Treatment by a Low-Energy HCEB", *Zashchita Metallov*, Vol. 29, No. 6, 1993.
9. A.V. Batrakov, G.A. Mesyats, D.S. Nazarov, G.E. Ozur, D.I. Proskurovsky, and V.P. Rotshtein, "Low-Energy, High-Current Electron Beams for Modification of the Properties of Surface Layers of Metallic Materials", *Intern. J. of Techn. Transfer*, No. 1, 1993.

Influence of *in situ* ion beam sputter cleaning on the conditioning effect of vacuum gaps

Shinichi Kobayashi, Hiroyuki Kojima and Yoshio Saito*

Saitama University, Department of Electrical and Electronic Engineering
255 Shimo-ookubo, Urawa, Saitama, 338, Japan

*National Laboratory for High Energy Physics
1-1 Oho, Tsukuba, Ibaraki, 305, Japan

ABSTRACT

An ion beam sputtering technique was used to clean the electrode surfaces of vacuum gaps. Ions of the sputtering gas were irradiated by means of an ion gun in a vacuum chamber attached to a breakdown measurement chamber. By providing *in situ* ion-beam sputter cleaning, this system makes it possible to make measurements free from contamination due to exposure to the air. The sputtering gas was He or Ar, and the electrodes were made of oxygen-free copper (purity more than 99.996%). An impulse voltage with the wave form of 64/700 μ s was applied to the test gap, and the pressure in the breakdown measurement chamber at the beginning of breakdown tests was 1.3×10^{-8} Pa. These experiments showed that ion-beam sputter cleaning results in higher breakdown fields after a repetitive breakdown conditioning procedure, and that He is more effective in improving hold-off voltages after the conditioning (Under the same ion current density, the breakdown field was 300 MV/m for He sputtering and 200 MV/m for Ar sputtering). The breakdown fields at the first voltage application after the sputter cleaning, on the other hand, were not improved.

1. INTRODUCTION

It is widely recognized that dielectric breakdown strength of a vacuum gap is influenced by the electrode surface conditions.¹ Before the electrodes are set into the vacuum chamber, their surfaces are processed in the atmosphere. Contamination and oxidation of electrode surfaces are thus inevitable. Vacuum gaps are therefore always conditioned after they are set, and various conditioning procedures (gas conditioning², repetitive spark conditioning³ etc.) are available.

To find out how electrode surface conditions and bulk characteristics influence vacuum breakdown strength, it is necessary to process the electrode surfaces and measure the breakdown strength in the same vacuum chamber, or to transfer the electrodes from a processing chamber to a measurement chamber through a vacuum. We have already described how the repetitive spark conditioning is affected by Ar ion sputter cleaning.⁴ Because an ion-beam sputtering technique can easily clean electrode surface,⁵ in the work presented here we compared the effects of *in situ* He sputter cleaning and Ar sputter cleaning.

2. EXPERIMENTAL

2.1. Apparatus

The experimental apparatus is shown schematically in Fig. 1. The sputter cleaning is carried out by an ion gun in Chamber 1. After cleaning the electrodes were transferred to Chamber 3 through Chamber 2, in which the surface can be analyzed by X-ray photoelectron spectroscopy (XPS). All the processes --that is, electrode surface cleaning, surface analysis, and breakdown measurements --can be carried out without the exposing the electrode to air.

The pressure in Chamber 2 and 3 was maintained at 1 to 3×10^{-8} Pa by sputter ion pumps and Ti-getter pumps. The voltages applied were positive impulses (peak value 100kV) with a 64 μ s rise time and 700 μ s decay time.

2.2. Electrode preparation and experimental procedure

The electrodes were made of oxygen-free copper (ASTM-F-68 Class1). Typical chemical compositions were as follows: copper was more than 99.996%, the hydrogen gas content was less than 0.5 ppm, and the oxygen content was less than 2 ppm. Sample electrodes were machined from this material, and the electrode surface was processed by turning.

After a sample electrode was put into Chamber 1, its surface was cleaned by the sputter ion-beam gun. Then the sputter-cleaned electrode was transferred to Chamber 2 for XPS analysis of the surface condition. After breakdown strength of the electrode was measured in Chamber 3, the electrode was returned to Chamber 2 for another analysis of its surface condition.

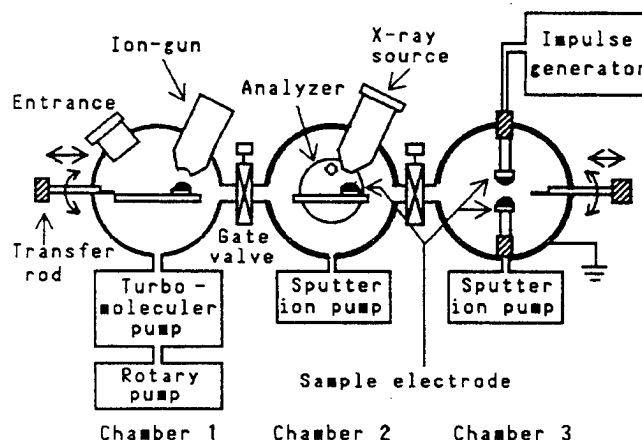


Fig. 1. Experimental system.

3. CONDITIONS OF ELECTRODE SURFACES

A scanning electron microscope (SEM) picture of the as-machined electrode surface (Fig. 2) shows traces of the turning, and that the surface is fairly flat.

The electrode surface conditions before and after sputtering are shown in Fig. 3. Before sputtering, a C_{1s} peak due to organic contaminants and an O_{1s} peak due to oxide layers on the electrode surface are seen in the wide-scan spectrum. The peak due to Cu (that is, Cu_{2p} , Cu_{3p} , and Cu_{Auger}) is very low. Electrode surfaces without any *in situ* surface processing, therefore, seem to be covered with organic contaminants and oxide layers. After sputtering by either He ions or Ar ions, on the other hand, the C_{1s} and O_{1s}

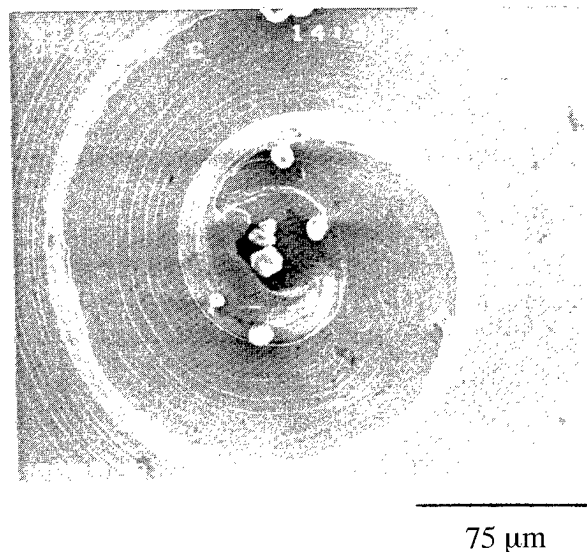


Fig. 2. SEM picture of as-machined electrode surface.

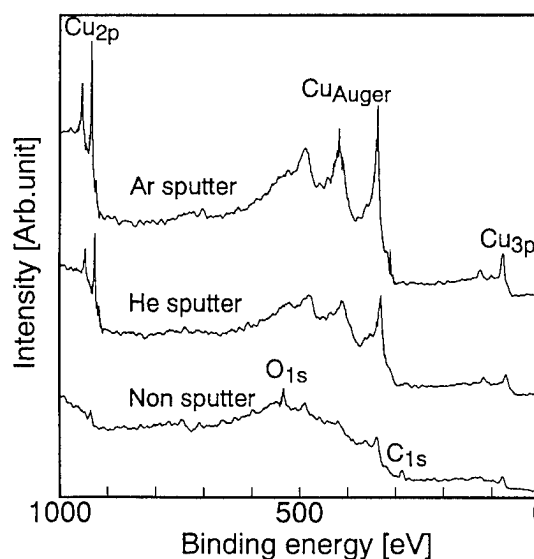


Fig. 3. XPS spectra of nonsputtered, He-ion-sputtered, and Ar-ion-sputtered electrode surfaces.

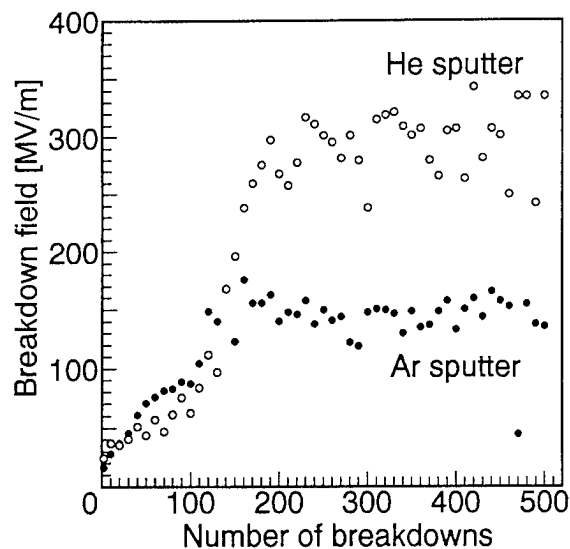
peaks are not evident and peaks due to Cu are obvious. The spectra thus show that ion-beam sputtering removes surface contaminants. *In situ* surface cleaning thus makes it possible to measure breakdown fields for electrodes without surface contamination.

4. BREAKDOWN STRENGTH AND SPUTTERED SURFACES

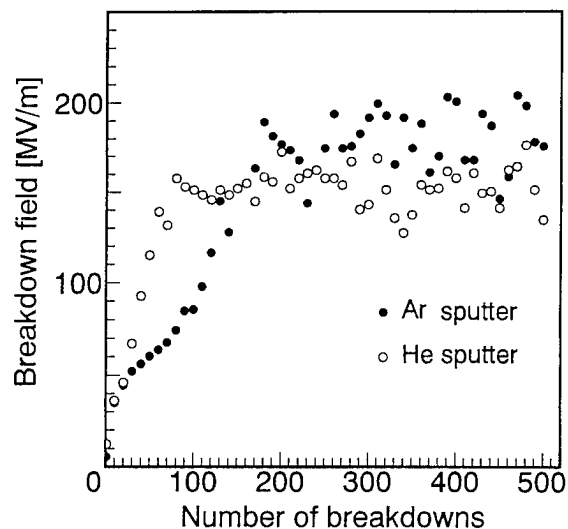
The strength of breakdown fields (breakdown voltage divided by gap length) is shown in Fig. 4. The results shown in Fig. 4(a) were obtained from electrodes sputtered under the same ion-beam current density for both He and Ar, and the results shown in Fig. 4(b) were obtained with ion-gun operating conditions that were identical for He and Ar. These figures show that breakdown fields first gradually increase with increasing numbers of breakdowns and then settle down to stable values. From Fig. 4(a) we can see that He ion sputtering is more effective than Ar ion sputtering, whereas from Fig. 4(b) we see that Ar ion sputtering is slightly superior to the He ion sputtering. These results confirm that the *in situ* ion sputter cleaning obtains good results in the conditioning effect and that the effect depends on sputtering conditions.

Breakdown fields at the first voltage application and after the values became stable are summarized in Table 1. The values listed in this table clearly show the effectiveness of *in situ* ion-beam sputter cleaning. The conditioning effect is far smaller for the electrodes that were not sputter cleaned, but the field strength at the first breakdown are similar for sputtered and unsputtered electrodes. This result suggests that the cleaning of electrodes is necessary for improving breakdown fields but is not sufficient.

It has been shown that the *in situ* sputter cleaning improves the conditioning effect for vacuum gaps. One cause of this effect is the removal of contaminants and oxide layers on the electrode surface. Ion-beam sputtering, however, also causes surface roughness and strains that will reduce the breakdown strength. We therefore



(a) same ion current density for He and Ar.



(b) identical ion-gun operating conditions for He and Ar.

Fig. 4. Breakdown strength.

Table 1. Breakdown fields.

Ion species	Ion current density (A/mm ²)	Breakdown fields (MV/m)		Number of breakdowns to attain final fields
		1st	conditioned	
Ar	0.16	17	145	120
He	0.16	25	300	170
Ar	0.025	5	185	180
He	0.014	12	157	80
None	---	13	112	500

observed the sputtered surface by using a scanning electron microscope. The surfaces of test pieces made of tough-pitch copper were polished to a mirror finish by using a diamond paste with a 0.5 μm grain size. The polished surfaces were then sputtered by either He ions or Ar ions.

The polished surface shown in Fig. 5(a) is smooth, whereas the sputtered surfaces shown in Fig. 5(b) and (c) are roughened. The roughness was dependent on the ion beam sputtering conditions. Ion-beam sputtering thus provided clean but rough surfaces. Cleaning surfaces tend to have higher breakdown fields, but the rougher surfaces tend to have lower breakdown fields. The resultant first breakdown field will thus be determined by the balance between these factors.

5.CONCLUSION

The findings of the present experiments are summarized as follows:

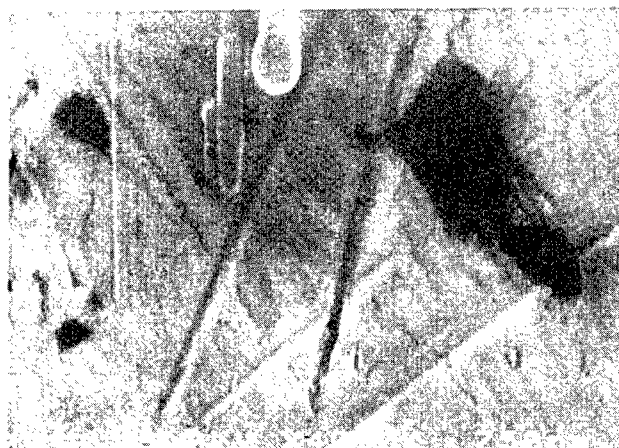
1. *In situ* ion beam sputter cleaning improves the conditioning effect of vacuum gaps, but does not effect the strength of the first breakdown field.
2. Ion-beam sputtering roughens electrode surfaces, contributing to lower first breakdown fields.

6.ACKNOWLEDGMENTS

We are indebted to Mr. Mitshuru Iida for obtaining the experimental data.

7.REFERENCES

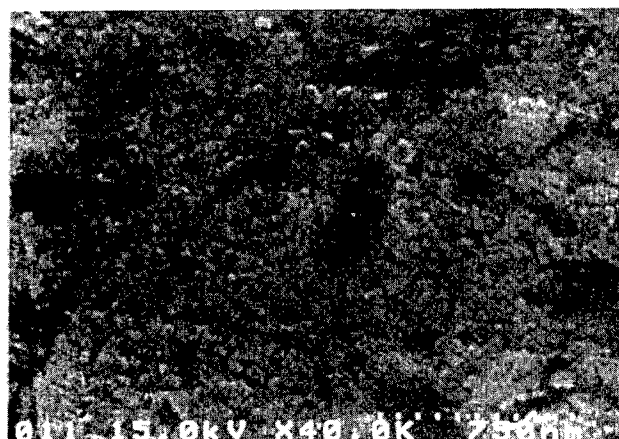
1. R.V. Latham, High Voltage Vacuum Insulation: The Physical Basis, Academic Press, London, 1981.
2. S. Bajic, A.M. Abbot and R.V. Latham, "The influence of gap voltage, temperature and gas species on the "gas conditioning" of high voltage electrodes," Proc. 13th International Symposium on Discharges and Electrical Insulation in Vacuum, J.M. Buzzi and A. Septier ed., Vol. 1, pp. 8-12, Les Editions de Physique, Paris, 1988.
3. J. Ballat, D. Konig and U. Reininghaus, "Spark conditioning procedures for vacuum interrupters in circuit breakers," IEEE Trans. on EI, Vol. 28, pp. 621-627, August, 1993.
4. S. Kobayashi, Y. Saito, Y. Nagai and Y. Yamamoto, "Vacuum breakdown strength of vacuum-degassed oxygen-free copper electrodes," IEEE Trans. on EI, Vol. 28, pp. 500-506, August 1993.
5. V.A. Nevrovsky, V.I. Rakhovsky and V.G. Zhurbenko, "Dc breakdown of ultra-high vacuum gap," Beit. Plasmaphys., Vol. 23, pp. 433-458, 1983.



(a) polished by 0.5 μm diamond paste.



(b) He-ion-sputtered surface
(5.3×10^{-4} Pa of He pressure).



(c) He-ion-sputtered surface
(2.7×10^{-3} Pa of He pressure).

750 nm

Fig. 5. Test piece surfaces.

Estimation of vacuum insulation degradation after long-lasting non-voltage state of the system

Krzysztof Siodła

Technical University of Poznań, The Institute of Electrical Power Engineering
3a Piotrowo St., 60-965 Poznań, Poland

ABSTRACT

The paper presents electrical strength estimation of vacuum insulating system after long period of storage, when voltage was not applied to the system. The test objects were commercially manufactured, high voltage extinguishing chambers of vacuum interrupter. The method of chamber preparation with conditioning process was described. Maximum charge of microdischarges and also microdischarges onset (inception) voltage were the parameters taken as the criteria to evaluate the electroinsulating state of vacuum system. It was found that there is a relation between breakdown voltage and the charge of microdischarges. The measurements were made after long-lasting period of time, when the chambers were stored without any voltage applied to them. The investigations proved that the increase of microdischarge charge resulted in the breakdown voltage decrease. On the other hand, microdischarge charge decreasing was accompanied by the breakdown voltage increase. Limiting of microdischarge intensity involves the increase of electric strength of a tested insulating system. Microdischarges maximum charge in vacuum insulating systems may be chosen as the one of quantities used for defining the electrical state of a chamber. It is important in a case when the measurement of breakdown voltage is impossible to conduct, or should not be done, because it may change the state of an investigated system.

1. INTRODUCTION

High voltage electrical devices with vacuum as an insulating medium, require employment of complex measuring procedures due to the fact that investigated breakdown voltage is a very unstable parameter, both in vacuum gap, and along the surface of dielectric material placed in vacuum. This instability of breakdown voltage is strictly connected with the state of electrode surface, which undergoes the permanent changes. It depends also on a kind of phenomena taking place in investigated system before the breakdown. Each breakdown occurring in a vacuum insulating device changes the parameters characterising state of this system such as: surface micro-relief, residual gas pressure, physical and chemical structure of electrodes [1,2,3]. An effective observation of all parameters describing vacuum system state is practically impossible, what makes precision evaluation of electric strength unrealisable. Therefore it is very important to find such a parameter, which may describe the state of the insulating system without necessity of the breakdown effect execution.

On the basis on our previously made investigations [4,5,6] above mentioned problem is possible to solve when we can measure the parameters characterising prebreakdown state. We use the fact that electric strength is depended on prebreakdown phenomena intensity and their complex measurement should give us opinion on vacuum system ability to initiate the breakdown.

One of the best criterion of vacuum gap strength is maximum charge carried by the most intensive microdischarge occurred in an investigated system. Microdischarges are self-limiting, low power impulses of current. They may be caused by small particles of electrode material which are pulled out from one electrode and strike the other electrode. Also a beam of electrons from the cathode can vaporise a small quantity of material from the surface of the anode. Presence of various kinds of contaminants on the electrodes' surface is a more common reason of microdischarge formation.

Other prebreakdown phenomena, like electron field emission, and other microdischarge parameters, like onset (inception) voltage, frequency of occurrence, total charge of impulses in a determined time interval, energy, radio frequency interference level also may be considered as criteria of the state of an insulating system [7].

The aim of this paper is to describe the possibility of usage such a parameter like maximum charge of microdischarges to evaluate the state of the vacuum insulating system, especially after long-lasting time of this system storage when voltage was not applied to it.

2. TEST OBJECTS AND EXPERIMENTAL SET-UP

The test objects were extinguishing chambers of vacuum interrupter of rated voltage equal to 12 kV and 24 kV. Electrodes were made of Cu-Cr sinter. Residual gas pressure was of the order of 10^{-3} Pa. The interelectrode gap was set to nominal distance equal to 12 mm for 12 kV chambers and 14 mm for 24 kV chambers.

For microdischarge measurements the typical arrangement for partial discharge investigation was used. The breakdown AC voltage was determined in a measuring set-up with 0.22/150 kV transformer.

Brand-new chambers were heated in high temperature to degas all its parts. Next the electrodes were eroded with a DC current arc to remove the contaminants from the surface of the contacts. Such a process leads up to the roughening this surface, what involves the decrease of the electric strength of the vacuum gap between electrodes. The conditioning process is necessary to improve the electric strength of the chamber. A series of breakdowns between the main electrodes was executed. Each successive breakdown usually occurred at a higher value of voltage, up to the limit of electric strength of the chamber. At that point breakdown voltage oscillates around a certain average value, several times higher than the voltage of the first breakdown. The chamber prepared in such a way is ready to use.

3. RESULTS AND DISCUSSION

If we assume that microdischarges are one of the reasons which lead to the final breakdown between the main electrodes, it should be checked if there is any relationship between the breakdown voltage and microdischarge. The maximum charge of microdischarges was taken as the most significant parameter characterising them. All investigations were made with the electrode set to the nominal distance. The maximum charge of microdischarges was measured during the conditioning process, just before each conditioning breakdown. It was found that the presence of microdischarges with high charge values is the reason of breakdown with relatively low voltage, as it is shown in Fig.1. Limiting of microdischarge intensity increases an electric strength of the interelectrode vacuum gap.

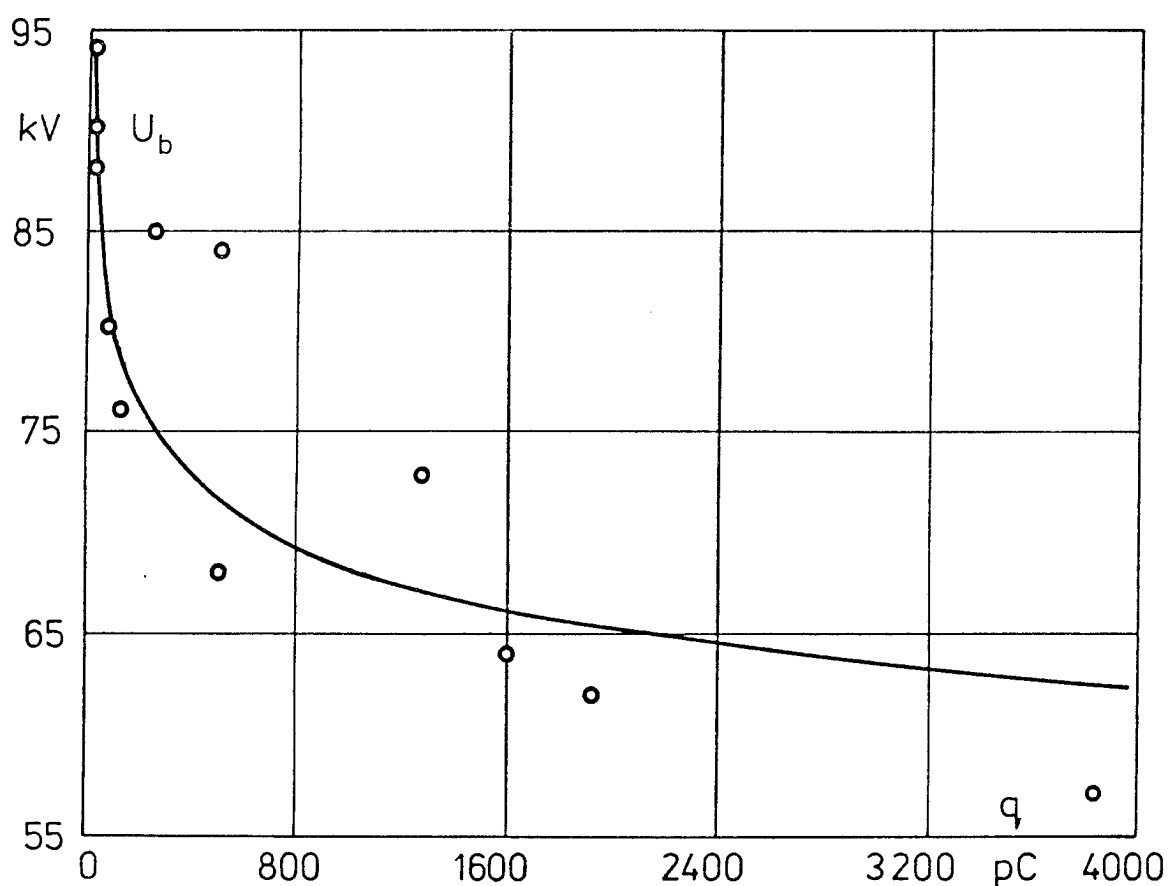


Fig.1. Breakdown voltage as a function of maximum charge of microdischarges. Voltage in peak values

The breakdown voltage strictly depends on microdischarge charge, what was found when the determination coefficient of corresponding quantities was analysed. Since this dependence is so strict, the maximum charge may be treated as an evaluation criterion of electric strength of the vacuum chambers. The efficiency of conditioning process manifests itself in a stabilisation of microdischarge charge and in non-diminishing of the breakdown voltage value. The microdischarge charge was measured just after the end of conditioning process, and next in some time intervals up to 90 days of storing the chambers. After this time also the breakdown voltage of all the chambers was measured. Fig.2 shows the values of microdischarge charge measured during long-lasting storage of the chambers, when voltage was not applied to them. In this figure, there are also included the values of breakdown voltage measured just after the end of the conditioning process and after the end of storage time. We can see that the good properties of the chambers obtained in an appropriate preparation process were preserved. This appears in a relatively low value of the maximum charge (comparing to Fig.1) during a whole storage period. The breakdown voltage was even higher than in the beginning of storage time, what may be involved by the limitation of microdischarge charge intensity.

Relatively high value of the charge in the 15-th day of storage for the 24 kV chamber should be treated as a random one, and confirms the complex and non-stable nature of microdischarges.

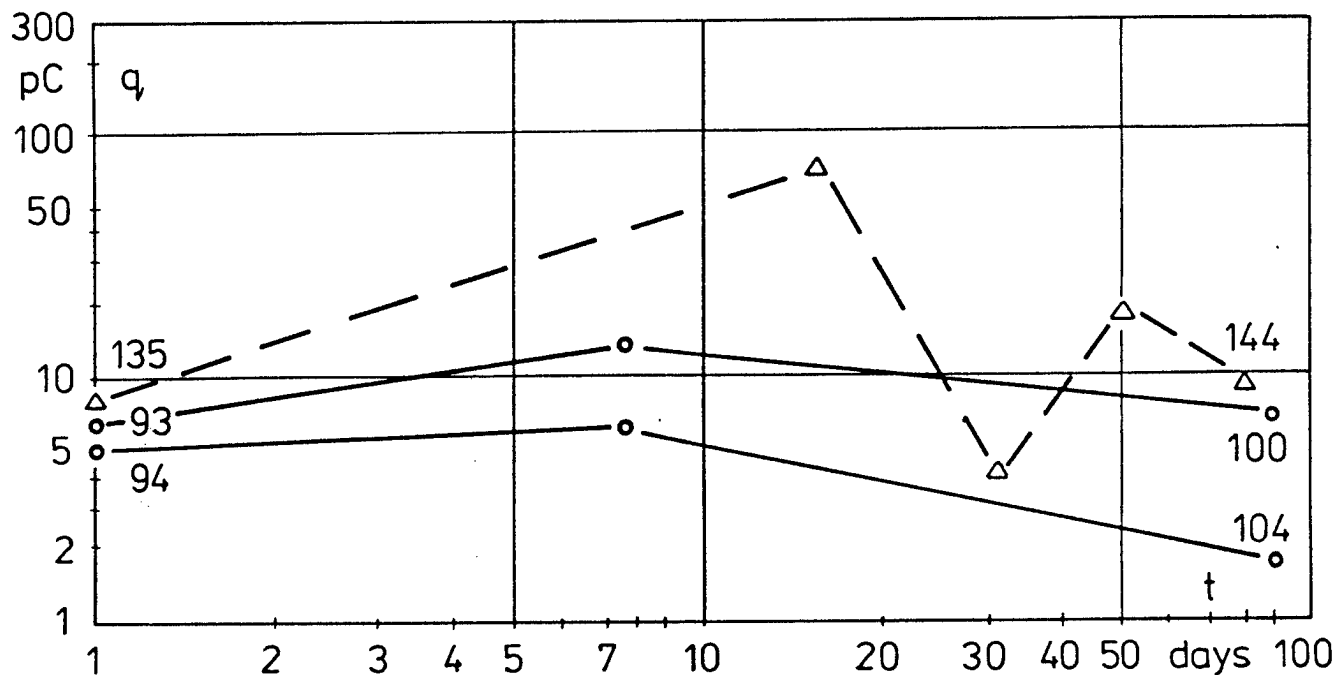


Fig.2. Changes of microdischarge charge during long-lasting storage of selected 12 kV chambers (solid line) and 24 kV chamber (broken line). Numbers inside the figure are the values of breakdown voltage (in peak values) taken after the end of conditioning process and next after the storage time of 90 days

4. CONCLUSIONS

1. Limiting of microdischarge intensity involves the increase of electric strength of the tested insulating vacuum system.
2. Properly prepared vacuum chambers keep their good electroinsulating properties without the changes in time.
3. The maximum charge of microdischarges may be considered as the quantity describing the vacuum chamber state in a case when the breakdown voltage can not be obtained, because the measurement of this voltage may change a state of the system.

5. REFERENCES

- [1] R.A.Latham, High Voltage Vacuum Insulation, The Physical Basis, Academic Press, London, 1981
- [2] G.A.Mesyats, D.J.Proskurovsky, Pulsed Electrical Discharge in Vacuum, Springer Verlag, Berlin, 1989
- [3] J.E.Thompson, "Vacuum Insulation, Conduction, Recovery And Applications; A Review", Proc. VI Int. Symp. on High Volt. Eng., New Orleans, USA, August 1989
- [4] H.Mościcka-Grzesiak, K.Siodła, W.Ziomek, "Relations of Breakdown Voltage and the Parameters Characterising Prebreakdown State in Vacuum in a Wide Range of the Electrode Distance", Proc. VII Int. Symp. on High Volt. Eng., Dresden, Germany, 1991
- [5] K.Siodła, "Microdischarges - the Prebreakdown Phenomenon in the Vacuum Interrupter", XIV Int. Symp. on Disch. and Electr. Insul. in Vacc., Santa Fe, USA, 1990
- [6] K.Siodła, W.Ziomek, "Electric Strength of Vacuum Gap Under Various Voltage Conditions", Vacuum, Pergamon Press, to be published
- [7] W.Ziomek, H.Mościcka-Grzesiak, "Relations of Breakdown Voltage and the Parameter Characterising Microdischarges in Prebreakdown state in Vacuum", Proc. XV Int. Symp. on Disch. and Electr. Insul. in Vacc., Darmstadt, Germany, 1992

Image processing analysis of discharge phenomena under non-uniform electric field in vacuum

H. Okubo M.Fujimori S.Yuasa N.Hayakawa and M.Hikita
(Nagoya University, Nagoya, JAPAN)

ABSTRACT

We observed the discharge type under non-uniform field in vacuum for air and He gas. In order to quantitatively discuss the change of the discharge type, we introduced an image processing method. In the first place, we newly proposed 4 shape parameters to characterize the discharge pattern: the area S_H , the flatness rate H/V , the location G of the center of gravity for the luminous area, and the length L of the positive column. The analysis with the image processing for air revealed that S_H , H/V and G continuously increased as the pressure decreased. Consequently, the discharge type in air was successfully classified into 3 regions with two boundary pressures 200 and 2000 Pa over the pressure range from 1.3×10^4 to 27 Pa. We also analyzed the discharge type in He gas in the same way. We newly introduced an another parameter: effective current density J_e which was defined as a ratio of the discharge current to the luminous area viewed from the vertical direction. J_e proved to be independent of the discharge current I_d , so that we suggested the possibility that J_e can be a universal parameter to classify the discharge type for non-uniform electric field in vacuum.

1. INTRODUCTION

Since space technology has been developing remarkably, application of high voltage technology in space is now underway.^{1,2} For instance, the technology for large power transmission receives a special attention. In this case, electrical insulation will play a decisive role in reliable operation of the power apparatus in space. In particular, the understanding of discharge characteristics in space environment is crucial for the application of high voltage technology to the power apparatus in space. Space environment is characterized by sever and special conditions such as low to ultra high vacuum, no gravity, wide temperature difference, ultra violet radiation, plasma, magnetic field and so on.³ For example, surface discharge due to charging of solid dielectrics in space caused even several satellites to lose their function. In such special circumstances, the terminology defined conventionally in the field of gas discharge technology may no longer be used: the definition of arc, glow and corona discharges. Even wrong terminology concerning discharges is sometimes used.

Although there have been extensive studies of discharge phenomena in vacuum simulating space environment, the type and mechanism of discharge under a non-uniform electric field in low and medium vacuum are not sufficiently clarified yet, especially discharges in low pressure He gas which is dominant in high altitude space. From the above points of view, we have been investigating discharge phenomena in low, medium and high vacuum simulating the space environment. In the first step, in this paper, an attempt is made to quantify the discharge phenomena and to classify the discharge type in vacuum of air and He gas under the non-uniform electric field. We employ image processing technique in order to analyze quantitatively the discharge type.

2. EXPERIMENTAL

Figure 1 illustrates the experimental setup, which consists of a vacuum chamber made of glass, a dc power supply, a video camera, a color monitor and an image processing unit. The point-plane electrode (point radius of the curvature is $50\mu\text{m}$) were placed in the vacuum chamber. After evacuation to almost 10^{-1} Pa , air or He gas was introduced into the chamber back to the atmospheric pressure. Then, the pressure was set at a given value between 0.1 MPa and 0.1 Pa. A dc ramp voltage with positive polarity was applied to the high voltage electrode at a rate of 0.1 kV/s. Discharge phenomena were observed with a video camera and recorded on a video tape. The recorded data were used for image processing to quantify the discharge pattern and classify the discharge type. All measurements were performed at room temperature.

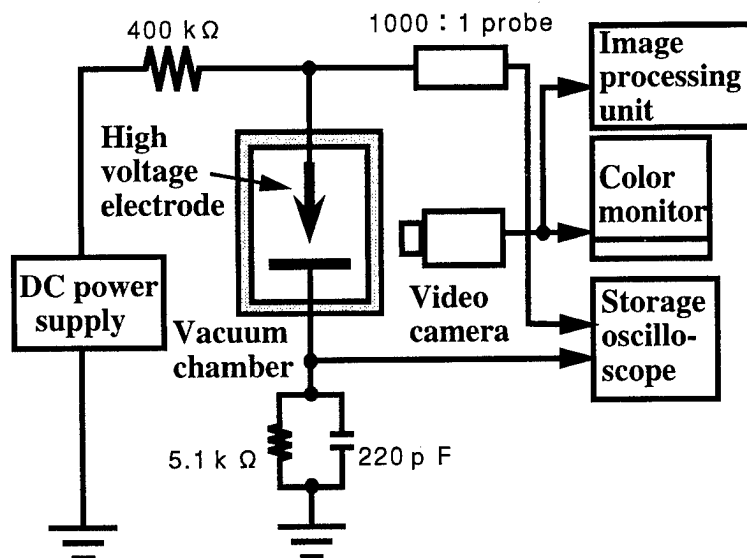


Fig.1 Experimental setup.

3. CHANGE OF DISCHARGE TYPE IN VACUUM

Figures 2 (a) to (c) show pictures of observed discharge pattern in air at 1.3×10^4 , 1.3×10^3 , 130 Pa, respectively, for the needle-plane electrode configuration with the gap length $d = 15\text{ mm}$. As seen from the picture (a), at $1.3 \times 10^4\text{ Pa}$, glow discharge takes place with emitting light only at the electrode edge. When the pressure decreases to $1.3 \times 10^3\text{ Pa}$ (b), positive column begins to emerge definitely. Further decrease of the pressure to 130 Pa (c) causes the positive column to disappear again and the luminous part of discharge to start spreading horizontally along the plane electrode. The discharge type of the luminous part is considered to correspond to negative glow.⁴ At 27 Pa, the glow discharge proved to diffuse in the form of a plane, and went up to the vicinity of the needle electrode edge.

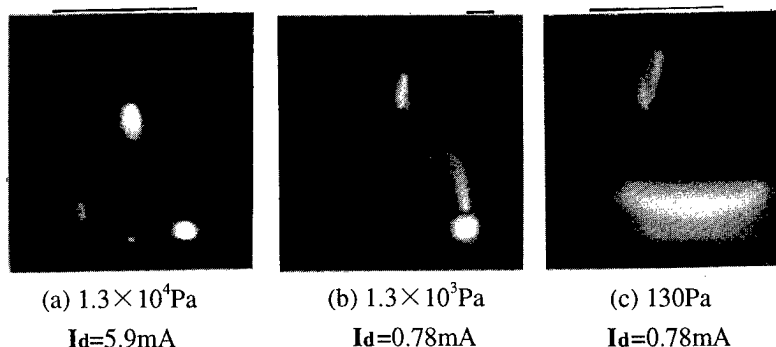


Fig.2 Pictures of observed discharge pattern in air for different pressure with the needle-plane electrode configuration and the gap length $d = 15\text{ mm}$ by applying the positive dc voltage.

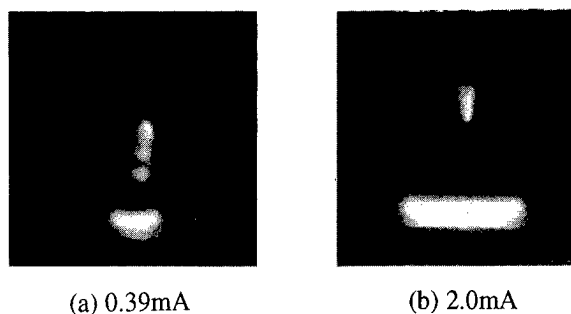


Fig.3 Pictures of discharge in air at 270 Pa for different discharge current I_d . The other conditions were the same as those in Fig.2.

To summarize the results, there were two major features in the change of the observed discharge type: i) As the pressure fell, the size of the negative glow floating above the plane electrode increased, the shape was getting flat, and it approached to the upper needle electrode. ii) The positive column emerged and disappeared again with decreasing the pressure.

On the other hand, the discharge type was found to change with the discharge current I_d . Figures 3 (a) and (b) depict pictures of discharge in air at 270 Pa for $I_d = 0.39$ and 2.0 mA, respectively; the other conditions were the same as those in Fig.2. It is evident from the figures that as I_d increases from 0.39 to 2.0 mA, the negative glow above the plane electrode begins to diffuse in the horizontal direction and the positive column disappears. Other experiments allowed us to confirm that the manner of the change of the discharge type in air with I_d was similar to that observed at 270 Pa.

4. APPLICATION OF IMAGE PROCESSING TO DISCHARGE TYPE CLASSIFICATION

In order to quantitatively discuss the change of the discharge shape obtained above, we introduce the image processing method. Let us newly introduce 4 shape parameters to characterize the discharge type as illustrated in Fig.4: the area S_H , the flatness rate H/V , the location G of center of gravity for the luminous part and the length L of positive column, where H and V are, respectively, the maximum width and maximum height of the luminous part parallel to and perpendicular to the plane electrode, and G is the distance between the center of gravity and the plane electrode. S_H is the cross sectional area of the discharge viewed from the horizontal direction. Note that the three parameters S_H , H/V and G are concerned with the discharge appearing above the plane electrode.

Figure 5 shows the image processing procedure from a given original image to a binary image. It should be noticed, as seen in the figure, that the binarization is eventually performed for one of the components R, G and B. Firstly, an original image is taken to the image processing unit through the video camera. After the color image get decomposed into R, G and B components, the intensity

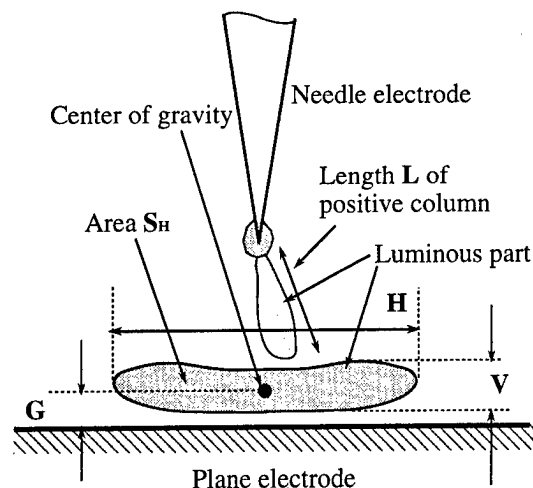


Fig.4 Illustration of four new shape parameters to characterize the discharge type .

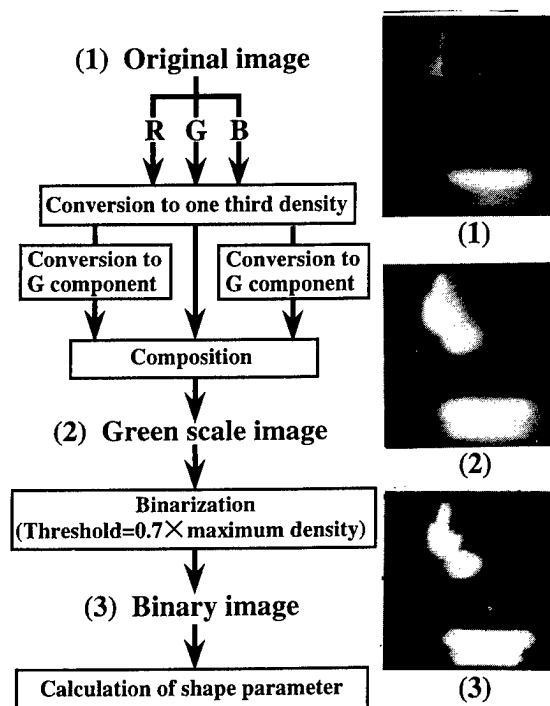


Fig.5 Image processing process from a given original image to a binary image.

of each component is divided by 3. Secondly, the image thus obtained is converted into one of the three components R, G and B, and then the intensity of one unmodified component and two modified ones are summed up. In Fig.5, R and B components turn into G component. Hence, an image reduced to one component (a green scale image in Fig.5) is obtained. The next step is the binarization of the monotone image. One has to determine a threshold level of light intensity for the binarization. In the present work, after comparing discharge shapes before and after the binarization, we have taken 70 % of the maximum intensity as the critical one. The shape feature measurement for the binary image allows the calculation of the 4 shape parameters on discharge type.

Figure 6 shows the area S_H of discharge and the flatness rate H/V as a function of gas pressure in air for different gap length with the positive dc voltage application. Dotted lines represent the two threshold pressures classifying the discharge type. It is seen that S_H and H/V begin to rise with decreasing the pressure. S_H and H/V exhibit the critical pressure, respectively around 2000 and 200 Pa, at which there exists the change in the first order derivatives of S_H and H/V with respect to the pressure. In other words, the above results indicate that the discharge type can be divided into three categories with two threshold pressures 2000 and 200 Pa under the present experimental conditions. It should be also noted that the two curves S_H and H/V vs. gas pressure are independent of the gap length.

Figure 7 shows the gas pressure dependence of the location G of center of gravity and the normalized length L/d of the positive column in air; the experimental conditions are the same as given in Fig.6. Note that the length L of the positive column is normalized by each gap length d . G sharply rises as the pressure decreases from around 200 Pa, as H/V does. The result implies that the negative glow approaches to the needle electrode with a reduction of the pressure. G is also independent of the

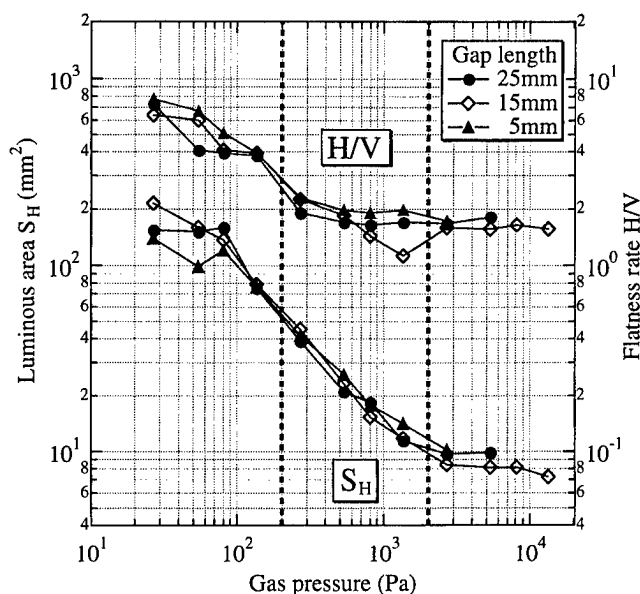


Fig.6 Gas pressure dependence of the area S_H and the flatness rate H/V of the luminous part of discharge in air for different gap length d for positive dc voltage application.

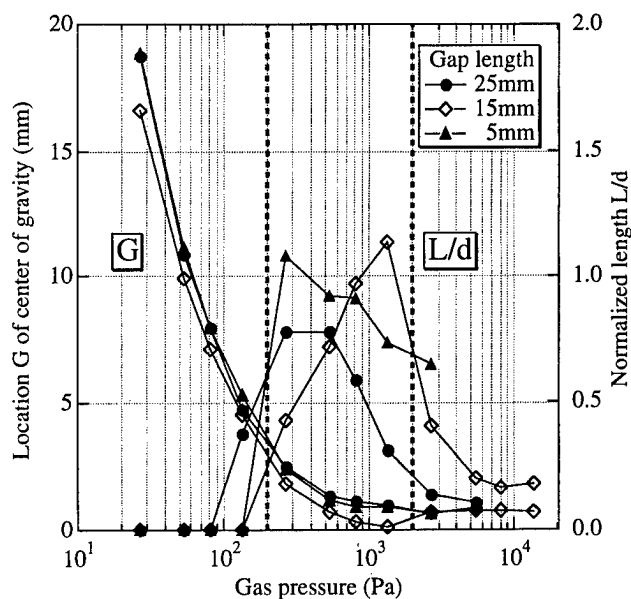


Fig.7 Gas pressure dependence of the location G of the center of gravity and the normalized length L/d of the positive column in air.

gap length. On the other hand, although the length L/d of the positive column changes with the gap length, the pressures at which the positive column emerges and disappears again are almost the same values for different d : 2000 and 200 Pa, respectively. Consequently, the image processing technique employed here allowed us to successfully classify the discharge type in air into 3 regions in the pressure range from 1.3×10^4 Pa to 27 Pa.

5. COMPARISON OF DISCHARGE TYPE BETWEEN AIR AND He GAS IN VACUUM

As shown in Fig.3, the discharge type also varied with the discharge current I_d . Figure 8 shows the relationship between S_H and I_d for different pressures in air and He gas with $d = 15$ mm. It is obvious that S_H increases with a rise of I_d at a constant gas pressure for both gases, and that S_H also increases as the pressure goes down. The image processing of the discharge type also revealed that H/V for both air and He gas exhibited the similar characteristics with a variation of the gas pressure and I_d as S_H did. It was also found that G was almost independent of I_d for a given pressure for both air and He gas. As the pressure fell down, G rose, indicating that the negative glow were approaching to the needle electrode.

It should be noticed that the positive column in He gas did not appear under the present conditions; this result remarkably differed from that in air. Consequently, it has been shown that although the values themselves of 3 shape parameters S_H , H/V and G are different by one order of magnitude between air and He gas at the same pressure, the manner how the three parameters change with I_d and gas pressure resembles in the two gases.

In addition, to discuss in more detail the classification of the discharge type observed in medium and low vacuum under the non-uniform field, we will introduce another new shape parameter J_e , the effective current density. Let us define J_e as expressed in eq.(1)

$$J_e = I_d / S_V \text{ [mA / mm}^2\text{]} \quad (1)$$

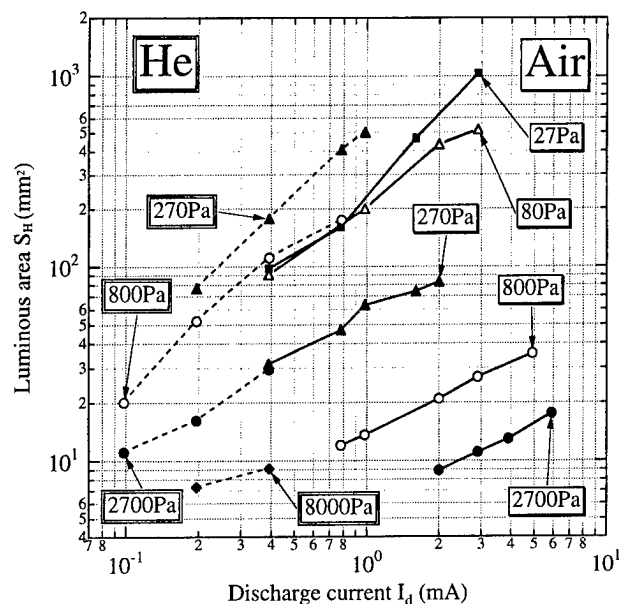


Fig.8 Relationship between area S_H and discharge current I_d for different gas pressures in air and He gas with gap length 15 mm for applying the positive dc voltage.

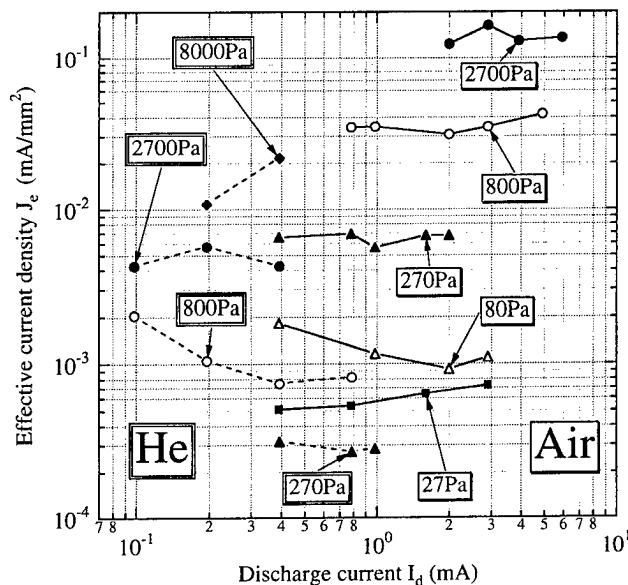


Fig.9 Relationship between the effective current density J_e and discharge current I_d for different gas pressures in air and He gas.

where $S_v = \pi (H/2)^2$, is the area of cross section of the luminous part of discharge viewed from the normal direction. Figure 9 shows the effective current density J_e as a function of discharge current I_d in air and He gas for different vacuum range. As seen in the figure, J_e is almost independent of I_d for a given constant pressure and is nearly proportional to the pressure. This indicates that the luminous area S_v of discharges increases with I_d . With the obtained results considered, the discharge type may lay in the first stage glow or the normal glow⁴ within the present conditions. It must be very useful that we get the parameter equivalent the current density even though it is a non-uniform field. Because of being independent of I_d , J_e can be a more universal parameter to classify the discharge type in comparison with the other preceding 4 parameters. Hence, there is the possibility that the use of J_e allows one to predict the gas pressure from discharge shape in a known gas or to identify gas component from a known pressure. Further investigation is necessary on the quantitative classification of discharge type in He gas and on the relationship between discharge mechanisms and the shape parameters derived from the image processing.

6. CONCLUSIONS

An attempt was made to quantify the pattern of discharge luminous part in vacuum using an image processing technique. As an example, we applied the image processing to the classification of the discharge type in low and medium vacuum for air and He gas under the non-uniform electric field by dc voltage application. In the first place, we newly introduced 4 shape parameters to characterize the discharge shape: the area S_H , the flatness rate H/V , the location G of the center of gravity of the discharge luminous part, and the length L of the positive column. The analysis with the image processing for air revealed that S_H , H/V and G continuously increased as the gas pressure decreased. It was also found that they were almost the same value irrespective of the gap length 5, 15 and 25 mm. Consequently, the discharge type was successfully classified into 3 regions with two boundary pressures 200 and 2000 Pa over the pressure range from 1.3×10^4 to 27 Pa. We also introduced the effective current density J_e , which was defined as a ratio of the discharge current I_d to the area of cross section of the luminous part viewed from the vertical direction. We pointed out that J_e can be a more universal parameter to identify the discharge type in vacuum for air and He gas than the preceding 4 parameters.

REFERENCES

1. M.Frank Rose: "Power Technology for Space Systems" 6th Int. Symp. High Voltage Eng. 45.01 (1989).
2. M.Gollor and K.Rogalla: "HV Design of Vacuum-insulated Power Supplies for Space Applications" IEEE Trans. on Elect. Insul., Vol. 28, No. 4, pp. 667-680 (1993).
3. M.LaurienTE and H.B.Garrett: "A Space Environment Data Resource" Proc. Spacecraft Charging Technology Conference 1989, p. 556 (1991).
4. Yuri P.Raizer: "Gas Discharge Physics" pp.167-171, Springer-Verlag (1991)

Influence of cobalt-molybdenum alloy coating on the surface
of copper electrodes upon electric strength of unconditioned
vacuum insulation systems

W. Opydo*, J. Mila*, R. Batura*, and J. Opydo**

*Department of Electrical Engineering, **Department of Chemistry
Technical University of Poznań, ul. Piotrowo 3, 60-965 Poznań, Poland

ABSTRACT

The paper presents the results of investigations of electric strength at AC voltage (50 Hz) of vacuum insulation systems which were not subject of conditioning. Plane electrodes with rounded-off edges of Rogowski's profile were used in the investigations. The electrodes, having diameters of 50 mm, were made of OFHC copper. The paper shows the influence of fundamental factors defining the conditions of a vacuum insulation system on its electric strength, such as: the value of pressure (within the scope of approximately 1 mPa - 1 Pa) and at constant value pressure approximately 1 mPa, the length of vacuum gap, and the presence of cobalt-molybdenum alloy layer coating the surfaces of the electrodes.

The experiments have shown that breakdown field strength of unconditioned vacuum insulation systems decreases with increasing the gap spacing between the electrodes and amounts to about 17 kV/mm for systems with copper electrodes at the electrode gap length of 1 mm, and about 9 kV/mm at the gap space between the electrodes equal to 6 mm. Cobalt-molybdenum alloy coating electrolytically deposited on the surface of copper electrodes, causes more than 25% increase of electric strength of unconditioned vacuum insulation systems.

1. INTRODUCTION

In literature there is little information on the electric strength, at AC voltage, of vacuum insulation systems which have not undergone the process of conditioning. In the course of time the electric strength of a conditioned vacuum insulation system left in the dead voltage condition decreases frequently to the level preceding the conditioning. Therefore, the knowledge of this level is of basic significance in designing devices with vacuum insulation.

Since elements conducting large currents for high voltage apparatus are usually made of copper, it was decided that the aim of the present paper will be to study the electric strength of unconditioned vacuum insulation systems with copper electrodes. Electric strength of vacuum insulation systems to a large degree depends on many factors determining the conditions of electrode surface of the systems. Surface impurities, including oxides, can deteriorate considerably electric strength¹. An oxide layer, visible even with the naked eye, on the copper electrode surface appears already a few minutes after polishing. Also the presence of microprotrusions of the height exceeding 1 μ m causes lowering the electric strength of the vacuum insulation system². This electrode surfaces must be mirror-like polished. Such a surface is little resistant against mechanical damages during mounting.

The mentioned above reasons made the authors look for coatings, which after depositing on electrode surfaces will protect these surfaces against oxidation will atmospheric oxygen, increase the resistance of these surfaces against mechanical damages. They are expected to increase the electric strength of the vacuum insulation system. This article presents study results of a cobalt-molybdenum alloy coating influence on electric strength of vacuum insulation system.

2. APPARATUS AND EXPERIMENTAL PROCEDURES

The experiments were carried out in a glass chamber pumped by means of a rotary and an oil diffusion pump. The electrodes were of plane shape with Rogowski's profile edges. The diameter of the electrodes was 50 mm and they were made of OFHC copper. Alternating 50 Hz high voltages were obtained from a 100 kV, 10 kVA test transformer. The voltage was applied to the insulation system through a 0.4 MΩ resistor.

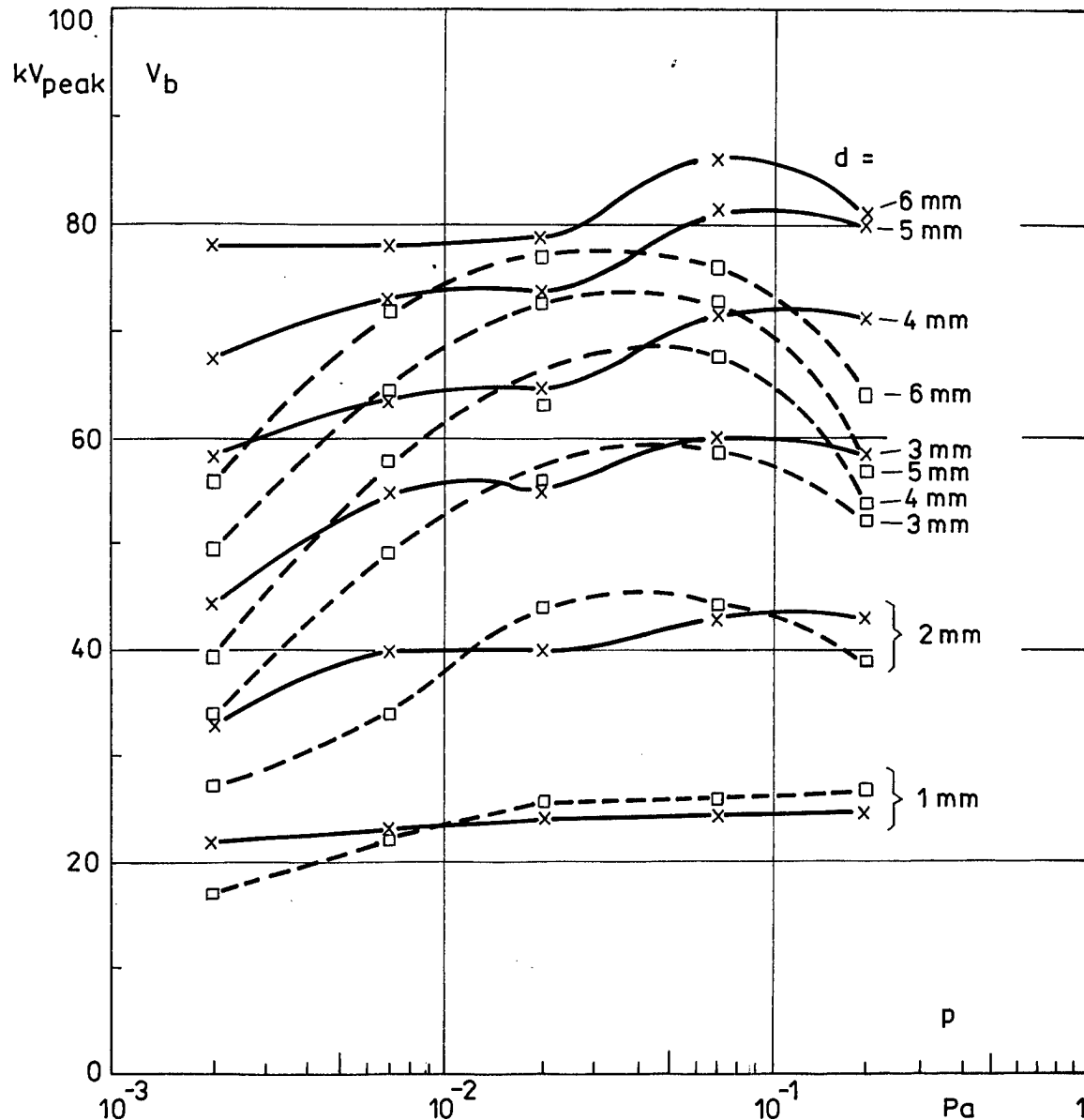


Fig. 1. Average breakdown voltages in vacuum insulation systems with various gap lengths (d), with electropolished electrodes (\square) and with electrodes having cobalt-molybdenum alloy coatings on surface (x) as a function of air pressure

The average breakdown voltage was determined from five results obtained by independent measurements, i. e. five runs on five separate pairs electrodes.

Electrode surfaces were mechanically polished. Some of these electrodes were polished electrochemically as has been described in the paper³.

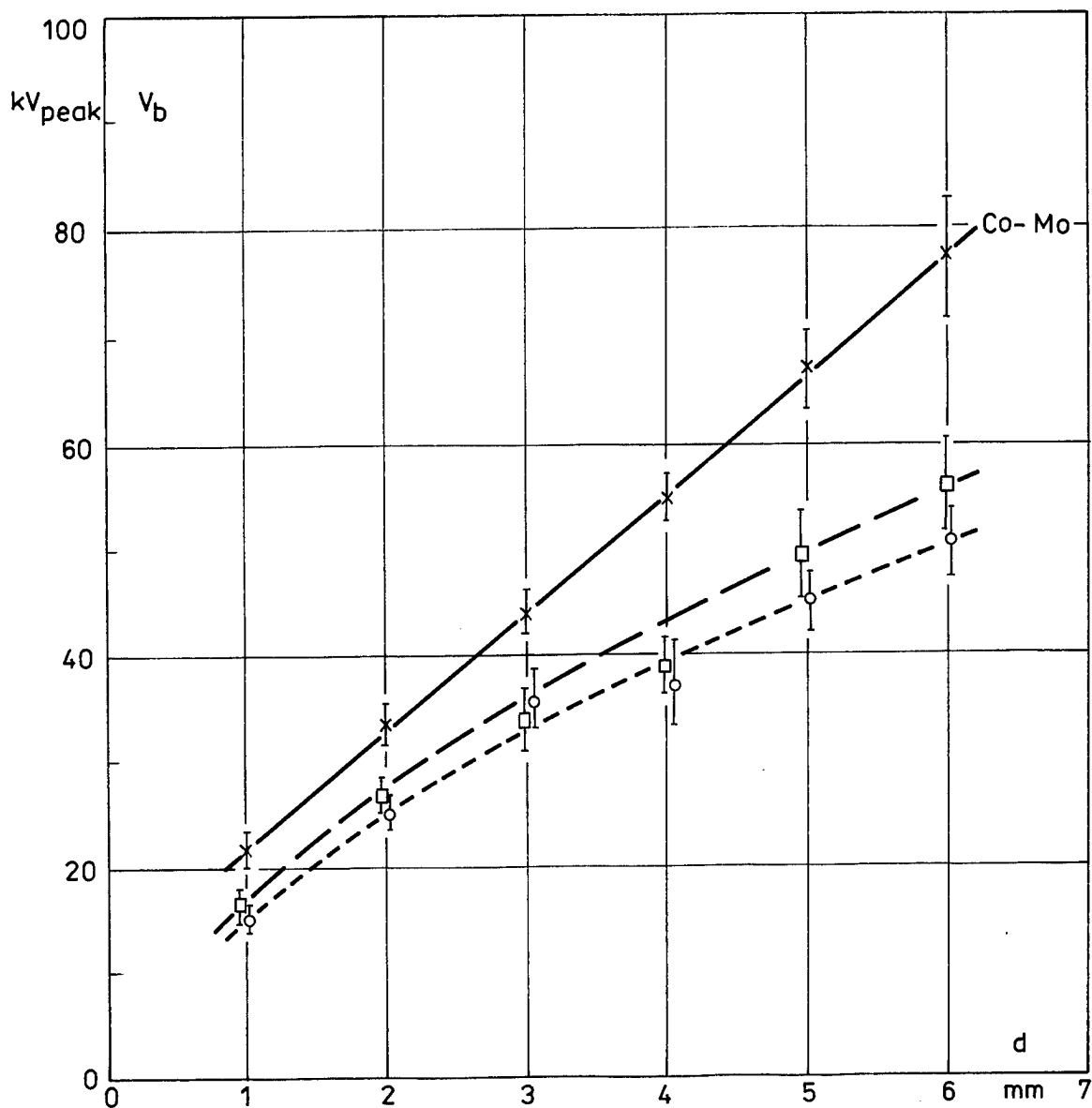


Fig. 2. Average breakdown voltages in unconditioned vacuum insulation systems with mechanically polished electrodes (o), electropolished electrodes (\square) and with electrodes having cobalt-molybdenum alloy coatings on surfaces (x), at the air pressure of 2 mPa, as a function of gap length. Error bars indicate the standard deviation of the mean

The cobalt-molybdenum alloy layer coating on the electropolished electrodes was obtained in a bath containing $\text{Na}_2\text{MoO}_4 \cdot 2\text{H}_2\text{O}$ - 20 g/l, $\text{CoSO}_4 \cdot 7\text{H}_2\text{O}$ - 60 g/l, citric acid - 40 g/l, and sodium citrate - 50 g/l. The bath temperature was 45°C, pH 4.0, and the cathode current density equalled to 2.5 A/dm². The process of electroplating lasted 20 min. The alloy (45% Co, 55% Mo) layer obtained in such a way was about 1 μm thick. The following basic procedure was used in the present studies. After mounting the investigated electrodes in a vacuum chamber, the latter was pumped off to a pressure of 2 mPa. At the electrode gap spacing equal to 1 mm, the breakdown voltage was measured once, increasing the voltage at the rate of about 3 kV/s. Then, the distance between the electrodes was enlarged by 1 mm and the breakdown voltage was measured once again, increasing the voltage at the above rate. This procedure was repeated and the distance between the electrodes was increased by 1 mm until it reached 6 mm. In a similar way, measurements were made at other values of pressure, each time pressure being increased by half order of magnitude. The measurements were finished at the pressure of 0.2 Pa, since further increase of pressure caused a very rapid reduction of electric strength in the investigated vacuum insulation systems.

3. RESULTS AND CONCLUSIONS

Investigations on the influence of cobalt-molybdenum alloy coating one copper electrode surfaces upon breakdown voltage in vacuum insulation system are illustrated by Fig. 1. This figure presents average breakdown voltage in vacuum insulated systems with various gap spacings (d) between electropolished electrodes and cobalt-molybdenum alloy plated electrodes as a function of pressure. Measurements of average breakdown voltages in the investigated insulation systems at the pressure of 2 mPa (previously partially shown in Fig. 1), admitted as the electric strengths of unconditioned vacuum insulation systems, are presented as a function of gap lengths between the electrodes in Fig. 2. The error bars represent the standard deviation of the mean, n=5. Fig. 2 shows that covering electrode surfaces of vacuum insulation systems with cobalt-molybdenum alloy coatings causes more than 25% increase in electric strength.

The following conclusions result from our investigations: Cobalt-molybdenum alloy coating about 1 μm thick, electrolytically deposited on the surface of copper electrodes, causes more than 25% increase of electric strength of unconditioned vacuum insulation systems. This is almost 10% more than we obtained covering copper electrode surfaces of the vacuum insulating system with a nickel layer³, but it is about 10% less than for covering the electrode surfaces with a cobalt-tungsten alloy layer⁴. An additional effect resulting from cobalt-molybdenum alloy coating on copper electrodes is a growth of surface resistance of the electrode to mechanical damage.

4. REFERENCES

1. R. V. Lathan, "High voltage vacuum insulation: the physical basis", chapter 8, Academic Press, London, 1981.
2. W. Opydo, J. Ranachowski, "Electrical properties of vacuum insulation systems under AC voltage", (in Polish), chapters 4 and 5, Wydawnictwo Naukowe PWN, Warszawa-Poznań 1993.
3. W. Opydo, R. Batura, J. Mila, and J. Opydo, "Electric strength at AC voltage of unconditioned vacuum insulation systems", Proc. of XV Inter. Symp. on Discharges and Electrical Insulation in Vacuum, pp. 100-102, Darmstadt, 1992.
4. W. Opydo, R. Batura, J. Mila, and J. Opydo, "Influence of cobalt-tungsten alloy coating on the surface of copper electrodes upon electric strength under AC voltage of unconditioned vacuum insulation systems", Proc. of XXI International Conference on Phenomena in Ionized Gases, pp. 17-18, Bochum, 1993.

High-Voltage Design of Vacuum Components

J.M. Wetzer and P.A.A.F. Wouters

High-Voltage and EMC Group, Department of Electrical Engineering
Eindhoven University of Technology, The Netherlands

ABSTRACT

In this contribution we discuss a number of practical implications from recent studies on high-voltage design concepts used in microwave tube technology. We show how the insights gained can be used in the design of for example insulators and cables, and how conditioning procedures and operating conditions (operating pressure, insulator charging) should be reflected in the design.

INTRODUCTION

For many vacuum devices such as electron tubes the high-voltage design is critical¹. Apart from the inside of vacuum devices, vacuum insulation is important in spacecraft where equipment is being used in the space environment. An additional problem then is the variation of the pressure: the satellite vacuum is deteriorated by outgassing, and atmospheric pressure is used during pre-launch tests. We have previously reported on DC surface flashover mechanisms, and presented some implications of this work to the design and conditioning of HV-insulators in vacuum^{2,3,4}. In this contribution we want to discuss a number of practical implications from recent studies on high-voltage design concepts used in microwave tube technology.

VACUUM DC-FLASHOVER MECHANISM

Primary electron emission

In an earlier study on insulators in vacuum it was found that the breakdown voltage strongly depends on the insulator shape, and in particular on the cathode triple junction field². This is due to primary electron emission. Insulators with a high cathode field have a lower breakdown voltage, but still perform rather well if stepped shapes are used to trap negative charge and thereby reduce the cathode field. If we plot the minimum breakdown voltage observed for different geometries versus the logarithm of the triple junction field⁴, we observe a clear trend indicating the vital importance of the cathode triple junction field (see Fig.1). We also observe a significant scatter, which indicates that other mechanisms must be considered as well.

Surface charging

Next to primary electron emission, surface charging was found to be a key mechanism in both the breakdown and in the conditioning process². It was shown that the breakdown voltage gain of insulators obtained by conditioning with a number of breakdowns with limited energy, is partly due to surface charging, and may be lost when the surface charge is removed by a low pressure nitrogen discharge (see the breakdown voltage evolution in Fig.2).

Electron impact

It was found that electrons impinging on the insulator surface have a detrimental effect on the breakdown voltage except when they are safely trapped. A field distribution by which electrons are drawn back to the surface, either by the chosen shape or by positive surface charge, causes a strong reduction of the breakdown voltage due to electron multiplication or due to desorption of gases⁴.

Implications for breakdown and conditioning

Insulating geometries can be characterized by quantities such as the initial and final breakdown values, conditioning speed and stability. In order to design an insulator it should be known whether and how it will be conditioned (for example with or without conditioning breakdowns), and whether or not it will be switched off for long periods of time (charge leakage) or exposed to whatever gas (discharging). If conditioning breakdowns are applied, the design should be such that the breakdown energy is high enough to be effective but not so high that damage may occur.

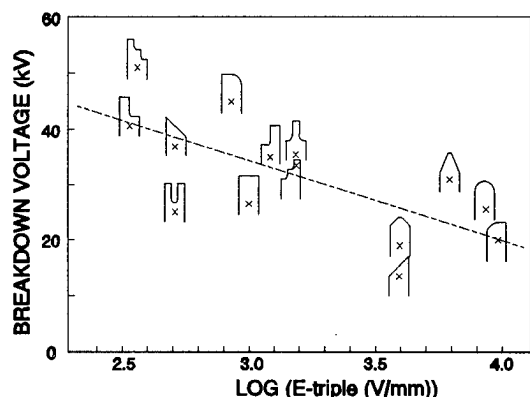


Fig.1 Minimum breakdown voltage versus the logarithm of the electric field amplitude close to the triple junction. The shapes involved are indicated (negative electrode on left hand side).

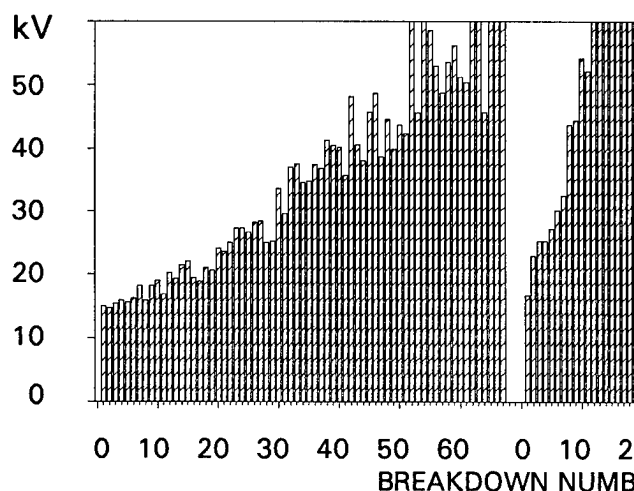


Fig.2 Example of measured breakdown voltage evolution. After 67 breakdowns the surface charge is removed with a low pressure nitrogen discharge.

INSULATOR DESIGN

Insulators between parallel electrodes

A number of different electrode shapes have been tested between parallel electrodes^{2,3}. All insulator samples are machined out of circular Alumina (Wesgo AL300) disks of 40 mm diameter and 5 mm thickness, metallized on top and bottom side with MoMn and Ni, and gold plated. The samples are subjected to test-series as shown in Figure 2. The results are shown in Table 1. A first design rule for insulators is to reduce the cathode field by enhancing the anode field. The cathode triple junction field may further be reduced by trapping the emitted electrons. This can be achieved by using stepped shapes, by using a small angle between insulator and electrode, or with cathode recesses⁴. With such traps the unconditioned breakdown voltage may increase drastically, provided that the electron/insulator interaction is not enhanced. A cathode recess (as in Fig.3A) does not improve the conditioned breakdown voltage, but it tends to make conditioning unnecessary.

Insulators for other than parallel electrodes

With the insights gained, insulators for different electrode geometries have been optimized. Some examples are shown in Figure 3. The optimized shape for **parallel electrodes** was discussed above (A). For most **cylindrical insulators** the distance between electrodes is large, and the cathode field is not effectively reduced by enhancing the anode field. Because of this distance, however, the situation is not critical, and it is sufficient to shield triple junctions (B). Example C shows a recommended design for insulating **concentric conductors**. The rod-type spacers often used for easy alignment can only be applied safely at low voltages: the breakdown voltage and the conditioning speed is low, and the conditioning effect is not stable. Two examples of **feedthrough** optimization are shown (D). The feedthroughs have one side in the tube vacuum, and the other side in vacuum (satellite) or in air (terrestrial). Inside the tube the cathode field is kept low by choosing a large conductor radius and conductor/insulator separation (right), or by shaping the insulator and shielding the triple junction (left). The inside of the insulator tube may be metalized but for DC the same effect is achieved by charging processes. A cathode recess could be used as in (A). Inside the tube the anode field is not harmful. Outside, different pressures may occur, and the field is controlled at both cathode and anode side.


CONDITIONING

Earlier, we have reported on different conditioning sequences, and found that conditioning is most effective at voltages close to the breakdown voltage³. The conditioning technique used should be reflected in the design. If breakdowns are applied in the conditioning process one should choose geometries with a high conditioning speed and stable performance. The breakdown energy should be high enough to be effective but low enough to avoid damage. Values of about 10-30 mJ were found to be safe and effective. If no conditioning breakdowns are applied, one should choose a geometry that effectively traps charge to reduce

the cathode field ("silent" conditioning). For components which may be switched off for long periods of time or which may be exposed to gases, stability is of major concern. Such designs should not rely on surface charging to attain a high breakdown voltage.

Table 1.

Results of breakdown evolution experiments. The averaged breakdown field is defined as the breakdown voltage over electrode distance (5 mm). All values are averaged over two samples. Before charge removal samples are conditioned up to 12 kV/mm. Maximum breakdown field is an average over 5 consecutive breakdowns.

Sample	Averaged breakdown field (kV/mm) MINIMUM	Averaged breakdown field (kV/mm) CHARGE REMOVED	Number of breakdowns to reach 10 kV/mm	Averaged breakdown field (kV/mm) MAXIMUM
	10.2	11.3	0	19.5
	9.0	12.0	1	16.0
	8.1	10.7	8	18.3
	7.4	12.0	5	20.0
	7.1	9.3	36	16.1
	7.0	11.8	24	14.3
	6.7	11.3	45	11.4
	6.2	7.0	40	12.2
	5.3	12.0	78	16.1
	5.1	9.3	61	13.4
	5.0	9.0	188	12.9
	4.0	5.4	25	14.1
	3.8	5.2	109	13.0
	2.7	3.5	71	15.4

BREAKDOWN IN VACUUM AND IN AIR

Spacecraft components designed to operate in vacuum are sometimes exposed to air (prelaunch tests) or to deteriorated vacuum (outgassing). Equipment designed for terrestrial use, such as high-voltage cables, may be incorporated in space hardware. Further, design rules for air operation (creepage distance) are sometimes applied to vacuum insulation and vice versa, although the breakdown mechanisms in vacuum and air are very different. In air, charge carriers are produced in an avalanche of a certain macroscopic distance⁵. Microscopic field enhancements are not very important. Long creepage distances are used to reduce the electric field parallel to (contaminated) insulators. The breakdown voltage obeys Paschen's law above 0.01 Torr.cm. In atmospheric air we can formulate a critical field strength above which partial discharges occur (30 kV/cm). Depending on the field distribution this discharge may develop into a streamer, and initiate breakdown. In vacuum, breakdown is initiated by electron emission from microscopic protrusions or imperfections at the negative electrode⁶. Secondary emission is caused by energetic electrons impinging on the insulator surface. The field components perpendicular and parallel to the insulator surface both contribute to the collision energy. Secondary electrons produced are harmful if they hit the surface again with increased energy. The creepage distance argument is not a valid design principle in vacuum. As a result of the different and sometimes conflicting design requirements for air and vacuum, equipment that operates safely in vacuum may fail in air (and vice versa). Tests in air are not representative for operation in vacuum (and vice versa), and may damage the equipment. Further, evaluation of the performance of vacuum equipment requires knowledge of the actual pressure. The most critical situation is a pressure cycle through the Paschen minimum with the voltage applied.

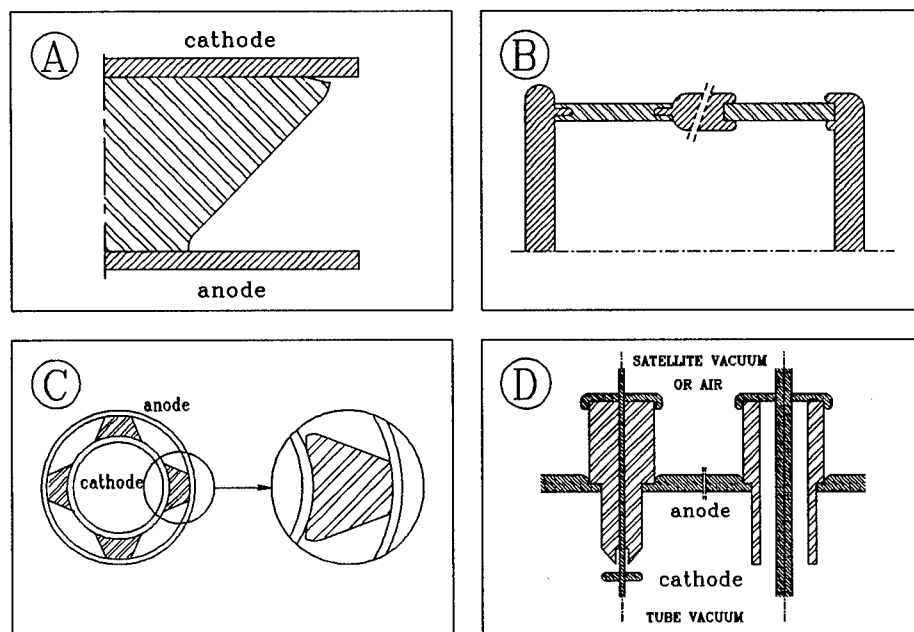


Fig.3 Examples of optimized insulator designs.

HIGH-VOLTAGE CABLES IN VACUUM

Multi-wire high-voltage cables, such as used in spacecraft, usually contain a number of wires made of tapewound and sintered dielectrics. The electric field in between insulated wires may be considerable. From a vacuum point of view a high-voltage cable is a poorly vented component. This makes the inside pressure uncontrolled. The combination of high fields and uncontrolled pressure may result in partial discharge activity, and finally in cable damage. The partial discharge activity may be eliminated by surrounding each insulated wire with a (semi-)conductive layer, and by using extruded, rather than tapewound and sintered, dielectrics. Such techniques are since long common practice in high-voltage cables for power distribution.

POTTED DESIGNS

Potting is often used in vacuum applications for mechanical support or to improve the high-voltage behavior. Properly applied pottings give reasonable results. This requires that the surfaces are clean before potting, and that the potting is applied under vacuum and is allowed to outgas. Improper potting causes partial discharge activity in voids at the interfaces or in the bulk material. Potting of flexible components (cables) may cause voids and partial discharge activity. Potting may further prevent the outgassing of the potted component which makes the inside pressure uncontrolled. A well-designed high-voltage component does not require potting for its high-voltage withstand capability.

REFERENCES

- 1 A.S. Gilmour, Jr., Microwave Tubes, Artech House, 1986.
- 2 J.M. Wetzer, P.A.A.F. Wouters, "The Effect of Insulator Charging on Breakdown and Conditioning", IEEE Transactions EI, Vol.28, No.4, pp. 681-691, 1993.
- 3 J.M. Wetzer, P.A.A.F. Wouters, "The Design of High-Voltage Insulators for Spacecraft Traveling Wave Tubes", IEEE Int.Symp.on Electrical Insulation, Baltimore, pp.31-35, June 7-10, 1992.
- 4 P.A.A.F. Wouters, J.M. Wetzer, P.C.T. van der Laan, "Optimization of Insulators for Bridged Vacuum Gaps", 8th.Int.Symp.on High Voltage Engineering, Yokohama, pp.299-302, August 1993.
- 5 E. Kuffel, W.S. Zaengl, HV Engineering, Pergamon Press, 1984.
- 6 R.V. Latham, HV Vacuum Insulation, Academic Press, 1981.

Electrical insulation problem in quasi-stationary
high-current relativistic E-beam injectors

M.A.Zavjalov, V.I.Perevodchikov

All-Russian Electrotechnical Institute, Moscow, Russia

This report deals with electrical insulation investigation of quasi-stationary high-current relativistic E-beam (REB) injectors (electron energy up to 400 keV, current up to 250 A, and pulse lengths of 250 mcsec). They were accomplished during REB injectors development and exploitation including regime of REB releasing into atmosphere.

The development quasi-stationary REB injectors widens (in comparison with nanoseconds technique) both REB physics research field, and perspectives of their practical using in next trends: REB energy transport, REB technology, plasma chemistry, beam-plasma microwave electronics, radiation technology. 3 types of REB injectors had been examined: 2 injectors with one-gap (diode-type) acceleration (with spherical cathode, and also with ring cathode and electrostatic compressor) and multi-jet three-electrodes injector.^{1,2,3} Large-dimension thermionic cathode was used in diode type injectors proceeding from limitation of accelerating gap electric strength and due to emission current density limitation. In its turn that demanded development of electron-optical system (EOS) with substantial linear compression of E-beams ($\sim 10-20$).

Quasi-Pierce-type EOS injector with 15 cm-diam. spherical cathode generates 1 cm-diam. REB with 120 A current, 350 keV electron energy and 250 mcsec pulse length (see Table and Fig. 1). The accelerating voltage up to 400 kV increasing (probably it's the limit for similar diode systems) led to pulse length reduction down to 50 mcsec due to breakdowns.

This system was examined in regime of bipolar diode with plasma anode for increasing E-beam current.⁴ Inflow of working gas Ar in gas-discharge source and presence of plasma with density $5 \cdot 10^{12} \text{ cm}^{-3}$ in anode area did not lead to breakdown of gap at accelerating voltage up to 300 kV.

REB propagation in a medium with increased gas pressure until the release into atmosphere through differential pumping out system has been examined. This system consists of three pumped out chambers divided by 1,5 cm-diam. aperture diaphragms and pulse gate with operation time of several msec. This hard working regime provided also creature of a 300 keV non-vacuum REB without breakdown accelerating gap.

In Fig. 2 EOS of REB injector with 40 cm-diam. ring cathode and electrostatic compressor is presented. Experimental setup with high voltage input is shown in Fig. 3. Unfortunately investigations showed E-beam instability displayed in ring beam destruction into separate cords at the compressor area ("compressive instability").²

Multi-jet three electrodes injector operates at raiser emission current density and it has smaller cathode dimension. The experiments were carried out with 7,5 cm-diam. cathode base (kern), in which 24 LaB₆ 0,8 cm-diam. tablets were fixed (Fig. 4).

Main parameters of REB injectors are presented in the table. The balanced state radius transported REB is equal about 0,5-0,75 cm.

Table. Main parameters of quasi-stationary REB Injectors
(pulse length 250 mcsec)

Injector type	Voltage kV	Current A	Beam diameter cm	Current density A/cm ²	Power MW	Power density W/cm ²	Note
Diode type EOS with 15 cm-diam. spherical cathode	350	120	1	150	40	$5 \cdot 10^7$	
EOS with 40 cm-diam. ring cathode and electrostatic compressor	270	220	-	-	60	-	compressive instability
Multi-jet triode type EOS with 7,5 cm-diam. spherical cathode	300	200	1,5	113	60	$3,4 \cdot 10^7$	

REFERENCES

1. G. N. Antypov, M. A. Zavjalov, V. N. Tshay, et al. 4 Symposium of High-Current Electronics (4 SHCE-82), Tomsk, 1982. P. 188-190; 5 SHCE-84, Tomsk, 1984. P.138-140.
2. E. K. Eroschenkov, A. B. Esychev, M. A. Zavjalov, V. I. Leyman. Sov.J. Plasma Phys. 11, 6, 1985. P. 700-706..
3. E. K. Eroschenkov, M. A. Zavjalov, V. D. Iljuschin, et al. 6 SHCE-86, Tomsk, 1986, P. 58-60, P. 61-63; 7 SHCE-88, Tomsk, 1988, P. 39-40.
4. M. A. Zavjalov, Yu. E. Kreindel, A. A. Novikov, L. P. Shanturin, "Plasma processes in technological electron guns." Moscow, Energoatomizdat, 1989.

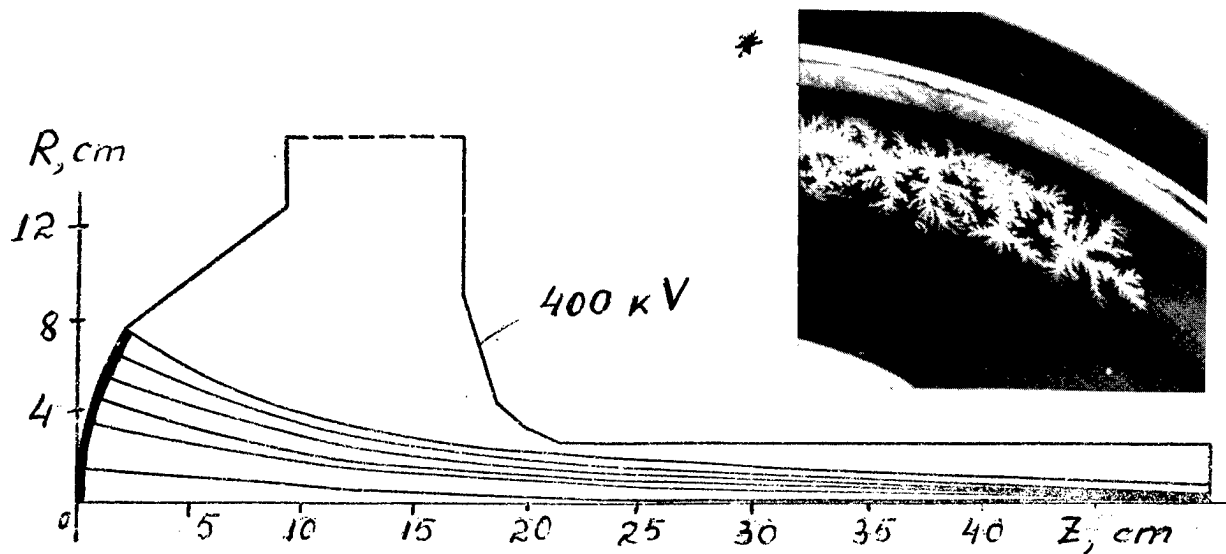


Fig. 1. EOS of Quasi-Pierce-type injector.

* Trace of breakdown on focusing cathode electrode.

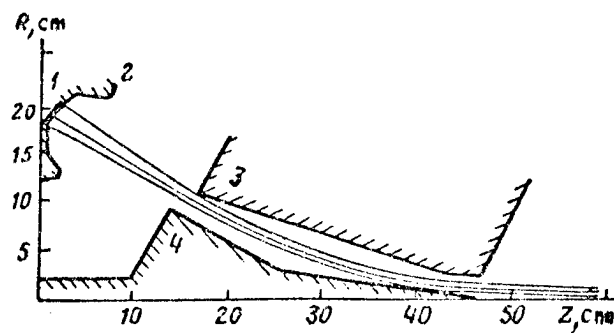


Fig. 2. EOS of injector with ring cathode and electrostatic compressor.

1 - ring cathode; 2 - focusing cathode electrode;
3, 4 - external and internal electrodes of compressor.

Cathode potential

$$\varphi_1 = -270 \text{ kV}; \quad \varphi_3 = 0; \quad \varphi_4 = 0, 1 \cdot \varphi_1.$$

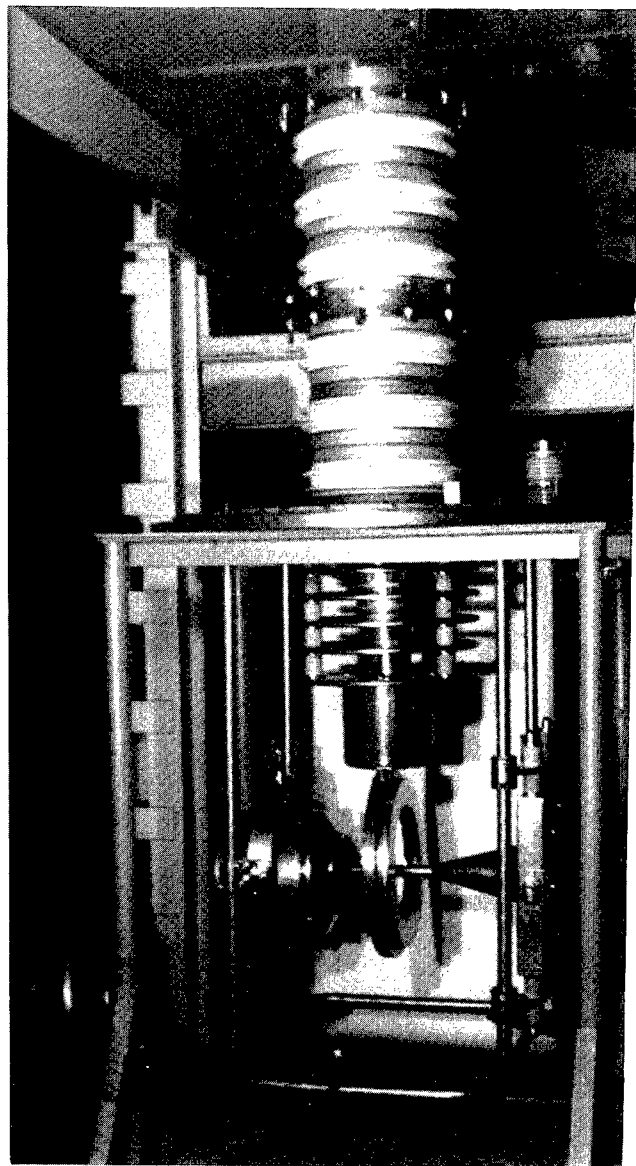


Fig. 3. Photograph of ring cathode injector removable part.

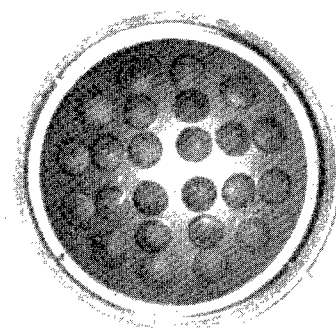


Fig. 4. Photograph of the cathode with 24 LaB₆ emitters installed in graphite base.

SESSION 6

High-Current Diodes and Intense Particle Beams

GENERATION AND TRANSFORMATION OF 0.4 MJ RIBBON BEAM AT THE U-2 DEVICE

A.V.Arzhannikov, V.B.Bobylev, V.S.Nikolaev,
S.L.Sinitsky and A.V.Tarasov

Budker Institute of Nuclear Physics, 630090 Novosibirsk, Russia

ABSTRACT

The paper presents the experimental results on generating and transforming the ribbon (3.5x130cm) beam with the electron energy 1MeV, beam current 70kA and pulse duration 8 μ s. The 70% efficiency of the energy transfer from a capacitor storage to the ribbon beam has been achieved. The close value of the efficiency has been obtained for transforming the ribbon beam to the compressed circular one at the optimal conditions. According to the measurements the angular spread of the compressed beam is less than 10^0 .

1. INTRODUCTION

Microsecond electron beams with a ribbon cross section should give possibility to achieve a total beam energy content about 1 MJ that is necessary for the plasma heating experiments on the nuclear fusion program¹. Besides that the ribbon beams may be used for generation of a microwave power at the wavelength about of some millimeters or even less² because of these beams may have a small angular spread at a large current per 1 cm of their width. Motivated by these applications we carry out experimental studies on the generation and transformation of the ribbon electron beams at the U-2 device.

2. EXPERIMENTAL SETUP

A schematic diagram of the experiments on the U-2 device is shown in Fig.1. This machine is operated by the following way. One megavolt pulse is applied to a fibrous graphite cathode (1) with 4.5x140 cm emission surface. Emitted electrons are accelerated in the magnetically insulated diode, pass through the anode slit (2) and then they are transported through a slit vacuum channel (3) with guiding magnetic field as a high current electron beam (7) with cross section 3.5x130 cm. The slit channel has a length 1m and inner dimensions 6x145 cm. After passing through the slit channel the ribbon beam enters into the transforming unit (4) intended for the transformation of the beam cross section. Due to geometry of the magnetic field lines in this unit the large dimension of the ribbon cross section is diminished and the small one is increased. After such kind of the cross section transformation the electron beam enters into the compression system (5). This system creates a region of a strong magnetic field where the beam cross section should be compressed in 10-20 times. The compressed beam is absorbed by the graphite collector-calorimeter (6) and the total energy of the beam is measured there.

First of all we should say that our experiments have shown³ the form and dimensions of the beam cross sections at various points on the beam way are close to the ones expected in accordance with the computer calculations. These cross sections are drawn in Fig.1. The initial ribbon cross section with dimensions 3.5x130 cm in the slit channel at 0.35 T magnetic field is transformed to the 13.5x23 cm cross section at the exit of the transforming unit and then it has become close to an ellipse with the dimensions 6x9 cm at the magnetic field 4 T in the compression system. By switching on a current in a special coils intended for correction of the beam cross section transforming we may achieve conditions at which the compressed beam cross section becomes close to a circle.

3. BEAM TRANSFORMING AT CHARGE NEUTRALIZATION BY GAS PUFFING

The first experiments on transforming and compressing the ribbon electron beam were carried out when the space charge of the compressed beam was neutralized by the beam electrons ionization of a residual gas. At the residual gas pressure $P_{res} \sim 7 \times 10^{-5}$ Torr when the possibility of the breakdown of the accelerating gap was still small during the beam pulse (10 μ s), the efficiency of the energy transfer from a capacitor storage to the compressed beam was obtained only about 38% because of the neutralization of the beam space charge was not enough. On this reason the next experiments have been done at the conditions when the continuous gas puffing into the region of the beam compression is realized. This gas puffing should remain a low (about 5×10^{-5} Torr) pressure in the accelerator diode gap. According to this limit we have possibility to increase the gas pressure in the compression system up to 2×10^{-4} Torr, not more.

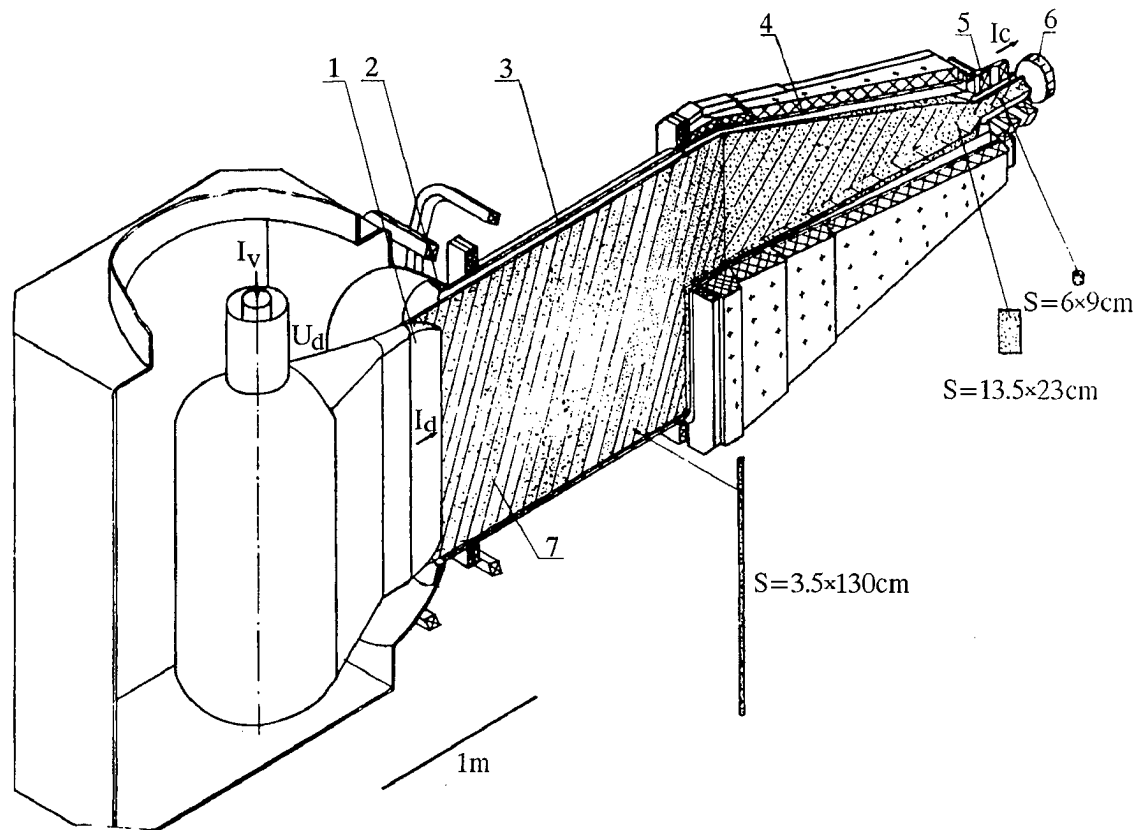


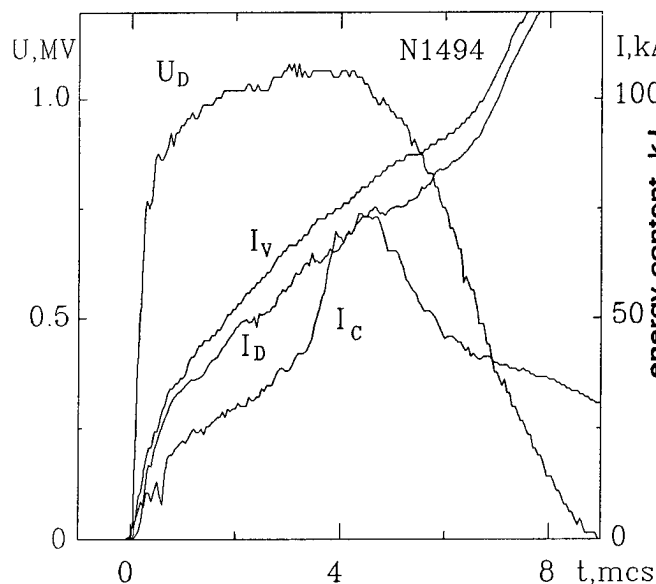
Fig.1. Schematic diagram of the ribbon beam transforming. 1 - cathode, 2 - anode slit, 3 - slit vacuum channel, 4 - transforming unit, 5 - compression system, 6 - collector, 7 - ribbon electron beam.

As a result at the continuous gas puffing the efficiency of the energy transfer from the capacitor storage to the compressed beam has been increased only up to 45%³ but not so essentially as we want.

The further increase of the efficiency was expected at the additional increase of the gas pressure in the vacuum chamber where the beam compression was realized. According to this conception we have carried out the experiments on searching for the necessary kind of a gas, its pressure and the optimal time delay between the pulse gas puffing and the beginning of the beam generation. At first we have investigated how the gas pressure in the vacuum chamber where the beam compression occurs, depends on the time delay from the opening of the gas puff at various gas pressure in the puffing system. It has been obtained that at the pressure $\sim 5 \text{ atm}$ in the gas puff the pressure in the beam compression system practically linear grows from $5 \times 10^{-4} \text{ Torr}$ up to $5 \times 10^{-3} \text{ Torr}$ at the increase of the time delay from 0 to 5ms. Hence by choosing the time delay of the beam generation from the start of the gas puffing we could vary the pressure in the vacuum chamber where the beam is compressed.

Fig.2 demonstrates a set of signals registered in one of the typical shots at the optimal conditions (the pressure of the air in the puffing system $\sim 5 \text{ atm}$, time delay 1.2ms and as a result the pressure in the vacuum chamber 10^{-3} Torr). In this shot more than the half of the 530 kJ energy stored in a high voltage generator has been transferred into the compressed beam. So the 54% efficiency has been reached at the energy content of the compressed beam close to 300 kJ. At the increase of the time delay from 1.2 ms up to 1.5 ms we have observed the decrease of the energy of the compressed beam in the experiments, which is connected with the breakdown of the accelerator diode gap in time shorter than $5 \mu\text{s}$. This breakdown has been caused by the increase of the gas pressure in the diode gap. If the time delay is decreased down to 1 ms the gas pressure in the region of the beam compression becomes insufficient for the space charge neutralization of the beam during the first two microseconds. The using for the pulse puffing the gases with a low atomic weight is turned out unacceptable because of the breakdown of the diode in a few microseconds in this case.

For analyzing the efficiency of the energy transfer the total energies in the beam pulse after passing through the various parts of the U-2 accelerator have been compared. This comparison is shown in the Fig.3. The total energy



$$Q_{PG}=530\text{kJ}, Q_v=450\text{kJ}, Q_D=410\text{kJ}, Q_c=280\text{kJ}$$

Fig.2. Set of signals characterizing the generation and transformation of the ribbon electron beam. U_D - diode voltage, I_v - current flowing from the pulse generator to the diode chamber, I_D - diode current, I_c - current of the compressed beam.

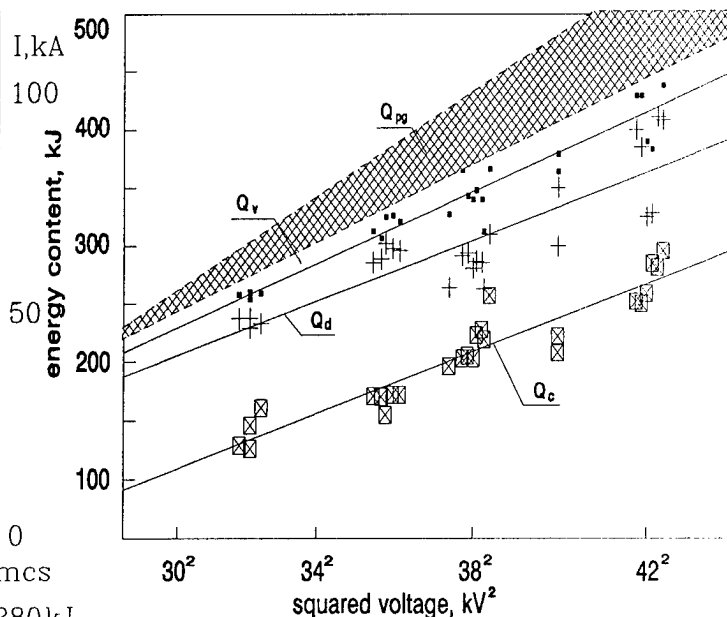


Fig.3. Total energy in the pulse passing through the various parts of the U-2 accelerator. Q_{pg} - energy in the capacitor storage, Q_v - energy transferred from the capacitor storage to the diode chamber, Q_D - energy of the ribbon beam in the diode, Q_c - energy of the circular compressed beam.

passing through the various parts of the accelerator as a function of a squared voltage on capacitor banks of the storage is shown there. The shaded region is the energy in the storage, points - energy transferred from the storage to the vacuum chamber, crosses - the energy of the electron beam which reached the anode of the diode and squares - the energy of the beam after its compression. The straight lines in Fig.3 have been drawn on the experimental data according to the least squares method. From the Fig.3 one can conclude that in a wide range of the experimental voltage the efficiency of the energy transfer from the capacitor storage to the ribbon electron beam in the diode is about of 70% and from the storage to the compressed circular beam it is closed to 50%.

4. MEASUREMENTS OF THE BEAM ANGULAR SPREAD

To measure the angular spread of the electron beam after the transformation and compression the collector-calorimeter at the exit of the compression system has been replaced by a detector of the angular spread⁴. Besides that an additional magnetic system has been constructed for the creation of the region of a homogeneous magnetic field on the detector axis. Almost all the electron beam outgoing from the compression system, is absorbed by a graphite plate and only 8mm diameter cylindrical flow of the electrons passes through a hole in the plate. This cylindrical flow is expanded at its motion in the decreasing magnetic field which has the value 0.6T at its homogeneous part in the angular spread detector. This detector looks like the graphite tube with the inner diameter 6mm. This tube is cut into four rings insulated each from other. The lengths of the rings are 1cm, 1cm, 2cm and 2 cm. During the flow passing through these rings some portion of the flow electrons is absorbed by the inner wall of the rings. The rest of the electrons goes out from the tube and comes to a graphite collector placed at the tube exit. For obtaining the angular spread of the beam electrons the currents of the electrons absorbed by the rings have to be compared with the results of computer calculations. The computer calculated electron current distribution along the axis of the tube for the various values of the angular spread are shown by the solid lines in the Fig.4. Crosses and circles in this figure are the results of the experimental measurements for two moments of the time $2\mu\text{s}$ and $4\mu\text{s}$ after the beginning of the beam generation. From the comparison of the experimental points with theoretical curves one can conclude that the angular spread of the beam electrons in the place where detector is located, is about $2-3^\circ$. The error of the obtaining this value of the angular spread is less than 1° . The value of the angular spread in the detector placement permits us to estimate the spread of the compressed beam in the magnetic field 4T. This parameter should be less than 10° . In addition these measurements allow to obtain the local current density of the compressed beam. This local current density has

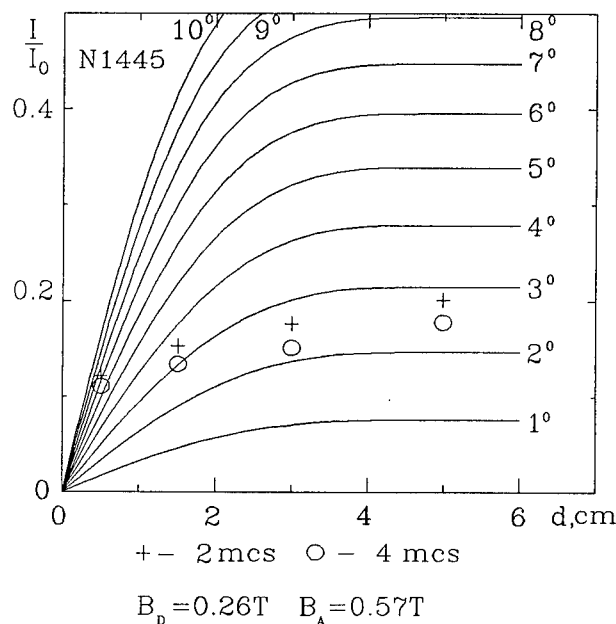


Fig.4. Comparison of the experimental data with theoretical curves characterizing the angular spread of the beam after transformation and compression. B_D - magnetic field in the diode, B_A - magnetic field in the angular spread detector.

a value about 1 kA/cm^2 and it is close to the average current density of the beam calculated by the derivation of the beam current on the beam cross section.

5. CONCLUSION

So, as a result of our investigations 0.4 MJ energy content of the ribbon electron beam has been achieved. It has been experimentally demonstrated that about 70% of the energy of this beam is transferred to the circular beam with the current density $1\text{--}1.5 \text{ kA/cm}^2$ and the angular spread less than 10° .

6. ACKNOWLEDGMENTS

This experimental studies have been performed as a base for the development of the E-beam-plasma interaction program which is carried out at Budker Institute of Nuclear Physics on the GOL-3 device. The authors wish to thank Prof. D.D.Ryutov and Dr. V.S. Koidan for helpful discussions on goals of the investigations on the microsecond electron beams, and the engineers A.D. Khilchenko, V.V. Konyukhov and A.G. Makarov for assistance of the U-2 device operating.

7. REFERENCES

1. A.V.Arzhannikov, A.V.Burdakov, V.V.Chikunov et al., "GOL-3 Programme", *Proc. 8-th Intern. Conf. on High-Power Particle Beams*, Vol.I, p.14, Novosibirsk, USSR, 1990.
2. A.V.Arzhannikov, V.S. Nikolaev, S.L. Sinitsky et al., "FEL Driven by High Current Ribbon REB and Operated with Two Dimensional Feedback", *Technical Digest 14-th Intern. Free Electron Laser Conf.*, p.214, Kobe, Japan, 1992.
3. A.V.Arzhannikov, V.B. Bobylev, V.S. Nikolaev et al., "Ribbon REB Research on 0.7MJ Generator U-2", *Proc. 9-th Intern. Conf on High-Power Particle Beams*, Vol.II, p.1117, Washington, DC, USA, 1992.
4. A.V. Arzhannikov, V.S. Koidan, S.V. Loginov, "Measurement of the angular spread of the magnetized electron beam by its passing through the microholes", *Pribery tekhnika experimenta*, v.4, p.36, 1983.

Relativistic electron beam generation in plasma filled diode and foilless injection into a dense plasma

V.S.Burmasov, I.V.Kandaurov, E.P.Kruglyakov, O.I.Meshkov

Budker Institute of Nuclear Physics, 630090, Novosibirsk, Russia

ABSTRACT

The traditional way of relativistic electron beam (REB) injection in the experiments on REB-plasma interaction is the injection through an anode foil that separates vacuum diode from plasma chamber. The presence of separating foil leads to the following: i) replacement of destroyed foil is required after each shot ii) the beam angular characteristics making worse. A beam with low angular spread can be obtained from foilless diode placed into strong guiding magnetic field; the problem is how to avoid the diode shortening in the presence of a dense plasma from the interaction chamber.

In the experiments on studying of Langmuir turbulence, carrying out on GOL-M device¹ it becomes possible to avoid a separating foil and to obtain a foilless injection of REB into a dense ($\geq 10^{16} \text{ cm}^{-3}$) plasma, utilizing a special drift pipe as an anode of the foilless axially symmetric magnetized diode.

1. EXPERIMENTAL SETUP

The schematic of the experiment is shown in Fig.1. The beam is injected into preliminary hydrogen plasma with the density $n_e \sim 10^{15} \div 10^{16} \text{ cm}^{-3}$ and the electron temperature $T_e = 1 \text{ eV}$. The plasma is created by high-voltage capacitor discharge in a longitudinal magnetic field of mirror configuration with 4.5 T in diode region and 2.5 T in homogeneous part. A length of the solenoid is 2.5 meters. The injected beam is stopped by graphite collector with shunt at the end of plasma chamber. The collector is separated from the plasma by foil.

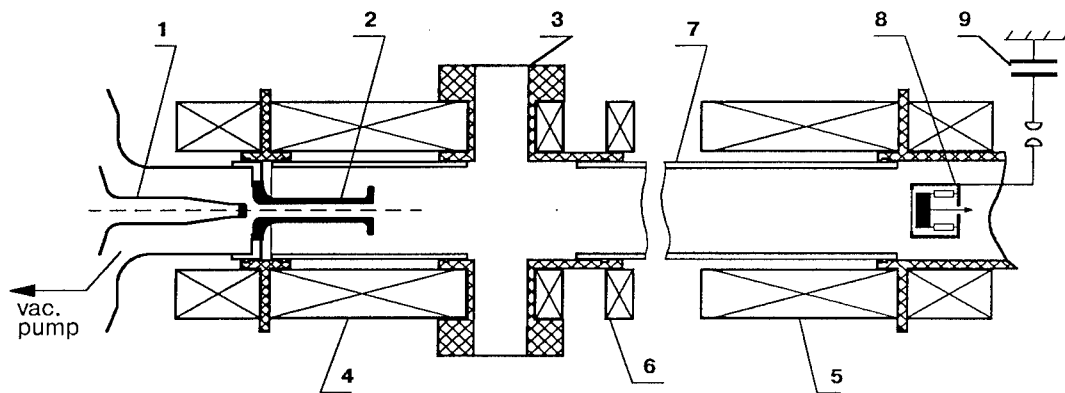


Figure 1. 1-cathode stalk, 2-anode pipe, 3-Thomson scattering system input/output ports, 4,5-mirror coils, 6-solenoid coils, 7-quartz tube, 8-collector/calorimeter, 10-foreplasma discharge capacitor bank.

The 1-MV pulse from coaxial water forming line is delivered to the hemispherical graphite cathode tip. The graphite anode is performed as a drift pipe separating the diode gap from the plasma chamber. The density of the preliminary plasma flowing into the diode gap through the pipe has been measured by Michelson interferometer with CO_2 laser ($\lambda = 10,6 \mu\text{m}$) as a source of light. The ratio R of average plasma density before and after the

anode pipe versus the length of the anode pipe l_A is shown in Fig.2. The inner diameter of the pipe in this experiment was 1.5cm, and the plasma density in the discharge chamber is around $4 \cdot 10^{15} \text{cm}^{-3}$

The pipe substantially reduces the plasma flowing into the diode gap, but do not stop it at all; thus the REB generation in the diode prefilled by plasma has taken place. A physics of REB generation in plasma-filled diode has been studied previously². The expanding ion sheath is formed near cathode surface and acts like virtual anode-cathode gap.

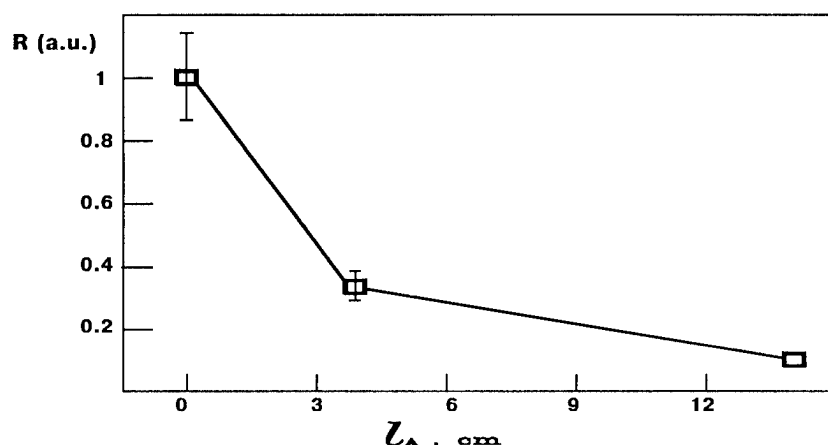


Figure 2.

2. EXPERIMENTAL RESULTS

To make clear the plasma influence on the beam generation, the output of the anode pipe was closed by 20 mkm titanium foil in special control experiments to avoid plasma flowing into the diode gap ("vacuum" magnetized diode regime).

In the case of plasma-filled diode two regimes of REB generation for any anode pipe dimensions could be distinguished depending on plasma density in the chamber. Typical traces of the beam current and the diode voltage for the pipe with inner diameter 1.3cm and length 13.5cm are given below in Fig.3.

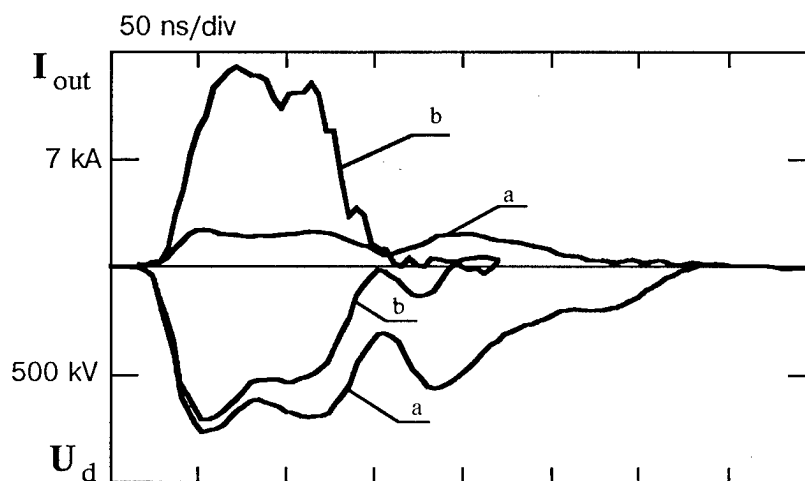


Figure 3

1) "Low-density" plasma regime ($n_e \leq 1 \cdot 10^{15} \text{ cm}^{-3}$). In this case the beam current exceeds slightly the current in "vacuum" regime or does not exceed it at all. The plasma influence on REB generation is negligibly small. Corresponding traces of the diode voltage and REB current are marked by symbol "a". 2) With the plasma density in the chamber increase ($2 \cdot 10^{15} \div 4 \cdot 10^{15} \text{ cm}^{-3}$) the REB current on the collector rises substantially; the pulse duration drops simultaneously (traces marked "b"). The significant spread of the beam parameters from shot to shot is observed in this regime. With further growth of the plasma density the diode shortens in most of shots. The lengthening of the anode pipe and the reducing of its inner diameter allows to inject the REB into the plasma of higher density.

The foilless injection of REB from plasma filled diode demonstrates more efficient dense plasma heating then that through a foil. The results of experiments with pipes of different sizes are presented on Fig.4. Each point on the plot gives the plasma electron temperature and density measured simultaneously by the Thomson scattering system (ruby laser, 5J, 50ns) after the REB injection

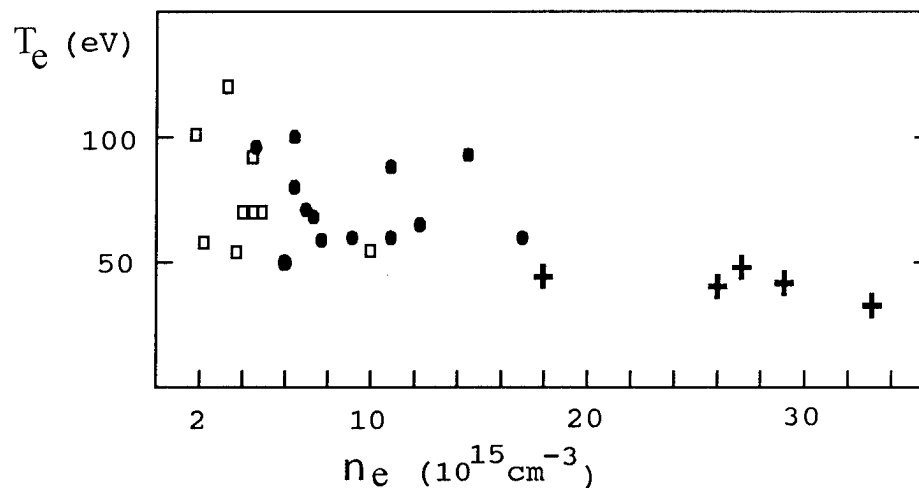


Figure 4. □ - anode pipe length 135mm and inner diameter 13mm;
● - 185mm and 10mm; + - 150mm and 7.5mm;

3. REFERENCES

- 1) I.V. Kandaurov et al., 9th Int. Conf. on High-Power Particle Beams, Washington, DC, 1992.
- 2) R.A. Miller, 1975, Phys. Rev. Lett 35(14), 940-943.

High current annular electron and ion beam sources based on magnetron discharge in the $E \times H$ fields

A.A. Chagin, E.M. Oks, and P.M. Schanin

Institute of High Current Electronics, Russian Academy of Sciences,
Siberia Division, Tomsk, 634055, Russia

ABSTRACT

The cylindrical geometry of the superdense magnetron type discharge system version in the crossed electric and magnetic fields is attractive in that it allows a high azimuthal uniform plasma emission surface to be formed. This geometry offers no problem with screening the cathode from the magnetic field of the beam transportation region. There is a stabilizing effect of magnetic field on the discharge, which provides high value of discharge current in the diffuse (without cathode spots) phase of discharge operation. Thus, for a cathode surface area of 300 cm² and a pulse duration of 15 μ s, the maximum current of a discharge in He was 1.5 kA, in a steady-state mode it was more than 10 A. The processes of electron and ion emission have some peculiar features, and the experimental results of this investigation are also presented. In our device, for a 20 μ s pulse duration and energy of 200 keV it was possible to obtain an electron beam current of 600 A with a current density of 75 A/cm². The beam mean diameter and width were, respectively, 10 cm and 1 mm. The electron current in the steady-state mode was 2 A with a 10 keV energy. The ion beam current constitutes of 10% of the discharge current. The application fields of these sources are microwave generation, surface properties modification, etc.

1. INTRODUCTION

Discharges in crossed electromagnetic and electric fields operating in electrode systems such as a magnetron attract attention because of the possibility they offer to create efficient charged-particle sources. Because of the electron oscillations, the discharge operates stably at low pressures, affording a high degree of ionization of the working gas and stability of the plasma parameters. Such a source, owing to highly efficient extraction of electrons and ions from the plasma, azimuthal uniformity of the emission parameters, simple construction, and the absence of heated cathodes, is competitive with hot-cathode devices. These advantages may particularly show up when the plasma source operates under rigorous vacuum conditions or in corrosive media (for example, in heat treatment of construction materials, in plasma chemical plants, etc.). An important plasma-source advantage is the possibility of producing both electron and ion beams in a single unit. This greatly extends the range of technological applications of such sources^{1,2}.

This paper presents the operational features of a charged-particle source with stationary and pulse annular electron and ion beams.

2. EXPERIMENTAL SETUP

The discharge was ignited between cylindrical coaxial electrodes — cathode 1 and anode 2 (Fig. 1) — made of stainless steel. The experiment used a discharge in the form of an "inverse magnetron". The magnetic field in the discharge chamber was created by using two short solenoids 3. An annular beam is formed by extracting particles from plasma through a 2-mm wide ring slit. The slit is made in end electrode 4, which is under the cathode potential. The voltage applied between electrode 4 and accelerating electrode 5 accelerates the particles up to the required energy. The current of the accelerated particles is detected by collector 6.

FIGURE NOT AVAILABLE
AT TIME OF PUBLICATION

Fig. 1. Source design

3. DISCHARGE PERFORMANCES

To obtain the required emission parameters in the source, it is necessary, above all, to provide conditions for stable ignition of the discharge. In the discharge used, these conditions are determined not only by the pressure of the working gas, but, to a considerable degree, by the magnitude of the magnetic field.

The experiments have shown that the characteristics of the discharge ignition are weakly affected by the type of plasma-forming gas. An increase in gas pressure results in a decrease in ignition voltage and in a shift of the ignition curve toward lower magnetic fields. The discharge ignition voltage can be lowered to the level of steady-state discharge voltage by a proper choice of the magnetic field induction. It considerably simplifies the construction of the electric power supply for the source, because no special ignition system is required.

The current-voltage characteristics of the discharge are presented in Fig. 2. A current growth with increasing voltage is inherent in the discharge. The increase in gas pressure, the higher magnetic-field induction, as well as the lighter plasma-forming gas lead to a decrease in discharge voltage. As seen from Fig. 2, owing to the stabilizing action of the magnetic field a considerably larger current can be obtained in the discharge in crossed fields than in an ordinary glow discharge. The probability of formation of a cathode spot and arc discharge rises as the magnetic field decreases. Electrode conditioning diminishes the probability of arc discharge and results in an increase in diffusion-discharge current.

FIGURE NOT AVAILABLE
AT TIME OF PUBLICATION

Fig. 2. Current-voltage characteristics for Xe (1), Ar (2), and N (3).

We used probes to measure the plasma parameters. The plasma density was estimated from the saturation current on the ion branch of the planar Langmuir probes. The plasma potential (φ) was determined by means of the "emission" probe, using the "floating" potential method.

The discharge was distinguished by a growing $I - V$ characteristic and a positive anode potential drop. The plasma density varied in direct proportion to the discharge current. The anode potential drop increased as a function of plasma density. Thus, at a discharge current of 70 A the discharge voltage was $U_d = 400$ V, the plasma density was 10^{12} cm^{-3} , and the plasma potential relative to the anode at the point equidistant from the anode and the cathode had a value of $\varphi = -20$ V. Increasing the discharge current to 200 A raised U to 200 V and changed φ to -40 V.

4. EMISSION PROPERTIES

In this discharge system the change in plasma and discharge parameters associated with electron emission depended on whether, the accelerating voltage was applied to the anode or cathode. In this regard we can distinguish two current extraction configurations.

In a system with a common anode (accelerating voltage applied to the anode) an increase in emission current I_e (the current drawn by the collector) was accompanied by a rise in plasma potential (Fig. 3a). Here the discharge ignition voltage decreased by a value approximately equal to φ . The current in the cathode circuit and the plasma density did not change, while the anode current decreased by I_e . When the electron extraction efficiency $K = 1$ was achieved, a further rise in the accelerating voltage led to a sharp increase in φ . This caused an increase in discharge (cathode) current, plasma density, and φ .

When the accelerating voltage was applied to the cathode, it was likewise found that electrons could be extracted from the plasma with high efficiency. But the reaction of the plasma to electron emission was very different. The increase in the current drawn by the collector was accompanied by a rise in cathode current by the amount I_e (Fig. 3b). The plasma density increased, while the current in the anode circuit remained the same. In this case, electron

emission caused an increase in anode potential drop and raised the discharge ignition potential. Note that the ignition potential rose by more than φ . Thus, the maximum change in the plasma potential was 12 V (Fig. 3b), while in this regime, the discharge operation potential rose from 600 to 660 V. In this case, the change in plasma parameters is the same as in the situation which occurs when the discharge current increases by I_e in the absence of current extraction. The distinctive difference is the constant current in the primary winding of the transformer supplying power to the discharge. This implies that the accelerating voltage has a major effect on the discharge ignition conditions.

The experimental results of the study of the discharge and emission in the extraction mode with the common anode can be explained as follows.

In fact, the transverse magnetic field restricts the access of the electrons to the anode. Because of the reduction in electron mobility, a layer of negative space charge develops near the anode and a corresponding positive anode potential drop appears. The accelerating voltage applied to the anode separates the electron and ion flows leaving the discharge gap. More and more of the electrons reach the collector by traveling along the magnetic field, while the ions continue to reach the cathode and anode. The electron lifetime in the discharge becomes shorter. This changes the degree of nonneutralization of the charged particles in the plasma and ultimately raises the plasma potential with respect to the anode.

The increase in the current to the collector results from the redistribution of the electron current between this electrode and the anode. For some value of the accelerating voltage

achieved or for some particular configuration of the magnetic field produced by the solenoid, the electron anode current "switches" totally to the collector. As can be seen from Fig. 3a, the plasma potential equals or even exceeds the anode potential. Thus, results in a discharge operation regime where the plasma is positively charged.

When electrons are extracted in the configuration with a common cathode, the anode current is stabilized by the external circuit. Electrons can be drawn off to collector only if additional electrons appear in the discharge gap. This means that the ionization rate in the discharge has to increase. Since in the experiments the rise in ignition voltage associated with electron extraction is not balanced by a corresponding change in anode potential drop, we can suppose that in this case the increase in discharge voltage is also associated with a rise in cathode potential drop. This probably causes an increase in the electron susceptibility to ionization. Note that the increase in cathode potential drop is associated with nonneutralization of the charge particles in the plasma, which is maintained by the electric field of the accelerating electrode. Similar processes take place in the case where electrons are extracted with a common anode having a fully "switched" current, since in this case additional electrons have to be produced in the discharge gap.

In the extraction regime with a common cathode, an increase in electron current drawn by the collector is accompanied by a rise in the ion current density to the cathode, since the emission current is added to the initial discharge current. This increases the probability of the cathode spot formation and the transition to the arc regime.

FIGURE NOT AVAILABLE
AT TIME OF PUBLICATION

Fig. 3. Emission characteristics:
 $n_0 = 10^{12} \text{ cm}^{-3}$, $\varphi_0 = -20 \text{ V}$,
 $I_{k0} = 70 \text{ A}$

5. CONCLUSION

The study of a magnetron discharge in cylindrical electrodes geometry gave rise to the creation of charged particle sources capable operating in both pulsed and stationary regimes. Thus, for a pulse length of $20\ \mu\text{s}$, at an accelerating voltage of 200 kV, the beam current from the source reached 600 A. The average current density of the electrons emitted by the plasma was $75\ \text{A}/\text{cm}^2$. In the steady-state regime, at an accelerating voltage of 10 kV, the beam current from the source reached 2 A. By switching the polarity of the collector potential, one can also efficiently extract ions from the magnetron discharge plasma. Thus, at an accelerating voltage of 10 kV, the beam current was 100 mA.

7. REFERENCES

1. E.M. Oks, A.A. Chagin, and P.M. Selanin, "Generation of a hollow electron beam of microsecond duration in a source with a plasma cathode," *Zh. Tekh. Fiz.*, Vol. 59, No. 10, pp. 188-, 1989.
2. E.M. Oks, A.A. Chagin, and P.M. Selanin, "A plasma source of stationary annular electron and ion beams", *Prib. i Tekhn. Eksperim.*, No. 2, pp. 189-, 1992.

ELECTRON BEAM FOCUSING AND UNFOCUSING EXPERIMENTS

A.L.Filatov, Y.A. Kotov, V.A. Motovilov, V.A.Scotnikov

Institute of Electrophysics Russian Academy of Sciences
Ural Division
34, Komsomolskaya Str, 620219 Ekaterinburg, Russia

Abstract

The paper presents experiments aimed at focusing and unfocusing pulsed electron beams of energy from 0.2 to 1.5 MeV by 3 to 35 kA currents with a duration of up to 200 ns. A cathode construction has been found experimentally which in recording on an X-ray film permits obtaining a resolution of 5 lines per millimeter with a penetrability of up to 40 mm of lead. A pulsating voltage with an amplitude over 10 kV is shown to exist at the prepulse voltage across the cathode. An electric generator substitution circuit has been found that explains the occurrence of a voltage pulsation across the cathode. The presence of the aforementioned voltage leads to the high-current diode being filled with plasma before a major high-voltage pulse arises. Conditions have been found experimentally which enable electron beam focusing or unfocusing.

2.Introduction

Experiments have been carried aiming to improve the radiography of fast processes that occur in dense media. The penetrability range that we consider is equivalent to 0-60 mm of lead with a separation of 1 m from the X-radiation source, the duration of X-radiation from 10

to 100 ns, and the spatial resolution is less than 0.5 mm. The investigations have been carried out on a VIR-1.5 generator, which incorporates a circuit with an intermediate inductive energy storage and a current interrupter based on electrically exploding wires (EEW) [1, 2] and on a generator with a semiconductor opening switch [3]. The generator's current being below the Alfvén current $I_A = 17\beta\gamma$, electron beam focusing is difficult to implement. It is the goal of the present paper to resolve this contradiction.

3. Generator substitution circuit

The fact that the prepulse voltage across the cathode has a strong effect on further electron beam propagation has been noted by many authors. As an example, we can make reference to the monograph [4], which analyzes a considerable number of publications. Therefore, special attention has been given to determining the form of the prepulse voltage. The difficulty resides in the fact that the voltages and currents cannot be measured directly in many parts of the installation. Apart from this, the constituent capacitances and inductances are not known. For this reason, the voltage values sought can be obtained only with the aid of calculations, from an analysis of the generator substitution circuit (fig. 1). The circuit has been obtained as a result of analyzing dozens of voltage, current, and current-derivative oscillograms for different generator components in different operation modes of the generator.

Using the simplex method, we have obtained numerical values of the components asterisked in the diagram. The values of the rest of the components have been evaluated from geometric dimensions. The calculated oscillograms give a fairly good fit to the measured

counterparts. The computational oscillogram for the voltage across the cathode prior to appearance of a high voltage pulse is presented in Fig 2.

As can be seen from the foregoing, a negative prepulse pulsating voltage with an oscillation amplitude of over 10 kV exists across the cathode during the inductive storage pumping time ($1 \mu s$). The effect of this voltage on electron beam propagation is considered below.

4. Experimental

The types of the cathodes and the electron beam autographs are shown in Fig.3 . The detector is placed behind the 50 μm titanium foil. Therefore the dark spots are due to only the electronic diode current component. The quality of focusing was determined from electron beam autographs, from the deviation from the law of inverse squares of γ -radiation intensity on the axis of installation behind the target, and from the radiographs of test objects.

Cathode 1 was used to create electrons beams without focusing. In terms of electron beam focusing, the best result came from cathode 2. A many- factor experiment was staged in order to choose thegeometric dimensions of this cathodes, in which the sizes of the edge, the needle diameter, the needle setting depths, etc. were varied. A feature distinguishing this cathode from those used only [2] is that the end face edge is rounded and the central needle is 0.3 to 0.5 mm in diameter. This promises the conclusion that it the electron emission occurs chiefly from the cathode plasma rather than the cathode rim. In the literature, examples are known of using in the cathode dielectric insets, which permitted electron beam focusing

either owing to the suppression of prepulse voltage [4] or owing to the production of the plasma on the cathode from an additional voltage source. In our case, as will be shown below, the plasma forms when the dielectric suffers a breakdown between the needle and the cathode body.

5. Discussion

The electron beam focusing results obtained can be explained by formation of cathode plasma. The latter arises at the prepulse voltage owing to the emission from the central needle (Fig.3) This emission gives rise to a potential difference of about 10 kV between the needle and the cathode, a voltage difference that leads to a breakdown along the dielectric surface in vacuum. The breakdown is accompanied by plasma formation. Owing to high mobility the electrons leave the plasma. Therefore, the diode gap will be filled with positively charged cathode plasma before the main voltage pulse arrives, a fact which permits compensation of the space charge of high-energy electrons. Estimates show that a plasma with a density of 10^{13} cm^{-3} is needed to realize this regime.

6. Conclusion

We have shown that a prepulse pulsating voltage of an amplitude higher than 10 kV exists across the cathode. Appropriate cathode designs have been chosen, which permit focusing and unfocusing an electron beam.

7. References

1. Kotov Yu.A., Rodionov N.E., Sergienko V.P., Sokovnin S.Yu. and Filatov A.L. *Pribory i Tekhnika Experimenta*, 1986, N2, p.138.
2. Filatov A.L., Kotov Yu.A., Mesyats G.A. et al. A $5 \cdot 10^7$ A/kg dose rate compact x-ray generator// *Laser and Particale Beams*, 1989. vol.7, part 4, p.755.
3. Kotov Yu.A., Mesyats G.A., Rukin S.N., Filatov A.L. and Lyubutin S.K. A novel nanosecond semiconductor opening switch for megavolt repetitive pulsed power technology: experiment and applications. 9th IEEE Pulsed Power Conf., June 21-23, 1993, Albuquerque, NM.
4. Генерация и фокусировка сильноточных релятивистских электронных пучков А.И.Рудаков, М.В.Бабыкин, А.В.Гордеев и др.; Под ред. А.И.Рудакова.- М. Энергоатомиздат, 1990. (Atomizdat, Moscow. 1990).

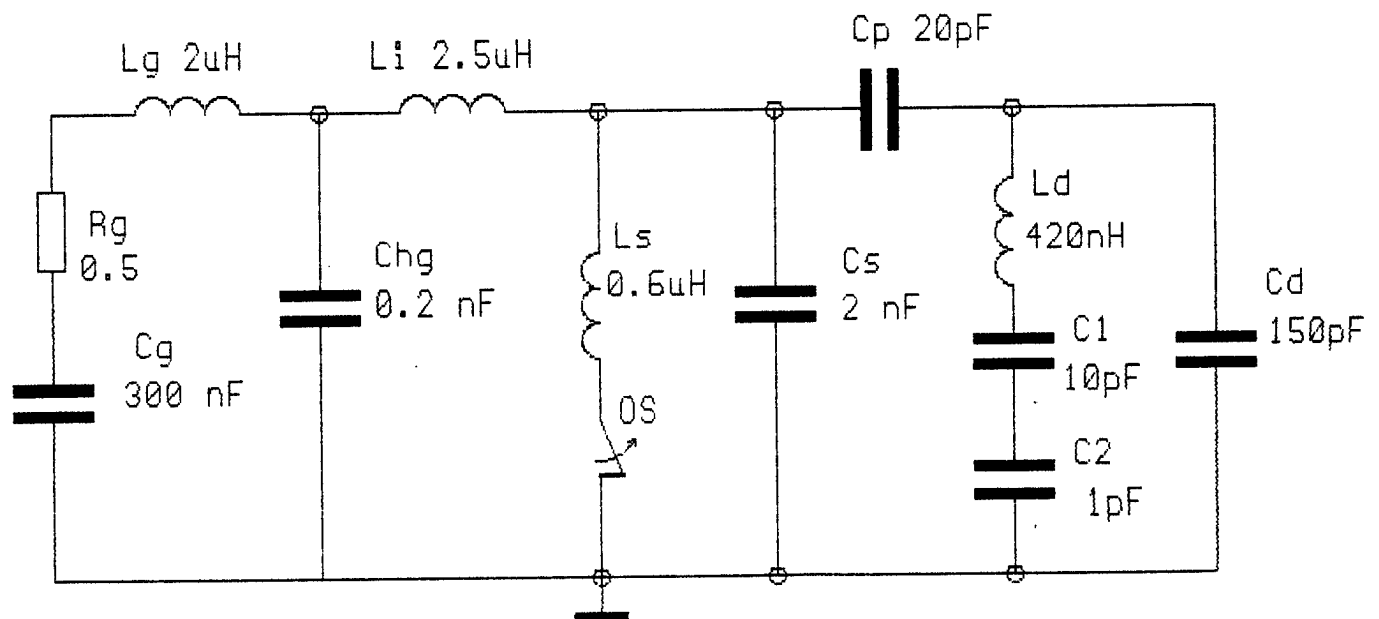


Fig.1. Generator substitution circuit

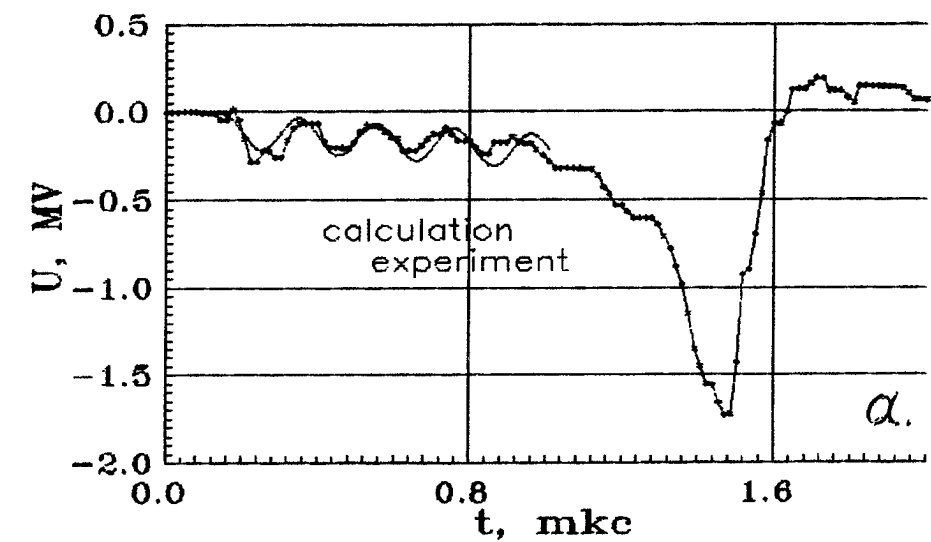


Fig.2. The oscillagram for the voltage across the opening switch - a, and the cathode prior to appearance of a high voltage pulse - b

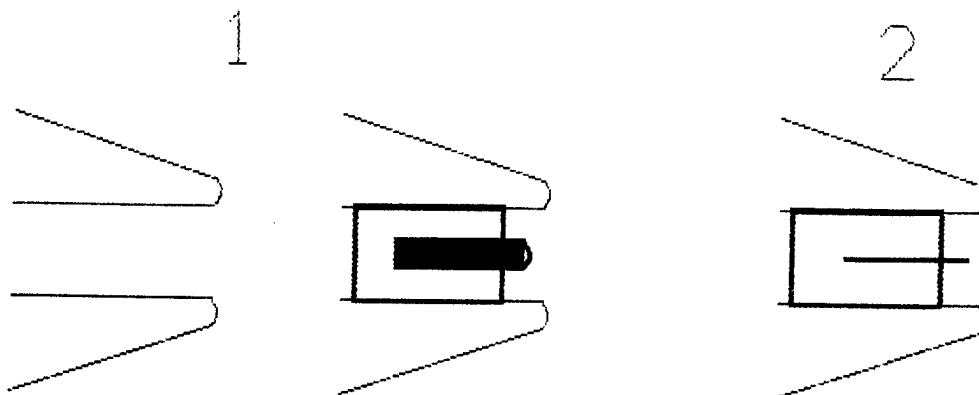
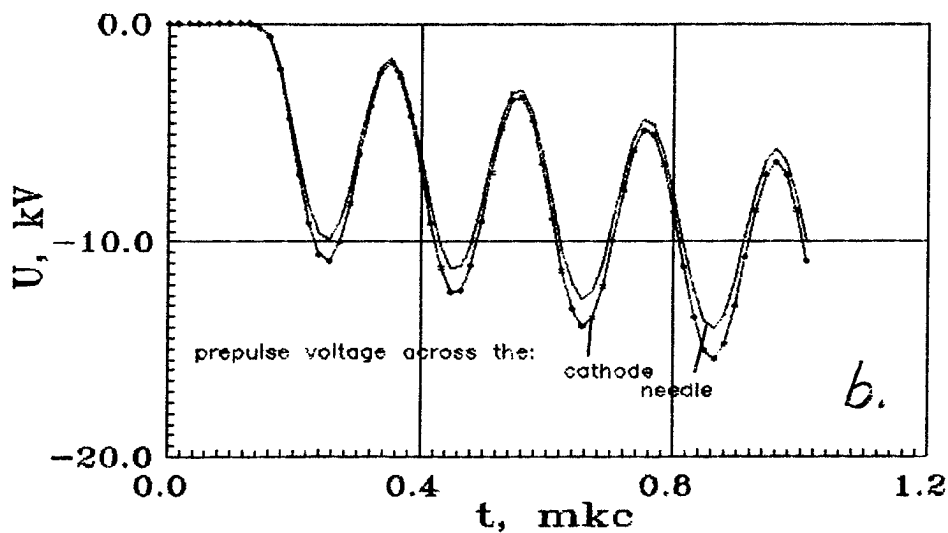


Fig.3. The types of the cathodes

Investigation of a ion-optical system of technological ion gas source

Dr. Nikolay V. Gavrilov*, Oleg M. Ivanov**, Dr. Alexander F. Stekolnikov**

* Institute of Electrophysics of Russian Academy of Sciences
34 Komsomolskaya str., Yekaterinburg 620219, Russia

** Byelorussian State University of Informatics and Radioelectronics
6 P.Brovka str., Minsk 220600, Byelorussia

EXPERIMENTAL INVESTIGATION

The formation of ion beams with a large current is provided by multiaperture ion-optical systems. Their characteristics are determined of properties of a single aperture of ion-optical system. A detailed experimental investigation of one-aperture ion-optical system was carried out¹ with the aim of determining of optimal conditions which provide the maximum current density j in the beam at a minimum angle of divergence ω . These requirements are produced to ion-optical systems of neutrals injectors for nuclear fusion setups.

The optimisation of ion-optical systems of technological ion sources for ion-implantation setups with forme beams of a big section² is aimed at creating of uniform beams at the distance $0.1-0.2\text{ m}$ from the ion-optical system. It is reached by increasing of a beam divergence in term of minimum particles loss on electrodes. The necessity of the determination of ion beam generation regimes for more heavy gases and smaller current density in comparison with the work¹ satisfying the mention above two conditions arises on elaborating of these sources. Due to it one does not possible to use results received¹.

A lot of factors which have influence on forming of a beam complicates the optimisation of ion-optical systems by experimental way makes expedient the use of numerical methods developed³. However, the comparing analyse of simulation and experiment is necessary to evalnate the degree of the reliability of results and to bring the algorithm of calculations what is the aim of this work.

Experiments were carried out with using of the impulse-periodic ion source on the base of the arc with the cathode spot screen². The one-aperture two-electrod ion-optical system with round holes of radius $r = 4 - 10\text{ mm}$, interelectrod distance $l = 10 - 20\text{ mm}$ and electrod thickness $d = 2\text{ mm}$ is used. The current density of argon ion emission changed in the limit $1 - 10\text{ mA/cm}^2$, the accelerating tension was $U = 10 - 40\text{ kV}$.

The full ion current on the collector with diameter 80 mm at the distance 200 mm from the ion-optical system and radial ion current density profiles which were received by the wire probe with a diameter 1 mm . The probe shifted radioly at the collector plane at the slit with the width 2 mm . Profiles $J(r)$ for one-aperture ion-optical system with $r = 4\text{ mm}$ and $l = 13\text{ mm}$ received for different U when $j = 5\text{ mA/cm}^2$ (a), and different j when $U = 40\text{ kV}$ (b) are presented in Fig.1.

NUMERICAL SIMULATION

Numerical simulation of the process of ion beam formation in ion-optical systems was based on generalized mathematical model which reduced to following:

$$j|_{f_\tau} = en_i \left(0.61 \sqrt{kT_e/M} - ds/dt \right) \bar{n},$$

$$dV/dt = -e/M \nabla \phi,$$

$$\nabla^2 \phi = -\rho/\epsilon_0,$$

$$\phi|_{f_\tau} = \phi_p,$$

$$ds/dt = (\epsilon_0 / (M n_i))^{1/2} \partial \phi / \partial \bar{n} |_{f_\tau} - (2 n_i k T_e / \epsilon_0)^{1/2},$$

$$\phi|_{f_1} = \phi_0^i,$$

$$\partial \phi / \partial \bar{n}_1 |_{f_2} = 0,$$

where j - ion current density, n_i - ion density, T_e - plasma electron temperature, e, M - ion charge and mass, ϕ - electric field potential, ρ - beam space-charged density, f_τ - plasma-ion beam boundary, \bar{n} - normal towards f_τ , f_1 - electrode boundary, f_2 - axis of beam symmetry, s - displacement of the plasma boundary from the initial position, ϕ_p - plasma potential, ϕ_0^i - potential of i -th electrode, \bar{n}_1 - normal towards f_2 .

Mathematical modeling of the charged-particles dynamics was done on a space grid 100×50 by large-particles method on the base of "Cloud-in-Cell" model⁴. The classical large-particles method was developed for this case taking into account a number of peculiarities in a large-particles motion near the plasma-ion beam boundary.

The algorithm of the numerical solution of the task consisted in setting the geometry of the calculation region, the electrodes potentials, beam current, large-particles parameters and the initial position of the plasma boundary; solving Laplace equation for the electric field potential and calculating the strength of the electric field; inletting a group of large particles with the ion-sonic velocity from the plasma boundary into the calculation region; solving the set of the equations of the large-particles motion; determining the grid density of the space charge and solving Poisson equation with the set boundary; defining the new position of the plasma-beam boundary according to Stefan condition and passing to the injection of the large particles and repeating all the calculations. If the displacements of the space-charge density cease to change within the set accuracy calculations are stopped and received results are taken as a task solution.

In order to calculate the output characteristics of the beam from the plasma boundary surface probe particles were injected and the equation of motion for them was solved throughout the whole region within the precalculated self-consistent field.

Results of numerical calculation of current density profiles in collector plane are presented in Fig. 2a and 2b correspondingly.

THE COMPARISON OF EXPERIMENTAL AND THEORETICAL DATA

The comparison of curves on Fig. 1 and Fig. 2 testifies about a good conformity of the theory to the experiment. Such behaviour of curves is explained that there is a characteristic beam perveance $P = j/U^{3/2} \approx 5 \times 10^{-10} \text{ A}/(\text{cm}^2 \text{ V}^{3/2})$ for this geometry when ω is minimal. It was shown⁵ that the increase r for $l = \text{const}$ leads to decreasing ω . However, as one can see from Fig. 1 and 2 the beam profile width in the ion-optical system with $r = 4 \text{ mm}$ provides the formation of uniform beam of a big section. This allows one to use large-cell ion-optical systems which are simple in the manufacture and the efficiency of using of mathematical simulation for a optimisation of such ion-optical systems.

REFERENCES

1. J. R. Coupland, T. S. Green, D. P. Hammond, A. C. Riviere, Rev. Sci. Instrum., Vol. 44, No 9, pp. 1258-1270, 1973.
2. N. V. Gavrilov, Yu. E. Kreindel, O. A. Shubin, "Источник мощных электронных и ионных пучков импульсно-периодического действия", ПТЭ, No 3, pp. 130-134, 1991. (In Russian)
3. A. F. Stekolnikov, "The boundary condition at the moving interface plasma-ion beam", Sov. Phys. Tech. Phys., Vol. 28, pp. 1369, 1983.
4. R. W. Hockney and J. W. Eastwood, *Computer Simulation Using Particles*, McGraw-Hill, New York, 1981.
5. A. F. Stekolnikov, O. M. Ivanov, "Численное моделирование динамики ионов в двухэлектродных ионно-оптических системах для формирования пучков большого сечения", Proc. 2-Soviet. Conf. "Модифика-

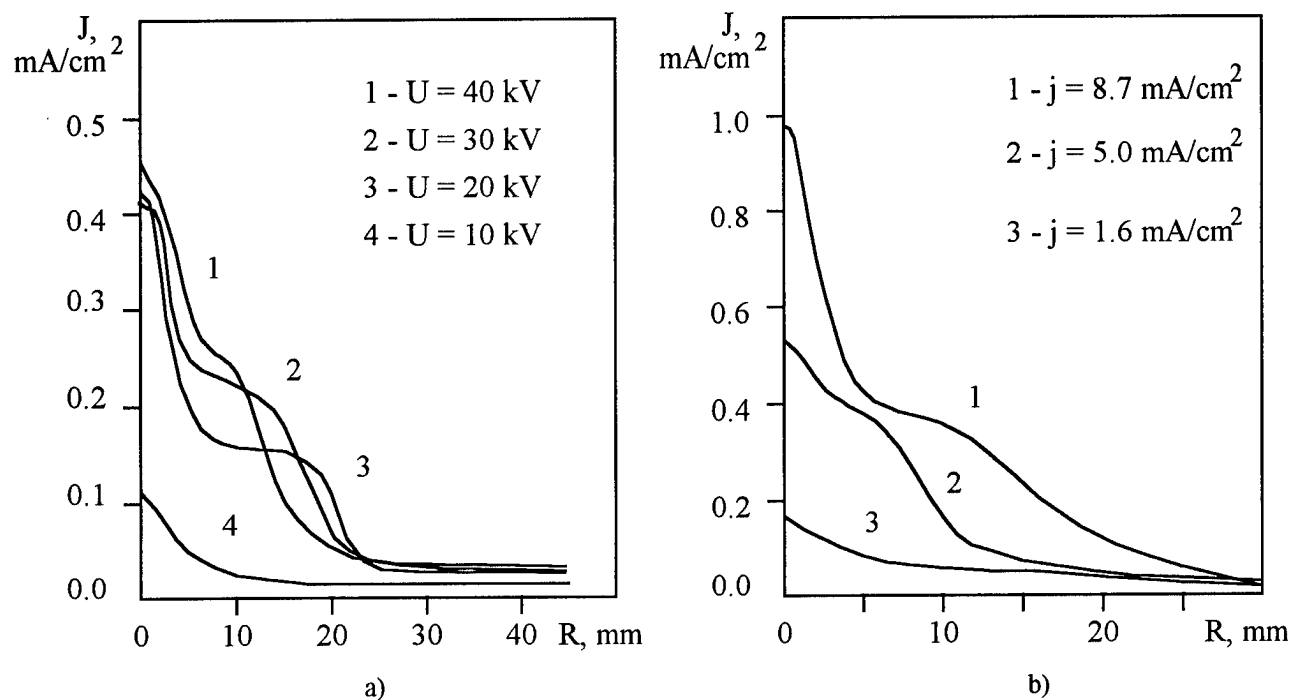


Fig. 1. Experimental curves of ion current density profiles on collector $l = 200$ mm.

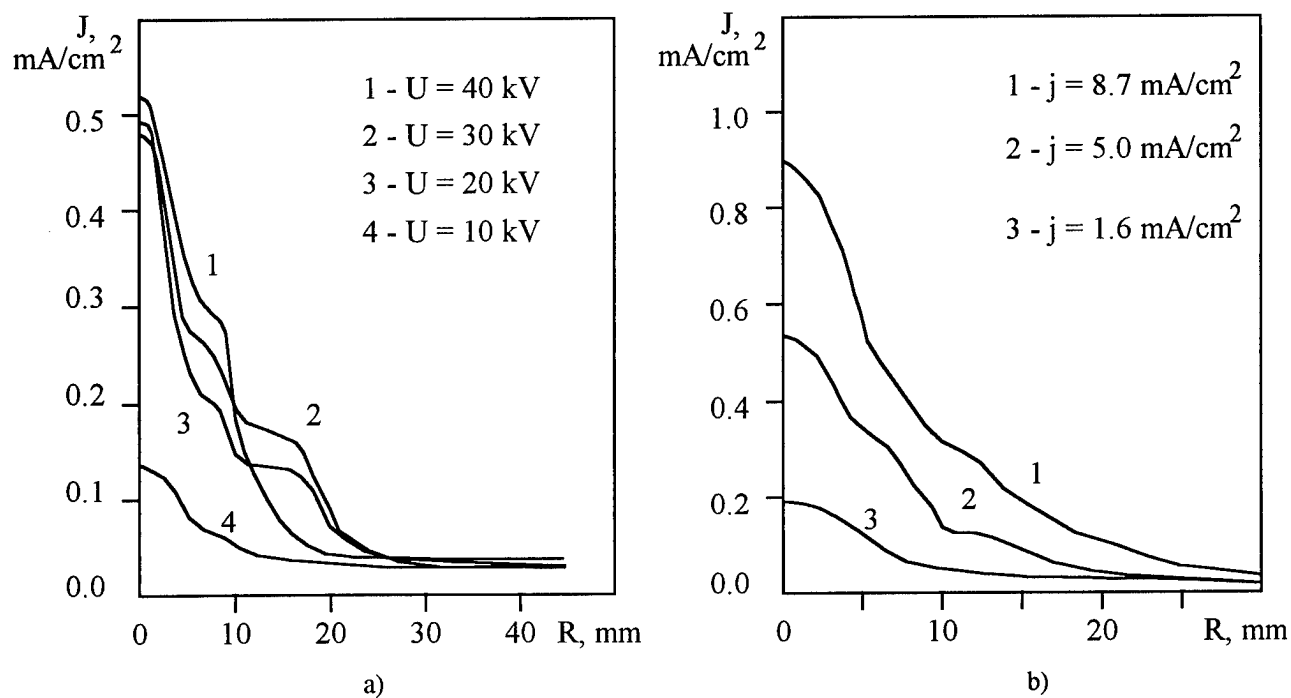


Fig. 2. Computed curves of ion current density profiles on collector $l = 200$ mm.

Intensive ion beams in the transverse magnetic field of an electromagnetic separator

A. Goncharov, N. Datsko, I. Soloshenko

Institute of Physics, Ukrainian Academy of Sciences, Kiev, Ukraine

Abstract

Based on the state-of-the-art knowledge, the processes of formation and transport of intensive ion beams in the transverse magnetic field of a commercial electromagnetic separator are analysed. For the first time, it is shown that suppressing the low-frequency noise oscillations in an arc discharge of an ion source allows for the formation of a highly stable ion beam with a minimum inner potential drop possible. At low pressures, the drop is determined by Coulomb's collisions between the beam particles and compensating electrons, the collisions being unremovable in principle.

1. INTRODUCTION

Intensive ion beams seem to have for the first time drawn close attention of physicists as far back as late 1940's, which was associated with necessity to produce fission material isotopes in abundance. The development of commercial calutrons required resolving quite a number of fundamental problems. First of all, high energy intensive ion beam sources had to be developed to provide for ion beams of different chemical elements with currents of the order of amperes and for the formation and transport of such beams in strong magnetic fields for distances of several metres. Stationary ion sources using the arc discharge in a magnetic field^{1,2}, developed for this purpose, allowed for the generation of ion beams of different chemical elements with total currents up to 1 A, which helped tackling problems the industry was faced with. There is a simple and effective way of intense ion beam transport within a separator, involving the accumulation of electrons compensating a positive space charge available, the electrons being produced by the knockout ionization of the residual ambient gas with fast particles of a moving beam. The very first test uses of calutrons revealed the disadvantages inherent in the then employed ion sources producing beams with a distinct (some 2 to 6 percent) modulation of the extracted currents, and disclosed a fundamental importance of the process of compensating the space charge of separated beams for the end quality of isotopes and the production of a particular device. An important role for the understanding of the mechanism of compensating the space charge of an ion beam in actual separator environments has been played by paper³, where it was shown that, provided $j_c \sigma_e n_a V_b \leq \omega j_v$ (n_a is the concentration of neutral atoms, σ_e is the cross-section for the production of electrons with ions of velocity V_b , j_c and j_v are the constant and variable components of the beam current density in a given elementary volume, respectively), the beam space charge will experience dynamic de compensation at frequency ω . Later in papers⁴, mechanisms were suggested causing the dynamic de compensation of the space charge of ion beams in separators. After the papers had been published, a great number of dedicated experiments were carried out in the course of multi-year understandings on electromagnetic isotope separation and a good deal of experimental data were obtained, which required developing new physical approaches and ideas. In the present paper, some new experimental results obtained with a commercial device for ion separation are reviewed on the basis of the state-of-the-art understanding of transport properties of the ion-beam plasma.

2. EXPERIMENTAL SETUP AND MEASUREMENT TECHNIQUES

The experimental studies with intensive ion beams were carried out using the chambers of large commercial separators. A typical chamber is a rectangular parallelepiped of dimensions 400cm×150cm×40cm. The side walls (400cm × 150cm) of the chamber constitute also magnetic poles. The magnetic field strength in the operating gap is $H \approx 3 \dots 6$ kOe. The bottom wall (400cm × 40cm) of the chamber has holes drilled to host ion sources and isotope collectors. The chamber is evacuated down to approximately $(1 \dots 3) \times 10^{-5}$ Torr. For the experiments, we have used an ion source¹ operating in the direct arc discharge mode subject to a strong magnetic field. The major source parts are as follows: an indirectly heated tungsten cathode, a chamber serving as anode, a crucible where a working substance is fed

to, and a vapour distributor. Such a source allows for extracting across the magnetic field strip ion beams of a total current I_{Σ} up to hundreds of milliamperes via slit $20 \text{ cm} \times 0,4 \text{ cm}$. The energy \mathcal{E}_b of the extracted single-charged ions is about 30 keV. The beam is formed with a three-electrode ion optical system including an intermediate electrode negatively biased at $U_i \leq -25 \text{ kV}$ with respect to the grounded one located at an extreme position. The negative potential prevents electrons from reaching a positive tip of the source set at a potential of 30 kV and provides for an increase of the electric field in the beam extraction space. Ion beams in commercial separators are fairly long, an average isotope separated beam length L being approximately 280 cm. The maximum initial current density amounts to $j_0 \approx 75 \text{ mA/cm}^2$ in experiments. Dynamic and stationary characteristics of the ion-beam plasma within the separator were measured using a diagnostic unit movable along the beam. The unit enabled the beam plasma to be subdivided into ten elementary beamlets and provided for the simultaneous measurement of the linear constant (j_c) and variable (j_v) current densities of both the beamlets and compensating electrons. The maximum space charge potential ϕ of the beamlets could be measured in parallel. To investigate particular regions of the beam, different aperture diaphragms and analysing azimuthally adjustable probes were employed.

3. MEASUREMENT RESULTS AND DISCUSSION

While operated in a routine technological mode, isotope ion beams are modulated by low frequency noises of an ion source, which causes a dynamic de compensation of a beam within the chamber of a separator. One may claim, based on numerous measurements $j_c(x)$, $j_v(x)$ and $\phi(x)$ established in papers⁴, x being the direction crosswise to the magnetic field, is only observed for relatively low total currents ranged as $I_{\Sigma} \leq 150 \text{ mA}$. In the domain of average currents $I_{\Sigma} \sim 150 \dots 250 \text{ mA}$, which is optimal for a commercially applied

separation, there is a distinct tendency toward the formation of a rectangular, or flat top, distribution for $j_c(x)$ and shifting $j_v(x)$ peaks into the peripheral region of $j_c(x)$ maximum gradients. This is accompanied by the failure of an interlink between the amplitude values of the variable current density and the extent of the beam de compensation (i.e. drop of potential within the beam). The amplitude values for j_v increase with the total current and are shifted toward peripheral regions while the drop of potential, as shown by numerous measurements, peaks at medium currents. Also, it has been established that the oscillation amplitudes for the variable current density j_v at the starting and middle points of the beam are approximately equal to each other. This gives evidence that no increase of the beam dynamic de compensation for its low frequency modulation takes place. Fig.1 shows typical dependencies of j_c , variable electron current amplitude j_v^e and space charge potential ϕ

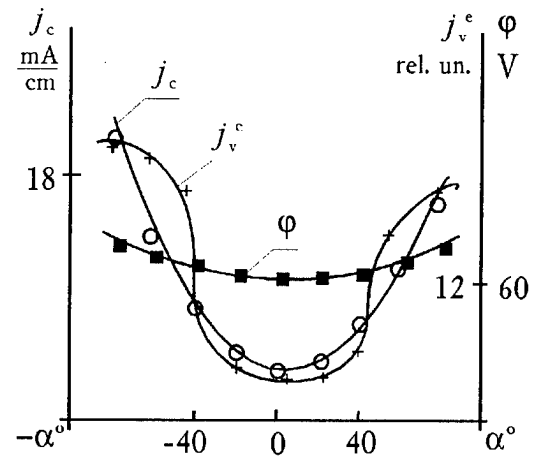


Fig. 1

vs the turning angle α of the azimuthally adjustable probe; α can be varied in arrange of $\pm 80^\circ$ about the beam central point. It can be seen that we have an essentially non-uniform system along the beam. For instance, in the middle of the beam trajectory its linear density goes down to a five times lower value. Similarly, there is a sharp decrease of the amplitude of the variable electron current. However, the space charge potential remains virtually constant, which reflects the availability of equipotential lines along the beam trajectory. One

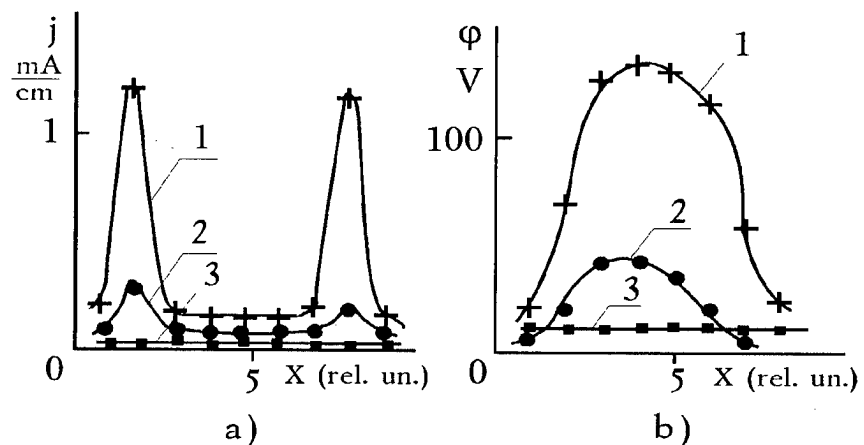


Fig. 2

of the authors (N.I.Datsko) has proposed and developed an efficacious technique of suppressing low frequency noises in arc discharges ignited in the vapour ambients of uncondensable materials which could be represented by the salts of quite a number of metals, e.g. under normal conditions, TiCl_4 is a gaseous entity. The above technique is associated with the insertion into the arc discharge of light element vapours, such as lithium vapour, which allows for the stabilization of the plasma collisionless flute instability and for a major suppression of pulsations in an extracted ion beam at low pressures inside the discharge chamber of an ion source. Experiments have been carried out to extract titanium ions from the plasma of a stabilized binary arc in TiCl_4+Li environments. Fig.2(a,b) shows measured data for a middle portion of the beam, describing the transverse distribution of amplitude $j_v(x)$ and of potential ϕ . It is clearly

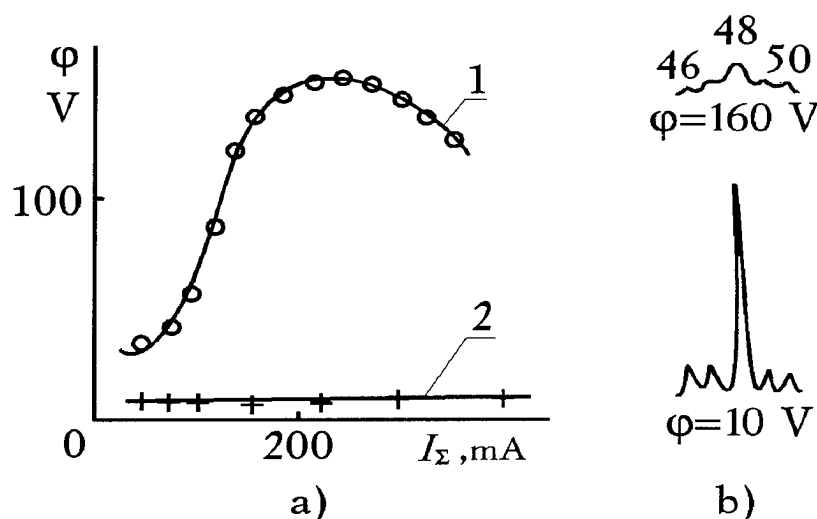


Fig.3

seen that incremental adding Li vapour into the arc discharge, curve 1 standing for a Li free case, suppresses j_v oscillations, makes potential ϕ 's maxim disappear, and lowers its value to a level of $\phi \leq 10 \text{ V}$ which is regarded as a record for commercial separators. It is to be pointed out that, in parallel, the residual gas pressure inside the drift chamber is maintained at a low enough level of $\sim 1.5 \times 10^{-5} \text{ Torr}$. It follows from Fig.3(a) that the degree of ion beam compensation inside the separator chamber remains fairly high within a wide variation range of the total current for a Ti^+ ion beam extracted from the binary plasma of an arc discharge. For the sake of comparison Fig.3(a) also shows a corresponding curve $\phi(I_\Sigma)$ revealing typical peaks at medium currents, obtained in the absence of Li vapour inside the source. Fig.3(b) is drawn to provide for a clear demonstration of the dynamic de compensation effects upon the quality of separation. For that purpose, the figure shows mass spectra of a Ti^+ beam on the case by case basis as established by Fig.3(a).

4. STEADY STATES AND STABILITY.

Peculiar features of the magnetic focusing in a separator determine a complicated ion beam configuration and control its transformation in the course of transport of the beam transverse profile. Based purely on particular geometrical reasoning for the first half of the beam path, one can evaluate the behaviour of the beam current density vs the longitudinal co-ordinate $Z \uparrow \uparrow V_b$ and one can be convinced that after the beam has been only transported at a distance of $Z \approx 14 S_0 / 25 \approx 5 \text{ cm}$ ($S_0 \approx 8 \text{ cm}^2$), its density becomes two times lower as compared the initial one. The first quarter of the beam path (i.e. $Z \leq 70 \text{ cm}$) deals with a sharp decrease of the beam density, which is followed by a rise within the second quarter ($Z > 70 \text{ cm}$).

Electrons are only produced in the course of ionization with the beam, their average lifetime within the beam being $\tau_c = 1/n_a \sigma_e V_b$ at low pressures. The presence of a quasi stationary space electric field E developing due to dynamic de compensation inevitably results in the removal of electrons from the area of their production at a velocity of $V_d \sim cE/H$. As the beam ends are cut off by outer potentials, the drift of electrons can, in principle, be closed within the beam volume. An average drift time is $\tau_d \sim 2L/V_b$. In the course of the beam transport, E is subject to substantial variations from hundreds to several V/cm, i.e. by approximately two orders of magnitude. Taking for estimate purposes $E \sim 50 \text{ V/cm}$, one could get convinced that τ_c and τ_d prove comparable under typical conditions. This means the electron drift along equipotential surfaces should substantially affect the stationary states of the ion beam plasma within a separator, which comes to explain the experimental data of Fig.1 and the absence of enhancement of dynamic de compensation along the

beam. In low-noise E -fields are essentially suppressed and electron drift becomes of no importance. Now, let us assume that an extreme value of a maintained static potential drop within the beam is governed by the following expression⁵ accounting for Coulomb's losses of an ion beam to heat up electrons:

$$\Delta\varphi \cong e\sqrt{3} \cdot l \cdot \sqrt{\frac{M_b}{m_e}} \cdot \sqrt{\frac{e\varphi_i}{\varepsilon_b}} \cdot \sqrt{\frac{n_b}{n_a\sigma_e}} \quad (1)$$

where l is Coulomb's logarithm of about 10, and φ_i is the ionization potential. Substituting values $n_b \leq 2 \times 10^9 \text{ cm}^{-3}$, $\varphi_i \approx 10 \text{ V}$, $\sigma_e \approx 5 \times 10^{-16} \text{ cm}^2$, which are typical for a medium part of the beam, into (1), we obtain $\Delta\varphi \approx 14 \div 15 \text{ V}$. The last figure conforms fairly well with the experimental one.

Intensive ion beam transport in a transverse H -field of a separator may well be seriously affected with the collective processes. This is unambiguously pointed to by the fact that the space potential within the beam goes up with the residual gas pressure inside the chamber of a separator. A theoretical consideration of potential collective phenomena in the ion-beam plasma of an electromagnetic separator has shown that, both for the initial part of the beam path, where the concentration of charged particles is fairly high ($\sim 10^{10} \text{ cm}^{-3}$) but the system itself is very non uniform, and for a long and quite uniform medium part with a particle concentration of about 10^9 cm^{-3} , the highest space growth rates are with the ion-electron instability can cause the emergence of not only variable fields in the beam but also of constant ones, which is indirectly supported by an increased removal of electrons from the beam along the magnetic field at the initial and end parts of its path (see Fig.1). Apart from an additional de compensation ($\varphi \approx 30 \text{ V}$), the above instability can result in a considerable broadening of the energy spectrum of an ion beam ($\Delta\varepsilon \geq 400 \text{ eV}$).

5. CONCLUSIONS

For the first time, it has been experimentally shown that suppressing the low-frequency oscillations of an arc discharge plasma by introducing easily ionized light element additives into an ion source provides for an adequate transport of a highly stable intensive ion beam with a minimum potential drop possible inside the chamber of an electromagnetic separator. Under low pressure conditions, when the ion-electron instability is of no importance because of a low growth rate and reduced space non uniformity of the beam, its inner potential is determined by Coulomb's collisions between the beam fast particles and compensating electrons, the collisions being in no way removable ones.

6. REFERENCES

1. P.M. Morozov, B.N. Makov, M.S. Ioffe et al, "An ion source for the separation of stable isotopes," Proc. Second Int. Conf., Vol. 4, pp. 111-116, United Nations, Geneva, 1959.
2. J.H. Freeman, "A new ion source for electromagnetic isotope separators," Nucl. Inst.&Methods, Vol. 22, N2, pp. 306-316, 1963.
3. L.P. Smith, W.E. Parkins, A.T. Forrester, "On the Separation of Isotopes in Quantity by Electromagnetic Means," Phys. Rev., Vol. 72, pp. 989-1002, 1947.
4. M.V. Nezlin, "Of mechanism oscillations of the space charge in quasicompensated ion beams," Zh. Tekhn. Fiz., Vol. 30, pp. 168-177, 1960.
5. M.D. Gabovich, "Ion-beam plasma and transport compensated intensive ion beams," Uspehi Fiz. Nauk, Vol. 121, N2, pp. 259-282, 1977.

Formation of an electron beam in its squeezed state

A.M.Ignatov,V.P.Tarakanov

General Physics Institute, Moscow, Russia

Abstract

The results of the computer simulations of electron beam emission and propagation in various spatially inhomogeneous systems are presented. It is shown that with the appropriate choice of the geometrical parameters the beam may be created in its squeezed state.

It is well-known that an electron beam propagating through a vacuum tube may be in one of two possible states. The normal one, observed in most experiments is characterized by the lower density and, correspondingly, higher velocity. Carrying the same current, another state is more dense and usually is thought of as unstable.

Our previous studies ¹ demonstrated that an electron beam injected into an inhomogeneous drift tube *e.g.*, of the shape depicted in Fig.1, under certain conditions may be squeezed by the additional electric field pressure produced by the outer wall step.

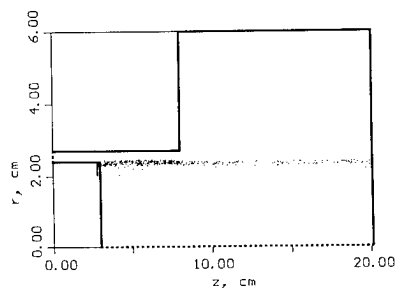


Figure 1.

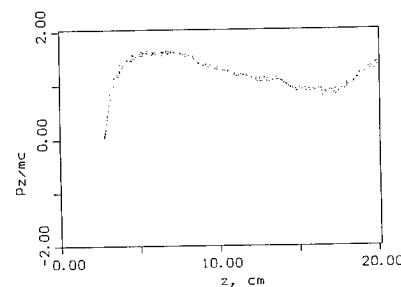


Figure 2.

However, in many experimental devices the magnetically insulated diode (MID) is not separated from the drift tube (Fig.1) and we are no longer able to distinguish the acceleration and the drift areas. The main problem we discuss in the present report is how the MID influences the electron beam in its squeezed state.

The outcoming current of the MID, I_{MID} , is always less than the limiting current of the drift tube, I_{lim} ². This limitation is illustrated by the stress vs. current plot (Fig.3).

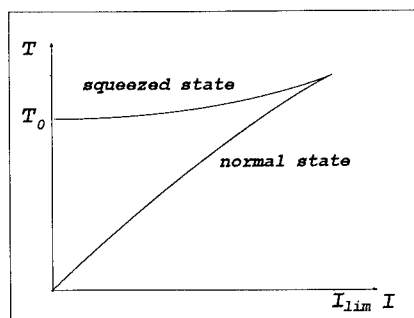


Figure 3.

$$T_0 = \frac{m^2 c^4}{4e^2 \ln(R/r_0)} (\gamma_0 - 1)^2,$$

where γ_0 stands for the diode voltage, R and r_0 is the outer and the inner radii of the MID, respectively. Since in the drift part of the device, far from the MID, the momentum flux carried by the beam in its squeezed state is in the interval

$$T_0 \leq T \leq T_{lim} = \frac{m^2 c^4}{4e^2 \ln(R/r_0)} (\gamma_0^{2/3} - 1)^2 (\gamma_0^{2/3} + 2),$$

the MID with a smooth outer wall cannot create the squeezed beam.

We have performed few computer runs by the axisymmetric version of the fully electromagnetic PIC code KARAT³ using various geometrical parameters and the same cathode potential, γ_0 .

First, we studied the electron beam emitted from the cathode and propagating through the device shown in Fig.1. If $I_{MID} < I_{lim_r}$, then there is no virtual cathode; the corresponding phase-space snapshot is shown in Fig.2.

If $I_{MID} > I_{lim_r}$, where I_{lim_r} is the limiting current of the wide tube, then there appears a vortex in the phase space (Fig.4). The emitted (I_{em}) and reflected (I_{ref}) currents were found to obey the relations: $|I_{em}| + |I_{ref}| = I_{MID}$, $I_{em} + I_{ref} = I_{lim_r}$. In this case, the single particle energy loss, e.g., due to the collisions, results in the formation of the squeezed state shown in Fig.5. This also may be caused by the emission of electromagnetic radiation, but it takes the beam much more time to relax to the squeezed state.

The upper part of this curve corresponds to the squeezed state of the electron beam. Besides the current, the MID produces some momentum flux, i.e., stress, that, in fact, was evaluated in². This stress, T_0 , marked in Fig.3, corresponding to the conducting bus with (in theory) zero velocity and infinite density is

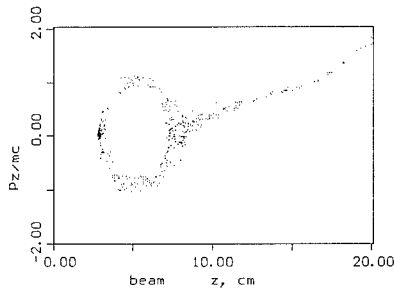


Figure 4.

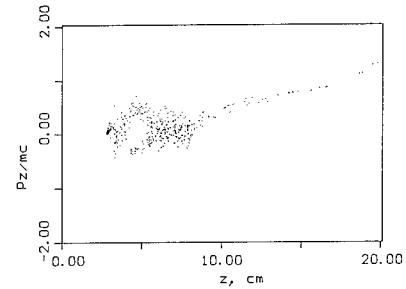


Figure 5.

In the device shown in Fig.6, the squeezed state appears in the middle tube (Fig.7) if $I_{MID} > (I_{lim_m} + I_{lim_r})/2$ even without any collisions and emission of e.m.waves.

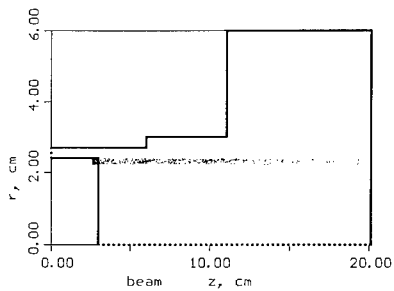


Figure 6.

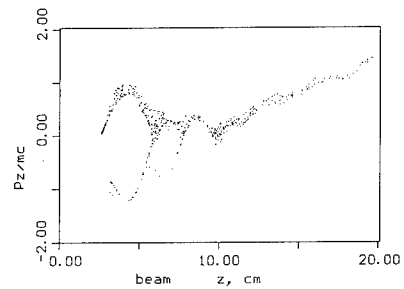


Figure 7.

References

1. Fedotov A.V., Ignatov A.M., Tarakanov V.P., *Proc. of BEAMS-92*, **2**, p.1373, (1992).
2. Fedosov A.I. et al., *Izvestija vuzov. Fizika*, n.10, p.134, (1977) (in Russian).
3. Tarakanov V.P., *User's Manual for Code KARAT*, BRA, Inc., V.A., USA, (1992).

Physics of electron emission from ferroelectric cathodes.

Gennady A. Mesyats

The Electrophysics Institute of the Russian Academy of Sciences,
Ural Division, 620219, Ekaterinburg, Russia.

1. INTRODUCTION

In the recent years a number of publications on the electron emission from ferroelectric cathodes have appeared. The most recent reviews are those by Schachter et al.¹ and by Gundel.² Ferroelectrics are ceramics containing the compounds PbZrO_3 , La_2O_3 , and PbTiO_3 . These ceramics are designated PLZT by the initial letters symbolising the metals involved. A cathode of this type is simple in construction. This is a PLZT ceramic plate of several millimeters in thickness with a solid silver layer fused into the plate from one side (a trigger electrode, TE). From the other side the plate is covered with a large number of silver strips parallel each other (a grid). The silver layer thickness is $\approx 1 \mu\text{m}$ on both sides. The anode to which an acceleration voltage is applied is placed parallel to the grid. The grid is grounded. An up to 2 kV trigger pulse of duration $\approx 10^{-7}$ s is applied to the TE. In the cathode-anode vacuum gap of the diode an electron current appears which is a hundred or more times higher than the Child-Langmuir current and shows a pronounced threshold depending on the voltage applied to the ceramics. Early in the pulse the electron current increases almost linearly with time; An investigation into the current structure has shown that it consists of individual bursts that merge into a single flow.²

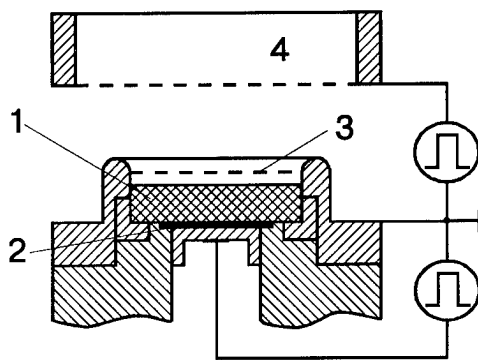


Fig. 1

Circuit diagram showing the connection of the electron source.

1 - dielectric, 2 - silver, 3 - grid, 4 - anode.

The PLZT ceramics possesses non-linear properties. The dependence of the charge on applied voltage has a hysteretic character.¹ The dielectric constant of the ceramics under normal conditions ranges³ within $(1-5) \times 10^{-3}$. The authors of the available publications do not propose a convincing theory of the emission observed, relating it, however, to special properties of the PLZT ceramics. It is even stated that the case in point is an essentially new type of electron emission that they call "ferroelectric electron emission".

Recall that electron emission from metal-dielectric cathodes has been known for a long time.⁴ Reviews of the relevant studies were made in Ref. 5,6, with electron currents up to 10^4 A achieved. The ferroelectric cathodes are absolutely identical in design to those described in Ref. 1 and 2 except that it was barium titanate (BaTiO_3 with $\epsilon \geq 10^3$) that was used as a ceramics component. (Below it will be referred to as BT ceramics.) The trigger electrode was made of fused silver, with the grid consisting of thin wires scratched (Fig. 1). The height of the T ceramic plate was several millimeters, and the trigger pulse had an amplitude up to 3 kV and duration of 100 ns. Thus, our BT cathode had the same design as the PLZT cathodes and the parameters close to the ones of the trigger circuit.

2. THE MECHANISM OF THE ELECTRON EMISSION FROM BT CATHODES

Studies of the BT cathodes⁴⁻⁷ have demonstrated that a fundamental part is played by the triple points (TP), metal-dielectric-vacuum, formed at the sites where the grid is in contact with the dielectric. At these sites a discharge over the dielectric surface occurs, whose current, when passing through the metal-dielectric contact, results in microexplosions of the microregions of the

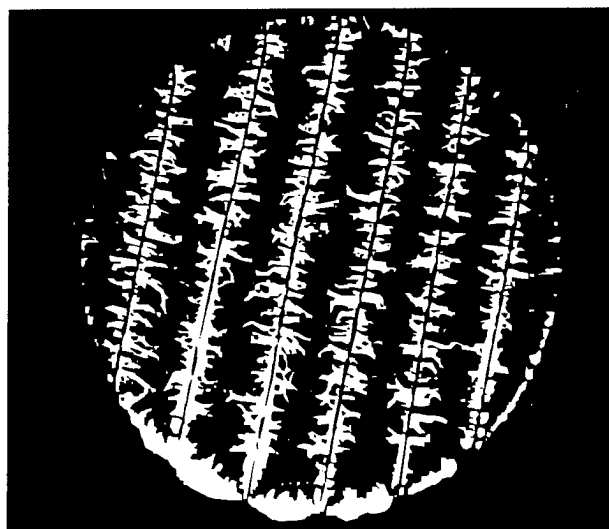


Fig. 2

The metal-dielectric cathode for electron production. Seen are the discharges on the surface of the dielectric.

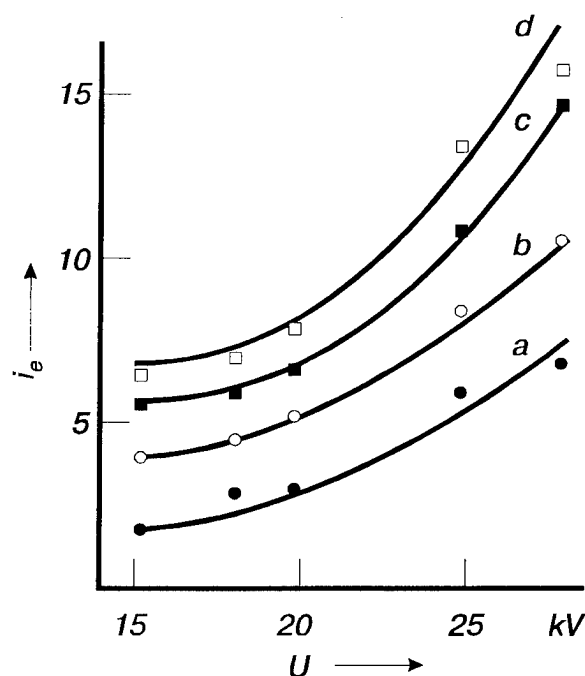


Fig. 3

Emission current from discharge plasma into vacuum as function of the voltage at the extractor, with point 3 being in positive polarity with respect to electrode 2. $U_0 = 1.8$ kV (a), 2.3 kV (b), 2.75 kV (c), and 3.1 kV (d).

The current in the region of a TP will be determined from the relationship $i = U_0 \partial C / \partial t$, where C is the dynamic capacitance created by the plasma and the TE. If $tv_d \ll \delta$, then we have $C = 4\epsilon_0 \epsilon v_d t$, where v_d is the velocity of expansion of the discharge plasma over the dielectric. Hence, the current is defined as $i = 4\epsilon_0 \epsilon A U_0^2$. Such a current will flow in the metal-

grid. This, in turn, causes well-studied explosive electron emission (EEE).⁶ These discharges over the surface of BTT ceramics are illustrated in Fig. 2. Used as a grid were thin copper wires tightly applied on the ceramics. The electron current from such a cathode was more than an order of magnitude higher than the Child-Langmuir current.⁵

To explore the part played by TPs a special experiment was carried out. On one side of a BT ceramic disk of thickness $\delta = 2$ mm a silver layer was applied, while against the other side a tungsten needle was retained. The needle served as a diode cathode, the anode being placed at a distance $d \sim 1$ cm from a cathode. Voltage pulses of amplitude $U_0 = 0.4$ to 4 kV and duration 2, 4, 20 and 50 ns were applied between the silver layer and the needle. The voltage, the current through the ceramics and the electron emission current from the needle tip were measured simultaneously and the discharge glow was photographed. A voltage pulse of amplitude U up to 30 kV and duration 25 ns was applied to the anode. A discharge near the needle occurred once the voltage exceeded some threshold value. Some time later an electron current appeared in the diode. The discharge glow had the shape of a sphere and expanded with a velocity $v_d = AU_0$, where $A = 5 \times 10^2$ and 2×10^3 cm/sV for positive and negative polarity of needle, respectively.

Figure 3 shows the electron current as a function of diode voltage U depending on the dielectric voltage U_0 . The increase in electron current is associated with a build-up of the emission area with speeding up the expansion of the discharge plasma.⁷

3. THE ELECTRON EMISSION FROM THE PLZT CATHODES

The above results furnish insight into the mechanism of the electron emission from PLZT cathodes.¹⁻³ The grid applied on the ceramics surface has numerous TPs on the silver strips. However, in order that these TPs be capable of initiating a discharge, there should be at least unit particles charged in the neighbourhood of TP. They may appear when the electric field E_m is high at the metal. With the uneven edges of the grid and the pores in the surface layer of the ceramics this field is defined as $E_m \approx U_0 \epsilon / \delta$ for $\delta \ll \epsilon \Delta$, where Δ is an effective gap at a metal-dielectric contact (Fig. 4). Since $U_0 / \delta \approx 10^4$ V/cm and $\epsilon > 10^3$, then we have $E_m > 10^7$ V/cm. Depending on the grid polarity this field causes an emission of positively or negatively charged particles which may initiate a surface discharge.

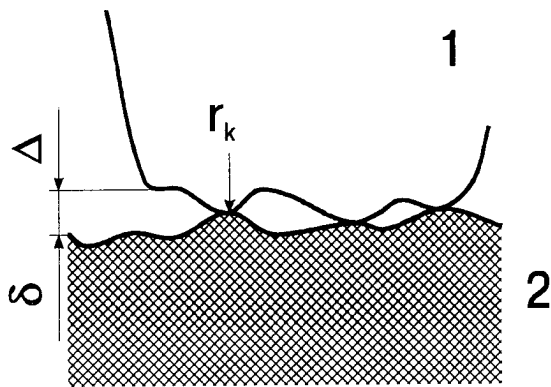


Fig. 4

Configuration of contact metal-dielectric.
1 - metal, 2 - dielectric.

dielectric contact through an area $S_k = \pi r_k^2$ (see Fig. 2). The current density through this contact will then be $j_k = 4\varepsilon_0 \varepsilon A U_0^2 / \pi r_k^2$. The metal in contact will explode in a time $t_e = \bar{h} / j_k^2$, where \bar{h} is a specific action which, to a first approximation, may be considered as a characteristic of the metal. The time t_e will then be found from the relationship:

$$t_e = \bar{h} \pi^2 r_k^4 / 16 \varepsilon_0 \varepsilon A^2 U_0^4 \quad (1)$$

To produce a uniform electron beam it is essentially that for a large number of TPs the time t_e be much shorter than the trigger pulse duration t_p , $t_e \ll t_p$.

$$r_k \ll \left(\frac{16 \varepsilon_0^2 \varepsilon^2 A^2 t_p U_0^4}{\pi^2 \bar{h}} \right)^{1/4} \quad (2)$$

For a silver contact we have $\bar{h} = 0.8 \times 10^9 \text{ A}^2 \text{cm}^4 \text{s}$. For $t_p = 10^{-7} \text{ s}$, $\varepsilon \approx 10^3$, $U_0 = 10^3 \text{ V}$, and $A = 5 \times 10^2 \text{ cm s}^{-1} \text{V}^{-1}$ we obtain from the relationship (2) $r_k \ll 2 \times 10^{-5} \text{ cm}$. This means that for the time t_p microexplosions of the metal will occur at all the triple points where the contact radius is less than 10^{-5} cm . From the explosion sites electrons will be emitted by EEE mechanism.

Reasoning from the above considerations we shall offer an explanation for some observations on PLZT cathodes.^{1,2} For instance, their high sensitivity to the voltage at the ceramics follows from Eq. (1), since the time to a microexplosion t_e is proportional U_0^{-4} . The short time current bursts are closely related to the mechanism of EEE.⁶ Once EEE has occurred, the cathode plasma starts propagating toward the anode with a velocity $v \approx 10^6 \text{ cm/s}$. For a plane electrode the electron current will be written as follows:⁶

$$I = a U^{3/2} s / (d - vt)^2 \quad (3)$$

where $a = 2.33 \times 10^{-6} \text{ AV}^{-3/2}$, U is the voltage across the diode, s - the cathode area and d - the cathode-anode separation. From Eq. (3) it follows that for $t \ll d/v$ the electron current will be given by

$$I \approx a U^{3/2} \frac{s}{d^2} \left(1 + \frac{2vt}{d} \right) \quad (4)$$

i.e. the current will increase linearly with time, which was just observed in experiment by Gundel.² Formally, Eq. (3) suggests that it is possible to produce an electron current considerably greater than the Child-Langmuir current $I_{ChL} = a U_0^{3/2} s / d^2$, and this was actually observed both by Schachter et al.¹ and by Gundel.² Moreover, this should be the case for both PLZT ceramics and BT ceramics. The diode may be preliminary filled with plasma so that the current would then flow in the plasma-filled diode.

The delay in the appearance of an electron current concerning the application of a voltage to the ceramics is, on the one hand, due to the delay in the appearance of EEE and, on the other hand, due to the fact that, according to the Eq. (3), the current increases as the cathode plasma propagates deeper in the cathode-anode gap. This is why the current is initially small and it is exactly this fact that is taken for a delay of the electron emission. Finally, Gundel² noted that as the temperature of the PLZT ceramics was elevated to 150°C , the charge of the electrons emitted by the cathode increases more than twice. Taken into account that the capacitance of the ceramics, and hence ε , increased almost three-fold,² we obtain that according to Eqs. (1) and (2) this causes an increase in both the number of microexplosions and the electron current from the cathode.

In conclusion it is worthy of note that the above estimates are of course rough. However, we believe that the concept of triple points and the explosive electron emission occurring at these sites seem to be highly promising for the explanation of the electron emission from PLZT ceramic cathodes. Furthermore, the emission properties attributed to PLZT ceramics are as well peculiar to the BT ceramics.^{4,7} This is quite evident that under certain conditions the electron emission will appear with other dielectrics used.

REFERENCES

1. Schachter L., Ivers J. D., Nation J. A. and Kerslick. Analysis of diode with a ferroelectric cathode. *J. Appl. Phys.* 73 (12), p.8097, 1993.
2. Gundel H. Electron emission by nanosecond switching in PLZT. *Integrated Ferroelectric*, v. 2, p.202, 1992.
3. Hench L. L., West J. K. *Principles of Electronic Ceramics*, John Wiley and Sons, 1991.
4. S. P. Bugaev, F. Ya. Zagulov, B. M. Kovalchuk and G. A. Mesyats, A pulsed source of great electron currents. - *Izv. Vyssh. Uchebn. Zaved. Fizika*, No 1, p.45, 1968.
5. G. A. Mesyats, Controllable electron sources. - In: *Cold cathodes*, Moscow: Sov. Radio, 1974, p.287.
6. G. A. Mesyats, Generation of high-power nanosecond pulses, Moscow: Sov. Radio, 1974.
7. S. P. Bugaev and G. A. Mesyats, Electron emission from the plasma of an uncompleted discharge over a dielectric in vacuum. - *Dokl. AN SSSR*, v. 196, p.324, 1971.

E-beam Behavior Accelerated by Short-time High-voltage Pulses.

Vladimir V. Osipov, Viktor M. Orlovsky,
Vladimir I. Solomonov.

Institute of Electrophysics, Ural Division, Russian Academy of Sciences,
34, Komsomolskaya str., Ekaterinburg, 620219, Russia.

The solution of the problem of a vacuum diodes development for a ribbon e-beams of nanosecond and subnanosecond time duration production meets some obstacles. They are defined both by electrotechnical problems and by difficulties arises from e-beam formation. This paper is devoted to investigation of main causes of a current amplitude limitations of the short-time e-beams.

A capacity C_n formed by extended cathode and a wall of vacuum diode (fig. 1) may be greater then equivalent capacity of high-voltage generator C_r during the short-time ribbon e-beam formation. This fact leads to decrease of high-voltage pulse amplitude due to charge of C_n . This effect appears as more as greater the ratio of C_n to C_r .

Moreover, this phenomenon makes one to doubt in opportunity to form ribbon e-beams of subnanosecond durations. Nevertheless, it is possible to avoid this problems if one performs the vacuum diode as a line with distributed parameters¹. In this case it is necessary to perform the following conditions:

$$t_f \leq t_o, \quad z_g \leq z_l, \quad (1)$$

where t_f - is pulse increase front, t_o - is time of double run of electric wave from cathode holder to the end of cathode, z_g - is wave resistance of generator, and z_l - is wave resistance of forming line.

The experiments to verify this approach was performed on e-beam accelerator. The latter was described in details in paper². Block-diagram of this accelerator is shown on fig.1. The forming line was used as accumulating element of the accelerator (C_r) and was formed by two cylinders with 200 mm and 150 mm diameters. The inside cylinder was of 400 mm length, the capacity of oil filled coaxial line was 150 pF. Wave resistance of the line was 10.2 Ohm. Blowing discharger filled by nitrogen at 10 atm. pressure was used as a switch P. Dimensions of case of vacuum diode (2) were 100x100x1000 mm, and dimensions of cathode holder (4) were 50x40x800 mm. Cathode (6) was designed in the form of two copper strips of 25 μ m thickness, 2 mm width, 10 mm height and 720 mm length and stuck on the dielectric substrate held in cathode holder (5) (substrate has not shown on fig.1). Wave resistance of the vacuum diode was 400 Ohm, the cathode-case (C_n) capacity was 130 pF. The charge voltage of the forming line rose up to 290 kV. When the conditions (1) were true the accelerator operated in the following way. When discharger P switched on, then the high-voltage pulse applied to cathode (6) from generator (1) via connector (3) in the input isolator (4). The pulse extended along the line formed by case of vacuum diode (2) and cathode's set up (5,6). The voltage occurred to be doubled when the pulse was reflected from the disconnected side of the line.

When the voltage rose up to breakdown in the gap between anode and cathode the current of accelerated electrons appeared in it and the last ones propagated through the foil (7) to the Faraday's cylinder.

High-voltage pulses with 1.1 ns rise time and 290 kV amplitude were applied to vacuum diode under conditions described above. The current of accelerated electrons with 7.1 kA amplitude and 4.7 ns time duration were obtained outside of the foil. Two types of experiments to register the change of the accelerator operation mode due to violation of conditions (1) were performed. In the first case high-voltage was applied to cathode via additional inductance extending the front rise time of the voltage pulse. The decrease of e-beam current more than in two times and t_f increase from 1.1 to 4.6 ns were shown. Nevertheless, the results explanation by the change of operation mode got rise the objections due to voltage decrease on the inductance.

Change of operation mode by shortening of emission length from 72 to 10 cm and cathode holder from 80 to 20 cm with the same characteristics of high-voltage pulse and number of emitting sharps was shown. In this case the current decreased from 7.1 to 2 kA. Indeed, in this case the run time along the line decreased and became significantly less than front of voltage increase. So diode lost the features of the line with distributed parameters and as a result the current of e-beam decreased. While existing theory predicted current of e-beam had to increase (at least not to decrease) due to decrease of C_n and increase of the voltage on the last one.

This approach permits to obtain not only ribbon subnanosecond e-beams but to diminish essentially vacuum diode overall dimensions which can be chosen by means cathode-case electric strength conditions. When the time duration of high-voltage pulse decreased from 3 ns to 0.3-0.5 ns the decrease of the accelerated electrons current was obtained in experiments to develop subnanosecond cathodoluminescent exited laser³. The subnanosecond e-beam was formed by the circuit adduced in paper⁴. 3 ns time duration and 200-300 kV amplitude high-voltage pulse was produced by the pulse generator of compact accelerator "RADAN-300"⁴. When the pulses were applied to vacuum diode 1 kA current amplitude and 3 ns time duration e-beam was obtained outside of the foil. The compressing line composed by sharpening and cutting off dischargers was installed between the vacuum diode and the forming line to form subnanosecond pulses. As a result the high-voltage pulses with the same amplitude and 0.3-0.5 ns time duration were applied to the accelerating gap.

The wave resistance of forming and transferring lines in the range of 40-100 Ohm not effected the energy transfer from forming line to e-beam and decrease of the interelectrode gap from 4.2 to 2.5 mm resulted only the slight increase of the energy was found. The cathode was built as a steel sharps located on the round with 6 mm diameter and 1 mm step. In this case 1 J was accumulated in the forming line and 1-2 mJ was transferred to e-beam. The energy of e-beam increased to 6-7 mJ and half height time duration increased from 0.3 to 0.5 ns when continuous plumbago electrode was installed. This fact may be related with specific activity of explosive emissive cathodes in subnanosecond pulse generation mode. Inasmuch as time formation of continuous plasma layer afterwards explosion of microsharp greater time formation of e-beam so the latter might consist of separate current filaments. Their quantity will correspond to quantity of exploded microsharps and current density would be controlled by rule " $3/2$ ".

The crystals CdS was stuck on anode aluminium foil as a mosaic with typical dimension not greater 0.5 mm to verify this suggestion. In the case of steel sharp cathode use the quantity of luminesced crystals increased from 4 to 9 when the length of vacuum gap was changed. Mentioned above suggestion was confirmed in our experiments with plumbago cathode. Separate luminescence could be registered when interelectrode gap was less 3.5 mm. Particularly when interelectrode gap $d \leq 1$ mm 1-2 of optionally not the same crystals began to luminesce.

Consider the mentioned above, let us estimate the current and the e-beam energy n-sharps emitter as⁴:

$$I = A \cdot U^{3/2} \cdot v \cdot t_n \cdot d^{-1} \cdot n \quad (2)$$

and e-beam energy as

$$W = I \cdot \varepsilon \cdot t_n, \quad (3)$$

where $A = 3.7 \cdot 10^{-5} \text{ A/V}^{-3/2}$, U - is potential between the electrodes of vacuum diode, $v = 2 \cdot 10^6 \text{ cm/s}$ - velocity of expanding anode plasma, ε - energy of single electron, t_n - pulse time duration. For our values $U = 2 \cdot 10^5 \text{ V}$, $\varepsilon = 1.2 \cdot 10^5 \text{ eV}$, $t_n = 3 \cdot 10^{-10} \text{ s}$, $d = 0.25 \text{ cm}$ and for steel cathode values $W = 2 \text{ mJ}$ and $I = 60 \text{ A}$ were obtained. The data obtained agrees with the experimental data quite well. As regards the plumbago cathode one can assume that quantity of emitting sharps on it's surface is greater in 2-3 times.

So this results indicate the need to use special procedures to form a good plasma surface to attain high accelerating voltage during subnanosecond e-beam formation.

References

1. V.M. Orlovsky, V.V. Osipov, A.G. Poter'ayev, V.G. Shpak. "Compact e-beam accelerator with vacuum diode in line with distributed parameters", Proc. VI All-Union Symp. High-current electronics. Tomsk, 1986, part II, pp. 103-105. (in Russian).
2. V.M. Karpov, Yu.G. Konev, V.V. Larin, V.M. Orlovsky, V.V. Osipov, M.M. Stain. "Components of pulse repetitive nanosecond e-beam sources", Sov. PTE 1987, #1, pp. 23-25.
3. G.A. Mesyats, V.V. Osipov, V.I. Solomonov, "Subnanosecond pulses of radiation generation", Sov. Pisma JTPH, 1991, v. 17, rel. 8, pp. 45-48.
4. V.M. Kovaltch'juk, G.A. Mesyats, V.G. Shpak, Development and application of intense ribbon beams", Novosibirsk, Nauka, pp. 179-181, (in Russian).

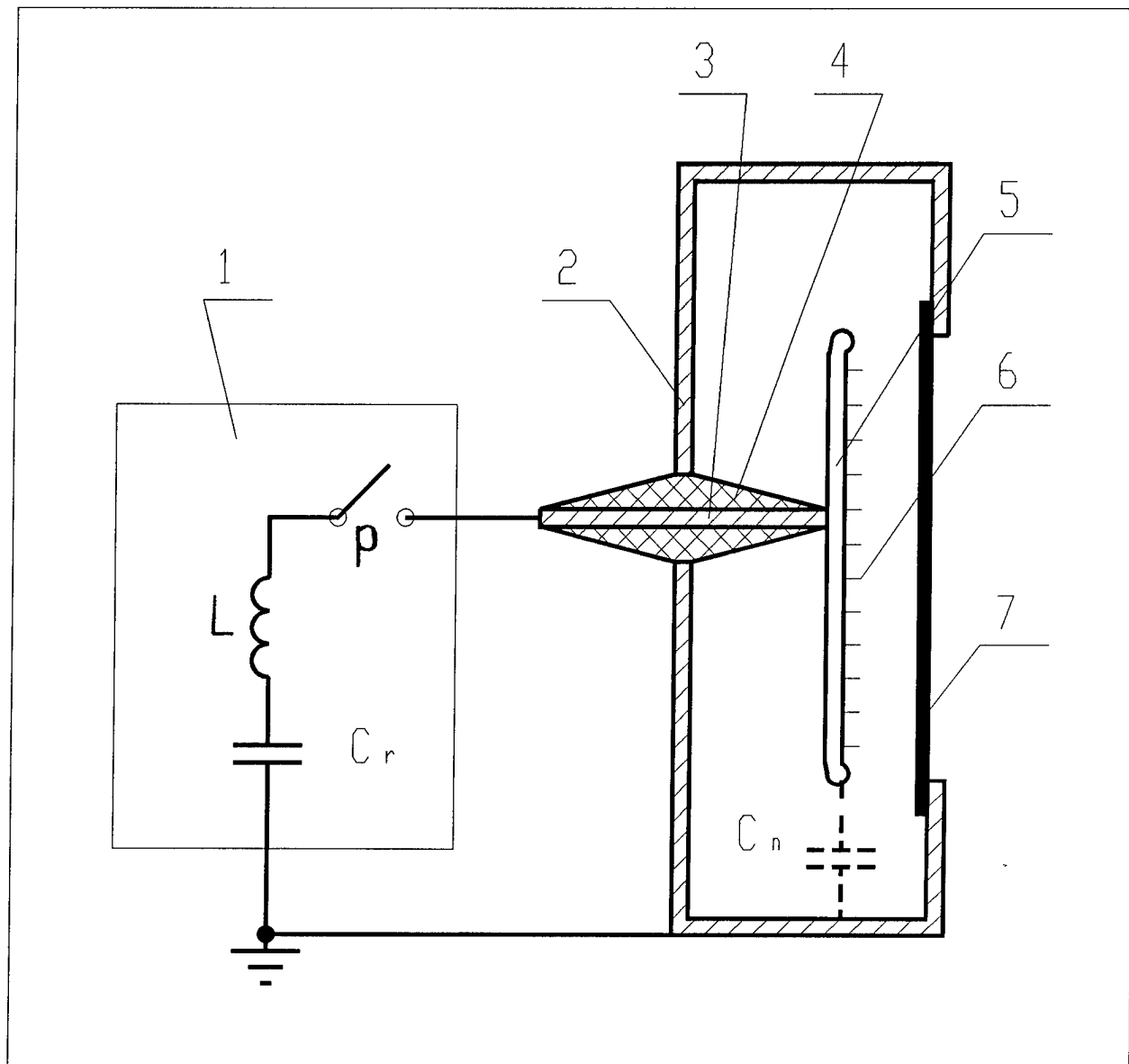


Fig. 1

Compact high-current ribbon e-beam diode

Valery G. Shpak, Michael I. Yalandin,
and Sergey A. Shunailov

Institute of Electrophysics,
Ural Division of the Russian Academy of Sciences
Ekaterinburg, 620219, Russia

ABSTRACT

High-current ribbon e-beam vacuum diode was designed to operate with RADAN 303 compact pulsed power source¹ for various laboratory research purposes and technological experiments. Maximum e-energy, 200 keV; peak e-beam current, 1.8 kA; beam cross section, $5 \times 110 \text{ mm}^2$; current pulse width, 4 ns; beam energy per pulse, 1.5 J; the average beam power (in air) is 40 W at replate of 25 pps. The parameters are given for the $40 \text{ }\mu\text{m}$ aluminum-beryllium foil window. The diode operates under a vacuum of 10^{-2} to 10^{-3} Torr. The metal-dielectric cathode and the foil life time exceeds more than 10^6 pulses. The pulsed power source permits one to control the diode voltage and change electron's energy. The possibility of varying the cathode length and anode-cathode gap of the vacuum diode is also present. Weight together with RADAN 303 is 31 kg.

1. INTRODUCTION

In some applications, such as gas laser pumping pulsed high current ribbon beams are demanded. The rise of irradiation area is also very important for pulsed radiation technology and surface sterilization. It can be achieved by combining a ribbon beam with conveyor where a treatment objects are placed.

The generation of a high current ribbon electron beams meets a range of difficulties. It is necessary to ensure:

- a smooth e-current distribution on the foil window,
- the sufficiently high impedance through all pulse duration,
- high energy efficiency of the supply source.

Using a compact pulsed power source one more difficulty takes place connected with the presence of a large own diode capacitance which frequently is compared with high voltage storage capacitance of such sources.

The design of easy in operation ribbon vacuum diode (Fig. 1) for RADAN 303 compact pulsed power source was the aim of our work.

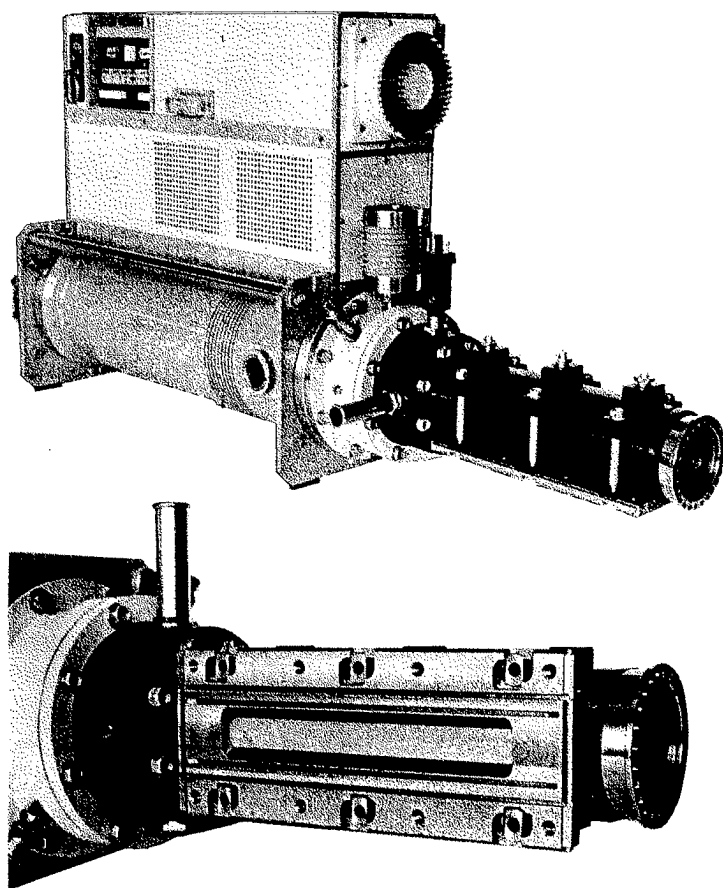


Fig. 1. High current ribbon vacuum diode with RADAN 303 compact pulsed power source.

2. RADAN 303 COMPACT MULTIPURPOSE PULSED POWER SOURCE

Compact RADAN-series high-current accelerators with a Tesla transformer have already demonstrated their large capabilities in the construction of diverse electrophysical apparatus, such as relativistic millimeter-band microwave oscillators, battery-supplied X-ray apparatus and gas lasers².

As with all RADAN systems, the backbone of this model is a fitted Tesla transformer with an open core made of steel. The total capacitance of the Blumlein forming lines is 170 pF. Principal RADAN 303 parameters are listed in Table 1. Smooth output voltage control is effected by varying the high pressure spark-gap electrode spacing without depressurizing the casing.

Table 1. SPECIFICATION OF RADAN 303 SOURCE

Output voltage with a 50 Ohm load	20 ÷ 200 kV
Forming line impedance	45 Ohm
Rise and fall time	<1 ns
Pulse width	4 ns
Maximum repetition rate:	25 pps
Maximum power consumption	250 W
Weight	27 kg
Power supply:	single phase mains 220 V, 50/60 Hz
Dimensions	405 x 190 x 635 mm ³

3. DESIGN OF THE RIBBON DIODE

In traditional T-construction ribbon diodes (Fig.2a.) anode-cathode capacitance is comparable to the capacitance of the compact RADAN 303 source. As a result the appreciable voltage losses occur and the energy efficiency of the supply source decreases. As we can not exclude this fact we try to use a running wave regime in diode and so don't charge the whole diode capacitance simultaneously. To do this the electrical length of the diode must be comparable to high voltage pulse width. Such liner diode (Fig.2b.) (L-diode) represents the part of a coaxial vacuum line with impedance equal to the impedance of the source. The cathode is disposed along the vacuum line. The high voltage pulse is reflected at the end of the line and redoubled.

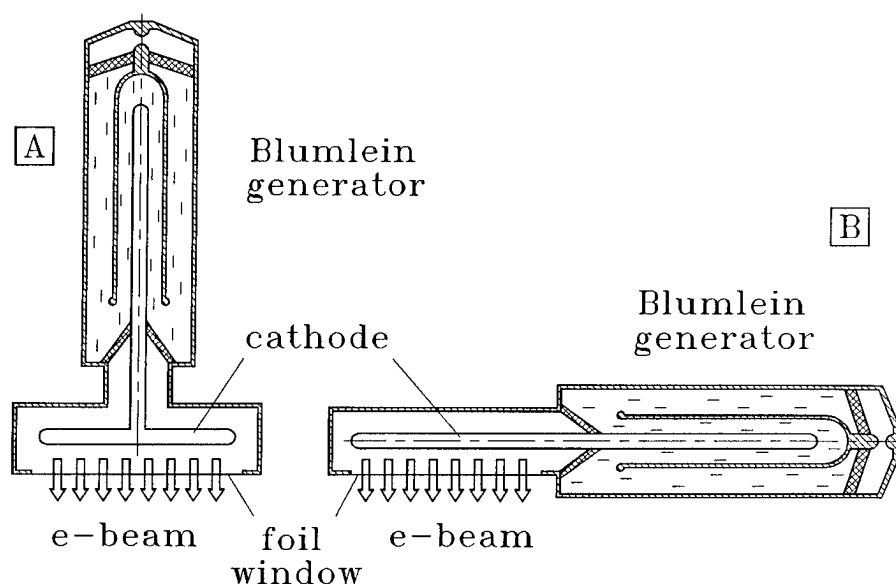


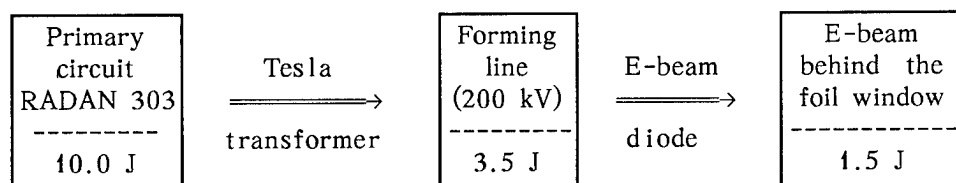
Fig.2. Different design of ribbon diodes.

To ensure a current density homogeneity on the foil is one of the main problems of any ribbon diodes. The appearance of spots with higher current density leads to local overheat and fast foil destruction. Metal points and blades as the cold cathodes have a limited life time because of sharp edges get blunted during operation. This fact increases the current density irregularity and parameters instability. We used the metal-dielectric cathode which work is founded on fire a plasma in the metal-dielectric contact in strong electric field. Such cathode represents a range of metal points pressed to dielectric plate. The wear of these points during operation does not change diode's characteristics because of a constant presence of the metal-dielectric contact. The installation of the dielectric plates at both edges of the cathode permits to form sharp borders of the beam on the foil and thus reduce the electron losses on inside walls of the diode. This construction makes it possible to design a diode window as a narrow slot and use the body of the diode in the capacity of radiator. Evenness of e-current density distribution along the foil is regulated by varying the points period and anode-cathode gap. Investigations carried out earlier³ show the parameters of such diodes don't depend on a dielectric constant of using dielectrics. Therefore thermal stable ceramic materials are chosen to increase the diode life time.

4. DIODE'S CHARACTERISTICS

Liner diodes testing shows there considerable advantages in operation with short 4 ns pulsed source. First of all such diodes do not require a high vacuum. The use of a trapless mechanical oil pump ensured a vacuum of 10^{-2} to 10^{-3} Torr is quite sufficient. The beam's homogeneity permits us to increase a current density on the foil up to 300 A/cm^2 at repetition rate of 25 pps. The $40 \mu\text{m}$ aluminum-beryllium foil shows as the best material for such purposes. Its high thermal conductivity permits to operate without a forced cooling. Due to a low heat conductivity of the $50 \mu\text{m}$ titanium foil window we can take a good picture of a current distribution. This foil is heating red in repetitive regime (Fig.3.). The sharp borders of e-beam show a good diode's efficiency.

Losses in small-sized accelerators operated in the repetitive regime lead to strong overheating of individual units. For the RADAN 303 source, an approximate energy balance per one pulse is as follows:



As can be seen, the largest losses occur in Tesla transformer. These losses are typical for such compact accelerators because of the need to have some voltage reserve for reliable operation of the uncontrollable high-voltage switch. Principal diode's parameters are listed in Table 2.

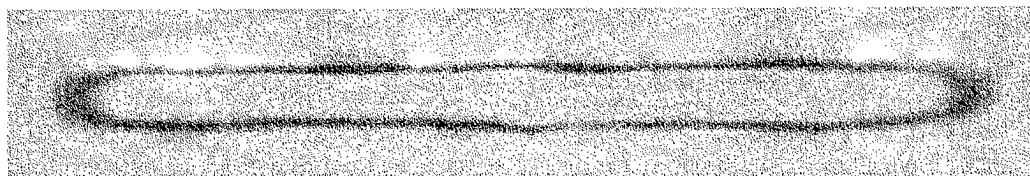


Fig.3. E-beam's track on the $50 \mu\text{m}$ titanium foil after 1000 pulses, 50 pps.

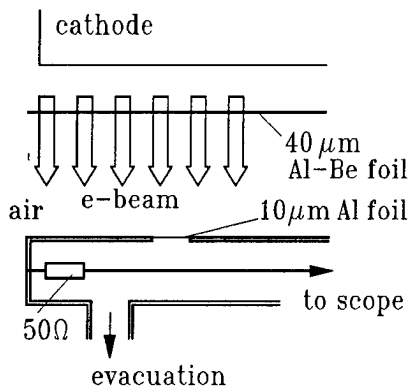
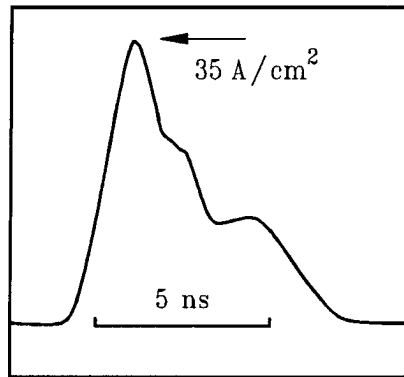


Table 2. SPECIFICATION OF THE RIBBON E-BEAM DIODE BEHIND THE 40 μm ALBEMET FOIL WINDOW

Maximum e-energy	200 keV
Peak e-beam current	1.8 kA
Current density on the foil	300 A/cm ²
Pulse width	4 ns
Beam cross section	5x110 mm ²
Pulsed e-beam energy	1.5 J
Repetition rate in prolonged mode	10 pps
short burst	50 pps
Average beam power (25 pps)	40 W
Weight (with RADAN 303)	31 kg

The measurement of the electron current in the air have met difficulties because of current leakage from probe across the ionized gas. Only using the vacuum probe let us to get a correct trace of e-current behind the foil (Fig.4.). The e-beam energy was measured by a calorimeter.

Fig.4. Trace of e-beam current behind the foil. Distance between the window vacuum probe is of 15 mm.

After more than 10^6 pulses of continuous operation (10 hours with repetition rate of 25 pps) the main characteristics of L-diode don't change. Only slight corrosion traces of the foil by products of an air radiolysis was noticed.

5. CONCLUSIONS

Using a running wave regime in vacuum high-current diode there is no need in high vacuum. High liner diode efficiency provides to use compact pulse power supply sources. The stability of characteristics and long life time of L-diode permits one to carry out not only laboratory research investigations but technological radiation experiments as well (e.g. for surface sterilization of small objects).

6. REFERENCES

1. V.G.Shpak, M.I.Yalandin, S.A.Shunailov. "Compact High-Current Accelerators Based on the RADAN SEF-303 Pulsed Power Source," *IEEE Proc.9th Int.Pulsed Power Conf.*, Albuquerque,NM,1993.
2. G.A.Mesyats, V.G.Shpak, M.I.Yalandin, S.A.Shunailov. "Compact High-Current Repetitive Pulse Accelerators," *IEEE Proc.8th Int.Pulsed Power Conf.*,San Diego,CA,pp.73-77,1991.
3. S.P.Bougaev, Yu.I.Terentyev, V.G.Shpak. "Electron Emission from Discharge Plasma over Dielectric in Vacuum," *Proc. 10-th Int. Conf. Phenomena in Ionized Gas.*, Oxford, P.93, 1971.

Current addition by MITL in vacuum.

Grabovskii E.V., Nedoseev S.L., Pichugin V.E.,
Smirnov V.P., Zajivikhin V.V.
Olejnik G.M.

TRINITI, Moscow region, Russia.

1. INTRODUCTION

Water is widely used as an insulator for high power forming lines. Its high breakdown voltage and high electrical permittance gives a possibility to produce high power density flux. But an optimal wave resistance for cylindrical water forming lines is several ohm. Consequently, the power addition schemes are necessary for low impedance loads. In greatest pulsed power installations "SATURN" and "PBFA-II" (SNL, USA) water power addition schemes are used. On the contrary, "ANGARA-5-1" (TRINITI, Russia) scheme of power addition uses eight separate MITL in vacuum. Some experimental results of the parallel current addition on a common load are described in this report. A jitter of parallel modules switching is a significant effect of "Angara-5-1" operation. Quantitatively it is a square mean of time delay of modules T1-T8, when voltage of every module gets 0.1 of its maximal value. These moments can be defined with ± 2 ns accuracy.

2. ANGARA-5 CONCENTRATOR DESIGN

The vacuum concentrator of "Angara-5-1" generator is aimed to addition of currents of eight separate modules. The output voltage of modules is equal to 1MV, module current - 0.6 MA, pulse duration ~ 90 ns. Different schemes of current concentrators were tested on "Angara-5-1" during 10 years of experiments (~ 3000 shots).

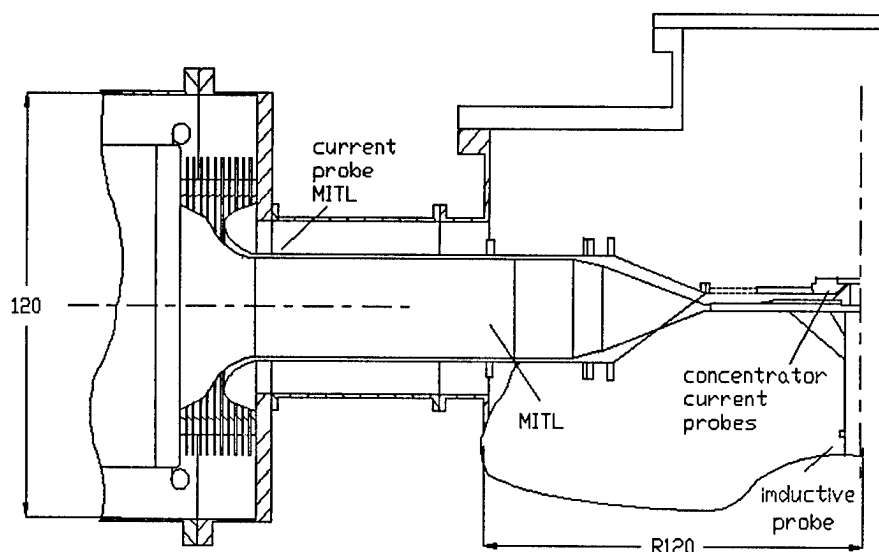


Fig.1. Angara-5 concentrator

Two discs concentrator was chosen as a most reliable and suitable one for physical experiments, in spite of its relatively high inductivity. The concentrator design is shown at Fig.1. It consists of eight cylindrical vacuum MITLs with diameter 30 cm connected to two flat disks with diameter 60 cm. The convolution from cylinder to

flat disk take place in distance 70-30 cm from center of concentrator. The gap between anode (top) and cathode (bottom) disks decreases from 3 cm at 30 cm radius to 1 cm in central part of concentrator. Cathode and anode have a cones with large diameter 280 mm in their central part. This cones shifts the load position from gap between disks upper the level of anode for diagnostic purposes. The total inductivity of disc concentrator is equal 10 nH for liner length 1 cm and liner diameter 30 mm. The total inductivity of all vacuum arrangement between water-vacuum interface is equal 17 nH for the same load sizes. The total current through the load was measured by magnetic probe, consisted of 8 magnetic loops, placed uniformly on radius 14 cm and connected in parallel. The signal from probe was registered by two registrators - oscilloscope-SRG-5 (1.5GHz, 1 GHz including cable line) for dI/dt measurements and digitizer (100MHz) for $I=I(t)$ measurements to obtain an instant information about current amplitude. An error of I measurements was $\pm 5\%$ with SRG-5.

3. EXPERIMENTAL RESULTS

The experimental data presented are taken from data base of double liner experimental program on "Angara-5-1". An imploding gas (Xe) shell of 100-200 mkg/cm linear mass surrounded coaxially an inner liner (4 mm, foam, agar-agar-50% + M0-50%, 200-300 mkg/cm). Current up to 4 MA passed through external shell, accelerated it to $V=5.10^7$ cm/s. In the moment of liners collision an energy, delivered by "Angara-5-1" generator in kinetic and magnetic modes, was transformed partially into soft X-ray radiation into inner liner. In some experiments foil cylinder was used as an inductive load.

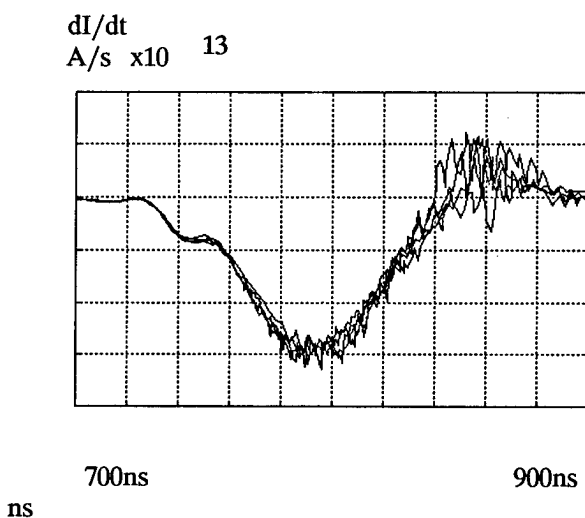


Fig.2. dI/dt signals.
liner mass-200mkg/cm

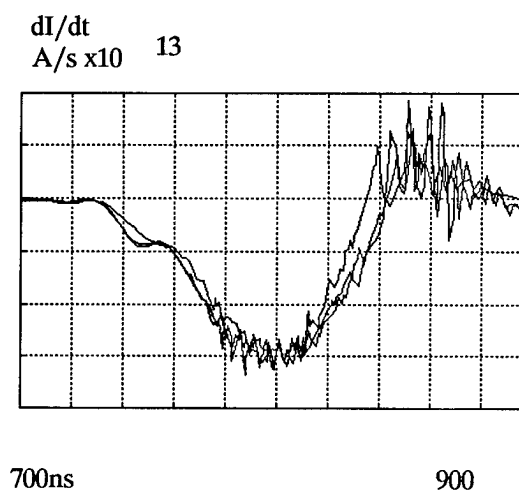


Fig.3. dI/dt -signals.
liner mass-120mkg/cm

4. dI/dt ANALYZIS

The dI/dt oscillograms for different external liner linear masses are shown at Fig. 2. and Fig.3. to outline the main features of dI/dt in our concentrator. There are three specific zones: 1-from signal beginning to maximum, 2- from maximum to zero, 3-residual part. In the first zone signal is independent on liner mass and it coincides with one for inductive foil load, having the same sizes and great mass in comparison with liner parameters. A plato on the signal is a result of superposition of effects electron leakage in MITLs and rising voltage of generators. Liner dynamics isn't significant in this period due to small liner velocity V and compression $c = r_0/r$, because linear liner impedance is $dL/dt = Vc/r_0$. The dynamics is more significant in the second zone, dI/dt depends on liner mass strongly. High frequency oscillations presents on dI/dt signals during time interval of MITL effective operation. The period of oscillations is 6 ± 0.4 ns.

5. JITTER EFFECTS

To analyze current-jitter dependence, we have chosen shots with approximately uniform distribution of pulse time T1-T8 in a band lesser than 20 ns. Current decreasing for large jitters is evident. A dependence between load current maximum and jitter value is significant only for the high load mass (200 mkg/cm), correlation factor ~ 0.8 . The correlation is absent for low load mass (120 and 160 mkg/cm).

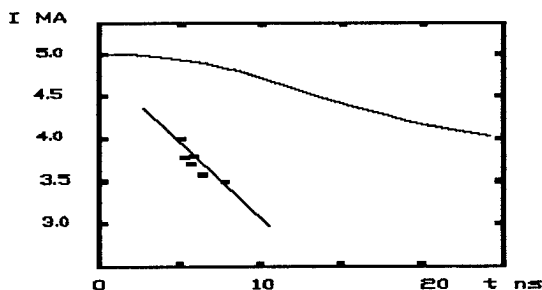


Fig.4. Dependence load current-jitter
top-calculation[1]
bottom-experiment.

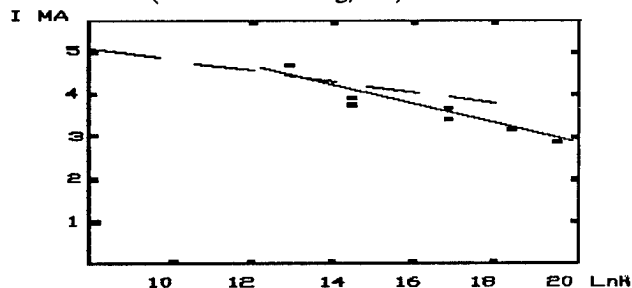


Fig.5. Dependence load current-load inductivity
dot line - calculation
solid line-experiment.

6. INDUCTIVE LOADS

Due to the impedance of imploded liner isn't accurately known, we have used metal cylindrical load, supposing its impedance retains without changes during the time of pulse. We use this load with different diameter and height. Dependence of current through such loads versus total inductance is shown on Fig.5. In the experiments presented on this figure the total module current almost doesn't change, as calculations predicts. Reasons of these losses may be similar to one observed in [5] and they aren't completely understood. Our measurements can't separate them. These losses may be due to disturbance of electron flow in a region of MITL - disk connection or due to ion currents. The total efficiency of current transmission reaches 90% for the minimal inductances from presented on Fig.5. This result is in agreement with calculations [1].

7. ELECTRON LOSSES CALCULATION

Calculations are based on the methods and code [1]. This paper developed codes for energy transmission through MITL. It takes into account current losses in areas where local current less than critical. Density of leakage current J was described by expression $J(U, I) = j(U) * F(I / I_m(U))$ where $I_m(U)$ - is a minimal current in Brilluen approximation, calculated in [3], F is a model function. F describes current losses decreasing with increasing of magnetic field. F equals zero if a line current I is larger than I_m . Function $j(U)$ is relativistic expression for "3/2 law". Calculations [1] describe the dependence of losses increasing in the case of nonzero jitter. This part of losses puts limitations on possible jitter value. Significant losses occurs when one module is late. In this case its current is subtracted from a total current of other modules. The early starting of one module doesn't increase the losses, but the late starting may be catastrophic for energy transmission to a load. Fig 4 shows calculated and experimental values of the current, transmitted to the equivalent load as a function of jitter value. Difference of experimental and calculated values is negligible for small jitter and it rises dramatically if the jitter is high.

8. DISCUSSION

Fig.2 shows good coincidence of dI/dt in zones 1-2 for 4 different shots with initial liner mass 200 mkg/cm. Consequently, an accelerated mass may be equal in these shots. On the contrary, an acceleration of

liners with smaller masses (120 mkg/cm) isn't so contemporary, it is shown at Fig.3. We can suppose that different masses are accelerated from shot to shot in this case. Taking into account the absence of "current-jitter" correlation in low mass case, we can conclude that some instability of initial parameters (current shell formation) or plasma current instability is significant for low mass liner implosion efficiency [6].

High frequency oscillations period is close to the period of electromagnetic self oscillations of concentrator volume, if a velocity of electromagnetic wave in operating MITL is equal to light velocity in vacuum. It allows us to propose that MITL+disk system concentrator is clean, there is no plasma and no current leakage in it during liner acceleration.

We can't explain now the difference of experimental and calculated values of the current for high jitter case.

9. REFERENCES

1. V.V.Bulan, V.V.Zajivikhin. Simulation of the magnetically selfinsulated multimodule system. Proceedings of "BEEM's-90",Novosibirsk, USSR, 1990.
2. Z.A.Albikov, e.a. Impulse thermonuclear installation Angara-5- 1. Sov.J.Atomic Energy, 1990, v.68, n.1, p.26-35.
3. F.V.Gordeev. Magnetic insulation of vacuum transmission lines. Preprint of Inst. of Atomic Energy, USSR, IAE-3076, 1978.
4. P.Sincerny, M.Di-Capua, R.Strigfield, S.Wong, C.Gilman, S.Ashby and T.Sheridan. The limit of power flow along a high-power MITL. Proc. of V Int.Conf. on High-Power Particle Beams.
5. A.V.Batunin, e.a. Plasmodynamic effects for magnetically insulated plasma. VIII Int. Conf. on High-Power Particle Beams. Abstracts, P2, p.243, Novosibirsk,,USSR, 1990.
6. A.N. Batunin, A.V.Branitsky et.al."Megaamper nanosecond current switching from external unstable light liner to inner load in vacuum on "Angara-5-1", to be published at this Conference.

Experiments on a microsecond electron beam generation in a plasma-filled diode.

S.V. Lebedev, M.A. Shcheglov, S.G. Voropaev.

Institute of Nuclear Physics, 630090, Novosibirsk, Russia.

ABSTRACT

Results of experimental study of a plasma-filled diode are presented. The diode was filled by a plasma from plasma guns. Two different regimes were tested. In the first one the plasma cloud was localized at the anode region. In this case there were not found a stable low impedance mode of a diode operation. In the second regime the diode was filled by plasma completely before a high voltage pulse and an additional plasma cloud was also created in the drift region. In this regime a low impedance accelerating gap, stable during up to $5 \mu s$ was formed.

1. INTRODUCTION

At the Budker Institute of Nuclear Physics microsecond electron beams with total energy about 100 kJ ¹ are used for plasma heating in solenoids². The beam is generated in an axial planar diode with cold emission cathode and then magnetically focused with compression coefficient up to 20. For efficient beam-plasma interaction it is necessary to use a beam with current density no less than 1 kA/cm^2 . This condition does not allow one to increase the diode gap that eliminates the pulse duration and, as a result, the total energy of the beam.

New opportunities for increasing of energy content are appeared in the case of using of a foilless plasma-filled diode. For such a diode there are no limitations on the geometrical diode gap, but an accelerating gap is set by initial plasma density in the diode and by the voltage applied to the diode. In our previous experiments³ we found that it is possible to produce a stable microsecond electron beam in plasma-filled diode. In this report new results obtained in the experiments on microsecond e-beam generation in a plasma-filled diode are discussed. An influence of the initial plasma density and operating regime of plasma sources on the beam generation is studied. The main feature of the operation of such a diode is a high current density of the beam from the very beginning of the pulse, while the diode voltage has its maximum value.

2. EXPERIMENTAL SETUP.

Experiments were carried out at the U-1 accelerator (1.6 MV, $0.2 \mu F$, 6 Ohm). Schematic of the experiments is given in Fig.1. High voltage pulse is applied to the graphite cathode with the 20 cm in diameter. Magnetic field is 0.5 T at the cathode and 10 T in the magnetic mirror. Beam collector

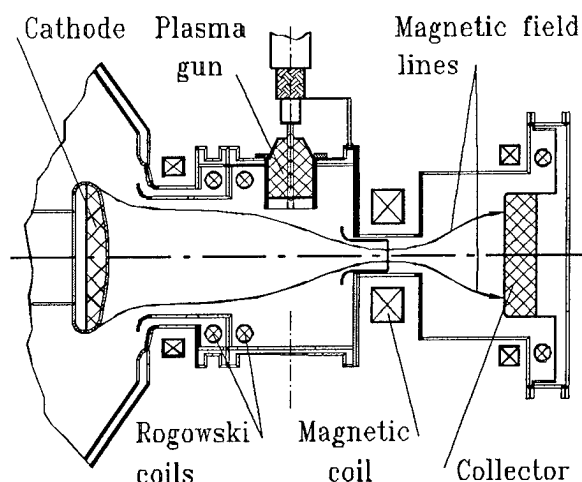


FIG.1

gradient of the magnetic field. In comparison with our previous experiments some changes in power supply of the guns were made and number of guns were increased from 3 to 6. These changes allowed us to decrease delay time between triggering of plasma guns and the moment of applying high voltage pulse to the diode and as a result to avoid breakdown of vacuum insulator. Typically the delay time in these experiments was in the range 100-200 μ s.

Diode voltage was measured by resistive divider. The beam current at the entrance and at the collector, as well as the net current have been measured by Rogowski coils. The difference between currents measured by different coils gives one the beam losses in the compression region. In some experiment a thin foil (10 μ m Al) was placed in the magnetic mirror.

3. EXPERIMENTAL RESULTS

Given in Fig.2 are typical diode voltage and current for the plasma-filled diode. It is seen that formation of the quasi-static accelerating gap is finished in $\sim 0.5 \mu$ s after the beginning of the pulse. In this moment rapid rise of the diode current ends and the current begins to follow the changes of a diode voltage. It seems that the time of acceleration gap formation is determined by inductance of high-voltage generator. Comparison of currents measured by different Rogowski coils shows that the losses of current ($\sim 15\%$) are exist in the transport region. This fact is also confirmed by erosion traces on the guns surfaces.

It is convenient to compare diode operation at different regimes by comparison of effective accelerating gaps, calculated from oscillograms of diode voltage and beam current. In Fig.3 the gaps calculated for different cases are presented: a) diode without plasma; b) one shot of plasma guns at

is situated behind the mirror in the magnetic field of 0.8 T to eliminate plasma formation at the collector.

For plasma production 6 surface discharge plasma guns were used. The guns were placed outside of the expected beam diameter so that the distance between the guns and the boundary magnetic surface corresponding to the cathode edge, was about 1 cm. To increase plasma diffusion across the magnetic field and as a result to improve the plasma homogeneity in the diode, plasma guns were placed in the region of maximal

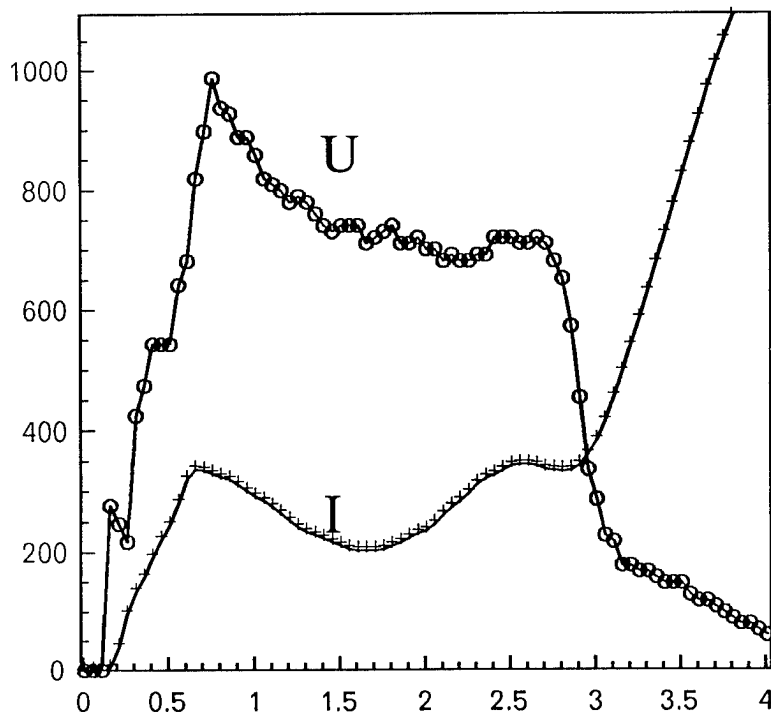


FIG.2

the beam was changed from shot to shot from 1 to 4 μs . Smooth decreasing of diode impedance at the end of the pulse, after 3 μs , occur as it seems, due to appearance and accumulation of electrons, oscillating between the cathode and magnetic mirror. These electrons lead to increasing of the ion current and appropriate increasing of the total diode current. The current raise leads to drop of diode voltage and to additional raise of number of oscillating electrons.

In the regime with preliminary filling of a diode with plasma (c and d, Fig.3) accelerating gaps are essentially smaller. The second plasma cloud which was created in these cases can be considered as a source of ion current. The existence of this additional plasma source of ions may be important because the plasma density responsible for charge separation at the distance ~ 5 cm at 1 MV voltage is about 10^{10} cm^{-3} and the ion density in the ion current is also about the same order of magnitude. In the experiments performed the density of second plasma cloud and, as a result, the ion current were varied by varying of the moment of guns switching. From comparison of the regimes (c) and (d) it is seen that the earlier creation of plasma cloud gives the possibility to obtain a low impedance of a diode from the very beginning of the pulse.

the moment 10 μs before diode voltage pulse; c) and d) - two shots of plasma guns, first 100 μs before diode voltage pulse and second at the moment of diode pulse (c) or 6 mks before diode voltage pulse (d). The largest accelerating gap is formed for the diode without plasma filling (a). In the regime (b) an accelerating gap is smaller at the beginning of pulse. The difference in the accelerating gap evolution may be connected with difference in acting sources of ions. In regime (a) the ions can be emitted from the collector surface and from transport region due to the space charge of the beam. In regime (b) the transport region do not filled with plasma totally and ions can be emitted only from the boundary of plasma cloud. In this regime the duration of

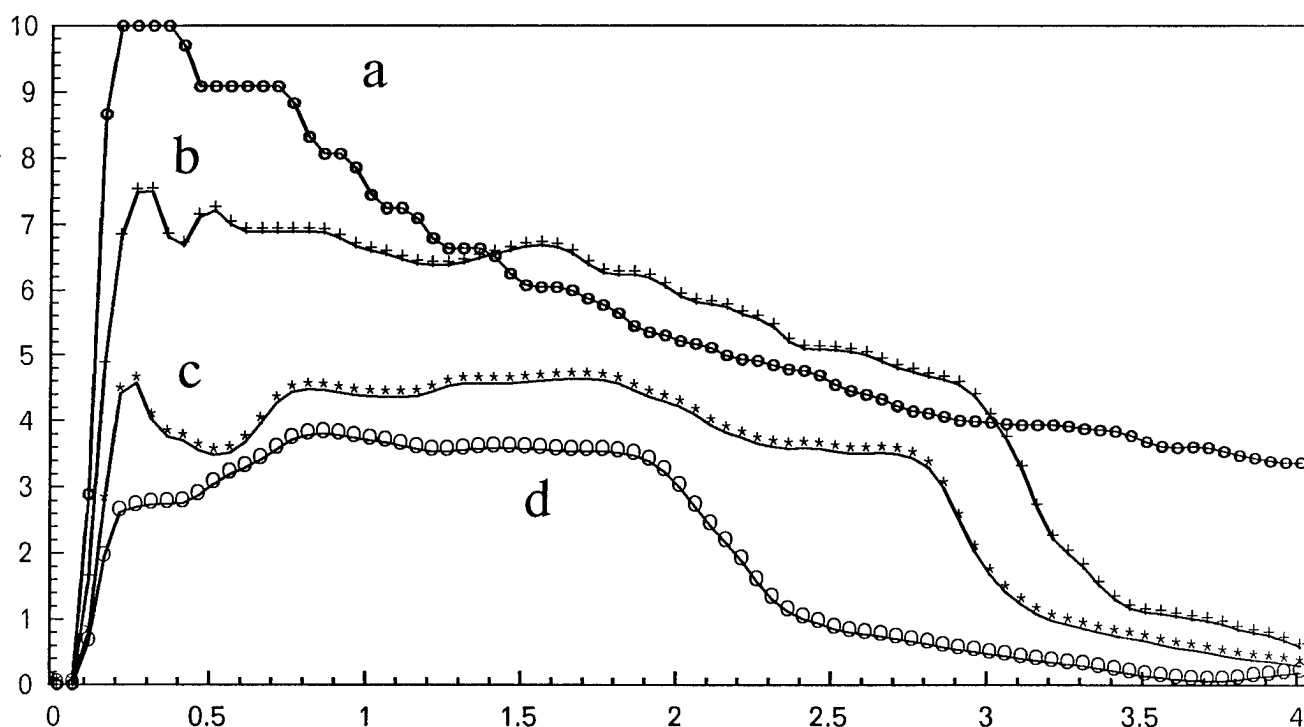


FIG.3

4. CONCLUSION.

The experiments performed allowed us to find conditions for beam generation in a plasma filled diode with an impedance practically fixed during the pulse. The current density of the beam ($\sim 100 \text{ A/cm}^2$) is practically constant during the beam pulse up to $5 \mu\text{s}$. It was found that it is better to use a regime with the diode completely filled by plasma, while for the plasma cloud localized at the anode region the diode operation was unstable.

5. REFERENCES.

1. Astrelin V.T. et al.- Proc. of 14th Intern. Symp. on Discharges and Electrical Insulation in Vacuum.- Santa-Fe, 1990, p.702-703.
2. Burdakov A.V. et al.- Proc. of 9th Intern. Conf. on High-Power Particle Beams.- Washington, DC, 1992, v.2. p.1049-1054.
3. Karyukin A.V. et al.- Proc. of 9th Intern. Conf. on High-Power Particle Beams.- Washington, DC, 1992, v.2. p.1015-1020.

POWERFUL WIDEBAND AMPLIFIER
BASED ON HYBRID PLASMA-CAVITY SLOW-WAVE
STRUCTURE.

M.A.Zavjalov, L.A.Mitin, V.I.Perevodchikov, V.N.Tskhai,
A.L.Shapiro.

All-Russian Electrotechnical Institute, Moscow, Russia.

ABSTRACT.

The powerful beam-plasma amplifier operating under continuous conditions is described. The amplifier is designed on the base of new principles using hybrid plasma-cavity electrodynamic structures. The theory and foundation of calculating the slow-wave structures having plasma filled propagation channel and interaction of electron beam with hybrid plasma-cavity system are considered. Considerably increased power of microwave radiation and expansion of the operating pass-band when the propagation channel is filled with plasma is shown.

1. INTRODUCTION.

The proposal and realization of the hybrid plasma-cavity waveguide [Refs.1-3] is a way to create the powerful wideband beam-plasma amplifier. This waveguide uses an electromagnetic-type waves excited in a chain of coupled cavities (CCC) to interact with the electron beam. The waves propagating in such a system are electromagnetic-plasma ones, the position of the maximum electric field strength on the plasma wave-guide axis coinciding with that of the power flux outside the propagation channel, which is passing through coupling slots in the walls of the CCC cells.

This made it possible to start the realization of hybrid plasma-cavity structure-based microwave amplifiers and generators in practice. Designing the amplifier required investigations to be performed in two directions. Firstly it was necessary to develop a theory and to work out a technique of calculating of hybrid plasma-beam device, secondly-to design construction and technology of the device the pressure of which could be varied from 10^{-6} to 10^{-3} torr in the area of slow wave structure. Here the main problem was to create a cathode and form a high power electron beam operating steadily under elevated pressure.

2. HYBRID WAVES IN PLASMA-CAVITY SLOW-WAVE STRUCTURE.

The method of partial regions for obtaining the dispersion relation have been used. In Fig.1 the region 1 corresponds to the propagation channel filled with the magnetized plasma and the region 2 does to the vacuum volume of a single resonator cell.

Based on this mathematical model the program of computing the characteristics of a system was realized, which allows to get frequency dependences of

the phase velocity, coupling resistance and ratio of energy fluxes inside and outside the plasma. In Fig. 2 the dispersion characteristic of hybrid waves of a system is presented for the case of dense plasma when the plasma frequency exceeds the frequency of the upper boundary of the CCC passband.

The efficiency of radiation of waves from plasma is determined by the ratio of the external energy flux to the internal. Such criterion allows to divide hybrid waves in two types: plasma-like and electromagnetic or structure-like.

In Figs. 3 the dependencies of coupling resistances R_c and ratios of energy fluxes outside and inside the plasma channel on the frequency are depicted for two types of hybrid waves, G_{01}^1 and G_{01}^2 . As it can be shown, the relative width of a frequencies band overlapped by the waves G_{01}^1 and G_{01}^2 together is about 55-60 %, and the coupling resistance is an order greater than that for a vacuum CCC.

3. INTERACTION OF AN ELECTRON BEAM WITH HYBRID WAVES.

As it was shown in periodic plasma-cavity systems the variety of hybrid waves corresponding to a plasma wave with a definite radial structure of fields arises which are plasma-like or electromagnetic. The energy fluxes of the plasma-like are almost completely localized in the propagation channel and they can be included into the space-charge field. And the electromagnetic waves have the energy fluxes localized primarily in cavities volume out of the channel. We consider the waves of electromagnetic type (G_{01}^1 and G_{01}^2 in one radial type approximation) as the active waves. Accordingly to this the equations of an ordinary plasma TWT [Refs. 4] can be used for the solution of the problem of amplification of waves by an electron beam in a plasma filled CCC.

In Fig. 4 the dependence of the efficiency on the axial coordinate for a hybrid plasma filled amplifier is presented. It can be high enough and is considerably greater than that for a vacuum device. This points to the possibility of creating of new type powerful microwave amplifiers.

Figs. 5 illustrate the results of studying of beam particles dynamics and bunching along the axial coordinate. Bunches are compact and contain up to 70 per cent of all particles what is connected with the strong bunching action of a space charge at negative values of the dielectric permittivity ϵ_z .

4. CONSTRUCTION AND TESTING OF THE PLASMA-BEAM AMPLIFIER.

Fig. 6 presents a schematic diagram of wideband plasma-beam amplifier within the centimeter wavelength range. The device is placed in a magnetic field of

a solenoid.

Fig.7 shows a microwave power radiated in the amplifier mode as a function of pressure in the slow-wave structure. The microwave power is increased 2-3 times with a pressure of about $1 \cdot 10^{-4}$ torrs to $1 \cdot 10^{-3}$ torrs. The power generated in continuous operation at a pressure of 10^{-3} torrs is up to 20kW, the electron efficiency (that is a ratio of microwave power to electron beam power) reaching up to 40%.

The extended operating band of beam-plasma amplifier is an essential advantage of the plasma mode of operation. Fig.8 gives amplitude frequency responses at a pressure of $1 \cdot 10^{-6}$ torrs (Curve 1) and $1 \cdot 10^{-3}$ torrs (Curve 2).

Fig. 9 shows the amplifier amplitude characteristics for different frequencies in the device service pass-band. It demonstrates a high quality of amplification in a wide range of frequencies and powers. The comparison of the presented experimental characteristics with the calculated ones shows the correctness of the theoretical representation of the operation of a hybrid beam-plasma amplifier.

The correlation of amplitude-frequency responses obtained for vacuum and plasma conditions is especially obvious. It confirms completely theoretically predicted expansion of the pass-band when using a plasma mechanism to amplify the oscillations.

5. CONCLUSION.

The obtained experimental results [4,5] support the theoretical representation of the benefits of hybrid beam-plasma amplifiers of microwave oscillations and show their real possibilities. The pilot devices of plasma-beam amplifiers are created to operate under continuous regime at power over 20kW, efficiency of 40 per cent and pass-band width of $\Delta f/f = 30$ per cent.

To our knowledge the attained combination of the above parameter values haven't yet been obtained with vacuum amplifiers. The theoretical representation shows even higher possibilities in the pass-band expansion and efficiency increase.

REFERENCES.

- [1] Ya.B. Fainberg, Yu.P. Blioh, L.A. Mitin et al. "Electrodynamics of hybrid plasma-waveguide structures," Doklady AN UkrSSR, no. 11, p.76. Dec. 1990.
- [2] L.A. Mitin, "Volume waves in a chain of coupled cavities with plasma filled propagation channel", Fizika plazmy, v.19, no.4, p.546, 1993.
- [3] L.A. Mitin, I.L. Volokitenkova, "Theory of hybrid plasma-beam amplifier", Radiotekhnika i elektronika, no.9, p.1671.
- [4] V.I. Perevodchikov, M.A. Zavjalov, V.F. Martynov, L.A. Mitin et al. "Generation of microwave oscillations in electrodynamic system with plasma-beam interaction," Abstr. of the Int. Conf. BEAMS'92, p. 183, Washington, May 1992.
- [5] G.I. Butskih, K.G. Gureev, M.A. Zavjalov et al. "Powerful amplifier of microwave oscillations based on hybrid beam-plasma electrodynamic system." Radiotekhnika i elektronika, no.9, pp.1682.

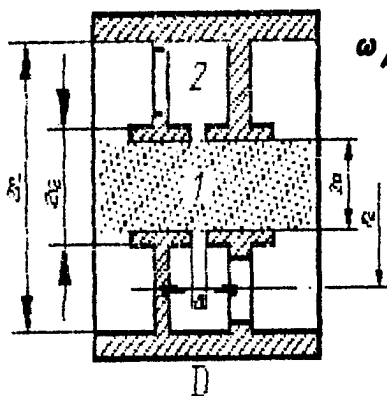


Fig. 1—Plasma filled cavity cell.

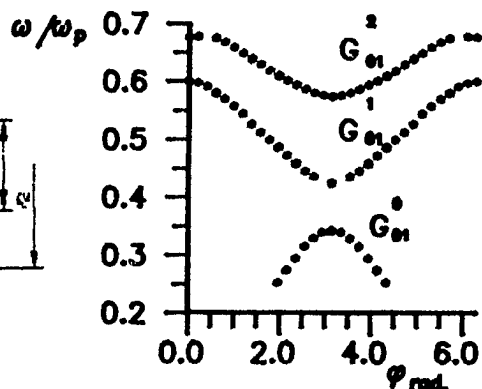


Fig. 2—Dispersion responses.

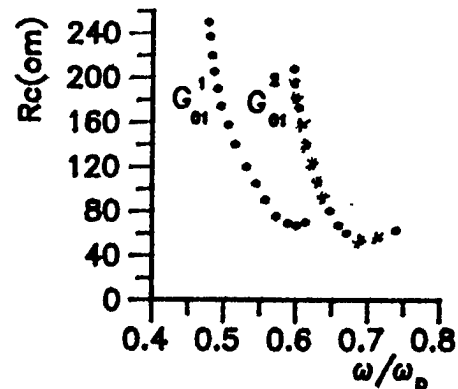


Fig. 3—Coupling resistance—frequency responses.



Fig. 6—Plasma-beam amplifier.

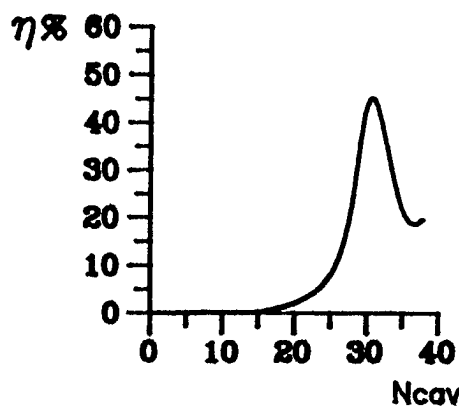


Fig. 4—Dependence of efficiency on number of cavity gap.

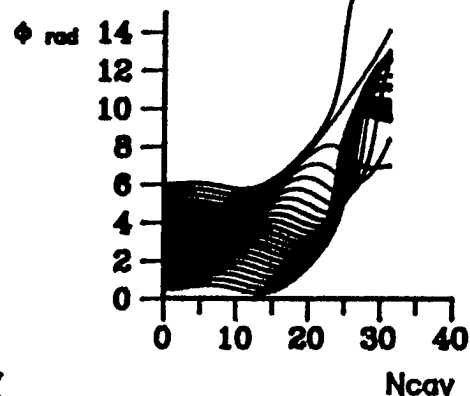


Fig. 5—Phase trajectories of beam particles.

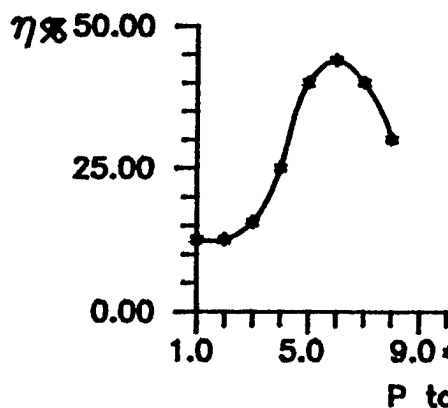


Fig. 7—Dependence of output power on gas pressure.

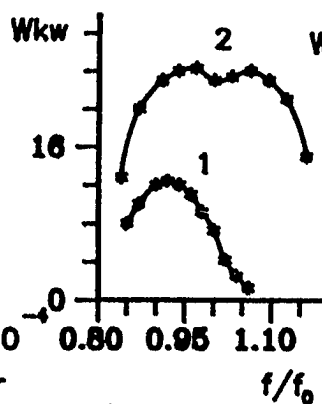


Fig. 8—Amplitude—frequency responses.

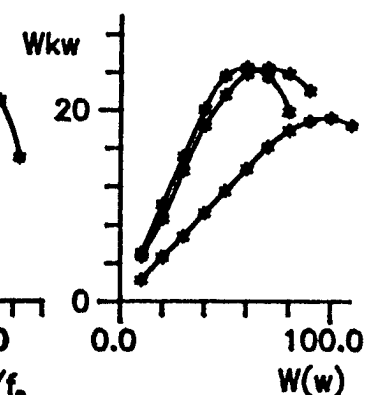


Fig. 9—Amplitude responses.

SESSION 7

Discharge in the Space Environment

Vacuum chamber simulation of high voltage breakdown in space

Andrew C. Logue and Lloyd B. Gordon

University of Texas at Arlington, Department of Electrical Engineering
P. O. Box 19380, Arlington, Texas 76019-0380

ABSTRACT

The Space Power Experiments Aboard Rockets (SPEAR) I, II, and III investigated (i) characteristics of high voltage in the space environment, (ii) various vacuum breakdown models applied to the space environment, (iii) designs for maintaining and utilizing high voltage in the space environment, and (iv) methods of grounding to control spacecraft charging. The ultimate goal of the SPEAR program was to develop design guidelines for system and component engineering for space power systems. SPEAR I investigated how exposed high voltage systems interact with the space environment. SPEAR II demonstrated that exposed high voltage power systems could be designed to operate in the space environment. SPEAR III tested the effectiveness of different methods of "grounding" the payload to the space environment.

A critical component of the program which preceded actual rocket launches was earth laboratory testing and full scale mockups of high voltage payloads. Such vacuum chamber tests permit the researcher to perform an experiment in a controlled environment at a comparatively lower cost. This environment allows for the testing of theoretical models and engineering designs prior to a costly launch, thus, the various SPEAR programs were simulated in vacuum chambers. A few of the parameters were plasma density, pressure, geometry of the payload, coupling of the payload to the plasma, payload experiments, and magnetic field orientation to the payload.

The mockup chamber tests for Space Power Experiments Aboard Rocket (SPEAR) I, SPEAR II, and SPEAR III will be examined in this paper. Specifically, high voltage results of mockup chamber tests will be compared with results of the flight hardware chamber tests and flight experiments. The authors will analyze the results obtained through the different phases of each of these programs and determine the effectiveness of the simulations that were performed in the vacuum chambers.

1. INTRODUCTION

Future missions in space will require higher electrical power levels to fulfill their objectives. Such missions will include the international space station, industrial manufacturing platforms, defense platforms, a lunar base, and a manned mars mission. The space station is expected to utilize 75 kW initially and 300 kW of power ultimately to fulfill the requirements for its operation and experimental objectives. Power figures for the other missions range from 100 kW to 1 MW of power. Currently the highest electrical power level of any U.S. spacecraft is the space shuttle with a maximum power level of 36 kW for brief periods of time.¹

The spacecraft that are currently in use today and the planned space station will use classical insulation on their power systems such as solid or gaseous dielectrics. These insulators have a large mass; suggesting that the power systems of future missions could compose up to 40% of the total mass of the spacecraft. Insulators could comprise up to 30 - 50% of the total mass of the power system. If the ambient atmosphere of low earth orbit (LEO) could be utilized as the insulation for the electrical power system then a large savings would result in mass reduction. Thus, a smaller launch vehicle or increased experimental hardware can be utilized for the mission.

2. DISCUSSION OF SPACE ENVIRONMENT

The space environment is a harsh environment in which to operate. Figure 1 reveals several different phenomena present such as plasma, micro debris, vacuum, microgravity, radiation, and atomic oxygen. Effects, such as spacecraft charging and temperature gradient, may be seen on the payload during its mission lifetime. These phenomena and effects require that designs for spacecraft be very resilient and impervious to the environment.

Power systems on the earth have a data base from previous experience that involves decades of time and thousands of research projects. Designing power systems to operate in the space environment is a relatively new field, thus designing power systems to utilize the ambient environment as an insulator is still in its infancy. The three SPEAR experimental missions start the data base.

3. SPACE POWER EXPERIMENTS ABOARD ROCKET PROGRAM

The Strategic Defense Initiative Organization performed many studies of advanced defense platforms that would require very high levels of power to meet mission requirements. It became clear that any reduction in the mass of these platforms would be worth substantial research effort. One of the areas that was singled out was eliminating the need for insulators by using the ambient vacuum as the insulating medium. This basic concept led to the SPEAR program.

The specific goals of the program were to determine the characteristics of exposed high voltage in the space environment. This included analyzing spacecraft charging and methods to minimize the phenomena, providing empirical data

for fine-tuning of theoretical models and computer simulations, and developing engineering designs that would operate in the space environment with exposed high voltage.

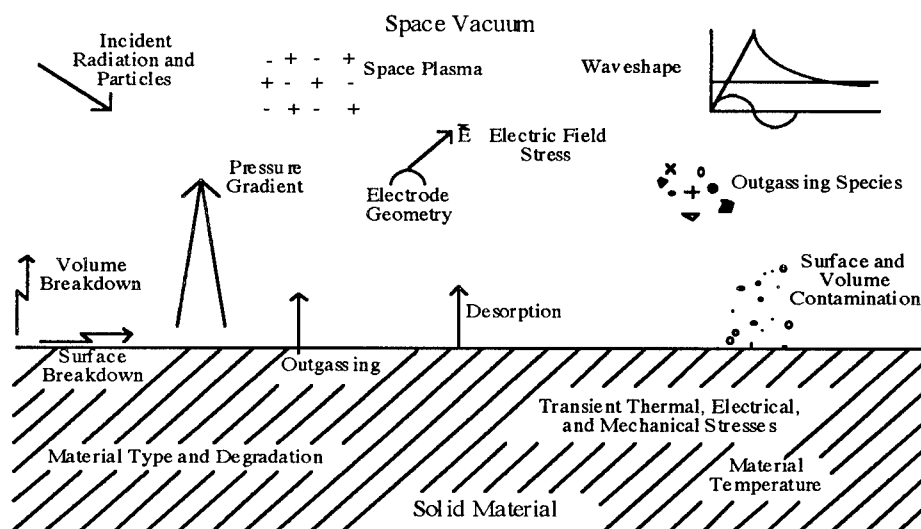


Figure 1. Phenomena present in the space environment and its effect on the spacecraft.

SPEAR I was the first spacecraft to expose such high levels of voltage to the space environment. Its objectives were to gain a better understanding of the physics involved in the use of exposed conductors. The waveform's effect (ramp vs. pulse) on discharges or breakdown were studied. Additionally, the response by the plasma and electron sheath were studied during the applied voltage. The last significant goal for the SPEAR I program was to quantify the predicted spacecraft charging levels during the discharges. Figure 2 shows that the payload consisted of two exposed conducting spheres with voltage graded insulating booms. The pulse forming network was contained in a gas insulated section of the body.

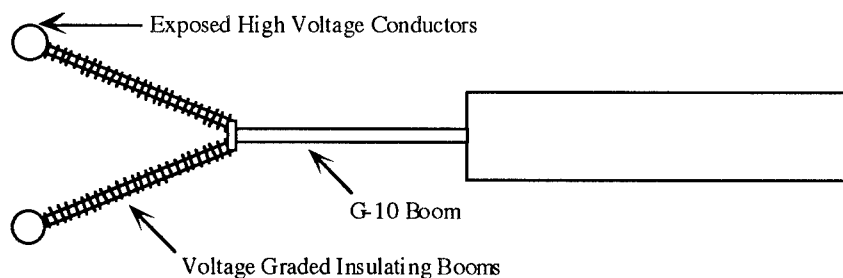


Figure 2. SPEAR I payload with booms deployed.

It was determined that an engineering proof of concept was to be SPEAR II's objective. This mission would establish new guidelines for the design of high power space systems that would use the vacuum of space as an insulator. Figure 3 illustrates the major innovations that were developed for the program which included: a pulse transformer, pulse shaping inductors, a voltage probe, a Klystron, high voltage bushings, and a fiber optic cable.² The spacecraft was to have exposed 100 kV at 1 MW of peak power and 335 kA at 125 MW peak power directly to the space environment with many of the electrical components using the ambient environment as an insulator.³

The final experiment of the program was SPEAR III. This payload investigated spacecraft charging as well as the possibility of the craft being "grounded" to the ambient plasma. This was done by using four different techniques which were thermionic electron emitter, field effect electron emitter, hollow cathode plasma contactor, and a neutral gas release system. Figure 4 illustrates the different grounding techniques and their location. Each of these techniques was tested in conjunction with a high voltage discharge to the exposed conductor to determine the effectiveness of its grounding capability.

In most of the SPEAR experiments substantial ground testing was performed on components, systems, and payloads. Prior to testing the payloads, a one-to-one scale mockup was tested to ensure proper experimental procedures. Breakdown thresholds in the space simulation chambers were determined so that the risk to the payload was minimized. These mockups had conductive profiles that were very similar to the payloads and had the capability to duplicate the experimental timeline of the payload. Mockups provide the researcher with a tool that is relatively inexpensive and can be

quickly modified for optimization of designs and theoretical models. The researcher also has the ability to determine the effects of a given phenomena of the space environment on the system or on a component.

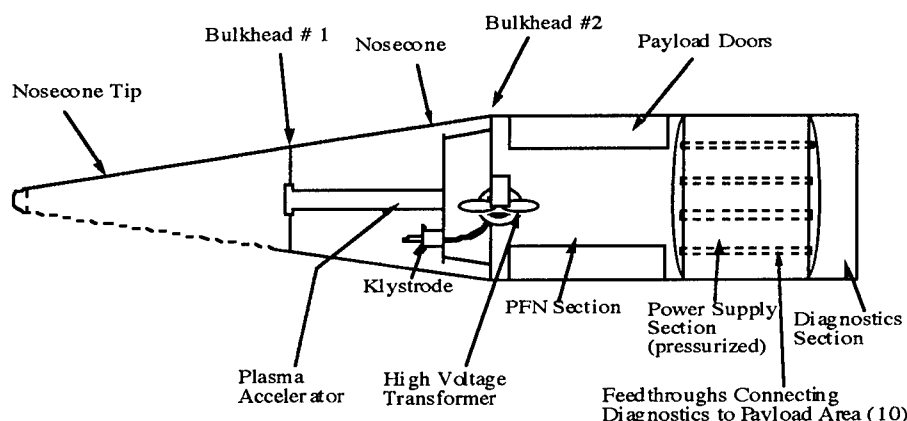


Figure 3. SPEAR II payload with several of the innovative engineering components illustrated.

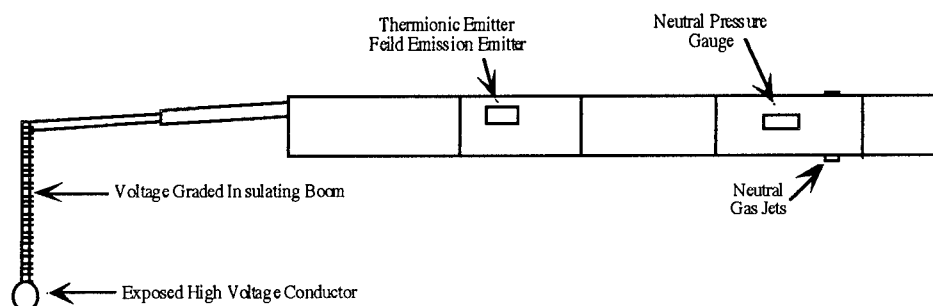


Figure 4. SPEAR III payload with the grounding techniques illustrated.

Space simulation chambers vary in their capabilities for simulating the space environment, however, some of the phenomena are too difficult or impossible to simulate on the earth. The chambers used in the SPEAR program can simulate one or more of the following: magnetic field orientation and amplitude, plasma density, pressure, real-time flight pressure profile, and illumination. A few of the parameters that could not be simulated by the chambers used in the program were: radiation intensity, particle debris, microgravity, and plasma species composition. The facilities that were utilized by the program were NASA's B2 chamber and the SPF chamber at the Plum Brook Vacuum Facility, the University of Maryland SPIE plasma chamber facility, Auburn University's space simulation facility, and the Naval Research Laboratory's space simulation chamber.

4. EXPERIMENTS AND RESULTS

The SPEAR program produced a tremendous amount of data from the different experiments performed on the ground as well as the flight experiments. A brief summary of some of the major results will be discussed in this section. In the SPEAR I program the simulations revealed new characteristics relating to current collection and breakdown under ionospheric conditions. During vacuum chamber tests with high voltage anodes (spheres), the presence of the chamber walls coupled with the existence of a weak magnetic field resulted in breakdown, even with low pressure neutral gases. The mechanism responsible for this breakdown was the trapping of secondary electrons, emitted by the walls when they were bombarded by the positive ions accelerated in the electric field of the anode.⁴ The sphere surfaces experienced high currents from the ambient environment for short periods when high voltages were applied to these surfaces. The vacuum chamber results led to speculation about whether or not equally high currents would occur during flight, causing electrical breakdowns in the equipment. To prevent such breakdowns during flight, protective components were added to the power circuitry.⁵ Several theories were developed from the pre-flight chamber tests and the results of the flight supported the following; no breakdowns would occur at the initial ionospheric vacuum condition, or at pressures below this minimum. The SPEAR I experiment showed that high positive voltages can be placed on isolated bodies in space without causing volume breakdowns.⁶

The SPEAR II program utilized simulation chambers extensively in all stages of the program. If there had been no chamber tests of the payload no significant data would have been obtained due to the loss of the payload shortly after launch. The use of these facilities led to the successful development of several key components for the payload. The pulse transformer is the best example of this. It went through several major redesigns before it would perform properly and this

would not have been possible without the use of the simulation facilities. The entire payload was also thoroughly tested in these chambers and was used to characterize and study the volume breakdown mechanism.⁷

In the last of the SPEAR missions vacuum chambers were of great use to the program. The mockup produced a large array of data that included all of the payload experiments as well as several experiments that provided data points that modelers requested. Some of the major observations from the mockup experiment were that the body of the craft was limited in charging when the sphere was grounded; the body had a discharge to the plasma when the sphere was grounded and a neutral gas was released; and the sphere had a discharge to the plasma at very low voltages and when this occurred the body was driven negative until 1 kV was reached and then breakdown occurred. After the main objectives of the experiments were accomplished a "torus killer" plate was installed to disrupt the electron sheaths around the sphere. The "torus killer" was a flat aluminum plate 1.22 m x 0.61 m. The plate was not grounded and was located in a vertical plane containing the axis of the high voltage boom. It came within 0.28 m of the sphere. Some observations were: the body breakdown threshold increased, the body went from negative potential to zero when a neutral gas discharge occurred, the sphere can maintain a higher potential, and the observed voltage division was 1/3 to the sphere and 2/3 to the negative body.

5. CONCLUSIONS

The SPEAR program made significant use of the available space simulation vacuum chambers. These included chambers at universities, industrial, and government facilities. These ground experiments allowed the researchers to test their theories, models, and designs and go through an iterative optimization procedure. This technique is a time, resource, and cost saver over performing experiments on payloads without some preliminary information from ground tests.

The SPEAR I program demonstrated the need for testing components, systems, and payloads in a ground facility. Several questions needed answers prior to the development of the payload such as should the boom with the sphere have voltage graded rings or not. Through chamber tests it was determined that graded rings were necessary. Models were fine tuned from data that was obtained from the SPEAR I chamber tests.

Vacuum chambers in SPEAR II were utilized the most extensively of all the phases of the program. SPEAR II would have produced no significant data from the payload if there had not been chamber tests. All of the exposed components were tested in ground facilities. These tests have begun the data base for future design of components that utilize the space environment as an insulator. The most significant use occurred in the development of a reliable, lightweight 6 to 100 kV, 1 MW pulse transformer that had greatly reduced bulk insulating media and solid insulators.⁷

SPEAR III was the final phase of the program. Many of the component designs were similar to those in SPEAR I. The experiments, however, greatly differed from SPEAR I. The mockup testing provided a baseline of information that could be utilized to examine the results from the flight experiment. This baseline included the experiments that would be performed by the payload and also experiments that provided insight into the interaction of the spacecraft with the space environment.

Simulation of the space environment in vacuum chambers has provided invaluable information for the SPEAR program in all three of its phases. This testing has insured that components, systems, and payloads have met their design requirements. Chamber tests have also provided data points for computer models to be compared with to insure accuracy and reliability. The use of these tests is clearly an asset to programs that are similar in nature to the SPEAR program.

6. ACKNOWLEDGMENTS

This research was supported by the Ballistic Missile Defense Organization Office of Innovative Science and Technology through Defense Nuclear Agency contract number DNA001-85-C-0181.

7. REFERENCES

- ¹Rose, M. Frank, "Specific Issues Associated with High Power Levels in Space," Proceedings of the 24th Intersociety Energy Conversion Engineering Conference, Vol. 1, Washington D. C., pp. 347 - 354, August 1989.
- ²Rustan, Pedro L. Jr., "SDIO Space Insulation Technologies," Conference Record of the 1992 IEEE International Symposium on Electrical Insulation, Baltimore, Maryland, pp. 2 - 12, June 1992.
- ³J. Benson, SPEAR II Preliminary Design Review, Seattle, Washington, June 16-18, 1987.
- ⁴Antoniades, John, Michael Alport, Derek Boyd, and Richard Ellis, "Ground Testing of the SPEAR I High Voltage Booms," XIII International Symposium on Discharges and Electrical Insulation in Vacuum, Vol. 1, Paris, France, pp. 273 - 275, June 1988.
- ⁵Allred, D. B., J. D. Benson, H. A. Cohen, "Exposure of High Power Systems to Space," XIII International Symposium on Discharges and Electrical Insulation in Vacuum, Vol. 1, Paris, France, pp. 267 - 269, June 1988.
- ⁶Allred, D. B., J. D. Benson, H. A. Cohen, "SPEAR: Rocket Flights to Investigate the Innovative Design of High Power Space Systems," Proceedings of the Space Structures, Power, and Power Conditioning, SPIE Vol. 871, Los Angeles, California, pp. 317 - 325, January 1988.
- ⁷Rustan, P., H. Garrett, and M. J. Schor, "High Voltages in Space Innovation is Space Insulation," IEEE Transactions on Electrical Insulation, Vol. 28, No. 5, pp. 855 - 865, October 1993.

Mechanics and physics of swift dust particle impact

N.A.Inogamov and S.I.Anisimov

Landau Institute for Theoretical Physics, Russian Academy of Sciences
GSP-1, 117940, Moscow, Kosigin street 2, Russian Federation

ABSTRACT

At present report we consider dust particle striking surface of a target. Swift impact is a reason of a whole sequence of mechanical and physical phenomena. It generates spallation and crater formation (#1), emission of matter (#2), plasma creation and radiation flash (#3). We have considered also dynamics of this plasma cloud (#4) in an external electric field (charge separation and charge extraction). This consideration is important from an experimental point of view for impact detection and analysis.

TEXT

0. In recent years there has been a noticeable increase in interest in the problems of impact¹. This is due to their fundamental applications in electrophysics (dust impact initiated high-voltage discharge)⁽¹⁻³⁾, space physics (damage by space dust fluxes) and others. Especially important these problems have been eight years ago during the successful exploration of dust coma of Halley comet⁽⁴⁻¹⁴⁾.

1. Here we want to give a short review of the problem and our results and also to present our previously unpublished results (concerning the plasma chemistry). Let's begin with mechanics of impact. Let a ratio of a kinetic energy per striking atom to a solid state bound energy per atom or $(v/c)^2$ is large (where v is a velocity of dust and c is a sound speed). Then a ratio of volumes of the crater and the particle is also large. Formation of the crater takes a lot of time in comparison with an impact time d/v (where d is a dust size). This is due to a size of the crater and a low velocity of its formation. The spallation of a plate from a back side can take place in the case of a barrier⁽⁶⁻⁹⁾. It depends on a thickness of this barrier. A through passage is formed at a small thickness.

2. Above we consider mechanics of the crater formation. Now let's try to describe mechanics of emission of matter. A knowledge of an energy of an expansion is important for a study of a process of the charge generation (cooling and evolution of ion composition) and separation (extraction of ions from moving cloud). Our final goal is emitted mass distributions at an kinetic energy scale and in an angular space. We will call them energy $(\partial m/\partial E)$ and angular $(\partial^2 m/\partial\theta\partial\phi)$ distributions or $f(\vec{v}) = \partial m/\partial\vec{v}$ distribution². We have different distributions for matter of the particle ($f_d(\vec{v})$) and the target ($f_t(\vec{v})$). In $\mu < 1$ case the $f_d(\vec{v})$ function is rather simple, where μ is a ratio of initial densities ρ_d to ρ_t of the dust particle and the target³. It maybe characterized by one average velocity \bar{v}_d . For $\mu \simeq 1$ the \bar{v}_d is several times smaller than v . For $\mu \rightarrow +0$ we have $\bar{v}_d \simeq v \sin(\alpha)$, where α is an angle of impact (it is measured from the target). Matter of the target removed from the crater are emitted into a surrounding space. The distribution $f_t(\vec{v})$ is a more complicated function than $f_d(\vec{v})$. A computer simulation^(10,11) shows that the distribution $f_t(\vec{v})$ consists from three (2 + 3 + 4) parts, see Fig.1, where these parts are shown in circles. In an expansion velocity space \vec{v} the asymptotic distributions $f_d(\vec{v})$ and $f_t(\vec{v})$ are contiguous with each other at some contact boundary d/t . At Fig.1 a part 1 (it is marked by digit 1 inside a circle) corresponds to the distribution $f_d(\vec{v})$. The distributions $f_d(\vec{v})$ and $f_t(\vec{v})$ are shown by dash and solid lines correspondingly. An overlap of the $f_d(\vec{v})$ and $f_t(\vec{v})$ distributions at Fig.1⁴ is due to an integration of the $\partial m/\partial\vec{v}$ distribution with respect to velocities v_x and v_y which are parallel to the surface of the target⁵.

The part 2 (in a circle) at Fig.1 is a high velocity "head" of the distribution $f_t(\vec{v})$. Its integral mass is of order of a mass of the dust particle m_d . If the densities ratio μ is significantly larger than 1 then the part 1 will be inside the part 2. This means that the "head" will expand with higher velocities than matter of dust will do. The

¹For example, special conference has been organised rather recently by Academy of Science (National thermophysics and thermoenergetics council, Institute for high temperature, National council for low temperature plasma and others): "Physics and technics of high velocity impact", Vladivostok, 1990.

²(i) Usually all of these distributions are normalized at a mass m_d and velocity v of the colliding particle.

(ii) Asymptotically at $t/(d/v) \rightarrow \infty$ one-to-one correspondence of points in lagrangian and velocity spaces is settled.

³This ratio is an important parameter of the problem of impact^(10,11).

⁴It seems that this is inconsistent with an existence of the d/t contact boundary in \vec{v} space.

⁵Here x, y axes belong to a plane surface of a target and z axis is perpendicular to this surface.

part 3 corresponds to a power law band of the velocity distribution⁽¹⁰⁾. This part is a some "bridge" which joins the high velocity "head" (the part 2) and a low velocity "tail" (the part 4) of the distribution $f_t(\vec{v})$. A density of mass (per $(km/sec)^3$ or km/sec) raises in a low velocity direction. Therefore the "tail" is an "infrared cutoff" of masses involved in motion. It contains the most part of mass. It consists of vapour, droplets and solid spolation fragments. Matter in this "tail" moves slowly. Its velocities is some fraction of c .

3.0. Impact gives us an example of an "interference" of hydrodynamical (mechanical) and physical⁶ phenomena. Physics of charge production is a most important question from a point of view of a break-down of a vacuum insulation. Let's consider this question. Let χ is an ionization degree. Then a contribution dQ in a total charge of given mass dm with its own local degree of ionization is $dQ = (dm/\bar{m}_i)\chi$, where \bar{m}_i is an average ion mass. A juxtaposition of lagrangian ("frozen-in") "maps" of mass (M), ionization degree (χ)⁷ and charge (Q) are shown in Fig.1 (circles 1-4 correspond to parts of the emission cloud described above). High velocity parts 1 and 2 give a main contribution into the total charge. They are hatched in Fig.1 (hatched rectangles). Matter contained in these parts have gone a maximum heating during impact.

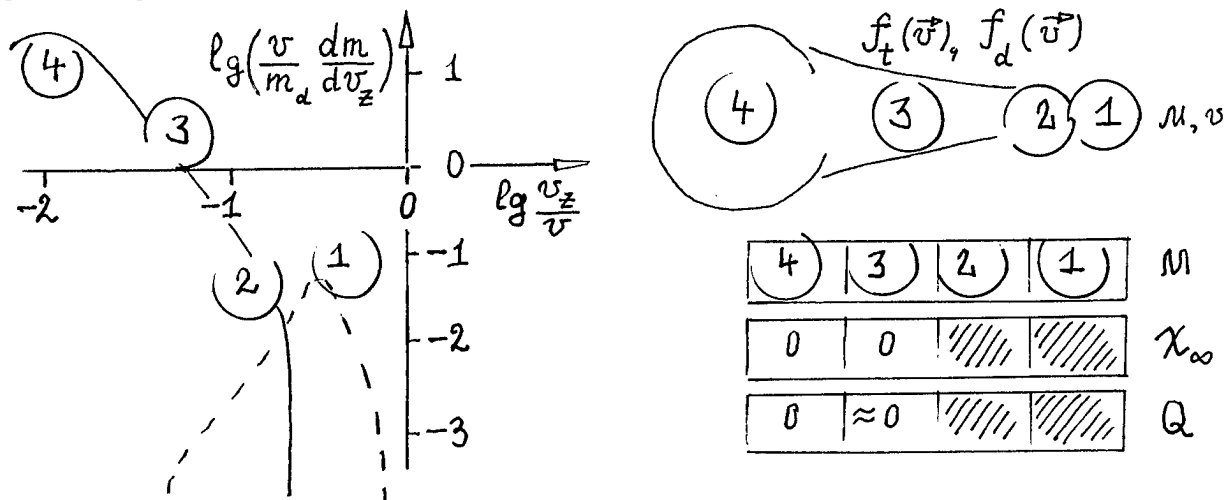


Fig.1. A structure of emission and a distribution of a residual ionization in emitted matter.

If we decrease velocity v of impact then a width of power law band (the part 3 in Fig.1) on a velocity axis will also decrease. The decrease of v leads to a coming together of characteristics of the parts 1 and 2 from one side to characteristics of the part 4 from another side. This leads to a decrease of the total charge. A case of very small⁸ values of χ requires to include into consideration a thermo- and autoelectronic and ionic processes at a surface. Here we consider the case of rather high velocity impact when the contribution of these processes is small. Now let's go to a description of our model.

3.1. The description consists of two parts. In the first we present an initial state of matter after impact. And in the second part (3.2) we describe an evolution of an ion composition during the expansion stage. This evolution is described by a system of ordinary differential equations. It is necessary to find an initial point to integrate this system. This point corresponds to the thermodynamic state after initial shock waves. A calculation of this state has been done in a following way. We have calculated shock adiabats for dust and target substances⁹. After that we have found an intersection of a pair of adiabats at an equal pressure. This intersection (Fig.2a) gives us the desired initial point. A free energy F have been approximated as a sum of ideal (electrons and ions) and non-ideal parts $F = F_{id} + F_{ss,e} + F_{ss,i} + F_{corr}$, where $F_{ss,e}$ and $F_{ss,i}$ are corrections due to an excluded volume for electrons and ions correspondingly and F_{corr} is a coulomb correction. This model are called a chemical model. It gives satisfactory values for an internal energy, temperature and ion composition. The only inadequacy is a excessive

⁶Physics of break down of substance at a load; equilibrium and non-equilibrium thermodynamics in a wide range of variation of parameters; plasma physics.

⁷Here is shown a distribution of a residual ionization χ_∞ . A definition of χ_∞ will be done below in chapter 3.2.

⁸In a very crude approximations the χ is of order of 10^{-6} in this case. Corresponding v is of order of several km/sec .

⁹It has been done for different pairs of substances, such as: H_2O , SiO_2 , Fe_2O_3 and Ag , Au , Pt .

softness of an equation of state¹⁰. We add terms F_{ss} , connected with the solid spheres volume (an index ss means solid spheres) to improve this. We forbid a stay inside spheres for electrons and ions both. This is a difference between our approach and an approach developed in a previous work⁽¹⁵⁾ of others authors. We choose such value for the relative volume of spheres ν to obtain experimental values for the compression, where ν is V_{ss}/V and V_{ss} is the volume of spheres. A variation of shock adiabats as a function of ν for Al are shown in Fig.2b. The best results have been obtained at $\nu = 7\%$ in matter before shock.

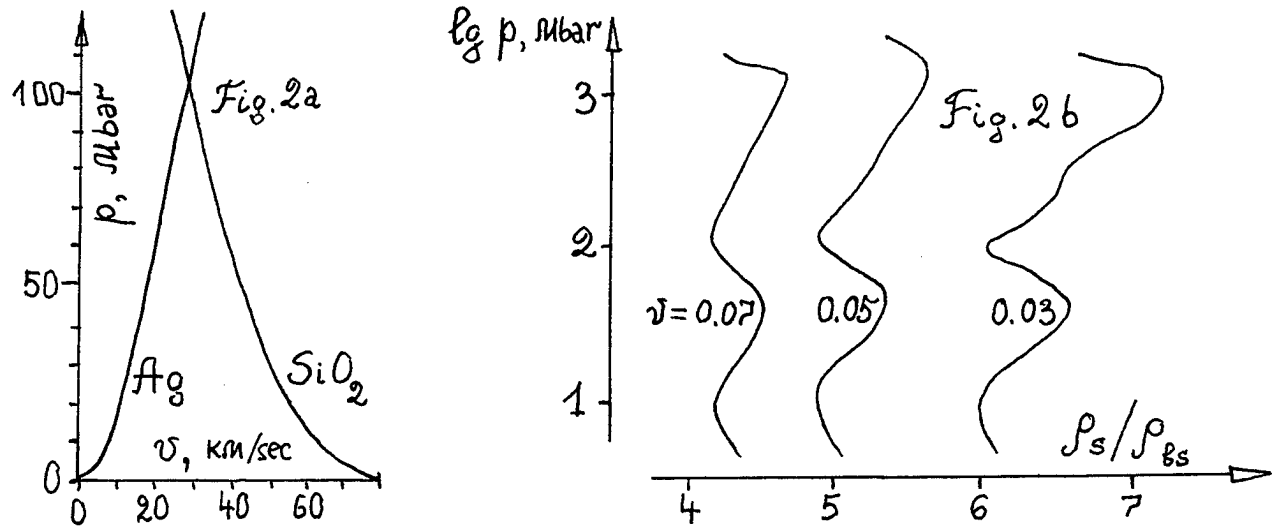


Fig.2a. The intersection of shock adiabats. Impact of Ag and SiO_2 with $v = 80 \text{ km/sec}$. Plasma parameters at the intersection point are: for SiO_2 : $\chi = 2.95$, $T = 42 \text{ e.V.}$, the internal energy $E = 280 \text{ e.V.}$, density after shock (g/cm^3) $\rho_s = 8.4$ and for Ag : $\chi = 4.05$, $T = 45 \text{ e.V.}$, $E = 397 \text{ e.V.}$ and $\rho_s = 37.7$. Fig.2b. An example of a family of adiabats for different values of ν , here ρ_{bs} is a solid state density before shock and ρ_s/ρ_{bs} is a compression factor.

3.2. Let's present a physical model of the evolution of the plasma composition. For an electrophysical applications the most important is a question about a residual ionization degree χ_∞ and a residual charge. An existence of χ_∞ is caused by a violation of a thermodynamic equilibrium. The evolution is described by a following system of kinetic equations: $dE/dt = -p\dot{V} - \dot{E}_{ehc} - \dot{E}_{rad}$; $dN_m/dt = \sum_n \Omega_{m,n} N_n$. Here the first equation describes a cooling ($p\dot{V}$, \dot{E}_{ehc} and \dot{E}_{rad} are mechanic, electron heat conduction and radiation losses) and the second the composition ($\Omega = \Omega^e + \Omega^{rad}$ are frequencies of collisional and radiation transitions). The internal energy equals to $E = 3(\chi+1)T/2 + W$, where $\chi = \sum_a \sum_m m N_{a,m}$, $N_{a,m}$ is a number of m -charged ions of element a . Indexes a and m numerates chemical elements in mixture and number of ionization¹¹ and $W = \sum_a \sum_m N_{a,m} Q_{a,m}$ is an energy stored in ionization, where $Q_{a,m} = \sum_{l=1}^m I_{a,l}$, $I_{a,l}$ -s are ionization potentials, $I_{a,0} = Q_{a,0} = 0$. The heat conduction losses are: $\dot{E}_{ehc} = 0.87 \cdot 10^{27} T^{3.5} v_h t / \chi / n$ ¹². Coefficients see^(16,17). The radiation losses are: $\dot{E}_{rad} = (\dot{E}_{bb}^{-1} + \dot{E}_{vol}^{-1})^{-1}$, where \dot{E}_{bb} is a black body radiation and \dot{E}_{vol} is a volume losses. The last equals to $\dot{E}_{vol} = \dot{E}_{bs} + \dot{E}_{phrec} + \dot{E}_{spnt}$, where \dot{E}_{bs} is a bremsstrahlung radiation, $\dot{E}_{phrec} = 3.72 \cdot 10^{-13} \chi \sum_a \sum_m (3T/2 + I_{a,m}) m^{2.4} N_{a,m} / V / T^{0.7}$ is a photorecombination and \dot{E}_{spnt} is a spontaneous lines emission due to transitions between excited states. Probabilities of spontaneous transitions have been calculated by Cramer's formula, populations of excited states have been estimated by Boltzmann formula and energies of excited states have been taken from reference book. Collisional matrixes Ω are: $\Omega_{m,m-1}^e = f_{elrec}(m \rightarrow m-1) = \beta \chi^2$, $\beta = 1.7 \cdot 10^{-28} \sqrt{I_{a,m}} / V^2 / T^{3/2}$ is a three body recombination, $\Omega_{m,m+1}^e = f_i(m \rightarrow m+1) = \alpha \chi$, $\alpha = 1 \cdot 10^{-6} \sqrt{I_{a,m}} e^{-I_{a,m+1}/T} / V$ is an electron shock ionization and $\Omega_{m,m}^e = -f_i(m \rightarrow m+1) - f_{elrec}(m \rightarrow m-1)$. Radiation matrixes Ω are photorecombination matrixes: $\Omega_{m-1,m}^{rad} = \phi_{phrec}(m \rightarrow m-1) = \alpha_{phrec} \chi$, $\alpha_{phrec} = 3.72 \cdot 10^{-13} m^{2.4} / V / T^{0.7}$, $\Omega_{m,m}^{rad} = -\phi_{phrec}(m \rightarrow m-1)$, $\Omega_{0,0}^{rad} = 0$.

¹⁰ A compression after shock wave is several times higher than an experimental one.

¹¹ We include multiple ions till to $m = 10$.

¹² Where \dot{E} is in e.V./sec , T and I in e.V. , $v_h (\text{km/sec})$ is a hydrodynamic expansion velocity taken from simulation of emission of matter after impact, t is a time in sec, $n (1/\text{cm}^3)$ is a density and V is a volume per particle in cm^3 .

The main difference between our model and those developed before^(13,18-21) is an inclusion of electron heat conduction losses¹³. It has been found, that this is important for small dust particles and high velocities of impact. Particularly it changes the dependence of χ on mass m_d in principal manner. In our model the dependence $\chi(m_d)$ has a maximum at some m_{crit} . In previous models $\chi(m_d)$ was a monotonic function. For v of order of several tenth of km/sec we have m_{crit} of order of $10^{-14} g$ (submicron particles). The decrease of m_d leads to the decrease of χ and to the increase of the coefficient of discrimination ξ of ions with high first potentials of ionization (see Table)¹⁴. In the case of oxides (double elements substances) ξ gives a ratio of the degree of ionization of element to degree of ionization of oxygen $\xi = \chi_{elmnt}/\chi_O$, $\chi_{elmnt=a} = \sum_m m N_{a,m} / \sum_m N_{a,m}$. If $\chi < 1$ then $\chi_{elmnt=a} \approx N_{a,1}/(N_{a,0} + N_{a,1}) \approx N_{a,1}/N_{a,0}$. An example presented in the Table is: *Ag* target, $v = 78 km/sec$, $\alpha = 30^\circ$.

Table. The fraction of the energy lost by the heat conduction, in the curly brackets values of χ_∞ and the coefficient of discrimination ξ . All of them as a function of a substance and mass of dust particle.

Mass (m_d), g	10^{-11}			10^{-14}			$10^{-15.5}$		
<i>H₂O</i> ($\bar{m}_i = 6$)	3%	{19%}	1	15%	{28%}	1	72%	{12%}	1
<i>SiO₂</i> ($\bar{m}_i = 20$)	3%	{69%}	2.3	19%	{70%}	2.2	45%	{43%}	2.5
<i>Fe₂O₃</i> ($\bar{m}_i = 33$)	4%	{71%}	2.3	27%	{73%}	2.3	88%	{12%}	6.8
<i>Fe</i> ($\bar{m}_i = 56$)	4%	{107%}		29%	{110%}		81%	{50%}	

4. A limitation of a text volume do not allow us to give a review of our results on self-consistent space charge.

5. Acknowledgments. This report have been prepared under a financial support of the Russian basic research foundation (RBRF), the project code is 93-02-3630. We also want to wish our coworkers E.N.Evlanov, S.B.Zhitenev, B.V.Zubkov, A.B.Konstantinov and V.N.Khromov.

REFERENCES

1. G.A.Mesyats and D.I.Proskurovskii, "Impulse electric discharge in vacuum," Nauka, Novosibirsk, 1984.
2. I.N.Slivkov, "Processes in high voltage in vacuum," Energoatomizdat, Moscow, 1986.
3. R.V.Latham, "High voltage vacuum insulation: the physical basis," Academic Press, London, 1981.
4. J.Kissel, R.Z.Sagdeev et al, "Comp.of comet Halley dust particles ...," *Nature*, Vol.321, pp.280-2, 1986.
5. R.Z.Sagdeev, S.I.Anisimov et al, "Tr.TOF MS imp.sour.ions," *Sov.Phys.Dokl.*, Vol.279, pp.613-7, 1984.
6. S.I.Anisimov, A.V.Bushman et al, "Phys.break down at high vel.impact," *JETP Lett.*, Vol.39, pp.9-12, 1984.
7. S.I.Anisimov, B.A.Demidov et al, "Sim.break.of Vega protect.by REB," *JETP Lett.*, Vol.41, pp.455-7, 1985.
8. V.A.Agureikin, S.I.Anisimov et al, "High vel.impact ...," *Teplophys.Visok.Temp.*, Vol.22, p.964, 1984.
9. S.I.Anisimov, V.P.Karyagin et al, "Exp.Foton on board Vega mission," *JETP Lett.*, Vol.44, p.477, 1986.
10. N.A.Inogamov, A.B.Konstantinov et al, "Emiss. at hypervel.IMP," *JETP*, Vol.99, pp.1699-1710, 1991.
11. S.I.Anisimov, S.B.Zhitenev et al, "Vel.distrib.emitt.matter...," *Sov.Tech.Ph.Lett.*, Vol.17, pp.57-61, 1991.
12. R.Z.Sagdeev et al, "...PUMA...," *Proc.20 ESLAB Symp.Expl.Halley,ESA*, SP-250, Vol.3, pp.345-8, 1986.
13. Yu.G.Malama, "Num.sim. ionization at high vel.impact," *Preprint Space Res.Inst.*, No.725, Moscow, 1982.
14. R.Z.Sagdeev et al, "...sensitiv.PUMA..ions prod.hyp.vel.IMP," *Astron.Astrophys.*, Vol.187, pp.179-82, 1987.
15. V.K.Gryaznov, I.L.Iosilevskii and V.E.Fortov, "...chem.model EOS," *Sov.Tech.Ph.Lett.*, Vol.8, p.1378, 1982.
16. D.R.Bates, D.Dalgarno, in: "At.Molec.Proc.," ed.D.R.Bates, Ac.Press, N.Y.-London, 1962.
17. L.M.Biberman et al, "Kinet.nonequil.low temper.plasma," Nauka, Moscow, 1982.
18. N.M.Kuznetsov, Yu.P.Raizer, *Zhurnal Prikladnoi Mekhaniki i Tekhn.Fiziki*, No.4, pp.10-9, 1965.
19. S.Drapatz and K.W.Michel, *Z.Naturforschung*, Band 29a, Heft 6, ss.870-79, 1974.
20. K.Hornung, S.Drapatz, "Resid.ioniz.after impact...," *Europ. Space Agency(ESA)*, SP-155, pp.23-32, 1982.
21. F.Arnaudean et al, "Giotto res.ion.," *Proc.Giotto PEWG Mtng,Switzerland, ESA*, SP-224, pp.21-35, 1984.

¹³Other differences are: (i) an approximation of an instantaneous "freezing" of the ion composition were frequently used and (ii) sometime authors did not calculate the thermodynamic state during the initial equilibrium stage of the expansion of matter and exchange the real dependence by an isoentropy curve with fixed index of adiabat γ .

¹⁴An oxygen and a hydrogen have the same potentials, therefore in the case of ice *H₂O* we have $\xi = 1$. A *Si* and *Fe* have smaller potentials, therefore in the case of significant cooling (if $\chi < 1$) we will have $\xi > 1$ and the ratio of numbers of single charged ions will not correspond to the stoichiometric ratio.

PHENOMENA OF FAULT ARC PROPAGATION ON CABLES AND WIRES FOR SPACE APPLICATIONS IN VACUUM, OXYGEN ENRICHED ATMOSPHERE AND AIR

F.R. Frontzek, D. König
Technical University of Darmstadt
High Voltage Laboratory
Landgraf-Georg-Str. 4
D-64 283 Darmstadt

M.D. Judd
ESA/ESTEC
Dept. QMO
Postbus 299
NL-2200 Noordwijk

H.J. Reher
DASA-ERNO
Abt. ROQ 115
Hünefeldstr. 11
D-28199 Bremen

ABSTRACT

Investigations of fault arc propagation on spacecraft cables under spacecraft specific conditions, e.g. vacuum, normal and oxygen enriched atmosphere have been performed. Typical patterns of fault arc extinction have been identified and their consequences with respect to causes of damages are discussed. The results indicate that for a given test current and test voltage the behaviour of the arc and the damages caused in a cable bundle depend strongly on the kind of insulation material, cable size and design as well as on the environmental conditions. For some cables the arc propagation effects are increased at higher oxygen partial pressure and significantly increased under vacuum. In many cases vacuum has turned out to be an important worst-case parameter. It was found that the amount of damage assessed by post-test measurements increases substantially, if the value of the test current grows.

1. INTRODUCTION

In many recorded incidents in air and space flights, the failure has been identified to be the result of fault arc propagation along bundles of polyimide cables through degradation of the insulation.^{1,2} At first this failure type was called "carbon arc-tracking" (because of the carbon or graphitic path created by thermal degradation of the insulation due to high arcing temperature) but the term "carbon" was quickly dropped and now even "tracking" seems inappropriate to describe this failure mechanism. At present, most accepted terminology refers to the process as "arcing failure" or "fault arc failure". This change in terminology follows the historical path of the phenomenon from the first identification of faults of polyimide cables to the analysis of the arcing effect on any cable insulation system. Aircraft organisations are aware of this phenomenon and have tried to provide solutions to cope with this new type of wire failure, i.e. modification of cable design and manufacturing processes as well as development of new test methods of cables. A comparison of some available "arc tracking" tests performed by TH Darmstadt and DASA-ERNO^{3,4} pointed out that these test methods and standards developed to qualify the aircraft cables do not cover the electrical and environmental conditions in spacecraft. Therefore a new test method should be established. Since the available database of arc failure testing of cables foreseen for application in spacecraft is very limited relevant investigations on harnesses under spacecraft specific conditions, e.g. vacuum, oxygen enriched atmosphere and normal air have been performed. The purpose of these investigations is to achieve fundamental information about the fault arc phenomenon and its relevance on spacecraft cables, especially its consequences for the operation ability of the spacecraft network. It is expected to achieve a database allowing one to develop a suitable test method for the assessment of fault arc resistance of different spacecraft cables.

2. TEST EQUIPMENT

A schematic diagram of the test system is given in Fig. 1. The test arrangement can be divided into seven independent units: the DC Power Source (1), the Power Control Unit (2), the Variable Resistor (3), Coil (4), Test Chamber (5), Vacuum and Gas System (6) and Measuring and Recording Devices (7). The DC power source (1) consisting of 11 DC battery elements of 12V/40 Ah in series and providing controlled voltage ranging from 12 V to 132 V is used to supply the electrical arc initiated on the cable bundle (test specimen). The power

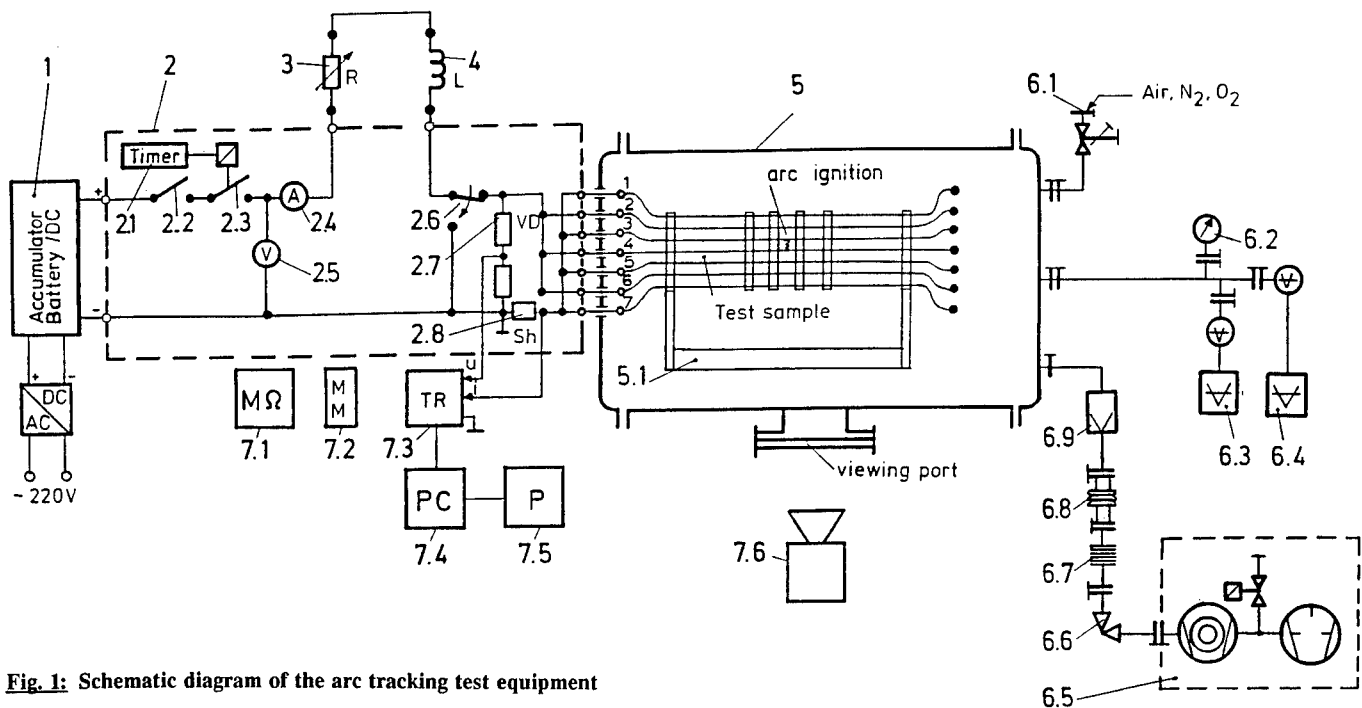
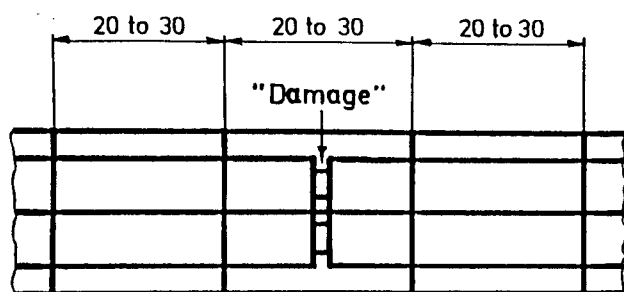


Fig. 1: Schematic diagram of the arc tracking test equipment

control unit (2) is used to switch on and switch off the test current and to adjust the relevant switching cycle and the test current value. A switching cycle is applied such as: C—ts—O—tp—C—ts—O, where C — close, O — open, ts — supply duration of 10 sec., tp — pause of 3 minutes. The power control unit consists of the following: manual safety disconnecting switch (2.2) and power contactor (2.3) controlled manually or by a timer (2.1), double-throw switch (2.6), measuring equipment such as meters for voltage (2.5) and current (2.4) as well as a voltage divider (2.7) and a shunt Sh (2.8) providing output signals for the transient recorder. A variable resistor (3) is provided for limiting the arc current and adjustment of the test current at the cable bundle under test. A coil (4) of 17 mH is applied for arc stabilizing. In order to conduct fault arc investigations under different environmental conditions, e.g. vacuum, oxygen enriched atmosphere, different internal pressure etc., the test chamber (5) is designed as a vacuum tube (T-shaped tube) made of stainless-steel of about 250 mm diameter and 50 cm length with two 250 ISO—K flanges at the tube ends. One of them is needed with respect to the connections to the vacuum and gas system and the other one is required as a carrier of the bushings being a part of the electrical system. An additional 250 ISO—K flange is used for the view port and is placed in the middle of the tube to enable visual observations. Inside the test chamber a mechanical support (5.1) is needed to stabilize the position of the test sample. The vacuum and gas system (6) consists of the turbomolecular pump and backing pump (6.5) with all necessary connecting and control elements for vacuum generation and internal pressure measurement. The pumping units produce hydrocarbon-free high and ultra-high vacuum (UHV) up to $1 \cdot 10^{-4}$ Pa. The pressure measurement system consists of two vacuum gauges for semivacuum (6.3) and UHV (6.4) and a manometer (6.2) for reduced pressure of about 10 ... 2000 hPa. The dosing valve (6.1) is used to adjust the gas pressure and the relevant gas mixture of O_2 and N_2 . Measuring devices such as AC RMS or DC current (2.4) and AC RMS or DC voltage (2.5) meters (precision 1%) is used for the measurement of the test current and test voltage. Arc current, arc duration and arc voltage are recorded by a transient recorder (7.3) with the help of a shunt (2.8) and a voltage divider (2.7). The test results are stored by the personal computer (7.4) and printed by a printer (7.5). A checker of conductor continuity and a megger of 500 V (7.1) is used for the post-test measurement and a video system (7.6) for the visual observation of testing.

The test specimen consists of an assembly of seven 200 to 250 mm long cables cut from a continuous piece. Each of the cable ends are stripped of insulation to permit electrical connection to the metallic terminals of the electrical circuit. Two of the cables of each cable bundle are damaged by inflicting a cut around the total circumference at the mid point of the total length by using a scalpel. The cut provides missing insulating material with a width of approx. 0.5 mm (Fig. 2). The two damaged cables are arranged with five undamaged cables in a six around one configuration as shown in Fig. 2. The cables 1 to 7 are numbered as shown in Fig. 2



View on arrow A

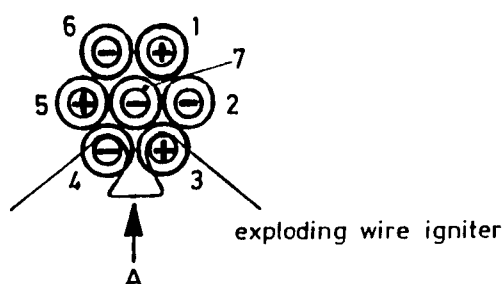


Fig. 2: Test sample configuration

Table 1: List of cable types tested

Sample No.	ESA SCC-SPEC	Wire Size AWG	Insulation Layers			
1/20	3901 001	20	PI	PI	PI (protective coating)	
1/12		12	"	"	"	
1 A/20	3901 002	20	PI	PI	(protective coating)	
2/20	3901 007	20	PI HR616	PI HR616	PTFE 50 % max. overl.	
3/20	3901 009	20	PTFE expanded	PI HR616	PI HR616	
4/20	3901 012	20	ETFE extruded			
5/20	-	20	Hybrid			
6/20	-	20	PTFE tape	PI 51 % overl.	PTFE varnish	
7/20	3901 013	20	PTFE expanded	PI coating		
8/12	3901 008	12	Gore-Tex	PI HR616	PI HR616	PTFE

ETFE = Ethylene Tetrafluoro-Ethylene; PI = Polyimide;
PTFE = Polytetrafluorethylene
HR616 = Special Design (see ESA SCC-Spec.)
Material of conductors/Plating: Copper/Silver

such that the damaged cables are number 3 and 4 and the centre cable is number 7. For the arc ignition one thin copper/silver strand of about 0.1 mm diameter and a resistance of about 2,0 Ω /m is used as an exploding-wire initiator, when connecting the two damaged cables in the area of the notches. The test specimen is arranged horizontally in the holder of the mechanical support inside the test chamber. One of the bundle ends is connected by means of a plug to the metallic terminals of the bushings at the test chamber flange while the other end of the bundle is connected to the terminal board of the holder (floating potential of terminals).

3. RESULTS

Investigations of the fault arc behaviour on cable bundles made of 9 different cable insulation systems (see Table 1) were performed with the help of the test system described above.

Test environments were defined as:

- normal air at atmospheric pressure
- dry gas mixture of 30% Vol O₂ and 70% Vol N₂ at a pressure of 700 hPa (socalled "emergency conditions")
- dry gas mixture of 24.5% Vol O₂ and 75.5% Vol N₂ at atmospheric pressure ("enriched oxygen conditions")
- vacuum ($p < 10^{-2}$ Pa).

Test currents were adjusted in the range of 6 A to 30 A at the quasi-constant test voltage of 125 V — 132 V,DC. Up to now more than 250 tests have been performed to gain basic understanding of physical phenomena related to fault arcs on cables and to define the main parameters of influence.

Transients of the arc current and the arc voltage provide very important information about the arc behaviour, e.g. arc ignition, arc burning and its extinction as well as the arc energy provided to the damaged part of the sample resulting from arc current, arc voltage and arc duration. Typical transients of the test current $i(t)$ and voltage $u(t)$ between the conductors during the time intervals T1 and T2 of the switching cycle are shown in Fig.3.

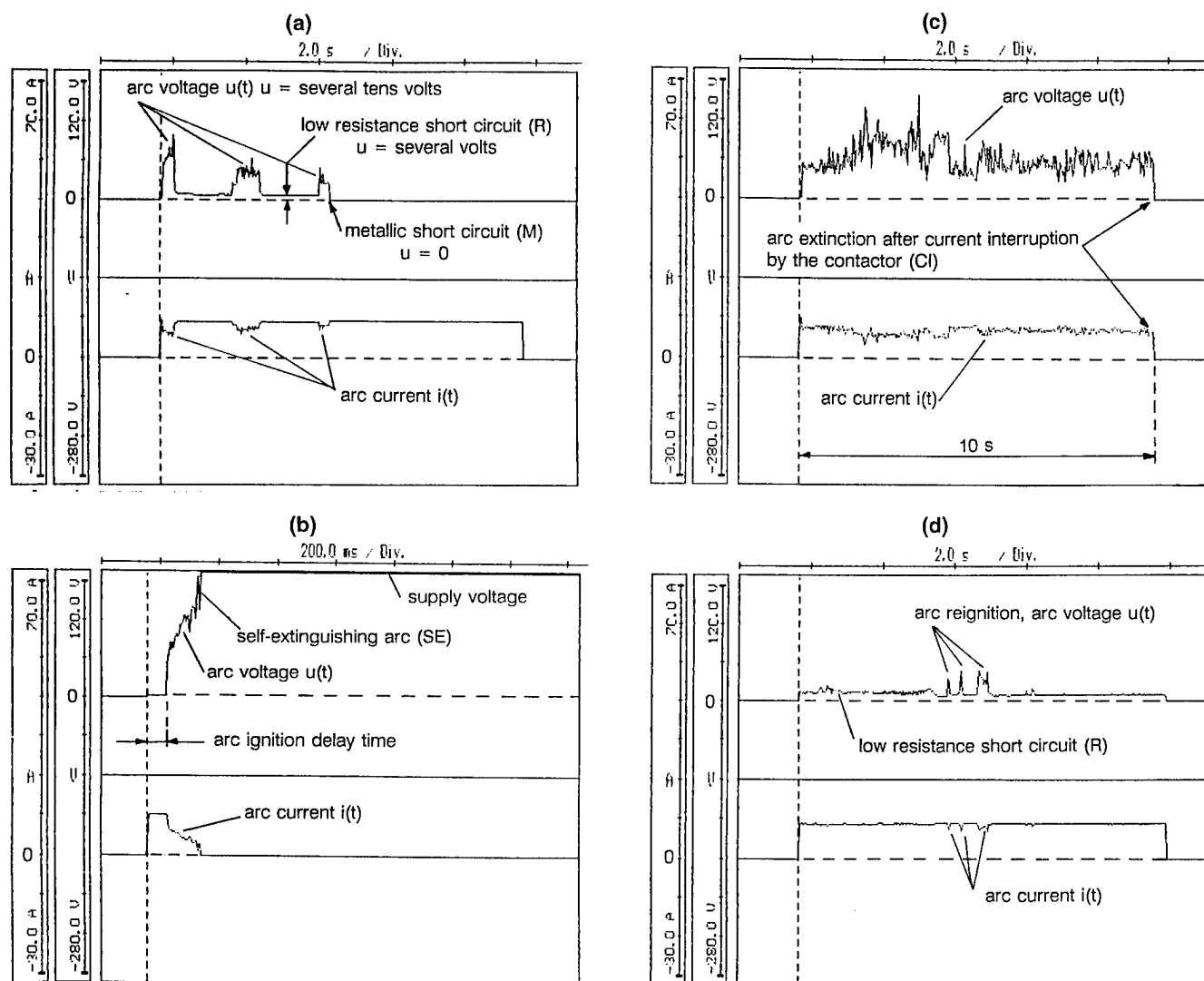


Fig. 3: Typical transients of test current $i(t)$ and voltage $u(t)$ between the conductors during the time interval T1 (a, b, c) and the time interval T2 (d) of the switching circle

Four typical cases of arc extinction have been observed:

- self-extinguishing arc (SE — Fig. 3b)
- arc extinction caused by metallic short circuit of conductors (M — Fig. 3a)
- arc extinction caused by low resistance short circuit of conductors (R — Fig. 3a)
- an arc extinction following the cut off of the current by the control contactor (CI — Fig. 3c).

After the arc extinction, the arc may reignite and the typical arc behaviour mentioned above may reappear, when the system is re-energised (time interval T2, Fig. 3d).

Mesurements of the following quantities were performed: arc duration, total arc path length, continuity check of conductors and insulation resistance before and after test as well as observations made with the help of the transient and video recorders. Fig. 4 shows average values of the arc duration obtained at testing of cables Nr. 2/20, 3/20 and 4/20 under different environmental conditions. The test current was 10 A and test voltage in the range of 125 V ... 132 V. For each environmental condition seven test specimens were used in case of cable types 2/20 and 3/20 and only two test specimens in case of cable 4/20. Arc path length is defined as the total length of the cable bundle, where the changes of cable insulation surface can be identified as a result of the arc activity. Fig. 5 shows the average values of the arc path length obtained at testing of the cable Nr. 2/20 and 3/20 under different environmental conditions. Average arc propagation velocity is defined as a quotient of the arc path length and the arc duration. Based on the individual results depicted of Fig. 4 and Fig. 5 the relevant average

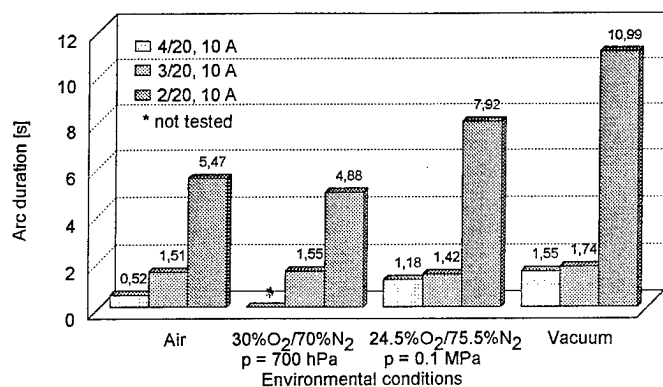


Fig. 4: Average values of arc duration for cables 2/20, 3/20 and 4/20 tested under different environmental conditions. Test current $I_t = 10$ A

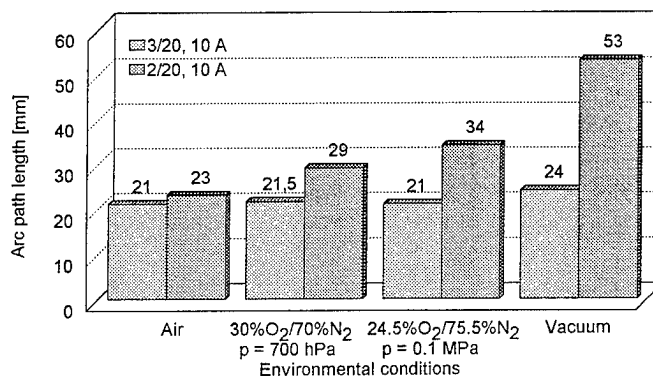


Fig. 5: Average values of arc path length for cables 2/20 and 3/20 tested under different environmental conditions. Test current $I_t = 10$ A

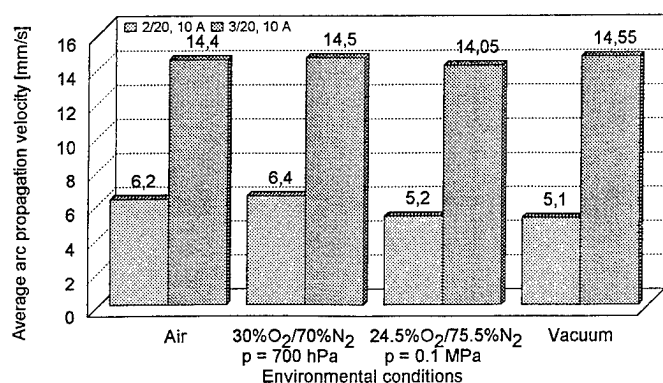


Fig. 6: Average values of arc propagation velocity for cables 2/20 and 3/20 tested under different environmental conditions. Test current $I_t = 10$ A

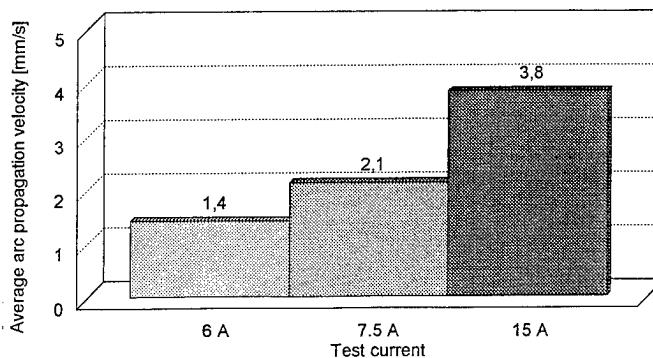


Fig. 7: Average values of arc propagation velocity for cable Nr. 8/12 tested at different test currents.

Table 2: Average values of arc duration, arc path length and arc propagation velocity evaluated by averaging the values obtained at different environmental conditions at a test current of 10 A for cable types: 1/20, 1A/20, 2/20, 3/20 and 4/20.

Cable type	Arc duration [s]	Arc path length [mm]	Arc propagation velocity [mm/s]	Number of tests performed
1/20	1.52	20	13.15	6
1A/20	1.49	25.5	17.1	6
2/20	7.99	38	4.75	19
3/20	1.55	22	14.2	22
4/20	1.06	17	16.0	6

values of arc propagation velocity are calculated and illustrated in Fig. 6. For two pure polyimide cables (1/20 and 1A/20), one pure ETFE insulated cable (4/20) and two hybrid cables (2/20 and 3/20) the average values of arc duration, arc path length and arc propagation velocity are calculated in such a way that the all test results obtained for a cable type are considered, averaging all data measured at different environments for a given test current. The result of calculations is presented in Table 2.

As an example, the dependence of the arc propagation velocity from the test current for the cable Nr. 8/12 is presented in Fig. 7.

Four further quantities are introduced in order to evaluate the damage caused by the fault arc. These are defined as follows:

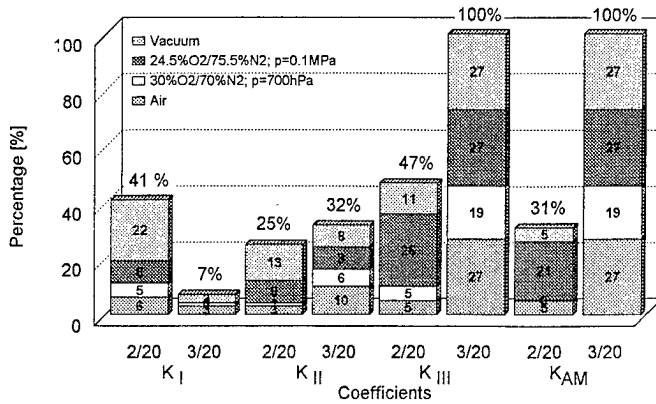


Fig. 8: Values of coefficients K_I , K_{II} , K_{III} and K_{AM} (defined in text) for cables 2/20 and 3/20 tested under different environmental conditions. Test current $I_t = 10$ A.

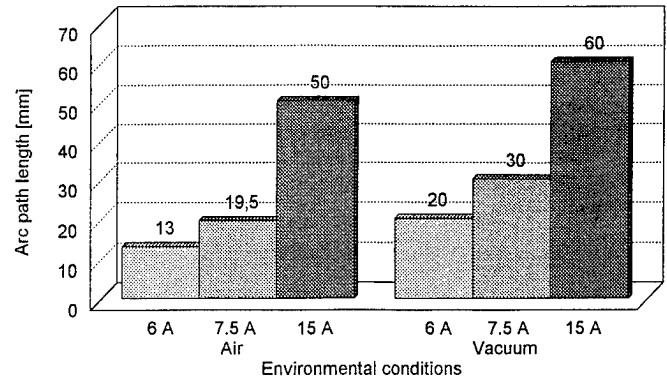


Fig. 9: Average values of arc path length for cable Nr. 8/12 tested at different test currents under normal air and vacuum.

$$k_I = \frac{\text{Number of cables with damaged conductor}}{\text{Number of cables tested}};$$

$$k_{II} = \frac{\text{Number of cables with damaged insulation}}{\text{Number of cables tested}}$$

$$k_{III} = \frac{\text{Number of tests, at which during the time interval T2 glowing or/and arcing was observed}}{\text{Number of tests performed for a given test current}}$$

$$k_{AM} = \frac{\text{Number of tests, at which during the time interval T2 the arc modes R/CI were observed}}{\text{Number of tests performed for a given test current}}$$

The values of the coefficients k_I , k_{II} , k_{III} and k_{AM} shown in Fig. 8 are based on post-test measurement results of continuity check of conductors and insulation resistance check as well as observations made with the help of transient and video recorders. The cable insulation is defined to be damaged if the insulation resistance is lower than $0.5 \text{ M}\Omega$. The test parameters are the same as those of Fig. 4, 5 and 6.

4. DISCUSSION

The amount of damage caused by the fault arc depends mainly on the arc duration, the electrical power delivered to the arc from the supply network being the product of instant values of arc voltage and arc current as well as the heat power generated as a result of chemical reactions initiated by the high temperature of the arc. On the other hand, the properties of the insulation materials used and the cable design strongly influence the fault arc and its behaviour. Interactions and feedbacks of different factors of influence make the total process even more complicated. The results obtained and the following considerations are intended to structure the knowledge and to discuss fault arc behaviour patterns and relevant consequences for the spacecraft network operation.

Short arc duration and self-extinguishing arcs (SE) as well as no arc reignition and no glowing after re-application the the power have been observed for ETFE insulated cables (Fig. 4, Tab. 2). At the same time the damage caused is minimised. However, the arc duration depends on the environmental condition. Increased arc durations are recorded for oxygen enriched atmosphere, whereas maximum arc duration occurs in vacuum (Fig.4). In case of pure polyimide insulated cables the arc duration is relatively short, too (Tab. 2) and nearly independent of the environmental conditions. However, the arc extinguishes as a result of the low-resistance short circuit of the conductor (R) and after reapplying the power to the cable bundle an arc and/or a glow propagation takes place (Fig. 8). A resistance (R) between conductors of some several hundred of $\text{m}\Omega$ to several Ω is a serious heat source in case of current flow. Depending on resistance and current values the heating power can be strong enough to cause glowing or reinitiation of the arc, which can subsequently propagate along the wire, resulting in the loss of an entire wiring harness. In spite of the use of similar insulating materials of the two hybrid cables 2/20 and 3/20 (see Table 1) their fault arc behaviour is quite different. While the relevant properties of the cable 3/20 are similar as those of pure polyimide cables, the properties of the cable 2/20 are a kind of mixture of a "arc self-extinction" and a "arc propagation" behaviour patterns. At the same test current

of 10 A the average arc duration of the cable 2/20 is significantly longer compared to that of cables 1/20, 1A/20, 3/20 and 4/20 (Tab. 2). Double PTFE layers between the conductors of a cable bundle seems to make it difficult to create a low resistance connection between the conductors. Therefore, in case of cable 2/20 a low-resistance short circuit of conductors is a rare event compared to polyimide cables (Fig. 8) and, if it happens at all more time is needed to create it (Tab. 2). Furthermore, the arc suppression property of PTFE seems to be less distinct than that of ETFE insulation. It was found that in case of cable insulation systems with basically dominant "self-extinguishing arc" behaviour, e.g. 2/20, 4/20 and 8/12 the amount of damage caused depends strongly on the test current (Fig. 9) and the environmental conditions (Fig. 4 and Fig. 5). The fault arc effects are increased in oxygen enriched atmosphere and significantly increased under vacuum. They decrease substantially, if the value of the test current is reduced (Fig. 7, Fig. 9). Therefore, it can be assumed that a threshold value of the test current exists, at which the amount of damage after testing is minimised and the neighbouring cables of the tested cable bundle are able to further operate in a spacecraft network. This threshold value can be used as a material test criterion to classify cables with respect to their fault arc resistance.⁵ The arc propagation velocity seems to be nearly independent from the environmental conditions (Fig. 6), but it is strongly influenced by the insulation system of the tested cable and the arc current (Fig. 7). For example, the arc propagation velocity of the cable Nr.2/20 (PI/PI/PTFE) is about three times lower than that of cable Nr.3/20 (PTFE/PI/PI).

5. CONCLUSIONS

The results obtained indicate that the damage caused by fault arcs depend strongly on the kind of insulation material, cable size and design, the test current value and the environmental conditions.

Four typical patterns of fault arc extinction (SE, M, R, CI) have been identified and their consequences with respect to causes of damage have been discussed. Two quite different behaviour patterns of fault arcs have been observed on ETFE and polyimide insulated cables. While the ETFE insulated cables show short arc duration and self-extinguishing arcs (SE) as well as no arc reignition and no glowing after reapplication of the power, the main characteristics of the pure polyimide cables on the other hand are an arc and/or a glow propagation along the wire after reapplying of the power to the cable bundle, being a potential hazard to lose an entire wiring harness.

For a certain cable type the average arc propagation velocity is nearly independent from the environmental conditions but increases when the test current grows. However, the severity of fault arc effects in terms of loss of conducting function of conductors and insulation damages depend on the environmental conditions. Compared to atmospheric air these effects are increasingly effective in oxygen enriched atmosphere and significantly increased under vacuum. Vacuum has turned out to be an important "worst case" parameter.

6. REFERENCES

1. J. Sylvester, "Aerospace Electrical Cable Arcing Failure", Report prepared at the request of MBB/ERNO, Bremen, Germany, January 1991.
2. M.W. Stavnes, A.N. Hammoud, "NASA Requirements and Applications Environments for Electrical Power Wiring", Proc. of 27th Intersociety Energy Conversion Engineering Conference, August 3 – 7, 1992, San Diego, CA, USA.
3. D. König, F.R. Frontzek, F. Dricot, H. Reher, M.D. Judd, "Principles of a New Arc Tracking Test of Cables and Wires for Spacecraft", Proc. of the Conference on Electrical Insulation and Dielectric Phenomena (CEIDP), October 18 – 21, 1992, Victoria, Canada, pp. 363 – 369
4. F. Dricot, H.J. Reher, "Survey of Arc Tracking on Aerospace Cables and Wires", Post-Deadline Proc. of the XVth Intern. Symp. on Discharges and Electrical Insulation in Vacuum, September 6 – 10, 1992, Darmstadt, Germany, pp. 24 – 30.
5. D. König, F.R. Frontzek, H. Reher, M.D. Judd, "A New Test Method for the Assessment of the Arc Tracking Properties of Wire Bundles in Air, Oxygen Enriched Atmosphere and Vacuum", to be published in Proc. of the 1994 Intern. Symp. on Electrical Insulation (ISEI), June 5 – 8, 1994, Pittsburgh, Pennsylvania, USA.

Vacuum insulation on the moon

Lloyd B. Gordon

University of Texas at Arlington, Department of Electrical Engineering
P.O. Box 19016, Arlington, Texas 76019

Krista L. Gaustad

Pacific Northwest Laboratory
P.O. Box 999 MS: K5-20, Richland, WA 99352

ABSTRACT

Vacuum insulation for high voltage electrical components has found widespread use in relatively small scale, controlled environments. Examples include vacuum tubes, vacuum switches, particle accelerators, and vacuum transmission lines. In general these applications utilize vacuum insulation over relatively small regions, when compared to air insulated transmission lines, and large scale solid and liquid dielectric components. In addition, the vacuum in such components is fairly well characterized and controlled.

In future space applications there will be increasing opportunity to utilize vacuum insulation on a much larger scale, and in environments with a much wider range of breakdown initiating stresses. Examples include high voltage solar arrays, pulse forming networks, and vacuum insulated power systems, used both in earth orbit and lunar base applications. These applications of vacuum insulation will present unique problems not encountered in typical vacuum components, including very large area electrodes, radiation, large thermal ranges, dust and gas contamination, and ionized plasma.

Vacuum insulation and high voltage experiments have been studied and discussed for the near earth orbit environment. Presentations at this conference and previously published work have covered such efforts. Little has been done, however, to present the challenges for large scale vacuum insulation for lunar base applications. This paper concerns the application of large scale vacuum insulation for the lunar environment, including vacuum-insulated large-area solar arrays, solid-state power converters, transmission lines, and manufacturing equipment. Voltages will potentially range up to 10's of kV with power levels up to 1 MW. This paper presents recent concepts and analysis on vacuum insulation issues in the lunar environment, including dust initiated breakdown, thermal management, gas contamination, and solar radiation effects.

1. POWER REQUIREMENTS FOR SPACE APPLICATIONS

As the application for electrical power systems in space increases there is a growing need for higher power levels. The high power requirements for large systems will promote an increase in the distribution voltage levels over those characteristically used in the past. Higher voltages are preferred over high currents in order to reduce the mass of the conductors of the power distribution system, and to assist in thermal management by keeping resistive losses to a minimum. In addition, many of the new applications will require higher voltage levels for operation. Systems include space platforms in earth orbit for research, defense, communication, and industrial applications; interplanetary spacecraft; and manned lunar/planetary bases.

Previous power levels in spacecraft have been limited to about 20 kW and exposed voltage levels have generally been below 200 V. For instance, Skylab used a power system at a bus voltage of 30 V supplying 20 kW. New space applications will require power levels approaching MWs and voltages up to 100's of kV. For example, the space station Freedom will initially have a power system supplying 75 kW at a bus voltage of 250 V [1]. Later growth of the station will require power levels up to 300 kW. High voltage solar array concepts propose exposed continuous voltage levels up to 570 V. The initial lunar base will have a 100 kW power system later expanding to include resource utilization units requiring power levels up to 1 MW. Interplanetary electrical propulsion concepts may utilize MW's of electrical power. In designing for voltages higher than 100's of volts, proper insulation is crucial to prevent electrical breakdown, and yet volume and mass must be kept to a minimum to minimize transportation costs. In addition, insulation lifetime is a key limiting factor in the reliability of electrical power systems. Reliability and lifetime are critical considerations for space applications due to inaccessibility, cost of replacement transport, and safety considerations for the crew.

2. VACUUM INSULATION

For space applications solid and liquid dielectrics are massive, and liquid and gaseous dielectrics are subject to loss. Solid dielectrics can be severely lifetime limited due to damage caused by stresses of the space environment such as radiation, temperature extremes, and microparticle impact. In order to minimize mass and exposure to the space environment, vacuum insulation is being considered for many space power applications, including large area solar arrays, power transmission, high power electronics, and manufacturing systems. Vacuum insulation of high voltage is used in earth applications such as power switchgear, particle accelerators, very high power transmission lines, and electronic devices. Under such controlled conditions very high breakdown strengths are achieved with long lifetimes.

For space applications high quality vacuum insulation systems would be ideally suited having minimum mass with high breakdown strength. Exposed to the space environment, however, reliability can be compromised by various stresses leading to electrical breakdown, including particulate and gaseous contamination, thermal degradation of materials, and radiation. These stresses affect the inter electrode gaps (breakdown voltages), the electrode surfaces (secondary electron emission), and the supporting dielectric materials (surface flashover).

3. VACUUM INSULATION IN EARTH ORBIT

Vacuum insulation may be utilized as electrical insulation in the power subsystems for the earth orbit environment. Special environmental considerations include: atomic oxygen, low gravity, ionizing radiation, thermal cycling, plasma, high velocity particle impact, and contamination [2]. Several system or component designs are under development for operation in the near earth space environment. For the Space Station Freedom large solar arrays 400 cells will be connected in series to produce 160 V dc. Taking all orbital environmental effects into consideration the 160 V dc is a compromise between the higher efficiency associated with high voltage and the lower probability of arcing associated with lower voltage [3]. Electronic subsystems include dc-dc converters between 160 V dc and 120 V dc buses [4].

The operation of high voltage components in the earth orbit vacuum environment has long been of concern for various satellites. Power supplies, solar arrays, high voltage wires [5], and traveling wave tubes must work reliably in the space vacuum. Transmission line designs for lengths up to 10 km have been proposed for the connection of nuclear power sources to a space station [6, 7].

4. VACUUM INSULATION FOR LUNAR POWER

Early phases of a lunar base will include an SP-100 or equivalent nuclear power source with an electric output of about 100 kW of electrical power. The first transmission of power will likely be a 100 kW, 5 km line from the nuclear power source to the habitat. The next phase will include large, high-voltage solar arrays and regenerative fuel cell systems with transmission to the habitat, science modules, and launch/landing facilities. Later phases will include a MW level power source (nuclear) to power resource utilization (mining and oxygen production) facilities. Solar arrays will most likely operate at levels from 150 V and up. Transmission lines, for efficiency, may operate at voltages up to 10 kV. Local buses and loads will operate, typically, at 10's to 100's of V. Thus, there will be power conversion distributed throughout the power system.

Critical areas of concern in the design of lunar base power systems are mass, reliability, and operation in the lunar environment. Mass and volume are very important due to the high cost of transportation of materials to the moon. Reliability is critical due to safety, inaccessibility, and cost of repair. The lunar environment presents a significant challenge for the operation of electrical power systems, specifically important issues include: vacuum, solar thermal radiation input, lunar surface temperature and thermal radiation characteristics, particulate radiation, micrometeoroid bombardment, lunar dust, gaseous contamination, night/day cycles, and ionizing radiation [8].

Vacuum insulation may find application in several power subsystems in a manned lunar base (see Fig. 1.). Large solar arrays will operate at 160 V and above. Using vacuum insulation for transmission lines can greatly reduce insulation mass and costs and has been proposed for both above ground and below the soil high-power transmission lines (up to 1 MW electrical power) [9]. To avoid the loss of gaseous and liquid dielectrics, and the degradation of solid insulation potting materials, vacuum insulation may find application in the high-power, solid-state converters used between sources, energy storage, transmission lines, local buses, and loads. Similarly, vacuum insulation may find application in the high power loads at the resource utilization equipment. For instance, oxygen production from the lunar regolith (soil) will require electrical power for mechanical equipment for crushing, pulverizing, and transport of soil material; heating circuitry for melting and chemical processes; and, control and monitoring.

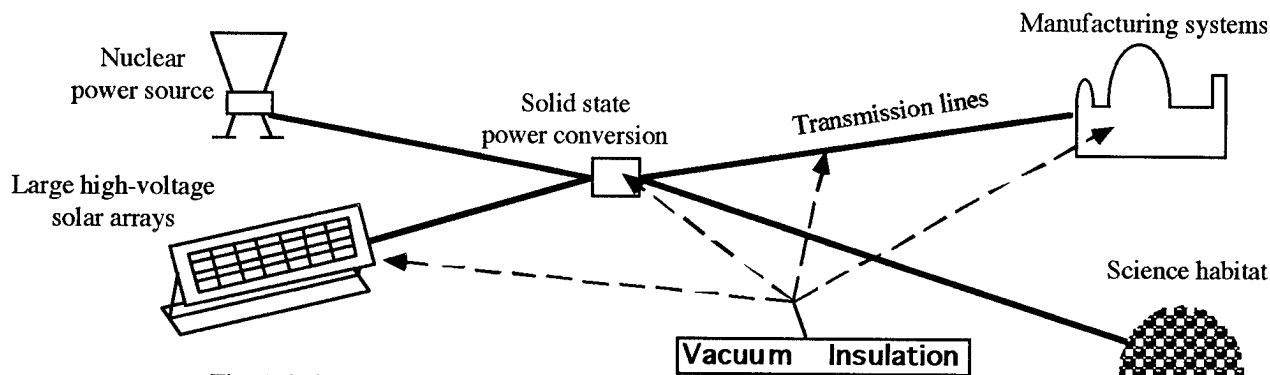


Fig. 1. Subsystems of a lunar base with potential locations of vacuum insulation.

5. BREAKDOWN ISSUES IN THE LUNAR ENVIRONMENT

There are a number of breakdown issues associated with the use of vacuum insulation in the lunar environment resulting from interaction with the lunar environment or human activities [10]. Breakdown between electrode gaps may be enhanced by interaction with (i) charged particles, (ii) gas contamination, (iii) lunar dust, and (iv) radiation. Electrode surfaces may have their secondary electron emission and microstructure characteristics altered by (i) surface contamination (gas or dust), (ii) thermal stresses, and (iii) radiation. Solid dielectrics used to support conducting structures can be damaged leading to bulk breakdown or surface flashover by (i) radiation, (ii) micrometeoritic impact, (iii) thermal cycling, (iv) exposure to vacuum, (v) surface contamination, and (vi) chemical degradation. And finally, for vacuum insulation structures near or in the lunar soil it will be important to characterize conduction, loss, thermal, and breakdown properties of the soil. Figure 2 illustrates some of the environmental factors which might affect, for instance, a vacuum-insulated transmission line.

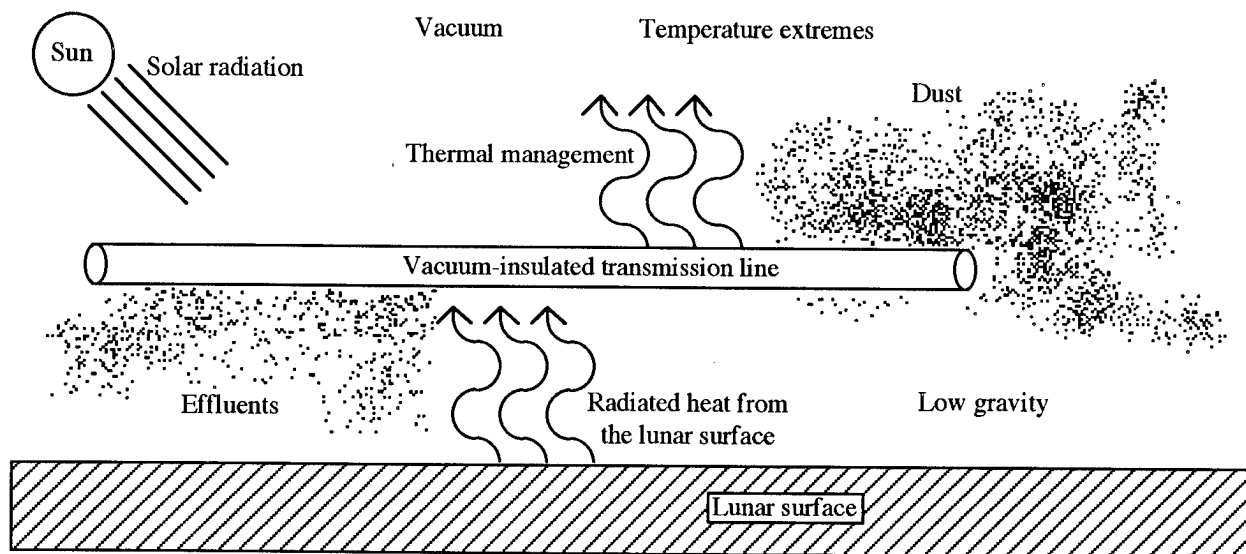


Fig. 2. Environmental considerations for vacuum insulation on the lunar surface.

The lunar vacuum is superior to that found in near earth orbit, in that there is no ambient plasma generating the problems of spacecraft charging, atomic oxygen erosion, and electrical breakdown. Nevertheless, the lunar environment can become contaminated by material outgassing, lunar base effluents, lunar dust, and micrometeoritic dust [11, 12]. The effects of gaseous contaminants are especially important near operations that deposit large amounts of effluents or dust in the vicinity of exposed high-voltage conductors. These conductors might be the large solar arrays or vacuum-insulated transmission lines. The sources of contamination might be rocket exhaust, hydrogen coolants, or the byproducts of a lunar manufacturing operation. Studies have been done to predict the effects of outgassing and effluent contamination of space vacuum around high voltage conductors [13,14]. Studies have included characterizing the nature of material outgassing as a function of material type, temperature, incident radiation, and history. Models were developed to predict the distribution of this gas around and within spacecraft structures as determined by the outgassing rates, the geometry of the structure, and the ambient pressure.

Although there is no significant ambient plasma on the lunar surface, there are mechanisms for charged particle generation [15, 16, 17]. Electrons in the vacuum environment will easily migrate possibly causing dielectric charging, leakage currents, and system noise.

Characteristics of high-power transmission line conductors exposed to simulated lunar soil in a vacuum environment have provided preliminary data [18]. The effects of the simulated lunar soil, the applied field strength, geometry and material of the transmission lines, and the ambient temperature on the operation of the high voltage transmission line were investigated. Experiments were conducted with parallel plate geometries and dc fields. The dc electrical characteristics of the simulated soil were studied for electric field strengths up to 4.4 kV/mm, including breakdown strength, dielectric constant, resistivity, and time dependency of these parameters.

6. CONCLUSIONS

Lunar bases will require the production, conversion, transmission, and utilization of electrical powers up to 1 MW at voltages as high as 10 kV. The cost of transportation and assembly, the unique lunar environment, and contamination generated by lunar base activities will result in new challenges for high voltage systems. Although vacuum insulation is a potentially ideal electrical insulation technique in the lunar environment the effects of environmental conditions and human activity on inter electrode breakdown strength must be considered. Although some effort has gone into the study of large solar array breakdown and simulated transmission lines there is uncertainty in breakdown thresholds, mechanisms, and long term reliability with such systems in the lunar environment.

7. REFERENCES

1. J. E. Maisel, "Identification of high performance and component technology for space electrical power," NASA-CR-183003, Dec. 5, 1988.
2. M. R. Curruth, J. A. Vaughn, and R. T. Bechtel, "Electrical breakdown of Space Station Freedom surfaces," Proc. of the 26th Intersociety Energy Conversion Eng. Conf. (IECEC), Vol. 1, pp. 357-361, Boston, Aug. 1991.
3. C. Y. Lu and H. K. Nahra, "Assessment of environmental effects on Space Station Freedom electrical power system," Proc. of the 26th Intersociety Energy Conversion Eng. Conf. (IECEC), Vol. 1, pp. 374-379, Boston, Aug. 1991.
4. D. K. Decker, L. Y. Inouye, and D. L. Rolandelli, "Multikilowatt power electronics development for spacecraft," Proc. of the 26th Intersociety Energy Conversion Eng. Conf. (IECEC), Vol. 1, pp. 104-109, Boston, Aug. 1991.
5. K. H. Geissler, "Intrinsic properties of high voltage wires that may cause sporadic discharges in space vacuum," Proc. of the European Space Power Conf., pp. 451-455, Madrid, Spain, Oct. 1989.
6. C. A. Switzer and D. J. Bents, "Coaxial tube array space transmission line characterization," pp. 565-570, Proc. of the 22nd Intersociety Energy Conversion Eng. Conf. (IECEC), Vol. 2, pp. 565-571, Philadelphia, Pennsylvania, Aug. 1991.
7. D. Bents, "Power transmission studies for tethered SP-100," Proc. of the 23rd Intersociety Energy Conversion Engineering Conference (IECEC), Vol. 3, pp. 733-741, Denver, Colorado, Aug. 1988.
8. J. E. Boretz and M. Koslover, "Synthesis of an Electrical Power System for a Manned Lunar Base," IEEE Trans. on Aerospace and Electronic Systems, Vol. AES-5, No. 5, pp. 770-788, Sept. 1969.
9. L. B. Gordon and K. L. Gaustad, "Vacuum Insulation for Lunar Transmission Lines", Proceedings of the XIVth Int. Symposium on Discharges and Electrical Insulation in Vacuum, pp. 768-773, Santa Fe, New Mexico, Sept 17-20, 1990.
10. L. B. Gordon, "The effects of extraterrestrial environments on high voltage distribution," Proc. of the 25th Intersociety Energy Conversion Engineering Conference (IECEC), Vol. 2, pp. 13-18, Reno, Nevada, Aug 12-17, 1990.
11. I. Fernini, J. O. Burns, G. J. Taylor, M. Sulkanen, N. Duric, and S. Johnson, "Dispersal of gases generated near a lunar outpost," J. Spacecraft, Vol. 27, No. 5, pp. 527-538, Sept./Oct. 1990.
12. J. E. McCoy and D. R. Criswell, "Evidence for a high altitude distribution of lunar dust," *Geochimica et Cosmochimica Acta*, Vol. 3, Supplement 5, pp. 2991-3005, 1974.
13. L. B. Gordon, J. Hamilton, J. Little, S. Merryman, and R. Phillips, "High voltage breakdown in the space environment," Proc. of the 6th Symp. on Space Nuclear Power Systems, pp. 749-754, Albuquerque, N. M., Jan. 1989.
14. L. B. Gordon, J. C. Little, and S. A. Merryman, "Breakdown Experiments in Gas Contaminated Vacuum Regions," Proc. of the 1989 Intersociety Energy Conversion Eng. Conf. (IECEC), pp. 2657-2662, Washington, D.C., Aug. 1989.
15. K. Knott, "Electrostatic charging of the lunar surface and possible consequences," J. of Geophysical Research, Vol. 78, No. 16, pp. 3172-3175, June 1973.
16. D. L. Reasoner, "Lunar nightside electron fluxes," Proc. of the 6th Lunar Sci. Conf., pp. 3023-3032, 1974.
17. B.E. Goldstein, "Observations of electrons at the lunar surface," J. of Geo. Res., V. 79, No. 1, pp. 23-35, Jan. 1974.
18. H. Kirkici and M. F. Rose, "High voltage transmission line operation in simulated lunar environment," Proc. of the 9th IEEE International Pulsed Power Conf., to be printed, Albuquerque, New Mexico, June 1993.

SESSION 8

Emission Processes

Thin superconducting films at field emission.

S.A. Barenholts, E.A. Litvinov, and I.V. Uimanov.

Institute of Electrophysics
Ural Division, Russian Academy of Sciences
Ekaterinburg 620219, Russia

ABSTRACT

An analysis of the kinetics of the electron subsystem of a superconductor based on a model with a phonon thermostat has shown that the nonequilibrium state of a superconducting thin-film cathode that appears at field emission changes the superconducting properties of the cathode as compared to the equilibrium state. The dependence of the superconducting gap on the intensity of the emissive source has been obtained.

1. INTRODUCTION

It is known that one of the principal reasons for breaking a vacuum electrical insulation is the heating and further destruction of the microprotrusions present on the cathode under the action of field emission current. The state of superconductivity eliminates one of the principal sources of heat release in field emission, the Joule heating. However, using superconducting field emission cathodes has not led to an increase in limiting field emission current densities^{1,2}.

The destroy of the superconducting state was related to the heat release due to the Nottingham effect. At the same time the problem concerning the efficiency of harnessing the phenomenon of superconductivity to increase the electric strength of a vacuum gap remains unresolved. The matter is that using thin superconducting films of thickness $\ell < \xi_0$ (where ξ_0 is the coherence length at $T = 0$) makes it possible to eliminate heating processes in the phonon subsystem of the superconductor. Under this condition, the phonons radiated in the process of relaxation of nonequilibrium electrons have time to leave the film and have no influence on their parent electron subsystem.

The present work is an extension of our preceding studies where it has been shown that field emission being a source of nonequilibrium in the electron subsystem of a superconductor may cause the cathode, at temperatures close to the superconducting transition temperature, to lose its superconducting properties^{3,4}. The paper presents the results of a study of the nonequilibrium processes at field emission from thin superconducting films at any temperature under the conditions where "heating" processes in the phonon subsystem can be neglected.

2. PROBLEM STATEMENT

The study of the nonequilibrium effects that take place at field electron emission from thin superconducting films is based on analyzing the kinetics of the electron subsystem of the superconductor in terms of a model with a phonon thermostat. The applicability condition for this model that imposes constraints on the film thickness ℓ and the character of its heat exchange with the surroundings are described, for instance, in Ref. 5.

It is also known that the characteristic scale of disturbances in the electron subsystem being of the order of the diffusion length of the quasiparticles l_E , is much greater than ℓ chosen in accordance with the above-mentioned condition, what allows one to assume that the problem is uniform with respect to the film thickness.

Consider a superconducting film of thickness ℓ to which an external electric field F_0 high enough for field emission to occur from the film surface is applied. Then the kinetic equation for the nonequilibrium energy distribution function for quasiparticles in quasi-steady-state case can be written as

$$Q^\pm(\varepsilon) + I^{(e-ph)}[n^\pm(\varepsilon)] = 0 \quad (1)$$

where $Q^\pm(\varepsilon)$ is the emissive source of quasiparticles which is just the source of nonequilibrium in the system, $I^{(e-ph)}[n^\pm(\varepsilon)]$ is the integral of electron-phonon collisions, $n^\pm(\varepsilon)$ is the quasiparticle energy distribution function

of the electron $n^+(\varepsilon)$ ($\xi_k > 0$) or hole $n^-(\varepsilon)$ ($\xi_k < 0$) type, respectively, $\varepsilon = \sqrt{\xi_k^2 + \Delta^2}$ is the quasiparticle energy reckoned from the level of the chemical potential for Cooper's pairs μ_s , $\xi_k = \frac{\hbar^2 k^2}{2m} - \mu_s$ is the single-particle energy for the Bloch state with a quasiwave vector \mathbf{k} , Δ is the superconducting gap.

For the case of an isotropic excitation distribution in the momentum space, the collision integral in accordance with Ref.5, can be written as:

$$I^{(e-ph)}[n^\pm(\varepsilon)] = \frac{\pi\lambda}{4(up_F)^2} \int_0^\infty \omega_q^2 d\omega_q \int_\Delta^\infty \frac{\varepsilon' d\varepsilon'}{\sqrt{\varepsilon'^2 - \Delta^2}} \times \\ \left\{ S_1(n^\pm, N_{\omega_q}, \Delta) \delta(\varepsilon' - \varepsilon - \omega_q) + \right. \\ S_2(n^\pm, N_{\omega_q}, \Delta) \delta(\varepsilon - \varepsilon' - \omega_q) + \\ \left. S_3(n^\pm, N_{\omega_q}, \Delta) \delta(\varepsilon + \varepsilon' - \omega_q) \right\}, \quad (2)$$

where the factor $S_{1,2,3}(n^\pm, N_{\omega_q}, \Delta)$ are defined as:

$$S_1(n^\pm, N_{\omega_q}, \Delta) = A^\pm(\varepsilon, \varepsilon', \Delta) \left\{ n_{\varepsilon'}^+(1 - n_\varepsilon^\pm)(1 + N_{\omega_q}) - n_\varepsilon^\pm(1 - n_{\varepsilon'}^+)N_{\omega_q} \right\} + \\ A^\mp(\varepsilon, \varepsilon', \Delta) \left\{ n_{\varepsilon'}^-(1 - n_\varepsilon^\pm)(1 + N_{\omega_q}) - n_\varepsilon^\pm(1 - n_{\varepsilon'}^-)N_{\omega_q} \right\}, \quad (3)$$

$$S_2(n^\pm, N_{\omega_q}, \Delta) = A^\pm(\varepsilon, \varepsilon', \Delta) \left\{ n_{\varepsilon'}^+(1 - n_\varepsilon^\pm)N_{\omega_q} - n_\varepsilon^\pm(1 - n_{\varepsilon'}^+)(1 + N_{\omega_q}) \right\} + \\ A^\mp(\varepsilon, \varepsilon', \Delta) \left\{ n_{\varepsilon'}^-(1 - n_\varepsilon^\pm)N_{\omega_q} - n_\varepsilon^\pm(1 - n_{\varepsilon'}^-)(1 + N_{\omega_q}) \right\}, \quad (4)$$

$$S_3(n^\pm, N_{\omega_q}, \Delta) = B^\mp(\varepsilon, \varepsilon', \Delta) \left\{ (1 - n_{\varepsilon'}^+)(1 - n_\varepsilon^\pm)N_{\omega_q} - n_\varepsilon^\pm n_{\varepsilon'}^+(1 + N_{\omega_q}) \right\} + \\ B^\pm(\varepsilon, \varepsilon', \Delta) \left\{ (1 - n_{\varepsilon'}^-)(1 - n_\varepsilon^\pm)N_{\omega_q} - n_\varepsilon^\pm n_{\varepsilon'}^-(1 + N_{\omega_q}) \right\}, \quad (5)$$

$$A^\pm(\varepsilon, \varepsilon', \Delta) = 1 \pm \frac{\sqrt{\varepsilon'^2 - \Delta^2} \sqrt{\varepsilon^2 - \Delta^2}}{\varepsilon' \varepsilon} - \frac{\Delta^2}{\varepsilon' \varepsilon}, \quad (6)$$

$$B^\mp(\varepsilon, \varepsilon', \Delta) = 1 \mp \frac{\sqrt{\varepsilon'^2 - \Delta^2} \sqrt{\varepsilon^2 - \Delta^2}}{\varepsilon' \varepsilon} + \frac{\Delta^2}{\varepsilon' \varepsilon}, \quad (7)$$

Here, u is the velocity sound, p_F is the quasi-momentum of an electron at the Fermi surface, $\lambda = \frac{mp_F}{2\pi^2} g^2$ is the dimensionless parameter of electron-phonon interaction, and g is the constant of electron-phonon interaction.

The presence in Eq. (2) the terms, which describe scattering processes where the number of quasiparticles is not preserved, causes the need to use additionally in this calculation scheme the continuity equation for the space charge density. This equation allows one to find, up to the terms of a first order infinitesimal in $\delta\mu_s$, an expression for the superconducting component for the case where the energy distribution function for quasiparticles deviates from equilibrium in the form

$$\delta\mu_s = - \int_\Delta^\infty [n^+(\varepsilon) - n^-(\varepsilon)] d\varepsilon, \quad (8)$$

where $\delta\mu_s = \mu_s - \varepsilon_F$, ε_F is the energy of Fermi.

For a great deviation of the electron system from equilibrium, the order parameter modulus Δ (which, for the case of spatial uniformity, can be chosen real and has the sense of a nonequilibrium gap) should be determined from the self-consistency equation⁵

$$1 = \lambda \int_{\Delta}^{\infty} \frac{1 - n^+(\varepsilon) - n^-(\varepsilon)}{\sqrt{\varepsilon^2 - \Delta^2}} d\varepsilon. \quad (9)$$

3. THE EMISSIVE SOURCE OF QUASIPARTICLES

The emissive source in Eq.(1) determines the time variation of the average number of quasiparticles with a given energy ε per unit volume in the superconducting film. The general equation for $Q^{\pm}(\varepsilon)$ can be written as

$$Q^{\pm}(\varepsilon) = \frac{1}{\ell \Sigma} \sum_{\mathbf{k}} \Gamma_{\mathbf{k}} \delta(\varepsilon - E_{\mathbf{k}}), \quad (10)$$

where $\Sigma = \sum_{\mathbf{k}, \sigma} \delta(\varepsilon - E_{\mathbf{k}})$ is the energy of a quasiparticle in the \mathbf{k} state, and the function $\Gamma_{\mathbf{k}}$ defines the quasiparticle flux from the given state characterized by the wave vector \mathbf{k} .

To calculate $\Gamma_{\mathbf{k}}$ the tunnel Hamiltonian method, first applied for the description of field emission in Ref.6, was used. We have obtained the following expression for $Q^{\pm}(\varepsilon)$:

$$Q^{\pm}(\varepsilon) = \mp \nu \frac{\sqrt{\varepsilon^2 - \Delta^2}}{\varepsilon} \left\{ \frac{1}{2} \left(1 \mp \frac{\sqrt{\varepsilon^2 - \Delta^2}}{\varepsilon} \right) \pm \frac{\sqrt{\varepsilon^2 - \Delta^2}}{\varepsilon} n^{\pm}(\varepsilon) \right\} \exp \left(\frac{\delta \mu_s \pm \sqrt{\varepsilon^2 - \Delta^2}}{d} \right), \quad (11)$$

where ν can be defined as a characteristic tunnel frequency at field emission

$$\nu = \frac{J_{\text{FN}}}{e d \ell 2N(0)} \quad (12)$$

Here J_{FN} is the emission current density in the Fowler-Nordheim theory, e is the electron charge, $2N(0)$ is the density of states at the Fermi level.

An analysis of Eq.(11) shows that $Q^+(\varepsilon) \neq Q^-(\varepsilon)$ and, moreover, these functions are opposite in sign what should inevitably lead to a disbalance in the population of the electron and hole spectrum branches in the system where the given source of nonequilibrium operates.

4. SOLUTION OF THE KINETIC EQUATION

The presence in Eq.(1) of a comparatively complex, in mathematical sense, term (the term describing electron-phonon collisions) causes the need to solve numerically the kinetic equation. In order that the generality of the solution to be obtained be preserved, it is convenient to rewrite Eq.(1) in a parametric form. First of all, integration in Eq.(2) with respect to ω_q using delta-functions and introduction, in accordance with Ref. 5, of an effective time for the relaxation in energy in normal state, τ_E , as

$$\frac{1}{\tau_E} = \frac{\pi \lambda (k_B T_c)^3}{4(u p_F)^2}. \quad (13)$$

reduces Eq.(2) to the form

$$I^{(e-ph)}[n^{\pm}(\varepsilon)] = \frac{1}{\tau_E (k_B T_c)^3} \left\{ \int_{\varepsilon}^{\infty} \frac{\varepsilon'(\varepsilon' - \varepsilon)^2 d\varepsilon'}{\sqrt{\varepsilon'^2 - \Delta^2}} S_1(n^{\pm}, N_{(\varepsilon' - \varepsilon)}, \Delta) + \int_{\Delta}^{\varepsilon} \frac{\varepsilon'(\varepsilon - \varepsilon')^2 d\varepsilon'}{\sqrt{\varepsilon'^2 - \Delta^2}} S_2(n^{\pm}, N_{(\varepsilon - \varepsilon')}, \Delta) + \int_{\Delta}^{\infty} \frac{\varepsilon'(\varepsilon + \varepsilon')^2 d\varepsilon'}{\sqrt{\varepsilon'^2 - \Delta^2}} S_3(n^{\pm}, N_{(\varepsilon + \varepsilon')}, \Delta) \right\}. \quad (14)$$

Recall that the kinetic equation for n^\pm involves a nonequilibrium gap, which depends of itself on the form of n^\pm . It can readily be shown that for case under consideration Eq.(9) is equivalent to the set of equations Ref.5:

$$\Delta = \Delta_0 \exp(-\bar{n}_+ - \bar{n}_-), \quad \bar{n}_\pm = \int_{\Delta}^{\infty} \frac{n^\pm(\varepsilon) d\varepsilon}{\sqrt{\varepsilon^2 - \Delta^2}}, \quad (15)$$

which can be included conveniently into overall iteration scheme.

The behavior of the nonequilibrium distribution function for excitation is illustrated by Fig.1 a,b. This figure presents the calculation results for Nb film. However, the procedure of seeking a solution of itself suggest that the qualitative picture will be the same for other metallic superconductors.

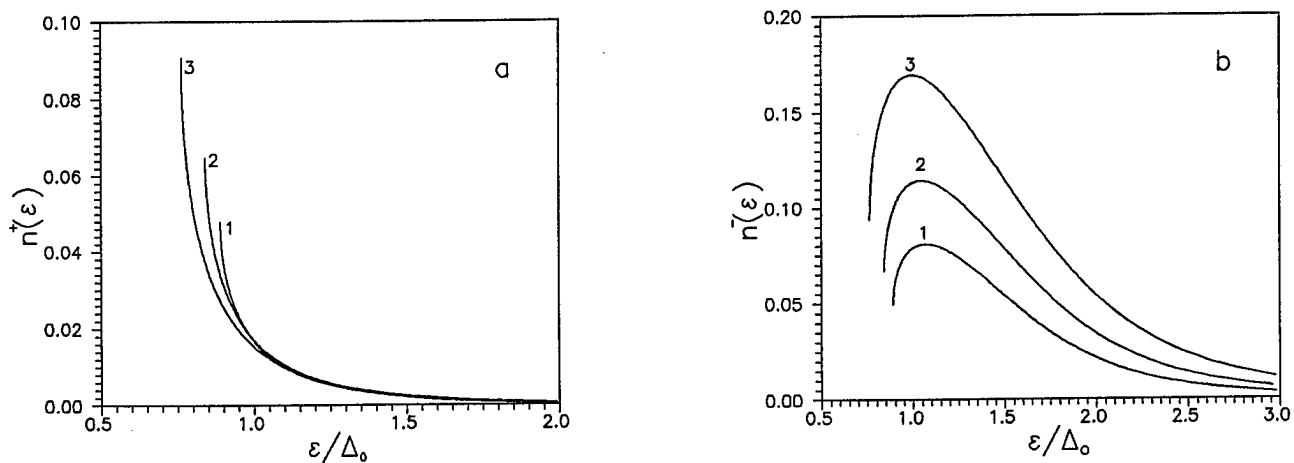


Fig. 1. Distribution functions for the electron- and hole-like excitations at $T = 0.2\Delta_0$: 1. $\alpha = 0.15$, 2. $\alpha = 0.3$, 3. $\alpha = 0.6$.

First of all, note the disbalance between the electron-like and hole-like excitations, that takes place in fact in any nonequilibrium situation. This confirms the conclusion that the properties of the emissive source of nonequilibrium are such that they should cause this disbalance and thereby determine the form of the nonequilibrium energy distribution function for quasi-particles. According to Eq.(8), the value of the disbalance directly determines the variation in the chemical potential of Cooper's pairs. The value of $\delta\mu_s$ of itself determines the value of electric field potential in a superconductor and it is always positive⁷. Therefore, the presence of extra excitations in the hole branch results in an an increase in the chemical potential of Cooper's pairs. From the viewpoint of emissive properties, this may be treated as a decrease in "emissive work function".

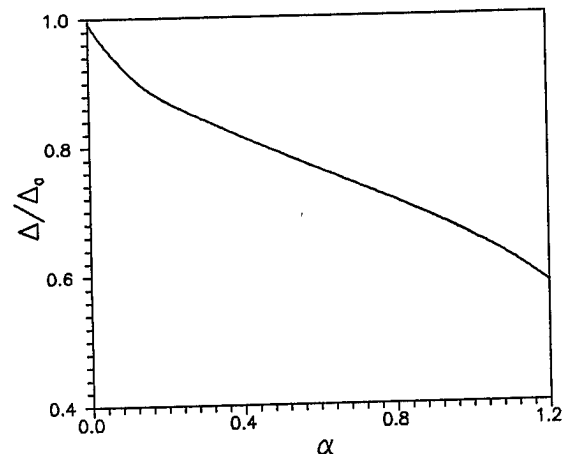


Fig. 2. Dependence of the superconducting gap Δ from the intensity of the emission source of the quasiparticles α at $T = 0.2 \Delta_0$.

Increasing the applied electric field (which is just responsible for an increase in $\alpha = \nu\tau_E$ in our consideration) substantially increases the degree of nonequilibrium, all excess excitations being concentrated in the region above the gap. This decreases the superconducting gap Fig. 2. and hence the critical parameters of the superconductor.

5. CONCLUSION

Thus, the above described analysis of the kinetics of the electron subsystem of a superconductor, performed in terms of a model with a phonon thermostat, allows the conclusion that using thin superconducting films will not increase the electric strength of a vacuum gap. Even with no heat release in the phonon subsystem of such a film, the field emission process of itself changes the electron subsystem, which may cause the film to lose its superconducting properties. At the same time, the performed study opens prospects for investigating fundamental properties of superconductors by field emission methods, and the way for controlling the superconducting properties of thin films by varying the field emission current can be used in the creation of various devices whose operation is based on the properties of nonequilibrium superconductivity.

The work is supported by Russian Foundation for Fundamental Research Grant No. 93-02-16878.

6. REFERENCES

1. G.N. Fursey, V.M. Zhukov, and L.M. Baskin, "Limiting FE Current Densities and Preexplosion Effects", in *Emission High Current Electronics*, Ed. G.A. Mesyats, Novosibirsk: Nauka, pp. 21-41, 1984 (in Russian).
2. S.A. Barengolts, S.I. Shkuratov, E.A. Litvinov, V.G. Mesyats, and V.F. Puchkarev, "Pulsed Electric Current and the Value of Critical Current at Cryogenic Temperature" *IEEE Trans. on Electr. Insul.*, Vol. 25, pp. 351-354, 1990.
3. N.E. Alekseevsky, "The Effect of Emission Current on Critical Parameters of Tantalum", *Dokl. AN SSSR* Vol. 242, pp. 816-818, 1978 (in Russian).
4. S.A. Barengolts, E.A. Litvinov, and I.V. Uimanov, "Superconducting switch based on field emission", *Pisma ZhTF (JTP Letters)* Vol. 19, No 19, pp. 20-23, 1993.
5. A. M. Gulyan and G. F. Zharkov, *Superconductivity in External Fields*, Moscow, Nauka, 1990.
6. J.W. Gadzuk, "Many-Body Tunneling Theory Approach to Field Emission of Electrons from Solids", *Surf. Sci.*, Vol. 15, pp. 466-482, 1969.
7. S.A. Barengolts, E.A. Litvinov, I.V. Uimanov, "Nonequilibrium effects in field emission from superconductors", *Surf. Sci.*, Vol. 266, pp. 132-136, 1992.

Field emission from nanometer protuberances at high current densities

G.N. Fursey, D.V. Glazanov,
S.A. Polezhaev

St.-Petersburg Bonch-Bruévitsch
Telecommunications University, Russia

The appearance or initial existence of microtips on the cathode surface is one of the main reasons of prebreakdown field emission (FE) currents^{1,2}. Thermal explosion of these tips leads to explosive electron emission and initiating of vacuum breakdown. In the last years the sufficient role of super small tips (10^{-6} - 10^{-7} cm) in prebreakdown phenomena and initiating vacuum breakdown^{1,3} was established. The amplification of electric fields on such tips leads to very high FE current densities ($J > 10^{10}$ A/cm²). So, the creation and decay of nanometer structures define the dynamics of the vacuum breakdown development. The investigations of FE from nanometer formations are very actual, as the emission properties and stability of such structures are connected with the problems of field cathodes fabrication and exploitation in the devices of vacuum micro- and nanoelectronics. In this report the results of preliminary investigation of high current densities FE from nano-emitters are presented.

EXPERIMENTAL RESULTS.

The objects of the investigation were the microprotuberances, created on the W surface by thermal-field build up process, and local spots of Zr and ZrO₂, formed by the selective adsorption on the tipped monocrystals of W. The FE research methods and electron microscopy of high resolution were used. Vacuum conditions were higher, than 10^{-9} torr.

The main mechanism of nanometer tips formation is the surface migration of atoms in the electric field. It is activated by the temperature growth, caused by outer heat source or self-heating of emission centers by high density FE current. Other processes, as

ion bombardment of the surface, also can have an influence.

1. The possibility of creation of nanometer tips by the build up process in the constant field ($F = 3-7 \cdot 10^{10}$ V/cm), when the cathode potential is positive, was studied. Temperature was 1700-2000 K. It was found out, according to our former results⁴, that submicrotips may be formed, when the field strength F is about $2 \cdot F_0$. $F_0 = (16 \pi \alpha / R)^{1/2}$ is the value of equilibrium between the electric pressure forces and the surface tension on the top of the basis monocrystal emitter (R - it's radius, α - the coefficient of surface tension). The time of microtips formation then is about several dozens of seconds (Fig. 1.a). When the exposition is about several hours, formation of tips is possible, if F is approximately equal F_0 ⁵. The new result is, that for such long times nanometer structures form even when $F < F_0 = F_0 / (2^{1/2})$. For such fields even on the tip apex the

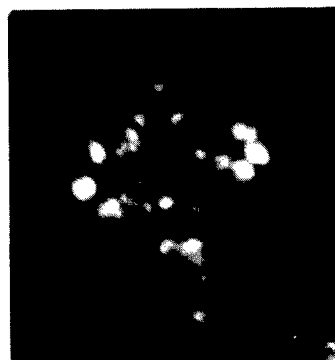


Fig. 1.a

mentioned equilibrium for atomic plane surface is not disturbed yet. We suppose, that this effect is connected with the natural roughness of surface

2. Microtips formation in pulsed fields was investigated. The cathode potential was negative; J was about $5 \cdot 10^{10}$ A/cm². Temperatures in prebreakdown stage were, probably, higher, than 2500 K, and therefore the build up process was activated by "self-heating." Under such conditions not only local nanometer tips, which look like presented on the Fig 1.a, but the edges and corners of atomic sharpness are formed⁶.

3. The rising of submicron tips was also explored in stationary fields, when cathode potential was negative.

The formation of big tips - so called "outgrowths" was observed (Fig. 1.b).

From our previous ⁷ and these results we can conclude, that such structures can appear not only, if cathode potential is positive, because of field evaporation ⁸, but also if cathode potential is negative and field evaporation is impossible.

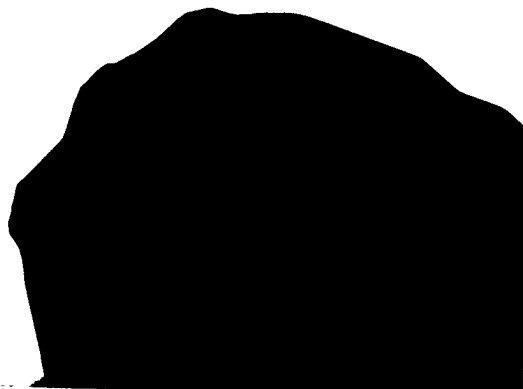


Fig. 1.b

The investigation of emission properties of structures, as presented on Fig. 1a shows, that the limit current densities for them are higher, than for smooth emitters. In ⁸ was shown, that the stability of emission and limit current densities are higher for the little emitters. This effect is emphasized, if the size of the tip is less than 10^{-6} cm - the character value of electrons free path length ⁹. In ⁹ was asserted, that the limit current densities for such tips are about 10^{11} A/cm². Our results shows, that such values, probably, are not attainable even in pulse fields (10^{-6} - 10^{-9} s). The exact definition of current density in such conditions is difficult, as the emitting surface size can be determined only approximately. However, the estimates give values of $J < 10^{10}$ A/cm².

4. The maximum values of J were achieved for the adsorption systems Zr/W and ZrO/W (Fig. 2). In the pulse regime J was about 5×10^{10} A/cm² according to our earlier results ¹⁰. In stationary field the values of J were up to 10^{10} A/cm². The minimum size of adsorbed spot was about 30Å, that is sufficiently less, than electrons free path length.

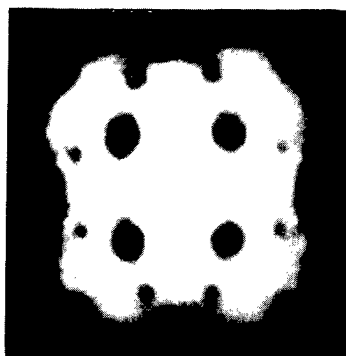


Fig. 2.a

W(001)



Fig. 2.b

Zr/W(001)

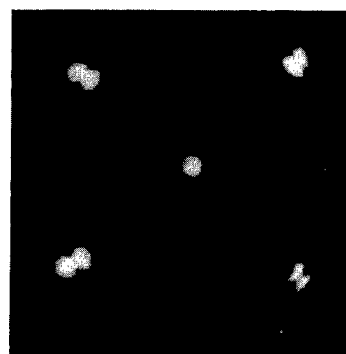


Fig. 2.c

ZrO/W(001)

THEORETICAL ANALYSIS OF THERMAL PROCESSES.

The strict formulation of the problem of thermal processes for localized emission must sufficiently differ from the traditional approach to "smooth" tip ⁸. The reason is, that typical sizes of microtips are about or even less than the characteristic length of electron-phonon interaction (several hundred Angstroms) - the length scale for electron and lattice temperatures become equal. Strictly

correct analysis may be done in frames of kinetic approach. Then the problem may be resolved without limitations of heat-transfer equation - the assumption about the "unlimited" velocity of heat expansion (which in reality cannot be greater than the speed of sound in the material), and about the "zero" phonon free path length.

However, the approach may be simplified. At the beginning of the process the main heat source is the Nottingham effect, as the Joule source is rather small, because the temperature and, therefore, the resistivity is rather low. For microtip Nottingham effect is the volume heat-source. For the little tip the heat extraction in its volume is negligible, because it's size is not enough for electron-phonon energy exchange. So, for the "basis" cathode, Nottingham effect can be considered as surface - as the boundary condition for heat transfer equation. If the localization of emission is provided by the adsorbate with low work function and the dimension of the spot is about the length of electron-phonon interaction, Nottingham heat source must be considered as the volume one. With fast temperature growth at the beginning of emission process, the length of particles energy exchange decreases and Nottingham source becomes boundary.

Due to exponential dependence of current density upon field (field amplification took place at the microtip) and upon work function (the adsorbate spot exists), the emission from the surface around the tip or spot can be neglected. This model can be marked as "strictly limited emission." The distribution of heat may be calculated on basis of heat-transfer equation with taking into account the dependencies of material characteristics and emission current density upon temperature. The common formulation of the problem is so analogous to α .

The characteristics of the process in dependence upon the radius of the emitting part of the surface (was taken about 0.1-0.2 μm) and the initial current density J_0 were numerically simulated. The values of J_0

were chosen more than 10^9 A/cm^2 - the limit densities for nanosecond time range. Then the instability of emission, which initiates vacuum breakdown, in the reality can be "pure" thermal. For the microsecond time range, the "pure" thermal instability does not develop and one of the main reasons of emitter destruction is the surface migration, stimulated by the temperature growth. The results are the time dependencies of 1) temperature distribution, 2) emission current, 3) power of volume and surface heat-sources.

Emitting part
of surface

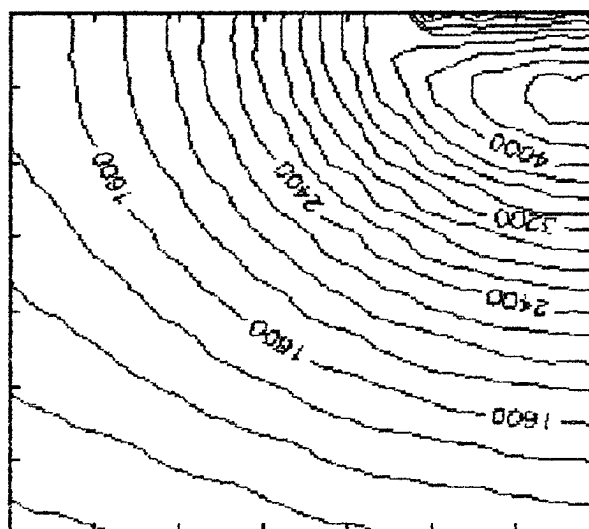


Fig. 3
Temperature distribution for $t = 8 \text{ ns}$
($J_0 = 6 \times 10^9 \text{ A/cm}^2$)

The total character of obtained results corresponds to the results for "smooth emitter." At the beginning maximum of temperature is on the surface in the middle of emitting area. The surface temperature is lower, than the inversion temperature of Nottingham-effect and so, the surface energy flow is heating. Later, the surface temperature becomes higher, than inversion temperature, and Nottingham flow becomes cooling. In combination with the Joule and Thompson volume heat sources this effect leads to the formation in the inner space of emitter the region of high temperature (Fig. 3), which can exceed the melting point of emitter material.

The main difference between the results for the model with localization and for non-localized one⁶ consists in the next. For almost any current densities (even non-realistic high) the "thermionic" instability of emission does not develop up to pulse durations, when the destroying of the emitter is inevitable due to thermoelastic strengths¹¹. For smooth emitter the calculations show, that thermal mechanism is enough for instability development. The avalanche growth of the current (due to the thermal addition) and the corresponding growth of the power of volume heat source (due to the resistivity growth with temperature) lead to the accelerating energy accumulation in the near apex region and, inevitably, to the explosion of emitter. So, there is no necessity to attract additional ideas about the mechanism of emitter destruction and breakdown initiation. When the emission is strictly localized such effect does not occur in the calculations. The reason is just the localization of emission: the heat transfer mechanism provides the distribution of heat to the inner space of the cathode and allows to avoid the avalanche growth of the variables. The possibility of heat transfer in radial direction - "around" the emitting spot is principle. In one-dimensional model, when energy distributes only in the direction, normal to the surface, the instability develops for any, even rather small J_0 . Therefore, we can conclude, that the limit value of initial current density grows up with the decreasing of the emitting area.

In the experiments the emitters (the "basis" radiuses about 1 mk) with microtips on their surface were studied. From such cathode the total current 6A was extracted without the explosion for pulse duration 20 ns. If estimate the limit current density for such emitter being smooth, using the relationship⁶

$$J_0^2 * t_{exp1}^{3/4} * R^{1/2} = B,$$

where t_{exp1} - the time of the instability development, R - radius of emitter apex. B - constant, equal for

tungsten 2.1×10^{15} in SI units. Total current may be calculated as $I = J_0 * S_{eff} * R^2$, where S_{eff} for such fields is about 2.5. The calculated limit value of total current for smooth emitter is $I_c = 2.8$ A. The experimental value 6 A is more than twice bigger than I_c . So, we can conclude that in frames of the considered model the rebuilt emitter with the localization of emission in several emitting centers can provide not only more high current densities, but also higher values of total current.

The quality analysis showed, that for nanometer tips, when the notion of temperature is already not correct the limit current density is more, than for rather big tips. So, the results, based on heat transfer equation, correspond with preliminary kinetic estimates.

REFERENCES

1. Fursey G.N., Vorontsov-Velyaminov P.N. *Zh.Tech.Fiz.* v.37, N 10, p. 1870-1888., 1967.
2. G.N. Fursey *IEEE Transactions on Electrical Insulation*, v. E1-20, N 4, p.659-670, 1985
3. S.F. Bugaev, A.M. Iskol'dskii, G.A. Mesyats, D.I. Proskurovskii *Zh.Tech.Fiz.* v.37, N 12, p. 2206-2208., 1967.
4. Ventova I.D., Fursey G.N., Polezhaev S.A. *Zh.Tech.Fiz.* v.47, N 4, p. 849-856., 1977.
5. Zhukov V.M. Polezhaev S.A., *Zh.Tech.Fiz.* v.57, N 6, p. 1133-1136., 1987.
6. D.N. Krotevitsch, V.E. Ptitsyn. G.N. Fursey, *Fiz. Tverd. Tela*, v. 28, N 12, p. 3722-3724, 1986.
7. G.N. Fursey, B.N. Movtschan, V.A. Shvarkunov, *Jorn. of. Tech. Phys. Lett.*, v. 16, N 20, p. 42-46, 1990.
8. D.V. Glazanov, L.M. Baskin, G.N. Fursey *Zh.Tech.Fiz.* v.59, N 5, p. 60-68., 1989.
9. V.G. Pavlov, A.A. Rabinovitsch, V.N. Shrednik, *Zh.Tech.Fiz.* v.45, N 10, p. 2126-2134., 1975
10. G.N. Fursey, S. Shakirova *Zh.Tech.Fiz.* v.36, N 6, p. 1125-1131., 1966.
11. L.M. Baskin, D.V. Glazanov, G.N. Fursey *Zh.Tech.Fiz.* v.59, N 5, p. 130-133., 1989.

Dynamic processes on a surface of iridium field emitters produced by action of high temperature and electric field

O. L. Golubev and V. N. Shrednik

A. F. Ioffe Physico-Technical Institute, 26 Polytekhnicheskaya st.
St Petersburg 194021, Russia

ABSTRACT

Field evaporation of Ir field emitters at high temperatures T and electric fields F was studied by means of field electron, ion and desorption microscopy. An initial emission of Ir-ions was observed only from the angles of build up emitters at relatively low F . The rise of F in 1.5 times in comparison with build up stage led to formation of microprotrusions. These microprotrusions moved along the edges between the angles of Ir-single crystal and played role of the centers of nucleation of new crystal layers. The macrooutgrowths on the close-packed planes were produced by field crystal growth and there were microprotrusions always on the corners of macrooutgrowths. Field evaporation of macrooutgrowths took place at definite T and F . This evaporation was observed as "effect of collapsing rings".

1. INTRODUCTION

This article is concerned with field evaporation of Ir at high temperatures $T = 1300\text{--}1700$ K, when the phenomena is complicated by diffusion and crystal growth processes. The process of low temperature field evaporation (field evaporation at cryogenic $T = 4.2\text{--}77$ K) was studied in many articles during a long time¹ but high temperature field evaporation was studied recently and there were only some papers²⁻⁶ dealing with "hot" field evaporation of W and Mo.

The process of high T field evaporation is very interesting both from scientific and applied point of view. It is interesting to extend the number of studied materials and to determine the fields F and T for specific processes on a surface. The tips under the action of high T and F can be used as sources of host material ions. These sources can operate for a long time with enough stability and play significant role in nanotechnology. It is hard to produce these sources of refractory metals by other methods. New data about local structure of emitting centers and possibility of their decreasing in dimension are very important for nanotechnology. Ir is of special interest because it is used in scanning tunnel microscopy as corrosion—preventive material.

2. EXPERIMENTAL METHOD

The experimental installation could operate as field electron, ion and desorption microscope. The installation consisted of pumping system, tube of microscope with image amplifier (two channel plates) and system for introduce of imaging gases (He, Ne, H₂). Field ion microscope enables to observe the surface of single crystal tip with atomic resolution at $T = 77$ K, field electron microscope enables to observe of this surface with resolution of $20\text{--}50\text{\AA}$ at $T = 77\text{--}1000$ K and field desorption microscope has a possibility to visualize the surface at the T up to nearly melting point by means of ions of host material of tip. When a negative voltage V was applied to the tip the installation operated as field electron microscope. When a positive voltage V was applied and the imaging gas was introduced into the chamber ($p = 10^{-5}\text{--}10^{-6}$ Torr) the device was operated as a field ion microscope. The regime of field desorption microscope took place when tip with positive voltage V was heated at the $T = 1300\text{--}1700$ K. The values of electric field strength F were obtained by means of Fowler-Norheim plots¹ $\lg(i/V^2) = f(1/V)$ (i —emission current) assuming that work function of Ir is $\varphi = 5.0$ eV.⁷ The slope of Fowler-Norheim plot produced the value of field factor $\alpha = F/V$, when α is known. The Ir-single crystal tips of annealed form (after heating in vacuum at high T) with the radii of curvature about $1\text{ }\mu\text{m}$ were used.

3. EXPERIMENTAL RESULTS AND DISCUSSION

The action of high F and T leads to significant shape changing of initial tip. Fig. 1 demonstrates the field electron images of main stages of shape changing process. These images were observed at the room T and show the final result of $T - F$ treatment.

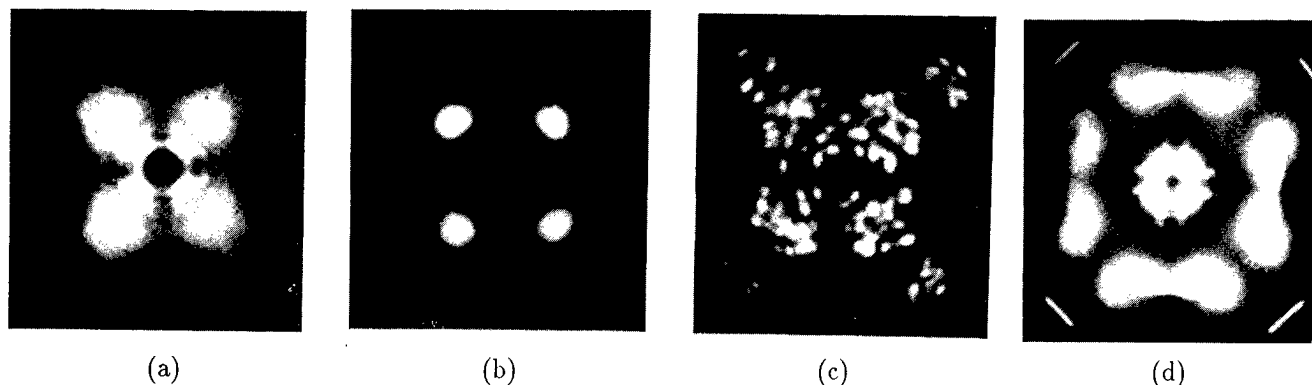


Fig. 1. Field electron images of the various stages of thermo-field shape changing of Ir-tip. The time of the treatment is 1 min. (a)—initial annealed form of the tip, $r \approx 11000 \text{ \AA}$. (b)—after $T-F$ treatment at $T = 1500 \text{ K}$ and $F = 0.3 \text{ V/\AA}$. (c)—after $T-F$ treatment at $T = 1500 \text{ K}$ and $F = 0.45 \text{ V/\AA}$. (d)—after smoothing of the tip in the state "c" at $T = 1800 \text{ K}$.

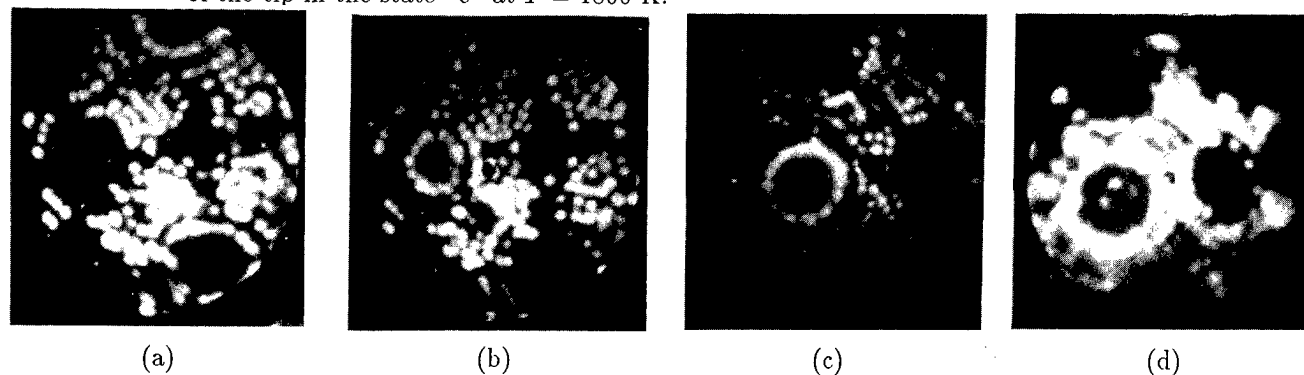


Fig. 2. Field desorption images of the surface of Ir-tip, $r = 9000 \text{ \AA}$ in Ir-ions (a)–(c), electron image (d). (a)— $T = 1340 \text{ K}$, $F = 1.55 \text{ V/\AA}$. (b)— $T = 1340 \text{ K}$, $F = 1.65 \text{ V/\AA}$. The collapsing ring is observed on the plane $(\bar{1}\bar{1}1)$. (c)— $T = 1340 \text{ K}$, $F = 1.65 \text{ V/\AA}$. The collapsing ring is observed on the center plane (001). (d)—The field electron image at $T = 300 \text{ K}$ of the surface corresponding to the Fig. 2c after collapse of the ring. The small macrooutgrowth remained on the center plane (001).

If the tip of initial annealed form (Fig. 1a) is heated at the $T \geq 900\text{--}1000 \text{ K}$ in the presence of $F = 0.3\text{--}0.4 \text{ V/\AA}$ well known phenomena of build up in electric field is observed. This process stops with the stage of fully build up⁸ when the tip is faced by most close-packed planes only: (111) and (100) for Ir. Fig. 1b demonstrates the image of this stage, only four bright emitting corners are observed in direction $\langle 023 \rangle$. The rise of F up to $0.45\text{--}0.5 \text{ V/\AA}$ allows to observe the image Fig. 1c consisting of spots arranged concentrically around the $\langle 111 \rangle$ and $\langle 100 \rangle$ poles. These spots correspond to images of thermo-field microprotrusions with the dimensions about $10\text{--}100 \text{ \AA}$. After gentle heating of the microprotrusions without F it is possible to observe the macrooutgrowths on the four planes $\{111\}$ and center plane (001) (Fig. 1d). The macrooutgrowths are comparable in dimensions with the planes of the tip on which they are grown and have the structure and faceting of the tip-crystal.

Field desorption microscope enables to observe the surface directly in the process of thermo-field treatment of the tip. At first the fully build up stage takes place and the same image as at Fig. 1b is observed. In this case the image is produced by Ir-ions evaporating from corners $\langle 023 \rangle$. The initial annealed form will be reconstructed when the pressure of electric field strength is more than the pressure of surface tension strength. The value of F necessary for build up of initial form of the tip is F of the treatment (F_{tr}). This F_{tr} ranges from 0.36 V/\AA to 0.25 V/\AA when T rises from 1300 K to 1700 K . If F_{tr} and T are constant the tip is reconstructed and sharpened and real F near the curved tip surface increases. This process is finished when the tip reaches the second stable form—fully build up form. When the ion emission is observed the final F (F_f) is higher than F_{tr} , of course. F_f varies from 0.94 V/\AA to 1.16 V/\AA and does not depend on T practically. The full build up form is a stable form and emission from the corners can be observed for a long time. Then if we want to observe the next stage we should increase F_{tr} up to

1.06–1.58 V/Å. Firstly one or some additional spots appear, these spots move along the edges between the corners of crystal. They are images of microprotrusions. These microprotrusions play a role of the centers of nucleation of new crystal layers.⁹ This is necessary for the process of the macrooutgrowths growth. This form is unstable because the shape of the tip is changed continuously. The third stable form is reached when the macrooutgrowths of enough height grow on the close-packed planes and the microprotrusions exist on the edges and corners of these macrooutgrowths. This form can be stable if the flow of atoms from the shank to the top of the tip is compensated by field evaporating atoms flow. The field desorption image at this stage is demonstrated by Fig. 2a.

Many spots are observed concentrically around the poles of (111) and (100). The increase of F_{tr} up to 1.16–1.65 V/Å leads to a new phenomena. The bright rings consisting of separate spots are formed on the periphery planes (111) and center plane (100). These rings are collapsed periodically.⁹ The radius of this ring decreases fast, the ring collapses to the center of the plane and disappears. Fig. 2b demonstrates such ring on the left plane (111) and Fig. 2c—on the center plane (100). The collapse of a ring continues for 1–2 seconds and the interval between collapses varies from some seconds to 30 seconds at various T and F . Therefore certain time is required to form a ring which is collapsed. This process was observed for 20–30 minutes at least and only on the close-packed planes.

The process of collapsing rings was observed at cryogenic T many times in field ion microscopy with atomic resolution.¹ This is well-known phenomena of field evaporation of two-dimensional monolayers consisting of the atoms of crystal tip at certain F and T when field is enough to evaporate the edge atoms of upper two-dimensional layer. In this case the radius of this layer decreases continuously and the layer disappears. This process takes place with constant velocity at invariable F . It is possible to determine the rate of field evaporation if the number of the collapsing-rings per second is known.¹ In our case we observed another phenomena, although it looks like effect of collapsing-rings at cryogenic T . The spots on the field desorption image represent not atoms but the microprotrusions. When we have the third stable form the rate of evaporation of the atoms from microprotrusions is equal to the rate of diffusion flow from the shank to the top of a tip. The rise of F leads to disturbance of the dynamic equilibrium and the rate of evaporation begins to prevail the rate of growth. In this case the evaporating macrooutgrowths decreases in dimensions. It is observed on the image as collapsing rings of microprotrusions existing on the edge of the macrooutgrowths. The scheme of this process is shown on Fig. 3.

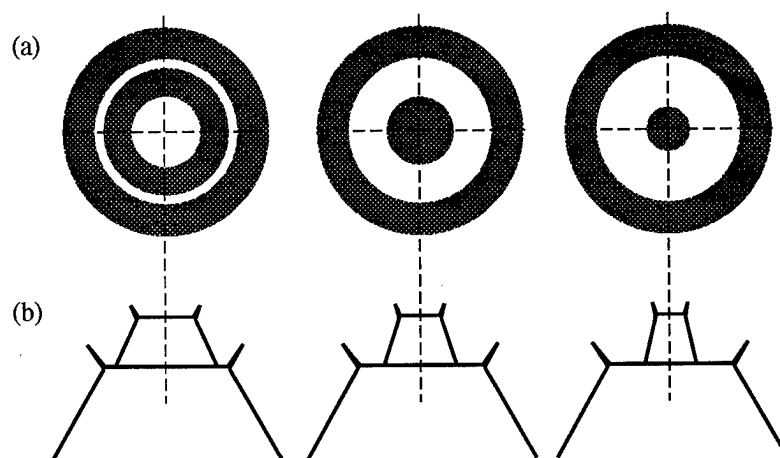


Fig. 3. The scheme of the process of collapsing ring: (a)—the views of the field desorption images; (b)—the profiles of a tip.

When the diameter of macrooutgrowth decreases the local F can increase and a rate of field evaporation increases too avalanche-like. The macrooutgrowth can be evaporated completely or a small part of this macrooutgrowth can remain at the center of the plane, where F is lower. This remained macrooutgrowth is observed on Fig. 2d at the center of the plane (001).

Thus the effect of collapsing rings on the field desorption microscope image corresponds to the field evaporation of single macrooutgrowth at high T through the microprotrusions. It is new mechanism of field evaporation, this mechanism was not observed previously. The form of tip with evaporating macrooutgrowths is relatively stable form too (the fourth stable form). This pulsating form can be observed for a long time in spite of the blunting of the tip at the process of field evaporation. It is interesting, that the F_{tr} for transition from the second to the fourth stable stage varies from 1.65 to 1.16 V/Å when T rises from 1300 to 1750 K, but F_f for the stage of collapsing rings varies from 0.94 V/Å to 1.06 V/Å. F_f is significantly lower than F_{tr} and does not depend on T practically. The form

with macrooutgrowths is "more blunt" in comparison with fully build up form and the rise of V_{tr} is compensated by decreasing of field factor α .

The tips with macrooutgrowths and microprotrusions evaporating the atoms can be used as the sources of refractory metal ions. We obtained the emission current of Ir-ions as $\cong 3 \times 10^{-10}$ A at the $T = 1400$ K and $F_f = 1.02$ V/Å. The current from single microprotrusion was about $(1-2) \times 10^{-12}$ A, i.e. 10^7 ions per second.

We have a possibility to estimate the value of the heat of evaporation of Ir in the presence of high F using Arrhenius law⁵ $v = 1/\tau_0 \exp(-Q_f/kT)$, where Q_f —heat of evaporation in the presence of field, $\tau_0 = 10^{-13}$ s. If $T = 1400$ K and $v = 10^7$ ions/s, $Q_f = 1.67$ eV. It is significantly lower than the heat of evaporation Q for Ir—6.93 eV. The value $F \cong 1.0$ V/Å decreases Q from 6.93 to 1.67 eV, but in the case of low temperature field evaporation evaporating field $F = 5.3$ V/Å decreases Q_f down to zero practically.

4. CONCLUSIONS

1. Four stable forms of tips exist in the process of thermo-field treatment—initial annealed form, build up form, form with macrooutgrowths and microprotrusions and form with evaporating macrooutgrowths.
2. The field of treatment F_{tr} necessary for transition from one to another form can be both higher and lower than final F_f for the final form.
3. The new observed mechanism of field evaporation is connected with pulsating dissolution of separate macrooutgrowths by means of evaporation through the microprotrusions. This mechanism manifests itself as effect of collapsing rings on the field desorption images.

5. REFERENCES

1. E. W. Muller and T. T. Tsong, "Field Ion Microscopy, Principles and Applications", Elsevier, Amsterdam, 1969.
2. Yu. A. Vlasov, V. G. Pavlov, and V. N. Shrednik, "High-temperature evaporation of thermofield microscopic protuberances", *Sov. Tech. Phys. Lett.*, Vol. 12, no. 5, pp. 224–225, 1986.
3. J. A. Vlasov, O. L. Golubev and V. N. Shrednik. "Progress in the study of thermo-field phenomena", *Journal De Physique*, Coll. C6, suppl. 11, Vol. 49, C6–131—C6–136, 1988.
4. V. T. Binh and N. Garcia. "Atomic metallic ion emission, field surface melting and scanning tunneling microscopy tips." *J. Phys. I*, Vol. 1, pp. 605–612, 1991.
5. V. T. Binh and N. Garcia. "On the electron and metallic ion emission from nanotips fabricated by field-surface-melting technique: experiments on W and Au-tips", *Ultramicroscopy*, Vol. 42–44, pp. 80–90, 1992.
6. Yu. A. Vlasov, O. L. Golubev and V. N. Shrednik, "Form changing of a metal tip at the competition of the field and surface tension forces", *Izvestija Akademii Nauk USSR, ser. fiz.*, Vol. 52, no 8, pp 1538–1543, 1988.
7. V. S. Fomenko, "The emission properties of the materials", Naukova Dumka, Kiev, 1980.
8. M. Benjamin and R. O. Jenkins. "The distribution of autoelectronic emission from single crystal metal points. I. Tungsten, Molybdenum, Nickel in clean state", *Proc. Roy. Soc. Lond. A*, Vol. 176, pp. 262–279, 1940.
9. Yu. A. Vlasov, O. L. Golubev and V. N. Shrednik, "Equilibrium and steady state forms of the heated crystals in the presence of high electric field", *Rost Kristallov*, Vol. 19, pp 5–21, Nauka, Moskva, 1991.
10. V. G. Butenko, O. L. Golubev, E. L. Kontorovich and V. N. Shrednik, "The effect of 'collapsing rings' at high temperature field evaporation of iridium", *Sov. Tech. Phys. Lett*, Vol. 18, no. 8, pp. 86–91, 1992.

Design of field electron emission spectrometer, field ion microscope and field electron emission microscope combination

S.N. Ivanov, S.N. Shilimanov and S.I. Shkuratov

Institute of Electrophysics, Urals Division of the Russian Academy of Sciences
34, Komsomolskaya Str., GSP-387, Ekaterinburg, 620219, Russia

ABSTRACT

A new set up is described which allows one to carry out field electron microscopic and spectroscopic study of cathode surfaces in direct correlation with their atomic structure.

1. EXPERIMENTAL INSTALLATION DESIGN

The investigations of the emissive properties of cathode microprotrusions, classical tip emitters and multi-tip systems in direct correlation with their real atomic structure provides new possibilities of interpretation of experimental data and, correspondingly, helps to raise vacuum insulation and improve technical characteristics of emission devices. This paper is concerned with the design of a new instrument enabling to investigate the emission properties, electronic and atomic structure of cathodes by using field emission methods. The set up comprises a dispersion-type field electron emission spectrometer (FEES) combined with a field ion (FIM) and a field electron emission (FEEM) microscopes fitted in a commercial ultra-high vacuum (UHV) chamber. Overall view of the experimental set up, top view of the work chamber and schematic drawing of the experimental set up are shown in fig. 1, 2 and 3, accordingly. Vacuum chamber manufactured from stainless steel has three-stage pumping system (the ultimate vacuum is higher than 10^{-10} Torr). The UHV installation is equipped with a lock chamber to replace a specimen without breaking vacuum in the main chamber and heating the vacuum system.

A specimen holder has eight isolated contacts which may be used for the temperature control, emission current measuring, specimen heating, etc. A specimen is cooled by liquid nitrogen or helium (specimen temperature is 115 K and 75 K, accordingly) with the use of specially developed cryogenic system, isolated from high-voltage elements. A precision UHV mechanical manipulator is capable of moving a specimen in three directions and rotating around its axis. Flexible link of specimen holder with cryosystem and contact set provides ability of moving of a specimen during experiments and allows to use all three methods of study in any sequence.

The FIM-FEEM (see fig.2) uses a microchannel amplifier 56 mm in diameter, the channel radius 12 μm . Emission images can be observed on a fluorescent screen and recorded by using either a photo- or videocamera. The microscopes design provides for applying a high voltage both to a specimen and a hall plate of microchannel amplifier, thereby allowing to take low-voltage measurements in the specimen circuit during experiment. In the latter case, the microchannel amplifier and fluorescent screen is fed from a specially designed high-voltage regulated power supply unit, isolated from the ground. In FIM regime, the spectrally pure neon, helium or molecular nitrogen can be used separately or in mixture as an imaging gas. Figures 4 and 5 shows FIM patterns of Nb cathode microprotrusion and Nb cathode tip, accordingly. Neon was used as an imaging gas.

FEES¹ (fig. 6) consists of seven cylindrical electrostatic lenses manufactured from nonmagnetic metal (titanium). Energy dispersion of electrons occurs due to chromatic aberrations in the filter, consisting of the lenses IV-VI. The analyser operates as an electronic counter. The high sensitivity is achieved by using the secondary electron multiplier of channel type. The analyser resolution, measured at 75 K by Young and Kuyatt criterion², is 30 - 70 meV depending on the high-voltage value at the anode. Fig. 7 shows electron spectra of Nb cathode microprotrusion (a) and Nb cathode tip (b) at 115 K.

A specimen holder impedance-matched with the transmission line that allows one to investigate electrical strength of vacuum diodes and critical densities of field emission current in static and pulsed regimes (response time 8 nsec).

The experiment is controlled and information is gathered by a IBM PC AT-286 computer with Microlink and IEEE-488 systems (see fig.3). Special computer programs enable to carry out an express-analysis of data in the course of the experiment, as well as to conduct a detailed analysis of results after the completion of the measurements.

The use of the device may give an important information about emissive properties of cathodes manufactured from refractory and low-melting metals, alloys and compounds, such as, for example, high-temperature superconductors.

2. REFERENCES

1. Yu. M. Yumaguzin, "Energy distribution of field emitted electrons from tungsten at high current densities", *Cand. Sci. Thesis*, Bashkirian University, USSR, Ufa, 1987.
2. R.D. Young and C.E. Kuyatt, "Resolution determination in field emission energy analyzers", *Rev. Sci. Instr.*, Vol.39, pp.1477-1480, 1968.



Fig.1. Overall view of the experimental setup.

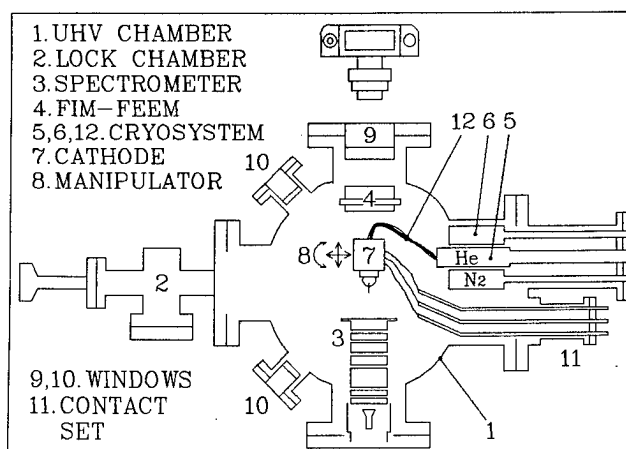


Fig.2. Top view of the work chamber.

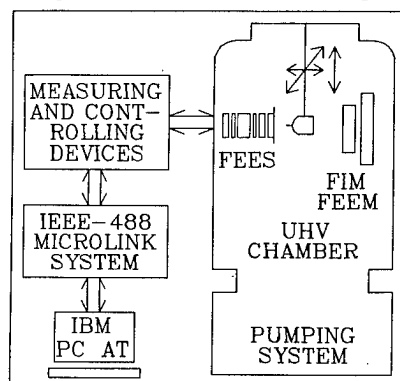


Fig.3. Schematic drawing of the experimental setup.

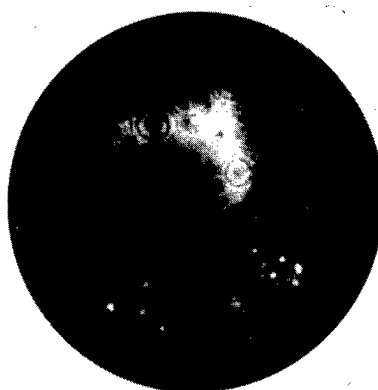


Fig.4. FIM pattern of Nb cathode microprotrusion ($P(\text{Ne})=3 \times 10^{-5}$ Torr, 115 K, 21.2 kV).

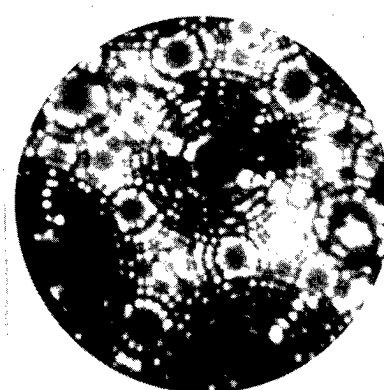


Fig.5. FIM pattern of Nb cathode tip ($P(\text{Ne})=3 \times 10^{-5}$ Torr, 115 K, 4.67 kV).

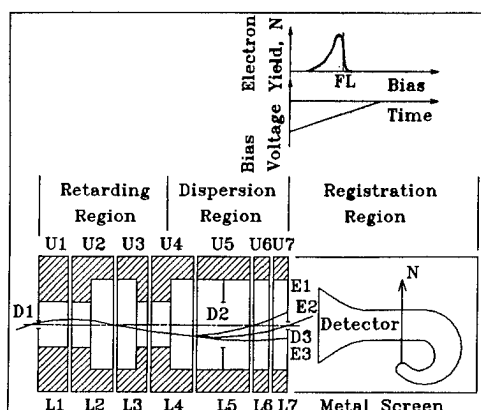


Fig.6. Schematic drawing of the field electron emission spectrometer.

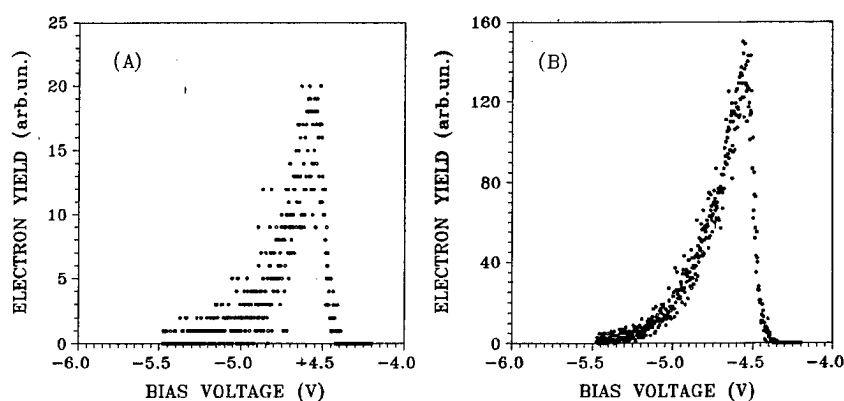


Fig.7. Electronic spectra of Nb cathode microprotrusion (a) and Nb cathode tip (b) at 115 K.

INTRODUCTION

Processes of field electron emission, field ionization and field evaporation of atoms from the emitter surface in intensive electric fields (10^7 – 10^8 V/cm) are determined, in particular, by the crystallographic structure of the emitting surface. For pure metals, wherein the nonuniformity of density distribution of field emission current is due to various values of factor $\varphi^{3/2}/E$, this was first shown by E.Muller¹. In the case of emission from the surface of metallic alloys the effect of the crystallographic structure on the distribution electron and field ion emission current density becomes more complicated. Such additional factors as the nature of interatomic forces responsible for structural transformations, different phase composition of various areas of the surface, the degree of long-range order in relevant sublattices, etc. begin to play a substantial role in emission processes.

The purpose of this investigation is to elucidate the effect of alloy atomic surface structure crystallography on the processes of field electron emission and field ionization in intensive electric fields (10^7 – 10^8 V/cm). Such experimental conditions exist in the field emission microscope, where the distribution of electron and field ion emission current density is influenced directly by the structure of an atom-clean surface.

2. EXPERIMENTAL RESULTS AND DISCUSSION

An analysis of electron and field ion emission current density distribution is based on the microimages of tip emitter surfaces of various alloys in the conversion duty of the field emission microscope.

The best alloys for solving the problems set in this work were found to be ones of the Pd(CuAg) type in which two phases with various kinds of structure are formed as a result of precipitation breakup: ordered PdCu phase with type B2 crystal lattice and AgPd solid solution with fcc structure². The distribution of ion emission from that part of the surface which is occupied by the PdCu phase is a typical (for an ordered alloy in neon) image with a distinct dependence on the sequence of morphological development of crystallographic faces (Fig 1a). The local variation in the ion current intensity in the microimage of the ordered crystal surface is also determined by various reactions of different species of atoms to processes of field ionization and field evaporation (depending on chemical nature and degree of long-range order in the alloy). The AgPd solid solution exhibits a typical irregular image with uniform distribution of ion current (indiscernible from the surface crystallography).



Fig.1. Field emission patterns of the Pd(CuAg) alloy at the early stages of the phase transition.
(a) Field ion image. (b) Field electron image. (c) Field ion image of partially aged Pd(CuAg) alloy having orientation $\langle 111 \rangle$ (the arrows show the interface boundary).

With the same voltage at the emitter the ion current density due to AgPd phase is much lower than that due to the PdCu ordered phase. At the same time the comparison of the intensity of the ion current due to PdCuAg solid solution with that of the ion emission from the AgPd phase, observed simultaneously in one microimage of the surface, shows that there is a marked difference in the density of current due to fcc disordered solid solutions with different contents of components, (Fig.1b).

The change in current density at the surface observed in the ion microimage, due to various (from the point of view of crystallography) phases can be explained as being brought about by selective ionization produced by atoms of various species. This selectivity of ionization is caused by the difference in the electric field intensity over the atoms. The higher the field intensity at a given location over a given atom, the brighter it glows on the screen. The difference in charge density at sites occupied by atoms of various species leads to a nonuniform field at these locations³.

In an alloy the charge distribution will show up in the transfer of a negative charge from atoms of a species featuring a smaller attraction between electron and nucleus to those having a stronger attraction. Hence, the field will grow in those places that are occupied by atoms of the species with a lower force of electron attraction, bringing about a brighter imaging of such atoms. This general mechanism links the probability of field ionization with field intensity at a certain position of the atom on the surface. The quantitative approximation involves the calculation of the actual probability of tunnelling of an electron moving from the imaging gas atom onto the Fermi surface in the metal⁴. However, these parameters are related to the set of atoms occupying the bulk of the pure metal. According to T.T.Tsong⁵, when considering the ion image due to an alloy one must proceed from the occupancy and density of atom states, changes taking place therein as a result of charge transfer within the bulk of the material and various degrees of charge reduction under the action of the applied potential. In⁶ the behaviour of two species of atoms in relation to such effects is described proceeding from the simple criterion of their relative forces of electron attraction. This makes it possible to estimate the relative brightness of their images.

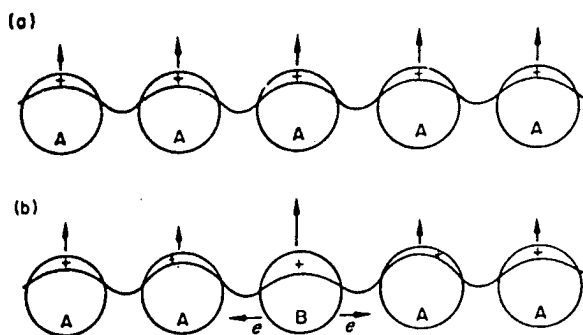


Fig.2. Schematic representation of an arbitrary surface plane under field ion imaging conditions. The length of the arrow is a measure of the ionization probability at its site⁶.
(a) Pure metal. (b) Solid solution alloy.

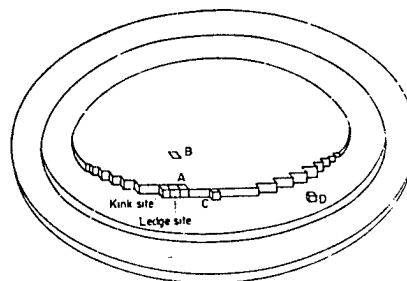


Fig.3. Schematic structure of a plane on the field-ion surface⁶.

It seems that the most suitable parameter is the electron work function since it characterizes not a free atom, but a set of atoms, at the same time being a measure of attraction of electron to the ion frame. When two metals are made to contact each other with their atoms their energy can be reduced by transfer of electron from a metal having a lower work function, to one with a higher work function, both Fermi levels coinciding when equilibrium is attained. Since the work function is a property of a large set of particles, it cannot be applied directly to individual atoms. Hence, it should be stressed that it is applied as a criterion of the relative force of attraction of an electron required for the prediction of the direction of electron transfer between atoms of different species in the alloy. One should note that while the ideal value of the work function must correspond to the internal Fermi potential⁷, experimentally obtained values are connected to this value on the surface, where the crystallographically dependent member, which

changes with the measurement technique, is added^{4,8}. Under the action of the potential applied to charge transfer yet another mechanism, equivalent to charge transfer, is added to the transfer of charges between two species of atoms within the bulk of the material. Fig.2 shows how in an alloy an atom species with a smaller electron attraction force impedes to a lesser degree the displacement of conduction electrons. Hence, the positive potential increases in this location and this species of atoms will be imaged more intensively. Similar to electron transfer between atoms of various species (in this case under the action of potential), the different capacity of atoms of various species to impede the displacement of conduction electrons is described. Indeed, for a given field F there exists a definite charge σ per unit of surface area, expressed as $F=4\pi\sigma$. Thus, if the total positive charge of one species of atoms decreases as a result of conduction electron displacement and in this way impedes the "penetration field" of applied potential, the charge at the atoms of the other species increases proportionally, balancing the whole system.

All the previous considerations pertained to atoms of various species located in identical geometric sites of the surface. Besides the dependence on the chemical nature of the atom, the intensity of its ion image is influenced by the location of the geometrical position of the atom on the surface. Because of the different positions of the atom on the surface, (Fig.3), the electric field intensity increases. One the one hand, it is called "geometrical", considering the classical picture of location of object of lesser radius on a conducting surface of larger radius. On the other hand, the more prominent atoms have the least coordination (for example, atoms at the step bend) and thus exhibit a higher polarization, i.e. provide a greater positive charge under the action of the applied potential (due to an easier displacement of conduction electrons).

In the pure metal the difference between coordination and "electronic size" does not affect the image intensity, since an atom having a lesser coordination will possess a larger "electronic size". In an alloy the "electronic size" is determined by the relative force of electron attraction by atoms of different species. Therefore, it was agreed to designate the field increase due to coordination as "geometrical increase" and that due to charge transfer as "electronic increase"⁶.

The density distribution of ion current drawn from the surface of an alloy is described in accordance with model⁶ with account taken of the secondary role of the mechanism of selective ionization as compared with the mechanism of selective field evaporation. Practically, the selective evaporation or retention of atoms of one of the components on the top faces of imaged planes is observed as "vacancy" contrast, inasmuch as atoms of one species create the surface microimage. The predominant evaporation of one species of atoms as compared to another species is determined by the parameter $\Delta F = F_A - F_B$, where F_A and F_B are evaporation fields of atoms of the solvent and dissolved element, respectively⁹. Taking into consideration that for element A the evaporation field is⁶:

$$F'_A = n_A^{-3} e^{-3} \left(\Lambda_A + \sum_n I_n(A) - n_A \varphi + n_A P_1 + P_2 \right)^2 \quad (1)$$

is the standard parameter of selective evaporation describing the difference of fields for atoms A and B, occupying the same place in the step bend $\Delta F_K = F'_A - F'_B$. The lower limit ΔF_K existing with placement of atom B in the centre of the given face as compared to position of atom A at the step bend, must be still greater than zero (ΔF_O), since no "geometrical" increase in field ΔF^* has yet been taken into account. It is obvious that for a predominant field evaporation of atom B the quantity $\Delta F_O - \Delta F^*$ must be positive. The direct calculation of field increase in the step bend, as compared to the field in the centre of this face, is impossible. Hence, as proposed by D.G.Brandon¹⁰, the quantity ΔF^* is taken in proportion to the height of the step of the plane, which decreases with the collapse of the top face.

A contrast of the "vacancy" type, i.e. the experimental registration of the predominant field evaporation, is possible as a rule with sufficient difference between evaporation fields of components making up the alloy. With small values of ΔF both types of atoms can show up in the image. Their relative brightness can be described with the help of the selective ionization model.

It follows from the above considerations that φ has a considerable effect on the density distribution of ion current drawn from the emitter surface. The smaller the work function of the alloy component electron, the brighter must be the image of this atom in the ion micrograph. On the other hand, the regularity of the annular image of the alloy surface is also an important factor. In an ordered structure an ion image similar in uniformity to that of a pure metal is typical, since only one species of atoms, as a rule, makes the main contribution to the ion current

drawn from the surface. It follows that for the ordered phase the distribution of ion current density is defined only by the "geometrical" growth of electric field, just as in the case of a pure metal. The difference in ion images will be determined by the type of crystallographic structure of the superlattice. In the case of a solid solution phase one must take into account, besides the "geometrical" field growth, also the "electronic size". At the same time the ion current density distribution is determined by the statistical arrangement of atoms at the crystal lattice sites (as a result of charge redistribution on the surface of the solid solution due to the action of the electric field). Parameter ΔF_K for concentrated solid solutions can also serve as a criterion of field evaporation selectivity⁶. In particular, in the case of phase AgPd we observe a predominant field evaporation of Ag atoms, the nonuniformity of the ion image being determined by the statistical arrangement of atoms at sites of the fcc lattice.

In the field emission duty the densities of cold emission currents drawn from the ordered phase PdCu and phase AgPd are interchanged. The density of field emission current of fcc phase is much higher than that from the phase ordered according to B2. Assuming that the mean magnitude of field E at the surface of a given emitter (Fig.1c) has a certain value, the nonuniformity of distribution of electron emission current density will depend on the crystallographic structure of the emitting surface. In other words, the work function of the given area on the surface becomes the main parameter affecting the change in the emission current density.

3. SUMMARY

The experimental data presented here on the character of distribution of density of current of electron and field ion emission from the surfaces of type Pd(CuAg) alloys show the effect of the crystallographic structure and the role of electron work function in emission processes taking place on the surfaces of solid solutions. The crystallographic structure type, the ordered arrangement of atoms, the nature of interatomic forces and the chemical type of alloy components remain essential factors in these processes.

4. ACKNOWLEDGMENTS

This work was supported, in part, by a Soros Foundation Grants awarded by the American Physical Society.

5. REFERENCES

1. E. W. Muller, *Zs. f. Phys.*, v.106, p.541-546, 1937.
2. N. N. Syutkin, V. A. Ivchenko and S. I. Noritsyn, "Structure of a palladium-copper-silver alloy studied in a field ion microscope", *Fiz. Met. Mettalloved.* v.57, p.776-781, 1984.
3. B. Ralph, D. G. Brandon, "A field-ion microscope study of some tungsten-rhenium alloys", *Phil. Mag.*, v.8, p.919-934, 1963.
4. R. Gomer, *Field emission and field ionization*, Cambridge, USA: Harvard University Press, 235p, 1961.
5. T. T. Tsong, *Field-ion microscopy of intermetallic Compounds: Platinum-Cobalt alloys /Applications of field-ion microscopy/*, Eds. R. F. Hochman, E. W. Muller and B. Ralph. Atlanta: Georgia Inst. of Technology, p.13-32, 1968.
6. H. N. Southworth and B. Ralph, "Image formation from alloys in the field ion microscope", *J. Microscopy*, v.90, p.167-197, 1969.
7. D. G. Brandon, "Image formation in the field-ion microscope", *Phil. Mag.*, v.7, p.1003-1011, 1962.
8. H. B. Michaelson, "Work functions of the elements", *J. Appl. Phys.*, v.21, p.536-540, 1950.
9. D. G. Brandon, "The field evaporation of dilute alloys", *Surf. Sci.*, v.5, p.137-146, 1965.
10. D. G. Brandon, "The structure of field evaporated surfaces", *Surf. Sci.*, v.3., p.1-18, 1965.

Liquid metal surface under the
artificial stimulation of
microcapillary waves

A.L. Kovalev, L.M. Baskin,
G.N. Fursey, L.A. Shirochin

St.-Petersburg Bonch-Bruévitsch
Telecommunications University, Russia

It is evident now that the internal mechanism of explosive electron emission and vacuum discharges is determined to a considerable extent by the dynamics of motion of the liquid phase at the cathode surface. The liquid phase is always present, if only on the individual sections of solid cathode, in every type of high voltage vacuum discharge. What is more, its presence is fixed actually even on carbon cathodes, although the formation of the liquid phase on it is fundamentally inhibited, since at normal pressures carbon sublimates by passing the melting stage¹. The interaction between the external fields and the liquid surface of the emitter leads to the emergency of different types of hydrodynamic instabilities. As a result, the surface microstructures of different types are formed². The characteristic dimensions of structures produced have the values which provide for the creation of the fields required for the emission sustaining. As our experiments show², the development of such instability in super-high frequency (SHF) fields results in a capillary wave swing, that, even with relatively low SHF-field strengths, may cause both field electron and field ion emission³. In this case, the high degree of reproducibility of small-scale irregularities of the microrelief of a liquid surface is, in our opinion, the reason such emitters are highly stable.

However, in static fields, such mechanism of the emission is impossible. The situation is determined by the uneven concentration of the external field at the individual microprotrusions which are arbitrarily reproduced after every regular actuation. Any attempt to increase the total current of the cathode leads to

the explosions of the irregularities, to formation of high density cathode plasma clusters, and to transition to the low-voltage stage of the discharge.

To solve the problem, it seems to be logical to create an artificially excited microrelief. Being initiated by the external source, which is connected immediately before the high voltage pulse, such structure should be able to result in a stable emission process. For this purpose, the method of ultra-sonic excitation of liquid metal has been selected. We treated a thin film, that is situated upon the substrate, vibrated normal to liquid surface. In this case, the layer of liquid swings as a single whole with the substrate and they both oscillate with the same frequency Ω and amplitude A . The volume density of the inertial force

$$F = n A \Omega^2 \sin \Omega t$$

stimulates the effective acceleration

$$a = A \Omega^2 \sin \Omega t \quad (1)$$

For the unviscous deep liquid, the dispersion equation for the capillary wave on its surface can be written as:

$$\theta = [\alpha * k^3 / n + g * k]^{1/2} \quad (2)$$

where α , n , and g are the surface tension, density, and gravity, respectively, of the liquid material.

The deep liquid approximation requires that $kH \gg 1$. As the estimates show, for the typical frequencies of ultra-sonic excitation (100 - 1000 KHz), and for the film thickness of $H > 10$ mcm, such a demand is always satisfied. Taking into account that the gravity is negligible ($g k = 0$) and combining (1) and (2), one can obtain a dispersion equation in a form:

$$\theta(k) = \theta_0 (1 + h \sin \Omega t)^{1/2} \quad (3)$$

where:

$$\theta_0 = (\alpha k^3 / n)^{1/2}$$

and

$$h = A \Omega^2 n / \alpha k^2 .$$

Now, the possibility of parametric instability development follows immediately from (3). This kind of oscillations can be excited on condition that the frequency of substrate vibration is close to the double frequency of the surface wave

$$\theta_0 = (\Omega - \beta) / 2$$

where $-h \theta_0 / 2 < \beta < +h \theta_0 / 2$, and $h \ll 1$.

In this case, the amplitude of the surface wave of frequency θ_0 will exponentially increase as $\exp(St)$. Here,

$$S = 1/2 [(h \theta_0 / 2)^2 - \beta^2]^{1/2} .$$

The surface perturbations with $\beta=0$ are the most rapidly increasing modes. They take place at $\Omega = 2 \theta_0$.

For an unviscous liquid, the characteristic time for the growth of amplitude of the most rapidly increasing mode is $\tau_c = 4 / h \theta_0$.

It is easy to present all the results as a function of ultra-sonic frequency Ω . The length of the most rapid mode will be:

$$L = 4 \pi (\alpha / 2 n \Omega^2)^{1/3} .$$

The characteristic time for the growth of this mode can be written as

$$\tau_c = 2^{5/3} \alpha^{1/3} / (A n^{1/3} \Omega^{5/3}) .$$

Note that the initial amplitude of the waves is a very small value because it defines only by the initial temperature of the liquid surface. As usual, it is a room temperature. That is why the full (real) time of surface structure formation τ_f is much longer than the value of τ_c ($\tau_f = 8 - 10 \tau_c$). The condition $h \ll 1$ can be expressed as

$$A \ll (\alpha / 16 n \Omega^2)^{1/3} .$$

For the effect study, a generator with a frequency of $\Omega = 1.63 \times 10^6 \text{ s}^{-1}$ (260 KHz), was used. Under these

conditions, for the liquid gallium, one can expect: $L = 35 \text{ mcm}$, $A \ll 1.6 \text{ mcm}$, $\tau_c = 70 \text{ mcs}$, and $\tau_f = 600 - 700 \text{ mcs}$.

With allowance for viscosity, the effect of threshold of instability is appeared:

$$h > h_{th} = (2^{8/3} n^{2/3} \mu \Omega^{1/3}) / \alpha^{2/3}$$

where μ is the kinematic viscosity. The threshold amplitude can be obtained as

$$A_{th} = (2^{4/3} n^{1/3} \mu) / (\alpha^{1/3} \Omega^{1/3})$$

and, for gallium, $A_{th} = 0.12 \text{ mcm}$.

As a result of threshold effect, the equation for character time of the growth is changed:

$$\tau_c = 2^{1/3} / \mu (\alpha / n \Omega^2)^{2/3} (A / A_{th} - 1)^{-1}$$

For liquid gallium it becomes to

$$\tau_c = 6 \times 10^{-5} [A / A_{th} - 1]^{-1} (\text{s}) .$$

It is not difficult to appreciate the value of power you need to excite the surface waves. A complete picture requires to take into account that one must to excite the layer of thickness H and of amplitude A as a whole, and that it should be done during the time of oscillation swing τ_f . Besides, it is necessary to create the surface wave, having amplitude, sufficient to the value to be registered. What is more, the energy dissipation, which takes place during the process of oscillation growth, is also required to be accounted. As the calculation show, required power is:

$$P = 0.02 H A^3 \{ \Omega^{1/3} n^{4/3} / \alpha^{1/3} \} +$$

$$0.2 \alpha^{2/3} n^{1/3} \Omega^{5/3} A +$$

$$0.5 \mu \alpha^{1/3} n^{2/3} \Omega^{4/3} [\text{Watt/cm}^2] .$$

For the film of thickness $H=20 \text{ mcm}$ one can obtain $P=(4-6) \text{ Watt/cm}^2$.

The process of surface oscillations growth can reach some stationary level. The conditions under which this situation is possible: the energy which is dissipated in near-surface layer is equal to the energy which is produced by the vibrating

surface. The amplitude of the stationary wave can be written as

$$a = 2.5 (\alpha^{1/6} / \mu^{1/2} n^{2/3} \Omega^{4/3}) P^{1/2}$$

For the liquid gallium a [mcm] = 7.6 [Watt/cm²]. Therefore, the input power is about 2-3 Watt/cm² will warrant the amplitude of the surface wave of (10-15) mcm.

It was found that the value of ultra-sonic threshold power is very close to the one, predicted by the theory

$$P_{\text{exper.}} = P_{\text{theor.}} = 0.1 \text{ Watt.}$$

Specifically, the structures with a character wave length of 10-15 mcm were fixed at the exciting frequency of $\Omega = 260$ KHz. As the experiments showed, such immobile waves may be kept for tens of seconds (Fig. 1).

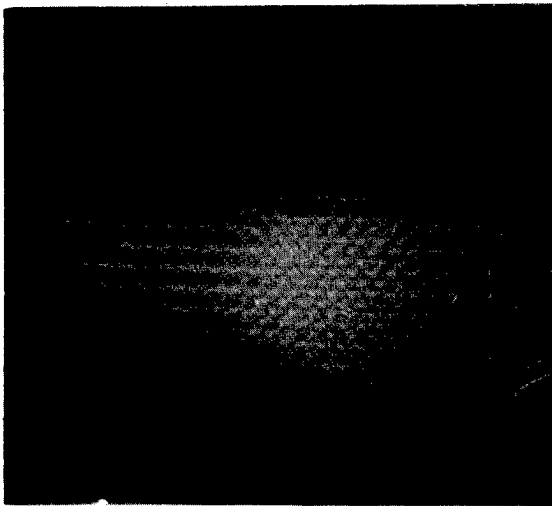


Fig. 1

Immobile wave on the liquid gallium in vacuum. A working area is about of 1mm². $\Omega = 260$ KHz, $L = 10$ mcm.

The dark stripes being observed on a photo are the positions of the immobile waves centers. Thus, the wave length is equal to a double distance between the neighboring strips. The amplitude of the wave has been defined by varying of microscope focal distance for focusing either at the top or at the hollow of the wave.

REFERENCES.

1. G.N. Fursey, B.N. Movtshan, S.M. Lupekhin et all. "Formation of the liquid phase and excitation of capillary waves at a carbon surface during explosive electron emission" Sov. Fiz. Dokl., v. 33, N 9, p. 696-698, Sept., 1988.
2. L. Baskin, L. Shirochin, A. Kantonistov, G. Fursey, I. Radchenko, "Field emission on the liquid metal surface at SHF fields", Radiotekhnika i Electronica, v. 36, N 7, p.1369-1376., 1991
3. A. Kantonistov, I. Radchenko, G. Fursey, L. Shirochin, "Field emission of liquid metals in alternating fields", Col. de Phys, Tome 50, colloque C8, Suppl. au n° 11, C8-203 - C8-207, Nov., 1989.

EXPERIMENTAL DETERMINATION OF WORK FUNCTION ABOUT SILVER ALLOYS

LEFORT André, AKBI Mohamed, PARIZET Marie-José

Laboratoire "Arc Electrique et Plasmas Thermiques"
CNRS : URA 828 - Université Blaise Pascal
24, Avenue des Landais - F 63177 AUBIERE CEDEX

ABSTRACT

Models about arc roots need a good knowledge of physical constants characterizing contact material. With pure metal, all the constants are well known ; but for alloys some are not known. In this paper we relate how we have measured work function of silver alloys.

Measuring method used is the Fowler one where photoelectronic current produced by different ultraviolet radiations is measured in high vacuum. Experimental set-up have been tested for pure materials and then, have been applied to some silver alloys.

Results about pure metals show an evolution of the work function with temperature ; it decreases when temperature increases.

Results about silver-nickel alloys show a large dependence of obtained results with the preparation of contact surface. For example, polishing and cleaning induce, because of atom migration, a large modification of the ratio of the two components on surface ; this phenomenon induces a variation of work function comparatively with obtained values with primary product. By heating alloy contact in high vacuum we have observed large variations of work function, which result from material component vaporisation by sheets. Surface analyses by electron microscope produce proves of the phenomenon.

An empirical relation is given to calculate work function of binary alloy when this constant is known for each alloy component.

1. INTRODUCTION

Modelization of phenomena describing arc root evolution needs accurate data on material that gives rise to it. Several authors^{1,2} have shown that surface state and its composition from initial ones, have an effect on cathodic spot duration, on their dimensions and cathode erosion ; this is due to electron crossing from electrode metallic state to plasma state of ionizing region. In this case, presence of materials different from basic one or existence of micro tips yields electric fields which extract electrons. To improve understanding of these phenomena, we have measured work function for different cases of basic material evolution. Experimental method developed and used³ is based on measuring, in vacuum, photoelectric currents emitted by electrode exposed to ultraviolet radiations of different wave lengths and same intensity.

In the first part of this paper, we give our results for three pure metals (silver, copper and nickel) versus temperature.

In second part, we show how varies work function of AgNi alloy versus physical conditions and its composition.

2. RESULTS FOR PURE METALS

Electrodes used, made with pure metal (99.99 %), have a cylindrical shape with 8 mm in diameter, 3.5 mm in height and are exposed to UV radiation ; their actived surface is curved with curvature radius of 18 mm. Before using them, contacts are polished and then cleaned and rinsed with distilled water.

Results obtained, at room temperature, for pure metals (copper, silver and nickel) are in good agreement with those of other authors³ and so that shows that our experimental method is valid.

Table 1 gives work function evolution when emitting electrode is heated at different temperatures, in vacuum. We have seen that the material, even perfectly cleaned, does not give immediately after putting it in vacuum chamber, stable and reproducing values. It is necessary to wait some hours ; that corresponds to evaporation in vacuum of non metallic particles included on surface.

Table 1 : Work function W_s variation versus temperature for pure metals.

Pure metal (99.99 %)	Temperature (k)	W_s (eV)
Silver	296	4.26 ± 0.03
	533	4.08 ± 0.07
	733	4.04 ± 0.08
Copper	296	4.41 ± 0.03
	533	4.23 ± 0.07
	693	4.23 ± 0.08
Nickel	294	4.51 ± 0.03
	533	4.24 ± 0.07
	673	4.23 ± 0.08

It did not be possible to use higher values of temperatures because a thermoelectronic current is then superposed to photoelectric one, and its fluctuations are of the same order of photoelectric current. Values on table 1 show that work function decreases when metal temperature increases. Variation of order of 0.2 eV has a significant effect on physical properties of the new-born spot ; underlying material does not reach immediately working temperature. It would be interesting to measure work function of material reaching its melting point.

3. MEASUREMENTS FOR AgNi ALLOYS

Results presented here concern two alloy compositions : 70 % in silver mass for the first and 60 % for second contact ; shapes are described on paragraph 2.

3.1. Influence of polishing and thermal effect in vacuum

Measurements, made with clean but non polished materials, at room temperature, have given, after several days in vacuum, stable values presented in table 2. We have to point out that variations are smaller than measure incertitude and that the effect of staying in vacuum at room chamber is not very appreciable.

Table 2 : Results at 298 K for non polished materials.

Materials	W_s (eV)
AgNi (70/30)	4.37 ± 0.03
AgNi (60/40)	4.40 ± 0.03

For polished contacts, used in the same conditions described above, we have find results shown on table 3. The obtained difference for polished and unpolished contacts is significant and shows the effect of polishing which enriches surface contact on silver. This conclusion has been confirmed by observations on electronic microscope and analysis of polished contact surface.

Table 3 : Results at 298 K for polished materials.

Materials	W_s (eV)
AgNi (70/30)	4.33 ± 0.03
AgNi (60/40)	4.34 ± 0.03

3.2. Influence of contact heating in vacuum

In this type of experiments, results are the same for unpolished contacts than for polished ones, for both composition values. Contacts in ultravacuum chamber are submitted to cycles of heating and cooling (several hours). After each cycle, at room temperature, work function is measured. Maximum value of reached temperature is modified for each cycle.

Maximum values are the following : 350 K, 600 K, 700 K and 1000 K. Many experiments have been made ; all of them show that work function varies between work function values of each of two components (4.26 eV for Ag and 4.51 eV for Ni).

The nature of AgNi alloy explains these results ; both metals do not mix like in a solution and they are generally arranged on successive layers. In vacuum when heating, both metals evaporate on surface and so surface layer composition varies between practically 0 % to practically 100 % for one of the components.

3.3. Temperature influence

For polished AgNi (70/30) contacts, we have made some measurements with heating temperature maintained to its maximal value during several hours. Results are given on table 4.

Table 4 : Work function variation for AgNi (70/30) alloy versus maximum temperature of the cycle.

Cycle	Maximal temperature (K)	Measurement temperature (K)	Work function (eV)
1	530	563	4.39
2	530	530	4.42
3	580	580	4.41
4	290	290	4.49

A comparison with table 1 values for Ag and Ni shows that there is inconsistency for cycles 1, 2 and 3 : work function of alloy is significantly higher than this of each component for the same temperature.

We have obtained similar results for AgNi (60/40). It is difficult to explain this inconsistency.

3.4. Work function variation with the number of applied arcs

Contacts are put in a contactor working repetitively on air. A cycle consists on opening contacts on charge with production of an electric arc with adjustable duration and closing some seconds after arc extinction on zero voltage.

For used contacts, adjustments were the following :

- arc duration : 4×10^{-3} sec
- arc current : linear variation with time from 36 to 12 amps
- arc voltage : linear variation with time from 12 to 35 volts
- maximal space between contacts : 5 mm
- separation velocity : 1 m/sec
- gas used : air at atmospheric pressure.

When submitted to 100 electric arcs, AgNi (60/40) contact work function varies from $(4.33 \pm 0.03 \text{ eV})$ to $(4.30 \pm 0.03 \text{ eV})$. To obtain a very good vacuum for work function measurement, we have to clean contact before measuring it. It is obvious that measurement value should not be the same if oxides created on surface remained on it.

Same measurement made after 500 arcs gives $(4.38 \pm 0.03 \text{ eV})$. In this case, increasing is due to progressive inclusion of oxide on alloy surface.

3.5. Composition influence

Comparison between results of table 1 and 2, for room temperature induces us to propose a variation law of work function versus alloy composition. Using results of E. Choi and S. Oh⁴ on charge transfer in $\text{Ni}_x\text{Pt}_{1-x}$ alloys function of atomic proportion x of Ni, we find a linear law for work function versus x .

For $\text{Ag}_x\text{Ni}_{1-x}$ alloy, we show, on figure 1, this linear law versus x .

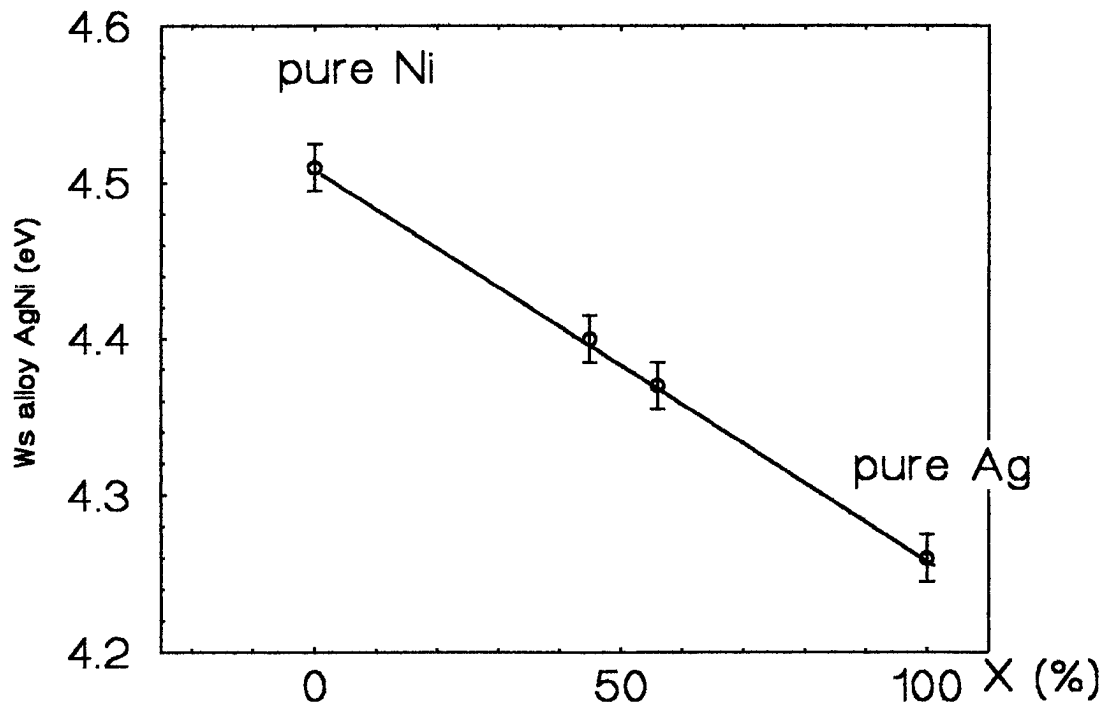


Figure 1 : Work function variation for $\text{Ag}_x\text{Ni}_{1-x}$ alloys.

4. CONCLUSION

Generally speaking, we can keep in mind from this study that work function of pure metals decreases with temperature increasing but this is not the case of alloys for which we found opposite result. These two results are significant because, using arc root models, it is possible according to the use of the contact (low currents, high currents, small arc duration, ...) to predict if contact material must be made with pure metal or with alloy. It should be interesting to carry on measurements for higher temperatures until melting point of the metal.

Background effect of thermoelectronic current could be minimized increasing UV radiation power on studied contact. It is obvious that the fact of putting contact in vacuum modifies its surface properties and cleans the surface when temperature increases.

Measurement method is well adapted to pure metal and their alloys, but it is necessary to be careful for composite material, particularly when surfaces are covered with oxide layer due to action of electric arcs.

REFERENCES

1. S. Anders and B. Jüttner, "Influence of residual gases on cathode spot behaviour", *IEEE Trans. Plas. Sci.*, Vol. 19, n° 5, pp. 705-712, 1991.
2. K.P. Nachtigall and J. Mentel, "Measurement of arc spot formation delay times at cold cathodes in air", *IEEE Trans. Plas. Sci.*, Vol. 19, n° 5, pp. 942-946, 1991.
3. A. Lefort, M. Akbi and M.J. Parizet, "Electron emission of silver alloying used for breakers", Cong. IC-ECAAA 2nd Int. Conf., Pekin, 1993.
4. E. Choi and S.J. Oh, "Charge transfer in $\text{Ni}_x\text{Pt}_{1-x}$ alloys studied by x-ray photoelectron spectroscopy", *Phys. Rev. B*, Vol. 43, n° 8, pp. 6360-6368, 1991.

Emission of a liquid metal interface in vacuum

G. Néron de Surgy (*), J.-P. Chabrier (*), J.-E. Wesfreid (**)

(*) Laboratoire de Génie Electrique de Paris (LGEP)

Plateau de Moulon, 91192 Gif-sur-Yvette France. URA CNRS 127

(**) Laboratoire d'Hydrodynamique et Mécanique Physique (LHMP)

ESPCI- 10, rue Vauquelin, 75005 Paris France. URA CNRS 857

ABSTRACT

The destabilization of an infinite plane surface of liquid metal by a normal electric field in vacuum has been the subject of different theoretical articles: above a critical field peaks grow on the liquid interface. A wavelength can be attributed to the resulting pattern. The electric field at onset and the corresponding wavelength only depends of the density and the surface tension of the liquid.

Above this critical field a whole range of wavelengths are excited, each growing with a different growth time: the fastest is the dominant wavelength.

We shall present the influence on dynamics of the liquid viscosity and of the liquid bath depth: it can be shown that the dominant wavelength is smaller with higher fields but differs if the liquid film is thick or thin, inviscid or viscous.

The further development of the pattern involves non-linear interactions. While a stable deformed interface has been observed on the analogous case of a magnetic fluid under magnetic field, experimentally (we worked with mercury) we only found stable non-plane interface for a confined geometry (disk with a diameter of a few mm) where the volume conservation makes the destabilization more difficult: indeed the critical field for the obtention of peaks is then greater than the value of the horizontally infinite surface. Otherwise, some peaks emit at their apex, killing the field: thus the peaks fall, do not emit any more and the electric field is installed again; this gives an oscillatory phenomenon.

For a sufficiently large liquid bath (compared to the wavelength so that the approximation of an infinite extension is valid) different wavelengths can be seen, depending on the electric field and the way this field was reached (slow or rapid installation). For confined geometries one or two peaks grow on the surface and the critical field can be significantly higher.

1. INTRODUCTION

We shall consider (see Fig.1) a conducting and incompressible layer of liquid metal laying on a metallic electrode. The undisturbed free surface of the liquid is at $z=0$ and the electrode at $z=-a$. Another electrode is disposed at $z=b$, with vacuum for $0 < z < b$ and a potential V is applied between the electrodes. The geometry will first be supposed to be unbounded for both x and y .

In the following we shall denote by ρ the density of the liquid, S its surface tension, η its dynamic viscosity, $\nu=\eta/\rho$ its kinematic viscosity, by ϵ_0 the permittivity of vacuum, g the gravitational field, by $\zeta(x,y)$ the vertical displacement of the interface, $\mathbf{v}(x, y, z)$ the velocity of the fluid, $\mathbf{e}(x, y, z)$ the electric field in vacuum and by $\mathbf{n}(x, y)$ the unit vector normal to the interface.

The stability of such a film under a normal electric field $E_0=V/b$ has already been studied in linear theory (Tonks ¹, Frenkel ², Taylor ³, Melcher ^{4, 5}, Nevrovskii ⁶, He *et al* ⁷, Néron de Surgy *et al* ⁸):

It is known that destabilization of an unbounded liquid surface occurs only above a critical field $E_c = \sqrt{\frac{2}{\epsilon_0} \sqrt{\rho} g S}$, for which

a pattern appears, associated with a critical wavelength $\lambda_c = 2\pi / k_c = 2\pi l_c = 2\pi \sqrt{\frac{S}{\rho g}}$, where k_c (resp. l_c) is the capillary wavenumber (resp. length). Above this field a whole range of wavelengths are excited, this range being limited by the curve of marginal stability. A linear analysis leads to a linear curve of marginal stability (Fig.2 for $b \gg l_c$), which is independant of viscosity η and fluid depth a .

We shall present the dynamics of the problem and an experimental study of the pattern where the restriction of a bounded geometry can affect the critical field value.

2. GENERAL CASE

2.1. The equations

The system is submitted to the following equations (for an incompressible fluid, and if η and S are constant):

$$\left\{ \begin{array}{l} \text{div } \mathbf{v} = 0 \\ \rho [\partial_t \mathbf{v} + (\mathbf{v} \cdot \text{grad}) \mathbf{v}] = -\text{grad } p + \eta \Delta \mathbf{v} + \rho \mathbf{g} \end{array} \right\} \text{ for } z < \zeta(x, y) \text{ (in the liquid metal)}$$

$$\left\{ \begin{array}{l} \text{curl } \mathbf{e} = 0 \\ \text{div } \mathbf{e} = 0 \end{array} \right\} \text{ for } z > \zeta(x, y) \text{ (in vacuum)}$$
(1)

with the following boundary conditions (where $\|X\| = X_2 - X_1$ = value above the interface - value under the interface,

$T_{ik} = \varepsilon_0 e_i e_k - \varepsilon_0/2 e^2 \delta_{ik}$, $\sigma'_{ik} = \eta (\partial_{x_k} v_i + \partial_{x_i} v_k)$ and R^{-1} = curvature of the interface (positive if towards the fluid)):

$$\left\{ \begin{array}{ll} \partial_t \zeta = v_z - v_x \partial_x \zeta - v_y \partial_y \zeta & \text{at } z = \zeta \quad (\text{free surface condition}) \\ -\|p\| n_i + \|T_{ik} + \sigma'_{ik}\| n_k - (S/R) n_i & \text{at } z = \zeta \quad (\text{stress balance at the interface}) \\ \mathbf{n} \times \mathbf{e} = 0 & \text{at } z = \zeta \quad (\text{liquid metal}) \\ \mathbf{v} = 0 & \text{at } z = -a \quad (\text{velocity equal to zero at the electrode}) \\ e_x = e_y = 0 & \text{at } z = b \quad (\text{electric field normal to the electrode}) \end{array} \right.$$
(2)

We limit ourselves to a linear analysis: using a Fourier expansion enables us to study the different modes apart. We therefore look at solutions with the following form:

$$A(\mathbf{r}, z, t) = A(x, y, z, t) = a(z) \exp(st - i\mathbf{k} \cdot \mathbf{r}).$$

It gives after some algebra the dispersion relation between the perturbation growth rate s and the wavenumber k (the modulus of the wavenumber \mathbf{k}) for a field E_0 :

$$4qk^3 [q - k \coth(ka) \coth(qa)] - (q^2 + k^2)^2 [q \coth(ka) \coth(qa) - k] +$$

$$+ \frac{4qk^2 (q^2 + k^2)}{\sinh(ka) \sinh(qa)} = \frac{\rho}{\eta^2} [Sk^3 - \varepsilon_0 E_0^2 k^2 \coth(kb) + \rho g k] [q \coth(qa) - k \coth(ka)]$$
(3)

$$\text{with } q^2 = k^2 + \frac{s}{\nu}$$

In the case of a vanishing viscosity, the equation (3) can be simplified; we retrieve the classical result of an inviscid layer:

$$\rho s_i^2 = [-Sk^3 + \varepsilon_0 E_0^2 \coth(kb) k^2 - \rho g k] \tanh(ka)$$

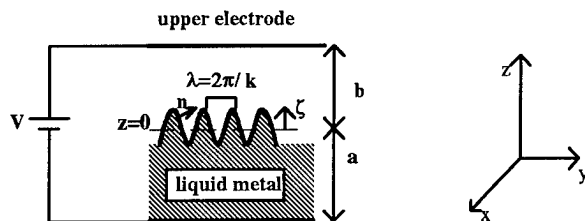


Figure 1. Principle of the experiment

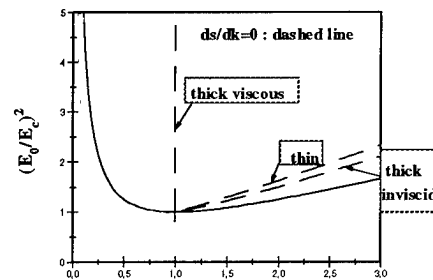


Figure 2. Curve of marginal stability and dominant modes (for $b \gg l_c = 1/k_c$, so that $\coth(kb) = 1$)

2.2. The dispersion equations for the different behaviours

The hypothesis used to derive the different equations should be verified around the dominant mode $s = s_{\max}$, obtained for $ds/dk = 0$, provided the potential has been applied sufficiently quickly: if the field is applied too slowly the transition will

occur before the maximal potential will be reached (for a very slowly applied field the transition occurs near the critical field) and once the instabilities have begun to grow, an increase of the potential will not change the wavelength. The time needed to put the potential should be smaller than the growth time (1/s) if we want that $ds/dk=0$ corresponds to the most important (dominant) mode.

The film is called thick (resp. thin) if $a >> 2\pi/\lambda$ (resp. $a << 2\pi/\lambda$) and inviscid (resp. viscous) if $\frac{\sigma}{\nu} >> \max(k^2, \frac{1}{a^2})$ (resp. $\frac{\sigma}{\nu} << \max(k^2, \frac{1}{a^2})$). We therefore encounter asymptotic behaviors that we summed up in Table I.

	thick	thin
inviscid	$\rho s_{tk,i}^2 = -Sk^3 + \epsilon_0 E_0^2 \coth(kb) k^2 - \rho g k$	$\rho s_{tn,i}^2 = [-Sk^3 + \epsilon_0 E_0^2 \coth(kb) k^2 - \rho g k] ka$
viscous	$s_{tk,v} = \frac{1}{2\eta} \left[-Sk + \epsilon_0 E_0^2 \coth(kb) - \frac{\rho g}{k} \right]$	$s_{tn,v} = \frac{(ka)^3}{3\eta} \left[-Sk + \epsilon_0 E_0^2 \coth(kb) - \frac{\rho g}{k} \right]$

Table I. Dispersion relations in asymptotic cases

The curve of marginal stability is defined by $s(k)=0$, which gives $\rho g - \epsilon_0 E_0^2 k \coth(kb) - Sk^2 = 0$, and plotted in Fig. 2 with the dominant mode for each case.

3. EXPERIMENTAL STUDY OF THE PATTERN

The liquid used is mercury. As usual for liquid metals viscosity can be neglected, and we shall work with sufficiently thick layers, unless otherwise stated.

The experimental device is showed in Fig. 3 and the electrical scheme in Fig. 4. The electric field is obtained thanks to two electrodes. The order of value of this field is 70 kV/cm. Is is well above the disruptive field of air (30 kV/cm) so that vacuum has to be made. The d.c. supply (Spellman DC Supply) allows tension up to 110 kV. We therefore took a value of b from 0.5 to 1 cm.

The geometry of the bath is axisymetric: the initial surface is a disk of radius R . An electrochemical treatment of the lateral boundaries has been performed leading to an anchorage of the liquid at $r=R$. The bath is filled so that the initial surface is flat (a consequence of the electrochemical treatment is that there is no fixed contact angle), see Fig. 5(a), and remains flat till the critical field (no deflection of zeroth order).

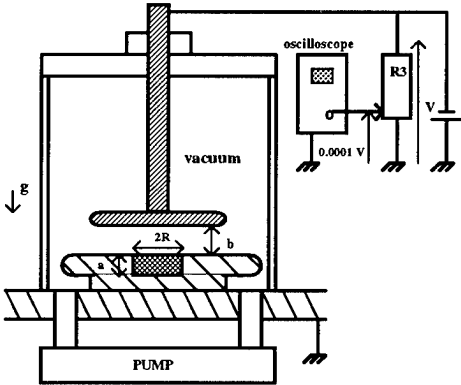
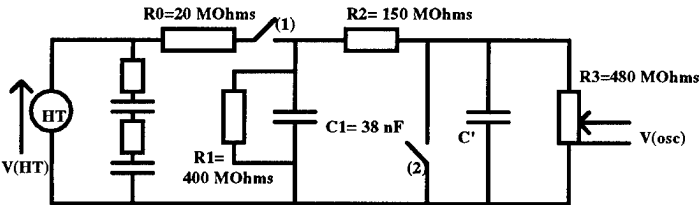


Figure 3. Experimental device



C' is the capacitance formed by the two electrodes

Figure 4. Electrical scheme

3.1. Laterally unbounded geometry

We shall first study the case of a large bath: it means that the pattern in the central part of the bath has enough place to forget the lateral boundary conditions, so the dimensions of the bath are great compared to the wavelength. The system can be considered as unbounded (in the horizontal directions).

Experimentally it is difficult to observe the initial linear stage of the phenomenon. As the peaks grow further non-linear interactions become important and the selection of the resulting pattern (squares, hexagones...as in other analogous situations^{10, 11}) is made by these interactions.

Once the peaks grow they emit at their apex when the radius of the tip is sufficiently small. A current I occurs so that the capacitance formed by the two electrodes is short-circuited: the tension at R_2 ($V_{R2}=R_2 \cdot I$) is sufficiently great so that $V_C=0$. Due to the current and to the alimentation potential it was not possible to obtain a stable emitter in vacuum.

We performed experiments with V positive and negative so that emission of electrons or ions occurs.

The value of the field that we found ($E_c=70$ kV/cm) was lower than the predicted one ($E_c=75$ kV/cm), with the listed properties of mercury ($\rho=13,5$ g/cm³, $S=450$ dyn/cm): an optical measurement of the surface tension gave a significantly lower value in air ($S=370$ dyn/cm, corresponding to the value given by Taylor and McDewan³): as the bath was filled in air without special preparation it can explain the value of S in vacuum and therefore the value of the critical field.

The non-stabilization and the emission of the peaks kill the field by the short-circuit. Once the field is zero again the instability tend to disappear and the current therefore stops. If the tension supply is still connected the field is installed again and the instability can grow another time.

This gives an oscillatory behavior that can be observed from the tension measured by an oscilloscope (Fig. 6). After some time one can see an oscillatory pattern with a given wavelength (Fig. 5(c)).

Increasing the tension of the alimentation then shortens the wavelength.

It is also seen that the phenomenon occurs with hysteresis: the oscillatory pattern, once obtained, continues to exist with an applied tension lower than the critical tension (Fig. 5(d)).

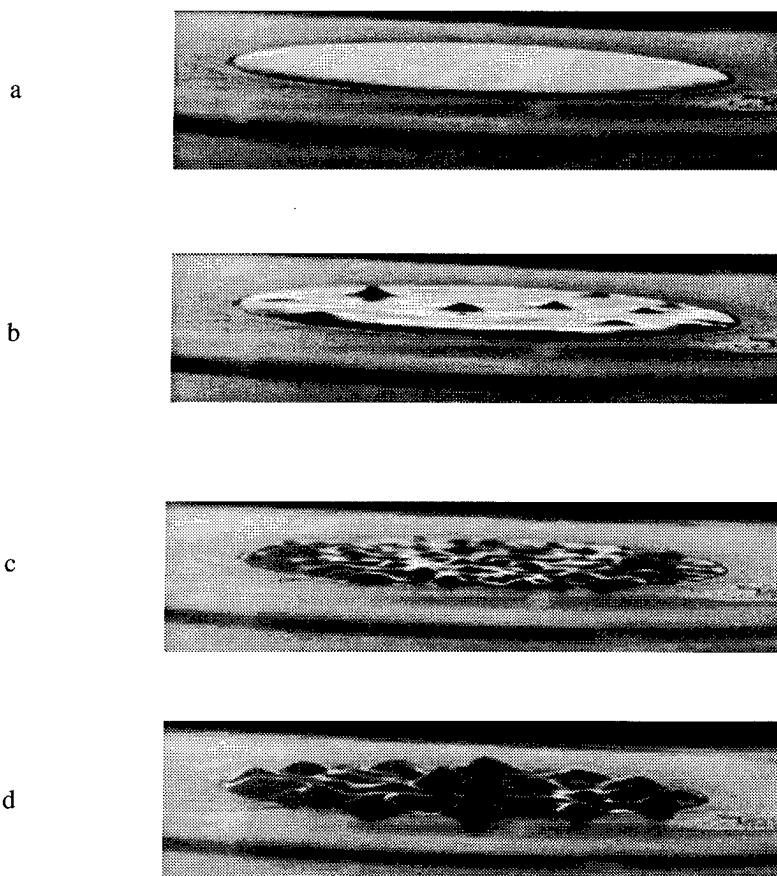


Figure 5. Patterns in large geometry ($R=2$ cm)

a: No electric field, b: At onset, c: Above onset, d: Under the critical field after transition (hysteresis)

Slow installation of the tension:

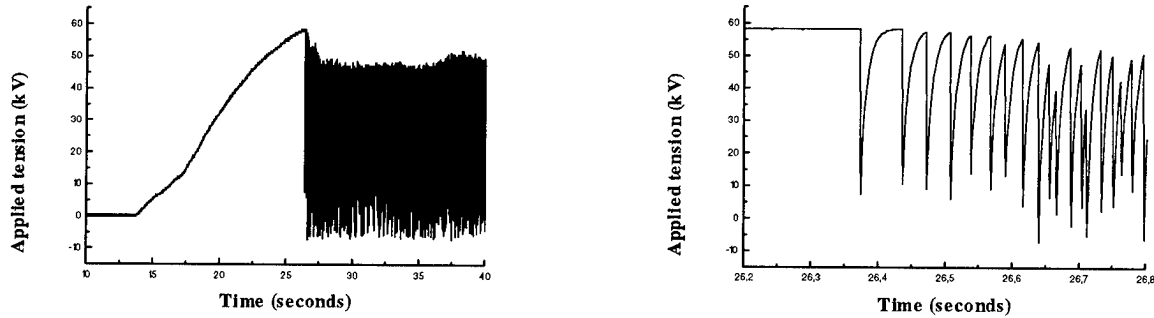


Figure 6. Typical evolution of the tension ($b = 8$ mm)

3.2. Confined geometry

For a confined geometry (i.e. the radius of the bath is of the order or less than the wavelength which corresponds for mercury to a diameter < 1 cm) one does not see a real pattern but a small number of peaks. The confinement makes the destabilization more difficult when the liquid is properly anchored at the lateral walls because the wavelength must fit the bath. The critical field is then higher (Table II) and a stable non-emitting deformed interface can be observed. A stable emitting surface was not obtained in vacuum (due to the current as explained above).

Radius R of the bath in cm	0.10	0.15	0.20	0.25	0.30	0.35	0.40	0.50	4.00
Field at onset (in kV/cm)	132	112	100	86	82	77	77	70	70

Table II. Critical field at onset for small radii of the bath

A rigorous calculation of the critical field for a radius R has been performed elsewhere⁹. The corresponding law fits well with the following form:

$$E_c(R)^2 = E_c(\infty)^2 \left(1 + \left(\frac{\xi_0}{R} \right)^2 \right) \quad (4)$$

where ξ_0 is a parameter (coherence length) of the order of l_c and $E_c(\infty)$ the critical field in unbounded geometry.

It is possible to observe that this deformation corresponds to a displacement of the surface combination of functions of the type $J_m(kr) \cos(m\theta)$ where J_m is the usual Bessel function of first kind. For small baths a single value of m leads to an approached solution near to the complete solution: a critical field $E_c(m, R)$ can be attached to each mode. If the fields are not equal the onset is reached for a given m (corresponding to $\min(E_c(m, R))$). In this case m is the number of peaks and $m=1$ is the first mode to be destabilized for small radii.

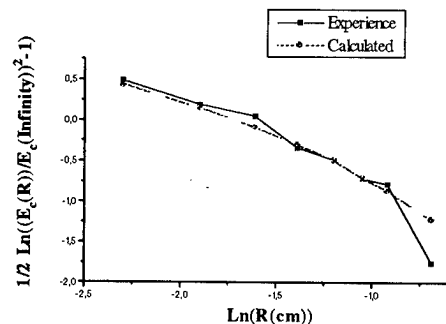


Figure 7. $\frac{1}{2} \ln \left(\left(\frac{E_c(R)}{E_c(\infty)} \right)^2 - 1 \right)$ vs $\ln(R)$

We have plotted in Fig. 7 $y = \frac{1}{2} \ln \left(\left(\frac{E_c(R)}{E_c(\infty)} \right)^2 - 1 \right)$ versus $x = \ln(R)$, with experimental and calculated ($m=1$ dashed line, with $S=370$ dyn/cm) data.

The equation (4) corresponds to $y = \ln(\xi_0) \cdot x$ and a linear regression gives (R was taken in cm in the formula): $y = \ln(0.18) - 0.98 x$. So it gives: $\xi_0 \approx l_c = 0.17$ cm.

For higher values of the field, the curvature becomes large enough and is not stable any more. The apex becomes significantly thinner and then begins to emit.

So a pattern can be observed on a large bath which appears for the well-known critical field of unbounded geometry. A small number of peaks appear for a small bath at a new and higher critical field $E_c(R)$, we then found a stable deflected surface. An intermediate case occurs for diameters that only allow a small number of peaks but for which the critical field is approximately equal to the one of the infinitely large case (diameter=1 cm). In this case no stabilization of the emitter has been observed in vacuum for our values of b . In very small bath ($R=1$ mm) we found a deflection of the surface which was not straightly followed by emission. For thin layers of mercury and gallium an experimental stabilization of the liquid emitter has been performed by replacing vacuum by paraffin oil: the current is then sufficiently small so that the electric field still exists.

4. CONCLUSION

The destabilization of a liquid interface by a normal electric field fits well with the usual linear theory. However, the effects of the lateral geometry can affect the critical value: for very small sizes of the bath the field necessary to obtain a deflection of the liquid surface is significantly higher. The obtention of the pattern was obtained thanks to the boundary conditions: anchorage of the fluid on the lateral bath boundaries and volume conservation; it prevents a destabilization of zeroth order before onset. Stabilization of the pattern was not observed in vacuum due to the current emission that killed the field, instead an oscillatory behaviour takes place: this prevents a full pattern of sharp peaks to be obtained. We observed that, once it has appeared, the instability grows till emission, except in very confined geometry.

5. ACKNOWLEDGMENTS

We would like to thank H. Gonzales for the theoretical aspect, R. Brimaud and F. Barata for the technical part of the experiment, and S. Assal for interesting discussions.

6. REFERENCES

1. L. Tonks, "A theory of liquid surface rupture by a uniform electric field," *Phys. Rev.*, Vol. 48, pp. 562-568, 1936.
2. Ya. I. Frenkel, "Tonks theory of liquid-surface rupture by a constant electric field in vacuo," *Zh. Eksp. Teor. Fiz.*, Vol. 6, p. 347, 1936.
3. G.I. Taylor and A. D. McDean, "The stability of a horizontal fluid interface in a vertical electric field," *J. Fluid Mech.*, Vol. 22, pp. 1-15, 1965.
4. J.R. Melcher, "Electrohydrodynamic and Magnetohydrodynamic Surface Waves and Instabilities," *Phys. Fluids*, Vol. 4, pp. 1348-1354, November 1961.
5. J.R. Melcher, *Continuum Electromechanics*, Chapter 8. The MIT Press, 1981.
6. V.A. Nevrovskii, "Instability of molten-metal film in an electric field," *Izvestiya Akademii Nauk SSSR, Mekhanika Zhidkosti i Gaza.*, Vol. 4, pp. 20-28, 1977.
7. J. He, N.M. Miskovski, P.H. Cutler and M. Chung, "Effects of viscosity on capillary wave instability of a planar liquid-metal surface in an electric field," *J. App. Phys.*, Vol. 68, pp. 1475-1482, August 1990. *Their equation (33) is different from our relation (3), which is equivalent only for thick films, because of a sign error in the determinant.*
8. G. Néron de Surgy, J.-P. Chabrierie, O. Denoux and J.-E. Wesfreid, "Linear growth of instabilities on a liquid metal under normal electric field," *J. Phys. II France*, Vol. 3, 1201-1225, August 1993.
9. H. Gonzales, G. Néron de Surgy and J.-P. Chabrierie, "Influence of bounded geometry on electrocapillary instability," *to be published*.
10. E.A. Kuznetsov and M.D. Spektor, "Existence of a hexagonal relief on the surface of a dielectric fluid in an external electric field," *Sov. Phys. JETP*, Vol. 44, pp. 136-141, 1976.
11. A. Gailitis, "Formation of the hexagonal pattern on the surface of a ferromagnetic fluid in an applied magnetic field," *J. Fluid Mech.*, Vol. 82, pp. 401-413, 1977.

Field evaporation of HTS-materials as a nonequilibrium process

Vladimir N. Shrednik

A. F. Ioffe Physico-Technical Institute, 26 Polytekhnicheskaya st.
St Petersburg 194021, Russia

ABSTRACT

The problem of field evaporation (FE) of the high temperature Superconductors (HTS) is discussed. The experimental data were obtained by techniques of wide-angle atom-probe and probe-hole atom-probe. These data are analyzed with the aims to estimate the binding energy λ of removing particle from the surface and to find some possible correlation between simultaneously detected species. Both results of these processing show that destroy of unit cell of HTS-crystal at the elementary act of FE is essentially nonequilibrium process, and that well developed FE-theory of metals is only partly valid for HTS-materials.

1. INTRODUCTION

Field Evaporation (FE)—cold evaporation of material of conducting sample in the presence of high electric field is now well studied for metals, alloys and some semiconductors.¹ This process as a kind of ion emission in high field can be involved in various breakdown (and especially prebreakdown) phenomena.

High Temperature Superconductors (HTS) promise to be applied in many electrical devices both in scientific and industrial fields. Therefore the problem of prebreakdown phenomena regarding to HTS-materials is significant and interesting in connection with main topics of this symposium. However, the behaviour of HTS-material in high electric field and the field evaporation of these materials in particular is still not so carefully and fully studied as for example in the case of refractory metals. Modern HTS-materials are multicomponent oxide crystals with composition and structure (usually some kind of perovskite lattice) essentially more complicated in comparison with metals. At the field evaporation of metals the removing of an atom does not change principally the situation for removing of the next one. Therefore we consider this process as equilibrium process in some approximation. At the field evaporation of HTS-material such reproducible situation could be realized when whole the unit cell of the HTS-crystal would be removed in elementary act of the field evaporation. However, the possibility of removing by FE as ion of individual atoms or small radicals i.e. only a part (and small part) of this unit cell is now well proved. In this case the situation for the next step of field evaporation after previous one will be changed periodically in spite of the keeping constant all the conditions of the experiment. Such situation we will consider as nonequilibrium.

The main aim of this paper is to analyze some experimental data regarding to the field evaporation of HTS-crystals and to show that the FE-process is really more complicated for the HTS-materials, than for the metals. We also try to find out some ways of obtaining the experimental data which enable to extend our theoretical understanding of such complex problem as field evaporation of HTS-material.

2. EXPERIMENTAL

Two kind of atom probe technique have been used for the field evaporation of HTS-materials: wide-angle atom probe and probe hole atom probe. Both devices are combination of field ion microscope with time of flight mass-spectrometer and enable to remove surface atoms (or group of them) after observation of surface structure usually in atomic scale. The operation of the device carries out usually in so called soft regime when one pulse of high voltage removes only one or two (and very seldom three or more) particles from the surface but more often it does not remove anything at all. Field electron and field ion calibration enables to obtain such data as field factor $\beta = F/V$ (F —field strength, V —voltage) and work function φ .² Field ion image (usually with nitrogen as image gas) was used for visualization of the surface structure and proving its purity and perfection. Measuring of evaporating voltage was used for evaporating field F_e determination. Liquid nitrogen could fill the cold finger and then solid nitrogen could be produced there by pumping. Therefore the experiments could be performed both at the temperature (T) reliable low than phase transition $T - T_c$ and at some higher T up to room temperature.

We have used in the FE-experiments the HTS-material such as (123) single crystals on the base of Tb, Eu and Gd. More detailed description of electrical and registration circuits and principals of results processing are presented in original papers.²⁻⁵

3. ESTIMATION OF BOND ENERGIES IN HTS SINGLE CRYSTALS

The theory of FE developed for metals¹ enables one to determine the bond energy λ of an atom leaving the surface⁶

$$\lambda = \sqrt{F_e n^3 e^3} - \sum_n I_n + n\varphi, \quad (1)$$

where F_e , φ and n (ion change) are measured and I_n —the energy of ionization to form n -fold charged ion—should be known from a handbook, e —is electron charge. The formal application of equation (1) to experimental data for Eu (123) crystal has given the result shown in Table 1.

Table 1

Ion species	Ba ⁺⁺	Eu ⁺⁺	Eu ⁺⁺⁺	Cu ⁺	Cu ⁺⁺	O ₂ ⁺	BaO ⁺	EuO ⁺
λ (eV)	4.73	3.63	-6.48	0.73	-7.17	-3.55	1.95	4.45

The binding energy λ has reasonable values for Ba⁺⁺ and Eu⁺⁺ only. They are close to the corresponding binding energies in the oxides BaO (5.8 eV) and (5.71 eV).⁷ It means that for these electropositive metal atoms (Ba and Eu) the classical theory of field evaporation is rather valid. Practically the ion Eu⁺⁺⁺ is observed in atom probe spectra more often than relatively rare ion Eu⁺⁺. However, the transformation of Eu⁺⁺ to Eu⁺⁺⁺ can be realized easily by post ionization in a very high field. Oxide ions BaO⁺ and EuO⁺ have also the λ values that is not too strange. May be it explains the great number of oxide ions in the FE-spectra of the HTS-materials. FE of species in oxide form can be energetically profitable. Nevertheless, the λ for many species typical for the FE-spectra are very strange: too small or even negative. It could mean that they release at the too small field as compared with the field expected from the theory of FE and formula (1). It is natural to suppose that some redistribution of interatomic bonds takes place after removing of some particles such as Ba, Eu, BaO, EuO from the unit cell of Eu (123). The disturbed part of the surface relaxes and shoots by some other ions practically simultaneously and at the same field necessary for release of some mentioned electropositive ions. This field is theoretically normal for the electropositive ion and too small for such species as Cu⁺, O⁺, Cu⁺⁺. The same estimation of λ with practically the same result were carried out recently for Tb (123).⁸ It is obvious from this λ -estimations that the theory of FE has to be developed taking into consideration the peculiarities of multicomponent chemically complicated conductors generally. From the idea of the relaxation of the unequilibrated unit cell becomes also clear that simultaneous release of some correlated pairs (or more large groups) of field evaporated species is quite probable.

4. SEARCH FOR CORRELATED ION GROUPS IN THE FE-SPECTRA

4.1. Experiments with wide-angle atom probe

An area of about 10^5 \AA^2 with about 10^4 surface atoms was analyzed in these experiments on the sample of well cleaned (by FE) single crystal of Eu (123). Practically every pulse removed from the surface one, two or three particles. Nevertheless such regime of FE has to be considered as soft one because of relatively large analyzing area. After 181 acting (non-zero) pulses (caused release at least one ion) more than 360 ions were detected. However, this removed material consisted of small part of the monoatomic layer. Then it reasonable to consider the overall field to be constant during the whole experiment. The integral FE-spectrum for this studied surface is shown for example in Ref. 6. The methods of processing of measured data are described in details.^{3,4} Here we present the results of the FE-experiments separately for three groups of detected ions (Fig. 1), for pulses when only one species was detected (Fig. 1a), when two species (Fig. 1b) and three species (Fig. 1c) were detected simultaneously.

Table 2

Type of pairs	Detected amount	Type of triplets	Detected amount
CuO ⁺⁺ -Cu ⁺⁺	34	CuO ⁺⁺ -Cu ⁺ -Eu ₂ O ₃ ⁺⁺⁺	11
Cu ⁺⁺ -Cu ⁺	7	CuO ⁺⁺ -Cu ⁺ -EuO ₂ ⁺⁺	2
CuO ⁺⁺ -EuO ₂ ⁺⁺	4	Cu ⁺⁺ -Cu ⁺ -Eu ₂ O ₃ ⁺⁺⁺	2
Eu ⁺⁺⁺ -Cu ⁺	3	Eu ⁺⁺⁺ -Cu ⁺ -Eu ₂ O ₃ ⁺⁺⁺	2
Eu ⁺⁺⁺ -Eu ₂ O ₃ ⁺⁺⁺	3		

Therefore we consider these three partial spectra. The experimental conditions are shown at figure capture. These spectra are so called line spectra, drawn with the assumption that time of flight error $\Delta\tau = \pm 5 \text{ ns}$.⁶ From

comparison of these three spectra is clear, that Eu^{+++} ion has peak of maximum height on the Fig. 1a spectrum. It means that release of Eu^{+++} species as single is more probable. Opposite to them such ions as CuO^{++} and Cu^{++} are released mainly as pairs. Heavy ions such as EuO^{++} and $\text{Eu}_2\text{O}_3^{+++}$ are not presented at Fig. 1a, they are released in pairs and $\text{Eu}_2\text{O}_3^{+++}$ mainly in triplets. The Table 2 summarizes the associates of lattice ions which were observed more often and shows the number of such associates.

It is easy to see that some most often observed pairs are included in most often observed triplets. The whole number of the detected pairs is 86 and of the detected triplets is 46. It is obvious that the great number of CuO^{++} – Cu^{++} pairs—34 (or even 47 if one takes into account 13 such pairs included in triplets) is more than expected value based on the idea of random events. The same conclusion could be done for Cu^{++} – Cu^+ associates and may be for some others. The more rigorous statistical analysis is here hardly possible because only the kind of species is well detected in these experiments. How many individual ions correspond to some certain peaks—it may be established not always, though too great number of ions in the peak (more than 2–3) is improbable.

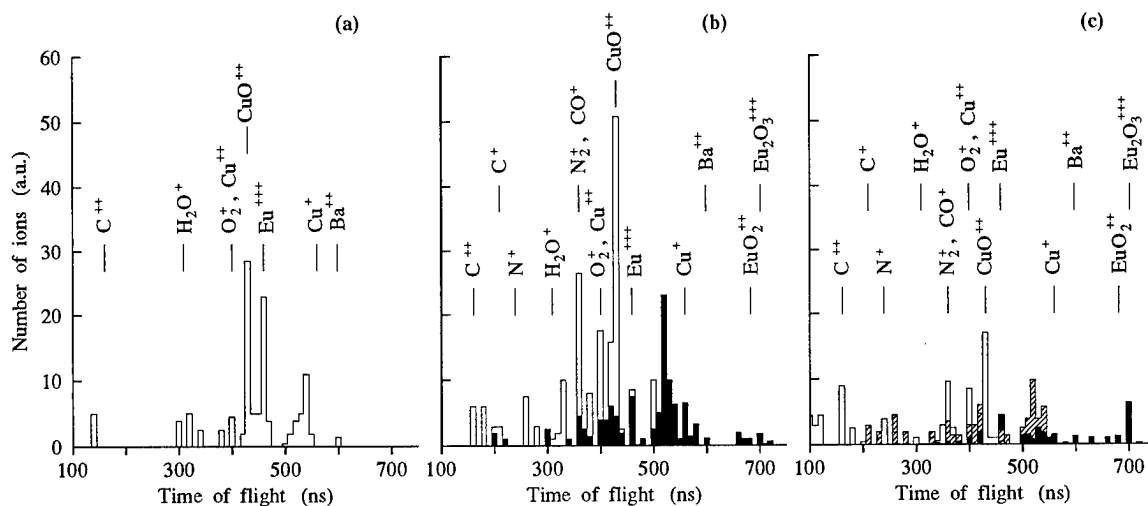


Fig. 1. Wide-angle atom probe spectra for Eu (123) ($T_c \cong 95$ K) obtained under the following conditions: vacuum is better than 10^{-9} Torr, liquid nitrogen cooling of the sample. Resulting voltage V is the sum of base steady state voltage V_0 and pulse voltage ΔV : $V = V_0 + \Delta V = (10 + 2)$ kV. Surface was reliably cleaned by field evaporation. (a) Line spectrum of single ions. (b) Line spectrum of pairs of ions. (c) Line spectrum of triplets of ions. The groups of ions at plots (b) and (c) are indicated by corresponding shading.

4.2. The experiments with probe-hole atom-probe

Fig. 2 shows the FE-spectrum for Gd (123) obtained at cryogenic temperature (liquid nitrogen cooling) in probe-hole atom-probe. It is typical for such spectra studied also for Sm (123) and Bi (2212) materials. These spectra consist of many detected lattice species such as metal and oxide ions. We analyze more detailed namely these Gd (123)-spectrum.

The regime of operation in these experiments was soft also. Only 264 pulses from 2587 were non-zero removing at least one particle from the surface. It enables us to believe that each elementary peak registered by detector corresponded to single ion, and rigorous statistical analysis was possible here. 9 kinds of ions: Cu^{++} (or O_2^+), Gd^{+++} , Ba^{++} , GdO^{++} , CuO_2^+ (or Gd_2^{+++}), $\text{Gd}_2\text{O}_3^{+++}$, Ba^+ , Gd^+ , GdO^+ were detected. From this set of ions 36 kinds of pairs could be formed principally. However, only 14 kinds of such pairs were detected in the real experiment. Some of them were detected several times (from 3 to 8), besides they could be involved in rather rare triplets and groups of 4 ions. From 264 effective pulses 219 have given single species, 35—two species (pairs), 8—triplets, and 2—four species. Choosing the pairs which were detected more than three times (including the groups with 3 and 4 species also) we have obtained that pairs: Gd^{+++} – Cu^{++} , GdO^+ – Ba^{++} , Gd^{+++} – Ba^{++} , Gd^{+++} – $\text{Gd}_2\text{O}_3^{+++}$, Gd^{+++} – GdO^{++} were formed essentially more often than it could be predicted on the base of theory of probability. The arising probability for all the pairs numerated above was at least three times higher than theoretically calculated one. More impressive difference between real probability of observation and predicted probability was revealed for triplets and especially for groups of 4 species. These observations seem to prove the idea of existence of correlated pairs (or groups) in the FE-spectra of HTS-materials. Some preliminary observations were carried out on other HTS-materials both at cryogenic and room temperatures. They have shown many individual peculiarities however

the observation of some groups of species as well as absence of some theoretically expected groups are not in good agreement practically always with the model of random events. More detailed this problem is discussed in Ref. 9.

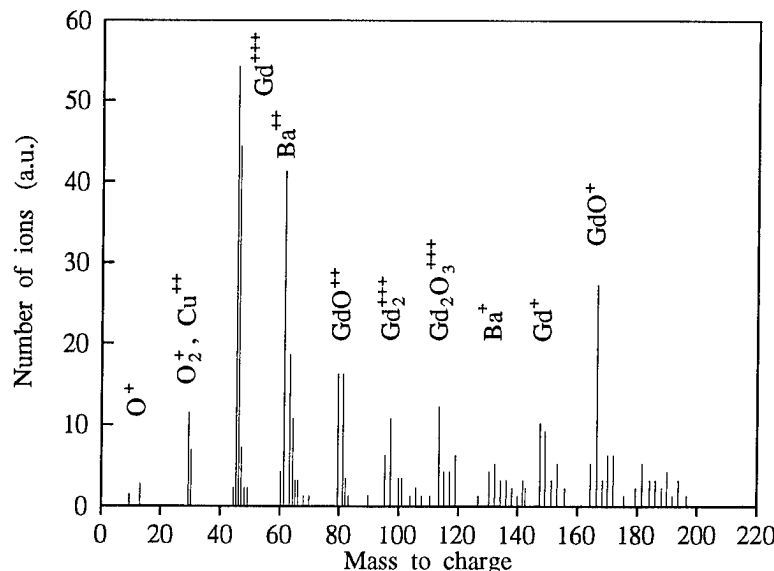


Fig. 2. Probe-hole atom-probe spectrum of Gd (123) ($T_c = 92$ K) obtained under the following conditions: vacuum is as 10^{-8} Torr, liquid nitrogen cooling of the sample. $V = V_0 + \Delta V = (7 + 3)$ kV.

5. CONCLUSION

All the material considered above shows that field evaporation of HTS-crystals is complicated and essentially nonequilibrium process of destroy of unit cell. The development of theory of FE of the multicomponent substances is necessary. The careful investigation of statistics of the field evaporating groups of species can shed some light on the nature of interatomic bonds and their changing at phase transition at T_c .

6. ACKNOWLEDGMENTS

I wish to express my sincere thanks to Dr. Yu. A. Vlasov and Mrs. E. L. Kontorovich and T. I. Sudakova for their kind assistance in preparing this paper.

7. REFERENCES

1. E. W. Muller and T. T. Tsong, "Field Ion Microscopy, Field Ionization and Field Evaporation," *Progress in Surface Science*, Vol. 4, part 1, 1973.
2. Yu. A. Vlasov, O. L. Golubev, N. A. Samokhvalov, N. N. Syutkin, E. F. Talantsev, N. M. Chebotaev and V. N. Shrednik, "Determination of work function of $\text{EuBa}_2\text{Cu}_3\text{O}_{7-x}$, $\text{TbBa}_2\text{Cu}_3\text{O}_{7-x}$ and $\text{DyBa}_2\text{Cu}_3\text{O}_{7-x}$ single crystals," *Sov. Tech. Phys. Lett.*, Vol. 15, no. 12, pp. 977-979, 1989.
3. Yu. A. Vlasov, O. L. Golubev, N. N. Syutkin, E. F. Talantsev and V. N. Shrednik, "Field desorption from the surface of superconducting perovskites," *Sov. Phys. Tech. Phys.*, Vol. 35, no. 10, pp. 1208-1210, 1990.
4. Yu. A. Vlasov, O. L. Golubev, E. L. Kontorovich and V. N. Shrednik, "Field evaporation of a $\text{Bi}_2\text{Sr}_2\text{Ca}_2\text{Cu}_3\text{O}_y$ single crystal," *Pis'ma Zh. Tekh. Fiz.*, Vol. 17, no. 24, pp. 5-9, 1991.
5. M. V. Loginov, O. G. Saveljev and V. N. Shrednik, "Field desorption of the protonated water clusters from HTSC surfaces," *Zh. Tekh. Fiz.*, Vol. 63, no. 8, August 1993 (in press).
6. Yu. A. Vlasov, O. L. Golubev, E. L. Kontorovich and V. N. Shrednik, "Estimation of bond energies for some atoms of HTSC single crystal lattice," *Pis'ma Zh. Tekh. Fiz.*, Vol. 18, no. 22, pp. 11-14, 1992.
7. *Energy of breaking chemical bonds, ionization potentials, and electronegativities*, Nauka, Moscow, 1974.
8. Yu. A. Vlasov, O. L. Golubev, E. L. Kontorovich and V. N. Shrednik, "Nonequilibrium character of destroy of the HTS-crystal unit cell at field evaporation," *Zh. Tekh. Fiz.*, Vol. 64, 1994 (to be published).
9. O. G. Saveliev and V. N. Shrednik, "Correlated groups of ions in HTS-material field evaporation spectra," *Zh. Tekh. Fiz.*, Vol. 64, 1994 (to be published).

Thermionic emission investigation of materials for directly heated cathodes of electron tubes

B.Gellert, W.Rohrbach
THOMSON ELEKTRONENRÖHREN AG
CH-5600 Lenzburg

ABSTRACT

Thermionic emission of new material compositions are studied. Combinations of rare earth materials and tungsten offer great potential as thermal electron emitter into vacuum. The thermal emission properties of these materials are studied and compared to thoriated tungsten as a well-known thermal emitter. The corresponding work functions and Richardson Dushman constants are evaluated. The chemistry involved and the emission mechanism are discussed.

1. INTRODUCTION

Thermal emitting cathodes are used in vacuum electron tubes for many applications as e.g. transmitters, industrial generators, lasers, microwave or radar applications. Thermionic emission has become also important for new applications in accelerators, high resolution microscopy or field emitter displays etc.

Standard materials for directly heated cathodes of electron tubes are based on thoriated tungsten (WTh). In the last years, however, new materials have been investigated^{1,2}. This is due to newly developed manufacturing technologies that allow for new material combinations and also because of stricter environmental and health legislation to avoid the handling of radioactive components like thorium. The reports of the past were mainly restricted to rare earth materials in a molybdenum matrix³. It was thereby possible to reduce the typical heating temperature of a cathode filament by up to 200 degrees to obtain the same emission as that of thoriated tungsten. The basic mechanism was not studied.

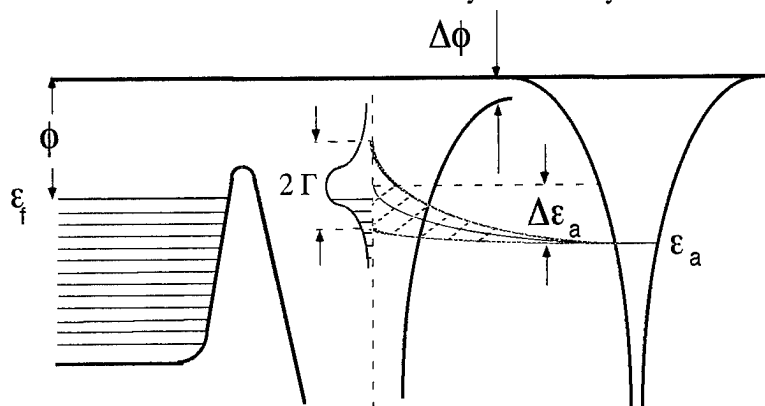
In this study we investigate fundamental aspects of thermionic emission of new materials (rare earth components in a tungsten base) and compare the results to standard material.

2. MODEL OF THERMIONIC EMISSION

Theoretical models of thermionic emission are well-known and can be found e.g. in⁴. The release of an electron from the bulk of a solid, e.g. a clean homogeneous metal, requires an energy given by the work function ϕ . The work function is defined by the potential difference between the Fermi level with energy ϵ_f and the energy of the vacuum level eV_∞ for infinite distance $x = \infty$ of an electron. Since measurements of physical parameters like the saturation current involves application of an accelerating field, the potential barrier at the surface can be lowered further by the Schottky effect.

Fig. 1

Static substrate model according to Gurney⁵
The model describes the energy levels of a solid with an adsorbed atom of energy ϵ_a that is broadened near the surface to result in a spectrum of local density states with FWHM 2Γ .



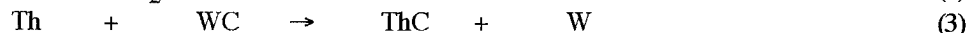
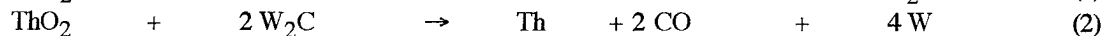
The situation is, however, not as simple, if a multi-component system is considered. The simplest approach is that for an emitting atom of type A placed on a solid metal of type B. This may be described by the static substrate model, which was originally developed by Gurney for adsorbed atoms⁵. The system of thoriated tungsten or rare earth atoms in tungsten can be dealt with in this manner, because mono-layers of thorium or rare earth atoms are formed on the surface of the tungsten base material. The model is depicted in fig. 1 (confer ref. 6). If a free atom approaches the bulk material and finally is attached to it, its energy level changes from a distinct value ϵ_a to a broadened spectrum of local density states near the surface due to the interaction with the atoms of the bulk material. Fig.1 shows the density of states with FWHM of 2Γ . The barrier for the electrons is at the same time reduced by the attached atom and new states can be filled up. These new states reduce the work function by $\Delta\phi$. For values of the lowering of the work function due to such effects see e.g. ref.7. The model becomes more complicated, if higher coverages occur. Then also interactions between the different mono-layers must be considered, i.e. mutual influence of the corresponding dipoles. This will lead to a deviation from the linear decrease of $\Delta\phi$ and is not wanted for applications like cathode filaments of electron tubes.

To obtain layers of thorium or rare earth atoms basically two ways are possible

- produce a coating of thorium or rare earth atoms on a pure substrate of tungsten, or
- utilise a multi-component substrate consisting of tungsten and a corresponding oxide (e.g. ThO₂).

The second method makes use of powder metallurgical processes to manufacture the substrates e.g. in the form of wires. In order to generate a layer of thorium or rare earth material at the surface of such a substrate, a special chemistry is necessary to continuously reduce the oxide. This can be accomplished by a W₂C coating around the tungsten base material. The process to coat tungsten wires in the appropriate way is known as "carburisation" and described e.g. in ⁸.

As an example the chemistry of thoriated tungsten is given. The rare earth reactions are corresponding. The following reactions play the most important part at the surface and in the layers



Reaction (1) describes the generation of thorium atoms at the surface even without W₂C coating. This reaction is important at high temperature. The W₂C coating allows a thorium production at lower temperature and therefore lower thorium evaporation by reaction (2). The unwanted side-reactions (3) and (4) contribute only little in the temperature range considered. Reaction (5) is the carburisation process itself, whereas reaction (6) is a loss process producing WC which again prohibits thorium formation at the surface e.g. by reaction (3). Optimum conditions for the formation of thorium layers are in the temperature range between 1400 K and 2200 K, in which the experiment was performed.

In this study mainly electrical properties were measured. The most easily obtainable physical parameter is the saturation current density J which is given for electrons emerging from clean homogeneous metal surface at temperature T by the Richardson-Dushman equation

$$J = A (1 - r_e) T^2 \exp(-\phi / k_b T), \quad (7)$$

$$A = 4 \pi m k_b e / h^3 = 120 \text{ A cm}^{-2} \text{ degree}^{-2},$$

$$m, e = \text{electron mass, charge}$$

$$h = \text{Planck's constant,}$$

$$k_b = \text{Boltzmann's constant}$$

$$r_e = \text{mean value of the zero-field reflection coefficient for the incident electrons}^6 \text{ (neglected in the evaluations below)}$$

3. EXPERIMENTAL ARRANGEMENT

The experimental set-up is sketched in fig. 2. Single wires are investigated. Each wire is mounted by a special holder to allow for experiments of particularly brittle carburised test wires. The complete set-up is mounted in a vacuum chamber. A typical vacuum of better than $5 \cdot 10^{-6}$ mbar is obtained by a turbo-molecular pump. Particular care is taken to install clean wires. They are fixed between insulated pincers and connected to a variable voltage source. In that way direct heating of the wires is possible under well-defined conditions. The test substrate is mounted concentrically in a cylindrical system made of molybdenum that functions as an anode. The cylindrical configuration consists of three parts. During the emission measurement the two outer parts are grounded to cathode potential in order to reduce distortions of the applied electrical field. The anode system has a slit of 1mm width to be able to measure the wire temperature pyrometrically. A two colour pyrometer is used that is carefully calibrated by comparison measurements. The gap spacing is chosen such that it is possible to take measurements with the applied pulsed source also in the space charge region. The source and measurement devices are in-house developed instruments to fulfil the special measurement requirements. A condensor is charged to voltages up to 2000V and discharged via a thyristor across the test sample under investigation. Pulse length is approximately 2ms. The voltage U between filament and anode cylinder is displayed versus emission current I_e simultaneously. The filament current I_f and voltage U_f are monitored as well. The display is calibrated by an internal calibration source. Lanthanum, cerium and thorium containing wires are manufactured by powder metallurgical methods. For the investigation of the thorium coverage of tungsten a wire with a thorium coating was produced by evaporating thorium from a substrate and coating a tungsten wire. All wires used in the experiments are pre-treated. The wires are electro-polished and carburised. At the end of the carburisation process special care is taken to make sure that no crack products of hydrocarbons from the carburisation process are present at the surface of the wire. After mounting into the

vacuum chamber the test samples are conditioned for several hours. Samples treated in that way show reproducible, optimised emission.

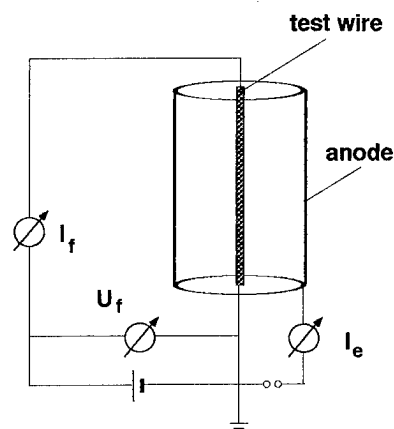
Fig. 2

Experimental arrangement

I_f : cathode filament current

U_f : cathode filament voltage

I_e : emission current

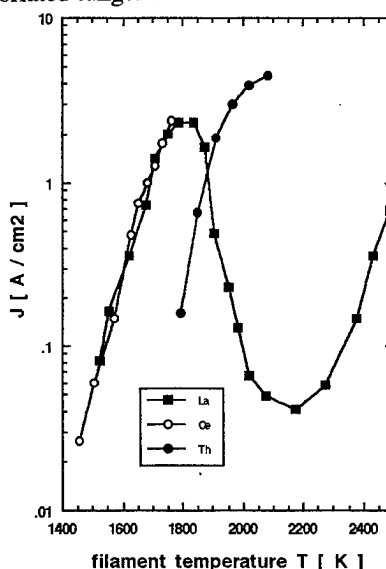


4. RESULTS AND INTERPRETATION

Fig. 3 shows the emission behaviour of a lanthanum (La) as well as a cerium (Ce) containing tungsten wires. For comparison also the typical emission of a thoriated tungsten (Th) wire is given that is used for directly heated cathode filaments in commercial electron tubes. A current density of several A/cm² can be achieved with the rare earth materials at temperatures of approximately 200 degrees lower than that of thoriated tungsten.

Fig.3

Measured temperature dependence of the current density of the materials thoriated tungsten (Th), lanthanated tungsten (La) and ceriated tungsten (Ce)



Three different ranges of emission can be distinguished. This is best seen for the case of lanthanum. In the temperature range up to approximately 1700 K the curve follows closely the Richardson-Dushman formula. For the evaluation of these measurements equation (7) was fitted to the data. For lanthanum on tungsten the Richardson constant $A(\text{La-W}) = 76 \text{ A/cm}^2 \text{K}^2$ and a work function $\phi(\text{La-W}) = 2.71 \text{ eV}$ were obtained. For cerium on tungsten the results are $A(\text{Ce-W}) = 62 \text{ A/cm}^2 \text{K}^2$ and $\phi(\text{Ce-W}) = 2.68 \text{ eV}$. Above 1700 K a saturation of the emission is observed for lanthanum. A distinct non-linear behaviour due to the exponential behaviour of equation (7) should result in a deviation from the curve only at higher temperatures. The observed reduction of the emission beginning at approximately 1700 K is due to strong evaporation of lanthanum atoms into vacuum at higher temperatures. Thereby a depletion of lanthanum in the tungsten matrix occurs which finally stops the emission from lanthanum atoms. Therefore the second range between approximately 1770 K and 2200 K is a transition region. Above 2200 K the measured curve again closely follows a Richardson Dushman behaviour. The corresponding evaluation reveals a constant $A = 160 \text{ A/cm}^2 \text{K}^2$ and a work function $\phi = 4.55 \text{ eV}$. These values demonstrate that pure tungsten emission occurs (theoretical for a pure metal $A = 60 \text{ A/cm}^2 \text{K}^2$, $\phi(\text{W}) = 4.5 - 4.8 \text{ eV}$). That is why the third range is the tungsten emission range.

In order to gain more insight into the transition region it was tried to estimate the rare earth coverage of the wires. For comparison again a thoriated tungsten test sample was evaluated that was coated by a monolayer of thorium. The coverage α can be evaluated by a fit of a superposition of the two Richardson Dushman equations $f(\phi, T)$ for the materials involved,

$$f\{\phi(x-W), \phi(W), T\} = \alpha f\{\phi(x-W), T\} + (1 - \alpha) f\{\phi(W), T\}, \quad (8)$$

where $x = \text{La}$ or Th . For the thorium coated wire it is known that for most efficient emission

$$\alpha = 1 = \text{constant}. \quad (9)$$

This occurs, when there is an equilibrium between diffusion of the thorium atoms to the surface and their evaporation into vacuum. Close to 1800 K the conditions of diffusion and evaporation are in equilibrium and therefore satisfy equation (9). For lanthanum highest efficiency is near 1500K. That is why values of the coverage of $\alpha = 1$ should be obtained at around 1800 K for tungsten and 1600 K for lanthanum. Deviations - in particular values of $\alpha > 1$ - will show, whether several mono-layers are present or not.

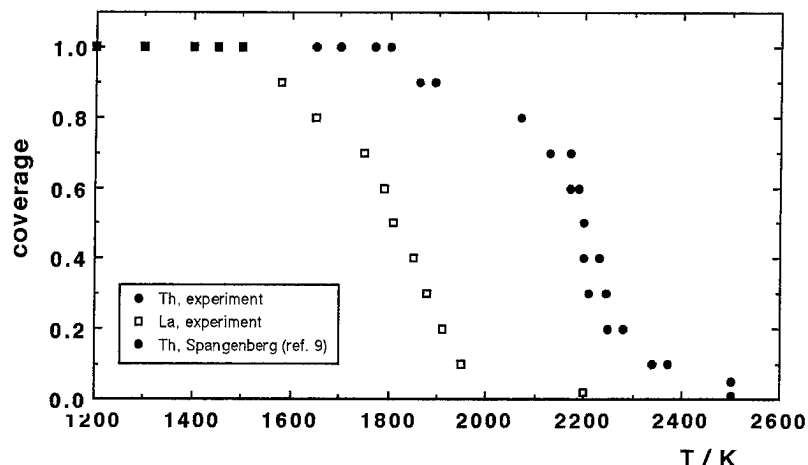


Fig.4

Measured coverage of tungsten base material by lanthanum (La), thorium (Th) this study and from Spangenberg ⁹

The dependence of the coverage as a function of filament temperature T is given in fig.4. The experimental values for thorium on tungsten (open circles) demonstrate that up to 1800 K there exists a monolayer of thorium ($\alpha = 1$), which is reduced and finally diminishes at around 2500 K. Also a plot from Spangenberg ⁹ is given (full squares) who investigated the diffusion of thorium in the same temperature range. Good correlation is found with the published data. The lanthanum behaviour (full dots) is in principle the same, but shifted by approximately 200 to 300 degrees towards lower temperature. Again mono-layers build up before the evaporation becomes too strong at high temperature. There is a slight deviation in the curvature of fig. 5 at about 1700 K for lanthanum and about 2000 K for thorium. Possibly at coverages of around 90 % the interaction between the bulk and the adsorbed atoms is more complicated to describe.

5. SUMMARY

We have studied thermionic emission of material combinations of rare earth material and tungsten. A simple model was given to describe the expected reduction of work functions involved. Lanthanum as well as cerium show similar emission behaviour as thoriated tungsten. In order to obtain the same emission current density as that of thoriated tungsten, it is possible to operate cathode filaments approximately 200 K lower than thoriated tungsten filaments.

Measured work functions are 2.71 eV for lanthanum and 2.68 eV for cerium. The value of cerium is close to the reported value of a cerium solid ⁷. Lanthanum shows the expected reduction of work function. The value reported in ⁷ could be confirmed precisely. Evaluation of the coverage revealed that up to 1700 K a mono-layer is present for lanthanum on tungsten with optimum emission properties. Application of these new materials will now depend mainly on an optimised composition of materials to enable a long lifetime of cathode filaments.

6. ACKNOWLEDGEMENTS

We should like to thank L.Schlapbach, O.Gröning (Université de Fribourg, Switzerland) and A.Kwetkus (ABB Corporate Research) for most valuable discussions and interesting information about thermal properties of materials.

7. REFERENCES

1. D.M.Goebel et al., "Large area LaMo electron emitters", Rev. Sci. Instr. 56 (19) , pp 1888, 1985
2. Zhou Meiling et al., "A study of the properties of Mo - La₂O₃ thermionic emission material" Proc.13th Int. Plansee Seminar, vol.1, Eds. H.Bildstein, R.Eck, Reutte (Austria) 1993
3. C.Buxbaum, G.Gessinger, CH-Patent 579 824, 1976
4. J.Hölzl, F.K.Schulte, Work function of Metals, Springer Tracts in modern Physics, vol. 85, Berlin, 1979
5. R.W. Gurney, "Theory of electrical double layers in adsorbed films", Phys. Rev. 47,479 pp., 1935
6. J.W.Gadzuk, The structure and chemistry of Solid Surfaces ed. G.A.Somorjai, Wiley, N.Y. 1969, p.43-1
7. V.S. Fomenko, Handbook of thermionic properties, ed. G.V.Samsonov, Plenum Press, N.Y. 1966
8. Walther H. Kohl, Materials and Techniques for Electron Tubes, Reinhold Publ., N.Y. 1960
9. K.R. Spangenberg, Vacuum Tubes, Mc Graw Hill, N.Y., 1948

SESSION 9

High-Power Microwaves

High power microwave Cherenkov oscillators with high current relativistic electron beams

S. D. Korovin, S. D. Polévin, I. V. Pegel, V. V. Rostov, A. M. Roytman,
V. L. Bratman*, G. G. Denisov*, and A. V. Smorgonsky*

Institute of High Current Electronics, Tomsk, RUSSIA

*Institute of Applied Physics, Nizhny Novgorod, RUSSIA

ABSTRACT

This paper is devoted to theoretical and experimental investigation of high power microwave Cherenkov oscillators using of high current nanosecond electron beams. The influence of non synchronous waves and additional (non Cherenkov) resonance on the process of microwave generation in 3 cm relativistic BWO are discussed. Experimental data presented in this paper show that the efficiency of 3 cm relativistic BWO can achieve 40% and pulsed microwave power - 500 MW. The enhancement of microwave power and efficiency of microwave generation was reached by creating of the non uniformity of the synchronous wave phase velocity and that of the coupling coefficient between the electrons and the electromagnetic wave. We experimentally studied the oversize Cherenkov oscillators in mm wavelength. One of them was 8 mm 120 MW orotron with TM_{13} -mode of the circular waveguide. The another one was two stage two electron beams 8 mm Cherenkov oscillator. The maximum of microwave power in this experiment was 600 MW, pulse duration was 10-15 ns. All of experiments were carried out by high current electron accelerators of type SINUS. The performance parameters of our accelerators are the following: electron energy from 100 to 2000 keV, beam current from 1 to 20 kA, pulse duration from 5 to 50 ns, repetition rate up to 200-300 pps.

1. INTRODUCTION

Cherenkov oscillators, due to their simplicity, were the first effective relativistic devices fabricated on the bases of high current electron accelerators with explosive-emission cathodes^{1, 2}. However, because of imperfection of early high current accelerators and methods of electron beam formation, only a simple (adaptive) version of Cherenkov oscillators, i.e., a relativistic backward wave oscillator (BWO), or a carsinotron operating at centimeter waves received primary attention in experiments for a rather long period of time. Recent progress in the field of high current accelerators³ has made it possible not only to increase the efficiency of the relativistic centimeter BWO⁴ and to create the millimeter BWO⁵, but to create a number of relativistic oscillators with resonant electrodynamic systems in millimeter wavelength: orotron⁶, surface wave oscillators⁷, BWO-twistron⁸, flimatron⁹. Here we describe some of our experiments on Cherenkov oscillators with vacuum electrodynamic systems in the form of sections of periodic metallic waveguides. We give here the short description of our experimental setups too.

2. RELATIVISTIC BWO

Cherenkov Backward Wave Oscillators are a self-sustained devices where radiation is generated under the conditions of synchronism between the electron beam and the -1st space harmonic of the backward wave of the periodic waveguide. BWO problem it is sufficient to make account of the interaction with the -1st space harmonic of the operating wave only, neglecting the influence the remaining wave fields. The increase of the efficiency of the device in doing so is much relied on the use of electrodynamic systems inhomogeneous in their coupling impedance^{1,2,4} or phase velocity of the -1st harmonic¹¹.

The design of BWO generally provides a microwave output onto a collector by reflecting the backward wave from the beyond-cutoff neck in the cathode side of the waveguide. The fundamental (0-th) harmonic of the traveling wave is not synchronous with the beam. Its phase velocity, however, is but slightly higher than that of the light ($\sim 1.1c$), while its amplitude may exceed manifold the amplitude at the -1st harmonic of the backward wave. Therefore, in the case of relativistic electron energies if is deemed necessary to take into account its effect on the beam modulation and energy exchange processes, also bearing in mind a potential increase in BWO efficiency.

2.1. Numerical simulation of BWO

The authors have constructed the numerical technique so that on the first stage by means of a stationary model were studied the processes of electron beam interaction with the -1st backward wave harmonic only. The results were then examined by more complex codes with subsequent account of other factors influencing the energy exchange: (i) the interaction of electron with the fundamental harmonic of the traveling wave and (ii) the influence of the forces of the intrinsic space charge of the beam.

The processes of bunching and energy exchange in a BWO are determined by the distribution of the synchronous field along the electrodynamic system. Efficiency of a homogeneous BWO is about 15%. The energy exchange can be made efficient by creating conditions which would simultaneously be favorable for electron bunching and provide for efficient decelerating of the majority of electrons which have fallen in the accelerating phases. This can be done by increasing the phase velocity of the synchronous wave, what would lengthen the time during which the initially accelerated electrons stay in the decelerating field phases and hence increase the interaction space length.

As it follows from calculations, the existence of favorable phasing of the high frequency (HF) current throughout a long interaction space increases the efficiency of the nonuniform phase velocity BWO. For the optimum regimes, the jump in phase velocity occurs within the first quarter of the corrugated electrodynamic system length and its amplitude is 10-20% of the initial phase velocity. The initial difference between the e-beam velocity and wave phase velocity turns out to be about a factor 1.5-2 as large as for a homogeneous electrodynamic system.

In calculations studying the influence of the traveling wave on the work of BWO it was assumed that the electrons penetrating the interaction space are subject to the influence of the field of two waves and interact simultaneously with both the -1st harmonic of the backward and the fundamental harmonic of the traveling waves. The character of this influence depends on several factors, the major being the ratios of amplitudes taking part in the interaction of harmonics (f) and their phases at the beginning of the interaction length. The change of the energy exchange processes in terms of the amplitude ratio was considered under the assumption of the phase coincidence. The amplitude ratio depends on the geometry of the electrodynamic system and on the radius of the tubular beam. In the experiments the value of f is normally of order of 2 to 6.

Calculations show that the presence of the traveling wave results in a stronger modulation of the beam and at $f < 4$ the high current phase is shifted to the center of the braking region of the -1st harmonic of the backward wave. In this operation mode beam, under the influence of the backward wave, loses up to 20% of its initial kinetic energy (Fig. 1). The energy exchange efficiency in a homogeneous oscillator may range from 10 to 30%. For $f > 5$ the electron modulation over velocity become so strong that one fails to provide favorable provide favorable phasing of HF current in the backward wave field. The efficiency of the energy exchange with the backward wave drops. The major role in the energy exchange is played by the traveling wave. Notwithstanding the decreasing efficiency of interaction with the backward wave, the overall efficiency of the device remains high. In the calculations performed, the operation with the maximum efficiency corresponded to the ratio $f = 6-8$, when the theoretical efficiency of the homogeneous oscillator reached 37%. For $f > 10$ the formation of compact long-life electron bunches in deteriorated and the efficiency of the device declines.

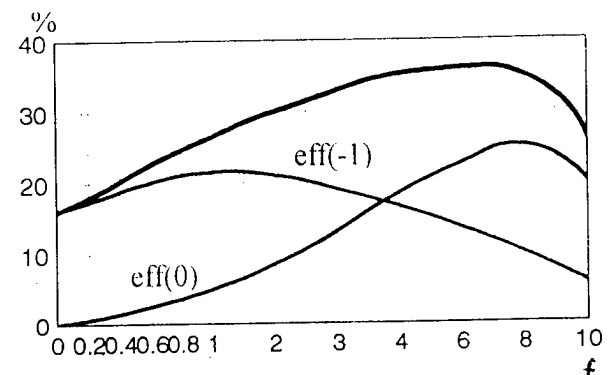


Fig. 1. Dependence of efficiency and dependences of energy exchange value with backward ($\text{eff}(-1)$) and traveling ($\text{eff}(0)$) waves on amplitudes ratio f .

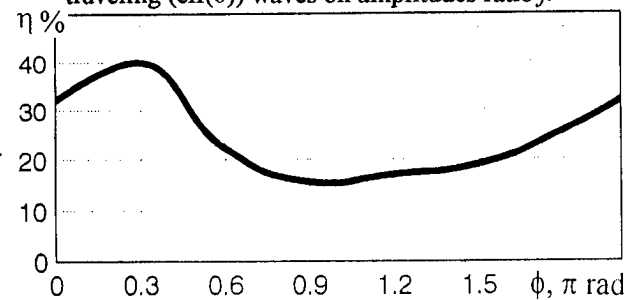


Fig. 2. Dependence of energy exchange efficiency on harmonics phase shift at beginning of interaction length in the homogeneous BWO. $f = 3$.

Modulation and energy exchange processes are dependent on the phase ratio harmonics of backward and forward propagating waves. The major reason for that is the fact that the shift in the wave phase leads to the shift of the initial phase of HF current with respect to the backward wave. The maximum efficiency of the energy exchange is reached at a small shift of the initial HF current phase to the backwave braking region. The efficiency decreases with the increase of the shift, reaching its minimum value in the case of opposite phase fields (Fig. 2.). Given the fixed geometry of corrugated structure and parameters of the beam current, the change in the phase relationship may result in termination of the stationary generation. Thus, the theoretical efficiency of homogeneous BWO in the presence of interaction with the traveling wave and under the assumption of the absence of space charge may reach 45%.

The influence of the intrinsic space charge of the electron flow on BWO operation can be taken into account even in simple models such as by solving the Poisson equation for electrostatic potential and calculating the relevant electric field. For simplicity the corrugation depth is taken to be small, as also the thickness of the walls of tubular e-beam.

As the calculations have shown, the relationship of the modulation and energy exchange processes in BWO described above do remain when the space charge is taken into account. But the electric field of the latter causes the e-bunches to be pushed apart and scattered out, preventing their effective grouping. In non-stationary calculations this is made manifest in the growth of the starter current of BWO, slow down of the oscillations built-up and generally in the shift of their oscillation frequency. In homogeneous BWO the space charge under certain conditions favors the growth of the BWO efficiency, while in the oscillators with high potential efficiency account of this charge invariably results in a sharp (up to 1.5-2 times) drop of the efficiency. Thus we may conclude that in BWO based on direct-action accelerators the influence of the space charge is strong and cannot be considered as a minor correction.

Note the preliminary results obtained by means of a 2.5-dimensional code "KARAT-2". The geometry of the calculation region is given in Fig. 3. It was assumed that the beam is injected through a foil at the edge of the beyond-cutoff neck. To avoid the reflection of the waves a weakly-conducting absorber is placed near right side of the device. The magnetic field strength of the coil reached 27 kOe on the quasi-homogeneous section. Simulation results agree satisfactory with the experiment. The generation power and frequency were 500 MW and 9.4 GHz, respectively (in the experiment with SINUS-6 accelerator they were 600 MW and 9.6 GHz). Note that in real-life experiment the operation of nonuniform BWO is very sensitive to physical parameters such as beam current, electron current, electron energy, etc., while in numerical experiment, in addition, model and calculations parameters are significant. Among the model parameters involved in the said calculations note the length of the beyond-cutoff neck, and the length of the absorber, the calculation parameters include the time step, which being too long, causes spurious cyclotron oscillations. Inappropriate selection of these parameters induces self-modulation and decline of the microwave power. It should also be mentioned, that numerical simulations of the homogeneous BWO showed a better stability.

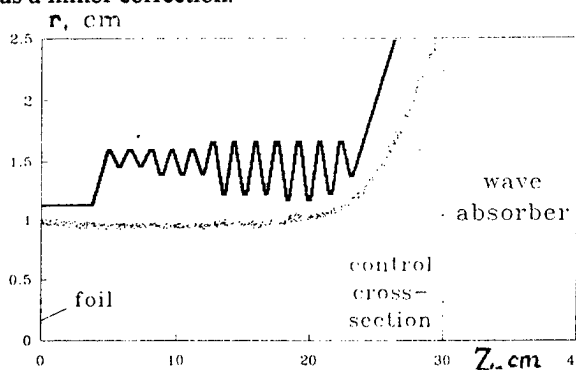


Fig. 3. Relativistic BWO particle simulation. System configuration.

2.2. Experimental investigation

The experiment was carried out on the "SINUS-6" accelerator. The TM_{01} -type wave in a circular waveguide was chosen as a working wave. The BWO electrodynamic system consisted of a stack of stainless-steel rings. The overall length of the homogeneous periodic structure was 161 mm, and the corrugation period was 16.1 mm. The corrugation depth was 2.2 mm, which for the cathode diameter of 18 mm gives $f = 3.5$.

The experiments studied the dependence of the microwave power on the coordinate of the withdrawal of the relativistic e-beam from interaction. By varying the length of the magnetic field we could change the location of the beam transfer. The results obtained are presented in Fig. 4. It is clearly seen that the interaction efficiency has a quasiperiodic dependence with the period corresponding to numerical calculation and connected with the period of electron flight within the phase of one sign of the fundamental harmonic of traveling wave. The power variation is not as

large as predicted theoretically. This could be accounted for by the scatter of the beam upon lowering magnetic field strength at the end of interaction space. Maximum power obtained in this series of the experiments constituted 300 MW with the efficiency 25%. The radiation wavelength was 3.25 cm.

Other experiments were aimed at optimizing the energy exchange efficiency over the shift of corrugated structure from the beyond-cutoff neck for various e-beam parameters. With a slot of 33-36 mm the peak power reached 550 MW with the efficiency of 25% and 400 MW with efficiency of 30%. It was observed that the shift of corrugated structure of fixed geometry with respect to the beyond-cutoff neck resulted in a periodic change of the output power and the operation mode of the oscillator (transition from stationary to non-stationary operation) (Fig. 5).

In experiments with inhomogeneous BWO the phase velocity increase along the interaction space was provided for by varying the corrugation pitch, the corrugation height being varied so that the coupling resistance would remain constant. In the experiment, the phase velocity jump was 10% for the length ratio of the initial phase velocity section to the jumped phase velocity 1/3. According to the simulation prediction, these parameters provide for an about 55% BWO efficiency. The maximum pulsed power achieved in the experiment was 500 MW for a pulse duration 12 ns. With a cathode voltage of 400 kV and an electron beam current of 2.8 kA, the efficiency reached 45%.

It was observed that on decreasing the beam current by mean mean of increasing the vacuum diode impedance there was an increase of the efficiency of stationary generation as well as of its stability. This could be accounted for by the decrease of the space charge of the beam.

3. OVERSIZED SINGLE-MODE CHERENKOV OSCILLATORS

Powerful millimeter-wave oscillators should generally have large, as compared to the wavelength, transverse dimensions. Therefore, realization of single-mode regimes with a high electron efficiency necessitates effective discrimination of parasitic oscillations. For this purpose we can use various electrodynamic and electron techniques. Electrodynamic mode selection by transverse indices can be effectively provided by making radiation slots in the resonator wall and introducing selective losses into the resonator. Thus an axisymmetric resonator with two longitudinal slots is essentially a two-mirror resonator where modes with the azimuthal index $m = 1$ have smallest losses. Modes with some transverse indices can also be discriminated using cylindrical or conical insertions coaxial to the resonator.

The radiation output of powerful generators should be such that selective properties of their electrodynamic systems not be deteriorated and too large (breakdown) field intensities do not occur. For this reason, a single-mode waveguide is generally undesirable. A "natural" diffraction output successfully used in subrelativistic gyrotrons, for example, is more favorable. Methods of electron selection are based primarily on the fact that not all modes of the electrodynamic system can be Cherenkov synchronism with the electron beam. For modes with different transverse structures, that are in synchronism with the beam simultaneously, selection is based on different dependences of the coupling coefficients on the electron beam radius. An effective method of electron mode selection in Cherenkov oscillators was proposed and realized in¹². For a focusing magnetic field that satisfied the condition $\omega_H \cong \hbar v_{||}$ the "basic" Cherenkov interaction is accompanied by cyclotron resonance absorption by a linear beam of all waves, but the operating one.

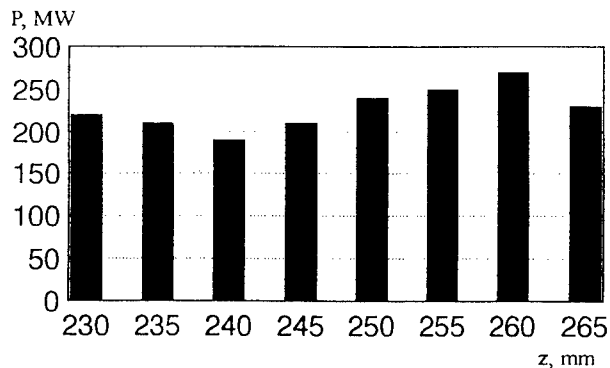


Fig. 4. Dependence of microwave power on the coordinate of the withdrawal of e-beam from interaction. Z is a distance from the beyond-cutoff neck of BWO

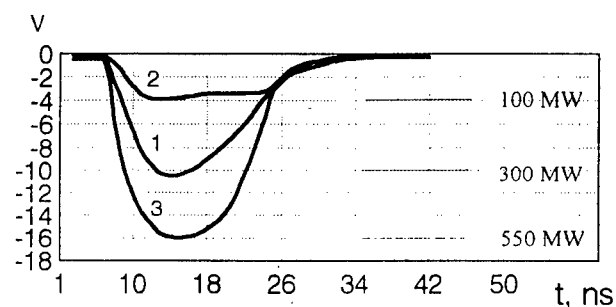


Fig. 5. Microwave pulse envelope waveforms:
1. without shifting of periodic structure from the cutoff neck
2. 11 mm shift
3. 36 mm shift

3.1. Relativistic Orotron

Unlike classical subrelativistic orotrons, high-current relativistic oscillators have resonators similar to the ones used in subrelativistic gyrotrons. Such a resonator is formed by a section of cylindrical waveguide with a cutoff narrowing at the cathode end and conical broadening for the radiation output at the collector end. The inner surface of the cylindrical section is corrugated. The early orotrons of the kind are realized at centimeter waves¹³ and at longer millimeter wavelengths for a multimode regime¹⁴. In our experiments the resonators had axisymmetric corrugation of the wall. With this corrugation, the $E_{1,3,1}$ mode was used as the operating one.

High-power oscillators need electrodynamic systems with a large (oversized) cross section and operation at higher modes. We chose $E_{1,3,1}$ because a higher waveguide mode $E_{1,3}$ and the waves close to it, $E_{3,2}$ and $E_{6,1}$, are somewhat isolated from the other waves. At the same time, their transverse structures differ significantly and, hence, one of them can be discriminated electro-dynamically. Thus two longitudinal 1/2-wide slots in the resonator wall provide the Q-factors of modes with the azimuthal indices $m = 3$ and $m = 6$ at last four times lower than Q-factor of the $E_{1,3,1}$ mode. The latter weakly depends on the slots and is defined, mainly, by the radiation through the output horn.

The experimental study was accomplished at the wavelengths $\lambda_1 = 8.0$ mm. The resonator Q factors and the number of corrugation periods in these orotrons were chosen so as to provide the maximum possible computed efficiency at an acceptable starting current. The starting currents of parasitic modes, when synchronism in the BWO regime was possible, were much higher than the computed values of the orotron operating currents: $I_{\text{stBWO}} \sim 10$ kA.

The radiation power close to the calculated one was attained at currents higher than 4 kA for 8-mm. At lower currents the level of generation was much smaller. This may be explained by the fact that oscillations did not have time enough to onset. The shape of the microwave pulses with lagging fronts is indicative of that. The radiation wavelengths of the orotrons thus obtained were in good agreement, within the measurement error, with the values determined in the "cold" experiments. The field distribution and the polarization of radiation also corresponded to $E_{1,3,1}$ wave. The maximum radiation power was 120 MW for the electron energy 500 keV and current 6 kA at the wavelengths 0.8 ± 0.1 mm. The electron efficiency was nearly 5 percent. The energy of single microwave pulse with the duration 7-10 ns at a half-power level amounted to 1.2 J. In good agreement with the calculations, the study of the generation versus the magnetic field focusing the particles for the 8-mm orotron showed clearly defined cyclotron absorption at maximum solenoid fields $H_0 = 27-30$ kOe. Besides the orotrons with wide selective slots in resonators, we investigated experimentally oscillators with very narrow slots (about 1/16 wide) that provided discrimination only of H modes. In this case, when electron beam parameters were highly stable, simultaneous generation of three modes, $E_{3,2,1}$, $E_{6,1,1}$, and $E_{1,3,1}$, with close frequencies was obtained. The polarizations and the ratios of the amplitudes of these modes varied randomly from pulse to pulse. Comparison of this generation and stable single-mode generation in the orotron with wide slots proved the necessity of effective mode selection in orotrons with a large cross section.

3.2. Two stage BWO-twistron oscillators

The two stage BWO-twistron oscillators include a single-mode driving oscillator (BWO) with a small cross-section which was excited by a relatively small part of a relativistic electron beam and a powerful output device with a large cross-section where the signal was amplified when interacting with the main part of the electron beam (a twistron) was investigated at high-current accelerator SINUS-6 to obtain greater power while preserving signal coherence. The twistron consisted of a modulating section, a short drift section and a short TWT section. The results of BWO-twistron investigations are given in Tab. 1.

Type of device	l , mm	P_{out} , MW	η , %	τ , ns
BWO	10.4	40	10	15
BWO-twistron	10.4	600	20	12

The wave E_{01} was used as an operating wave in BWO. The power of TWT can be varied by changing the focusing magnetic field around its resonance value (35 kHe) that corresponds to cyclotron wave absorption. The output twistron section (TWT) was made in a form of a section of an oversize corrugated waveguide with circular cross-section 3λ in diameter. In this section a slowed wave E_{01} was also taken as an operating one. When removing a driving BWO from the generator or when replacing the output section with a section with smooth walls, the radiation power became negligibly small. Radiation frequency of the generator within the limit of the measurement accuracy corresponds to BWO frequency. Space corresponds to BWO frequency. Space structure emitted from the generator through a smoothly expanding cone and a vacuum window was close to the directivity diagram of E_{01} wave.

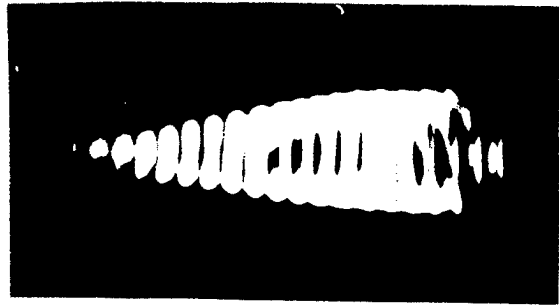


Fig. 6.

To additionally verify the measured high value of the output radiation power, an experiment on the air breakdown at atmospheric pressure was carried out (Fig. 6.). Here the radiation was focused by a spherical metallic mirror which was coaxial to the radiating horn. The observed frequency breakdown had a form of a converging cone 10 cm in length at maximum diameter of 2.5 cm.

5. REFERENCES

1. N. F. Kovalev, M. I. Petelin, M. D. Raizer, A. V. Smorgonsky, and L. E. Tsopp, "Generation of powerful electromagnetic radiation pulsed by a beam of relativistic electrons", JETP Lett., vol. 18, pp. 138-140, 1973.
2. Y. Carmel, J. Ivers, R. E. Kribel, and J. Nation, "Intense coherent Cherenkov radiation due to the interaction of a relativistic electron beam with a slow-wave structure", Phys. Rev. Lett., vol. 33, pp. 1278-1282, 1974.
3. A. S. El'chaninov, F. Ya. Zagulov, S. D. Korovin, G. A. Mesyats and V. V. Rostov, "High current pulse-periodic electron accelerators for microwave oscillators, Relativistic HF Electronics, Gorky: IPF USSR Acad. Sci., vol. 2, pp. 5-21, 1981.
4. A. S. El'chaninov et al., "Highly efficient relativistic backward-wave tube", Sov. Tech. Phys. Lett., vol. 6, p. 191, 1980.
5. A. S. El'chaninov, S. D. Korovin, et al., "Generation of high-power microwaves with use of high-current mini-accelerators". Sov. J. Reports of USSR Acad. Sci., vol. 279, N 3, pp. 624-626, 1984.
6. V. L. Bratman, V. P. Gubanov, G. G. Denisov, S. D. Korovin, S. D. Polevin, V. V. Rostov, and Smorgonsky, "Relativistic orotrons-powerful sources of coherent millimeter-wave radiation", Sov. Tech. Phys. Lett., vol. 10, pp. 807-811, 1984.
7. V. L. Bratman, G. G. Denisov, B. D. Kolchugin, S. D. Korovin, S. D. Polevin, V. V. Rostov, "Powerfull millimeter-wave generators based on the stimulated Cherenkov radiation on relativistic electron beams", Int. J. of Infrared and Millimeter Waves, vol. 5, N. 9, pp. 1311-1332, 1984.
8. V. L. Bratman, V. P. Gubanov, G. G. Denisov, S. D. Korovin, S. D. Polevin, V. V. Rostov, and A. V. Smorgonsky, ""Experimental investigation of sectional oscillator with relativistic electron beam", Sov. Tech. Phys. Lett., vol. 14, pp. 9-14, 1984.
9. V. L. Bratman, G. G. Denisov, M. M. Ofitserov, S. D. Korovin, S. D. Polevin, V. V. Rostov, "Millimeter-wave HF relativistic electron oscillators", IEEE Trans. on Plasma Sci., vol. PS-15, pp. 2-15, 1987.
10. N. F. Kovalev, V. I. Petruhina, "Ultrarelativistic carsinotron with a jump in beam-rf coupling", Electr. Techn. SVCH, vol. 7, pp. 101-105, 1977.
11. S. D. Korovin, D. D. Polevin, A. M. Roytman, V. V. Rostov, "Relativistic BWO with variate phase velocity", Sov. Tech. Phys. Lett., vol. 18, N 8, pp. 63-67, 1992.
12. E. B. Abubakirov, M. I. Petelin, et al., "Experimental realization of cyclotron-resonance mode selection in HF relativistic electron Cherenkov oscillators", Sov. Tech. Phys. Lett., vol. 9, N 9, pp. 533-537, 1983.
13. A. V. Gaponov, M. I. Petelin, and V. A. Flyagin, "Achievements and problems of relativistic HF electronics", Proc. Xth European Conf. Contr. Fusion and Plasma Phys., vol 2, pp. 48-50, 1981.
14. A. F. Alexandrov et al., "Study on a millimeter-wave relativistic generator with diffraction radiation", Sov. Tech. Phys. Lett., vol. 7, N 10, pp.587-589, 1981.

Surface breakdown phenomena in alumina rf windows

Y.Saito

KEK-National Laboratory for High Energy Physics
Tsukuba, Ibaraki, 305 JAPAN

ABSTRACT

The multipactor and flashover phenomena of alumina rf windows used in a high-power klystron have been investigated. Multipactoring due to the high yield of secondary electron emission takes place during rf operation. A spectrum analysis of luminescence due to multipactoring shows that multipactor electron bombardment causes an F-center of alumina, thus leading to surface melting. From the results of a high-power examination of rf windows with several kinds of alumina ceramics, it was found that an alumina material with a crystallized grain-boundary and without any voids between the boundaries, thus having a low loss-tangent value, is not liable for F-centers, even under multipactoring. Flashovers in a tree-like pattern of alumina luminescence occasionally take place on a TiN-coated surface where multipactoring is suppressed. A sapphire window, whose surface was polished and having pre-existing F-centers, shows a lower flashover threshold. The annealing effect of polished window surfaces was also investigated.

1. INTRODUCTION

Alumina ceramic has been widely used as an electrical insulator in vacuum devices, such as switching tubes and microwave tubes. Since it has high stability for thermal treatment and a low outgassing rate as well as high dielectric and mechanical strengths, it is a suitable material for insulators having good vacuum performance. However, the property of a ceramic having a high yield of secondary electron emission often induces breakdown phenomena under a high electric field applied to the devices. Especially, in an rf field once electrons impinge upon the alumina surface, secondary emitted electrons are accelerated so as to impinge again onto the surface due to an alternating rf field; this causes a multiplication of the secondary electrons. The primary electrons are most likely generated at the triple junction of the window periphery due to field emission, or are created at the window surface due to ionization of adsorbed molecules, such as contamination and water molecules. This breakdown, generally known as multipactoring, is one of the characteristic phenomena in high-power rf windows.¹

TiN coatings on alumina surfaces can effectively suppress multipactoring when the thickness is optimized so as to reduce the number of secondary electrons and to avoid any excessive heating due to ohmic loss.² However, flashovers in a tree-like pattern of alumina luminescence occasionally take place on the coated surface; the threshold of the flashover depends on the alumina materials.³ In order to investigate the fundamental process of rf window breakdown several experiments have been carried out on the S-band (2856 MHz) pill-box type of alumina windows used for pulsed high-power klystrons (3.5 μ s, 30 MW). In this paper, multipactor and flashover phenomena, both of which are characteristic of rf breakdown in alumina windows are reported.

2. MULTIPACTOR PHENOMENA

2.1. Luminescence caused by electron bombardment

An rf window comprises a high-purity alumina ceramic disk (3.5 mm thick, 92 mm in diameter) and a pill-box type housing. The window structure shown in Fig.1 was designed to meet the requirement of impedance matching. An alumina material having a low-loss tangent is chosen so as to avoid excessive heating.

It is often observed that breakdown takes place with rf wave reflection and a pressure rise in the vacuum. Such a breakdown usually causes coloring, localized surface melting and puncturing of the alumina ceramic disk. As a pre-breakdown phenomenon, the optical emission on the alumina is observed during rf operation. Especially, when it is localized like spots and its intensity increases, surface melting, and additional puncturing are formed.⁴ A spectral analysis of the optical emission was carried out using a monochromator attached to the waveguide viewport. The spectrum shows a structure with a broad band centered at about 300 nm and a line at 694 nm. Since the latter can be identified as being ruby color attributed to Cr impurities in the alumina and the former F⁺-center of oxygen vacancies of alumina, it is indicated that

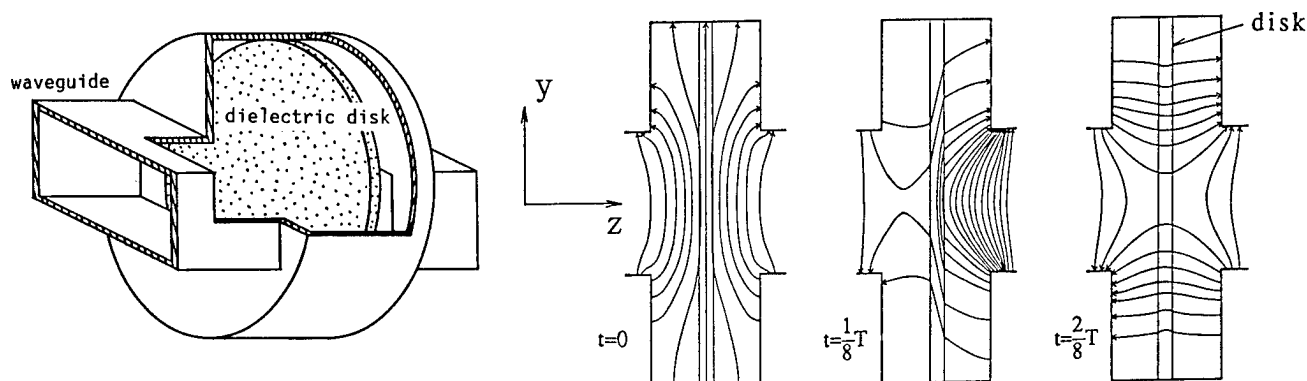


Fig.1. Schematic of pill-box type rf window, and electric force lines in the window (on the plane $x=0$) at each $1/8$ cycle.

the optical emission is not due to ionized or excited gas molecules, but rather luminescence of the alumina ceramic due to electron bombardment. In fact, the cathodoluminescence spectrum obtained for a disk irradiated by an electron beam (12 nA) using a scanning-electron microscope is very similar to that observed during rf operation.⁵ From these facts it is concluded that the breakdown phenomena leading to surface melting is induced by electron bombardment accompanied by luminescence of alumina.

Fig.2 shows the luminescence from the window surface, where TiN (2 nm thick film) and MgO (10 nm) films are partly coated. It is found that the luminescence intensity depends on the materials of the outermost surface. However, the spectral structures observed during rf operation are identical to the alumina luminescence in every case. Therefore, the impinging electrons pass through the films and excite the alumina, thus causing luminescence. Since these electrons are considered to come from those first emitted from the outermost surface, and are then accelerated by an rf field so to impinge again onto the surface, multipactoring possibly takes place in a manner of multiplying secondary electrons by electron impingement (Fig.3). The difference in the luminescence intensity should thus be due to the number of secondary emitted electrons from the outermost surface.

2.2 Multipactor due to secondary electrons

In order to ascertain multipactor occurrence, secondary electron emission (SEE) yields were measured using the pulsed electron beam (100 pA peak, 1 ms) of a scanning-electron microscope as primary electrons for avoiding any charge built-up.⁵ The result shows that the TiN-coated surface has the lowest yield compared to any others, and overlaid MgO on TiN film has a higher yield as well as MgO on alumina (Fig.4). It is thus concluded that the higher intensity of alumina luminescence during rf operation can be attributed to the higher SEE yield of the outermost surface and that the electron bombardment accompanies the multiplication of secondary electrons. A TiN film has also been ascertained to be effective to suppress multipactoring by reducing the SEE yield when coated on the outermost surface of the alumina window; absorbing secondary electrons from alumina.

A further estimation of electron behavior in the multipactor phenomenon was carried out through a trajectory simulation

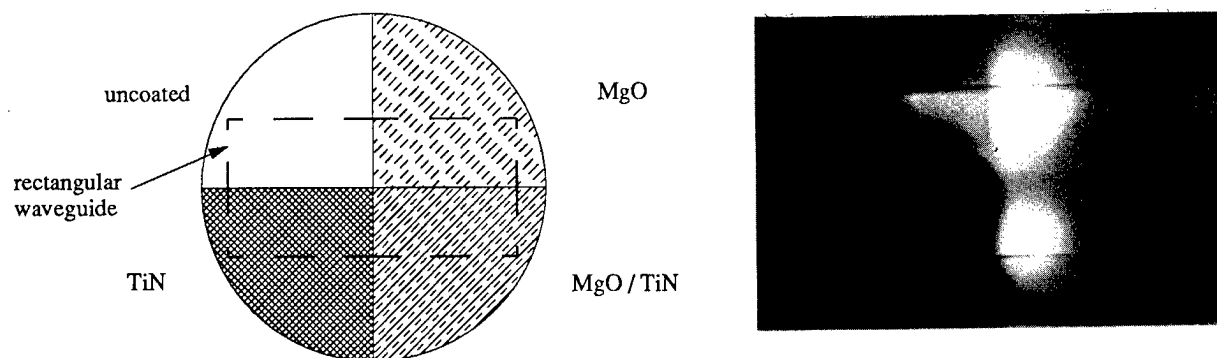


Fig.2. Luminescence from the window surface where TiN and MgO films are coated. An operation power is 27 MW.

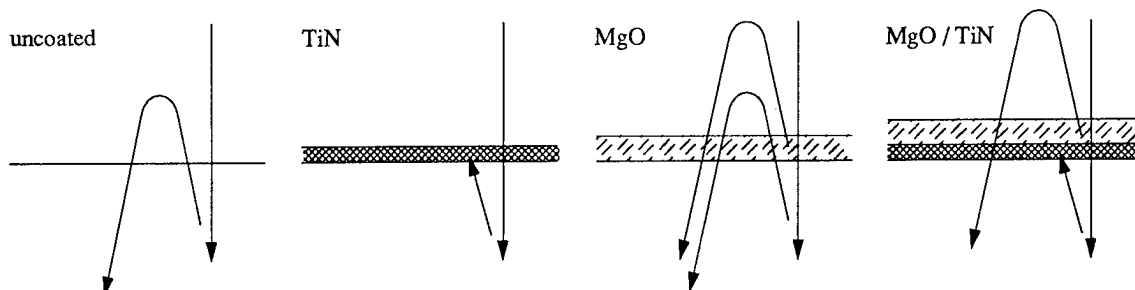


Fig.3. Model of secondary electron emission and multipactor of Fig.2.

of electrons in the window.⁶ A calculation of the rf electric field in the pill-box structure was made using the 3-dimensional MAFIA code (Fig.1); the trajectories and re-impinging energies of secondary emitted electrons in these fields were then simulated using a Monte-Carlo method. Based on the results, the incident energy distribution weighted by the re-impinging rate was elucidated to be very similar to pattern of the colored and opaque areas which are observed for typically failed windows. This indicates that multipactor electron bombardment on the alumina surface causes a coloring as well as luminescence. Since the calculated incident energy of the multipactoring electrons is about 8 keV at its maximum (when an rf power of 30 MW is being transmitted), the electron range in the alumina crystal is roughly estimated to be on the order of micrometers.⁶ The lack of transparency of the alumina disk is due to alumina degeneration, not only on the surface, but also in the bulk adjacent to the surface; the range is so long as to penetrate the MgO/TiN films of Fig.2 and exciting the alumina luminescence.

It is interesting to directly observe the secondary electron multiplication during multipactoring. Fig.5 shows the time dependence of the luminescence intensity when an X-band (11.4 GHz) rf pulse of 50 ns is transmitted through the pill-box window with a power of 30 MW. The intensity increases for a few tens of nanoseconds, which corresponds to a few hundreds cycles of the rf field. Though a detailed analysis has not yet been performed for the multipactor rise time, this would be explained in the terms of the life time of the successively emitted electron; some coincidence condition exists between the emission timing and the accelerating phase of the rf field.

3. SURFACE BREAKDOWN

3.1 F-centers in oxygen vacancy of alumina

The influence of multipactor bombardment on alumina materials has been characterized by cathodoluminescence

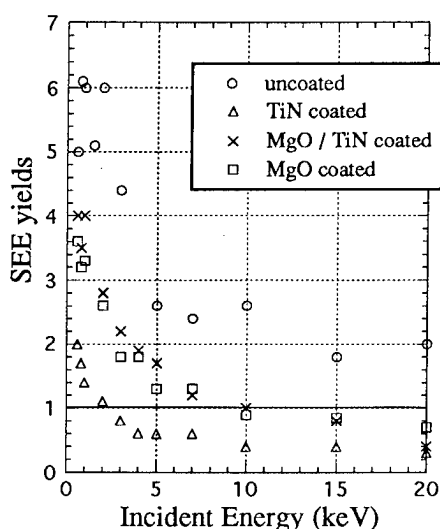


Fig.4. Secondary electron emission (SEE) yields measured by pulsed-beam method.

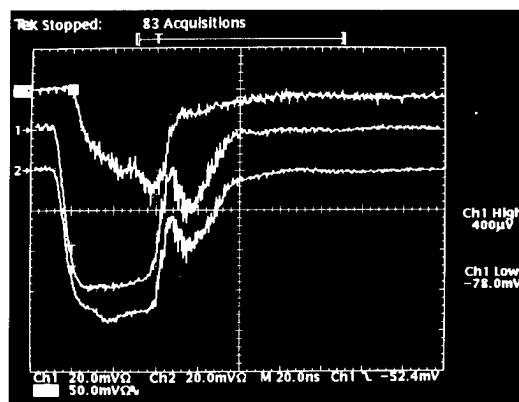


Fig.5. Time dependence of luminescence intensity (upper) during rf operation with a pulsed power (bottoms) of 30 MW.

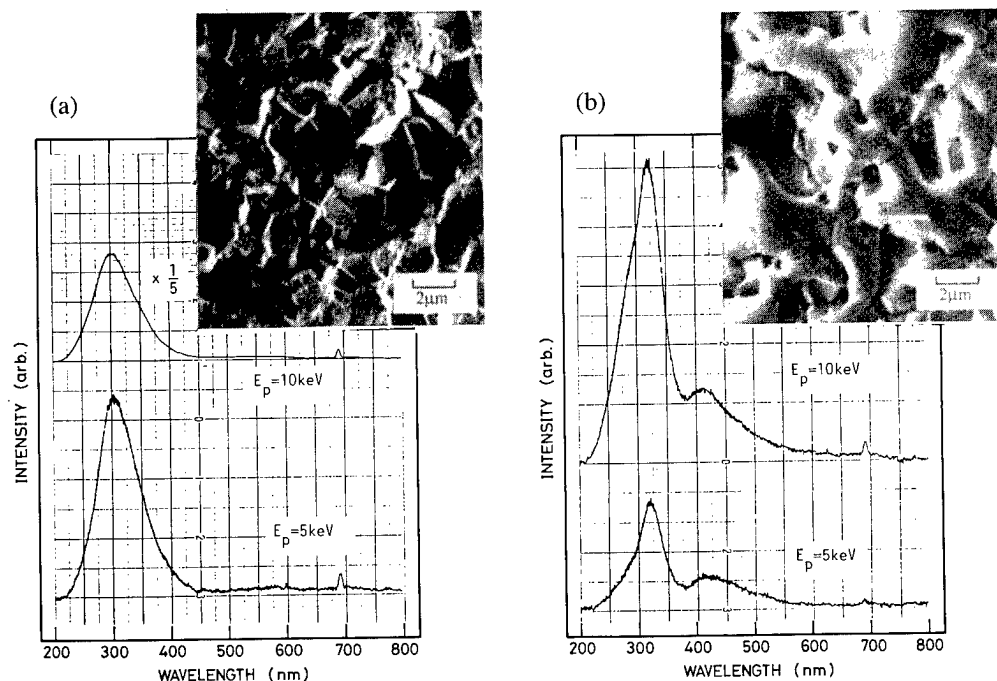


Fig.6. Cathodoluminescence spectra; (a)unmelted and (b)melted surfaces.

measurements. The spectrum observed for a melted surface resulting from breakdown is shown in Fig.6. Another band at 410 nm appears in addition to the characteristic structure of the unmelted surface. This band is attributed to F-centers of oxygen vacancies with two trapped electrons;⁷ F^+ -centers have one trapped electron. It is considered that the F-centers created by the multipactoring should result in conductive charges of free ions or electrons,⁸ thus inducing an increase in the loss tangent at the alumina surface. The surface temperature would then rise not only due to electron bombardment, but also due to rf dissipation, which should cause an additional increase in the loss tangent, thus melting the surface. It is expected that only alumina material not liable to F-centers must be durable, even when multipactoring occurs. In order to study the relation between the material properties and the durabilities, characterization and high-power examinations were carried out for several kinds of alumina materials,⁹ and a sapphire¹⁰ of alumina single-crystal disk having an optically flat surface.

Their characterizations were made by measuring the terms of the SEE yield, loss tangent, electric resistivity and cathodoluminescence spectra, as listed in Table 1.¹¹ UHA-99, which is pre-treated with highly pressurized forming before sintering, has the smallest grains (1~2 μm in diameter) and thinner boundaries comprising sintering additives. The higher value of its specific gravity should be attributed to such a dense structure; the high electrical resistivity observed is probably due to smaller amount of sintering additives. HA-997 is specially sintered in order to make the boundary additives crystallized, which contributes to a reduction in the loss tangent to be as small (10^{-5} at 3 GHz) as that of sapphire. To obtain an alumina ceramic with a high purity of 99.9%, such as XKP-999, a sintering process without using additives is carried out. In this process, a spray-dried powder must be manufactured, which usually produces a small amount of residual micro-porosities in the ceramic structure. We consider that the relatively high value of the loss tangent in XKP-999 is due to the microstructure with porosities. As for a sapphire disk, the smallest value of the loss tangent, as well as the highest

Table 1. Characterization of alumina materials for rf window use.

alumina material	purity (%)	specific gravity	ϵ	$\tan \delta$ 10^{-5}	resistivity $10^{15} (\Omega \text{ cm})$	SEE @1 keV, @ 10 keV	sintering additives	CL spectra (before rf op.)
UHA-99	99.0	3.90	9.81	9.4	>1000	6.0, 2.0	SiO_2 , MgO, CaO	F^+ , Cr^{3+}
HA-997	99.7	3.93	9.95	4.2	6.7	5.2, 2.0	SiO_2 , MgO	F^+ , Cr^{3+}
XKP-999	99.9	3.91	9.67	13.3	3.3	6.7, 2.2	—	F^+ , Cr^{3+}
sapphire	100	3.98	10.16	2.3	>1000	10.1, 3.7	—	F^+ , F(unannealed) F^+ (annealed)

Table 2. High-power test results of alumina materials for rf window use.

alumina material	characteristics	transmittable power (MW)	remarks	CL spectra (after rf op.)	
				TiN-coated	uncoated
UHA-99	dense structure, high resistivity	>220	colored yellow (uncoated surface)	F ⁺ , Cr ³⁺	F ⁺ , Cr ³⁺ , F
HA-997	crystallized additives, low loss tangent	>220	no coloring	F ⁺ , Cr ³⁺	F ⁺ , Cr ³⁺
XKP-999	micro-porosities, higher loss tangent	144	melting, (uncoated surface)	F ⁺ , Cr ³⁺ , F	F ⁺ , Cr ³⁺ , F
sapphire	pre-existing F-center, low loss tangent	75 (unannealed) 100 (annealed)	melting (uncoated surface)	F ⁺ , F (unannealed) F ⁺ (annealed)	F ⁺ , F F ⁺ , F

value of the specific gravity, are observed. However, in the cathodoluminescence spectrum of sapphire, it was found that there are pre-existing F-centers. The surface residual stress in microcracks or dislocations which have been mechanically introduced by polishing seems to change electronic states in vacancies, and then an excess electron is trapped as an F-center. Indeed, by annealing the disk at 1500 C in air, which probably relaxes such stress, these pre-existing F-centers vanished.

High-power examinations of the rf windows with these disks were performed using a resonant ring³. A TiN film was formed on three quarters of the area of each disk surface in order to distinguish the multipactor effect on F-centers. Though multipactoring takes place on an uncoated surface of every disk, the maximum powers transmittable through the windows are different, depending on the materials used, as summarized in Table 2. UHA-99 and HA-997 were found to have high durabilities for rf operation of up above 220 MW. Moreover, in HA-997 no F-centers have been observed, even on an uncoated surface. On the contrary, XKP-999 and sapphire, though having a higher purity, are not durable under high-power operation; F-centers have been found even on the TiN-coated surface of XKP-999.

Based on these results it is concluded that high-purity dielectric materials having a microscopically dense structure (without residual porosities) and crystallized sintering-additives, and consequently having low loss tangent values, are not liable to F-centers. This indicates that F-centers are formed not only by direct trapping of the impinging electrons, but also by rf-loss heating; it is reported that the F⁺-center in alumina is converted to an F-center when heated in a vacuum.¹²

The annealed sapphire window shows a higher value of the transmittable power than the unannealed one. However, since F-centers are formed again on an uncoated surface by multipactoring, the impinging electrons are considered to be excessively trapped in oxygen vacancies. Annealing in air is, therefore, not sufficient to reduce the number of trapping centers, though it is effective to de-trap F-center electrons.

3.2. Surface charging and flashover

Not only surface melting induced by multipactor (as described above), but also flashovering with both outgassing and rf wave reflection are characteristic of breakdown in rf windows. Occasional flashovers were observed at rf powers of 75 and 220 MW on the sapphire (unannealed) and alumina ceramic disks, respectively.³ These flashovers take place selectively on the TiN-coated surface, and are accompanied by tree-like patterns of alumina luminescence, as shown in Fig.7. After a high-power examination the flashover tracks of surface melting with tree-like pattern are observed (Fig.8). *In situ* measurements



Fig.7. Surface discharge on sapphire window.
Three quarters of the area is coated with TiN.

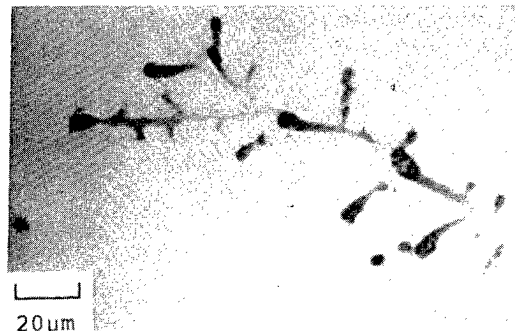


Fig.8. Discharge tracks on the sapphire.

of surface charging before and after flashovers have been carried out.³ Several nC of positive charges are observed after flashover; tens to hundreds pC of negative or positive charges before flashover. From these observations, we can conclude that a localized accumulation of electrons is first formed and then released, possibly in the film-dielectric interface during an avalanche, which causes luminescence and melting of the alumina. It thus leaves positive charges on the tracks.

Though the charge-accumulation mechanism under a high rf-field has, at present, not been clearly explained, it is considered that any mobile charges which exist in conductive films or in F-centers of dielectrics are retrapped in deeper energy levels of such defects as dislocations or microcracks introduced by polishing.¹³ Charge accumulation should therefore depend on the defect density in the dielectrics and on the surface residual stress.^{14, 15} In fact, an annealed sapphire window shows a higher threshold of about 100 MW than unannealed sapphire.

4. SUMMARY

Breakdown phenomena in alumina rf windows for high-power use have been investigated. Multipactoring due to a high yield of secondary electron emission takes place on the alumina surface accompanied by alumina luminescence, which causes F-centers of oxygen vacancy. It is considered that the F-centers should result in conductive charges of free ions or electrons, thus inducing an increase in the loss tangent at the alumina surface and leading to surface melting.

The durability of alumina materials under rf operation does not always depend on their purities, but rather on their microstructures. It is elucidated that alumina materials having a dense structure and crystallized sintering-additives, and consequently having low loss tangent values, are not liable to F-centers. This indicates that F-centers are formed not only by direct trapping of the impinging electrons, but also by rf-loss heating. Although an in-air annealing treatment for polished materials with a surface having a residual stress is effective to de-trap electrons from F-centers, it is not so sufficient to reduce the number of trapping centers.

Occasional flashovers with a tree-like pattern of luminescence are observed for a TiN-coated surface where multipactoring is suppressed. The results of surface charging measurements indicate a localized accumulation of electrons and its avalanche. The charge-accumulation mechanism under a high rf-field is considered in which any mobile charges in conductive films or in F-centers of alumina are retrapped in deeper energy levels of such defects as dislocations or microcracks. Charge accumulation should therefore depend on the defect density in the dielectrics.

5. REFERENCES

1. R. Hayes, "Research on Microwave Window Multipactor and its Inhibition," *Final Report*, #AD256295, Eitel-McCullough, CA, June 1964.
2. S. Michizono et al., "TiN film coatings on alumina radio frequency windows," *J.Vac.Sci.Technol.*, Vol. A4, pp.1180-1184, 1986.
3. Y. Saito et al., "Surface Flashover on Alumina rf Windows for High-power Use," *IEEE Trans. on Electr. Insul.*, Vol. 28, pp.566-573, 1993.
4. Y. Saito et al., "Breakdown of alumina rf windows," *Rev. Sci. Instrum.*, Vol. 60, pp.1736-1739, 1989.
5. Y. Saito et al., "Breakdown of Alumina Rf Windows," *IEEE Trans. on Electr. Insul.*, Vol. 24, pp.1029-1032, 1989.
6. S. Yamaguchi et al., "Trajectory Simulation of Multipactoring Electrons in S-band Pillbox RF Window," *IEEE Trans. on Nucl. Sci.*, Vol. 39, pp.278-282, 1992.
7. A. Al Ghamdi et al., "Ion Beam Excited Luminescence of Sapphire," *Nucl. Instr. and Meth.*, Vol. B46, pp.133-136, 1990.
8. K. H. Lee et al., "Luminescence of F-center in Sapphire," *Phys. Rev.*, Vol. B19, pp.3217-3221, 1979.
9. NTK CO., Nagoya, Aichi, Japan.
10. ASGAL CO., Sambu, Chiba, Japan.
11. S. Michizono et al., "Dielectric Materials for Use as Output Window in High-power Klystrons," *IEEE Trans. on Electr. Insul.*, Vol. 28, pp.692-699, 1993.
12. K. H. Lee et al., "Additive Coloration of Sapphire," *Appl. Phys. Lett.*, Vol. 33, pp.273-275, 1978.
13. T. Asokan et al., "Dependence of the Surface Flashover Properties of Alumina on Polishing Abrasive Parameters," *IEEE Trans. on Electr. Insul.*, Vol. 28, pp.535-544, 1993.
14. C. Le Gressus et al., "The Influence of Surface Phenomena on the Initiation of Discharge in Vacuum," *IEEE Trans. on Electr. Insul.*, 24, pp.969-977, 1989.
15. C. Jardin et al., "Behavior of α -alumina insulator surfaces under electron irradiation," *J. Material Sci.*, Vol. 26, pp.3019-3024, 1991.

PREBUNCHED-BEAM FREE ELECTRON MASER (FEM)

M. Arbel, D. Ben-Chaim, M. Cohen, M. Draznin, A. Eichenbaum,
A. Gover, H. Kleinman, A. Kugel, Y. Pinhasi, S. Witman, Y. Yakover.

Faculty of Engineering - Physical Electronics Dept.
Tel-Aviv University (TAU), Ramat-Aviv 69978, ISRAEL

ABSTRACT

The development status of a prebunched FEM is described.

We are developing a 70KeV FEM to allow high gain wideband operation and to enable variation of the degree of prebunching. We intend to investigate its operation as an amplifier and as an oscillator. Effects of prebunching, frequency variation, linear and nonlinear effects, will be investigated.

The prebuncher consists of a Pierce e-gun followed by a beam modulating section. The prebunched beam is accelerated to 70KeV and injected into a planar wiggler containing a waveguide.

The results obtained to date will be presented. These include: characterization of the e-gun, e-beam transport to and through the wiggler, use of field modifying permanent magnets near the entrance and along the wiggler to obtain good e-beam transport through the wiggler, waveguide selection and characterization.

1. INTRODUCTION

The theory of prebunched beam FEL was described by Schnitzer and Gover¹. The prebunched FEM under development at TAU uses a 1.5Amp, 70KeV e-beam and a planar wiggler with a period $\lambda_w = 4.4$ cm; this leads to an operating frequency near 4.8GHz. Fig. 1a is a schematic of the FEM.

The prebuncher has an e-gun and the first two modulating section of a traveling wave tube (TWT). The gun end is continuously pumped by a 11 l/sec auxiliary pump. The e-beam from a shielded Pierce-type electron gun is on-off modulated by a grid located in close proximity to the cathode. The gun provides a 1.5Amp e-beam at 10.5KV with a radius of less than 1mm. The e-gun is described in sec. 2.

The helix traveling wave prebuncher operates in the 3.8 to 12GHz range. The rf signal is absorbed at the end of the prebuncher and a 1.5mm dia, density-modulated e-beam exits. The e-beam focussing in the prebuncher is by periodic permanent magnets (PPM). The modulated e-beam is accelerated to 70KeV and focussed by solenoid magnets to the wiggler entrance (sec. 3)

The TW and e-gun portions of the system are shielded from the magnetic field of the solenoids and can be closed from the rest of the system by a vacuum valve. The transport of the e-beam into and through the planar wiggler requires a matching magnetic field section near the entrance to the wiggler (sec. 4). Lateral (x) beam focussing in the wiggler is provided by use of long permanent magnets at the sides of the wiggler. At the exit from the wiggler there is another set of magnetic field matching magnets. The wiggler system is described in sec. 4.

The rf guide is located in the wiggler. For efficient interaction the waveguide must provide a strong electric field in the x direction within the e-beam area. The microwave system is discussed in sec. 5. The spent beam is collected at a depressed collector. Beam transport experiments are described in sec. 6.

2. THE E-GUN

The Pierce-type gun provides a laminar space charge limited 1.5Amp e-beam with the grid pulsed to $V_g = +150$ Volts and with the anode at $V_a = 10.5$ KV. It is cut off for $V_g = -60$ Volts.

To test possibilities of obtaining lower e-beam currents we investigated e-beam conditions from cutoff to full space-charge-limited flow² by varying the grid voltage from -60V to +160Volts.

In the range $120 < V_g < 160$ Volts approximately 90% of the cathode current passed the helix section, with 9% of the cathode current intercepted by the grid (as expected based on grid transparency). The corresponding cathode current range is $1\text{Amp} < I_c < 1.7\text{Amp}$. For $V_g = 0$ Volt the cathode current is 0.25Amp, but the intercepted helix

current is 50%. The e-flow is highly nonlaminar with large transverse velocities. The useful range of currents from the gun is, therefore, 1Amp to 1.7Amp.

3. BEAM TRANSPORT FROM PREBUNCHER TO WIGGLER

Numerical calculations were carried out for our FEM configuration using the "Envelope"³, e-gun⁴ and 3D codes⁵. The programs include space-charge and finite emittance effects. Regions of acceleration, drift, solenoid magnetic fields and magnetic shields were included. The beam exits from the TW modulator with a 1.5mm dia; the beam is focussed and matched to the wiggler acceptance.

The calculated³ axial magnetic field B required for beam focussing and the envelope of the resulting beam vs z are shown in Fig. 1. Coils were positioned and currents adjusted to provide this field. Beam transport experiments carried out thus far (sec. 6) verified the magnetic focussing system design.

4. MODIFICATION TO THE WIGGLER MAGNET SYSTEM

The wiggler is shown in Fig. 2. It is 74.8cm long with $\lambda_w = 4.4$ cm. The magnet stacks, a distance D apart, accomodate the interaction guide. For a first-order estimate of the transport of an axially symmetrical e-beam through the wiggler we used a "wiggler field" code to find the 3D wiggler field⁶ and calculated trajectories of single electrons moving through the wiggler.

4.1 Tapered magnet configuration at wiggler input and output

Electrons entering an unmodified wiggler are rapidly deflected and do not pass the guide in the wiggler. We calculated trajectories for several tapered magnet configurations near the wiggler input, and found a configuration which allows electrons to transport through the wiggler with x-wiggles of the order of 2.5mm and without any average deflection. The magnet configuration⁷ allowing for such a transport is shown in Fig. 3. PM1 and PM2 are half the size and strength of the main wiggler magnets. The position of these magnets can be adjusted and the effective field under PM2 can be varied by a coil above it producing an additional magnetic field. The y position of PM3 can be changed by use of shims. Experiments on electron transport in the wiggler were carried out using these 3 input matching magnets at the wiggler entrance (sec. 7.1) verifying the effectiveness of the above design.

4.2 Lateral focussing magnets

For a $B(x)$ increasing with x , a force toward $x=0$ keeps the beam focussed laterally.

The required $\alpha = \frac{\partial B_w}{\partial x}$ to keep the beam circular inside the wiggler for our FEM was

found to be⁸ approximately 5 Gauss/cm for a B_w of 300 Gauss. In a scheme proposed by Prof. Gover at TAU this gradient is obtained by use of two long permanent magnets as shown in Fig. 3. For such a configuration the required distance X_0 between the magnets

becomes: $X_0 = \left[\frac{16h dB_r}{\pi \alpha} \right]^{1/3}$ where h and d are the height and width of the long magnets, B_r

is the remanent magnetic field of the long magnet. A housing was made which permits adjustment of X_0 . Calculated trajectories for electrons entering the wiggler with a large angular spread⁹ showed good transmission through a 1cm dia tube in the wiggler.

5. The microwave interaction waveguide

A microwave interaction waveguide is used in the wiggler (Fig. 2). The electron beam passes inside of the guide; it enters and leaves the guide through nonradiating holes in the waveguide bends (Fig. 1) Several guides were investigated¹⁰ with the objective of attaining: propagation in a mode suitable for FEM interaction in the 4 to 6GHz frequency range, high rf electric field in the x -direction, low transmission losses, small D dimension required for attaining a large magnetic field and large gain, large d dimension (Fig. 4) to allow e-beam advance along the guide without interception.

Waveguides of crossection shown in Fig. 4 were compared theoretically and experimentally. The maximum squared rf field value $|E_{\text{max}}|^2$ in the e-beam area of guide 3) is 5 times larger than that of 1) and 50% larger than that of 2) making 2) and 3) favorite choices. The predicted gain for our FEM is high (about 2) making also 1) useful as a waveguide in initial experiments, since beam transmission through 1) is easiest ($d_1 = 3d_2 = 3d_3$). Guide 1) also has the lowest loss and highest power carrying capability of the guides studied.

6. Electron transport experiments

E-beam transport experiments to date include:

6.1 Low density e-beam transport

The e-gun and premodulator shown in Fig. 1 were replaced by a TV gun. The low density e-beam is first accelerated to 70KV and subsequently drifts in a region focussed by coils. The e-beam impinges on a 10 μ aluminum foil and phosphor screen, located after the second diagnostic cube. A beam diameter of about 1.5mm was obtained. An extension tube was mounted beyond the second diagnostic cube containing a phosphorescent screen. The phosphor screen was adjusted to be 160mm inside of the wiggler by moving the wiggler toward the TV gun over that extension tube. The x-displacement of the beam spot was measured as the wiggler was drawn away from the gun (phosphor screen moves from inside of the wiggler to the wiggler entrance).

The measured results showed that:

- 1) The beam passed 160mm into the wiggler with peak-to-peak deviations in the x direction of 5mm (theory predicts 4mm peak-to-peak deviations for a 2mm dia beam).
- 2) The average period of beam wiggling was close to 4.4cm (the wiggler period).
- 3) The e-beam passed the wiggler entrance and subsequent tube, indicating that the matching magnets at the wiggler entrance were adequate.

It should be noted that prior to placement of the matching magnets at the wiggler entrance the beam was deflected and could not even enter the wiggler.

6.2 Full e-beam current transport

Initial experiments were carried out on e-beam transport from the traveling wave buncher to the diagnostic cube. For a 1.5Amp cathode current approximately 1.1Amps were transported to an aluminum foil and quartz window mounted at the end of that cube¹¹. The magnetic field distribution between the traveling wave buncher and the cube is as described in Sec. 3. Work is continuing on passing the full e-beam through the wiggler.

7. REFERENCES

1. I. Schnitzer and A. Gover, Nucl. Instr. and Meth., A237(1985)124.
2. A. Eichenbaum, C. Kleinman, D. Ben-haim, "TAU Report" (1993).
3. A. Kugel, "E-beam Envelope Radius Calculations" TAU Report (1991).
4. W.B. Herrmannsfeldt e-gun code SLAC (1988).
5. M. Cohen and A. Gover, TAU "3-D code" (to be published 1993).
6. M. Draznin, TAU (1993) based on L. Elias, RCJHO, G. Ramian Quant. Inst. Rep. UCSB QIFEL 023 ('83).
7. A. Gover and M. Draznin, Internal TAU communication.
8. M. Cohen and A. Gover, TAU Report PBFEM5 (1993).
9. S. Witman, TAU - internal communication.
10. D. Ben-Haim, TAU - internal communication.
11. M. Arbel, TAU-internal communication.

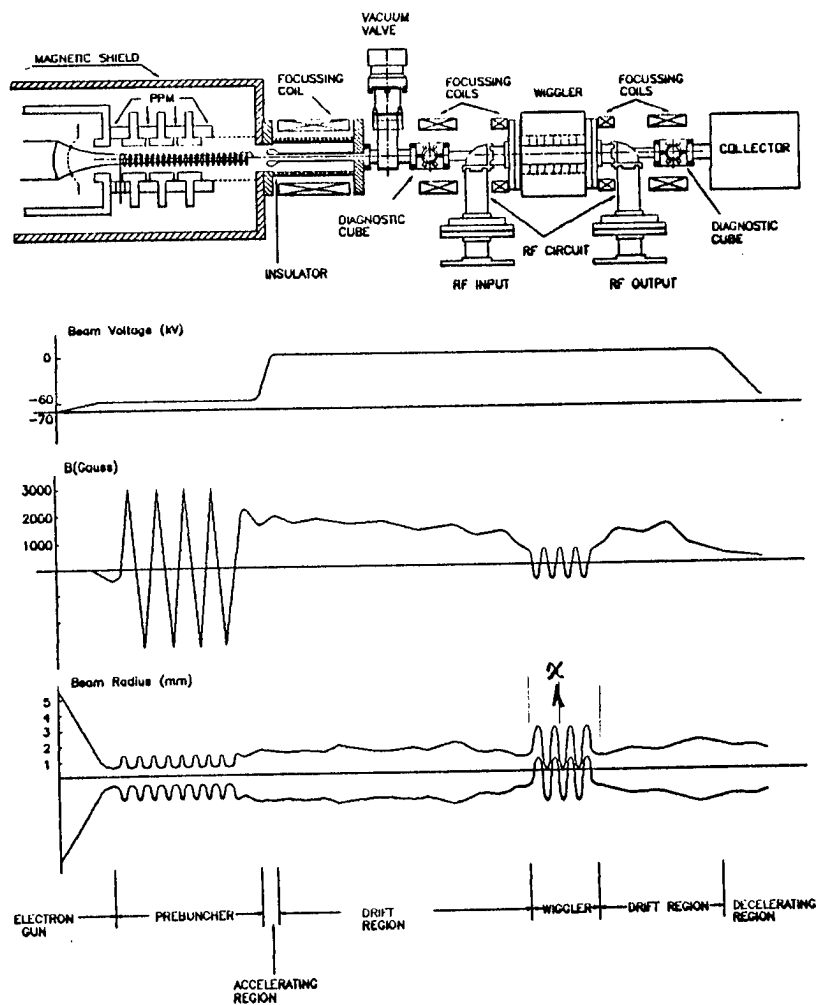


Fig. 1 a) Schematic of Prebunched FEM b) Voltage distribution
c) Magnetic field distribution d) Beam radius and x displacement

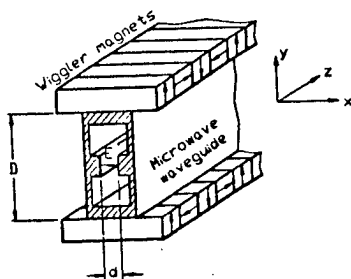


Fig. 2 Wiggler containing waveguide

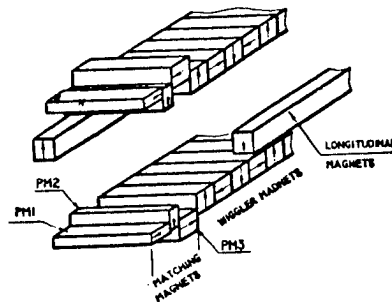


Fig. 3 Wiggler including input matching magnets and lateral focussing long magnets

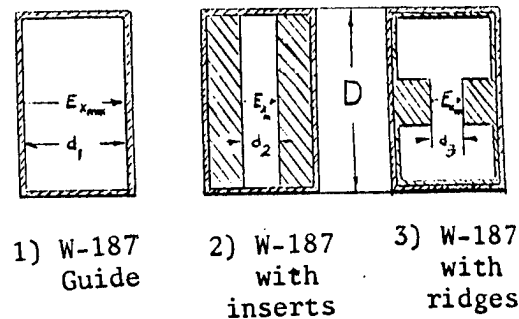


Fig. 4 Microwave waveguide crosssections for use in FEM

EXPERIMENTS WITH AN S-BAND VIRCATOR

by

D E T F Ashby, J Allen and K C Hawkins

AEA Technology, Culham Laboratory, Abingdon, Oxfordshire OX14 3DB

ABSTRACT

The experiments described used a Vircator operating in the frequency range 2.5 - 3.5 MHz and powered by a 10 ohm, 100 ns pulse generator operating at voltages up to 600 kV. The Vircator had a tunable resonant cavity and power was coupled out from one side. A series of experiments were carried out to elucidate various aspects of the Vircator's behaviour. The first experiment conclusively demonstrated reflexing in which electrons from the virtual cathode region re-enter the anode/cathode gap and affect the diode impedance. The second experiment demonstrated the effect of the anode/cathode gap on the behaviour of the reflexing electrons. The third experiment showed that the power output depended upon the thickness of the anode foil, and more surprisingly, on the thickness of the foil forming the adjustable rear wall of the cavity.

1. INTRODUCTION

The experiments to be described used the Vircator shown in Fig 1; it was originally supplied by Physics International but has undergone several modifications. The results presented demonstrate in a simple direct fashion the effects of reflexing electrons.

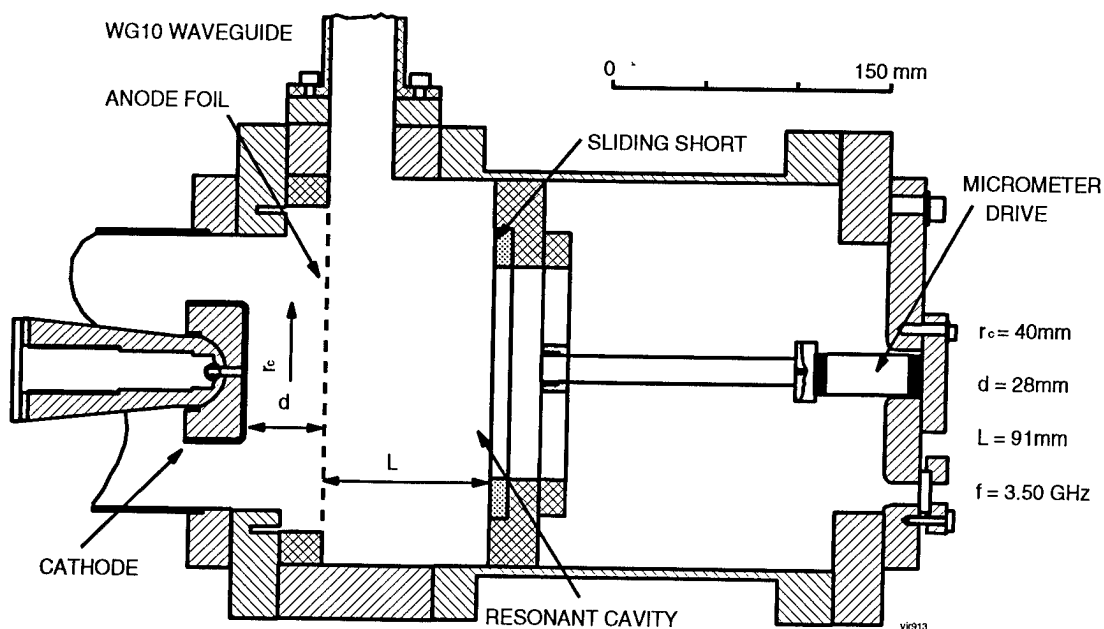


Figure 1: The Vircator assembly.

2. EXPERIMENTAL RESULTS

It appeared that electrons from the virtual cathode region in the RF cavity might be re-entering the diode region by passing through the anode foil (i.e. reflexing). The first indication of this was that the diode current failed to increase as d^{-2} as the anode/cathode gap was decreased; a series of measurements then demonstrated that the Child-Langmuir law for space charge limited flow was not being obeyed.

If reflexing occurs then the electrons re-entering the diode space will affect the space charge fields and consequently the current flow. Reflexing was demonstrated unambiguously by replacing the anode foil with a 1 mm aluminium plate which completely absorbed the electrons striking it. Figure 2 compares the current pulses obtained when the foil was replaced by the aluminium plate and shows that the current amplitude is increased by using a thick anode.

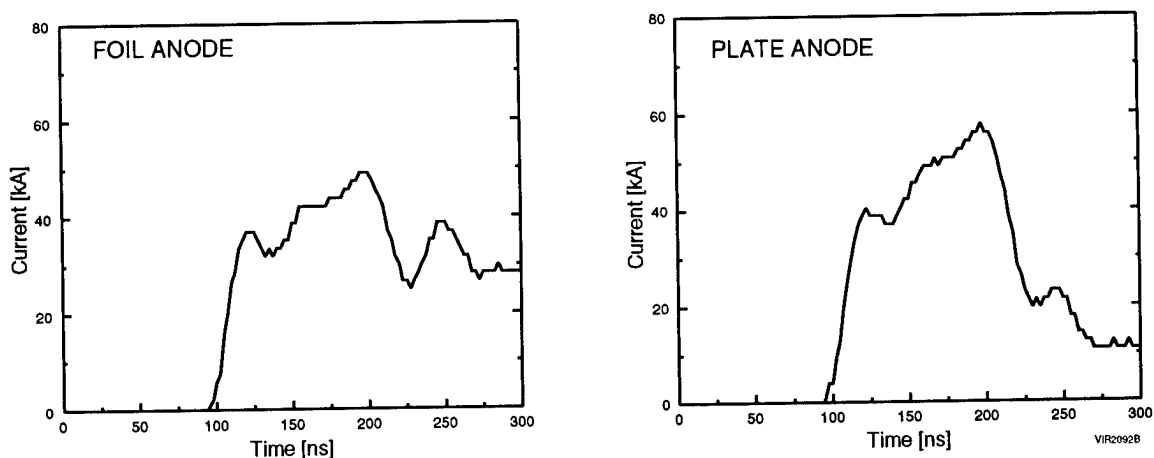


Figure 2: Oscillograms of current showing the effect on the current pulse of replacing anode foil by an aluminium plate to absorb the electrons.

The presence of electrons from the RF cavity in the diode region was also demonstrated by the signal from a small B-dot which monitored the RF activity in the diode region. The B-dot signal was split into two with one half going to an integrator to monitor current while the other half was filtered and rectified to give the amplitude of the RF fluctuations. Signals at the Vircator frequency were detected that corresponded to current fluctuations of about 1%.

The second experiment showed that the anode/cathode gap affected the behaviour of the reflexing electrons and had a strong influence on the power output and frequency of the Vircator. The cathode geometry was changed and the cavity enlarged by removing the sliding short-circuit. (See Fig 3). With this new cathode the bulk of the electron emission comes from the outer of the cathode. This part of the cathode is connected to the cathode support via a sliding contact; hence the distance d_2 between the centre of the cathode and the anode can be varied without affecting the total current as long as d_1 is left unchanged by adjusting the length of the cathode stalk.

Figure 4 shows that changing the gap d_2 had a drastic effect on the operation of the Vircator. The oscillograms shown compare power outputs, as measured by a directional coupler and crystal detector, and heterodyne signals for the two cases $d_2 = 45$ mm and $d_2 = 0$.

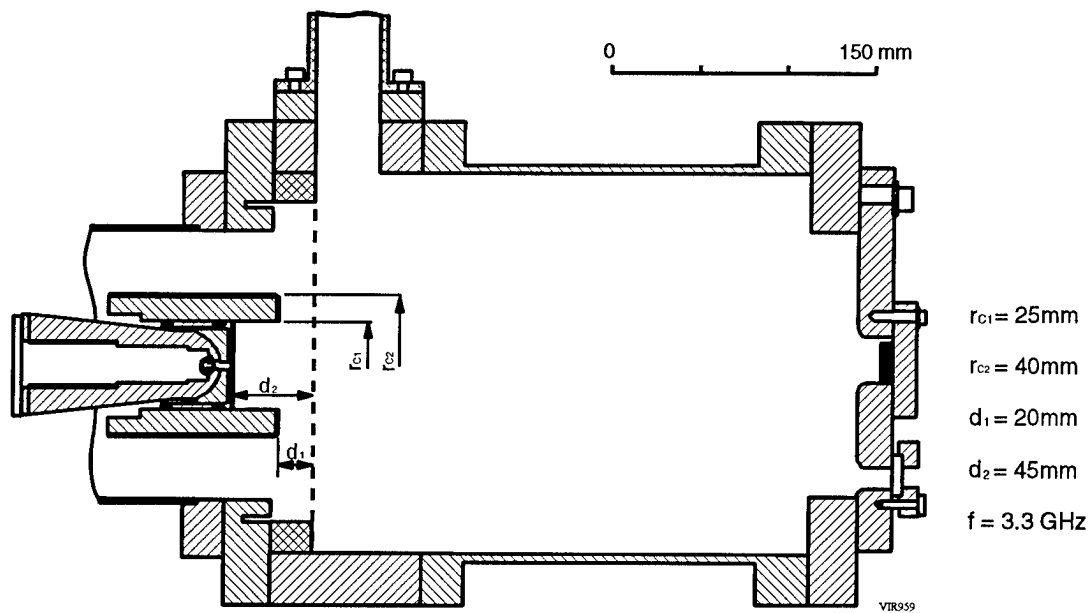


Figure 3: Diagram showing the Vircator with a recessed cathode.

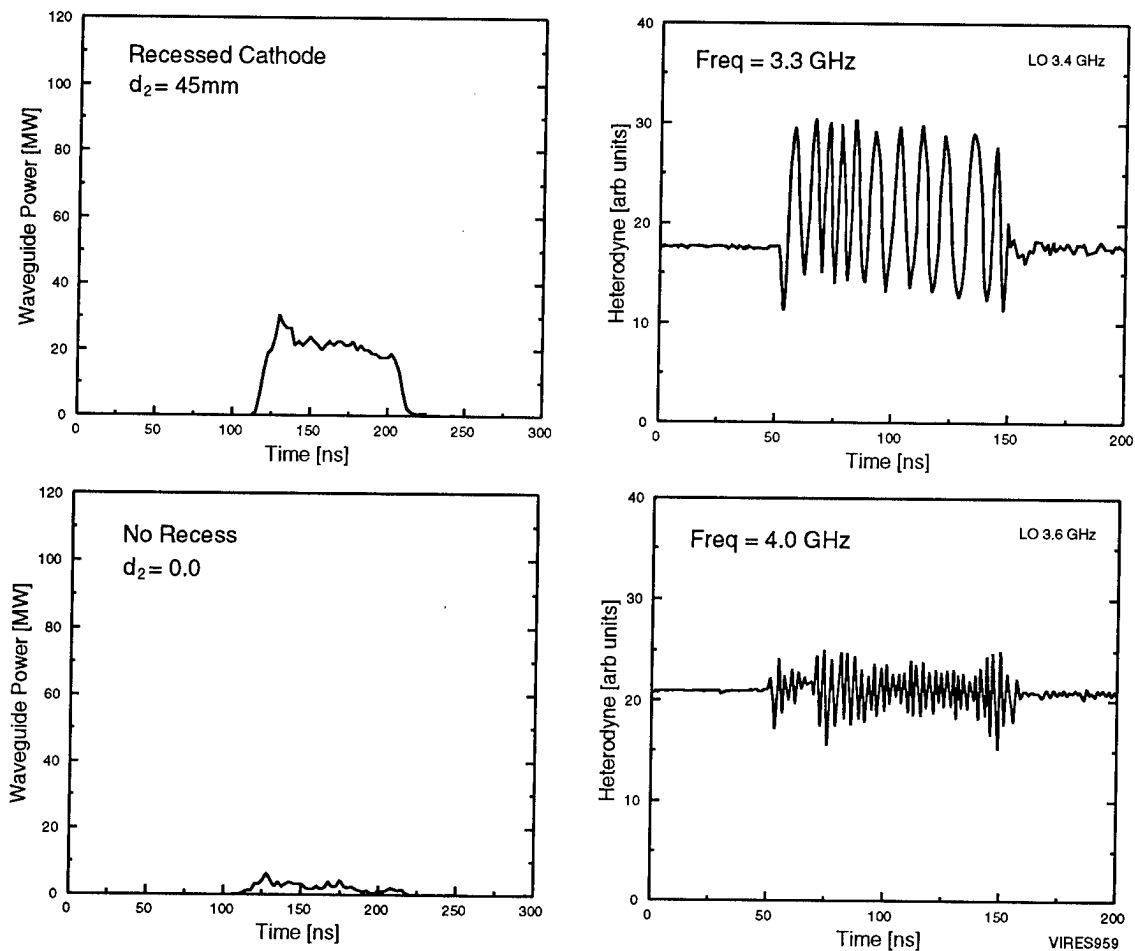


Figure 4: Oscillograms showing the effect of the recessed cathode on Vircator performance.

From the experiment with the recessed cathode it is evident that the anode/cathode gap affects the operating frequency by two separate mechanisms, firstly by one involving reflexing electrons and secondly by the normally quoted mechanism depending upon current density and plasma frequency¹. It is important to note that the recessed cathode shown in Fig 3 enables both mechanisms to be optimised independently.

In the Vircator assembly shown in Fig 1 the front face of the sliding short as well as the anode is made from aluminium foil which is largely transparent to high energy electrons. In the third experiment the effect of foil thickness on power output was investigated. The reasoning behind the experiment was based on the possibility that the passage of high energy electrons through the foil would produce secondary electrons, and possibly surface plasma, which would reduce the power output by loading the cavity; such an effect is likely to depend upon foil thickness.

The oscillograms in Fig 5 show that the power output increases as the foil thickness is decreased; the thickness of both the anode foil and the rear foil affects the power output. Although the pulses shown in Fig 5 are of irregular shape repeated pulses showed that the mean amplitude was essentially constant from one pulse to the next and that the increase in power was a real effect.

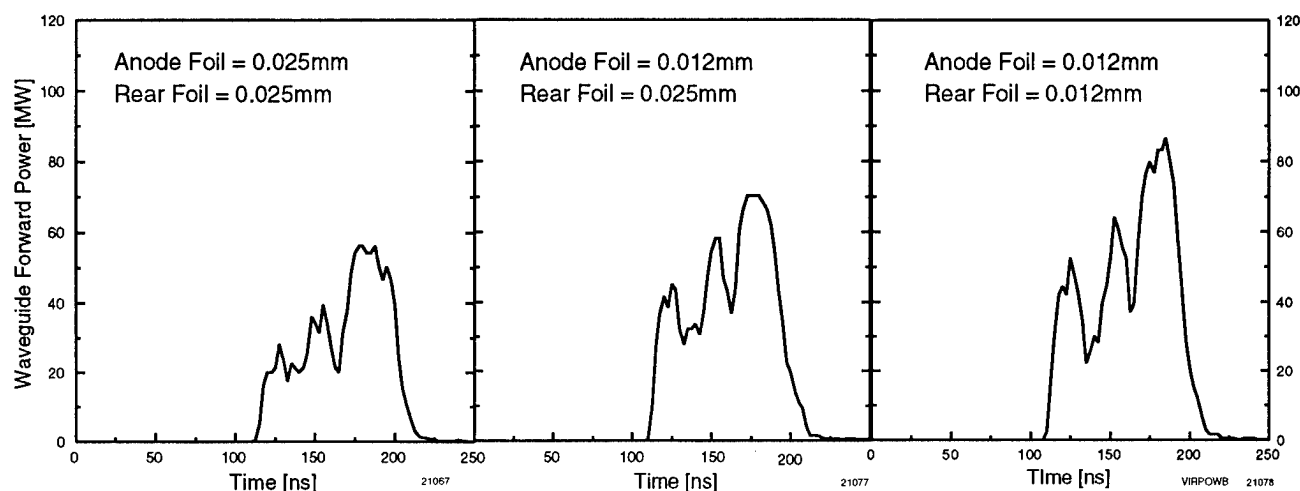


Figure 5: Oscillograms showing how power output is affected by the thickness of foil used in the resonant cavity of the Vircator.

3. ACKNOWLEDGEMENT

The work described has been carried out under contract RAE 1B/1a for DRA Farnborough.

4. REFERENCES

- [1] James Benford and John Swegle, "High Power Microwaves" Artech House, p311, 1991.

COMPARISON BETWEEN EXPERIMENT AND COMPUTER MODELLING FOR SIMPLE MILO CONFIGURATIONS

by

D E T F Ashby, J Allen, J W Eastwood, K C Hawkins and L M Lea

AEA Technology, Culham Laboratory, Abingdon, Oxfordshire OX14 3DB

ABSTRACT

A detailed comparison of experimental results and computer simulation have been made for a number of simple axisymmetric MILO structures designed to operate at 1 GHz. The structures were built from a set of demountable components which enabled the number of cavities and their dimensions to be rapidly altered. Measurements were made of the fluctuating magnetic fields at the end of each cavity and of the applied voltage and current pulse. The amplitude and depth of RF modulation of the magnetic fields, although repeatable, changed drastically from one configuration to the next. These parameters were compared with predictions from VIPER, a 2-D electromagnetic PIC code^{1,2}. Good quantitative agreement was obtained between experiment and simulation in most situations, however, late in the current pulse, after about 100 ns the level of RF began to decay; a phenomenon which became more pronounced as the applied voltage was increased. The effect was attributed to plasma formation on the cavity vanes and subsequent electron emission; this explanation was verified by computer modelling electron emission and by using vanes made from polished stainless steel in place of aluminium vanes.

1. INTRODUCTION

The Magnetically Insulated Line Oscillator (MILO) is a relatively new type of co-axial crossed field device that uses the self-magnetic field produced by current flow in the central cathode to cut-off electron flow to the anode¹. This paper describes the detailed comparison between computer simulations using the VIPER software^{2,3} and a series of MILO experiments specifically designed to test how well the numerical modelling matches experiment.

2. THE EXPERIMENTS AND COMPUTER MODELLING

The azimuthally symmetric MILO apparatus, shown in Fig 1, was chosen to facilitate direct comparison of experimental measurement and results from the two dimensional axisymmetric PIC code. The length of the long entry section can be adjusted, thus enabling the diode gap to be varied under vacuum. The apparatus is demountable, and by changing the vane width and cavity size six different slow wave structures were used; both the number of cavities and the diode gap were varied.

The voltage and current measurements are standard and are measured at the entrance to the MILO. However, the B -dot measurements need some explanation. Each cavity contains a small calibrated loop which measures the magnetic field at the top of the cavity; for monochromatic oscillations this field takes the form

$$B = B_0 + \tilde{B} \sin \omega t \quad (1)$$

The signal from the loop is split into two channels and processed separately to give two signals proportional to B_0 and \dot{B} respectively. The first channel goes through a passive integrator and measures the current flowing through the MILO at the position of the cavity; the second channel goes through a high-pass filter and is then rectified to give a signal proportional to the oscillating magnetic field.

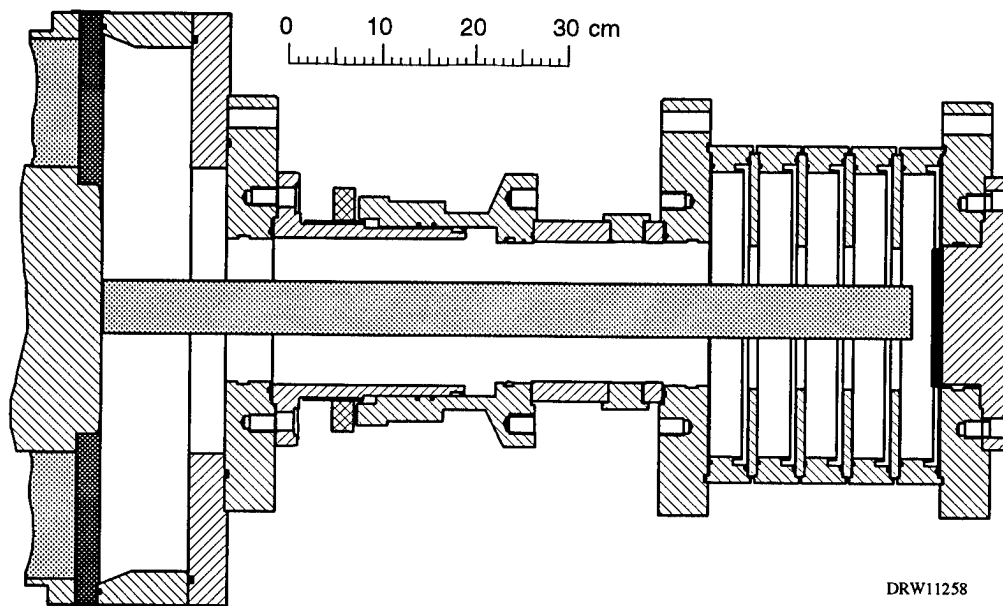


Figure 1: Diagram showing a 5 cavity MILO used in the current study.

3. RESULTS

Six different periodic slow wave structures were tested, all with the π -mode at approximately 1 GHz. The π -mode is the usual oscillation mode, but some structures had a poor match between the wave phase velocity (which is proportional to the periodic length) and the electron flow velocity; in such cases, the MILO was reluctant to oscillate at 1 GHz and was sensitive to small changes in the diode gap and to the amplitude and shape of the voltage pulse from the Pulser. This behaviour is not typical; normally the MILO is a robust device that is insensitive to small changes in operating conditions; however modelling reproduced all the phenomena displayed by the experiments.

Only one set of results are displayed here because of space restrictions. Figure 2 compares experiment and modelling for a 5-cavity MILO configuration. The curves marked 'current' are derived from the B_0 signals obtained from the B-dot loops while those marked 'RF' are derived from the \dot{B} signals; for ease of understanding both signals have been normalized to current.

The agreement between experiment and computer simulation was good. The mean measured amplitudes of both B_0 and \dot{B} were compared with those obtained from computer simulation for all of the experiments; the mean of all these results was 0.96 ± 0.05 .

A minor difference between the experimental results and the computer simulation is that in the experiment the RF signals have a tendency to decay slightly while the opposite occurs in the simulation. This difference is attributed to plasma formation on the resonator vanes and subsequent electron emission. This hypothesis is supported by Fig 3 which shows the effect of changing the vane material for aluminium alloy to polished stainless steel for the configuration used in Fig 2. Note that with stainless steel vanes the gradual decay in the RF signals is absent.

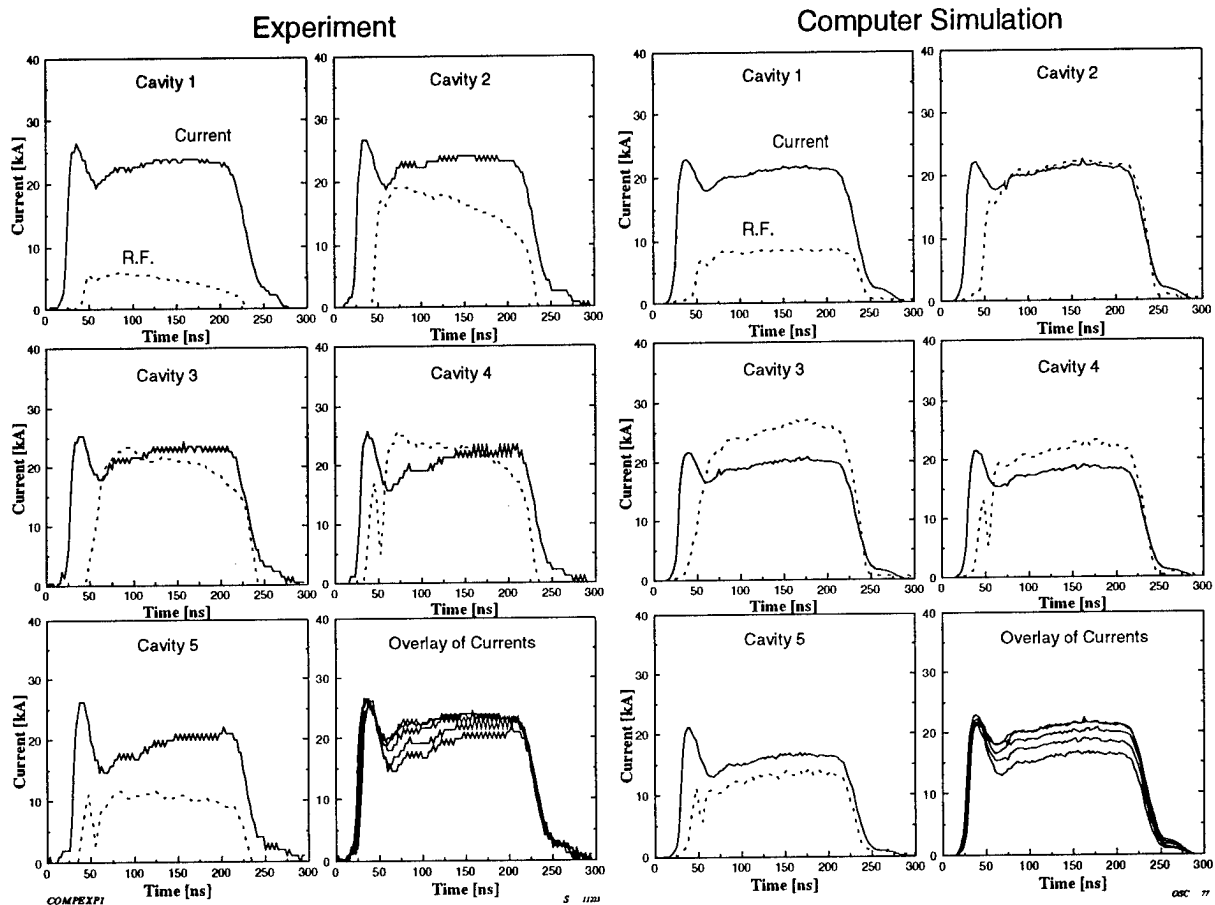


Figure 2: Comparison between experiment and computational simulation for a 5-cavity MILO using 4 cm cavities and 1 cm vanes. The simulation was driven using the experimentally measured voltage pulse.

The effect shown in Fig 3 became much more pronounced at higher operating voltages. At 450 kV the MILO using aluminium alloy vanes showed strongly anomalous behaviour; the RF signals quickly reached a maximum and then rapidly decayed throughout the pulse to about a third or a quarter of their maximum. By contrast the MILO with stainless steel vanes showed somewhat larger RF signals which exhibited only a slight droop throughout the pulse.

This anomalous behaviour has been duplicated in computer modelling by making the cavity vanes electron emitters; this results in the RF signals decreasing by a factor of about three which is close to that observed experimentally.

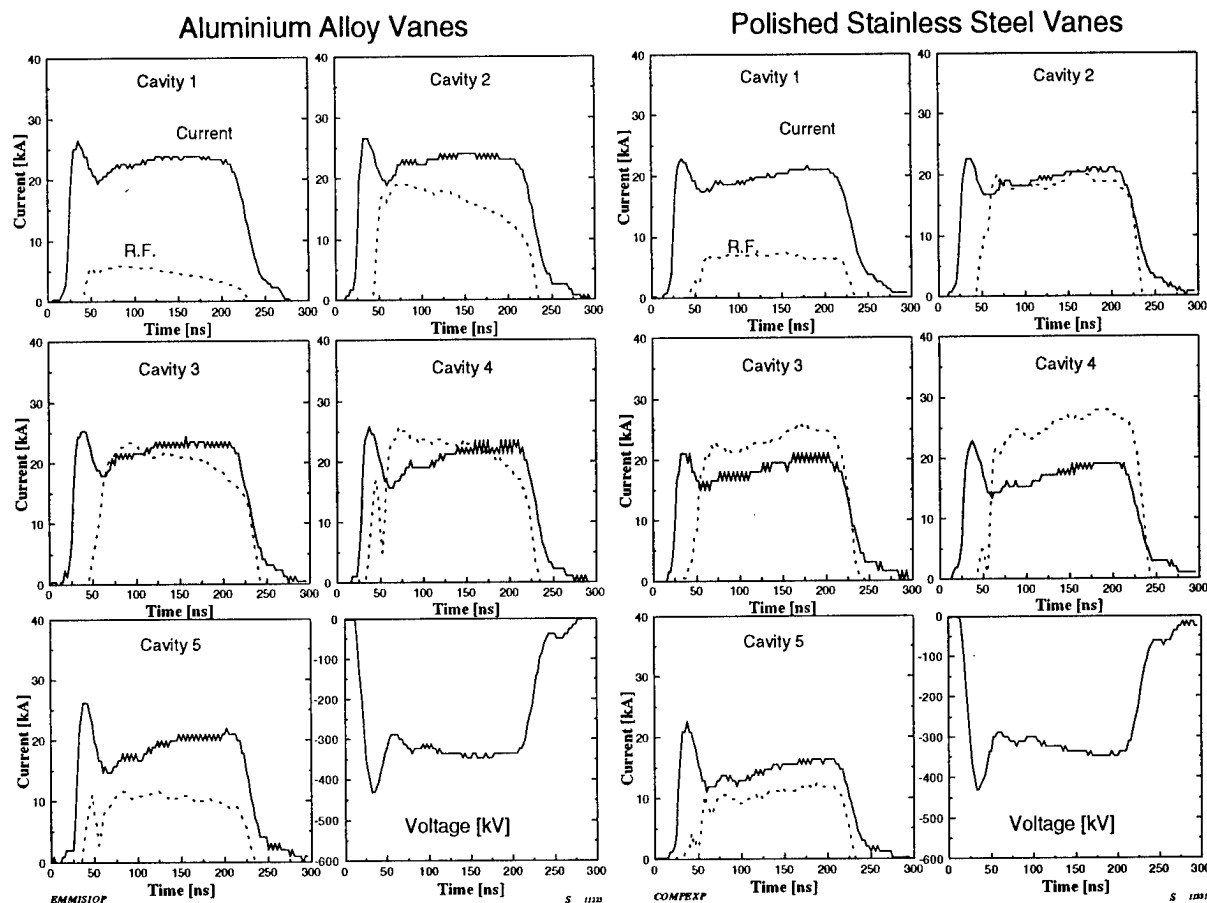


Figure 3: Comparison between two sets of experimental data, showing the difference in operation when polished stainless steel vanes are used instead of the aluminium alloy vanes normally used.

4 ACKNOWLEDGEMENT

The work described has been carried out under contract RAE 1B/1a for DRA/Farnborough.

5 REFERENCES

- [1] M. C. Clark, B. M. Marchev and L. D. Bacon, "Magnetically Insulated Transmission Line Oscillator", *Appl. Phys. Lett.* Vol. 52, p78, 1988.
- [2] J. W. Eastwood, "Virtual Particle Electromagnetic Particle-Mesh Algorithms for Microwave Tube Modelling" *7th Ann. Rev. Prog. App. Comp. Electromag.* 655-660, 1991.
- [3] J. W. Eastwood, "The Virtual Particle Electromagnetic Particle-Mesh Method", *Computer Phys. Commun.* 64, 252-266, 1991.

Excitation of UHF-oscillations in magnetic insulated slow-wave line

V.A.Balakirev, D.Yu.Sidorenko, G.V.Sotnikov, Yu.V.Tkach

NSC Kharkov Institute of Physics & Technology,
310108, Ukraine, Kharkov, Akademicheskaya Str., 1

ABSTRACT

The theory of electromagnetic radiation excitation by an electron flow is considered for a flat magnetically insulated transmission line with a comb anode. The dispersion relation describing the excitation of electromagnetic oscillations by the Brillouin flow in the slow-wave structure is derived. The numerical analysis of dispersion equation has shown that in the presence of the slow-wave structure, an essential increase in increments of unstable oscillations takes place. The conditions for optimum generation of microwave power are found. Efficiency estimates are given for the oscillators of the type considered.

1. INTRODUCTION

In magnetically insulated transmission lines the Brillouin electron flow forms¹. The electrons, emitted from cathode, drifts along the electrodes in crossed self-consistent electrical and magnetic fields. Being strongly non-equilibrium, such a flow is unstable². In transmission lines with slow waves (coaxial lines, flat lines with a corrugated anode, comb-shaped structures) the synchronism of the Brillouin flow with slow waves of the structure is possible. The instability, arising under these conditions, will lead to the excitation of intense electromagnetic oscillations. The systems of this type can be used as powerful microwave amplifiers and oscillators. In the Magnetically Insulated Line Oscillator(MILO) the electron flow formation and the generation of radiation are combined. For the given geometry of the transmission line, the only external parameter which defines the characteristics of the oscillator is the voltage applied.

2. INTERACTION OF THE ELECTRON FLOW WITH THE SLOW-WAVE LINE

The geometry of the flat slow-wave line is shown in fig.1. The anode has a comb structure. The potential difference applied to the electrodes is sufficient to cause the explosion emission. As a result, the Brillouin flow with thickness x_* , pressed to the cathode, forms in the line. We shall describe the comb using the long-wave approximation $kl \ll 1$, where k is the longitudinal wave number, l is the comb period. The dispersion equation for TM waves can be obtained by matching the field impedance in the vacuum gap $d > x > x_*$ to the impedances of the comb and the electron flow. As a result, we shall obtain

$$\zeta_b = (\zeta_s - \tanh pB) / (\zeta_s \tanh pB - 1), \quad (1)$$

where $B = D - X_*$, $D = d\omega_c/c$, $X_* = x_*\omega_c/c$,

$$\zeta_s = (w/p) \tan(wA), \quad \zeta_b = \Gamma \gamma_*^2 \Omega_*^2 / p(\Delta'_*/2 + \Delta_* F'_*/F_*), \quad (2)$$

$\zeta_{s,b}$ are the field impedances at the boundaries of the comb $x = d$ and the electron flow $x = x_*$, $p = (K^2 - w^2)^{1/2}$, $w = \omega/\omega_c$, $K = kc/\omega_c$ are the dimensionless frequency and longitudinal wavenumber, c is the speed of light, $\omega_c = eH_c/mc$ is the cyclotron frequency, H_c is the magnetic field on the cathode, $A = a\omega_c/c$, $\Gamma = w^2 - K^2 - 1$, $\Omega_* = w - KV_*$, $V_* = v_*/c$, v_* is the velocity, γ_* is the relativistic factor of electrons at the flow boundary $x = x_*$, $\Delta_* = \gamma_*^2 \Omega_*^2 - 1$, $\Delta' = d\Delta/dX|_{X=X_*}$, $F = F(X_*)$, $F'_* \equiv dF/dX|_{X=X_*}$, $X = x\omega_c/c$, the function $F(X)$ is the solution of the differential

equation

$$d^2 F/dX^2 + (\Delta'/\Delta)(dF/dX) - p^2 F = 0, \quad (3)$$

$\Delta = \gamma^2 \Omega^2 - 1$, $\gamma = \cosh X$, $\Omega = \omega - KV(X)$, $V(X) = \tanh X$. On the cathode, the longitudinal component of electric field goes to zero, therefore, $F(0) = 0$.

Now we shall analyse the Brillouin flow instabilities in the slow-wave structure. In the extreme case of $K \ll 1$, from the dispersion equation (1) we shall obtain the expression for phase velocities of waves

$$V_{ph}^{\pm} = \frac{\sinh X_* \cosh X_* \pm [s(s-1) + s\nu(s - \cosh^2 X_*)]^{1/2}}{\sinh^2 X_* + s(1 + \nu)}, \quad (4)$$

where $s = d/x_*$, $\nu = a/d$. If we exclude the electron flow by introducing extreme transition $X_* \rightarrow 0$, then from Eq.(4) we shall obtain the expressions for the phase velocities of forward and backward waves of the "cold" structure. The Brillouin flow not produce new branches of oscillations, but it "distorts the "cold" branches. The LF-instability arises when the discriminant is negative $D = s(s-1) + s\nu(s - \cosh^2 X_*) < 0$. The flow with the minimal current $s = \cosh^2 X_*$ is stable. In this case as in the smooth anode line the phase velocity of the slow wave V_{ph}^- is equal to zero. Phase velocity of the quick wave $V_{ph}^+ = \tanh 2X_*/(1 + \nu \cosh^2 X_*/\cosh 2X_*)$ is lower than that in the line with smooth electrodes.

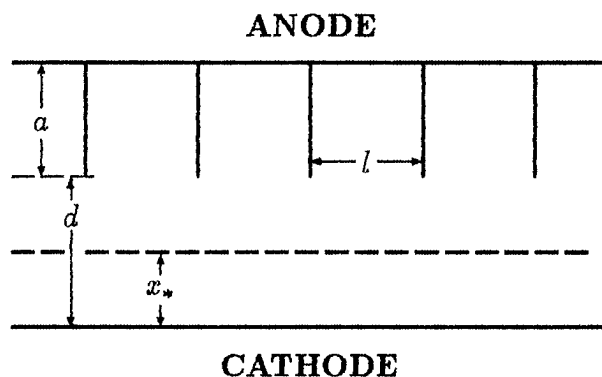


Fig.1. The slow-wave transmission line

The dispersion equation (1) was solved numerically for the minimal current and different slow-wave structure geometries and applied voltage values. The frequency (fig.2a) and the instability growth rate (fig.2b) versus wavenumber were obtained for slow-wave structure with $d/a = 4$ and the applied voltage $U = 0.6$ MV. For small K , in accordance with analytical treatment, the Brillouin flow is stable and two waves propagate in it. The quick wave branch breaks. This feature is also observed for the line with smooth walls². Oscillations grow in the frequency range $W > 1$. The growth rate as a function of the wavenumber has a peak. The gain in the growth rate is due to the wave being in resonance with the slow-waves structure. Outside of the resonance region K , the instability has the same behavior as in the line with smooth walls. As the voltage increases, the growth rate peak shifts to the low frequency region, and the increment value at the maximum decreases. For high voltages $U > 2.4$ MV, the resonance instability growth rate is essentially less than the growth rate of magnetron instability², which arises in the line with smooth walls. Therefore, in this case, the slow-wave structure will influence weakly the excitation of oscillations in the transmission line. The results of numerical calculations for the slow-wave structure with the parameters $d/a = 2$ and an applied voltage of 1 MV are represented in fig.3. Here the wave with

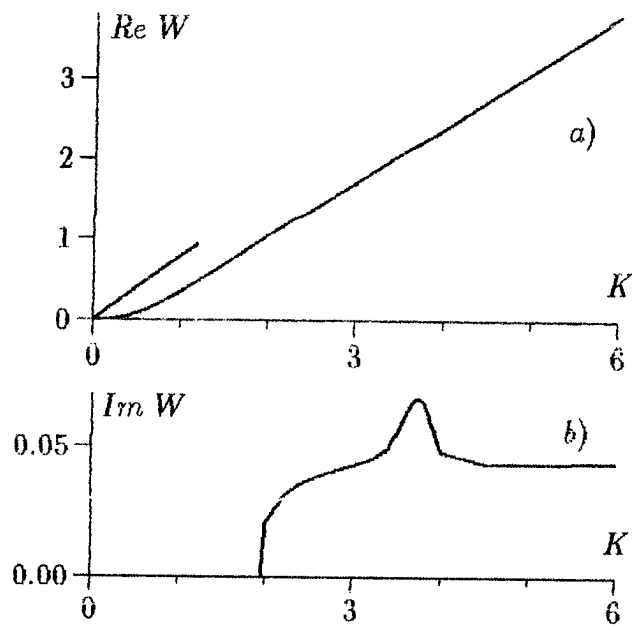


Fig. 2.

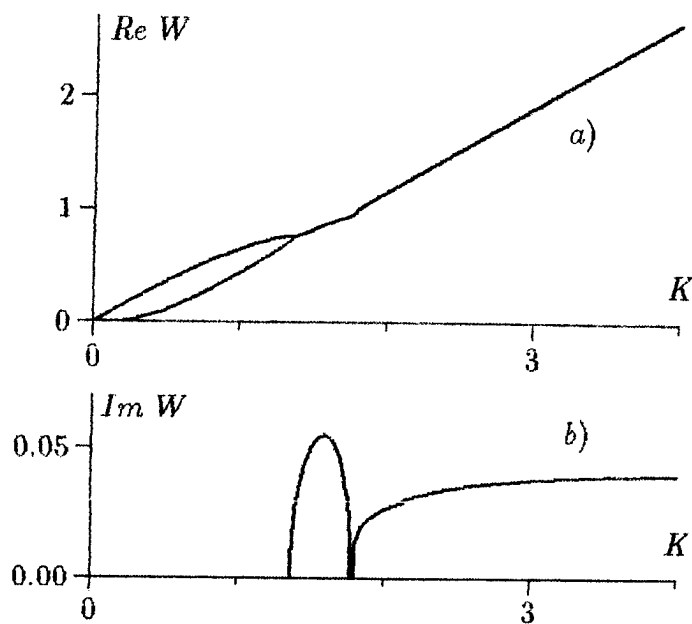


Fig. 3.

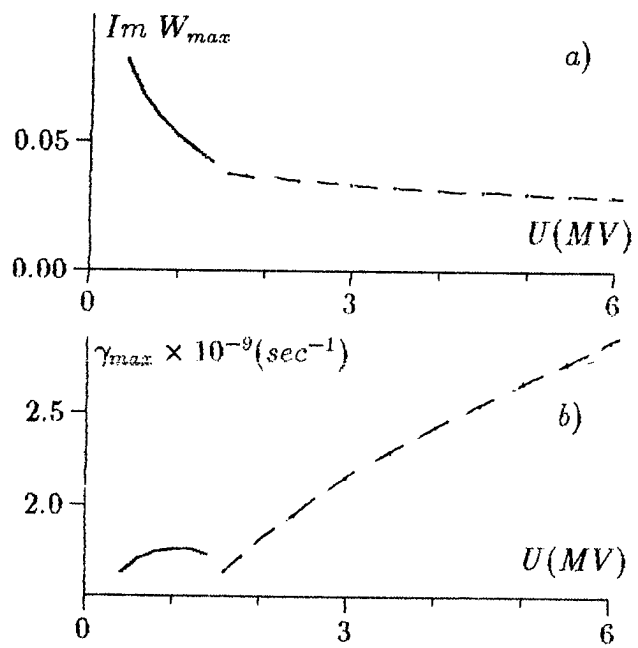


Fig. 4.

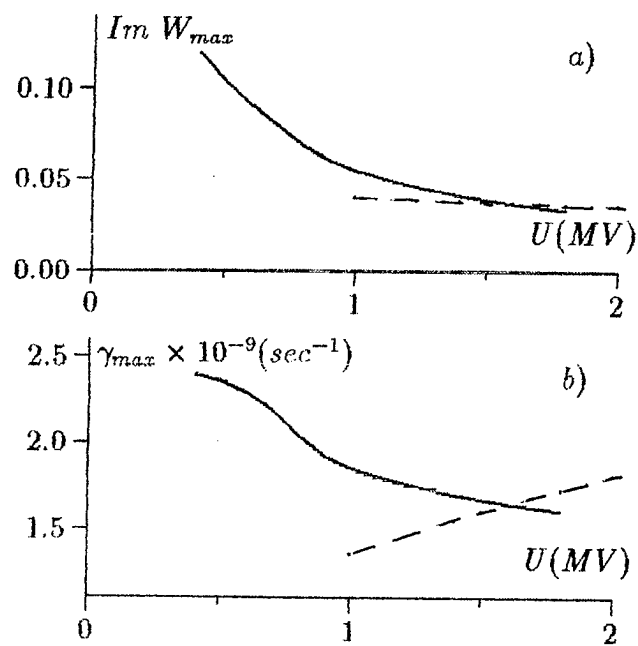


Fig. 5.

the frequency $W = 0.8$ has the greatest growth rate. And this wave is stable in the transmission line with smooth electrodes. The region $K > 1.8$ corresponds to the magnetron instability, and $1.8 > K > 1.3$ — to the resonance instability.

The maximum dimensionless (a) and dimensional (b) increments vs applied voltage for $d = 2$ m and $a = 0.5$ m are represented in fig.4. Similar functions dependencies for $d = 2$ m and $a = 1$ cm are shown in fig.5. The greatest growth rate of resonance instability is depicted by a solid line. The dotted line depicts the greatest growth rate of magnetron instability. As the applied voltage increases, the dimensionless growth rates decrease, and dimensional growth rate behave differently. The resonance instability growth rate decreases and the magnetron one increases. For relatively low voltages the resonance instability is dominating. This instability takes place only in the slow wave structure. For high voltages, the magnetron instability is determining. The frequency of the wave, excited by resonance instability practically does not depend on voltage. The anode efficiency of the oscillator can be determined as

$$\eta = K_i(\gamma - \gamma_*)/(\gamma - 1), \quad (5)$$

K_i is the ratio of the flow current to the total current in the line, $\gamma = 1 + eU/mc^2$. In particular, for $U = 0.5$ MV we obtain $\eta = 17\%$. Formula (5) must be considered as the top efficiency estimation. In reality the efficiency value will be always lower.

3. CONCLUSION

The theoretical analysis has shown MILO to be promising as a superpower microwave oscillator. Under the fixed geometry of the line, the output oscillator parameters, such as microwave power and efficiency, depend only on voltage applied. On the other hand, the generated frequency is practically voltage independent, and this will ensure frequency stability during operation with voltage variations.

REFERENCES

1. L.I. Rudakov et.al. Generation and focusing of the high-current relativistic electron beams. M.:Energoatomizdat, 1977.
2. J. Swegle, E. Ott, "Linear waves and instabilities on magnetically insulated gaps", Phys.Fluids, Vol.24, pp.1821-1835, 1981.
3. R.W. Lemke, M.C. Clark, "Theory and simulation of high-power microwave insulated transmission line oscillator", J.Appl.Phys., Vol.62, pp.3436-3440, 1987.
4. B.M. Marder, "Simulated behavior of the magnetically insulated oscillator", J.Appl.Phys., Vol.65, pp.1338-1349, 1989

L.G.Blyachman, V.E.Nechaev

Institute of Applied Physics, Russian Academy of Science
Nizhny Novgorod, Russia, 603600

1. ABSTRACT

Secondary Emission Discharge (SED) is one of the critical factors, which limit energy possibilities of the powerful HF-electronic devices with great magnetostatic fields (e.g., relativistic generator and amplifiers); it initiates a breakdown mechanisms. The most dangerous, nonlocalised variety of the SED, which develops with the highest speed, is the one-sided resonance discharge [1,2]. It is formed by electrons that oscillate near one of the Me surfaces and are driven back to this surface by the magnetic field \mathbf{H}_0 , which is directed in parallel or at some angle to this discharge surface. Characteristics of such secondary emission resonance discharge (SERD) have not been studied yet in the cases of arbitrary direction of the field \mathbf{H}_0 to the discharge surface. However, near the walls of various devices (e.g., electrodynamic structures of generators) the angle of the direction of the field \mathbf{H}_0 with respect to the surface can change in a wide range. The basic concepts of the theory of SERD starting regimes are studied in this report.

2. BASIC CONCEPTS

An avalanche rise of the SERD can take place in several conditions [1,2]. Discharge is built by the essential nonrelativistic electrons with the size of oscillation $a \sim \beta\lambda$ (λ - wavelength, $\beta=v/c$ - ratio of the electron velocity to velocity of light) much smaller than the wavelength and the curvature radius of the surface in the typical practice situations [1]. Therefore the surface can be approximate by the plane and one can describe the motion in the coordinates and fields as it is shown on Fig.1 (x - along normal, α - is the angle between \mathbf{H}_0 and z -axis).

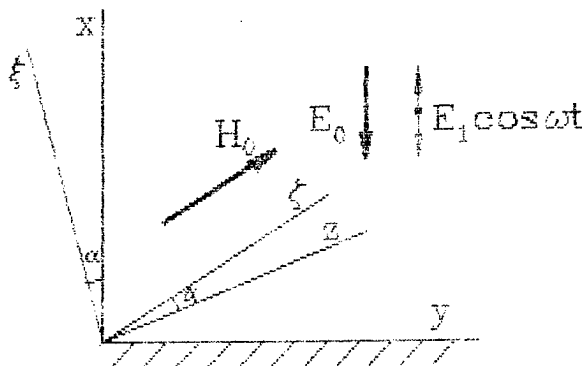


Fig. 1. Coordinates and fields for the SERD model

It is comfortable to present the electric field, taking into account the possibility of the existence of the static component (from the device electrodes and different charges, e.g., electron beams), as

$$\mathbf{E} = -\mathbf{x}_0 [E_1 \cos \omega t + E_0] \quad (1)$$

Then the motion of the electrons at the starting stadium of the SERD can be described in the terms of the undimensional transit angle $T = (\omega t - \omega t_0)$ with the marked particles initial phase $\varphi = \omega t_0$ with the use of the two main parameters $\varepsilon = E_0/E_1$ and $\nu = \Omega/\omega$ (the ratio of the free oscillations frequency in \mathbf{H}_0 -field to the forced oscillations frequency) with fixed inclination angle and the oscillation size $a = eE/m\omega^2$. The initial velocities could be neglected.

The motion can be presented as a superposition of the two displacements along and across the magnetic field:

$$\zeta = a \sin \alpha f_{\parallel}; \quad \xi = a \cos \alpha v^{-2} f_{\perp}, \quad (2)$$

where

$$f_{\parallel} = \varepsilon T^2 / 2 + \cos \varphi (1 - \cos T) - \sin \varphi (T - \sin T);$$

$$f_{\perp} = \varepsilon (1 - \cos vT) + \frac{v^2}{v^2 - 1} \left[\cos \varphi (\cos T - \cos vT) - \sin \varphi \left(\sin T - \frac{\sin vT}{v} \right) \right], \quad (3)$$

so, that f_{\parallel} and f_{\perp} are comparable in the region of high magnetic fields, that is of the practical interest. The coordinate projections of the motions can be counted from the following expressions:

$$x/a = \cos^2 \alpha v^{-2} f_{\perp} + \sin^2 \alpha f_{\parallel};$$

$$z/a = \cos \alpha \sin \alpha [f_{\parallel} - v^{-2} f_{\perp}];$$

$$dy/dT = v^{-1} \cos \alpha df_{\perp}/dT. \quad (4)$$

There can be resonance groups of electrons in case of some relations between v , ε and α (H_0 , E_0 -fields and the angles of the field \mathbf{H}_0 direction, if ω and E_1 are fixed). These groups have the finish flight time T_f , which is multiple to the forced oscillation period. During the following cycles these motions are reproduced by the increasing groups, if the secondary emission coefficient $\sigma > 1$, i.e. in the known interval of the bombing energy [2]. Such electrons belong to the resonance phase φ_r to be found. Neighbour electrons can move close to or move away from the resonance electrons in the time of motion cycle ($T_f = 2\pi$) - by the moments of the interaction with the surface ($x=0$). This is to define stability of the resonance phase. The discharge develops when

$$\left| 1 + \left(\frac{dT}{d\varphi} \right)_{\varphi=\varphi_r} \right| < \sigma, \quad (5)$$

i.e. when resonance phase is stable or unstable in such limits, in which the electron flight away is compensated with excess by their reproduction at the moments of interaction with surface.

Estimations and countings show, that the discharge with the multipactλxon periods, equal to the one period of HF-oscillations $T=2\pi$, have the largest starting zones by the magnetic field and also the highest velocities of the build-up. That is why we limit only by its analysis.

3. SOME RESULTS AND THEIR ANALYSIS

The common picture of the motion can be presented without direct counting of the resonance and close to them motion $x(T)$ with the numerical algorithms, if v, ε, α are given. The situation does not to be clear, mainly when, as (3,4), the $v^2 \text{tg}^2 \alpha$ - parameter has the value near to 1 (when the inclination of great field \mathbf{H}_0 is small, or when the slope of moderate \mathbf{H}_0 is moderate). When $v^2 \text{tg}^2 \alpha \gg 1$, the motion is similar to the one in the parallel fields $\mathbf{E} \parallel \mathbf{H}$, in the opposite case (when $v^2 \text{tg}^2 \alpha \ll 1$) the motion is as in crossed fields $\mathbf{E} \perp \mathbf{H}$ [1,2]. We should like to demonstrate some common regularity, including the ability of step-by-step "penetration" of the discharge with the rising of the inclination angle α of \mathbf{H}_0 -field into the area of large v (it has a great importance in the work of powerful relativistic HF-devices). We will present the analyze of the possibility of the idealizing the motion by the single-dimension motion along the \mathbf{H}_0 -direction with the suitable characteristics. It is obviously, that with the increase of \mathbf{H}_0 such idealization becomes true with angles α becoming smaller and smaller. But, we must note, that the single-dimension idealization can distort the accuracy of the image of the angle of bombing of the surface: when $\alpha=0$ the bombing, as (2-4), takes place in normal direction, but when $\alpha \neq 0$, $H_0 \Rightarrow \infty$ the bombing takes place by angle α . In the real situations the appearance of y,z-component of bombing velocity can enlarge the range of HF-fields E_1 , in which the effective reproduction of the electrons by their interaction with the surface, can take place.

For the lower possible boundary of the discharge zone $\epsilon_{\min}(\nu)$ as a result of the necessary condition on the initial acceleration ($\epsilon + \cos\varphi > 0$) from (3,4) it follows

$$\epsilon_{\min}(\nu) = -\cos\varphi_m; \quad \text{tg}\varphi_m = -\frac{2\pi \text{tg}^2\alpha + \frac{1 - \cos 2\pi\nu}{\nu^2(1 - \nu^2)}}{2\pi \text{tg}^2\alpha + \frac{\sin 2\pi\nu}{\nu(1 - \nu^2)}} \quad (6)$$

Also, from (6) one can see the importance of the $\nu^2 \text{tg}^2\alpha$ -parameters. The position of the discharge zones is shown on the Fig.2.

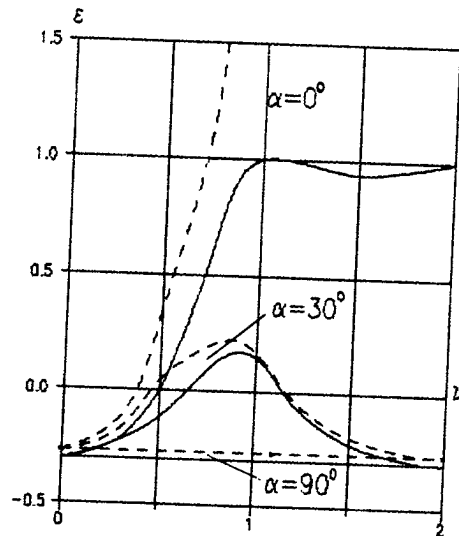


Fig.2. Position of the SERD zones. Solid lines - $\epsilon_{\min}(\nu)$, dashed lines - $\epsilon_{\max}(\nu)$.

Here $\epsilon_{\max}(\nu)$ is the boundary of the resonance phase stability, which has been marked above. The area of the admissible acceleration fields decreases gradually and then eliminates with the rising of the inclination angle α . With the rising of ν , the boundary $\epsilon_{\min}(\nu)$ quickly becomes closer to the value -0,303, which is characteristic of the discharge in $\mathbf{E} \parallel \mathbf{H}$ -fields. With α rising, the discharge "comes through" the cyclotron resonance to the area of $\nu > 1$, with values of electrostatic field getting smaller and smaller (smaller ϵ). The direct analysis of the cyclotron resonance motion ($\nu=1$)

$$x/a = \cos^2\alpha \left\{ \epsilon(1 - \cos T) + \frac{T \sin(T + \varphi) - \sin\varphi \sin T}{2} \right\} + f_1 \sin^2\alpha \quad (7)$$

near of the resonance phase φ_r

$$\sin\varphi_r = \frac{\pi\epsilon}{1 - (1/2)\text{ctg}^2\alpha}; \quad \left| 1 + \frac{dT}{d\varphi_{\varphi=\varphi_r}} \right| = \frac{\epsilon + \cos\varphi_r}{1 + (1/2)\text{ctg}^2\alpha \cos\varphi_r} \quad (8)$$

make it possible to find with the method, mentioned above, the boundaries of the discharge zones of ϵ ; look at Table:

α (degrees)	0	15	30	60	90
ϵ_{\max}	∞	1.71	0.16	-0.24	-0.27
ϵ_{\min}	1	0.88	0.15	-0.26	-0.30

It is seen, that in this concrete, but very important to the hydro-resonance systems, case, the discharge zone moves along ε extremely: starting from the large electrostatic fields $\varepsilon > 1$ (when $\alpha = 0$) up to the essentially braking fields $\varepsilon < 0$ (when $\alpha \Rightarrow \pi/2$). In the absence of the electrostatic fields, discharge can develop near the surface parts, where $\alpha \approx 35$ degrees.

When ν is large, the discharge characteristics should not much changed, therefore the most simple counting for the whole value ν can be of interest. In this case, the resonance conditions are independent of the inclination angle α and equal to the case $\mathbf{E} \parallel \mathbf{H}$ -fields: $\sin \varphi_r = \varepsilon \pi$, besides the boundaries $\varepsilon_{\min} = -\cos \varphi_r$, $\varepsilon_{\max} = -0,5 \cos \varphi_r$. Dependencies $f_{\parallel}(T)$, $f_{\perp}(T)$ are about to be stable whatever ε in the SERD-zone, therefore they are shown on the Fig.3 for the case of ε_{\min} .

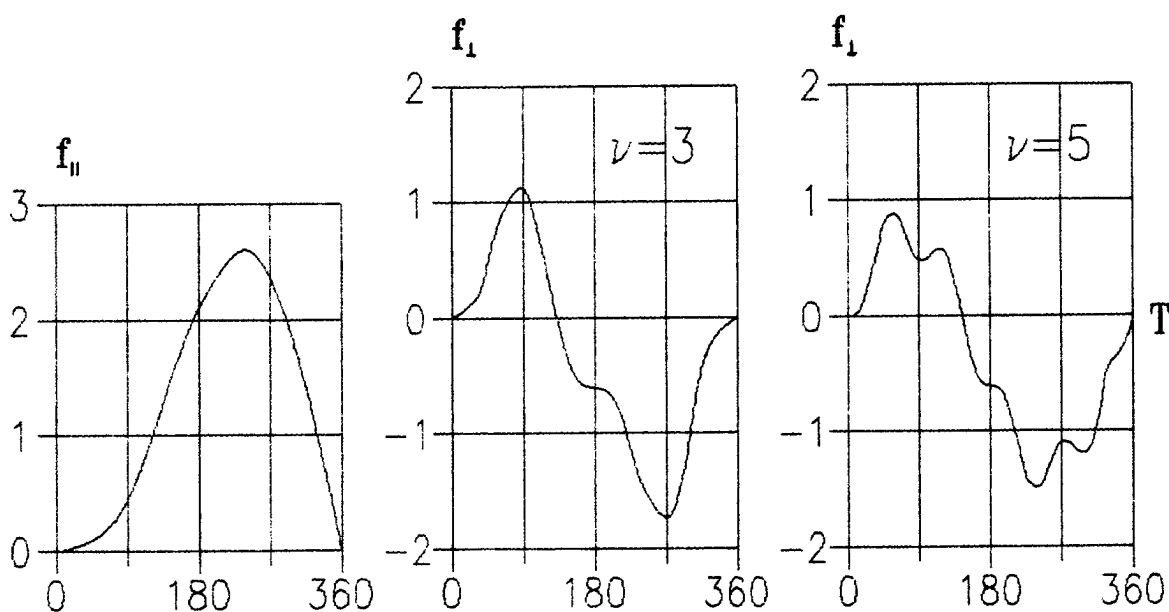


Fig. 3. The resonance motion components for the whole values ν .

It can be seen, that $f_{\perp}(T)$ -part of the motion consists of the considerable one-period forced oscillation and the "fast" free oscillations (in the \mathbf{H}_0 -field), diminishing with the ν rising. It can be seen, by comparing this curves, taking (4) into account, that condition $\nu \tan \alpha \sim 1$ separates the situations, where the resonance electron groups can exist or can not: there is $x(T) > 0$ everywhere in the motion cycle or there is not. That is why the condition (6) is sufficient, but not necessary, and the precision boundaries of the zones $\varepsilon(\nu)$ in the region $\nu > 1$ must be found from some special calculations.

So, the magnetic fields inclination to the surface helps the SERD penetration into the large \mathbf{H}_0 -fields area and even with small inclinations of the surface to the "insulating" \mathbf{H}_0 -field in real devices, e.g., with corrugated waveguides, when ν is often near 5-10, are created a suitable conditions for the build-up of the one-sided SERD, which can be counted in single-dimension approximation in the cases of $\nu^2 \tan^2 \alpha \gg 1$. In the more complicated situations ($\nu^2 \tan^2 \alpha \sim 1$) the analyses with concrete counting are necessary.

In conclusion we must be note, that the SERD can have the starting electric fields about tens of kV/cm and more [1], the build-up times about tens of nanoseconds and the powers, confiscated of HF-fields and given by the electron bombing to the metal wall (discharge surface), about tens and hundreds kW/cm².

4. REFERENCES

1. L.G.Blyachman and V.E.Nechaev, "Starting conditions of vacuum resonance HF-discharge in magnetostatic field", *ZH.T.R.H.*, Vol. 50, No 4, pp.720-727.
2. L.G.Blyachman and V.E.Nechaev, "Near-wall secondary emission HF-discharge in insulating magnetostatic field", *ZH.T.P.H.*, Vol 54, No 11, pp.2163-2168

Relativistic pulse-periodic mm-wavelength cyclotron masers with hot cathodes

V.L.Bratman, I.E.Botvinnik, Yu.V.Grom, Yu.K.Kalynov, M.M.Ofitserov

Institute of Applied Physics, Russian Academy of Science

46 Ulyanov Str., Nizhny Novgorod, 603600, Russia

ABSTRACT

The specialized high-voltage installation for the investigation of cyclotron autoresonance masers (CARMs) as possible prototypes of HF source for fusion has been put in operation. The main parameters of the system are as follows: the maximal voltage 300 kV, the electron-beam current up to 300 A, the pulse duration 10 μ s, the pulse-repetition frequency up to 2 Hz. Experiments with the electron-optic system on the basis of the magnetron-injector gun (MIG) being traditional for subrelativistic gyrotrons, are carried out. As an initial stage of the experiments, the relativistic gyrotron with the wavelength 4.4 mm and the operating mode $TE_{4,3}$ is studied.

1. MOTIVATION

For cyclotron resonance masers (CRMs) the transition from subrelativistic electron energies to relativistic ones permits us, in principle, to enlarge not only radiation power but radiation frequency as well. Besides, it opens the ways to broadband frequency tuning. One has to pay attention that in the case of the fixed magnetic field strength the radiation frequency of gyrotrons decreases with the electron energy increase because of the relativistic dependence of the electron cyclotron frequency on the energy. Another type of CRM - cyclotron autoresonance maser (see, for example, the review¹) where, like in the free-electron laser (FEL), the Doppler up-conversion of the radiation frequency is used - is known to avoid this disadvantage. According to the theory, CARM represents a rather perspective device at the range of mm and sbmm wavelengths, where it needs significantly smaller magnetic fields, than in gyrotron, and significantly smaller electron energies, than in free-electron lasers. However, an Achilles heel of CARM, like FELs, is the electron-beam quality. Up to now in CARMs, with only exception², electron-optic systems, based on explosive-emission cathodes, have been used. As a rule, such systems form electron beams with a rather large spread in parameters. Correspondingly, CARM efficiency was several times smaller than it had been calculated for ideal electron beams, and not larger than 10 %. So, at IAP RAS simultaneously with attempts of creation of explosive-emission electron-optic systems with a small spread in particle parameters, the work for creation of CARM on the basis of conventional thermoemitters is being carried out. The goal of this work is design of high-efficiency short-mm-wavelength CARM with relatively long pulse duration, that could be a competitionable prototype of HF source, needed for tokamaks of the next generation.

2. INSTALLATION

The installation consists of the pulse-modulator power supply, the accelerating section, the source of strong magnetic field, electron-optic and microwave systems (Figs.1 and 2). The pulse modulator represents the drive generator (1) and the pulse line (2), connected with the load by a transformer. The accelerating tube (4) is formed by ceramic insulator rings. The voltage distribution is provided by resistors. In order to operate at repetitive regime, the cryomagnet (5) is used to provide a strong magnetic field with the strength up to 70 kOe. The diameter of the cryomagnet hot bore is 150 mm, the length of homogeneous magnetic field is about 20 mm (for CARM experiments another cryomagnet with the length of homogeneous field 400 mm has been designed, manufactured and tested).

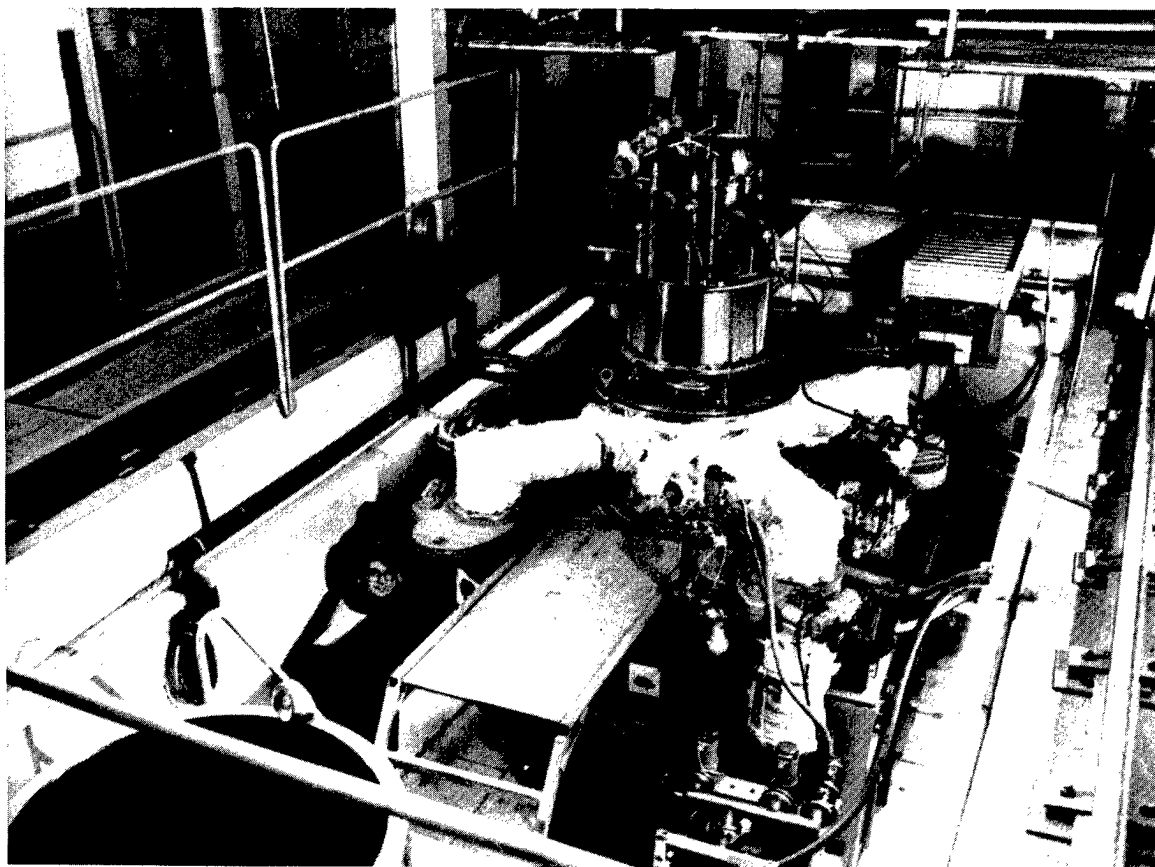


Fig. 1. The high-voltage installation.

3. RELATIVISTIC GYROTRON WITH WAVELENGTH 4.4 MM

(TEST EXPERIMENT)

As an initial step, a simple HF source, namely, relativistic gyrotron with the electron energy 200 keV is realized. The tubular electron beam is formed by the MIG (6). The gun anode is isolated from the cavity, its voltage is applied through the resistive divider, placed on the accelerating tube. At the anode voltage 85 kV and the ratio of magnetic fields in the cavity and close to the emitter 60, the calculated pitch angle of particles in the interaction space is close to 45° . The beam radius in the cavity corresponds to the first maximum of the connection impedance for the operating mode. After the cavity electrons move to the copper cylindrical collector with the diameter 70 mm.

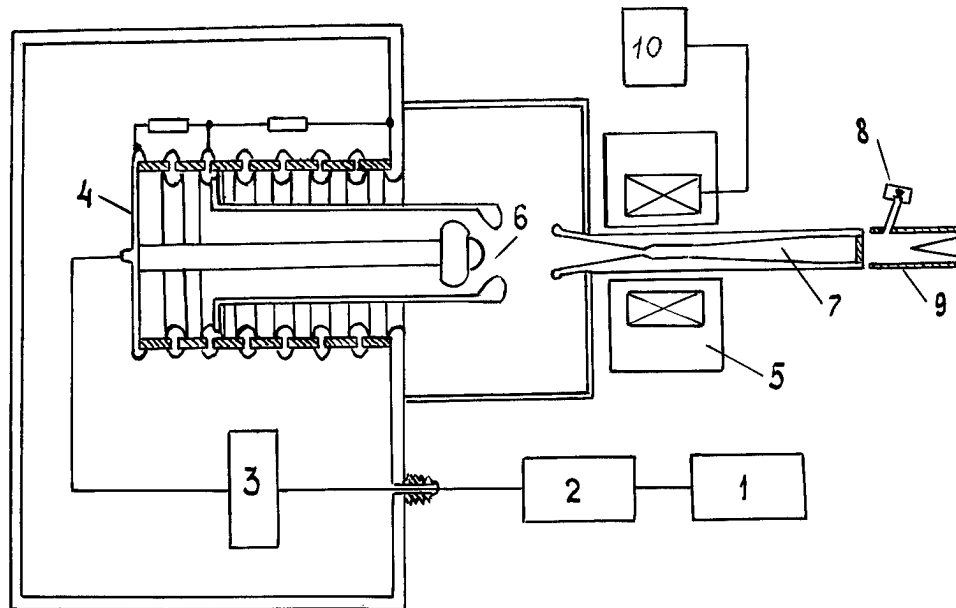


Fig.2. The scheme of the high-voltage installation.

The microwave system of the relativistic gyrotron has been chosen in the form being traditional for subrelativistic gyrotrons: the axisymmetric cavity with a diffraction radiation output (7). The operating mode is transverse-electric $TE_{4,3}$. The radiation energy is withdrawn by this mode through the half-wavelength quartz window.

The HF radiation is observed by means of hot electron detector (8), the output radiation power is measured calorimetrically (9). In the experiment at the electron energy 200 keV, the radiation power more than 2MW with the pulse duration 10 μ s (Fig.3) and the efficiency more than 25% is obtained. The typical repetition rate is equal to 1 Hz. The magnetic field tuning band of generation is about 5%, that coincides with calculations.

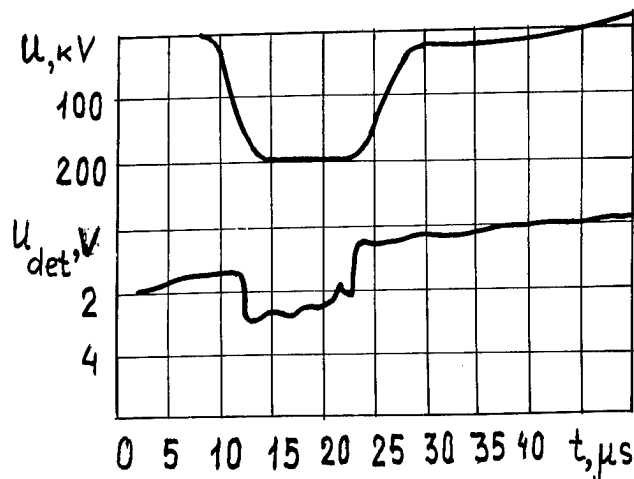


Fig.3. Pulses of voltage at the accelerating tube
and of the detected HF signal.

4. ACKNOWLEDGMENTS

Authors are grateful to Russian Foundation of Fundamental Investigations (Project No.93-02-842) for financial support

5. REFERENCES

1. V.L.Bratman and G.G.Denisov, "Cyclotron autoresonance masers - recent experiments and prospects," - Int.J.Electronics, Vol.72, pp.969-981, May-June 1992.
2. S.Alberti, B.G.Danly, G.Gulotta, E.Giguet, T.Kimura, W.L.Menninger, J.L.Rullier, and R.J.Temkin, "Experimental study of a 28 GHz high-power long-pulse cyclotron autoresonance maser oscillator," Phys.Rev.Letts., Vol.71, pp.2018-2021, Sept. 1993.

Interaction of REB with electromagnetic field in overmoded slow-wave structures near the high-frequency boundary of the transmission band

I.A. Chernyavsky, M.P. Deichuly, V.I. Koshelev

High Current Electronics Institute, Siberian Division of Russian Academy of Sciences, Tomsk 634055, Russia

and V.M. Pikunov

Moscow State University, Physics Department, Moscow 119899, Russia

ABSTRACT

The relativistic electron beam (REB) — electromagnetic field interaction near the high-frequency boundary of the TM_{01} -mode transmission band in overmoded uniform and sectioned structures with different slowing-down value has been studied experimentally and theoretically by means of the linear theory. The detailed comparison of the numerical simulation and the experimental data has been carried out for the three regimes: TWT-, TWT-BWO-, BWO-ones.

1. INTRODUCTION

In multiwave Cerenkov generators (MWCGs)^{1,2} with $D/\lambda \gg 1$ (D is the structure diameter, λ is the radiation wavelength), the beam interaction with the TM_{01} -mode field near the π -mode oscillations is used to select frequency. More detailed experimental investigation of the beam — field interaction in a wide range of electron energies at a successive regime transition from BWO- to TWT-BWO- (π -mode oscillations) and TWT-types seemed to be necessary for a better understanding of the processes in MWCG, choosing the ways for increasing the generation efficiency and the stability of the radiation parameters. It was necessary to carry out investigations of this kind for single- and multisectional (with equal periods) structures with different slowing-down of the TM_{01} -mode wave for a comparative analysis of the processes.

Hierarchy of physical and mathematical models — linear, nonlinear, nonstationary ones and so on — is necessary for theoretical studies. In the given work, the linear stationary theory³ allowing one to calculate the starting current, the radiation spectrum, and the transverse and longitudinal field structures was used for numerical simulation of experimentally studied Cerenkov microwave devices.

2. EXPERIMENTAL SETUP AND MEASURING TECHNIQUE

Experiments were carried out on the "Sinus-7M" accelerator. Hollow electron beams with diameter $D_b = 10$ to 11.6 cm, thickness of 2 to 3 mm and current $I_b = 1.5$ to 13 kA were formed in a coaxial diode with magnetic insulation at the diode voltage $U_d = 300$ to 1100 kV and pulse duration $\tau_p = 40$ ns. The magnetic field in the beam transport region varied from 5 to 15 kG. To indicate microwave radiation and measure its characteristics, germanium and lamp detectors were used. The radiation spectrum was measured by band filters with the bandwidth 0.5%. The radiation power was determined by the directivity diagrams in two (θ - and φ -) polarizations measured in the atmosphere. Radiation losses in the antenna were not monitored.

Slow-wave structures using periodic waveguides of two dimension types were investigated. The first and second waveguide diameters were $D = 13$ and 13.1 cm and their periods were $l = 1.4$ and 1.3 cm, respectively. Periodic waveguide geometric parameters were chosen from the condition that the π -mode oscillation wavelength was equal to that of the TM_{01} -mode ($\lambda_\pi = 3.25$ and 3.22 cm for the first and second waveguides, respectively). The wave slowing-down factor V_{ph}/c (V_{ph} is the wave phase velocity, c is the velocity of light) near the π -mode oscillations of the TM_{01} -mode was equal to 0.864 and 0.808, respectively. The construction allowed smooth controlling the section lengths L and drift tube length L_{dr} between them.

3. EXPERIMENTAL RESULTS

Experimental investigation of slow-wave structures with $l = 1.4$ and 1.3 cm was carried out at $U_d = 600$ to 1100 kV and 300 to 900 kV, respectively. The region where the dispersion characteristic of the TM_{01} -mode intersects the

space charge slow wave (SCSW) line occupies the BWO- ("1"-space harmonic) and TWT- ("0"-space harmonic) branches with tuning out from λ_π on both branches by 1% and 1–3% for the structures with $l = 1.4$ and 1.3 cm, respectively. Preliminary investigation results for the structures with $l = 1.4$ cm are given in Ref. 4. We shall consider the experimental results for one- and then two- and more sectioned slow-wave structures. The generator starting length is $L_{st} = (13 - 14)l$ and it depends on the beam parameters. The directivity diagrams show that the radiation with θ - and φ -polarizations is present. The radiation diagram with θ -polarization is close in form to the TM_{01} -mode diagram. Usually, the power ratio for the two polarizations is $P_\varphi = (0.3 \text{ to } 0.5)P_\theta$. The radiation spectra for the two polarizations coincide. The subsequent discussion of experimental and theoretical results is related to the radiation with θ -polarization only, if not mentioned specially.

In the radiation spectrum, one to three maxima are observed. Next to the main narrowband ($<1\%$) spectrum, additional lateral maxima (satellites) are indicated. The spectrum form depends on the structure length. The wavelength of the main maximum in the spectrum decreases as the voltage is increased for both structures. The frequency tuning out ω of these maxima from the SCSW and TM_{01} -mode synchronism at fixed U_d depends on the structure length as $1/L$. This dependence is more exact for the ratio $(V_{SCSW} - V_{ph})/V_{SCSW} \approx l/L$, where $V_{ph} = \omega/k_z$ is the wave phase velocity determined by the dispersion characteristic of the TM_{01} -mode without a beam. A stepwise violation of this dependence occurs at $U_d > U_d^{opt}$, where U_d^{opt} is the diode voltage at which the generation efficiency reaches a maximum. Note that for $U_d > U_d^{opt}$ the directivity diagram undergoes a change consisting in the fact that the narrowing of the diagram, characteristic of the TM_{01} -mode, as well as the appearance of an additional maximum with a large angle occur. For the structure with $l = 1.3$ cm at $U_d > 600$ kV, a stepwise transition to a longer radiation wavelength with an increase in diode voltage takes place. Two spectrum groups may be distinguished. The first spectrum group is characterized by the fact that it develops in time after the radiation appearance on the shorter wavelength and is due to nonlinear processes in the beam. The second spectrum group corresponds to the usual development of the radiation generation process.

The region of U_d where the generation efficiency increases by a factor of 1.5 and 2 at $l = 1.3$ and 1.4 cm, respectively, is of greatest interest. When the slow-wave structure length decreases from the optimal $L_{opt} = 24l$ ($l = 1.4$ cm) to the essentially starting one $L = 14l$ ($L_{st} = 13l$), U_d^{opt} increases from 750 to 1050 kV. The resonance region becomes less pronounced, the maximum efficiency decreases from 7% to 3% and the SCSW and TM_{01} synchronism point for U_d^{opt} moves aside from the π -mode along the TWT-branch. Note that at $L = L_{opt}$, the total power ($P_\theta + P_\varphi$) reached 500 to 800 MW with the 10%-efficiency in the radiation extracted into the atmosphere. For a structure with a larger slowing-down ($l = 1.3$ cm), the resonance region width is narrower and an increase in efficiency is smaller. The SCSW and TM_{01} synchronism point for U_d^{opt} does not move to the TM_{01} -mode TWT-region.

The microwave radiation pulse duration is limited by the beam pulse duration. The pulse form depends on the tuning out on the main spectral maximum frequency from the synchronism frequency of the SCSW with the TM_{01} -mode. In case $U_d \approx U_d^{opt}$, the trapezoid pulse form turns into a triangular or bell-like form cut by peaks of low amplitude and time scale.

In this part we shall consider the investigation results for MWCG with a two-sectional slow-wave structure. The first section length was usually $L_1 < L_{st}$. It was studied how the lengths of the second section, the drift tube, the beam radius, the magnetic field might be varied to optimize the generation. The influence of these parameters as well as of the diode voltage on the radiation spectrum and directivity diagram form was studied. The main results are as follows. Similar to one-sectional structures, the two-sectional radiation spectra have satellites, the θ - and φ -polarization spectra coincide, and the radiation wavelength decreases as the voltage is increased. The power ratio is also $P_\varphi = (0.3 \text{ to } 0.5)P_\theta$. The optimal magnetic field is $B = 8$ to 10 kG. The generation efficiency has no marked maximum in U_d , it grows with increasing U_d and decreasing the wave slowing-down. The maximum generation efficiency according to the total radiation ($P_\theta + P_\varphi$) into the atmosphere reached 20% and 10% at $l = 1.4$ and 1.3 cm, respectively. The maximum power reached 2 GW at a radiation pulse duration of 35 ns. The existence of U_d^{cr} the exceeding of which results in sharp increase in generation instability ($>30\%$), the appearance of spectral lines with $\lambda < \lambda_\pi$ of the TM_{01} -mode and the disappearance of the generation with $\lambda > \lambda_\pi$, are general. The values of U_d^{cr} are approximately equal to 550 to 600 kV and 1100 kV at $l = 1.3$ and 1.4 cm, respectively, and are somewhat higher than U_d at which the SCSW and TM_{01} -mode synchronism point makes the transition from the "1" to the "0" space harmonic.

The second section optimal length is $L_2 \leq L_{st}$ ($l = 1.4$ cm). When L_2 is increased, the power grows not smoothly but with a step at $L_2 \simeq 10l$. The directivity diagram also changes sharply (the main diagram lobe angle decreases from 14° to 8°). At $L_2 \geq 16l$, the main diagram lobe angle decreases to 2° and the P_ϕ share increases. At $U_d \approx U_d^{cr}$, the diagram takes the Gaussian form (the power maximum in the center), the stability drops, and the spectral line shifts to the non-transmission band of the TM_{01} -mode. In case $l = 1.3$ cm, the generation instability becomes more apparent, the P_ϕ share is larger and the power dependence on L_2 has no marked optimum. It follows from the experiments that the optimal beam radius is less at $l = 1.4$ cm than at $l = 1.3$ cm.

The radiation parameter dependencies on the drift tube length have two scales ($\gg l$ and $\sim l/2$). The large-scale L_{dr} changes determine the radiation power, $L_{dr}^{opt} = (5 \text{ to } 8)l$. Low-scale L_{dr} changes essentially affect the directivity diagram form, the radiation spectrum, the power, and the generation stability.

As mentioned above, the U_d and L_2 increase in the structures with $l = 1.3$ cm rapidly increases the generation instability. When the section lengths were decreased, the generation efficiency dropped. To eliminate the contradictory requirement to increase beam — field interaction length with decreasing the structure Q , an experiment with the structure consisting of five short equal sections with $L = 5l$ connected by drift tubes of equal length was performed. At $U_d > U_d^{cr}$, stable generation with a 12%-efficiency on the 3.42-cm-wavelength was obtained. In a two-sectional device $\lambda = 3.25$ to 3.3 cm.

4. NUMERICAL SIMULATION RESULTS AND COMPARISON WITH EXPERIMENTAL DATA

To begin with, we consider numerical simulation results for one-sectional devices. By solving a boundary-value problem, several first longitudinal resonances of the TM_{01} -mode were determined. The resonance ordinal number is counted out from the π -mode oscillations. The starting currents I_{st} were determined from the condition of a strong power amplification (40 to 75 dB) at a small change of the beam current. The starting currents strongly depend on the beam diameter and increase with the resonance number. When the electron energy was changed, the presence of starting current minima was found. Measurements of the first longitudinal resonance starting current carried out agree well with the value calculated. At optimal parameters ($U_d^{opt} = 900$ kV, $L = 18l$, $l = 1.4$ cm) the ratio $I_b/I_{st} \approx 3$. For a structure with larger slowing-down ($l = 1.3$ cm) near U_d^{opt} , the ratio $I_b/I_{st} \approx 15$ for the first resonance.

Theoretical dependencies of the generation wavelength on voltage agree with the experimental ones. For a structure with $L = 18l$ ($l = 1.4$ cm), the wavelengths correspond to the first longitudinal resonance excitation (the second resonance starting currents are $I_{st} \geq I_b$). For a structure with $L = 18l$ ($l = 1.3$ cm) at a low diode voltage ($U_d \leq 550$ kV) the first longitudinal resonance becomes excited. With the U_d growth, the second and third longitudinal resonances become excited subsequently. An analysis of experimental data also shows the appearance of spectral line between first and second and then between the second and the third resonances due to nonlinear processes in the beam. It should be noted that the radiation wavelength tuning out from the longitudinal resonance of the structure without a beam decreases with the diode voltage growth. It follows from the calculations that the consecutive transition of regimes from BWO to TWT-BWO and TWT results in changes in electromagnetic field longitudinal distributions, toward and backward power flows, and the alternating component of the beam kinetic power.

In this part, we consider MWCG numerical simulation results. Structures with $l = 1.4$ cm were studied only. The superposition of the resonances appeared in the sections of the periodic and smooth waveguides results in the appearance of complex longitudinal resonances in the generator. The drift tube length, second section, diode voltage, beam radius effects on the spectrum and the starting current of the first three (counted from the π -mode) longitudinal resonances were investigated.

To begin with, we consider the drift tube influence on the processes in MWCG. It follows from the calculations that the resonances appearing in the drift tube increase the shift to the low frequency region and substitute each other. The resonance location near the π -mode repeats with the period of 1.6 cm that shows good agreement with a half-wavelength of the smooth waveguide TM_{01} -mode $\lambda_w/2$ on generation frequencies. This indicates that the connection between sections is effectively realized by the TM_{01} -mode. When L_{dr} is increased by $\lambda_w/2$, an additional phase increase in the standing wave period is realized in the drift tube. All the resonances shift on the wavelength

by one number and a new resonance corresponding to the first one appears. The sectional structure peculiarity is the appearance of resonances in the non-transmission band of the TM_{01} -mode. The resonance starting currents also change with $\lambda_w/2$ period and depend on the resonance number. Two types of the drift tube differing in essence in the field structure and, respectively, the periodic waveguide section matching can be noted. For the matched and mismatched structures, the drift tubes differ in length by $\lambda_w/4$.

Complete comparative analysis of calculation and experimental results is difficult, since even at obvious excitation of TM_{01} -mode in the experiment, side by side with θ -polarization, a radiation with φ -polarization is present in the diagram. The latter is evidently due to the presence of the beam disadjustment and incomplete synchronization of the beam — field interaction region. The presence in the experiment of the generation spectral lines in the TM_{01} -mode non-transmission band is difficult to associate with the calculation results, since at $\lambda < \lambda_\pi$ share of P_φ increases, which may pointed to nonsymmetrical mode excitation. The latter were not studied either experimentally or theoretically. It follows from the experiment that the transition from the drift tube $L_{dr} = 6l \approx 2.65\lambda_w$ to the one $L_{dr} = 5.5l \approx 2.4\lambda_w$ results in an increase in the wavelength of the main spectral maximum from 3.27 to 3.32 cm. According to the calculations, this corresponds to the transition from the first to the second resonance. This transition is due to the I_{st} increase for the first resonance and I_{st} decrease for the second one. The radiation parameter stability should be noted to increase during the transition to $L_{dr} \approx 2.4\lambda_w$.

All subsequent calculations were performed for MWCG with $L_{dr} \approx 2.65\lambda_w$. It follows from a comparison of numerical and experimental data that the wavelengths of the main spectral maxima correspond to the first resonance excitation. The radiation wavelength generation dependence on U_d in MWCG is realized by the BWO-type, by analogy with a one-sectional structure. It follows from the calculations that in the investigated range of electron beam parameters and slow-wave structure geometry, simultaneous excitation of the first two resonances is possible. In the experiment, excitation of the first resonance only as well as of both the first and the second ones is realized. In the latter case, the power is maximum. Comparison of experimental and theoretical results shows that in the optimal regime $I_b/I_{st} \approx 3$, which agree with a one-sectional structure ($l = 1.4$ cm). According to the calculations and experiments (for the main spectral maximum), the MWCG radiation wavelength weakly depends on the beam radius and the second section length.

5. CONCLUSIONS

The generation efficiency increase in MWCG with a two-sectional slow-wave structure is due to the use of high electron energy beams (> 1 MeV) and the decrease in slowing-down. More complex multisectional structures are necessary to increase the generation efficiency at ≤ 1 MeV-electron energies. This requires that the formation of bunches be optimal, and the accumulated and taken out electromagnetic fields be matched. In this case, promising are the regimes of beam — field interaction tuned out of the TM_{01} -mode π -type.

6. REFERENCES

1. S.P. Bugaev, V.I. Kanavets, V.I. Koshelev, and V.A. Cherepenin, *Relativistic Multiwave Microwave Generators*, Nauka, Novosibirsk, 1991.
2. S.P. Bugaev, V.A. Cherepenin, V.I. Kanavets, A.I. Klimov, A.D. Kopenkin, V.I. Koshelev, V.A. Popov, and A.I. Slepko, "Relativistic multiwave Cerenkov generators", *IEEE Trans. Plasma Science*, Vol. 18, pp. 525-536, 1990.
3. V.M. Pikunov and I.A. Chernyavsky, "Linear theory of the relativistic superdimensional Cherenkov devices", *SPIE Proc. Series*, Vol. 1872, pp. 358-367, 1993.
4. A.N. Batrikov, S.P. Bugaev, I.A. Chernyavsky, M.P. Deichuly, P.A. Khryapov, V.I. Koshelev, V.V. Lopatin, N.S. Sochugov, K.N. Sukhushin, A.N. Zakharov, V.I. Kanavets, V.M. Pikunov, and A.I. Slepko, "The state of art of investigations of relativistic multiwave microwave generators", *Proc. IX Intern. Conf. on High-Power Particle Beams*, Vol. 3, pp. 1586-1591, 1992.

Superradiance of ensembles classical electron-oscillators as
a method for generation of ultrashort electromagnetic pulses

N.S.Ginzburg, Yu.V.Novozhilova,A.S. Sergeev

Institute of Applied Physics, Russian Academy of Science,
46 Uljanov Str., 603600 N.Novgorod, Russia

ABSTRACT

We considered the superradiance of ensembles of electrons rotating in the uniform magnetic field. It is demonstrated that such processes may be used for generation of powerful ultrashort microwave pulses.

The effects of the superradiance of ensembles of inverted atoms in quantum electronics have long been an object of theoretical and experimental investigations. Recently, interest was aroused in such phenomena in ensembles of classical oscillators¹⁻⁵. A classical analogue of the superradiance effect is radiative instability in space-localized ensembles of electron-oscillators having infinite lifetime. As a consequence of the development of nonthreshold superradiance instabilities, the energy of oscillatory motion is emitted in the form of a short electromagnetic pulse with the duration of about several periods of HF oscillations. Powerful ultrashort microwave pulses are interesting for radiotechnical applications, as well as for investigations of nonlinear phenomena in plasmas and solid matter. Superradiative instabilities may develop when an intense e.m. pump wave or undulator field affects on the moving electron cluster³⁻⁵. Here we analyze superradiance in a layer of electrons rotating in a uniform magnetic field $\vec{H} = z_0 H_0$.

Let the electrons have equal transverse momenta $p_{\perp 0} = m\gamma v_{\perp 0}$ and be (to an accuracy of small fluctuations) distributed uniformly over the cyclotron rotation phases at the initial moment of time. The unperturbed static electron charge is compensated by the ion background. The particles' motion will be described by the following equations

$$\begin{aligned} \frac{dp_+}{dt} &= i\omega_H p_+ - eE_+ - ie\beta_z H_+, \\ \frac{dp_z}{dt} &= \frac{e}{mc\gamma} \text{Im}(p_+ H_+^*) + F_{\text{coul}}, \quad \frac{dz}{dt} = \frac{p_z}{m\gamma} \end{aligned} \quad (1)$$

where $p_+ = p_x + ip_y$, $H_+ = H_x + iH_y$, $E_+ = E_x + iE_y$ is electric field, $\omega_H = eH_0/mc\gamma$ is the relativistic gyrofrequency, $\gamma = (1 + |p_+|^2/(mc)^2)^{1/2}$ is the relativistic mass-factor, F_{coul} is the Coulomb force. The layer considered will radiate circularly polarized waves in the $\pm z$ -directions.

$$E_+ = -\frac{2\pi}{c} \int_{z-ct}^{z+ct} j_+(z', t - |z-z'|/c) dz' \quad (2)$$

where $j_+ = -ep\langle v_+ \rangle$ is the electron current density, ρ is the electron density, and $\langle v_+ \rangle$ is the average electron velocity in the given cross section. We will now assume that the electrons are subrelativistic ones, and radiate near the nonrelativistic gyrofrequency ω_{H0} . Representing

$$E_+ = A(z, t) e^{i\omega_{H0}t}, \quad H_+ = \frac{c}{\omega_{H0}} \frac{\partial A}{\partial z} e^{i\omega_{H0}t}, \quad p_+ = \hat{p}_+ e^{i\omega_{H0}t}$$

we reduce the set of equations (1)-(2) to the form

$$\begin{aligned} \frac{dp_{\perp}}{d\tau} &= -i\mu p_{\perp} |p_{\perp}|^2 - a, \quad \frac{d\hat{p}_z}{d\tau} = 2\mu \text{Re}(ip_{\perp} \frac{\partial a^*}{\partial Z}) + F_{\text{coul}}, \quad \frac{dZ}{d\tau} = \hat{p}_z, \\ a(Z, \tau) &= \frac{I}{2\pi} \int_0^{2\pi} \int_0^B p_{\perp} \exp(-i|Z-Z'|) dZ_0 d\vartheta_0 \end{aligned} \quad (3)$$

with the initial conditions $p_{\perp}|_{\tau=0} = \exp(i\vartheta_0 + i\text{rcos}\vartheta_0)$, $\vartheta_0 \in (0, 2\pi)$, $\hat{p}_z|_{\tau=0} = 0$.

The following dimensionless variables are used here: $\tau = \omega_{H0}t$, $Z = \omega_{H0}z/c$, $p_{\perp} = p_+/p_{\perp 0}$, $\hat{p}_z = p_z/mc$, $a = eA/m\omega_{H0}v_{\perp 0}$, $I = \omega_p^2/2\omega_{H0}^2$,

ω_p is the plasma frequency, $\mu = v_{\perp 0}^2/2c^2$, the parameter $r \ll 1$ characterizes the initial electron modulation over the cyclotron rotation phases, Z_0 is the initial electron coordinate, ϑ_0 is the initial rotation phase.

In the small signal approximation we obtain the characteristic equations from eqs.(3) to determine the frequencies $\Omega = \omega/\omega_{H0} + \mu - 1$ and spatial structure of eigenmodes:

$$\begin{aligned} \operatorname{tg}(\Gamma B/2) &= i/\Gamma \text{ for symmetric mode,} \\ \operatorname{ctg}(\Gamma B/2) &= -i/\Gamma \text{ for antisymmetric mode} \end{aligned} \quad (4)$$

Here $B = \omega_{H0}b/c$, b is layer width, and Γ is the normalized wave number inside the layer, which are given by the dispersion equation

$$\Gamma^2 - 1 = -2I(\mu(\Gamma^2 - 1)/\Omega^2 + 1/\Omega) \quad (5)$$

The behaviour of the gain $|\operatorname{Im}\Omega|$ as a function of the layer width B for symmetric and antisymmetric modes is shown in fig.1. With the growth of B the gain at first increases, then it decreases. In the case of wide layers, when $B \gg 1$, the gain tends to the value

$$|\operatorname{Im}\Omega| = \frac{\omega_p^2}{2\omega_{H0}^2} \sqrt{2\beta_{\perp 0}^2 \omega_{H0}^2 / \omega_p^2 - 1} \quad (6)$$

for $\omega_p^2/\omega_{H0}^2 < 2\beta_{\perp 0}^2$ and to zero for $\omega_p^2/\omega_{H0}^2 > 2\beta_{\perp 0}^2$. For the case of a thin layer, when $B \ll 1$, the gain is equal to

$$|\operatorname{Im}\Omega| = \frac{\omega_p \beta_{\perp 0}}{\omega_{H0} \sqrt{2}} \quad (7)$$

Spatial structures of eigenmodes are shown in Fig.2.

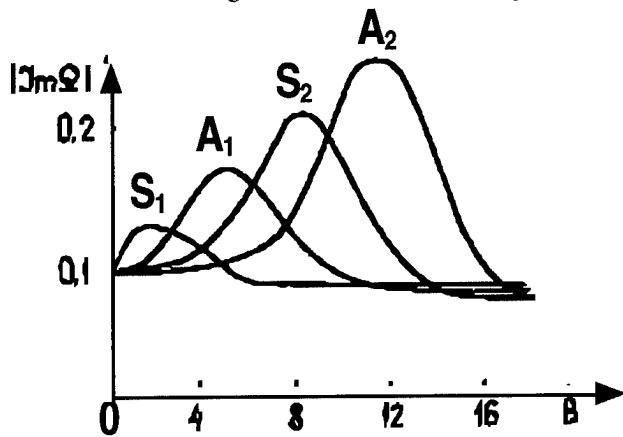


Fig. 1. Superradiative instability growth rate as a function of layer width for different eigenmodes.

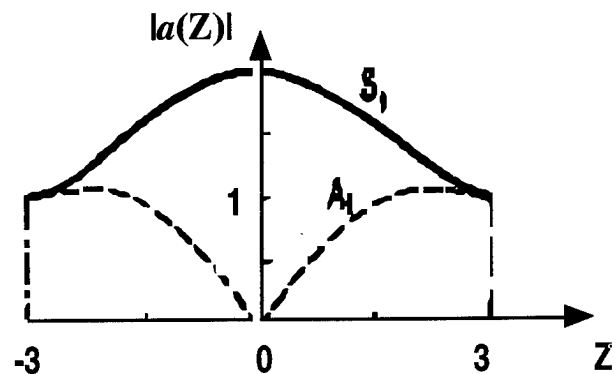


Fig. 2. Spatial profile for first symmetric (S_1) and first antisymmetric (A_1) modes.

The nonlinear stage of the cyclotron superradiance was investigated by numerical simulation of Eqs.(3). The time dependence of the radiation power $W = |a|^2|_{z=0}$ and the total electron efficiency

$$\eta = 1 - (1/B) \int_0^B \langle |p_{\perp}|^2 + p_z^2 / \beta_{\perp 0}^2 \rangle_{\infty} dZ'$$

are given in Fig.3. Figure 4 displays the formation of the spatial structure of the fundamental symmetric mode at the initial linear stage of radiation ($\tau < 60$), and the stochastization of this structure at the nonlinear stage ($\tau > 60$).

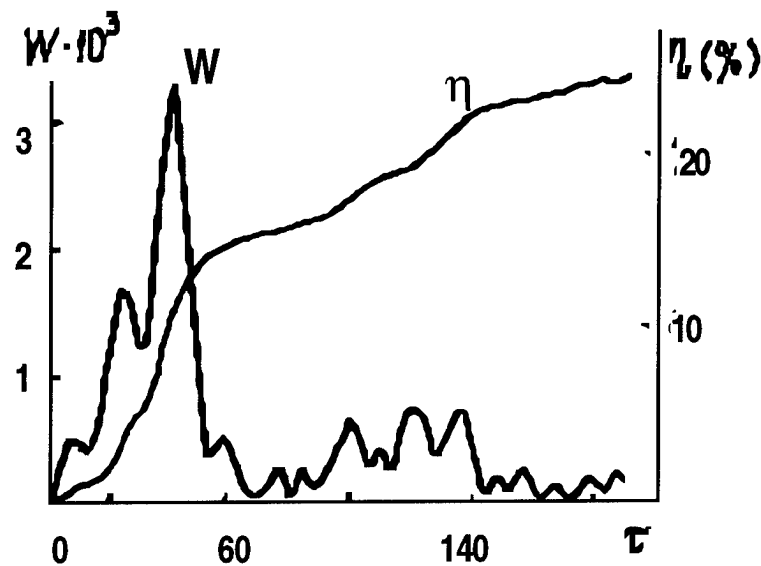


Fig. 3. Superradiance power and electron efficiency vs time: $I=0,1$; $\mu=0,1$; $B=6$.

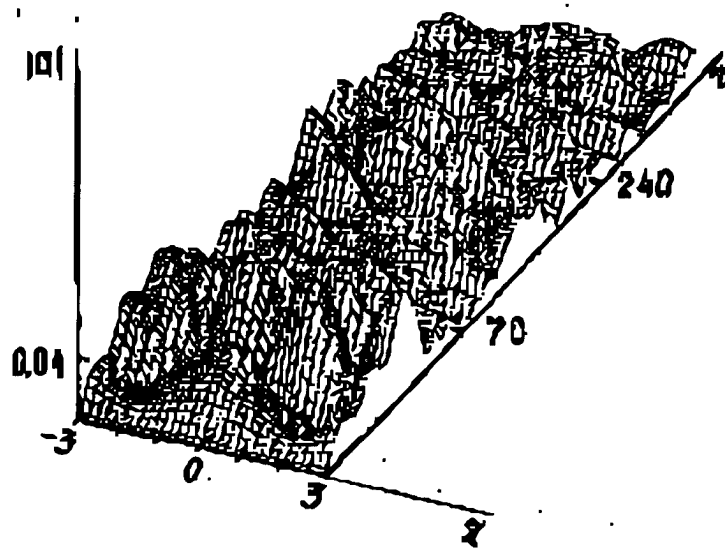


Fig. 4. Evolution of electric field profile inside of the electron layer: $I=0,1$; $\mu=0,1$; $B=6$.

Important to note that it is possible to increase the superradiance power essentially and to shift the frequency to the short-wave part of the spectrum by imparting to electrons translational velocity close to the light velocity. In a such case in accordance with Doppler effect, the relation between frequencies of waves propagating in $+z$ - and $-z$ -directions is following: $\omega^+/\omega^- = 4\gamma_0^2$. The electromagnetic energy flux densities in immovable points on both sides of the layer are differ significantly: $S^+/S^- = 16\gamma_0^4$. The duration of radiation pulse in $\pm z$ -directions from the layer for observer in laboratory reference frame is equal to

$$\Delta t^{\pm} = (1 \mp v_z/c) \gamma_0 \Delta t' \quad (8)$$

where $\Delta t'$ is the pulse duration in comoving frame.

Let us estimate the possibility to use the modulator with picosecond pulse duration⁶ for generation of short superradiative pulses. Let the electron density $n=10^{12} \text{ cm}^{-3}$, ($\omega_p=5,5 \cdot 10^{10} \text{ s}^{-1}$), electron pulse length 1.5 cm, and the electron energy 300 keV. We suppose that electrons pass through the region with inhomogeneous magnetic field where

electrons acquire transverse velocity $v_{\perp 0}=0.45c$. Then particles radiate in uniform magnetic field with strength $H_0=6.6\text{kOe}$. The radiation wavelength $\lambda=1.5\text{cm}$. These values of parameters correspond to $I = 0.1$, $\mu=0.1$ and $B = 6$. From fig.2 for the normalized radiation power we obtain $W_{\text{max}}=3\cdot 10^{-3}$. Therefore in dimensional variables the peak power per square unit 6 MW/cm^2 . The pulse duration of the superradiance is about 300 ps.

In the case of moving electron layer with particles' energy 2.5 MeV, $v_{\perp 0}=0.1c$, $v_{z0}=0.98c$, $n=0.2\cdot 10^{12}\text{cm}^{-3}$, with electron pulse length 0.28cm (in the comoving reference frame these parameters correspond to described above) for the short-wave component of radiation with wavelength 0.15 cm, power emitted per unit square will achieve 0.6 GW and the e.m. pulse duration will be about of 30 ps.

REFERENCES

1. V.V.Zheleznyakov, V.V.Kocharovsky, V.I.V.Kocharovsky, "Synchrotron superradiance as a classical analog for Dicke' superradiance", *Izv.vuzov, radiophysica*, Vol.29, N 9, pp.1095-1116, 1986.
2. N.S.Ginzburg, A.S.Sergeev, "Radiative instabilities in layers of excited oscillators", *Physica plasma*, Vol.17, N 11, pp.1318-132, 1991.
3. N.S.Ginzburg, A.S.Sergeev, "Superradiance of electron cluster, moving in periodic magnetic field", *Pis'ma v ZheTF*, Vol. 54, N 8, pp.445-448, 1991.
4. R.H.Bonifacio, W.M.Sharp, W.M.Fawley, "Simulation of superradiant free-electron laser", *Nucl.Instr.and Meth.Phys.Res.*, Vol. A285, pp. 217-223, 1989.
5. N.S.Ginzburg, Yu.N.Novozhilova, "Collective acceleration of electron cluster in plane electromagnetic wave, caused by the superradiative instability effect", *Pis'ma v ZhTF*, Vol. 15, N 19, pp.60-64, 1989.
6. G.A.Mesyats, et al, "Pulse-periodic high-voltage generator of subnanosecond pulses", *Proc.of 9-th Symp.on High-Current Electronics*, pp.236-237, July 1992.

The use of two-dimensional distributed feedback for synchronization of radiation of powerful sheet and tubular relativistic electron beams

N.S.Ginzburg, N.Yu.Peskov, A.S.Sergeev

Institute of Applied Physics RAS, 46 Ulyanov str., 603600, Nizhny Novgorod, Russia

Abstract

It is proved that there is the possibility to use 2-D distributed feedback to ensure powerful spatial-coherent microwave emission of sheet and tubular relativistic electron beam with transverse size exceeding wavelength by the factor $10^2 - 10^3$.

Introduction

For generation of superpower microwave radiation it is perspective to drive FEL's by intense sheet and tubular (hollow) relativistic electron beams with particle energy 1-2MV, total current up to 100kA and power up to 100GW. However, the typical transverse size of such beams runs up to 10^2 cm [1,2]. As a result, the main problem is to provide spatial coherence of emission from different parts of electron beams. For solving this problem in [3,4] the use of two-dimensional distributed feedback, which may be realized in a planar and coaxial 2-D Bragg resonator, proposed. The additional transverse electromagnetic energy fluxes arising in these resonators should synchronize radiation of electron beams with the transverse size essentially exceeding the wavelength.

FEL with Planar 2-D Bragg Resonator and Sheet Electron Beam

Let us consider the planar 2-D Bragg resonator (Fig.1a) formed by two metal plates with width l_x , length l_z and distance between them a_0 , which are corrugated as $a = a_1(\cos(\bar{h}x - \bar{h}z) + \cos(\bar{h}x + \bar{h}z))$, where $\bar{h} = \sqrt{2}\pi/d$, d is corrugation period, a_1 is corrugation depth. Assuming $\bar{h}a_1 \ll 1$ we will seek the field in the resonator in the form of four coupled waves: \mathcal{A}_{\pm} propagating in the $\pm z$ and \mathcal{B}_{\pm} propagating in the $\pm x$ directions:

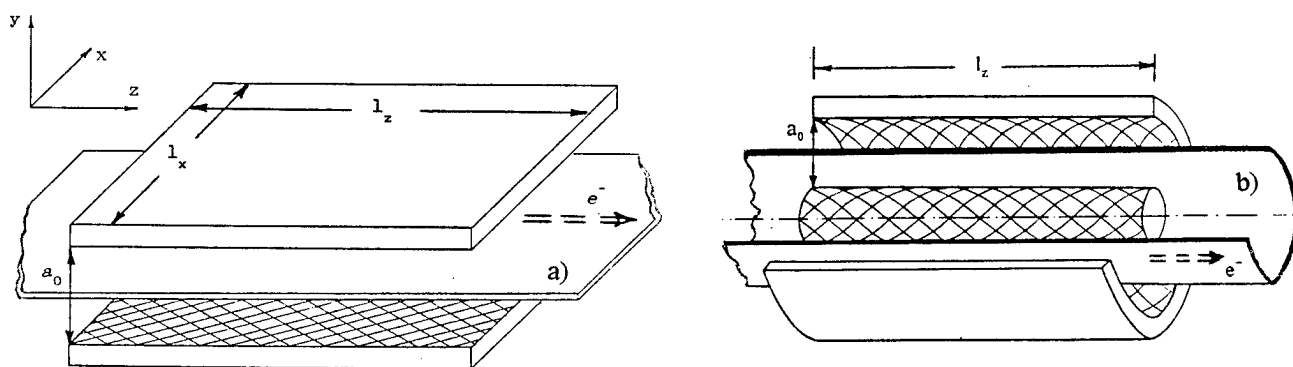


Fig.1 The general scheme of FEL-generator with two-dimension Bragg resonator driven by sheet (a) or tubular (b) electron beam (the drift velocity of electrons directed along z coordinate)

$$\vec{E} = \text{Re} \left[\bar{y}_0 (\mathcal{A}_+(x, z, t) e^{-i\bar{h}z} + \mathcal{A}_-(x, z, t) e^{i\bar{h}z} + \mathcal{B}_+(x, z, t) e^{-i\bar{h}x} + \mathcal{B}_-(x, z, t) e^{i\bar{h}x}) e^{i\omega t} \right], \quad (1)$$

where $\omega = \bar{h}c$ is Bragg frequency.

We investigate here excitation of the 2-D Bragg resonator by a sheet relativistic electron beam. Suppose that electrons oscillate either in the undulator field (ubitron) or in the uniform axial magnetic field (cyclotron autoresonance maser). In assumption that only the \mathcal{A}_+ wave is synchronous to the electrons moving in the $+z$ direction and the rest partial waves do not interact with the beam, the oscillations build-up can be described by the following system of equations:

$$\begin{aligned} \left(\frac{\partial}{\partial Z} + \beta_{gr}^{-1} \frac{\partial}{\partial \tau} \right) \mathcal{A}_+ + \sigma \mathcal{A}_+ + i\alpha (\mathcal{B}_+ + \mathcal{B}_-) &= \frac{1}{\pi} \int_0^{2\pi} e^{-i\theta} d\theta_0, & \left(\frac{\partial}{\partial Z} + \beta_{gr}^{-1} \frac{\partial}{\partial \tau} \right)^2 \theta &= \text{Re}(\mathcal{A}_+ e^{i\theta}) \\ \left(-\frac{\partial}{\partial Z} + \beta_{gr}^{-1} \frac{\partial}{\partial \tau} \right) \mathcal{A}_- - \sigma \mathcal{A}_- + i\alpha (\mathcal{B}_+ + \mathcal{B}_-) &= 0, & \left(\pm \frac{\partial}{\partial X} + \beta_{gr}^{-1} \frac{\partial}{\partial \tau} \right) \mathcal{B}_{\pm} \pm \sigma \mathcal{B}_{\pm} + i\alpha (\mathcal{A}_+ + \mathcal{A}_-) &= 0. \end{aligned} \quad (2)$$

Boundary conditions for Eqs.(2) take the form

$$\begin{aligned} \mathcal{A}_+(X, -L_z/2) = 0, \quad \mathcal{A}_-(X, +L_z/2) = 0, \quad \mathcal{B}_+(-L_x/2, Z) = 0, \quad \mathcal{B}_-(+L_x/2, Z) = 0 \\ \theta|_{Z=-L_z/2} = \theta_0 \in [0, 2\pi), \quad \left(\frac{\partial}{\partial Z} + \beta_{gr}^{-1} \frac{\partial}{\partial \tau} \right) \theta \Big|_{Z=-L_z/2} = -\Delta. \end{aligned} \quad (3)$$

Here $Z = \bar{h}zC$, $X = \bar{h}xC$, $\tau = \omega tC$, α is wave coupling coefficient, $C = \left(\frac{eI_0 \lambda^2 \kappa^2 \mu}{8\pi \gamma_0 m c^3 a_0} \right)^{1/3}$ is gain parameter,

$v_{gr} = \beta_{gr}c$ is group wave velocity, θ is electron phase relative to synchronous wave, Δ is initial mismatch of synchronism, κ is parameter proportional to the oscillatory particles velocity, μ is bunching parameter, I_0 is electron current, $L_{x,z} = \bar{h}l_{x,z}C$, $\sigma = \sigma/C$ is ohmic losses (these losses are important for FEL with coaxial Bragg resonator, so in this section we suppose $\sigma = 0$).

Dependencies of efficiency on time at the region of parameters, where the establishment of the stationary regime of generation takes place, are presented in Fig.2. At the stationary regime spatial structures of partial waves \mathcal{A}_{\pm} and \mathcal{B}_{\pm} are close to the structures of corresponding waves for the most high-Q mode of "cold" resonator (compare Fig.3 and Fig.3 in Ref.[4]). The frequency of this mode, as well as the oscillations frequency, coincides with the Bragg one. It is important to note that transverse distribution of the amplitude of synchronous wave \mathcal{A}_+ does not depend on transverse coordinate x that provides equal energy extraction for all parts of the electron beam.

From Eqs.(2) it can be shown that at stationary conditions ($\partial/\partial\tau = 0$), when the fundamental mode is excited, distribution of waves along longitudinal coordinate, as well as efficiency, does not change when conditions $\alpha^2 L_x = \text{const}$ and $L_z = \text{const}$ are satisfied. Such a scaling gives us the possibility to increase the width of the interaction space simultaneously decreasing coupling parameter (for example, decreasing corrugation depth). Computer simulation of nonstationary equations (2) confirms this conclusion. If $L_z \leq 5$ the synchronization regime is stable at least up to $L_x \leq 30$

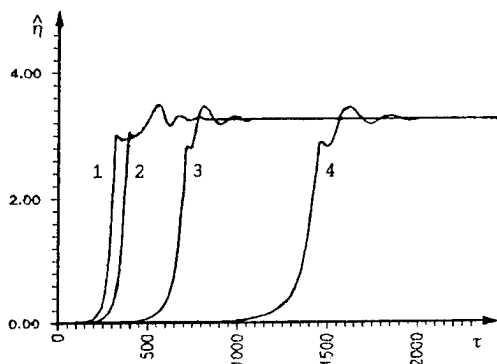


Fig.2 Build up stationary regime of oscillations.

Dependencies of normalized efficiency on time:

$$L_z = 4, \Delta = -1,82, \alpha^2 L_x = 1,25 :$$

1. $L_x = 0,8$; 2. $L_x = 3,2$; 3. $L_x = 12,8$; 4. $L_x = 28,8$.

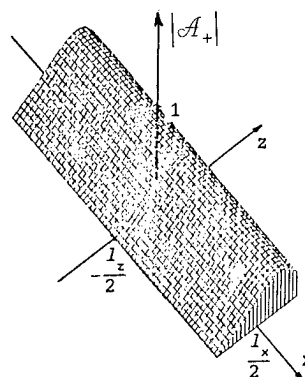


Fig.3 Spatial distribution of partial wave amplitude A_+ in the stationary regime of oscillations:

$$L_z = 4, \Delta = -1,82, L_x = 12,8, \alpha = 0,32 .$$

However, the transitional time increases with increasing system's width (see Fig.2).

Using the theory carried out we have designed the FEL with wavelength 4mm and output power up to 20GW driven by relativistic electron beam with transverse size 140cm, electron current 1kA/cm, particles energy 1MeV and pulse duration 10^{-6} s (accelerator U-2, INP RAS, Novosibirsk [1]).

FEL with Coaxial 2-D Bragg Resonator and Tubular Electron Beam

Scheme of the FEL with tubular electron beam and coaxial 2-D Bragg resonator is presented in Fig.1b. For this scheme double-periodic corrugation of the walls couples the A_{\pm} waves propagating in $\pm z$ direction and the B_{\pm} waves propagating in the azimuthal $\pm\phi$ one. Let us assume that the resonator radius R exceeds essentially the distance between the plates and the wavelength ($R \gg \lambda, a_0$). Under these conditions, neglecting low curvature of the plates, we can describe excitation of this resonator by tubular electron beam with the help of Eqs.(2), where $X = R\phi$ is coordinate along the perimeter of the resonator. Boundary conditions (3) in the longitudinal direction for waves A_{\pm} and for electrons don't change, while in the transverse direction the conditions of cyclicity are valid

$$A_{\pm}(-L_x/2, Z) = A_{\pm}(+L_x/2, Z), \quad B_{\pm}(-L_x/2, Z) = B_{\pm}(+L_x/2, Z), \quad (4)$$

where $L_x = 2\pi RC$ is normalized perimeter of the resonator. According to relations (4) it is possible to expand solutions of Eqs.(2) in Fourier series and considered every term as a mode with azimuthal index m .

An important specific feature of coaxial 2-D Bragg resonator is excitation of a nondisappeared azimuthal-symmetric eigenmode (i.e. a mode with the infinite quality factor), if we don't take into account ohmic or diffraction losses for the partial waves B_{\pm} . At the same approximation, azimuthal nonsymmetric eigenmodes ($m \neq 0$) have finite losses (finite quality). Therefore, under excitation of such a resonator by electron beam selective discrimination azimuthal nonsymmetric modes arise. However, establishment of stationary generation regime the losses ($\sigma \neq 0$) for partial waves B_{\pm} have principal importance.

Transient process may be divided into two stages. At the first, relatively short, stage during several passes of partial

waves over resonator azimuthal symmetric distributions of waves amplitudes are formed. At the next stage lasting for a longer time than the first one, storage of electromagnetic energy in resonator occurs. At the end of this stage the stationary single-frequency generation regime establishes. This conclusion is illustrated by Fig.4 that represents the time-dependencies of different azimuthal harmonics in spectrum \mathcal{B}_\pm in the cross-section $Z = L_z$.

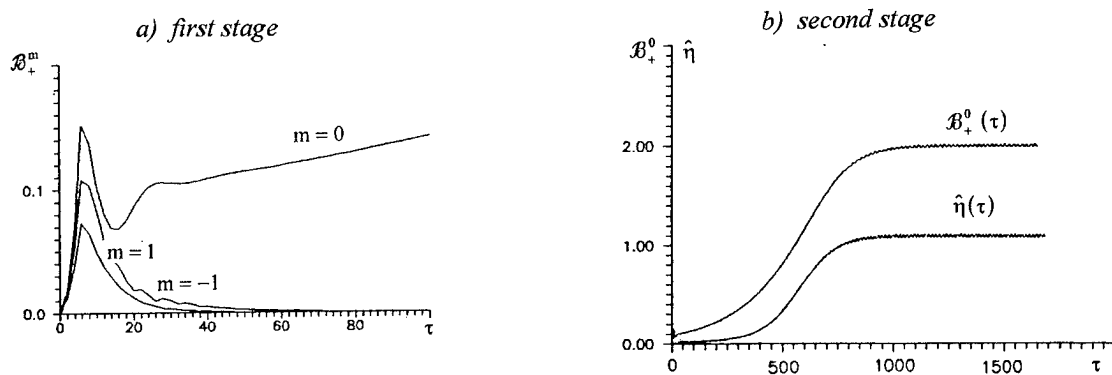


Fig.4 Normalized efficiency and amplitudes of azimuthal harmonics in spectrum of partial wave \mathcal{B}_+ vs time:

$$L_z = 6,8, \Delta = -0,65, L_x = 12,8, \alpha = 0,1, \sigma = 0,1$$

At time $t=0$ we take the wave \mathcal{A}_+ as initial perturbation, in the spectrum of which amplitudes of different harmonics with number $m \in \{-1, 0, 1\}$ are equal. At first, transformation of the wave \mathcal{A}_+ into the waves \mathcal{B}_\pm takes place and the amplitude of all harmonics in spectrum of \mathcal{B}_\pm growth. But then, amplitudes of all harmonics except $m=0$ fall practically to zero. As is clear from comparing Fig.4a and Fig.4b, the main part of the transitional process occupies the second stage (stage of energy storage) when distribution of waves amplitudes is azimuthal symmetric and equal energy extraction from different parts of electron beam take place. Due to this reason, total transitional time only to a small degree depends on the perimeter of the system L_x . Characteristics of stationary regime of generation do not depend on full perimeter too.

Note that the establishment of stationary regime we observe in the computer simulation at least to the value of normalized perimeter $L_x = 30$ what corresponds to $R/\lambda \approx 10^2$ under gain parameter $C = 10^{-2}$. This confirms the possibility of using large size tubular electron beams for generation of powerful spatial-coherent radiation.

References

1. Arzhannikov A.V., Nikolaev V.S., Sinitsky S.L. e.a. "Generation and transport of 140 kJ ribbon electron beam", J. of Appl. Phys., vol.72, no.4, pp.1657-1659, 1992.
2. A.N.Bastrikov, S.P.Bugaev, I.N.Kiselev e.a. "Hollow microsecond electron beam formation at megavolt voltages on a diode", Zh. Tekh. Fiz., vol.58, no.3, pp.483-488, 1988.
3. Ginzburg N.S., Peskov N.Yu., Sergeev A.S. "The use of two dimensional distributed feedback in free electron lasers", Pis'ma v Zh. Tekh. Fiz., vol.18, no.9, pp.23-28, 1992 (Sov. Tech. Phys. Lett., vol.18, no.5, pp.285-287, 1992).
4. Ginzburg N.S., Peskov N.Yu., Sergeev A.S. "Two-dimension double-periodic Bragg resonator for free electron lasers", Optics Commun., vol.96, no.4-6, pp.254-258, 1993.

Nonlinear processes in relativistic Cerenkov microwave resonance sources

Kanavets V.I., Nifanov A.S., Slepikov A.I., Bakharev I.G.

Moscow State University, Physical Department. Russia.

ABSTRACT

The peculiarities of the self-congruent interaction of surface fields of the superdimensional periodic waveguide and the relativistic hollow electron beam are considered with using methods of linear multimode and nonlinear nonstationary theories. The longitudinal and transversal electromagnetic field structure, the efficiency and the spectrum of radiation are determined.

INTRODUCTION

When the electron beam is synchronized with the electromagnetic field on the frequencies near the band cutoff the resonance effects arise. This peculiarity is used for the electron mode selection in amplifiers and generators with superdimensional periodic waveguides¹⁻³. Beam's influence on the mode selection is studied unsufficiently. Particularly this relates to "hot" cutoff moving and changing of "hot" synchronism conditions².

The numerical simulation of physical processes in Cerenkov sources was executed by using linear and nonlinear approach. The matrix multimode method⁴, consisting in the consideration of the field in the periodic waveguide in linear approach, is used for analysis of the field configuration. Theoretical analysis of oscillations evolution in Cerenkov generator is made according to nonlinear nonstationary methods. The assumption about a main role of electron and field of surface wave interaction in Cerenkov generator is in the basis of this method. This peculiarity of the beam radiation in superdimensional periodic waveguide are confirmed by results of multimode method⁴. The supposition permits to use the approximate nonlinear method, based on surface field describing with using the network method, replaced by equivalent circuit. In limits of the model, used for the analysis of nonstationary processes, we make the assumption about slow changing of processes in the time. Particularly, there is pick out the basic frequency equals the frequency of beam and field synchronism.

1. FIELD AND WAVES IN AMPLIFIER AND GENERATOR

We consider the results of the numerical analysis of the surface and electron mode formation in the relativistic amplifier with large diameter ($D \gg \lambda$) with beam current $I=1-10$ kA and electron energy of $E=0.3-1.0$ MeV. These modes often correspond to eigenwaves, which are increased along the system and characterize signal amplifying.

Eigenwave's field structure in any cross-section is determined as a superposition of regular waveguide modes and waves in the beam. So, we may determine the sign of power, which is carried out by electromagnetic field of individual wave. One of four combinations of imaginary part of propagation constant $\text{Im}(k_z d)$ (d -period of the system) and power of vortex field P corresponded to each eigenwave. In this way, we may to distinguish amplifying and dumped regimes for forward and backward waves.

The beam's wave (dotted line) and the vortex field power in dependence on frequencies are showed on fig.1. Dependencies correspond to waves, which have a complex propagation constant. Umov-Poynting vector change it's sign at $2d/\lambda=0.82$ (π -type of band cutoff is at $2d/\lambda_{\pi}=0.865$). This value of $2d/\lambda$ may be called "hot" band cutoff because the waves with complex propagation constant dumped when $2d/\lambda>0.82$. The power of an electromagnetic field $P>0$, and $\text{Im}(k_z d)>0$ if $2d/\lambda<0.82$ and, therefore, there is amplifying of input signal along the system.

Numerical results for section of the system, having 10 periods confirm the conclusion about wave amplifying on this frequencies. Vortex field configuration in the section of Cerenkov source is showed on fig 2. It show longitudinal component of vortex electrical field E_z in dependence on radius in different cross-section of the system - on the first ($s=1$), third, fifth, seventh and tenth period of the system, $2d/\lambda=0.82$. The field structure inside the system is similar to the surface wave. Beam and surface wave synchronism results in the essential increasing of the surface field component along the system. Near the end of section there is the maximum of field on the axis of the system, which corresponds to surface wave scattering on periodical unhomogeneities of the structure.

2. NONSTATIONARY PROCESSES IN GENERATOR

The two typical cases of system matching was chosen to consideration the Cerenkov radiation efficiency on frequencies near π -type band cutoff. The first case is the case of ideal "cold" matching, when we connect equivalent resistors which are equal to wave resistance of infinite system at the enter and the exit of the system. In the second case additional dismatching was used at the system enter and so reflection from technology unhomogeneities was simulated. The investigations of generation processes development was made for different values $k_{zo} d$ - the electron transit angle of an individual period, which is determined by beam and field kinematic synchronism.

The generation frequency in all regimes is not equal the frequency of the beam and field kinematic synchronism. It is shifted to the range of lowest frequencies. The results of the numerical simulation are presented at fig.3. The curve 1 corresponds to the case of ideal matching; curve 2 - the system at the enter is dismatched; dotted line - line of the kinematic synchronism. Generation frequency (at fig.3 frequency normalized on π -type frequency) shift to inside of the band is corresponded to linear analysis data; the electron shift of the band cutoff is existed at this frequencies and the generation arises first of all at the frequencies of the "hot" band cutoff. The dependence of the average efficiency on $k_{zo} d$ for one section generator is shown on fig. 4 (Curve 1 conform to ideal matching, 2 - to dismatched system at the enter). The radiation power at the π -type frequency ($k_{zo} d=\pi$) reached the minimum value. The insignificant variation of the transit angle results in the increase of exit power. In all cases mechanisms of TWT and BWT are presented simultaneously, so the beam and the backward harmonic interaction determine value of internal feedback and section self-excitation condition (starting length, starting current), and interaction with the traveling wave leads to additional amplification. Particularly, acceleration voltage decrease connected with the intensification TWT mechanism role, results in the increase

of the radiation power. The analysis of generation in systems with different length showed, that the generation frequency is determined, in the main, by waveguide properties of the system and depend on its length insignificantly.

REFERENCES

1. Bugaev S.P., Cherepenin V.A., Kanavets V.I. et al. Relativistic Multiwave Cerenkov Generators. IEEE Transactions on Plasma Science, 1990, 18, 525-536.
2. Kanavets V.I., Mozgovoy Ju.D., Slepko A.I. The radiation of the high power electron beams in the resonance slow-wave structures. Moscow. MSU. 1993. 208 p
3. Bugaev S.P., Kanavets V.I., Koshelev V.I., Cherepenin V.A. Relativistic Multiwave Microwave Generators. Novosibirsk: Nauka, 1991.
4. Kanavets V.I., Nifanov A.S, Slepko A.I. Normal waves of periodical waveguide loaded by electron beam. Vestnik Moskovskogo Universiteta. Seriya 3. Fizika. Astronomija. 1990. V.31, N 6. p.80-83.

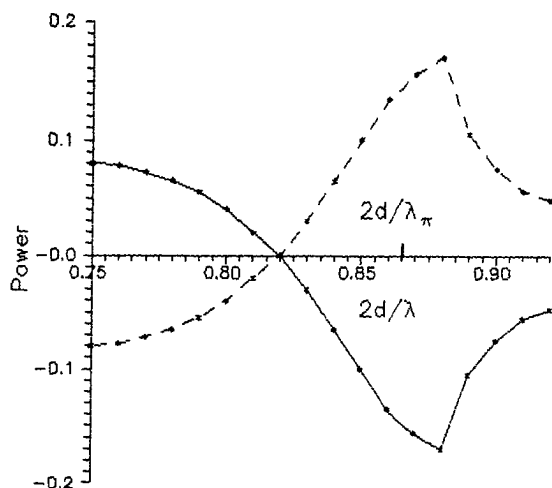


Fig.1

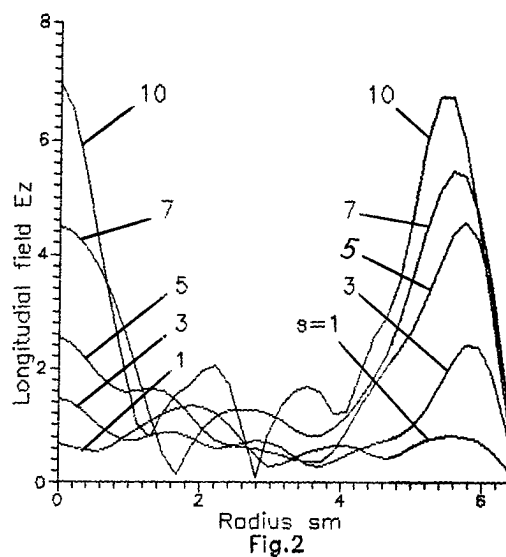


Fig.2

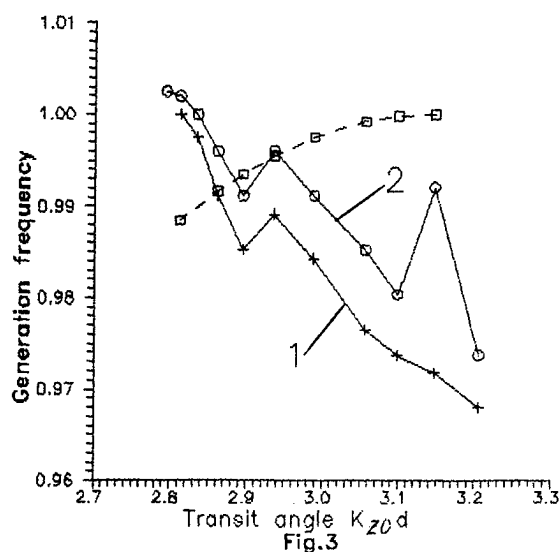


Fig.3

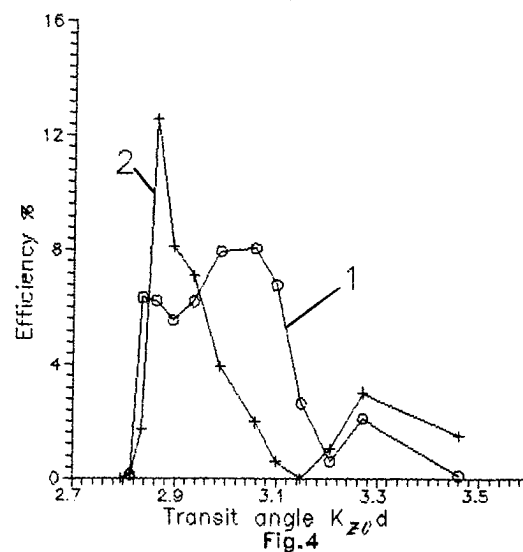


Fig.4

Powerful microwave oscillator of microsecond pulse duration
driven by relativistic electron beam

O.T.Loza, P.S.Strelkov

General Physics Institute,
Vavilov Str., 38, Moscow, 117942, Russia

ABSTRACT

The present work continues experimental investigations of high-power microwave oscillator driven by relativistic electron beam. We studied the possibility to design a microwave source of microsecond pulse duration, usually restricted by plasma generation due to a few reasons. It is shown that the breakdown is determined by microwave discharge, initiated, in turn, by electron beam destruction and bombardment of the slow-wave structure walls. To depress the process of plasma accumulation we propose to apply a gyrotron with axially-symmetrical TE-type mode.

Carrying out this work we tried to find out ways for realizing repetitively-rated microwave pulse oscillators with high mean power: more than 100 kW. Availability of such devices is vital e.g. for plasma chemistry, heating plasma, etc. The rep-rate of oscillators is restricted principally by the value ~ 100 Hz, so a microwave pulse should contain ≥ 1 kJ. There exist microwave oscillators driven by high-current relativistic electron beams (REB) with the power of the order of 1 GW, but pulse duration does not usually exceed ~ 100 ns irrespectively to that of REB. To accomplish the proposed goal it is necessary to increase pulse duration substantially.

The microwave pulse shortening is due to plasma generation in a powerful vacuum device in different parts of it. The preventing of microwave pulse shortening is possible, therefore, only by complete elimination of plasma or, at least, its influence on the device operation.

To create REBs with high current (of a few kA) explosive cathodes are applied. Plasma that emits electrons expands transversely to the guiding magnetic field and changes the electron beam geometry. This is one of the reasons for preliminary termination of microwave radiation. We succeeded in stabilizing the beam geometry by varying magnetic field in the diode, but with the goal of rep-rated device operation we managed to generate a hollow circular REB with invariant radius and thickness in a steady-state magnetic field. Fig.1 demonstrates the radial distribution of beam current density for a REB of 500 keV, 3 kA, 750 ns in different moments. No diaphragm was applied here.

Having this problem solved, we got rid of plasma on the entrance diaphragm (that is usually used to restrict the outer beam radius), and the collector plasma was merely removed with its originator far from the waveguide². The slow-wave structure was the only area where plasma could appear.

Investigation carried out at our setup³ shows that microwave discharge with plasma creation in the residual gas can be avoided by a proper choice of its pressure. Moreover, beginning from some value of

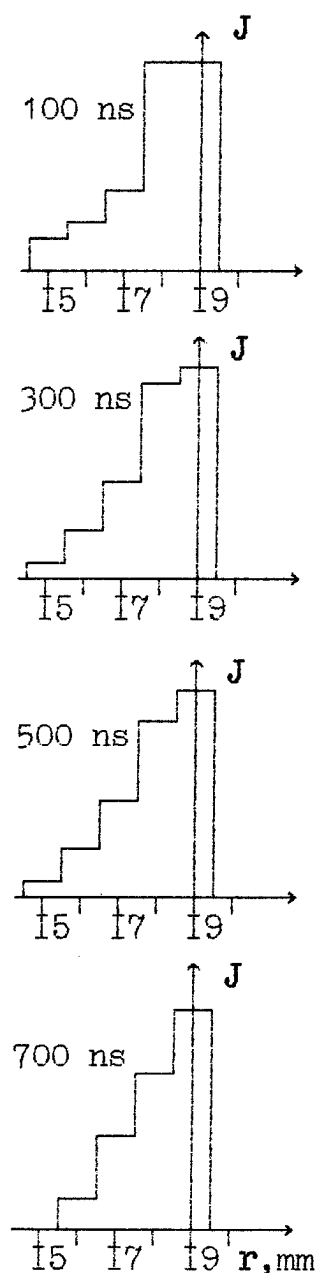


Fig. 1.

microwave electric field the breakdown threshold tends to rise up, because the cross section of electron-molecule interaction drops down with the increase of oscillation velocity of the particles. Maintaining low pressure (≤ 0.1 mTorr) is also the cure for intensive plasma accumulation due to collisions of relativistic electrons (~ 1 kA/cm²) with gas during the beam propagation (~ 1 μ s).

The waveguide inner wall is one more source of plasma. High-power microwaves have sufficient energy to create great amount of it by means of near-wall secondary emission electron discharge with the following accumulation of plasma. This effect may be obviated if REB space charge electric field on the wall is always more than electric component of microwaves. But if the surface was previously screened by sufficiently dense plasma layer (even a very little spot of it), microwave discharge will develop.

Our estimations show that such "ignition" plasma may appear after bombardment of the walls by a weak flux of relativistic electrons: < 1 A/cm². These electrons may appear either as the consequence of well-known REB destruction in microwave field or after backscattering on the collector.⁴ Moreover, if this initial plasma forms the enclosed circumference, unimpeded azimuthal drift of ~ 100 eV electrons (with comparatively large interaction cross section) in crossed axial magnetic and radial electric fields causes fast plasma accumulation well before the appearance of microwaves and prevents it. It was confirmed by a special experiment.

BWO oscillator with the remote (asymmetrical) collector² produced 50 MW radiation of 300 ns duration with 100 ns time delay from the beginning of REB propagation. Solenoids providing the beam turn to the collector being switched off, the emitting horn played the role of the collector in a completely symmetrical geometry, and the radiation process did not even start. Observa-

tions of backscattered electrons by sensitive films⁴ showed that, unlike the first case, the enclosed ring of relativistic electrons bombarded the rippled walls of BWO. And our preliminary studies brought out clearly

that 100 ns were not sufficient for collector plasma to spoil the device.

To eliminate the backscattered electrons completely, the method of spatial separation of the direct and the backstreaming electron fluxes was proposed.⁵ It uses the property of electrons to drift in an inhomogeneous (curved) magnetic field to the same side irrespectively to their longitudinal velocity. To achieve the separation it is necessary to bend the direct beam in the collector chamber. We implemented this method turning the beam through angle of π in magnetic field of 0.1 T.

Backscattered electrons disappeared from the slow-wave structure, but nevertheless the radiation process terminated before the end of REB current. Now only direct particles could be responsible for this breakdown, producing plasma layer on the walls and providing the mechanism of plasma accumulation in microwave field. This conclusion is supported by the following.

A TMO2 BWO (carsinotron) was in use, based on well-known cyclotron mode selection. This meant that due to finite thickness of hollow REB electron cyclotron frequency Ω/γ (γ - relativistic factor) should be a little (up to 30%) greater than microwave frequency with Doppler shift: $\omega - ku$. Absorbing energy of microwaves, relativistic electrons increased their γ . Achieving the resonance, and if the initial phase was appropriate, electrons flew to the walls, promoting plasma creation. Total amount of such "wasted" particles depends on different reasons, but first of all - on the initial values of the two frequencies. The more close they were to each other, the more particles occurred in these conditions, as was seen in our numerical simulations. And the experiment showed that Ω/γ being risen up from $\omega - ku$, both microwave power and pulse duration increased from zero level. The latter can not be explained only by microwave discharge development.

The described experiments prove, we believe, that in absence of all the deleted reasons for plasma appearance mentioned above, the two-stage model of microwave breakdown does take place: first plasma "screen" is produced by wasted electrons of direct REB, and the following plasma accumulation is determined by microwaves with strong electric field on the wall. The resonance principle of the device operation played its negative role, but the value of microwave power of ~ 50 MW was comparatively modest as well. To depress the beam deterioration it would be possible to use e.g. TMO1 carsinotron, not so sensitive to magnetic field value. But it should be kept in mind that in the powerful oscillator⁶ current leakage to the walls reached 10%, so it would be hardly possible to prevent electron bombardment of the walls completely in a powerful device.

Much more promising way to avoid fast breakdown it seems to be the next one. An axially-symmetrical TE-type mode of a circular waveguide has vanishing component of electric field on the wall. So one may hope, that initial plasma, created by relativistic electrons on the wall, will not have sufficient energy supply. Such type of electromagnetic wave can be generated in a gyrotron, for example.

Rigid requirements are imposed by a gyrotron upon the electron beam quality, including its thickness. Following this demand, we created a hollow REB (500 kV, 2 kA) with ~ 1 mm thick walls in a steady-state magnetic field. Its current radial profile is shown in Fig.2. As for Fig.1, no₇ diaphragm was applied. And our experience in design of Q-band gyrotron⁷ witnesses, that the problem of microsecond REB generation with helical electron trajectories may be solved.

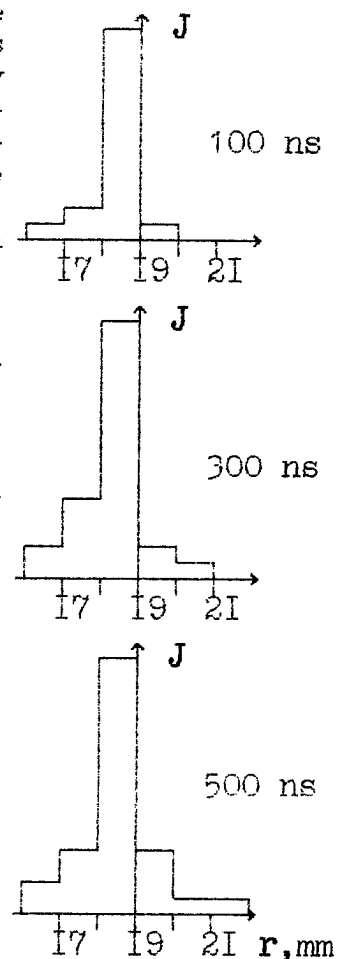


Fig.2.

CONCLUSION

The results of present investigation may be summed up as following. The breakdown of microwave radiation in a powerful oscillator driven by REB is determined by plasma creation inside the vacuum device. Numerous reasons for plasma appearance exist, overwhelming majority of them can be eliminated. On the base of experimental data, a mechanism of intensive plasma accumulation is proposed, comprising a few consequent processes.

First, strong microwave field causes destruction of REB, dispatching a part of electrons to the wall. The electron bombardment creates a layer of plasma on the surface. This plasma screens the electrostatic field of electron beam space charge, that initially had prevented secondary emission electron discharge in the microwave field. The discharge becomes possible, and amount of plasma increases up to the moment of preliminary termination of microwave radiation, e.i. breakdown.

It is difficult (or maybe impossible) to avoid electron bombardment completely. To obviate the established mechanism of plasma accumulation it is proposed to use an axially-symmetrical TE-type mode of a gyrotron. Electron beams with invariant geometry are available.

REFERENCES

1. Voronkov S.N., Loza O.T., Strelkov P.S., "Influence of cathode plasma upon the radiation pulse duration of vacuum microsecond relativistic microwave generator", Proc. of the IX Int. Conf. on High-Power Particle Beams (BEAMS'92), v.3, p. 1550-1555, Washington, DC, USA, May 25-29, 1992 // Sov. Journ. of Plasma Physics, vol.19, N.4, 1993.
2. Voronkov S.N., Loza O.T., Strelkov P.S. "Restriction of radiation pulse duration in microwave generators using microsecond REB", Proc. of the VIII Int. Conf. on High-Power Particle Beams (BEAMS'90), v.2, p.1147-1152, Novosibirsk, USSR, July 2-5, 1990. // Sov. Journ. of Plasma Physics, vol.17, N.6, p. 439-442, 1991.
3. N.S.Tsagareishvili, "Gas breakdown at low pressures in ultrastrong nonuniform microwave fields", Sov. Journ. of Plasma Physics, vol.16, N.11, p.803-804, 1990.
4. Aleksandrov A.F., Galuzo S.Yu., Karavichev M.V., Kubarev V.A., "Study of REB backscattering on a collector in magnetic field", USSR VII Simp. on High-Current Electronics, v.2. p. 154-156, Tomsk, 1988.
5. Loza O.T., Strelkov P.S., Voronkov S.N., "The reason for the microwave radiation breakdown in a relativistic carsinotron", Proc. of the II Int. workshop "Strong microwaves in plasmas", S-32, N-Novgorod, Russia, August 15-22, 1993 // Sov. Journ. of Plasma Physics, vol.20, N.4, 1994.
6. S.P.Bugaev, V.I.Kanavets, A.I.Klimov et al, "Interaction of electron flux and electromagnetic field in a multiwave Cherenkov oscillator with the power of 10^{10} W", Radiotekhnika i elektronika, vol.32, N.7, p.1488-1496, 1987.
7. S.N.Voronkov, V.I.Krementsov, P.S.Strelkov, A.G.Shkvarunets, "A stimulated cyclotron radiation of high-current relativistic electron beam in the millimeter wavelength band", Zhurnal tekhnicheskoi fiziki, v.52, p.106-108, 1982.

Investigation of TW output circuit for relativistic klystrons

Dmitry V. Fedyaev, Victor M. Pikunov, Aleksandr N. Sandalov

Physics Department
Moscow State University
119899 Moscow, Russia

ABSTRACT

Relativistic klystron amplifiers (RKA) for the linear collider usually used a iris loaded waveguides as an output circuit [1]. The behavior of electron and electromagnetic waves in travelling wave (TW) output structure of relativistic klystron with electron beams loading have been investigated. The linear interaction of space-charge waves of electron beam and electromagnetic waves of TW structure were studied and increment of radiation gain of TW's cell was determined. Longitudinal and transversal distributions of electron wave EM fields and their effect on TW circuit characteristics has been shown.

1. INTRODUCTION

A future linear colliders if it operate at X Band will require a microwave power level more than 100 MW. The conventional klystron with relativistic electron beam formed by thermionic cathode is more convenient for the realization of 100 MW RF power level. The principal problem are in output circuit. To avoid the pulse length shortening and very high EM fields gradients, interaction between circuit and electron beam must be over an extended space, rather than the traditional short gap or double-gap cavity at RKA [2]. The extended output circuit must be as multy-gap cavity, couple-gap cavity or superdimensional structure [3,4].

There are also the RKA with the iris loaded output structure [1] and for the understanding the physics of electromagnetic and electron waves interaction as the first step is the study of structure dispersion diagram. It's the base of understanding the EM excitation, parasitic oscillations and RF discharge at the output circuit. That principal problem can be studied theoretically by means of the methods based on linear theory. It includes the linearized motion and continuity equations and electrodynamic prescription of electromagnetic fields in output circuit.

Galerkin's method [5-8] for electron wave equations is more useful and it gives the possibility to find the synchronism frequency regions and the interaction type of electron beam and the circuit EM modes, can be determined the gain per cell and so on. Follows we used that method for RKA output circuit as nonregular periodic waveguide study.

2. THEORY AND MODELING

We assumed that extended output circuit excited by the sets of electron bunches comes from the RKA buncher (fig.1) with the parameters of electron beam: beam current - $I_0 = 300$ A, beam voltage - $V_0 = 1$ MV, beam radius $r_0 = 0.4$ cm, the fundamental frequency - 14 GHz [1]. The dispersion diagram of electron waves for the output circuit as diaphragm waveguide with the follows dimensions: external diameter - $2r_0 = 24.24$ mm, inner diaphragm diameter - 16 mm, the structure period $d = 5$ mm and the diaphragm thickness - 2 mm is shown on fig. 2. Output circuit operates on $k_z d = \pi/2$ oscillation mode.

The real dispersion diagram part (solid line on fig. 2.) is responsible for the phase shift of selected mode and imaginary part gives the amplification (attenuation) value $8.686 \text{Im } k_z d'$ [dB/cell] per period of slow wave structure. On the dispersion diagram is shown the interception region of "0" and "-1" spatial harmonics of related modes E_{01} . There are frequency regions in which interaction of electron beam with the electromagnetic fields of output circuit are present.

In lower frequency region may be possible the TWT interaction type on operating frequency $f_0 = 14$ GHz. On the upper threshold frequency region $f^{(0)}_{th}$ of mode E_{01} will be interaction $E^{(0)}_{01} + \text{SWSC}$ type and determined by interaction of E_{01} mode of diaphragm waveguide with the slow wave of space-charge (SWSC) of electron beam.

In threshold region of dispersion diagram $f < f^{(0)}_{th}$ will be interaction SWSC + FWSC type which coupled with the interaction of fast wave (FWSC) and slow wave of space-charge of electron beam. The same situation are at slow wave structure as waveguide with the partial dielectric filling and called by low frequency Cherenkov's instability [7].

In the upper frequency range there are BWO interaction regions. As the frequency spectrum of electron bunches usually has the intense amplitudes of second - $2f_0$ and third - $3f_0$ fundamental current harmonics, the design of output circuit must be out off that interaction region.

The different electron waves transversal distribution which will be excited in output circuit on fundamental frequency 14 GHz is shown on fig. 3 a-c. The operating frequency are in TWT interaction region. On fig.3a there are transversal structure of coupled electron waves SWSC + $E^{(0)}_{01}$ in diaphragm cross-section. The transversal distribution structure of FWSC and "-1" spatial harmonic of E_{01} mode is shown on fig.3b and fig.3c respectively. The transversal distribution of the longitudinal component of electric field of "0" spatial harmonic $E^{(0)}_{01}$ of E_{01} mode slightly differ from that on fig.3c. The beam loading gives a distortion of transversal field of "0" spatial harmonics and exciting the operating mode SWSC + $E^{(0)}_{01}$ with a transversal field distribution like shown on fig. 3a.

The linear theory permit us to estimate the value of electric field strength. The calculations were made for the possible 50% RKA overall efficiency it gives the 150 MW RF power level. It was estimate also the maximum of longitudinal and transversal components of electric fields between the diaphragms which has a values equaled $E_r = 201$ kV/cm and $E_z = 347$ kV/cm.

The longitudinal electromagnetic energy distribution for the RKA extended output circuit are on fig. 5 for the shape shown on fig.4. The excitation of output structure was by sine-shaped velocity modulated electron beam. On fig.5 the $S^{(+)}$ - is the energy flow transmitted by waves downstream to energy extract and $S^{(-)}$ = transmitted to the entrance of output circuit, so $S = S^{(+)} + S^{(-)}$. The energy flows distribution between the neighborhood diaphragms looks like that in klystron cavities.

The longitudinal distribution of alternating component of convectional current for linear regime calculations is shown on fig.6. The curve maximum in linear regime comes from the taking into account the boundary conditions on the ends of slow wave structure.

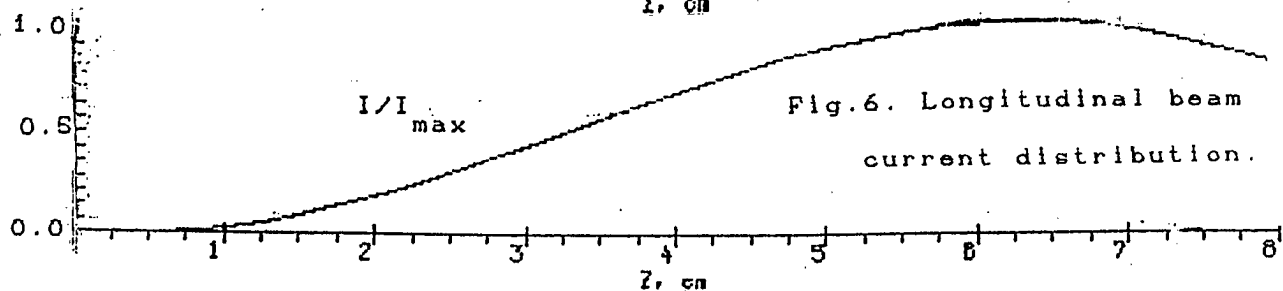
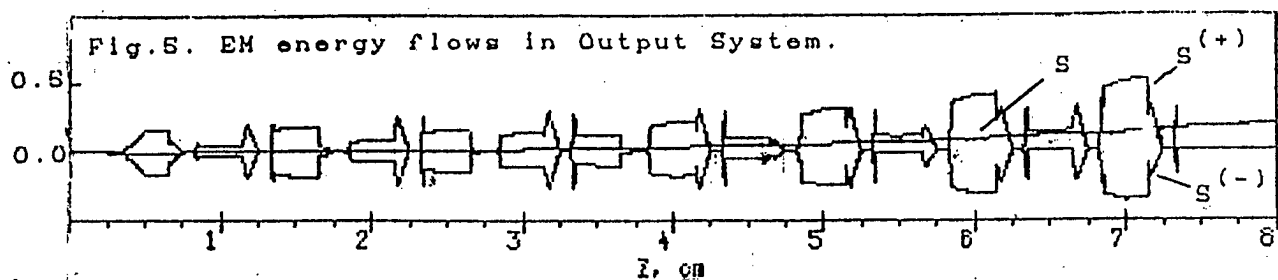
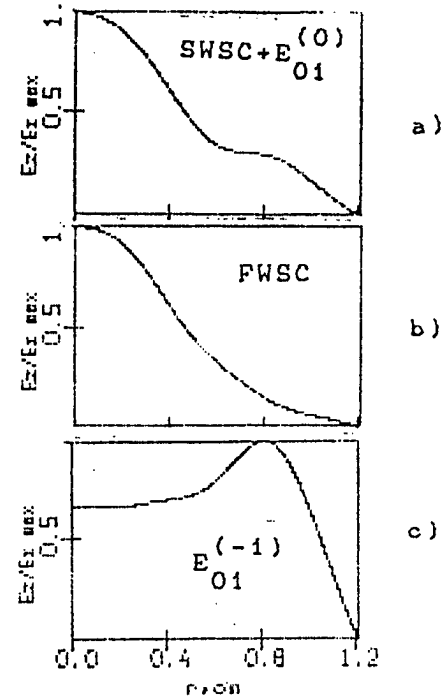
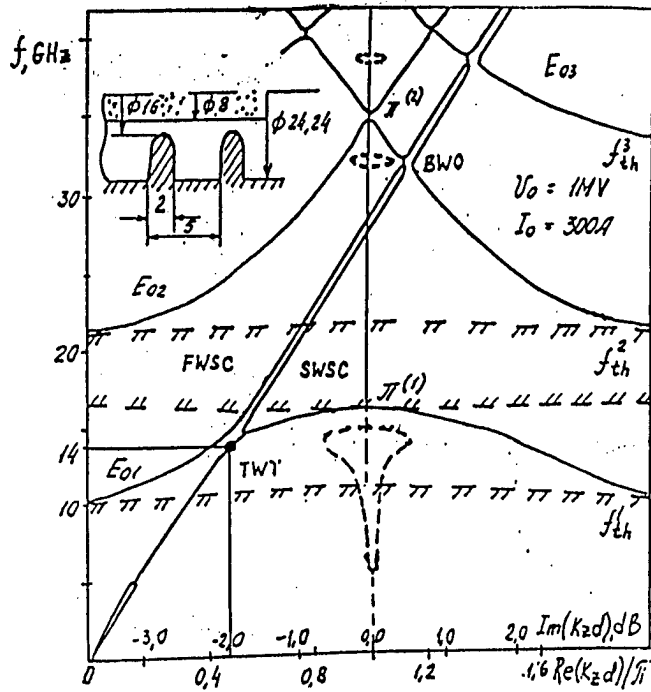
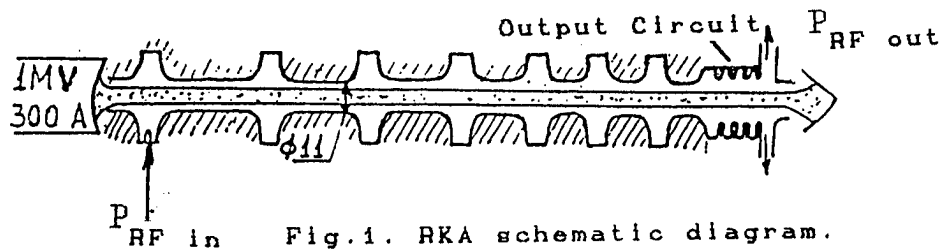
For the testing of linear theory the "cold" measurements of output circuit in several points of dispersion diagram was made. The results of comparison are on table 1.

Table 1.

Oscillation mode	Measured wavelength, cm	Calculated wavelength, cm
$\pi/2$	1.869	1.860
π	1.539	1.512

3. REFERENCES

1. V.E. Balakin// LC - 91 - Protvino, September 1991.
2. I.G. Artiukh, A.N.Sandalov, A.S.Sulakshin et al// Obzory po elektronnoi tekhnike. s.1, v.17(1490), 1989, 70p.
3. A.N.Sandalov, V.M.Pikunov, V.E.Rodiakin, A.A.Stogov//Proc. BEAMS 92, 1993, v.3., pp.1673-1678.
4. A.N.Sandalov, A.V.Terebilov// Radio Engineering and Electron Physics. 1983, v.27, n.9.
5. D.B.Luzianin, V.M.Pikunov// ibid, 1991, v. 36, N.1.
6. V.M.Pikunov, I.A.Chernyavsky//ibid, 1992, v.37, N. 11.
7. V.M.Pikunov, I.Yu.Kolesnikova//ibid, 1988, v.33, N. 11.
8. V.M.Pikunov, A.N.Sandalov, D.V.Fedyaev//Proc.of All-Union conf. "Physics and microwave application.", MSU, 1991, v.1, p. 144.



Measurement of spectrum and power of microwave radiation
from relativistic plasma microwave oscillator

Shkvarunets A.G., Ulyanov D.K.

General Physics Institute of Russian Academy of Sciences
Vavilov Str., 38, Box 117942, Moscow, Russia

ABSTRACT

Experimentally studied microwave radiation from plasma waveguide when relativistic electron beam (600 keV, 2÷4 kA, 100 ns) propagate axially the plasma waveguide. Spectrum of microwave radiation was measured by multi resonator spectrometer power was measured by broadband calorimeter. The calorimeter measured the total microwave energy emitted from output horn. Emitting microwave power strongly depended on plasma density, interaction length and gap between annular tube beam and annular tube plasma column. Spectrum of radiation was ~ 50%.

1. INTRODUCTION

Plasma microwave electronics devices differ from the vacuum ones by the presence in their electrodynamics systems the sufficiently dense plasma. The plasma allows to achieve the electron beam currents beyond a limit current in vacuum. The plasma provides slowing of electromagnetic waves, which allows the fulfillment the Cherenkov resonance between the beam electrons and some eigen mode of electromagnetic waves in such devices. As a result in the devices of plasma microwave electronics a possibility appears of utilization of beam currents higher than in corresponding vacuum microwave devices and the attainment more high radiation power levels in the more compact geometry.

2. EXPERIMENTAL RESULTS

The annular REB produced by the "Terek-3" accelerator with an energy $E = 550-650 \text{ keV}$, beam current - 2, 3, 4 kA and pulse duration $\approx 100 \text{ ns}$ is injected into cylindrical waveguide of the radius $R = 1.8 \text{ cm}$. The main radius of the beam $r_b = 0.6 \text{ cm}$ and the thickness $\Delta_b = 0.1 \text{ cm}$. The magnitude of guiding external magnetic field $B_0 = 2 \text{ T}$. In the Fig.1 a schematic diagram of the experimental apparatus is shown. The REB is emitted by cathode K and accelerated in the vacuum diode. Then it propagates through the waveguide 2 and reaches the graphite collector 6. The preliminary plasma is produced by the low energy electron beam with energy 600 eV and current $\leq 100 \text{ A}$, which ionizes the neutral gas in the waveguide (Xe at $P = 2 \cdot 10^{-3} \text{ Torr}$). The time of the plasma density increasing is 10-15 ns, the thickness of plasma layer $\Delta_p = 0.1 \text{ cm}$, the mean radius is varied $r_p = 0.8$ and 0.9 cm and density $10^{12} \text{ cm}^{-3} \leq n_p \leq 8 \cdot 10^{13} \text{ cm}^{-3}$.

Experiment had two stages.

- A measurement of output microwave power by a powerful semiconductor detector, operating on "hot carriers" at the room temperature. The de-

tector had following parameters: the frequency band $f = (8-14) \text{ GHz}$ and the range of the measured power $10 \div 200 \text{ kW}$. This detector received $\sim 1/400$ part of the output radiation. Measurements were performed for above parameters of beam and plasma. The interactions lengths L were 13, 20, 25 and 30 cm.

- A measurement of the total power and spectrum of the radiation for optimal parameters with maximum of the radiated power. The total power was measured using a calorimeter with a large cross-section, which overlapped the whole area of the horn. The calorimeter absorption coefficient was about 90% in the frequency range from 4 to more than 30 GHz. A sensitivity of the calorimeter was about 0.05 J. The spectrum of the radiation was measured by 5-channel wide-band spectroanalyser. The frequency values were 8, 10.4, 12.7, 15 and 17.3 GHz. The band of each channel was $\sim 10\%$.

Now we discuss some results of a first stage.

- 1. A microwave power was practically absent (less than 1 MW) at $L = 13 \text{ cm}$ for all above written parameters.

- 2. At $L = 20, 25$ and 30 cm was obtained a dependence of the radiated power on n_p about the same for all values of the beam currents I_b and r_p . If $n_p \leq 2 \cdot 10^{12} \text{ cm}^{-3}$ the radiated power did not exist; if $n_p \geq 2 \cdot 10^{12} \text{ cm}^{-3}$ the radiated power increased while the n_p increased to value $2 \cdot 10^{13} \text{ cm}^{-3}$, then the power decreased with the increasing n_p up to $4 \cdot 10^{14} \text{ cm}^{-3}$. The radiated microwave power depended on the beam current, the plasma radius and did not depend on the length of the plasma waveguide, if the lengths were 20, 25 and 30 cm. If the beam current was equal to 3 kA , the power was maximum. With decreasing plasma radius the power increased. The highest microwave power took place at following parameters: $I_b = 3 \text{ kA}$, $r_p = 0.8 \text{ cm}$, $L = 25 \text{ cm}$ and n_p about 10^{13} cm^{-3} . It was this set of parameters measurements of microwave radiation characteristics were performed.

The results of the second stage. For more precise measurement of the whole microwave power we used an energy calorimeter with big cross-section, which overlapped whole areas of the horn. Simultaneously we measured the time dependence of microwave radiation pulse, which allowed us to define the power. The results of such measurements are presented in the Fig. 2. It is seen that the band of n_p , in which the generation takes place is $2 \cdot 10^{12} \text{ cm}^{-3} \leq n_p \leq 7 \cdot 10^{13} \text{ cm}^{-3}$. The radiation power reaches the maximum value $\approx 350 \text{ MW}$ at $n_p = 2 \cdot 10^{13} \text{ cm}^{-3}$, which corresponds to the radiation efficiency $\approx 20\%$.

The results of spectral measurements of 14 shots are presented in the Fig. 3. Here the vertical lines are signals from spectroanalyzer channels. At the left of the spectral lines set are written the radiated power in MW and plasma density in cm^{-3} for every shot. From the Fig. 3 it

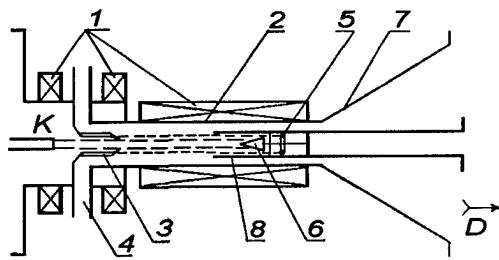


Figure 1.

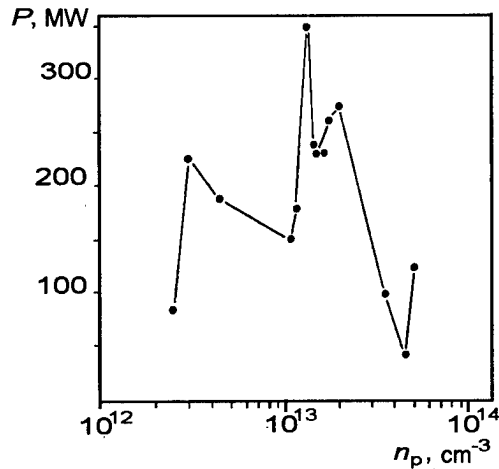


Figure 2.

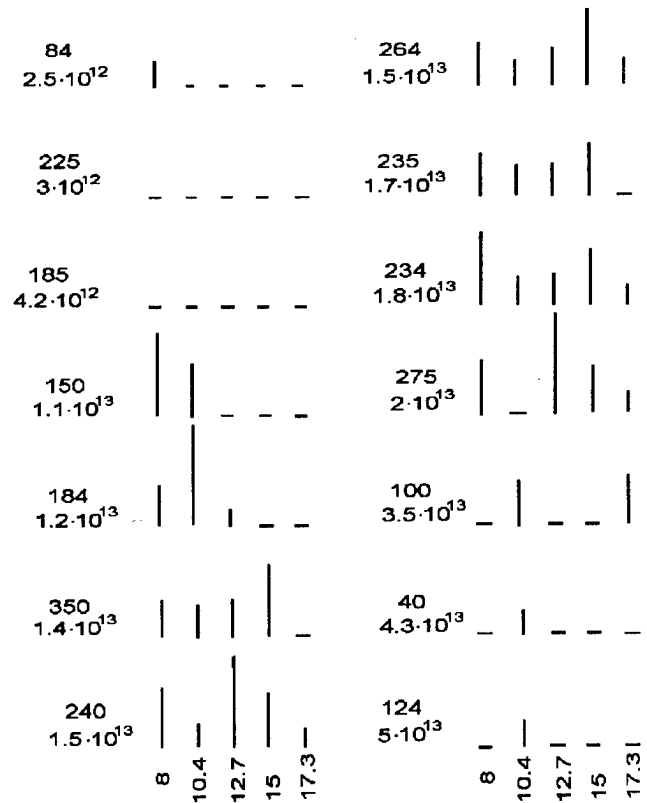


Figure 3.

is seen that the radiation frequency band is below 8GHz near the n_p -threshold of generation. Increasing n_p shifts the spectrum to more high frequencies. At n_p about $1.2 \cdot 10^{13} \text{cm}^{-3}$ the spectrum covers all frequency band of our spectranalyser practically uniformly. At the high plasma density the radiation spectrum is higher the band of spectranalyzer. Under the optimum conditions of wave excitation ($U = 600 \text{keV}$, $I_b = 3 \text{kA}$, $r_p = 0.8 \text{cm}$, $L = 25 \text{cm}$ and $n_p \approx 2 \cdot 10^{13} \text{cm}^{-3}$) the relative frequency width is of the order of $\Delta f/f \approx 0.5$, radiation spectrum extends from 6GHz up to 20GHz and the whole radiation power achieves $200 \div 250 \text{MW}$.

3. COMPARISON OF EXPERIMENTS WITH NUMERICAL SIMULATION

In the steady-state model the microwave radiation power in the output of the system was calculated as a function of the wave frequency for several values of plasma density^{2,3,4}. Input parameters such as wave frequency f , power and radial structure of the excitation mode (E_{01}) are given. All calculations were done at $R = 1.8 \text{cm}$ and $r_p = 0.9 \text{cm}$, $r_b = 0.55 \text{cm}$, $U = 0.512 \text{MeV}$, $L = 30 \text{cm}$, $I_b = 3.2 \text{kA}$, which are close to experiment. In the Fig.4 the dependences of the quantity (the linear power amplification) $10 \lg P/P = K$ are presented as a function of f for several values of n_p (1 - $n_p = 3.3 \cdot 10^{12} \text{cm}^{-3}$, 2 - $7.5 \cdot 10^{12}$, 3 - $1.33 \cdot 10^{13}$, 4 - $2.1 \cdot 10^{13}$, 5-

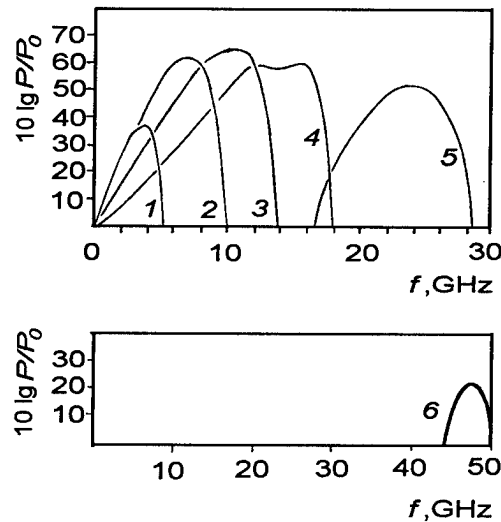


Figure 4.

$4.1 \cdot 10^{13}$, $6 - 8.3 \cdot 10^{13} \text{ cm}^{-3}$). We see that the band of amplified frequencies increases with increasing n_p . The power amplification increases also, while $n_p \leq 2 \cdot 10^{13} \text{ cm}^{-3}$, then it drops with increasing n_p . Up to $n_p = 2 \cdot 10^{13} \text{ cm}^{-3}$ there is a wide band amplification in a frequency range $0 \leq f \leq f_{\max}$, but if $n_p \geq 4 \cdot 10^{13} \text{ cm}^{-3}$ the amplification exists only in the high frequency range ($f_{\min} < f < f_{\max}$) as it is shown in the Fig.4. In the nonlinear and steady-state model the highest output power $P_{\text{out}} \approx 450 \text{ MW}$ was obtained at follows parameters: $I_b = 3.2 \text{ kA}$, $R = 1.8 \text{ cm}$, $r_p = 0.9 \text{ cm}$, $r_b = 0.55 \text{ cm}$, $L = 25 \text{ cm}$ and $n_p = 1.7 \cdot 10^{13} \text{ cm}^{-3}$ and for $f = 12.4 \text{ GHz}$ and $P_{\text{in}} = 20 \text{ kW}$.

In conclusion let us note that a wideband relativistic plasma microwave oscillator was realized. A radiated frequency band corresponds to calculated one for linear and, presumably, for nonlinear amplification coefficient. It means that a system emits the radiation of all frequencies, for which it has a ability to amplify. The reason is that such a amplifier has a big linear amplification coefficient - 60 dB and a nonlinear optimal one substantially below - 30 dB .

The authors wish to thank prof.A.A.Rukhadze and prof.P.S.Strelkov for helpful discussions throughout the course of this investigation.

4. REFERENCES

- 1.M.V. Kuzelez, A.A.Rukhadze, P.S.Strelkov, A.G.Shkvaruhets, "Relativistic plasma microwave electronics", *Uspekhi fiz. nauk*, Vol.146, N4, pp.709-712, 1985.
- 2.A.F.Aleksandrov et all, *Radiotekhnika i elektronika*, Vol.37, N8, pp.152-159, 1982.
- 3.M.V.Kuzelev et all, *Vestnik MGU, serija fizika i astronomija*, Vol.33, N6, pp.3-10, 1992.
- 4.M.V.Kuzelev et all, *JETP*, Vol.101, pp.460-478, 1992.

Multiwave interaction in high-current microwave devices

Alexander N. Vlasov

Moscow State University, Department of Physics
Moscow, 119899, Russia,

Vladimir A. Cherepenin

Institute of Radioengineering and Electronics of Russian Academy of Sciences
Mokhovaja St., 11, Moscow, GSP-3, 103907, Russia

ABSTRACT

Physics processes in multiwave microwave devices are discussed. One of the important peculiarities of high-power microwave devices is multiwave interaction between electron beam and electromagnetic field. Multiwave interaction effects are illustrated for well-known microwave devices such as multiwave Cerenkov's and diffraction generators.

1. INTRODUCTION

Main goal of relativistic microwave electronics is enhancement of coherent output radiation power. This problem can be solved by using high-current electron beams or by optimization of efficiency of electron beam energy transformation to coherent electromagnetic radiation. The spatial development of electrodynamic structure is required in both cases as well in perpendicular direction for limiting current increasing as tapering in longitudinal direction for interaction between electron beam and electromagnetic field optimization. There are two known ways how to provide effective interaction. First, we select one eigenmode of electrodynamic structure and provide interaction with this eigenmode only. Second, to escape mode selection and to provide electron beam interaction with a number of eigenmodes at the same frequency. We are interesting in second type of interaction. The single mode interaction based on usual induced radiation but multiwave interaction based on Rayleigh scattering¹.

2. BASIC DEFINITIONS AND ASSUMPTIONS

We defined multiwave interaction as interaction between electron beam and a set of eigenmodes of electrodynamic structure at certain frequency ω . We assume those eigenmodes satisfy Maxwell's equations and boundary conditions on electrodynamic structure surface. This definition is clear for amplifiers and can be extended to oscillators. In oscillator's case we name processes with a number of resonator's eigenmodes at certain frequency ω that occurred as a result of interaction between electron beam and eigenmodes, see as an illustration figure 1, where spectra of resonator's eigenmodes are plotted and 1,2,3,4 correspondent to different eigenmodes. It is necessary to stress that the identical synchronism conditions are assumed

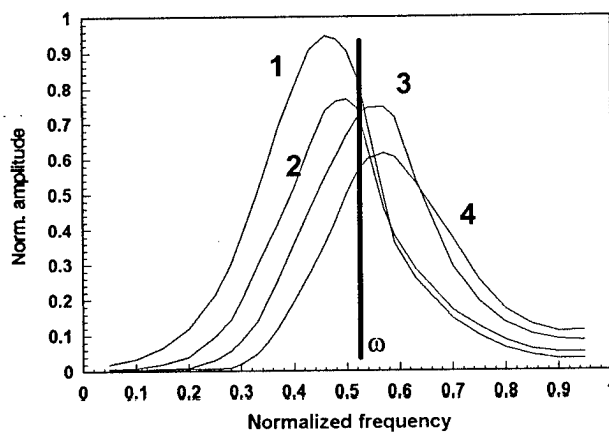


Fig. 1

for all eigenmodes. For example, there are eigenmodes of periodical electrodynamic structure with set of longitudinal wavenumbers $k_{z,i}$, where i is number of eigenmode. The different spatial harmonics with number n are able to provide Cerenkov or cyclotron synchronism. We can summarize synchronism conditions for multiwave interaction as:

$$\Delta_{\min} \frac{c\pi\beta_z}{L} \leq |\omega - (k_{z,i} + \frac{2\pi}{d}n)v_z - m\frac{\omega_B}{\gamma}| \leq \Delta_{\max} \frac{c\pi\beta_z}{L}, \quad (1)$$

where $\Delta_{\min}, \Delta_{\max}$ are minimal and maximum value of detuning, d is period of structure, ω_B is cyclotron frequency, v_z is longitudinal velocity of electrons, L is length of interaction region, $m = 0, \pm 1, \pm 2, \dots, n = 0, \pm 1, \pm 2, \dots$ are possible values of indexes for different kind of synchronism conditions, m, n should be constant for all eigenfunctions involved in multiwave interaction.

It is necessary to remark that we should to use different definitions for v_z and $k_{z,i}$ in low efficiency and high efficiency cases. In the simplest case of low efficiency (low signal approximation) when :

$$\max_{0 \leq z \leq L} |\Delta v_z| \ll v_{z,0}, \quad (2)$$

the synchronism conditions are the simplest and set of interacting eigenfunctions can be found from initial parameters. In high-efficiency case $\Delta v_z \sim v_z$ and eigenmodes with k_z different from set of k_z found from initial parameters will be able to interact with electron beam under the same synchronism conditions.

There are different approaches for multiwave interaction theoretical description. The rigorous solution of this problem includes Maxwell's equation and equation of motion simultaneous solution. However, usually it is more simply to use formalism based on coherent electron bunches radiation. It is convenient to use electromagnetic field representation as sum of eigenmodes synchronous with electron beam. For amplifier's model the direct solution of Maxwell's equations at certain frequency ω is useful. There are exact solutions of Maxwell's equations for diffraction problems too. For non-stationary models of multiwave interaction we can select the processes that provide coherent radiation at ω frequency. There are non-stationary solutions refer to mode competition, stochastic oscillations, etc. We are not interesting in this kind of solutions here. We can use the peculiarities of electron bunch coherent radiation for multiwave devices designing and parasitic generation suppression. The multiwave devices efficiency is higher than efficiency of common relativistic devices. It is can be explained easily: when electrons go out interaction under one mode synchronism condition they will interact with different mode under similar synchronism condition. We will discuss some examples of high-current devices based on multiwave interaction.

3. MULTIWAVE CERENKOV GENERATOR

Multiwave Cerenkov generator (MWCG)² is typical example of multiwave high-current devices. High output power MWCG can be based on electron beam with high electron's energy (1-2 MeV) and high current (tens kA). High operating current requires a high transverse size of hollow cylindrical beam. Therefore, the following conditions are common for MWCG:

$$D \gg \lambda, L \sim D, \quad (3)$$

where D – is diameter, L – is length of MWCG electrodynamic structure, moderate value of electron's energy ($\gamma \approx 3 \div 4$) is reason for the second condition. The MWCG electrodynamic system consists on two sections of overmode corrugated waveguide and smooth walled drift section separating these two sections. There are a number of

axially symmetrical and non-symmetrical modes of this structure with longitudinal wavenumber satisfied to Cerenkov synchronism condition. The distance between longitudinal wavenumbers of two nearest modes ($k_{z,i} - k_{z,i-1}$) is smaller than $\frac{\pi}{\gamma^2 L}$ under conditions:

$$L < 0.1 \left(\frac{\pi R}{\gamma d} \right)^2 d \quad (4)$$

The factor 0.1 will increase up to one if we will take into account both symmetric and non-symmetric modes. It is mean that interaction between electron beam and electromagnetic field in MWCG is always multiwave.

The electrodynamic structure of MWCG is open system with high diffraction losses. Numerical simulation of MWCG^{2,3} shown that transverse distribution of electromagnetic field is changed along longitudinal axis. This dependence of transverse and longitudinal distributions of electromagnetic field along longitudinal axis is due to electron beam loading. Electromagnetic field in this case can not be represent as single eigenmode of periodically corrugated waveguide or eigenmode of open resonator. Experimentally measured directivity diagram of MWCG output radiation^{2,3} was essentially different from certain eigenmode directivity diagram. However, spectrum of MWCG output radiation is monochromatic with 0.5% accuracy⁴.

4. MULTIWAVE DIFFRACTION INTERACTION

Physical processes in microwave devices based on Smith-Purcell (diffraction) radiation^{2,5} is more complicate than in MWCG. The main reason is simultaneous excitation of volume and surface component of electromagnetic field. Amplitudes of surface and volume electromagnetic field components are changed versus frequency. The most sufficient changes occur near resonant frequencies. There is resonance near Wood's anomalies conditions:

$$\frac{d}{\lambda} = \frac{|n|\beta_z}{1 + \beta_z}, \quad (5)$$

where $|n|$ — is absolute value of spatial harmonic number, and near internal " $n\pi$ " type resonance of periodic structure:

$$\frac{d}{\lambda} = \frac{|n|\pi}{2}, \quad (6)$$

these two resonant wavelengths are approximately equal for relativistic electron beams.

Peculiarities of electromagnetic field in open periodical structures can be illustrated by electromagnetic field in open structure consist on N circular cylinders infinitely long in perpendicular direction. This electrodynamic structure is excited by pre bunched at frequency ω electron beam. Integral equation's technique is used :

$$\frac{1}{2} u(P) + \frac{1}{2\pi} \int_S G(P, Q) u(Q) dQ = u_0(P), \quad (7)$$

where S — are surfaces of cylinders, $u(P), u_0(P)$ — surface current distribution and exciting current, $G(p, Q)$ — scalar Green's function. We assumed amplitude of electron beam bunching constant and calculate by using Green's function electromagnetic field near surface, because this part of electromagnetic field provides interaction with electron beam. Sufficient increasing of electromagnetic field amplitude is obtained at frequencies correspondent to resonance conditions (5),(6) for infinitely long periodic structure. The most important difference between electromagnetic fields in infinitely long structure and finite length structure is continuous spectrum of longitudinal wavenumbers for finite structure against discrete for infinitely long. In case of finite length structure we should to take into account a set of planar waves or continuous spectrum of planar waves. The calculated spectrum of electromagnetic field near structure is presented on figure 2. The spectral distribution of surface and volume components of electromagnetic field are different. The bandwidth of wavenumbers is dependent not only on number of cylinders but on cylinder's radius, ratio of operating frequency to resonant frequency. It is necessary to remark that bandwidth $\Delta k_z / k_{z,0}$ near resonance is greater than $1/N$ to 2+5 times. Parameters of electrodynamic structure correspond to surface wave excitation for infinitely long structure,

but there is volume electromagnetic field in finite length structure. The main part of volume field is radiated to directions located near direction of electron beam propagation and opposite direction.

All these resonant effects exist in corrugated overmode waveguide sections used as electrodynamic structure of relativistic diffraction generators. In this case quality factor Q decrease sufficiently, up to 10^3 times due to near-axis radiation. The directivity diagram is formed by direct radiation from corrugated surface to free space what is very different from usual eigenmodes radiation. The experimental measurements of diffraction generator's radiation directivity diagram shown that the direction of maximum radiation is different from direction of maximum radiation for any eigenmode of electrodynamic structure.

This direction is correspondent to direction of maximum radiation from finite length periodic structure.

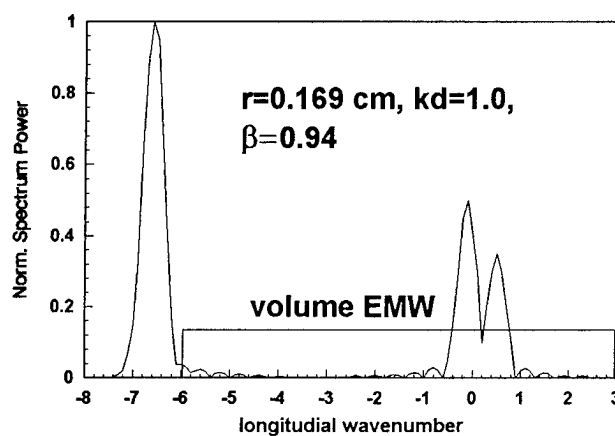


Fig. 2

5. REFERENCES

1. V.A.Cherepenin, "Multiwave relativistic electron devices: progress and prospects", *Proc. of 9th Intern. conf. on high power particle beams, BEAMS-92*, Vol. III, pp. 1596-1600, Washington DC, 1992.
2. S.P.Bugaev, V.I.Kanavets, V.I.Koshelev, B.A.Cherepenin, *Relativistic multiwave microwave generators*, Nauka, Novosibirsk, 1991 (in Russian).
3. S.P.Bugaev, V.A.Cherepenin, V.I.Kanavets, A.I.Klimov, A.D.Kopenkin, V.I.Koshelev, V.A.Popov and A.I.Slepkov, "Relativistic multiwave Cerenkov generators", *IEEE Trans. on Plasma Science*, Vol. 18, pp. 525-536, June 1990.
4. D.K.Abe, T.Antonsen Jr., Y.Carmel, B.Levush, S.M.Miller and A.Bromborsky, "Recent results from the University of Maryland overmoded BWO and MWCG program", *Proc. of 9th Intern. conf. on high power particle beams, BEAMS-92*, Vol. III, pp. 1607-1612, Washington DC, 1992.
5. S.P.Bugaev, V.A.Cherepenin, V.I.Kanavets, V.I.Koshelev, V.A.Popov and A.N.Vlasov, "Investigation of millimeter-wavelength-range relativistic diffraction generator", *IEEE Trans. on Plasma Science*, Vol. 18, pp. 518-524, June 1990.

A 400 kV, 400 A microsecond electron accelerator with a hot cathode

N.I.Zaitsev, E.V.Ilyakov, G.S.Korablyov, I.S.Kulagin

Institute of Applied Physics, Nizhny Novgorod, Russia

The description of an electron accelerator of microsecond pulse duration and the results of experiments with a relativistic carcinotron and a gyrotron, carried out on its base, is submitted in the report.

A three-electrode magnetron-injection gun¹ forms a hollow electron beam either with rectilinear or with helical trajectories of electrons, depending on magnitude and configuration of the magnetic field and also on potential distribution at the electrodes. Configuration of the gun electrodes is shown in Fig. 1. The electron beam diameter is in the range of 10-40 mm at the wall thickness being in the range of 1-4 mm respectively. A relatively low-temperature barium-aluminate cathode maintaining the emission current density to be not less than 10 A/cm^2 at the heating temperature of 1150°C , is used. The scheme of the accelerator is shown in Fig. 2. The cathode heating is carried out by a heater which is fed by a transformer with a secondary winding being one turn of a high-voltage cable with 500 kV insulation. The secondary winding passes through 10 toroid cores with primary windings connected in parallel. Heating power is controlled by varying the repetition rate of pulses from a special oscillator.² The nominal heating power of the cathode with an emitting belt diameter of 100 mm accounts for 1.2 kW.

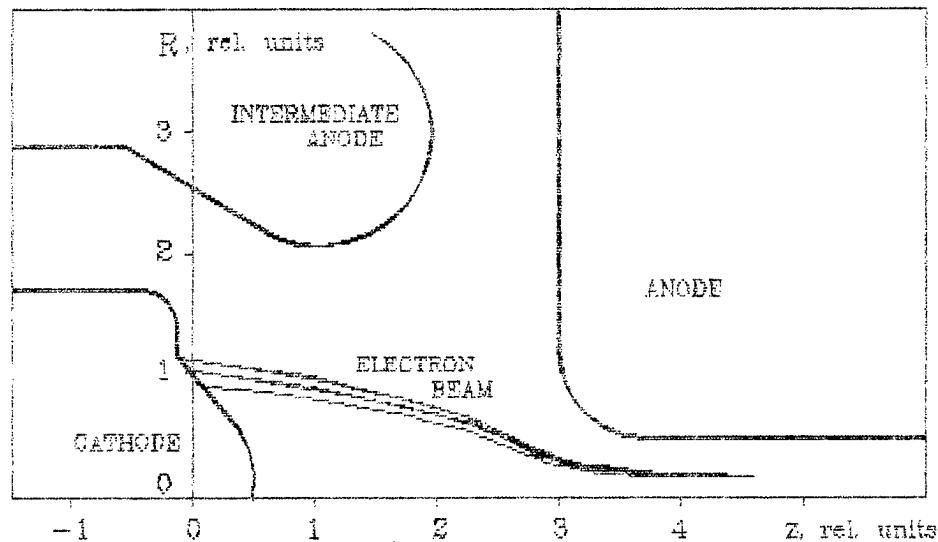


Fig. 1. Configuration of gun electrodes

Mutual disposition of the gun electrodes is fixed by a sectioned insulator that consists of alternating aluminium and porcelain rings. Electric potential is distributed along the insulator sections by a resistive divider with total resistance $10 \text{ k}\Omega$.

The vacuum system evacuation up to pressure of the order of 10^{-7} mm Hg is carried out by cryogetter pumps.

An 11-sectioned Marx generator with two-sectioned forming circuit that makes pulse flat-top inhomogeneity to be no more than $1.5\%^3$ is used as a high-voltage source.

Depending on forming circuit parameters, the accelerator can operate in two regimes with the following maximum parameters:

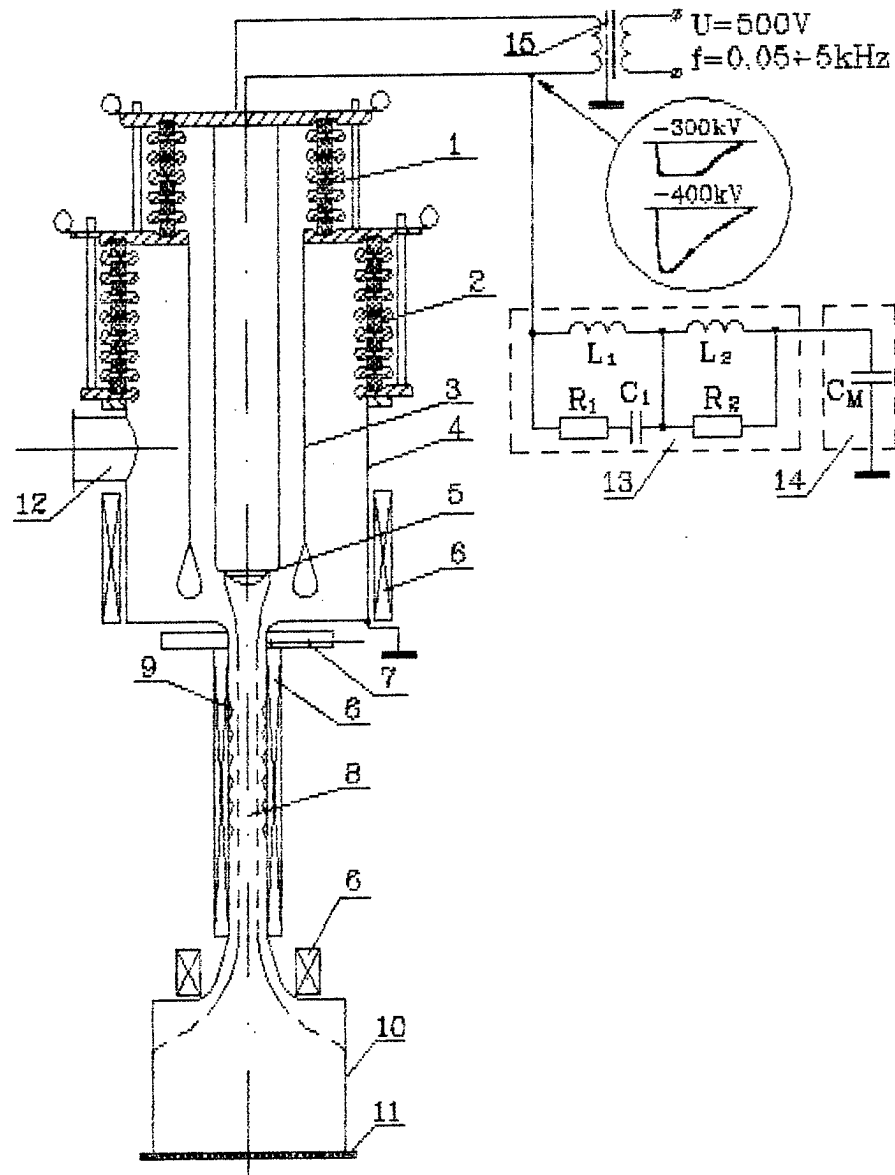


Fig. 2. Scheme of the accelerator: 1 - cathode insulator; 2 - anode insulator; 3 - intermediate anode; 4 - vacuum casing; 5 - cathode; 6 - coils; 7 - valve; 8 - drift channel; 9 - slow-wave structure; 10 - collector; 11 - window; 12 - pipe branch for pumping out; 13 - forming line; 14 - Marx generator; 15 - cathode-heating transformer

1) energy of electrons 300 keV, current 300 A, pulse flat-top duration 7 μ s;

2) energy of electrons 400 keV, current 400 A, pulse flat-top duration 1 μ s. Beam current density reaches 350 A/cm² in the latter regime.

The investigation of a beam with rectilinear trajectories of electrons has shown that the current-density radial distribution was close to a right-angled one in the space-charge current limitation regime (Fig.3). These measurements were carried out by means of a sectioned collector consisting of four diaphragms with sequentially decreased diameters of the holes. The spread in longitudinal velocities, measured by the reflecting potential method for the modeling regime did not exceed 2%.

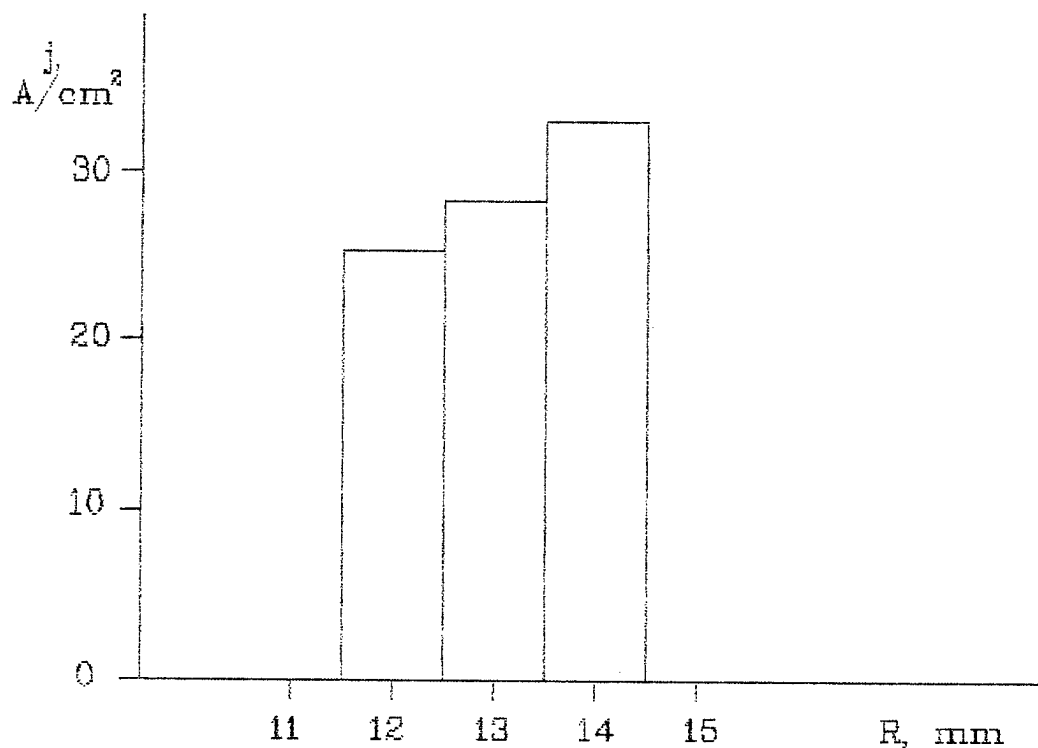


Fig. 3. Current density distribution in the regime of space-charge limitation depending on radial coordinate at the accelerating voltage of 115 kV.

The formed rectilinear beam has been used to excite a relativistic carcinotron operating at wavelength of 6.5 cm and at E_{01} mode. For beam current of 260 A and voltage of 230 kV one has obtained the radiation corresponding in its pulsewidth to total duration of the high-voltage pulse and having pulse energy 60 J (7 MW, 9-10 μ s, efficiency 12%). This microwave pulse is shown in Fig. 4.

The beam with helical trajectories of electrons has been used to excite a gyrotron operating at H_{01} mode and wavelength of 1.5 cm (this gyrotron was counted on and designed by an IAP employee S.V.Samsonov). At the regime of 200 kV, 17 A one has obtained radiation of power of 1.2 MW, efficiency of 35% and pulsewidth corresponding to the total duration of a high-voltage pulse.

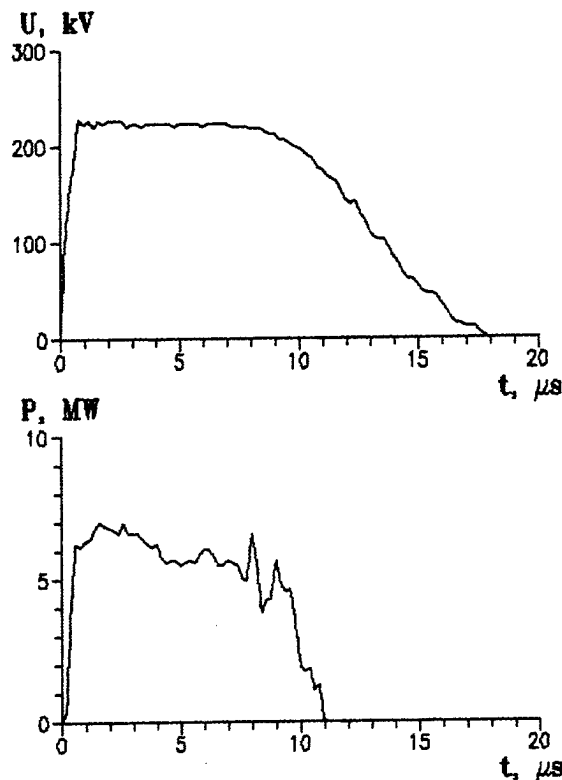


Fig. 4. High-voltage and microwave pulses for the relativistic carcinotron experiment

As it was to be expected, the H_{01} mode, that is free from electric microwave fields at the cavity walls, had the maximum breakdown strength of all the modes that can be excited in the gyrotron cavity. Further output power increase for the devices of both types has resulted in shortening of the radiation pulsewidth owing to the RF breakdown.

REFERENCES

1. I.K.Batrak, V.N.Glazman, N.I.Zaitsev et al., "Thermoemission gun with a high magnetic compression of a hollow microsecond 400 kV, 400 A electron beam," In: *Proceedings of the 8-th Int. Conf. on High-Power Particle Beams (Beams'90), Novosibirsk, USSR, July 2-5, 1990*. Eds. B.N.Breizman, B.A.Knyazev, Vol.1, pp.581-585, World Scientific, Singapore, 1991.
2. E.A.Kopelovich, V.V.Bondarenko, "A hot cathode supply," *Pribory i tekhnika eksperimenta*, N1, pp.146-148, 1990.
3. B.Z.Movshevich, M.Yu.Kryl'tsov, "A generator of high-voltage pulses with small inhomogeneity of a flat top," *Pribory i tekhnika eksperimenta*, N2, pp.128-132, 1986.

Radio-frequency interference generated by high voltage system with vacuum insulation

Waldemar ZIOMEK, Hanna MOŚCICKA-GRZESIAK

Technical University of Poznań, The Institute of Electrical Power Engineering
3a Piotrowo Str., 60-965 Poznań, POLAND

ABSTRACT

The paper presents a problem of radio-frequency interference (RFI) generated by complex high-voltage insulating system, i.e. extinguishing chamber of vacuum interrupter. A typical RFI measurement system with receiving antenna has been used to investigate prebreakdown phenomena in the extinguishing chamber. The experimental results allow to decide whether the vacuum chamber may be a source of RFI. Moreover, a strong relation between breakdown voltage and the RFI level in prebreakdown stage has been shown.

1. INTRODUCTION

Radio-frequency interference (RFI) is a term for short pulse voltage and current oscillations. RFI may propagate in the air as an electromagnetic wave or move along transmission line wires as a current wave. In this case, wires act as a waveguide and as a transmitting antenna. RFI may be singularly troublesome. In particular it affects the quality of RTV reception and the work of data transmission systems. It may also disturb the work of control systems and the work of computer equipment. All kinds of partial discharges in solid and fluid insulation, corona discharge, microdischarges in reduced-pressure gas insulation and in vacuum could be the sources of potentially very strong interference. For that reason, the work voltage of a high-voltage device ought to be much lower than the voltage at which partial discharges occur. The RFI generated by a high-voltage object may be considered an unwanted phenomenon, to be reduced or eliminated. On the other hand, however, the RFI is a useful source of information about the insulating system, since the interference results from different kinds of partial discharges. In general, two methods of measuring interference are used. In the first, a system of receiving antennas is used to measure the electromagnetic field of interference in space. In the second method, the voltage drop on measuring impedance is measured, caused by the interference current in the wire. The first method allows for remote measurement, while in the second method the RFI generating object must be connected with a RFI meter. In open space only the first method is used. In an electromagnetic insulated lab both methods may be used [1].

The research has been carried out for the extinguishing chamber of a vacuum interrupter. For long vacuum gap (over 10 mm) and also in some cases for interelectrode distances from transient area (1 ... 10 mm), the most characteristic prebreakdown phenomena are microdischarges. Microdischarges appearing in vacuum insulating system are accompanied by optical effects, x-rays, electromagnetic waves and pulses of current in an external circuit. Measurements of the parameters describing phenomena accompanying microdischarges render possible determination of microdischarges intensity. In this paper the electromagnetic field of RFI generated by microdischarges has been analysed. A typical RFI measurement system via antenna has been used to investigate prebreakdown phenomena in the extinguishing chamber for the voltage level much higher than the rated voltage. On the other hand, the RFI has been also investigated for rated voltage, for nominal interelectrode distance. The results of the latter experiment allow to decide whether the extinguishing chamber of the vacuum interrupter may be a source of RFI.

2. THE EXPERIMENT

The interference field was measured by an analog RFI meter (the measuring range 0.14–300 MHz, voltage range 0–120 dB where 0 dB corresponds to 1 mV). The RFI meter is a selective microvoltmeter yielding the quasi-peak value of the input voltage. The meter was used to measure the voltage induced in the measuring antennas. The interference level, measured for frequency which was being changed in a continuous way, was automatically recorded by an X-Y recorder. In general, the level of interference generated by the tested objects decreased with the increase in the measuring frequency. Beyond the 30 MHz frequency the RFI level dropped below 0 dB. Therefore the investigations were conducted for the frequency range 140kHz–30MHz.

In order to suppress the RFI propagating in the air, the test room was specially shielded. The walls, floor and ceiling were covered by a 1 mm thick steel sheet, which ensured the suppressing of the magnetic component of the interference

field. Next, all surfaces were additionally covered by $0,1\text{ mm}$ aluminum foil, in order to improve the suppression of the electric component of the interference field. To suppress the interference current in the supply network wires, low-pass LC filters were used, while the RFI meter was supplied from a V-type artificial network. Also, only 30% of the voltage range of the 100 kV (rms) , 50 Hz test transformer was used to ensure an appropriately low level of partial discharges in the said transformer (about 0.05 pC) [2].

In order to reduce the corona discharge in the high-voltage part of the measuring system, large diameter pipe wires were used, and electrodes which control the electric field distribution were placed on the wire connectors. All elements of the measuring equipment and additional equipment were carefully one-point grounded by very short copper wires [3].

The tested object was the extinguishing chamber of a vacuum interrupter. The rated voltage of the chamber was 12 kV , and the rated current was 630 A . The contacts were made of Cu-Cr sinter material. The nominal distance of contacts was 12 mm , but there was possible to change the contacts distance from 0 to 14 mm during the experiment. In the extinguishing chamber, for high enough voltage there can appear various kinds of partial discharges, between open contacts, on the outer surface of the insulating envelope (in the air) and on its inner surface (in vacuum). Partial discharges are one of the causes of RFI.

3. RESULTS OF THE EXPERIMENT

The experiment was conducted by measuring the voltage induced in an antenna by the interference electromagnetic wave. The wire antenna used was placed 0.5 m away from the tested chamber. Fig.1 shows the level of interference generated by the extinguishing chamber for frequency ranging between $0.1 \dots 30\text{ MHz}$. The interelectrode distance in the chamber was 6 mm and voltage was 30 kV . Fig.2 presents, for chosen range of measuring frequency, the level of RFI generated by investigated object and additionally the level of RFI produced by background. The level of the latter interference is very low and therefore proves that the test room and the measuring system were well prepared for the experiment. The high level of interference generated by the extinguishing chamber is due to the fact that the voltage was $2,5$ times higher than the rated voltage, and the interelectrode distance 2 times shorter than the rated distance. For nominal rating, i.e. 12 kV voltage and 12 mm interelectrode distance, the interference generated by a well conditioned chamber was too small to be measured.

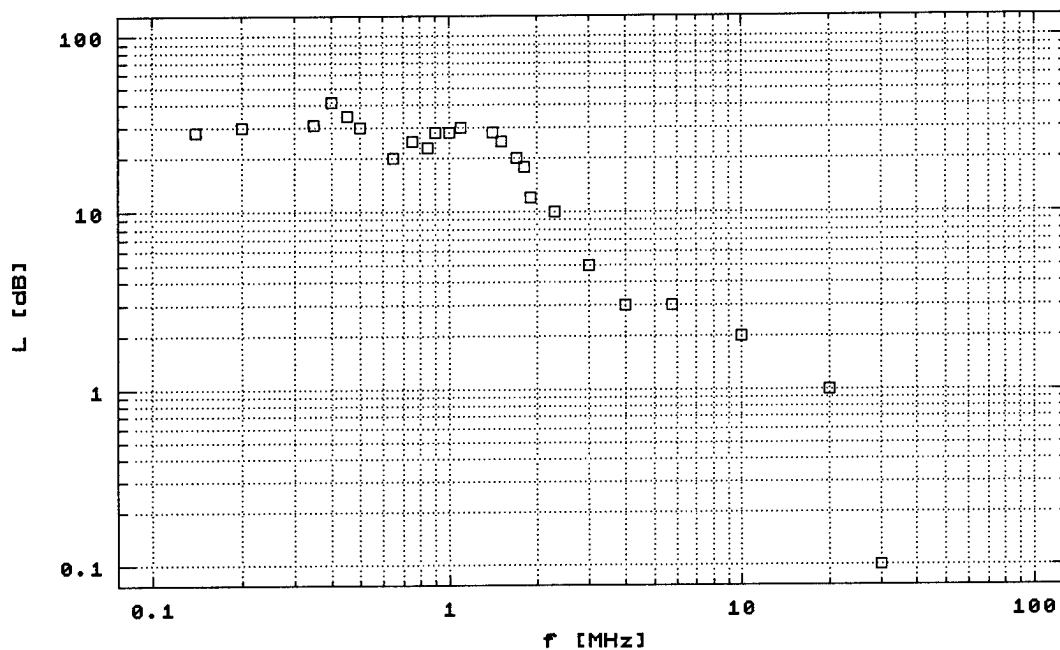


Fig.1. The level of RFI generated by extinguishing chamber of vacuum interrupter under voltage of 30 kV , interelectrode distance 6 mm , measuring frequency $0.14 \dots 30\text{ MHz}$.

The application of the RFI measurement method yields valuable information about the state of a high-voltage system with vacuum insulation. Electric strength is a very important quantity characterizing a high-voltage insulating system. Electric strength in vacuum, however, is an ambiguous notion. In a series of breakdowns, almost each breakdown occurs for the higher voltage value than previous one. The conditioning effect is observed. The electric strength measurement procedure actually changes the said electric strength (Fig.3). Therefore other quantities characteristic for the prebreakdown stage are needed, such that there is a definite relationship between these quantities and the electric strength. Moreover, the measurement of these quantities must not change the state of the system [4]. For purpose of this research as prebreakdown quantity describing the insulating system state, the level of RFI generated by a vacuum chamber under preselected voltage in prebreakdown stage has been chosen.

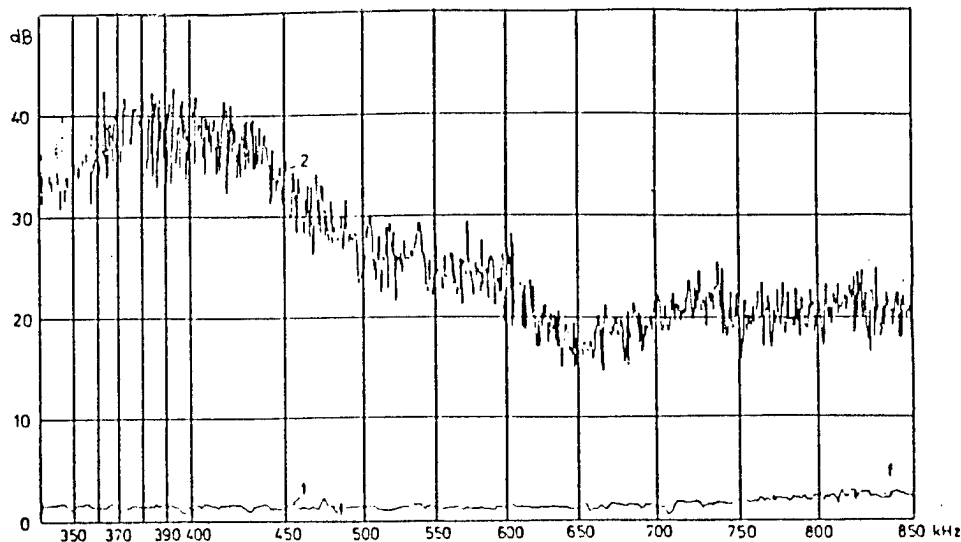


Fig.2. The level of RFI generated by background (1) and the vacuum chamber (2) under 30kV, interelectrode distance 6mm, frequency range 300 ... 850 kHz.

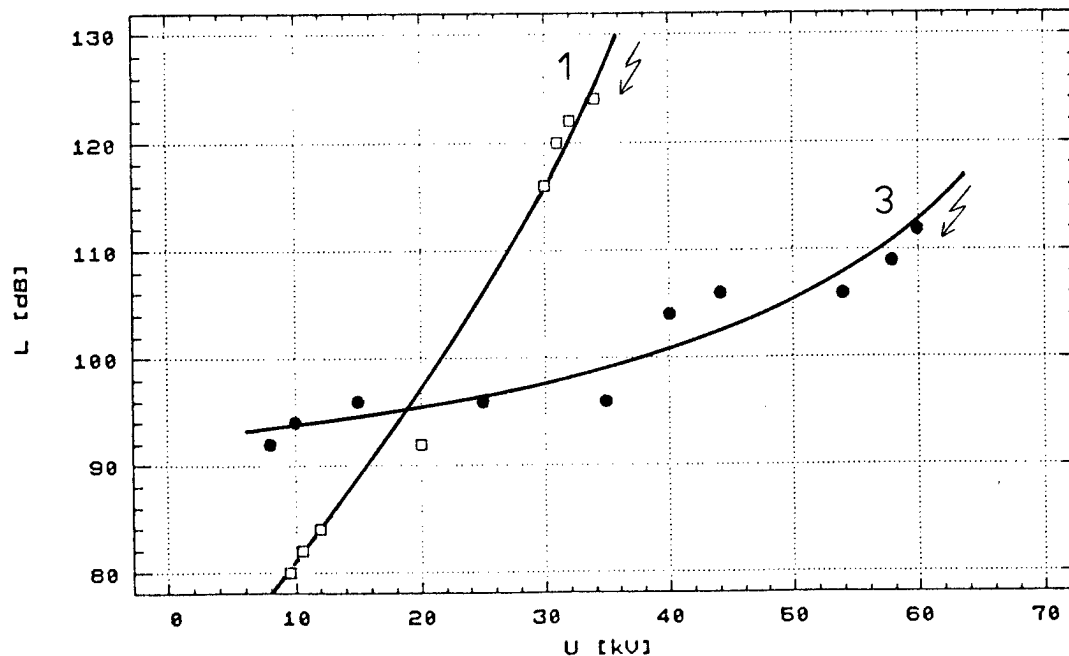


Fig.3. The level of RFI generated by the vacuum chamber at frequency 180 kHz, interelectrode distance 6 mm, characteristics before first breakdown (1) and third breakdown (3).

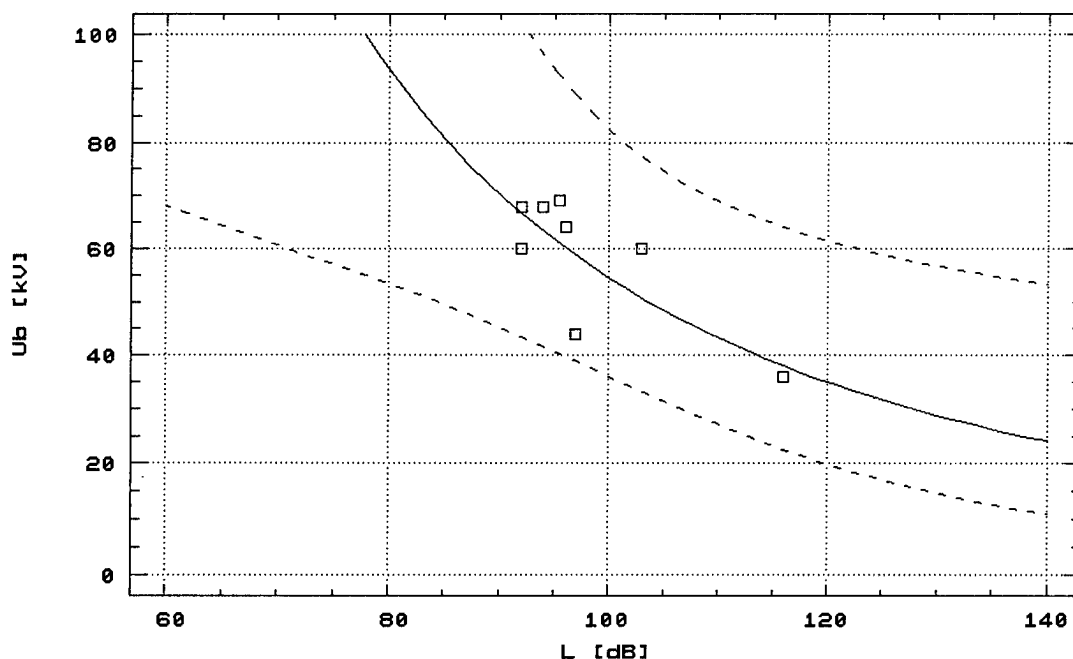


Fig.4. Relation between breakdown voltage U_b [kV] and the level L [dB] of RFI generated by the vacuum chamber in prebreakdown stage at 30 kV, measuring frequency 180 kHz, interelectrode gap 6 mm

$$U_b = 3.27 \cdot 10^6 L^{-2.42} \quad \text{at } r^2 = 0.62$$

The experiment shows that there exists a relation between breakdown voltage in vacuum and the RFI level in prebreakdown stage (Fig.4). The big value of the determination coefficient proves the existence of a close relation of the breakdown voltage to the RFI level in prebreakdown stage. Therefore it may be expected that the measurement of the RFI level in the extinguishing vacuum chamber will allow to predict the breakdown voltage. Moreover, there is a possibility of a distant reading of the measurement results, without connecting the tested object to the measuring system. This is an additional advantage of the measuring procedure.

4. CONCLUSIONS

The investigations of the RFI generated by the extinguishing chamber of the vacuum interrupter yielded the following results: (i) For zero current and for open contacts, the interference level depends strongly on the interelectrode distance and on the voltage. (ii) For nominal rating, i.e. 12 kV voltage and 12 mm interelectrode distance the RFI generated by a well conditioned chamber is too low to be measured. However, when the interelectrode distance decreases and the voltage increases, the interference increases up to tens of dB (50 – 60 dB for the 30 kV voltage). The RFI measurement method may be successfully used to investigate prebreakdown phenomena in high-voltage systems with vacuum insulation. The investigations have shown a strong relation between the breakdown voltage in vacuum and the RF interference level measured at preselected voltage in prebreakdown stage of the system.

REFERENCES

- [1] CISPR Publication 1. "Specification for CISPR radio interference measuring apparatus for the frequency range 0.15 MHz to 30 MHz", Geneva, 1963
- [2] W. Ziomek "Relation between breakdown voltage and parameters characterizing prebreakdown phenomena in selected vacuum insulating systems" (Polish), Ph.D. thesis, Technical University of Poznań, 1992
- [3] N.Hylten-Cavallius, High Voltage Laboratory Planning, ASEA – Haefely, 1986
- [4] W. Ziomek, H.Mościcka-Grzesiak, "Relations of breakdown voltage and prebreakdown microdischarge parameters in vacuum", IEEE Transaction on Electrical Insulation, Special Issue, 1993

SESSION 10

Commercial Application and Opportunities

Project of a microwave amplifier based on a compact high voltage modulator

E.B. Abubakirov, M.I. Fuchs, N.F. Kovalev, N.I. Zaytsev
Institute of Applied Physics, Nizhny Novgorod, Russia
J.P. Brasil, G. Jean-Francois, M. Simon
Thomson - Shorts - Systemes, France

ABSTRACT

The subject of the project is to develop a version of a high-power pulse microwave amplifier similar to the conventional travelling wave tube (TWT or TWA) on the basis of a relativistic electron beam emitted by a field emission electron gun. Anticipated parameters of the system are: electron beam energy 0.8 MeV, beam current 7 kA, radiation frequency 9.3 GHz, microwave output power up to 1 GW, microwave pulse duration 50 ns, gain about 40 dB.

1. GENERAL PROBLEMS OF HIGH-CURRENT MICROWAVE AMPLIFIERS

The demand of powerful microwave sources with controlled amplitude and phase for supercolliders, radars with high resolution and other applications has made a recent impact to the research in the field of powerful nanosecond amplifiers, which use high-current relativistic electron beams. Design of a powerful relativistic amplifier requires that the following problems should be solved:

- elimination of possible high-frequency breakdowns in the electrodynamic system (electric reliability);
- spatial coherence of radiation;
- operation in the short-pulse regime;
- reduction of the interference with inherent noises of an intense electron beam;
- high amplification coefficient (40 dB and higher).

One of the most important problems in high-frequency relativistic electronics is the problem of making the system stable to high-frequency breakdowns, which change the electrodynamic characteristics of the interaction space (increase of electric reliability). The most fundamental way to increase output power preserving electric reliability is to expand the transverse dimensions of the interaction space and the cross-section of the output waveguide line while retaining the values of high-frequency fields, current density in the electron beam and the flow of high-frequency power.

The use of over-sized electrodynamic systems is hindered by the problem of providing spatial coherence of the fields in the interaction space, and, accordingly, coherence of the output radiation. The ways to provide the coherence somewhat differ in oscillators and amplifiers [1]. The problem can be solved for oscillators by application of this or that method of mode selection, i.e., by conditioning the appearance of only one mode: a self-consistent structure with a high temporal increment. For amplifiers this problem can be solved by mode filtration, which is understood as providing conditions for spatial increase of only one self-consistent structure of the field. Coherence of the output radiation is one of the most complicated problems and there are no universal receipts for its solution. As a rule, the way to filter out (to select) modes is chosen for each specific developed device individually.

The need for a high amplification coefficient is caused by a considerable difference between the characteristic power of relativistic electron beams (1-10 GW) and the expected level of the amplifier's output microwave signal, on the one hand, and the power of possible sources of the primary signal (less than 1 MW, if one takes into account traditional electron microwave devices), on the other. Note that high amplification adds to the risk of spurious self-excitation of the amplifier, which is possible in over-sized systems not only at the operating wave, but at other eigenmodes of the electrodynamic structure, too. Besides that high amplification is impeded by high level of inherent noises of electron beam injected by field emission electron gun.

It is evident that integrated solution of the problems that have been mentioned is possible, as a rule, only as a trade-off of high amplification coefficient against resistance to self-excitation, of narrowing of the operation frequency band to reduce the

influence of the beam self-noises against adaptivity of the device (resistance of the system to variations of beam parameters), etc..

2. SECTIONED DEVICES

A perspective way to achieve simultaneously high amplification and spatial coherence is to divide the interaction space into separate sections resistant to self-excitation [2]. By that, the sections may perform various functions in the device and be connected only by the electron beam. Each section can have its own set of modes, and the matched work of all sections in this case is possible only when the band of the operating mode in a separate section overlaps with amplification bands of the neighboring sections. The number of mode combinations that can provide matched functioning of all the sections lowers fast with an increase in the number of sections, thus the selective work of the device can be achieved. Besides, the use of separate selective sections in the device also enhances selective properties of the whole device.

One of the simplest versions of sectioned amplifier is a cascade joint of TWT and BWO modulator (backward-wave oscillator operating as amplifier below the excitation threshold) [3,4]. The BWO, due to its internal feedback, has high adaptive quality as to variations of parameters of the electron beam. Selectivity is provided by narrowing the BWO amplification band $\Delta\lambda/\lambda \sim 1 - J/J_{st}$, when the BWO works in the regime of regenerative amplification (amplifier with positive feedback) and the operating current, J , approaches the start current J_{st} . At the same time, the BWO amplification coefficient also grows $G \sim (1 - J/J_{st})^{-1}$.

The amplification band and amplification coefficient are limited only by instability of the high-voltage modulator and corresponding instabilities of the electron beam parameters, which keeps the system from coming as close to the self-excitation threshold as possible. It is natural, then, that the BWO is calculated such as to make the start current of the operating mode lower than the start currents of other modes.

3. VERSION OF AN AMPLIFIER BASED ON A COMPACT HIGH-VOLTAGE MODULATOR

It is supposed the designed accelerator will be power-supplied by a high-voltage modulator [5] with the following parameters:

output voltage	up to 1.2 MV,
pulse energy	up to 3 kJ,
erected capacitance	4.17 nF,
series inductance	less than 1 μ H.

When the modulator works with an active 50 Ohm load, pulse duration is about 150 ns with front duration less than 50 ns. Low inductance of the modulator due to compact design permits to feed electron gun of the amplifier without adding of pulse forming elements.

The operation range of the amplifier (X-band) combined with the source's being high-current (pulse current of the load up to 20 kA) gives grounds to think that the most expedient version of the amplifier is a device of the Cherenkov type with a rectilinear electron beam. Among the Cherenkov relativistic devices the most suitable scheme for an amplifier based on the high-voltage modulator is the scheme with a modulating BWO and an amplifying TWT section. A relativistic amplifier of a similar type for the 3-cm wavelength band with output power up to 100 MW was developed and tested experimentally at the IAP, RAS [3]. This version of the amplifier is advantageous for

- possibility to achieve strong amplification by means of sectioning the system;
- adaptivity of the sections to variations of beam parameters;
- relative simplicity of the system forming the electron beam;
- possibility to form the required structure of the output radiation by choosing a suitable wave in the output section;
- possibility to use microwave input space as the drift channel for the electron beam.

We propose to use for amplifier the following disposition of section (Fig.1):

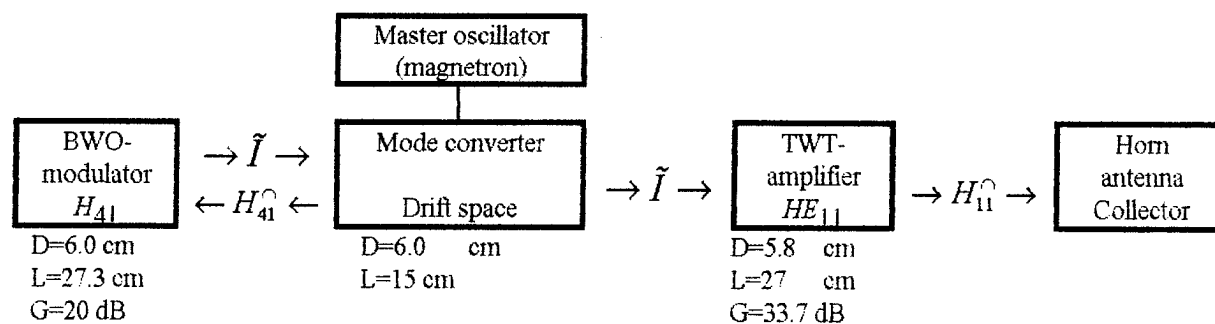


Fig. 1. Block diagram of the amplifier project design,
D is waveguide diameter, L is section length, G is "linear" amplification

The following values will be assumed as initial for the project of the amplifier:

working wavelength	3.25 cm;
energy of electrons in the beam	0.8 MeV;
beam current	7 kA.

The working wavelength at the present stage is determined mainly by the parameters of the primary generator. The value for the energy of beam electrons is chosen such as to have possibility to tune the amplifier by changing the modulator voltage. Electron beam current was limited by 7 kA to simplify the conditions for beam transportation through the working channel (the current is low as compared to the limiting value) and to realize the regime of operation with relatively low parameters of the high-frequency space charge.

TWT AMPLIFIER. The simplest way to make the structure of the output radiation close to the Gaussian wave beam is to choose as the working wave of the TWT section the lowest hybrid slow HE_{11} wave of the cylindrical corrugated waveguide. With the appropriate choice of waveguide parameters this wave is easily transformed into a structure close to the wave beam in the output horn antenna.

Theoretical analysis and experimental investigations of relativistic microwave generators with similar electrodynamic systems [2] show that working with a slow wave one can realize increments that correspond to the amplification over 1 dB/cm. When the transverse cross-sections of the electrodynamic system was $D \sim 2\lambda$, the output microwave power realized in the studied generators exceeded 1 GW, which proves that the electric reliability of such systems is acceptable. It has been also obtained experimentally that using sufficiently simple means, such as smooth matching transitions at the ends of the corrugated electrodynamic system one is able to realize stable to self-excitation TWT sections with calculated amplification up to 40 dB (in the growing wave).

BWO MODULATOR. BWO is one of the most reliable and adaptive devices that can be used as a pre-amplifier, which converts the input electromagnetic signal into a modulation of an electron beam. It is reasonable to choose one of the whispering-gallery modes of the H_{n1} type as the working mode of the BWO, since such modes have the maximum coupling with the beam. The choice of the magnetic wave is also expedient due to the fact that in the high-frequency input of the amplifier that acts as a drift channel for the electron beam such a wave does not influence the process of high-frequency current formation. For better matching between the sections and simplification of transportation of electron beam it is convenient to use waveguide in the BWO-amplifier with cross section, which is close to cross-section of TWT. Since the diameter of the electrodynamic system of the TWT section is $D \sim 2\lambda$, the most suitable wave for that cross-section will be the H_{41} mode of the circular waveguide, whose ratio between the diameter and the critical wavelength is 1.7.

It is assumed that the BWO will work in the regime of regenerative amplification (amplification with positive feedback) near the start regime of the working mode, for which the start current should be lower than the start currents of other modes. The regenerative regime provides efficient narrow-band generation, and that is an additional factor for mode selection in the

device. When the modulator nears the start parameters, its amplification grows with no limitations. We suppose that in the working regime the modulator will provide amplification of the order of 20 dB.

HIGH-FREQUENCY INPUT AND DRIFT SPACE. The input signal from the primary generator is fed into the BWO through a converter, which converts the H_{10} mode of the rectangular waveguide into the H_{41} mode of the cylindrical one. The converter is a quasi-optical device, in which the wave from the cut of a rectangular waveguide falls on the caustic surface for the H_{41} mode of the cylindrical waveguide. Such a converter can be matched with the electron beam and does not effect its structure actively. This high-frequency input is a drift channel for the beam at the BWO modulator output.

4. ANALYSIS OF AMPLIFIER OPERATION

Nonlinear analysis of the amplifier operation was performed for the disposition of the sections shown at Fig. 1. The results of numerical investigation of the described version of the amplifier are presented in Figs. 2 and 3 as dependencies of efficiency, output power and amplification coefficient on the power of the input signal. Analysis shows that the proposed version of the amplifier provides the following calculated output characteristics: total amplification up to 45 dB with efficiency over 30%, and output power over 1 GW.

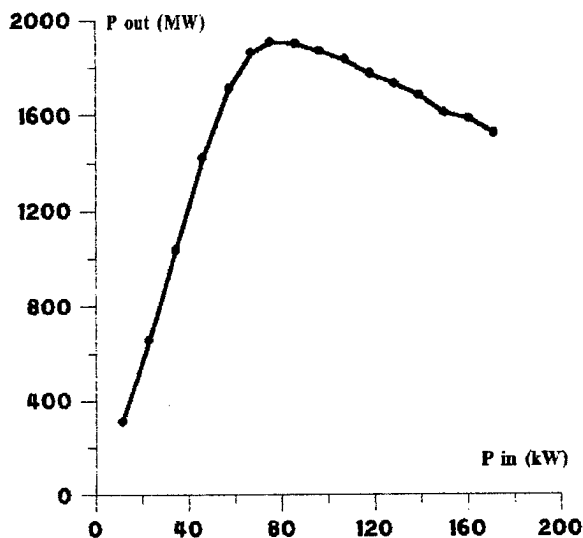


Fig. 2. Output power of the amplifier vs input power

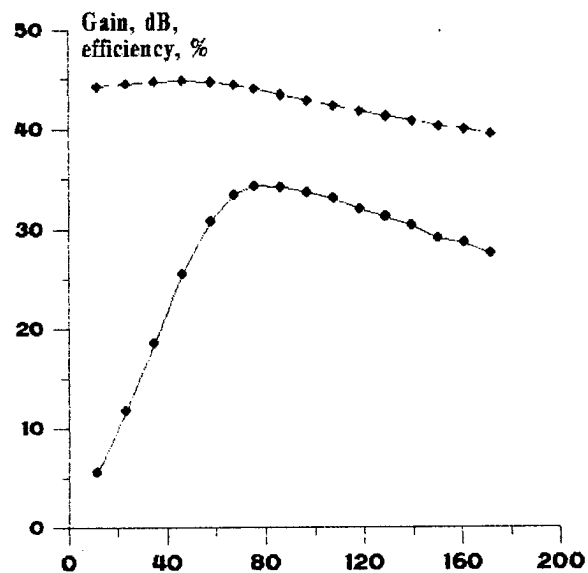


Fig. 3. Gain (◆) and efficiency (●) of the amplifier vs input power

REFERENCES

1. N.F.Kovalev, M.I.Petelin. "Mode selection in microwave relativistic electron generators with distributed interaction." Relativistic microwave electronics (Russian), IAP, AS USSR, Gorky, issue 2, pp.66-100, 1981.
2. E.B.Abubakirov, M.I.Fuchs, V.A.Gintsburg et al. "Cherenkov relativistic oscillators of coherent electromagnetic radiation with multimode sectioned electrodynamic systems". Proc. of "Beams-90" Conf., World Scientific, vol.2, pp.1105-1110, 1991.
3. A.B.Volkov, N.I.Zaitsev, E.V.Ilyakov et.al. "Realization of high gain in power microwave pulse amplifier with explosive emission gun". Pis'ma v Zh.Tekh.fiz. (Russian), vol.18, no.12, pp.6-10, 1992.
4. W.Kleen, K.Poschl. "Einführung in die mikrowellen elektronik". S.Hirzel Verlag Stuttgart. vol.2, 1958.
5. O.Becke et al., 8-th IEEE International Pulse Power Conf., San-Diego, pp. 998-1000, 1991.

Pseudospark switches for high power applications

A. Görtler, J. Christiansen, S. Döllinger, K. Frank, U. Herleb, S. Insam, T. Mehr, M. Schlaug, A. Schwandner, R. Tkotz

Department of Physics, University of Erlangen - Nuremberg,
Erwin-Rommel-Str.1, D-91058 Erlangen, Germany

ABSTRACT

In the recent years pseudospark switches (pss) have been developed to replace conventional switches like thyratrons, ignitrons, and spark gaps in certain applications. For fast electrical circuits in gas lasers a medium power switch with integrated deuterium reservoir is available. This device is designed for a peak current of 30 kA at a hold-off voltage of 32 kV and a pulse length of up to 500 ns. With those devices a current rise of up to $8 \cdot 10^{11}$ A/s (10%-90%) was measured. In addition to this medium current device also pseudospark switches for high current applications were developed. Currents up to 400 kA at a hold-off voltage of about 25 kV and pulse length of some microseconds are typical for these pss. This large charge transfer must be distributed on parallel discharge channels to reduce lifetime limiting electrode erosion. Longterm tests with several electrode materials and discharge channel arrangements were performed. Two possible geometries were tested, a radial and a coaxial one. Optical fast shutter technique, and spectroscopic and interferometric methods were used to get more information about the discharge-character, the pinching of the discharge channels due to magnetic forces, and the erosion mechanism. The homogeneous ignition and the equal distribution of the current into the individual discharge channels was proved by fast photography and current measurements. At currents exceeding some kA the pseudospark transforms from a specific hollow cathode discharge into a metal-vapour-arc like behaviour. Measurements of the forward voltage drop provide values of less than 100 V which are typical for metal-vapour-arcs. Also cathode spots and their traces on the electrode surface were observable. The performance of these switches in pulsed power devices will be reported.

1. INTRODUCTION

The pseudospark is a low pressure gas discharge in a special electrode geometry. Typical are the hollow cathode and the central hole in the electrodes. The fast current rise and the pulsed electron beam generated in the breakdown phase are characteristic for the pseudospark. Found in 1977 by Christiansen and Schultheiß¹ the application as a fast closing switch was discussed soon afterwards. Switch development started at CERN, Geneva in collaboration with the University of Erlangen at the begin of the eighties.² In 1986 the investigation of a pseudospark switch (pss) for high power gas lasers began with the aim to provide an alternative for commercial thyratrons. Now this type of switch is available in metal ceramic technology with an incorporated deuterium reservoir. Typical data of this pss are: 32 kV holdoff voltage, 30 kA peak current at a pulse length of 500 ns maximum. Near the self breakdown a jitter of less than 5 ns can be achieved. By means of an auxiliary electrode inside the hollow cathode the jitter is reduced to less than 2 ns. Therefore this type of pss can be used in parallel. At a current of 9.4 kA (70 ns FWHM) a repetition rate of 1.8 kHz was achieved.³ The lifetime of the pss is limited by electrode erosion. To confirm extrapolated data a longterm test was performed with an excimer laser test circuit at the Siemens AG, Erlangen.⁴ The parameters were: holdoff voltage 22 kV, anode current 10 kA, reverse current < 1 kA, pulse length 170 ns (FWHM). The max. repetition rate was 233 Hz. After 129 million pulses which correspond to a total charge transfer of 219 kC the test was stopped even though the switch was still working. During operation the delay decreased from original 750 ns to 420 ns at the end of the test whereas the jitter kept constant at about 5 ns (rms). After conditioning of the switch its misfiring rate was below one ppm and was always due to a prefiring. This test showed that the pss has a lifetime similar to that of thyratrons. Advantages of the pss like high current rise rate and capability of 100 % current reversal makes it to an interesting alternative to commercial available switches. For switching high currents of about 50 to 500 kA at holdoff voltages up to 30 kV and pulse length of some μ s a special type of pss is under development. The main problem is the great erosion of the electrodes transferring such a high amount of charge per shot which is of the order of some coulomb. At these high currents the discharge transforms to a metal vapour arc with an erosion comparable to spark gaps. To achieve a higher lifetime of these pss multichannel devices have to be used for high current applications. Multichannel pss can be realized with different arrangements of the discharge channels. The actual stand of development of high current pss is reported in the following.

2. PSS FOR HIGH CURRENT TRANSFER

2.1. Test data of a one channel pss

For high charge transfers a one channel pss was investigated initially. The pss is triggered by a surface flashover in the back of the hollow cathode. The trigger is protected against erosion by the main discharge by mounting it behind the hollow cathode. This measure results in a delay of 500 ns and a jitter of about 30 ns due to the large distance between trigger discharge and cathode hole. These features are sufficient for most applications of high current switches. The insulator is made of alumina and connected via UHV flanges with copper seals to the electrodes. The inner diameter of the insulator is 85 mm. The insulator wall is shielded by special structures on the molybdenum electrodes. The electrode apertures are 5 mm in diameter, and the gap distance is 3 mm. This pss was tested with a current reversal of about 90 %. The peak current was 120 kA at 30 kV holdoff voltage at a pulse halfwave (damped sinusoidal wave) of 2 μ s. The repetition rate was about 0.5 Hz limited by the test circuit and the water cooling system. Results of erosion measurements and longterm tests with the one channel pss have been reported earlier.⁵ With tungsten and carbon electrodes the best results were found. To get information about the discharge at high charge transfer plane electrodes without protecting screens have been used in connection with a glass insulator. With a fast shutter camera the temporal evolution of the discharge was observed.⁵ The discharge starts in the center, widens up to the edge of the central apertures and contracts after about 500 ns to a small filament, if the current exceeds 20 kA. The filament moves away from the central bore region to the plane electrode surface, which may also cause erosion of the shielding structures normally used in this pss. The spot localization changes statistically from shot to shot. By interferometric methods an electron density of the filament of more than $10^{17} \cdot \text{cm}^{-3}$ was determined.⁵ Measurements of the forward voltage drop showed voltages of about 100 V if the current exceeds 500 A.⁶ These results are typical for metal vapour arcs. Also the erosion rate is comparable to that of metal vapour arcs. The lifetime of the one channel pss of 15,000 pulses is too short for real applications. To increase lifetime the investigation of multichannel devices was started. The lower current density per channel leads to an erosion reduction of the single discharge channels and to an increase of life time.

2.2. Multi channel pss development

Two arrangements of multi-channel pss (mups) were investigated: coaxial and radial devices as shown in Fig. 1. A linear arrangement is although possible⁷, but should be used only in special strip line circuits because of the complex geometry. The main problem of the multi-channel pss is homogeneous ignition of all channels by the trigger discharge. The coaxial design has separated hollow cathodes, the radial design a common one. In the last case the trigger of a one channel pss can be used.³ Triggering with a surface flashover in the back of the hollow cathode is possible, too. For the coaxial mups a special trigger design is necessary.⁸

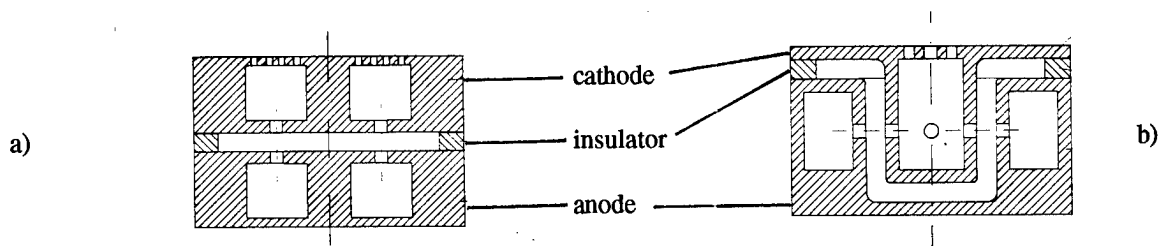


Figure 1: Schematic drawing of the coaxial (a) and the radial (b) mups design

2.2.1. Radial mups

With a 3-channel device homogeneous discharge ignition was investigated by fast shutter photography through a window in the anode. The light emission is equally distributed among the channels during the whole discharge. Measurements of the current distribution were done by dividing the anode into three insulated segments. The current through each segment was measured by three independent current transformers. The deviation from the mean current was less than 5 % for each of the three channels. This deviation is shown in Fig. 2 in dependence on the gas pressure and the trigger method. With a surface flashover trigger (SFT) the deviation is enlarged a few percent in comparison to the pulsed

charge injection trigger (CIT). The experiments proved the equal distribution of the discharge current in a wide range of test parameters. A three channel device with molybdenum electrodes was tested at a peak current of 120 kA at 15 kV holdoff voltage with 2.2 μ s pulse length (half period) and 90 % current reversal. After 25,000 shots no change in the switching characteristic was observed. The erosion at the apertures was small in comparison with the one channel switch. The lifetime is about five times higher. Devices with 5 and 7 discharge channels work as well. Therefore the lifetime should be about at least one order of magnitude higher in comparison to that of a one channel pss. A total charge transfer of more than 300 kC can be expected.

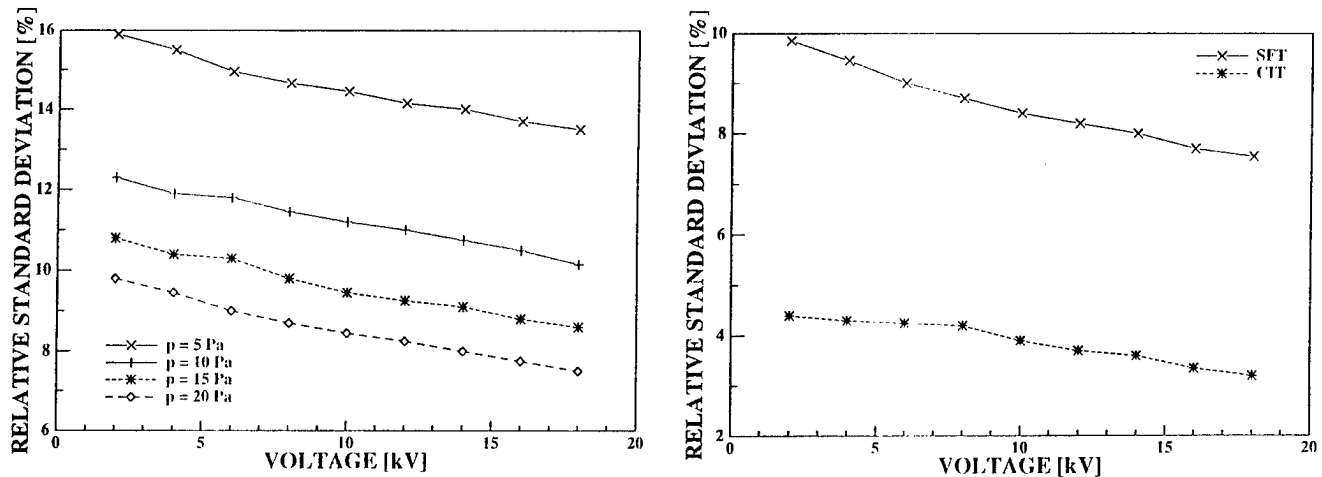


Figure 2: Deviation of the single current of each of the three channels of a radial mups from the mean current depending on the gas pressure (left) and the trigger method (right) (SFT: surface flashover trigger, CIT: charge injection trigger).

2.2.2. Coaxial mups

With the coaxial design tests were performed at a peak current of 100 kA and a pulse length of 2.2 μ s. A 3-channel mups was tested. The trigger used was a pulsed hollow cathode discharge as described in ref. 8. The electrode holes were arranged at a hole circle of 24 mm and had a diameter of 5 mm. The gap distance was 3 mm. About 300 ns after current rise an acceleration of the discharge channels from the electrode apertures into the center can be observed. This behaviour can be explained by the forces of the magnetic field and is similar to that of a z-pinch discharge. Depending on the applied voltage the channels merge at axis after about 650 ns to 1.2 μ s. At the later part of the half wave the single discharge channel moves statistically in the central area of the electrodes. Figure 3 shows a fast shutter photography of the discharge at current rise and in the beginning of contraction. The pinching of the discharge channels at axis causes an enhanced erosion at this region, whereas erosion at the bore is negligible. Therefore the lifetime of this type of mups is reduced in comparison to the radial arrangement at high current applications with long cycle times. The application of this switch is restricted for pulse generators adapted to the pinching of the discharge channels. The limit of the maximum current at different cycle times will be investigated in near future.

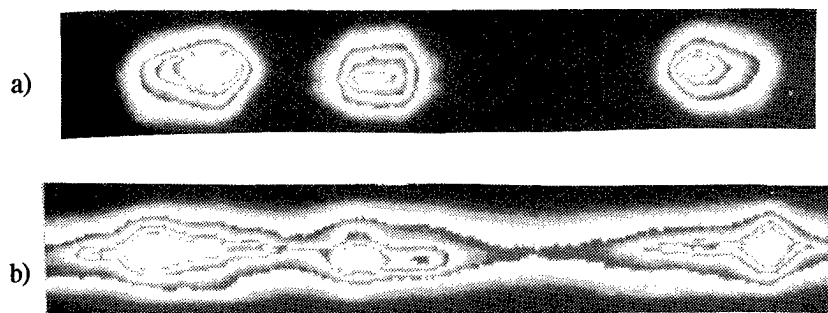


Figure 3: Fast shutter photographs of a coaxial mups arrangement at a) start of the discharge and b) after the pinching in the center. Note that there is a different scale of the photographs.

3. SUMMARY

Pseudospark switches have been developed for several applications in the last years. For pulsed gas lasers a sealed-off pss with incorporated deuterium reservoir is available. For high current applications first multi-channel prototypes were tested (s. Table 1). Both, the coaxial and the radial design showed homogeneous ignition of all the discharge channels, but the radial pss is easier to trigger. The equal current distribution among the channels during the current pulse was proved by fast photography and current measurements with a segmented anode. The coaxial multi-channel pss showed a pinching of the single discharge channels to the center after a few hundred ns. This may lead to increased erosion at the center of the electrode and therefore to a shorter lifetime if generator parameters are not choosen carefully. The discharge transforms to a metal vapour arc if the transferred current exceeds some kA. This is proved by the erosion pattern, measurements of the forward voltage drop and determination of the electron density. Lifetime tests with a one channel pss showed that with tungsten and carbon the lowest erosion rates were achieved. In further experiments the influence of peak current and of new materials on the erosion rate will be studied. According to results the number of parallel discharge channels necessary to achieve a considerable lifetime for a certain application will be determined. Operation with up to 7 discharge channels is already proved. In the future the development of multi channel pss for currents up to 400 kA will be the goal.

Table 1: Data of the high current pseudospark switches.

	high current mups	high current pss
number of channels	3, radial design	1
holdoff voltage / peak current	30 kV / 200 kA	30 kV / 120 kA
trigger method	surface flashover	surface flashover
charge transfer per puls	3 C	1.5 C
maximum repetition rate	0.3 Hz	0.5 Hz
dI/dt	$6 \cdot 10^{11}$ A/s	$4 \cdot 10^{11}$ A/s
delay / jitter	500 ns / < 30 ns	500 ns / < 30 ns
lifetime	> 25,000 / 50 kC	> 15,000 / 27 kC

4. ACKNOWLEDGEMENTS

We thank Dr. W. Hartmann and J. Stroh, Siemens AG, Erlangen for performing the longterm test of the sealed-off pss.

5. REFERENCES

1. J. Christiansen and C. Schultheiss, "Production of High Current Particle Beams by Low Pressure Spark Discharges", *Z. Phys. A* 290, pp. 35-41, March 1979.
2. P. Billaut, H. Riege, M. van Gulik, E. Boggasch, K. Frank, R. Seeböck, "Pseudospark Switches" *Yellow Report CERN 87-13*, December 1987.
3. P. Bickel, J. Christiansen, K. Frank, A. Görtler, W. Hartmann, R. Kowalewicz, A. Linsenmeyer, C. Kozlik, R. Stark, P. Wiesneth, "High-Repetition Rate Sealed-Off Pseudospark Switches for Pulsed Modulators", *IEEE Trans. on Electr. Dev.*, Vol. 38, No. 4, pp. 712-716, April 1991.
4. A. Görtler, H. Arenz, P. Bickel, J. Christiansen, K. Frank, U. Herleb, T. Mehr, M. Schlaug, A. Schwandner, R. Tkotz, "Pseudospark Switches for Excimer-Lasers and Pulsed CO₂-Lasers", *Proc. Int. Symposium on High Power Lasers and Laser Applications V*, Wien, April 1994 (to be published).
5. A. Görtler, A. Schwandner, J. Christiansen, K. Frank, H. Granzer, "Development of a High Current Pseudospark Switch and Measurement of Electron Density", *IEEE Trans. on Pl. Sci.*, Vol. 21, No. 5, pp.516-521, October 1993
6. A. Görtler, H. Granzer, J. Christiansen, K. Frank, A. Schwandner, R. Tkotz, "Measurements of the Forward Voltage Drop in Pseudospark Switches", *Proc. 21. Int. Conf. on Phenomena in Ionized Gases*, Bochum, Vol. 2, pp. 321-322, September 1993.
7. G. Mechttersheimer, R. Kohler, "Multichannel Pseudo-Spark Switch (MUPS)", *J. Phys. E: Sci. Instrum.* 20, pp. 270-273, 1987
8. T. Mehr, J. Christiansen, K. Frank, A. Görtler, M. Stetter, R. Tkotz, "Investigations about Triggering of Coaxial Multichannel Pseudospark Switches", *IEEE Trans. on Plasma Sci.*, Vol. 22, No. 1, February 1994 (to be published).

Unsteady shock wave propagation from electrical foil explosion

N. G. Karlykhanov, S. V. Dem'yanovskiy, I. V. Glazyrin, A. A. Kondrat'ev,
Yu. A. Kucherenko, A. T. Litvin, A. V. Pavlenko, M. S. Timakova, A. D. Zoubov

Federal Nuclear Center — All-Russian Scientific Research Institute of Technical Physics
P.O.Box 245, 454070, Snezhinsk, Russia

ABSTRACT

A computational analysis is performed to investigate unsteady shock wave (SW) formation from electrical foil explosion. The velocity of SW vs. generator power is investigated: results for momentary power release are compared with ones are obtained for electrical circuit parameters calculation with effects in foil consideration. Physical effects in the foil have been considered in detail. The special case of SW profile formation is analyzed. Results of calculations compared to the experimental data.

1. INTRODUCTION

Production of intense unsteady shock wave from electrical foil explosion is one of the great interest for various applications, in particular, for investigation of hydroinstabilities (Rayleigh-Taylor, Richtmyer-Meshkov etc.) development¹. The configuration of installation is sketched in Fig.1.

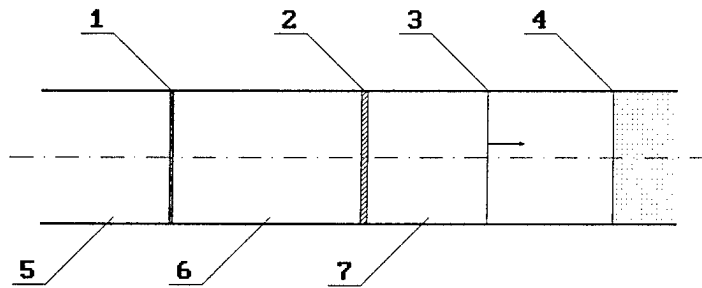


Fig.1. Design of shock tube using foil explosion for hydroinstabilities investigation.

The installation works as follows: two different shock waves propagate in air in opposite directions after the foil (2) explosion. Shock wave (3) which propagates to the right side, reaches the subject of research (4). Another shock wave which propagates to the left in the intermediate tube (6), reaches a nitrocellulose film (1), bursts one and expands into vacuum chamber (5). As a result a rarefaction wave propagates to the right and forms the required time profile of shock wave (3).

The experiment which has been simulated consists of foil electrical explosion due to high-current generator discharge. The generator consists of several GNUV modules with following parameters: charged energy is about 24 kJ, current amplitude ~ 0.62 MA, half-period current rise time $\sim 4 \mu\text{s}$ (total inductance 80 nG, capacity 66 μF , charged voltage 27 kV). Copper foil 17 μm thickness and cross-section of $138 \times 138 \text{ mm}^2$ is used.

2. THE MODEL

To resolve the whole task it is necessary to take into account phenomena which differ in length appreciably: a). μm width foil explosion; and b). SW propagation in extended gas region of 1 m scale. Therefore the task has been divided into two parts: first one includes the simulation of processes in foil for determination of transmission efficiency of charged energy to SW kinetic energy; second one consists of simulation of SW moving in gas region.

2.1. Foil explosion model

The macroscopic foil behavior is described by single-fluid MHD approximation. The radiation effect is neglected because the temperature of matter exceed few eV. In this context the heat propagation and physical viscosity did not consider. Kinetic features (nonequilibria properties due to microinstabilities development) are ignored too. Equations of state taking into account the phase state transitions and mixtures were used for metal². Coefficients of electrical conductivity have been taken from paper³. Boundary condition for magnetic field is determinated from the equations for current which traverses the generator external circuit. Magnetic field diffuses into foil due to chosen electrical conductivity. Conductivity in surrounding air is not considered.

2.2. Model of shock propagation

Shock wave which is generated by foil explosion propagates in gas region. SW velocity exceeds Mach number of $M_s \geq 6$ and then decreases with time. In early time the shock wave is strong. The gas is air at room temperature. We assumed that the gas was compressible. Kuznetsov's tables⁴ of thermodynamic coefficients were used for air. The model considers air which has only translational degrees of freedom, so that corresponding relaxation time is much less than the relaxation time of the vibrational degrees of freedom. In air there are no effects considered of electron excitation and ionization. Moreover, dissociation cannot appear.

3. NUMERICAL SCHEME

All calculation was performed with the 1-D Lagrangian code ERA⁵, using a plane coordinate system. The method used for SW modeling is a second-order scheme both on time and on coordinate using an Neumann-Richtmyer artificial viscosity to description of SW front.

Vacuum region is taken into account by means of boundary condition: when the time less t_0 – the moment when left-propagating SW reaches the nitrocellulose film (1) (see Fig.1), the condition keeps $v = 0$ (v – velocity). After t_0 the condition changes to $p = 0$ (p – pressure).

4. RESULTS AND DISCUSSION

4.1. Calculation of experiment

The calculation of the experiment described above was performed in two stages. First one consists of calculation of foil explosion. Obtained solution for energy release is then overlayed onto large scale for complex modeling.

Figure 2 shows energy time-histories for the calculated results and experimental data. There is some differences between these results. They are connected probably on the one hand with chosen transport coefficients and equation of state in model and on the other hand with methods of treatment of experimental data. For general problem it is necessary 2D modeling. It is interesting to note that 1) the time of energy release is few μs and time of SW motion to the subject of research (4) (Fig.1) is 300 – 400 μs (see Fig.3); 2) the calculated energy is approximately equal to experimental one. Therefore at later stages of flow development we use calculated dependence of release power in foil vs. time for SW propagation modeling.

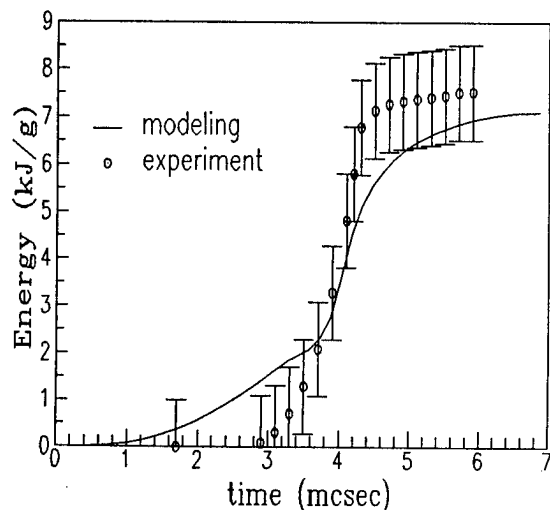


Fig.2. Energy release in foil vs. time

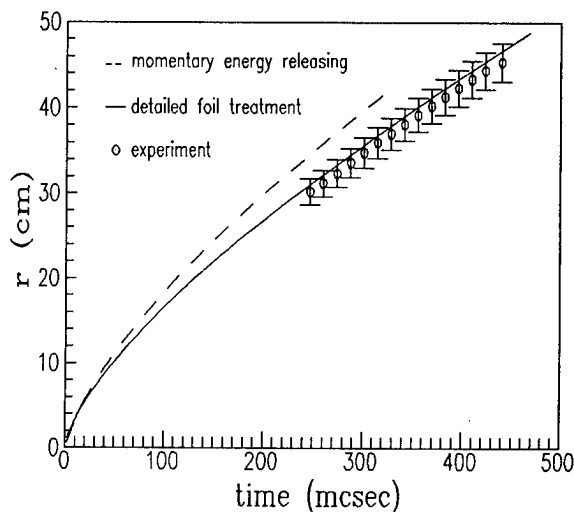


Fig.3. Shock wave front coordinate vs. time

Fig.3. shows comparison of calculated SW front position to experimental measurements. Case of momentary energy release in foil ($t_{foil} = 0$) is shown by dashed lines. Although $t_{foil} \sim 6 \mu sec$ is very small compare to the time of SW motion, there is no satisfactory agreement with the experimental data for $t_{foil} = 0$. Only the calculation with processes in foil consideration (Fig.3, solid line) shows good agreement with the experiment in timing of SW front.

Summary up describing above one could conclude that the physical-mathematical model satisfactory simulates the foil explosion and SW motion. Next step would be a SW profile calculation by the model in a complex region

sketched in Fig.1.

4.2. Shock wave profile formation

The problem of SW profile formation is the subject of experimental studies. These experiments are performed in order to explore some of the mechanisms occurring in the implosion of inertial confinement fusion targets as a consequence of instabilities. For Richtmyer–Meshkov instability investigation it is necessary to obtain δ – similar form of acceleration of a shocked interface with different densities and for Rayleigh–Taylor one need to have close to constant acceleration. The present calculations are directed to investigation of this problem. The objective of this numerical study is to optimize the length of intermediate tube (6) (see Fig.1) for required SW profile. Some computations have been performed for a range of the tube lengths.

In Fig.4, the right coordinate of exploded foil increases in time, reaches the value r_0 and begins to oscillate around r_0 . It could be explained by nonlinear processes of interaction of metal vapor with surrounding gas. In the beginning hot dense metal plasma of exploded foil expands into cold low-density air. During the expansion metal plasma is cooled and at r_0 its pressure becomes approximately equal to gas pressure. Foil bound motion continue for some time due to inertia and then return to the equilibria point. Oscillation is damped through three or four cycles.

These oscillations have an influence on position of interface (4) time-history. It could clear see in Fig.5 where the velocity of shocked interface vs. time is shown for two cases: without and with vacuum region. Upper curve (after ... μsec) shows the velocity without vacuum region. Oscillations are explained by described above processes. In presence of vacuum region the foil "suck up" by vacuum and the velocity becomes negative. Corresponding acceleration (close to constant) is approximately equal to 10^6 m/s^2 , so that the value defined of instability development $gt^2 \sim 1 \text{ m}$.

Obtained results show that form of acceleration corresponding to both cases models Richtmyer–Meshkov instability. Using vacuum region one could delive from oscillations and continued the acceleration action.

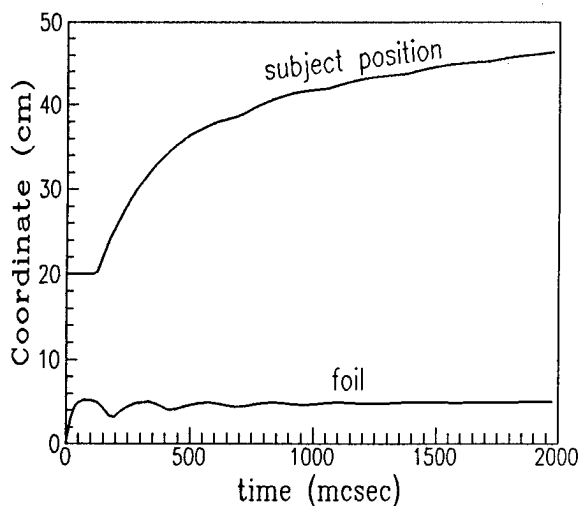


Fig.4. Coordinates of foil and subject of research vs. time

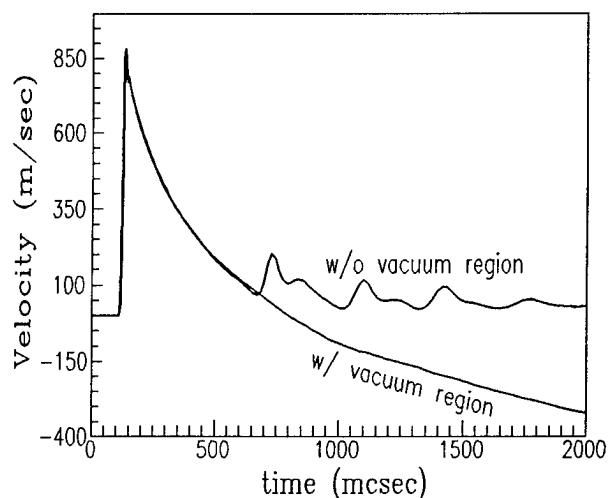


Fig.5. Subject of research velocity vs. time with and without vacuum region

5. CONCLUSIONS

Building up physical-mathematical model realized in 1-D ERA code was shown to calculate efficiency and accurately electrical foil explosion and SW propagation from the foil. The computation satisfactory models the main flow features in the tube special designed for SW profile formation for hydroinstabilities investigation.

The estimation of acceleration value is overrated because for correct simulation of subject position it will be necessary to consider the turbulent mixing development⁶, induced by shock wave passage through the interface. Model of the mixed region need to be refined to account for all phases of perturbation growth and their transition.

6. ACKNOWLEDGMENTS

The authors wishes to thank Dr. Yu. Matveenko for helpful discussions regarding air thermodynamics properties.

7. REFERENCES

1. R. F. Benjamin, D. Besnard and J.-F. Haas, "Richtmyer-Meshkov instability of shocked gaseous interfaces", *Proceedings of the 18th Int. Symp. on Shock Waves*, Ed. K. Takayama, Vol. I, pp. 325-330, Springer-Verlag, Sendai, Japan, 21-26 July 1991.
2. A. T. Sapozhnikov, A. V. Pershina, VANT, Ser.: Metodiki i Programmy Chisl. Resheniya Zadach Matem. Fiziki, **3** (16), p. 29, 1984 (in Russian).
3. Yu. D. Bakulin, V. F. Kuropatenko, A. V. Luchinskiy, Zh. Tehn. Fiz., Vol. 46, No. 9, pp. 1963 - 1969, 1976 (in Russian).
4. N. M. Kuznetsov, *Termodinamicheskie funktsii i udarnye adiabaty vozduha pri vysokikh temperaturakh*, Mashinostroenie, Moskva, 1965 (in Russian).
5. N. M. Barysheva, A. I. Zuev, N. G. Karlykhanov, V. A. Lykov, V. E. Chernyakov, Zh. Vych. Matem. i Matem. Fiz., Vol. 22, No. 2, pp. 401 - 410, 1982 (in Russian).
6. V. Rupert "Shock-interface interaction: Current research on the Richtmyer-Meshkov problem", *Proceedings of the 18th Int. Symp. on Shock Waves*, Ed. K. Takayama, Vol. I, pp. 83-94, Springer-Verlag, Sendai, Japan, 21-26 July 1991.

Erwin Keil

Bundesforschungs- und Prüfzentrum Arsenal (BFPZ), Institute of Electrical Engineering,
Department Electrical Machines and Plants; A-1030 Wien, Faradaygasse 3

ABSTRACT

This report deals with A.C. measurements of H.V. insulating arrangements on site and in Laboratory.

The inspection of H.V. insulation of electrical equipment is first of all to recognize defects of these insulations as early as to prevent breakdown of apparatus. The special difficulty of these inspections results from the large dimensions of this equipment.

The PD-measurements consider the test-circuit transfer characteristic influenced by the large physical and geometrical dimensions, the individual conditions of the test objects and the disturbance levels found on several places.

For state evaluations of electrical insulations different test arrangement and measuring devices are used.

The report gives a comparison between such methods with regard to the impact on the PD-signal and its spectrum from the generation up to the evaluation.

2. INTRODUCTION

The PD-measurement is a sensitive measuring method and enables in contrast to all other known methods the detection of singular failures in an insulation system.

For this reason the above mentioned method gains increased importance specifically for quality control on high voltage insulations in production and to obtain specific characteristic qualities for the assessment of the operating conditions for a entire plant.

In the past a lot of reports have been published about the use and suitability of PD-measurements.^{1,2,3}

3. DISPLAY OF CURRENTLY MEASURED VALUES

The high electrical quality of the major insulation of H.V. equipments leads to small overall dimensions.

Depending on the shape and arrangement of metal parts and insulation leads could be exposed to high electrical field concentrations of major insulations.^{4,5,6}

A defect can be given also by free conducting particles in a gas insulated system.^{7,8}

Because each failure type has its own PD-behaviour the quality and condition of insulation can be estimated.

This described method of PD-measurement deals with sampling the frequency spectrum, of the PD-signals are

uncoupled at the terminals of H.V. equipments, in the range of 10 kHz to 5 MHz with rather narrow bandwidth (up to 25 Hz).

Test results of two different defects in insulations of H.V. equipments are shown at different conditions in fig. 1

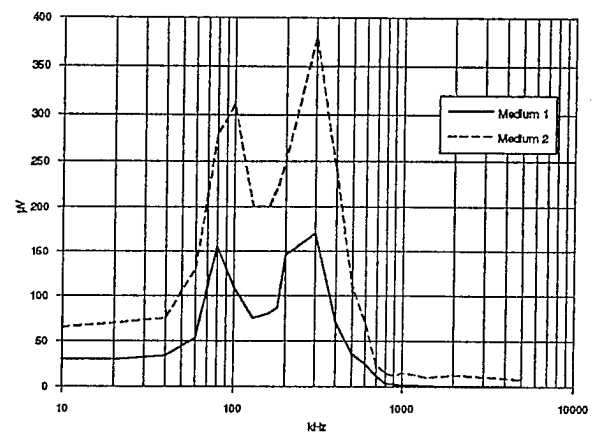


fig. 1a

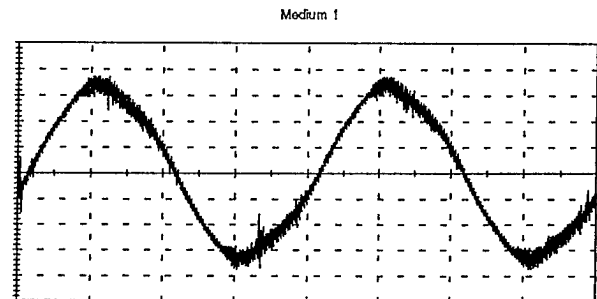
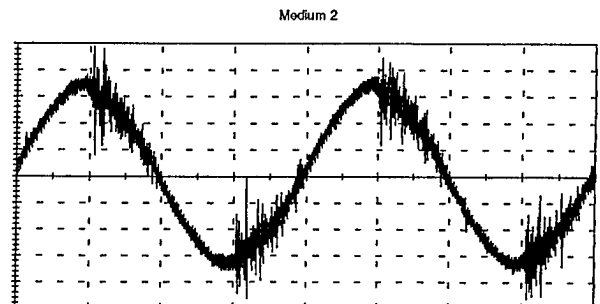


fig. 1b



4. TEST RESULTS

For the assessment of the failure type the dependence of the PD-values on the polarity and the position in relation to the applied AC-voltage and the typical frequency spectrums are used.

All available data are processed, averaged, and stored in a parametered processing cycle.

Scanning rates are selected according to use conditions or are adjusted to the letter.

In order to limit the amount of data to be handled, results are stored.

There will be discussed the three principal applications of this method.

4.1. Test results of Offline measurements

A typical Offline test result is shown in fig. 2

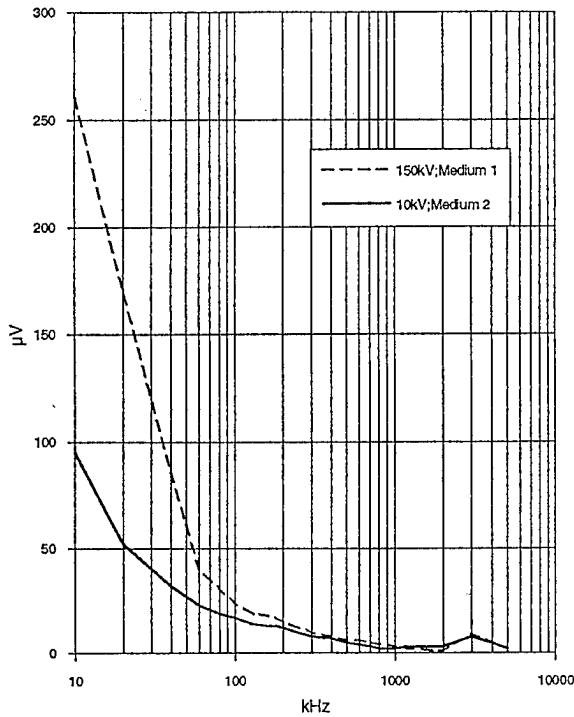


fig. 1c

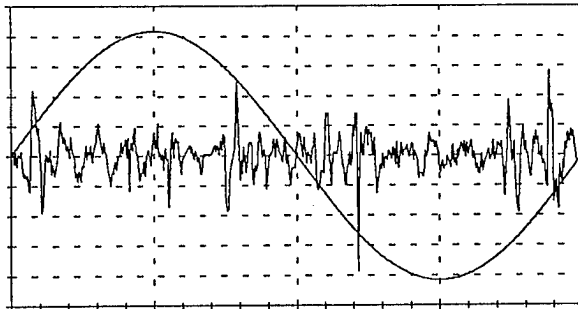


fig. 1d

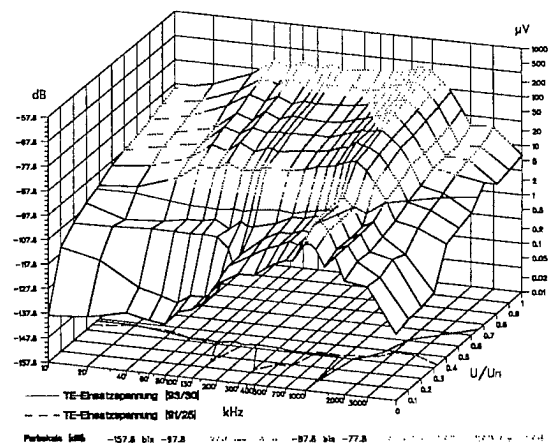


fig. 2a

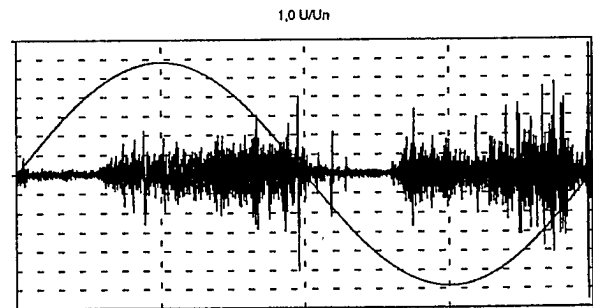


fig. 2b

4.2. Test results of Online measurments

A typical Online test result is shown in fig. 3

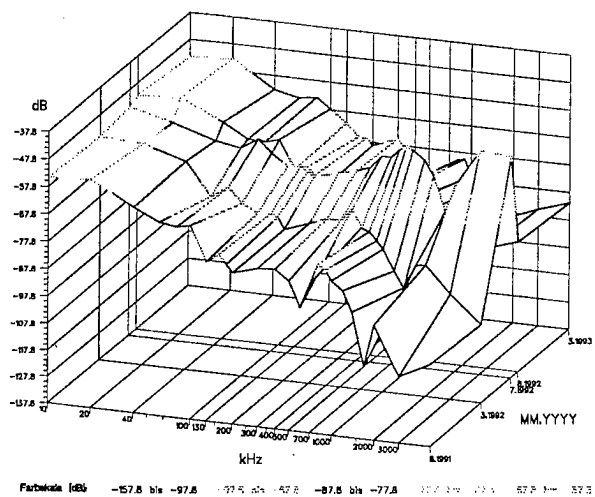


fig. 3a

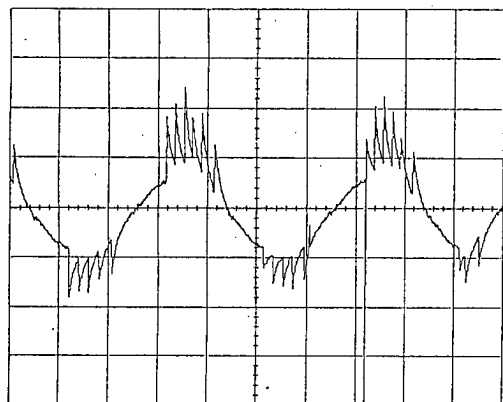


fig. 3b

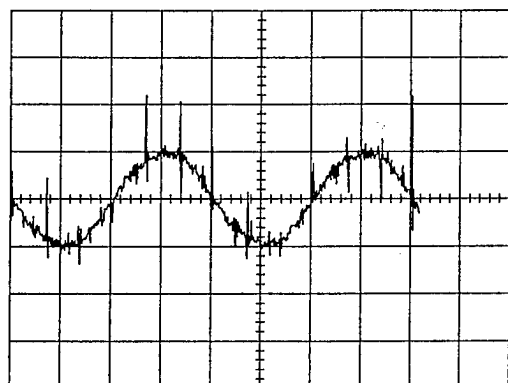


fig. 3c

4.3. Test results of PD-measureings in connection with H.V.-tests

A typical PD-measuring result in connection with H.V.-test is shown in fig. 4

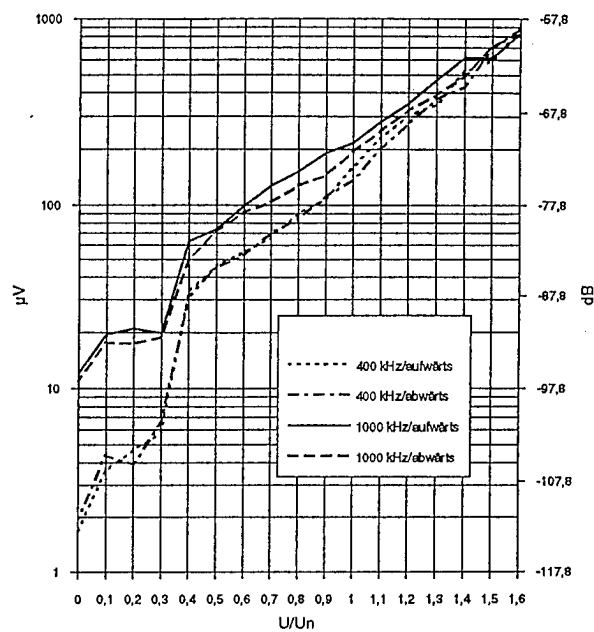


fig. 4a

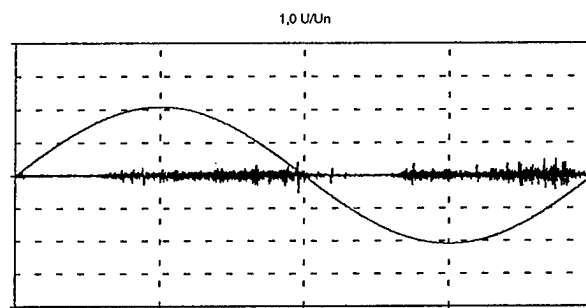


fig. 4b

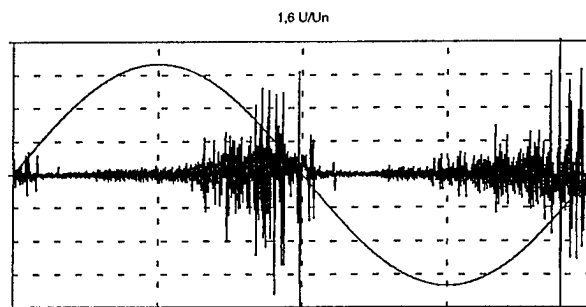


fig. 4c

5. RESUME

Power plants represents such a substantial economic value that all conceivable steps should be taken to assure maximum availability.

In recent years this PD-method for the monitoring of such plants have been developed from the BFPZ Vienna.

With early error detection, damages can either be avoided or at least limited.

With the reduction of time needed for revisions, availability of the plant is substantially increased. Monitoring systems should not only be incorporated in new plants; they also constitute an important instrument- and often the only way - to make use of yet untapped reserves without exceeding the thresholds for the operation of an older plant. This last point, in particular, becomes increasingly important for optimum utilization of existing energies and installed capacities.

6. REVERENCES

1. E. Keil, "Die Untersuchung an Hochspannungs-isolierungen-ein Beitrag zur Beurteilung der Lebensdauer elektrischer Betriebsmittel der Energietechnik" E.u.M. Vol.94 (1977) pp. 244-250

2. P. Blasius, G. Buerger, D. Koenig, K. Moellenbeck, K. Moeller, K.B. Mueller, C. Neumann, K. Schon, K.H. Weck, A. Wichmann, ua.: 50. VDE-Seminar ueber Teilentladungen in Betriebsmitteln der Energietechnik, Muenchen, 1982

3. D. Koenig, H.G. Kranz, E. Lemke, G. Luxa, K.B. Mueller, C. Neumann, D. Peier, K. Schon, K.H. Weck, A. Wichmann, ua.: VDE-ETG-Fachtagung, "Teilentladungen in Betriebsmitteln der Energietechnik", Techn. Akademie Esslingen, 1985

4. U. Brand, M. Marckmann: Outdoor High-voltage compressed-gas capacitors using SF₆-insulated bushings with potential control, Messwandlerbau GmbH W. Germany

5. E. Philippow, "Taschenbuch Elektrotechnik" Band 6 Systeme der Elektroenergietechnik; Abschnitt Hochspannungs-isoliertechnik, Carl Hauser Verlag Muenchen 1982

6. W. Schmidt, P. Högg, A. Eidinger, "Vor-Ort-Hochspannungsprüfung von SF₆-isolierten metallgekapselten Schaltanlagen und Rohrgaskabeln", Baden; Brown Boveri Mitt. 11-77, pp.640-645

7. W. Boeck, "Durchschlag von Isoliergasen", VDE Darmstadt; etza-a Bd. 97 (1976) H.1, pp. 35-37

8. V. Berthold, "Zum Einfluß der Spannungsform auf den partikelgezündeten Durchschlag von SF₆-Isolierungen", KTD Dresden; Elektrie 30 (1976) H.8, pp. 444-446

Compact PC-controlled tester of electric strength

Okunev V.D., Pozdnyakov V.I., Puzanov S.V., Yashnov Y.M.

Moscow Institute of Radio-Electronics and Automatics,
Scientific-Research Institute "Titan", Moscow

ABSTRACT

The tester is a convenient and useful unit for complex damage-free test of current leakage of vacuum and ceramic insulation in a wide range of high voltage. PC-control and processing provide information about the leakage nature and characteristics of the electrodes' surfaces.

The tester is designed for leakage control of vacuum and dielectric insulation, reveal of the leakage nature, breakdown voltage forecast with the breakdown most probable nature, vacuum gaps geometry control.

The tester operation principle is based on the takeoff and processing of leakage voltage-current characteristics (VCC).

Vacuum gaps leakage current (also called pre-breakdown currents) are highly sensitive electric strength investigation and control means. It is associated with that fact that pre-breakdown current having on the hole field-emission nature is the main reason of electric strength failure - breakdown. Therefore field emission surface characteristics are determined by means of prebreakdown current VCC and hence the quality of electrode treatment technology. Moreover by determined by means of VCC micro-field-emitters form parameters and a breaking point for it of a current density and the limit for an anode electron bombardment power are evaluated and hence a breakdown voltages are calculated accordingly for cathode and anode breakdown nature.

Exponential dependance of field-emission current on electrode spacing at the present voltage gives the possibility to control the vacuum gap geometry by means of pre-breakdown current measurement and to reveal drifts from predetermined geometry stipulated both by imperfection of a technology (assembly of poor quality, welding stress relaxation) and parts thermal deformation with switching on the thermocathode filament.

Pre-breakdown current VCC are used for identification of leakage current which can be in practice of field-emission, ohmic (over the ceramic surface) and thermoemission nature. The division of leakages by their physical nature is possible owing to the essential difference in the form of their VCC, especially with a good chosen coordinate system.

In particular for this purposes the Fowler-Nordheim coordinates are appeared to be suitable (Fig.1) so far as in this coordinates a field-emission part

is represented in the form of a straight line with a negative inclination (section 1) and a part of ohmic leakage over ceramic - in the form of a logarithmic curve (section 2).

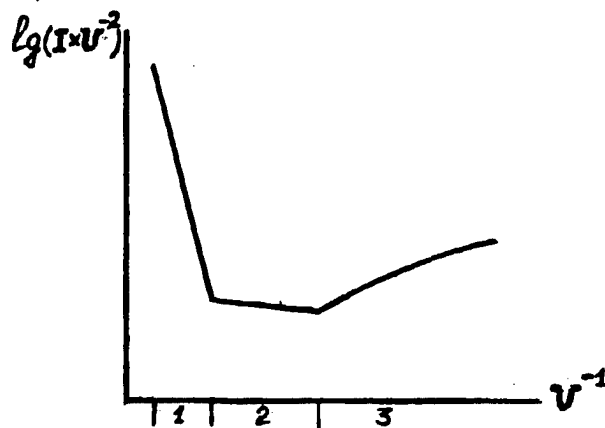


Fig.1. An approximate drawing of a vacuum gap VCC: 1-field emission leakage range; 2-transition range; 3-ohmic leakage range

When drawing the tester the main characteristics were chosen range of taken off currents and voltages and way of supply a high voltage to the vacuum gap. The range of pre-breakdown current to be measured was chosen to be from 5 nA to 50 mcA so far as maximum prebreakdown current levels without the breakdowns occurring are hundreds mcA and leakage current less than some nA are permissible practically for all types of power vacuum tubes. The range of recorded leakage current in four decades is quite sufficient for determination of vacuum insulation characteristics.

The high voltage (HV) range from 0 to 25 kV was chosen proceeding from a nomenclature of produced electronic devices (including TV cathode ray tubes), from a required portability, compactness of the tester (higher voltage require big overall dimensions of HV elements even when poured by a compound) and also by the choice of complete equipment items - HV rectifiers-multipliers, step-up transformers, HV capacitors.

As a source of changing HV (for VCC taking off) a capacitor was chosen relatively slow discharging through discharge resistors of an ohmic HV divider and vacuum gap under the test.

The capacitor charging is carried out from a HV during 1 sec, which is much less than time of its discharge (some 100 sec). After charging of the capacitor the HV source is switched off that allows to conduct measurements of weak currents (the vacuum gap leakage current and current through the HV divider) without HV oscillation noise.

Voltage and current measurements in the tester are carried out by means of electrometric amplifiers. The leakage current measurements are carried out over two channels with different upper limits that provides the necessary range

of recorded current by means of manufactured controllers with 10(12)-bits analogue-to-digit converters (ADC).

Analogue signals from amplifiers outputs to ADC inputs of and control signals of the controller are transmitted through galvanic opto-insulator (insulation breakdown voltage 200 V).

The tester operation is PC-controlled, with introduction of necessary data carried from the keyboard and data library of electrode materials.

When processing the recorded VCC the parts with different leakage nature are distinguished, microfield-emitter (supposed to be a protrusion) and breakdown voltages (both for anode and cathode breakdown nature) are calculated in the field emission part of the VCC, and the ceramic ohmic resistance in the ohmic part of the VCC.

Measurements and processing results are displayed on the screen, printer and stored in the archive files.

The tester block diagram is given in Fig.2.

The tester main specification are as follows:

- test voltage range - 0.5-25 kV;
- test voltage polarity - positive;
- recorded leakage current range - 5 nA - 50 μ A;
- one VCC measurement and processing time - up to 4 min.;
- power consumption - 220 V, 50 Hz, 50 W;
- overall dimensions 300*300*130 mm;
- weight - up to 8 kg.

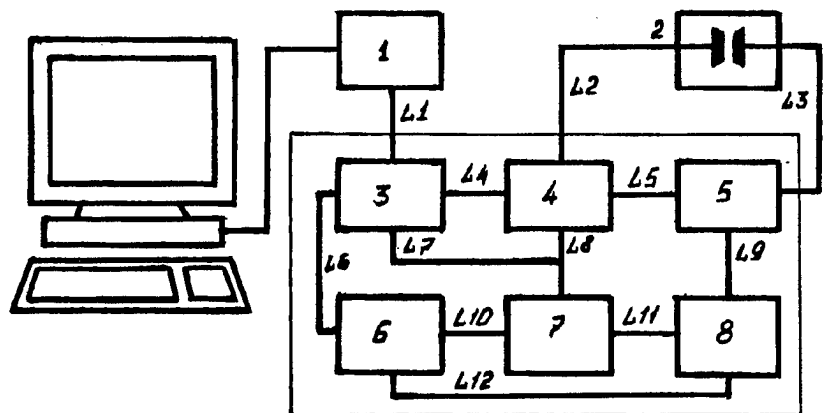


Fig.2. The tester block diagram: 1-controller (input to a slot of the PC motherboard); 2-the tested vacuum gap; 3-opto-insulator board; 4-amplifiers board; 5-HV source; 6-TTL-pulse generator; 7-DC source; 8-pulse current source; L1-tester-PC connecting line; L2-leakage current line; L3-HV-supply cable; L4-amplifiers-output line; L5-HV divider-output line; L6-pulse generator switch line; L7,L8,L10,L11-DC supply lines; L9-pulse current supply line; L12-TTL-pulse line.

DESIGNING FIELD EMISSION DEVICES TO AVOID IMPEDANCE COLLAPSE

Roy Olson

Emeritus Professor of Physics
California State University, Northridge
Northridge, California 91330

ABSTRACT

It is asserted that Impedance Collapse is due to a partial vanishing of space charge which limits current in an improperly designed field emitting device. Empirical support for this contention is presented.

1. INTRODUCTION

The phenomenon known as "Field Emission" was given what is perhaps a misnomer upon its discovery in 1897⁽¹⁾, as it was thought to be a stream of electrons somehow pulled out of a metal by a sufficiently strong electric field. After an unsuccessful attempt in 1923⁽²⁾ to show analytically that this is the case, the matter remained a mystery until 1928 when it was shown to be a quantum mechanical tunnelling of electrons through a potential barrier which had been narrowed as well as lowered by the presence of an electric field⁽³⁾. An excellent review article cites numerous examples of empirical studies which demonstrate agreement with the tunnelling analysis⁽⁴⁾.

The dependence of the emitted current density, J , on the effective applied electric field, F , is essentially

$$J = KF^2 e^{-k/F} \quad (1)$$

where K and k are constants which involve among other things, the work function of the metal. This dependence is plotted and labelled in Figure 1 as the more steeply inclined line, with the slowly varying F^2 term ignored for simplicity. The slope of that line depends on the work function of the emitting metal, and the value for tantalum was chosen for this example, as this is the emitting substance mentioned below in section 3.

At current densities below about 10^7 amperes per square centimeter the current is steady and there is excellent agreement between experimental results and Equation 1. However, if the current density is caused to exceed this value, either by increasing the voltage or decreasing the radius of curvature of the emitter (which increases the effective field) the current is characterized by abrupt surges or pulses⁽⁵⁾. Attempts to extract 10^8 to 10^9 amperes per square centimeter usually result in such violent outbursts of emitted current that the emitter is destroyed by melting and evaporation. This violent increase is frequently referred to as "Impedance Collapse", or "Diode Closure".

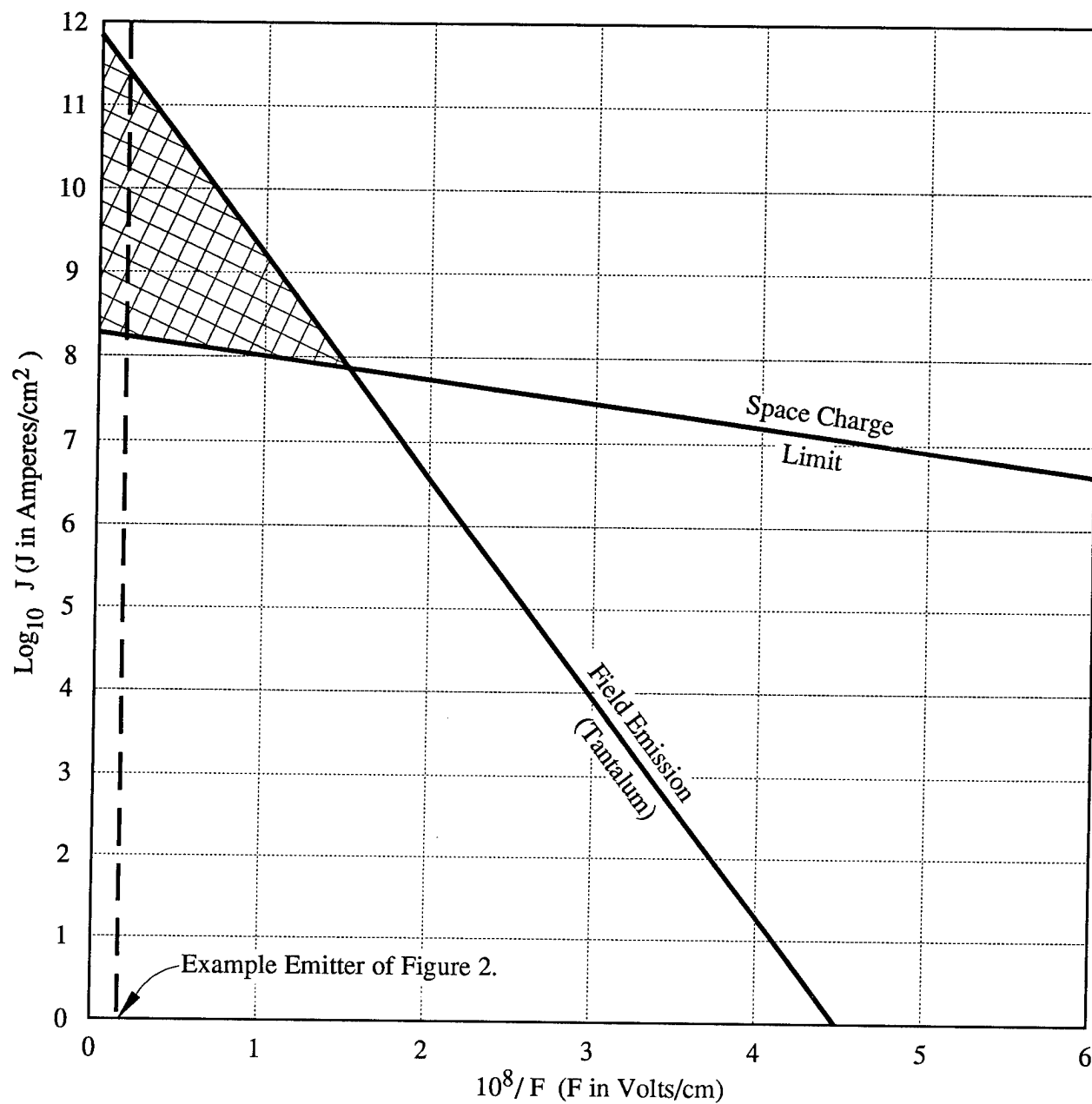


Figure 1. Space Charge Limiting superimposed upon a plot of Field Emission Current Density, J , as a function of Enhanced Field, F .

2. THE EFFECTS OF SPACE CHARGE

After the electrons have tunnelled out from the emitting metal they are accelerated by the electric field toward the anode, but their finite mass causes them to linger in the vicinity of the emitter's surface for a short time, resulting in a negative space charge which tends to reduce the effective field, and hence, the emitted current. In equilibrium the current is referred to as being "space charge

limited", shown by theory⁽⁶⁾ and experiment to be given approximately by

$$J = \frac{CF^{3/2}}{\sqrt{d}} \quad (2)$$

The symbol C refers to another constant and d is an effective value of electrode separation. Equation 2 is plotted and labelled in Figure 1 as the line with the smaller slope. As shown there in the figure, the two lines intersect somewhere, the location of the intersection depending somewhat on electrode geometry and the metal's work function. To the right of the intersection the current is determined by the field emission phenomenon, Equation 1, and to the left it is space charge limited, Equation 2.

3. THE CAUSE, NATURE, AND CURE OF IMPEDENCE COLLAPSE

If the current is space charge limited and the electric field is sufficiently strong to increase the current by an order of magnitude if the space charge were removed, rather obviously the amount of current is sensitive to perturbations in the quantity of space charge present. A disturbance which lowers the space charge increases the emitted current density. Ionization of residual gases or material ejected by some means from the emitter decreases the space charge density due to the fact that the more massive positive ions remain near the emitter while the electrons are accelerated away. The resulting increased current density causes more ionization and the self regenerating phenomenon appears externally as a current surge. A particularly violent current surge, "Impedance Collapse", can damage or destroy the emitter. A field emitter being subjected to an electric field to produce a space charge limiting current would begin operating on the space charge limit line in Figure 1, at the bottom of the crosshatched area indicated. As some ionization begins to occur, the space charge decreases and the operating point moves upward through that area toward its upper limit, the field emission line.

Figure 2 shows an electron microphotograph of the edge of a thin tantalum sheet which had been used as a field emitter. The intense emission caused localized heating which resulted in melting, and image forces pulled the liquid into the convex surface, whose radius of curvature is 5.6 microns. Impedance Collapse was noted as the device was operated at 375 kilovolts. Dividing the applied voltage by the radius of curvature gives the effective field, establishing that the operating point is on the line indicated in Figure 1. It is significant to note that the line passes through the crosshatched area in which impedance collapse is to be expected, as explained above.

Impedance collapse can be avoided by designing the electrodes in such a way that the crosshatched

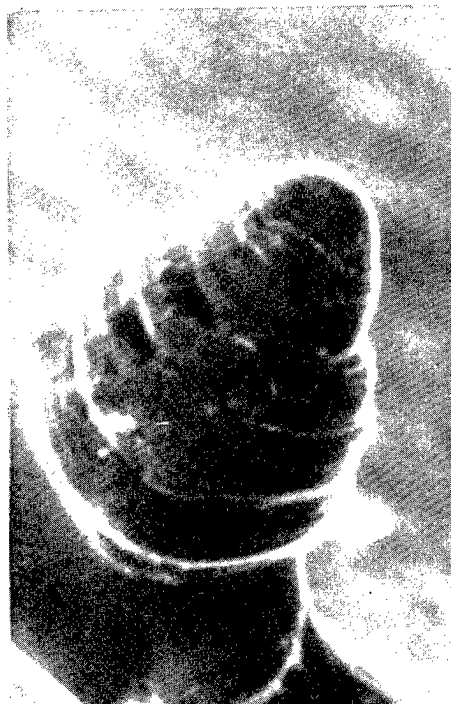


Figure 2. Tantalum Emitter

area of Figure 1 is avoided by the operating point. Such an emitter is shown in Figure 3, and the resulting emitted current trace when it was subjected to a 350 kilovolt pulse is shown in Figure 4.

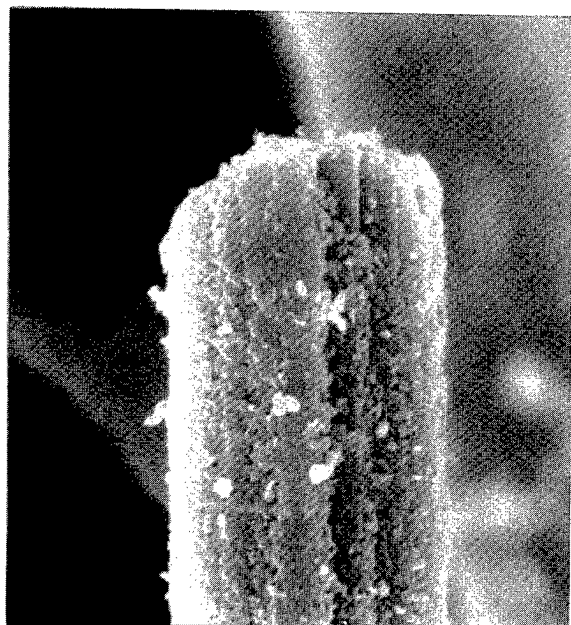


Figure 3. A Graphite Emitter

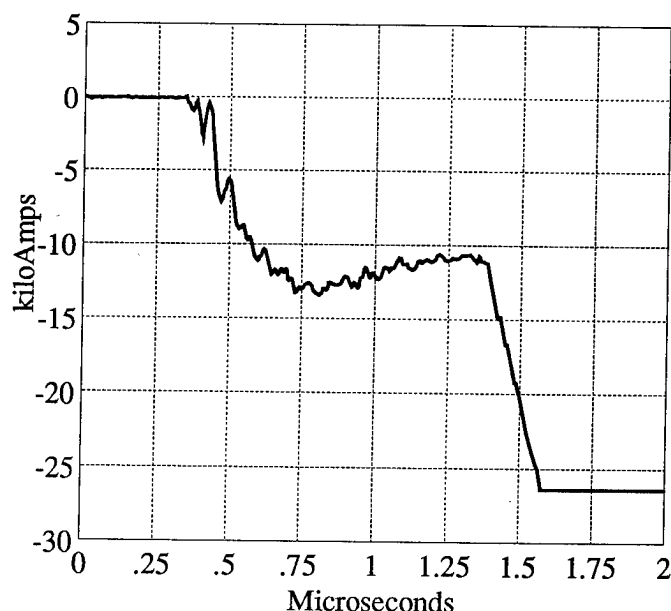


Figure 4. The Current Trace

The radius of curvature is about 30 microns which places the operating point near the intersection of the lines in Figure 1. The emitter contained myriads of such protrusions, yet the current was fairly steady, as can be seen in Figure 4. The applied pulse was terminated by a shorting bar after one microsecond for a reason which did not involve the emitter.

No impedance collapse is seen in Figure 4, demonstrating that it can be avoided by designing the emitter so that no space charge effect will limit the current. That is, choosing an operating point outside of the crosshatched area in Figure 1.

4. ACKNOWLEDGEMENTS

The author thanks Mr. K. Williams for the use of Figure 2, Mr. L. Hale for Figure 3, and Mr. D. Burde for Figure 4. The author thanks Mr. E. Olson for preparing the manuscript.

5. REFERENCES

1. R. W. Wood, *Phys. Rev.* **5**, p. 1, 1897
2. W. Schottky, *Zeit. für Phys.* **14**, p. 63, 1923
3. R. W. Fowler and L. W. Nordheim, *Proc. Roy. Soc. A* **119**, p. 173, 1928
4. W. P. Dyke and W. W. Dolan, Advances in Electronics and Electron Physics VOL VIII, pp. 89-184, Academic Press, New York, 1956
5. See, for example: G. N. Fursey and V. M. Zhukov, *Sov. Phys. Tech. Phys.* **21**, p. 176, 1976
6. E. Child, *Phys. Rev.* **32**, p. 492, 1911

Self-propagating phase transformations in metastable media induced by ion bombardment

Vladimir V. Ovchinnikov

Institute of Electrophysics,
Urals Division of the Russian Academy of Sciences;
34 Komsomolskaja Str., Ekaterinburg, 620219, Russia

ABSTRACT

Resistometry, X-ray and NGR methods have been used to investigate phase transformations long-range type in submillimetre layers of $Fe_{69}Ni_{31}$ and Pd_2AuFe alloys under ion bombardment. In situ measurements were made simultaneously resistivity and temperature on plate specimens 100-400 μm thick. The observed transformations are considered to be a new type of radiation-induced self-spreading phase transformations similar to combustion and detonation phenomena, propagating at a speed equal to or exceeding that of sound in the material. In accordance with the proposed model the transformations take place in metastable media at solitary wave fronts generated as a result of evolution of atom collision cascades. Equations are proposed describing the emergence of undamped solitary waves with self-regulating amplitudes which bring about such transformation.

1. INTRODUCTION

Ion implantation is now established as one of novel techniques for processing of the stable and metastable metallic surface alloys [1-3]. At present detailed studies have been made of phenomena connected with ion bombardment in the zone of direct penetration of ions, as well as in the adjacent subsurface layers having a thickness, as a rule, not exceeding several ion projected ranges R_p .

In [1,2] it was reported about unknown up to now effects of generation of nonthermal structural phase transitions, self-spreading in the bulk of the material, induced by continuous and pulse repetitive high-current ion beams. These transformations are observed with energy inputs insufficient for any noticeable heating of the samples in subsurface layers, the thickness of which is 10^3 - 10^4 times greater than the projected range of ions in the irradiated materials. The effect of heating, static stress and radiation enhanced diffusion in [1,2] was precluded by decreasing the fluence of 20 keV Ar^+ and N^+ ions (which caused such transformations) down to $5 \cdot 10^{14}$ - $10^{15} 1/cm^2$, the thickness of iron-rich alloy specimens being 30-600 μm and with good heat abstraction ensured.

Emphasizing the special nature of this new type of transformations, it should be noted that they are essentially opposed to the destruction of the narrow subsurface zone under ion bombardment or to the increase of dislocation density at a large depth. Indeed, in publications already mentioned [1-3] there were observed "long-range effects" which consisted in the transition of deep-lying layers of materials (several R_p to 10^3 - $10^4 R_p$) into a more ideal state, approaching that of an equilibrium.

This paper is devoted to the study by resistometry technique of the kinetics of phase transitions $bcc \rightarrow fcc$ and (disorder state) \rightarrow (long-range atomic order) in submillimeter specimens of $Fe_{69}Ni_{31}$ and Pd_2AuFe , first with continuous heating-cooling in the absence of irradiation, and then with combined action of heating and Ar^+ irradiation (Fe-Ni) and in the course of Ar^+ irradiation using various fluences at different fixed temperatures (Pd-Au-Fe). All measurements of resistivity (ρ) with simultaneous measurement of temperature were carried out in situ. For monitoring the depth at which transformations occur use was made of X-ray diffraction. Diffraction pictures were taken both of irradiated and non-irradiated sides of specimens. The magnetic state was monitored by transmission Mossbauer spectroscopy of foils 30 μm thick made from investigated plates by means of mechanical and electrolytic polishing.

2. BCC \rightarrow FCC PHASE TRANSITION INDUCED BY ION BOMBARDMENT IN $Fe_{69}Ni_{31}$ ALLOY

Measurements were made in situ of resistivity of $Fe_{69}Ni_{31}$ alloy plates, measuring $10 \times 10 \times 0.4$ mm³ (cut out from the same plate), while under continuous bombardment by an Ar^+ ($E=20$ keV, $J=80 \mu A/cm^2$) ion beam with simultaneous monitoring of temperature. Before irradiation (after being held in liquid nitrogen at $-196^\circ C$) the plates had bcc-structure with a small (5-10%) residual fcc-phase. Resistivity vs temperature (Fig., curves 1 and 2) practically coincide in the absence of ion irradiation. This is evidence of good stability of the initial state of specimens

(their components and phase composition, etc.). The temperatures of the start and end of the $bcc \rightarrow fcc$ irradiation induced phase transitions drop by about $50-60^\circ\text{C}$, the transition temperature interval width remaining the same. The resistivity values of the fcc phase formed as a result of ion irradiation are substantially (on the average by 10-12%) higher than those of the fcc phase formed by ordinary heating. Ion bombardment also leads to the increase of the alloy TRC from $3.2 \cdot 10^{-4}$ up to $3.6 \cdot 10^{-4} \mu\text{Ohm} \cdot \text{m/K}$.

The change of ρ and TRC can be explained by the emergence of a short-range order under irradiation (of the K-state type),

Mossbauer studies of foils $30 \mu\text{m}$ thick made of specimens 1,2 and 3 after their transition to the fcc phase and cooling show that the ion bombardment produces a substantial effect not only on electrical, but also on magnetic properties of the fcc phase being formed (similar to [3]).

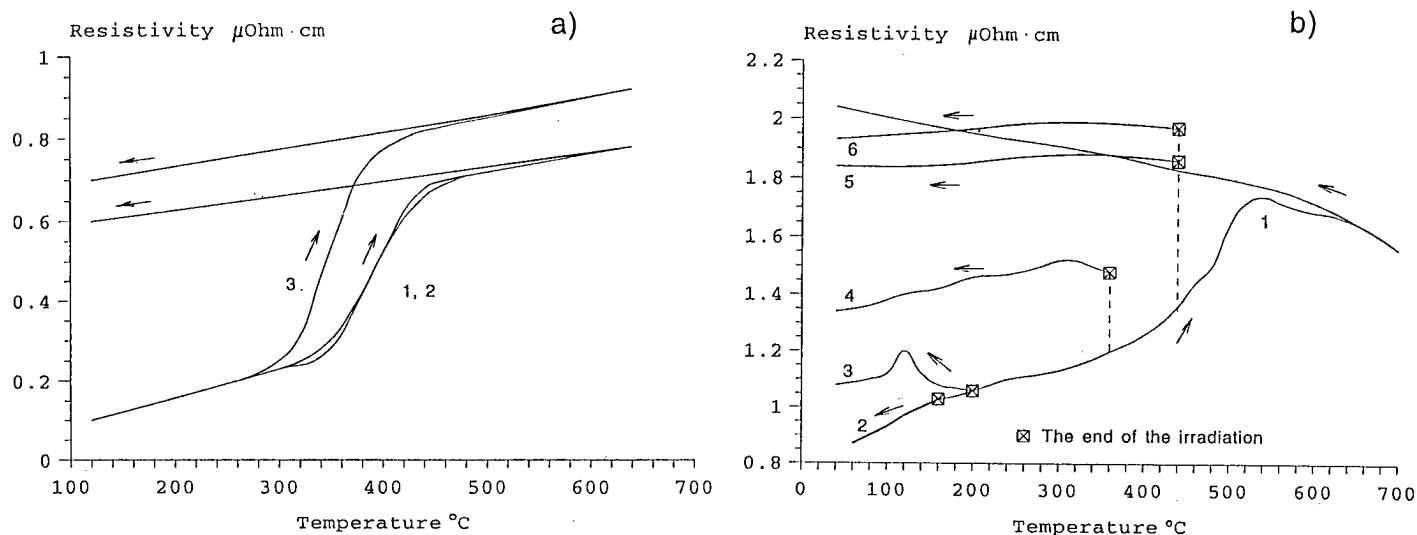


Fig. Temperature dependence of resistivity of $\text{Fe}_{69}\text{Ni}_{31}$ (a):
 1, 2 - in the absence of irradiation;
 3 - under irradiation by Ar^+ ions ($E=20 \text{ keV}$, $j=80 \mu\text{A}/\text{cm}^2$).
 Temperature and irradiation dependences of resistivity Pd_2AuFe (b):
 1 - thermal curve (heating and cooling);
 2, 3, 4, 5, 6 - heating, irradiation at different temperatures and subsequent cooling (2, 3, 4, 5 - $D = 1 \cdot 10^{17} \text{ 1/cm}^2$; 6 - $D = 3 \cdot 10^{17} \text{ 1/cm}^2$).

3. EXCITATION OF THE LOW-TEMPERATURE ATOM MOBILITY AND CHANGE OF ELECTRICAL PROPERTIES OF Pd_2AuFe ALLOY INDUCED BY ION BOMBARDMENT

The effect of Ar^+ ion beams (20 keV and $j=80-100 \mu\text{A}/\text{cm}^2$) on the electrical properties of ordering alloys Pd_2AuFe was studied. Temperature dependencies of resistivity ($\rho(T)$) of Pd_2AuFe specimens ($10 \times 10 \times 0.1 \text{ mm}^3$) measured both with the usual heating without ion bombardment (curve 1) and under ion bombardment at various fixed temperatures (curves 2-6) are presented in Fig. The usual heating of specimens up to temperatures not exceeding 350°C with subsequent cooling does not bring about any deviation of $\rho(T)$ from the initial dependence (curve 1). Atom mobility is stimulated by ion bombardment at temperatures below the diffusion-defreezing threshold, this being confirmed by results of X-ray diffraction analysis: a long-range atom ordering takes place in irradiated Pd-Au-Fe specimens. The emergence of superstructural lines was clearly observed both from the irradiated and the non-irradiated sides of specimens. An exception is the specimen irradiated at 210°C , where only an increase of diffuse X-ray scattering is noted, this showing that a short-range ordering is taking place. The changes in the atomic structure and properties occur at depths several orders of magnitude greater than the projected range of ions having such energies.

Mossbauer investigation shows changes not only in the electrical, but also in the magnetic properties of this alloy. We suggest to apply the ion irradiation effect produced on and TRC (curve 5 demonstrates a practically zero value of TRC over a wide temperature range) with the purpose of improving the electrical characteristics of precision wirewound resistors made of Pd_2AuFe alloys, in particular, to enhance their temperature stability.

4. ABOUT THE INITIATION MECHANISM OF SELF-SPREADING PHASE TRANSFORMATIONS. DISCUSSION.

Theoretical analysis in the continuum approximation [4] and molecular dynamic method [5] have shown that as a result of evolution of atom collision cascades in a substance there can arise shock waves which on propagating into the bulk of the substance attenuate rapidly, breaking up into an elastic and inelastic components. In view of the rapid attenuation of such waves their emergence cannot explain long-range effects observed during ion bombardment. For the explanation of the observed phenomena the idea may be advanced that with a given ratio of medium parameters and the wave propagating therein, the latter can become undamped.

Suppose that the medium, in which the wave propagates, is metastable with potential barrier energy equal to Δf , and with its transition to the stable state there is released energy ΔF . In certain conditions when the energy density at the wave front $\varepsilon_0 \geq \Delta f$, it is possible that the energy of the wave propagating in the medium will be fed with energy liberated by phase transition induced by such a wave. Assuming that the wave front propagates together with the transformation front, we can instead of writing the usual damping equation

$$\frac{d\varepsilon}{dV} = -2\frac{\beta}{S}\varepsilon, \quad (1)$$

write down

$$\frac{d\varepsilon}{d\xi} = -2\beta\varepsilon + \frac{\Delta F'}{k\Gamma}, \quad (2)$$

where $\beta = \frac{\delta}{v}$ for the plane wave and $\beta = \frac{\delta}{v} + \frac{1}{\rho}$ for the spherical wave ($dV = Sdx$ or $dV = Sd\rho$), x and ρ are wave front coordinates, V is the wave velocity, $\varepsilon = \frac{E}{k\Gamma S}$ is the energy density at the solitary wave maximum, S is the area of wave front, k is a coefficient taking into account the wave form (for a Gaussian wave form $k = \sqrt{\pi/4\ln 2} \approx 1.06$), Γ is the width of the solitary wave at half-height, $\Delta F'$ is the energy returned to the wave ($\Delta F = -\Delta F'$ is the change of the system free energy when it passes from metastable state to the stable).

The solution of this equation for a plane wave ($\xi = x$, $\beta = \frac{\delta}{v}$) is as follows

$$\varepsilon(x) = \frac{v\Delta F'}{2\delta k\Gamma} + (\varepsilon_0 - \frac{v\Delta F'}{2\delta k\Gamma})e^{-\frac{2\varepsilon}{v}(x-x_0)} \quad (3)$$

when

In case of a special wave the solution has a somewhat more complicated form, but the general character of $\varepsilon(\rho)$ is the same as that of $\varepsilon(x)$. The most interesting case is when $\varepsilon \geq \Delta f$ and $\Delta F' > 0$ (i.e. when attenuation is compensated for by energy released as a result of transformation) and the amplitudes of solitary waves become self-regulating.

With $\varepsilon > \Omega$ ($\Omega = \frac{v\Delta F'}{2\delta k\Gamma}$) the wave is attenuated not down to zero value, but to Ω with $x, \rho \rightarrow \infty$, while with $\varepsilon < \Omega$ it even increases in the limit up to the same value Ω . Any fluctuations in the wave amplitude, caused by inhomogeneities in the medium, are restored automatically.

We shall attempt, basing on our findings, to explain some regularities in the transformations induced by ion bombardment in alloys.

In iron-rich alloys of the Fe-Ni system, in which the rate of components at $t < 500^\circ C$ is extremely low, phase transformations at real rates of heating and cooling exhibit a mainly diffusionless martensitic-like character. In the ideal case $bcc \rightarrow fcc$ transitions on heating and cooling must take place at temperature T_0 , when the free energies of bcc and fcc phases are equal, i.e.: $\Delta F = \Delta E - T\Delta S = 0$, and, consequently, $T_0 = \Delta E/\Delta S$. In a real case because of contributions (apart from chemical energy ΔE) of elastic energy ΔE_e , surface energy ΔE_s , magnetic energy ΔE_m and because of the dependence of these contributions on temperature and transformation percent, the problem gets more complicated. Phase transitions start with considerable overcooling $\Delta T_1 = (\Delta E_{e1} + \Delta E_{s1} + \Delta E_{m1})/\Delta S_1$ (on cooling) and considerable overheating $\Delta T_2 = (\Delta E_{e2} + \Delta E_{s2} + \Delta E_{m2})/\Delta S_2$ (on heating), and the temperature interval

becomes extended (indices 1 and 2 correspond to the direct and inverse transformations, respectively). Overheated and overcooled phases are metastable and the above results are applicable to them.

In case of Fe-Ni alloys the initiation of $bcc \rightarrow fcc$ transformations by ion bombardment requires the heating of the system to a temperature just above T_0 by an amount $\delta T \ll \Delta T_1$, when the bcc phase becomes metastable (i.e. $\Delta F' = -\Delta F > 0$). Hence, the necessary and sufficient condition for the initiation of self-spreading phase transition in the given model is $\varepsilon_0 > \Delta f$. Considering that initially the amplitude of generated shock waves can exceed the theoretical elasticity limit of solids, the condition $\varepsilon_0 > \Delta f$ is quite real. The traveling solitary compression wave can, probably, stimulate $bcc \rightarrow fcc$ transformations, inasmuch as an fcc lattice can be obtained from a bcc one by compression of the latter along two mutually perpendicular directions.

The initiation of phase transitions (disorder state) \rightarrow (long-range atomic order) in Pd_2AuFe alloys can also be explained within the framework of the proposed model. Let us suppose, that with the propagation of solitary waves with an amplitude sufficient for effecting plastic flow of material, correlated atom restructuring takes place at their front, leading (because of differences in the energies of pairwise interactions of alloy components) to an increase in the degree atomic order. In this case the energy released by the medium and returned to the wave is given by:

$$\Delta F \approx \sum_{i=1}^n \frac{F}{\eta_i} \Delta \eta_i \quad (4)$$

where $\eta_1, \eta_2, \dots, \eta_n$ are a set of order parameters describing atomic ordering (i.e. characterizing the degree of long-range atomic order) in the alloy. With the passage of each consecutive wave the degree of long-range order in the alloy increases by a certain vector $\Delta \vec{\eta} = \Delta \eta_1, \Delta \eta_2, \dots, \Delta \eta_n$, this corresponding to an increment of free energy $\Delta F' = -\Delta F > 0$. With the approach of the degree of perfection of atomic order to its maximum, the quantity $\Delta F'$ apparently decreases, however the passage of each separate solitary wave does not create a scorched zone behind it.

It should be kept in mind that for the complete analysis of the mechanism of generation of radiation-induced self-spreading phase transformations it is necessary to solve equations in hydrodynamics, just as it is done when solving combustion and detonation problems. In each case a detailed knowledge of the state of the medium equation is required.

5. REFERENCES

- 1.S.N. Borodin, Yu.E. Kreindel, G.A. Mesyats, V.V. Ovchinnikov, V.A. Shabashov, Nonthermal Phase Transitions and Long-Range Effects Produced by Irradiation of Alloys with Accelerated Ions. *Pizma v JTF*, 1989, V. 15, N 17, pp. 51-55 (in Russian).
- 2.Yu.E. Kreindel, V.V. Ovchinnikov, Structural Transformations and Long-Range Effects in Alloys Caused by Gas Ion Bombardment. *Vacuum*, 1990, V. 42, N 1/2, pp. 81-83.
- 3.V.V. Ovchinnikov, Yu.D. Kogan, N.V. Gavrilov, A.K. Shtoltz, The Formation of Extraordinary Magnetic States in Iron-Nickel Alloy with BCC \rightarrow FCC Transitions Induced by Ion Irradiation. *Coating Technology*, 1994, 64/1, pp. 1-4.
- 4.V.P. Zhukov, A.V. Demidov, Calculation of Shift Peak in the Continuous Medium Approximation. *Atomnaya energia*, 1985, V.59, B1, pp. 29-33 (in Russian).
- 5.V.G. Chudinov, R.M.J. Cotterill, V.V. Andreev, Kinetics of Diffuse Processes within a Cascade Region in the Sub-Threshold of F. C. C. and H. C. P. Metals. *Phys. Stat. sol. (a)* (1990), 122, pp. 111 - 120.

Plasma flare of pulsed microwave surface discharge in vacuum for thin films deposition and materials processing

Alexander A. Ravaev, Alexander V. Medvedovsky, and Pavel S. Chernyshev

Moscow Radiotechnical Institute, Russian Academy of Sciences
Warshawscoe Shosse, 132, Moscow 113519, Russia

ABSTRACT

A plasma flare generated by a surface discharge on a target in vacuum under action of high intensity pulse microwave (MW) beam may become a new tool for depositing a variety of materials in thin film form and for materials processing. Besides well known, advantages of *pulsed* MW deposition include: (1) convenience and efficiency of the MW energy remote supply; (2) controllability of a plasma non equilibrium degree and ion energy spectrum; (3) no requirements for a "working gas," as on sputtering; (4) wide choose of operating regimes -- both active and "afterglow" regimes, in both active and "post discharge" reactor zones. The use of superpower ($\sim 1\text{GW}$) MW generators based on relativistic electron beams will give: (5) flexibility in a process scaling and possibility of a large surface treatment; (6) achievement of MW intensities up to 10 MW/cm^2 , typical values for pulsed laser deposition techniques.

The present report consists of three parts. The first one is a brief review of experimental works accomplished in MRT Institute and devoted to a study of nonlinear interaction of strong microwaves (in X-band at intensities of $0.01\text{--}10\text{ MW/cm}^2$ and pulse duration from $50\text{--}100\text{ nsec}$ up to $1\text{--}10\text{ }\mu\text{sec}$) with a plasma flare, and of attendant physical processes. The small experimental plasma reactor bench is described in the second part. And the third part of our report reflects the first qualitative experiments on pulsed microwave deposition of thin carbon and metal films on various substrates. Obtained practical results and technique perspectives are discussed in detail.

1. INTRODUCTION

There is no doubt that *pulsed power microwave* discharge will occupy an important place among other plasma-chemical techniques of new materials creation. Recent experimental investigations devoted to applications of indicated discharges in gases^{1,2} confirm that well. For instance, the authors¹ were the first to carry out low-temperature plasma reduction of such hard powdered oxides as silica and alumina.

This is especially true for hard films deposition, semiconductor surface etching and doping in *vacuum* conditions. Such a technique may become a principally, physically novel tool in the field of advanced materials processing and surface plasma treatment. The only example: Batanov, Ivanov et al.³ have performed the plasma treatment of LiF crystal surface in the plasma flare of pulsed high-power MW discharge in vacuum. New advantages and a good efficiency of the process were achieved in their experiments. Thus, plasma flare of pulsed high-power MW discharge on a target surface in vacuum is of great interest not only from fundamental, but from practical view point as well.

The main process characterizing interaction of strong microwaves with a plasma cloud in vacuum is the creation of so-called plasma-resonance layer in front of this cloud moving toward radiation source. This phenomenon has been studied extensively in General Physics Institute and is fully described in review articles, Ref. 4,5. Notice that generation of strong Langmuir waves and following electrons' acceleration in a listed plasma resonance region cause an effective transformation of MW energy into plasma, creation of high plasma potentials, and production of ions with energies from thermal to as high as tens keV. The last is of more direct interest to us, as ion source for thin film deposition.

Above mentioned experimental investigations^{4,5} have been conducted at MW intensities $J = 10\text{--}100\text{ kW/cm}^2$ and pulse duration $\tau_p = 1\text{--}100\text{ }\mu\text{sec}$. Recent works, performed in Moscow Radiotechnical Institute with super-power MW generator - relativistic carsinotron, enabled us to carry out analogous experiments at MW intensities up to 10 MW/cm^2 and pulse duration $\tau_p = 50\text{--}100\text{ nsec}$.⁶⁻⁸ In particular, we have observed high plasma potentials above 100 kV ^{6,7} and very effective conversion of MW energy into quasi-stationary electric currents.⁸ New results confirm the validity of considered phenomenon physical model.⁴

Apparently the use of relativistic MW generators, with output power of 1-10 GW, will lead to production of high-energy ion electroless sources for deposition and other beam techniques. But, what is more important, high-power MW generators give rise to a technological process scaling and to possibility of a large surface treatment. So, the studies of new plasma-deposition techniques at "usual" MW intensities of 1-10 kW/cm² are of practical interest today.

2. EXPERIMENTAL SETUP

Experimental equipment used in our investigations is schematically depicted in Fig. 1. It consists of MW source (magnetron plus its pulse modulator), waveguide with accessories (including wave rectifier, directed tap - for testing an incident MW power, etc.), focusing dielectric lens, and stainless-steel vacuum chamber with its ancillaries. Operating parameters of microwave source are given in the figure. Pulse repetition rate may range from "0" to ~ 100 Hz depending on a value of MW pulse duration τ_p . Generator's output is butted with rectangular waveguide (2.3×1.0 cm²). Besides mentioned accessories, MW transmission-line is also supplied with a pumping up system for rising waveguide electrical strength. The necessary gauge air pressure in the system is about 1.5-2.0 atm.

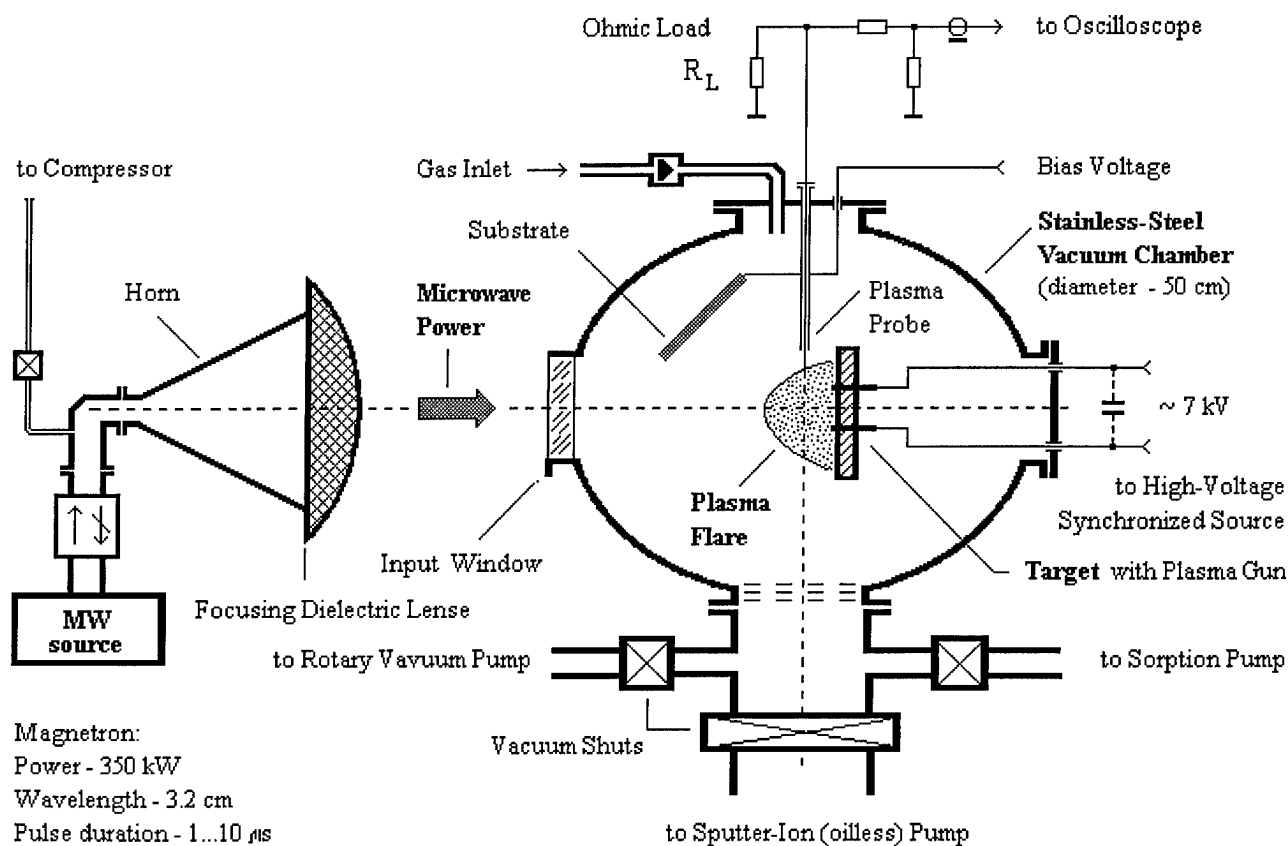


Fig. 1. Experimental equipment for pulsed microwave deposition

Focusing polyethylene lens, of 25 cm in diameter, is placed at the output aperture of the conic horn. The lens forms microwave beam with cross-section $\sim 2 \times 6$ cm² in focal region; longitudinal caustic is of 8 cm long. Thus, a maximum MW intensity in the focus is approximately equal to 30 kW/cm².

The construction of spherical vacuum chamber and auxiliary equipment are readily illustrated in Fig.1. Holders of the target and substrates are made of quartz or kapron tubes. In most of instances we have used erosion plasma gun being fed from an external synchronized high-voltage source. Gun electrodes and a target itself were made of materials to be sputtered, graphite, titanium and others.

Vacuum system consists of various type pumps, Fig. 1, that allows to work both in high vacuum and at intermediate pressures ranging from 10^{-3} ... 10^{-1} to above 100 Torr. In experimental conditions described below, working vacuum in the system was about 10^{-5} Torr, not better. It is caused by a high outgasing rate during the sputtering process.

Diagnostic instrumentation, including optic and X-ray detectors, construction of the plasma probe, etc., is similar to that used in cited above experimental works.⁵⁻⁷ There is no need to describe our diagnostics more detail.

3. FIRST RESULTS AND DISCUSSION

The data obtained with the plasma probe experiments are presented below, Fig. 2 and 3. Typical oscilloscope pictures of MW and the probe voltage pulses are depicted in Fig. 2. There is a time delay τ_d between the point $t = 0$ and the beginning of the probe signal. The last matches with the beginning of MW surface breakdown of a target; and τ_d depends on the value of MW intensity J , Ref.9. In case of using plasma gun, as would be expected, $\tau_d \rightarrow 0$.

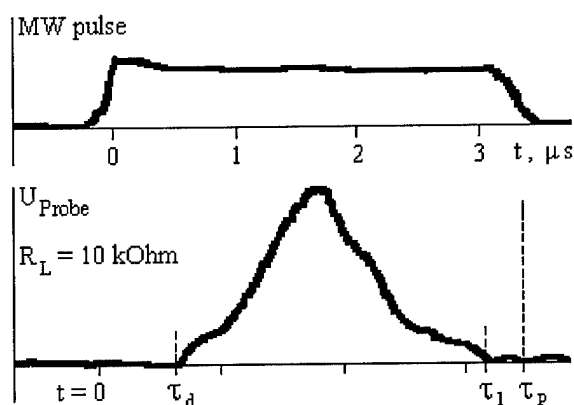


Fig. 2. Oscillograms of MW and probe pulses

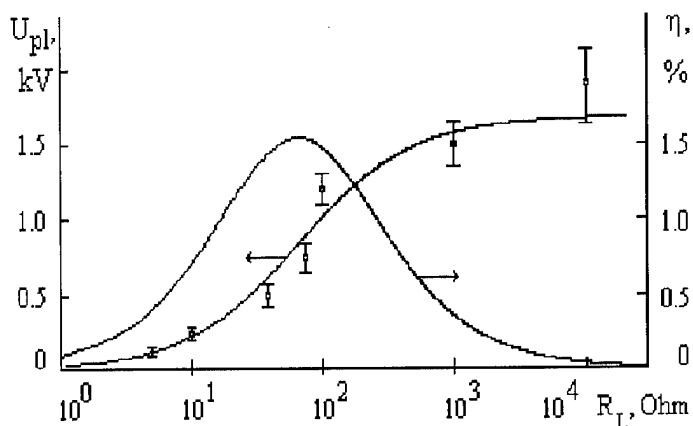


Fig. 3. Probe plasma characteristics

Some plasma characteristics measured with the probe are shown in Fig. 3. The maximum probe potential, $U_p \approx 1.5$ - 2.0 kV, was observed at non inductive load equal to 65 ± 15 Ohm. The outlined value U_p is in a good agreement with theoretical predictions:

$$eU_p \approx E_e \approx \frac{1}{2\pi} E_0 \sqrt{\lambda L}, \quad E_0 = \sqrt{2JZ}, \quad Z = 120\pi \text{ [Ohm]} \quad (1)$$

where E_e is an average energy of "fast" electrons accelerated in the plasma resonance region,⁴⁻⁶ and the plasma non-uniformity scale $L \sim \lambda$. Microwave intensity J was about 10-20 kW/cm².

Dependence $\eta(R_L)$, the efficiency MW energy conversion into plasma electron fluxes, was calculated with the following formula:

$$\eta = \frac{\frac{1}{R_L} \int_{\tau_d}^{\tau_1} U_p^2(t, R_L) dt}{P_{mw} \cdot \tau_1} \quad (2)$$

Corresponding results are presented in Fig. 3b. Changing the denominator of the formula (2) to $P_{mw} (\tau_1 - \tau_d)$, we will obtain $\eta \geq 3$ %. It is quite satisfactory value for our purposes and corresponds to using external pre-ionizing source, the listed synchronized plasma gun.

Now consider some experimental results of our preliminary attempts of films deposition. We have not gotten any satisfactory products in case of applying only microwave energy. The film deposition processes took place under

indispensable condition of using both MW and erosion plasma gun energy simultaneously. This fact may be explained, first, by the absence of an effective target sputtering under action of MW discharge only. On the other hand, erosion gun itself produces "something" being difficult to call "a film". Obviously, there is a certain MW "treatment" of the erosion plasma cloud with the accompanying formation of the necessary ion energetic spectrum.

Some metallic (Cu, Ti) and carbon films were deposited onto silicon, steel and quartz substrates. Besides this, the metal sputtering in vacuum and the following treatment of a metallic film in a gas-discharged plasma - without breaking the process - permits to produce some more chemical complexes, such as TiN and other films.

It should be notice, the volume structure, quality and adhesion forces of the films created were not enough good yet. In apparent, the reason is that the previous qualitative treatment of a substrate surface and an external substrate heater are a prime necessity. But the use of an external heater is undesirable from the viewpoint of technology perspectives, id est of a process scaling. We hope, this obstacle will be overcome with an increasing of MW pulse repetition rate up to several kilohertz. The last may, also, give such a possibility as to exclude the erosion gun from the technical process at all.

There is one problem else. Saegner, in his review article devoted to pulsed laser deposition techniques⁹ has pointed out the negative role of target's particulates and other outside impurities leading to a films' quality lowering. Possibly, the use of magnetic separation method, of external bias voltage applied to substrate, and, mainly, excluding of an erosion plasma source will help to "clean" the ion fluxes onto substrates.

Mentioned in Abstract advantages and perspectives of the new deposition technics, considered here, and our preliminary results are sufficient to allow definite conclusions and stimulate the future investigations.

Acknowledgments. The authors would like to thank Alexej Khomenko and Marina Loza for technical assistance, Eugene Galstjan and Pavel Sopin for useful discussions, and other colleagues from Moscow Radiotechnical Institute for their help and support at this difficult time.

REFERENCES

1. V. A. Brukvin, A. A. Ravaev, I. K. Tagirov, and P. S. Chernyshev, "Low-temperature reduction of silicon, boron and aluminum oxides in the powerful microwave produced plasma," *IV Sov. Conf. on Application of Electron-Ion Processing in National Economy*, Moscow Energetic Inst., pp. 59-60, Oct. 21-24, 1991 (in Russian).
2. G. M. Batanov, E. F. Bol'shakov, A. N. Voronin, A. A. Gorbunov, A. A. Dorofejuk, V. I. Kononov, and I. A. Kossiy, "Plasma-chemical deposition of thin films in the free-localized pulsed microwave discharge," *Zhurn. Tekhn. Fiziki*, vol. 63, no. 6, pp. 87-95, June 1993 (in Russian).
3. G. M. Batanov, V. A. Ivanov, M. E. Konyzhev, V. A. Konjushkin, and S. B. Mirov, "Production of an optically opaque layer on the surface of LiF crystal during painting in microwave discharge," *Pis'ma Zhurn. Tekhn. Fiziki*, vol. 19, no. 20, pp. 42-45, Oct. 1993 (in Russian).
4. G. A. Askar'jan, G. M. Batanov, and I. A. Kossiy, "Energy conversion of intense radiation in plasma flare," *Proc. of General Physics Inst. - Generation of Nonlinear Waves and Quasi-Stationary Currents in Plasmas*, vol. 16, pp. 3-10, Nauka, Moscow, 1988 (in Russian).
5. G. M. Batanov, V. A. Ivanov, "Plasma-flare microwave-electrical current energy conversion," *Ibidem*, pp. 16-45.
6. G. M. Batanov, V. A. Ivanov, M. E. Konyzhev, A. A. Ravaev, V. D. Seleznev, and A. I. Khomenko, "Generation of high potentials in the plasma by the interaction with intense microwave radiation," *Proc. I Int. Workshop on Strong Microwaves in Plasmas. Sec. N, Nonlinear Processes in Plasmas* (Sept. 18-23, 1990. Suzdal, USSR), vol. 2, pp. 553-558, IPFAN, Nizhny Novgorod, 1991.
7. V. A. Ivanov, M. E. Konyzhev, M. I. Loza, and A. A. Ravaev, "Generation of high potentials and fast electron diagnostics in microwave produced plasma flare," *Proc. XX Intern. Conf. on Phenomena in Ionized Gases*, Pisa, Italy, vol. 5, pp. 1091-1092, July 8-12, 1991.
8. A. A. Ravaev, M. I. Loza, "Microstrip antenna - an effective plasma converter of microwave radiation energy into quasi-stationary current," *Radiotekhnika i Elektronika*, vol. 36, pp. 1505-1509, 1991 (in Russian).
9. K. L. Saegner, "Pulsed laser deposition. Part I. A review of process characteristics and capabilities," *Processing of Advanced Materials*, vol. 3, no. 1, pp. 1-24, March 1993.

Ion Beam Surface Treatment: A New Capability For Rapid Melt And Resolidification Of Surfaces

R. W. Stinnett, D. C. McIntyre, R. G. Buchheit, Sandia National Laboratories
John B. Greenly, and Michael O. Thompson, Cornell University

ABSTRACT

The emerging capability to produce high average power (5-250 kW) pulsed ion beams at 0.2-2 MeV energies is enabling us to develop a new, commercial-scale thermal surface treatment technology called Ion Beam Surface Treatment (IBEST). This new technique uses high energy, pulsed (≤ 100 ns) ion beams to directly deposit energy in the top 2-20 micrometers of the surface of any material. The depth of treatment is controllable by varying the ion energy and species. Deposition of the energy with short pulses in a thin surface layer allows melting of the layer with relatively small energies and allows rapid cooling of the melted layer by thermal diffusion into the underlying substrate. Typical cooling rates of this process (10^9 - 10^{10} K/sec) cause rapid resolidification, resulting in the production of non-equilibrium microstructures (nano-crystalline and metastable phases) that have significantly improved corrosion, wear, and hardness properties.

We have conducted IBEST feasibility experiments with results confirming surface hardening, nanocrystalline grain formation, metal surface polishing, controlled melt of ceramic surfaces, and surface cleaning.

INTRODUCTION

Recent advances in high average power, pulsed ion beam systems are enabling a new technology to achieve rapid melt and resolidification of surfaces. Researchers at Sandia National Laboratories and Cornell University have developed the capability to produce 5-250 kW average power pulsed ion beams at 0.2-2 MeV energies using a repetitively pulsed (up to 120 Hz) concept designed for long component lifetimes. This new capability is enabling us to develop a commercial-scale thermal surface treatment technology called Ion Beam Surface Treatment (IBEST). This new technique uses high energy, pulsed (typically ≤ 100 ns) ion beams to directly deposit energy in the top 2-20 micrometers of the surface of any material. The depth of treatment is controllable by varying the ion energy and species. Deposition of the energy in a thin surface layer (Figure 1) allows melting or vaporization of the layer with relatively small energies (1 - 10 J/cm² for metal surfaces) and allows rapid cooling of the melted layer by thermal diffusion into the underlying substrate. Solidification of metals at the cooling rates typical of this process (10^9 - 10^{10} K/sec) results in the production of non-equilibrium microstructures (nano-crystalline and metastable phases) in the surface layer. Experiments with both laser and ion beams¹⁻⁸ have shown that surfaces produced by this rapid thermal quenching have significantly improved corrosion, wear, and hardness properties.

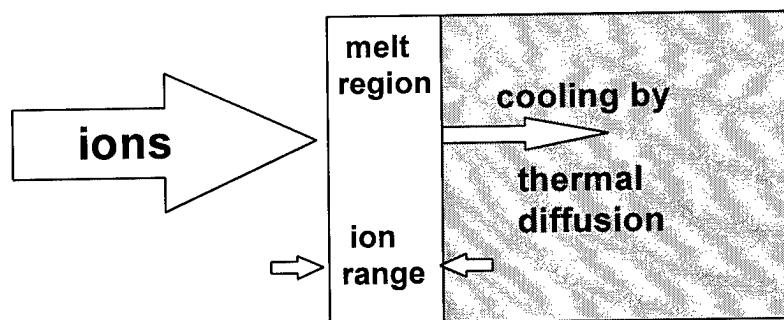


Figure 1. Ion BEam Surface Treatment (IBEST) uses a pulsed, high energy (0.2-2 MeV) ion beam to deposit energy over the classical ion range, typically 2-20 microns, in a surface, raising its temperature to melt. Thermal diffusion rapidly (10^9 - 10^{10} K/sec) cools the surface, leading to the formation of amorphous layers and the production of non-equilibrium microstructures by rapid quenching.

Ion Beam Surface Treatment (IBEST) is a thermal process that does not significantly change the atomic composition of the sample. The ion pulse rapidly heats a thin surface layer to melt using typically only 3×10^{13} ions per pulse. Over the ion range the implanted ion concentration is less than 10^{-3} atomic percent. The short pulse length allows the heated depth to be confined to approximately the ion range by limiting the effect of thermal diffusion. Thermal diffusion lengths in 60 ns are 1 and 4 microns in stainless steel and aluminum respectively, less than the proton range in the materials at typical IBEST ion energies of 0.4-1 MeV. The use of a new Magnetically-confined Anode Plasma (MAP) ion beam system¹¹⁻¹⁴ described later allows any gas ion to be used to deposit energy in materials. Protons, having the largest range in materials, can provide relatively deep treatment ranging from 5-15 microns in aluminum for energies of 0.5 to 1 MeV respectively.

The effects of Ion Beam Surface Treatment are similar to surface treatment using pulsed lasers but IBEST technology provides unique capabilities that allow it to avoid many problems intrinsic to laser technology including energy coupling to metals, edge effects, and high cost due to its in-depth energy deposition, large energy per pulse, and the low capital cost of hardware.

The energy coupling of ion beams to a material is independent of the surface preparation and only weakly dependent on the actual material. The availability of a clean, single species ion source opens up new areas for metal studies, especially in the solidification behavior of simple alloys. Thermal quench rates and the corresponding solidification velocities can be controlled by varying the beam energy and the ion species.

The typical area treated by a single IBEST pulse ranges from 100-1000 cm² depending on the application. This capability and our new repetitive pulse technology are key elements enabling high volume commercial applications.

Results Of Initial Experiments

IBEST experiments have been performed on several facilities including Sandia's Repetitive High Energy Pulsed Power (RHEPP) facility, Cornell University's LION accelerator, and LANL's Anaconda accelerator. These experiments are supported by an integrated team of researchers in pulsed power, beam physics, and materials science from Sandia National Laboratories, Cornell University, Los Alamos National Laboratories, and the UNM/LANL/SNL Advanced Materials Laboratory. Single pulse and burst-mode tests at 1/3 Hz have been used to produce initial treated samples while hardware for full scale repetitive operation is being optimized. Results from initial analysis confirm surface hardening, amorphous layer and nanocrystalline grain size formation, metal surface polishing, controlled melt of ceramic surfaces, surface cleaning of hydrocarbon layers from 304 stainless steel, oxide layer removal, and corrosion resistance.

These initial experiments clearly demonstrate the ability of Ion Beam Surface Treatment to significantly modify the properties of materials. The ion source for all of these initial experiments was a "flashover" source which produces a mixed species ion beam. Other experiments¹⁵ at Cornell University using this ion source have indicated that these beams are made up of approximately half H⁺ ions and half heavier ions, predominantly C⁺ and C⁺⁺. Future experiments will be done using the new, single species, Magnetically-confined Anode Plasma ion source described later in this article. The following sections describe some of our initial experiments in more detail.

Treatment O-1 tool steel

These samples were treated using Cornell University's LION accelerator (1 MeV, 4Ω, 40ns FWHM). The ion energy during the FWHM of the power pulse varied from approximately 0.5-1 MeV. The ion energy delivered to the surface was approximately 10 (+/- 30%) J/cm² as measured by biased and apertured ion collectors and the load voltage monitor. The samples were located approximately 25 cm from the beam system. Treatment was done at a vacuum level of approximately 2x10⁻⁴ torr.

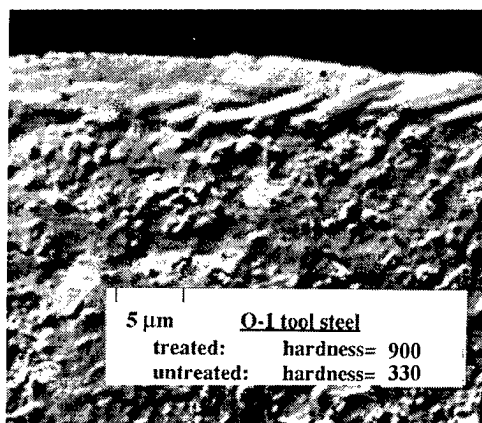


Figure 2. This cross sectional view of an O-1 tool steel sample shows the effects of rapid surface melting and cooling by a 50 ns, 10 J/cm², 0.5-1 MeV mixed proton and carbon beam.

Cross-sections of IBEST-treated O-1 tool steel samples were examined¹⁸ using an optical microscope as well as cross-sectional and plan view Transmission Electron Microscopy (TEM). An optical micrograph of the cross-section of an IBEST-treated sample is shown in Figure 2. The near-surface several microns of the sample were featureless. In contrast,

the underlying untreated tool steel material had an equilibrium structure composed of α -Fe (bcc-iron) and large iron carbides. The results of the optical metallography evaluation suggested that the iron carbides in the treated region had been largely redissolved into the bcc-iron matrix. The TEM examination of the IBEST-treated O-1 tool steel sample revealed that the near surface region of the sample was composed of microcrystalline grains approximately 20 nm in diameter. Hardness testing on the O-1 tool steel samples was performed using a Shimadzu microindentation hardness tester. Knoop indentations were made using a 25 gr load on the Knoop tip yielding a Knoop hardness (H_K) of $H_K = 900$ for the treated surface and $H_K = 330$ for the untreated surface of O-1 tool steel.

Both the optical metallography and TEM results indicate that carbon was dissolved into the Fe matrix during the pulsed beam treatment. The kinetics of the iron carbide dissolution process during heating, melting, and resolidification were apparently more rapid than the kinetics required for carbide reprecipitation during cooling. The presence of FeO in the treated layer suggests that oxide was incorporated into the layer from the oxidized, untreated surface when melting occurred during treatment. Oxygen may also have been incorporated during melting from the background gasses in the treatment chamber.

Polishing of Ti-6Al-4V

In other experiments we treated Ti-6Al-4V on the Anaconda accelerator (400kV peak voltage, 40 kA total current, 500 ns pulse duration) at a treatment level of 7 J/cm^2 (+/- 30%) at 250-400 keV using a 400 ns ion pulse. The surfaces were treated using 4 pulses separated by at least 5 minutes between pulses. The untreated and treated surfaces are shown in Figure 3. The surface roughness of the untreated, machined surface was approximately 5 microns. IBEST treatment resulted in a reduction of roughness to 0.1 micron. The energy deposited in the top 3-4 microns of the near surface region in these experiments was more than sufficient to raise the temperature to the melting point and was likely large enough to cause some ablation of the surface. The time the surface was above the melting point can be roughly estimated from the energy deposition profile and the calculated thermal diffusion properties of the material to be 250-500 ns.

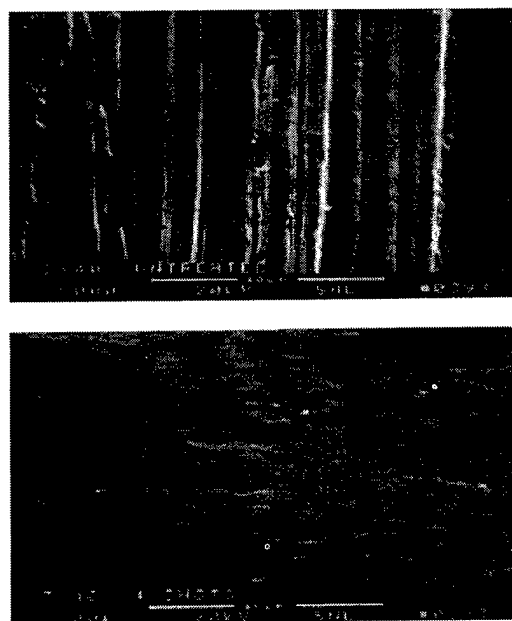


Figure 3. IBEST treatment of a Ti-6Al-4V machined surface (top) treated with 4 pulses of a 400 ns duration, 7 J/cm^2 mixed proton and carbon beam demonstrates significant surface smoothing to a 0.1 micron scale roughness.

Corrosion resistance

Initial corrosion resistance studies have been performed on the RHEPP facility at Sandia National Laboratories. In this work, samples were treated using a 700 keV, 60 ns, mixed proton-carbon beam at $2\text{-}3 \text{ J/cm}^2$. Corrosion resistance of the treated aluminum alloy surfaces has been assessed by electrochemical testing and by salt spray exposure testing. Treated alloys tested thus far include 2024-T3 (Al-4.4Cu-1.5Mg-0.6Mn), 6061-T6 (Al-1.0Mg-0.6Si), and 7075-T6 (Al-5.6Zn-2.5Mg-1.6Cu). Electrochemical tests used include anodic polarization and electrochemical impedance spectroscopy (EIS) conducted in an aerated aqueous 0.5M NaCl solution. Exposure testing has been conducted at controlled temperatures in a

saturated salt fog environment per ASTM B117. Anodic polarization of 2024-T3 has shown that passive current densities are reduced and pitting potentials are shifted to more positive potentials indicating improved resistance to localized corrosion. Figure 4 illustrates these results.

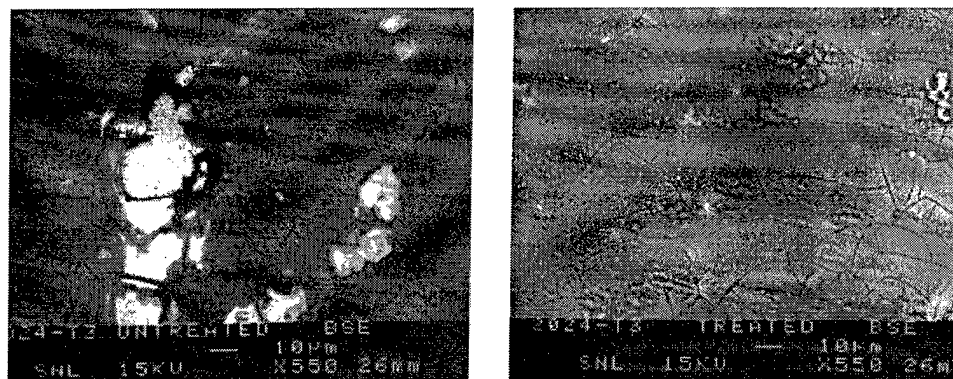


Figure 4. A 168 hour salt fog test (ASTM B117) of untreated and treated samples of Aluminum 2024-T3 shows resistance to pitting due to IBEST treatment.

Controlled melt and resolidification of alumina surface

On the LION accelerator at Cornell University we treated a polished Al_2O_3 sample with a single pulse at a level of 10-20 J/cm^2 to demonstrate controlled melt and resolidification. The result is shown in Figure 5. This technique shows promise for surface porosity reduction but also shows some microcracking on a 0.1 micron scale.

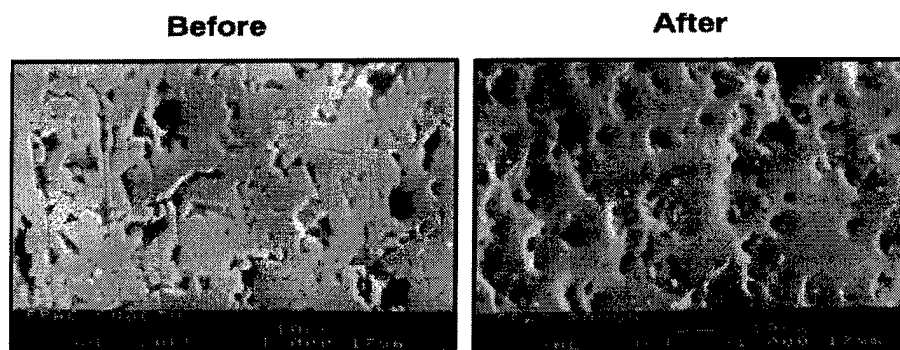


Figure 5. This alumina sample was treated using a single pulse, 0.6-1 MeV mixed proton and carbon beam at 10 J/cm^2 . The result shows controlled melt and resolidification of the ceramic surface without serious problems although some 0.1 micron scale cracking was observed. The width shown is 100 microns.

Enabling Technologies For IBEST

Until recently pulsed ion beams have not been considered a viable technology for routine materials processing applications because of their inability to deliver the multi-kilowatt average powers with long component lifetimes needed for commercial processing applications. During the past few years there has been significant progress in two complementary technologies that now enable the design of 5-500 kW average power, $>10^8$ shot lifetime ion beam surface treatment systems for materials processing.

The first of these advances is the development of a compact, electrically efficient, repetitively pulsed, magnetically switched pulsed power system capable of 10^9 pulse component lifetimes. This prototype system, the Repetitive High Energy Pulsed Power (RHEPP) facility¹⁰ (0.8 MV matched voltage, 35Ω, 60 ns FWHM pulse duration, 120 Hz repetition frequency), began operation this year at Sandia National Laboratories. This new facility, the first of its kind in the world, is designed to operate continuously at 120 Hz, delivering 150kW average power. This system has demonstrated operation at

50% electrical efficiency from the wall plug to energy delivered to a matched load. RHEPP is also designed to allow operation at reduced pulse rates or in single pulse mode if desired. Its capability to efficiently produce high average power, high voltage electrical pulses using a compact design is a breakthrough for the commercial application of pulsed power.

The second advance is an ion beam system that is capable of operating repetitively and efficiently to transform the pulsed power of RHEPP into an ion beam. An ion beam system capable of operating at repetitive pulse rates of 100 Hz in 10 pulse burst mode (active cooling was not part of the design) was demonstrated¹³ at the Cornell University Laboratory of Plasma Studies. An improved version of this system is now being fielded on the RHEPP facility at Sandia for operation in burst mode. This system, the Magnetically-confined Anode Plasma (MAP) ion source, shown in Figure 6, is based on the concept of drawing ions from a single species plasma anode rather than the solid, flashover anode used in standard single pulse ion beam systems. The plasma can be formed from any gas ion.

The MAP ion beam system produces an annular beam which is brought to a broad focus symmetric about the axis shown in the figure. In the cathode (ground potential) electrode assembly (A), slow (100 μ s risetime) magnetic field coils (B) produce magnetic flux which provides the magnetic insulation of the accelerating gap between the cathode and the anode (high voltage) electrode assembly (C) connected to the output of the RHEPP generator. The ion source that supplies ions to the accelerating gap is contained within the anode assembly. The MAP source operates in the following way: a fast gas valve (D) on the axis of the anode assembly produces a rapid (200 μ s) gas puff which is delivered through a supersonic nozzle (E) to produce a highly localized volume of gas (F) directly in front of the surface of a fast-driving coil (G) located in an insulating support structure (H). After preionization by a 1 μ s induced electric field, the fast coil is energized, inducing a loop voltage of 20 kV on the gas volume, driving a breakdown to full ionization, and moving the resulting plasma toward the flux-excluding anode field-shaping electrodes (C) in about 1.5 μ s, to form a thin magnetically-confined plasma layer. The RHEPP pulse is then applied to the anode assembly, accelerating ions from this plasma layer to form the ion beam. The magnetic flux surfaces (J) at the time of beam extraction are shown. The beam propagates in vacuum to a broad focal area at the target plane at the right of the figure, where material samples are placed for treatment.

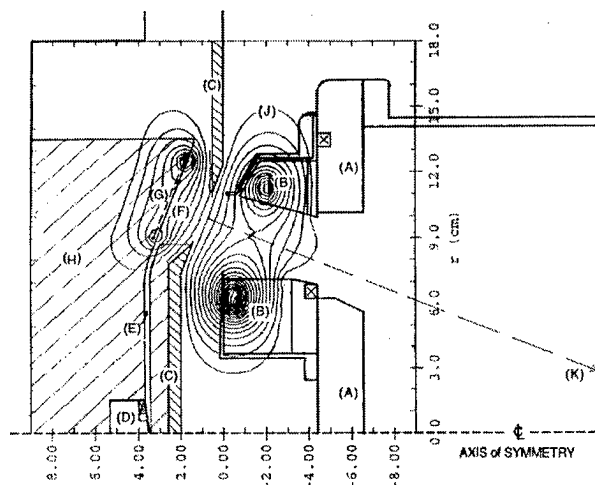


Figure 6. MAP Ion Diode for RHEPP. The cathode assembly (A) with slow magnetic field coils (B); the anode electrodes/magnetic flux shapers (C); the fast gas valve (D); the gas nozzle (E); the gas breakdown and plasma formation region (F); the fast-driving magnetic field coil (G) in the insulation support structure (H), the magnetic flux of the slow and fast coils, as they are at the time of the RHEPP accelerating pulse (J); the ion beam propagation direction to the material target (K).

Conclusions

We have demonstrated that Ion Beam Surface Treatment (IBEST) can significantly alter the microstructures of the near surface region of materials and thus the material properties. The effects of IBEST include hardening, corrosion resistance, polishing and cleaning. Initial results from these experiments indicate that IBEST can provide new capabilities for cost-effective surface treatment for a variety of applications.

Acknowledgments

Our Ti-6Al-4V smoothing experiments were conducted on the Anaconda accelerator at Los Alamos National Laboratory with the assistance of D. Rej, and W. Waganaar.

References

1. E. M. Breinan, B. H. Kear, L. E. Greenwald, and C. M. Banas, "Laser Glazing, a New Process for Production and Control of Rapidly Chilled Metallurgical Microstructures," Lasers in Modern Industry, (Dearborn, Michigan 1979), 147-166.
2. H.-W. Bergmann, B. L. Mordike, "Laser and Electron-Beam Melted Amorphous Layers," J. Mat. Sci., (1981), 863-869.
3. R. Fastow, "Pulsed Ion Beam Surface Modification of Materials", Ph.D. thesis, Cornell University, 1985.
4. R. Rastow, Y. Maron, and J. Mayer, "Pulsed ion beam melting of silicon", (Phys. Rev. B, 31,893 (1985)
5. G. E. Remnev, and V. A. Shulov, "Practical Applications of High-Power Ion Beams," 9th International Conference on High-Power Particle Beams, Washington, D.C., 5/25-29, 1992.
6. S. A. Chistjakov, A. M. Gagarin, R. G. Koishibaev, Yu Yu Rjuchkov, V. A. Kuzminikh, V. M. Milutin, V. A. Pirogov, V. A. Perov, A. D. Pogrebnyak, S. V. Plotnik, G. E. Remnev, Yu G. Rusin, and V. P. Janovskii, "Ion Mixing of Near Surface Layers in Au-Cu, Cu-Mo Systems Irradiated by HPIB," Physics Letters, Vol. 131, No. 1, 8/1, 1988, 73-77.
7. V. L. Kutuzov, M. Yu. Ovsyannikov, I. G. Romanov, A. D. Pogrebnyak, and G. E. Remnev, "Mechanical and Frictional Properties of Tool Steels Exposed to HPIB Irradiation," Mechanical and Frictional Properties of Tool Steels, 11/8, 1988, 361-364.
8. Y. Shimotori, M. Yokoyama, H. Isobe, S. Harada, K. Masugata, K. Yatsui, JAP **63**, 968 (1988).
9. TRIM-90.05, J. Ziegler and J. Biersack
10. H. C. Harjes, K. J. Penn, K. W. Reed, C. R. McClenahan, G. E. Laderach, R. W. Wavrik, J. L. Adcock, M. E. Butler, G. A. Mann, G. E. Pena, G. J. Weber, D. VanDeValde, L. E. Martinez, D. Muirhead, P. D. Kiekel, D. L. Johnson, E. L. Neau, "Initial results from the RHEPP module", Proc. 9th Int. Conf. on High Power Particle Beams, Washington D.C., May 25-29, 1992, 333-340.
11. J. B. Greenly, M. Ueda, G. D. Rondeau and D. A. Hammer, "Magnetically Insulated Ion Diode with a Gas-Breakdown Plasma Anode," J. Appl. Phys **63**, 1872 (1988).
12. J. B. Greenly, L. Brissette, A. Dunning, S. C. Glidden, D. A. Hammer and W. A. Noonan, "Plasma Anode Ion Diode Research at Cornell: Repetitive Pulse and 0.1 TW Single-Pulse Experiments," Proceedings of the 8th Intl. Conf. on High Power Particle Beams, B. N. Breizman and B. A. Knyazev, Eds., Novosibirsk, 1990 (World Scientific), p. 199.
13. W. A. Noonan, Ph.D. thesis, Cornell University, 1993.
14. M. Ueda, J. B. Greenly, G. D. Rondeau and D. A. Hammer, Rev. Sci. Instr. **64**(10), 2737 (1993).
15. G. Rondeau, Ph.D. Thesis, Cornell University, 1989.
16. J. H. Scofield, J. Electron Spectroscopy **8**, 129 (1976).
17. D. J. Rej, R. R. Bartsch, H. A. Davis, R. J. Fael, D. C. Gautier, J. B. Greenly, I. Henins, T. W. Linton, R. E. Muenchausen, W. J. Waganaar, "Intense Ion Beam Research at Los Alamos", Proceedings of the 9th Intl. Conf. on High-Power Beams, David Mosher and Gerald Cooperstein, Eds., Washington D. C., 1992 (NTIS PB92-206168)
18. R. W. Stinnett, R. G. Buchheit, F. A. Greulich, C. R. Hills, A. C. Kilgo, D. C. McIntyre, J. B. Greenly, M. O. Thompson, and D. J. Rej, "Thermal Surface Treatment Using Intense, Pulsed Ion Beams," Accept. for pub. in JMRS.

The atomic structure and phase state of quenched FePd₂Au alloy after bombardment by Ar⁺ ions

E.F. Talantsev, N.N. Syutkin, V.V. Ovchinnikov and V.I. Chernoborodov

Institute of Electrophysics, Urals Division of the Russian Academy of Sciences
34, Komsomolskaya Str., GSP-387, Ekaterinburg, 620219, Russia

ABSTRACT

Field ion microscopy techniques have been used to investigate the atomic structure of quenched FePd₂Au alloy before and after bombardment by Ar⁺ ions (ion energy E=20 keV, fluence D=2·10¹⁷ ions/cm²). It has been confirmed that ion bombardment induces a "disorder-order" phase transformation in a subsurface layer more than 20 μm deep.

1. INTRODUCTION

The modification of surfaces of metals and alloys by beams of accelerated ions can initiate various types of structural phase transformations [1]. The physical-and-chemical processes running in a thin surface layer of a solid bombarded by ions have, as a rule, a destructive character. This, in particular, can lead either to a partial or a full amorphization of the crystal lattice in the thin surface layer having a thickness of several ion projective ranges [1]. It was reported [2,3] that in Fe-Al and FePd₂Au alloys under ion bombardment the entire bulk of the crystal (excluding the said surface layer) undergoes a phase transformation of the "disorder - order" type.

X-ray diffraction studies, as well as measurements of resistivity of FePd₂Au in situ directly under ion bombardment [3] have led to the conclusion that in a disordered FePd₂Au alloy under ion bombardment there takes place a phase transformation of the atomic ordering type (this may be considered as improvement of alloy structure under ion bombardment). According to [3] the alloy gets ordered to a depth of up to several hundreds of micrometers, this exceeding the calculated projective range of Ar⁺ ions in FePd₂Au. Ordering under ion bombardment proceeds at temperatures below the threshold diffusion defreezing temperature T_f (i.e. that temperature below which the diffusion coefficient is so small that any noticeable diffusion atom restructuring during meaningful intervals of time are impossible).

In this investigation we have attempted to identify the phase state and carry out by means of an ultramicroscopic technique - field ion microscopy (FIM) [4] a detailed study of the atomic structure of quenched FePd₂Au alloy before and after ion bombardment. The use of FIM ensures the acquisition of data on the three-dimensional structure of metals and alloys [4], as well as of metal-oxide superconductors [5] at individual atom level. Micro-volumes of FePd₂Au alloy which were at least several ion projective ranges (0.3 - 25 μm) away from the irradiated surface were investigated.

2. EXPERIMENTAL

Ordering processes in disordered alloys of the FePd_{3-x}Au_x system begin to run at temperatures above T= 690 K. Ion bombardment leads to an increase in atom mobility in FePd₂Au alloy so that the emergence of an ordered phase is possible in the temperature interval T= 493-673 K [3].

In this investigation the following ion bombardment regime was chosen: the target was heated by means of a microheater to $T = 475\text{--}461\text{ K}$, then acted on by Ar^+ ions ($E = 20\text{ keV}$). The ion current density was adjusted so that the temperature of the target in the course of the bombardment was maintained within $T = 598\text{--}608\text{ K}$. The integral radiation dose was $D = (2.2\text{--}2.3) \cdot 10^{17}\text{ ions/cm}^2$.

The technique of FIM investigations practically did not differ from the traditional one: the initial specimens of the disordered FePd_2Au alloy were first certified in a field ion microscope, then subjected to ion bombardment and after this studied by FIM.

Needle emitters were made from FePd_2Au wire blanks (diameter 0.1 mm) which underwent thermal treatment: $T = 1273\text{ K} - 1\text{ h}$, quenching in water. Electrochemical polishing at $U = 3\text{--}7\text{ V d.c.}$ in a 10% solution of HClO_4 in ethylene glycol monobutyl ether yielded needle emitter with the required radius of curvature at the tip apex ($R = 10\text{--}100\text{ nm}$).

After having been certified in a field ion microscope the FePd_2Au needle emitters were welded to a nickel holder in the measuring cell and the whole was placed in the ion implantation setup. The ion beam was directed perpendicular to the axis of the tip emitters. The temperature of the nickel holder was measured to within $\pm 1.5\text{ K}$. A thermostat was used to set the initial temperature of the nickel holder to within $\pm 3.0\text{ K}$ in the range $T = 313\text{--}673\text{ K}$ [3].

The ion source based on reflex discharge with a hollow cold cathode ensured a continuous Ar^+ ion beam with $E = 20\text{ keV}$ and current density within $J = 50\text{--}150\text{ mA/cm}^2$.

3. RESULTS AND DISCUSSION

FIM images of quenched FePd_2Au alloy are characterized by irregular ion contrast typical of the disordered state (Fig.1). The sequence of (HKL) faces showing up in the ion micrographs in the decreasing order of morphological prominence is as follows: (111), (002), (022), (113), etc., which is typical of fcc lattice.

The ion contrast of irradiated FePd_2Au alloys is qualitatively different from that of quenched alloys (Fig. 2). FIM images show a high regularity of ion contrast. The highest prominence is exhibited by (001) face, then follow dodecahedron (011), octahedron (111) faces, etc (Fig.2). On the whole ion micrographs of FePd_2Au after ion bombardment correspond to micrographs of ordered alloys and intermetallic compounds having the L1_2 superstructure (for example, Pt_3Co [4]).

The emergence of a superstructure in an irradiated FePd_2Au alloy is also confirmed by transmission electron microscopy investigations of tip emitters (Fig.3).

Families of superstructural planes (for example, (001), (011)) are imaged in FIM micrographs in the form of alternating bright and dim rings, which correspond to the edges of single atom (HKL) planes packed chemically with different atoms. Crystallographic analysis of ion contrast has revealed that predominantly palladium and gold atoms show up in the ion images (i.e. iron atoms occupying one of four simple cubic lattices in the L1_2 superstructure are not visible in the micrographs).

The main superstructural defects in the irradiated FePd_2Au are antiphase domain boundaries. The registered antiphase boundaries practically always lie in cubic (100) planes, this being typical of antiphase boundaries of thermal origin in the L1_2 superstructure [6].

The irradiated needle specimens were subjected to controlled electrochemical polishing and then examined in a field ion microscope with the purpose of evaluating the depth at which the phase transformation takes place. No disordered phase was revealed in the bulk of the needle emitters. Preliminary estimates permit us to assert that the depth down to which the FePd_2Au alloy gets ordered under ion bombardment exceeds $20\text{ }\mu\text{m}$.

4. CONCLUSIONS

1. It has been established that under ion bombardment a phase having long-range order emerges in a disordered alloy. The phase transformation occurs at temperatures below the threshold diffusion defreezing temperature T_f .

2. The phase transformation induced by ion bombardment extends to a depth exceeding $20\text{ }\mu\text{m}$.

5. ACKNOWLEDGEMENTS

The authors wish to thank L.N. Tyulenyev for the specimens they kindly supplied and A.Yu. Volkov for help in the transmission electron microscopy investigations. The help of Mr. B.V. Holin in the preparation of this manuscript is very appreciated. This work was supported, in part, by a Soros Foundation Grants awarded by the American Physical Society.

6. REFERENCES

1. H. Ryssel and I. Ruge, *Ion Implantation*, John Wiley & Sons, New York, 1986.
2. Yu.E. Kreindel and V.V. Ovchinnikov, "Structural transformations and long-range effect in alloys caused by gas ion bombardment," *Vacuum*, Vol. 42, pp. 81-83, 1991.
3. Yu.G. Ignatenko, V.I. Chernoborodov and V.V. Ovchinnikov, "Influence of ion bombardment on electrical properties of ordered alloys $(\text{Pd}_{1-x}\text{Au}_x)_3\text{Fe}$," *Proc. of the IX Symposium of High-Power Electronics (Ekaterinburg-Moscow, Russia)*, pp. 360-361, 1992.
4. E.W. Müller and T.T. Tsong, *Field Ion Microscopy. Principles and Applications*, Elsevier, New York, 1969.
5. G.A. Mesyats, N.N. Syutkin, V.A. Ivchenko and E.F. Talantsev, "Atomic structure of superconductor $\text{YBa}_2\text{Cu}_3\text{O}_{7-x}$ in field ion microscope", *Journal de Physique (Paris)*, Vol. C6-49, pp. 477-481, 1988.
6. N.S. Stoloff and P.G. Davies, *The Mechanical Properties of Ordered Alloys*, Progress in Materials Science, Vol. 13, Pergamon Press, New York, 1967.

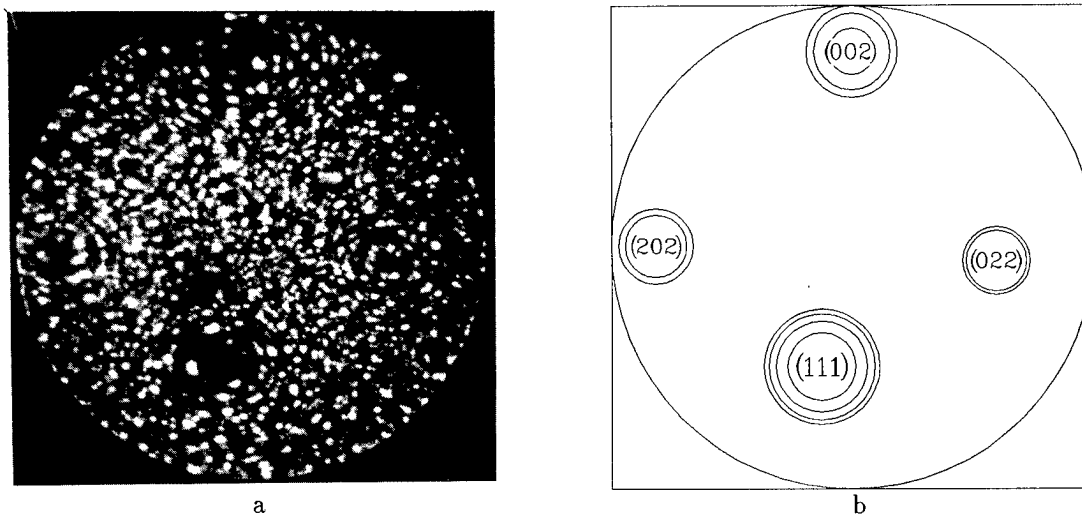


Fig. 1. Field ion micrographs of quenched FePd_2Au alloy (a) and corresponding stereographic projection (b).

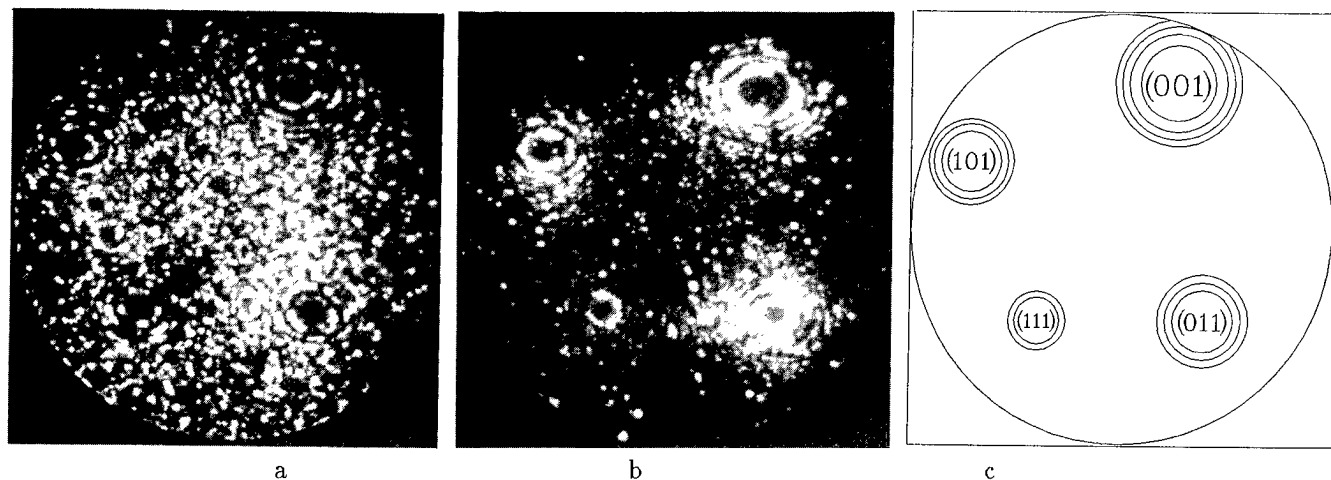


Fig. 2. Field ion micrographs of quenched FePd_2Au alloy after ion bombardment (a,b) and corresponding stereographic projection (c). Field ion micrographs taken at best image voltage (a) and just below best image voltage (b).

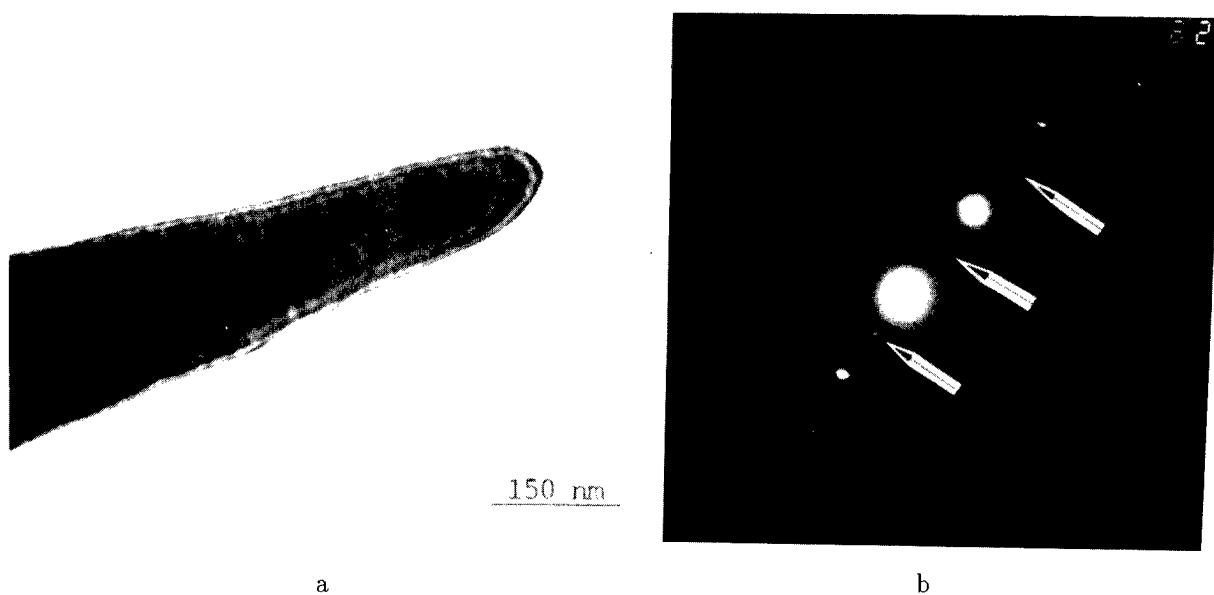


Fig. 3. Transmission electron micrograph of a FePd_2Au needle (a) and diffraction pattern of the same needle (b) (long-range order reflections arrowed).

Composite plastic coatings and face rolled materials technology, energy- and environment-saving, based on irradiation of liquid monomers by broad and high-current electron beams in vacuum

David Vaisburd

Tomsk Polytech University and High-Current Electronics Institute Russian Academy of Sciences Siberian Division
4 Akademicheski Avenue Tomsk 634055 Russia

ABSTRACT

The technology is based on the well-known process of hardening some organic liquid monomers and oligomers (resins and lacquers) under the action of ionizing radiation, i.e. electron, ion, ultra-violet, laser, and X-ray beams. The main mechanism of hardening is three-dimensional polymerization of initial monomers induced by irradiation. First of all one-dimensional polymer chains are created. And the next stage is cross-linking of them. Numerical attempts to apply such a process for plastic materials production met some earnest difficulties. Our decision to perform the whole processing in vacuum changed radically the main properties of radiation induced hardening technology. The inhibition of polymerization by reactive oxygen became unessential. The output window foil of accelerator became unnecessary. Application of super broad beams such as 1 sq. m became possible. The entire efficiency of grid electricity was increased to 60% and it was not the limit. One of the main advantages is that the processing carried out in vacuum may satisfy the highest ecological standards. The technology developed is contamination free and environment-saving.

1. HISTORICAL BACKGROUND

The first steps of decorative plastic coatings processing by means of electron beam irradiation of thin transparent lacquer layer deposited on decorative film glued onto a furniture surface were carried out in the early 50-s in the Great Britain and the USA. Low-current electron accelerators with thermal cathodes were used as other didn't exist. The electron beam was scanned across a conveyor. But such a technology met some earnest difficulties.

The beam ionized the air and created plasma containing oxygen and nitrogen ions and their molecules and radicals. Reactive oxygen penetrating into the lacquer inhibited greatly the hardening process in the thin surface sublayer. The radiated lacquer layer became acutely heterogeneous, it consisted of easily hardened body and hard hardened surface. Americans proposed and applied the nitrogen blow over the radiated lacquer surface to eliminate the hardening inhibition by oxygen-containing radicals. This method helped a bit, but significantly complicated the processing and increased the prime cost.

In the middle 60-s a significant progress occurred in electron beams technology. High-current accelerators were designed and made in Russia and the USA. They were based on the gigantic amplification of cold cathode self-emission in the super-high pulsed electric field. The record currents of electron beams jumped up by 10^4 times.

Tomsk is one of the world recognized centers of high current accelerators owing to creative scientific engineering and business activities of Professor Mesyats and his collaborators from High-Current Electronics Institute (HCEI) of Russian Academy of Sciences and Tomsk Polytech University (TPU).

In the middle 70-s Mesyats became acquainted with lacquer hardening technology by means of electron irradiation. And proposed the pulsed power electron beams to be applied in such processing. He expected that under intense irradiation the lacquer would be quickly polymerized before slow oxygen diffusion inhibited it. Followed scientific research carried out by Chmukh and Sakharov in HCEI and TPU confirmed the expectations. Lacquer's surface was hardened out by pulsed power electron beam in air without nitrogen blow.

Mesyats and his collaborators undertook an attempt to adopt the pulsed power electron beams in industry for producing polishing faces of TV set wooden cases at Lvov Plant. Professor Kreindel and Professor Schanin with collaborators developed and made powerful electron accelerator with plasma cathode and broad beam for that purpose. Industrial tests of pulsed power beams in hardening technology proved that the first problem arisen, i.e. "oxygen inhibition of polymerization" might be overcome¹. But others appeared.

The second and the most essential was great harm for ecology. Powerful electron beam in air generated intensively aerosols, ozone, nitric oxide. The latter, for example, combining with atmospheric moisture produces nitric acid.

The third hard problem is following. The output of power electron beam from accelerator's vacuum chamber into the atmosphere required a complicated cooling system for output foil, which had a short life-time.

2. PLASTICS PROCESSING BY IRRADIATION IN VACUUM

In 1991 author proposed to perform whole sequence of basic technological operations in vacuum of $10^{-5} \div 10^{-1}$ Torr, including irradiation without fail. We decided to develop and build up process equipment for thin plastic composites producing in the form of face materials like washable wallpapers. There is great demand for such goods in Russia. The main consumers are population, agriculture and various industries: furniture- and wood-processing, building, aircraft, etc. By our request Professor Schanin and his collaborators made a high-current electron accelerator with plasma cathode. Its parameters are: pulse duration $1 \div 30 \mu\text{s}$, energy $0.18 \div 0.22 \text{ MeV}$, mean reiteration frequency $1 \div 50 \text{ Hz}$, cross-width $0.7 \div 1.0 \text{ m}$.

Our proposal to perform the whole processing in the vacuum was tested on a working lowered model of technological machinery. We produced various samples of the plastic composite ribbons using the liquid lacquer, from one side, and paper tape, fiber glass, fiber carbon, metal networks, from the other side, as the primary products. The samples of such goods displayed high mechanical strength; chemical stability to the action of acids, alkalies and many others vehicles; heat stability up to 500 K ; and fine appearance.

Our decision to realize the whole processing in vacuum changed radically the main properties of the radiation induced hardening technology. The variety of hard problems naturally disappeared and some advantages appeared:

1. The inhibition by reactive oxygen became unessential.
2. The accelerator's output window foil became unnecessary.
3. Application of super-broad beams such as $1 \times 1 \text{ m}^2$ became possible.
4. The whole efficiency of grid electricity was increased to 60% and it was not the limit.
5. One of the prior advantages is that the production carried out in vacuum may satisfy the highest ecological standards. The technology became contamination free and environment saving.

3. PROCESS EQUIPMENT

Now the full process equipment set is ready (Fig.). It consists of big vacuum chamber, inner machine-tool working in vacuum, pulsed-power repetitive accelerator producing broad electron beam and truck for moving the machine-tool off and into the vacuum chamber. Its productivity is expected of $300\,000 - 500\,000 \text{ sq. m}$ of plastic composite ribbon per one year. Electric power consumption is 35 kW .

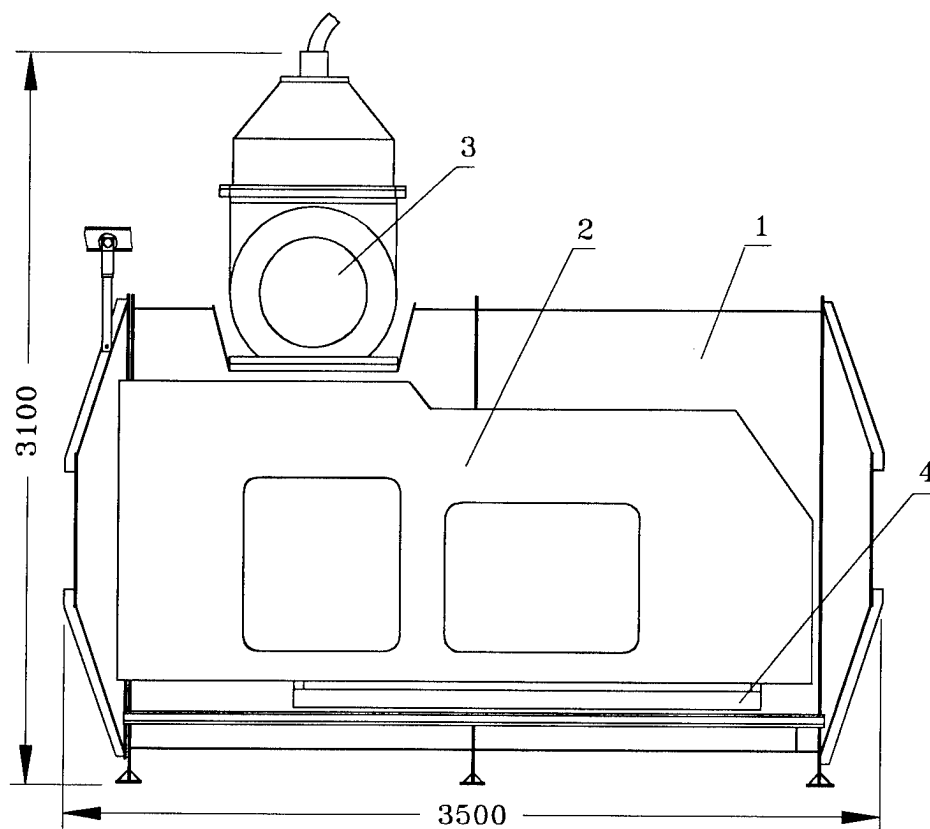


Fig. Process equipment: 1 - big vacuum chamber, 2 - inner machine-tool working in vacuum, 3 - pulsed power repetitive accelerator, producing broad electron beam, 4 - truck for moving the machine-tool off and into the vacuum chamber.

4. REFERENCES

1. E.N.Abdullin, D.I.Vaisburd, N.N.Koval, Yu.E.Kreindel, G.A.Mesyats, V.N.Chmukh, and P.M.Schanin, "Pulsed-power electron beam application for polymerization of polyethers", Letters to JTP, Vol. 4, No. 4, pp. 213-215, February 1978.

SESSION 11

Additional Papers

In situ Surface Charge Distribution Measurement of Alumina Insulator Surfaces After Impulse Voltage Application in Vacuum

Tumiran,* Shinichi Kobayashi,* Hiroshi Imada,* Mitsuaki Maeyama,*
Takahide Ishii,* Yoshio Saito,** Noriaki Sato* and Noriyuki Kawada.***

*Saitama University, 255 Shimo-ookubo, Urawa, Saitama,
338, Japan

**National Laboratory for High Energy Physics, 1-1 Oho,
Tsukuba, Ibaraki, 305, Japan.

***Mitsubishi Heavy Industries, Ltd, Kan-on-shinmachi,
Hiroshima, 733, Japan.

ABSTRACT

This paper investigates the surface charge distribution of an alumina insulator surface after flashover tests by impulse voltage application. The measurement of surface charge distribution and the voltage testing were both done in vacuum (*in situ*). The vacuum chamber for the voltage flashover testing experiments was maintained at the pressure of 1.3×10^{-8} Pa. Impulse voltage was applied with positive and negative polarity. The surface charge was measured for both positive (flashover and unflashover) and negative (flashover and unflashover) polarity. Applying the positive impulse polarity produces a positive charge on the alumina surface, when the impulse polarity is reversed both the positive and negative charges were detected in case of flashover, and only negative charge was detected in case of unflashover.

1. INTRODUCTION

It has been known that the dielectric strength of a solid insulator surface in vacuum is inferior to that of the insulator itself. Therefore, the ability of the insulator to sustain high voltage in vacuum is limited by surface flashover. Various attempts have been made to improve the holdoff voltage of insulator surfaces in vacuum¹. Many have concluded that the flashover voltage of the insulator surface in vacuum is dependent of the insulator material, geometry, surface conditions and electrode geometries.^{1,2,3} Many theories have been proposed to explain the flashover mechanism along the surface of insulator.¹ The role of surface charge in flashover phenomena has been reported,^{4,5} but the correlation between surface charge distribution and surface flashover voltage of an insulator in vacuum has not been determined.

We have investigated the correlation between surface charge distribution and surface flashover voltage of an insulator in vacuum² by measuring the charge on an alumina surface in air. However, the presence of water vapour in the air strongly influenced the charge. Thus to correctly determine the correlation, the surface charge distribution measurements and the flashover voltage measurements should both be done in vacuum (*in situ*).

In this paper, the surface charge distribution measurement system and the characteristic of charge distribution on alumina surfaces after voltage application are described. We also discuss the charge distribution of alumina surfaces after voltage application for both flashover and unflashover by applying positive and negative impulse voltage.

2. EXPERIMENTAL PROCEDURE

The samples were 99.8% pure alumina discs with a diameter of 23 mm and a thickness of 5 mm. The electrode configuration used in voltage application included a needle electrode (length: 15 mm, diameter: 3 mm, radius of curvature is 1.5 mm) and a back side electrode, both made of stainless steel (Figure 1). The creeping distance was 11.5 mm. The voltage measurements were made in an ultra-high vacuum chamber in which the pressure was maintained within the range of 1.3×10^{-8} Pa by a sputter ion pump and a Ti-getter pump. This experimental system is explained elsewhere.³ The applied impulse voltage waveform had a 64 μ s rise and 700 μ s decay. The pulses of positive and negative polarities were applied.

The change in polarity (positive to negative) was involved only the needle electrode (the backside electrode was grounded). All alumina samples were ultra-sonically cleaned for 15 minutes before being placed into the vacuum chamber.

After applying the impulse voltage, the alumina and the holder (backside electrode) were moved from the breakdown measurement chamber to the charge measurement chamber by a transfer rod in vacuum. Then the surface charge distribution on the alumina surface was measured. This system allows measurement of the surface charge on the alumina surface unaffected by the presence of water vapour. The charge measurements were made with an electrostatic probe in the form of a capacitive voltage divider connected to an electrometer (Monroe model # 145A). The system used to measure surface charge distribution is illustrated in Figure 2. The capacitance between the tip of the probe and the ground is 5 pF. This capacitor divides the input signal voltages by the probe-to-surface capacitance. The diameter of the probe tip, which governs for the probe-to-surface capacitance, was 0.076 mm. It was surrounded by a shielding electrode. The probe was shielded by the probe housing. The spacing between the alumina surface and the probe tip is maintained at 1 mm.

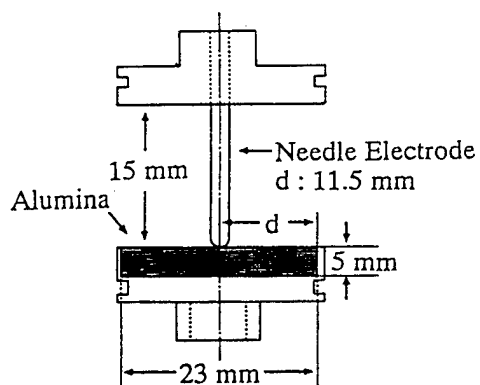


Figure 1.
Electrode configuration.

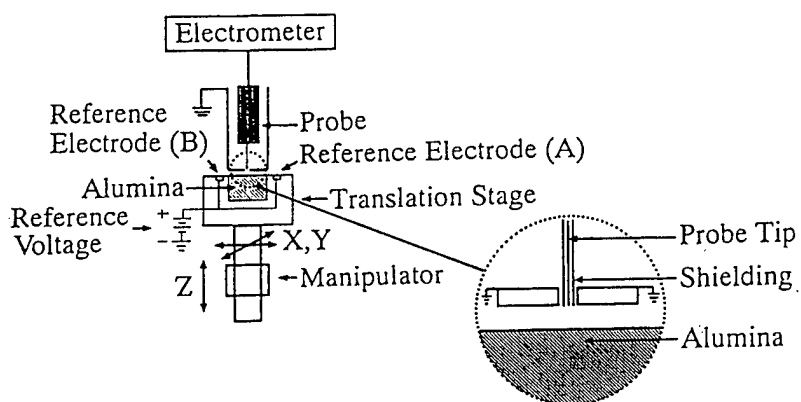


Figure 2.
Charge distribution measurement system.

The 1 mm spacing was chosen to prevent arcing to the probe from the charged alumina surface. The alumina was placed on an X-Y-Z translation stage and could be manipulated from outside the vacuum chamber without affecting the vacuum. The charge measurements started from the reference electrode on one side (point A) and progressed across the surface of the alumina along the X axis to the reference electrode on the other side (point B). The moving of alumina in the X-Y plane was driven by two stepping motors.

3. EXPERIMENTAL RESULTS AND DISCUSSION

3.1. Surface charge distribution with positive impulse voltage.

Figure 3 shows the surface charge on an alumina surface after a series of flashovers. The polarity of the applied impulse voltage was positive. The surface charges were measured after the sixth flashovers, which was at 54 kV. The surface charge distribution was measured on the center line of the alumina surface. The ordinate in the figure is surface potential, which is proportional to the charge density. The surface charge shows that the surface is charged positively by positive applied impulse voltage (flashover), and the surface potential is higher near the cathode side (backside electrode) than on the anode side (needle electrode, point C). The charge distribution pattern obtained in this experiment is similar to the one previously in air before.²

The surface potential near the cathode was nearly 600 volts, on the anode side the surface potential was 0 volts. This surface potential is higher than previous measurements.² When we measured the surface charge distribution in air, the humidity strongly influenced the charge on the alumina surfaces, but in vacuum the influence of water vapour can be neglected.

The surface potential is higher in the vicinity of the cathode than in the anode region; that is, positive charges accumulate in the cathode region. The result indicates that the alumina surface region struck by electrons emitted from the cathode

triple junction becomes positively charged, if the secondary electron emission coefficient is above unity. This positive charge accumulation will enhance the electric field at the triple junction. These processes continue until complete breakdown occurs. Other researchers⁵ have concluded that for positive polarity the charge density in the cathode region is higher than that in the anode region.⁵ The surface potential measured on the anode side is zero, we suppose that the positive charge at the anode position (needle electrode, point C) is discharged to the needle electrode.

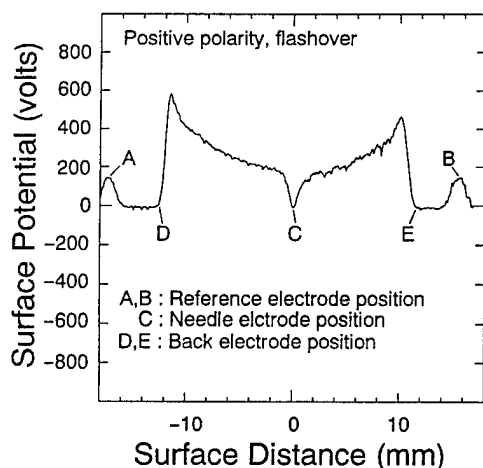


Figure 3.
Surface charge distribution
after 6 flashovers.
Positive polarity.

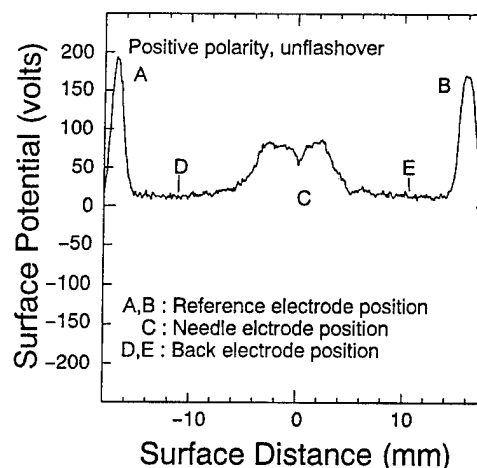


Figure 4.
Surface charge distribution.
Flashover did not occur.
Positive polarity.

Figure 4 shows the surface charge on the alumina surface after application of positive impulse (unflashover). The applied voltage was 22.5 kV, and the alumina surface was charged four times. The positive charges are distributed around the anode region. On the other hand no charges were detected at the cathode region.

The surface potential is slightly lower at the needle electrode (point C) than in the area far from the anode. The surface potential on the alumina surface was extremely lower for unflashover than for flashover.

3.2. Surface charge distribution with negative impulse voltage.

Figure 5 shows the surface charge distribution on the alumina surface after application of negative impulse voltage (flashover). The surface charges were measured after the 15th flashover, which was at 33 kV. The surface charge was measured along the center line of the alumina in the X direction. The result shows that in the vicinity of the cathode (point C) the surface has a strong negative charge, and part of the anode region is charged positively (points F to E). On the another side of the anode region, the negative charge was also detected, but this phenomenon is still unexplained.

The surface potential produced by negative trapped charge at point C was more than -800 V, while the positive potential produced by the positive charge at point F is nearly 200 V. When a negative impulse is applied to the cathode (needle electrode), electrons emitted from the cathode triple junction strike the alumina surface with high energy. The alumina surface is charged positively, if the secondary electron emission coefficient exceeds 1. As a result, the electric field at the cathode triple junction increases rapidly. That is why the flashover voltage for the negative impulse is lower than that of the positive impulse.

Figure 6 shows the surface charge on the center line of the alumina surface after the negative impulse voltage application (unflashover). The applied voltage was 12 kV. For unflashover, positive charges were not detected. The region close to the cathode had a strong negative charge, and the surface measured potential is more than -800 V. The surface potential in part of anode region was also detected, but this phenomenon is still unexplained. The result indicates that the alumina surface is not uniformly charged by a negative charge after negative impulse voltage application.

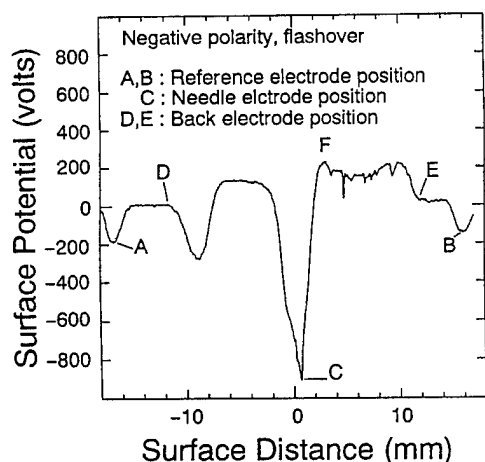


Figure 5.
Surface charge distribution
after 15 flashovers.
Negative polarity.

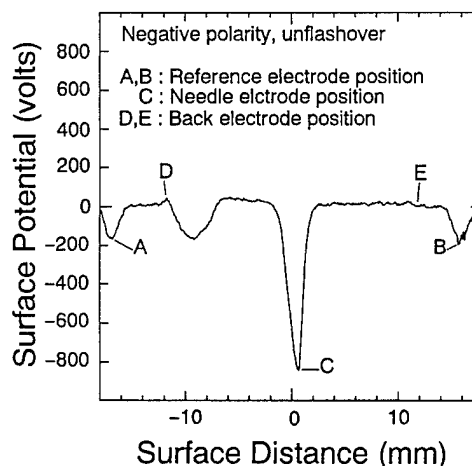


Figure 6.
Surface charge distribution.
Flashover did not occur.
Negative polarity.

4. CONCLUSIONS

1. After flashover voltage application, the surface potential for both positive and negative impulse polarity is higher than after unflashover voltage application.
2. For both positive and negative impulse voltage application (flashover), the surface potential near the cathode side is higher than on the anode side.
3. For unflashover (positive), positive charges were detected only in the area close to the anode, and the surface potential was lower than 100 V; for negative polarity, the surface close to the cathode had a very negative charge, and the surface potential was more than -800 V.

5. REFERENCES

1. H. Craig Miller, "Flashover of Insulators in Vacuum, Review of the Phenomena and Technique to Improve Holdoff Voltage," *IEEE Transactions on Electrical Insulation*, Vol. 28, No. 4, pp. 512-527, 1993.
2. Tumiran, S. Kobayashi, H. Imada, K. Kiyokawa, Y. Saito and N. Sato, "Surface Flashover Properties and Surface Charge Distribution of Alumina Insulators in Vacuum," *Proc. 8th International Symposium on High Voltage Engineering*, Vol. 1, pp. 469-472, Yokohama, 1993.
3. S. Kobayashi, Tumiran, K. Kiyokawa, Y. Saito and N. Sato, "The Influence of Surface Polishing on the Flashover Voltage of Alumina in Vacuum," (in Japanese), *Japan Vacuum Society*, pp. 171-172, Osaka, 1992.
4. J.M. Wetzer and P.A.A.F. Wouters, "The Effect of Insulator Charging on Breakdown and Conditioning," *IEEE Transaction on Electrical Insulation*, Vol. 28, No. 4, pp. 681-691, 1993.
5. N.C. Jaitly and T.S. Sudarshan, "In-Situ Insulator Surface Charge Measurement in Dielectric Bridged Vacuum Gaps Using an Electrostatic Probe," *IEEE Transaction on Electrical Insulation*, Vol. 23, No. 2, pp. 261-273, 1988.

Enhanced field emission from extremely small metallic microtips.

By

R.Z.Bakhtizin and V.G.Valeyev

1.Introduction

Electron field emission from microscopic metal cathodes subjected to high electric fields is observed at fields being much below the value predicted by the Fowler-Nordheim law for flat metallic surface. Understanding for this phenomenon is important for high field vacuum applications [1]. This enhanced field emission (EFE) is known to originate from localized microparticles on a broad area cathode [2-5]. The characteristic size L of the microtip was estimated to be of order of $10^{-7} - 10^{-8}$ cm. However, the physical mechanism of EFE is not clear up to now. The case of extremely small microtips is analysed below.

Depending on the correlation of the microtip size and length of elastic (l_i) and inelastic (l_e) electron scattering, three modes of emission may be realized: ballistic ($l \ll l_e, l_i$), diffusional ($l_i \ll l \ll l_e$), and thermal ones ($l \gg l_e, l_i$). In the latter case the principal solution may be obtained by means of hydrodynamic approximation [6]. Otherwise, in the case under consideration, the analysis should be based upon the direct solution on the kinetic equation for the electron distribution function. For metallic microcontacts such a programme in the single-particle approximation is realized in [7]. In this case the energy scattering length $\lambda_e = (l_i l_e)^{1/2} \gg l$, thus heat discharges in a region of volume λ_e^3 , exceeding considerably the region of formation of microtip tunneling resistance ($\sim l^3$). According to [3], it is this particular phenomenon that causes the microtip thermal stability at greater values of the current density.

2.Theoretical Consideration

2.1 The case of d-c field emission

Proceeding from [7], let us build a microscopic theory of the electron field emission from microtips satisfying specific conditions (Fig.1).

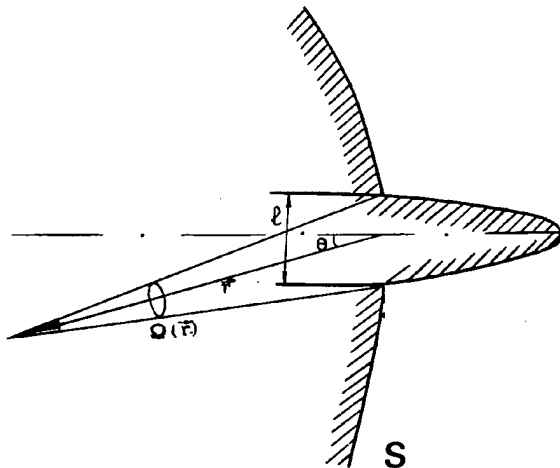


Fig 1. Microtip on the surface S of the field emitter; $\Omega(r)$ is the space angle inside the cathode, under point r the microtip base may be observed

Our consideration will be based on the Boltzmann kinetic equation for the single-electron distribution function (this is possible for microroughness with $l \gg h/p_F \approx 10^{-8}$ cm),

$$V \frac{\partial f}{\partial \mathbf{r}} + eF \frac{\partial f}{\partial p} = \hat{I}\{f\} \quad (1)$$

where $\hat{I}\{f\}$ is the electron inelastic collision integral. Is considered electron-phonon scattering a source of energy relaxations [8]. The electric field $F = -\nabla\Phi(r)$ found in (1) should be obtained by solving the Maxwell equation with the charge and current densities corresponding to the distribution function f ,

$$\rho = 2e \sum_p f(r, p) \quad (2)$$

$$j = 2e \sum_p V \cdot f(r, p) \quad (3)$$

As is known in metals the equation for the electric field F reduces to the condition of local electrical neutrality $\delta\rho = 0$,

$$\sum_p \left[f(r, p) - n_0 \left(\frac{E_p - \mu}{T} \right) \right] = 0 \quad (4)$$

Let us assume that emission occurs only from the microtip $z=0$. At a distance from a cathode surface the current density and electric field are equal to zero while the distribution is equilibrium. With these assumptions made the boundary conditions to (1) and (4) acquire the form

$$f(r, p)|_{z \rightarrow -\infty} = n_0 \left(\frac{E_p - E_F}{T} \right) \equiv f_0(E_p) \quad (5)$$

$$\Phi(r)|_{z \rightarrow -\infty} = 0 \quad (6)$$

$$f(r, p)|_{z=0, p_z < 0} = [1 - D(p)] \cdot f(r, p)|_{z=0, p_z > 0} \quad (7)$$

$$j|_s = 0 \quad (8)$$

$D(p)$ in (7) is the surface potential barrier transparency. In the approximation of zero order in the parameter $1/l_e$ one has the collision free Boltzmann equation

$$V \frac{\partial f^{(0)}}{\partial t} + eF^{(0)} \frac{\partial f^{(0)}}{\partial p} = 0 \quad (9)$$

Taking into account the boundary conditions (5) to (8), its solution will take the form

$$f^{(0)} = f_0(E_p + e\Phi^{(0)}(r)) \cdot \theta(V \notin \Omega(r)) + (1 - D) f_0(E_p + e\Phi^{(0)}(r)) \cdot \theta(V \in \Omega(r)). \quad (10)$$

This solution is exact if we ignore scattered reflection of electrons from the sides of the microtip. Provided $\delta\rho = 0$, we have for $\Phi^{(0)}$

$$\left(\frac{\partial n}{\partial \mu} \right) e\Phi^{(0)}(r) = \sum_p D(p) n_0 \left(\frac{E_p - e\Phi^{(0)}}{kT} \right) \cdot \theta(V \in \Omega(r)). \quad (11)$$

Let us confine ourselves to the WKB approximation for the barrier transparency.

A simple analysis of (11) makes it possible to establish the character of the change of $\Phi^{(0)}(r)$ in the metal at large distances from the surface (see Fig.1),

$$\Phi^{(0)}(r) \approx \Phi_0 \begin{cases} \frac{1}{\sin 2\theta} \frac{l}{r}; \frac{l}{r} \ll \max\{1, |\operatorname{tg} 2\theta|\}, \\ \left(\frac{l}{r}\right)^2; |\operatorname{tg} 2\theta| \ll \frac{l}{r} \ll 1. \end{cases}, \quad (12)$$

$\Phi^{(0)}$ is the potential within the microtip, it is constant throughout the length of the latter. It can be seen that the electric field penetrates the cathode to a depth of $\approx l \gg \lambda_{Th-F}$. The constant $\Phi^{(0)}$ is determined by the equation

$$y - \frac{1}{3\sqrt{\lambda}} e^{-C} (\lambda + y)^{3/2} M\left[2, \frac{5}{2}, -\frac{3C}{2}(\lambda + y)\right] = 0, \quad (13)$$

where $C = (0.68 \varphi^{3/2} / F_0) \theta (3.79 F_0^{1/2} / \varphi)$, $\lambda = E_{F/\varphi}$, $y = -e\Phi_0 / \varphi$, $M(x, y, z)$ is the Whittaker function F_0 the field near the microtip (in 10 V/nm), φ the electron work function (eV), θ the Fowler-Nordheim function (see [9]). It can be seen that in zeroth approximation in the parameter l_e / l shift $e\Phi_0$ of the electron chemical potential appears near the microtip, which is conditioned by carrier heating by the external electric field. the shift $\Phi^{(0)}$ manifests itself in the corresponding shift of the maximum of the electron distribution function towards the high-energy region, bringing forth an increase of the emission total current by a factor $\exp(|e\Phi_0|/d)$, where $d^{-1} = (1.025 \varphi^{3/2} / F_0) t (3.79 F_0 / \varphi)^{1/2}$ (see [9]).

EfE is now seen to be the feature of the nonequilibrium microtip state, described above.

The Nottingham energy source on the tip surface was then studied as a function of electric field. Definitely nonequilibrium increase δT_i of the Nottingham inversion temperature T_i was found to be created by the field penetration:

$$\delta T_i = \frac{e\hbar F}{(2m)^{1/2} \varphi^{3/2}} |e\Phi_0| \quad (14)$$

Selfconsistent consideration of the energy exchange processes which are decisive for the thermal stability of the tip in prebreakdown state is to be reported else where.

References

- [1] Latham R.V. 1988 IEEE transactions in Electrical Insulation 23 № 881
- [2] V.G.Pavlov, A.A. Rabinovich, and V.N. Shrednic, Zh. tekhn. Fiz. 45, 2126 (1975).
- [3] V.G.Pavlov and V.N. Shrednic, Proc. 7th Internat. Symp. Discharges and Electrical Insulation in Vacuum, Academy Sciences of the USSR, Siberian Branch, Novosibirsk 1976 (p.213).
- [4] I.D. Ventova and G.N.Furse, Zh. tekhn. Fiz. 47,1417 (1979).
- [5] Niedermann Ph. et al. 1989 Inst. Phys. Conf. Ser. № 99 Section 6 173-176
- [6] E.A.Litvinov and A.N.Starobinets, in : Emissionnaya synnototchnaya electronica, Izd. Nauka, Novosibirsk 1984 (in Russian).
- [7] I.O. Kulik, A.N. Omelyanchuk, and R.I. Shechter, Fiz. nizkikh Temp. 3,1543 (1977).
- [8] E.M.Liphshits and L.P. Pitaevsky, Fizicheskaya kinetika, Izd. Nauka, Moscow 1979 (in Russian).
- [9] R.E. Buggers, H. Kroemer, and J.M. Houston, Phys. Rev.90,515 (1953).

Author Index

- Abdullin, E. N., 239
 Abubakirov, E. B., 582
 Akbi, Mohamed, 486
 Alferov, D. F., 243, 247
 Allen, J., 522, 526
 Alterkop, B., 76
 Anders, Andre, 195
 Anders, Simone, 195
 Anisimov, S. I., 448
 Arbel, M., 518
 Arbilly, David, 90
 Arzhannikov, A. V., 392
 Ashby, D. E. T. F., 522, 526
 Asokan, T., 328
 Bakharev, I. G., 554
 Bakuto, I. A., 96
 Balakirev, V. A., 530
 Barahvostov, S. V., 53
 Barengolts, S. A., 464
 Barinov, N. U., 251
 Baskin, Lev M., 2, 483
 Batrakov, A. V., 2, 360
 Batunin, A. N., 254
 Batura, R., 378
 Bauville, Gérard, 273
 Bazhenov, G. P., 239
 Beilis, Isak, 76, 90, 140, 164
 Belenki, G. S., 251
 Ben-Chaim, D., 518
 Ben-Shalom, Amir, 90
 Blaise, G., 348
 Blyachman, L. G., 534
 Bobylev, V. B., 392
 Bochkov, V. D., 317
 Bogoslovskaya, A. B., 258
 Bolotov, Alexander V., 82
 Borisov, D. P., 86
 Boruta, Z., 219
 Botvinnik, I. E., 538
 Boussoukaya, Mustapha, 6
 Boxman, Raymond L., 76, 90, 122, 140, 164
 Branitsky, A. V., 254
 Brasil, J. P., 582
 Bratman, V. L., 506, 538
 Brown, Ian G., 195
 Buchheit, R. G., 613
 Bulan, Vladimir, 262
 Burmasov, V. S., 396
 Bushik, A. I., 96
 Chabrerie, Jean P., 491
 Chagin, A. A., 399
 Chalmers, I. D., 332
 Chaly, A. M., 105
 Chalyi, A. M., 100
 Chebotarev, A. V., 58
 Chekrygin, V. N., 14
 Cheng, Li-chun, 211, 215, 312
 Cheng, Zhongyuan, 109
 Cherepenin, Vladimir A., 569
 Chernoborodov, V. I., 619
 Chernyavsky, I. A., 542
 Chernyshev, Pavel S., 609
 Chesnokov, S. M., 239
 Chistyakov, S. P., 291
 Christiansen, Jens, 586
 Cichos, Frank, 207
 Coaker, B. M., 10
 Cohen, M., 518
 Curtoni, Aline, 6
 Damstra, Geert C., 266, 270
 Datsko, N., 412
 Deichuly, M. P., 542
 Delmas, Alain, 273
 Dem'yanovskiy, S. V., 590
 Denisov, G. G., 506
 Dickinson, Michael R., 195
 Döllinger, S., 586
 Dolgachev, G. I., 251
 Draznin, M., 518
 Eastwood, J. W., 526
 Eichenbaum, A., 518
 Emelianov, A. A., 160
 Engel, Thomas G., 277
 Erokhin, G. P., 239
 Etlicher, Bernar, 262
 Fayeulle, S., 348
 Fedyaev, Dmitry V., 561
 Filatov, A. L., 403
 Frank, K. H., 586
 Frantz, O. B., 317
 Frolov, I. N., 254
 Frontzek, F. R., 452
 Fuchs, M. I., 582
 Fujimori, M., 372
 Fursey, G. N., 469, 483
 Galstjan, Evgeni A., 340
 Gaustad, Krista L., 459
 Gavrilov, Nikolay V., 118, 409
 Gavrilov, V. N., 114
 Gellert, Bernd, 232, 501
 Gidalevich, Evgeny, 90, 122
 Ginzburg, N. S., 546, 550
 Glazanov, D. V., 469
 Glazyrin, I. V., 590
 Glinkowski, Mietek T., 153
 Görtler, Andreas, 586
 Goldsmith, Samuel, 76, 90, 122, 140, 164
 Golubev, O. L., 473

- Goncharov, A., 412
 Gordeev, E. M., 283
 Gordon, Lloyd B., 444, 459
 Gover, Avraham, 518
 Grabovsky, E. V., 254, 431
 Gradinaru, G., 336
 Greenly, John B., 613
 Greenwood, Allan, 153
 Grigoriev, Y. V., 49
 Grom, Y. V., 538
 Hantzsche, Erhard, 128, 132
 Hara, T., 354
 Hashimoto, Yasuyuki, 17
 Hatfield, Lynn L., 277
 Hawkins, K. C., 522, 526
 Hayakawa, N., 372
 Hayashi, M., 354
 He, Junjia, 312
 Heinzinger, Jan, 207
 Herleb, U., 586
 Hikita, M., 372
 Homma, M., 35
 Ignatov, A. M., 416
 Ilyakov, E. V., 573
 Inogamov, N. A., 448
 Insam, S., 586
 Ishaya, Amiel, 90
 Ivanov, Oleg M., 409
 Ivanov, R. Yu., 136
 Ivanov, S. N., 477
 Ivanov, V. P., 287
 Ivchenko, V. A., 479
 Jagnov, V. A., 287
 Jean-Francois, G., 582
 Jones, F. J., 10
 Judd, M. D., 452
 Jüttner, B., 70, 132, 170
 Kalynov, Y. K., 538
 Kamikawaji, T., 35
 Kanavets, V. I., 554
 Kandaurov, I. V., 396
 Kaneko, Eiji, 35, 203
 Kaplan, Larissa, 90
 Karlykhanov, N. G., 590
 Kassirov, G. M., 14
 Keidar, Michael, 90, 140
 Keil, Erwin, 594
 Kiselev, V. V., 239
 Kleinman, H., 518
 Kobayashi, Shinichi, 17, 364
 König, D., 452
 Kojima, Hiroyuki, 364
 Kolensky, I. L., 58
 Kolesnikov, A. V., 317
 Kondrat'ev, A. A., 590
 Korablyov, G. S., 573
 Korolev, V. D., 283
 Korolev, Yuri D., 64, 82, 317
 Korony, G., 336
 Korovin, S. D., 506
 Koshelev, V. I., 542
 Kotov, Y. A., 403
 Koval, N. N., 64, 86
 Kovalev, A. L., 483
 Kovalev, N. F., 582
 Kovalev, Yu. I., 251
 Kozlov, I. V., 146
 Kozyrev, Andrey V., 82
 Kristiansen, Magne, 277
 Kruglyakov, E. P., 396
 Krukovsky, A. Yu., 199
 Kucherenko, Yu. A., 590
 Kugel, A., 518
 Kulagin, I. S., 573
 Kulikov, J. A., 58
 Kutzner, J., 219
 Kuznetsov, D. V., 254
 Ladyzhensky, O. B., 239
 Lamerichs, Nico J. G., 203
 Latham, R. V., 10, 60
 Le Gressus, C., 348
 Lea, L. M., 526
 Lebedev, S. V., 435
 Lefort, André, 486
 Lei, J. H., 332
 Li, C. R., 344
 Li, Hongun, 203, 224
 Li, Mao-lin, 215
 Liksonov, V. I., 283
 Lindmayer, M., 170
 Lisitsyn, A. G., 254
 Litvin, A. T., 590
 Litvinov, E. A., 114, 146, 464
 Löffler, W., 70
 Logatchev, A. A., 105, 149
 Loginov, L. V., 21
 Logue, Andrew C., 444
 Loza, O. T., 557
 Ma, Zhiying, 295, 304
 MacGill, Robert A., 195
 Markov, Alexey B., 360
 Matsuura, H., 354
 Mazulin, A. V., 287
 McIntyre, D. C., 613
 Medovschikov, S. F., 254
 Medvedovsky, Alexander V., 609
 Mehr, T., 586
 Melnik, A. V., 58
 Meshkov, O. I., 396
 Mesyats, Gennady A., 25, 114, 419
 Mila, J., 378
 Mishensky, V. O., 254
 Mitin, L. A., 439
 Mościcka-Grzesiak, Hanna, 577
 Motovilov, V. A., 403
 Nagai, Yasuchika, 17
 Nechaev, V. E., 534
 Nedoseev, S. L., 254, 431

Nemirovskii, A. Z., 160
 Neron de Surgy, G., 491
 Nevrovsky, V. A., 100, 321
 Nifanov, A. S., 554
 Nikitin, M. M., 30
 Nikolaev, V. S., 392
 Nikulin, Sergey P., 118
 Novozhilova, Y. V., 546
 Ofitserov, M. M., 538
 Ohshima, Iwao, 35
 Oks, E. M., 399
 Okubo, H., 372
 Okunev, V. D., 598
 Olejnik, G. M., 254, 431
 Olson, Roy, 601
 Opydo, J., 378
 Opydo, Wladyslaw, 378
 Orlovsky, Viktor M., 423
 Osipov, Vladimir V., 423
 Otochin, A. A., 199
 Ovchinnikov, Vladimir V., 605, 619
 Ozur, Gregory E., 360
 Parizet, Marie-José, 486
 Pavlenko, A. V., 590
 Pegel, I. V., 506
 Perevodchikov, V. I., 386, 439
 Pertsev, A. A., 291, 321
 Peskov, N. Yu., 550
 Pichugin, V. E., 431
 Pikunov, Victor M., 542, 561
 Pinhasi, Y., 518
 Podrezov, A. A., 53
 Pokrovskaya-Soboleva, A. S., 21
 Polevin, S. D., 506
 Polezhaev, S. A., 469
 Popov, Sergey A., 2
 Poulussen, H. B. F., 266
 Pozdnyakov, V. I., 598
 Proskurovsky, Dmitry I., 2, 360
 Pursch, H., 170
 Puzanov, S. V., 136, 598
 Rabotkin, V. G., 317
 Ravaev, Alexander A., 340, 609
 Reher, H. J., 452
 Rohrbach, W., 501
 Rosenthal, H., 164
 Rostov, V. V., 506
 Rotshtein, Vladimir P., 360
 Roytman, A. M., 506
 Rusteberg, C., 170
 Ryjkov, V. M., 287
 Rylskaya, L. A., 291, 321
 Sadovskaya, E. Yu., 146
 Saito, Yoshio, 17, 364, 512
 Sandalov, Aleksandr N., 561
 Sasorov, P. V., 254
 Schanin, P. M., 399
 Schellekens, H., 183
 Schlaug, M., 586

Schülke, Thomas, 191
 Schulman, M. Bruce, 179
 Schwandner, A., 586
 Scotnikov, V. A., 403
 Sekisov, F. G., 14
 Sergeev, A. S., 546, 550
 Shang, W., 183
 Shapiro, A. L., 439
 Shchanin, P. M., 64, 86
 Shcheglov, M. A., 435
 Shcolnikov, E. Ja., 58
 Shemyakin, I. A., 317
 Shilimanov, S. N., 477
 Shilov, V. A., 96
 Shioiri, T., 35
 Shirochin, L. A., 483
 Shkol'nik, S. M., 105, 149
 Shkuratov, Sergei I., 39, 477
 Shkvarunets, A. G., 565
 Shmelev, D. L., 114
 Shpak, Valery G., 427
 Shrednik, Vladimir N., 473, 497
 Shunailov, Sergey A., 427
 Sidorenko, D. Yu., 530
 Sidorov, V. A., 243, 247
 Siemroth, Peter, 191
 Simon, M., 582
 Sinitsky, S. L., 392
 Siodła, Krzysztof, 368
 Skvortsov, Vladimir A., 199
 Slepkov, A. I., 554
 Smeets, Rene P. P., 203, 224, 266
 Smirnov, V. P., 254, 431
 Smorgonsky, A. V., 506
 Solodovnikov, S. G., 287
 Solomonov, Vladimir I., 423
 Soloshenko, I., 412
 Sotnikov, G. V., 530
 Starostin, A. N., 254
 Stekolnikov, Alexander F., 409
 Stinnett, R. W., 613
 Stoving, Paul, 153
 Strelkov, P. S., 557
 Sudarshan, Tangali S., 328, 336, 344
 Sugano, Takeshi, 17
 Syutkin, N. N., 479, 619
 Takeuchi, Kiyomatsu, 17
 Talantsev, E. F., 619
 Tarakanov, V. P., 416
 Tarasov, A. V., 392
 Tatarinova, Nina V., 45, 49
 Thompson, Michael O., 613
 Timakova, M. S., 590
 Tkach, Y. V., 530
 Tkotz, R., 586
 Treheux, D., 348
 Trofimov, S. V., 254
 Tskhai, V. N., 439
 Uimanov, I. V., 464

Ulyanov, D. K., 565
 Ulyanov, K. N., 258
 Ushakov, A. G., 251
 Utjugov, E. G., 254
 Vaisburd, David, 623
 Vallayer, B., 348
 Vershinin, Y. N., 53
 Vlasov, Alexander N., 569
 Vogel, Nadja, 207
 Volkov, G. S., 254
 Voropaev, S. G., 435
 Vozdvijenskii, V. A., 243, 247, 287
 Wang, Chengyu, 295, 301, 304
 Wang, Hao, 211, 215
 Wang, Jimei, 187, 295, 301, 304, 308
 Wang, Yi, 308
 Weber, C., 70
 Wesfreid, J. E., 491
 Wester, S. L., 277
 Wetzer, J. M., 382
 Witke, Thomas, 191
 Witman, S., 518
 Wouters, P. A., 382
 Wu, Jian-wen, 308
 Xu, N. S., 10, 60
 Yakover, Y., 518
 Yalandin, Michael I., 427
 Yamamoto, O., 354
 Yamamoto, Yoshiki, 17
 Yang, B., 332
 Yang, Hong-lin, 211, 215
 Yang, Lei, 211
 Yashnov, Y. M., 136, 598
 Yuan, Shun, 187, 308
 Yuasa, S., 372
 Yukimura, K., 354
 Zachepilo, P. S., 96
 Zaitsev, N. I., 573
 Zajivikhin, Vladimir V., 262, 431
 Zakatov, L. P., 251
 Zakharov, S. V., 254
 Załucki, Z., 219
 Zavjalov, M. A., 386, 439
 Zaytsev, N. I., 582
 Zazhivikhin, V. V., 283
 Zeitoun-Fakiris, Anne, 6
 Zhang, X., 270
 Zhitomirsky, Vladimir, 90
 Ziegenhagen, G., 70
 Ziomek, Waldemar, 577
 Zou, Jiyan, 109, 211, 215, 312
 Zoubov, A. D., 590
 Zurin, M. V., 254